Talanta

The International Journal of Pure and Applied Analytical Chemistry

Aims & Scope

Talanta provides a forum for the publication of original research papers, preliminary communications, and reviews in all branches of pure and applied analytical chemistry. Analytical data should be submitted only if they are clearly related to new analytical measurements. Original research papers on fundamental studies and novel sensor and instrumentation development are especially encouraged. Novel or improved applications in areas such as clinical chemistry, environmental analysis, geochemistry, and materials science and engineering are welcome. Methods should be validated by comparison with a standard method or analysis of a certified reference material, and relevant literature should be cited. Since classical spectrophotometric measurements and applications, solvent extraction, titrimetry, chemometrics, etc. are well established, studies in such areas should demonstrate a unique and substantial advantage over presently known systems. New reagents or systems should demonstrate clear advantage, and their presentation should be comprehensive rather than generating a series of similar papers for several analytes. Modifications of reagents should demonstrate significant improvements. Solvent extraction methods in particular, but others as well, should focus on the use of non-hazardous material substitutes and the minimization of waste generation. But obvious application of known chemistries or methods to established techniques are discouraged. Application of classical analytical approaches to relatively sample matrices having no major interferences, such as pharmaceutical preparations or reconstituted samples, are discouraged unless considerable improvements over other methods in the literature are demonstrated. Papers dealing with analytical data such as stability constants, pK_a values, etc. should be published in more specific journals, unless novel analytical methodology is demonstrated, or important analytical data are provided which could be useful in the development of analytical procedures.

Flow injection wetting-film extraction system for flame atomic absorption spectrometric determination of cadmium in environmental waters

Ibrahim S.I. Adam, Aristidis N. Anthemidis[*]

Laboratory of Analytical Chemistry, Department of Chemistry, Aristotle University, Thessaloniki 54124, Greece

ABSTRACT

A newly simple flow injection wetting-film extraction system coupled to flame atomic absorption spectrometry (FAAS) has been developed for trace amount of cadmium determination. The sample was mixed on-line with sodium diethyl dithiocarbamate and the produced non-charged Cd(II)–diethyl dithiocarbamate (DDTC) chelate complex was extracted on the thin film of diisobutyl ketone (DIBK) on the inner wall of the PTFE extraction coil. The wetting-film with the extracted analyte was then eluted by a segment of the cover solvent, and transported directly to the FAAS for evaluation. All the important chemical and flow parameters were optimized. Under the optimized conditions an enhancement factor of 35, a sample frequency of 22 h^{-1} and a detection limit of $c_L = 0.7\,\mu g\,l^{-1}$ Cd(II) were obtained for 60 s preconcentration time. The calibration curve was linear over the concentration range 1.5–45.0 $\mu g\,l^{-1}$ Cd(II) and the relative standard deviation, R.S.D. ($n = 10$) was 3.9%, at 10.0 $\mu g\,l^{-1}$ concentration level. The developed method was successfully applied to cadmium determination in a variety of environmental water samples as well as waste-water sample.

© 2008 Elsevier B.V. All rights reserved.

1. Introduction

The environment is continuously contaminated with large amount of toxic elements as consequence of human activities. Exposure to these toxic pollutants imposes not only risks to human health, but also potentially unacceptable ecological risks to plants, animals and microorganisms [1]. As the result, years of effort have been devoted to the development of more effective, fast, precise and accurate approaches for the determination of different elements like cadmium, in various environmental matrices using numerous analytical methods. The adverse effects of cadmium are the result not only of its high toxicity even at trace concentrations, but also of its bioaccumulation processes along the food chain and into vital human organs like kidney.

Flame atomic absorption spectrometry (FAAS) is among the most widely used techniques for determination of heavy metals, however, its sensitivity is usually insufficient for monitoring the low level concentrations of these metals in environmental samples. In addition, the interfering effect of the matrix components of complicated samples like sea-water, many times is a serious problem in the determinations by atomic spectrometry (AS). Consequently, a preconcentration and/or separation process is usually required prior the measurement. Although, liquid–liquid extraction (LLE) has proven to be a reliable and efficient separation and/or preconcentration technique for metal determination, it is time and reagent consuming, as well as tedious and laborious procedure and hence, potentially prone to contamination of sample and environment, when it is performed in batch (off-line) mode. However, the marriage of LLE with flow injection (FI) [2,3] offers a great ease to the analysis eliminating to a great extent, many of the drawbacks encountered in the batch mode.

In classical FI–LLE systems, the on-line extraction process is accomplished by three major operations: (i) segmentation, (ii) extraction and (iii) separation [4]. The extraction efficiency into the narrow tube of the extraction coil is usually high and it is completed in a few seconds. These parameters are attributed to the formation of a very thin film of one phase on the inner wall of the extraction coil, surrounding the segments of the other phase. The material of the coil (hydrophobic or hydrophilic) defines which phase will form the wetting-film according to the polarity of the solvent [5].

However, FI–LLE has not been widely accepted for routine analysis, due to the critical instrumentations, segmentor and phase separator, which affect significantly the reproducibility, stability and robustness of the method. Their design construction and operation performance have been studied in detail [6–8]. On the other hand, several efforts have been made to eliminate the need for segmentation and phase separation.

* Corresponding author. Tel.: +30 2310997826; fax: +30 2310997719.
E-mail address: anthemid@chem.auth.gr (A.N. Anthemidis).

A new concept called wetting-film extraction (WFE) has been proposed for sequential injection (SI) systems, without the need of segmentor and phase separator [9]. Wetting-film extraction is based on the formation of a thin film coating on the inner wall of the extraction coil, with major aim on sample preconcentration and separation. When an organic solvent is passed through a hydrophobic tube such as PTFE, a stationary thin film of the solvent is formed on the inner wall of the tube. When an aqueous solution with extractable analyte complex is aspirated into the tube extraction/preconcentration takes place at the interface of the organic thin film with the aqueous phase. After that, the preconcentrated analyte can be eluted, with a small plug of suitable solvent or back-extraction solution. The theoretical aspects and fundamentals of the WFE technique have been well presented by Miró et al. in a recent comprehensive review [10]. Christian and co-workers, developed a SI-WFE system for speciation of Cr(VI)/Cr(III) [11] and V(IV)/V(V) [12] and also for trace Mo(VI) determination in natural water samples [13]. In this case the consumption of the organic solvent was reduced tenth time than in the conventional automated FI-LLE. Paterson et al. [14] demonstrated that WFE is also suitable for sample preparation prior to high-pressure liquid chromatography (HPLC). Miró et al. [15] presented a flow-reversal SI-WFE set-up for radionuclide ^{90}Sr (b-emitter) determination in environmental samples and daily products. van Staden and Taljaard [16] determined seven heavy metals as dithizone complexes in environmental and biological samples. Cai et al. [17] established a microflow WFE for determination butyl rhodamine B and Chen et al. [18] coupled WFE in a FI system for copper determination by FAAS.

Diethyl dithiocarbamate (DDTC) form strong and mostly neutral complexes with a large number of heavy metals such as Cd(II), Cu(II), Pb(II), Ni(II), Zn(II) and Fe(III) [19–21], which can be separated from large excess of alkali and alkaline earth elements. In addition the complex formation is sufficiently rapid. These attributes makes the above chelating reagent ideal for the on-line preconcentration procedures of heavy metals in natural waters sample as well as in sea-water samples.

In the present work wetting-film extraction is exploited as versatile automatic approach for the implementation of liquid–liquid extraction in a simple low cost manifold for on-line metal preconcentration and determination by flame atomic absorption spectrometry. To the best of our knowledge, there is only one paper in the literature, dealing with WFE and FAAS [18], which presents copper determination and suffers from the complexity of the manifold and the procedure. The proposed method was evaluated for determination of Cd in natural water, using diisobutyl ketone (DIBK) as coating solvent and sodium diethyl dithiocarbamate as chelating reagent.

2. Experimental

2.1. Apparatus

A PerkinElmer, Norwalk, Connecticut, U.S.A. (http://las.perkinelmer.com) model 5100 PC flame atomic absorption spectrometer with deuterium arc background corrector was exploited as detection system. Cadmium electrodeless discharge lamp (EDL) was used as light sources operated at 5 W. The wavelength was set at 228.8 nm resonance line, while the slit was fixed at 0.7 nm. A time-constant of 0.2 s was used for peak height evaluation. The flame conditions were slightly leaner than those recommended by the manufacturer, in order to compensate the effect of DIBK, which serves as additional fuel during the measuring step. The air and acetylene flow rate was set at 10.0 and 0.9 l min^{-1}, respectively.
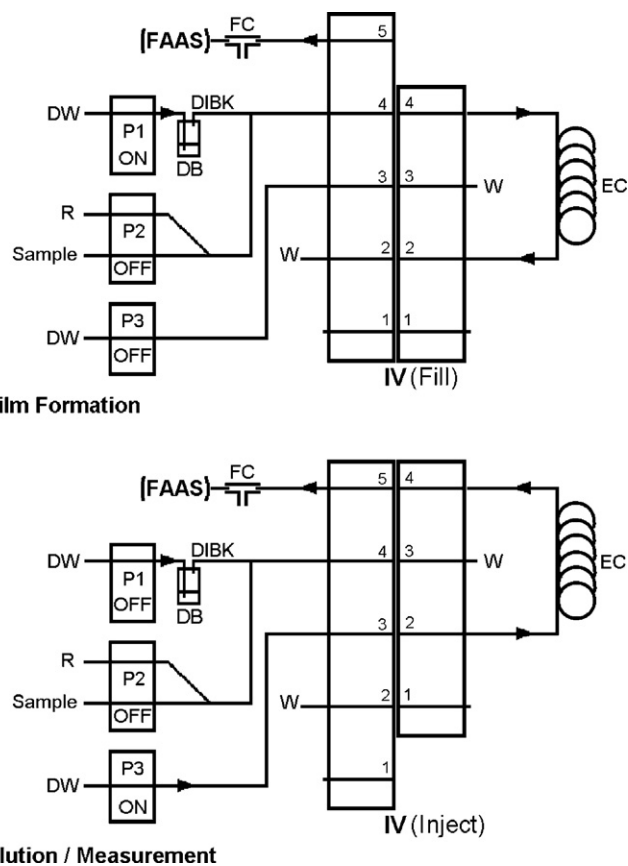
Fig. 1. Schematic diagram of the FI–WFE manifold and the two operation sequences, for metal determination. R, 0.2% (m/v) DDTC; P1, P2, P3, peristaltic pumps; IV, injection valve; DB, displacement bottle; EC, extraction coil; FC, flow compensation adapter; DW, distilled water; W, waste.

In that case the nebulizer's free uptake rate was 5.5 ml min^{-1}. A flow spoiler was employed into the spray chamber for better nebulization conditions. The spectrometer was set to work in the FI-FAAS mode and peak height was used for signal evaluation. The electrothermal atomization mode of the above PerkinElmer atomic absorption spectrometer equipped with zeeman background corrector was used as a standardized method for cadmium determination in the water samples.

A PerkinElmer Norwalk, Connecticut, U.S.A. model FIAS-400 flow injection analysis system was coupled to the flame atomic absorption spectrometer for automatic processing of the method and operated in normal mode. The whole system was controlled by a personal computer and the AA Lab. Benchtop version 7.2 application program. The FIAS-400 system, which is shown schematically in Fig. 1, consisted of three peristaltic pumps P1, P2, P3, a 5-port 2-position (Fill/Inject) injection valve and it was connected to the spectrometer's nebulizer using a short PTFE capillary 20.0 cm length, 0.5 mm i.d., in order to minimize the eluent dispersion. A flow compensation (FC) unit was used just before the nebulizer inlet, in order to compensate the lack of nebulizer free uptake flow rate as described elsewhere [22]. Peristaltic pump tubing of "Tygon" type was adopted to deliver the aqueous solutions and a displacement bottle (Tecator, Hoganas, Sweden http://www.foss.dk) was used to deliver the organic solvent, diisobutyl ketone. The extraction coils of 0.75 mm i.d. in different lengths in the range 150–400 cm were coiled on 30 mm i.d. cylinder. All other conduits used for various connections were of 0.5 mm i.d. PTFE tubing.

2.2. Reagents and samples

All chemicals were of analytical reagent grade and were provided by Merck (Darmstadt, Germany, http://www.merck.de). Ultra-pure quality water was used throughout which was produced by a Milli-Q system (Millipore, Bedford. USA, http://www.millipore.com). Working standard solutions of Cd(II) were prepared by appropriate stepwise dilution of a 1000 mg l^{-1} stock standard solution (Titrisol, Merck) to the required μg l^{-1} levels. The acidity of the standards was adjusted with dilute HNO$_3$. Sodium diethyl dithiocarbamate (DDTC) (Aldrich) solution in water (0.2%, m/v) was prepared fresh daily. Diisobutyl ketone was used without any purification.

Natural water samples (tap, river, and costal sea-water) were collected from Northern Greece, filtered through 0.45 μm membrane filters, acidified to 0.1 mol l^{-1} HNO$_3$ and stored at 4 °C in acid-cleaned polyethylene bottles, in order to determine the "dissolved metal" fraction.

2.3. Procedure

The operation sequence of the on-line wetting film extraction method for metal determination with FAAS runs through three steps and is summarized in Table 1. In step 1 (Fig. 1, Film formation), the injection valve, IV is in the "Fill, F" position and pump P1 feeds DIBK into the extraction coil (EC) in order to remove the possible residuals of the previous cycle and for thin film formation of organic solvent into the PTFE tube. In the mean time the nebulizer of the FAAS aspirates air through the flow compensation adapter (FC). During step 2, pump P2 delivers sample solution mixed with complexing agent, 0.2% (m/v) DDTC through the EC for 60 s. The on-line formed metal–DDTC complex was extracted in the thin film of DIBK into the EC. In step3 (Fig. 1, Elution/Measurement), IV is turned in the "Inject, I" position. Deionized water (DW) is propelled by pump P3 through the EC in reverse direction than that of the sample loading, delivering the small amount of the coating solvent (DIBK), which has accumulated at the end of the EC, through the extraction coil to the nebulizer, executing the elution procedure. The baseline was stable. Five replicate measurements per sample were made in all instances and direct calibration for quantification.

3. Result and discussion

3.1. Development of the FI wetting film extraction system

Two aspects should be considered developing an effective FI–WFE system. The choice of the organic solvent, that could form a thin film on the inner wall of the hydrophobic PTFE tubing and the kinetic properties of the metal complex for the extraction processes, which are defined by the partition coefficient of the analyte between the organic and aqueous phase [9]. The coating solvent should form a thick and stable wetting film with the lower solubility in aqueous phase. The larger the ratio of viscosity and interfacial tension the thicker is the wetting film and the larger are the volume of organic solvent and the extraction capacity. On the other hand, the capacity of the film for the analyte is competitive with the ease with which the film can be eluted. Thick films have higher capacity but are more difficult to elute. Hence, the film should be thick enough that it does not break up during sample loading and also it must be possible the quantitatively elution of the film [11].

The most appropriate organic solvents compatible with FAAS (good burning and atomization characteristics), which also have excellent liquid–liquid extraction properties are methyl isobutyl ketone (MIBK) and diisobutyl ketone (DIBK). Both of them were examined as coating solvents. The performance of MIBK wetting-film was unstable and it was easily destroyed by the fluctuation of the flow during the sequences of the method, resulting in losses of analyte. The above-mentioned problems were probably due to the high solubility of MIBK in water (2%, v/v at 20 °C). On the other hand, DIBK possessing good combustion properties, high boiling point and very low miscibility with water (0.05%, v/v at 20 °C), is an excellent alternative to MIBK for FAAS. The main property, which has encouraged the wide use of MIBK in FAAS methods, is the greater sensitivity compared with other solvents. However, it has been shown that the loss of sensitivity incurred by the use of DIBK is only about 20% on average [23]. It was found that DIBK could form stable wetting-film on the PTFE tubing, and the film offered higher extraction efficiency for the studied metal. Hence, DIBK was chosen as a coating solvent for the proposed method. The DIBK loading flow rate and the loading time were defined from the volume of the extraction coil (1.1 ml, for 2.5 m length/0.75 mm i.d.). During step 1 (Table 1) the extraction coil should be washed from residents of the previous cycle and filled with the cover solvent. Thus, DIBK loading flow rate and the loading time were fixed at 4.8 ml min^{-1} and 30 s, respectively, for accurate film formation.

In the early stages of the present study, a six port two position injection valve with a variable sampling loop (50–300 μl) was utilised in cooperation with the FIAS-400 system, in order to introduce accurate volumes of the eluent, as segment in distilled water carrier stream. The elution procedure was performed in opposite direction to that of the sample loading, in order to reduce the analyte dispersion. With this manifold and using a defined volume of MIBK or other organic solvent as eluent, a double peak of absorbance was observed. The first peak was higher and produced from a small amount of the coating solvent, which has been pushed, scrunched and accumulated at the end of the tubing of the extraction coil during the extraction step. On the other hand the second peak, which was significant lower, was owed in the eluent segment.

In order to solve the above problem the manifold was modified, deducting the injection valve and maintaining the distilled water stream, as it is shown in Fig. 1. After this modification the elution of the analyte is performed solely by the accumulated segment of the coating solvent. This segment was efficiently delivered through the extraction coil by the water stream during the third step (Fig. 1, Elution/Measurement). The recorded peak with this manifold is equivalent with the first of the two peaks observed with previous manifold. In addition it is proportional with the analyte concentration of the sample.

The extraction capacity of the wetting-film depends on the volume of the organic film, which adhered on the inner surface of the PTFE tubing and thus on the length of the extraction coil. Moreover, the volume of the wetting-film is proportional to the inner diameter of the extraction coil [9]. The length of the extraction coil was studied in the range 150–400 cm with 0.75 mm inner diameter for a fixed sample loading time and sample flow rate at 60 s and 2.2 ml min^{-1}, respectively. The absorbance levelled off at 250 cm length, probably due to increased back pressure at higher lengths, which would lead to lower loading of sample. As optimum extraction coil for the proposed method was selected the PTFE tubing 2.5 m in length and 0.75 mm i.d.

3.2. Factors affecting the on-line wetting-film extraction

Sample acidity is a critical variable for the metal–chelate complex formation and also for the wetting-film extraction efficiency. The effect of pH on the absorbance of 20.0 μg l^{-1} Cd(II) was studied in the range from 0.4 to 3.5 by adjusting it with dilute nitric acid or ammonia. As it is shown in Fig. 2, the maximum absorbance was recorded in the pH range 1.0–1.5. This fact enables the use of the

Table 1
Operation sequences of the FI–WFE method for Cd(II) determination by FAAS

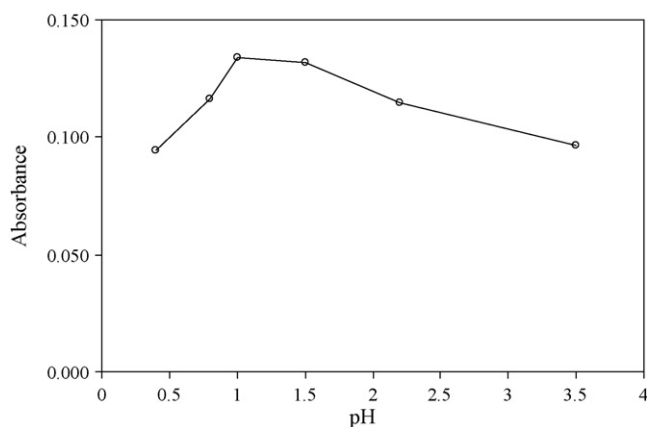| Step	IV	Pumps			Delivered medium	Flow rate (ml min^{-1})	Time (s)	Operation
		P1	P2	P3				
1	F	ON	OFF	OFF	DIBK	4.8	30	Extraction coil washing, Film formation
2	F	OFF	ON	OFF	Sample	2.2	60	Extraction
					DDTC	0.7		
3	I	OFF	OFF	ON	Water	1.4	60	Elution
4	I	OFF	OFF	ON	Water	1.4	10	Absorption measuring

Fig. 2. Effect of sample pH on the peak height absorbance of 20.0 μg l^{-1} Cd(II). All other parameters as in Table 1.
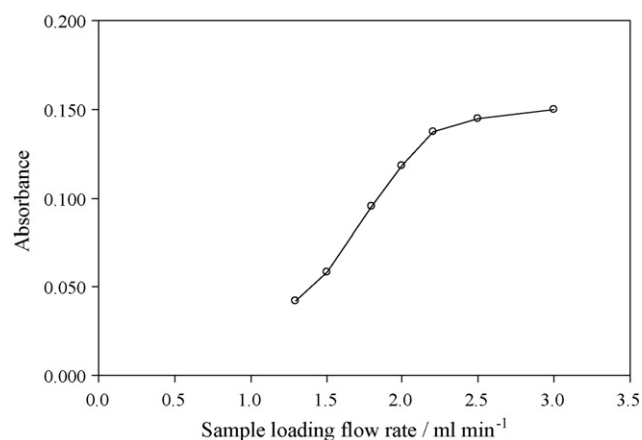

Fig. 3. Effect of sample loading flow rate on the absorbance of 20.0 μg l^{-1} Cd(II). All other parameters as in Table 1.

method directly in many types of aqueous samples after common acid preservation, without any laborious precise pH adjustment. Therefore, the sample acidity was adjusted to pH 1.0 for further experiments.

Three chelate reagents, DDTC, ammonium pyrrolidine dithiocarbamate (APDC) and ammonium diethyldithiophosphate (DDPA) were investigated for the effective extraction of cadmium via wetting-film extraction procedure. It was found that all reagents could form extractable complexes in acidic sample solution with cadmium, but DDTC gave the highest absorbance. Thus, the DDTC was chosen for the proposed method. The effect of DDTC concentration was studied in the range of 0.01–1.0% (m/v) at fixed flow rate 0.7 ml min^{-1}. The maximum signal was maintained in the DDTC concentration range 0.1–0.5% (m/v). Hence, aqueous solution of 0.2% (m/v) DDTC was chosen for subsequent studies.

Addition of an ionic substance to the sample might also affect the extraction process as it increases the ionic strength of the aqueous phase. Depending on the solubility of the analytes, extraction is usually enhanced with an increase in ionic strength as the solubility of hydrophobic species such as the Cd–DDTC complex in the aqueous phase is decreased. In order to study this effect, NaCl was added to the sample solution in the concentration range 0–2.0 mol l^{-1}, before the wetting-film extraction procedure. No significant variation on Cd(II) extraction observed by increasing the content of NaCl. Consequently, no addition of NaCl to the sample solution was adopted.

The effect of sample loading flow rate on the absorbance (Fig. 3) was investigated in the range 1.3–3.0 ml min^{-1} at fixed 0.7 ml min^{-1} DDTC flow rate. The obtained results revealed that the absorbance of 20.0 μg l^{-1} Cd(II) was increasing almost linearly, by increasing the sample flow rate up to 2.2 ml min^{-1} and levelled off for higher flow rates, because the contact time of aqueous phase with wetting-film solvent was not enough for effective extraction. A sample flow rate of 2.2 ml min^{-1} was adopted as optimum.

The influence of preconcentration time (sample loading time) was studied in the range from 30 to 120 s, at a sample flow rate of 2.2 ml min^{-1}. As it is shown in Fig. 4, it was found that the absorbance increased as the sample loading time increased up to 60 s. For longer loading time, the analytical signal decreases due to a partial missing of the wetting-film. This fact allows the use of preconcentration time up to 60 s, which was chosen as optimum for the proposed method.

The effect of the elution flow rate on the absorbance was studied in the range 1.0–1.8 ml min^{-1}. Optimum sensitivity with sharp peak was achieved at elution flow rate 1.4 ml min^{-1}. For lower values the recorded peak appeared a broadening, due to higher analyte dispersion, into the extraction coil. At flow rate higher than 1.4 ml min^{-1} the absorbance was decreased, probably because the much higher linear velocity of the organic segment do not allow the
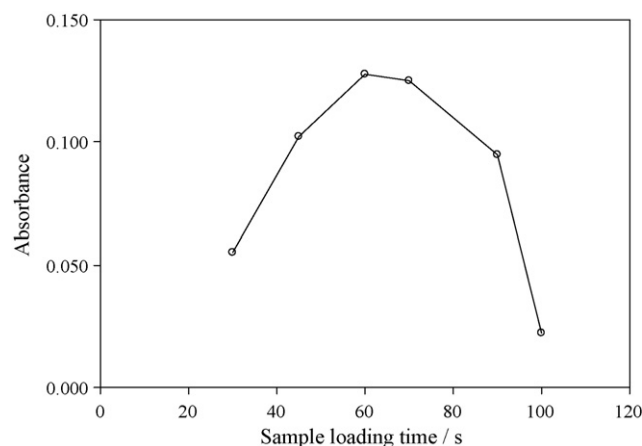

Fig. 4. Effect of the sample loading time on the absorbance of 20.0 μg l^{-1} Cd(II). All other parameters as in Table 1.

Table 2
Analytical performance characteristics of the proposed FI–WFE–FAAS method for Cd(II) determination

Preconcentration time (s)	60
Sampling frequency (h^{-1})	22
Sample consumption (ml)	2.2
Enhancement factor	35
Linear range ($\mu g\,l^{-1}$)	1.5–45.0
Regression equation ($n = 6$, $\mu g\,l^{-1}$)	$A = 0.0012 + 0.0062[Cd(II)]$
Correlation coefficient, r	0.9956
RSD (%), $n = 10$, $10.0\,\mu g\,l^{-1}$	3.9
Detection limit, c_L ($\mu g\,l^{-1}$)	0.7

Table 3
Analytical results for the determination of cadmium in water samples (determination in "dissolved metal" fraction) by the proposed method and ETAAS

Sample	Added ($\mu g\,l^{-1}$)	Found[a] ($\mu g\,l^{-1}$)	Recovery[b] (%)	ETAAS[c] ($\mu g\,l^{-1}$)
Tap-water	–	$<c_L$		$<c_L$
	5.0	4.8 ± 0.5	96	4.9 ± 0.6
	10.0	9.6 ± 0.4	96	9.5 ± 0.8
River-water	–	$<c_L$		$<c_L$
	5.0	4.7 ± 0.6	94	5.1 ± 0.6
	10.0	10 ± 1	97	9.8 ± 0.9
Sea-water	–	1.1 ± 0.1[d]		1.2 ± 0.2
	5.0	6.2 ± 0.6	102	6.0 ± 0.7
	10.0	10.8 ± 0.8	97	11 ± 1
Waste-water	–	4.1 ± 0.4		4.0 ± 0.5
	5.0	8.9 ± 0.8	96	9 ± 1
	10.0	14 ± 1	95	14 ± 2

[a] Mean value ± standard deviation based on three replicate determinations.
[b] Recovery obtained from spiked samples.
[c] Direct injection of 35 μl of sample.
[d] The resulting concentration is between LOD and LOQ and it is reported only as estimation.

establishment of mass transfer from the wetting-film towards the eluent.

3.3. Analytical performance characteristics

Under the optimum conditions described above, the analytical performance characteristics of the proposed FI–WFE–FAAS method for Cd(II) determination are summarized in Table 2. For a 60 s preconcentration time (corresponding to 2.2 ml of sample solution being loaded) the sampling frequency was 22 h^{-1} and the enhancement factor was 35 (calculated as the ratio of the slopes of calibration curves with and without preconcentration). The limit of detection (LOD) calculated by 3s criterion and found to be $c_L = 0.7\,\mu g\,l^{-1}$, while the limit of quantitation (LOQ) calculated by 10s criterion and was $c_Q = 1.5\,\mu g\,l^{-1}$. The precision, as relative standard deviation (RSD), was $s_r = 3.9\%$, calculated from 10 replicate measurements at $10.0\,\mu g\,l^{-1}$ concentration level of Cd(II).

The proposed method was applied also to the analysis of tap-water, river- and sea-water samples as well as waste-water and validated by spiking the analyzed samples with known amounts of Cd(II). The accuracy of the proposed method was evaluated by comparing the obtained results with those obtained by the use of electrothermal atomic absorption spectrometry (ETAAS). The obtained results are presented in Table 3, and the recoveries were varied in the range 94–102%.

3.4. Investigation of the potential interferences

The effect of potential interferences encountered in aqueous samples on the recovery of $10.0\,\mu g\,l^{-1}$ of Cd(II) was examined with individual interferent ions added in the standard solution. Taking as criterion for interference every deviation of the recovery higher than ±5%, the obtained results showed that Fe(III), Mn(II) and Zn(II) are tolerated up to $10\,mg\,l^{-1}$, Pb(II), Co(II), and Ni(II) are tolerated up to $5\,mg\,l^{-1}$, while Cr(VI), Cu(II), Hg(II) is tolerated up to $0.5\,mg\,l^{-1}$.

4. Conclusions

The present work testifies the applicability of FI wetting-film extraction system coupled with FAAS for cadmium determination in aqueous samples. The proposed method is simple with reasonable sample throughput. A significant advantage has been arisen from the elimination of the need for segmentation and phase separation, simplifying thus the manifold as well as reducing the reagents and sample. The use of DIBK as wetting-film coating solvent is advantageous providing good extraction efficiency properties. Enhancement factor equivalent with on-line solid phase extraction methods can be achieved. An interesting feature of the proposed system is the fact that the elution can be accomplished only with water without the need for extra organic solvent segment. Finally, it was indicated that samples with difficult matrices like sea-water or waste-water could be analyzed successfully by the proposed method.

References

[1] M. Miro, J.M. Estela, V. Cerda, Talanta 63 (2004) 201.
[2] Z.-L. Fang (Ed.), Flow Injection Atomic Absorption Spectrometry, John Wiley & Sons, Chichester, UK, 1995.
[3] M. Miró, E.H. Hansen, On-line Sample Processing Methods in Flow Analysis, Wiley-VCH, Weinhem, in press.
[4] V. Kuban, Crit. Rev. Anal. Chem. 22 (1991) 477.
[5] C.A. Lucy, K.K.-C. Yeung, Anal. Chem. 66 (1994) 2220.
[6] G.-H. Tao, Z.-L. Fang, Spectrochim. Acta B 50 (1995) 1747.
[7] J.-H. Wang, E.H. Hansen, Anal. Chim. Acta 456 (2002) 283.
[8] A.N. Anthemidis, G.A. Zachariadis, C.G. Farastelis, J.A. Stratis, Talanta 62 (2004) 437.
[9] Y. Luo, R. Al-Othman, J. Ruzicka, G.D. Christian, Analyst 121 (1996) 601.
[10] M. Miró, J.M. Estela, V. Cerda, Curr. Anal. Chem. 1 (2005) 329.
[11] Y. Luo, S. Nakano, D.A. Holman, J. Ruzicka, G.D. Christian, Talanta 44 (1997) 1563.
[12] S. Nakano, Y. Luo, D.A. Holman, J. Ruzicka, G.D. Christian, J. Flow Injection Anal. 13 (1996) 148.
[13] S. Nakano, Y. Luo, D. Holman, J. Ruzicka, G.D. Christian, Microchem. J. 55 (1997) 392.
[14] K.L. Paterson, B.K. Logan, G.D. Christian, J. Ruzicka, Anal. Chim. Acta 337 (1997) 99.
[15] M. Miró, E. Gomez, J.M. Estela, M. Casas, V. Cerda, Anal. Chem. 74 (2002) 826.
[16] J.F. van Staden, R.E. Taljaard, Talanta 64 (2004) 1203.
[17] Z. Cai, H. Chen, B. Chen, C. Huang, Talanta 68 (2006) 895.
[18] H. Chen, J. Liu, X. Mao, Anal. Chim. Acta 370 (1998) 151.
[19] M. Sperling, X. Yin, B. Welz, J. Anal. At. Spectrom. 6 (1991) 295.
[20] Z.-L. Fang, T. Guo, B. Welz, Talanta 38 (1991) 613.
[21] R. Ma, W. Van Mol, F. Adams, Anal. Chim. Acta 285 (1994) 33.
[22] A.N. Anthemidis, S.-J.V. Koussoroplis, Talanta 71 (2007) 1728.
[23] K.M. Bone, W.D. Hibbert, Anal. Chim. Acta 107 (1979) 219.

Simultaneous determination of Co²⁺, Ni²⁺, Cu²⁺ and Zn²⁺ ions in foodstuffs and vegetables with a new Schiff base using artificial neural networks

Abbas Afkhami [a,*], Maryam Abbasi-Tarighat [a], Hamid Khanmohammadi [b]

[a] Faculty of Chemistry, Bu-Ali Sina University, Hamadan 65174, Iran
[b] Department of Chemistry, Faculty of Sciences, Arak University, Arak, Iran

ARTICLE INFO

ABSTRACT

New complexes of Co^{2+}, Ni^{2+}, Cu^{2+} and Zn^{2+} with a recently synthesized Schiff base derived from 3,6-bis((aminoethyl)thio)pyridazine were applied for their simultaneous determination with artificial neural networks. The analytical data show the ratio of metal to ligand in all metal complexes is 1:1. The absorption spectra were evaluated with respect to Schiff base concentration, pH and time of the color formation reactions. It was found that at pH 10.0 and 60 min after mixing, the complexation reactions are completed and the colored complexes exhibited absorption bands in the wavelength range 300–500 nm. Spectral data was reduced using principal component analysis and subjected to artificial neural networks. The data obtained from synthetic mixtures of four metal ions were processed by principal component-feed forward neural networks (PCFFNNs) and principal component-radial basis function networks (PCRBFNs). Performances of the proposed methods were tested with regard to root mean square errors of prediction (RMSEP%), using synthetic solutions. Under the working conditions, the proposed methods were successfully applied to simultaneous determination of Co^{2+}, Ni^{2+}, Cu^{2+} and Zn^{2+} in different vegetable, foodstuff and pharmaceutical product samples.

© 2008 Elsevier B.V. All rights reserved.

1. Introduction

Metal ions play significant roles in biological processes, such as the functions of enzymes, the transport of oxygen, and the health of teeth and bones. They play important role in diseases like transmissible spongiform encephalopathies (Creutzfeldt-Jakob and related diseases), Alzheimer's, Parkinson's, Huntington's, Wilson's and Menkes' diseases, as well as in familial amyotrophic lateral sclerosis and others [1,2].

Zinc and copper are essential trace elements for human nutrition and health [3–6]. When people absorb too little zinc, they can experience a loss of appetite, decreased sense of taste and smell, slow wound healing and skin sores. Zinc-shortages can even cause birth defects [7,8]. The deficiency of zinc and copper marked by severe growth retardation and arrested sexual development [3]. Copper deficiency is rare, but can be caused by excess zinc from supplementation. Growth retardation, altered immune response, prematurely pregnancy, weight loss, anorexia, etc. are other effects of the Zn^{2+} deficiency consequences [3].

Cobalt and nickel share right/left-sided cell receptors and are considered essential to human health too. While a cobalt and vitamin B12 relationship is well documented, a similar, less documented affiliation applies to nickel and vitamin C [9]. Also less documented is the control nickel and cobalt exert over the muscular walls of the body's arteries. Nickel interacts with RNA and DNA [10].

All of examples show that a balance of cations in the body is essential to maintain human health. The excess amounts of heavy metals can lead to imbalances in others resulting in disease. It seems that it is important since intake of even low concentrations of metal ions can cause serious toxic effects. Therefore, detection and determination of trace amounts of metals in pharmaceutical and food products for their quality control is very important. In the literature, due to a strong environmental and biological impact, trace metal ions determination has received particular attention in the last years. Atomic absorption spectrometry [11], X-ray fluorescence spectrometry [12], inductively coupled plasma-optical emission spectrometry [13], flow injection combined with inductively coupled plasma mass spectrometry [14], polarography [15], chromatography [16] and spectrophotometry [17–20] have been used for the determination of metal ions in different samples.
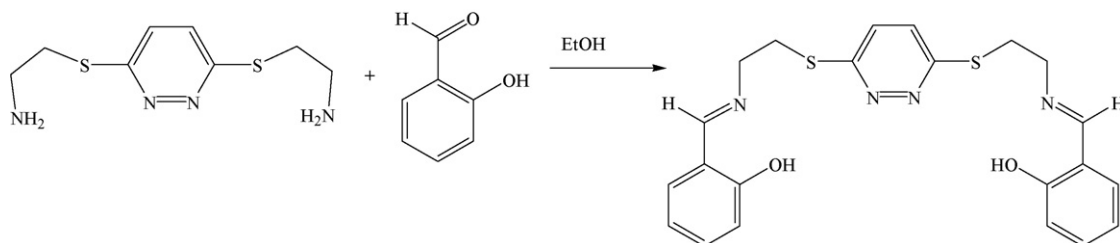
Scheme 1. Preparation of PATS.

Multivariate calibration methods (partial least squares (PLS) or principal component regression (PCR)) can be applied to multi-component determination [21,22]. These methods are not suitable when non-linearity is observed in the system. Artificial neural networks (ANNs) approach has several advantages over the multivariate calibration of data including easily programming of the network architecture, not necessity for any priori assumption on the behavior of the data, ability to process input data containing some degree of uncertainty and handling non-linearity due to analyte–analyte interaction, the synergistic effect and so on. Due to these advantages ANNs have attracted the interest of many researches in the field of chemistry as modeling tools for multivariate calibrations [23–26]. Among neural networks, the most popular is the multi-layer feed-forward neural networks (FFNNs) with the back-propagation learning algorithm. A radial basis function network (RBF) is an ANN which uses radial basis functions as activation functions offer interesting alternatives to feed-forward neural networks, in the sense that they allow local and also very fast training [27–31].

The most popular method for data compression in chemometrics is principal component analysis (PCA). In practice, principle components (PCs) are often successfully used as inputs. Even if there is some non-linearity in data set, all relevant information is usually contained in the first PCs [23]. PCA became ideal tool to remove possible complications caused by multicollinearity from the independent variables. Reducing the number of inputs to a network reduces the training time and repetition in the input data. So noise filtered data which contains that only the significant independent variables are responsible for the determination of amounts of metal ions [32–34].

The non-linearity due to synergistic effect, which is the main factor to the error of the kinetic analysis, has attracted much attention, and some works has been performed for solving this problem in non-linear systems with the aid of chemometrics [35]. In the literature, there are several papers which solve the synergistic effect in simultaneous determination of analytes with different network architectures for simultaneous modeling [35–38]. So the use of non-linear modeling technique makes it possible to describe accurately synergistic effects if presented in the novel area of food processing.

Schiff base ligands have played an integral and important role in coordination chemistry since the late 19th century and containing strong donor sites like phenoxo oxygen atoms as well as imine nitrogen atoms and find extensive applications in different fields for their special coordination ability with transition metal ions. Schiff bases have been developed as chelating ligands/catalysts for oxygenation and oxidation reactions of organic compounds [39], redox systems in biological processes [40], aldol reactions [41], degradation of dyes through decomposition of hydrogen peroxide and other reagents [42], epoxidation [43] and many other applications [44–46].

Copper, nickel, cobalt and zinc are metals that appear together in many real samples. Few reports have been published on the simultaneous determination of these ions in different samples

[47]. This paper describes simultaneous spectrophotometric determination of Co^{2+}, Ni^{2+}, Cu^{2+} and Zn^{2+} based on their complexes with potential active Schiff base ligand, 3,6-bis((2- aminoethylsalicyliden)thio)pyridazine (PATS)), with the aid of chemometric approaches, feed forward neural networks(FFNNs) and radial basis function networks (RBFNs).

2. Experimental

2.1. Reagent and standard solutions

All solutions were prepared with analytical grade reagents. Stock solutions of Cu^{2+}, Co^{2+}, Ni^{2+} and Zn^{2+} (1000 mg L^{-1}) were prepared by dissolving $CuCl_2$, $CoCl_2$, $NiCl_2 \cdot 6H_2O$ and $ZnCl_2$ (Fluka, Buchs, Switzerland) in water. A 0.026 mol L^{-1} Schiff base solution was prepared by dissolving it in a 80:20 (v/v) dimethylformamide (DMF):H_2O mixture. A pH 10.0 ammonium buffer solution (0.2 mol L^{-1}) was prepared from ammonium chloride and ammonia [48]. n-Hexane, methanol, ethanol and salicylaldehyde was purchased from Merck (Darmstadt, Germany) and used without further purification.

2.2. Preparation of 3,6-bis((2-aminoethylsalicyliden)thio)pyridazine (PATS)

PATS was synthesized from 3,6-bis((aminoethyl)thio)pyridazine (PTA). PTA was prepared as described previously [49] and used for preparation of PATS as follows (Scheme 1). A solution of 3,6-bis((aminoethyl)thio)pyridazine (PTA) (1 mmol) in absolute EtOH (10 mL) was added to a stirring solution of salicylaldehyde (2 mmol) in absolute EtOH at 50 °C over a period of 10 min. The solution was heated in water bath for 2 h at 70 °C with stirring, then cooled and let to stand at 0 °C. The obtained yellow solid was filtered off, washed with cooled n-hexane/methanol (4/1), and dried in air. Overall Yield: 75%, m.p. = 109–110 °C. ^{1}H NMR (CDCl$_3$, ppm): δ 3.59 (t, 4H), 3.90 (t, 4H), 6.88 (m, 4H), 7.31 (m, 2H), 7.46 (m, 4H), 8.57 (s, 2H), 13.22 (br, 2H). IR (KBr, cm^{-1}); 1635(C=N), 1610, 1578, 1497(C=C), 1281(C—O), 1150, 750.

2.3. Apparatus and data processing

Visible absorbance spectra were recorded on a PerkinElmer Lambda 45 UV–Vis spectrometer using 1-cm quartz cells and a slit of 0.5 cm. A short program was written in MATLAB 7.1 for performing principal component analysis of the data and the networks calculations were performed using nnet–Toolbox for MATLAB 7.1.

2.4. Procedure

Three sets of standard solutions containing Cu^{2+}, Co^{2+}, Ni^{2+} and Zn^{2+} were prepared as calibration, prediction and validation sets. The correlation between concentrations of the desired cations was avoided. Each set was selected so that the concentrations of the

Table 1
Composition of calibration, prediction, and validation samples in quaternary mixtures for simultaneous determination of Zn^{2+}, Co^{2+}, Ni^{2+} and Cu^{2+} with ANNs

Concentration ($mg\,L^{-1}$)

Calibration set				Prediction set				Validation set			
Zn^{2+}	Co^{2+}	Ni^{2+}	Cu^{2+}	Zn^{2+}	Co^{2+}	Ni^{2+}	Cu^{2+}	Zn^{2+}	Co^{2+}	Ni^{2+}	Cu^{2+}
5.0	5	4	4	2	4	5.2	5	4	4	3	2
8	5	5.1	5	2	2	2	2.2	4.2	3	2	1
4	2	5.1	5	2	2	2	2	3	3.2	3	3
1	10	1	4.5	4	1	2.2	4	2	3.2	5	2
2	2	3	2	5.1	2	2	3.1	2	5	10	5.2
4	4	5	5	5	5.1	6	4	10	10.2	3	5
5	4	4	4	3	2	6	3	10	2	1	6
10	2	2	4.5	10	2	2.2	6				
1	5	8	3	2	10	6	2				
3	2	1	4	6	2	4	4.5				
6.2	5	3	2	2	5	5.1	5.1				
6	2	1	2	3.2	10	10	5				
3	5	6.1	6	2.5	2	1	10				
2.5	5.1	4	4	1	1	3	5				
4	2	4	3								
4	2	1	3								
6	3	3	2								
2.5	6	1.5	7								
5	3	2	2								
4	1	1	3								

analytes were approximately covered the entire ranges of the analytes. Appropriate amounts of Zn^{2+}, Cu^{2+}, Co^{2+} and Ni^{2+} solutions, 1.0 mL buffer solution and 0.8 mL of $0.023\,mol\,L^{-1}$ PATS solution were added to a 5.0 mL volumetric flask. The flask was made up to the mark with water and allowed to stand for 60 min. A portion of the solution was transferred into a 1 cm quartz cell to record the absorbance spectra against a blank solution in the wavelength range 300–500 nm with 1 nm intervals. Calibration, prediction and validation sets contained 20, 14 and 7 samples, respectively. Table 1 shows the three sample sets.

2.5. Preparation of multivitamin tablet sample

Ten tablets were weighted and powdered in a mortar. A tablet amount and 2 mL concentrated HNO_3 was transferred to a 50 mL flask and diluted to the mark with doubly distilled water. The content of the flask was mechanically shaken for a period of 30 min and filtered. After that the developed methods were applied to the final solution [20].

2.6. Preparation of tea leaves samples

A 0.2 g of the sample was taken in a beaker and dissolved in concentrated nitric acid (5 mL) with heating. The solution was cooled, diluted and filtered. The filtrate was made up to 100 mL with distillated water in a volumetric flask. This solution was applied for analysis [50].

2.7. Preparation of vegetable and foodstuff samples

Lettuce, cabbage, soybean meal, burley and spinach samples available on the local markets in Hamadan were purchased for investigation. First, lettuce, cabbage and spinach samples were cleaned with tap water and double distilled water. Then, the samples were dried at 110 °C. Each of the dried varieties of samples were ground to reduce particle size and then thoroughly mixed to ensure homogeneity samples individually. Masses of 500 mg of cabbage, lettuce, spinach, and burley and soybean meal were transferred into separate 250 mL beakers and 5 mL of $0.5\,mol\,L^{-1}$ nitric acid was added to moisten the samples thoroughly. This was followed by adding 10 mL of concentrated nitric acid and heating on a hot plate (130 °C) for 3 h. After cooling to room temperature, 5 mL of concentrated perchloric acid was added drop wise. The beaker was heated gently until completion of sample decomposition resulting in a clear solution. This was left to cool down and then was transferred into a 100 mL volumetric flask by rinsing the interior of the beaker with small portions of $0.1\,mol\,L^{-1}$ nitric acid and the solution was filled to the mark with the same acid [51].

3. Results and discussion

3.1. Spectra and composition of complexes

Fig. 1 shows the absorption spectra for Zn-PATS, Cu-PATS, Co-PATS and Ni-PATS complexes at pH 10.0 in wavelength range
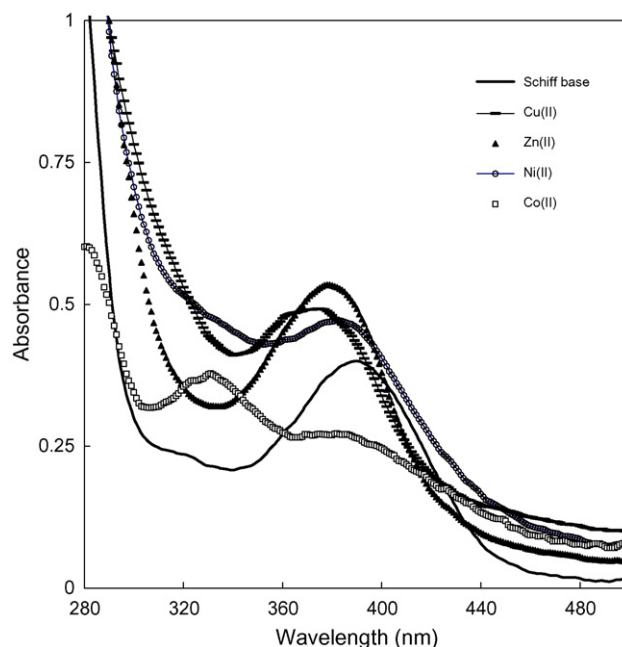

Fig. 1. Spectra for Schiff base $(5 \times 10^{-4}\,mol\,L^{-1})$ and its complexes with Ni^{2+} $(5.0\,mg\,L^{-1})$, Co^{2+} $(5.0\,mg\,L^{-1})$, Cu^{2+} $(2.0\,mg\,L^{-1})$ and Zn^{2+} $(2.0\,mg\,L^{-1})$.
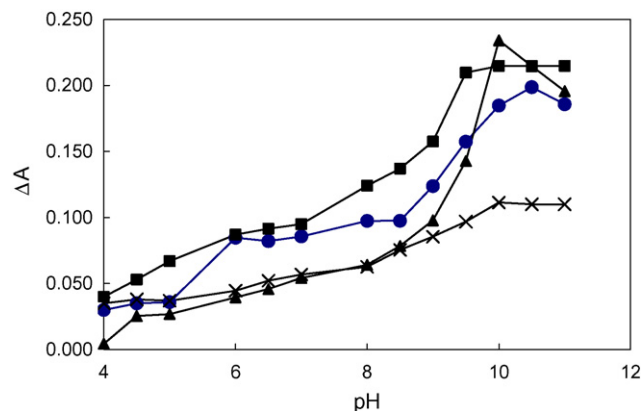
Fig. 2. Effect of pH on ΔA signals of Ni^{2+} ($\times$), Co^{2+} ($\bigcirc$), Zn^{2+} ($\blacktriangle$), Cu^{2+} ($\square$).

300–500 nm. The composition of complexes was determined by continuous variation method. Job's plot for Zn^{2+}, Cu^{2+}, Co^{2+} and Ni^{2+} complexes confirmed a 1:1 (M:L) composition for all the investigated complexes. As Fig. 1 shows, the absorption spectra of the complexes overlap, and therefore the metal ions interfere in the spectrophotometric determination of each other.

3.2. Influence of experimental factors

The overall processes are influenced by pH of the solution, concentration of Schiff base and time of the reactions which affect the absorbance of the colored products. So, the various experimental parameters affecting the development of the colored complexes were carefully studied and optimized.

3.2.1. Effect of pH

The complex formation reactions of metal ions with PATS depend on pH. In order to find the optimum pH, the effect of pH in the range 3–11 on the complex formation reactions of a constant concentration of each cation with PATS was investigated (Fig. 2). pH studies were carried out using sodium acetate–acetic acid (pH 3.4–6.5), ammonium chloride–ammonia and phosphate buffers (pH 7.0–11.0). From the results, it was observed that the complexes exhibit maximum absorbance in the pH range 9.5–10.5.

Fig. 3. Effect of PATS concentration on ΔA signals of Ni^{2+} ($\times$), Co^{2+} ($\bigcirc$), Zn^{2+} ($\blacktriangle$), Cu^{2+} ($\square$).

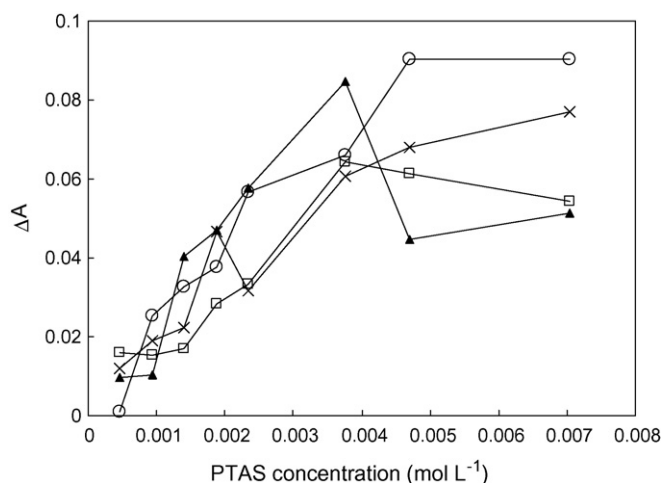Hence, further studies were carried out at pH 10.0 of ammonia buffer solution.

3.2.2. Effect of reagent concentration

The effect of PATS concentration over the range 4.6×10^{-4} to 8.0×10^{-3} mol L^{-1} on the determination of 2.0 mg L^{-1} each of Zn^{2+}, Cu^{2+}, Co^{2+} and Ni^{2+} ions at pH 10.0 buffer solution was studied to obtain the maximum color formation. As Fig. 3 shows, it is apparent that lower concentrations of PATS lead to lower complex formations. Therefore from the absorbance values, it was observed that, 3.23×10^{-3} mol L^{-1} PATS, eightfold excess over maximum concentration of metals, was sufficient to get maximum complex formation.

3.2.3. Time effect

To measure completeness of complex formation reaction, the absorbance values of metal-PATS complexes were monitored at different intervals of time. For Zn^{2+} ion, complex formation was completed after 20 min but for Cu^{2+} it was completed after 35 min and for Ni^{2+} and Co^{2+} it was completed after 60 min. Therefore, absorption measurements were performed at 60 min after mixing of reagents.

Table 2
Optimized parameters used for construction of PC-FFNNs and ANNs for simultaneous determination of Zn^{2+}, Co^{2+}, Ni^{2+} and Cu^{2+}

Parameter	Method	Zn^{2+}	Co^{2+}	Ni^2	Cu^{2+}
Input nodes	PCFFNNs	8	7	5	8
	FFNNs	Original sets	Original sets	Original sets	Original sets
Hidden nodes	PCFFNNs	4	5	3	5
	FFNNs	5	5	5	7
Output nodes	PCFFNNs	1	1	1	1
	FFNNs	1	1	1	1
Learning rate	PCFFNNs	0.01	0.01	0.01	0.01
	FFNNs	0.01	0.01	0.01	0.01
Momentum	PCFFNNs	0.001	0.001	0.001	0.001
	FFNNs	0.001	0.001	0.001	0.001
Number of iteration	PCFFNNs	520	520	520	520
	FFNNs	1200	1200	1200	1200
Hidden layer transfer function	PCFFNNs	Logsig	Tansig	Logsig	Logsig
	FFNNs	Logsig	Tansig	Logsig	Logsig
Output layer transfer function	PCFFNNs	Purelin	Purelin	Purelin	Purelin
	FFNNs	Purelin	Purelin	Purelin	Purelin
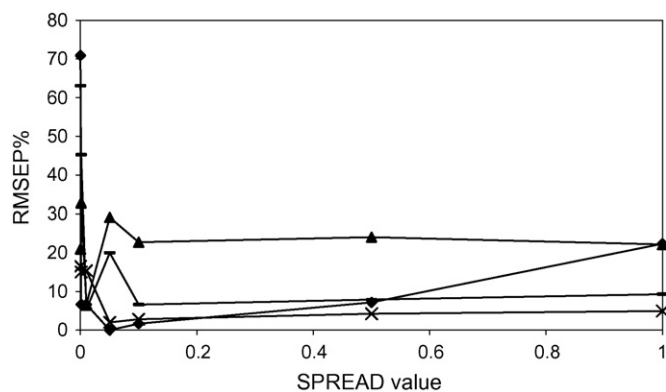
Fig. 4. Plots of RMSEP% as a function of SPREAD value for Ni^{2+} ($\times$), Co^{2+} ($\blacktriangle$), Zn^{2+} ($\blacksquare$), Cu^{2+} ($-$) for construction of RBFN.

3.3. Individual calibration graphs

A set of sample solutions with different metal ions concentrations were prepared and measurements were carried out under the optimum conditions according to the experimental procedure described in Section 3.2. The calibration curves of four analytes measured at different ranges were linear in the ranges 0.5–12.0 mg L^{-1}, 1–10.0 mg L^{-1}, 0.5–8.0 mg L^{-1}, 1.0–10.0 mg L^{-1}, 1.0–7.0 mg L^{-1}, and 1.0–12.0 mg L^{-1} for Zn^{2+}, Co^{2+}, Ni^{2+} and Cu^{2+}, respectively. Typical equations of the calibration curves were as follows: $A = 7.88 \times 10^{-2}C + 2.3 \times 10^{-3}$, $r^2 = 0.9979$; $A = 8.81 \times 10^{-2}C + 1.7 \times 10^{-2}$, $r^2 = 0.9997$; $A = 8.92 \times 10^{-2}C + 2.5 \times 10^{-3}$, $r^2 = 0.9995$ and $A = 1.81 \times 10^{-1}C + 2.0 \times 10^{-2}$, $r^2 = 0.9989$ for Zn^{2+}, Co^{2+}, Ni^{2+} and Cu^{2+}, respectively. Where C is the concentration of metal ions in mg L^{-1}. Limit of detection (LOD) were determined as 0.056, 0.098, 0.123 and 0.108 mg L^{-1} for Zn^{2+}, Co^{2+}, Ni^{2+} and Cu^{2+}, respectively. Also, limit of quantitation (LOQ) was determined as 0.186, 0.320, 0.410 and 0.360 mg L^{-1} for Zn^{2+}, Co^{2+}, Ni^{2+} and Cu^{2+}, respectively.

3.4. Optimizing the network variables in PCFFNNs

ANNs are mathematical or computational models based on biological neural networks. They consist of an interconnected group of artificial neurons and process information using a connectionist approach to computation. For the optimization of a neural network, a trial and error method has to be used to find the best neural network architecture. One layer of nodes in the output layer is common topological suggestions, when an ANN is used as a model of calibration. In this study some factors such as number of principal components, number of nodes (neurons) in hidden layer, learning function and number of epochs were optimized.

Performance of methods were tested with root mean square errors prediction (RMSEP), using synthetic solutions of metal ions as prediction set. The results obtained in the quantification of the samples in the training and prediction sets are expressed as

$$\text{RMSEP} = \sqrt{\frac{\sum_{i=1}^{n}(\hat{y}_i - y_i)^2}{n}} \tag{1}$$

where $\hat{y}_i$ and y_i are the desired output and the actual output sets, respectively, and n is the number of prediction set samples. Reducing the data volume before using ANNs for multivariate calibration was suggested as a preprocessing step in many of the previous studies [27,52].

If the number of weights exceeds the number of samples for the training of ANN to some extent, "over fitting" may be caused [53]. Also, in the case of a high number of input variables meaningful variables could be hidden [54], the probability of chance correla-

Table 3
RMSEP% values for prediction samples for determination of Zn^{2+}, Co^{2+}, Ni^{2+} and Cu^{2+} with PCFFNNs and PCRBFNs

Method	RMSEP (%)			
	Zn^{2+}	Co^{2+}	Ni^{2+}	Cu^{2+}
PCFFNN	4.81	3.37	3.51	1.24
FFNNs	6.80	6.89	5.23	5.44
PCRBFNs	1.45	1.53	1.15	0.72
RBFNs	3.32	3.08	3.15	2.66

tion increases [55], and may prevent ANN from finding optimized models [56]. Therefore, PCA input selection is necessary in order to improve the predicted results of different ANN.

In this work, spectrophotometric data were employed in different kinds of ANN to predict the concentrations of the corresponding analytes.

Therefore, the spectrophotometric data, before building the ANNs models, were subjected to principal component analysis and decomposed to PC scores. The numbers of input nodes were selected as optimal numbers of PC scores. The FFNN including one to ten PC scores were trained. The lowest RMSEP% values were obtained with eight, seven, five and eight input factors for Zn^{2+}, Co^{2+}, Ni^{2+} and Cu^{2+}, respectively. In order to determine the optimal number of hidden layer networks, neural networks with different numbers of hidden nodes were trained. The number of hidden nodes was varied from one to ten to train the networks. According to RMSEP% values versus the number of hidden layer nodes, the best number of hidden layer nodes were four, five, three and five for Zn^{2+}, Co^{2+}, Ni^{2+} and Cu^{2+}, respectively. To get the best network architecture, different transfer functions in hidden and output layer were also tested. The best transfer functions as well as some other parameters such as number of epochs, learning rate and momentum are summarized in Table 2. In order to predict metal ions concentrations in prediction set, ten times replications were performed in optimum conditions and finally the RMSEP% values were calculated and applied for comparing the applicability of the methods.

Simultaneous determination of four metal ions was studied with optimized architecture of Zn^{2+} (see Table 2). The RMSEP% results were more than 10 for Ni^{2+}, Co^{2+} and Cu^{2+} and more than 6 for Zn^{2+} ions. It may be due to complications caused by multicollinearity from the independent variables. These results showed that the best results could be calculated when optimized architectures for each metal ion were used.

In order to compare the PCFFNNs models with FFNNs, original spectrophotometric data, as input nodes, were subjected to FFNNs. The topology parameters were shown in Table 2. Comparison of PCFFNNs with ANNs models shows that the PCFFNNs models appear the shorter training time because of the fewer input nodes and iterations. Subsequently, RMSEP% values of ANNs models are shown in Table 3. RMSE% values in ANNs models were worse than

Table 4
Effect of foreign ions on the simultaneous determination Zn^{2+}, Co^{2+}, Ni^{2+} and Cu^{2+} (4.0 mg L^{-1} of each metal ion)

Foreign ion	Tolerance limit (mg L^{-1})
Na$^+$, K$^+$	1000
F$^-$, SO$_4^{2-}$, SCN$^-$, C$_2$O$_4^{2-}$	>200
CH$_3$CO$_2^-$, NO$_3^-$	>500
Thiourea	600
Thioacetamide	150
Mn^{2+}	70
Ag$^+$	20
Fe^{3+}	10
Hg^{2+}, Pb^{2+}	2

Table 5
Simultaneous determination of Zn^{2+}, Co^{2+}, Ni^{2+} and Cu^{2+} in different vegetable and foodstuff samples by proposed methods and flame atomic absorption spectrometry (FAAS) as a standard method (mg g^{-1})

Metal	Method	Sample							
		Tea	Spinach	Lettuce	Cabbage(1)	Cabbage(2)	Soybean meal	Barley	Tablet
Zn^{2+}	FFNN	0.058	0.136	0.080	0.058	0.075	0.068	0.226	0.042
	RBFN	0.058	0.139	0.069	0.056	0.075	0.076	0.268	0.038
	FAAS	0.054	0.132	0.072	0.054	0.064	0.078	0.300	0.036
Co^{2+}	FFNN	0.703	0.028	0.240	0.036	0.056	0.601	0.120	–
	RBFN	0.690	0.029	0.228	0.034	0.052	0.481	0.167	–
	FAAS	0.722	0.033	0.204	0.033	0.048	0.460	0.146	ND[a]
Ni^{2+}	FFNN	0.128	0.148	0.048	0.180	0.063	0.072	0.168	–
	RBFN	0.128	0.145	0.045	0.168	0.062	0.082	0.140	–
	FAAS	0.132	0.145	0.036	0.162	0.076	0.076	0.141	ND
Cu^{2+}	FFNN	0.072	0.222	0.005	0.100	0.025	0.007	0.025	0.218
	RBFN	0.070	0.194	0.003	0.115	0.022	0.006	0.024	0.225
	FAAS	ND	0.196	ND	ND	ND	ND	ND	0.251

[a] ND: not detected.

those in PCFFNNs models. The results indicate the PCFFNNs models have more advantages over ANNs models.

3.5. Optimizing the network variables in PCRBFNs

RBFNs typically have three layers: an input layer, a hidden layer with a non-linear RBF activation function and a linear output layer. Due to pure estimation by using too low hidden layer units or over fitting of data by using many hidden layer units, the challenge of designing an RBFN, lies in properly placing the best values of variables which affected performance of RBFN.

The two primary variables are the number of hidden units and the Gaussian SPREAD. By the *exact fit* type of radial basis function networks (from ANN Toolbox of MATLAB version 7.1); the numbers of hidden nodes are equal to the number of nodes in the input layer. The best value of the SPREAD is the value that entire input space of interest is covered with minimum overlap. Finding optimal values is usually made empirically, rather than through automatic training methods. So PC scores from application of PCA on spectral data were used as input variables. RMSEP% for the prediction of the complexes at the number of inputs from one to ten, and SPREAD values of 0.0001–1 were investigated. Four PC scores for Zn^{2+}, Ni^{2+} and Cu^{2+} and three PC scores for Co^{2+} were used as input variables. Based on the data in Fig. 4, the SPREAD value of 0.05 was used for Zn^{2+} and Ni^{2+} and, a value of 0.01 was used for Co^{2+} and Cu^{2+} in the final trained PCRBFN networks. Concentrations of Zn^{2+}, Co^{2+}, Ni^{2+} and Cu^{2+} were estimated in optimal parameters after three replicates. The RMSEP% values of the results were calculated and are given in Table 3.

Original spectrophotometric data as input nodes were subjected to RBFNs and the obtained results of this method were compared those obtained by PCRBFNs. In this case the SPREAD values was used as the same values used in PCRBFNs and RMSEP% values of ANNs models was calculated. As Table 3 shows, RMSEP% values in ANNs models were worse than those obtained in PCRBFNs models. Therefore, PC-FFNNs or PCRBFNs models advantageous over ANNs models.

As Table 3 shows, improvements in the estimated RMSEP% were observed when RBFN was applied instead of FFNN. In the case of using RBFN, the obtained results from repetition of training procedure for each condition were the same. Also comparing the RMSEP% obtained by two networks (Table 3) shows that the RBFNs can predict concentration of analytes better than FFNNs. This is due to utilizing better local distribution of the training samples and less parameters in optimization. Fast training and producing similar

prediction values causes the stability of the network and very fast convergence in each network repetition. Therefore the precision and accuracy of RBFNs results are better than FFNNs results.

3.6. Study of interferences

The effects of foreign species on the simultaneous determination of Zn^{2+}, Co^{2+}, Ni^{2+} and Cu^{2+} were investigated by measuring the absorbance of the solutions containing 4.0 mg L^{-1} of each metal ion in the presence of various amounts of other ions. The tolerance limit was taken as the amount of added ion causing less than 5% relative error in the determination of Zn^{2+}, Co^{2+}, Ni^{2+} and Cu^{2+}. Table 4 summarizes the maximum tolerances of the investigated cations and anions.

3.7. Applications

Application of the proposed methods to the analysis of synthetic mixtures (Table 2) showed satisfactory results for the simultaneous determination of Zn^{2+}, Co^{2+}, Ni^{2+} and Cu^{2+}. To demonstrate the applicability of the optimized methods to real samples, it was applied to the simultaneous determination of Zn^{2+}, Co^{2+}, Ni^{2+} and Cu^{2+} in lettuce, cabbage, soybean meal, burley, spinach, multivitamin tablet and tea leaves, which contain desired elements in different amounts. The concentration of Zn^{2+}, Co^{2+}, Ni^{2+} and Cu^{2+} were determined by the FFNNs and RBFNs. Concentrations of Zn^{2+}, Co^{2+}, Ni^{2+} and Cu^{2+} in the samples were also determined by flame atomic absorption spectrometry (FAAS). The results are given in Table 5. The amounts of metal ions obtained by the proposed methods were in good agreement with those obtained by FAAS. Moreover the calculated results proved that the proposed neural networks approach based on the PCA input selection was suitable for the simultaneous determination of Zn^{2+}, Co^{2+}, Ni^{2+} and Cu^{2+} in complex mixtures.

4. Conclusion

Simultaneous determination of Zn^{2+}, Ni^{2+}, Co^{2+} and Cu^{2+} directly performed by spectrophotometric measurements using a new Schiff base, as an analytical reagent, and chemometric modeling. Two networks (PCFFNNs and PCRBFNs) were optimized and used to the determination of Zn^{2+}, Ni^{2+}, Co^{2+} and Cu^{2+}. This study showed that the RBFN and FFNN are efficient methods for simultaneous determination of mixtures of Zn^{2+}, Ni^{2+}, Co^{2+} and Cu^{2+}.

High analytical potential of the ANNs created satisfactory results. A comparison between PCRBFNs and PCFFNNs shows that in RBFNs less parameters should be optimized. Also training procedures in RBFNs are faster than those in PCFFNNs. So reproducibility and lower training time of networks in the PCRBFNs are among the main advantage of these networks compared to PCFFNNs. The structure of the PCRBFNs and PCFFNNs were simplified by using the corresponding important principal components as input variables instead of original spectral data. Totally, comparison of constructed networks showed that the results obtained by PCRBFNs are better than those obtained by PCFFNNs and also PCRBFNs created, surprisingly, lower RMSEP% values. The methods offer good procedures for the analyzing of complex mixtures, using simple spectrophotometer, which is available in most laboratories and without any separation steps.

Acknowledgements

References

[1] A. Sigel, H. Sigel, R.K.O. Sigel, Neurodegenerative Diseases and Metal Ions: Metal Ions in Life Sciences, vol. 1, 2006.
[2] C.W. Levenson, Physiol. Behav. 86 (2005) 399.
[3] G.M. Wardlaw, Perspectives in Nutrition, 4th ed., WCB McGraw-Hill, Boston, 1999.
[4] G.A. Cypher, Copper and Human Health and Safety, International Copper Association Limited, New York, NY, USA, 1985.
[5] L. Del Corso, F. Pastine, M.A. Protti, Panminerva Med. 42 (2000) 273.
[6] C.D. Romero, P.H. Sanchez, F.L. Blanco, E.R. Rodriguez, L.S. Majem, J. Trace Elem. Med. Biol. 16 (2002) 75.
[7] J.C. Wallwork, H.H. Sandstead, J. Nutr. 113 (1983) 47.
[8] M. Hambidge, J. Nutr. 130 (2000) 1344S.
[9] V.K. Gupta, A.K. Singh, S. Mehtab, B. Gupta, Anal. Chim. Acta 566 (2006) 5.
[10] http://www.acu-cell.com/nico.html.
[11] A. Martın-Esteban, R.M. Garcinuno, S. Angelino, P. Fernandez, C. Camara, Talanta 48 (1999) 959.
[12] G. Zarazua, P. Ávila-Pérez, S. Tejeda, I. Barcelo-Quintal, T. Martínez, Spectrochim. Acta Part B 61 (2006) 1180.
[13] M.A. Hamilton, P.W. Rode, M.E. Merchant, J. Sneddon, Microchem. J. 88 (2008) 52.
[14] H.F. Maltez, M.A. Vieira, A.S. Ribeiro, A.J. Curtius, E. Carasek, Talanta 74 (2008) 586.
[15] Z. Shen, Z. Wang, Fensi Huaxane 21 (1993) 1313.
[16] N. Xie, C. Huang, H.D. Pu, Chem. Abstr. 113 (1990) 094170.
[17] A. Afkhami, M. Bahram, Spectrochim. Acta Part A 61 (2005) 869.
[18] A. Afkhami, M. Bahram, Anal. Chim. Acta 526 (2004) 211.
[19] V. Ravi, H. Kurniawan, P.N.K.P. Thai, R. Kumar, J. Appl. Soft Comput. 8 (2008) 305.
[20] A. Afkhami, T. Madrakian, M. Abbasi-Tarighat, Food Chem. 109 (2008) 660.
[21] T. Madrakian, A. Afkhami, M. Borazjani, M. Bahram, Spectrochim. Acta Part A 61 (2005) 2988.
[22] R. Ghavami, A. Najafiand, B. Hemmateenejad, Spectrochim. Acta 70 (2008) 824.
[23] F. Despagne, D.L. Massart, Analyst 123 (1998) 157R.
[24] T.B. Blank, S.D. Brown, Anal. Chim. Acta 277 (1993) 273.
[25] Y. Akhlaghi, M. Kompany-Zareh, Anal. Chim. Acta 331 (2005) 537.
[26] P.J. Gemperline, J.R. Long, V.G. Gregoriou, Anal. Chem. 63 (1991) 2313.
[27] A. Afkhami, M. Abbasi-Tarighat, M. Bahram, Talanta 75 (2008) 91.
[28] B. Walczak, D.L. Massart, Anal. Chim. Acta 331 (1996) 177.
[29] Y. Xiong-Zhang, Talanta 73 (2007) 68.
[30] Y. Ni, Y. Wang, S. Kokot, Food Chem. 109 (2008) 431.
[31] E.P.P.A. Derks, S.M.S. Pastor, L.M.C. Buydens, Chemom. Intell. Lab. Syst. 28 (1995) 49.
[32] S.M. Al-Alawi, S.A. Abdul-Wahab, C.S. Bakheit, Environ. Model. Softw. 23 (2008) 396.
[33] A. Afkhami, M. Abbasi-Tarighat, Anal. Sci. 24 (2008) 779.
[34] Y.X. Zhang, Talanta 73 (2007) 68.
[35] A. Safavi, H. Abdollahi, M.R. Hormozi Nezhad, Talanta 59 (2003) 515.
[36] A.H. Geeraerd, C.H. Herremans, L.R. Ludikhuyze, M.E. Hendrickx, J.F. Van Impe, Math. Comput. Simulat. 48 (1998) 53.
[37] M. Hasani, L. Yaghoubi, H. Abdollahi, Anal. Biochem. 365 (2007) 74.
[38] M. Hasani, M. Moloudi, F. Emami, Anal. Biochem. 370 (2007) 6.
[39] A. Nashinaga, H. Ohara, H. Tomita, T. Matsuura, Tetrahedron Lett. 24 (1983) 213.
[40] L.F. Lindoy (Ed.), The Chemistry of Macrocyclic Ligand Complexes, Cambridge University Press, Cambridge, 1989.
[41] K. Maruyama, K. Kubo, Y. Toda, K. Kawasa, T. Mashino, A. Nishinaga, Tetrahedron Lett. 36 (1995) 5609.
[42] T. Nakamura, K. Niwa, M. Fujiwara, T. Matsushita, Chem. Lett. 28 (1999) 1067.
[43] W. Zhang, E.N. Jacobsen, J. Org. Chem. 56 (1991) 2296.
[44] M. Shi, C.J. Wang, Tetrahedron-Asymmetr. 13 (2002) 2161.
[45] R.I. Kureshy, N.H. Khan, S.H.R. Abdi, S.T. Patel, P. Iyer, E. Suresh, P.I. Dastidar, J. Mol. Catal. A: Chem. 160 (2000) 217.
[46] Z.H. Yang, L. Wang, Z. Zhou, Q. Zhou, C. Tang, Tetrahedron-Asymmetr. 12 (2001) 1579.
[47] J. Ghasemi, Sh. Ahmadi, K. Torkestani, Anal. Chim. Acta 487 (2003) 181.
[48] J.A. Dean, Analytical Chemistry Handbook, McGraw-Hill, Inc., 1995, p 14.33.
[49] S.S. Tandon, L.K. Thompson, J.N. Bridson, Inorg. Chem. 32 (1993) 32.
[50] M.A. Taher, Anal. Chim. Acta 408 (2000) 153.
[51] S. Baytak, Acta Chim. Slov. 54 (2007) 385.
[52] S. Ventura, M. Sliva, D. Perez-Bendito, C. Hervas, J. Chem. Inf. Comput. Sci. 37 (1997) 287.
[53] I.V. Tetko, A.I. Luik, G.I. Poda, J. Med. Chem. 36 (1993) 811.
[54] M.B. Seasholtz, B. Kowalski, Anal. Chim. Acta 277 (1993) 165.
[55] D.J. Livingstone, D.T. Manallack, J. Med. Chem. 36 (1993) 65.
[56] D. Broadhurst, R. Goodacre, A. Jones, J.J. Rowland, D.B. Kell, Anal. Chim. Acta 348 (1997) 71.

Determination of ^{235}U/^{238}U atom ratio in uranium samples using liquid scintillation counting (LSC)

D. Alamelu, S.K. Aggarwal*

Fuel Chemistry Division, Bhabha Atomic Research Centre, Trombay, Mumbai 400 085, India

ARTICLE INFO

ABSTRACT

A correlation has been developed for the determination of ^{235}U/^{238}U atom ratio in uranium samples using liquid scintillation counting (LSC). The ^{235}U/^{238}U atom ratio determined by thermal ionization mass spectrometry (TIMS) was correlated to the ratio of (i) α-count rate and (ii) Cerenkov count rate due to ^{234m}Pa in the sample; both measured by LSC. This correlation is linear over the range of ^{235}U/^{238}U atom ratio encountered in the nuclear fuel samples, i.e. the low enriched uranium (LEU) samples with ^{235}U < 20 atom%. The methodology based on this correlation will be useful for the quick determination and verification of ^{235}U/^{238}U atom ratios in fuel samples using cost effective technique of LSC.

© 2008 Elsevier B.V. All rights reserved.

1. Introduction

Determination of isotopic composition and concentration of uranium (U) is very important in nuclear industry due to its strategic importance. Moreover, low enriched uranium (LEU < 20 atom% ^{235}U) is used as a nuclear fuel in light water reactors such as boiling water reactor (BWR) and pressurized water reactor (PWR). Determination of the isotopic composition and the trace elemental composition in the nuclear fuel is an important step for the chemical quality assurance of the reactor fuel. These data are used to calculate the fissile content of the fuel in the reactor.

Thermal ionization mass spectrometry (TIMS) is a well-recognized technique for the determination of isotopic composition of U in different matrices [1]. Other mass spectrometric techniques such as inductively coupled plasma mass spectrometry (ICP-MS), secondary ion mass spectrometry (SIMS) and glow discharge mass spectrometry (GDMS) can also be employed for the isotopic analysis of uranium [2–4]. In the event of non-availability of mass spectrometer, radiometric techniques such as alpha spectrometry [5] and gamma spectrometry [6] can also be employed. However, these radiometric techniques have limited applicability since the data on all the U isotopes cannot be obtained.

Development of isotope correlations is promising since it is possible to obtain the data on the amounts of different isotopes with minimal experimental effort employing simple experimental techniques such as alpha spectrometry and liquid scintillation counting (LSC). The correlations are also useful for obtaining the isotopic composition data when the amount of sample available is limited and is just sufficient to quantify major isotopes namely, ^{235}U and ^{238}U using mass spectrometry. Moreover, since the sample preparation steps involved for LSC are minimal, the correlation can be employed for obtaining the isotopic composition data in a cost effective manner.

A methodology for determining ^{234}U/^{238}U in U samples using LSC has been reported recently [7]. In this method, the spectra were de-convoluted for obtaining the contribution of ^{234}U and ^{238}U and the ^{234}U/^{238}U alpha activity ratio was then correlated to % enrichment of ^{235}U in the sample. Certified reference materials up to ^{235}U enrichment of 5% were used for developing this methodology, which gave satisfactory results except for the most depleted sample. When considering ^{235}U contents greater than 0.26%, the average discrepancy with respect to the reference values was 3.5% (with a maximum of 6.4%). This methodology showed a general tendency to under-estimate ^{235}U which was attributed to the approximation of neglecting the contribution of ^{235}U decays present in the region between the ^{238}U and ^{234}U peaks. The activity due to ^{235}U was assumed to give a greater contribution to the ^{238}U peak than to the ^{234}U peak.

LSC method has also been reported for the determination of U, using Cerenkov counting [8]. The daughter product ^{234}Pa

($T_{1/2}$ = 6.70 ± 0.05 h) [9] in the decay series of ^{238}U is in secular equilibrium with ^{238}U and this equilibrium is established in around 240 days. ^{234m}Pa with a half-life of 1.17 min has a β_{max} of 2.269 ± 0.004 MeV [9] and hence can produce scintillations due to Cerenkov radiation, in solutions with suitable refractive index. When natural U is considered, this radiation can be correlated to the amount of U using suitable calibration. In the above reported work, it was found that there was no effect on Cerenkov efficiency with volume of scintillator, while the efficiency increased with increase in acidity of the solution. It was also observed that there was no interference due to in-growth of the daughter products of the other isotopes of U while using Cerenkov counting. The Cerenkov counting efficiency was determined as 62.35% which is high in comparison to the other radiometric methods such as alpha spectrometry. It was also reported that the Cerenkov counting could be useful when the amount of uranium used is sufficiently high for analysis.

In this paper, we discuss the application of LSC for determination of $^{235}U/^{238}U$ atom ratio in enriched U fuel samples using Cerenkov counting in 0.1 M HNO_3 for determining ^{238}U in the sample and the total α counts due ^{234}U, ^{235}U and ^{238}U by LSC. The ratio of total α count rate observed to Cerenkov count rate in the same aliquot was then correlated to the $^{235}U/^{238}U$ atom ratio determined by TIMS. The correlation was found to be linear over the entire range of samples used in the study (1–15 atom% of ^{235}U).

2. Experimental

Nine synthetic fuel samples of low enriched uranium (LEU) with ^{235}U content in the range of 1–15 atom% were prepared by mixing natural uranium and NIST CRM-500. Of the nine samples, seven samples were used for obtaining the calibration and two were used as unknowns for checking the validity of the correlation. The uranium samples were purified from most of the daughter products by anion exchange procedure using Dowex 1 × 4 in 4 M HCl, where only U is held while Th and Pa are washed out in the effluent. After loading of U, the column was washed sufficiently with 4 M HCl to remove Th and Pa. Uranium was eluted from the column with 0.1 M HNO_3.

The U solution in 0.1 M HNO_3 was loaded onto the sample filament, which is made of high purity rhenium, of the double filament assembly. The $^{235}U/^{238}U$ and $^{234}U/^{238}U$ atom ratios were obtained using a Finnigan MAT-261 (Bremen, Germany) TIMS equipped with multi Faraday cup detection system employing static mode of multi-collection. The sample and the ionization filaments were heated to appropriate temperatures corresponding to heating currents of 2.2 and 6 A, respectively, for obtaining sufficient intensity of U^+ ions at m/q 235 and 238. The mean value of $^{235}U/^{238}U$ atom ratio was determined by taking average of data from three blocks, each block consisting of 10–12 peak scans.

The purified uranium solution was then taken in the LSC vial for LSC counting after a period of 7 days from the completion of elution. The rationale for choosing this time gap is later discussed in this paper. However, it is to be noted that in case of actual enrichment samples, the separation procedure need not be performed, since the date and time of sampling can itself be used as the time of separation of uranium from its daughter products. In such cases, care should be exercised to account for different quench levels between unknown samples and calibration standards while doing Cerenkov counting as well as LSC. For determination of ^{238}U using Cerenkov radiation, about 100 μL of U solution was taken in a glass scintillation vial. 5 mL of 0.1 M HNO_3 was added to these samples. The samples were kept in slightly acidic medium to avoid any precipitation of uranium. The Cerenkov radiation was then monitored in

the 0–50 keV region of the multi-channel analyser (MCA) covering an energy range of 0–2000 keV using a low background Liquid Scintillation Spectrometer (Packard Tri-Carb 2900 TR) for 10 min to reduce the statistical uncertainties in counting. 12 mL of Ultima Gold AB scintillator [di-isopropyl naphthalene (DIN)-based] was then added to the solution in the same vial. The mixture was subjected to ultra-sonication for complete mixing of aqueous phase with the scintillation cocktail and the vial was counted again in the LSC system for one minute and the counts in the 70–250 keV region of the MCA of the LSC system, which corresponded to the total α-count rate of the different U isotopes were recorded. It may be mentioned that Ultima Gold AB which is particularly useful to discriminate α and β was used in the present work since this was readily available to us without any specific advantage of α and β discrimination. In the present case, we found that it was also not necessary to apply α-β discrimination for determining the α-count rate in the sample, and hence no α-β discrimination was employed in the present work.

3. Results and discussion

Fig. 1 shows the increase in the activity, calculated using the Bateman's formula, of the daughter product ^{234}Pa in the ^{238}U decay series as a function of time after purification using $T_{1/2}$ values of (24.1 ± 0.03) d and (6.70 ± 0.05) h for ^{234}Th and ^{234}Pa, respectively [9]. As can be seen, secular equilibrium between ^{238}U and ^{234}Pa is obtained in around 240 days. Based on these calculations, it can be seen that the increase in the activity of ^{234}Pa is around 17% of its equilibrium concentration in 7 days after purification and may be used for the determination of ^{238}U in the sample without the attainment of secular equilibrium. This growth period is also sufficient to reduce the uncertainty due to small differences (of a few hours) on the time elapsed between purification and starting of the Cerenkov counting of the actual samples.

Fig. 2 shows the correlation obtained between $^{235}U/^{238}U$ atom ratio and the ratio of α-count rate (cpm) and Cerenkov count rate (cpm) in the present work. The increase in the α-count rate would be due to increase in both ^{234}U as well as ^{235}U atom% abundances, which would also be a case in actual enrichment samples. As can be seen, the correlation is linear over the range of $^{235}U/^{238}U$ atom ratios (0.02–0.16) of the mixtures used for study. Although in the present case of synthetic samples, a linear correlation was obtained for the entire range of $^{235}U/^{238}U$ atom ratio of LEU samples, the same may not be the case for samples with much higher enrichments, since the $^{235}U/^{234}U$ atom ratio may not be independent of
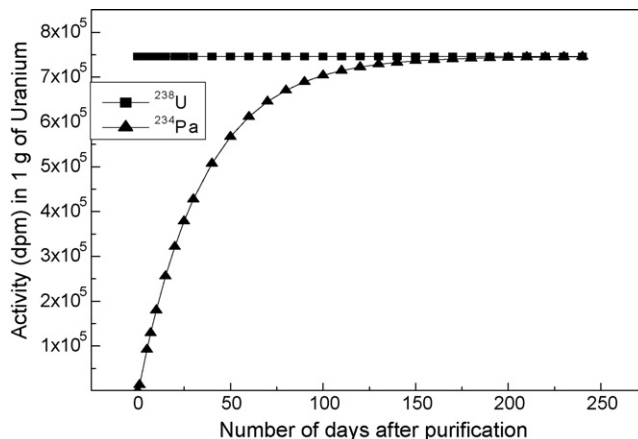

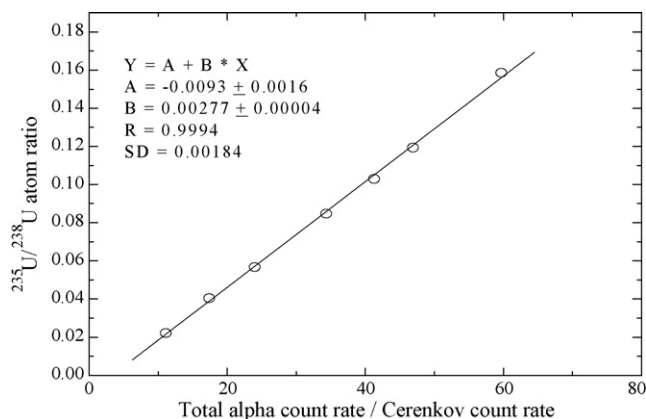**Fig. 1.** Increase in the activity of ^{234}Pa as a function of time elapsed after purification.

Fig. 2. Correlation between ^{235}U/^{238}U atom ratio and the ratio of total α-count rate to Cerenkov count rate.

the ^{235}U enrichment level and would also be dependent on the enrichment process employed.

Table 1 gives the data obtained on Cerenkov count rate and α-count rate for the synthetic samples. It is to be noted that the Cerenkov count rate was renormalized using the data from Fig. 1 to obtain the equilibrium concentration of ^{234}Pa. The table also includes the data on SIS (spectral index of the sample) and tSIE (transformed spectral index of the external standard ^{133}Ba γ-source, (half-life 10.53 year; E_γ 0.356 MeV)) for the synthetic samples used. Both these parameters are generally used to measure the quench level; the latter (tSIE) being more versatile [10]. This is because the value of SIS which reflects the end point or maximum energy of the sample pulse height spectrum as well as the magnitude and shape of the spectrum depends not only the end point energy but also on the level of activity in the sample. The higher the end point energy, smaller is the quench correction and higher the activity, more accurate is the value of SIS. Even though the SIS value may change appreciably due to quenching when dealing with high energy β-radiation, but there is no marked effect on counting efficiency of the sample. In the present work, an SIS value of about 20 corresponds to an efficiency between 60 and 70% for the Cerenkov radiation. The value of tSIE is independent of the activity level in the sample as well as is independent of the radioisotope involved. The value of tSIE ranges from 1000 (for unquenched cocktail mixture) to about 100 (for highly quenched samples).

In the present work, the SIS value is a good indicator of quench level for Cerenkov radiation since the compton electrons from the external gamma source namely ^{133}Ba for obtaining the tSIE have much lower energy in comparison to the $β_{max}$ of ^{234m}Pa, the tSIE will not be a correct indication of quench level. Hence SIS was used for indicating the quench level while obtaining the Cerenkov count rate in the samples.

It is obvious from the data given in Table 1 on SIS and tSIE values that the quenching in the LSC samples is quite significant but is consistent for all the samples used. It should be noted the volume of the sample has to be optimized for the highest efficiency for Cerenkov counting. The quenching can be reduced by using small volume of acid (upto 100 μL) in the cocktail which is possible when sufficient amount of U is available. This would also be important in considering the reduction in the volume of organic radioactive waste containing U, generated in LSC counting. These problems could be circumvented by performing two separate measurements, one for obtaining Cerenkov count rate using significant amount of U in solution and the second using the same uranium sample (100 μL) on weight/volume basis for obtaining the α-count rate. These were not considered necessary in the present studies since our aim was to demonstrate the applicability of the correlation to LEU samples.

The above-developed correlation was then applied for the determination of ^{235}U/^{238}U atom ratio in the two synthetic samples which were used as unknowns. The experimental data obtained for these samples are shown in Table 2. It is seen that the ^{235}U/^{238}U atom ratio in these synthetic LEU samples could be determined with an accuracy of about 2%.

Though the correlation discussed in this work was obtained using synthetically prepared LEU samples, it can be applied to actual uranium samples obtained during ^{235}U enrichment by different processes. The methodology could not be employed for real enrichment samples, obtained from natural U as the starting material, due to the non-availability of such samples. However, it must be noted that change in atom% abundances of ^{234}U and ^{235}U would depend on the enrichment process employed and hence a similar correlation must be developed for specific enrichment process prior to employing this methodology.

It may also be noted that the time of starting the counting of the samples subjected to enrichment and the calibration standards, i.e. the samples used for developing the above correlation, should be nearly the same as far as possible, in case secular equilibrium is not established as was done in the present work. Alternatively, in case

Table 1
Thermal ionization mass spectrometric (TIMS) and LSC data of different synthetic samples

Sample number	Cerenkov count rate (cpm) (A)	SIS[a] of samples for Cerenkov counting	Total α-count rate by LSC (cpm) (B)	tSIE[b] of samples for LSC counting	Total α-count rate/ Cerenkov count rate (B/A)	^{235}U/^{238}U atom ratio by TIMS
1	1993	22.43	21,955	333.64	11.15	0.0222
2	305	25.79	4,886	360.84	17.39	0.0404
3	302	24.66	6,669	359.58	23.99	0.0568
4	1678	22.82	56,794	341.28	34.34	0.0847
5	2133	21.95	87,038	337.58	41.27	0.1029
6	1764	22.29	81,603	338.34	46.90	0.1194
7	447	24.07	25,240	358.71	59.67	0.1586

[a] SIS denotes spectral index of the sample.
[b] tSIE denotes transformed spectral index of the external standard.

Table 2
Determination of ^{235}U/^{238}U atom ratio in unknown samples by LSC counting and using correlation given in Fig. 2

S. no.	Cerenkov count rate (cpm)	SIS of samples for Cerenkov counting	α-Count rate with cocktail (cpm)	tSIE of samples for counting with cocktail	α-Count rate/ Cerenkov count rate	^{235}U/^{238}U atom ratio		C/D
						Using correlation (C)	TIMS (D)	
1	2706	21.42	76909	324.01	28.68	0.0701	0.0684	1.025
2	1381	22.72	71159	345.66	52.44	0.1360	0.1375	0.989

of differences in the time elapsed after purification for the unknown samples and the calibration standards, renormalization should be done to the observed Cerenkov count rate to obtain the equilibrium value.

Similar correlations can be developed using the data from irradiated fuel dissolver samples for the other U isotopes, e.g. ^{236}U as well as for ^{234}U in enriched U samples [11]. These correlations are also useful to check the internal consistency of the data on samples from the same type of reactor.

It would be interesting to develop and test the correlation mentioned in this work, by other laboratories, who are actually involved in the ^{235}U enrichment work by taking both the depleted and the enriched U samples.

Acknowledgements

References

[1] I.T. Platzner, Modern Isotope Ratio Mass Spectrometry, John Wiley & Sons, New York, USA, 1997.
[2] M. Betti, L. Aldave de las Heras, Spectrosc. Eur. 15 (2003) 15.
[3] S.F. Boulyga, T. Prohaska, Anal. Bioanal. Chem. 390 (2008) 531.
[4] Xiaolin Hou, Per Roos, Anal. Chim. Acta 608 (2008) 105.
[5] S.K. Aggarwal, P.M. Shah, J. Radioanal. Nucl. Chem. 230 (1998) 265.
[6] R.O. Korob, G.A. Blasiyh Nuno, Appl. Radiat. Isotopes 64 (2006) 525.
[7] D. Bianchi, P. Cortese, G. Dellacasa, I. Merlano, Nucl. Instrum. Meth. Phys. Res., A 553 (2005) 543.
[8] R. Blackburn, M.S. Al-Masri, Analyst 119 (1994) 465.
[9] R.B. Firestone, V.S. Shirley, Table of Isotopes, vol. II, 8th ed., John Wiley & Sons, 1999.
[10] Michael F.L. Annunziata, Michael J. Kessler, in: Michael F.L. Annunziata (Ed.), Handbook of Radioactivity Analysis, Academic Press, San Diego, CA, 2003 (Chapter 5).
[11] D. Alamelu, R. Govindan, Raju Shah, P.S. Khodade, S.K. Aggarwal, Paper No. CP-12, in: Proceedings of the 12th Indian Society for Mass Spectrometry Symposium cum Workshop on Mass Spectrometry (12th ISMAS-WS 2007), March 25–30, 2007, Goa, India (CD compiled by D. Alamelu, P.G. Jaison, S.K. Aggarwal, ISBN: 978-81-904442-0-0).

Applying sequential injection analysis (SIA) and response surface methodology for optimization of Fenton-based processes

Allan C.V. dos Santos, Jorge C. Masini *

Instituto de Química, Universidade de São Paulo, C.P. 26077, 05513-970 São Paulo, SP, Brazil

ABSTRACT

This work presents the use of sequential injection analysis (SIA) and the response surface methodology as a tool for optimization of Fenton-based processes. Alizarin red S dye (C.I. 58005) was used as a model compound for the anthraquinones family, whose pigments have a large use in coatings industry. The following factors were considered: $[H_2O_2]$:[Alizarin] and $[H_2O_2]$:$[FeSO_4]$ ratios and pH. The SIA system was designed to add reagents to the reactor and to perform on-line sampling of the reaction medium, sending the samples to a flow-through spectrophotometer for monitoring the color reduction of the dye. The proposed system fed the statistical program with degradation data for fast construction of response surface plots. After optimization, 99.7% of the dye was degraded and the TOC content was reduced to 35% of the original value. Low reagents consumption and high sampling throughput were the remarkable features of the SIA system.

© 2008 Published by Elsevier B.V.

1. Introduction

Environmental protection has been an important factor for development of new coatings technologies [1]. Waterborne systems, high solid coatings and restriction/elimination of toxic raw material in coatings are just some examples of how the paints industries are dealing with environmental challenges. Most part of the efforts is dedicated to product development and little attention has been given to wastewater treatment improvement. A high capacity coatings industry may generate around $320\,m^3$/month of effluent [2], whose quality and possible contaminants may greatly vary according to specific site production, construction/design or management [3]. Only a recent work [4] was found to deal with alkydic resin wastewater (a sub product of one of the paint components) and the use of advanced oxidative processes (AOP's) for its treatment.

AOP's are processes based on the generation of the hydroxyl radical, •OH, a species that acts as a strong oxidant to a wide variety of organic and inorganic compounds [5]. A special kind of AOP is the Fenton reaction, in which the hydroxyl radical is formed from the reaction between H_2O_2 and Fe(II) ions. The hydroxyl radical can degrade the pollutant to harmless compounds, or even mineralize it to CO_2, water and inorganic salts [6]. Pignatello et al. [7]

showed the scientific interest on this theme: a search of the keyword "Fenton reaction" yielded over 2500 scientific articles since 1945.

Response surface methodology is an optimization technique based on factorial planning [8,9]. It was introduced around the 1950s and has been used with great success for modeling many industrial processes [10]. This methodology was already applied for the optimization of Fenton reaction parameters [11,12]. Sequential injection analysis (SIA), a flow technique proposed by Ruzicka and Marshall [13], can be used to reduce reagents consumption, and to facilitate the execution of experiments necessary for the construction of the response surface. This technique was already used as a tool for monitoring metal cations such as Cd(II), Pb(II) and Cu(II) in wastewater samples from coatings industry [14] and a review of SIA as an alternative approach to process analytical chemistry was presented by Barnett et al. [15].

Alizarin red S was used as a model compound for the anthraquinones family, whose pigments have a large use in coatings industry. Before this study, it was found only one article by Iqbal and Ashiq [16] dealing with alizarin removal from aqueous solution by adsorption on activated charcoal. An effluent, however, can be depurated by adsorption, but the contaminants are only transferred to another phase. At this new phase, the volume to be treated is lowered, but the degradation problem concerning the pollutants still remains [17].

The present work shows, for the first time, how a SIA system can help to define optimum process conditions for degradation of
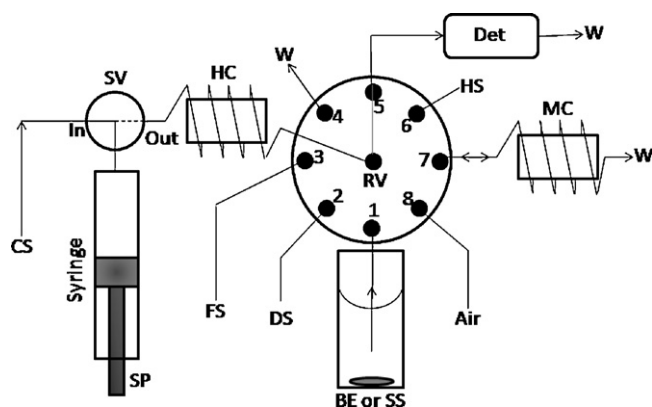

Fig. 1. Sequential Injection Analysis manifold for optimization of Fenton reaction. SP, syringe pump; RV, rotary selection valve; SV, solenoid valve for "in" and "out" positions of the system; HC, holding coil (3 m long, 0.8 mm i.d.); CS, carrier solution (deionized water); DET, spectrophotometric detector; MC, mixing coil (polyethylene, 25 cm, 2 mm i.d.); FS = 50 mmol L^{-1} FeSO$_4$ solution; HS = 200 mmol L^{-1} H$_2$O$_2$ solution; W, waste; BE, beaker containing 50 mL of 0.100 mmol L^{-1} alizarin stock solution under continuous stirring; SS = 0.100 mmol L^{-1} alizarin stock solution (calibration mode); DS, dilution solution (deionized water adjusted with HNO$_3$ to desired pH). *Note*: Alizarin stock solution previously adjusted with HNO$_3$ to desired pH.

alizarin red S using Fenton reaction with the help of the response surface methodology.

2. Experimental

2.1. Reagents

All reagents were of analytical grade and the working solutions were prepared in deionized water obtained from a Simplicity 185 system from Millipore coupled to an UV lamp (Millipore, São Paulo, SP, Brazil).

Alizarin red S, specifically alizarinsulfonic acid sodium salt, molecular formula C$_{14}$H$_7$NaO$_7$S (CAS 130-22-3) and molar mass of 342.26 g mol^{-1} was acquired from Merck (Merck Brazil, Rio de Janeiro, RJ).

Iron sulfate stock solution was prepared by dissolving FeSO$_4\cdot$7H$_2$O salt. This stock solution was purged with N$_2$ and protected from atmospheric O$_2$, thus avoiding rapid oxidation of Fe(II). Any pH adjustments (sample or standard solutions) were performed only with HNO$_3$.

Table 2
Complementary data for the in line construction of the calibration curve.

In line standard concentration (μmol L^{-1})	Volume (μL) for step 3	Volume (μL) for step 4	Volume (μL) for step 10
10	65	435	775
25	120	280	750
50	270	230	870
75	390	110	880
100	800	0	800

2.2. Apparatus and procedure

A FIAlab 3500 system (FIAlab Instruments, Bellevue, WA, USA) was used in all experiments in the sequential injection mode according to Fig. 1. Solutions were driven by a 5.00 mL syringe pump (SP) and an eight port rotary valve (RV) (Valco Instrument Co., Houston). The holding coil (HC) was made of 3 m of Teflon (polytetrafluoroethylene, PTFE) tubing (0.8 mm i.d.). Connections from port 5 to the flow detection cell and from port 1 to the sample beaker were made of 53.5 and 42 cm long PTFE tubings, respectively (0.8 mm i.d.). The mixing coil (MC) was made of 25 cm of polyethylene tubing (2 mm i.d.). All other tubing connections were made of 0.8 mm i.d. PTFE tubing and PTFE nuts and ferrules (Upchurch, Oak Harbor, WA, USA). A Micronal B382 spectrophotometer (Micronal, São Paulo, SP, Brazil) was used as detector fitted to a 10 mm light path length flow cell with 80 μL of internal volume from Hellma (Hellma GmbH & Co. Mülheimheim, Baden, Germany), performing absorbance measurements at 422 nm. Spectral curve was previously obtained in a Hitachi spectrophotometer model U-3000 using a quartz batch cell of 10 mm optical path length.

From a 100 μmol L^{-1} alizarin standard solution, the SIA system can generate a five points calibration curve by dilution of this standard in the MC and HC using the monosegmented flow approach [14,18]. To perform this task, suitable volumes of the standard and diluting solutions (SS and DS, respectively) are aspirated to HC, as described in Table 1, forming 800 or 1000 μL monosegments (Table 2). To facilitate the homogenization of the monosegment, the total volumes of SS and DS are fragmented twice (steps 3 and 4, Table 1) using the volumes described in Table 2, generating alizarin concentrations from 10 to 100 μmol L^{-1}. Homogenization is improved by pumping the monosegment toward the mixing coil (MC, Fig. 1) and then aspirating it back to HC (steps 7 and 8, Table 1). Even with these steps the homogenization is not complete in all solution elements of the monosegment, so that the absorbance

Table 1
Sequence of steps for in line construction of the calibration curve.

Step	SV	RV port	SP	Volume (μL)	Flow rate (μL s^{-1})	Comments
1	In	–	Aspirate to syringe	3000	200	Aspirate CS into the syringe
2	Out	8	Aspirate air to HC	50	75	Starts forming the monosegment
3	Out	1	Aspirate SS to HC		75	See Table 2 for SS volume
4	Out	2	Aspirate DS to HC		75	See Table 2 for DS volume
5	–	–	Repeat steps 3 and 4	–	–	Completes the sequence of SS and DS zones[a]
6	Out	8	Aspirate air to HC	200	75	Forms the monosegment inside HC
7	Out	7	Dispense to MC	1000	100	Homogenization of the monosegment
8	Out	7	Aspirate to HC	900	100	Completes homogenization of the monosegment, leaving part of the bubble in MC
9	–	–	–	–	–	Start data acquisition
10	Out	5	Dispense to DET		75	See Table 2 for dispensed volume. Monosegment directed to detector for absorbance readings
11	–	–	Delay 10 s	–	–	Data acquisition period
12	Out	5	Empty syringe	–	200	Cleans detection system
13	–	–	–	–	–	Stop of data acquisition

[a] For 100 μmol L^{-1} in line standard solution preparation, step 5 is not executed. SS and DS were fractioned twice to improve homogenization.

Table 3
Sequence of steps to perform Fenton reagents addition and subsequent reaction monitoring by SIA (spectrophotometric detection).

Step	SV	RV port	SP	Volume (μL)	Flow rate (μL s^{-1})	Comments
1	In	–	Aspirate to syringe	500	200	Aspirate CS into the syringe
2	Out	8	Aspirate air to HC	350	50	Separation of CS and FS
3	Out	3	Aspirate FS to HC		50	See Table 4 or 6 for FS volumes
4	Out	1[a]	Dispense FS to BE		50	Consider 300 μL + volume of step 3, so that air fills the port 1 tubing
5	Out	1[a]	Aspirate air to HC	280	50	Aspirates part of the air to HC, starting the segmentation of the next step.
6	Out	6	Aspirate HS to HC		50	See Table 4 or 6 for HS volumes
7	Out	1[a]	Dispense HS to BE		50	Consider 300 μL + volume from step 6, leaving air in the port 1 tubing
8	Out	4	Empty syringe	–	200	End of reaction mixture preparation
9	In	–	Aspirate to syringe	3000	200	Aspirate CS into the syringe
10	Out	1[a]	Aspirate BE to HC	250	50	Displaces air inside port 1 tubing, aspirating it to HC
11	Out	4	Dispense BE to W	500	50	Clean HC (air elimination)
12	Out	8	Aspirate air to HC	50	50	Start segmentation
13	Out	1[a]	Aspirate BE to HC	750	50	Aspirate mixture sample for monitoring process
14	Out	8	Aspirate air to HC	50	50	Completion of segmentation
15	–	–	–	–	–	Start of data acquisition
16	Out	5	Dispense to DET	800	50	Monosegment is directed to detector
17	–	–	Delay 3 seconds	–	–	Data acquisition period
18	Out	5	Empty syringe	–	200	Cleans detection system
19	–	–	–	–	–	Stop of data acquisition
20	Out	8	Aspirate air to HC	300	200	Prepare to purge tubing from port 1
21	Out	1[a]	Empty syringe	(300)	200	Purges port 1 tubing
22	–	–	Repeat steps 9–21	–	–	Monitoring of reaction for 9 times

[a] This port is connected to a tube with capacity of 280 μL.

readings were made in a previously selected portion of solution corresponding to the absorbance read for off-line prepared standards. This portion was defined by the volumes injected in step 10 (Table 1) and described in Table 2.

The degradation experiment is performed with 50 mL of 100 μmol L^{-1} alizarin solutions previously adjusted to the desired pH using only HNO$_3$. The SIA system adds previously defined volumes of 50 mmol L^{-1} FeSO$_4$ and 200 mmol L^{-1} H$_2$O$_2$, in this order, to a beaker containing alizarin solution under continuous stirring. Using a bubble, reagent solutions are separated from the carrier solution (water) during this process. By dilution, the final desired concentrations of H$_2$O$_2$ and FeSO$_4$ are obtained. For computation

Fig. 2. Registered data for construction of a calibration curve consisting of five alizarin concentration levels: 10, 25, 50, 75 and 100 μmol L^{-1} at pH 3.5, measured in triplicate. Data were smoothed by a 10 points adjacent averaging method.

purposes, it is considered that the final volume of reaction mixture is not significantly varied by addition of the reagents. Finally, the SIA system starts the on-line sampling and analysis of the reaction medium using the monosegmented flow analysis approach [18], performing 10 measurement cycles (monitoring step). Details about this procedure are given in Table 3. Besides to each run with alizarin, a blank run was also performed and the resulting absorbance difference was used for statistical evaluation of the dye degradation.

For statistical analysis, a face centered central composite response surface was considered; six repetitions were performed at the central point. All statistic values and graphics were obtained with Minitab release 14 software (Minitab Inc., State College, Pennsylvania) at a confidence level of 95% ($\alpha = 0.05$).

Analysis of total organic carbon (TOC) was performed in a Shimadzu TOC analyzer model 5000A (Kyoto, Japan) in accordance to standard methods [19], always as an average of three determinations.

3. Results and discussion

3.1. General features

The monosegmented flow approach was used to minimize the dispersion of the Fenton reagents with the carrier solution, assuring quantitative transference from the stock recipients (ports 3 and 6 of RV, Fig. 1) to the reaction beaker, without significant increase of the transference volume. The monitoring of the alizarin concentration and the generation of the calibration curve by diluting a single stock solution could be done either by segmented or non segmented approaches, but we preferred to work using segmentation. Dimensions of tubing connecting the ports 1 and 5 of RV to the reaction beaker and flow cell, respectively, were as short as possible to keep the system compact and to avoid long washing times between runs. These tubings work as transmission lines between the reactor and the detector and not as reaction coils. Dimensions
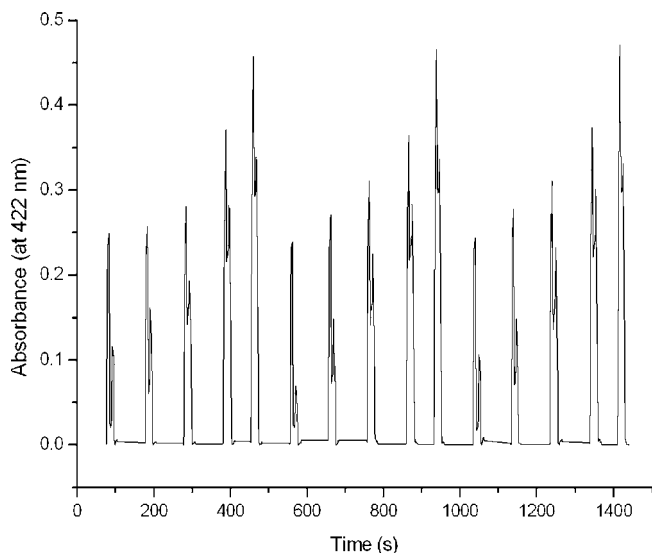
Table 4
First response surface design.

Run	[H_2O_2]:[Alizarin]	[H_2O_2]:[$FeSO_4$]	pH	$FeSO_4$[a]	H_2O_2[b]	Color removal (%)
1	4	2	2.5	200	100	36.6
2	10	8	2.5	125	250	76.2
3	10	2	4.5	500	250	32.3
4	4	8	4.5	50	100	17.5
5	7	5	3.5	140	175	58.6
6	7	5	3.5	140	175	58.6
7	10	2	2.5	500	250	89.0
8	4	8	2.5	50	100	4.5
9	4	2	4.5	200	100	38.1
10	10	8	4.5	125	250	67.7
11	7	5	3.5	140	175	58.9
12	7	5	3.5	140	175	58.6
13	4	5	3.5	80	100	19.6
14	10	5	3.5	200	250	85.2
15	7	2	3.5	350	175	59.6
16	7	8	3.5	88	175	37.7
17	7	5	2.5	140	175	63.1
18	7	5	4.5	140	175	55.7
19	7	5	3.5	140	175	59.3
20	7	5	3.5	140	175	58.9

[a] Injected volume (μL) of 50 mmol L^{-1} $FeSO_4$ solution (Table 3 – step 3).

[b] Injected volume (μL) of 200 mmol L^{-1} H_2O_2 solution (Table 3 – step 6).

of MC were defined to accommodate the monosegment, allowing one to perform well controlled dilutions of a single stock of standard using a total volume of up to 1000 μL of solution plus 250 μL of air (Tables 1 and 2).

Molecular absorption spectra of alizarin solutions adjusted to pH 2.5, 3.5 and 4.5 (only with HNO_3) show that, in the visible range of spectra, 422 nm is the wavelength of maximum molar absorptivity, being used for monitoring the degradation of the compound. It was also verified that alizarin absorbance read at 422 nm obeyed a linear relation for concentrations between 10 and 100 μmol L^{-1} at any pH from 2.5 to 4.5. Calibration of the system by dilution of a single 100 μmol L^{-1} alizarin stock solution was achieved in 24 min, including three repetitions at each concentration level of a five points calibration curve (Fig. 2). Washing MC at the end of each cycle was not necessary because the air bubble prevents dispersion from one sample solution into the next one, as is evidenced in Fig. 2 by the high reproducibility of the 10 μmol L^{-1} alizarin solution signal obtained just after processing the 100 μmol L^{-1} solution. The analytical signals were considered as the mean absorbance values read in the valley between the two sharp peaks generated by the air bubbles passing through the detector.

After addition of reagents, the reaction mixture (including alizarin) becomes dark-cloudy, followed by a fast pH decrease, more remarkably at pH 4.5 (decreased around 1 pH unit). Other pH (2.5 and 3.5) were less affected, being observed a decrease of less than 0.5 pH unit. As the reaction goes to completion, solution turns transparent or sometimes slightly yellow because of the iron content. No precipitation was observed during the experiment.

Table 5
Estimated regression coefficients for the first response surface design.

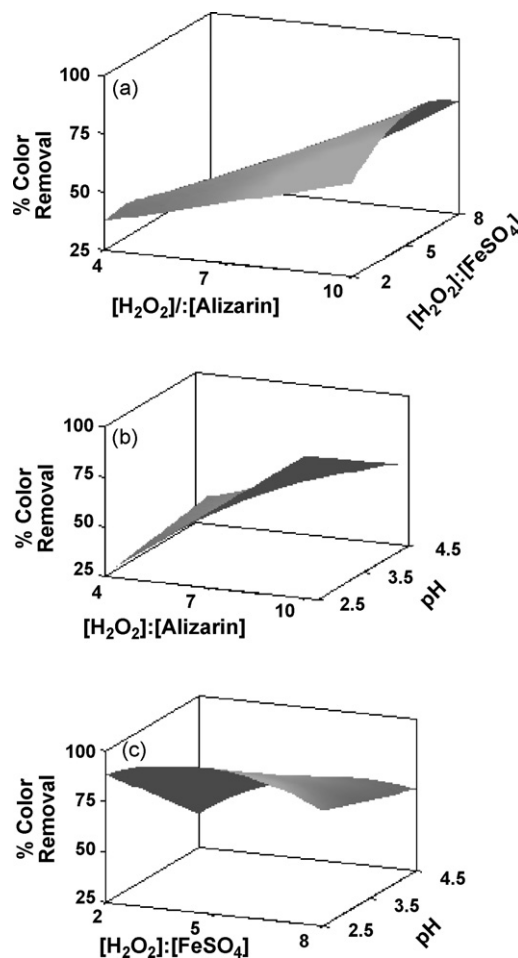| Term	Coefficient	Standard error of the coefficient	p-value
Constant	−1.780	28.9522	0.952
A	14.197	3.2343	0.001
B	−4.727	4.8961	0.353
C	4.998	7.3256	0.508
B^2	−1.303	0.3428	0.003
AB	1.046	0.2710	0.002
AC	−3.321	0.8130	0.002
BC	2.488	0.8130	0.010

Fig. 3. Response surfaces for percentage of color removal as a function of: (a) [H_2O_2]:[Alizarin] and [H_2O_2]:[$FeSO_4$] molar ratios (hold value: pH 3.5); (b) [H_2O_2]:[Alizarin] molar ratio and pH (hold value: [H_2O_2]:[$FeSO_4$] = 5); (c) [H_2O_2]:[$FeSO_4$] molar ratio and pH (hold value: [H_2O_2]:[Alizarin] = 10).

Table 6
Second response surface design performed at pH 3.5.

Run	$[H_2O_2]:[Alizarin]$	$[H_2O_2]:[FeSO_4]$	$FeSO_4$[a]	H_2O_2[b]	Color removal (%)
1	10	3	333	250	83.0
2	16	3	533	400	84.0
3	10	7	143	250	86.0
4	16	7	229	400	99.7
5	13	5	260	325	89.4
6	13	5	260	325	89.7
7	13	5	260	325	83.7
8	10	5	200	250	84.1
9	16	5	320	400	90.7
10	13	3	433	325	79.1
11	13	7	186	325	92.7
12	13	5	260	325	83.7
13	13	5	260	325	85.7
14	13	5	260	325	91.1

[a] Injected volume (μL) of 50 mmol L^{-1} FeSO$_4$ solution (Table 3 – step 3).
[b] Injected volume (μL) of 200 mmol L^{-1} H$_2$O$_2$ solution (Table 3 – step 6).

Table 7
Estimated regression coefficients for the second response surface design.

Term	Coefficient	Standard error of the coefficient	p-value
Constant	92.8827	14.9204	0.000
A	−1.4625	1.1285	0.224
B	−4.1875	2.8383	0.171
AB	0.5292	0.2146	0.033

3.2. First response surface

Table 4 shows the results obtained from the first response surface, a three factors central composite design, face centered, with 8 cube points, 6 axial points and 6 center points (from cube and axial portions), thus resulting in 20 runs. Factors and levels considered were: $[H_2O_2]:[alizarin]$ ratio (from 4 to 10); $[H_2O_2]:[FeSO_4]$ ratio (from 2 to 8) and pH (from 2.5 to 4.5). All ratios are mol based on a fixed value of 5 μmol of alizarin (the content in the beaker). Table 4 also shows the volumes of H$_2$O$_2$ and FeSO$_4$ solutions used in each run (complementary data from Table 3).

Table 5 summarizes the estimated regression coefficients from the quadratic model, where A = $[H_2O_2]:[Alizarin]$, B = $[H_2O_2]:[FeSO_4]$ and C = pH. The quadratic terms A^2 and C^2 were previously removed (not significant). This model has a high R^2 value (93.9%) and fails to describe points 3, 8 and 13, resulting in a model with lack of fit of experimental data. Despite of this poor fitting, the obtained response surfaces (Fig. 3) provided the following information: (a) best results were obtained at pH 2.5 and 3.5; (b) increasing $[H_2O_2]:[Alizarin]$ and decreasing $[H_2O_2]:[FeSO_4]$ ratios may lead to higher percentages of color removal; (c) the lower the $[H_2O_2]:[FeSO_4]$ ratio the higher becomes pH effect, and for higher pH values, less amounts of iron are needed. The best point was obtained at run 7, but considering reagents saving, run 14 also presented a close value to the best result.
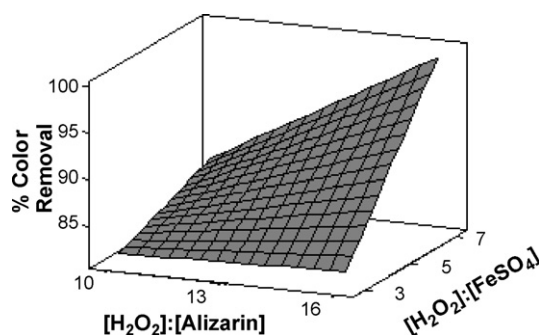

Fig. 4. . Second response surface for percentage of color removal as a function of the $[H_2O_2]:[Alizarin]$ and $[H_2O_2]:[FeSO_4]$ ratios at pH 3.5.

3.3. Second response surface

A second surface was constructed at pH 3.5 in order to better explore this region; other pH values were not considered because of the low process efficiency (pH 4.5) or high reagent consumption (pH 2.5), which could be economically prohibitive for large amounts of effluents. A two factors central composite design, face centered, with 6 center points, results in 14 runs. Factors and levels considered were: $[H_2O_2]:[alizarin]$ ratio (from 10 to 16) and $[H_2O_2]:[FeSO_4]$ ratio (from 3 to 7). The molar ratios, the set of volumes of H$_2$O$_2$ and FeSO$_4$ solutions used in each run (complementary data from Table 3) and the final results are presented in Table 6.

Table 7 summarizes the estimated regression coefficients from the linear and interactions model, where A = $[H_2O_2]:[Alizarin]$, B = $[H_2O_2]:[FeSO_4]$. Only the interaction term is statistically significant. This model has a R^2 value (81.4%) lower than that obtained by the first model, but the lack of fit error does not occur. Residues follow a normal distribution, according to Anderson–Darling nor-
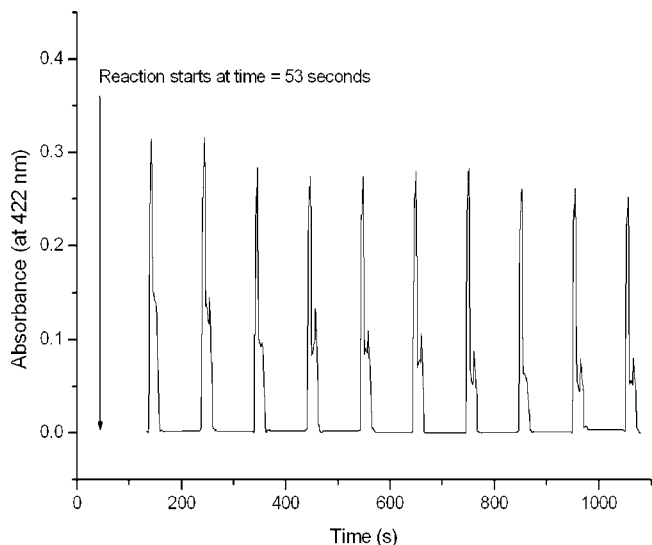
Table 8
Analysis of variance (ANOVA) for second response surface model.

Source of variation	Degrees of freedom	Sequential sum of squares	Adjusted mean square	F-value	p-value
Regression	3	289.82	96.606	14.57	0.001
Linear	2	249.50	7.391	1.11	0.366
Interaction	1	40.32	40.323	6.08	0.033
Residual error	10	66.29	6.629		
Lack of fit	5	13.24	2.648	0.25	0.923
Pure error	5	53.05	10.610		
Total	13	356.11			

Fig. 5. Registered data for run number four of the second response surface design. Data were smoothed by a 10 points adjacent averaging method. Blank reading was not subtracted in the graph.

mality test [20]. ANOVA results are presented in Table 8 and the final response surface is shown in Fig. 4.

A maximum color removal (99.7%) is obtained at run 4, where $A = 16$ and $B = 7$. Fig. 5 shows all registered data for run 4. Theoretical TOC value of a $100\,\mu\mathrm{mol\,L^{-1}}$ alizarin solution is $16.8\,\mathrm{mg\,L^{-1}}$. Experimental result for this solution is $17.0\,\mathrm{mg\,L^{-1}}$, being in agreement with the expected value. For the solution resulting from run 4 the TOC value was $5.8\,\mathrm{mg\,L^{-1}}$, implying in a TOC removal (sample mineralization) of 65%. The high $[\mathrm{H_2O_2}]$:$[\mathrm{FeSO_4}]$ ratio suggests an oxidation reaction mechanism where catalytic decomposition of $\mathrm{H_2O_2}$ ($2\mathrm{H_2O_2} \rightarrow 2\mathrm{H_2O} + \mathrm{O_2}$) accompanies the oxidation of $\mathrm{Fe^{2+}}$ ions [21].

4. Conclusions

The association of sequential injection analysis with the response surface methodology was shown to be a valuable approach to process optimization based on Fenton reaction. The large number of experiments needed to construct the response surface was automatically performed by the SIA system, without human interference during the reagent addition and color monitoring steps. This is an interesting feature that can be explored further in the application of the proposed methodology to construct response curves for degradation/mineralization of real wastewaters from coating industries. This procedure can also be used to

make inferences about reaction kinetics, since it is possible to change reagents initial concentrations and monitor the reaction progress.

The statistical model obtained was suitable for predicting and optimizing color removal within the range of variables used. In the first 15 min of the Fenton reaction, more than 95% of color removal can be achieved. This finding suggests an industrially feasible pretreatment process because fast color removal and significant TOC reduction were achieved in a very short period of time, a feature that would not be possible by using only direct biological treatments [11]. The main drawback associated with the use of Fenton oxidation in industrial scale would be the need for pH reducing followed by post-reaction neutralization.

References

[1] J.M.R. Fazenda, Tintas e Vernizes: Ciência e Tecnologia, vol. 1, 2nd ed., ABRAFATI, Brasil, 1995.
[2] A.C.V. dos Santos, Uso de técnicas eletroanalíticas em fluxo no estudo da adsorção de Cd(II), Pb(II) e Cu(II) em vermiculita visando tratamento alternativo para efluentes da indústria de tintas, MSc dissertation, Instituto de Química – USP, São Paulo, Brazil, 2006.
[3] A.C.V. dos Santos, J.C. Masini, Appl. Clay Sci. 37 (2007) 167.
[4] I.S. de Oliveira, L. Viana, C. Verona, V.L.V. Fallavena, C.M.N. Azevedo, M. Pires, J. Hazard. Mater. 146 (2007) 564.
[5] R.F.P. Nogueira, A.G. Trovó, M.R.A. da Silva, R.D. Vila, Quim. Nova 30 (2007) 400.
[6] E. Neyens, J. Baeyens, J. Hazard. Mater. B 98 (2003) 330.
[7] J.J. Pignatello, E. Oliveros, A. MacKay, Crit. Rev. Environ. Sci. Technol. 36 (2006) 1.
[8] B.B. Neto, I.E. Scarminio, R.E. Bruns, Como Fazer Experimentos – Pesquisa e Desenvolvimento na Ciência e na Indústria, 2ª edição, Editora da UNICAMP, Campinas, 2003.
[9] S.J. Kalil, F. Maugeri, M.I. Rodrigues, Process Biochem. 35 (2000) 539.
[10] S.D.M. Hasan, D.N.C. Melo, R.M. Filho, Chem. Eng. Process 44 (2005) 335.
[11] N.S.S. Martínez, J.F. Fernández, X.F. Segura, A.S. Ferrer, J. Hazard. Mater. B101 (2003) 315.
[12] C.T. Benatti, C.R.G. Tavares, T.A. Guedes, J. Environ. Manage. 80 (2006) 66.
[13] J. Ruzicka, G.D. Marshall, Anal. Chim. Acta 237 (1990) 329.
[14] A.C.V. dos Santos, J.C. Masini, Anal. Bioanal. Chem. 385 (2006) 1538.
[15] N.W. Barnett, C.E. Lenehan, S.W. Lewis, TrAC Trends Anal. Chem. 18 (1999) 346.
[16] M.J. Iqbal, M.N. Ashiq, J. Hazard. Mater. B139 (2007) 57.
[17] R.S. Freire, R. Pelegrini, L.T. Kubota, N. Duran, Quím. Nova 23 (2000) 504.
[18] C. Pasquini, W.A. Oliveira, Anal. Chem. 57 (1985) 2575.
[19] Standard Methods for the Examination of Water and Wastewater, 20th ed. American Public Health Association/American Water Works Association/Water Environment Federation, Washington, DC, 2003.
[20] R.B. D'Agostino, M.A. Stephens, Goodness-of-Fit Techniques, Marcel Dekker, New York, 1986.
[21] M.L. Kremer, Phys. Chem. Chem. Phys. 1 (1999) 3595.

Microfluidic-based electrochemical genosensor coupled to magnetic beads for hybridization detection

Francesca Berti [a], Serena Laschi [a], Ilaria Palchetti [a], Joël S. Rossier [b], Frédéric Reymond [b], Marco Mascini [a,c], Giovanna Marrazza [a,*]

[a] *Università degli Studi di Firenze, Dipartimento di Chimica, Via della Lastruccia 3, 50019 Sesto Fiorentino, Italy*
[b] *DiagnoSwiss S.A., Rte de l'Ile-au-Bois 2, 1870 Monthey, Switzerland*
[c] *Istituto Nazionale Biostrutture e Biosistemi (INBB), Unit of Florence, Viale delle Medaglie d'Oro 305, 00136, Roma, Italy*

ARTICLE INFO

ABSTRACT

This paper describes the development of a rapid and sensitive enzyme-linked electrochemical genosensor using a novel microfluidic-based platform. In this work, hybridization was performed on streptavidin-coated paramagnetic micro-beads functionalized with a biotinylated capture probe. The complementary sequence was then recognized via sandwich hybridization with a capture probe and a biotinylated signaling probe. After labeling the biotinylated hybrid with a streptavidin–alkaline phosphatase conjugate, the beads were introduced in a disposable cartridge composed of eight parallel microchannels etched in a polyimide substrate. The modified beads were trapped with a magnet addressing each microchannel individually. The presence of microelectrodes in each channel allowed direct electrochemical detection of the enzymatic product within the microchannel. Detection was performed in parallel within the eight microchannels, giving rise to the possibility of performing a multiparameter assay. Quantitative determinations of the analyte concentrations were obtained by following the kinetics of the enzymatic reaction in each channel. The chip was regenerated after each assay by removing the magnet and thus releasing the magnetic beads. The system was applied to the analytical detection of PCR amplified samples with a RSD% = 6. A detection limit of 0.2 nM was evaluated.

© 2008 Elsevier B.V. All rights reserved.

1. Introduction

In the last decade, several procedures and applications have been developed in order to obtain simple and portable devices for DNA diagnostics. In this context electrochemical genosensors couple the selectivity of the hybridization event with the sensitivity, compatibility with micro-fabrication, low cost and portability of electrochemical devices [1]. However, a recurring problem with electrochemical DNA detection is the background interference. The absorption of non-specific DNA sequences or enzymatic labels at the electrode surface, in fact, can reduce the sensitivity of the assay. To overcome this problem, in the past few years many researchers exploited the possibility of performing the hybridization event on the surface of paramagnetic micro- and nano-beads and several formats of magnetic bead-based electrochemical genosensors have been reported in literature [2–9]. Both label-free and enzyme-linked methods have been proposed by Wang et al. [2,3,6]. Palecek et al. [4] showed an enzyme-linked immunoassay for the detec-

tion of DNA hybridization event performed on paramagnetic beads with covalently bound a $(dT)_{25}$ probe, able to hybridize with target DNAs containing adenine stretches. Target DNAs were modified with osmium tetroxide,2,2′-bipyridine and the immunogenic DNA-Os, bipy adducts were determined by enzyme-linked immunoassay or, alternatively, by direct measurement of the Osmium signal by square wave voltammetry. Another interesting way to amplify the electrical signal was found by Kawde and Wang [7], who achieved a detection limit of 0.1 ng/mL using oligonucleotides functionalized with polymeric beads carrying gold nanoparticles. Lermo et al. [8] developed a genomagnetic assay for the detection of food pathogens based on a graphite–epoxy composite magneto electrode (m-GEC) as electrochemical transducer. The assay was performed in a sandwich format by double labeling the amplicon ends during PCR with a biotinylated capture probe, to achieve the immobilization on streptavidin-coated magnetic beads and a digoxigenin signaling probe, to achieve further labeling with the enzyme marker (anti-digoxigenin horseradish peroxidase).

These examples show interesting features; however, a significant challenge for all biosensor systems is minimizing sample preparation, requirements, operational complexity and time. Microfluidic-based platforms show great potential in responding

* Corresponding author. Tel.: +39 0554573320; fax: +39 0554573396.
E-mail address: giovanna.marrazza@unifi.it (G. Marrazza).

to these demands due to significant decrease in sample/reagent consumption and cost, and dramatically reduction in time [10]. Therefore, microfluidic devices have found great application in the proteomic [11,12] and genomic area [13,14]. Further advantages have been demonstrated by incorporating paramagnetic beads as transportable solid support [15–17]: analytes were captured by probe (i.e. DNA)-modified beads in flow through format. Small-diameter particles, in fact, help to enhance the surface area-to-volume ratio thus increasing the sensitivity. Moreover, magnetic properties greatly facilitate the delivery and removal of reagents through the microfluidic channels.

In this work, we report the development of a rapid and sensitive enzyme-linked electrochemical genosensor using a commercially available microfluidic-based platform. This was obtained by integrating the existing technology with a new electroanalytical procedure based on the use of paramagnetic beads. The proposed assay allowed the rapid analysis of PCR amplicons.

Only few examples of analytical procedures based on microfluidic platform coupled to paramagnetic beads for hybridization electrochemical detection were reported in literature [18,19]. Baeumner and co-workers [18] reported an interesting approach based on liposomes entrapping the electrochemical marker (ferro/ferricyanide couple).

The novelty of the proposed procedure was the combination of a sensitive electrochemical platform and a proper microfluidic with a simple and effective enzyme signal amplification technology.

In our approach, streptavidin-coated paramagnetic micro-beads were modified with a biotinylated capture probe. The complementary sequence was then recognized via sandwich hybridization with a capture probe and a biotinylated signaling probe. After labeling the biotinylated hybrid with a streptavidin–alkaline phosphatase conjugate, the particles were introduced in a disposable cartridge composed of eight parallel microchannels etched in a polyimide substrate (called chip) [20]. The modified particles were trapped with a magnet addressing each microchannel individually. The presence of microelectrodes in each channel allowed direct electrochemical detection of the enzymatic product within the microchannel. Detection was performed in parallel within the eight microchannels, giving rise to the possibility of performing a multiparameter assay. Quantitative determinations of the analyte concentrations were obtained by following the kinetics of the enzymatic reaction in each channel. The chip was regenerated after each assay by removing the magnet and thus releasing the magnetic beads. The system was applied to the analytical detection of PCR amplified samples. Our attention was focused on the detection of a 182 bp fragment of Cor a 1.04, the major hazelnut allergen [21–25].

The assay was also carried out using disposable electrochemical sensors as electrochemical transducers to optimize some parameters such as hybridization time, enzyme concentration and incubation.

2. Materials and methods

2.1. Reagents

Dithiothreitol (DTT), streptavidin–alkaline phosphatase, α-naphthyl phosphate, bovine serum albumin (BSA), magnesium chloride and diethanolamine were obtained from Sigma–Aldrich. Disodium hydrogenphosphate, ethylendiamine tetraacetic acid (EDTA) and potassium chloride were purchased from Merck. MilliQ water was used throughout this work. TE buffer $20\times$ (200 mmol/L Tris/HCl; 20 mmol/L EDTA; pH 7.5), Picogreen and λ-DNA standard solution (100 µg/mL), used for fluorescent measurements, were obtained from Molecular Probes.

p-Aminophenyl phosphate was purchased from DiagnoSwiss S. A. (Monthey, Switzerland). Streptavidin-coated paramagnetic beads (iron oxide particles with the diameter of approximately 1.0 ± 0.5 µm) were purchased from Promega (USA). Synthetic oligonucleotides were obtained from MWG Biotech AG. Genomic DNA from hazelnut was obtained using the extraction kit Sure Food PREP-Allergen (Congen). *Taq* polymerase, dNTP mixture and PCR buffer were obtained from Takara. The sequences of synthetic oligonucleotides, PCR primers and the PCR amplicon are reported below:

Capture probe (24 mer): biotin-5′-GGA GAT CGA CCA CGC AAA CTT CAA-3′ Signaling probe (20 mer): 5′-ATA CTG CTA CAG CAT CAT CG-TEG-biotin-3′ where TEG (tetra-ethyleneglycol) was used as spacer arm Forward primer (24 mer): 5′-GGA GAT CGA CCA CGC AAA CTT CAA-3′ Reverse primer (23 mer): 5′-CCT CCT CAT TGA TTG AAG CGT TG-3′ PCR amplified fragment of the Cor a 1.04 gene (182 bp) of hazelnut: 5′-GGAGATCGACCACGCAAACTTCAAATACTG-CTACAGCATCATCGAGGGAGGTCCA TTGGGGCACACACTGGAGAAGA-TCTCTTACGAGATCAAGATGGCGGCAGCCCCTCATGGAGGAGGATCCA TCTTGAAGATCACCAGCAAGTACCACACCAAGGGCAACGCTTCAATCAA TGAGGAGG-3′.

2.2. Disposable screen-printed electrodes

Screen-printed electrochemical cell (SPEC) consists of a carbon working electrode, a carbon counter electrode and a silver pseudo-reference electrode. Materials and procedures to screen-print the transducers are described elsewhere [26].

The DPV electrochemical measurements were performed with µAutolab type II PGSTAT with a GPES 4.9 software package (Metrohm, Rome, Italy). All potentials were referred to the Ag/AgCl pseudo-reference electrode. All experiments were carried out at room temperature (25 °C).

To perform electrochemical measurement SPECs were kept horizontally and a magnet holding block was placed on the bottom part of the electrode, to better localize the beads onto the working surface. Then a known volume of a solution containing the enzymatic substrate was added on the SPEC surface to close the electrochemical cell. In further sections these disposable electrochemical sensors will be called "drop-on system".

2.3. Microfluidic-based platform

A microfluidic-based platform, produced by DiagnoSwiss S.A., was used. This platform consists of a disposable cartridge called ImmuChip™, an instrument called ImmuSpeed™ and its associated software ImmuSoft™.

ImmuChip™ consists of eight parallel microchannels etched in a polyimide substrate at distances compatible with conventional 96-well plate automation [11]. The fabrication process of the microchannel systems was described elsewhere [11,12]. Each microchannel contains a housing with a sample deposition reservoir (well), and it was etched in a polyimide body with inlet/outlet in contact with microelectrode tracks. The microchannels have a length of 1 cm and a total volume of 65 nL. The upper part of each channel contains an array of 48 gold working microelectrodes. A counter electrode and an Ag/AgCl pseudo-reference electrode are placed at the bottom of the well, near the channel entrance. ImmuChip™, called simply chip throughout the text, is shown in the Fig. 1A.

ImmuSpeed™ is composed of an interface to plug the disposable cartridge, a temperature controller, a multichannel pumping device and valves as well as a multiplexer electrochemical detector for sequential detection occurring in each of the eight channels (Fig. 1B).
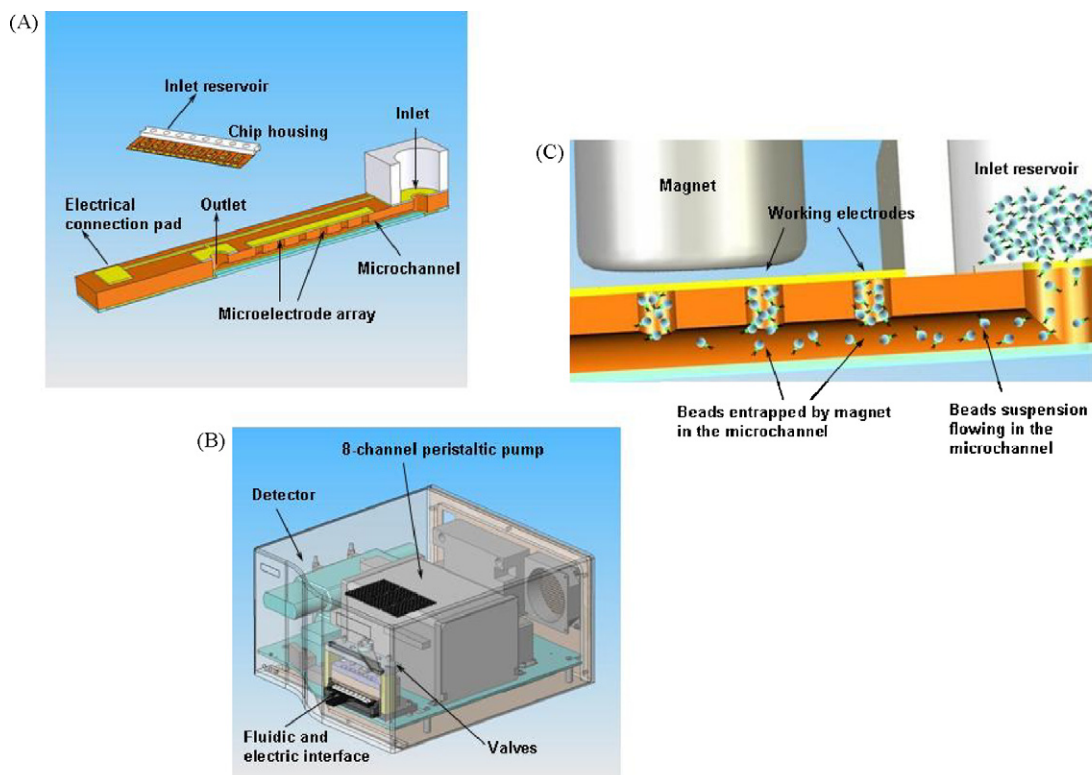
Fig. 1. (A) Technical drawing of the chip: ImmuChip™; (B) technical drawing of the microfluidic-based platform ImmuSpeed™; (C) technical drawing of a microchannel cross-section with flowing magnetic beads being captured by a magnet.

A special software (ImmuSoft™) has been created to integrate the fluidic and the electrochemical detection. The software enables the application of independent protocols in the different channels. Sample and reagent solutions are aspirated from the inlet reservoir through the reaction channel to the waste, but the solution flow can be directed in both directions, allowing the construction of protocols with back flow. The fluidic can also be regulated in order to alternate times in which the liquid flows into the channels with times where the solution remains static: in this case parameters as well as the time during which the liquid should flow through the channels, the flow rate and the turnover at which this mode should be repeated, in order to have more "loading cycles", can be also varied. This last procedure allows to increase the contact time of the solution with the well of channels and ensures an efficient steady state of the solutions during the incubation and/or detection steps.

An electrochemical detection step is then added to complete the protocol. This is performed by real-time chronoamperometric technique, in which the kinetics of the enzyme-label reaction are followed, by measuring the current alternatively on each channel and then reporting it vs. time. Detection parameters are introduced to the protocol by the user. Apart from the applied potential, parameters that can be tuned are the time interval between two chronoamperometric measurements as well as the number of such measurements cycles, which are influencing the duration of each measurement (acquisition time).

In this particular application, the chip was integrated with a dedicated magnet to capture the beads into the channel, as described in Fig. 1C. Eight cylinder magnets, supported in a bar, were inserted between the chip and instrument interface in order to capture the beads flowing through the channel at the electrode position.

All experiments were carried out at 37 °C.

2.4. DNA modification of streptavidin-coated paramagnetic beads

The modification of the beads with biotinylated capture probe was carried out on aliquots of 0.75 mL, containing 1 mg/mL of beads. The beads were washed three times with 600 μL of phosphate buffer 0.5 M, pH 7.0 (using a magnetic particle concentrator – MagneSphere Magnetic Separation Stand, Promega) and re-suspended in 500 μL of buffer containing 1.0 nmol of capture probe/mg of beads. After an incubation of 30 min, under continuous mixing, the beads were washed three times with phosphate buffer. Finally, the modified beads were incubated for 15 min with 500 μL of 500 μM solution of biotin in phosphate buffer, to block the remaining streptavidin active sites on the probe-functionalized surface, in order to prevent the undesired binding of other biotinylated oligonucleotides. After the treatment, the beads were then washed three times with phosphate buffer and re-suspended to 1 mg/mL in buffer. The modified beads can be stored at 4 °C until use [6]. Their stability was experimentally demonstrated by hybridization experiments performed using the same aliquot of beads freshly modified, after 1 week and after 1 month. By comparing signals obtained for a 5 nM oligonucleotide target sequence (100 ± 4 nA for freshly modified beads, 95 ± 1 nA after 1 week, 90 ± 2 nA after 1 month) only a 10% decrease was observed after 1 month.

2.5. PCR amplification

The conditions for the PCR amplification of the gene sequence codifying for Cor a 1.04 allergen were adapted from the procedure reported in literature [24]. The DNA template was extracted from raw hazelnuts using the commercial kit Sure Food PREP-Allergen (Congen), according to the manufacturer's instructions. The PCR reaction was carried out in a final volume of 50 μL containing PCR buffer 1× 1.5 mM MgCl₂, 1.2 U/mL of *Taq* polymerase, 200 μM of

dNTPs (deoxyribonucleotide triphosphates), 0.25 µM of forward primer, 0.25 µM of reverse primer and 500 ng of genomic DNA. The PCR was performed with a MJ Research PTC 150 thermocycler (MJ Research Inc.) using the following conditions: activation of *Taq* polymerase at 95 °C for 5 min, followed by a 40 two-step cycles (94 °C for 30 s, 63 °C for 30 s) and a final extension at 72 °C for 10 min. Prior to use, PCR amplicons were purified using Millipore Montage PCR centrifugal filter devices according to the manufacturer's protocol. Their concentration was finally determined by fluorescence measurements using the Picogreen dye and a TD-700 fluorometer (Analytical Control).

2.6. Hybridization procedure

Hybridization experiments were carried out in a sandwich-like format (see Fig. 2). Synthetic target and PCR amplicons were diluted with a solution 0.15 µM of biotinylated signaling probe in phosphate buffer. In the case of PCR amplicon, the double-stranded DNA was thermally denatured by using a boiling water bath (5 min at 100 °C); amplicon strand re-annealing was retarded by cooling the sample in an ice-water bath for 1 min. Both the PCR blank and non-complementary PCR products were used as negative controls. For every assay 20 µL of probe-modified beads were employed. Using the magnetic particle concentrator, the buffer was removed carefully and then the beads were incubated with 50 µL of the hybridization solution for 15 min. After hybridization, the beads were washed three times with 100 µL of DEA buffer (0.1 M diethanolamine, 1 mM $MgCl_2$, 0.1 M KCl; pH 9.6), to remove non-specifically adsorbed sequences.

2.7. Labeling with alkaline phosphatase

After the hybridization and washing steps, the beads were incubated with 50 µL of a solution containing 0.75 U/mL of the streptavidin–alkaline phosphatase conjugate and 10 mg/mL of BSA (blocking agent) in DEA buffer. After 20 min, beads were washed three times with 100 µL of DEA buffer.

2.8. Electrochemical detection: drop-on system

After washing, the beads were re-suspended in 25 µL. The electrochemical measurements were performed by placing a magnetic particle concentrator under the SPEC; 10 µL of enzyme-labeled bead suspension was deposited on the working electrode surface, and the liquid was carefully removed with a pipette without touching the electrodes. Then, the planar electrochemical cell was covered with 50 µL of 1 mg/mL α-naphthyl phosphate in DEA buffer. After 5 min, the electrochemical signal of the enzymatically produced α-naphthol was measured by DPV (modulation time 0.05 s; interval time 0.15 s; step potential 5 mV; modulation amplitude 70 mV; potential scan from 0 to +0.6 V). Upon scanning the potential, the α-naphthol was irreversibly converted into an electro polymerized derivative; the height of its oxidation peak was taken as the analytical signal. Reported results are the average of at least three measurements and the error bars correspond to the standard deviation.

2.9. Electrochemical detection: microfluidic-based platform

After washing, the beads were re-suspended in 135 µL. A volume of 20 µL of bead suspension was added in each inlet reservoir of the ImmuChip™. The solution was then introduced in the microchannels by applying the optimized loading cycles; during the loading cycles, a suitable magnet was used in order to allow for the blocking of the beads within each microchannel. Once all the suspensions

were introduced and the beads captured, the substrate solution was added. Following the manufacturer's instructions, *p*-aminophenyl phosphate (10 mM in DEA buffer) was used as enzymatic substrate.

The chronoamperometric measurement of the enzyme kinetics was performed in a static mode, i.e. without flow. The eight channels were then sequentially measured, each 2 s, at a potential of +250 mV vs. Ag/AgCl, for a total acquisition time of 3 min; in this way many measuring cycles are recorded, and a plot of current as function of time is obtained for each channel. The slope of the linear portion of the plot, which is a direct measure of the *p*-aminophenol concentration and hence of the enzyme concentration, was used as analytical data. An example of enzyme kinetics acquisition data, obtained by adsorbing only alkaline phosphatase enzyme in the microchannels, is reported in the Fig. 3. The data elaboration was performed using the software incorporated in the DataFitX fitting tool (Oakdale Engineering, USA).

3. Results and discussion

3.1. Optimization of magnetic bead-genosensor assay using drop-on system

The magnetic beads assay scheme is shown in Fig. 2. Preliminary experiments were performed using disposable electrochemical sensors in order to optimize some parameters (i.e. modification of beads, assay times and procedures). This allowed us to control the reliability of the DNA beads modification process with an experimental set-up already tested for other analytical applications [27] and thus by avoiding any effect due to flow conditions. The experiments were performed using 10 nM solution of hazelnut amplicon corresponding to Cor a 1.04 gene.

The influence of the probe concentration was firstly investigated. The declared binding capacity of paramagnetic beads is 0.75 nmol of biotinylated oligonucleotides/mg of beads. However, in the analysis of long, double stranded sequences, as PCR products, the base-pair recognition might be decreased by electrostatic repulsions and the high steric interference. By varying the probe concentration, different densities of biorecognition sites can be obtained on the beads with, consequently, variations in hybridization efficiency. The experiment was performed by modifying five aliquots of beads with different concentrations of capture probe solution (0.15, 0.75, 1.0, 3.2, 7.5 nmol/mg). Results obtained (not shown) demonstrated that using a solution of 1 nmol/mg a good compromise between intensity of signal and amount of employed reagents could be achieved. The analytical signal obtained was, in fact, $1.3 \times 10^{-8} \pm 2 \times 10^{-9}$ A, whereas for lowest concentration tested (0.15 nmol/mg) was $0.70 \times 10^{-8} \pm 3 \times 10^{-9}$ A and for the highest (7.5 nmol/mg) a value of $1.5 \times 10^{-8} \pm 3 \times 10^{-9}$ A was obtained.

Afterwards, the hybridization time was optimized. Probe-modified and biotin-blocked beads (20 µg) were incubated with 50 µL of the hybridization solution for 10, 15, 30, 45, 60 min. As reported in Fig. 4, the hybridization occurred with maximum efficiency after 15 min. The reported results exhibit very low specific vs. non-specific signal ratio. Thus, 15 min of incubation time was used for further measurements.

Then, the labeling step was investigated. Thus, five aliquots of beads, modified with biotinylated hybrid, were exposed to 50 µL of solution containing different concentrations of streptavidin–alkaline phosphatase and 10 mg/mL of BSA in DEA buffer. As reported in Fig. 5, signal shows a dramatic increase with the enzyme concentration. Only for concentrations higher than 0.75 U/mL a considerable signal amplification can be observed. Probably for a small amount of enzyme, which is moreover dis-
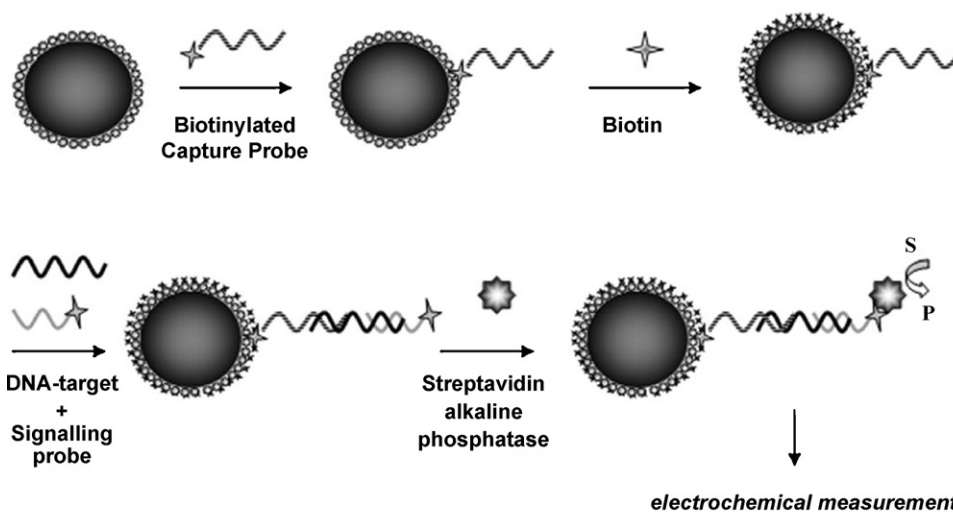
Fig. 2. Scheme of the genomagnetic assay: streptavidin-coated paramagnetic microparticles were functionalized with a biotinylated capture probe and the remaining streptavidin active sites were blocked with biotin. The complementary sequence was hybridized with capture probe in the presence of a biotinylated signaling probe. The biotinylated hybrid was labeled with a streptavin–alkaline phosphatase conjugate. Subsequently, the particles were magnetically absorbed onto the working electrode. The electrochemical cell was then covered with the substrate and the enzymatic product was measured.

persed in a highly viscous solution (BSA), the kinetic of association with biotinylated hybrid is too slow. The best specific vs. non-specific signal ratio (20:1) was obtained for a concentration of 0.75 U/mL of streptavidin–alkaline phosphatase. This concentration was used for further experiments. The influence of the enzyme–biotin association time on analytical signal was finally examined. Results are showed in Fig. 6. The kinetics of reaction appear very fast since high analytical signal can be observed after very short times. The optimal value was found to be 10 min for the enzyme–biotin association time and no relevant increasing of the signal can be observed for longer periods.

A calibration experiment of PCR amplicons was finally performed using the optimized conditions. The voltammet-ric response increased with the target concentration up to 10 nmol/L ($r^2 = 0.98$), then slowly decreased (Fig. 7). This behavior has been elsewhere explained as a consequence of the re-annealing of the two complementary strands [28]. When the amount of target in solution is relatively high, random collisions of reagents make re-annealing of the two complementary sequences favored over formation of the probe-amplicon hybrid. The non-specific signal, obtained using a non-complementary sequence, resulted negligible even at the highest investigated concentration, thus confirming the good selectivity of the genosensor.

The reproducibility of the measurements (evaluated as relative standard deviation over 8 results for a 10 nmol/L solution) was 8%.
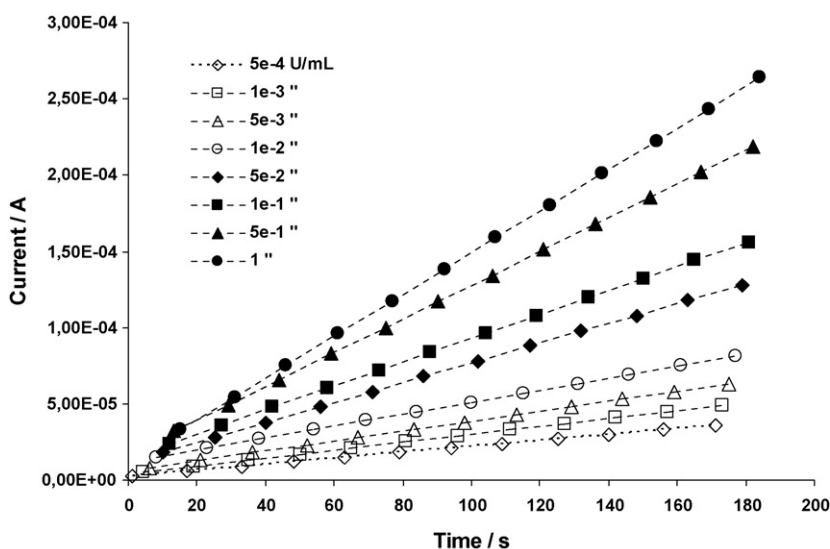

Fig. 3. Chrono-amperometric detection of enzyme kinetics in a chip. The experiment was performed by adsorbing on the walls of the microchannels different amounts of alkaline phosphatase (from 1 to 5 10^{-4} U/mL, in channel from 1 to 8) and then introducing the enzyme substrate. Each symbol represents a single current acquisition value. Data were then elaborated using the DataFitX fitting tool, obtaining for each channel a plot of current as a function of time. The slope of the linear portion of the plot, which is a direct measure of the *p*-aminophenol concentration and hence of the enzyme concentration, was used as analytical data. The chrono-amperometric detection was performed at +250 mV vs. Ag/AgCl.
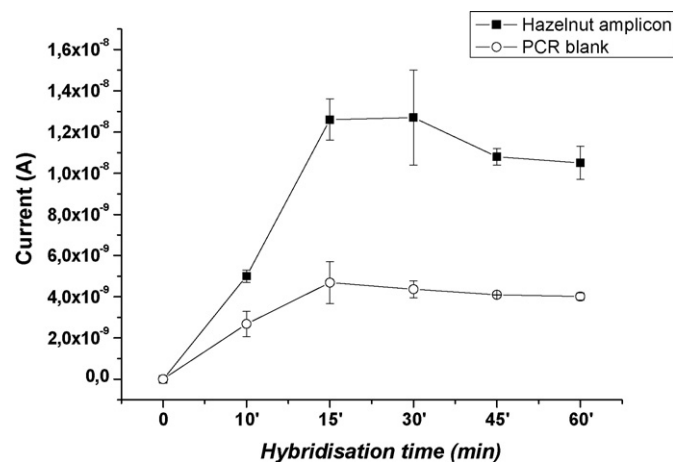
Fig. 4. Influence of hybridization time on the analytical signal. 20 µg of probe-modified and biotin-blocked beads were incubated with 50 µL of the hybridization solution for 15, 30, 45, 60 min. The experiments were performed using drop-on system. See detail in the text.

3.2. Procedure optimization using microfluidic-based platform

Key parameters to test the magnetic bead-based genosensor in the microfluidic-based platform were the procedure for bead capture in the microchannel of the chip and protocols for the electrochemical evaluation of the enzyme kinetic. This set of experiments was performed using beads modified with a target concentration of 10 nM and the assay conditions as optimized in paragraph 3.1.

The first set of experiments was devoted to develop a suitable procedure for beads capture within the microchannels. For this reason, two different loading operations were compared. The experiments were performed by depositing a volume of 20 µL of beads suspension into each of the eight inlet reservoirs of a chip. In the first loading protocol, after placing the magnet, as illustrated in Fig. 1C, a flow rate of 10 µL/min was applied for 2 min until the bead suspension was completely introduced into each channel. The flow was, then, reversed and kept at a rate of 5 µL/min in order to

Fig. 6. Influence of enzyme–biotin interaction time on the analytical signal. After the hybridization step, beads were incubated with 50 µl of solution containing 0.75 of streptavidin-alkaline phosphatase and 10 mg/ml of BSA in DEA buffer for different times (5, 10, 20, 40 min.). Then, the cell was covered with 50 µL of 1 mg/ml α-naphthyl phosphate in DEA buffer and incubate for 5 min. The experiments were performed using drop-on system. See detail in the text.

allow the complete capture of the beads. After 4 min, the solution was removed from the wells, and 20 µL of 20 mM p-aminophenyl phosphate was added and introduced into the channel at a flow rate of 2 µL/min. After 30 s, the flow was stopped and sequential chronoamperometric measurements of 2 s for a total time of 6 min were carried out. The same experiment was performed with two different bead suspension amounts (1 and 3 mg/mL, respectively); results demonstrated that this strategy was characterized by low reproducibility for both amounts and it was considered as not useful (data not shown). Thus, more loading cycles were introduced and the reverse phase was eliminated, in order to increase the efficiency of the assay. In this approach, each loading step comprised 2 s at 2 µL/min flow through and 3 s of steady state without flow. A total number of 100 loading cycles was used, and then the electrochemical detection step was carried out as previously. Four different
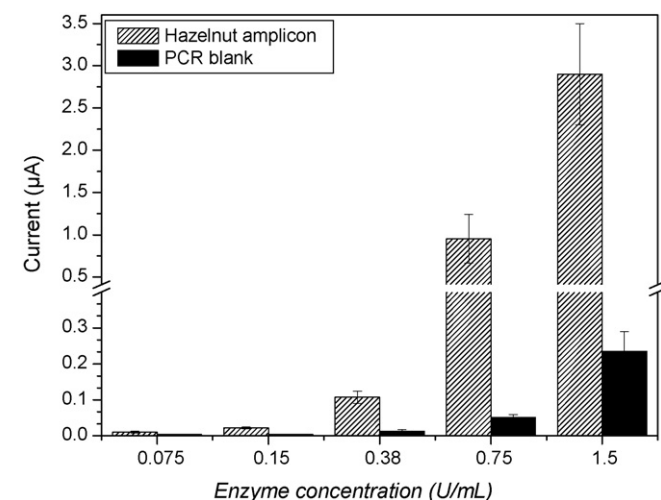

Fig. 5. Influence of enzymatic conjugate concentration on the analytical signal. After the hybridization step, beads were incubated with 50 µl of solution containing different concentrations (0.075, 0.15, 0.38, 0.75, 1.5 U/ml) of the streptavidin–alkaline phosphatase conjugate and 10 mg/ml of BSA (blocking agent) in DEA buffer for 20 min. The experiments were performed using drop-on system. See detail in the text.
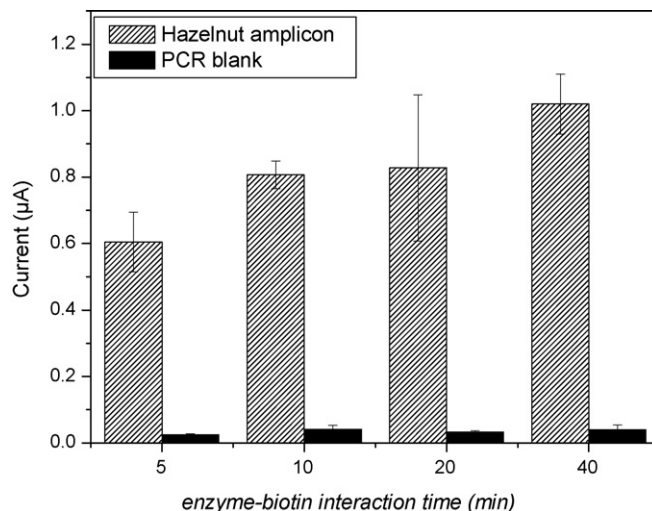

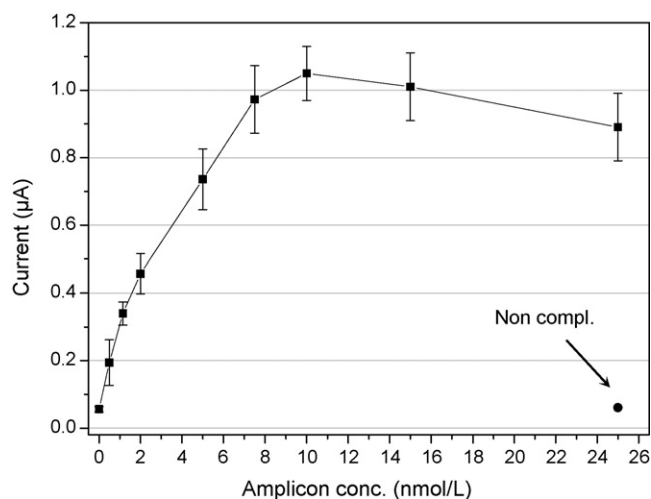**Fig. 7.** Calibration plot for Cor a 1.04 amplicons. Probe-modified and biotin-blocked beads were incubated for 15 min with 50 µL of thermally denatured target solutions, diluted to the desired concentration (0, 1, 2, 5, 7.5, 10, 15, 25 nmol/L) with a solution 0.15 µM of a biotinylated signaling probe in phosphate buffer. The experiments were performed using drop-on system. See detail in the text.

Table 1
Evaluation of *p*-aminophenyl phosphate concentration on the sensitivity of the assay

PAPP concentration (mM)	Acquisition time: 3 min	
	Linear slope (μA/s)	r^2
20	$(9.4 \pm 0.3) \times 10^{-8}$	0.999
10	$(4.2 \pm 0.6) \times 10^{-6}$	0.990
5	$(5.1 \pm 1.2) \times 10^{-7}$	0.55

Experiments were performed with the microfluidic-based electrochemical platform. Other details in the text.

bead suspensions (0.15, 0.5, 1.0, 3.0 mg/mL) were tested. The higher sensitivity was obtained by decreasing the beads amount (data not shown). These results could be due to the fact that high amount of beads reduced the flow efficiency into the microchannels. For 0.5 mg/mL beads suspension, a sensitivity of $(4 \pm 1) \times 10^{-6}$ A/nM was observed; this was the highest sensitivity obtained, but associated with a large standard deviation (RSD% = 25). The best result was obtained for a concentration of 0.15 mg/mL, where a lower slope was observed (2×10^{-6} A/nM) but with the highest reproducibility (RSD% = 10, n = 8). This amount of beads was then used for further experiments.

Finally, the concentration of *p*-aminophenyl phosphate was optimized in order to get the higher sensitivity and to avoid the inhibition of the enzymatic activity due to the substrate concentration excess. During the electrochemical measurement step, three different *p*-aminophenyl phosphate concentrations were used, in combination with two different acquisition times, 6 and 3 min, respectively. In the case of 6 min it was found that, between the three *p*-aminophenyl phosphate concentrations tested (20, 10 and 0.5 mM), a linear slope trend (r^2 = 0.999) was obtained only for the 20 mM concentration. Otherwise, by decreasing the data acquisition time from 6 to 3 min, a higher sensitivity with a good linear correlation (r^2 = 0.990) was obtained for 10 mM as substrate concentration (Table 1). Thus, this concentration was then used for the assay, taking advantage from the minor reagent consumption coupled with a shorter detection time.

3.3. Analysis of PCR-amplified samples

Experiments of PCR amplicons were then performed. Different amplicon concentrations (0, 2, 5, 10, 15, 20, 30 nM) and a 30 nM of non-specific sequence solution were analyzed. Each concentration was tested in a different channel. After measurement, the
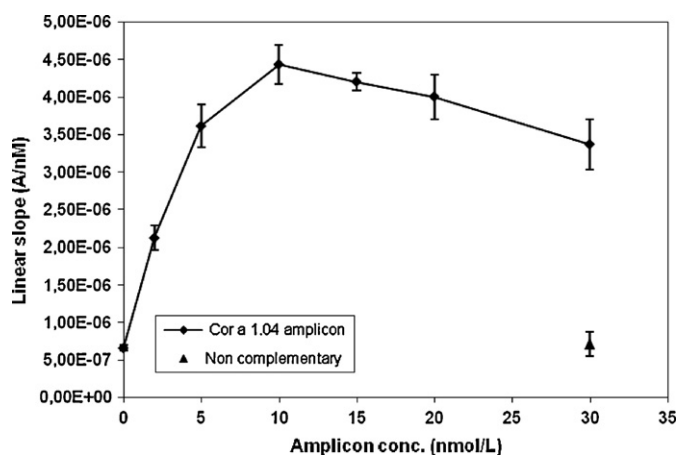
magnet was removed and the microchannels were washed with deionized water for 5 min with a flow rate of 5 μL/min. Then, fresh aliquots of beads were added in the microchannels and measurements were repeated. This procedure was performed for three times. As reported in Fig. 8, the response increased with the target concentration up to 10 nmol/L, and then slowly decreased. This behavior was the same observed with "drop-on sensor" system (Fig. 7), even if the electrochemical measurement procedure was different. In our opinion, the key factor to explain this trend is that the bead modification process (i.e. capture probe concentration, target hybridization time, enzyme concentration) was the same for both the measurement strategies.

The overall procedure (including sample amplification, target hybridization and labeling, measurement, data presentation) takes approximately 90 min.

The reproducibility of the measurements (evaluated as relative standard deviation over three results for 10 nM solution) was 6%.

We demonstrated that target concentrations at nM levels can be easily detected. Moreover, the reliability of the method was also demonstrated, with the low signal of the non-specific sequence ($7 \pm 2 \times 10^{-7}$ A/nM).

A detection limit of 0.2 nM was calculated considering the slope of the linear portion of the calibration curve (0–5 nM), fitting in the following equation $Y = 6 \times 10^{-7}X + 9 \times 10^{-7}$ the mean of the blank solution response plus three times its standard deviation.

4. Conclusions

In this work a rapid and sensitive enzyme-linked electrochemical genomagnetic assay using a microfluidic system was developed. The integration of microfluidic-based platform with a new analytical procedure based on the use of paramagnetic beads allowed the possibility to measure nM level of DNA sequences, with high reproducibility. The hybridization reaction has been carried out on probe-modified paramagnetic micro-particles, freely moving in solution, thus favoring random collisions between reagents. Moreover, magnetic properties of the particles allow an easy separation from the solution with the consequent possibility of avoiding the absorption of non-specific DNA sequences or enzymatic labels at the electrode surface.

Further work will be devoted to investigate the possibility of automation of beads modification and integration in the microfluidic-based platform, in line with the concept of Lab-on – a chip technology. Even if the procedure was demonstrated with DNA sequences, however other affinity biomolecules such as aptamers or classical antibodies can undoubtedly benefit from the use of paramagnetic beads integrated in a microfluidic-based platform, using the set-up developed in this work.

Fig. 8. Calibration plot for Cor a 1.04 amplicons. Probe-modified and biotin-blocked beads were incubated for 15 min with 50 μL of thermally denatured target solutions, diluted to the desired concentration. Experiments were performed with the microfluidic-based electrochemical platform. Other details in the text.

References

[1] F. Lucarelli, G. Marrazza, A.P.F. Turner, M. Mascini, Biosens. Bioelectron. 19 (2004) 515.
[2] J. Wang, A. Kawde, A. Erdem, M. Salzar, Analyst 126 (2001) 2020.
[3] J. Wang, R. Polsky, D. Xu, Langmuir 17 (2001) 5739.
[4] E. Palecek, S. Billovà, L. Havran, R. Kizek, A. Miculkova, F. Jelen, Talanta 56 (2002) 919.
[5] E. Palecek, M. Fojta, Talanta 74 (2007) 276.
[6] J. Wang, D. Xu, A. Erdem, R. Polsky, M.A. Salazar, Talanta 56 (2002) 931.
[7] A.N. Kawde, J. Wang, Electroanalysis 16 (2004) 101.
[8] A. Lermo, S. Campoy, J. Barbè, S. Hernadez, S. Alegret, M.I. Pividori, Biosens. Bioelectron. 22 (2007) 2010.
[9] A. Erdem, D.O. Ariksoysal, H. Karadeniz, P. Kara, A. Sengonul, A.A. Sayiner, M. Ozsoz, Electrochem. Commun. 7 (2005) 815.
[10] M. Pumera, A. Merkoci, S. Alegret, Trends Anal. Chem. 25 (2006) 219.
[11] J.S. Rossier, C. Vollet, A. Carnal, G. Lagger, V. Gobry, H.H. Girault, P. Michel, F. Reynold, Lab. Chip 2 (2002) 145.
[12] J.S. Rossier, F. Reymond F, in: Alegret and Merkoçi (Eds.), Comprehensive Analytical Chemistry, vol. 49, Elsevier, pp. 885–905.

[13] R.H. Liu, J. Yang, R. Lenigk, J. Bonanno, P. Grodzinski, Anal. Chem. 76 (2004) 1824.
[14] D. Liu, R.K. Perdue, L. Sun, R.M. Crooks, Langmuir 20 (2004) 5905.
[15] Z.H. Fan, S. Mangru, R. Granzow, P. Heaney, W. Ho, Q. Dong, R. Kumar, Anal. Chem. 71 (1999) 4851.
[16] M.A. Hayes, N.A. Polson, A.N. Phayre, A.A. Garcia, Anal. Chem. 73 (2001) 5896.
[17] H. Zhang, S.M. Mitrovsky, R. Nuzzo, Anal. Chem. 79 (2007) 9014.
[18] S. Kwakye, V.N. Goral, A.J. Baeumner, Biosens. Bioelectron. 21 (2006) 2217–2223.
[19] V.N. Goral, N.V. Zaytseva, A.J. Baeumner, Lab. Chip 6 (2006) 414–421.
[20] D. Hoegger, P. Morier, C. Vollet, D. Heini, F. Reymond, J.S. Rossier, Anal. Bioanal. Chem. 387 (2007) 267.
[21] M. Besler, Trends Anal. Chem. 20 (2001) 662.
[22] A. Germini, E. Scaravelli, F. Lesignoli, S. Sforza, R. Corradini, R. Marchelli, Eur. Food Res. Technol. 220 (2005) 619.
[23] H. Hird, J. Lloyd, R. Goodier, J. Brown, P. Reece, Eur. Food Res. Technol. 217 (2003) 265.
[24] T. Holzhauser, A. Wangorsh, S. Vieths, Eur. Food Res. Technol. 211 (2000) 360.
[25] O. Stephan, S. Vieths, J. Agric. Food Chem. 52 (2004) 3754.
[26] S. Laschi, I. Palchetti, G. Marrazza, M. Mascini, J. Electroanal. Chem. 593 (2006) 211–218.
[27] S. Centi, E. Silva, S. Laschi, I. Palchetti, M. Mascini, Anal. Chim. Acta 594 (2007) 9.
[28] M.L. Del Giallo, F. Lucarelli, E. Cosulich, E. Pistarino, B. Santamaria, G. Marrazza, M. Mascini, Anal. Chem. 77 (2005) 6324.

Differentiation of the volatile profile of microbiologically contaminated canned tomatoes by dynamic headspace extraction followed by gas chromatography–mass spectrometry analysis

F. Bianchi[a], M. Careri[a], A. Mangia[a], M. Mattarozzi[a], M. Musci[a,*],
I. Concina[b,c], M. Falasconi[b], E. Gobbi[d], M. Pardo[b], G. Sberveglieri[b]

[a] *Dipartimento di Chimica Generale ed Inorganica, Chimica Analitica, Chimica Fisica, Università degli Studi di Parma, Viale Usberti 17/A, 43100 Parma, Italy*
[b] *SENSOR Laboratory, CNR-INFM, Dipartimento di Chimica e Fisica per l'Ingegneria e per i Materiali, Università di Brescia, Via Valotti 9, 25133 Brescia, Italy*
[c] *CNR-Istituto di Biofisica, Via La Malfa 153, 90146 Palermo, Italy*
[d] *DBADP, Università di Udine, Via Scienze 208, 33100 Udine, Italy*

ARTICLE INFO

ABSTRACT

The aromatic profile of microbiologically contaminated canned tomatoes was analyzed by the dynamic headspace extraction technique coupled with gas chromatography–mass spectrometry. Canned tomatoes contaminated with *Escherichia coli*, *Saccharomyces cerevisiae* and *Aspergillus carbonarius* were analyzed after 2 and 7 days. About 100 volatiles were detected, among which alcohols, aldehydes and ketones were the most abundant compounds. Gas chromatographic peak areas were used for statistical purposes. First, principal component analysis was carried out in order to visualize data trends and clusters. Then, linear discriminant analysis was performed in order to detect the set of volatile compounds ables to differentiate groups of analyzed samples. Five volatile compounds, i.e. ethanol, β-myrcene, *o*-methyl styrene, 6-methyl-5-hepten-2-ol and 1-octanol, were found to be able to better discriminate between uncontaminated and contaminated samples. Prediction ability of the calculated model was estimated to be 100% by the "leave-one-out" cross-validation. An electronic nose device was then used to analyze the same contaminated and not contaminated canned tomato samples. Preliminary results were compared with those obtained by dynamic headspace gas chromatography–mass spectrometry, showing a good agreement.

© 2008 Elsevier B.V. All rights reserved.

1. Introduction

Tomato is a basic component of the Mediterranean diet and it is frequently consumed in several European countries, both fresh and processed. Fresh and processed vegetables can be exposed to safety risk related to the presence of microbial contaminants, like bacteria, yeasts and fungi [1,2], due both to their high-water content and to their pH values within the growth range of different spoilage microorganism.

The microbial contamination of food represents a serious health concern, since it can cause foodborne outbreaks. Among bacteria, *Escherichia coli* is regarded as responsible for serious illness associated with the consumption of contaminated food, including vegetables [3]; in addition, it is able to survive in acidic food and beverages, including fresh and processed tomato products [4,5]. Aflatoxins contamination is another issue of great concern [6]: aflatoxins are mainly produced by fungi, belonging to *Aspergillus genus*. Other microorganisms, like yeasts, can be present in tomato products owing to their ability to survive at acidic pH values [7].

On the basis of these considerations, a strict control of microbiological quality of food is essential. However, conventional microbiological methods, based on total count of bacteria, present some drawbacks, mainly related to a long-incubation time, preventing early detection of the microbial spoilage. Obviously, it is important to detect microbiological spoilage as soon as possible, to enable producers to act rapidly and effectively in order to avoid the selling of contaminated products.

In the recent years, alternative methods, originally developed to analyze volatile compounds from various sample

* Corresponding author at: Dipartimento di Chimica Generale ed Inorganica, Chimica Analitica, Chimica Fisica, Università degli Studi di Parma, Parco Area delle Scienze 17/A, 43100 Parma, Italy. Tel.: +39 0521 905128; fax: +39 0521 905556.
E-mail address: marilena.musci@unipr.it (M. Musci).

matrices, based both on headspace extraction coupled to gas chromatography–mass spectrometry (HS-GC–MS) [8–13] and on gas-sensor arrays called electronic noses (EN) [14–19], have been successfully applied to the early detection of microbial contamination in food [20]. All these studies were carried out to elucidate the relationship among the volatile profile of contaminated food and the source of microbiological contamination, so detecting volatile markers for food spoilage. In fact, microbial contamination of food can not only be harmful for consumer's health, but it can also affect the organoleptic quality of the products, enhancing the production of volatile metabolites. The characteristic pattern of the volatile profile of microbiologically contaminated samples could be a useful indicator of the microbial contamination, thus allowing the identification of specific microorganisms responsible for the spoilage on the basis both of the type and of the amount of the detected volatile metabolites [21].

This study was firstly aimed at the characterization of the volatile fraction of microbiologically contaminated processed tomatoes by using the dynamic headspace extraction (DHS) followed by GC–MS analysis. Chromatographic data were then submitted to statistical analysis as principal component analysis (PCA) and linear discriminant analysis (LDA) [22,23] in order to detect the volatile compounds able to differentiate the samples of tomatoes under investigation. Finally, a comparison was made among the results obtained by analyzing the headspace of inoculated and not inoculated tomato samples with DHS-GC–MS and EN, showing a good agreement.

2. Materials and methods

2.1. Samples

Three microorganisms, namely one bacterium (*E. coli*), one fungus (*Aspergillus carbonarius*) and one yeast (*Saccharomyces cerevisiae*) were used for inoculation.

Commercial tins of peeled tomatoes (500 ml) were inoculated with 20 μl suspension (10^7 cfu ml^{-1}) of each species inserted through a small hole produced in the upper side of each tin and hermetically sealed with silicone rubber after inoculation. Initial contamination level was 400 cfu ml^{-1}. Artificial inoculations were performed under rigorous sterile conditions. For each microorganism, three tins were produced, incubated at 37 °C and analyzed at 2 and 7 days after contamination. In addition, three not-inoculated tins were incubated at 37 °C for 2 days.

2.2. Dynamic headspace extraction (DHS)

After incubation, tins were opened and the liquid phase was divided into 50 ml aliquots and maintained at −20 °C until analysis. Each aliquot was then placed in a 250 ml Erlenmeyer flask at 40 °C. After an equilibration time of 15 min, purified helium (75 ml min^{-1}) was passed through the system for 10 min and the extracted volatiles were adsorbed on a glass tube (16 cm × 0.4 cm i.d.) trap filled with Tenax TA (90 mg, 20–35 mesh) (Chrompack, Middelburg, The Netherlands). The volatile compounds were subsequently thermally desorbed and transferred into the GC system by using a TCT thermal desorption cold trap (TD800, Fisons Instruments, Milan, Italy). Desorption was performed at 280 °C for 10 min under a helium flow (10 ml min^{-1}) and the substances were cryofocused in a glass lined tube at −120 °C with liquid nitrogen. The volatile components were injected into the GC capillary column by heating the cold trap to 220 °C.

Three independent extractions were performed for each sample. To assess possible environmental contamination, blank analyses were carried out using an empty 250 ml Erlenmeyer flask fol-

lowing the same procedure used for the samples. In addition, in order to verify the absence of carry-over effects, the adsorbent trap was desorbed before and after each entire sampling procedure.

2.3. Gas chromatography–mass spectrometry

Gas chromatography–mass spectrometry analysis of the tomato headspace was carried out using a system consisting of a TRACE GC 2000 gas chromatograph and of a TRACE MS quadrupole mass spectrometer (Thermo Electron Corporation, Milan, Italy). Transfer line and source temperatures were kept at 230 and 200 °C, respectively. Electron impact mass spectra were recorded at 70 eV ionization energy (scan time, 0.5 s; electron multiplier voltage, 350 V) scanning the mass spectrometer from m/z 35 to 350. The carrier gas was helium (pressure, 70 kPa). Chromatographic separation was performed on a fused-silica bonded-phase capillary column Supelcowax 10^{TM} (30 m × 0.25 mm; d.f. = 0.25 μm) (Supelco, Palo Alto, CA, USA). The following GC oven temperature program was applied: 50 °C for 8 min, 6 °C min^{-1} to 160 °C, 20 °C min^{-1} to 200 °C, 200 °C hold for 1 min.

The mass spectrometer data acquisition was performed using the release 1.2 Xcalibur^{TM} software (Thermo Electron Corporation).

The identification of the volatile compounds was achieved by comparing their mass spectra with those stored in the National Institute of Standards and Technology US Government library (NIST, 1998). In addition, retention indices (RIs) were calculated for each peak with reference to the normal alkanes C6–C16 series according to the following equation [24]:

$$RI = 100z + 100 \frac{RT_i - RT_z}{RT_{z+1} - RT_z}$$

where RI is the retention index of the unknown peak, RT_i is the retention time of the unknown peak, RT_z and RT_{z+1} are the retention times of the *n*-alkanes that bracket the unknown peak, z is the number of carbon atoms of the *n*-alkane eluting just before the unknown peak. C6–C16 normal alkanes used for RIs calculation were supplied by Sigma–Aldrich (Milan, Italy). Calculated RIs were then compared with those stored in a proprietary database obtained by injecting 250 volatile compounds usually found in a variety of food samples [25]. Compounds were considered positively identified when both mass spectra and retention indices led to the same identification, taking into account that a maximum difference of 10 RI units can be considered acceptable, since different commercial stationary phases and temperature programs were used.

Finally, pure standards were injected, when available, in order to confirm identification.

In order to evaluate quantitative differences in the aromatic profile of the samples investigated, GC peak areas were calculated as total ion current (TIC) for all the analytes with the exception of coeluting compounds for which the signal of one or more characteristic ions (quantifier ions) was extracted and integrated (Table 1).

2.4. Electronic nose sampling

The commercial electronic olfactory system ESO835 (Sacmi scarl, Imola, Italy), whose detailed description can be found in previous works [17,26], was equipped with an array of six metal oxide semiconducting gas sensors. Every thin film sensor was based on a different metal oxide in order to improve the selectivity of the array. Electronic nose device was only used for analyzing headspace of sample tomatoes after 2 days from inoculation. Headspace sampling working parameters were as similar

Table 1
Volatile compounds identified in the analyzed samples

Volatile compounds	RI_{calc}	RI_{tab} [a]	ΔRI	ID[b]	Occurrence[c]
Alcohols					
Ethanol	936	932	+4	MS, RI, RT	0, 1, 2, 3
2-Butanol	1038	1035	+3	MS, RI, RT	0, 1, 2, 3
1-Propanol ($m/z = 59, 60$)[d]	1056	1052	+4	MS, RI, RT	0, 1, 2, 3
2-Methyl-1-propanol ($m/z = 74$)[d]	1102	1097	−5	MS, RI, RT	0, 1, 2, 3
3-Pentanol ($m/z = 59$)[d]	1116	1112	+4	MS, RI, RT	0, 1, 2, 3
1-Butanol	1152	1152	0	MS, RI, RT	0, 1, 2, 3
1-Penten-3-ol	1177	1176	+1	MS, RI, RT	0, 1, 2, 3
3-Methyl-1-butanol	1216	1215	+1	MS, RI, RT	0, 1, 2, 3
Unsaturated alcohol ($m/z = 41, 57$)[d]	1241			MS (tentatively identified)	0, 1, 2, 3
1-Pentanol ($m/z = 55, 70$)[d]	1258	1256	+2	MS, RI, RT	0, 1, 2, 3
4-Methyl-1-pentanol	1325			MS (tentatively identified)	1
3-Methyl-1-pentanol ($m/z = 56, 69$)[d]	1335	1325	+10	MS, RI, RT	0, 1, 2, 3
1-Hexanol	1359	1354	+5	MS, RI, RT	0, 1, 2, 3
3-Hexen-1-ol	1392	1391	+1	MS, RI, RT	0, 1, 2, 3
1-Heptanol ($m/z = 56, 70$)[d]	1461	1460	+1	MS, RI, RT	0, 1, 2, 3
6-Methyl-5-hepten-2-ol	1470			MS (tentatively identified)	0, 1, 2, 3
2-Ethyl-1-hexanol	1495	1492	+3	MS, RI, RT	0, 1, 2, 3
1-Octanol ($m/z = 55, 69, 84$)[d]	1564	1561	+3	MS, RI, RT	0, 1, 2, 3
Phenyl ethyl alcohol	1880			MS (tentatively identified)	1
Ketones					
Acetone ($m/z = 58$)[d]	820	814	+6	MS, RI, RT	0, 1, 2, 3
2-Butanone ($m/z = 57, 72$)[d]	907	901	+6	MS, RI, RT	0, 2, 3
2,3-Butandione	988	986	+2	MS, RI, RT	0, 1, 2, 3
2,3-Pentandione ($m/z = 57, 100$)[d]	1072	1071	+1	MS, RI, RT	0, 1, 2, 3
2-Heptanone ($m/z = 58$)[d]	1188	1185	+3	MS, RI, RT	0, 1, 2, 3
2-Methyl-6-heptanone	1244			MS (tentatively identified)	0, 3
2-Octanone ($m/z = 58$)[d]	1282	1280	+2	MS, RI, RT	0, 1, 2, 3
3-Hydroxy-2-butanone	1291	1289	+2	MS, RI, RT	1
2,2,6-Trimethyl ciclohexanone	1318			MS (tentatively identified)	0, 1, 2, 3
6-Methyl-6-hepten-2-one	1327			MS (tentatively identified)	0, 1, 2, 3
6-Methyl-5-hepten-2-one	1344	1340	+4	MS, RI, RT	0, 1, 2, 3
1-(2-Furanyl)ethanone	1529			MS (tentatively identified)	0, 1, 2, 3
6-Methyl-3,5-heptadien-2-one	1613			MS (tentatively identified)	0, 1, 2, 3
Acetophenone	1662	1660	+2	MS, RI, RT	1, 2
Aldehydes					
Propanal ($m/z = 58$)[d]	808	801	+7	MS, RI, RT	0, 1, 2, 3
2-Methyl propanal ($m/z = 72$)[d]	820	814	+6	MS, RI, RT	0, 1, 2, 3
2-Methyl butanal	915	914	+1	MS, RI, RT	0, 1, 2, 3
3-Methyl butanal	918	917	+1	MS, RI, RT	0, 1, 2, 3
Hexanal	1084	1080	+4	MS, RI, RT	0, 1, 2, 3
2-Methyl-2-butenal	1100			MS (tentatively identified)	0, 2, 3
Heptanal ($m/z = 55, 70$)[d]	1198	1196	+2	MS, RI, RT	0, 1, 2, 3
Octanal ($m/z = 69, 84$)[d]	1286	1286	0	MS, RI, RT	0, 1, 2, 3
Nonanal	1395	1396	−1	MS, RI, RT	0, 2, 3
2-Furaldehyde	1480	1474	+6	MS, RI, RT	0, 1, 2, 3
Decanal	1500	1502	−2	MS, RI, RT	0, 2, 3
Benzaldehyde	1530	1528	+2	MS, RI, RT	0, 1, 2, 3
α-Cyclocitral	1636			MS (tentatively identified)	0, 1, 2, 3
Aromatic hydrocarbons					
Toluene ($m/z = 91, 92$)[d]	1044	1040	+4	MS, RI, RT	0, 1, 2, 3
Aromatic hydrocarbon ($m/z = 91, 106$)[d]	1116			MS (tentatively identified)	0, 2
Ethylbenzene	1130	1125	+5	MS, RI, RT	1, 2, 3
m-Xylene	1134	1132	+2	MS, RI, RT	0, 1, 2, 3
o-Xylene	1184	1182	+2	MS, RI, RT	0, 1, 2, 3
Styrene ($m/z = 78, 104$)[d]	1265	1261	+4	MS, RI, RT	0, 1, 2, 3
Cymene	1266	1264	+2	MS, RI, RT	0, 1, 2, 3
Aromatic hydrocarbon	1280			MS (tentatively identified)	0, 1, 2, 3
o-Methyl styrene	1367			MS (tentatively identified)	2
Ethynyl benzene	1370			MS (tentatively identified)	2
Dimethylstyrene	1442			MS (tentatively identified)	1, 2
Terpenes					
ß-Myrcene	1169	1167	+2	MS, RI, RT	1, 2, 3
Limonene ($m/z = 68$)[d]	1194	1194	0	MS, RI, RT	0, 1, 2, 3
Ocimene	1247	1237	+10	MS, RI, RT	2
Terpene	1274			MS (tentatively identified)	0, 1, 2, 3
α-Pyronene	1295			MS (tentatively identified)	0, 2, 3
p-Ment-8-en-2-ol	1305			MS (tentatively identified)	3
Terpene	1377			MS (tentatively identified)	0, 1, 2, 3

Table 1 (*Continued*)

Volatile compounds	RI$_{calc}$	RI$_{tab}$[a]	ΔRI	ID[b]	Occurrence[c]
β-Isophorone	1400			MS (tentatively identified)	0, 1, 2, 3
2-Bornene	1528			MS (tentatively identified)	0, 1, 2, 3
Linalool	1560	1554	+6	MS, RI, RT	0, 1, 2, 3
Furans					
Furan (m/z = 39, 68)[d]	809	802	+7	MS, RI, RT	0, 1, 2, 3
2-Methyl furan	880	876	+4	MS, RI, RT	0, 1, 2, 3
3-Methyl furan (m/z = 81, 82)[d]	897	893	+4	MS, RI, RT	0, 1, 2, 3
2-Ethyl furan	949	945	+4	MS, RI, RT	0, 2, 3
2-Ethyl-5-methyl furan	1042			MS (tentatively identified)	0, 1, 2, 3
2-Acetyl-5-methyl furan (m/z = 109, 124)[d]	1061			MS (tentatively identified)	0, 1, 2, 3
Vinyl furan (m/z = 65)[d]	1082			MS (tentatively identified)	0, 1, 2, 3
2-Pentyl furan	1240	1240	0	MS, RI, RT	0, 1, 2, 3
3-(4-Methyl-3-pentenyl) furan (perillen)	1423			MS (tentatively identified)	0, 1, 2, 3
Sulfur compounds					
Dimethyl sulfide	750	745	+5	MS, RI, RT	0, 1, 2, 3
Mercapto acetone (m/z = 43, 90)[d]	1058			MS (tentatively identified)	0, 1, 2, 3
Dimethyl disulfide (m/z = 79)[d]	1080	1075	+5	MS, RI, RT	0, 1, 2, 3
2-Methyl tiophene	1095	1090	+5	MS, RI, RT	0, 1, 2, 3
3-Methyl thiophene (m/z = 97)[d]	1115	1120	+5	MS, RI, RT	0, 1, 2, 3
Dimethyl trisulfide	1378	1383	+5	MS, RI, RT	0, 2, 3
2-Propyl thiazole	1383			MS (tentatively identified)	1, 2
2-*sec*-butyl thiazole	1399			MS (tentatively identified)	0, 1, 2, 3
2-Isobutyl thiazole	1402	1396	+6	MS, RI, RT	0, 1, 2, 3
Esters					
Ethyl acetate (m/z = 61, 70, 88)[d]	897	893	+4	MS, RI, RT	0, 1, 2, 3
sec-Butyl acetate	995			MS (tentatively identified)	0, 1, 2, 3
Isobutyl acetate	1022	1018	+4	MS, RI, RT	0, 1, 2, 3
Terpentyl acetate (m/z = 55, 70, 101)[d]	1075			MS (tentatively identified)	0, 1, 2, 3
Ethyl hexanoate	1241	1238	+4	MS, RI, RT	1
Ethyl octanoate	1440	1438	+2	MS, RI, RT	1
Nitrogen compounds					
Acetonitrile	1012			MS (tentatively identified)	0, 1, 2, 3
3-Methyl butanenitrile	1132			MS (tentatively identified)	0, 1, 2, 3
Nitrometane	1174			MS (tentatively identified)	0, 1, 2, 3
1-Nitropentane	1342			MS (tentatively identified)	0, 1, 2, 3
1-Nitrohexane (m/z = 41, 57)[d]	1455			MS (tentatively identified)	0, 2, 3
Benzonitrile	1626			MS (tentatively identified)	1, 2
Hydrocarbons					
Cis-1,1,3,5-tetramethyl cyclohexane	1312			MS (tentatively identified)	1
Trans-1,1,3,5-tetramethyl cyclohexane	1315			MS (tentatively identified)	1
Cyclohexen-3,5,5,-trimethyl	1600			MS (tentatively identified)	0, 1, 2
Halogen compounds					
Chloroform	1024	1018	+6	MS, RI, RT	0, 1, 2, 3
Not identified					
m/z = 67, 82	812			MS (tentatively identified)	0, 1, 2, 3
m/z = 67, 111	964			MS (tentatively identified)	0, 1, 2, 3
m/z = 43, 55, 97	997			MS (tentatively identified)	0, 1, 2, 3
m/z = 82, 96, 125	1093			MS (tentatively identified)	0, 1, 2, 3
m/z = 111, 126	1098			MS (tentatively identified)	0, 1, 2, 3
m/z = 111, 126	1109			MS (tentatively identified)	0, 1, 2, 3
m/z = 107, 122	1256			MS (tentatively identified)	0, 1, 2, 3
m/z = 68, 83	1475			MS (tentatively identified)	0, 1, 2

[a] RI$_{tab}$: RI values from home-made database.

[b] ID: MS, identification by comparison with NIST mass spectrum; RI, identification by comparison with RI tabulated data; RT, identification by injection of pure standards.

[c] Occurrence: 0, compounds identified in the uncontaminated samples; 1, compounds identified in the samples inoculated with *S. cerevisiae*; 2, compounds identified in the samples inoculated with *E. coli*; 3, compounds identified in the samples inoculated with *Aspergillus carbonarius*.

[d] Fragments used for GC–MS peaks integration.

as possible to those used for the DHS-GC–MS analyses: 50 ml of the liquid phase were conditioned in 500 ml vials for 15 min at 40 °C; a continuous chromatographic air flow (150 ml min^{-1}) drew the headspace into the sensing chamber. Sensor array was exposed to the chromatographic air flow for 0.2 min, then to sample headspace for 3 min and finally again to chromatographic air for 20 min, in order to recover the baseline before the next measurement. Explorative data analysis was performed by using the EDA software package developed at SENSOR Laboratory [27].

2.5. Multivariate analysis

Mean, standard deviations and coefficient of variation were calculated on chromatographic peak areas.

Comparison between the volatile profile of sample inoculated with the same microorganism after 2 and 7 days from inoculation were performed by means of a *t*-test (α = 0.05).

PCA and LDA were performed on the areas of the chromatographic peaks detected in the tomatoes samples. Prior to analysis, peak area data were auto scaled to mean zero and unit variance.
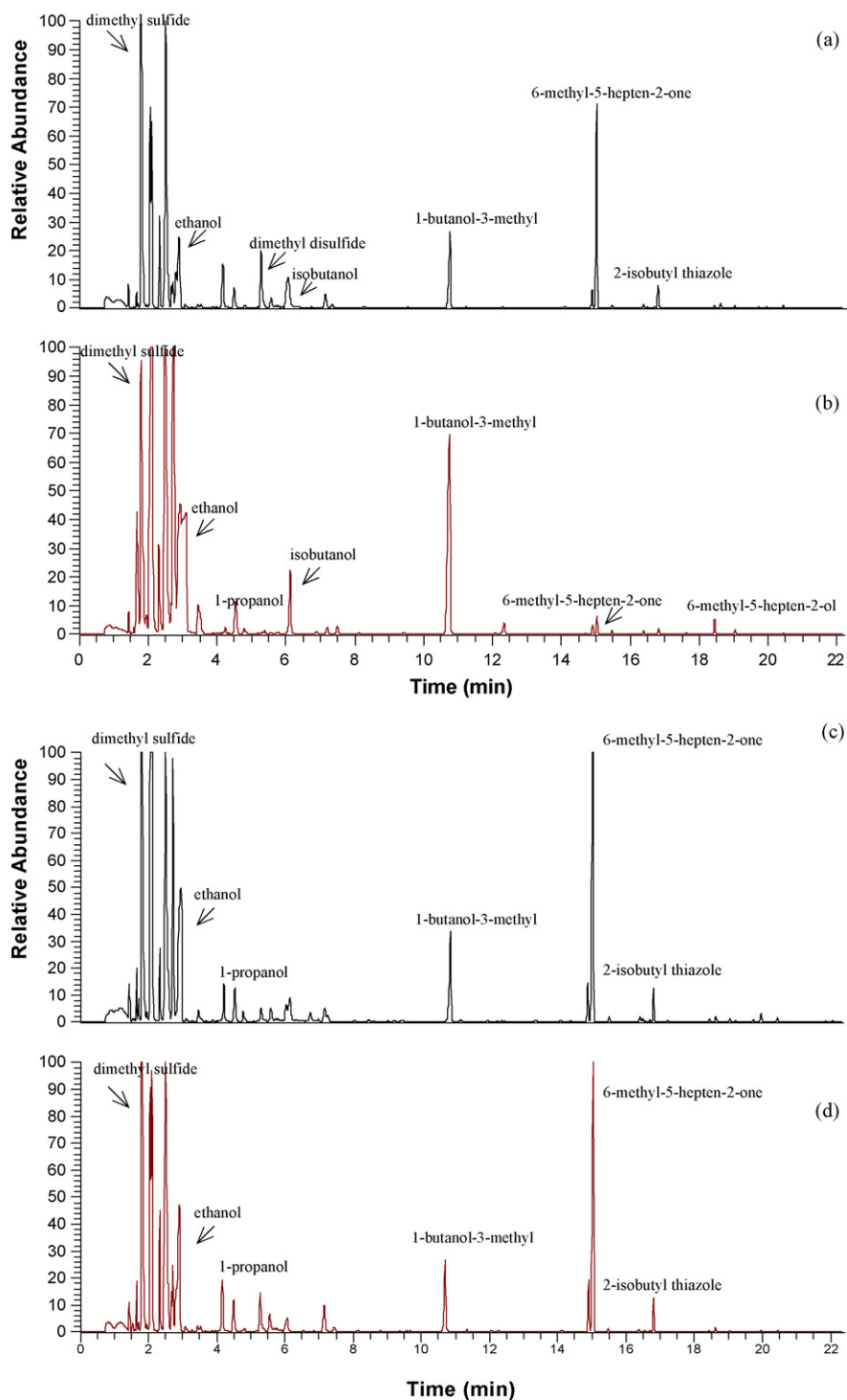
Fig. 1. GC–MS chromatograms of tomato samples: (a) not inoculated, (b) inoculated with *Saccharomyces cerevisiae*, (c) inoculated with *Escherichia coli* and (d) inoculated with *Aspergillus carbonarius*, after 2 days from inoculation.

PCA on DHS-GC–MS data for 2-day inoculated samples was carried out on a 12 × 109 matrix, where 12 is the number of samples (three samples for each kind of microorganism plus three not inoculated samples) and 109 is the number of the variables (volatile compounds). As for 7-day inoculated samples, PCA was carried out on a 21 × 109 matrix.

Stepwise LDA based on Wilk's lambda (*F*-to-enter = 0.05, *F*-to-remove = 0.1) was then performed on the same dataset in order to compute discriminant functions and to detect the variables more contributing to differentiate the aromatic profile of the inoculated and not inoculated samples.

The predictive ability of the calculated model was then evaluated by the "leave-one-out" cross-validation: each sample was removed one-at-time from the initial matrix of data, then the classification model was rebuilt and the case removed was classified in the new model.

3. Result and discussion

3.1. Characterization of the volatile profile

As known, the typical aroma of fresh and canned tomato can not be ascribed only to few compounds, but it depends on a large number of volatiles, the nature and relative amount of which can be related to the tomato composition as well as to ripening and processing conditions [28–32].

Fig. 1 shows typical gas chromatograms of DHS extracts obtained from the analysis of tomato samples not contaminated and contaminated with *S. cerevisiae, E. coli* and *A. carbonarius* after 2 days of incubation. Table 1 lists the compounds detected in the samples analyzed after 2 days from inoculation.

As for the uncontaminated samples a total of 84 volatile compounds belonging to different chemical classes were identified: among them, 17 alcohols, 13 aldehydes, 12 ketones, 9 furans, 8 sulfur compounds, 7 aromatic hydrocarbons, 7 terpenes, 5 nitrogen compounds, 4 esters, 1 hydrocarbon and 1 halogen compound.

The most abundant compound was dimethylsulfide, accounting for 26% of the total GC area, followed by 3-methyl-furan (18%), 6-methyl-5-hepten-2-one (10%), acetone (8%) and ethanol (7%).

The presence of some of the detected tomato volatiles can be explained taking into account both their original (endogenous) presence in the fresh fruit and their development/increase during processing from precursors like carotenoids, lipids and aminoacids as a consequence of carotenoids co-oxidation, lipoxygenase activity and Maillard reactions [33–35]. In particular, the thermal sterilization treatment in the production of canned tomatoes can be responsible for the increased amount of some compounds like 6-methyl-5-hepten-2-one, one of the most abundant volatile identified in the analyzed samples. In fact, the amount of this compound, naturally present in the fresh fruit [29,33], can increase as a consequence of the thermal degradation of carotenoids and more precisely from the oxidative cleavage of lycopene [36,37]. Other compounds identified in the analyzed samples and derived from carotenoids were α-isophorone, α-cyclocitral, toluene and xylenes [36,37].

The presence of C_6, C_7 and C_9 carbonylic compounds in canned tomato samples, such as aldehydes (hexanal, heptanal, nonanal) and ketones (2-heptanone) can be related to fatty acids oxidation [38].

As for volatiles derived from amino acids, 2-methylbutanal and 3-methylbutanal can be produced from isoleucine and leucine by Strecker degradation, whereas volatile sulfur compounds like dimethylsulfide, dimethyldisulfide, dimethyltrisulfide, 2-*sec*-butyl thiazole and 2-isobutylthiazole can be produced from sulfuric aminoacids in foods submitted to thermal treatment. In the volatile fraction of uncontaminated canned tomatoes were also identified some nitro-compounds like nitrometane, nitropentane and nitrohexane, that can be derived from the oxidation of aminoacids [31].

Another important class of compounds detected in the analyzed tomato products is represented by heterocyclic compounds like furans, thiazoles and thiophenes: all these volatiles have been already detected in previous studies [39,40].

As for microbial contamination of tomato, it is known that microorganisms as bacteria, fungi and yeasts can affect the development of different volatile metabolites, which nature and amount depend on the ability of the microorganisms to selectively transform precursor compounds present in the analyzed matrix. In addition, some microorganisms, as yeasts and filamentous fungi, possess *O*-glycoside hydrolases that can catalyze the enzymatic hydrolysis of glycosides, thus releasing additional volatile compounds [41]. In particular, the capability of *S. cerevisiae* to release volatiles from glycosidic precursors is well documented [42]. However, little is known about the production of volatile compounds from microbial contamination; further studies need to be performed to elucidate the role of yeasts in food spoilage and in the production of volatile metabolites [43].

As for the volatile profiles of contaminated canned tomatoes, 87 volatiles were identified in the samples inoculated with *S. cerevisiae*, namely 19 alcohols, 12 ketones, 10 aldehydes, 8 aromatic hydrocarbons, 8 sulfur compounds, 8 furans, 7 terpenes, 6 esters, 5 nitrogen compounds, 3 hydrocarbons and 1 halogen compound. Canned tomatoes contaminated with *S. cerevisiae* were characterized by the highest number and abundance of alcohols being 3-methyl-1-butanol (23%) and ethanol (21%) the most abundant compounds, followed by ethyl acetate (10%), 3-methyl furan (7%) and dimethylsulfide (12%). The great presence of alcohols in these samples can be ascribed to the fermentative activity of the added yeast. In particular, phenyl ethyl alcohol was detected only in the samples inoculated with this yeast; its origin can be related to the degradation pathway of phenylalanine or to the enzymatic hydrolysis from the glycosidic precursor as already discussed in previous studies [44].

As for the aromatic profile of the tomato samples inoculated with *E. coli*, 92 compounds, namely 17 alcohols, 13 aldehydes, 12 ketones, 11 aromatic hydrocarbons, 9 terpenes, 9 furans, 9 sulfur compounds, 6 nitrogen compounds, 4 esters, 1 hydrocarbon and 1 halogen compound were identified. The most abundant compounds were dimethylsulfide (20%), 6-methyl-5-hepten-2-one (16%), ethanol (11%), ethyl acetate (10%) and 3-methyl furan (7%). With respect to the other contaminated samples, those inoculated with *E. coli* were characterized by higher amounts of aldehydes.

Finally, in the samples inoculated with *A. carbonarius* a total of 85 compounds were identified, i.e. 17 alcohols, 13 aldehydes, 12 ketones, 9 terpenes, 9 furans, 8 sulfur compounds, 7 aromatic hydrocarbons, 5 nitrogen compounds, 4 esters and 1 halogen compound. As for the aromatic profile of samples contaminated with *A. carbonarius,* it resulted to be similar to that obtained from the analysis of uncontaminated samples; indeed few volatile compounds attributable to the fungal metabolism were detected. In this case, dimethylsulfide was the most abundant compound (24%) followed by 3-methyl furan (18%), acetone (10%) and ethanol (9%).

In general, volatile profiles of the samples analyzed after 7 days from inoculation did not significantly differ from those obtained after 2 days, without regard to the kind of inoculation. As for tomato samples inoculated with *S. cerevisiae*, no significant differences were found for the amount of most of the volatile compounds after 2 and 7 days from inoculation, with few exceptions, mainly regarding some alcohols, ketones and aromatic hydrocarbons, for which a slight decrease in the chromatographic signals was observed along the time. On the contrary, a significant increase in the GC responses was observed for nonanal and decanal after 7 days from inoculation, being these compounds absent in the analyzed samples after 2 days from inoculation.

A significant decrease in the GC responses after 7 days from inoculation was observed for a limited number of volatile compounds also for the aromatic profile of samples inoculated with *E. coli* and *A. carbonarius*.

These findings could be explained supposing a decrease in the microorganism activity during the time. In addition, the volatile compounds produced after incubation could be absorbed by the matrix and further metabolized [8].

Statistical analysis on volatile data was performed by using the SPSS package v. 9.0 (SPSS Italia, Bologna, Italy).

PCA was also carried out on preliminary data obtained from electronic nose.

Table 2
Component matrix for PC1 and PC2 on DHS-GC–MS data from samples analyzed after 2 days from inoculation

Variable	PC1
Nitrohexane	0.93
2-Furaldehyde	0.92
4-Methyl-1-pentanol	−0.91
3-Hydroxy-2-butanone	−0.9
Styrene	−0.89

Variable	PC2
2-Propyl thiazole	0.93
NI (RI = 1475)	0.93
Hexanol	0.91
3-Hexen-1-ol	0.89
Dimethylstyrene	0.88

3.2. Multivariate analysis

A direct comparison among the volatile profiles of differently inoculated samples is not easy to be performed, due to the high number of chromatographic peaks present in the chromatograms. In this case, comparison can be performed by submitting GC peak areas to multivariate analysis by means of chemometric techniques as PCA and LDA. Three independent analyses were performed on each canned tomato sample showing a very good reproducibility (R.S.D. ≤15%) for most of the compounds.

In order to evaluate the capability of the DHS-GC–MS method for an early detection of microbial contamination, in the first step only data obtained by analyzing the samples after 2 days from inoculation, were elaborated.

PCA is an unsupervised statistical method, allowing to describe data without the constraint of initial assumptions on the analyzed samples. It is a convenient tool for data dimension reduction and visualization of similarities among samples.

Five principal components were needed to explain about 90% of the total variance; PC1 accounting for 37% of the total variance and PC2 accounting for 29% of the total variance. Table 2 list component matrix for PC1 and PC2, i.e. the volatile compounds mostly contributing to the two first principal components.

As it can be seen from the PC plot (Fig. 2), the aromatic profile of tomato samples inoculated with *S. cerevisiae* (group 1) and that of samples inoculated with *E. coli* (group 2) resulted to be very different, whereas the aromatic profile of sample inoculated with *A. carbonarius* (group 3) was similar to those of not inoculated samples (group 0), as previously observed on the basis of the nature and relative abundance of volatile compounds detected in the samples. Therefore, a complete separation among group of samples could not be achieved by means of PCA.

LDA was then applied in order to calculate discrimination functions for the classification of samples in the corrected group and to find the most useful variables in the differentiation among the classes. LDA is a supervised chemometric method widely used for classification of food samples [19,45–48]. This method minimizes the variance within categories and maximizes the variance between categories. LDA renders a number of orthogonal linear discriminant functions equal to the number of categories minus 1; when four classes are considered, three linear discriminant functions are obtained. The importance of each variable in discrimination was investigated by analyzing its coefficients in the discriminant functions. In addition, the calculation of the values of these functions for each sample makes it possible to allocate it to the group for which the probability of belonging is highest. Three discriminant functions were calculated, the first accounting for 98.8% of the variance. According to the standardized
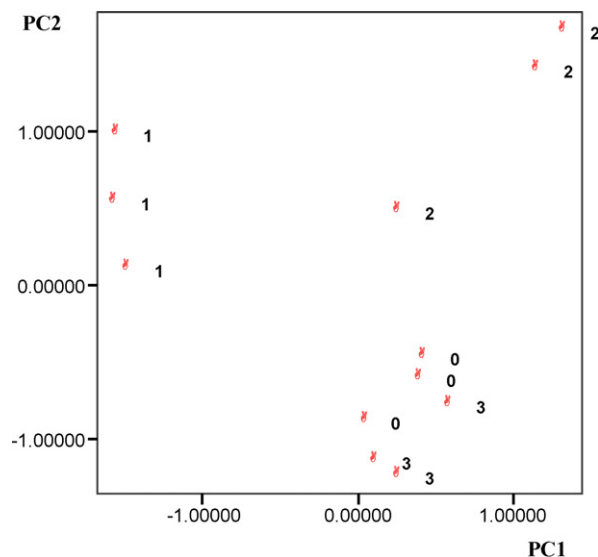

Fig. 2. PCA score of not contaminated samples and of contaminated samples after 2 days from inoculation (0: uncontaminated samples; 1: samples inoculated with *S. cerevisiae*; 2: samples inoculated with *E. coli*; 3: samples inoculated with *A. carbonarius*).

discriminant coefficients, five variables were found able to discriminate among the considered groups, namely ethanol, β-myrcene, *o*-methyl styrene, 6-methyl-5-hepten-2-ol and 1-octanol. Standardized canonical discriminant coefficient are reported in Table 3.

Fig. 3 shows the plot of discriminant scores of the analyzed samples.

The discriminant functions allowed the correct classification of all the samples into their respective group with a success rate of 100%, thus achieving a perfect discrimination (Table 4). The prediction capacity of the discriminant model was evaluated by the "leave-one-out" cross-validation in order to determine the

Table 3
Standardized canonical discriminant function coefficients for DHS-GC–MS data from samples analyzed after 2 days from inoculation

Variable	Function		
	1	2	3
Ethanol	12.615	0.109	−0.18
β-Myrcene	−11.639	−1.814	1.586
o-Methyl styrene	8.756	2.364	−0.236
6-Methyl-5-hepten-2-ol	−12.91	1.297	−0.145
1-Octanol	5.43	−1.011	−0.912

Table 4
Classification and cross-validation results (DHS-GC–MS data from samples analyzed after 2 days from inoculation)

	Predicted group membership			
	Group 0	Group 1	Group 2	Group 3
Original model				
Group 0	100%	0	0	0
Group 1	0	100%	0	0
Group 2	0	0	100%	0
Group 3	0	0	0	100%
Cross-validated model				
Group 0	100%	0	0	0
Group 1	0	100%	0	0
Group 2	0	0	100%	0
Group 3	0	0	0	100%

Fig. 3. Plot of discriminant scores of the analyzed samples after 2 days from inoculation.
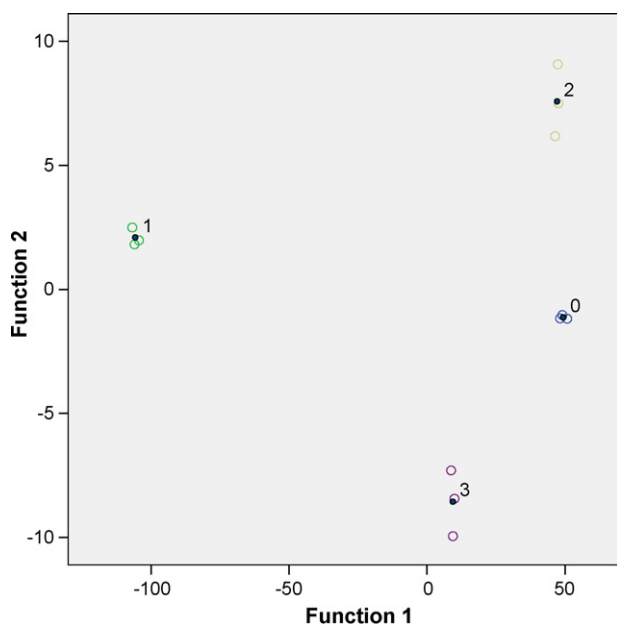
Fig. 4. PCA score plot of EN analysis of uncontaminated and contaminated samples after 2 days from inoculation.

stability of the model. During the validation procedure each sample is removed one-at-time from the initial matrix of data; then the classification model is rebuilt and the case removed is classified in this new model. Discriminant analysis model based on metabolic fingerprints of inoculated samples correctly classified the 100% of the observations based on cross-validation. The results obtained from LDA can be considered very satisfactory, since a small number of selected volatile compounds were able to guarantee an early detection of canned tomato samples inoculated with different microorganisms.

DHS-GC–MS data obtained by analyzing canned tomato samples after 7 days from inoculation were then submitted both to PCA and LDA. Despite little differences were observed in the volatile profile of 2- and 7-day inoculated samples, as previously discussed, chemometric multivariate techniques revealed differences between volatile metabolic production of the analyzed samples depending on time from inoculation, so allowing not only to discriminate samples on the basis of the source of the microbial contamination, but also on the basis of time.

A set of 10 variables was selected in order to discriminate samples submitted to LDA: ethyl octanoate (standardized coefficient = 30; it was found only in samples inoculated with *S. cerevisiae*), 4-methyl-1-pentanol (standardized coefficient = −29), 2-methyl propanal (standardized coefficient = 3.57), 2-*sec*-butyl thiazole (standardized coefficient = 2.67), not identified compounds at RI = 1475 (standardized coefficient = −2.00), acetone (standardized coefficient = −1.47), 3-methyl butanenitrile (standardized coefficient = 1.40), *o*-methyl styrene (standardized coefficient = 0.87), ocimene (standardized coefficient = −0.7) and dimethylstyrene (standardized coefficient = 0.268). Also in this case, 100% of correct classification was obtained.

3.3. Electronic nose analysis

EN analyses were performed on the headspace of canned tomato samples after 2 days from inoculation, in order to investigate its capability to distinguish between pure and contaminated samples.

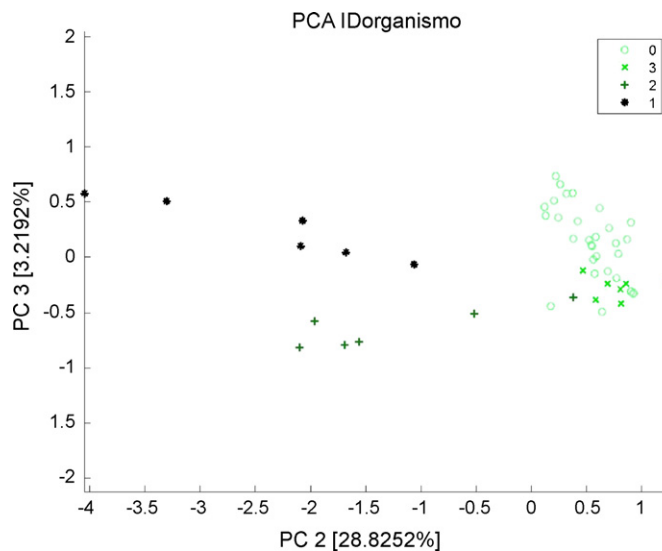Exploratory data analysis was performed by extracting the feature R/R_0 for each sensor, being R the resistance value of a sensor during the exposition to the sample headspace and R_0 the corresponding value of the baseline. Since PC1 was found to be mainly related to the intrinsic variance of the samples, PC2 and PC3 were taken into account.

PCA analysis (Fig. 4) showed that the EN was able to clearly distinguish samples spoiled by *E. coli* and *S. cerevisiae*, whereas the data related to the samples contaminated by *A. carbonarius* overlapped those corresponding to uncontaminated product. The obtained results were similar to those achieved in the DHS-GC–MS study, thus suggesting the use of EN as a useful tool for the early detection of microbial spoilage.

4. Conclusions

The DHS-GC–MS analysis of contaminated and not contaminated canned tomatoes evidenced significant differences in the nature and relative abundance of volatile compounds. In addition, LDA allowed to identify the set of variables better discriminating the analyzed samples. The characterization of the aromatic profile of canned tomatoes inoculated with different microorganisms could provide the potential for identification of the organism responsible for spoilage and determination of both quality and shelf life.

Preliminary findings from EN analyses carried out on not contaminated and contaminated samples showed a good agreement with the results obtained by means of DHS-GC–MS and suggested the usefulness of EN as early spoilage detection tool.

References

[1] E. Kokkinakis, G. Boskou, G.A. Fragkiadakis, A. Kokkinaki, N. Lapidakis, Food Control 18 (2007) 1538.
[2] R.H. Bishop, C.L. Duncan, G.M. Evancho, J. Food Sci. 47 (1982) 437.

[3] B.A. Del Rosario, L.R. Beuchat, J. Food Prot. 58 (1995) 105.
[4] L. Koodie, A.M. Dhople, Microbios 104 (2001) 167.
[5] B. Eribo, M. Ashenafi, Food Res. Int. 36 (2003) 823.
[6] S. Muhammad, K. Shehu, N.A. Amusa, Food Sci. 34 (2004) 72.
[7] J.M. Jay, Modern Food Microbiology, 6th ed., Springler-Verlag, New York, 2006.
[8] K. Yu, T.R. Hamilton-Kemp, D.D. Archbold, R.W. Collins, M.C. Newman, J. Agric. Food Chem. 48 (2000) 413.
[9] H.N. Chinivasagam, H.A. Bremner, A.F. Wood, S.M. Nottingham, Int. J. Food Microbiol. 42 (1998) 45.
[10] B. Zierler, B. Siegmund, W. Pfannhauser, Anal. Chim. Acta 520 (2004) 3.
[11] J.J. Jouffraud, F. Leroi, C. Roy, J.L. Berdaguè, Int. J. Food Microbiol. 66 (2001) 175.
[12] P. Ragaert, F. Devlieghere, E. Devuyst, J. Dewulf, H. Van Langenhove, J. Debevere, Int. J. Food Microbiol. 112 (2006) 162.
[13] N. Sabatini, M.R. Mucciarella, V. Marsilio, LWT (2008), available online.
[14] Y. Blixt, E. Borch, Int. J. Food Microbiol. 46 (1999) 123.
[15] N. Magan, A. Pavlou, I. Chrysanthakis, Sens. Actuat. B 72 (2001) 28.
[16] R. Needham, J. Williams, N. Beales, P. Voysey, N. Magan, Sens. Actuat. B 106 (2005) 20.
[17] M. Falasconi, E. Gobbi, M. Pardo, M. Della Torre, A. Bresciani, G. Sberveglieri, Sens. Actuat. B 108 (2005) 250.
[18] J.E. Haugen, K. Rudi, S. Langsrud, S. Bredholt, Anal. Chim. Acta 565 (2006) 10.
[19] S. Balasubramanian, S. Panigrahi, B. Kottapalli, C.E. Wolf-Hall, LWT 40 (2007) 1815.
[20] K. Arora, S. Chand, B.D. Malhotra, Anal. Chim. Acta 568 (2006) 259.
[21] G. Fisher, R. Schwalbe, M. Moller, R. Ostrowski, W. Dott, Chemosphere 39 (1999) 795.
[22] J.N. Miller, J.C. Miller, Statistics and Chemometrics for Analytical Chemistry, 4th ed., Pearson Education, London, 2000.
[23] D.L. Massart, B.G.M. Vandeginste, L.C.M. Buydens, S. De Jong, P.J. Lewi, J. Smeyers-Verbeke, Handbook of Chemometrics and Qualimetrics. Part A and Part B, Elsevier, Amsterdam, 1997.
[24] H. van den Dool, P.D. Kratz, J. Chromatogr. 11 (1963) 463.
[25] F. Bianchi, M. Careri, A. Mangia, M. Musci, J. Sep. Sci. 30 (2007) 527.
[26] M. Falasconi, M. Pardo, G. Sberveglieri, I. Riccò, A. Bresciani, Sens. Actuat. B 110 (2005) 73.
[27] M. Vezzoli, A. Ponzoni, M. Pardo, M. Falasconi, G. Faglia, G. Sberveglieri, Sens. Actuat. B 131 (2008) 100.
[28] R. Buttery, L.C. Ling, J. Agric. Food Chem. 35 (1987) 540.
[29] J. Song, L. Fan, L.R. Beaudry, J. Agric. Food Chem. 46 (1998) 3721.
[30] M. Servili, R. Selvaggini, A. Taticchi, A.L. Begliomini, G.F. Montedoro, Food Chem. 71 (2000) 407.
[31] A.Z. Berna, J. Lammertyn, S. Saevels, C. Di Natale, B.M. Nicolai, Sens. Actuat. B 97 (2004) 324.
[32] J. Beltran, E. Serrano, F.J. Lopez, A. Peruga, M. Valcarel, S. Rosello, Anal. Bioanal. Chem. 385 (2006) 1255.
[33] R.G. Buttery, in: R. Teranishi, R.A. Flath, H. Sugisawa (Eds.), Flavor Research: Recent Advances, Marcel Dekker Inc., New York, 1981, pp. 175–216.
[34] P.N. Onyewu, H. Daun, C.-T. Ho, in: T.H. Parliament, R.J. McGorrin, C.-T. Ho (Eds.), Thermal Generation of Aromas, ACS Symposium Series 409, American Chemical Society, Washington, 1989, pp. 247–257.
[35] E. Rodriguez-Bustamante, S. Sanchez, Crit. Rev. Microbiol. 33 (2007) 211.
[36] J. Crouzet, P. Kanasawud, Methods in Enzimology, vol. 213, Academic Press Inc., San Diego, 1997.
[37] J.J. Rios, E. Fernandez-Garcia, M.J. Minguez-Mosquera, A. Perez-Galvez, Food Chem. 106 (2008) 1145.
[38] D.A. Gray, S. Prestage, R.S.T. Linforth, A.J. Taylor, Food Chem. 64 (1999) 149.
[39] C.-T. Ho, N. Ichimura, LWT 15 (1982) 340.
[40] R.G. Buttery, R. Teranishi, R.A. Flath, L.C. Ling, in: R. Teranishi, R.G. Buttery, F. Shahidi (Eds.), Flavor Chemistry. Trends and Developments, ACS Symposium Series 388, American Chemical Society, Washington, 1989, pp. 213–222.
[41] P. Ortiz-Serrano, J.V. Gil, J. Agric. Food Chem. 55 (2007) 9170.
[42] J.V. Gil, P. Manzanares, S. Genoves, S. Valles, L. Gonzales-Candelas, Int. J. Food Microbiol. 103 (2005) 57.
[43] P. Ragaert, F. Devlieghere, S. Loos, J. Dewulf, H. Van Langenhove, I. Foubert, P.A. Vanrolleghem, J. Debevere, Int. J. Food Microbiol. 108 (2006) 42.
[44] D.M. Tieman, H.M. Loucas, J. Young Kim, D.G. Clark, H.J. Klee, Phytochemistry 68 (2007) 2660.
[45] F. Bianchi, C. Cantoni, M. Careri, L. Chiesa, M. Musci, A. Pinna, Talanta 72 (2007) 1552.
[46] I.S. Arvanitoyannis, M. van Houwelimgen-Koukaliaroglou, Crit. Rev. Food Sci. Nutr. 43 (2003) 173.
[47] D. Ollivier, J. Artaud, C. Pinatel, J.P. Durbec, M. Guérère, Food Chem. 97 (2006) 982.
[48] J.S. Câmara, M.A. Alves, J.C. Marques, Talanta 68 (2006) 1512.

Mesoporous silica hollow sphere (MSHS) for the bioelectrochemistry of horseradish peroxidase

Zhaoxia Cao [a,b], Jian Zhang [a,b], Julan Zeng [a,c], Lixian Sun [a,*], Fen Xu [a,*], Zhong Cao [c], Ling Zhang [c], Daowu Yang [c]

a Dalian Institute of Chemical Physics, Chinese Academy of Sciences, Materials & Thermochemistry Laboratory, 457 Zhongshan Road, Dalian 116023, Liaoning Province, China
b Graduate School of the Chinese Academy of Sciences, Beijing 100049, China
c School of Chemistry and Environmental Engineering, Changsha University of Science and Technology, Changsha 410076, China

ARTICLE INFO

ABSTRACT

In this work, novel mesoporous silica hollow spheres (MSHS) were chosen as an immobilization matrix, to construct a mediator-free third-generation HRP biosensor. UV–vis spectroscopy revealed that horseradish peroxidase (HRP) entrapped in MSHS could retain its native structure. FTIR spectroscopy and nitrogen adsorption–desorption isotherms indicated that HRP are intercalated into the mesopores. The direct electron transfer of HRP entrapped in MSHS was observed. A pair of stable and well-defined redox peaks of HRP with a formal potential of about -0.150 V (vs. Ag/AgCl) in 0.1 M pH 7.0 phosphate-buffered solution (PBS) were obtained. The biosensor exhibited a fast amperometric response to H_2O_2 with a linear range of 3.9×10^{-6} to 1.4×10^{-4} M ($R = 0.997$, $N = 20$). The detection limit was 1.2×10^{-6} M based S/N = 3.

© 2008 Published by Elsevier B.V.

1. Introduction

Electrochemical sensors, such as third-generation amperometric biosensors, which are based on the direct electron transfer between the enzyme and the electrode, have attracted considerable attentions in recent years [1–3]. Direct electrochemical detection of hydrogen peroxide is of practical importance in chemical, biological, clinical, and many other fields. However, proteins exhibit a rather slow rate of heterogeneous electron transfer at conventional electrodes due to inaccessibility of the electroactive centers as well as its absorptive denaturation and unfavourable orientation of proteins on the electrode surface [4,5]. Therefore, the immobilization of enzyme is essential to the performance of biosensors.

In order to achieve direct electron transfer between HRP and electrode, surfactant [6], polymer [7,8], and nanomaterials like the inorganic oxide such as antimony oxide bromide (AOB) [9], TiO_2 [10], ZrO_2 [11,12], $CaCO_3$ [13] and composite materials [14–16] have been used as the immobilization matrices. Among these materials, mesoporous silicas (MSs), have several advantages [17–19]: MS possess large surface areas, highly ordered pore structures, very narrow pore size distributions, and variable pore diameters,

and hence are good candidates as host materials for biomolecules [20,21].

Previous studies show that either mesostructure or morphology has a significant influence on the adsorption behavior of proteins and the performance of biosensor in addition to their framework composition and surface properties [22–26]. Liu et al. synthesized mesoporous silica of various morphologies and structures and investigated the lysozyme adsorption behaviors [27]. The highest lysozyme adsorption capacity of 536 mg g^{-1} was obtained on the mesoporous silica with cellular foam structure. Mesoporous hollow spheres with a rough surface exhibit the fastest adsorption rate and can adsorb more than 97% of lysozymes from the solution within 5 min.

Dai et al. reported that hexagonal mesoporous silicas (HMSs) can promote direct electrochemistry of many proteins such as myoglobin, hemoglobin and horseradish peroxide [28–30]. Taking account of the novel properties of silica hollow spheres (MSHS), it might serve as a promising host material for the redox protein to construct electrochemical biosensor. However, to our best knowledge, direct and unmediated voltammetry of HRP or any other redox enzyme incorporated in mesoporous silica hollow spheres has not been reported until now. In this paper, HRP was used as a simple model to study the feasibility of using this material in bioelectroanalysis. With isoelectric point (pI) at 8.8, HRP was positively charged at pH 7.0, and thus could easily assemble on this novel material which is negatively charged. As an enzyme immobilization

matrix, MSHS can incorporate the enzyme through physical or chemical actions without the need for any complicated and time-consuming covalent attachment process. Combined with Nafion (a perfluorosulfonate linear polymer with excellent film-forming ability and stability), MSHS/entrapped with HRP was easily designed to construct a stable biosensor. The enzyme film could efficiently retain the bioactivity of the entrapped protein. Meanwhile, dramatically facilitated direct electron transfer of HRP and excellent bioelectrocatalytic activity towards H_2O_2 were obtained.

2. Experimental

2.1. Materials

HRP (EC 1.11 1.7, >250 U mg^{-1}) was from Sigma and used without further purification. Hydrogen peroxide (H_2O_2, 30%, w/w) was from Beijing Chemical Engineering Plant, its dilute solution was freshly prepared daily. Phosphate buffer solutions (PBS, 0.1 M) with different pH values were prepared by mixing the standard stock solutions of Na_2HPO_4 and NaH_2PO_4 and adjusting the pH with 1.0 M H_3PO_3 or NaOH. Other reagents were of analytical reagent grade and used as received. The method of synthesis of Mesoporous silica hollow sphere was described else where [27].

2.2. Measurements and apparatus

UV–visible (UV–vis) absorption spectroscopy was carried out by using a GBC-cintra 20 spectrophotometer. FTIR Spectra were obtained on a Bruker Equinox 55 Fourier transform infrared spectrometer (FTIR).

In adsorption experiments, 40 mg of mesoporous silica was dispersed in a solution of HRP (5 mg/mL, pH 7.0). The resulting mixture was continuously shaken in a shaking bath at room temperature for 24 h to reach adsorption equilibrium, then centrifuged at 10,000 rpm for 10 min. The supernatant was analyzed by UV absorbance at 403 nm. Adsorbed amounts were measured by the difference in the concentration of the enzyme before and after adsorption.

N_2 adsorption–desorption measurements were conducted on a micromeritrics ASAP 2000 apparatus at 77 K using nitrogen as the adsorption gas. MSHS (150 mg) was dispersed in a solution of HRP (5 mg/mL, pH 7.0) and shaken for 3 h for enzyme absorption. The bioconjugates, denoted as MSHS–HRP, were then centrifuged and washed with distilled water three times, and dried prior to N_2 adsorption–desorption measurements.

Electrochemical measurements were performed on an IM6e electrochemical workstation (Zahner-Elektrik, Kronach, Germany) with conventional three-electrode cell. The as-prepared enzyme electrode, a platinum electrode and an Ag/AgCl (saturated with NaCl) were used as the working electrode, counter electrode and reference electrode, respectively. All experimental solutions were deoxygenated by bubbling high-purity nitrogen for at least 20 min and maintained under nitrogen atmosphere during measurement. Experiments were carried out at room temperature (18 ± 2 °C).

2.3. Preparation of enzyme electrodes

Prior to use, the glassy carbon electrode (GC, 3 mm in diameter) was polished to a mirror-like surface with 1.0, 0.3, and 0.05 μm alumina slurry followed by rinsing thoroughly with doubly distilled water. The electrodes were successively sonicated in 1:1 nitric acid, acetone and doubly distilled water in an ultrasonic bath, and then allowed to dry at room temperature.

The enzyme electrode was prepared by a simple casting method. Typically, 5 μL of a homogenous solution (pH 7.0) containing

Table 1
Physicochemical properties of mesoporous silica and the amounts adsorbed of HRP.

Mesoporous silica	Pore diameter (Å)	BET surface area (m^2 g^{-1})	Total pore volume (cm^3 g^{-1})	Adsorbed amounts (mg g^{-1})
MSHS-110	110	320	0.94	246
MSHS-90	90	758	1.00	216
MSHS-82	82	690	0.94	145

2.5 mg mL^{-1} MSHS (pore size 11 nm), 2.5 mg mL^{-1} HRP and 1/5 (v_{nafion}/v_{total}) Nafion was dropped on the surface of pretreated GC electrode to prepare the HRP/MSHS/GC electrode. A breaker was covered over the electrode so that water can evaporate slowly in air and a uniform film electrode can be formed, the dried enzyme electrode was stored at 4 °C in refrigerator while not in use.

3. Results and discussion

3.1. Enzyme adsorption

The as-prepared samples have hollow spherical morphology with different pore sizes ranging from 8.2 to 11.0 nm, see in Ref. [27]. HRP molecules possess an oval-shaped structure with a molecular size of 4.3 nm × 3.7 nm × 6.4 nm which is smaller than the pore diameter of the hollow spherical samples. At pH 7.0, the HRP (pI, 8.8) should be positively charged, and the silica surface is negatively charged [31]. Thus the adsorption properties of the mesoporous material under the present conditions can be related to the mesostructure of the materials. The results of adsorption capacity of MSHS were summarized in Table 1.

The mesoporous hollow sphere materials showed the adsorption of large amounts of HRP, 141–246 mg g^{-1}. And MSHS with the largest pore diameter (11.0 nm) exhibited the highest HRP adsorption capacity. This is consistent with the findings of lysozyme adsorption behaviors [27].

Protein could be fixed in the pores of mesoporous materials by simply immersing the mesoporous material in the protein solution [32]. To clarify the effect of HRP on mesoporous materials, the N_2 adsorption isotherms after HRP loading were investigated (Fig. 1). For MSHS (pore size: 11 nm), the pore size decreased to 9.9 nm after HRP loading treatment and pore volume (0.64 cm^3 g^{-1}) was 68.8% of that of MSHS (0.94 cm^3 g^{-1}), indicating HRP intercalated into the
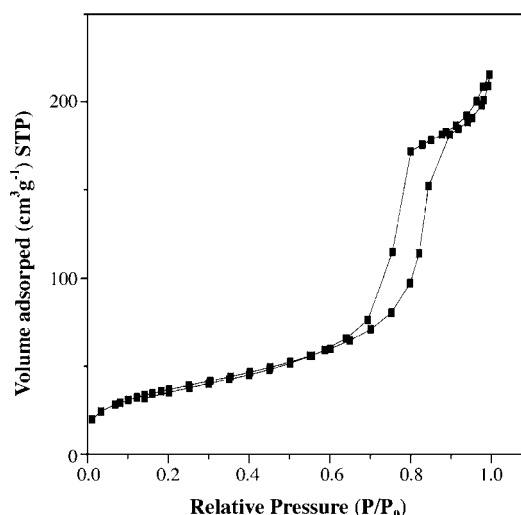

Fig. 1. N_2 adsorption–desorption isotherms after immobilizing of HRP on MSHS.
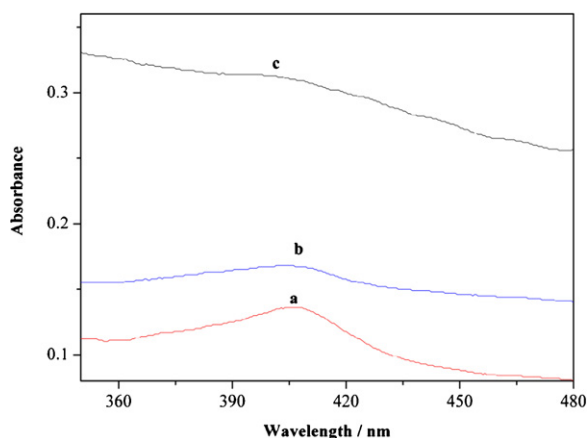
945

Fig. 2. UV–vis spectra of (a) HRP in solution, (b) dry MSHS/HRP and dry HRP/MSHS/Nafion composite films on quartz glass.

internal surface of MSHS [33]. Thus MSHS is a good matrix for HRP immobilization.

3.2. Spectroscopic characteristics of the MSHS/HRP

UV–vis spectroscopy is sensitive for the characteristic structure of proteins. The position of Soret absorption band of heme may provide information about possible denaturation of heme proteins. From Fig. 2, HRP entrapped in MSHS (curve b) or Nafion-MSHS (curve c) has a characteristic Soret absorption band at 403 nm, the same as that of native state of HRP in PBS (curve a), and retains its biological activity. This result suggests no significant denaturation occurs.

Fig. 3 shows the FTIR spectra of free HRP with that of HRP entrapped in the MSHS. For the pure MSHS (curve a) the absorption bands due to H_2O (1631 cm^{-1}), Si—O—Si (ν_{as}, 1092 cm^{-1}, ν_s, 804 cm^{-1}) and Si—OH (ν_s, 970 cm^{-1}) are observed, where ν_{as} = asymmetric stretching, ν_s = symmetric stretching [34]. This indicates that the as-formed MSHS contain a large amount of OH groups and H_2O on their surfaces [35]. Curve b is the FTIR spectrum of free HRP. The amide I band of HRP, which is caused by C=O stretching vibrations of peptide linkages, appears at 1654.9 cm^{-1}. The signal at 1535.3 cm^{-1} indicates the characteristic of amide II, which results from a combination of N—H in plane bending and C—N stretching vibrations of the peptide groups [36]. Curve c, the spectra of amide I and amide II bands (1656.8 and 1539.2 cm^{-1}) of HRP
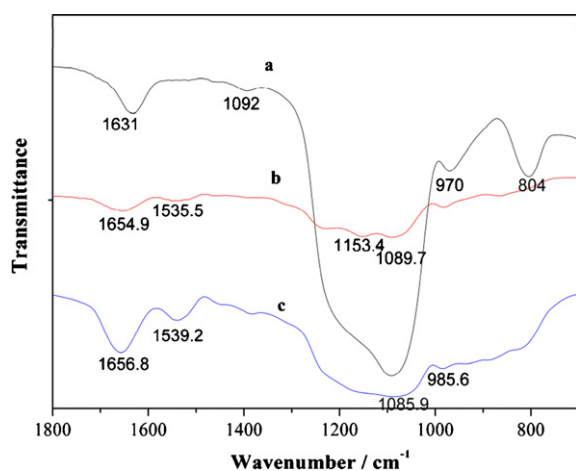

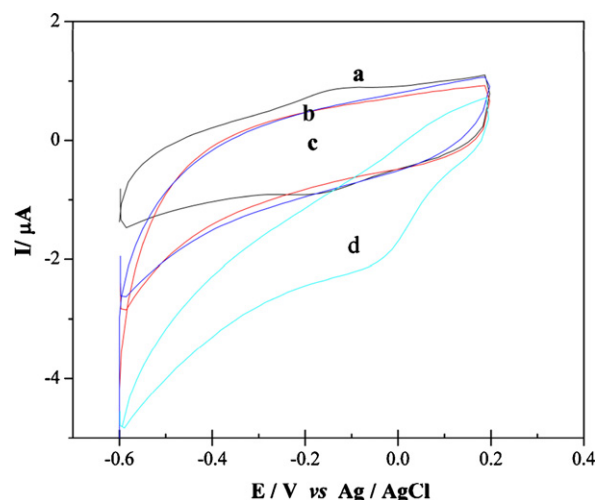**Fig. 3.** FTIR spectra of (a) MSHS, (b) HRP and (c) MSHS/HRP.

Fig. 4. CV of different modified electrodes in PBS (pH 7.0) at a scan rate of 100 mV s^{-1}: (a) HRP/MSHS/Nafion/GC, (b) MSHS/Nafion/GC, (c) bare GC and (d) HRP/Nafion/GC.

in MSHS are nearly the same as those obtained for native HRP. The similarities of the two spectra suggest that HRP retains the essential features of its native secondary structure in HRP–MSHS. The MSHS may provide a promising matrix for enzyme immobilization and biosensor fabrication because of its satisfactory biocompatibility. It should be pointed that upon adsorption of the HRP on MSHS, the bands at 1631 and 970 cm^{-1} shifted to 1656 and 985 cm^{-1}, respectively. The shift of water vibration adsorption band resulted from the interaction of NH_3^+ groups of HRP with Si groups in MSHS [37]. The shifts of framework vibration bands to higher frequency were due to the effect of the intercalated HRP on the pore size. This might result from the interaction between HRP and some specific sites on the pore internal surface of MSHS, consisting with the result of the N_2 adsorption isotherm.

3.3. Electrochemistry of HRP/MSHS/Nafion/GC electrode

Fig. 4 depicts the typical of HRP/MSHS/Nafion/GC (curve a), MSHS/Nafion/GC (curve b), bare GC (curve c) and HRP/Nafion/GC (curve d) electrode in 0.1 M phosphate buffer solution of pH 7.0 at 100 mV s^{-1}. As shown in CV (curve a), a pair of redox peaks was observed at the −0.217 and −0.085 V, which was related to the redox of the immobilized HRP. The low redox potential might imply special interactions between the molecular of HRP and MSHS, which could strongly affect the heme microenvironment. For HRP/Nafion/GC electrode, only a broad redox peak could be observed which shows that a direct electron transfer process could not take place. While the MSHS/Nafion/GC and bare GC displayed no redox peaks in the potential window, indicating electro-inactiveness. We also investigated the effect of pore size of MSHS on the properties of enzyme electrodes. The enzyme electrode modified with MSHS possessing largest pore size showed best performance (data not shown). So following electrochemistry measurements were done with MSHS (pore size: 11.0 nm).

Fig. 5 displays the direct electron transfer behavior of the immobilized HRP at various scan rates. With increasing scan rate, the redox peak currents of the adsorbed HRP increased, coupled with slightly enlarged peak-to-peak separation. The cathode peak currents showed linear response to scan rate from 50 to 1000 mV s^{-1} (inset of Fig. 5). All these result are in accordance with the surface-confined electrochemical behavior [38].
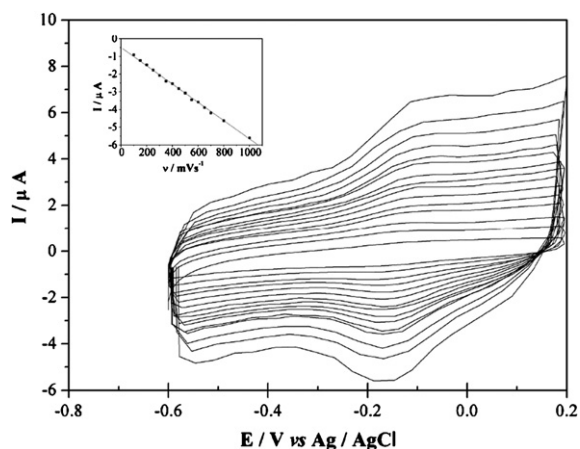
Fig. 5. CV of HRP/MSHS/GC electrode in PBS (pH 7.0) at 50, 100, 150, 200, 250, 300, 350, 400, 450, 500, 550, 600, 700, 800, 1000 mV s^{-1} (from inner to outer). Inset: plot of cathode peak current vs. scan rate.

3.4. Electrochemical response to hydrogen peroxide of HRP/MSHS/Nafion/GC electrode

The immobilized HRP undertakes a direct electron transfer reaction and exhibits an excellent electrocatalytic response to the reduction of H_2O_2 in PBS (Fig. 6). An obvious increase in the cathodic peak current was observed when H_2O_2 was added to a phosphate buffer indicating that a fast direct electron transfer reaction between the heme site of the immobilized HRP and the electrode surface was achieved [39,40]. These results illustrate that HRP in the MSHS can retain its bioelectrocatalytic activity.

As shown in Fig. 7, the amperometric response of the HRP/MSHS/Nafion/GC electrode to successive addition of different concentrations of H_2O_2 at the working potential of −0.2 V was also investigated. Upon addition of an aliquot of hydrogen peroxide to the buffer, the reduction current increased steeply to reach a stable value. The enzyme electrode achieved 95% of the steady-state current within 5 s. The calibration plot (inset of Fig. 7) shows a good linear response range to H_2O_2 in the wide range of 3.9×10^{-6} to 1.4×10^{-4} M ($R = 0.997$, $N = 20$), with detection limit of 1.2×10^{-6} M ($S/N = 3$) and sensitivity of 0.56 A m^{-1} cm^{-2}. Which is comparable
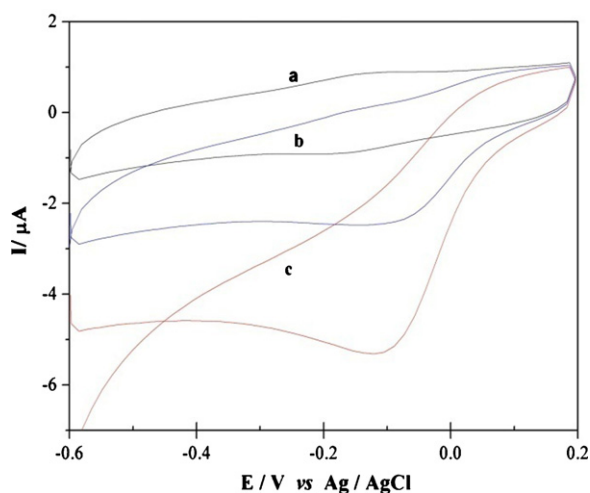

Fig. 6. Electrocatlysis of HRP/MSHS/Nafion/GC electrodes towards H_2O_2 in PBS (pH 7.0) at a scan rate of 100 mV s^{-1}. H_2O_2 concentrations: (a) 0 μM, (b) 7.8 μM and (c) 15.6 μM.
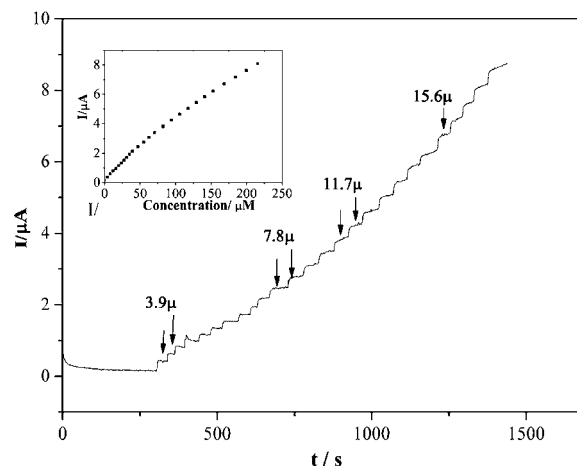

Fig. 7. Amperometric responses of HRP/MSHS/GC electrode upon successive additions of H_2O at −0.2 V in PBS (pH 7.0). Inset: plot of electrocatalytic current vs. H_2O_2 concentration.

to HRP immobilized in TiO$_2$ nanoparticle [41] film on PG electrode (linear response range: 7.5×10^{-6} to 1.23×10^{-4} M, detection limit: 2.5×10^{-6} M). The sensitivity is higher in comparison with that (0.184 A m^{-1} cm^{-2}) obtained by other immobilized HRP electrode reported previously [14]. The higher sensitivity may be related to novel architectures of MSHS that provided better mass transport and allowed more HRP loading. The apparent Michaelis–Menten constant (k_m) is calculated to be about 0.22 mM according to the Lineweaver–Burke equation, which was less than those of 1.38 mM for HRP immobilized in poly (ethylene glycol) [42], 2.3 mM for HRP immobilized on a colloid/cysteamine modified gold electrode [43] and 5.5 mM for HRP immobilized in polymer [40]. The small k_m shows a good affinity between the intercalated HRP in MSHS and H_2O_2.

The stability of the enzyme electrode has been studied as well. Even the 50 continuous cyclic scans were carried out in the potential range from −0.6 to 0.2 V at a scan rate of 100 mV s^{-1}, no obvious change of the CV curve could be observed. When the electrode was stored in pH 7.0 PBS buffer solution at 4 °C for 20 days, the CV curve was still well retained, which suggested that the electrode had an excellent stability.

What we should point out is that MSHS is not suitable to construct a third-generation glucose biosensor according our experiments (see supplementary data). Although we could observe the direct electrochemistry of the glucose oxidase (GOD), the response was too poor to be used. The poor response may be due to a low GOD loading which resulted from the repulsion between GOD (pI, 4) and silica surface (both negatively charged) except a larger size than HRP molecular [31].

4. Conclusion

In this work, the direct electrochemical behavior of HRP immobilized in the silica hollow sphere and the feasibility of a reagentless mediator-free third-generation HRP biosensor has been investigated. The enzyme electrode has a fast response, wide linear detection range and low detection limit. The unique mesoporous silica hollow spheres could provide a desirable microenvironment for HRP to undergo facile electron transfer reaction. It also provides a good biosensing platform for redox-active proteins and enzymes, and may find wide potential applications in direct electrochemistry, biosensors, biocatalysis and biomedical devices.

Acknowledgments

Appendix A. Supplementary data

Supplementary data associated with this article can be found, in the online version, at doi:10.1016/j.talanta.2008.06.043.

References

[1] Y.H. Song, L. Wang, C.B. Ren, G.Y. Zhu, Z. Li, Sens. Actuators B 114 (2006) 1001–1006.
[2] Q. Xu, C. Mao, N.N. Liu, J.J. Zhu, J. Sheng, Biosens. Bioelectron. 22 (2006) 768–773.
[3] Y. Xu, W.J. Peng, X.J. Liu, G.X. Li, Biosens. Bioelectron. 20 (2004) 533–537.
[4] J.F. Rusling, Acc. Chem. Res. 31 (1998) 363–369.
[5] A. Heller, Acc. Chem. Res. 23 (1990) 128–134.
[6] K. Chattopadhyay, S. Mazumdar, Bioelectrochemistry 53 (2000) 17–24.
[7] Y.T. Kong, M. Boopathi, Y.B. Shim, Biosens. Bioelectron. 19 (2003) 227–232.
[8] S.Y. Xu, B. Peng, X.Z. Han, Biosens. Bioelectron. 22 (2007) 1807–1810.
[9] X.B. Lu, Z.H. Wen, J.H. Li, Biomaterials 27 (2006) 5740–5747.
[10] S.Q. Liu, A.C. Chen, Langmuir 21 (2005) 8409–8413.
[11] S.Z. Zong, Y. Cao, Y.M. Zhou, J.H. Xu, Langmuir 22 (2006) 8915–8919.
[12] Z.Q. Tong, R. Yuan, Y.Q. Chai, Y. Xie, S.H. Chen, J. Biotechnol. 128 (2007) 567–575.
[13] D. Shan, M.J. Zhu, H.G. Xue, S. Cosnier, Biosens. Bioelectron. 22 (2007) 1612–1617.
[14] W.Y. Cai, O. Xu, X.N. Zhao, J.J. Zhu, H.Y. Chen, Chem. Mater. 18 (2006) 279–284.
[15] L. Qian, X.R. Yang, Talanta 68 (2006) 721–727.
[16] Y. Liu, J.P. Lei, H.X. Ju, Talanta 74 (2008) 965–970.
[17] Y.J. Wang, F. Caruso, Chem. Mater. 17 (2005) 953–961.
[18] R. Ravindra, S. Zhao, H. Gies, R. Winter, J. Am. Chem. Soc. 126 (2004) 12224–12225.
[19] J. Fan, C. Yu, F. Gao, J. Lei, B. Tian, L. Wang, B. Tu, D. Zhao, Angew. Chem. Int. Ed. 42 (2003) 3146–3150.
[20] J. Lei, J. Fan, C. Yu, L. Zhang, S. Jiang, B. Tu, D. Zhao, Micropor. Mesopor. Mater. 73 (2004) 121–128.
[21] Y.Z. Xian, Y. Xian, L.H. Zhou, F.H. Wu, Y. Ling, L.T. Jin, Electrochem. Commun. 9 (2007) 142–148.
[22] J.M. Sun, H. Zhang, R. Tian, D. Ma, X. Bao, D.S. Su, H. Zou, Chem. Commun. 12 (2006) 1322–1324.
[23] S.Z. Qiao, H. Djojoputro, Q.H. Hu, G.Q. Lu, Prog. Solid State Chem. 34 (2006) 249–256.
[24] A. Vinu, V. Murugesan, M. Hartmann, J. Phys. Chem. B 108 (2004) 7323–7330.
[25] B. Li, H. Takahashi, Biotechnol. Lett. 22 (2000) 1953–1958.
[26] H. Takahashi, B. Li, T. Sasaki, C. Miyazaki, T. Kajino, S. Inagaki, Chem. Mater. 12 (2000) 3301–3305.
[27] J. Liu, C.M. Li, Q.H. Yang, J. Yang, C. Li, Langmuir 23 (2007) 7255–7262.
[28] Z.H. Dai, X.X. Xu, H.X. Ju, Anal. Biochem. 332 (2004) 23–28.
[29] Z.H. Dai, S.Q. Liu, H.X. Ju, H.Y. Chen, Biosens. Bioelectron. 19 (2004) 861–867.
[30] Z.H. Dai, H.X. Ju, H.Y. Chen, Electroanalysis 10 (2005) 862–868.
[31] H. Liu, P. Wright, J. Mater. Chem. 15 (2005) 3690–3700.
[32] J.F. Diaz, K.J. Balkus Jr., Mol. Catal. B: Enzym. 2 (1996) 115–126.
[33] H. Takahashi, B. Li, T. Sasaki, C. Miyazaki, T. Kajino, S. Inagaki, Micropor. Mesopor. Mater. 44 (2001) 755–762.
[34] M.W. Anderson, J. Klinowski, J. Chem. Soc. Faraday Trans. 1 (82) (1986) 1449–1469.
[35] A. Kioul, L. Mascia, J. Non-Cryst. Solids 175 (1994) 169–186.
[36] J.K. Kauppinen, D.J. Moffate, H.H. Mantsch, D.G. Cameron, Appl. Spectrosc. 35 (1981) 271–276.
[37] B. Liu, R. Hu, J. Deng, Anal. Chem. 69 (1997) 2343–2348.
[38] R.W. Murray, A.J. Bard (Eds.), Electroanaytical Chemistry, 13, Marcel Dekker, New York, 1984, p. 191.
[39] T. Ferri, A. Poscia, R. Santucci, Bioelectrochem. Bioenerg. 44 (1998) 177–181.
[40] T. Ferri, A. Poscia, R. Santucci, Bioelectrochem. Bioenerg. 45 (1998) 221–226.
[41] Y. Zhang, P.L. He, N.F. Hu, Electrochim. Acta 49 (2004) 1981–1988.
[42] Y. Xu, W. Peng, X. Liu, G. Li, Biosens. Bioelectron. 20 (2004) 533–561.
[43] Y. Xiao, H.X. Ju, H.Y. Chen, Anal. Biochem. 278 (2000) 22–28.

Contents lists available at ScienceDirect

Talanta

journal homepage: www.elsevier.com/locate/talanta

Ultrasensitive flow-injection electrochemical method for detection of anticancer drug tamoxifen

Parandis Daneshgar[a], Parviz Norouzi[a,b,*], Mohammad Reza Ganjali[a,b], Hassan Ali Zamani[c]

[a] Center of Excellence in Electrochemistry, Department of Chemistry, University of Tehran, Tehran, Iran
[b] Endocrinology & Metabolism Research Center, Tehran University of Medical Science, Tehran, Iran
[c] Department of Applied Chemistry, Quchan Islamic Azad University, Quchan Branch, Iran

ARTICLE INFO

ABSTRACT

This paper presents the optimization of instrumental and solution parameters for determination of tamoxifen in urine and plasma and formulation by fast Fourier transform square wave voltammetry (SWV) using a gold microelectrode in flow-injection system. The samples are subjected by the same buffer solution and are injected in the flow-injection apparatus. By applying a novel square wave voltammetry method to perform as a sensitive method the voltamograms are recorded. The method used for determination of tamoxifen by measuring the changes in admittance voltammogram of a gold ultramicroelectrode (in $0.05 \, mol \, L^{-1} \, H_3PO_4$ solution) caused by adsorption of the tamoxifen on the electrode surface. The best sensitivity was achieved using a frequency of 600 Hz and a medium composed of $0.05 \, mol \, L^{-1}$ phosphate buffers at pH 2.0. The best performance was obtained with the pH value of 2, pulse amplitude 25 mV, frequency 600 Hz, accumulation potential of $-100 \, mV$ and accumulation time of 0.5 s. Furthermore, signal-to-noise ratio has significantly increased by application of discrete fast Fourier transform (FFT) method, background subtraction and two-dimensional integration of the electrode response over a selected potential range and time window. Calibration plots are given for solutions containing 1.0×10^{-11} to $3.0 \times 10^{-6} \, mol \, L^{-1}$ of tamoxifen. The detection limit is calculated to be $3.0 \times 10^{-12} \, mol \, L^{-1}$ ($\sim$2 pg mL^{-1}). The relative standard deviation at concentration 2.0×10^{-8} M is 6.1% for five reported measurements.

© 2008 Elsevier B.V. All rights reserved.

1. Introduction

Trans isomer of (Z)-2-[p-(1,2-diphenyl-butenyl)phenoxy]-N,N-dimethyletylamine (tamoxifen) is a hormone treatment developed over 20 years ago. It lowers the risk of breast cancer coming back (recurring) or developing in the other breast. It belongs to a class of drugs called selective estrogen receptor modulators (SERMs), which have both estrogenic and antiestrogenic effects. Tamoxifen has the same nucleus as diethylstilbestrol but possesses an additional side chain (trans isomer) which accounts for its antiestrogenic activity [1]. Tamoxifen is extensively metabolized after oral administration. N-desmethyl tamoxifen is the major metabolite found in plasma. N-desmethyl tamoxifen activity is similar to tamoxifen. The prolonged binding of tamoxifen to the nuclear chromatin of these results in reduced DNA polymerase activity, impaired thymidine utilization, blockade of estradiol uptake,

and decreased estrogen response [2,3]. There were some reports on determination of that by using Capillary gas chromatographic in the presence of a number of antidepressants in urine [4] and Capillary zone electrophoresis [5], but these methods are so expensive and time consuming. The method which introduced in this paper is too sensitive, inexpensive and fast for detection of tamoxifen.

The combination of ME with square wave voltammetry (SWV) has recently been shown to be advantageous for environmental detection of several compounds [6]. The adaptation of this technology to ASV of tamoxifen on gold ME could provide a substantial improvement for rapid analysis [7–9]. This paper describes a fundamentally different approach to SWV measurement, in which the detection limits are improved, while preserving the information content of the SW voltammogram. The approach is designed to separate the voltammetric signal and background signal in frequency domain by using discrete fast Fourier transformation (FFT) method. This separation allows, digitally filtrating some of the noises and decreasing the bandwidth of the measurement. Further improvement in the signal was gained by two-dimensional integration of the electrode response over a selected potential range and time window of the signal. Although at sufficiently high scan

rates CV can approximate an ac voltammetric technique and can be used to investigate electrode surface phenomena such as physical adsorption, FFT–SWV may be a more appropriate technique for monitoring analyte adsorption, as the potential dependence of analyte adsorption may be more clearly characterized. SWV measures the current response while rapid alternating potentials are applied during a staircase scan, whereas CV, which uses only a forward and reverse linear dc scan, is not sensitive to the potential dependence of changes that occur in the double layer.

2. Experimental

2.1. Apparatus and reagents

All solutions were prepared in double-distilled water using analytical grade reagents. Reagents in use in preparation of the stock eluent solution for flow-injection analysis (0.05 mol L^{-1} H$_3$PO$_4$ and NaOH 1 mol L^{-1} used for adjusting pH of the eluent) were obtained from Merck Chemicals. In all experiments all solutions were made up in the background electrolyte solution, and were used without removal of dissolved oxygen.

The equipment for flow-injection analysis included a 10 roller peristaltic pump (Home made) and a four-ways injection valve (Supelco Rheodyne Model 5020) with a 50 μL sample loop. In all experiments, described in this paper, the flow rate of eluent solution was 0.5 mL min^{-1}.

The Au–ME was constructed from a 25 μm diameter gold wire (Goodfellow). It is the same as what we used in our previous papers [10–20]. In all measurements, an Ag (s) | AgCl (s) | KCl (aq, 1 mol L^{-1}) reference electrode was used. The auxiliary electrode was made of a Pt wire, 1 cm length and 0.5 mm in diameter.

2.2. Sample preparation assay

Twenty tablets were weighed, finely powdered and portions equivalent to 20 mg tamoxifen were transferred into 100 mL volumetric flask; 50 mL distilled water was added, shaken thoroughly to dissolve, made up to volume and mixed well. Suitable aliquots of solution were filtered through a Millipore filter (0.45 μm). 1 mL of the filtered solution was diluted with distilled water in a 100 mL volumetric flask. Then 50 μL of the resulting solution was added to a 100 mL volumetric flask and made up to volume with 0.05 mol L^{-1} phosphoric acid to yield starting concentration of 2.0 ng mL^{-1}.

2.3. Determination of tamoxifen in human urine and plasma

1 mL of untreated urine containing 50 ng mL^{-1} tamoxifen was placed into a 5 mL volumetric flask and diluted with water to the mark. A 1 mL of this solution was diluted with pH 2 buffer solution to 10 mL into a volumetric flask. Then 50 μL aliquot was injected into the FIA system.

For the determination of tamoxifen in plasma, 100 μL aqueous tamoxifen solutions (50 ng mL^{-1}) were added to 100 μL of untreated plasma. The mixture was vortexed for 30 s. In order to precipitate the plasma proteins, the plasma samples were treated with 20 μL perchloric acid HClO$_4$ 15%. After that, the mixture was vortexed for a further 30 s and then centrifuged at 6000 rpm for 5 min. Then 50 μL aliquot of the obtained supernatant was injected into the FIA system. The voltammograms were recorded according to the above recommended procedure. The voltammograms of samples without tamoxifen do not show any signal that can interfere with the direct determination, so external calibration can be used.
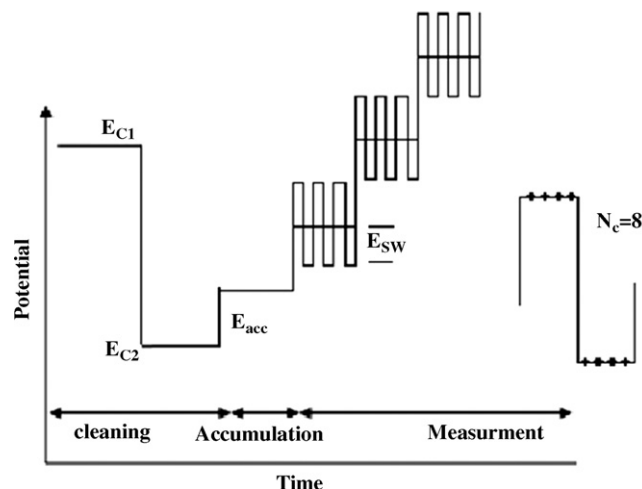

Fig. 1. The diagram of potential waveform used in measurements.

2.4. Electrochemical setup

All electrochemical experiments were done using a setup comprised of a PC PIV equipped with a data acquisition board (PCL-818H, Advantech Co.) was used to output an analog waveform to the working electrode and acquire current readings from the working electrode that connected to a custom made potentiostat. Most of the waveform parameters could be modified from within the software; including the pre- and post-scan potential/time, square wave frequency/amplitude, dc ramp initial/final potential, and ramp time.

In this new method, to improve the detector sensitivity, the FFT–SWV technique was modified in the potential excitation waveform and current sampling and data processing. Fig. 1 shows the potential waveform consisted of three sections; (a) electrode conditioning and (b) accumulation part (c) measurement the potential waveform contained three additional potential steps, E_{c1} to E_{c2} (for cleaning the electrode surface) and Es (for accumulation of tamoxifen). As is shown in Fig. 1, the measurement part of the waveform contains multiple SW pulses with amplitude of E_{SW} and frequency of f_0, were superimposed on a staircase potential function, which was changed by a small potential step of ΔE. The values of potential pulse of SW (E_{SW}) and ΔE were in a range of few mV (10–50 mV). In potential ramp, the currents sampled four times per each SW polarization cycle.

3. Results and discussion

Fig. 2 shows the changes in the electrode admittance, of the gold electrode in 0.05 mol L^{-1} H$_3$PO$_4$ into the eluent solution, caused by the injection of a solution of 50 μL of 5.0 × 10^{-8} mol L^{-1} tamoxifen. The FFT–SW modulation had amplitude of 10 mV and a frequency of 800 Hz. Before each scan, the electrode was held at E_{c1} potential (1400 mV) for 60 ms, the E_{c2} potential at −200 mV for 60 ms and accumulation potential; Es at −100 mV for 500 ms.

The single peak at potential 1000 mV at the voltammogram is due to the adsorption process of drug and inhibition of redox behavior of gold electrode as shown in Eq. (1). When the electrode potential passes the zero charge potential, changes in the double layer capacitance is caused by the reorientation of water molecule and ion exchange at the Helmholtz layer. Since such processes (e.g., water molecule reorientation) are too fast, the pseudo capacitance peak can be observed easily in various electrolytes even at frequencies above 1 MHz. The second peak, with a shoulder, is related to
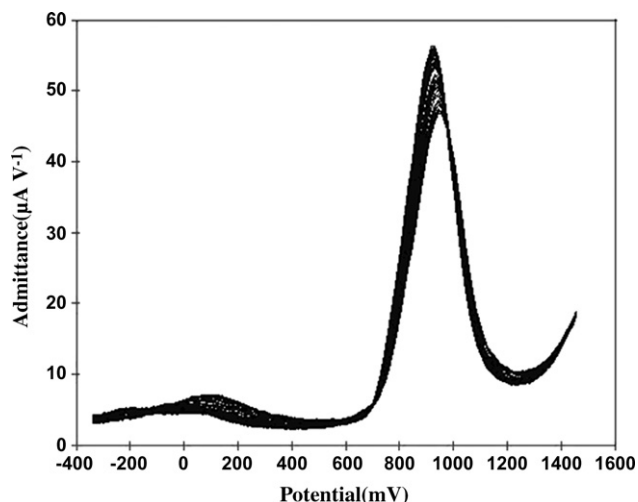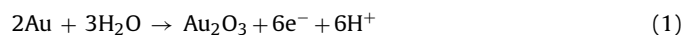
Fig. 2. Two-dimensional square wave voltammogram of 1.0×10^{-7} mol L^{-1} tamoxifen in H$_3$PO$_4$ 0.05 mol L^{-1} at an Au UME to show the change of current because of compound adsorption.

oxidation of the electrode surface,

$$2Au + 3H_2O \rightarrow Au_2O_3 + 6e^- + 6H^+ \tag{1}$$

which, led to formation of oxide layer.

At Fig. 3a the peak current change is clear during time after injection of analyte. The analyte signal appears as a current decline in certain potential at the FFT–SWVs admittance. It is result of the inhibition of the electrode surface processes by the adsorbed tamoxifen. The differential form of the voltammograms is shown in Fig. 3b. In the differential graphs, it can be also noted that the analyte signal extends over a potential range of the FFT–SWV.

Unlike redox reactions, adsorption is much more general phenomenon. Adsorption of organic molecules onto a gold surface can be an extremely complex process which also involves the desorption of adsorbed water molecule, hydroxyl, or electrolyte anions. Although there will be some dependence on the structure of the molecule, adsorption onto metal electrodes will occur in varying degrees with most organic compounds. Moreover, adsorption of species onto an electrode has been avoided in flowing systems as it causes electrode fouling and analyte carryover. Such changes in the electrode surface concentrations and diffusion layer conductivity will result in a change in the charging current response. When FFT–SWV is used to monitor a flowing system, analyte adsorption will cause a measurable change in the admittance response. In addition to this, faradic FFT–SWV current may be result from chemisorptions of the analyte onto the gold surface. Actually, this system would be very useful for detection of electroactive and non-electroactive compounds (by using the adsorption behavior or redox behavior of substances) and coupling by chromatographic method make the system so powerful to separation and determine the trace amount of compounds.

Norouzi et al. [10–26] reported a detection method by using flowing systems cyclic voltammetry (CV) to monitor the adsorption of several inorganic and organic molecules onto Au electrode. Similarly, using FFT–SWV technique, these current responses (in response to an alternating potential) can be examined to determine the time dependence of the change in the current response due to analyte adsorption. It should be noted that in this method all processes studied involve adsorption of analytes hence both charging and faradic currents may potentially carry useful analytical information. It is advantageous in FFT–SWV to collect more current samples near the end of the forward and reverse pulses and use

signal averaging to increase the ΔQ. It is well known that, in the traditional Osteryoung SWV method, the current is sampled at two points for each square wave, t_1 (the end of the first SW pulse) and t_2 (the end of the second SW pulse). The difference current [(current at t_2) − (current at t_1)] for each square wave is plotted versus dc ramp potential to obtain a peak-shaped voltammogram for an electroactive species. In the Osteryoung technique, the majority of the charging current will have decayed at the end of each pulse, allowing the faradic current to be sampled independently. FFT–SWV is able to sample the current across the entire SW period and use a selected portion of the forward and reverse voltammogram to calculate the difference current by taking this point that most of the current response was used to calculate the difference current (i.e., 0–20% of the initial current rejected), the ΔQ was lower, possibly due to the charging component of the current interfering with the measurement of the faradic current. One of the advantages of scanning approaches for electrochemical detection is that different parts of voltammogram can be selected for a calculating the detector signal, based on response integration. A total absolute difference
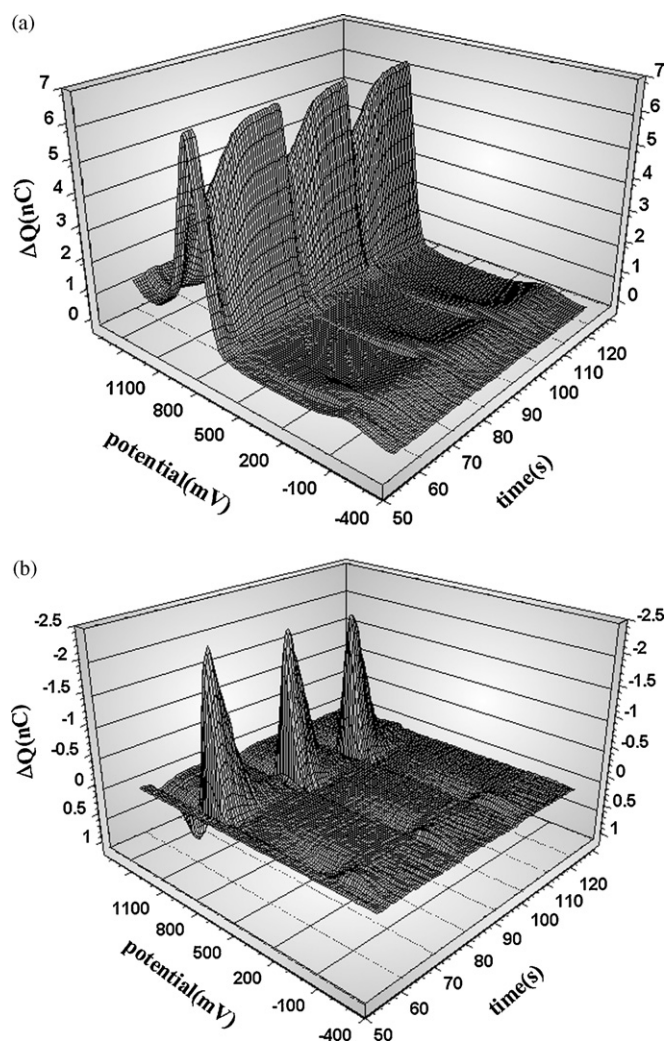
Fig. 3. (a) FFT square wave voltammograms at a 15 μm Au UME recorded during a flow-injection experiment. The eluent was 0.05 mol L^{-1} H$_3$PO$_4$, the flow rate was 0.5 mL min^{-1}, and the frequency was 800 Hz. The injected solution (50 μL) contained 1.0×10^{-6} mol L^{-1} tamoxifen in 0.05 mol L^{-1} H$_3$PO$_4$. (b) Graph (a), when the average of five Au FFT SW voltammograms (in 0.05 mol L^{-1} H$_3$PO$_4$) subtracted from the displayed voltammograms, (c) overlapping FFT SW voltammograms all conditions as in graph (a).

function (ΔQ) can be calculated by using the following equation:

$$\Delta Q(s\tau) = \Delta t \left[\sum_{E=E_i}^{E=E_v} \left| A(s, E)E - A(s_r, E)E \right| + \sum_{E=E_v}^{E=E_i} \left| A(s, E)E - A(s_r, E)E \right| \right]$$

(2)

where, s is the sweep number, τ is the time period between subsequent sweeps, Δt is the time difference between two subsequent points on the FFT–SW curves, $A(s, E)$ represents the admittance of the FFT–SW curve recorded during the s-th sweep and $A(s_r, E)$ is the reference admittance of the FFT–SW curve. E_i and E_v are the initial and the vertex potential, respectively. The reference FFT–SW curve was obtained by averaging a few FFT–SW curves (10–30) recorded at the beginning of the experiment (i.e., before injection of the analyte). By optimizing accumulation potential and time, the square wave amplitude and frequency and selecting suitable flow rate of the FFT–SW response, the ΔQ adsorption-based response can be maximized.

3.1. Optimization of FFT–SW frequency and amplitude

In fast voltammetric analysis, the SW frequency and amplitude are important factors since analyte signal, background noise, and peak shape rely on speed of excitation signal. It should be noted that the solution resistance, electrode diameter, and stray capacitance of the system will limit the sensitivity gains obtained by raising the SW frequency. However, increasing the SW frequency will increase the SW peak current, or the sensitivity, but this will be tempered by a higher charging/faradic current ratio. Due to this fact that, the SW frequency acts similar to sweep rate in cyclic voltammetry. For example, in this method, in order to achieve a scan rate equal to or greater than 10 V/s the SW frequency should be at least 500 Hz (assuming an increment of 20 mV with each SW cycle). Therefore, using very high SW frequencies causes a shorter potential scan times, consequently, the response peak for the flow analysis becomes smaller and skewed, due to insufficient time for oxidation of the electrode surface. While application of lower SW frequencies results to a longer potential scan times, which result to lower number of potential scan for each injected sample zone. To study the effect of those factors, the SW frequency range 600–2200 Hz and amplitude 5–40 mV were examined. In Fig. 4 the importance of fre-
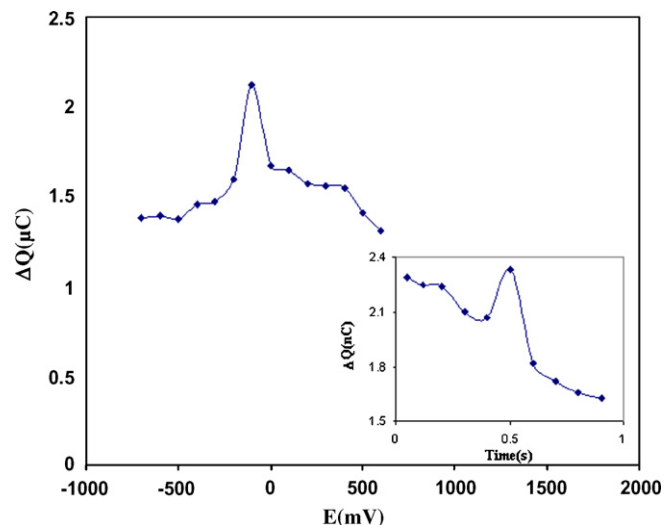

Fig. 5. The effect of frequency and amplitude on the signal-to-noise ratio of Au UME response to the injection of 5.0×10^{-8} mol L^{-1} tamoxifen in 0.05 mol L^{-1} H$_3$PO$_4$.

quency and amplitude is demonstrated for solution of tamoxifen. A series of SW frequencies were examined to determine the optimal frequency for the detection of tamoxifen. A plot of SW frequency versus ΔQ showed that a frequency of 800 Hz was the instrumental limit for this system. Above this frequency, excessive charging currents interfered with the measurement of the faradic current, decreasing the tamoxifen ΔQ.

Theoretically, the optimal square wave amplitude for a reversible system is 50/n mV. To determine influence of SW amplitude on ΔQ, various amplitudes were investigated. Fig. 5 shows the effect of SW amplitude on increasing ΔQ was observed with increasing amplitude until 25 mV, after which ΔQ plateaued and then began to decrease when amplitudes greater than 25 mV were used. Low frequency noise (baseline drifting) was more pronounced when SW amplitudes above 10 mV were used. SW amplitude of 25 mV and frequency of 600 Hz was found to be optimal.

3.2. Effect of instrumental variables

As mentioned before, this system used of change in charge because of adsorption of analyte on the surface of gold electrode. Similar to stripping voltammetric techniques, in this method, the high sensitivity is mainly attributed to analyte pre-concentration via physical, chemical, or electrochemical adsorption. In Fig. 6 the importance of accumulation time and potential is demonstrated for solution of tamoxifen. In this method, it is also possible to make use of the fact that many analytes will adsorb at electrodes at suitably applied potentials, Es. To optimize the performance of FFT–SWV detection in FIA, the effect of accumulation time on electrode response and peak shape was evaluated. An accumulation time range of 0.05–0.9 s and an accumulation potential range −700 to 700 mV were examined.

If analytes cannot be accumulated in the selected time, then some loss in ΔQ would be expected. Therefore, in order to reach a maximum surface coverage, or maximum sensitivity, the accumulation time should be long enough. However, long accumulation times also reduced the number of data points (at lest 10 data points need to plot analyte peak) for plotting the electropherogram; thus, accumulation times of 500 ms were selected as a compromise between maximum ΔQ and minimum peak broadening. The losing data point was noted when accumulation time was more than 800 ms, likely due to short retention time of analyte zone in
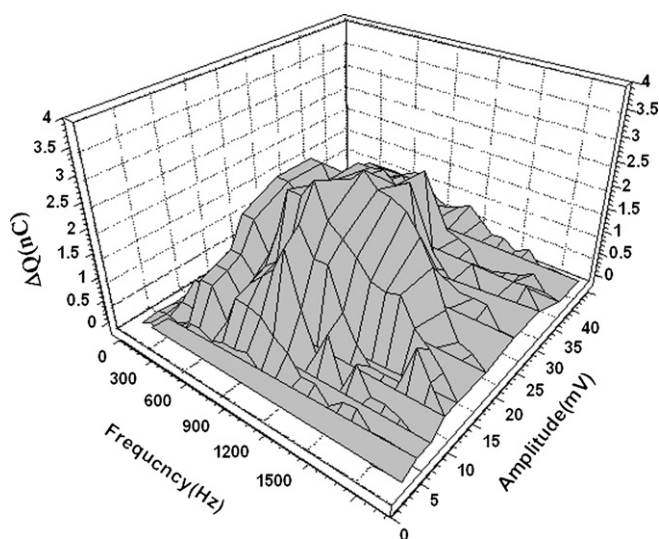

Fig. 4. The effect of accumulation time and potentialon the response of 15 μm Au UME to the injection of 5.0×10^{-8} mol L^{-1} tamoxifen in 0.05 mol L^{-1} H$_3$PO$_4$.
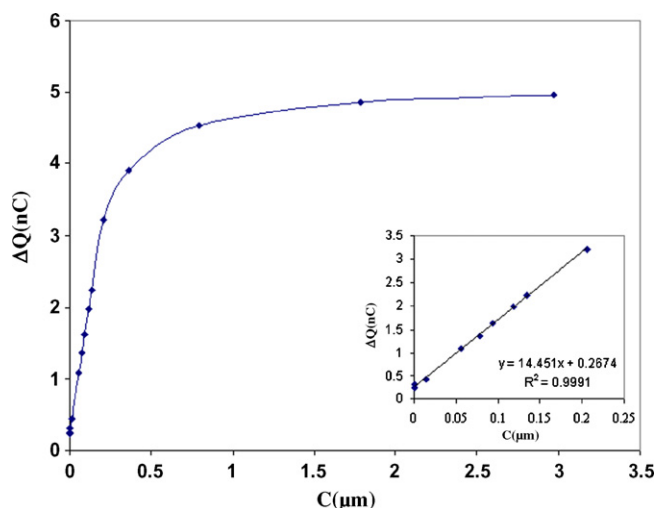
Fig. 6. Calibration curve for tamoxifen in 0.05 mol L^{-1} H$_3$PO$_4$ under optimum condition at flow-injection system.

the electrochemical cell for the flow analysis. So after data analyzing the accumulation time 500 ms and accumulation potential −100 mV was chosen.

3.3. Calibration and precision

As mentioned above the electrode response could be expressed in various ways as peak heights or peak areas. For this reason, the magnitude of the flow-injection peaks depends on the choice of the data processing methods. Like stripping voltammetry methods, here, the electrode response is proportional to the electrode coverage. This assumption, however, may be less obvious when inhibition of oxide formation by adsorbates (tamoxifen is considered, but not unlikely). Fig. 6 illustrates the obtained calibration carves for measurements of tamoxifen in 0.05 mol L^{-1} H$_3$PO$_4$. The experimental conditions were set at optimum values in order to obtain the best detection limits. Results shown in this figure represent the integrated signal for 3–5 consecutive flow injections of the standard solution. It has been shown that a decrease of charge in the oxide formation region on gold caused by adsorption of species is proportional to the surface coverage [27]. Measurements carried out for small analyte concentrations allow the estimation of the detection limit C_{DL}:

$$C_{DL} = \frac{3s_b}{slope} \tag{3}$$

where s_b is the standard deviation (or noise) of the baseline around the flow-injection peak.

The linearity was evaluated by linear regression analysis, which calculated by the least square regression method [28]. The calibration curves constructed for tamoxifen were linear over the concentration range of 1.0×10^{-11} to 7.0×10^{-8} mol L^{-1}. Peak areas of tamoxifen were plotted versus its concentration and linear regression analysis performed on the resultant curve. A correlation coefficient of $R = 0.9968$ with %R.S.D. values ranging from 0.23% to 3.7% across the concentration range studied were obtained following linear regression analysis. Typically, the regression equation for the calibration curve was found to be $Y = 14.45X + 0.2674$. Fig. 6 shows the calibration graph that obtained for the monitoring of tamoxifen in a 0.05 mol L^{-1} H$_3$PO$_4$. The LOD was measured as the lowest amount of the analyte that may be detected to produce a response which is significantly different from that of a blank. Limit of detection was approved by calculations based on the standard

deviation of the response (δ) and the slope (S) of the calibration curve at the levels approaching the limits according to equation LOD = 3.3 (δ/S) [28]. The LOD for tamoxifen was 3.0×10^{-12} mol L^{-1}. The LOQ was measured as the lowest amount of analyte that can be reproducibly quantified above the baseline noise, for which triplicated injections resulted in a R.S.D. ≤1.75%. A practical LOQ giving a good precision and acceptable accuracy was found to be 8.0×10^{-12} mol L^{-1}.

3.4. Precision

Precision of the assay was investigated with respect to both repeatability and reproducibility. Repeatability was investigated by injecting nine replicate samples of each of the 5.0×10^{-6}, 5.0×10^{-9} and 5.0×10^{-10} mol L^{-1} standards where the mean concentrations were found to be 5.6×10^{-6}, 4.8×10^{-9} and 4.5×10^{-10} mol L^{-1} with associated %R.S.D.'s of 2.5, 1.30 and 0.5, respectively. Inter-day precision was assessed by injecting the same three concentrations over 3 consecutive days, resulting in mean concentrations of tamoxifen of 5.5×10^{-6}, 4.5×10^{-9} and 5.1×10^{-10} mol L^{-1} and associated %R.S.D. of 3.10%, 1.5% and 0.9%, respectively.

3.5. Accuracy

Accuracy of the assay was determined by interpolation of replicate ($n = 6$) peak areas of three accuracy standards (5.0×10^{-6}, 5.0×10^{-9} and 5.0×10^{-10} mol L^{-1}) from a calibration curve prepared as previously described. In each case, the percent relevant error and accuracy was calculated. The resultant concentrations were $(5.4 \pm 0.3) \times 10^{-6}$, $(4.6 \pm 0.2) \times 10^{-9}$ and $(5.1 \pm 0.2) \times 10^{-10}$ mol L^{-1} with percent relevant errors of 2.6%, 1.1% and 0.23%, respectively.

3.6. Ruggedness

The ruggedness of the method was assessed by comparison of the intra- and inter-day assay results for tamoxifen undertaken by two analysts. The %R.S.D. values for intra- and inter-day assays of tamoxifen in the cited formulations performed in the same laboratory by the two analysts did not exceed 3.5%, thus indicating the ruggedness of the method. Also the robustness of the method was investigated under a variety of conditions such as small changes in the pH of eluent, in the flow rate, in the buffer composition and in the laboratory temperature. The result showed that the percent recoveries of tamoxifen was between 99.8% and 101.1% which were good under most conditions and did not show a significant change when the critical parameters were modified.

3.7. Recovery

A known amount of tamoxifen standard powder was added to aliquots ($n = 20$) of tablets contents, mixed and the powder was extracted, diluted and analyzed. The final nominal concentration of tamoxifen was found to be 2.0×10^{-9} mol L^{-1}. The assay was repeated ($n = 9$) over 3 consecutive days to obtain intermediate precision data. The resultant %R.S.D. for this study was found to be 1.2% with a corresponding percentage recovery value of 99.95%.

3.8. Assay of tablets

The method developed in the present study was applied for the determination of tamoxifen in tablets from the Iranian market. The results showed a percent recovery of 99.92% and a R.S.D. of 1.85%.

Table 1
Comparison of the detection limit of the proposed method with the other reported.

Added (pg/mL)	Interpolated concentration	R.S.D (%)	R.E. (%)
2500 (plasma)	2530 ± 20	2.7	2.33
1000 (urine)	1100 ± 10	1.7	1.53

Data obtained from five replicates at each concentration. Interpolated concentration data expressed as mean ± S.D.

Table 2
Application of the proposed method to the determination of tamoxifen in spiked humane plasma and urine.

Method	Detection limit	Ref. no.
Capillary zone electrophores	3 ng/mL	[5]
Capillary gas chromatographic	2.4 ng/mL	[4]
FFT–SWV	2 pg/mL	This work

3.9. Determination of tamoxifen in urine and plasma samples

After the application of the method to the Iranian market injection, the resulting data showed a recovery percentage value of 99.88% and a respective R.S.D. value of 1.95%. The proposed method was also applied to the determination of tamoxifen in spiked urine and plasma samples. The results of analysis of spiked human plasma ($n = 5$) and urine ($n = 5$) are shown in Table 1. The results are satisfactory, accurate and precise. No interference was noticed from the urine content after just dilution with the supporting electrolyte. The major advantage of the method as applied to plasma and urine is that no prior extraction step is required.

3.10. Comparison of the sensitivity of the method and other previously reported methods

Table 2 compares the detection limit of the proposed method with the other reported methods. As it is immediately obvious, the sensitivity of the method is superior to all previously reported methods. The data in Table 2 reveal that the detection limit of the method is about 1200 times lower than the most sensitive reported method.

4. Conclusions

This report described a novel, sensitive, and widely applicable FFT–SWV FIA detection method using of UME gold electrode. FFT–SWV was demonstrated to provide sensitive detection of a wide range of analytes based on oxidation of the electrode surface. Currently, work is progressing on the enhancement of the detection electronics and FIA cell to allow incorporation of a second sensing electrode positioned away from the detection zone which will enable automatic, analog subtraction of the background response. It is hoped that this will make FFT–SWV easier to use as well as provide enhanced sensitivity. Also, application of FFT–SWV to high-performance liquid chromatography is being considered.

References

[1] B. Fisher, J. Dignam, J. Bryant, A. DeCillis, D.L. Wickerham, N. Wolmark, J. Costantino, C. Redmond, E.R. Fisher, D.M. Bowman, L. Deschenes, N.V. Dimitrov, R.G. Margolese, A. Robidoux, H. Shibata, J. Terz, A.H.G. Paterson, M.I. Feldman, W. Farrar, J. Evans, H.L. Lickley, J. Natl. Cancer Inst. 88 (1996) 1529.
[2] B. Fisher, J.P. Costantino, D.L. Wickerham, C.K. Redmond, M. Kavanah, W.M. Cronin, V. Vogel, A. Robidoux, N. Dimitrov, J. Atkins, M. Daly, S. Wieand, E. Tan-Chiu, L. Ford, N. Wolmark, J. Natl. Cancer Inst. 90 (1998) 1371.
[3] Z. Desta, B.A. Ward, N.V. Soukhova, D.A. Flockhart, J. Pharmacol. Exp. Ther. 310 (2004) 1062.
[4] J. Rodriguez, J.J. Berzas, A.M. Contento, M.P. Cabello, J. Sep. Sci. 26 (2003) 915.
[5] J.R. Flores, J.J.B. Nevado, A.M.C. Salcedo, M.P.C. Diaz, Anal. Chim. Acta 512 (2004) 287.
[6] T. Yu-Chen, A. Barry, R. Coles, G. Compton, F. Marken, Electroanalysis 13 (2001) 639.
[7] S.H. Tan, S.P. Kounaves, Electroanalysis 10 (1998) 364.
[8] D. Rurikova, I. Kunakova, Chem. Papers 53 (1999) 246.
[9] R.M. Wightman, D.O. Wipf, in: A.J. Bard (Ed.), Electroanalytical Chemistry, vol. 15, Marcel Dekker, New York, 1989.
[10] P. Norouzi, M.R. Ganjali, S. Shirvani-Arani, A. Mohammadi, J. Pharm. Sci. 95 (2007) 893.
[11] P. Norouzi, S. Shirvani-Arani, P. Daneshgar, M.R. Ganjali, Biosens. Bioelectron. 22 (2006) 1068.
[12] P. Norouzi, M.R. Ganjali, A.A. Moosavi-Movahedi, J. Brazil. Chem. Soc. 18 (2007) 231.
[13] P. Norouzi, M.R. Ganjali, P. Daneshgar, Anal. Lett. 40 (2007) 547.
[14] P. Norouzi, M.R. Ganjali, L. Hajiaghababaei, Anal. Lett. 39 (2006) 1941.
[15] P. Norouzi, M.R. Ganjali, P. Daneshgar, Sens. Actuators B 123 (2007) 1125.
[16] P. Norouzi, M.R. Ganjali, P. Daneshgar, T. Alizadeh, A. Mohammadi, Anal. Biochem. 360 (2007) 175.
[17] P. Norouzi, M.R. Ganjali, P. Daneshgar, J. Pharmacol. Toxicol. Methods 55 (2007) 289.
[18] P. Norouzi, M.R. Ganjali, A.A. Moosavi-movahedi, B. Larijani, Talanta 73 (2007) 54.
[19] P. Norouzi, M.R. Ganjali, M. Zare, A. Mohammadi, J. Pharm. Sci. 96 (2007) 2009.
[20] P. Norouzi, M.R. Ganjali, B. Akbari-Adergani, Acta Chim. Slov. 53 (2007) 499.
[21] G. Nabi Bidhendi, P. Norouzi, P. Daneshgar, M.R. Ganjali, J. Hazard. Mater. 143 (2007) 264.
[22] P. Norouzi, M.R. Ganjali, S. Labbafi, A. Mohammadi, Anal. Lett. 40 (2007) 747.
[23] P. Norouzi, M.R. Ganjali, P. Daneshgar, P. Dinarvand, A.A. Moosavi-Movahedi, A.A. Saboury, Anal. Chim. Acta 590 (2007) 74.
[24] P. Norouzi, G.R. Nabi Bidhendi, M.R. Ganjali, A. Sepehri, M. Ghorbani, Microchim. Acta 152 (2005) 123.
[25] P. Norouzi, M.R. Ganjali, T. Alizadeh, P. Daneshgar, Electroanalysis 18 (2006) 947.
[26] M.R. Ganjali, P. Norouzi, M. Ghorbani, A. Sepehri, Talanta 66 (2005) 1225.
[27] J. Lipkowski, L. Stolberg, Adsorption of Molecules at Metal Electrodes, VCH, New York, 1992.
[28] J.C. Miller, J.N. Miller, Statistics for Analytical Chemistry, vol. 22, Ellis Horwood, Chichester, 1984, p. 82.

An aqueous two-phase system as a strategy for serum albumin depletion

Marcelo Anselmo Oseas da Silva, Marco Aurélio Zezzi Arruda *

*Group of Spectrometry, Sample Preparation and Mechanization (GEPAM), Department of Analytical Chemistry, Institute of Chemistry,
PO Box 6154, University of Campinas (UNICAMP), 13084-862 Campinas, SP, Brazil*

ABSTRACT

An aqueous two-phase system, based on the cloud point phenomenon, was proposed for blood plasma albumin depletion prior to gel electrophoresis (SDS-PAGE) analysis. Albumin removal was evaluated using a mixture of Triton® X-114 and SDS. Variables affecting phase separation and the partition coefficient (K), such as pH (from 5.0 to 7.6) and salt composition, were first optimized to carry out phase separation at room temperature and to promote albumin removal (15 min with *ca.* 95% efficiency) to the surfactant-rich phase, in a global process that results in reduction of 12% α-helix structures, confirmed through circular dichroism analysis. Gel electrophoresis analyses were carried out to compare crude human plasma composition with human plasma submitted to the cloud point procedure as well as the same plasma submitted to the separation of albumin using a commercially available system based on a chromatographic affinity column. The cloud point extraction procedure allowed identification of 18 protein bands present in the surfactant-poor phase, resulting in a more detailed electrophoretic profile, when compared with crude plasma (10 protein bands).

© 2008 Elsevier B.V. All rights reserved.

1. Introduction

Albumin represents approximately 50% of total blood plasma proteins. Although it presents great importance to the sample [1], the high albumin concentration in a given system can also be considered a significant problem in studies involving biomarker analyses. Thus, albumin removal from a sample becomes fundamental for obtaining adequate separation [2], since these biomarkers are commonly present at lower concentration levels in a sample, and must be isolated from major proteins before analysis [3].

Thus, the development of efficient and fast methodologies for protein extraction and purification is of utmost importance [4,5]. Methods applying aqueous two-phase systems as cloud point extraction (CPE) can be an attractive alternative to promote albumin depletion. In fact, CPE has been receiving a large amount of attention for isolating and concentrating important biomolecules, including proteins [6–12], because only a few minutes are needed to bring most two-phase systems into equilibrium and biocompatible conditions, in terms of pH and temperature are attained [6]. Such conditions are attractive features of easy scale-up [6,13].

In a general way, CPE systems are based on the application of nonionic surfactant solutions with controlled temperature and ionic strength, leading to a coacervation process: above the critical micellar concentration (CMC) surfactant monomers tend to

form aggregates, which are denominated micelles. By increasing the solution temperature and/or the ionic strength by using cosmotropic ions a reduction of the monomer solubility due to dehydration of oxyethylene groups can be attained. As a consequence, two immiscible phases are formed: one of them containing a high surfactant concentration, called the rich phase, and other containing a lower surfactant concentration, near to the CMC, denominated the poor phase [14].

Due to the complexity, variability and instability of the analytes (proteins), universal or official methods for protein depletion are difficult to establish. The present work describes a CPE system, offering a new alternative for serum albumin depletion. Since this strategy depends on several variables, such as pH, temperature, type and concentration of the surfactant, net charge, etc., they were first optimized, and circular dichroism (CD) analysis was carried out using the optimized system to highlight those biocompatible characteristics attained with this new albumin depletion procedure. Finally, gel electrophoresis analyses were carried out for comparisons between the rich and poor phases when CPE was applied, as well as for checking the CPE albumin depletion efficiency when compared with a commercially available system.

2. Materials and methods

2.1. Reagents, solutions and samples

All reagents were of analytical grade. The nonionic surfactant polyoxyethylene (8) isooctylphenyl ether (trade name as Triton®

X-114) was obtained from Sigma–Aldrich (Steinheim, Germany). Sodium dodecyl sulphate (SDS) was from USB (Cleveland, USA). The reagents applied in gel electrophoresis were from Amersham Biosciences (Uppsala, Sweden). All other chemicals (including phosphoric acid, potassium dihydrogen phosphate, sodium hydroxide, hydrochloric acid, Coomassie Brilliant Blue G-250, ammonium acetate, methanol, ethanol, tris(hydroxymethyl)-aminomethane and the albumin standard) were obtained from Merck (Darmstadt, Germany) and J.T. Baker (Phillipsburg, NJ, USA). All solutions were prepared with deionized water ($\geq 18.2\,M\Omega\,cm$) obtained using a Milli-Q water purification system (Millipore, Bedford, USA).

All tests were carried out in a buffered medium, including albumin standards, using a phosphate/NaOH buffer. Concentrations and pH were adjusted accordingly.

In order to optimize the entire albumin extraction process, a surfactant concentration study was carried out. Adequate volume of Triton® X-114 and a 10% (w/v) SDS stock solution, prepared in phosphate buffer, were mixed into 10-mL test tubes, to produce solutions with final concentrations ranging from 1.0% to 5.0% (v/v) Triton® X-114 and from 0.1% to 1.0% (w/v) SDS. Finally, a $500\,mg\,L^{-1}$ albumin standard stock solution prepared in phosphate buffer was added to each solution to produce a $125\,mg\,L^{-1}$ albumin solution. This final concentration allows adequate rich phase volume to the protein added mass, avoiding rich phase saturation, as well as minimization of sample dilution effects, once that at higher degree they can impair circular dichroism analysis.

Human plasma, free of disease, was provided by the Clinical Hospital of UNICAMP. Clinical controls of the samples were made at the hospital, and the bags were received in our laboratory with their seal of approval. They were stocked at $-20\,^\circ C$ until analysis.

2.2. Phase separation procedure

Cloud point (CP) measurements were visually performed by inserting the test tubes in a thermostated water bath (Amersham Biosciences, Multi Temp III, Freiburg, Germany). A heating rate of $0.5\,^\circ C$ each 30 s was applied, until obtaining permanent anisotropic solutions, characterizing the CP [4].

Solutions were centrifuged at $1780 \times g$ for 5 min and fractions of the rich (lower) and the poor (upper) phases were collected for protein quantification.

2.3. Protein quantification

The Bradford method [15] was applied for all protein quantification. Since the presence of surfactant led to interference in this method, the collected fractions were first submitted to a precipitation procedure. Each sample volume was mixed with five volumes of $0.1\,mol\,L^{-1}$ ammonium acetate in methanol. This mixture was kept at $-20\,^\circ C$ for 3 h. Then, the supernatant was removed, and the pellet dissolved with $0.1\,mol\,L^{-1}$ phosphate buffer at pH 7.2. Aliquots of $200\,\mu L$ were placed in a plastic cell followed by the addition of 2.5 mL of Bradford reagent [15]. Absorbance values were measured at 595 nm in a UV–vis spectrophotometer (Micronal, São Paulo, Brazil), after a 5-min reaction. Bovine serum albumin (BSA) solutions ($25–100\,\mu g\,mL^{-1}$), in $0.2\,mol\,L^{-1}$ phosphate buffer at pH 7.2, were applied as standards in the analytical curve.

Extraction efficiency was evaluated in terms of partition coefficient, K, defined as the ratio between rich and poor phase protein concentrations, respectively. It was obtained via total protein quantification using the Bradford method.

2.4. Circular dichroism analysis

CD analyses were carried out in a Jasco automatic recording spectropolarimeter, model 720 (Tokyo, Japan). A cell with a path-length of 0.1 cm was used. CD spectral parameters used wavelengths ranging from 195 to 250 nm; a cell temperature at $20\,^\circ C$; resolution of 1 nm and 100 mdeg of sensitivity.

Protein analyses were carried out in the rich phase, after precipitation with ammonium acetate $0.1\,mol\,L^{-1}$ in methanol. The pellet was dissolved with $0.2\,mol\,L^{-1}$ phosphate buffer at pH 5.0 to obtain $1.3\,\mu mol\,L^{-1}$ albumin solution. As reference, a $1.3\,\mu mol\,L^{-1}$ albumin standard solution, also in phosphate buffer, previously submitted to the precipitation procedure with ammonium acetate $0.1\,mol\,L^{-1}$ in methanol and dissolved with phosphate buffer was used.

The results were expressed in terms of mean residue molar ellipticity (θ), in units of $deg\,cm^2\,dmol^{-1}$. For secondary structure estimations, four different algorithms (Selcon 2 and 3 [16], K2D [17] and CONTIN [18,19]) were applied.

2.5. Gel electrophoresis analysis

Gel electrophoresis analysis (SDS-PAGE) were carried out in order to evaluate albumin removal from plasma samples. For this study, $100\,\mu L$ of human plasma were added to test tubes containing previously optimized surfactant concentrations: 4.0% (v/v) Triton® X-114, 0.8% (w/v) SDS in $0.2\,mol\,L^{-1}$ phosphate buffer at pH 5.0.

After the phase separation procedure, 1.0 mL of poor phase and 1.0 mL of rich phase were collected in different test tubes and precipitated with 4.0 mL of acetone. The mixtures were kept at $-20\,^\circ C$ for 3 h. Then, the supernatants were removed and the pellets were dissolved using a denaturant electrophoresis buffer composed by a mixture of Tris (hydroxymethyl)-aminomethane 60 mM at pH 6.8 (adjusted using concentrated HCl); 10.0% (w/v) glycerol; 20% (v/v) SDS; 5.0% (v/v) β-mercaptoethanol and 0.001% (w/v) bromophenol blue [20]. In order to obtain well defined gels, solutions containing $320\,\mu g\,mL^{-1}$ of protein (solution A) and $160\,\mu g\,mL^{-1}$ of protein (solution B) were prepared.

$25\,\mu L$ of solutions A (8 μg of protein) and B (4 μg of protein) were used for SDS-PAGE analysis. The separation using a 10.0% (w/v) acrylamide gel and the protein stain were carried out according to Garcia et al. [21]. The protein markers (#SM0431, MBI Fermentas, Hanover, USA) were used for molecular mass estimation.

Two other electrophoretic runs were carried out in order to compare the proposed method. In the first, crude plasma was diluted with denaturant electrophoresis buffer [20] in order to obtain a solution with final concentration of $320\,\mu g\,mL^{-1}$. In this case, $25\,\mu L$ of diluted plasma (8 μg of protein) was applied in the gel.

The second one received a previously depleted sample, which was submitted to a commercially available system (Montage Albumin Depletion Kit, Millipore, USA), based on an albumin affinity column. For this sample, the standard kit's protocol, described in the user's guide was applied.

The gels were scanned and images were analyzed using the Gel-Pro Analyzer® 3.1 software (Media Cybernetics Inc., Silver Spring, USA), to estimate the protein molar masses of samples.

3. Results and discussion

Application of CPE for albumin extraction has some limitations related to the high hydrophilicity of this protein, disabling its migration to the interior of hydrophobic micelles [6]. In this way, in the optimization process, charge characteristics of the system were taken into account, as can be noted through the discussion section, once that it is fundamental to attain high partition coefficient values.

3.1. Effect of SDS concentration on CP temperature and micelle formation

Protein extraction procedures using nonionic surfactants only, such as Triton® X-114 or Triton® X-100, are based on excluded volume interactions involving hydrophobic micelles interiors and hydrophobic protein regions [22]. Low extraction efficiencies are frequently attained for these systems, when they are applied for hydrophilic molecules extraction due to the hydrophobic micelle cores [23]. However, this class of surfactant is commonly used because it provides lower CP, allowing phase separation at biocompatible conditions.

The problem in using ionic surfactants only is the difficulty to promote phase separation, due to the presence of charged micelles. To attain the CP under these conditions, the addition of inorganic acids, such as hydrochloric acid, is necessary. Even though this procedure can be applied for metal extraction [24], it is not applicable for proteins, since conditions with low pH induce to the denaturation of the proteins.
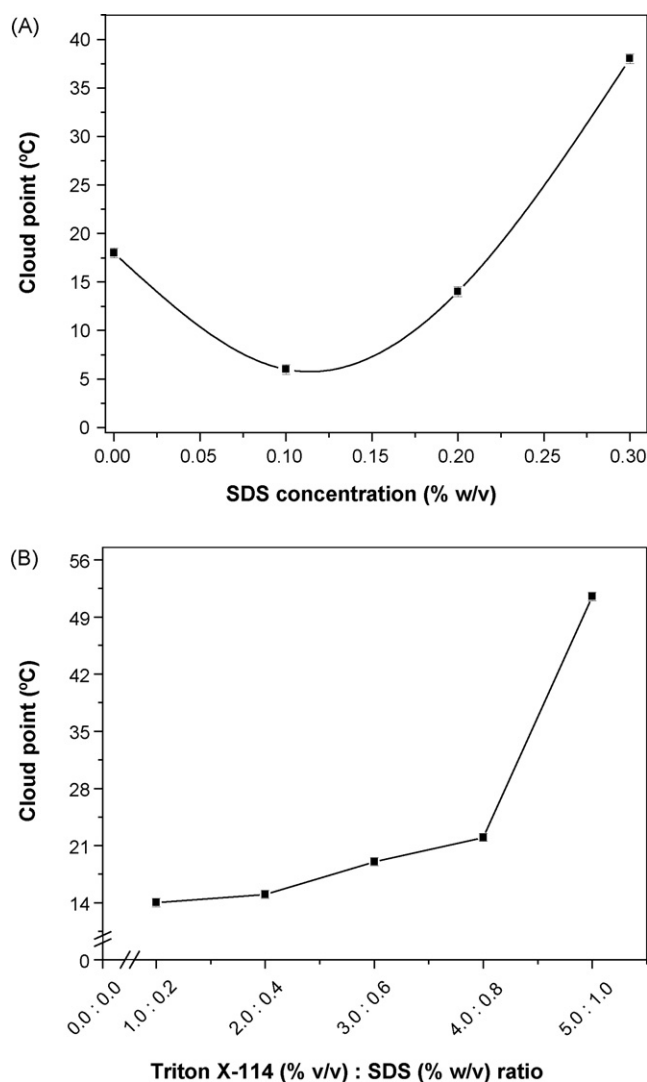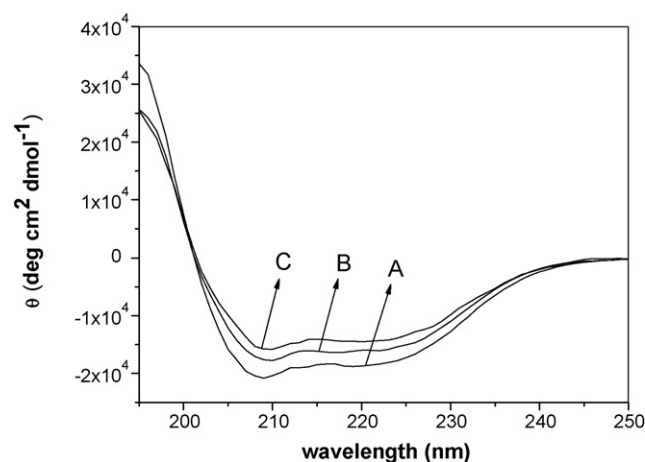

Fig. 2. Circular dichroism analysis. (A) BSA prepared in 0.2 mol L^{-1} phosphate buffer at pH 5.0; (B) BSA prepared in 0.1 mol L^{-1} phosphate at pH 5.0 after precipitation process with 0.1 mol L^{-1} ammonium acetate in methanol; (C) BSA prepared in 0.1 mol L^{-1} phosphate buffer at pH 5.0 after proposed extraction procedure and later precipitation with 0.1 mol L^{-1} ammonium acetate in methanol.

To resolve this, a mixture involving both ionic and nonionic surfactants to promote efficient protein removal procedures is usually applied. Parameters involved in this extraction process include the shape of the formed micelles, hydrodynamic protein and micelle radii and their charges.

In this sense, SDS concentration ranging from 0.1% to 0.5% (w/v) was the first parameter evaluated. Triton® X-114 concentration was fixed at 1.0% (v/v) and 100 mM phosphate buffer at pH 7.2 was applied. Two antagonic effects can be noted (see Fig. 1A): the first one is related to the cloud point decrease at SDS concentrations between 0.1% and 0.2% (w/v), when compared with a solution containing Triton® X-114 only. For these solutions, a reduction in the cloud point from 18 to 6 °C and from 18 to 14 °C, respectively, can be observed due to the grade of micelles monomers hydration [25]. The second effect consists on the cloud point increase due to the ionic surfactant predominance in the micelles composition. For concentrations higher than 0.3% (w/v), poor cloud point values were attained. According to obtained results, a mixture composed by 1.0% (v/v) Triton® X-114 and 0.2% (w/v) SDS (ratio of Triton® X-114/SDS at 5) was chosen to carry out the optimization once that this mixture presented low cloud point with the highest possible ionic micelles composition.

3.2. Triton® X-114 and SDS concentrations

Five Triton® X-114/SDS concentrations were evaluated while maintaining the ratio of Triton® X-114 to SDS at 5. Phase separa-

Fig. 1. Concentration studies. (A) Effect of SDS on cloud point for solutions containing 125 μg mL^{-1} BSA and 1.0% (v/v) Triton® X-114 in the presence of 100 mM phosphate buffer at pH 7.2. (B) Effect of SDS/Triton® X-114 ratio on cloud point for solutions containing 125 μg mL^{-1} BSA in the presence of 0.1 mol L^{-1} phosphate buffer at pH 7.2.

Table 1
Estimated percentages of α-helix structures

Method	Estimated α-helix structures (%)		
	Conditions		
	A	B	C
Selcon 2	58	50	45
Selcon 3	55	51	44
K2D	65	58	60
CONTIN	71	53	50
Average value[a]	62 ± 7	53 ± 4	50 ± 7

Using data obtained from CD analysis, for BSA under three different conditions: (A) 0.2 mol L^{-1} phosphate buffer at pH 5.0; (B) after precipitation with 0.1 mol L^{-1} ammonium acetate in methanol; (C) after proposed extraction procedure and posterior precipitation with 0.1 mol L^{-1} ammonium acetate in methanol.

[a] Mean ± sampling standard deviation.

tion is carried out at higher temperatures (above 30 °C, see Fig. 1B) using surfactant mixtures of 5.0% (v/v) Triton® X-114 and 1.0% (w/v) SDS or even higher. However, with this surfactant mixture, the micelles presented significant ionic surfactant characteristics,

being its application not suitable for protein extraction. Thus, for the optimization studies, a mixture of 4.0% (v/v) Triton® X-114 and 0.8% (w/v) SDS was used. It has higher ionic surfactant composition, providing better extractions results.
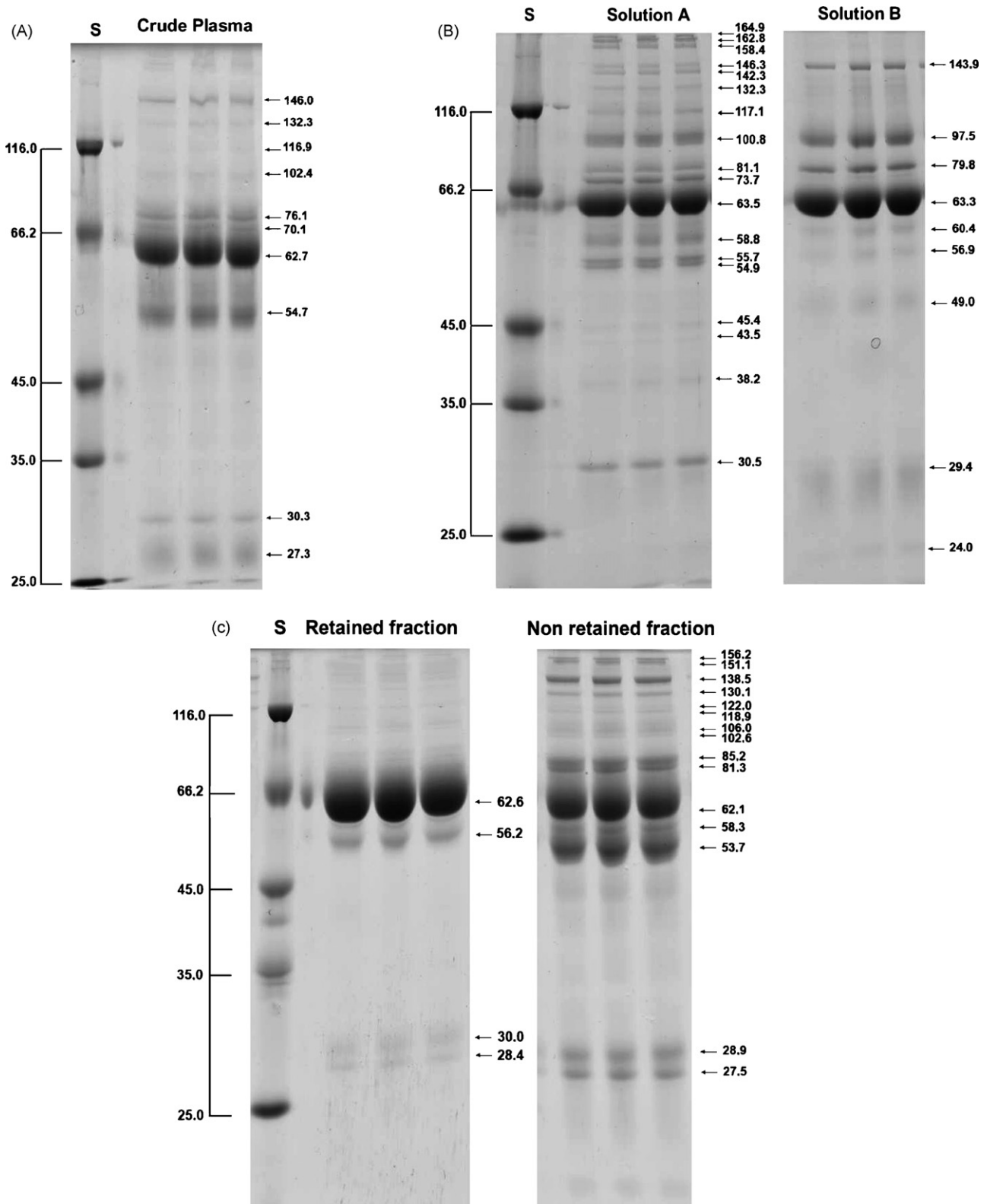
Fig. 3. Gel electrophoresis profiles. (A) 8.0 μg of crude plasma diluted with an adequate volume of denaturant electrophoresis buffer; (B) 8.0 μg of proteins contained in solution A (proteins presented in the poor phase) and 4.0 μg of proteins contained in solution B (proteins presented in the rich phase); (C) proteins retained on an albumin affinity column and non-retained proteins. The recommended protocol was used. Protein standards are represented by (S).

For all conditions evaluated, the poor phase was visually cloudy after the centrifugation process. The addition of 1.0% (w/v) NaCl in each test solution was applied to assure complete phase separation process.

3.3. Effect of pH

Protein extraction based on cloud point extraction is pH dependent [26,27]. The partition coefficient was obtained close to physiological conditions, ranging from 5.0 (albumin isoelectric point) to 7.6, using the optimized surfactant concentrations and 0.1 mol L^{-1} phosphate buffer at different pH.

The results obtained reveal that K was greatly increased (from 0.10 ± 0.09 at pH 7.2 to 2.8 ± 0.7) when the solution pH was close to the albumin isoelectric point (pH 5.0). At the isoelectric point, the overall albumin charge is close to zero. However, it presents side chains of aminoacids containing positive charges that can interact with micelles through electrostatic interactions. In addition, at this pH, albumin solubility is reduced, favoring its migration to surfactant-rich phase. This behavior is observed even with reduction of the association constants for albumin and ionic surfactant complex formation [28], as a consequence of a highly compacted protein structure, minimizing its residue and cavity exposure that make interactions with the surfactants difficult.

3.4. Influence of electrolyte

Sodium chloride was added to the solution for promoting effective phase separation, maximizing protein extraction. However, an adverse effect on protein extraction was noted: micelle charge neutralization. Sodium ions are disposed on the micelle surfaces by electrostatic interactions, contributing for both a CP temperature decrease and albumin–surfactant interactions [29,30]. Thus, replacement of NaCl by KH$_2$PO$_4$ was evaluated by increasing the phosphate buffer concentration from 0.1 to 0.2 mol L^{-1}.

The results show an increase in the K values at pH 5.0 from 2.8 ± 0.7 to 9.2 ± 0.5, representing *ca.* 95% extraction efficiency, according to quantitative protein analysis using Bradford method. This behavior can be explained in terms of the phosphate ions, which present cosmotropic characteristics (higher hydration capability), thus drastically reducing charge neutralization effects.

3.5. Contact time study

The contact time is defined as the period in which the proteins are in contact with surfactant, before the phase separation process is completed. The results obtained for protein extraction, using solutions containing 4.0% (w/v) Triton® X-114 and 0.8% (v/v) SDS in 0.2 mol L^{-1} phosphate buffer at pH 5.0, show only slight variations in partition coefficient ($K = 3.1 \pm 0.5$) when contact time ranged from 10 to 50 min.

3.6. Circular dichroism analysis

BSA CD analysis (Fig. 2) and (Table 1) obtained for protein present in a medium containing 0.2 mol L^{-1} phosphate buffer at pH 5.0 confirm the presence of *ca.* 62% α-helix structures (Fig. 2, spectrum A). This value is in accordance with the literature [31], providing evidences that α-helix structures is kept constant for BSA molecules prepared in phosphate buffer.

Analysis carried out for BSA submitted to the precipitation procedure using 0.1 mol L^{-1} ammonium acetate in methanol (Fig. 2, spectrum B) shows a reduction in α-helix structures to 53%, indicating protein denaturation due to the precipitation process induced with high salt concentrations: excess of ammonium acetate reduces

albumin solvation as well as the protein excluded volumes as a consequence of preferential solvent coordination (water) with ions from the precipitating agent. This necessity of local charge solvation and the reduction of protein–solvent interactions results in attraction between side chains of BSA aminoacids residues, as well as protein structure changes [32,33].

Results obtained for BSA submitted to the extraction procedure followed by the precipitation step (Fig. 2, spectrum C) indicate reduction in α-helix structures to 50% as a consequence of precipitation procedure, as well as interactions involving BSA and surfactant monomers. In this case, band reduction at *ca.* 208 and 220 nm are mainly referred to magnetically allowed transitions involving free electrons from oxygen. It is important to note that BSA presents a relative structural stability conferred due to the presence of disulfides bounds [34,35].

3.7. Electrophoretic profile evaluation after albumin depletion procedure

Fig. 3 presents the SDS-PAGE gel separations for crude plasma (Fig. 3A) solutions A (poor phase) and B (rich phase) (Fig. 3B), and a commercial system (Fig. 3C). In crude plasma 10 bands were detected, including albumin (*ca.* 63 kDa), as well as other high abundance plasmatic proteins, including immunoglobulin (*ca.* 146 kDa and 30 kDa), and transferrin (at 76 kDa). An undefined band at 54 kDa can also be observed.

As expected, the gel obtained after electrophoresis solution B (Fig. 3B) presented a high albumin concentration, due to the presence of an intense band *ca.* 63 kDa. Another eight bands can also be observed, indicating an unselective extraction. For this separation, application of higher sample mass could produce an excess of protein, albumin particularly, making the analysis difficult.

Solution A (Fig. 3B), representing proteins contained in the poor phase from CPE, revealed an interesting and highly detailed electrophoretic profile. Eighteen bands are visualized in the gel, including those identified in the gel obtained using crude plasma. Albumin was also present in this solution (band *ca.* 63 kDa), showing an incomplete removal. The 54-kDa band is now divided into two bands, *ca.* 54.9 and 55.7 kDa, which can be attributed to immunoglobulin and antitrypsin.

Comparison between the cloud point procedure and the extract from a commercial system shows that non-retained proteins (equivalent to the poor phase) presented a similar electrophoretic profile, resulting in a gel with *ca.* 15 bands. The retained fraction (equivalent to the rich phase) showed albumin as the major protein, but other abundant plasmatic proteins can also be noted.

4. Conclusions

The initial purpose of this work was attained, once that a simple, fast (*ca.* 15 min) and inexpensive (less than US$ 1.00 per sample, considering reagents only) procedure is presented for albumin depletion using an aqueous two-phase system. An optimized solution (4.0% (v/v) Triton® X-114, 0.8% (w/v) SDS in 0.2 mol L^{-1} phosphate buffer at pH 5.0) allowed albumin extraction to the surfactant-rich phase at room temperature, due to charge interaction between micelles and target protein. The control of pH and ionic strength were the most important factors involving the extraction process: the first acts by changing the overall charge of the proteins, allowing their migration to the surfactant-rich phase, while the second defines the micellar surface charge, which is responsible for micelle–protein interactions.

The presence of electrostatic interactions involving micelles surface and BSA, as well as the precipitation step for promoting

surfactant removal, resulted in 12% α-helix reduction, indicating changes in the protein structure. However, the proposed method does not present limitation due to these conformational alterations.

Gel electrophoresis showed preferential albumin extraction to the rich phase when the optimized system was applied to blood plasma samples. Less abundant proteins were observed in the poor phase, resulting in a highly detailed electrophoretic profile. A commercial system for albumin depletion, based on a protein affinity column, produced similar results to the obtained with the CP procedure, pointing out that this new strategy for albumin depletion can successfully and routinely be applied for this purpose.

Acknowledgements

References

[1] T. Peters Jr., Adv. Protein Chem. 37 (1985) 161.
[2] K. Björhall, T. Miliotis, P. Davidsson, Proteomics 5 (2005) 307.
[3] L.A. Echan, H.Y. Tang, N.A. Khan, K. Lee, D.W. Speicher, Proteomics 5 (2005) 3292.
[4] C.S. Magalhães, J.S. Garcia, A.S. Lopes, E.C. Figueiredo, M.A.Z. Arruda, in: M.A.Z. Arruda (Ed.), Trends in Sample Preparation, Nova Science Publishers, New York, 2007, pp. 245–288.
[5] B.A. Chromy, A.D. Gonzales, J. Perkins, M.W. Choi, M.H. Corzett, B.C. Chang, C.H. Corzett, M. Maloney, J. Proteome Res. 3 (2004) 1120.
[6] A.S. Lopes, J.S. Garcia, R.R. Catharino, L.S. Santos, M.N. Eberlin, M.A.Z. Arruda, Anal. Chim. Acta 590 (2007) 166.
[7] J.X. Xiao, U. Sivars, F. Tjerneld, J. Chromatogr. B 743 (2000) 327.
[8] T. Saitoh, W.L. Hinze, Talanta 42 (1995) 119.
[9] T. Zhang, H. Liu, J. Chen, Sep. Sci. Technol. 35 (2000) 143.
[10] D.T. Kamei, J.A. King, D.I.C. Wang, D. Blankschtein, Biotechnol. Bioeng. 80 (2002) 233.
[11] G.C. Kresheck, Z. Wang, J. Chromatogr. B 858 (2007) 247.
[12] C.O. Rangel-Yagui, H. Lam, D.T. Kamei, D.I.C. Wang, A. Pessoa Jr., D. Blankschtein, Biotechnol. Bioeng. 82 (2003) 445.
[13] Y. Wang, K. Kimura, P.L. Dubin, Macromolecules 33 (2000) 3324.
[14] W. Hinze, E. Pramauro, Crit. Rev. Anal. Chem. 24 (1993) 133.
[15] M.M. Bradford, Anal. Biochem. 72 (1975) 248.
[16] N. Sreerama, R.W. Woody, Anal. Biochem. 209 (1993) 32.
[17] M.A. Andrade, P. Chacon, J.J. Merelo, F. Moran, Protein Eng. Des. Sel. 6 (1993) 383.
[18] S.W. Provencher, Comput. Phys. Commun. 27 (1982) 213.
[19] S.W. Provencher, Comput. Phys. Commun. 27 (1982) 229.
[20] C.S. Magalhães, M.A.Z. Arruda, Talanta 71 (2007) 1958.
[21] J.S. Garcia, P.L. Gratao, R.A. Azevedo, M.A.Z. Arruda, J. Agric. Food Chem. 54 (2006) 8623.
[22] Y.J. Nikas, C.L. Liu, T. Srivastava, N.L. Abbott, D. Blankschtein, Macromolecules 25 (1992) 4797.
[23] R.J. Robson, E.A. Dennis, J. Phys. Chem. 81 (1977) 1075.
[24] C.C. Nascentes, M.A.Z. Arruda, Talanta 61 (2003) 759.
[25] M. Jönsson, H. Johansson, J. Chromatogr. A 983 (2003) 133.
[26] H. Tani, T. Kamidate, H. Watanabe, Anal. Sci. 14 (1998) 875.
[27] J. Gutenwik, B. Nilsson, A. Axelsson, Biochem. Eng. J. 19 (2004) 1.
[28] E.L. Gelamo, C.H.T.P. Silva, H. Imasato, M. Tabak, Biochem. Biophys. Acta 1594 (2002) 84.
[29] D.J. Shaw, Introduction to Colloid and Surface Chemistry, 2nd ed., Oxford Press, Butterworth-Heinemann, UK, 1992.
[30] Y. Moroi, Miceles: Theoretical and Applied Aspects, 1st ed., Plenum Press, New York, 1992.
[31] D. Güzey, Í. Gülseren, B. Bruce, J. Weiss, Food Hydrocoll. 20 (2006) 669.
[32] R.A. Curtis, L. Lue, Chem. Eng. Sci. 61 (2006) 907.
[33] D.E. Kuehner, H.W. Blanch, J.M. Prausnitz, Fluid Phase Equilibr. 116 (1996) 140.
[34] J.D. Hirst, K. Colella, A.T.B. Gilbert, J. Phys. Chem. B 107 (2003) 11813.
[35] Y. Li, X. Wang, Y. Wang, J. Phys. Chem. 110 (2006) 8499.

Automated solid phase extraction, on-support derivatization and isotope dilution-GC/MS method for the detection of urinary dialkyl phosphates in humans

G.K. Hemakanthi De Alwis*, Larry L. Needham, Dana B. Barr

Division of Laboratory Sciences, National Center for Environmental Health, Centers for Disease Control and Prevention, 4770 Buford Highway, NE, Mailstop F 17, Atlanta, GA 30341, USA

ABSTRACT

We developed an analytical method based on solid phase extraction, on-support derivatization and isotope dilution-GC/MS for the detection of dialkyl phosphate (DAP) metabolites, dimethyl thiophosphate, diethyl thiophosphate, dimethyl dithiophosphate, and diethyl dithiophosphate in human urine. The sample preparative procedure is simple and fully automated. In this method, the analytes were extracted from the urinary matrix onto a styrene-divinyl benzene polymer-based solid phase extraction cartridge and derivatized on-column with pentafluorobenzyl bromide. The ester conjugated analytes are eluted from the column with acetonitrile, concentrated and analyzed. Compared to extraction–post extraction derivatization methods for the analysis of DAP metabolites, this on-support derivatization is fast, efficient, and less labor-intensive. Furthermore, it has fewer steps in the sample preparation, uses less solvent and produces less interference. The method is highly sensitive with limits of detection for the analytes ranging from 0.1 to 0.3 ng/mL. The recoveries were high and comparable with those of our previous method. Relative standard deviation, indicative of the repeatability and precision of the method, was 1–17% for the metabolites.

Published by Elsevier B.V.

1. Introduction

Organophosphorus (OP) pesticides are widely used as insecticides in agriculture on crops, in residential settings for pest control and in public health programs to control vector-borne diseases. Because of this extensive use humans are at potential risk for exposure to OP pesticides. In humans these OP pesticides are metabolized to form dialkyl phosphates and the measurement of urinary DAPs is commonly used as a means of biological monitoring for OP pesticide exposure. The most commonly used DAP metabolites are dimethyl phosphate (DMP), diethyl phosphate (DEP), dimethyl thiophosphate (DMTP), diethyl thiophosphate (DETP), dimethyl dithiophosphate (DMDTP), and diethyl dithiophosphate (DEDTP) (Fig. 1). Direct determination of DAPs using liquid chromatography has not been very common owing to the low sensitivity associated, and majority of the

methods of OP analysis are based on gas chromatographic determination of derivatized DAP metabolites. A conventional sample preparation involves two steps: an extraction step which isolates metabolites from the urine matrix followed by a derivatization step that yields the desired derivative. The high polarity and high water solubility of the DAPs have often posed a considerable problem in isolating them from a polar urinary matrix and, to address this issue, many extraction methods including liquid–liquid extraction [1–5], solid phase extraction [6–8], anion exchange [9], extractive-derivatization [10], azeotropic distillation [11–16], lyophilization [17–20] have been tried in the past, which were often time consuming and/or labor-intensive. Furthermore, some methods failed to give clean extracts affecting subsequent derivatization and interfering in the GC analysis and, therefore, necessitating pre- or post-derivatization cleanup [14,11]. For example, azeotropic distillation resulted in a viscous gummy urine residue [12,15] in which DAPs were speculated to be encapsulated hindering efficient derivatization [15]. We have applied solid phase extraction successfully to pre-concentrate OP metabolites from a urinary matrix on a styrene-divinyl benzene (SDVB) polymer-based sorbent material with a subsequent acid wash to produce a relatively cleaner eluate containing the metabolites

* Corresponding author. Present address: Food and Drug Administration, FDA Center for Veterinary Medicine, Office of Research, 8401 Muirkirk Road, Laurel, MD 20708, USA. Tel.: +1 301 210 4581; fax: +1 301 210 4653.
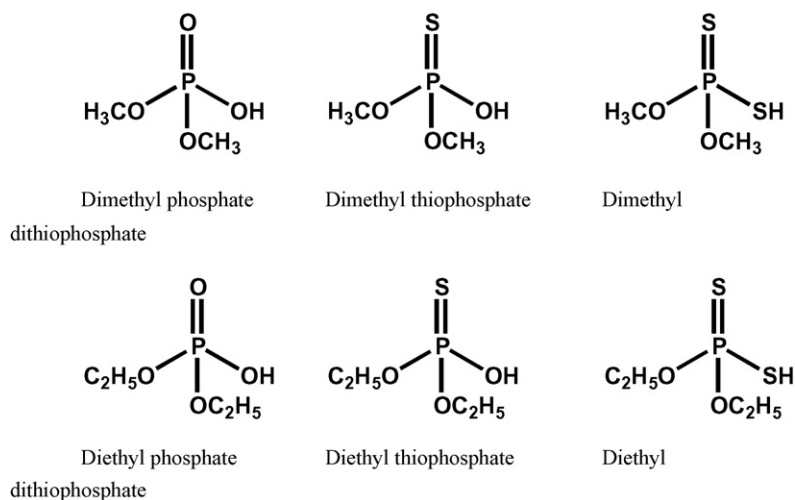*E-mail address:* hemakanthi.dealwis@fda.hhs.gov (G.K.H. De Alwis).

Fig. 1. Dialkyl phosphate metabolites.

which were derivatized to give good recoveries of the alkylated products [21,22].

It is reported that SDVB macroreticular polymeric resins serve as good solid supports for analytical derivatization reactions [23–31]. Combined with its high surface area and high adsorptivity which allows sorption of the analytes by hydrophobic binding [32], the SDVB polymers proved to be good materials to enable simultaneous extraction and derivatization from aqueous solution of a variety of compound classes [28]. The high retention of the DAP metabolites on the SDVB polymer prompted us to investigate the feasibility of derivatization of the metabolites on this solid support, which could, if works well, provide us with a fast sample preparative method that could be fully automated.

Here we report some preliminary findings of this investigation. An analytical method was developed for the detection of DMTP, DETP, DMDTP and DEDTP in human urine based on automated solid phase extraction on-support derivatization and isotope dilution-GC/MS. In this method, acidified urine is passed through the SDVB SPE cartridge to retain the analytes followed by the derivatizing agent, pentafluorobenzyl bromide, to alkylate the analytes concurrently on the solid support. This method is simple, rapid and highly labor efficient.

2. Experimental

2.1. Analytical standards and reagents

All organic solvents were analytical grade. Acetonitrile and toluene were purchased from Tedia Co., Inc. (Fairfield, OH, USA). Anhydrous sodium sulphate was obtained from Mallinckrodt Baker, Inc. (Paris, KY, USA). Concentrated hydrochloric acid, anhydrous potassium carbonate and tributyl phosphate (TBP) (99%) were purchased from Aldrich Chemical Co., Inc. (Milwaukee, WI, USA). 2,3,4,5,6-Pentafluorobenzyl bromide (99%) (PFBBr) was purchased from Sigma–Aldrich Co., Inc. (St. Louis, MO, USA). Analytes DMP and DEP (98%) were purchased from Pfaltz and Bauer, Inc. (Waterbury, CT, USA) and Acros Chemicals (Fairlawn, NJ, USA), respectively. DMTP (98%) and DMDTP (98%) were purchased from Cambridge Isotope Laboratories (Andover, MA, USA). DETP (98%) and DEDTP (90%) were purchased from Aldrich Chemical Co., Inc. (Milwaukee, WI, USA). The isotope-labeled analogues of the analytes, D6-DMP (dimethyl-d_6), D10-DEP (diethyl-d_{10}), D6-DMTP (dimethyl-d_6), D6-DMDTP (dimethyl-d_6), D10-DETP (diethyl-d_{10}) and ^{13}C4-DEDTP (diethyl-^{13}C$_4$) were custom synthesized by Cambridge Isotope Lab-

oratories (Andover, MA, USA). All isotopically labeled standards had chemical and isotopic purities of at least 99%. A 3 M hydrochloric acid solution was prepared by diluting 25 mL of concentrated acid with 75 mL deionized water. Deionized water was organically and biologically purified with a Barnstead Nanopure Infinity ultra-pure water purification system (Barnstead/Thermolyne, Dubuque, IA, USA). Ultra high purity grade nitrogen was purchased from Airgas Inc. (Radnor, PA, USA).

2.2. Preparation of standard solutions and quality control (QC) materials

Stock solutions and working solutions of native standards, isotope-labeled internal standards and TBP internal standard were prepared and stored as previously described [21,22]. Calibration standards were prepared daily by spiking 2 mL of blank urine with 12.5 μL of the analyte standard spiking solution and 12.5 μL of isotope-labeled internal standard spiking solution. TBP internal standard (12.5 μL) was added when necessary. QC materials, at levels low (QCL, 10 ng/mL) and high (QCH, 20 ng/mL), were prepared as previously described [21].

2.3. Sample preparation and automated SPE

The flow diagram in Fig. 2 summarizes the DAP extractive-derivatization procedure. Human urine (2.0 mL) was thawed, treated with 3 M hydrochloric acid (30 μL), spiked with isotope-labeled internal standard (12.5 μL) and vortex mixed. The automated SPE procedure was performed on RapidTrace extractor (Zymark Corporation, Hopkinton, MA, USA) using 500 mg/3 mL Bond Elut PPL SPE cartridges (Varian Sample Preparation Products, Harbor City, CA, USA) as follows: The reagent lines were primed by purging them with water, acetonitrile, and diluted aqueous hydrochloric acid (dil. HCl) (pH ~ 1). Urine samples were placed on the sample rack and SPE cartridges were placed on the column turret. After conditioning the SPE cartridge with acetonitrile (4 mL) and dilute HCl (4 mL) at a flow rate of 1 mL/min urine sample was loaded at 0.38 mL/min. The cartridge was dried by passing nitrogen (~30 psi) through it for 5 min. Next, 15% aqueous potassium carbonate solution (0.5 mL) was passed through the cartridge followed by 5 min drying with nitrogen. The derivatizing agent, 3% solution of PFBBr in acetonitrile (0.5 mL), was then applied to the cartridge at 0.38 mL/min and let stand for 15 min to complete reaction. Elution was accomplished with acetonitrile (4 mL) at a rate of
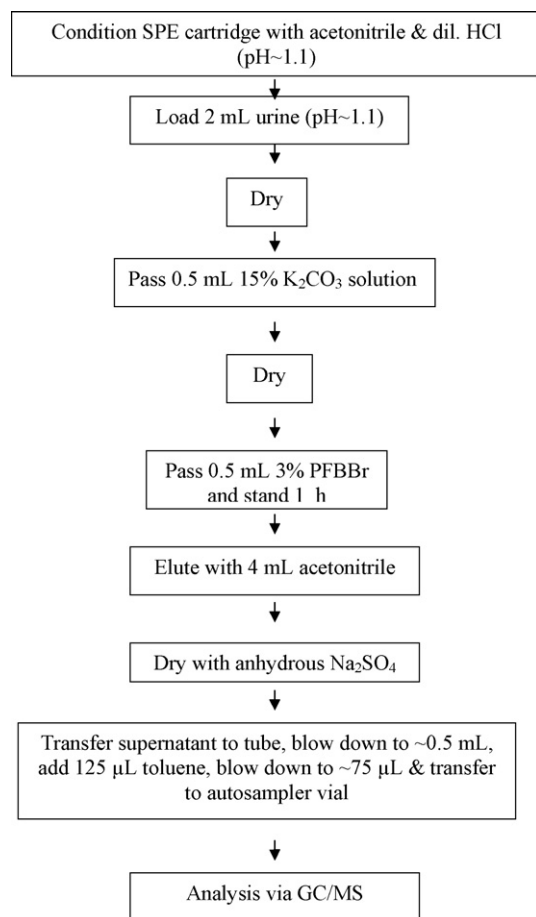
Fig. 2. Flow diagram for analysis of dialkyl phosphate metabolites in urine.

Fig. 3. A sample daily calibration curve for DEDTP. The values are weighted (1/X) by the Xcalibur software. The plot was linear across the range from 0 to 60 ng/mL with correlation coefficient typically exceeding 0.99. The inset shows curve at low concentrations.

0.5 mL/min into a 10 mL vial containing the drying agent, anhydrous sodium sulphate (∼2 g). After allowing for about 5 min in contact with sodium sulphate the supernatant was transferred to a 10 mL vial and concentrated in a Turbovap LV evaporator to about 0.5 mL. Toluene (125 μL) was then added to the sample, re-concentrated to a final volume of about 75 μL and transferred to an autosampler vial for analysis.

2.4. Instrumental analysis

Analysis was performed under the same conditions as specified elsewhere [22] using a Hewlett Packard 6890 Gas Chromatograph equipped with an Agilent 5973 mass selective detector (Agilent Technologies Inc. Palo Alto, CA, USA). Sample injection (1 μL) was performed by the splitless technique onto a J & W Scientific (Folsom, CA, USA) DB-5MS ([5%-Phenyl]-methylpolysiloxane) capillary GC column (30 m, 0.25 mm ID, 0.25 μm) using a Hewlett Packard 7683 autosampler (Agilent Technologies Inc. Palo Alto CA, USA). The mass spectrometer was operated in electron impact ionization mode at 70 eV and ions were monitored in the selected ion monitoring mode. The retention times and the detected ions for the metabolites, TBP and the isotope-labeled compounds are as given previously [22]. The data files, acquired using ChemStation software on a PC-based data system, were converted to XCalibur® files and manually evaluated. The identity of the metabolites was confirmed by matching retention times with the isotope-labeled internal standard. Quantification was done by the isotope dilution method [33].

2.5. Limits of detection

Five of the lowest standards were extracted five times each and the standard deviation was plotted against their concentrations. The intercept of the best-fit line was taken as S_0 which is the standard deviation as the concentration approaches zero. The analytical limit of detection (LOD) was calculated as $3S_0$ [34]. This LOD was verified by spiking urine samples at or near the LOD level to ensure that the analytes could be easily detected.

2.6. Recoveries

Blank urine samples that were SPE-extracted and concentrated were spiked with the native standard and TBP internal standard and then derivatized and analyzed. In parallel, blank urine samples, spiked with only the native standard, were taken through the extractive-alkylation and spiked with TBP and analyzed. Recovery, determined at three spiked levels, 1, 5 and 50 ng/mL with five replicates representing each level, was calculated using the ratio of the amount of analyte recovered after extractive-alkylation to the amount representing 100% analyte.

2.7. Relative recovery (accuracy)

The relative recovery was determined by enriching urine samples at three concentrations (i.e., 1.25, 6 and 40 ng/mL), and comparing the calculated concentrations to the spiked concentrations. For each concentration, five replicate samples were analyzed. A slope of 1.0 of a linear regression analysis of the expected value versus the calculated value indicates a 100% relative recovery.

2.8. Precision

The relative standard deviation (R.S.D.%) which is a measure of precision was determined by analyzing QC materials at the two concentration levels ($n = 10$ for each level) over a period of 2 weeks.

3. Results and discussion

The analytical method presented here can determine DMTP, DETP, DMDTP and DEDTP in human urine. This method, which is based on automated on-column solid phase extraction-derivatization and isotope dilution-GC/MS, is simple, fast, highly sensitive, repeatable, and requires only minimal analyst handling. We obtained linear calibration curves for all analytes over three

Table 1
Specifications of the analytical method

Analyte	R^2 of calibration line (% error of slope)	LOD ng/mL ($n=5$)	Recovery[a] ± S.D.[b] (%; $n=5$) relative to previous method[c]			Relative recovery (%; $n=5$)	Relative standard deviation[d] (R.S.D.%) ($n=10$)	
DMTP	0.996 (0.6)	0.30	63 ± 3	71 ± 3	73 ± 6	94.5	13	17
DMDTP	0.999 (0.3)	0.10	128 ± 11	120 ± 11	87 ± 5	105.0	2	2
DETP	0.999 (1.6)	0.10	75 ± 6	61 ± 4	73 ± 6	105.5	5	2
DEDTP	0.999 (1.3)	0.10	67 ± 3	70 ± 4	85 ± 3	101.3	1	2

[a] Recovery at 1, 5 and 50 ng/mL.
[b] S.D., Standard deviation.
[c] Reference [22].
[d] R.S.D.% for DAP concentrations of urine samples spiked at 10 and 20 ng/mL.

orders of magnitude with correlation coefficients exceeding 0.99 (Fig. 3, Table 1). The limits of detection (LODs), calculated from repeated analyses ($n=5$) of urine spiked with low DAP standards are shown in Table 1. The LOD values for all analytes compare well with those obtained before [22], except for a slightly higher value for DMTP.

The relative standard deviation (R.S.D.%) values (Table 1), <5% for all analytes except DMTP, which was ~15%, indicate the high repeatability of this method (Table 1). A linear regression analysis of the expected versus calculated concentrations of urine samples resulted in excellent slopes showing high relative recovery for all analytes (Table 1) ranging from 95 to 106%. We observed excellent agreement between calculated concentrations derived from this method and our previous method [22] (slope 0.996; R^2 0.993) (Fig. 4). A typical chromatogram of a spiked blank urine sample is given in Fig. 5.

We could not determine the absolute recovery of the overall analytical procedure due to the unavailability of the authentic standards of the pentafluorobenzyl esters. Neither could we determine an SPE recovery as we did in our previous methods [21,22] since this is a simultaneous extractive-derivatization procedure. Under the circumstances we calculated recoveries of this method relative to those of our previous method [22]. The results show that DMDTP and DEDTP recoveries were higher compared to our previous method while DETP showed a similar recovery and DMTP slightly lower recovery. It was noted that at concentrations 1 and 5 ng/mL DMDTP recoveries were greater than 100% indicating that on-column derivatization was more efficient than the derivatization separately carried out.

In this analytical procedure, urine is acidified (pH ~ 1.25) before passage through the cartridge so the DAPs are in their protonated/un-ionized form to be extracted effectively on the solid support. The aqueous potassium carbonate solution that is passed next converts the analytes to their anionic form for efficient derivatization. It also serves the purpose of a wash liquid. The drying step that follows removed most of the moisture from the cartridge. The residual water that may have been present did not seem to affect the reaction of DAPs with PFBBr which was subsequently applied to the column.
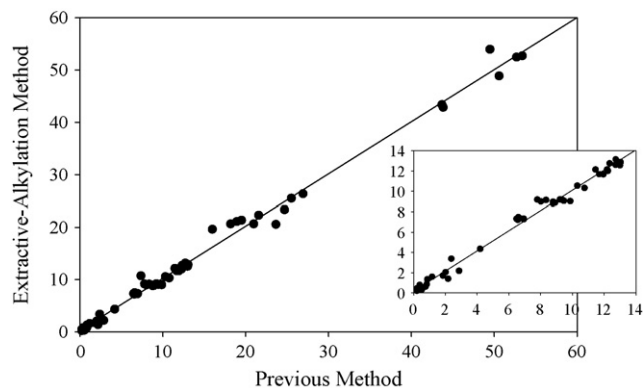
Analytical derivatization is an important step in the determination of organic compounds. It could increase stability of analytes, enhance volatility, improve chromatographic response and yield greater structural information [28,35]. However, these benefits of derivatization are overshadowed by the additional steps involved, higher material consumption, and the time, labor and costs associated. Furthermore, the reactions can produce side products that could interfere with the analysis [28,35]. Solid phase analytical derivatization (SPAD), which has gained much interest in the recent past, was found to be a solution to these problems [28,36]. SPAD involves simultaneous sorption and derivatization of the analytes from aqueous matrix onto the solid phase or sorption immediately followed by derivatization. The formed derivatives are also retained on the solid support and could be selectively eluted. SPAD is fast, has fewer steps in the sample preparation and produces less side products that may interfere with the analysis. Furthermore, SPAD is amenable to automation. Among many sorbents, polystyrene-divinyl benzene (SDVB) copolymer has been found to be an effective

Fig. 4. DAP Concentrations (ng/mL) of a series of standards analyzed by previous PFBBr GC/MS method and new method (62 data points). The gradient of 0.996 and R^2 value of 0.993 obtained indicate a good agreement between the two methods.
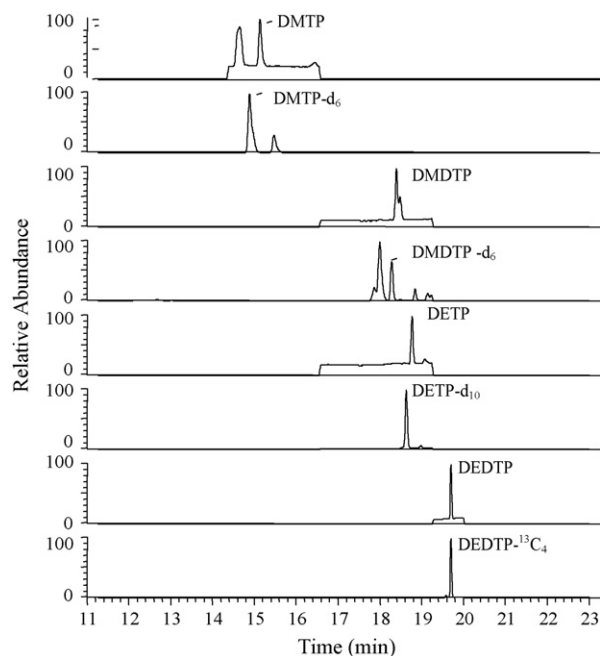

Fig. 5. Sample MS chromatogram for a spiked human urine extract containing ~2.0 ng/mL of the analytes and their labeled internal standards (~10 ng/mL) on a DB-5MS ([5%-Phenyl]-methylpolysiloxane) capillary column.

material for SPAD of many classes of analytes including carbonyl compounds [27,28], carboxylic acids [24,25], cannabinoids [23,28], bisphenol A and alkyl phenols [29] from biological/aqueous matrices. The SDVB polymer has a high surface area and high adsorptivity, is compatible with many solvents and can withstand extremes of pH [25,30]. Furthermore, it acts as a catalyst for some derivatization reactions [27]. The sorbent that we used in our method is a functionalized form of SDVB polymer that has even a greater hydrophobicity and a surface area that could retain even the most polar classes of compounds through non-polar interactions. On this solid support the analytes, DMTP, DMDTP, DETP and DEDTP were sorbed and derivatized from the urinary matrix with high yields. Although DMP and DEP are effectively extracted on to the sorbent as we previously demonstrated [21,22] they did not alkylate efficiently at room temperature under which the extractive-alkylation procedure is performed. The extent of derivatization seen was hardly enough for a meaningful evaluation of these two analytes.

Most of the work in the past [23–28] were performed using SDVB beads in a reaction vessel. In this SPAD procedure either the derivatizing agent is first immobilized on the beads and added to the biological matrix so the analytes are derivatized and adsorbed on the surface of the beads or the analytes are first adsorbed from the biological matrix, the liquid aspirated and the reagent added to the beads for the derivatization. After removing the liquid phase by filtration the derivatives are extracted from the beads using an organic solvent. In our work we used commercially available cartridges with the added advantage of fully automating the sample preparation using a RapidTrace extractor system which resulted in less labor-intensive, unattended extraction of samples. Furthermore, it reduced the solvent consumption drastically compared to the immobilization method. Application of derivatizing agent after the initial analyte sorption worked best for us.

With regard to many aspects as discussed above, a potential fully automated solid phase extractive-alkylation method that could determine all six metabolites would be a vast improvement on the procedures currently available for DAP analysis. Our work in this field is by no means complete as the method reported here has the limitation of not being able to determine DMP and DEP due to the low reactivity of these two analytes at room temperature with PFBBr. Work is, therefore, underway in our laboratory to find a suitable derivatizing agent that reacts efficiently at ambient temperature with all six metabolites and that could be applied effectively in the extractive-derivatization process. Such a reagent would greatly enhance the analytical capability of OP exposure assessment studies to evaluate relevant health effects.

Acknowledgements

References

[1] L.E. St.John, J. Lisk, J. Agric. Food Chem. 16 (1968) 48.
[2] D.E. Bradway, R. Moseman, R. May, Bull. Environ. Contam. Toxicol. 26 (1981) 520.
[3] Z. Vasilic, V. Drevenkar, V. Rumenjak, B. Stengl, Z. Frobe, Arch. Environ. Contam. Toxicol. 22 (1992) 351.
[4] T. Shafik, D.E. Bradway, H.F. Enos, A.R. Yobs, J. Agric. Food Chem. 21 (1973) 625.
[5] J. Hardt, J. Angerer, J. Anal. Toxicol. 24 (2000) 678.
[6] E.M. Lores, D.E. Bradway, J. Agric. Food Chem. 25 (1977) 75.
[7] S.S. Park, H. Pyo, K.-J. Lee, S.-J. Park, Bull. Korean Chem. Soc. 19 (1998) 45.
[8] C. Weisskopf, J. Seiber, in: R.G. Wang, C.A. Franklin, R.C. Honeycutt, J.C. Reinert (Eds.), Biological Monitoring for Pesticide Exposure. Measurement, Estimation, and Risk Reduction, American Chemical Society, Washington, DC, 1989, p. 206.
[9] C.D. Brokopp, J.L. Wyatt, J. Gabica, Bull. Environ. Contam. Toxicol. 26 (1981) 524.
[10] A. Miki, H. Tsuchihashi, K. Ueda, M.Y. Yamashita, J. Chromatogr. 718 (1995) 383.
[11] S.J. Reid, R.R. Watts, J. Anal. Toxicol. 5 (1981) 126.
[12] R. Fenske, J.T. Leffingwell, J. Agric. Food Chem. 37 (1989) 995.
[13] B.P. Nutley, J. Cocker, Pesticide Sci. 38 (1993) 315.
[14] C. Aprea, G. Sciarra, L. Lunghini, J. Anal. Toxicol. 20 (1996) 559.
[15] T.F. Moate, C. Lu, R.A. Fenske, R.M. Hahne, D.A. Kalman, J. Anal. Toxicol. 23 (1999) 230.
[16] R. Bravo, W.J. Driskell, R.D. Whitehead, L.L. Needham, D.B. Barr, J. Anal. Toxicol. 26 (2002) 245.
[17] J.E. Davies, J.C. Peterson, Ann. N. Y. Acad. Sci. 837 (1997) 257.
[18] N. Kupfermann, H. Schmoldt, J. Steinhart, J. Anal. Toxicol. 28 (2004) 242.
[19] A.N. Ogloblîne, G.E. O'Donnell, R. Geyer, G.M. Holder, B. Tattam, J. Anal. Toxicol. 25 (2001) 153.
[20] R. Bravo, L.M. Caltabiano, G. Weerasekera, R.D. Whitehead, C. Fernandez, L.L. Needham, A. Bradman, D.B. Barr, J. Exposure Anal. Environ. Epidemiol. 14 (2004) 249.
[21] G.K.H. de Alwis, D.B. Barr, L.L. Needham, J. Chromatogr. B 843 (2006) 34–41.
[22] G.K.H. de Alwis, D.B. Barr, L.L. Needham, J. Anal. Toxicol., accepted for publication, 26 may 2008.
[23] J.M. Rosenfeld, R.A. McLeod, R.L. Foltz, Anal. Chem. 58 (1986) 716.
[24] J.M. Rosenfeld, M. M-Russell, S. Yeroushalmi, J. Chromatogr. B 358 (1986) 137.
[25] J.M. Rosenfeld, S. Yeroushalmi, E.Y. Osei-Twum, Anal. Chem. 58 (1986) 3044.
[26] J.M. Rosenfeld, Y. Moharir, S.D. Sandler, Anal. Chem. 61 (1989) 925.
[27] S.M. Breckenridge, X. Yin, J.M. Rosenfeld, Y.H. Yu, J. Chromatogr. B 694 (1997) 289.
[28] J.M. Rosenfeld, J. Chromatogr. A 843 (1999) 19.
[29] Z. Kuklenyik, J. Ekong, C.D. Cutchins, L.L. Needham, A.M. Calafat, Anal. Chem. 75 (2003) 6820.
[30] H.L. Lord, J. Rosenfeld, S. Raha, M.J. Hamadeh, J. Sep. Sci. 31 (2008) 387.
[31] J. Rosenfeld, M. Kim, A. Rullo, J. Chromatogr. Sci. 44 (2006) 333.
[32] J.J. Pesek, M.T. Matyska, in: N.J.K. Simpson (Ed.), Solid-Phase Extraction Principles, Techniques, and Applications, Marcel Dekker, Inc., New York, NY, 2000.
[33] L. Valentin-Blasini, B.C. Blount, H.S. Rogers, L.L. Needham, J. Exposure Anal. Environ. Epidemiol. 10 (2000) 799.
[34] J.K. Taylor, Quality Assurance of Chemical Measurements, CRC Press, Boca Raton, FL, 1987.
[35] J.M. Rosenfeld, Trends Anal. Chem. 22 (2003) 785.
[36] A. Salvador, C. Moretton, A. Piram, R. Faure, J. Chromatogr. A 1145 (2007) 102.

Univariate and multivariate optimization of the separation conditions for the analysis of five bisphenols by micellar electrokinetic chromatography

Jessica Felhofer [a], Grady Hanrahan [b], Carlos D. García [a,*]

[a] *Department of Chemistry, The University of Texas at San Antonio, One UTSA Circle, San Antonio, TX 78249, USA*
[b] *Department of Chemistry, California Lutheran University, Thousand Oaks, CA 91360, USA*

A B S T R A C T

In this paper we used a chromatographic response function (CRF) that included an output for each of the two performance parameters (resolution and analysis time) to optimize the separation of five bisphenols by micellar electrokinetic chromatography (MEKC) using multivariate response surface methodology (RSM). To validate the real utility of this approach, we have also compared the efficiency of the proposed optimization method with a traditional univariate analysis. For both methods, the selected variables of the analysis were: buffer concentration, pH, amount of organic solvent, and concentration of surfactant. The predictive nature of a validated response surface design allowed for the elucidation of a strong interactive effect and resulted in a more labor-efficient optimization when compared to the univariate approach.

Published by Elsevier B.V.

1. Introduction

Among many different alternatives used to improve separations by capillary electrophoresis (CE), a commonly encountered mode is micellar electrokinetic chromatography (MEKC) [1,2]. MEKC is performed by adding surfactants to the background electrolyte (BGE) in amounts above the critical micelle concentration (CMC). Under these conditions, surfactant molecules aggregate, and the resulting micelles form a pseudo-stationary phase [3]. The differential analyte/micelle interactions are the key factors determining the selectivity of MEKC. Although more hydrophobic analytes typically show more affinity for the micelles with respect to analytes of a more hydrophilic character, other factors such as molecular weight, shape, and dipolar moment may play a fundamental role in the separation. These interactions can be altered in many ways, such as by changing the pH, by changing the type of surfactant, or by adding organic solvents to the BGE [4]. Due to its low cost, short analysis time, and great versatility, MEKC has been used for the quantification of a wide variety of analytes including amino acids, biomarkers, antiretroviral agents, drugs, pharmaceutical preparations, dyes, flavonoids, antioxidants, and pesticides [5–8]. An additional advantage of MEKC is that in some cases, the same surfactant used to create the micelles can be used, even below the CMC, to control the electro-osmotic flow (μ_{EOF}) [9–11] and improve the performance of the detector [12,13].

It is therefore clear that many different factors can influence the resolution and efficiency of separations by MEKC. Separation voltage, buffer concentration, type and concentration of surfactant, type and concentration of organic modifier, and pH have shown to have drastic effects on performance [14,15]. Consequently, different approaches have been proposed to optimize the separation conditions by MEKC [16–19]. Although the univariate approach is the simplest and probably the most commonly used method to optimize separations by MEKC [20–23], it is generally time consuming, labor intensive, and assumes the absence of interactions between the factors. If interactions between factors exist, then simultaneous variations in the levels of these factors should be considered in order to optimize the separation to the greatest extent [24]. In this regard, statistically designed experiments, traditionally used to optimize chromatographic separations [25–29], have been applied to MEKC [24,30–36]. It is interesting to see however, that in most of these reports a single output parameter (extraction efficiency, resolution between two adjacent peaks, selectivity, number of peaks, etc.) was selected [24,31,32,37].

In order to be able to optimize an entire electropherogram (when more than a single analyte is important) [30] several outputs should be factored into a single function. Using resolution as the main factor to determine the output of the model, Berridge
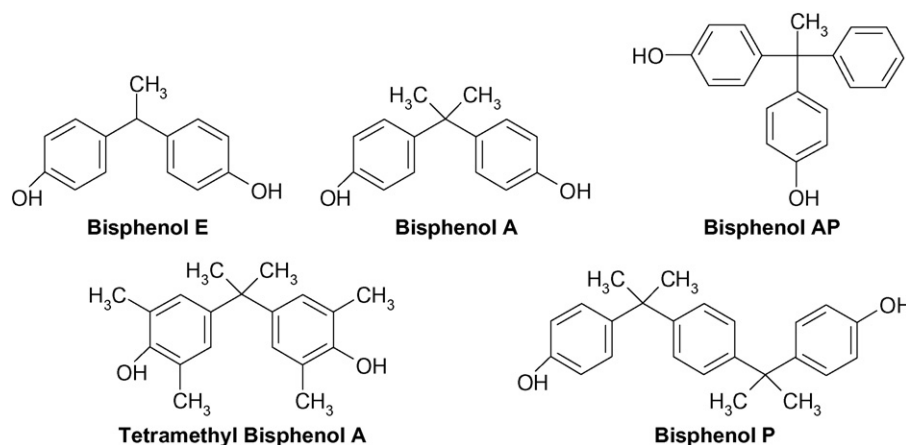
Fig. 1. Chemical structures of the five selected bisphenols.

proposed the use of a chromatographic response function (CRF) [38] to evaluate the quality of a given separation. Similarly, the Derringer's desirability function (which is based on the transformation of the measured property to a dimensionless scale for each criterion [39]) was applied to the simultaneous optimization of several chromatographic performance goals [40]. A modified version of Derringer's desirability function was later applied to the analysis of transition metals [41]. Although the importance of short analysis times in CE and MEKC separations has always been acknowledged [17], it has only been rarely included as part of the parameters to consider during optimization [42–46].

In this paper we used a CRF that included a function for each of two performance parameters (resolution and analysis time) to optimize the separation of five bisphenols by MEKC using multivariate analysis. To validate the real utility of this approach, we have also compared the efficiency of the proposed optimization method with a traditional univariate analysis. For both methods, the selected factors of the analysis were: buffer concentration, pH, amount of organic solvent, and concentration of surfactant. In the case of univariate analysis (changing one variable at the time while keeping the rest at a constant level), the migration time and separation efficiency were considered in order to sequentially select the best analytical conditions. For the multivariate analysis, the electropherograms obtained were processed to obtain the migration time and peak width for each analyte, resolution, and the total analysis time. Then, a CRF was calculated for each separation condition using a modified version of the method proposed by Divjak et al. [41]. The procedure and the results for both the univariate and the multivariate method of optimization are herein described.

2. Experimental

2.1. Materials and reagents

All chemicals were analytical reagent grade and used as received. The selected bisphenols, namely 4,4′-isopropylidene-bis(2,6-dimethylphenol) (tetramethyl bisphenol A); 4,4′-(1,4-phenylenediisopropylidene)bisphenol (bisphenol P); 4,4′-isopropylidenediphenol (bisphenol A); 4,4′-ethylidenebisphenol (bisphenol E); 4,4′-(1-phenylethylidene)bisphenol (bisphenol AP) were purchased from Sigma–Aldrich (Saint Louis, MO). The chemical structure of the selected bisphenols is shown in Fig. 1. Sodium borate ($Na_2B_4O_7 \cdot 10H_2O$) and sodium hydroxide were

purchased from Fisher Scientific (Fair Lawn, NJ). Sodium dodecyl sulfate (SDS) and acetonitrile (ACN) were purchased from Sigma–Aldrich (Saint Louis, MO). Stock solutions of bisphenols (10 mM) were prepared weekly in ACN and stored at 4 °C (protected from light) until use. Aqueous solutions were prepared using 18 MΩ cm water (NANOpure Diamond, Barnstead; Dubuque, IA) and were filtered using a hollow fiber filter (0.2 μm, Barnstead). The pH of the solutions was adjusted using either 1 M NaOH or 1 M HCl (Fisher Scientific; Fair Lawn, NJ) and measured using a glass electrode and a digital pH meter (Orion 420A+, Thermo; Waltham, MA).

2.2. Apparatus and procedures

A Beckman–Coulter P/ACE MDQ (Fullerton, CA) capillary electrophoresis system and fused silica capillaries (50 μm i.d. × 375 μm o.d. × 30 cm long; Polymicro Technologies; Phoenix, AZ) were used. Data acquisition was performed using Karat 32 software (Beckman–Coulter; Fullerton, CA) on an IBM personal computer. Unless otherwise noted, samples were introduced into the capillary by a 3 s, 0.5 psi pressure injection, and subsequently separated ($E = 666.6$ V/cm) at 25 °C. Direct UV detection was performed using a wavelength of 280 nm, through the capillary at a window located 20 cm from the inlet.

2.3. Measurement of the critical micellar concentration

As expected, the CMC is a key parameter in MEKC and can be affected by a wide variety of factors including the structure and charge of the surfactant, the type and concentration of the supporting electrolyte, type and concentration of the organic solvents, solution pH, and temperature. Because most of these factors have been used to optimize the separation in this report, the CMC of SDS was determined using CE [47]. For these experiments, the electrophoretic mobility of a neutral marker (bisphenol E) as a function of surfactant concentration (in the premicellar and micellar regions) was followed (data not shown). The highest CMC value measured under the selected experimental conditions (vide infra, Table 2) was 4.18 ± 0.01 mM. Although similar results were obtained by setting the lower limit of SDS concentration to zero (data not shown), the lowest limit for the experimental design-matrix was set at the minimum possible, 4.2 mM. As a result, micelles are present at all the selected conditions, and the only separation method involved in the study is MEKC.

2.4. Desirability functions

Since the two performance goals for the separation were good resolution among all five bisphenol peaks and short total analysis time, the CRF was a product of two types of desirability functions, as used by Divjak et al. [41]. Resolution (R) between two adjacent peaks in an electropherogram was calculated using Eq. (1), where t_m^k, w^k, t_m^{k+1}, and w^{k+1} are the migration time and the peak width at base for each of the two consecutive peaks named k and $k+1$, respectively,

$$R^{k,k+1} = \frac{t_m^{k+1} - t_m^k}{(w^{k+1} + w^k)/2} \tag{1}$$

Two analytes that give only one peak (co-migration) result in the resolution of zero. Two Gaussian-shaped peaks are theoretically resolved at $R^{k,k+1} > 0.6$ and therefore resolution values lower than 0.5 were considered not acceptable. A resolution of 1.5 implies a slight overlap of two equal width peaks and is generally considered sufficient for baseline resolution of equal height peaks. Significantly larger R-values are not necessarily beneficial as the only factor contributing to the improvement in resolution is a larger difference in migration time of each analyte. Since the peaks are already resolved, this only leads to an increase in the total analysis time. The value $R^{k,k+1}$ can be transformed by Eq. (2) to give $S^{k,k+1}$, a dimensionless value between 0 and 1 corresponding to poor resolution ($R^{k,k+1} < 0.5$) and maximum resolution ($R^{k,k+1}$ approaching 2.5), respectively,

$$S^{k,k+1} = \frac{1}{1 + e^{-2.20R^{k,k+1}+3.30}} \tag{2}$$

To account for the resolution between adjacent peaks in a separation of N analytes, the final form of the desirability function for resolution (f) was calculated (Eq. (3)) as the geometrical average of all individual desirability values $S^{k,k+1}$:

$$f = \left(\prod_{k=1}^{N-1} S^{k,k+1} \right)^{1/(N-1)} \tag{3}$$

The desirability function that scales the total analysis time (g) is also a sigmoidal transformation that gives values close to zero for analysis times (T) greater than 45 min and values approaching one for total analysis times close to 6 min. Preliminary experiments, mostly performed by the univariate approach, were used to set these limits,

$$g = \frac{1}{1 + e^{0.09T-1.94}} \tag{4}$$

The final CRF is the product of the desirability function for resolution (f) and the desirability function for analysis time (g):

$$CRF(f, g) = fg \tag{5}$$

Eq. (5) enables evaluating an entire electropherogram on a dimensionless scale from 0 (poor) to 1 (desirable) corresponding to poor separation and/or long total analysis time to good resolution with short analysis time, respectively.

2.5. Experimental design

A Box–Behnken response surface design was employed to locate the optimum analytical conditions for the separation by mapping the CRF as a function of the different analytical factors. The Box–Behnken is considered an efficient option in response surface methodology and an ideal alternative to central composite designs. This approach combines a fractional factorial with incomplete block designs to avoid the extreme vertices and to present an approximately rotatable design with three levels per variable.

Table 1
Experimental factors and levels used in the Box–Behnken design

Factor examined	Level (−)	Level (0)	Level (+)
Borate concentration (mM)	5.0	15	25
Acetonitrile (%)	5.0	15	25
pH	8.8	9.3	9.8
SDS concentration (mM)	4.2	30	50

In order to select factors and their corresponding limits, preliminary results obtained by the univariate approach were used. If such results are not available, the experience of the analyst should provide a set of reasonable values for the model. Table 1 shows the four factors and three corresponding levels of each variable selected for the optimization experiments. Although these factors were selected based on the significant effect that each has on the outcome of a separation by MEKC based on previous experience and results, initial experiments could be defined by the following general guidelines [14,48,34,49]. It is worth noting that the design codes used in Table 1 (−, 0, +) may imply equally spaced levels for all the factors. This is true for borate concentration, acetonitrile, and pH. Although the selected values for SDS concentration (4.2, 30, and 50 mM) are not equally spaced, preliminary experiments performed setting the lower limit at either 0 mM (no SDS) or 1 mM (SDS present at sub-micellar concentrations) did not affect the optimum conditions predicted by the model (data not shown). As previously stated, the lower limit for SDS concentration was set at 4.2 mM to ensure the presence of micelles at all conditions.

The concentration of borate and the pH can affect the total analysis time due to ionic strength effects and zeta potential effects on the electro-osmotic flow (μ_{EOF}) [9,10,12,13,20,50–52]. The concentration of SDS clearly affects the separation and therefore the resolution since interactions of the analytes and the pseudo-stationary phase formed only when micelles are present is the basis of the separation. The amount of ACN can also affect the analysis because it affects both the partition coefficient of the analytes and the formation of micelles [3,14,15]. Since varying the pH or ACN is known to affect the aggregation of micelles, the multivariate model may also show any significant interactive effects that the pH and ACN concentration have with the SDS concentration, revealing interactions between commonly used factors that have not been considered in previous studies or that have been considered in a smaller experimental domain [30,44].

2.6. Response surface characterization

As reported elsewhere [53], the generalized model used in this study had the quadratic form described in Eq. (6), where the terms X_1, X_2, X_3, and X_4 correspond to borate concentration, ACN concentration, pH, and SDS concentration, respectively,

$$
\begin{aligned}
CRF = {} & \beta_0 + \beta_1 X_1 + \beta_2 X_2 + \beta_3 X_3 + \beta_4 X_4 + \beta_{11} X_1^2 + \beta_{22} X_2^2 + \beta_{33} X_3^2 \\
& + \beta_{44} X_4^2 + \beta_{12} X_1 X_2 + \beta_{13} X_1 X_3 + \beta_{14} X_1 X_4 + \beta_{23} X_2 X_3 \\
& + \beta_{24} X_2 X_4 + \beta_{34} X_3 X_4
\end{aligned}
\tag{6}
$$

Eq. (6) contains linear terms for all factors, squared terms for all factors, and products of all pairs of factors. The regression coefficient, β, gives a measure of the rate of change in CRF per unit change in each of the factors.

All the generated data were analyzed using JMP (SAS Institute; Carey, NC) statistical software. Factor significance was calculated in analysis of variance (ANOVA) models that were estimated and run up to their first order interaction terms. ANOVA for a linear regression partitions the total variation of a sample into

components. These components were then used to compute an *F*-ratio (ratio of mean square for lack of fit to mean square for pure error) that evaluates the effectiveness of the model. If the probability associated with the *F*-ratio is small, then the model is considered a better statistical fit for the data than the response mean alone. For all the calculations it was assumed that higher order interaction terms did not contribute significantly to the behavior of the selected statistical model.

3. Results and discussion

For these experiments a group of five bisphenols (tetramethyl bisphenol A, bisphenol P, bisphenol A, bisphenol E, and bisphenol AP) was selected as a model mixture. The selection was based on several criteria. First, because these compounds have different structures, molecular weights, and polarities they allow a simple evaluation of the advantages and limitations of the proposed approach. Second, bisphenols are widely employed in the manufacture of plastics used in food and beverage packaging, baby bottles, dental composites [54], adhesives, protective coatings, flame-retardants, water supply pipes, and compact disks [55]. Third, bisphenol A has a tendency to leach from those products [56], and therefore contamination and the consequent exposure among humans, have motivated multiple studies about their potential effects on fertility [57], development, and cancer [55,58,59]. Fourth, although few reports described the analysis of bisphenol A (and related compounds) by electrophoretic techniques [54,60–64], bisphenols are still mainly analyzed by traditional chromatographic techniques [65–67]. This is, to the best of our knowledge, the first report describing the separation of five bisphenols by MEKC.

3.1. Univariate analysis

Under the selected conditions, bisphenols are non-ionic species and can be separated by MEKC. It is well known that the BGE concentration has a significant effect on separations by CE and MEKC [68]. The BGE concentration may not only affect the zeta potential of the capillary tube, but also the CMC of the surfactant used. The concentration of BGE is, therefore, one of the factors that can affect other factors. In order to study the effect of borate concentration on the separation of the five selected bisphenols, solutions in the range of 5–30 mM were studied (pH 9.3, 30 mM SDS, 15% (v/v) ACN). The results showed that although higher borate concentrations had little effect on the separation efficiency or migration order of the analytes (bisphenol E, bisphenol A, bisphenol AP, tetramethyl bisphenol A, and bisphenol P), they reduced the μ_{EOF} (data not shown) giving long analysis times. This reduction in μ_{EOF} was believed to be the main reason for the baseline separation of the bisphenols obtained at borate concentrations above 20 mM. In order to minimize the analysis time, while preserving the separation, 20 mM was selected as the optimum borate concentration and used throughout the rest of the experiments. SDS has shown to be one of the most suitable surfactants for MEKC. Additionally, it has been shown that the selectivity of SDS micelles can be altered by a wide variety of modifiers making it an attractive choice to test the proposed (univariate and multivariate) approaches. Consequently, the effect of the SDS was studied in the range of 0–50 mM, using a BGE consisting of a mixture (v/v) of 85% 20 mM borate, pH 9.3 and 15% ACN. No separation was observed when SDS was not included in the BGE. As the SDS concentration was progressively increased, the separation of the five selected compounds was gradually improved. Using 30 mM SDS, well-defined resolved peaks were obtained for the selected compounds. Along with the obvious increases in resolution (consequence of the increased concentration of micelles), longer analysis times were also obtained. In agreement with previous reports [9,50,69], the observed increases in analysis time were mainly attributed to a decrease in μ_{EOF} produced by the higher ionic strength of the BGE. It is worth mentioning that no Joule heating was observed. Based on these results, 30 mM was selected as the optimum concentration of SDS and subsequently used to optimize the concentration of acetonitrile (as organic modifier) present in the BGE. Organic solvents are commonly used in MEKC to increase the solubility of hydrophobic compounds, to control the μ_{EOF} [4,70,71], and to control retention in MEKC [14,36,72,73]. Therefore, the effect of ACN concentration on the separation of the five selected bisphenols was analyzed in the 5–25% (v/v) range. It was observed (data not shown) that consecutive increases in migration time occurred in the range of 5–25% (v/v). This effect was particularly important in the case of bisphenol P, in which t_M increased from 2.96 ± 0.04 min at 5% to 12.50 ± 0.04 min at 25%. The separation efficiency (*N*) also followed the same trend, allowing baseline separation of all the selected compounds at ACN concentrations above 15%. Considering the separation efficiency and analysis time, 15% (v/v) ACN was selected as the optimum amount. It is well known that changes in the buffer pH also affect the zeta potential on the capillary, the μ_{EOF}, the separation selectivity, and the resolution. In order to study the effect of pH on the separation of the selected bisphenols, a series of buffer solutions were prepared at pH values ranging from 8.3 to 10.3, using a BGE consisting of 20 mM borate, 30 mM SDS, and 15% (v/v) acetonitrile. No significant enhancements in the separation efficiency (data not shown) were observed at pH values lower than 9.3. However, considerable increases in migration times (and consequently total analysis time) were obtained at pH values above 9.3 (data not shown). These changes in migration time have been attributed to a combination of decrease in μ_{EOF} and ionization of the selected bisphenols, which like other phenolic compounds have a typical pKa above 10 [74]. Although a wide range of values have been reported for. This effect was particularly significant in the case of bisphenol AP, tetramethyl bisphenol A, and bisphenol P. Although pH values >10 may provide a means to separate the selected compounds by a combination of MEKC and capillary zone electrophoresis, a pH value of 9.3 was selected as the optimum pH value for the analysis. At this pH value the five bisphenols can be baseline separated with the lowest analysis time. As previously stated, the separation in MEKC is dictated by the interaction between the micelles and the analytes. Clearly, in this case the molecular weight of the bisphenols is the
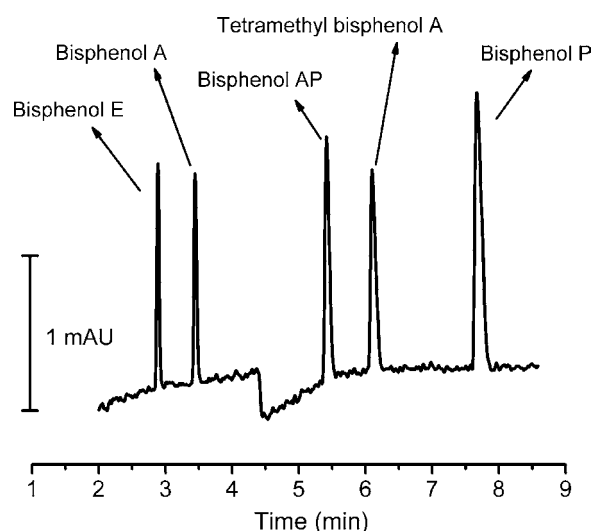

Fig. 2. Electropherogram produced with conditions optimized by the univariate method: 20 mM borate, 30 mM SDS, 15% (v/v) ACN, and pH 9.3. Other conditions: $V_{separation}$ = +20,000 V, injection = 3 s, 0.5 psi, and temperature = 25 °C.
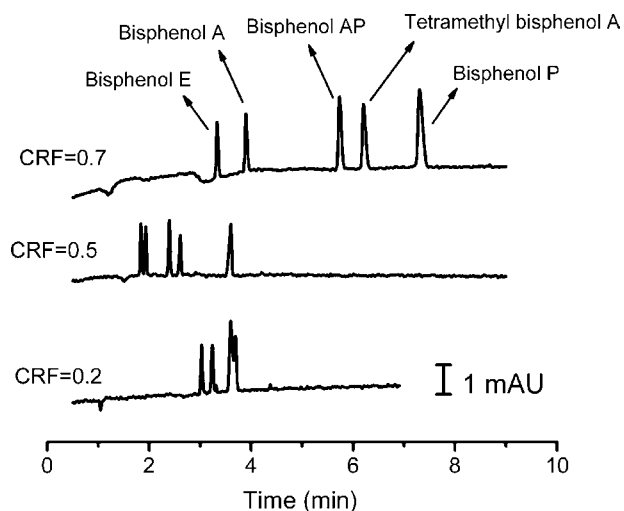
Fig. 3. Representative electropherograms for the Box–Behnken design and corresponding CRF values. From bottom to top: experiment 18, 2, and 5 (see Table 2). Other conditions: $V_{separation}$ = +20,000 V, injection = 3 s, 0.5 psi, and temperature = 25 °C.

Fig. 4. Whole model leverage plot of actual response vs. predicted response.

main factor determining this interaction and dictating the overall sequence. The inversion observed for bisphenol AP (290.37 g/mol), which elutes before tetramethyl bisphenol A (284.40 g/mol) can be attributed to the significant difference in molecular shape (see Fig. 1). Overall, the univariate optimization determined that 20 mM borate, 30 mM SDS, 15% (v/v) ACN, and a solution pH of 9.3 were the best conditions to separate the five selected bisphenols. A typical electropherogram obtained under these conditions is shown in Fig. 2. The separation produced five resolved peaks (bisphenol E (t_M = 2.88 ± 0.01 min), bisphenol A (t_M = 3.44 ± 0.01 min), bisphenol AP (t_M = 5.42 ± 0.01 min), tetramethyl bisphenol A (t_M = 6.10 ± 0.02 min), and bisphenol P (t_M = 7.67 ± 0.02 min)) with a total analysis time of less than 8 min. Considering that the univariate approach involved 4 variables, 6 levels, and 5 analytes, a mini-

mum of 120 experiments were required. This calculation already considers that preliminary results (not counted) have enabled selecting a set of conditions that are close to the final optimum conditions. Depending on the experience and skills of the analyst, the number of iterations and experiments could be much larger.

3.2. Multivariate analysis

As stated in Section 2, a design-matrix for the Box–Behnken study was generated (using four factors at three levels) resulting in a total of 27 analytical conditions. Evidently, a larger number of experiments were necessary to optimize the separation conditions by the standard univariate approach. The design-matrix as well as the corresponding model-predicted and actual CRF response values is shown in Table 2. The system was fully optimized using the experiments described within. Here, three center point experiments

Table 2
Experimental design-matrix with mean actual and model-predicted CRF values

Experiment no.	[Borate] (mM)	ACN (%)	pH	[SDS] (mM)	Experimental CRF	Predicted CRF
1	5	5	9.3	30	0.2	0.2
2	5	25	9.3	30	0.5	0.5
3	15	15	9.8	50	0.7	0.7
4	15	15	8.8	50	0.7	0.7
5	25	15	8.8	30	0.7	0.7
6	15	15	9.8	4.2	0.1	0.1
7	15	15	8.8	4.2	0.1	0.1
8	25	5	9.3	30	0.3	0.4
9	25	25	9.3	30	0.5	0.6
10	15	25	9.3	4.2	0.0	0.1
11	25	15	9.8	30	0.7	0.6
12	15	5	9.3	4.2	0.2	0.2
13	15	15	9.3	30	0.7	0.7
14	15	15	9.3	30	0.7	0.6
15	15	15	9.3	30	0.7	0.6
16	15	25	9.3	50	0.6	0.6
17	5	15	8.8	30	0.5	0.4
18	15	5	9.3	50	0.2	0.2
19	5	15	9.3	50	0.6	0.4
20	15	5	9.8	30	0.2	0.3
21	15	25	9.8	30	0.5	0.5
22	5	15	9.3	4.2	0.1	0.1
23	5	15	9.8	30	0.7	0.7
24	25	15	9.3	50	0.6	0.6
25	15	5	8.8	30	0.4	0.3
26	15	25	8.8	30	0.5	0.6
27	25	15	9.3	4.2	0.1	0.2

(numbers 13–15) were incorporated to compute an estimate of the error term that does not depend on the fitted model. This allows estimation of the experimental variance and examines the loss of linearity between the levels chosen for each variable chosen.

Fig. 3 presents representative electropherograms and the corresponding CRF values from experiments 2, 5, and 18. These results illustrate the operating conditions with various degrees of optimization quantified numerically as the mean actual CRF value in Table 2. It is important to note that the quantitative measure of optimization, the CRF, scales with the qualitative assessment one can make by inspection. For example, experiment 5 has the best average resolution and the shortest analysis time among the three electropherograms, and consequently, the highest CRF value (0.7). Further, inspection from experiments 2 and 18 shows an obvious decrease in quality of resolution and accordingly, a decrease in CRF.

The mean actual CRF values and the mean CRF values predicted by the model were also included in Table 2. The quality of fit is shown in Fig. 4 by a whole leverage plot of experimental vs. model-predicted responses (based on all effects) with the quality of fit expressed by the coefficient of determination. This coefficient is variation in the response around the mean that can be attributed to terms in the model rather than to random error. The term leverage is used because a point exerts more influence on the fit if it is farther away from the middle of the plot. If the extremes are considered, the differences of the residuals before and after being constrained by the hypothesis are greater and thus contribute a larger part of the sums of squares for a given effect's hypothesis test. The distance from a point to the line of fit shows the actual residual. Ostensibly, the mean line in a leverage plot represents the model where the hypothesized value of the effect is constrained to zero. Again, we have shown a whole model leverage plot. Here, multiple effects representing a partially constrained model instead of a model fully constrained to a single mean value. The whole model plot dramatizes the test that all the parameters (except intercepts) in the model are zero. The same test is reported as in a typical analysis of variance report. The intuitive interpretation of the plot is the same whether for simple or multiple regressions. The goal is to examine if the line of fit on the effect's leverage plot carries the points significantly better than does the horizontal line. As shown, the confidence curves (dashed lines) cross the horizontal line, thus the test is considered significant at the 5% level. Overall, an r^2-value of 0.91 was obtained with a mean predicted response of 0.42.

ANOVA for a linear regression partitions the total variation of a sample into components, which are used to compute an F-ratio that evaluates the effectiveness of the model. Prob > F is the significance probability for the F-ratio, which states that if the null hypothesis is true, a larger F-statistic would only occur due to random error. It is the probability of obtaining a greater F-value by chance alone if the variation due to lack of fit variance and the pure error are the same. Significance probabilities of 0.05 or less are often con-

Table 3
Effect test results for the Box–Behnken design

Source	DF[a]	Sum of squares	F-ratio[b]	Prob > F
Borate (mM)	1	0.046904	1.8963	0.1864
Acetonitrile (%)	1	0.690267	27.906	<.0001
SDS (mM)	1	0.001600	0.0647	0.8023
pH	1	0.013379	0.5409	0.4721
Borate (mM) × acetonitrile (%)	1	0.000025	0.0010	0.9750
Borate (nM) × pH	1	0.182533	7.3796	0.0147
Borate (mM) × SDS (mM)	1	0.000029	0.0012	0.9730
Acetonitrile (%) × pH	1	0.000025	0.0010	0.9750
pH × SDS (mM)	1	0.000093	0.0038	0.9517
Acetonitrile (%) × SDS (mM)	1	0.000023	0.0102	0.8965

[a] Degrees of freedom.
[b] F-Ratio of mean square for lack of fit to mean square for pure error.

Fig. 5. Electropherogram produced with conditions optimized multivariate: 14.6 mM borate, 15% (v/v) ACN, pH 9.25, and SDS 28.5 mM. Other conditions: $V_{separation}$ = +20,000 V, injection = 3 s, 0.5 psi, and temperature = 25 °C.
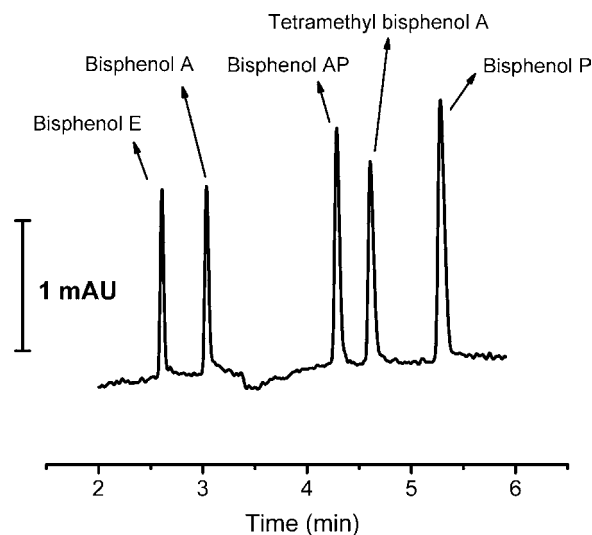
sidered evidence that there is at least one significant regression factor in the model. An examination of Prob > F from the effect test results (Table 3) revealed that ACN had a significant single effect (Prob > F = <0.001) on the CRF. ACN affects the affinity of the bisphenols for the micelles and therefore should have a strong effect on the separation of the five analytes. Because at all three levels of pH each analyte was neutrally charged [54,75] (see also Section 3.1), the solution pH was not significant as an individual variable. However, it displayed a strong interactive effect with borate concentration (Prob > F = 0.0147). Changing the pH of the solution either to a higher or lower value requires the addition of a solution of HCl or NaOH. This in turn increases the ionic strength of the solution, and in conjunction with varying the levels of borate buffer, can significantly alter the total ionic strength and in the end, affect the total analysis time and consequently, the CRF. This interactive effect would not have been determined by a simple univariate approach alone.

A *post hoc* review of our model revealed optimum critical values of: 14.6 mM borate, 15% (v/v) ACN, pH 9.25, and SDS 28.5 mM. As can be observed in Fig. 5, baseline separation of the five selected compounds (bisphenol E (t_M = 2.60 ± 0.01 min), bisphenol A (t_M = 3.01 ± 0.01 min), bisphenol AP (t_M = 4.28 ± 0.01 min), tetramethyl bisphenol A (t_M = 4.60 ± 0.01 min), and bisphenol P (t_M = 5.27 ± 0.02 min)) was obtained in less than 6 min. Finally, a series of validation experiments using 0.5 mM standard solutions of each bisphenol were performed at the predicted critical values. Under the optimum conditions, a mean experimental CRF of 0.7 ± 0.1 was obtained with a 8% discrepancy difference from the model predicted. The repeatability of the method was evaluated by performing multiple injections of a standard containing the five bisphenols using the optimum critical values. Results (data not shown) indicate that the optimal operating conditions result in highly repeatable electropherograms (statistically non-significant differences), as analyzed by a two-factor ANOVA at a significance level of α = 0.05.

4. Conclusions

The standard univariate approach commonly used for the optimization of separation conditions was successfully applied to the separation of five bisphenols by MEKC. These results were weighed

against the results obtained by a multivariate approach, which used a combination of a CRF composed of two desirability functions (based on resolution of each analyte peak and the total analysis of the separation) and response surface methodology. The results highlight the utility of combining several outputs into a common factor (such as the CRF) to evaluate the overall quality of a given separation, to discover interactive effects between the factors and to optimize the separation in a timely fashion.

Acknowledgments

References

[1] S. Terabe, Anal. Chem. 76 (2004) 240A.
[2] T. Watanabe, S. Terabe, J. Chromatogr. A 880 (2000) 295.
[3] T.J. Pappas, M. Gayton-Ely, L.A. Holland, Electrophoresis 26 (2005) 719.
[4] S.F. James, Electrophoresis 24 (2003) 1530.
[5] M. Molina, M. Silva, Electrophoresis 23 (2002) 3907.
[6] P. Iadarola, G. Cetta, M. Luisetti, L. Annovazzi, B. Casado, J. Baraniuk, C. Zanone, S. Viglio, Electrophoresis 26 (2005) 752.
[7] S. Manuel, Electrophoresis 28 (2007) 174.
[8] V. Kostal, J. Katzenmeyer, E.A. Arriaga, Anal. Chem. 80 (2008) 4533.
[9] C.D. Garcia, B.M. Dressen, A. Henderson, C.S. Henry, Electrophoresis 26 (2005) 703.
[10] M.F. Mora, C.E. Giacomelli, C.D. Garcia, Anal. Chem. 79 (2007) 6675.
[11] M.F. Mora, J. Felhofer, A. Ayon, C.D. Garcia, Anal. Lett. 41 (2008) 312.
[12] Y. Ding, C.D. García, Electroanalysis 18 (2006) 2202.
[13] Y. Ding, M.F. Mora, G.N. Merrill, C.D. Garcia, Analyst 132 (2007) 997.
[14] F.G. Tonin, A.V. Jager, G.A. Micke, J.P. Farah, M.F. Tavares, Electrophoresis 26 (2005) 3387.
[15] A.V. Jager, F.G. Tonin, M.F. Tavares, J. Sep. Sci. 28 (2005) 957.
[16] A.W.M. Lee, W.-F. Chan, F.S.Y. Yuen, K.P.K. Tse, Y. Liang, K.-T. Fang, Chemometr. Intell. Lab. Syst. 39 (1997) 11.
[17] A.M. Siouffi, R. Phan-Tan-Luu, J. Chromatogr. A 892 (2000) 75.
[18] A. Ben Hameda, S. Elosta, J. Havel, J. Chromatogr. A 1084 (2005) 7.
[19] S.L.C. Ferreira, R.E. Bruns, H.S. Ferreira, G.D. Matos, J.M. David, G.C. Brandao, E.G.P. da Silva, L.A. Portugal, P.S. dos Reis, A.S. Souza, W.N.L. dos Santos, Anal. Chim. Acta 597 (2007) 179.
[20] R.W. Hompesch, C.D. Garcia, D.J. Weiss, J.M. Vivanco, C.S. Henry, Analyst 130 (2005) 694.
[21] E. Mejia, Y. Ding, M.F. Mora, C.D. Garcia, Food Chem. 102 (2007) 1027.
[22] X. Zhao, Y. Wang, Y. Sun, J. Pharm. Biomed. Anal. 44 (2007) 1183.
[23] X. Liu, J. Zhang, X. Chen, J. Chromatogr. B 852 (2007) 325.
[24] J.C. Ehlen, H.E. Albers, E.D. Breyer, J. Neurosci. Methods 147 (2005) 36.
[25] J. Havel, E.M. Peña, A. Rojas-Hernández, J.P. Doucet, A. Panaye, J. Chromatogr. A 793 (1998) 317.
[26] L. Mutihac, R. Mutihac, Anal. Chim. Acta 612 (2008) 1.
[27] K.M. Pierce, J.C. Hoggard, R.E. Mohler, R.E. Synovec, J. Chromatogr. A 1184 (2008) 341.
[28] S.L.C. Ferreira, R.E. Bruns, E.G.P. da Silva, W.N.L. dos Santos, C.M. Quintella, J.M. David, J.B. de Andrade, M.C. Breitkreitz, I.C.S.F. Jardim, B.B. Neto, J. Chromatogr. A 1158 (2007) 2.
[29] F. Marini, R. Bucci, A.L. Magrì, A.D. Magrì, Microchem. J. 88 (2008) 178.
[30] M. Thorsteinsdóttir, D. Westerlund, G. Andersson, P. Kaufmann, Chromatographia 47 (1998) 141.
[31] E. Nemutlu, M. Celebier, B. Uyar, S. Altinoz, J. Chromatogr. B 854 (2007) 35.
[32] R. Gotti, S. Furlanetto, S. Pinzauti, V. Cavrini, J. Chromatogr. A 1112 (2006) 345.
[33] T.R.I. Cataldi, D. Orlando, D. Nardiello, A. Rubino, G. Bianco, S. Abate, R. Ciriello, A. Guerrieri, Anal. Chim. Acta 597 (2007) 129.
[34] S. Mikaeli, G. Thorsen, B. Karlberg, J. Chromatogr. A 907 (2001) 267.
[35] H. Wan, M. Öhman, L.G. Blomberg, J. Chromatogr. A 916 (2001) 255.
[36] C.A. Silva, E.A. Pereira, G.A. Micke, J.P.S. Farah, M.F.M. Tavares, Electrophoresis 28 (2007) 3722.
[37] A. Alnajjar, H.H. AbuSeada, A.M. Idris, Talanta 72 (2007) 842.
[38] J.C. Berridge, J. Chromatogr. 244 (1982) 1.
[39] G. Derringer, R. Suich, J. Qual. Technol. 12 (1980) 214.
[40] B. Bourguignon, D.L. Massart, J. Chromatogr. 586 (1991) 11.
[41] B. Divjak, M. Moder, J. Zupan, Anal. Chim. Acta 358 (1998) 305.
[42] A.V. Pirogov, M.M. Platonov, I.V. Pletnev, O.N. Obrezkov, O.A. Shpigun, Anal. Chim. Acta 369 (1998) 47.
[43] Y.C. Guillaume, E. Peyrin, Talanta 50 (1999) 533.
[44] S. Orlandini, S. Fanali, S. Furlanetto, A.M. Marras, S. Pinzauti, J. Chromatogr. A 1032 (2004) 253.
[45] S. Furlanetto, S. Orlandini, A.M. Marras, P. Mura, S. Pinzauti, Electrophoresis 27 (2006) 805.
[46] F. Priego Capote, J.M.L. Rodriguez, M.D. Luque de Castro, J. Chromatogr. A 1139 (2007) 301.
[47] C.-E. Lin, J. Chromatogr. A 1037 (2004) 467.
[48] M.A. Rodriguez Delgado, M.L. Pérez, R. Corbella, G. González, F.J. García Montelongo, J. Chromatogr. A 871 (2000) 427.
[49] E. Baher, M.H. Fatemi, E. Konoz, H. Golmohammadi, Microchim. Acta 158 (2007) 117.
[50] C.D. Garcia, C.S. Henry, Anal. Chim. Acta 508 (2004) 1.
[51] Y. Ding, C.D. Garcia, Electrophoresis 27 (2006) 5119.
[52] Y. Ding, M.F. Mora, C.D. Garcia, Anal. Chim. Acta 561 (2006) 126.
[53] A. Gonzalez, K.L. Foster, G. Hanrahan, J. Chromatogr. A 1167 (2007) 135.
[54] A. Musenga, A. Schedle, U. Demelbauer, L. Kremser, M.A. Raggi, E. Kenndler, J. Chromatogr. A 1034 (2004) 221.
[55] C. Dash, M. Marcus, P.D. Terry, Mutat. Res. Rev. Mutat. 613 (2006) 68.
[56] C.-M. Chang, C.-C. Chou, M.-R. Lee, Anal. Chim. Acta 539 (2005) 41.
[57] R.A. Keri, S.-M. Ho, P.A. Hunt, K.E. Knudsen, A.M. Soto, G.S. Prins, Reprod. Toxicol. 24 (2007) 240.
[58] W. Volkel, T. Colnot, G.A. Csanady, J.G. Filser, W. Dekant, Chem. Res. Toxicol. 15 (2002) 1281.
[59] J.K. Hess-Wilson, K.E. Knudsen, Cancer Lett. 241 (2006) 1.
[60] M. Katayama, Y. Matsuda, T. Sasaki, K.-I. Shimokawa, S. Kaneko, T. Iwamoto, Biomed. Chromatogr. 15 (2001) 437.
[61] S. Takeda, A. Omura, K. Chayama, H. Tsuji, K. Fukushi, M. Yamane, S.-I. Wakida, S. Tsubota, S. Terabe, J. Chromatogr. A 979 (2002) 425.
[62] A. Schedle, M. Ivanova, E. Kenndler, J. Chromatogr. A 990 (2003) 231.
[63] F. Regan, A. Moran, B. Fogarty, E. Dempsey, J. Chromatogr. A 1014 (2003) 141.
[64] S.-I. Wakida, K. Fujimoto, H. Nagai, T. Miyado, Y. Shibutani, S. Takeda, J. Chromatogr. A 1109 (2006) 179.
[65] F. Regan, A. Moran, B. Fogarty, E. Dempsey, J. Chromatogr. B 770 (2002) 243.
[66] H. Yoshida, H. Harada, H. Nohta, M. Yamaguchi, Anal. Chim. Acta 488 (2003) 211.
[67] R. Braunrath, M. Cichna, J. Chromatogr. A 1062 (2005) 189.
[68] K. Poouthree, W. Soonthorntantikul, N. Leepipatpiboon, A. Petsom, T. Nhujak, Electrophoresis 28 (2007) 3705.
[69] C.D. Garcia, C.S. Henry, Electroanalysis 17 (2005) 1125.
[70] J.J. Berzas Nevado, G. Castaneda Penalvo, M.J. Pinilla Calderon, J. Chromatogr. B 773 (2002) 151.
[71] M. Wang, D. Wu, Q. Yao, X. Shen, Anal. Chim. Acta 519 (2004) 73.
[72] O. Nuñez, J.-B. Kim, E. Moyano, M.T. Galceran, S. Terabe, J. Chromatogr. A 961 (2002) 65.
[73] G.T. Roman, K. McDaniel, C.T. Culbertson, Analyst 131 (2006) 194.
[74] H. Sambe, K. Hoshina, K. Hosoya, J. Haginaka, J. Chromatogr. A 1134 (2006) 16.
[75] C.A. Staples, P.B. Dome, G.M. Klecka, S.T. Oblock, L.R. Harris, Chemosphere 36 (1998) 2149.

Comparative analysis of the volatile fraction from *Annona cherimola* Mill. cultivars by solid-phase microextraction and gas chromatography–quadrupole mass spectrometry detection

Liseth Ferreira, Rosa Perestrelo, J.S. Câmara*

Centro de Química da Madeira, Departamento de Química, Universidade da Madeira, Campus Universitário da Penteada, 9000-390 Funchal, Portugal

ABSTRACT

The analysis of volatile compounds in Funchal, Madeira, Mateus and Perry Vidal cultivars of *Annona cherimola* Mill. (cherimoya) was carried out by headspace solid-phase microextraction (HS-SPME) combined with gas chromatography–quadrupole mass spectrometry detection (GC–qMSD). HS-SPME technique was optimized in terms of fibre selection, extraction time, extraction temperature and sample amount to reach the best extraction efficiency. The best result was obtained with 2 g of sample, using a divinylbenzene/carboxen/polydimethylsiloxane (DVB/CAR/PDMS) fibre for 30 min at 30 °C under constant magnetic stirring (800 rpm).

After optimization of the extraction methodology, all the cherimoya samples were analysed with the best conditions that allowed to identify about 60 volatile compounds. The major compounds identified in the four cherimoya cultivars were methyl butanoate, butyl butanoate, 3-methylbutyl butanoate, 3-methylbutyl 3-methylbutanoate and 5-hydroxymethyl-2-furfural. These compounds represent 69.08 ± 5.22%, 56.56 ± 15.36%, 56.69 ± 9.28% and 71.82 ± 1.29% of the total volatiles for Funchal, Madeira, Mateus and Perry Vidal cultivars, respectively. This study showed that each cherimoya cultivars have 40 common compounds, corresponding to different chemical families, namely terpenes, esters, alcohols, fatty acids and carbonyl compounds and using PCA, the volatile composition in terms of average peak areas, provided a suitable tool to differentiate among the cherimoya cultivars.

© 2008 Elsevier B.V. All rights reserved.

1. Introduction

The family of annonaceae that includes *Annona squamosa*, *Annona muricata*, *Annona reticulata* and *Annona cherimola* contains a considerable number of plants with economic significance because of their edible fruits around the world, namely tropical America, Australia, Africa, India, Malaysia and Mediterranean Europe [1]. The edaphoclimatic conditions of the Madeira Islands are favourable for the production of tropical and subtropical fruits. *Annona cherimola* Mill. (cherimoya) production in Madeira Islands remains from its colonization and nowadays have an important role for the economic development with an annual production around 1000 Ton per year, exporting to the mainland, France, Spain and England markets.

The pulp of this fruit is creamy, very sweet and pleasantly flavoured. It is well known as a dessert fruit and has a lot of applications in ice creams and beverages [2]. The cherimoya fruit is used by

the natural products industry due to the high presence of secondary metabolites that show antimicrobial activity. The cherimoya is also known as a medicinal plant. Tea made from leaves and bark is relaxing. The pulp is moderately laxative and benefits the digestion with a particular taste as result of the harmonic combination of acids and sugars.

In fruits, aroma is one of the most appreciated characteristics on their consumption [3]. The volatile compounds (e.g. esters, terpenes, alcohols, carbonyl compounds, furanic compounds, among others) that form the fruit flavour are produced through metabolic pathways during ripening, harvest, post-harvest and storage which depends on many factors related to the species, variety and type of technological treatment [4]. The main volatiles identified in tropical fruits belong to esters such as methyl and ethyl esters [5]. The ester compounds play a role in the ripe fruit, serving both as "biological bribes" for the attraction of animals and as protectants against pathogens. In the case of some fruit species like apple, pear, annona, banana and others, they are the major volatile compounds on their characteristical aroma profile [6]. Several studies report that cherimoya fruit contains about 208 volatile compounds, 23 hydrocarbons, 58 esters, 47 carbonyl compounds, terpenoids
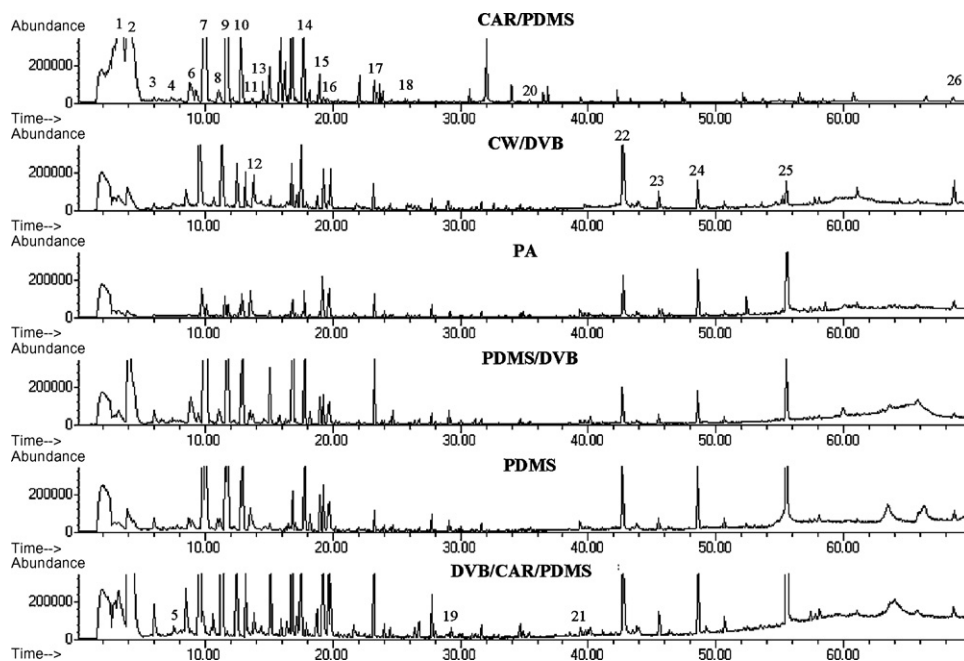
Fig. 1. TIC chromatogram obtained by HS-SPME/GC–qMSD analysis of Mateus cultivar with different fibre coatings during 30 min at 25 °C under constant magnetic stirring (800 rpm).

(mono and sesquiterpens), 54 miscellaneous structures of alcohols as butan-1-ol, 3-methylbutan-1-ol, hexan-1-ol, linalool and 3-methyl butanoate [1,7,8]. For the analysis of the volatile compounds in the annonaceae family, some publications are available using gas chromatography–quadrupole mass spectrometry detection (GC–qMSD) followed by liquid–liquid extraction and steam distillation [1,7,8]. These techniques, however, have some disadvantages such as higher costs, extent time-consumption and larger volumes of organic solvents used [9]. Recently, the headspace solid-phase microextraction (HS-SPME) technique emerges as an attractive alternative for volatile analysis because it offers many advantages like high sensitivity and reproducibility, combines extraction and pre-concentration in a simple step without pre-treatment of samples and does not require solvents. This technique is fast, inexpensive, requires low volume of sample and can be easily automated [10–12]. It is an equilibrium technique that requires a previous optimization step of the sampling conditions in order to obtain high recoveries of volatiles and a good precision of the method [13]. The analysis of headspace volatile compounds by HS-SPME is greatly influenced by the vapour pressure of flavour compounds of the matrix. Since the first HS-SPME fibres became commercially available, they have been used in several applications, including a wide range of food analysis, like volatile

composition in wines [14–16], beers [17,18], whiskeys [19,20], honeys [21], medicinal plants [22,23] and several kinds of fruits [24,25]. Up to now, this technique has been widely applied in the several matrixes. At the moment, no references have been found on the use of HS-SPME to describe the volatile composition of any cherimoya species. The purpose of this study was to develop and optimize an HS-SPME methodology coupled with GC–qMSD for the analysis of the volatile composition of four different cherimoya cultivars from Madeira Island. A preliminary screening of six commercial available fibres with different polarities was carried out in order to select the best coating for the matrix and other parameters that affect the HS-SPME procedure like extraction time and temperature were also tested and evaluated and using PCA the volatile composition in terms of average peak areas, provided a suitable tool to differentiate among the cherimoya cultivars.

2. Experimental

2.1. Fruit samples

The four cherimoya cultivars were kindly provided by "Direcção Regional de Agricultura – Divisão de Fruticultura" of Madeira Islands. Each fruit pulp was separated from the seeds and bark,
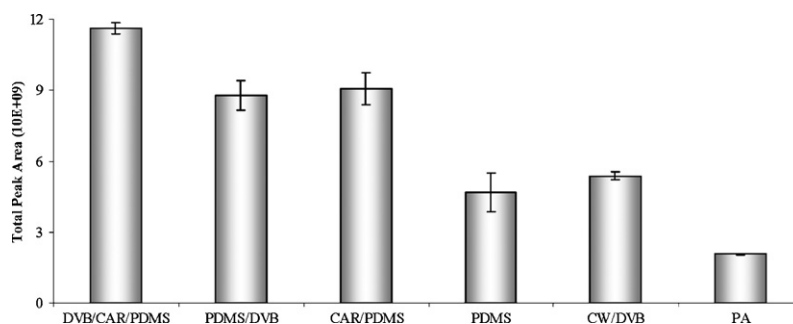
Fig. 2. Sorption capacity of different fibres for extraction of Mateus volatile compounds during dynamic HS-SPME method, expressed as total peak area (30 min at 25 °C). Error bars represent standard error of the mean ($n = 3$ for each data point).
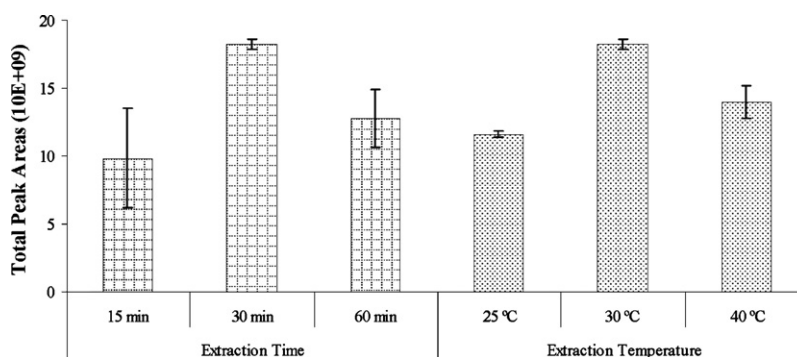
Fig. 3. Effect of the extraction time (DVB/CAR/PDMS coating at 30 °C) and extraction temperature (DVB/CAR/PDMS coating during 30 min) on the extraction efficiency of the volatile compounds from Mateus cultivars. Error bars represent standard error of the mean (*n* = 3 for each data point).

homogenised with a home blender, added with an amount of calcium chloride ($CaCl_2$) in order to inhibit the enzyme activity and finally stored in polyethylene bottles at −20 °C until analysis.

2.2. Standards and materials

All reagents used were analytical quality and all solvents were HPLC grade. Sodium chloride (99.5%) was supplied from Panreac (Spain, Barcelone). C8–C20 *n*-alkanes were run under the same chromatographic conditions as the samples to calculate the Kovats indices of the compounds were purchased from Sigma–Aldrich (Switzerland, Buchs). Water Mili-Q purification system (Milipore). SPME fibres and SPME holder for manual sampling were obtained from Supelco (Bellenfonte, PA, USA).

2.3. HS-SPME procedure

To determine the volatile compounds in cherimoya cultivars, the sample extraction is a key technique for those who are always present at very low concentrations. To obtain the optimal HS-SPME conditions, the experimental parameters including different fibre coating, extraction time, extraction temperature and sample amount, which can affect the extraction efficiency were systematically studied.

For the fibre screening, six commercially available fibres: carbowax-divinylbenzene (CW/DVB, 70 μm), divinylbenzene/carboxen/polydimethylsiloxane (DVB/CAR/PDMS, 50/30 μm), carboxen/polydimethylsiloxane (CAR/PDMS, 75 μm), polyacrylate (PA, 85 μm), polydimethylsiloxane/divinylbenzene (PDMS/DVB, 65 μm) and polydimethylsiloxane (PDMS, 100 μm) were tested and examined. All the fibres were of the same length (1 cm) and conditioned prior to use, according to the manufacturer's instructions. Before daily analysis each fibre was conditioned for 15 min at 250 °C. For each extraction, fibres were exposed to the headspace of a 4 mL septum-sealed glass vial containing 2 ± 0.001 g of sample, 0.5 mL of water, 1 μL of internal standard (3-octanol, 4.22 mg L^{-1}) and 0.10 g of NaCl for 30 min at 25 ± 1 °C under constant magnetic stirring (800 rpm). Once sampling was finished, the fibre was withdrawn into the needle and inserted into the GC system injection port at 250 °C for 6 min where the analytes are thermally desorbed from the fibre coating and transferred directly to the GC system column. Blank runs were conducted between extractions to check the absence of carry over which would cause memory effects and misinterpretation of results.

HS-SPME operating conditions were optimized with extractions at different extraction temperatures (25 °C, 30 °C and 40 °C), extrac-

tion times (15 min, 30 min and 60 min) and sample amounts (1 g, 2 g and 4 g).

2.4. Gas chromatography–quadrupole mass spectrometry detection (GC–qMSD) analysis

The analyses were carried out with an Agilent 6890 N gas chromatograph system (Agilent Technologies, Palo Alto, CA, USA) coupled to an Agilent 5975 quadrupole inert mass selective detector. The extracted compounds were separated on a BP-20 fused silica capillary column (30 m × 0.25 mm I.D. × 0.25 μm film thickness). Splitless injection was employed with helium as the carrier gas (Helium N60, *Air Liquide*, Portugal) at a flow rate of ≈1 mL min^{-1} (column head pressure 13 psi). The initial oven temperature was 40 °C, followed by a linear programmed temperature from 40 °C to 220 °C held for 10 min at a rate of 3 °C min^{-1}. The injection and ion source temperatures were 250 and 220 °C, respectively. The mass spectra of the compounds were acquired in electron-impact (EI) mode at 70 eV. The electron multiplier was set to the auto tune procedure. All data were obtained by collecting the full-scan mass spectra within the range of 30–300 *m/z*.

2.5. Qualitative and quantitative analysis

The volatile compounds were identified by matching mass spectra with spectra of reference compounds in National Institute of Standards and Technology (NIST05) mass spectral library. The relative amounts of individual components were expressed as percent peak areas relative to total peak areas.
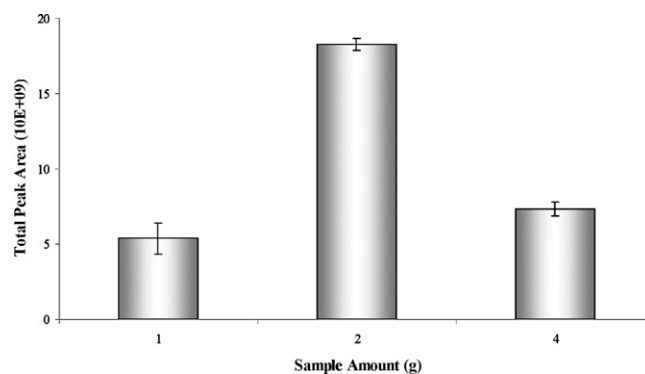

Fig. 4. Extraction efficiencies measured for different Mateus cultivar amounts at 30 °C during 30 min under constant magnetic stirring (800 rpm) with DVB/CAR/PDMS fibre. Error bars represent standard error of the mean (*n* = 3 for each data point).

Table 1
Identification of volatile compounds in Mateus cultivars by dynamic HS-SPME/GC–qMSD using different fibre coatings (extraction temperature: 25 °C, extraction time: 30, 800 rpm)

RT (min)	Peak no.	Compounds	CAR–PDMS	CW/DVB	DVB/CAR/PDMS	PA	PDMS	PDMS/DVB
3.12	1	Ethanol	x	x	x	x	x	x
3.96	2	Methyl butanoate	x	x	x	x	x	x
5.58	3	β-pinene	x	x	x	x	x	x
7.07	4	Butyl propanoate	–	–	x	–	x	x
7.65	5	Butan-1-ol	x	–	x	–	–	–
8.16		β-mircene	x	–	–	–	–	–
8.56	6	Methyl hexanoate	x	x	x	x	x	x
9.48		3-Methylbutan-1-ol	–	–	x	x	x	x
9.69	7	Butyl butanoate	x	x	x	x	x	x
10.78	8	Butyl pentanoate	x	x	x	x	x	x
11.47	9	3-Methylbutyl butanoate	x	x	x	x	x	x
12.68	10	3-Methylbutyl 3-methylbutanoate	x	x	x	x	x	x
12.90	11	1-Hydroxypropan-2-one	–	x	–	–	–	–
13.83	12	Hydroxyacetaldehyde		x				
14.78	13	Pentyl butanoate	x	–	x	x	–	x
15.05		Hexan-1-ol	x	x	x	x	x	x
15.80		Methyl 3-hydroxy-3-methylbutanoate	–	–	x	–	x	x
16.31		(Z)-3-hexen-1-ol	–	–	x	–	–	x
16.65		Methyl octanoate	–	–	–	–	–	x
17.68	14	Hexyl butanoate	x	x	x	x	–	x
18.22		Hexyl 2-methylbutanoate	x	x	x	x	x	x
18.96	15	Hexyl 3-methylbutanoate	x	x	x	x	x	x
19.13	16	Acetic acid	x	x	x	x	x	x
19.52		(Z)-3-Hexenyl butanoate	x	–	x	–	–	–
19.69		2-Furfural	x	x	x	x	x	x
20.24		2,5,5-Trimethyl-1,3,6-heptatriene	–	–	–	–	x	–
20.80		2-Ethylhexan-1-ol	–	–	x	x	–	x
21.29		1-(2-Furanyl)-ethanone	–	–	–	–	x	–
21.83		Benzaldehyde	x	–	x	–	–	–
23.24	17	Linalool	x	x	x	x	x	x
24.03	18	5-Methyl-2-furfural	–	x	x	–	x	x
24.50		2-Cyclopenten-1,4-dione	–	–	–	–	x	–
25.15		Methyl decanoate	–	–	–	–	x	–
25.76		Hexyl hexanoate	–	–	–	–	x	–
25.87		2-(2-etoxyethoxy)-ethanol	–	x	–	–	–	–
26.38	19	Butanoic acid	x	x	x	–	–	x
27.73		2-Furanmethanol	–	x	x	x	x	x
28.01		3-Methylbutanoic acid	x	x	x	x	–	–
28.38		Diethyl succinate	–	–	x	–	–	–
29.29		3-Methoxybutan-1-ol	–	x	x	–	–	–
30.92		(5H)-Furan-2-one	–	x	x	–	x	x
31.62		2-Hydroxy-2-cyclopenten-1-one	–	x	x	x	x	x
32.97		2-Cyclohexen-1-ol	–	x	x	–	x	x
34.65	20	Hexanoic acid	x	x	x	x	x	x
35.44		Phenylmethyl butanoate	x	x	x	–	x	–
36.84		2-Phenylethanol	–	–	x	x	–	x
39.37	21	2,5-Furandicarbaldehyde	–	–	x	–	x	x
40.01		Methyl 2-furoate	–	–	–	–	x	–
42.69	22	Dihydroxyacetone	–	x	x	x	–	–
45.49	23	2-Hidroxy-γ-butyrolactone	–	x	x	–	–	–
45.65		Octanoic acid	–	x	x	–	x	x
48.57	24	3-Hydroxy-2,3-dihydromaltol	–	x	x	x	x	–
55.48	25	5-Hydroxymethyl-2-furfural	–	x	x	–	x	x
58.13		DHF[a]	–	x	x	–	x	–
68.61	26	n-Hexadecanoic acid	x	x	x	x	–	x
Total compounds identified per fibre			25	35	44	26	35	34

–: Not detected.

[a] DHF: 5,6-Dihydro-4-ydroxy-(3H)-furan-2-one.

3. Results and discussion

3.1. HS-SPME optimization

The extraction time, extraction temperature and sample amount are important variables influencing the vapour pressure and equilibrium of the aroma compounds in the headspace, therefore they were chosen and optimized in this study [3,26]. The optimization method evaluated the effect of one variable at a time, keeping all other variables constant during the assays. Before carrying out the optimization of the HS-SPME conditions for the analysis of the volatile compounds of cherimoya cultivars, fibre screening was carried out. The Mateus cultivar was selected as the matrix for the optimization of this methodology. The results were expressed in terms of the total peak areas obtained by GC–qMSD analysis using HS-SPME technique.

3.1.1. SPME fibre

The selection of the most appropriate SPME fibre depends on the compounds targeted and therefore on the plant material under
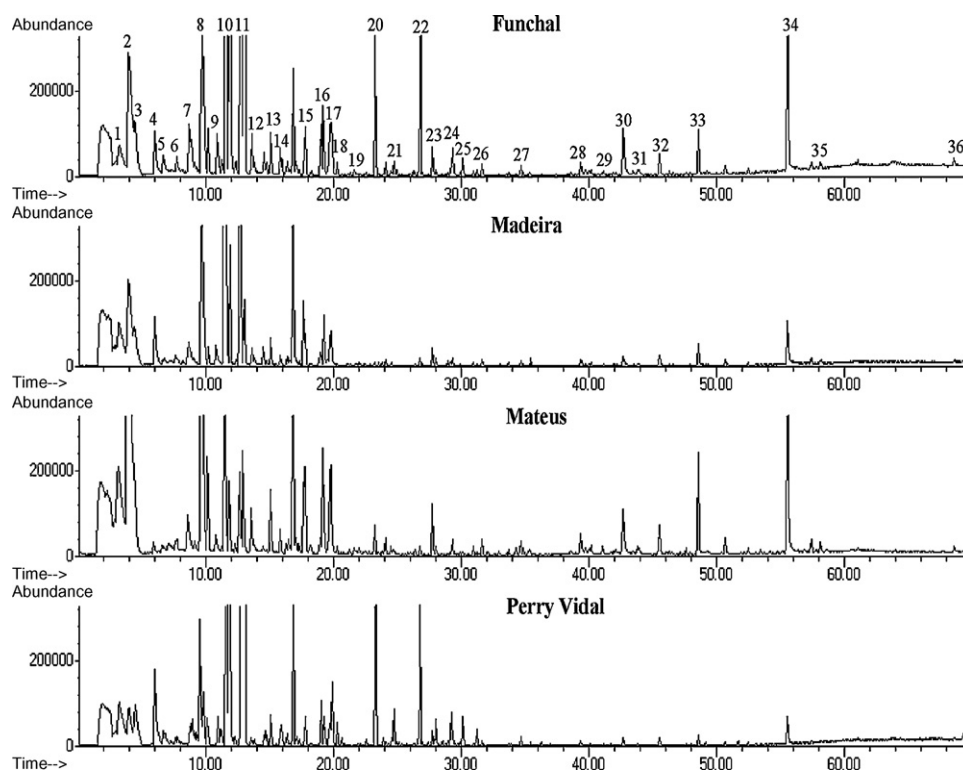
Fig. 5. TIC chromatogram obtained for Funchal, Madeira, Mateus and Perry Vidal cultivars using HS-SPME$_{DVB/CAR/PDMS}$/GC–qMSD methodology at 30 °C during 30 min under constant magnetic stirring (800 rpm).

study [22]. So, the six fibres (CW/DVB, DVB/CAR/PDMS, CAR/PDMS, PDMS/DVB and PDMS) were tested and compared individually to evaluate the effect of different fibre coatings on the extraction of volatile compounds in Mateus samples. Fig. 1 shows the typical total ion chromatograms (TIC) obtained for 2 g of Mateus cultivar using different fibre coatings with 30 min of extraction at 25 °C under constant magnetic stirring (800 rpm). The comparison among the six types of fibre coatings used in this study showed different GC responses, their performances were determined based on the intensity of the response observed including extraction efficiency, number of identifiable compounds in the extract and reproducibility (Table 1). Each extraction was done in triplicate and the repeatability (RSD%) was lower than 20%. The results in terms of total peak areas are illustrated in Fig. 2. According to the results, CAR/PDMS and DVB/CAR/PDMS fibre coatings had much better extraction efficiencies than the others, however, CAR/PDMS and PDMS/DVB fibre presented similar extraction efficiency. Of these three fibres, the retention ability of DVB/CAR/PDMS fibre for the volatile compounds in the Mateus samples is much stronger than the rest of the other fibres. Given to the better profile shown by this coating, this fibre was selected for the extraction of the volatile compounds of cherimoya cultivars [10,11].

3.1.2. Extraction time

Time affects the mass transfer of the analytes between the three system phases in HS-SPME technique. The optimal time for extraction should be the time of equilibrium since this methodology is based on the equilibrium between analyte and the fibre coating [10]. Assays focusing on the dynamics of Mateus volatiles were conducted with 15, 30 and 60 min of exposure time of the fibres into the headspace. The results are illustrated in Fig. 3. The best extraction efficiency was obtained at 30 min. The decline of the total peak after 30 min probably resulted from a partial desorption of some high volatile compounds from the fibre coating, the same behaviour was

observed by Zhang et al. [11], due to competition phenomenon. The high values of % RSD that were observed at 15 min are due to the fact of the system may have not reached the equilibrium. According to these results, the time of extraction selected was 30 min.

3.1.3. Extraction temperature

The extraction temperature has a significant role in the extraction of the analytes because it can influence the distribution coefficients of the compounds between the sample and the headspace and between the headspace and the fibre [26]. Therefore, it is an important parameter because it controls the diffusion rate of the analytes into the coating. In order to determine the best temperature for the extraction of volatile compounds of Mateus cultivar, the effect of this parameter in the extraction of the analytes was checked. Fig. 3 reports the results of the three temperatures tested using the DVB/CAR/PDMS fibre during 30 min of extraction and 2 g of sample under constant magnetic stirring (800 rpm). As can be
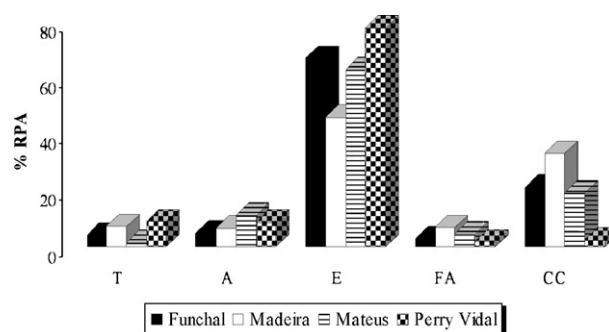

Fig. 6. Distribution of chemical families identified for the cherimoya cultivars (T: terpenes and sesquiterpenes; A: alcohols; E: esters; FA: fatty acids; CC: carbonyl compounds).

Table 2
Chemical components in the HS-SPME$_{DVB/CAR/PDMS}$ volatile compounds detected in Funchal, Madeira, Mateus and Perry Vidal cherimoya cultivars

KI	Compounds	Peak no.	Odor description [28–30]	Molecular weight	Funchal		Madeira		Mateus		Perry Vidal	
					Content	Similarity	Content	Similarity	Content	Similarity	Content	Similarity
966	Ethanol	1	Sweet	46.07	2.04	78	4.66	83	7.66	82	4.24	90
1018	Methyl butanoate	2	Ether, fruity, sweet	102.13	5.98	90	6.80	91	20.52	90	2.40	91
1042	α-Pinene	3	Pine, turpentine	136.23	1.99	90	2.60	96	–	–	2.30	95
1105	β-pinene	4	Pine, resin, turpentine	136.23	0.79	94	3.60	95	0.91	91	2.66	91
1128	Isoamyl acetate	5	Banana	130.18	0.63	74	0.48	72	0.29	72	0.71	90
1143	Butyl propanoate	6	Sweet, fruity	130.18	–	–	–	–	0.32	72	–	–
1159	Butan-1-ol		Medicine, fruit	74.12	–	–	–	–	0.87	70	0.45	83
1182	Methyl hexanoate	7	Fruity, fresh, sweet	130.18	2.24	73	2.00	70	2.97	80	1.76	78
1205	3-Methylbutan-1-ol		Alcohol, malt, fusel	88.15	–	–	–	–	–	–	1.61	90
1212	Butyl butanoate	8	Fruity, apple	144.21	5.15	83	7.27	90	16.83	78	2.22	91
1244	Butyl pentanoate	9	Sweet, fruity, green	158.24	1.04	83	0.82	80	1.03	83	1.16	90
1262	3-Methylbutyl butanoate	10	Fruity, green	158.24	21.10	83	18.61	90	9.74	78	25.14	83
1292	3-Methylbutyl 3-methylbutanoate	11	Sweet, fruity, green	172.26	27.80	90	7.05	91	4.06	91	41.28	90
1297	1-Hydroxypropan-2-one		–	74.08	0.92	77	–	–	2.22	74	–	–
1313	Hydroxyacetaldehyde	12	–	60.05	0.77	78	0.41	78	0.7	76	0.24	87
1319	(Z)-2-Penten-1-ol		Green, plastic, rubber	86.13	0.24	74	0.62	86	–	–	0.15	76
1342	Pentyl butanoate		Banana	158.24	0.55	70	0.62	70	0.39	77	0.58	72
1348	Hexan-1-ol	13	Resin, flower, green	102.17	0.59	78	0.60	83	1.64	78	0.53	83
1364	Methyl 3-hydroxy-3-methylbutanoate		–	132.16	0.51	83	0.28	73	0.41	74	0.68	78
1374	(Z)-3-hexen-1-ol	14	Grass	100.16	0.22	70	0.21	79	0.53	76	0.22	83
1402	Hexyl butanoate	15	Apple peel	172.26	0.85	91	1.00	91	4.57	83	0.72	91
1417	Hexyl 2-methylbutanoate		Strawberry	186.29	0.09	76	–	–	0.5	79	0.09	73
1418	5-Methyl-(3H)-furan-2-one		–	98.10	0.11	70	0.13	73	–	–	–	–
1436	Hexyl 3-methylbutanoate	16	Sweet, green, fruity	186.29	0.78	80	0.37	80	0.85	83	0.95	80
1441	Acetic acid		Acid, spicy	60.05	1.23	91	1.66	91	3	91	0.52	91
1451	(Z)-3-Hexenyl butanoate		Wine, green	170.25	0.21	79	–	–	0.13	74	0.22	72
1455	2-Furfural	17	Bread, almond, sweet	96.08	1.71	95	1.89	94	1.58	95	0.35	81
1471	Methyl 3-hydroxybutanoate	18	–	118.13	0.06	74	–	–	0.19	90	–	–
1494	1-(2-Furanyl)-ethanone		Balsamic	110.11	0.11	72	0.14	86	0.16	86	0.04	80
1521	DMDF[a]		–	144.12	0.09	74	0.10	72	0.25	73	–	–
1530	Propanoic acid	19	Pungent, rancid, soy	74.08	0.04	76	0.20	90	0.11	74	0.07	74
1540	Linalool	20	Flower, fresh	154.25	0.95	86	0.18	80	0.59	80	3.28	93
1558	5-Methyl-2-furfural		Almond, caramel, burnt sugar	110.11	0.37	95	0.73	94	0.38	95	0.07	90
1568	2-Cyclopenten-1,4-dione		–	96.08	0.11	72	0.39	83	0.21	87	–	–
1574	Caryophyllene	21	Wood, spice	204.35	0.24	80	0.32	90	0.23	72	0.18	83
1611	Butanoic acid		Rancid, cheesy, sweet	88.11	0.09	75	0.28	70	0.14	83	0.03	74
1622	4,4-Dimethylhexan-3-ol	22	–	130.23	1.70	70	0.16	75	0.24	72	1.54	75
1650	2-Furanmethanol	23	Burnt	98.10	0.52	96	0.68	96	0.97	96	0.25	96
1657	3-Methylbutanoic acid		Cheesy, spicy, rancid	102.13	0.07	74	0.37	78	0.19	78	0.34	78
1683	α-Terpineol		Pine, teil, íris	154.25	0.04	79	0.10	90	–	–	0.05	90
1689	D-Germacrene		Wood, spice	204.35	0.11	95	0.35	97	–	–	0.22	97
1692	3-Methoxybutan-1-ol	24	–	104.15	0.09	70	0.34	76	0.29	73	0.17	70
1715	γ-Elemene	25	–	204.35	0.14	76	0.17	78	–	–	0.23	93
1740	(5H)-furan-2-one		–	84.07	0.10	90	0.29	91	0.15	90	–	–
1748	γ-Cadinene		Thyme, wood	204.35	0.07	77	0.21	99	0.14	73	0.13	98
1760	2-Hydroxy-2-cyclopenten-1-one	26	–	98.10	0.22	90	0.25	80	0.31	86	0.08	83
1798	2-Cyclohexen-1-ol		–	98.14	0.05	70	0.17	70	0.09	73	–	–
1847	Hexanoic acid	27	Sweet, fatty, cheesy	116.16	0.11	73	0.24	74	0.24	74	0.08	70
1854	Dihydromaltol		–	128.13	0.15	79	0.86	78	–	–	–	–
1869	Phenylmethyl butanoate		Plum	178.23	0.04	83	0.20	91	0.27	74	0.04	91
1873	Maltol		Caramel	128.13	0.17	72	0.38	80	0.16	86	–	–
1973	2,5-Furandicarbaldehyde	28	–	124.09	0.53	91	1.48	87	0.61	87	0.12	90
1989	Methyl 2-furoate		Fruity, mushroom, sweet	126.11	0.21	72	0.52	88	0.19	80	–	–
2122	Furaneol	29	Caramel, strawberry	128.13	0.17	74	0.42	75	0.2	91	–	–

RI	No.	Compound	Odour	MW	RPA%	%	RPA%	%	RPA%	%	RPA%	%
2178	30	Dihydroxyacetone	–	90.08	2.03	74	1.28	83	1.46	72	0.19	73
2204	31	γ-Ethylbutyrolactone	Coumarin, sweet	114.14	0.19	70	0.18	78	0.17	78	–	–
2269	32	2-Hidroxy-γ-butyrolactone	–	102.09	0.36	78	0.93	74	0.77	72	–	–
2294		5-Acetoxymethyl-2-furfural	–	168.15	0.23	74	0.70	88	0.1	80	–	–
2311	33	3-Hydroxy-2,3-dihydromaltol	–	144.13	2.16	94	3.59	91	2.49	87	0.24	87
2314		5-Hydroxymaltol	–	142.11	0.25	78	0.85	91	0.28	74	–	–
2334		Benzoic acid	Urine	122.12	0.18	73	0.97	87	0.15	91	0.08	79
2335	34	Furancarboxylic acid	–	112.08	0.24	80	0.27	72	0.21	74	0.07	70
2343	35	5-Hydroxymethyl-2-furfural	Cardboard	126.11	9.05	95	16.65	95	5.54	94	0.78	94
2355		DHF[b]	–	102.01	0.65	74	0.81	74	0.5	73	–	–
2395	36	n-Hexadecanoic acid	Sightly fatty, waxy	256.42	0.57	94	2.58	98	0.3	76	0.55	78

–: Not detected.

[a] DMDF: 2,5-Dimethyl-2,4-dihydroxy-(2H)-furan-3-one.

[b] DHF: 5,6-Dihydro-4-hydroxy-(3H)-furan-2-one.

observed, the higher temperature does not contribute positively for the extraction efficiency, due to thermodynamic reasons; decrease of partition coefficients, and to the decrease of the extraction by the fibre coating. Thus, the highest temperature used in this study was 40 °C, to avoid the possible loss of thermally unstable analytes and thermal degradation of some compounds present in matrix [13,21]. All the extractions were carried out in triplicate. From these results, the temperature of 30 °C was selected for further experiments.

3.1.4. Sample amount

For a given volume vial, sample amount has a positive effect on the peak areas of the compounds. But this does not mean that the larger the sample amount, the better the results [11]. In this assay, the sample amounts tested were 1, 2 and 4 g and the results of the effect of sample amount on the total peak areas are shown in Fig. 4. Considering the results, the sample amount of 2 g was chosen for the present study. Between 2 and 4 g of sample amount it was observed that a decrease in total peak area may be due to the saturation of the fibre coating.

3.2. Analysis and comparison of the volatile components in Funchal, Madeira, Mateus and Perry Vidal cultivars

The TIC chromatograms of the HS-SPME/GC–qMSD methodology with the optimized sampling conditions for Funchal, Madeira, Mateus and Perry Vidal cultivars are shown in Fig. 5. Each sample was analysed in triplicate. A total of 66 volatile compounds, among them 23 carbonyl compounds, 17 esters, 9 alcohols, 9 fatty acids and 8 terpenes, were tentatively identified by matching mass spectra with spectra of reference compounds in NIST mass spectral libraries with a resemblance percentage above 70%. The Kováts retention indices were calculated, under the same chromatographic conditions as the samples, for each compound and compared with the literature in order to certify the compound identification. In general, Funchal, Madeira and Mateus cultivars showed a similar aroma complexity profile comparatively to Perry Vidal. The relative amount percent of the individual components was expressed as percent peak areas relative to total peak areas (RPA%) and are listed in Table 2. The qualitative data analysis showed that the presence of the volatile compounds tentatively identified in this study are characteristic for the annonaceae family [1,27]. The RPA% values obtained for the different chemical families in Funchal, Madeira, Mateus and Perry Vidal are shown in Fig. 6. Esters, carbonyl compounds, alcohols, terpenes and fatty acids represent, in average 63.62 ± 7.89%, 18.92 ± 7.58%, 7.98 ± 1.57%, 5.47 ± 1.21% and 4.02 ± 1.70% for the total volatile profile, respectively.

Tropical fruits can be classified into two broad categories based on whether esters and terpenoids predominate in the volatiles. Flavour volatiles of cherimoya are reported to be composed of esters, especially butanoate and 3-methyl butyl esters [1], therefore this specie is included in the first category, the same results were obtained by Idstein [7]. According to the results, the volatile compounds of all cultivars were also predominantly shared by esters, which contribute for total volatiles with 46.02%, 63.26%, 67.24% and 77.25% for Madeira, Mateus, Funchal and Perry Vidal, respectively. Methyl butanoate (8.93 ± 1.80%), butyl butanoate (7.87 ± 2.06%), 3-methylbutyl butanoate (18.65 ± 1.51%) and 3-methylbutyl 3-methylbutanoate (20.05 ± 1.25%) were the main compounds identified in this chemical family. These compounds contribute to the fruity and floral odors for the cherimoya cultivars. These compounds make a positive contribution to the general quality of cherimoya cultivars, being responsible for their fruity and flowers sensory proprieties (Table 2).

The carbonyl compounds were the main chemical family identified (23 compounds), on the other hand quantitatively this chemical

Table 3
Percentage of variance and percentage of cumulative variance explained by the two first principal components

Component	Total variance explained					
	Extraction sums of squared loadings			Rotation sums of squared loadings		
	Total	% of Variance	Cumulative %	Total	% of Variance	Cumulative %
Raw						
1	27.113	51.156	51.156	27.110	51.150	51.150
2	17.866	33.710	84.866	17.869	33.715	84.866
Rescaled						
1	27.113	51.156	51.156	27.110	51.150	51.150
2	17.866	33.710	84.866	17.869	33.715	84.866

Extraction method: Principal component analysis.

family has the second major contribution to the total volatile profile. In average, the major carbonyl compounds detected in the analysed cultivars were 1-hydroxypropan-2-one (1.57 ± 0.19%), 2-furfural (1.38 ± 0.42%), 1,3-dihydroxypropan-2-one (1.24 ± 0.47%) and 5-hydroxymethyl-2-furfural (8.01 ± 3.67%). In Perry Vidal, 2-furfural and 1,3-dihydroxypropan-2-one were found in less amount compared with the other cultivars that reported the similar contents. The same behaviour was observed for 5-hydroxymethyl-2-furfural, but its content in Madeira cultivars (16.65%) was higher than Funchal (9.05%), Mateus (5.54%) and Perry Vidal (0.78%).

Alcohols are formed as enzymatic degradation products of unsaturated fatty acids [1]. This chemical family contributes with 4.93%, 6.76%, 8.91% and 11.32% for total volatiles profile in Funchal, Madeira, Perry Vidal and Mateus, respectively. 3-Methylbutan-1-ol (1.61%) was only detected in Perry Vidal and represents the second major alcohol content. Butan-1-ol was only detected in Mateus and Perry Vidal, still (Z)-2-penten-1-ol and 2-cyclohexen-1-ol were not detected in Mateus and Perry Vidal, respectively.

The dominating terpenoids found in the analysed cultivars were α-pinene, β-pinene and linalool. In Mateus, α-pinene was not detected and the amount between the others cultivars were similar (not significantly different at the 95% level). The contribution of linalool for the total volatile profile was more significant in Perry Vidal (3.28%) than Funchal, Madeira and Mateus which had a contribution lower than 1%. This chemical family contributes with pine, flowers odors to the cherimoya cultivars studied.

Another group of aroma compounds that have been studied were the fatty acids. Within this family the acetic acid and *n*-hexadecanoic acid were notable for their higher contributions. Acetic acid or its biosynthetic equivalent, acetyl CoA contributes significantly to the synthesis of fatty acids and also to aromatic compounds [1]. The Madeira cultivar, presents the highest contribution for the total volatile profile (6.79%). The fatty acids contribution in Funchal and Perry Vidal cultivars was not significantly different at the 95% level. The odors of fatty acid are described as being cheesy, fatty and rancid (Table 2).

3.3. Multivariate analysis

The proposed HS-SPME/GC–qMSD methodology was applied to Funchal, Madeira, Mateus and Perry Vidal cultivars. Their differentiation was possibly due to the different total peak areas of each volatile compound determined in the four cherimoya cultivars. Data analysis multivariate techniques represent a powerful statistical tool that explains this differentiation. The 66 analytical variables used for statistical purposes were included into five different chemical families, such as terpenes, esters, alcohols, fatty acids and carbonyl compounds. When principal component analysis (PCA) was applied to the total peak area of the different chemical families, two factors were extracted and 74.97% of the total variance was explained. The redundant variables (13) not contributing to the explanation of total variance (coefficients magnitude <0.7)
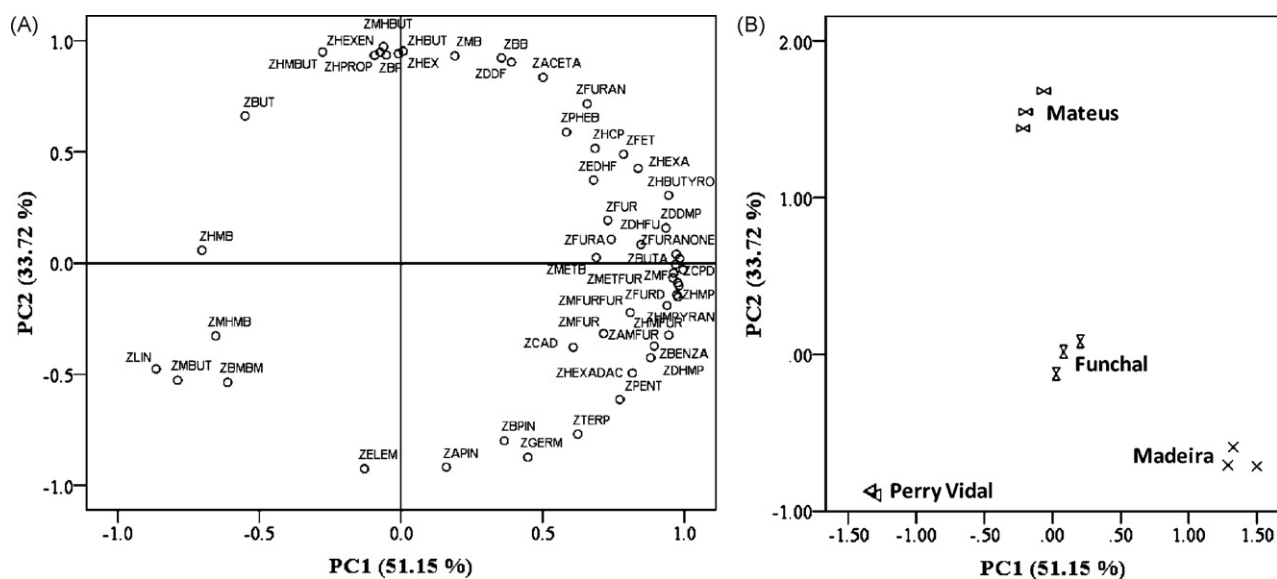

Fig. 7. PC1 and PC2 scatter plot of the main sources of variability between cherimoya cultivars. (A) relationships between the chemical compounds (loadings); (B) Distinction between the samples (scores).

Table 4
Prediction abilities for the different cultivars, using stepwise discriminant analysis (Anonacul: Anona cultivars)

	Anonnacul	Classification results[a,b]				Total
		Predicted group membership				
		Funchal	Madeira	Mateus	Perry Vidal	
Original						
Count	Funchal	3	0	0	0	3
	Madeira	0	3	0	0	3
	Mateus	0	0	3	0	3
	Perry Vidal	0	0	0	3	3
%	Funchal	100.0	.0	.0	.0	100.0
	Madeira	.0	100.0	.0	.0	100.0
	Mateus	.0	.0	100.0	.0	100.0
	Perry Vidal	.0	.0	.0	100.0	100.0
Cross-validated[c]						
Count	Funchal	0	0	1	2	3
	Madeira	0	1	2	0	3
	Mateus	0	2	1	0	3
	Perry Vidal	0	0	0	3	3
%	Funchal	.0	.0	33.3	66.7	100.0
	Madeira	.0	33.3	66.7	.0	100.0
	Mateus	.0	33.3	66.7	.0	100.0
	Perry Vidal	.0	.0	.0	100.0	100.0

[a] 100.0% of original grouped cases correctly classified.

[b] 41.7% of cross-validated grouped cases correctly classified.

[c] Cross validation is done only for those cases in the analysis. In cross validation, each case is classified by the functions derived from all cases other than that case.

were removed with the purpose to maximize the total variance from the data set. So, the first two components explain 84.87% of the total variance of the initial data set (Table 3). Furaneol (0.99), 2-cyclopenten-1,4-dione (0.98) and methyl 2-furoate (0.98) are the variables with the highest contribution on the first component (51.15%); 33.72% of total variance, corresponding to second component, was correlated with methyl 3-hydroxybutanoate (0.98), hexyl 2-methylbutanoate (0.96) and hexan-1-ol (0.94).

Fig. 7 reports PC1 and PC2 scatter plot of the main sources of variability between cherimoya cultivars. Madeira and Funchal cultivars (four quadrant) are essentially characterized by α-terpeneol, furaneol, benzoic acid, methyl 2-furoate, 3-methoxybutan-1-ol, 5-methyl-(3H)-furan-2-one and (Z)-2-penten-1-ol. The Perry Vidal (third quadrant) is described by linalool, 3-methylbutyl 3-methylbutanoate, 3-methylbutan-1-ol and methyl 3-hydroxy-3-methylbutanoate. The Mateus cultivar localized in the second quadrant is characterized by butyl propanoate (Z)-3-hexen-1-ol and methyl-3-hydroxybutanoate.

A linear discriminant analysis (LDA) was run, using the above-mentioned variables, in order to obtain suitable classification rules. Fig. 8 shows a projection of the investigated cultivars of cherimoya in two-dimensional space, generated by the two first discriminate functions that explain 99.9% of the total variance. Four groups representing Funchal, Madeira, Mateus and Perry Vidal cultivars, were clearly observed. The good agreement achieved indicates that very acceptable classification functions can be deduced. The leave-one-out classification method was used as cross-validation procedure to evaluate the classification performance (Table 4). From the results it can be concluded that headspace SPME coupled to GC–qMSD and chemometrics is a very appropriate sampling technique to distinguish the different cherimoya cultivars growing in Madeira Islands studied based on their volatile profile.

4. Conclusions

A simple, rapid and solvent-free method to extract and determine the volatile compounds in cherimoya cultivars with the HS-SPME/GC–qMSD was developed. The volatile compounds play an important role in assessing the classification of this fruit. The qualitative profile of the volatile compounds of Funchal, Madeira and Mateus was similar, but their relative abundance showed several differences. The esters, alcohols, fatty acids and terpenes constitute important aroma group compounds which contribute with fruity, cheese/fatty and flowers notes to cherimoya cultivars sensory properties. Using PCA, the volatile composition in terms of average peak areas, provided a suitable tool to differentiate among the cherimoya cultivars.

Acknowledgements

Fig. 8. Differentiation between *Annona Cherimola* Mill. cultivars by applying LDA.

References

[1] M.N. Shashirekha, R. Baskaran, L.J. Rao, M.R. Vijayalakshmi, S. Rajarathnam, LWT – Food Sci. Technol. 41 (2008) 236.
[2] N.V. Chikhalikar, A.K. Sahoo, R.S. Singhal, P.R. Kulkarni, J. Sci. Food Chem. 80 (2000) 1339.
[3] E. Carasek, J. Pawliszyn, J. Agric. Food Chem. 54 (2006) 8688.
[4] E. Ibañez, S. López-Sebastián, E. Ramos, J. Tabera, G. Reglero, Food Chem. 63 (1998) 281.
[5] N. Narain, J.N. Almeida, M.S. Galvão, Cienc. Tecnolo. Aliment 24 (2004) 212.
[6] J. Beekwilder, M. Alvarez-Huerta, E. Neef, F.W.A. Verstappen, H.J. Bourwmeester, A. Aharoni, Plant Physiol. 135 (2004) 1865.
[7] H. Idstein, W. Herres, P. Schreier, J. Agric. Food Chem. 32 (1984) 383.
[8] A.J. MacLeod, N.M. Pieris, J. Agric. Food Chem. 29 (1981) 488.
[9] D. Sandi, J.B.P. Chaves, A.C.G. Sousa, J.F.M. Parreiras, M.T.C. Silva, P.B.L. Constant, Braz. Arch. Biol. Technol. 47 (2004) 233.
[10] J.S. Câmara, M.A. Alves, J.C. Marques, Anal. Chim. Acta 555 (2006) 191.
[11] C. Zhang, M. Qi, Q. shao, S. Zhou, R. Fu, J. Pharm. Biomed. Anal. 44 (2007) 464.
[12] J.C.R. Demyttenaere, C. Dagher, P. Sandra, S. Kallithraka, R. Verhé, N. De Kimpe, J. Chromatogr. A 985 (2003) 233.
[13] E. Coelho, S.M. Rocha, A.S. Barros, I. Delgadillo, M.A. Coimbra, Anal. Chim. Acta 597 (2007) 257.
[14] C. Pizarro, N. Pérez-del-Notario, J.M. González-Sáiz, J. Chromatogr. A 1166 (2007) 1.
[15] S.M. Rocha, P. Coutinho, A. Barros, I. Delgadillo, M.A. Coimbra, J. Chromatogr. A 1114 (2006) 188.
[16] Q. Xiao, C. Xu, J. Xing, B. Hu, J. Chromatogr. A 1125 (2006) 133.
[17] F. Rodrigues, M. Caldeira, J.S. Câmara, Anal. Chim. Acta 609 (2008) 82.
[18] J.S. Câmara, J.C. Marques, R.M. Perestrelo, F. Rodrigues, L. Oliveira, P. Andrade, M. Caldeira, J. Chromatogr. A 1150 (2007) 198.
[19] M. Caldeira, F. Rodrigues, R. Perestrelo, J.C. Marques, J.S. Câmara, Talanta 74 (2007) 78.
[20] M. Pontes, J.C. Marques, J.S. Câmara, Talanta 74 (2007) 91.
[21] C. Bicchi, S. Drigo, P. Rubiolo, J. Chromatogr. A 892 (2000) 469.
[22] E.M. Gioti, Y.C. Fiamegos, D.C. Skalkos, C.D. Stalikas, J. Chromatogr. A 1152 (2007) 150.
[23] T.T. Liu, T.S. Yang, J. Agric. Food Chem. 50 (2002) 653.
[24] X.M. Wan, R.Y. Stevenson, X.D. Chen, L.D. Melton, Food Res. Int. 32 (1999) 175.
[25] E. Sánchez-Palomo, C. Díaz-Maroto, M.S. Pérez-Coello, Talanta 66 (2005) 1152.
[26] F. Pellati, S. Benvenuti, F. Yoshizaki, D. Bertelli, M.C. Rossi, J. Chromatogr. A 1087 (2005) 265.
[27] E.H.A. Andrade, M.G.B. Zoghbi, J.G.S. Maia, H. Frabricius, F. Marx, J. Food Compos. Anal. 14 (2001) 227.
[28] R. Perestrelo, A. Fernandes, F.F. Albuquerque, J.C. Marques, J.S. Câmara, Anal. Chim. Acta 563 (2006) 154.
[29] E. Campo, V. Ferreira, A. Escudero, J.C. Marques, J. Cacho, Anal. Chim. Acta 563 (2006) 180.
[30] A. Genovese, A. Gambuti, P. Piombino, L. Moio, Food Chem. 103 (2007) 1228.

Chemiluminescence from singlet oxygen that was detected at two wavelengths and effects of biomolecules on it

Yusuke Harada [a], Kosuke Suzuki [a], Masahiko Hashimoto [a], Kazuhiko Tsukagoshi [a],*, Hideshi Kimoto [b]

[a] Department of Chemical Engineering and Materials Science, Doshisha University, 1-3 Miyakodani, Tatara, Kyotanabe 610-0321, Japan
[b] Kimoto Electric Co. Ltd., Funahashi-cho Tennoji-ku, Osaka 543-0024, Japan

ARTICLE INFO

ABSTRACT

We developed the detection apparatus that equipped with the two-photomultiplier tubes for chemiluminescence from singlet oxygen. Singlet oxygen was generated with reaction between sodium hypochlorite and hydrogen peroxide. The chemiluminescence from singlet oxygen, the dimol light emission (ca. 634 nm) and the monomol light emission (ca. 1270 nm), was observed simultaneously for the same reaction cell. The effects of sodium azide as an antioxidant, human serum albumin, and α-amino acids on the chemiluminescence based on the both emissions were examined; the observed chemiluminescence could provide direct information with regard to the reaction between singlet oxygen and antioxidant/biomolecules. The apparent rate constants for quenching singlet oxygen in the presence of human serum albumin were calculated to be ca. 3.3×10^9 and ca. $8.8 \times 10^8 \, M^{-1} \, s^{-1}$ for the dimol and monomol light emissions, respectively, under the present conditions. The chemiluminescence intensities of the dimol emission decreased in the presence of His, Asp, Phe, Ser, and Tyr, and that of the monomol decreased in the presence of Cys and Trp. The chemiluminescence observed in the presence of biomolcules was discussed together with the reactivities of sodium hypochlorite and hydrogen peroxide to biomolecules.

1. Introduction

Singlet oxygen that is one of active oxygen has been focused on from the viewpoint of not only specific chemical species in chemical reactions but also medical science with regard to disease factors and health maintenance. Singlet oxygen reacts rapidly with many biological molecules, such as nucleic acids, lipids, amino acids, peptides, and proteins [1,2]. Singlet oxygen can be readily produced upon an irradiation of a photosensitizer that transfers its exited state energy to ground-state or triplet oxygen [3,4]. The reaction between singlet oxygen and biomolecules was usually confirmed by examining the reaction products with spectroscopic methods, such as mass spectrometry and Raman spectrometry [1,5,6].

Singlet oxygen possesses unique chemiluminescence (CL) property, the dimol light emission (ca. 637 nm) and the monomol light emission (ca. 1270 nm) [6]. The observation of CL from singlet oxygen in the presence of biomolecules might easily provide direct information with regard to the reaction between singlet oxygen

and biomolecules. However, as far as we know, there were few investigations about an observation of CL from singlet oxygen in the presence of biomolecules [7]; at least there were no reports examining the CL from singlet oxygen simultaneously at the two wavelengths for the dimol and monomol light emissions. When an irradiation using ultra-violet or visible light is combined with CL detection comprising a photomultiplier tube (PMT), the optical system including a light source, spectroscopic parts, and light detection devices must become extremely complicated.

In this study we developed the detection apparatus that equipped with the two PMTs for the CL from singlet oxygen, the dimol and monomol light emissions. Singlet oxygen was generated with chemical reaction between sodium hypochlorite (NaClO) and hydrogen peroxide (H_2O_2) without using any light irradiation systems. The reaction equations are shown below [8]:

$$NaClO + H_2O_2 \rightarrow {}^1O_2 + H_2O + NaCl,$$

$$2({}^1O_2) \rightarrow 2\,{}^3O_2 + h\nu(634\,nm) \text{ or } {}^1O_2 \rightarrow {}^3O_2 + h\nu(1270\,nm).$$
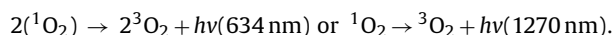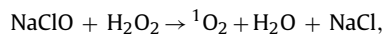
The reactivity of singlet oxygen to antioxidant, human serum albumin (HSA), and α-amino acids were examined through the simultaneous observation of the CL from singlet oxygen, the dimol

* Corresponding author. Tel.: +81 774 65 6595; fax: +81 774 65 6803.
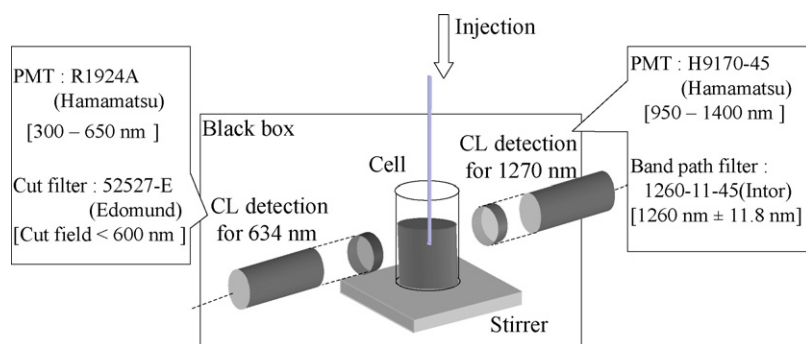E-mail address: ktsukago@mail.doshisha.ac.jp (K. Tsukagoshi).

Fig. 1. Schematic diagram of the CL detection apparatus equipped with the two PMTs.

and monomol light emissions, for the same reaction cell. That is, the information about the reactivity of singlet oxygen was obtained easily, quickly, and directly through the observation of the CL by the present method. The spectrometric analyses of the reaction products related to singlet oxygen are as a matter of course significant in this research area, but it is hard to examine trace amounts of the reaction products online due to the limitation in sampling and sample preparation. The present method becomes an alternative way for investigating the reactivity and property of singlet oxygen to biomolecules.

2. Experimental

2.1. Reagents

Water was purified with Elix UV 3 (Millipore). All reagents used were of commercially available and analytical grade. Sodium hypochlorite, H_2O_2 solution (30 wt.%), sodium azide, potassium permanganate were purchased from Nacalai Tesque. Human serum albumin and 20 α-amino acids used here were purchased from Sigma Co.

2.2. Analysis of NaClO and H_2O_2

We used an SBT Kit (ZK01-50; Dojindo), which uses a colorimetric method developed to determine chloride radical concentration, to examine the concentration of NaClO in the reaction cell in accordance with the manufacturer's instructions. The concentration of H_2O_2 in the reaction cell was determined by a normal titration method using potassium permanganate.

2.3. Apparatus and procedures

The CL detection apparatus equipped with the two kinds of PMTs is shown in Fig. 1. The experiments were carried out as follows; a definite amount of H_2O_2 solution (100 mM carbonate buffer (pH 10.8)) was added to a definite amount of NaClO solution (100 mM carbonate buffer (pH 10.8)) in the reaction cell through a PTFE tube. When the effects of antioxidant/biomolecules were examined, they were placed in the reaction cell in advance. The CL of the dimol emission (ca. 634 nm) was detected by PMT (R1924A, Hamamatsu) (sensitive region, 300–650 nm) and cut filter (52527-E, Edomund) (cut field <600 nm). The CL of the monomol emission (ca. 1270 nm) was detected by PMT (H9170-45, Hamamatsu) (sensitive region, 950–1400 nm), which was cooled at −60 °C with thermoelectric refrigeration under vacuum, and band path filter (1260-11-45, Intor) (1260 ± 11.8 nm). The CL from the dimol and monomol of singlet oxygen were simultaneously detected with the both PMTs for the same reaction solution in the cell. They

were treated with an integrator (Chromatopac C-R8A; Shimadzu Co.).

3. Results and discussion

3.1. Typical CL profiles of singlet oxygen

When each 10 mM of NaClO and H_2O_2 solutions was used, we observed the CL profiles at ca. 634 and ca. 1270 nm, as shown in Fig. 2. The CL appeared quickly after injecting H_2O_2 solution and disappeared within several seconds. The half-life of singlet oxygen is short. Although it is dependent on the solvent [9], e.g., 3.3 μs in water and 68.0 μs in heavy water, it is micro-second order. Judging from the CL profiles in Fig. 2, the reaction rates between the hypochlorite and H_2O_2 is comparatively first. As we do not have standard light source for 634 and 1270 nm, we have not compared the CL amount between the both CL emissions.

The effect of H_2O_2 concentration on the CL from singlet oxygen was examined at both wavelengths (ca. 634 and 1270 nm). As described in the caption of Fig. 3, H_2O_2 concentrations were changed from 0.1 to 10 mM. The CL intensities (CL peak heights) were observed with the detection limits of 0.1 mM H_2O_2 at both wavelengths and increased with increasing of the H_2O_2 concentration up to ca. 5 mM (Fig. 3). Above the concentrations the CL intensities were not changed, or saturated. The vertical line means the relative CL peak heights; they were estimated based on 100 for the addition of 10 mM H_2O_2. It was found that the reaction between NaClO and H_2O_2 might produce with equimolar to generate equivalent singlet oxygen.

On the other hand, dissolved oxygen concentration in water is generally calculated to be ca. 0.3 mM under atmosphere at a room temperature by Henry's law. When the dissolved oxygen concentration, ca. 0.3 mM, was taken into consideration, singlet oxygen generated in the reaction cell seemed to be detected with sufficient sensitivity by the present method, corresponding to the detection
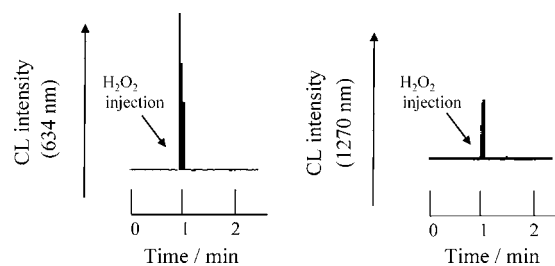

Fig. 2. The CL profiles of singlet oxygen obtained for dimol and monomol light emissions. Conditions: 10 mM H_2O_2 in 100 mM carbonate buffer (pH 10.8) (1 ml) was added to 10 mM NaClO in 100 mM carbonate buffer (pH 10.8) (5 ml) in the reaction cell.
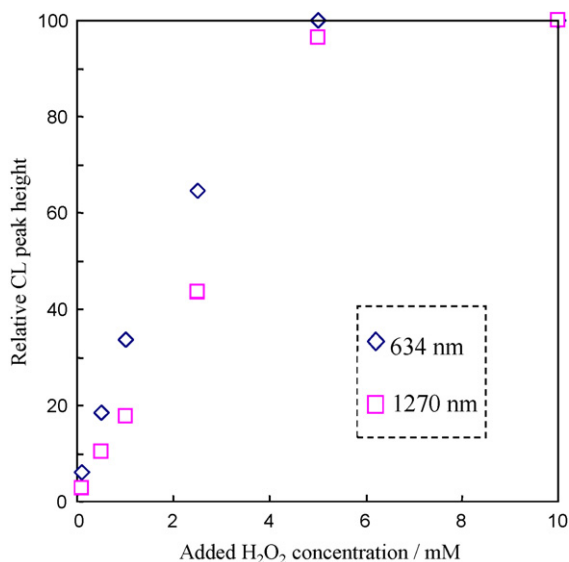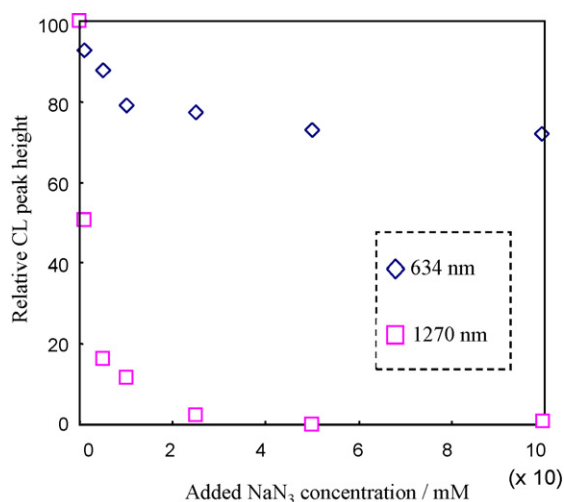
Fig. 3. The effect of H_2O_2 on CL intensities of dimol and monomol light emissions. Conditions: 0.1–10 mM H_2O_2 in 100 mM carbonate buffer (pH 10.8) (1 ml) was added to 1 mM NaClO in 100 mM carbonate buffer (pH 10.8) (5 ml) in the reaction cell.

limit of ca. 0.1 mM singlet oxygen where dissolved singlet oxygen may reach to supersaturation temporarily.

3.2. Effect of sodium azide on CL profiles

Sodium azide is well known antioxidant for singlet oxygen and is also known not to react with NaClO and H_2O_2. We examined the effect of sodium azide in the reaction cell on the CL profiles. The concentrations of sodium azide in the cell, 1–100 mM, were used. The obtained results are shown in Fig. 4. The vertical line means the relative CL peak heights; they were estimated based on 100 for no addition of sodium azide.

The both CL, from the dimol and monomol, decreased with increasing of sodium azide concentrations. The CL intensity due to monomol (ca. 1270 nm) disappeared at ca. 50 mM sodium azide. On the other hand, the CL due to dimol (ca. 634 nm) was almost constant above 20 mM sodium azide. Such observed phenomena

Fig. 4. The effect of sodium azide on CL intensities of dimol and monomol light emissions. Conditions: 10 mM H_2O_2 in 100 mM carbonate buffer (pH 10.8) (1 ml) was added to 10 mM NaClO in 100 mM carbonate buffer (pH 10.8) (5 ml) containing 1–100 mM sodium azide in the reaction cell.
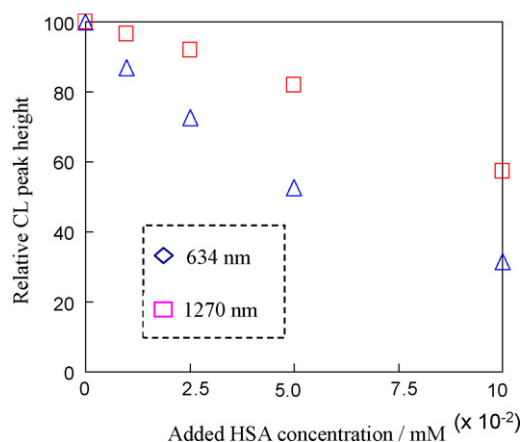
Fig. 5. The relationship between HSA concentrations and relative CL peak heights of singlet oxygen. Conditions: 10 mM H_2O_2 in 100 mM carbonate buffer (pH 10.8) (2.5 ml) was added to 10 mM NaClO (8.0 ml) in 100 mM carbonate buffer (pH 10.8) plus 0.01–0.1 mM HSA (2.0 ml) in 100 mM carbonate buffer (pH 10.8) in the reaction cell.

may be caused by the difference in the existing ratio between the dimol and the monomol in singlet oxygen, the reaction rate between singlet oxygen (the dimol or the monomol) and sodium azide, and the extinguish rate from singlet state (the dimol or the monomol) to triplet state. However, the reason has not been clear yet. Anyway, as the CL from the both states of dimol and monomol are simultaneously determined for the same reaction solution, the obtained data can be evaluated with high reliability. We will continue examining the CL profiles from singlet oxygen with the dimol and monomol emission in the presence of various other antioxidants.

3.3. Reactivity of singlet oxygen to HSA

As described in Section 1, the observation of CL from singlet oxygen in the presence of biomolecules might easily provide direct information with regard to the reaction between singlet oxygen and biomolecules. Furthermore, it is known that proteins and some α-amino acids positioning in protein side-chains are the major targets for singlet oxygen due to the abundance of proteins within most biological systems. Therefore, we decided as a first step to examine the reaction of singlet oxygen with HSA and α-amino acids by use of the present method newly developed for CL observation concerning singlet oxygen.

First, the reactivity of singlet oxygen to HSA was examined through the observation of the CL at the both wavelengths. Human serum albumin was added in the reaction cell and the concentrations were changed over the range of 0.01–0.1 mM as described in the caption of Fig. 5. The CL intensities decreased with increasing of the HSA concentrations at both detection wavelengths for the reaction (Fig. 5). The decreasing line of the relative CL peak heights of dimol showed larger slope than that of monomol.

We tried to calculate the apparent rate constants for quenching singlet oxygen with HSA from Stern–Volmer plots [10]. Stern–Volmer equation is expressed by $(I_0/I) = 1 + (k_q \tau [Q])$; the symbols mean that I_0: CL intensity in the absence of HSA, I: CL intensity in the presence of HSA, $[Q]$: HSA concentration, τ: lifetime of singlet oxygen (3.3 μs) [9], and k_q: rate constant for quenching singlet oxygen. The numbers of I_0/I are plotted against the quencher or HSA concentrations; the apparent rate constants for quenching were estimated from the slopes of the lines. They were ca. 3.3×10^9 and ca. 8.8×10^8 M^{-1} s^{-1}, respectively, for dimol and monomol. The apparent rate constant for quenching singlet

oxygen at 634 nm detection was larger than that at 1270 nm. Wei et al. [1] reported that the reaction rate constants of singlet oxygen with His, Trp, and carnosine (dipeptide) were calculated to be 3.2×10^8, 7.7×10^7, and 1.3×10^8 M^{-1} s^{-1}, respectively, through a quite different way using Eu^{3+} luminescence probe. Although there is quite difference in a measurement and a quencher between their data and ours, the apparent rate constants for quenching in the present method for HSA possessing much larger molecular weight seemed to be enough reasonable.

As NaClO and H_2O_2 are also oxidants, we examined the reactivity of them to HSA. Human serum albumin solution (0.1 mM HSA) was mixed with NaClO solution under the same conditions of CL measurement experiments of Fig. 5, the solution being left in 5 min, the concentration of NaClO was determined by use of the commercial SBT Kit for NaClO determination as mentioned in Section 2. There was no difference in the concentration of NaClO between without HSA and with HSA for 5 min solutions. Also, we examined the reactivity of H_2O_2 to HSA (0.1 mM) under the same conditions of CL measurement experiments of Fig. 5; the concentration of H_2O_2 was determined by a normal titration method using potassium permanganate. There was no difference in the concentration of H_2O_2 between without HSA and with HSA for 5 min solutions. It was concluded from the results that as all CL peaks were observed with in several seconds, the CL decreased in the presence of HSA must be based on the reaction of singlet oxygen to HSA, not on the reaction of NaClO or H_2O_2 to HSA.

3.4. The reactivity of singlet oxygen to α-amino acids

The photooxidation of His and Trp by singlet oxygen was investigated by a Eu^{3+} luminescence probe and UV Raman spectroscopy under physiological conditions (pH 7.5) [1], also, His, Tyr, Met, Cys, and Trp are known to be oxidized by singlet oxygen at physiological pH [11]; there have been no distinction between dimol and monomol singlet oxygen. We examined the CL intensities for dimol and monomol emissions in the presence of the 20 α-amino acids under the present conditions; 10 mM H_2O_2 in 100 mM carbonate buffer (pH 10.8) (2.5 ml) was added to 10 mM NaClO (8.0 ml) in 100 mM carbonate buffer (pH 10.8) combining 1 mM α-amino acids (2.0 ml) in 100 mM carbonate buffer (pH 10.8) in the reaction cell. Table 1 shows the relative CL peak heights for the 20 α-amino acids; the values were averages for 10 measurements for each α-amino acid and the relative CL peak heights were estimated for 100 in the absence of α-amino acids.

The standard deviations in the absence of α-amino acids were calculated using 10 measurements to be 3.3 and 6.0 for the dimol and monomol emissions, respectively. Some α-amino acids showed the relative CL peak heights lower than 90 for dimol and 82 for monomol that corresponded to 100 minus three standard deviations ($3.3 \times 3 = 9.9$ for dimol and $6.0 \times 3 = 18.0$ for monomol). In this study, as a valuation standard, we admitted that α-amino acids that showed the relative CL peak heights lower than 90 for dimol emission and 82 for monomol emission could possess effective influences on the CL from singlet oxygen. To be concrete, His (87), Asp (87), Phe (85), Ser (84), and Tyr (81) were thought to influence the CL of dimol emission, as well as Cys (81) and Trp (70) were to influence the CL of monomol emission; the values in parentheses indicated the relative CL peak heights shown in Table 1.

We also examined the reactivity of NaClO and H_2O_2 to α-amino acids under the same conditions of the CL measurement experiments of Table 1 in a similar way to HSA by use of an SBT Kit for determining chloride radical concentration and a normal titration method using potassium permanganate. There was no difference in the concentrations of NaClO and H_2O_2 between without α-amino

Table 1
Effect of α-amino acids on the CL from singlet oxygen

α-Amino acid	Relative CL peak height	
	634 nm	1270 nm
Blank	100	100
Met	103	95
Thr	100	97
Leu	100	101
Cys	100	(81)
Gln	100	101
Val	100	98
Glu	99	99
Asn	99	101
Asn	99	101
Ile	98	99
Pro	97	92
Arg	96	100
Ala	96	100
Trp	96	(70)
Lys	92	93
His	(87)	96
Asp	(87)	98
Phe	(85)	92
Ser	(84)	100
Tyr	(81)	93

Conditions: 10 mM H_2O_2 in 100 mM carbonate buffer (pH 10.8) (2.5 ml) was added to 10 mM NaClO (8.0 ml) in 100 mM carbonate buffer (pH 10.8) plus 1 mM α-amino acid (2.0 ml) in 100 mM carbonate buffer (pH 10.8) in the reaction cell.

acids and with α-amino acids for 5 min, except for NaClO concentration with His for 5 min decreased to 51% of that without His.

It was concluded from the results that the CL of dimol emission decreased in the presence of Asp, Phe, Ser, and Tyr must be based on the reaction of singlet oxygen to these α-amino acids, not on the reaction of NaClO or H_2O_2 to α-amino acids, as well as the CL of monomol emission decreased in the presence of Cys and Trp must be based on the reaction of singlet oxygen to them. As far as His, considering that the existence of His decreased the CL intensity of dimol but not that of monomol and that all CL peaks were observed within several seconds, the decrease of the dimol emission of singlet oxygen might not be caused through the interaction between His and the hypochlorite (although the existence of His decreased NaClO concentration for 5 min). That is, for the moment, we thought that the existence of His decreased the CL of the dimol through the reaction between singlet oxygen and His, similar to Asp, Phe, Ser, and Tyr.

As described in the above section, HSA quenched both the dimol and monomol light emissions, although the apparent rate constant for quenching singlet oxygen at 634 nm detection was larger than that at 1270 nm. On the other hand, some α-amino acids quenched either the dimol or monomol light emission. The reason has not been clear yet. However, such observed phenomena may be caused by the matching in the reaction rate between singlet oxygen (the dimol or the monomol) and α-amino acid as well as the extinguish rate from singlet state (the dimol or the monomol) to triplet state; that is, for providing CL decrease from singlet oxygen, some α-amino acids might need to react with singlet oxygen (the dimol or the monomol) with their individual reaction rate before singlet oxygen turns to triplet oxygen. For supporting this assumption, the dimol of singlet oxygen having larger energy and specific association is required to feature shorter life-time than the monomol of singlet oxygen through its self-extinguishment and/or dissociation.

4. Conclusions

Singlet oxygen possesses unique chemiluminescence (CL) property, the dimol light emission (ca. 637 nm) and the monomol light

emission (ca. 1270 nm). We newly developed the detection apparatus that equipped with the two PTMs for the CL from singlet oxygen, the dimol and monomol light emissions. Singlet oxygen was generated with chemical reaction between NaClO and H_2O_2 without using any light irradiation systems. The effects of antioxidant/biomolecules on the CL based on the both emissions were examined for the same sample solution; the observed CL could provide direct information with regard to the reaction between singlet oxygen and antioxidant/biomolecules. We are now interested in a difference in reactivity or property for antioxidant/biomolecules between dimol and monomol singlet oxygen.

Acknowledgments

References

[1] C. Wei, J. Yuan, Z. Feng, G. Jia, C. Li, J. Photochem. Photobiol. A: Chem. 189 (2007) 39.
[2] M.J. Davies, Biochem. Biophys. Res. Commun. 305 (2003) 761.
[3] A.M. Edwards, E. Silva, J. Photochem. Photobiol. B 63 (2001) 126.
[4] E. Clo, J.W. Snyder, N.V. Voigt, P.R. Ogilby, K.V. Gothelf, J. Am. Chem. Soc. 128 (2006) 4200.
[5] J.-L. Ravanat, M.H.G. Medeiros, P.D. Mascio, J. Cadet, Tetrahedron 66 (2006) 10709.
[6] E.A. Almeida, G.R. Martinez, M.H.G. Medeiros, P.D. Mascio, Anal. Chim. Acta 482 (2003) 99.
[7] Y. Wenli, Z. Yaping, Biochim. Biophys. Acta 1725 (2005) 30.
[8] E.A. Almeida, S. Miyamoto, G.R. Martinez, M.H.G. Medeiros, P.D. Mascio, Anal. Acta Chim. 482 (2003) 99, and the references cited therein.
[9] M.A.J. Rodgers, J. Am. Chem. Soc. 105 (1983) 6201.
[10] M.Y. Li, C.S. Cline, E.B. Koker, H.H. Carmichael, C.F. Chignell, P. Bilski, Photochem. Photobiol. 74 (2001) 760.
[11] J. Kim, M. Guoc, M.E. Kenney, N.L. Oleinick, V.E. Anderson, Free Radic. Biol. Med. 44 (2008) 1700.

Rapid identification and high sensitive detection of cancer cells on the gold nanoparticle interface by combined contact angle and electrochemical measurements

Fang He [a], Qin Shen [a], Hui Jiang [a], Jian Zhou [a], Jian Cheng [b], Dadong Guo [a], Qingning Li [a], Xuemei Wang [a,*], Degang Fu [a], Baoan Chen [b]

[a] *State Key Laboratory of Bioelectronics (Chien-Shiung Wu Laboratory), School of Biological Science and Medical Engineering, Southeast University, Nanjing 210096, China*
[b] *Department of Hematology and Oncology, Affiliated Zhongda Hospital, Southeast University, DingJiaQiao 87, Nanjing 210009, China*

ARTICLE INFO

ABSTRACT

In this study, we have proposed a novel strategy for the rapid identification and high sensitive detection of different kinds of cancer cells by means of electrochemical and contact angle measurements. A simple, unlabeled method based on the functionalized Au nanoparticles (GNPs) modified interface has been utilized to distinguish the different cancer cells, including lung cancer cells, liver cancer cells, drug sensitive leukemia K562/B.W cells and drug resistant leukemia K562/ADM cells. The relevant results indicate that under optimal conditions, this method can provide the quantitative determination of cancer cells, with a detection limit of $\sim 10^3$ cells mL^{-1}. Our observations demonstrate that the difference in the hydrophilic properties for target cellular surfaces and in the uptake efficiency of the anticancer drug daunorubicin for different cancer cells could be readily chosen as the elements of cancer identification and sensitive detection. This raises the possibility to advance the promising clinic diagnosis and monitoring of tumors with the aim of successful chemotherapy of human cancers.

© 2008 Elsevier B.V. All rights reserved.

1. Introduction

Cancer is one of the most serious and lethal diseases around the world. The research of fast identification and high-sensitive detection of cancer cells is extremely important for cancer diagnosis and therapy, which can be utilized to explore and monitor the relevant biological process of cancers and is critical for the early cancer diagnosis and clinical treatments.

The intensive interests and efforts in the early cancer diagnosis reflect the increasing demand of relevant biosensors with good sensitivity and selectivity, rapidness, and easy operation [1,2]. Several protocols have been developed to detect and identify cancerous cells, including those based on polymerase chain reaction (PCR) [3], quartz crystal microbalance (QCM) measurement [4], microarrays [5,6], monoclonal antibody-coupled ferromagnetic nanoparticles [7], aptamer-modified fluorescent nanoparticles [8], carbohydrate-mediated cell recognition using gold glyconanoparticles [9], immunophenotyping by means of flow cytometry [10], amperometric detection of enzymatic reaction products [11] chemiluminescence (CL) [12] or diffraction-based cell detection

[13], etc. Many of the currently available detection methods require enrichment of the target cells in the sample or expression of fluorescent protein markers or antibodies in the cells, and tend to include additional steps and time-consuming assay procedures. For example, PCR-based methods are indirect ways of detecting cells and require prolonged isolation steps before analysis. Besides, the variable sensitivity of PCR can limit its effectiveness as a diagnostic technique and lead to false-negative results [3]. Moreover, the common immunophenotypic analyses on basis of flow cytometry, which require multiple antibody probes for accurate cell detection, are usually time-consuming, complex and costly. In view of these challenges, a simple detection system that can achieve high selectivity and sensitivity without the need for target amplification and labeling is highly desirable.

Recently, nanotechnology has been located in a unique position to transform cancer diagnostics and to produce a new generation of biosensors and medical imaging techniques for highly sensitive and precise recognition. Large quantities of biocompatible nanomaterials have attracted much interest of numerous scientists in various biomedical research areas due to their unique properties. Among them, gold nanoparticles (GNPs), the known biocompatible nanomaterials, have been widely concerned in the fields of biomedical imaging and biosensing applications during the last ten years [14–17]. Our recent study indicates that the relevant GNPs have

* Corresponding author. Tel.: +86 25 83792177; fax: +86 25 83792177.
E-mail address: xuewang@seu.edu.cn (X. Wang).

negligible effect on cellular drug uptake of daunorubicin (DNR) of normal cells but have significant effect on the intracellular drug accumulation of DNR on leukemia cancer cells [17]. Besides, the functional GNPs-based materials have been well adopted for the biosensing of biomacromolecules based on their unique mechanical and electronic properties [18–22].

Considering the plentiful merits of GNPs, in this study we have utilized them for highly sensitive detection of cancer cells. The strategy of a simple identification and sensitive detection of the drug sensitive and drug resistant leukemia K562 cells, lung cancer cells and liver cancer cells on the functionalized GNPs modified interface has been developed by using anticancer drug daunorubicin as the electrochemical probe. Meanwhile, according to the different hydrophilic characteristics of the relevant cancer cells on the GNPs modified interface, we could utilize the contact angle measurement to identify above different kinds of cancer cells. The researches have realized the cancerous cell detection by electrochemical and contact angle measurements with high sensitivity, selectivity and simplicity.

2. Experimental

2.1. Reagents

Daunorubicin, mercaptopropionic acid (MPA) and hydroxyethylpiperazine ethanesulfonic acid (HEPES) were purchased from Aldrich. 1-Ethyl-3-(3-dimethyl aminopropyl)-carbodiimide hydrochloride (EDC) was purchased from Sinopharm. Co. Ltd., China. Daunorubicin stock solutions were freshly prepared and stored in the dark at 4 °C. Phosphate buffer solution (PBS) and HEPES buffer was prepared with double distilled water. All other reagents were of analytical grade. The functionalized GNPs were synthesized according to the literature [23] by the ligand exchange reaction between triphenyl phosphine (PPh$_3$)-stabilized precursor nanoparticles and MPA. The concentration ratio between original Au (III) and MPA was adjusted at 1:100.

2.2. Cells and cell culture

Lung cancer cells, liver cancer cells, leukemia K562/ADM and K562/B.W cell lines were purchased from Institute of Hematology of Tianjin, Chinese Academy of Medical Sciences and cultured in a flask in RPMI 1640 medium (GIBCO) supplemented with 10% fetal calf serum (FCS, Sigma), penicillin (100 U mL^{-1}), and streptomycin (100 μg mL^{-1}) at 37 °C in a humidified atmosphere containing 5% CO$_2$. The drug resistant leukemia K562 cells (K562/ADM cells) were maintained with 1 μg mL^{-1} Adriamycin (Sigma).

The real leukemia cell lines were collected and separated from the mixture of peripheral blood of leukemic patients, PBS (0.1 M, pH 7.2) and lymphocytes separation medium with the ration of 1:1:2 (v/v/v) by centrifugation 2500 rpm for 30 min.

2.3. Electrode preparation

The glassy carbon electrode (GCE) was polished to a mirror using 0.3 and 0.05 μm alumina slurry (Beuhler) followed by rinsing thoroughly with double distilled water. The electrodes were then pretreated electrochemically by applying a potential of +1.75 V in PBS (0.1 M, pH 5.0) for 300 s, and scanned between +0.3 and +1.25 V and then +0.3 and −1.3 V until a steady-state current–voltage curve was observed [24]. This process led to the formation of hydroxyl groups on the GCE surface and increased surface hydrophilicity of the GCE. Then the pretreated electrode was immersed thoroughly into the blending solution with 100 μL GNPs and 100 μL HEPES buffer solution (0.1 M, pH 7.2) containing 0.5 mmol EDC for about

10 h. The hydroxyl groups on GCE were linked to the MPA stabilized GNPs with the assistance of the EDC linker. The GNPs modified GCE was then rinsed thoroughly with double distilled water to remove the non-covalent nanoparticles before use.

2.4. Atomic force microscopy (AFM) measurements

The AFM measurements were performed through a simultaneous monitoring of both the amplitude and the phase of the oscillating cantilever in tapping mode. All AFM data were collected on a Digital Instruments using a Nanoscope III controller (Veeco Instruments, New York) and an E-scanner operating in tapping mode in air. Imaging was accomplished using diving board TESP tips with integral square pyramidal tips. All data were plane fit and flattened prior to analysis using the Nanoscope software.

2.5. Electrochemical investigation

The leukemia K562 cells at a concentration of 6×10^5 mL^{-1} with anticancer drug daunorubicin at a concentration of 5.3×10^{-5} M were firstly incubated at room temperature. After the targeted cells with DNR were pretreated for a series of incubated time, the suspensions were centrifuged for 10 min. Then all medium samples outside leukemia K562/ADM cells were collected and diluted with sterilized PBS (0.1 M, pH 7.2). The electrochemical signal of DNR residue in these samples was determined with differential pulse voltammetry (DPV) assay for each sample by CHI660C electrochemical analyzer. All measurements were performed at ambient temperature (22 ± 2 °C) in a three-component electrochemical cell consisting of the GNPs modified glassy carbon electrode (GNPs–GCE) as the working electrode, a Pt wire as the counter electrode and a saturated calomel electrode (SCE) as the reference electrode.

2.6. Contact angle detection

Contact angle detection was performed with a CAM2000 optical contact angle analyzer (KSV Instruments, Finland) using a CCD video camera and a horizontal light source to illuminate the liquid droplet. The droplets of solution were placed on the surface of the GNPs–GCE and the contact angle measurements were carried out at ambient temperature (22 ± 2 °C). To extract the precise contact angle values, the drop images were fitted using the Young–Laplace equation [25]. The contact angle values were determined with the precision of ±0.5°.

3. Results and discussion

3.1. Characterization of the GNPs–GCE

After the preparation of the GNPs–GCE according to the procedure described above, the GNPs–GCE was first characterized by AFM, which is an effective way to provide nanoscale surface topography and phase images. The AFM studies can afford direct evidence for the morphologies of the functionalized GNPs film covered on the GCE. As shown in Fig. 1, the typical topographic images of the bare GCE and the GNPs–GCE have been explored and characterized by AFM studies. The pretreated bare GCE exhibits a relatively planar interface (Part A, Fig. 1), while the GNPs film appears more rough and highlighted in the AFM graphs (Part B, Fig. 1). The average sizes of GNPs were about 15 nm and in coincidence with the sizes of dispersed GNPs obtained by TEM (not shown), indicating the assembly of GNPs on the surface produces little aggregation.

In addition, the electrochemical performance of the GNPs–GCE has also been investigated by cyclic voltammetry. As shown in
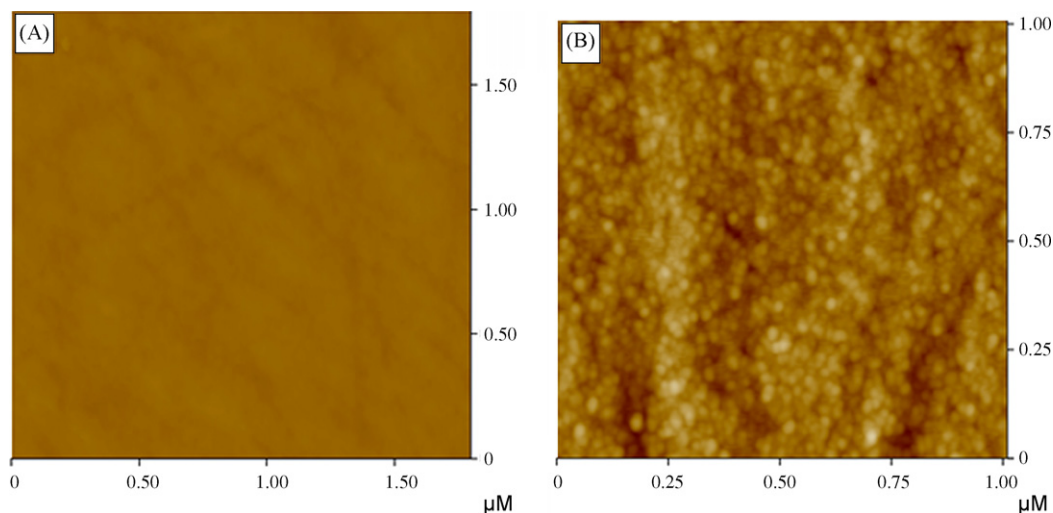
Fig. 1. Topological AFM images of the GCE surface before (A) and after (B) functionalized GNPs modification.
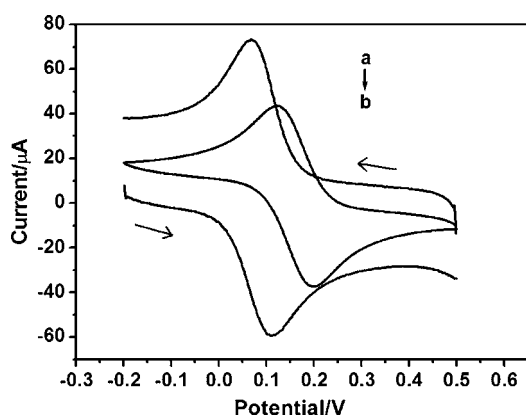

Fig. 2. Cyclic voltammograms of 1 mM $K_3[Fe(CN)_6]$ (containing 0.1 M KCl electrolyte) at (a) the functionalized GNPs–GCE, and (b) the bare GCE. Scan rate: 0.1 V/s.

Fig. 2, compared with the bare GCE, the electrochemical current of $[Fe(CN)_6]^{3-}$ at the GNPs–GCE enhances ca. 45%, indicating a considerable improvement in the electron transfer. Besides, a negative shift of ca. -70 mV in the $[Fe(CN)_6]^{3-}$ redox peak potentials is observed for the GNPs–GCE in comparison with that of the bare GCE.

3.2. Identification of cancer cells by contact angle detection

Based on these studies, the multi-signal responsive biosensing interface was further explored by tailoring the relevant cell (i.e., lung cancer cells, liver cancer cells, leukemia drug sensitive K562/B.W cells, and leukemia drug resistant K562/ADM cells) covering GNPs–GCE, where a 10 μL droplet of target cell solution was pipetted onto the modified surface and dried with nitrogen. By

combination of the respective cancer cells with the GNPs–GCE, our observations indicate that contact angle technique could offer a new strategy for the rapid identification and detection of different cancer cells. Fig. 3 shows the pixel images of the initial contact angle values of PBS (pH 7.2, 0.1 M) droplet on the respective cell covered GNPs–GCE. The contact angle values of relevant droplet on lung cancer cells, liver cancer cells, drug sensitive leukemia K562/B.W cells, and drug resistant leukemia K562/ADM cells covered modified electrodes were ca. 77°, 70°, 64°, and 53°, respectively. It is evident that the different cancer cells can be distinguished from each other by using the contact angle detection. The rational behind this may be due to the difference in the expression of the membrane proteins (such as P-glycoprotein (P-gp) and others) on the cellular surface, which greatly influences the hydrophilicity of the cellular surface. Thus, the different cells could be identified based on the hydrophilic characteristics of them, using the contact angle measurements.

The stability of the contact angle measurements of PBS on these cancer cells covered GNPs surface have also been investigated (as shown in Fig. S1 in Supporting Information). It is observed that the contact angle values of the droplets on the relevant surfaces almost kept constant in 30 s. The stable and convincing results guarantee the simple and fast identification of target cancer. So, according to the distinct contact angles of PBS on target cells covered GNPs–GCE, we can fast and simply identify the drug sensitive and drug resistant leukemia K562 cells, lung cancer cells and liver cancer cells.

3.3. Identification of cancer cells based on electrochemical detection

In view of the above studies, the more sensitive DPV technique has been explored for the identification and detection of the cancer cells (i.e., lung cancer cells, liver cancer cells, leukemia drug sensitive K562/B.W cells, and leukemia drug resistant K562/ADM
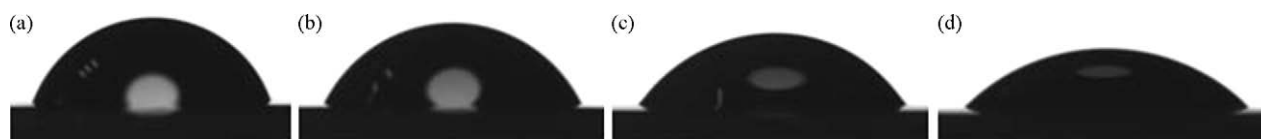

Fig. 3. Typical initial contact angle images of 7 μL PBS droplets on (a) lung cancer cells, (b) liver cancer cells, (c) leukemia K562/B.W cells, and (d) leukemia K562/ADM cells covered GNPs–GCE. During the preparation of the cells covered GNPs–GCE, a 10 μL droplet of cell solution (6×10^7 cells mL^{-1}) was pipetted onto the modified electrodes surface and dried with nitrogen. The contact angle values were determined with the precision of ±0.5°.
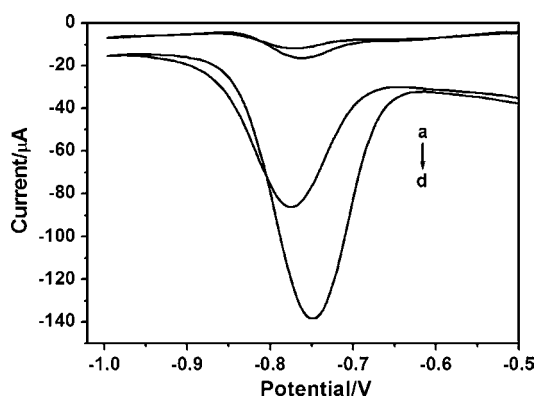
Fig. 4. Differential pulse voltammetry of DNR residue after the leukemia K562/ADM cells (a and c) or leukemia K562/B.W cells (b and d) were incubated with DNR (5.3×10^{-5} M) for 2 h at bare GCE (a and b) and GNPs–GCE (c and d). Pulse amplitude: 0.05 V. Pulse width: 0.05 s. Pulse period: 0.1 s. The significant enhancement on the GNPs–GCE can be observed.

cells). As well known, multidrug resistance (MDR) is a dominating limit in the current chemotherapy of cancers. It is mainly associated with the overexpression of several proteins on the cellular surface, the most important being P-gp. Failure of chemotherapy to the malignant tumor is usually attributed to the overexpression of P-gp, which is considered to act as an energy-dependent drug efflux pump that causes a decrease in cytotoxic drug accumulation [26]. Another failing factor of chemotherapy is that anticancer drugs not only kill cancer cells but also poison healthy cells. Therefore, it is much important to distinguish the drug sensitive and drug resistant cancer cells to monitor the cancer therapy. Meanwhile, with the anticancer drug DNR as the electrochemical probe, the DNR uptake efficiency for different cancer cells could be probed by the DPV technique [27].

On the basis of these considerations, in this contribution, the DNR uptake efficiency by the different cancer cells has been investigated. As we know, when different cells were treated with DNR, the unadsorbed DNR molecules are still in the environmental solution, and the electrochemical response of this part of the molecules can be readily detected. Thus, the DNR residue (unadsorbed DNR) can be adopted as the referential value of the cellular uptake efficiency. As shown in Fig. 4, our study indicates that the DNR detection sensitivity could be remarkably enhanced by using the functionalized GNPs–GCE than that of the bare GCE. It is proved that the GNPs–GCE could remarkably enhance the DNR detection sensitivity and selectivity for identification of the cancer cells.

It is evident that by combining with anticancer drug DNR as an electrochemical probe, the residual amount of the DNR outside the target cancer cells can be adopted as the referential value of the efficiency. So, we have explored the possibility to identify and detect the four kinds of cancer cells mentioned above by electrochemical means. Fig. 5 illustrates the DPV study of DNR residue on the GNPs–GCE after the cells have been incubated with DNR for 2 h. The distinct electrochemical responses of the DNR residue in the buffer for the four different cancer cells appear at ca. −750 mV (vs SCE) on the modified electrodes. Notably, the DPV peak current of the DNR residue for the drug resistant leukemia K562/ADM cells is much greater than that of the drug sensitive leukemia K562/B.W cells, suggesting that much more DNR molecules have been absorbed into drug sensitive cancer cells than that of the drug resistant cancer cells. This is consistent with the cellular surface properties of the leukemia K562/ADM cells, i.e., the overexpression of P-gp on the leukemia K562/ADM cells will extrude the positively charged DNR out of the cells and lead to the less DNR accumulation in the leukemia K562/ADM cells than that in the leukemia K562/B.W cells.
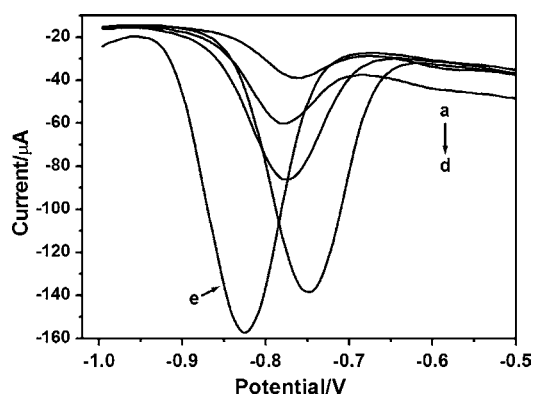

Fig. 5. Differential pulse voltammetry study on the GNPs–GCE for DNR residue outside (a) lung cancer cells, (b) liver cancer cells, (c) leukemia K562/B.W cells, (d) leukemia K562/ADM cells after the cells were incubated with DNR (5.3×10^{-5} M) for 2 h. DPV of DNR (5.3×10^{-5} M) itself was also shown as the reference (e). All cell concentrations are 6×10^5 cells mL^{-1}. Pulse amplitude: 0.05 V; Pulse width: 0.05 s; Pulse period: 0.1 s.

With a same incubation period, the relative decrease percentage in the peak current of DNR in the buffer is 17% for leukemia K562/ADM cells, 53% for leukemia K562/B.W cells, 74% for lung cancer cells and 89% for liver cancer cells, respectively, indicating that different cancer cells have different uptake facility of DNR. Scheme 1 illustrates the relevant strategy for the identification of cancer cells by contact angle and electrochemical study. Thus, by checking the corresponding electrochemical behavior of the DNR residue in the buffer for different cancer cells, we can quickly and sensitively identify these different kinds of cancer cells based on the respective GNPs–GCE.

The time dependence of the drug uptake efficiency has also been researched (as shown in Fig. S2 in Supporting Information), since the interaction time of DNR with target cancer cells is important for the fast and high-sensitive identification of the four different cancer cells mentioned above. The corresponding electrochemical response of DNR residue outside the lung cancer cells, liver cancer cells, and leukemia K562/B.W cells are found to decrease with an increasing incubation time, while only the current of the leukemia K562/ADM cells keep stable during the period. In all cases, the peak currents of DNR residue can reach to a constant value after incubation for about 2 h. Therefore, to distinctly identify the target cancer cells with rapidness and accuracy, the optimal incubation time should be 2 h.

Furthermore, we have applied this procedure to real world sample analyses. We analyzed the peripheral blood of leukemic patients before and after injected with anticancer drug. As shown in Fig. S3 in Supporting Information, the result was consistent with the foregoing experiments. After injected with anticancer drug for a period of time, the cancer cells in the body of patient became leukemia drug resistant cells which less anticancer drug could be absorbed into. So, its electrochemical responses of the DNR residue in the buffer was stronger than that of patient without injection, and both of them had some positive shift of the peak potential, suggesting its potential application as the new strategy for the development of the clinic diagnosis and monitoring of tumors.

3.4. Electrochemical method for cell quantification

To quantitatively describe the performance of the multi-signal responsive biosensing interface, leukemia K562/B.W cell line was chosen as the paradigm. When incubated with the same concentration of DNR, the DPV peak current of DNR residue in the buffer decreased with the increasing concentration of K562/B.W cells. The peak current was proportional to the concentration of leukemia
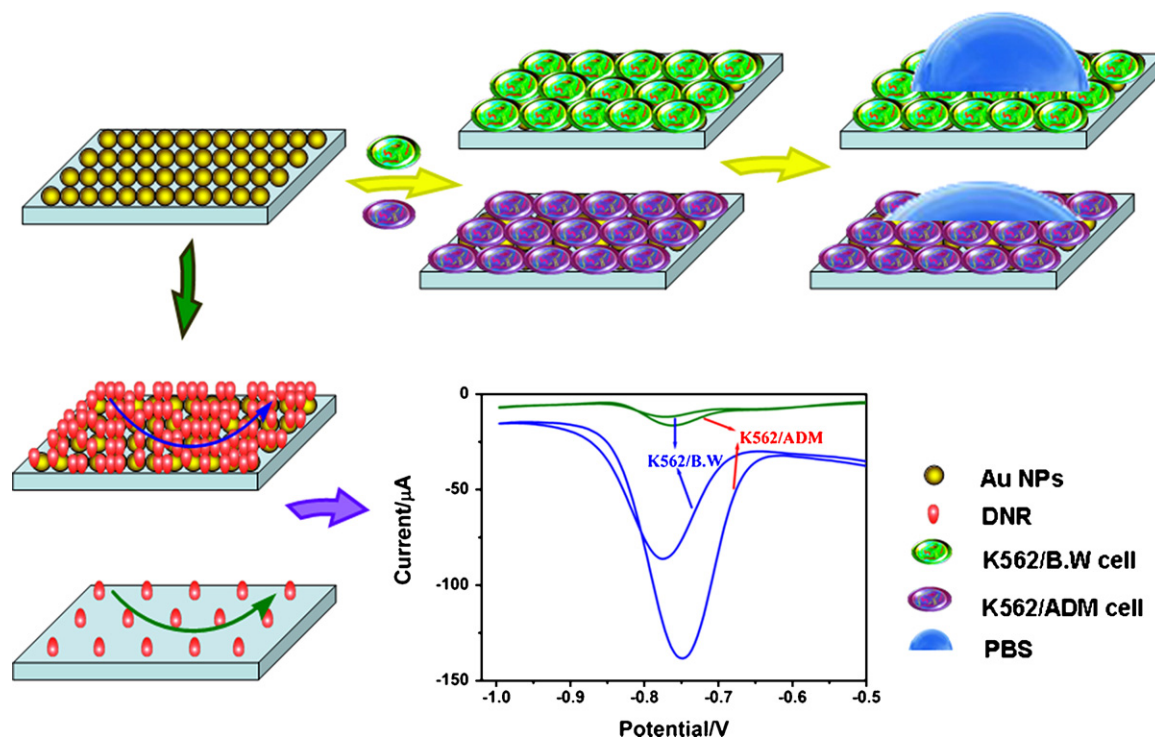
Scheme 1. Scheme for the illustration of electrochemical and contact angle detection of cancer cells based on functionalized GNPs–GCE interface.

K562/B.W cells ranging from 2.0×10^4 to 8.0×10^5 cells mL^{-1}, with a correlation coefficient of 0.99 (as shown in Fig. S4 in Supporting Information). The detection limit for cell number was calculated to be approximate 1000 cells mL^{-1} (based on the signal of DNR with S/N = 3 criterion) and much lower than those of several methods developed by other researchers, such as 1.0×10^5 cells mL^{-1} by immunomagnetic separation/flow injection systems coupled with mediated amperometric detection [28], and 1.0×10^4 cells mL^{-1} by immunosensor for detection of *Salmonella* species on a QCM [29]. This indicates that the presented strategy could provide a simple and applicable way for cancer cell quantification with high sensitivity and fine accuracy.

4. Conclusions

In summary, we have demonstrated a novel strategy for the rapid identification and high sensitive detection of target cancer cells by electrochemical and contact angle measurements based on the functionalized GNPs–GCE. On the basis of these observations, the approaches described here may be readily adopted as a significant way to detect and identify various cancer cells and advance clinic diagnosis and monitoring of tumors with the aim of successful chemotherapy of human cancers. This could provide a promising powerful tool for cancer early diagnosis and thus guide how to treat it, a challenge faced by the relevant cancer therapy. Further, in vivo applications of this new strategy to detect and distinguish different kinds of cancerous cells by using electrochemical and contact angle detection simultaneously are ongoing in process.

Acknowledgements

Appendix A. Supplementary data

Supplementary data associated with this article can be found, in the online version, at doi:10.1016/j.talanta.2008.07.063.

References

[1] D. Pan, J.L. Turner, K.L. Wooley, Chem. Commun. 19 (2003) 2400.
[2] P.E. Andreotti, G.V. Ludwig, A.H. Peruski, J.J. Tuite, S.S. Morse, L.F. Peruski Jr., Biotechniques 35 (2003) 850.
[3] P. Belgrader, W. Benett, D. Hadley, J. Richards, P. Stratton, R.M. Mariella Jr., F. Milanovich, Science 284 (1999) 449.
[4] H. Wang, H. Zeng, G.L. Shen, R.Q. Yu, Anal. Chem. 78 (2006) 2571.
[5] M.D. Disney, P.H. Seeberger, Chem. Biol. 11 (2004) 1701.
[6] P. Francoisa, M. Bentoa, P. Vaudauxa, J. Schrenzela, J. Microbiol. Methods 55 (2003) 755.
[7] A.G.J. Tibbe, B.G. de Grooth, J. Greve, P.A. Liberti, G.J. Dolan, L.W.M.M. Terstappen, Nat. Biotechnol. 17 (1999) 1210.
[8] J.K. Herr, J.E. Dmith, C.D. Medley, D.H. Shangguan, W.H. Tan, Anal. Chem. 78 (2006) 2918.
[9] A. Carvalho de Souza, K.M. Halkes, J.D. Meeldijk, A.J. Verkleij, J.F.G. Vliegenthart, J.P. Kamerling, Chem. Biol. Chem. 6 (2005) 828.
[10] S. Cobbe, S. Connolly, D. Ryan, L. Nagle, R. Eritja, D. Fitzmaurice, J. Phys. Chem. B 107 (2003) 470.
[11] M. Másson, Ö.V. Rúnarssona, F. Jóhannsona, M. Aizawa, Talanta 64 (2004) 174.
[12] J. Matsui, K. Akamatsu, S. Nishiguchi, J. Matsui, K. Akamatsu, S. Nishiguchi, D. Miyoshi, H. Nawafune, K. Tamaki, N. Sugimoto, Anal. Chem. 76 (2004) 1310.
[13] S.H. Chen, K. Kimura, Langmuir 15 (1999) 1075.
[14] A.B. Lowe, B.S. Sumerlin, M.S. Donovan, C.L. McCormick, J. Am. Chem. Soc. 124 (2002) 11562.
[15] J.G. Worden, Q. Dai, A.W. Shaffer, Q. Huo, Chem. Mater. 16 (2004) 3746.
[16] K. Kerman, H.B. Kraatz, Chem. Commun. 47 (2007) 5019.
[17] J.Y. Li, X.M. Wang, C.X. Wang, B.A. Chen, Y.Y. Dai, R.Y. Zhang, M. Song, G. Lv, D.G. Fu, Chem. Med. Chem. 2 (2007) 374.
[18] J. Matsui, K. Akamatsu, S. Nishiguchi, D. Miyoshi, H. Nawafune, K. Tamaki, N. Sugimoto, Anal. Chem. 76 (2004) 1310.
[19] G.P. Goodrich, M.R. Helfrich, J.J. Overberg, C.D. Keating, Langmuir 20 (2004) 10246.

[20] G. Acharya, C.L. Chang, C. Savran, J. Am. Chem. Soc. 128 (2006) 3862.
[21] H.K. Li, J.H. Huang, J.H. Lv, H.J. An, X.D. Zhang, Z.Z. Zhang, C.H. Fan, J. Hu, Angew. Chem. 117 (2005) 5230.
[22] T. Koshiyama, N. Yokoi, T. Ueno, S. Kanamaru, S. Nagano, Y. Shiro, F. Arisaka, Y. Watanabe, Small 4 (2008) 50.
[23] G.H. Woehrle, L.O. Brown, J.E. Hutchison, J. Am. Chem. Soc. 127 (2005) 2172.
[24] Z. Dai, F. Yan, J. Chen, H.X. Ju, Anal. Chem. 75 (2003) 5429.
[25] X.M. Wang, A.B. Kharitonov, E. Katz, I. Willner, Chem. Commun. 13 (2003) 1542.
[26] H. Hamada, T. Tsuruo, Cancer Res. 48 (1988) 4926.
[27] M. Song, R.Y. Zhang, Y.Y. Dai, F. Gao, H.M. Chi, G. Lv, B.A. Chen, X.M. Wang, Biomaterials 27 (2006) 4230.
[28] L. Yang, Y.B. Li, G.F. Erf, Anal. Chem. 76 (2004) 1107.
[29] Y.Y. Wong, S.P. Ng, M.H. Ng, S.H. Si, S.Z. Yao, Y.S. Fung, Biosens. Bioelectron. 17 (2002) 676.

Preliminary study of a microbeads based histamine detection for food analysis using thermostable recombinant histamine oxidase from *Arthrobacter crystallopoietes* KAIT-B-007

Takeshi Ito [a,*], Tetsuya Hiroi [a], Tsutomu Amaya [a], Satoru Kaneko [a], Mayumi Araki [a], Toshiyuki Ohsawa [a], Akira Yamamura [b], Kunio Matsumoto [b]

[a] *Kanagawa Industrial Technology Center, Shimo–imaizumi 705-1, Ebina, Kanagawa 243-0435, Japan*
[b] *Kanagawa Institute of Technology, Shimo–ogino 1030, Atsugi, Kanagawa 243-0292, Japan*

ARTICLE INFO

ABSTRACT

We designed and prepared a micro biosensing system consisting of a flow through system with a sub-micro liter injection valve and a sub-micro liter volume bioreactor. An electrochemical detector was combined with the reactor for immediate detections. The volumes of the reactor and the sample loop for the injection were 850 nl and 320 nl, respectively. This paper described about the characteristics of the sensing system in the case of histamine detection for food analysis. Histamine oxidase from KAIT-B-007 was prepared by using a gene recombination technique and they were immobilized with chitosan beads (ϕ = 70–105 μm). The detection less than one minute after injection made possible fast analysis for histamine. The biosensing system also showed a high performance for histamine detection in wide range of 1 μM–1 mM. In addition, we practically measured histamine content in raw tuna stored at room temperature and 35 °C up to 96 h. As a result of the comparison between our sensing system and HPLC method, there was good agreement. These results show that our microfluidic biosensing system has the potential to assist miniaturization with small sample volume and short determination time for a sequential food analysis.

© 2008 Elsevier B.V. All rights reserved.

1. Introduction

Histamine is one of important primary amines in food analysis. Histamine is a well known factor to cause an allergy-like food poisoning [1,2], and is produced in a fish or fish product as a result of the bacterial decarboxylation of histidine which exists in high amounts in a lean fish of bluefish species like tuna, herring, mackerel, horse mackerel, etc. It is important for fishery industries and food-processing companies to manage the freshness of the lean fish, for an example, a food engineering process for canned tuna. In such a situation, a compact analytical system with easy-to-use and fast analysis for sequential measurement is in great demand. Histamine is usually detected by separation techniques like high performance liquid chromatography (HPLC) with spectrophotometric or fluorometric detection [3–6]. However, these techniques need a quite long time to determine the amount of histamine because of complicate preparations. While, a biosensor immobilized with enzymes which were amine oxidase [7,8], histamine oxidase (HOD) [9,10],

methylamine dehydrogenase [11,12] and histamine dehydrogenase (HmDH) [13], is a candidate for sensing method to satisfy these demands because of their substrate specificity.

HOD from *Arthrobacter crystallopoietes* KAIT-B-007 was purified and well characterized, and it had advantages in thermostability and in specificity of substrate [14]. This enzyme catalyzes the oxidation of histamine to imidazole acetaldehyde, ammonia, and hydrogen peroxide. However, it took long time to purify the enzyme with complications from culturing KAIT-B-007, and then we got small quantity of the purified enzyme. In this paper, the enzyme was produced using a gene recombination technique to enhance the productivity through the process.

Flow injection analysis (FIA) has advantages for continuous monitoring of many samples and is known as an analytical way with highly reproducible and user friendly. In fact, automatically system with FIA is commercially available, however, the system is still under miniaturization. For downsizing the sensing system with sequential measurement, microbeads based enzyme reactor is proposed as a microfluidic device in this study. The enzyme reactor was completed by putting the immobilized chitosan beads into a microchannel with a step structure to retain the beads. The device was fabricated by using a build-up technique, which was

---

well known in printed-wiring assembly (PWA). An electrochemical (EC) detector was combined with the reactor and measured the current on oxidizing hydrogen peroxide generated from the enzyme reaction. In this paper, we demonstrated that our sensing system had the potential to detect histamine in ultralow volume for a food administration.

2. Experimental

2.1. Reagents and chemicals

Pyrex wafers (0.5 mm thick) were purchased from Mitorika Glass Co., Ltd. (Ibaraki, Japan). Pt tablets, Ti grains, Ag grains and Cr grains were obtained from Kojundo Chemical Laboratory Co., Ltd. (Saitama, Japan). Photosensitive sheets were obtained from Hitachi Chemical Co., Ltd. with the thickness of 25 μm (ME-1025) and the 50 μm (ME-1050). Phosphate buffer solution (1/15 M, pH 7.0), sodium carbonate, 4-aminoantipyrine (4-AA), Triton X-100, sodium dodecyl sulfate (SDS), histamine dihydrochloride, peroxidase (POD), laccase, isopropyl-β-D(−)-thiogalactopyranoside (IPTG), ampicillin, sodium chloride, sodium hydroxide, phenylisothiocyanate (PITC), ethanol and triethylamine were purchased from Wako Pure Chemical Industries, Ltd. (Osaka, Japan). Bacto tryptone and bacto yeast extract were obtained from Becton Dickinson (MD, USA). Chitosan beads (Chitopearl BCW25) were purchased from Fujibo (Tokyo, Japan). Glutaraldehyde solution of 8 wt% was obtained from TAAB (Berkshire, GB). TALON™ Metal Affinity Resins and pCold I Vector Set were purchased from Takara Bio Inc. (Shiga, Japan). E. coli BL21star(DE3) strain was purchased from Invitrogen Japan K.K. (Tokyo, Japan). N-Ethyl-N-(2-hydroxyl-3-sulfopropyl)-3,5-dimethoxyaniline (DAOS) was purchased from Dojindo Laboratories (Kumamoto, Japan).

2.2. Enzyme purification, assay and immobilization

When the histamine oxidase gene was amplified by polymerase chain reaction (PCR), chromosomal DNA from *Arthrobactor crystallopoietes* KAIT-B-007 was used as a template. The oligonucleotides of 5′-GGATCCATGACCCTTCAGACCGCCTC-3′ and 5′-AAGCTTGCTCGCTCCTTCGTTTG-3′ were used as primers. After PCR product was cloned into pCold I plasmid vector to yield the pCold I-HOD vector which produced a histidine-tagged HOD upon expression, it was transferred into *E. coli* BL21star(DE3).

LB medium of 1 l contained bacto tryptone of 10 g, bacto yeast extract of 5 g, NaCl of 10 g and NaOH (5N) of 200 ml. After an autoclave sterilization, the transformed *E. coli* BL21star(DE3) cells were grown at 37 °C in the LB medium supplemented with ampicillin at 5 mg/l. When the absorbance at 600 nm reached 0.6 using a spectrophotometer (Hitachi, U-2000A), the LB medium was cooled down and kept at 15 °C for 30 min. After IPTG was added at the final concentration of 1 mM, the LB medium was incubated for 24 h at 15 °C to include the expression of recombinant HOD. The cells were harvested by centrifugation, and resuspended in sodium phosphate buffer solution (50 mM, pH 7.0) contained 300 mM NaCl (Buffer A). The cells were broken by sonication for 5 min. The resulting suspension was centrifuged at $10,000 \times g$ for 5 min at 4 °C to obtain a crude enzyme solution which was loaded onto the TALON™ Metal Affinity Resins column equilibrated with Buffer A. After washing the column with Buffer A, the enzyme elution was prepared with Buffer A contained 150 mM imidazole. The amount of protein was estimated by the absorbance at the wavelength of 280 nm using the spectrophotometer.

The enzyme assay was performed following to the Ref. [14]. The reaction mixture contained 0.2 ml of 10 mM histamine dihy-

drochloride, 0.5 ml of 5 mM DAOS, 0.5 ml of 7.5 mM 4–AA, 0.5 ml of POD (25 units/ml), and 0.3 ml of ion–exchange water, and was incubated at 37 °C for 5 min. The reaction was terminated by addition of 0.5 ml of SDS solution (5%). The absorbance was measured at the wavelength of 600 nm using the spectrophotometer.

After the purification, recombinant HOD was immobilized with chitosan beads using a glutaraldehyde cross-linking technique. Diameter of the beads was filtered between 70 and 105 μm. The beads were fed into a microtube and shaken for 1 h with 2% gultaraldehyde solution which was prepared by diluting 8% gultaraldehyde solution with the phosphate buffer solution. After the beads were rinsed 5 times with 1 ml of ion-exchanged water, they were dipped in the enzyme solution of 500 μl (1.4 U/ml) at 4 °C for 18 h.

2.3. Sample preparation from raw fish

The lean fish from raw tuna was stored at 25 °C and 35 °C up to 96 h. The sample of 1.5 g on each storage temperature and storage time was minced and put into the phosphate buffer solution. After the sonication was carried out for 5 min, each solution was enlarged to be 6 ml and filtered. Sample solution added with 1 U laccase was left at room temperature for 5 min. After they were kept on hot water over 95 °C for 5 min, a centrifugal separation was carried out with 15,000 rpm for 5 min. Finally, supernatant solutions were used as sample solutions.

2.4. Fabrication of the microfluidic device

A microfluidic device was fabricated by using the build-up technique commonly used in PWA as described in elsewhere [15]. The detail of the fabrication process was described previously [16]. A schematic of the device at the step structure is presented on the lower side of Fig. 1. The upper Pyrex wafer had an inlet port for the microbeads and solutions, and an outlet port for the waste. The bottom Pyrex wafer had the EC detector composed of a thin Pt/Ti film as a working electrode (WE, 1 mm long) and a counter electrode (CE, 2.5 mm long), and a thin Ag/Cr film as a reference electrode (RE, 0.5 mm long). These electrodes were separated from each other by a distance of 0.25 mm. The width of the electrode was the same as the microchannel width (0.3 mm). All the electrodes were patterned using the photolithography technique. After ME-1050 was laminated on the bottom wafer as a first layer microchannel, it was patterned using a mask aligner (Mikasa, MA-20), and development (developer: 1 wt% Na₂CO₃) was carried out for 5 min followed by rinsing with ultra pure water. The microchannel upstream of the step was fabricated on the upper wafer in the same manner. In this case, photosensitive sheets of ME-1025 and ME-1050 were laminated in sequence to increase the channel depth (75 μm thick). After the upper and bottom wafers were aligned and fixed in position by lamination, the wafers were adhered together at 160 °C for 1 h. Finally, the microchannel depth upstream and downstream of the step was 125 and 50 μm, respectively.

2.5. System set up and electrochemical detection

A schematic of the histamine detection system using FIA is presented in Fig. 1. After the immobilized microbeads were introduced from the inlet port, a fused silica capillary was connected with each equipments and devices. As a result, the volume of the reactor was 850 nl when the microbeads were filled the microchannel upstream of the step, including the inlet port. The phosphate buffer solution was used as a carrier solution, and a microsyringe pump (CMA Co., Ltd., CMA-102) fed the carrier solution from a microsyringe (1 ml, Hamilton Co.) to the microfluidic device through a 6-port
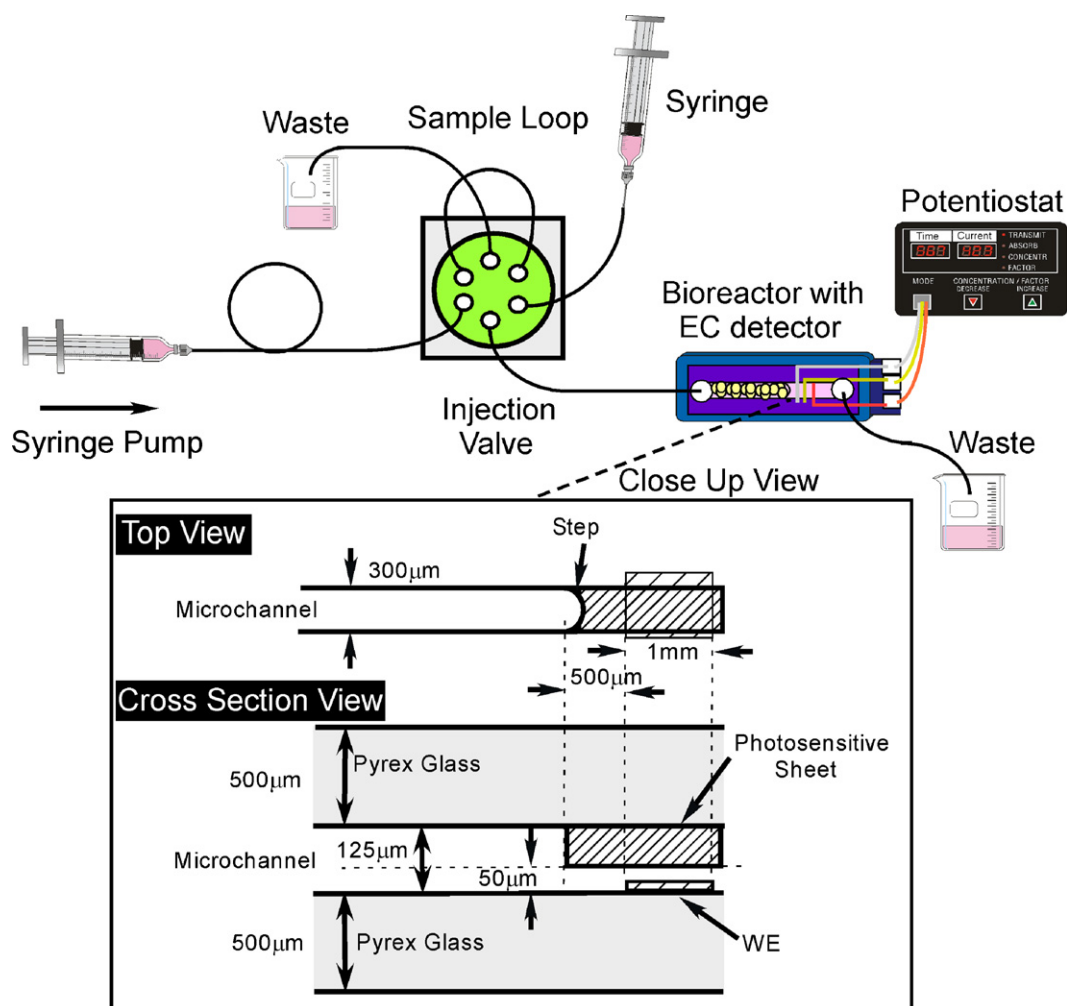
Fig. 1. Schematic figure of a flow through sensing system. Sample injection was carried out electrically by using an injection valve with a dead volume of 35 nl. Sample loop was set to be 320 nl. Close-up and cross-section view of the microfluidic device is indicated on the lower side. The microchannel had 300 μm width, 125 μm depth and 50 μm depth at upstream and downstream of the step structure, respectively.

injection valve (V-485-DC, Upchurch Scientific). Histamine dihydrochloride was dissolved into the phosphate buffer solution to be 100 nM–5 mM. Sample loop made of Teflon tube was cut to be 320 nl. The dead volume of the injection valve was 35 nl. All of the capillary and the Teflon tube had outside and inside diameter of 360 and 100 μm, respectively, and they were obtained from Upchurch Scientific. After the electrodes of the EC detector were connected to a potentiostat (ALS Co., Ltd., ALS 832), amperometric detection was carried out. The WE potential was set to be 0.6 V vs. the RE to oxidize hydrogen peroxide produced from the enzyme reaction. All the measurements were carried out at room temperature.

2.6. HPLC detection

HPLC experiments were carried out by using Pico-Tag HPLC system (Waters Co., MA, USA) consisting of 486 tunable absorbance detector, 510 HPLC pump, 712 WISP autosampler, and Pico-Tag column (150 mm × 3.9 mm i.d.). The chromatographic conditions and the derivatization process have been reported with a precolumn derivatization method using PITC [17]. After derivatization of samples with a derivative reagent (PITC:water:ethanol:triethylamine = 1:1:7:1), histamine content was determined with a linear solvent gradient at the flow

rate of 1.0 ml/min. The column temperature was kept at 38 °C, and absorbance detection was carried out at the wavelength of 254 nm.

3. Results and discussions

3.1. Expression and purification of the recombinant histamine oxidase

The histamine oxidase gene was expressed with C-terminal His-Tag in *E. coli* using the pCold I expression system and the product was purified to homogeneity as a soluble protein. To check the purity of a resultant histamine oxidase, a sodium dodecyl sulfate-polyaclylamide gel electrophoresis (SDS-PAGE) was carried out for a crude and a final enzyme preparation. SDS-PAGE was performed with a 12.5% polyacrylamide gel and the protein was visualized by Coomassie Brilliant Blue Staining. As a result of SDS-PAGE, the enzyme showed a single band at the purified enzyme solution without any subunits as shown in Fig. 2. SDS-PAGE showed a subunit molecular mass of 81 kDa which was same as that of the histamine oxidase from *Arthrobacter crystallopoietes* KAIT-B-007 [14]. This result indicates that recombinant HOD was obtained by using pCold I expression system and was purified only one step using the metal affinity column. On the enzyme assay, one unit of activity was
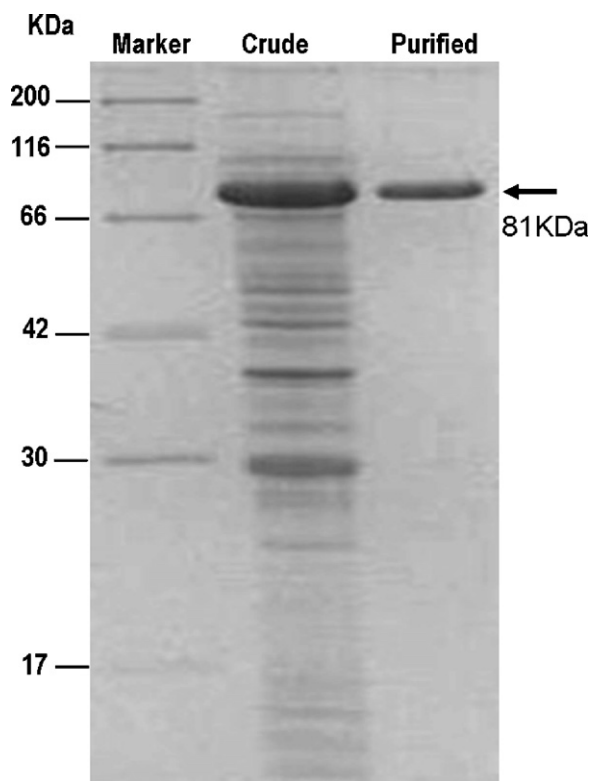
Fig. 2. SDS-PAGE of the recombinant HOD. SDS-PAGE was performed with a 12.5% polyacrylamide gel and the protein was visualized by Coomassie Brilliant Blue Staining. Left, middle and right lane show a standard marker protein, a crude enzyme and a purified enzyme, respectively.

defined as the amount of enzyme which liberated 1 μmol of hydrogen peroxide per min under the specified conditions. The result of the purification was summarized in Table 1. The specific activity of the purified recombinant HOD was 2.8 U/mg-protein. We achieved high purification yield over 90%, which was much higher than that on the purification from strain of KAIT-B-007.

3.2. Characteristics of the device for histamine detection

An oxidation current peak which was generated on oxidizing hydrogen peroxide produced from the enzyme reaction was observed in relation to the injection. A typical response on 0.1 mM histamine at the flow rate of 5 μl/min was presented in Fig. 3. Height of the current peak and peak area were determined as I_p and Q, respectively. Electric charge Q shows the amount of hydrogen peroxide oxidized on the electrode, and was calculated as an integration of current at the current peak using a software attached to the potentiostat. With the efficiency of enzyme reaction of 100%, electric charge on the condition of 0.1 mM histamine with 320 nl injection was calculated as 3.09×10^{-6} C. However, electric charge calculated using data from Fig. 3 was 7.95×10^{-8} C, which was much smaller than the simulated data. Unoptimized condition of enzyme reaction on our system contributed to the low efficiency, since HOD from KAIT-B-007 had the optimum pH of 9 and the optimum temperature of 45 °C [14]. The relative standard deviation (R.S.D.) of Q for 0.1 mM histamine was 1.0% ($n = 4$), this value is acceptable for
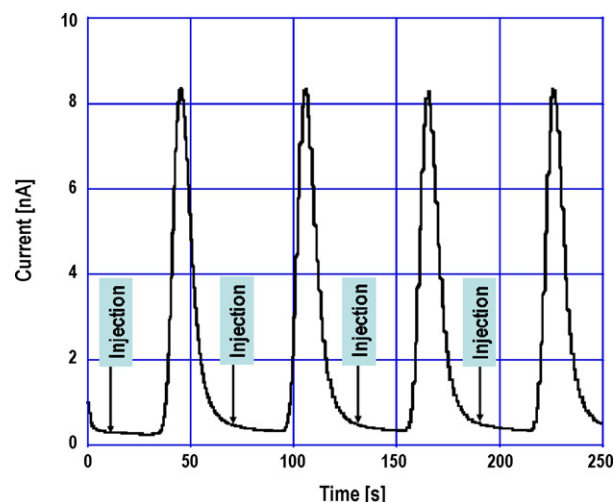

Fig. 3. Simultaneous flow-injection analysis of 0.1 mM histamine. The injection volume and the flow rate were 320 nl and 5 μl/min, respectively.

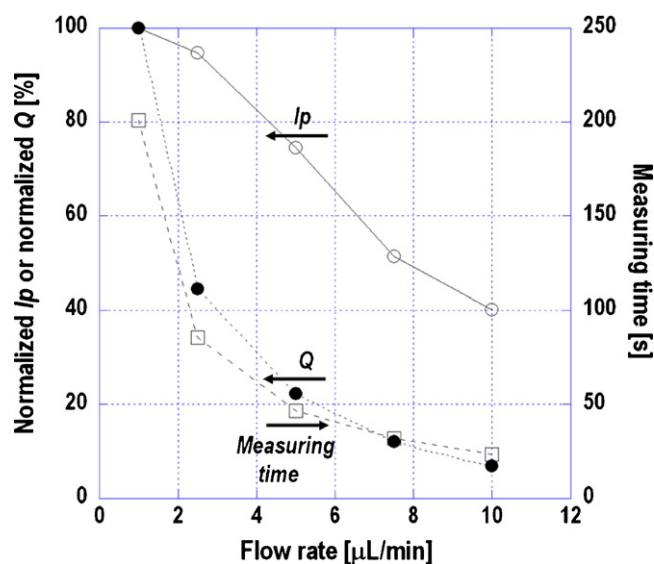**Fig. 4.** Dependency of I_p, Q and measuring time against the flow rate which was set from 1 to 10 μl/min. Histamine concentration was 0.1 mM. I_p and Q were normalized at 1 μl/min. Opened circles, closed circles and opened squares show I_p, Q and measuring time, respectively.

food analysis. The flow rate against I_p, Q, and measuring time were studied at the histamine concentration of 0.1 mM. I_p and Q were normalized at the flow rate of 1 μl/min. Measuring time was calculated as "Measuring time = Peak end time − Injection time". As shown in Fig. 4, I_p and Q decreased with increasing the flow rate. The amount of the product from the enzyme reaction increased with the reaction time which was equal to the time spent in the reactor. In fact, the lower flow rate increased the residence–time in the reactor. These results indicate that lower flow rate might make sensitivity higher, however, long time determination is required. Judging from the measuring time (within 60 s) and the magnitude of the responses, we made a calibration curve both on I_p and Q at the

Table 1
Purification of histamine oxidase using DNA recombinant technique

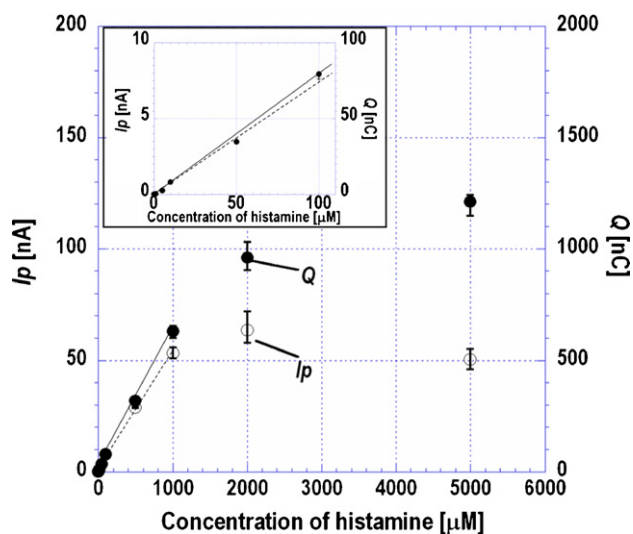| Activity on crude enzyme solution (units)	Total activity (units)	Total protein (mg)	Specific activity (units/mg)	Yield (%)
49.25	44.86	16	2.8	91.1

Fig. 5. Calibration curve using I_p and Q for histamine dissolved in the phosphate buffer solution at the flow rate of 5 µl/min. Opened and closed circles show I_p and Q, respectively. The inset showed calibration curve from 0 to 100 µM. The WE potential was set to be 0.6 V vs. RE.

flow rate of 5 µl/min since it took only 35 s from sample injection to peak top and 47 s from sample injection to peak end at this flow rate.

I_p and Q were measured with the histamine concentration from 100 nM to 5 mM by four times measurements at each concentration. The responses of I_p and Q are shown in Fig. 5. The relationship between I_p and histamine concentration was linear in the range from 1 µM to 1 mM with correlation coefficient of 0.9986. The detection limit of 3.4 µM (S/N = 3) indicated that the system could detect 1.09 pmol of histamine. Therefore, the relationship between Q and histamine concentration had triple-digit linearity in the range from 1 µM to 1 mM with correlation coefficient of 0.9997. I_p and Q deviated down ward from the calibration curve at high histamine concentration, since there was not enough dissolved oxygen. We examined the lifetime of the enzyme reactor at room temperature by monitoring responses of the device for 0.1 mM histamine. Though the flow rate was 0.5 µl/min on intervals of the monitoring to avoid drying the chitosan beads, it was set to be 5 µl/min on the measurements. The reactor had the activity level around 90% to the initial state within 27 h, however the activity level decreased gradually to be lower than 40% after the storage time of 98 h. Reusability might be the critical factor for a next generation device. By using our device, the microbeads could be removed for recycling by adding the negative pressure from the inlet port. This characteristic help to supply flesh immobilized microbeads.

3.3. Analysis of histamine in fish samples

Our sensing system practically detects histamine in food sample. The sample solution from raw tuna with storage time for 0 h was tested for recovery experiments. Standard solution of histamine was added to the solution. The results were listed in Table 2. In these cases, a recovery from 100 to 102% was observed. To compare the performance of our sensing system with traditional method, we

Table 2
Recovery experiments by adding standard solutions of histamine

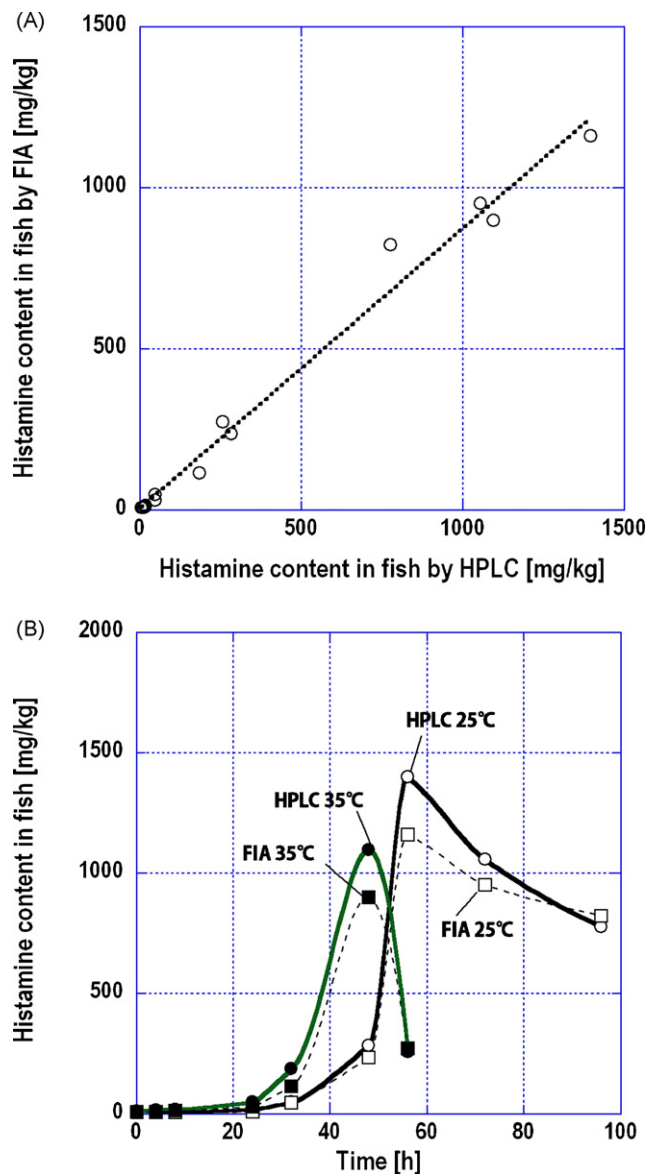| Added (µM)	Found (µM)	Recovery (%)
0	13.1 ± 3.5	
50	64.6 ± 4.8	102
100	112.9 ± 4.2	100

Fig. 6. (A) The comparison between the FIA system and HPLC method on histamine detection in raw tuna. (B) Histamine content in tuna samples stored at 25 °C and 35 °C up to 96 h. Opened and closed circles show histamine content determined by using HPLC method at the storage temperature of 25 °C and 35 °C, respectively. Opened and closed squares show histamine content determined by using the FIA system at the storage temperature of 25 °C and 35 °C, respectively.

measured histamine content in fish samples by using the FIA system and HPLC method. At the higher concentration of histamine, sample solution was diluted ten times thinner by adding the phosphate buffer solution. Fig. 6(A) shows the correlation on histamine detection in raw tuna of 1 kg using the FIA system and HPLC method. There was good agreement between them with correlation coefficient of 0.993 (n = 16), and the regression equation was Y = 0.87 X + 1.84. Here, X and Y show the histamine content (mg/kg in fish) determined using HPLC method and using the FIA system, respectively. The slope of the regression equation was slightly deviated down ward from 1.0, since the condition of enzyme reaction was not optimized. Fig. 6(B) shows the relationship between the storage time and histamine content on each detection method. The histamine content at 25 °C increased with the storage time after 48 h drastically. It reached a peak on 56 h, but gradually decreased at the end of the experiment. On the other hands, the histamine

content at 35 °C increased sooner than that at 25 °C. These characteristics were observed on both detection methods, and there was good agreement between them. Based on the perspective of a food sanitation and quality management of food product, Hazard Analysis Critical Control Point (HACCP) is worth noting on a global scale. HACCP decides defect action level of histamine as 50 ppm and toxicity level of that as 500 ppm. Our results indicated that histamine content with storage at 25 °C over 56 h and storage at 35 °C over 48 h transgressed the toxicity level. As a result, our sensing system had a potential to determine histamine content in situ.

4. Conclusion

Histamine was determined by using the nano-litter volume reactor integrated with EC detector. HOD was immobilized with chitosan microbeads and stored in the microchannel as the enzyme reactor. For continuous measuring, our device was combined with flow injection system which had the nano-litter volume injector. To increase productivity of enzyme, we succeeded to purify recombinant HOD from *Arthrocbacter crystallopoietes* KAIT-B-007 by using pCold I expression system. Fast analysis could be carried out with high sensitivity and linearity from 1 μM to 1 mM of histamine dissolved in phosphate buffer solution. In addition, histamine detection was carried out on raw tuna. As a result, histamine content determined by using the FIA system showed good agreement with that using HPLC method. These results demonstrated that the proposed micro biosensing system is useful with high sensitivity of small sample and enzyme volume, and the system has the potential to provide a miniaturized sensing system with both simple and disposable for a food evaluation on filed site.

References

[1] S.L. Talor, S.S. Sumner, Seafood Quality Determination, Elsevier Science Publishers B.V., Amsterdam, 1986, p. 235.
[2] L. Lehane, J. Olley, Int. J. Food Microbiol. 58 (2000) 1.
[3] N. Garacía-Villar, J. Saurina, S. Hernández-Cassou, Anal. Chim. Acta 575 (2006) 97.
[4] V. Frattini, C. Lionetti, J. Chromatogr. A 809 (1998) 241.
[5] J. Lange, K. Thomas, C. Wittmann, J. Chromatogr. B 779 (2002) 229.
[6] D. Kutlán, P. Presits, I. Mohnár–Perl, J. Chromatogr. A 949 (2002) 235.
[7] J.M. Hungerford, A.A. Arefyev, Anal. Chim. Acta 261 (1992) 351.
[8] M.–A. Carsol, M. Mascini, Talanta 50 (1999) 141.
[9] O. Niwa, R. Kurita, K. Hayashi, K. Torimitsu, K. Maeyama, K. Tanizawa, Sens. Actuators, B 67 (2000) 43.
[10] Y. Sekiguchi, A. Nishikawa, H. Makita, A. Yamamura, K. Matsumoto, N. Kiba, Anal. Sci. 17 (2001) 1161.
[11] M.G. Loughran, J.M. Hall, A.P.F. Turner, V.L. Davidson, Biosens. Bioelect. 10 (1995) 569.
[12] K. Zeng, H. Tachikawa, Z. Zhu, V.L. Davidson, Anal. Chem. 72 (2000) 2211.
[13] K. Takagi, S. Shikata, Anal. Chim. Acta 505 (2004) 189.
[14] Y. Sekiguchi, H. Makita, A. Yamamura, K. Matsumoto, J. Biosci. Bioeng. 97 (2004) 104.
[15] T. Ito, T. Kawaguchi, H. Miyoshi, K. Maruyama, S. Kaneko, S. Ohya, Y. Iwasaki, O. Niwa, K. Suzuki, J. Micromech. Microeng. 17 (2007) 432.
[16] T. Ito, M. Kunimatsu, S. Kaneko, S. Ohya, K. Suzuki, Anal. Chem. 79 (2007) 1725.
[17] M. Calull, R.M. Marce, J. Fabregas, F. Borrull, Chromatgraphia 31 (1991) 133.

A highly sensitive resonance scattering spectral assay for IgG using Fehling reagent–glucose–immunonanogold reaction

Zhiliang Jiang [a,b,*], Sumei Wang [b], Aihui Liang [b], Fuxin Zhong [b]

[a] *Guangxi Key Laboratory of Environmental Engineering, Protection and Assessment, Guangxi Normal University, Guilin 541004, China*
[b] *Key Laboratory of New Processing Technology for Nonferrous Metals and Materials of Education Ministry, Guilin University of Technology, Guilin 541004, China*

ARTICLE INFO

ABSTRACT

Nanogold exhibits strong catalytic effect on the slow reaction between glucose and Fehling reagent at 70 °C. The production of Cu_2O particles have two stronger resonance scattering (RS) peaks at 390 nm and 505 nm. The catalytic effect of nanogold-labeled goat anti-human IgG (AuIgG) on the reaction was investigated with the RS technique. Coupled the immunoreaction and the immunonanogold catalytic reaction and centrifugal technique, a highly sensitive and selective RS method was developed for the detection of immunoglobulin G (IgG) as a model. With the concentration of IgG increased, the RS intensity at 505 nm decreased. The decreased intensity at 505 nm $\Delta I_{505\ nm}$ was proportional to IgG concentration in the range of 0.13–53.3 ng mL^{-1}, with a detection limit of 0.04 ng mL^{-1} IgG. This new immunonanogold–catalytic Cu_2O–particle RS bioassay was applied to the determination of IgG in serum sample, with high sensitivity, good selectivity, and low cost.

© 2008 Elsevier B.V. All rights reserved.

1. Introduction

Nanogold has high electron density, good monodispersion, good biocompatibility, high catalytic activity and novel surface plasmon resonance (SPR) phenomenon, and was applied to immunology, histology, pathology, cell biology and bioassay. Since 1971 year, Faulk and Taylor firstly reported that antibody coated by nanogold was used to immunocyte chemical study using electron microscope, the immunonanogold technique as fourth label developed rapidly [1]. Combining nanogold-labeled and immunoreaction and DNA hybridization, some selective and sensitive bioassays were proposed with optical and electrochemical detection [2]. In 1983 year, Danscher and Norgaard [3] developed a gold-silver staining (GSS) technique using silver-developer to enhance the visibility of nanogold at the optical microscopic level, and applied to immunone histochemistry and bioassay. Afterward, Holgate et al. [4] proposed an immunogold-silver staining (IGSS) technique, using immunonanogold as catalyst that catalyzed the reduction of Ag(I) to Ag on the surface of nanogold.

Recently, Xu et al. reported an immunonanogold-silver enhancement light scattering technique to assay nucleic acid, with a detection limit of 10 fmol L^{-1} [5]. However, the immunonanogold-silver enhancement technique has some shortages. For example, the enhancer is unstable and the Cl^{-} in serum sample interfered with the determination [3–5]. To overcome the shortages and to enhance the detection signal, immunonanogold-gold enhancement technique was proposed [6–8]. Brown and Natan [6] and Brown et al. [7] examined the nanocatalytic mechanism of nanogold–NH$_2$OH–Au^{3+}, and prepared monodispersion nanogold in big size. Ma and Sui [8] used HAuCl$_4$–NH$_2$OH·HCl enhancement solution to enlarge the immunonanogold fixed on pyroxylin film to detect human-IgG by naked eye, with a detection limit of 10.0 pg mL^{-1}. Willner et al. [9] used immunonanogold-gold enhancement quartz crystal microbalance sensor to determine 3×10^{-16} mol L^{-1} DNA. A glucose optical biosensor was fabricated using immunonanogold-gold enhancement [10]. Nanogold exhibited catalytic effect on NADH–HAuCl$_4$ particle reaction [11], and was utilized to assay NADP with an optical sensor. Because the immunonanogold-catalytic gold-enhancement reaction carried out at room temperature, the reaction was stopped difficultly, the operation was not convenience, and precious reagent of HAuCl$_4$ was used. Thus, it was necessary to explore a new immunonanogold–catalytic reaction technique with high sensitivity, good reproducibility, simplicity and low-cost.

* Corresponding author at: School of Environment and Resource, Guangxi Normal University, Guilin 541004, Guangxi Province, China. Tel.: +86 7735846141; fax: +86 7735846201.
E-mail address: zljiang@mailbox.gxnu.edu.cn (Z. Jiang).

Resonance scattering (RS) spectral technique was sensitive and simple, and was applied to analysis of trace inorganic ions, nucleic acids and proteins [12–14]. Some RS assays for protein were based on the simple interaction between protein and small molecule such as dye, their selectivity was not high. Our results [15–17] showed that coupling RS effect of nanogold and immunoreaction was used to develop RS immunoassay for proteins, with high sensitivity, good selectivity, and simplicity. In addition, the combining RS technique with inorganic catalytic reaction and enzyme catalytic reaction was applied to analysis of trace inorganic ion and organic compound, with satisfactory results [15–18]. Up to date, there is no report about the immunonanogold–catalytic Cu_2O–particle RS assay for IgG. In the present work, a simple and highly sensitive immunonanogold–catalytic Cu_2O–particle RS bioassay for IgG was proposed, coupling the nanogold labeled immunoreaction, immunonanogold catalytic reaction and RS effect of Cu_2O particles.

2. Experimental

2.1. Apparatus and reagents

A model LS-55 spectrofluorometer (PerkinElmer Company, MA, USA), model UV1900PC UV–vis spectrophotometer (Yayan Electron Company, Shanghai, China), model JSM-6380LV scanning electron microscope (Electronic Stock Limited Company, Japan), model H-600 transmission electron microscope (TEM) (Electronic Stock Co., Ltd., Japan), model SK8200LH ultrasonic reactor with 450 W and 59 kHz (Kedao Company, Shanghai, China), model Sigma 3K3D high-speed refrigeration centrifuge (Sigma Company, Harz, Germany), and model Nano-ZS90 nano-granularity and Zeta potential meter (Malvern Company, Worcestershire, England) were used.

A 1.0% $HAuCl_4$ (National Pharmaceutical Group Chemical Reagents Company, Shanghai, China), 1.0% trisodium citrate, $3.25\,mg\,mL^{-1}$ goat anti-human IgG with a titer of 1:128 (Jiemen Biotechnological Company Limited, Shanghai, China), $30.0\,mg\,mL^{-1}$ IgG (Jiemen Biotechnological Company Limited, Shanghai, China), $0.1\,mol\,L^{-1}$ K_2CO_3, 10.0% KCl, Fehling solution including $0.28\,mol\,L^{-1}$ $CuSO_4$ and $1.23\,mol\,L^{-1}$ potassium sodium tartrate (KNaT) containing $6.25\,mol\,L^{-1}$ NaOH, $10\,mg\,mL^{-1}$ glucose, pH 6.0–7.8 NaH_2PO_4–Na_2HPO_4, $2.0 \times 10^{-3}\,mol\,L^{-1}$ $AgNO_3$, $1.0 \times 10^{-5}\,mol\,L^{-1}$ K_2PtCl_6, fresh 0.2% KBH_4 solutions were prepared. All reagents were of analytical grade, and water was doubly distilled.

2.2. Preparation of nanogold

Nanogold in size of 15 nm was prepared by trisodium citrate procedure [19]. The preparation of 23.2 nm nanosilver was as follows. A 0.30 mL 1.0% trisodium citrate, 1.1 mL $2.0 \times 10^{-3}\,mol\,L^{-1}$ $AgNO_3$ were added to a teflon jar. The solutions were mixed well and irradiated 4 min at 0.9 MPa by model XT-9900 microwave instrument. Then the mixture was diluted 10 mL to obtain a $2.2 \times 10^{-4}\,mol\,L^{-1}$ nanosilver. A 7 nm nanoplatinum was prepared as follows [20], into a 50 mL beaker containing 5.0 mL $1.0 \times 10^{-5}\,mol\,L^{-1}$ K_2PtCl_6 and 10 mL water, a 0.6 mL 0.2% KBH_4 and were added under the magnetic stirring. Then the mixture was diluted to 20 mL to obtain a $2.5 \times 10^{-6}\,mol\,L^{-1}$ Pt. The mean size of the three nanoparticles was measured by TEM.

2.3. Preparation of the immunonanogold probe

The pH and goat anti-human IgG amount were optimized. The preparation was as follows. Into 100 mL $58.0\,\mu g\,mL^{-1}$ nanogold with pH 6.5 under the magnetic stirring, a 4.0 mL $0.13\,mg\,mL^{-1}$ goat anti-human IgG was added slowly. Ten minutes later, a 1.63 mL 3.0%

PEG 20000 as stabilizer was added, continue stirring 30 min. The concentration of nanogold-labeled goat anti-human IgG (AuIgG), calculated as nanogold, was $54.1\,\mu g\,mL^{-1}$.
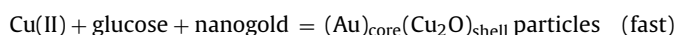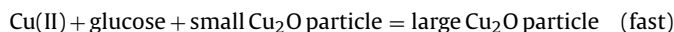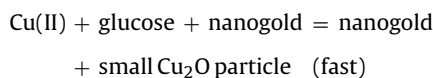
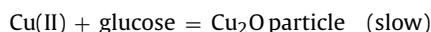### 2.4. Procedure

Into a graduated test tube, 0.30 mL pH 7.0 NaH_2PO_4–Na_2HPO_4 buffer solutions, 0.60 mL $54.1\,\mu g\,mL^{-1}$ AuIgG, a certain amount of IgG, and 0.80 mL of $300\,mg\,mL^{-1}$ PEG-6000 solutions were added, and then diluted to 3.0 mL with water, mixed well and incubated in an ultrasonic reactor for 20 min. The solution was centrifuged at 16,000 rpm for 20 min to remove the immunonanogold complex, and the supernatant was taken out for use.

A 30 μL $0.28\,mol\,L^{-1}$ $CuSO_4$ solution, 0.15 mL $1.23\,mol\,L^{-1}$ KNaT, 80 μL of the supernatant, and 0.20 mL $10\,mg\,mL^{-1}$ glucose was added successively to a 5 mL graduated test tube, diluted to 3.0 mL, mixed well and placed them in a bath at $70\,°C$ for 7 min. Stop the reaction by tap-water cooling. A part of the solutions was transferred into a quartz cell. The settings were as follows, volt = 650 V, excited slit = emission slit = 7.0 nm, emission filter = 1%T attenuator. The RS spectrum of the system was recorded by means of synchronous scanning of the excitation wavelength and emission wavelength (excitation wavelength = emission wavelength). Then, the RS intensity at 505 nm ($I_{505\,nm}$) was recorded, and the $(I_{505\,nm})_b$ of blank solutions without IgG were measured. The $\Delta I_{505\,nm} = (I_{505\,nm})_b - I_{505\,nm}$ was calculated.

3. Results and discussion

In the medium of potassium sodium tartrate–NaOH at $70\,°C$, Cu(II) was slowly reduced to Cu_2O particles by weak reducer glucose. Addition of nanogold, large amounts of Cu_2O particles in yellow were observed. Similar to the catalytic effect of nanogold on the reduction of Ag(I) to silver particles by hydroquinone, the nanogold exhibited catalytic effect on the reduction of Cu(II) to Cu_2O particles by glucose. First, nanogold catalyzed the reduction of Cu(II) to form small Cu_2O nanoparticles, and the nanogold did not enwrapped by Cu_2O molecules in the process. Second, the small Cu_2O nanoparticles also catalyzed the reduction of Cu(II) to form large Cu_2O nanoparticles, this is called as autocatalysis. The main reactions were as follows:

$$Cu(II) + glucose = Cu_2O\,particle \quad (slow)$$

$$Cu(II) + glucose + nanogold = nanogold + small\,Cu_2O\,particle \quad (fast)$$

$$Cu(II) + glucose + small\,Cu_2O\,particle = large\,Cu_2O\,particle \quad (fast)$$

$$Cu(II) + glucose + nanogold = (Au)_{core}(Cu_2O)_{shell}\,particles \quad (fast)$$

After goat anti-human IgG coated by nanogold, the immunoactivity did not change. The nanogold labeled immunoreaction can be also used to RS assay of IgG [21], with a detection limit of $0.78\,ng\,mL^{-1}$. The nanogold labeled immunocomplex can be removed by centrifuging, the excess AuIgG in the supernatant exhibited catalytic effect on the slow Cu_2O particle reaction of Fehling reagent–glucose. More Cu_2O particles formed in the catalytic system. Thus, the RS intensity at 505 nm enhanced greatly. Similar to the nanogold catalysis, AuIgG, like a common catalyst, catalyze the Cu(II)/Cu(I) reduction in solutions to produce Cu_2O particles as in Fig. 1. On the other hand, AuIgG, as seed catalyst, accelerate the Cu(II)/Cu(I) reduction on the surface of
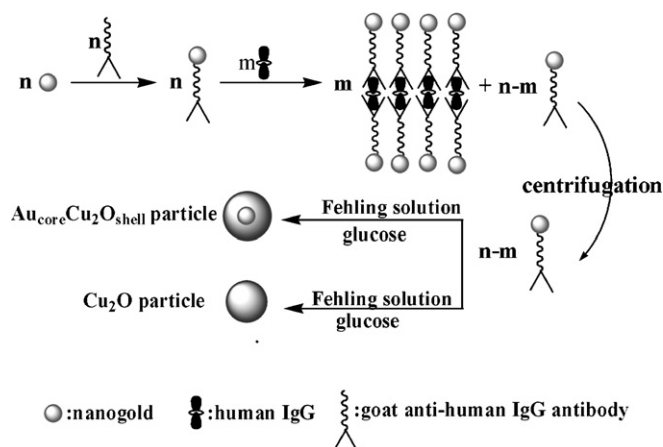
Fig. 1. Principle of immunonanogold–catalytic Cu_2O amplification.

Fig. 3. Absorption spectra of IgG–AuIgG–glucose–Cu(II) catalytic particle reaction. (a) 2.76×10^{-3} mol L^{-1} CuSO$_4$–6.13 $\times 10^{-2}$ mol L^{-1} KNaT–3.7 $\times 10^{-2}$ mol L^{-1} glucose–0.29 μg mL^{-1} AuIgG–0.0 ng mL^{-1} IgG; (b) a–6.67 ng mL^{-1} IgG; (c) a–26.67 ng mL^{-1} IgG; (d) a–53.34 ng mL^{-1} IgG; (e) 2.76×10^{-3} mol L^{-1} CuSO$_4$–6.13 $\times 10^{-2}$ mol L^{-1} KNaT–3.7 $\times 10^{-2}$ mol L^{-1} glucose.

nanogold to form $(Au)_{core}(Cu_2O)_{shell}$ particles. With addition of IgG, the nanogold labeled immunocomplex increased, the excess AuIgG in the supernatant decreased, and the RS intensity at 505 nm decreased. The decreased RS intensity at 505 nm was linear to the IgG concentration. On those grounds, a new RS immunoassay for IgG was proposed.

3.1. Electron microscope and laser scattering

Nanogold was characterized by TEM, was in spherical shape with average diameter of 15 nm. When the nanogold particles were labeled with the antiserum, their original diameter did not change. According to the procedure, the immunonanogold catalytic reaction solutions were spread uniformly into a copper pole that coated electronic glue. After natural dryness, the scanning electron microscope (SEM) was showed in Fig. 2. The Cu_2O particles have a spherical shape in size of 1–7.0 μm. Their laser scattering diameter distribution showed that the average size was about 2.2 μm.

3.2. Absorption spectra

In the presence of 6.13×10^{-2} mol L^{-1} KNaT–0.37 $\times 10^{-3}$ mol L^{-1} glucose, Cu(II) exhibited a weak absorption peak at about 650 nm (Fig. 3e). According to the procedure, the blank system without IgG appeared a stronger absorption peak at about 650 nm (Fig. 3a), and
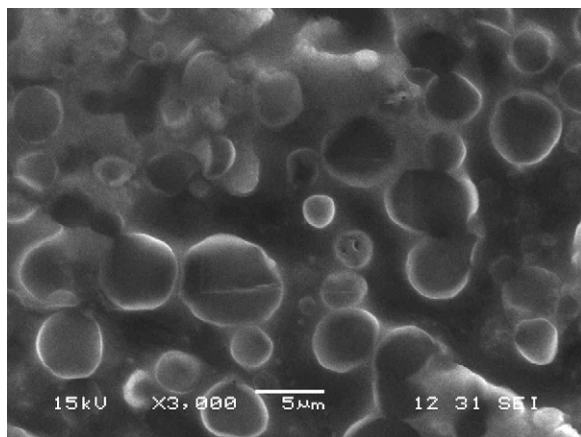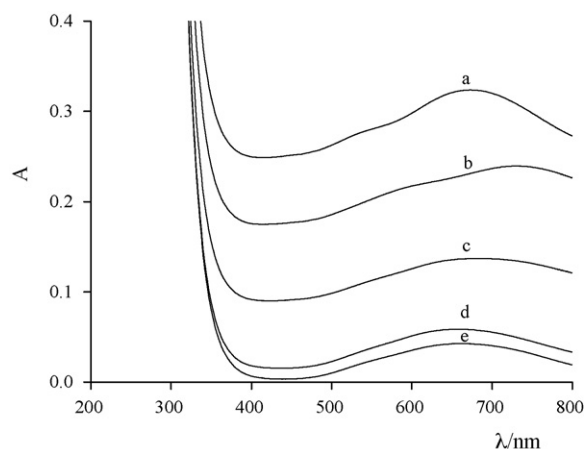
the system was in yellow color owing to formation of particles. The particle may be Cu_2O and/or Cu [22,23]. We known that glucose was a weak reducer, and was difficult to reduction of Cu(II) to Cu(0). In organic chemistry, the product of Fehling reagent–aldehyde was Cu_2O particle. Thus, the particle was Cu_2O in the Cu(II)–glucose catalytic system. Upon addition of IgG, the absorption value decreased because the nanocatalyst of AuIgG in the supernatant decreased, and the number of formed Cu_2O particles decreased (Fig. 3b–d).

AuIgG–glucose–Cu(II) system without heating (Fig. 4a–d), and AuIgG (Fig. 4e) all have a surface plasmon resonance absorption peak at 528 nm. When those systems were heated at 70 °C for 7 min, the systems of Fig. 4f–h all exhibited a wide absorption peak at about 660 nm, the surface plasmon resonance absorption peak for Fig. 4i and j systems exist still. For the systems of Fig. 4h–j, its mole ratio of [AuIgG]/[Cu(II)] was about 1/120, 1/60 and 1/30, that is, Cu(II) concentration was higher than the AuIgG. The results
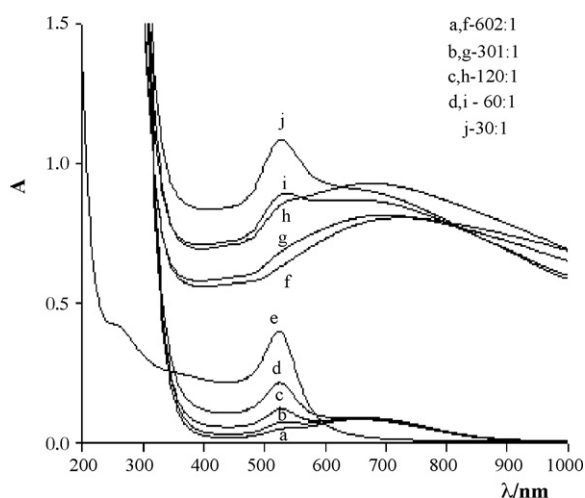

Fig. 2. SEM of IgG–AuIgG–glucose–Cu(II) catalytic particle reaction. 6.13×10^{-2} mol L^{-1} KNaT–2.76 $\times 10^{-3}$ mol L^{-1} CuSO$_4$–3.7 $\times 10^{-2}$ mol L^{-1} glucose–0.29 μg mL^{-1} AuIgG–26.7 ng mL^{-1} IgG.

Fig. 4. Absorption spectra of AuIgG–glucose–Cu(II) system. (a) 2.76×10^{-3} mol L^{-1} CuSO$_4$–6.13 $\times 10^{-2}$ mol L^{-1} KNaT–0.90 μg mL^{-1} AuIgG–3.7 $\times 10^{-2}$ mol L^{-1} glucose, un-heating; (b) a–1.80 μg mL^{-1} AuIgG, un-heating; (c) a–4.51 μg mL^{-1} AuIgG, un-heating; (d) a–9.02 μg mL^{-1} AuIgG, un-heating; (e) 18.03 μg mL^{-1} AuIgG; (f) 2.76×10^{-3} mol L^{-1} CuSO$_4$–6.13 $\times 10^{-2}$ mol L^{-1} KNaT–0.90 μg mL^{-1} AuIgG–3.7 $\times 10^{-2}$ mol L^{-1} glucose, 70 °C for 7 min; (g) a–1.80 μg mL^{-1} AuIgG, 70 °C for 7 min; (h) a–4.51 μg mL^{-1} AuIgG, 70 °C for 7 min; (i) a–9.02 μg mL^{-1} AuIgG, 70 °C for 7 min; (j) a–18.03 μg mL^{-1} AuIgG, 70 °C for 7 min.
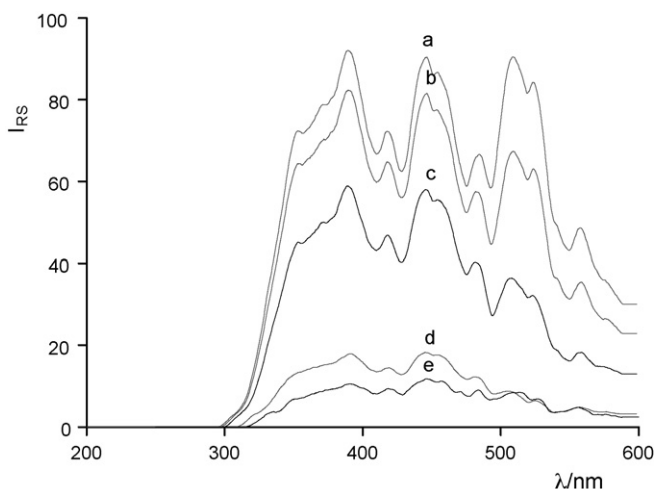
Fig. 5. RS spectra of IgG–AuIgG–glucose–Cu(II) particle reaction. (a) 2.76×10^{-3} mol L^{-1} CuSO$_4$–6.13×10^{-2} mol L^{-1} KNaT–3.7×10^{-2} mol L^{-1} glucose–0.29 μg mL^{-1} AuIgG–0.0 ng mL^{-1} IgG; (b) a–6.67 ng mL^{-1} IgG; (c) a–26.7 ng mL^{-1} IgG; (d) a–53.3 ng mL^{-1} IgG; (e) 2.76×10^{-3} mol L^{-1} CuSO$_4$–6.13×10^{-2} mol L^{-1} KNaT–3.7×10^{-2} mol L^{-1} glucose.

Fig. 6. Effect of AuIgG concentration. 2.76×10^{-3} mol L^{-1} CuSO$_4$–6.13×10^{-2} mol L^{-1} KNaT–3.7×10^{-2} mol L^{-1} glucose–29.8 ng mL^{-1} IgG.

indicated that there are AuIgG particles in the systems of Fig. 4h–j after reaction. That is to say, AuIgG particles also catalyzed the reduction of Cu(II) to form Cu$_2$O particle in body phase solutions.

3.3. Resonance scattering spectra

Light scattering is a commonly optical phenomenon, and is the interaction between the incident photon and the interface electron on the particle such as nanoparticle and supermolecule, etc. It was known that there are some electrons on the nanoparticle surface, in which electrons located in the ground state or excited state. The energy between the ground state and the excitation state was called as excited energy. If changing the incident photon energy by scanning the excited wavelength in the visible region, the incident photon energy is same or close at the excited energy of surface electrons, in which the incident photon resonate with the electron, that cause the scattering signal enhanced greatly. This optical phenomenon was called as resonance scattering (RS) effect or resonance light scattering (RLS) effect. This synchronous scattering spectrum, including RS effect, was called as RS spectrum. In our RS study of metal, nonmetal and semiconductor nanoparticles, color particles in liquid commonly exhibited RS effect and RS peak.

The RS spectra of the IgG–AuIgG–glucose–Cu(II) nanocatalytic reaction system was showed in Fig. 5. There are three stronger synchronous scanning scattering peaks at 390 nm, 450 nm and 505 nm. The synchronous scattering spectra of inorganic nanometal in liquid phase indicated that lamp, free molecular absorption and RS effect of nanoparticles are three factors that cause synchronous scattering peak. The strongest emission of the apparatus located at 450 nm that produce a synchronous scattering peak at 450 nm. The free Cu(II) ion absorption can be neglected in the visible region.
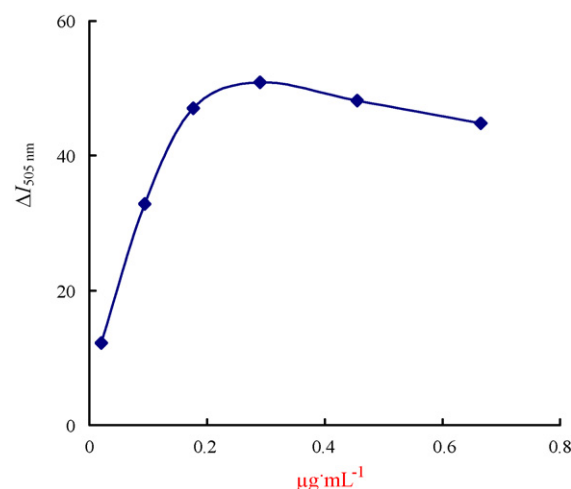
Furthermore, if there is no (Au)$_{core}$(Cu$_2$O)$_{shell}$ particle the peak at 390 nm and 505 nm disappeared. Thus, the peak at 390 nm and 505 nm were caused by their RS effect, and was called as RS peak. A wavelength of 505 nm was selected for use, because the selectivity was better.

3.4. Catalytic effect of nanoparticles on the glucose–Cu(II) reaction

Nanocatalysis has undergone an explosive growth during the past decade [24]. Catalytic effect of metal nanoparticles was related to its properties, size and shape, etc. Table 1 showed that nanogold, nanosilver and nanoplatinum particles all exhibited catalytic effect on the glucose–Cu(II) particle reaction. With the addition of nanoparticles, the RS intensity at 505 nm enhanced. The enhanced RS intensity (ΔI_{RS}) was linear to the nanocatalyst concentration. Compared with 15 nm nanogold and AuIgG, the catalytic effect of AuIgG was weaker, owing to the nanogold surface coated by the antibody tightly. Nanogold had good biocompatibility, and the preparation of 15 nm nanogold was convenience. Thus, the 15 nm nanogold was used in the following study.

3.5. Effect of nanogold labeled immunoreaction conditions

Effect of pH 6.0–7.8 NaH$_2$PO$_4$–Na$_2$HPO$_4$ buffer solution, AuIgG and PEG-6000 concentration, ultrasonic irradiation time on the $\Delta I_{505 nm}$ was examined, respectively. Fig. 6 indicated that the $\Delta I_{505 nm}$ increased when AuIgG concentration was up to 0.17 μg mL^{-1}. When the concentration was in the range of 0.17–0.67 μg mL^{-1} AuIgG, the $\Delta I_{505 nm}$ was bigger and changed weakly. Thus, 0.27 μg mL^{-1} AuIgG, that is, adding 0.60 mL 54.1 μg mL^{-1} AuIgG, was chosen for use. Results showed that 0.30 mL pH 7.0 NaH$_2$PO$_4$–Na$_2$HPO$_4$, 0.80 mL 30% PEG-6000, and

Table 1
Relationship between nanocatalyst concentration and ΔI_{RS}

Catalyst	Size (nm)	Linear range (ng mL^{-1})	Regress equation	Related coefficient	DL (ng mL^{-1})
Au	5	0.19–3.86	$\Delta I_{RS} = 12.0c + 5.27$	0.9940	0.06
Au	10	0.32–6.44	$\Delta I_{RS} = 5.77c + 4.11$	0.9968	0.12
Au	15	0.64–9.66	$\Delta I_{RS} = 6.49c + 13.8$	0.9875	0.27
AuIgG	15	0.64–8.50	$\Delta I_{RS} = 5.55c + 4.90$	0.9999	0.28
Ag	23	3.24–54.0	$\Delta I_{RS} = 1.00c + 9.96$	0.9877	1.74
Pt	7	1.29–13.1	$\Delta I_{RS} = 4.51c + 8.99$	0.9886	0.51
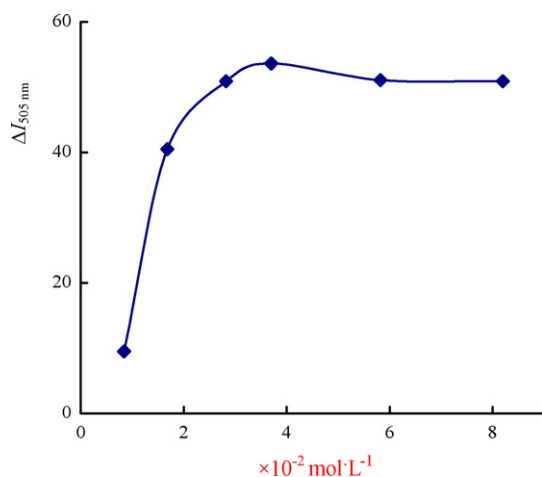
Fig. 7. Effect of glucose concentration. 2.76×10^{-3} mol L^{-1} CuSO$_4$–6.13×10^{-2} mol L^{-1} KNaT–0.29 μg mL^{-1} AuIgG–29.8 ng mL^{-1} IgG.

ultrasonic irradiation for 20 min, gives biggest $\Delta I_{505\,nm}$ value, and was selected for use.

3.6. Selection of the immunonanogold–glucose–Cu(II) reaction conditions

Effect of centrifugal speed and time on the $\Delta I_{505\,nm}$ was examined, respectively. When centrifugal speed was in the range of 8000–16,000 rpm, the $\Delta I_{505\,nm}$ increased. When it was higher than 16,000 rpm, the $\Delta I_{505\,nm}$ decreased. The $\Delta I_{505\,nm}$ increased when centrifugal time was within 30 min. Prolonged the time, the $\Delta I_{505\,nm}$ decreased. Thus, 16,000 rpm for 30 min was chosen. In basic medium, KNaT was a good complex for Cu(II) to avoid formation of Cu(OH)$_2$ precipitation to hold active concentration of copper ions [25]. Effect of KNaT concentration on the $\Delta I_{505\,nm}$ was considered. A 6.13×10^{-2} mol L^{-1} KNaT, giving biggest $\Delta I_{505\,nm}$ value, was chosen for use. Effect of CuSO$_4$ and glucose concentration on $\Delta I_{505\,nm}$ was examined, respectively. Results showed that when CuSO$_4$ concentration was 2.76×10^{-3} mol L^{-1}, the $\Delta I_{505\,nm}$ was biggest, and was chosen for use. Glucose was a weak reducer and a good stable reagent for Cu$_2$O particles, and can be used to control reaction rate to obtain good dispersion Au$_{core}$Cu$_2$O$_{shell}$ particles [26]. As in Fig. 7, when the glucose concentration was 3.7×10^{-2} mol L^{-1}, the $\Delta I_{505\,nm}$ was biggest, and was chosen for use. Effect of reaction temperature in the range of 30–100 °C on the $\Delta I_{505\,nm}$ was considered. Owing to the nanocatalytic reaction of nanogold–glucose–Cu(II) being endothermic reaction [27,28], the reaction do not take place at 30–50 °C, the $\Delta I_{505\,nm}$ was very small. When the temperature was higher than 50 °C, the $\Delta I_{505\,nm}$ increased greatly (Fig. 8). When the temperature was higher than 80 °C, the uncatalytic reaction rate of Cu(II)–glucose increased also, the $\Delta I_{505\,nm}$ decreased quickly. To obtain high sensitivity and low blank value, a reaction temperature of 70 °C was chosen for use. The $\Delta I_{505\,nm}$ value increased linearly with reaction time within 6 min at 70 °C. After 6 min, the $\Delta I_{505\,nm}$ was biggest and stable. A reaction time of 7 min was selected. After stopping the catalytic reaction by tap-water cooling, the influence of the measurement time on $\Delta I_{505\,nm}$ was examined. The $\Delta I_{505\,nm}$ was stable within 30 min, longer than 30 min the $\Delta I_{505\,nm}$ decrease slowly. If the solution was mixed again, the $\Delta I_{505\,nm}$ remains original value. According to this operations, the $\Delta I_{505\,nm}$ remains within 2 h. The reason was that the O atoms in the Cu$_2$O particle can interact with water-soluble glucose molecule by H-bond and molecular interaction forces that protected and suspended the bigger Cu$_2$O particle

in the basic medium. Effect of supernatant volume on the $\Delta I_{505\,nm}$ was considered. When the supernatant volume (V) within 80 μL increased, the $\Delta I_{505\,nm}$ value increased linearly. Its regress equation was $\Delta I_{505\,nm} = 1.03V + 9.88$, with a relative coefficient of 0.9886. An 80 μL supernatant was selected.

3.7. Linear range

According to the procedure, the $\Delta I_{505\,nm}$ for different concentration of IgG was recorded. The $\Delta I_{505\,nm}$ was proportional to IgG concentrations c_{IgG} in the range of 0.13–53.3 ng mL^{-1}. The regression equation was $\Delta I_{505\,nm} = 1.43c_{IgG} + 8.36$, with a correlation coefficient of 0.9904. A detection limit of 0.04 ng mL^{-1} IgG was calculated from the mean plus 3 standard deviation of a blank value ($n = 10$). Compared with IgG assays reported [21,29–34], including chemiluminescent, anodic stripping voltammetry, resonance scattering, surface-enhanced Roman scattering and ICP-MS assay, this RS assay for IgG had very high sensitivity.

3.8. Influence of foreign ions

According to the procedure, the influence of foreign ions on the determination of 26.7 ng mL^{-1} IgG was examined, with a relative error of ±5%. Results showed that 40,000 ng mL^{-1} urea, 10,700 ng mL^{-1} EDTA, 5300 ng mL^{-1} L-serine, L-leucine, L-arginine, lysine, L-histidine, L-tryptophan, L-phenylalanine, and glutamic acid, 2670 ng mL^{-1} L-cystine, 1300 ng mL^{-1} L-aspartate, and L-tyrosine, 3000 ng mL^{-1} L-proline, and DL-threonine, 2700 ng mL^{-1} Zn^{2+}, Ca^{2+}, and Fe^{3+}, 1000 ng mL^{-1} HSA, human chorionic gonadotrophin, and IgA, 800 ng mL^{-1} BSA, and prealbumin, 500 ng mL^{-1} IgM, and ceruloplosmin do not interfere with the assay. This indicated that this assay has good selectivity.

3.9. Analysis of samples

Twenty samples of healthy people sera were obtained from the Attached Hospital of Guilin Medical Institute. After dilution of 150-fold, a 30.0 μL of the diluted sample was assayed according to the procedure. The mean value by this assay was 11.98 mg mL^{-1} IgG. The results obtained by this RS assays were consistent with the
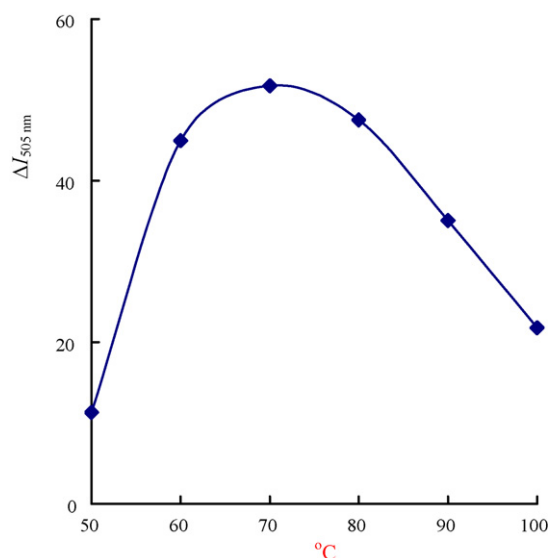

Fig. 8. Effect of reaction temperature. 2.76×10^{-3} mol L^{-1} CuSO$_4$–6.13×10^{-2} mol L^{-1} KNaT–3.7×10^{-2} mol L^{-1} glucose–0.29 μg mL^{-1} AuIgG–29.8 ng mL^{-1} IgG.

immunoturbidimetry. The linear regression analysis of both assay results revealed a correlation coefficient, slope, and intercept of 0.9961, 1.002, and 0.15 mg mL^{-1}, respectively.

4. Conclusion

Catalytic effect of nanogold labeled goat anti-human IgG probe on Fehling reagent–glucose particle reaction was studied by resonance scattering spectral technique. A novel and highly sensitive immunonanogold–catalytic Cu_2O–particle RS bioassay was developed for IgG, combing the immunoreaction, nanocatalytic reaction, centrifugal technique and RS detection technique. Comparing with the silver, gold and copper particle reaction techniques reported, the Cu_2O particle reaction technique has high sensitivity and selectivity, simplicity and low cost.

Acknowledgments

References

[1] S.Q. Xu, H.C. Liu, Immunological Test, Peoples Health Press, Beijing, 2006, p. 10.
[2] L.A. Lyon, M.D. Musick, M.J. Natan, Anal. Chem. 70 (1998) 5177.
[3] G. Danscher, S.O. Norgaard, J. Histochem. Cytochem. 31 (1983) 394.
[4] C.S. Holgate, P. Jackson, P.N. Cowen, C.C. Bird, J. Histochem. Cytochem. 31 (1983) 938.
[5] X.Y. Xu, D.G. Georganopoulou, H.D. Hill, C.A. Mirkin, Anal. Chem. 79 (2007) 6650.
[6] K.R. Brown, M.J. Natan, Langmuir 14 (1998) 726.
[7] K.J. Brown, D.G. Walter, M.J. Natan, Chem. Mater. 12 (2000) 306.
[8] Z. Ma, S.F. Sui, Angew. Chem. Int. Ed. 41 (2002) 2176.
[9] I. Willner, F. Patolsky, Y. Weizmann, B. Willner, Talanta 56 (2002) 847.
[10] M. Zayats, R. Baron, I. Popov, I. Willner, Nano. Lett. 5 (2005) 21.
[11] X. Yi, V. Pavlov, S. Levine, T. Niazov, G. Markovitch, I. Willner, Angew. Chem. Int. Ed. 43 (2004) 4519.
[12] S.P. Liu, H.Q. Luo, N.B. Li, Z.F. Liu, W.X. Zheng, Anal. Chem. 73 (2001) 3907.
[13] Y.F. Long, C.Z. Huang, Y.F. Li, J. Phys. Chem. B 111 (2007) 4535.
[14] Z.Q. Han, L. Qi, G.Y. Shen, W. Liu, Y. Chen, Anal. Chem. 79 (2007) 5862.
[15] Z.L. Jiang, S.J. Sun, A.H. Liang, W.X. Huang, A.M. Qin, Clin. Chem. 52 (2006) 1389.
[16] Z.L. Jiang, Q.Y. Liu, S.P. Liu, Talanta 58 (2002) 635.
[17] Z.L. Jiang, S.J. Sun, A.H. Liang, C.Y. Kang, X.C. He, Anal. Chim. Acta 571 (2006) 200.
[18] Z.L. Jiang, G.X. Huang, Clin. Chim. Acta 376 (2007) 136.
[19] L.P. Zhu, X.Q. Chen, Common Immunological Methods, Peoples Army Press, Beijing, 1999, p. 426.
[20] S.N. Ding, Y.J. Lu, B.K. Jin, J. Anhui Univ. 26 (2002) 74.
[21] Z.L. Jiang, Y. Li, S.J. Sun, B. Chen, Chin. J. Chem. 25 (2007) 1282.
[22] P. Joanna, M.E. Cason, B.J. Thompson, J. Phys. Chem. B 105 (2001) 2297.
[23] N. Arul Dhas, C. Paul Raj, A. Gedanken, Chem. Mater. 10 (1998) 1446.
[24] R. Narayanan, M.A. El-Sayed, J. Phys. Chem. B 109 (2005) 12663.
[25] X. Zhang, Y. Xie, F. Xu, X.H. Liu, D. Xu, Chem. Commun. 6 (2003) 1390.
[26] D.B. Wang, D.B. Yu, M.S. Mo, X.M. Liu, Y.T. Qian, J. Colloid Interface Sci. 261 (2003) 565.
[27] Z.H. Wang, X.Y. Chen, J.W. Liu, M.S. Mo, L. Yang, Y.T. Qian, Solid State Commun. 130 (2004) 585.
[28] H. Zhang, X. Ren, Z.L. Cui, J. Cryst. Growth 304 (2007) 206.
[29] Z.P. Li, C.H. Liu, Y.S. Fan, Y.C. Wang, X.R. Duan, Anal. Biochem. 359 (2006) 247.
[30] Z.P. Li, Y.C. Wang, C.H. Liu, Y.K. Li, Anal. Chim. Acta 551 (2005) 85.
[31] J. Ni, R.J. Lipert, G.B. Dawson, M.D. Porter, Anal. Chem. 71 (1999) 4903.
[32] C.S. Zhang, Z.Y. Zhang, B.B. Yu, J.J. Shi, X.R. Zhang, Anal. Chem. 74 (2002) 96.
[33] H.Q. Chen, F.G. Xu, S. Hong, L. Wang, Spectrochim. Acta Part A 65 (2006) 428.
[34] A. Ambrosi, M.T. Castaneda, A.J. Killard, M.R. Smyth, S. Alegret, A. Merkoçü, Anal. Chem. 79 (2007) 5232.

Determination of total nitrogen in atmospheric wet and dry deposition samples

Sathrugnan Karthikeyan[a], Jun He[a], Sundarambal Palani[b], Rajasekhar Balasubramanian[a,*], David Burger[c]

[a] *Division of Environmental Science and Engineering, National University of Singapore, Engineering Drive 1, Singapore 117576, Singapore*
[b] *Tropical Marine Science Institute, National University of Singapore, Engineering Drive 1, Singapore 117576, Singapore*
[c] *Deltares, P.O. Box 177, 2600 Delft, The Netherlands*

ABSTRACT

A microwave-assisted persulfate oxidation method followed by ion chromatographic determination of nitrate was developed for total nitrogen determination in atmospheric wet and dry deposition samples. Various operating parameters such as oxidation reagent concentrations, microwave power, and extraction time were optimized to maximize the conversion of total nitrogen to nitrate for subsequent chemical analysis. Under optimized conditions, 0.012 M $K_2S_2O_8$ and 0.024 M NaOH were found to be necessary for complete digestion of wet and dry deposition samples at 400 W for 7 min using microwave. The optimized extraction method was then validated by testing different forms of organic nitrogen loaded to pre-baked filter substrates and NIST SRM 1648 (urban particulate matter), and satisfactory results were obtained. In the case of wet deposition samples, standard addition experiments were performed. The suitability of the method for real-world application was assessed by analyzing a number of wet and dry deposition samples collected in Singapore during the period of March–April 2007. The organic nitrogen content was 15% (wet) and 30% (dry) of the total nitrogen. During the study period, the estimated wet fluxes for nitrate (NO_3^-), ammonium (NH_4^+), organic nitrogen (ON), and total nitrogen (TN) were 16.1 ± 6.5 kg ha^{-1} year^{-1}, 11.5 ± 5.7 kg ha^{-1} year^{-1}, 3.8 ± 1.5 kg ha^{-1} year^{-1} and 31.5 ± 13.2 kg ha^{-1} year^{-1}, respectively, while the dry fluxes were 2.5 ± 0.8 kg ha^{-1} year^{-1}, 1.4 ± 0.9 kg ha^{-1} year^{-1}, 2.3 ± 1.4 kg ha^{-1} year^{-1} and 7.5 ± 2.6 kg ha^{-1} year^{-1}, respectively.

1. Introduction

In recent years, atmospheric nitrogen deposition onto surface water has received considerable attention, particularly in the context of eutrophication of aquatic systems. Global industrialization and increased vehicular emissions are the major contributors to the cultural modification of atmospheric nitrogen cycle [1–3]. Until now, most of atmospheric research pertaining to nitrogen budgets has focused mainly on inorganic nitrogen in terms of identifying its sources and understanding its deposition patterns [4–6]. However, the environmental implications of atmospheric organic nitrogen are relatively less well understood [5,7–9]. An improved qualitative and quantitative understanding of organic nitrogen component is needed to complement the well-established knowledge-base pertaining to nitrate and ammonium deposition.

Although organic nitrogen is ubiquitous, it is still a poorly characterized component of atmospheric deposition of nutrients [8]. This lack of database is mainly because no single analytical technique can analyze the entire range of organic forms of nitrogen present. The limited results available to-date in the literature indicate that the organic nitrogen (ON) can be ~10–40% of total nitrogen depending on their sources and locations. Aliphatic amines, free amino acids, total hydrolysable amino acids, urea, and aromatic nitrogen are the various compounds reported to be present in wet and bulk deposition samples. Amorphous largely uncharacterized macromolecules like humic materials also contribute significantly to DON (dissolved organic nitrogen). Nevertheless, the current practice is to only measure bulk DON through difference between the total nitrogen and inorganic nitrogen [5].

Total nitrogen determination involves releasing the nitrogen from organic molecules by chemical oxidation to NO_3^-; thermal/catalytic oxidation to NO; kjeldahl conversion; or by photolysis [7,10–12]. Though new techniques such as high-temperature catalytic oxidation (HTCO) have facilitated the determination of organic nitrogen, older techniques (kjeldahl method, or persulfate oxidation) are still being used [5]. Kjeldahl method is the oldest of the methods, and is still widely used. However, the nitrogen present in forms other than amines, or amides is not sufficiently converted to ammonium. Furthermore, the method requires a tedious digestion procedure using concentrated sulfuric acid, followed by

distillation of ammonia under alkaline medium. An alternative method for the determination of organic nitrogen is the alkaline persulfate digestion technique which promotes efficient hydrolysis and oxidation of most nitrogenous compounds resulting in nitrate ions. The final step requires the analysis of nitrate either by ion-chromatography (IC), or a colorimetric technique.

Persulfate oxidation is carried out either in an autoclave, or in a pressure cooker with the digestion time being generally in the range of 30–60 min [5,10]. On the other hand, microwave digestion is a well known technique for rapid sample preparation for inorganic and organic compounds in environmental samples. This advantage of this digestion is that unlike conventional extraction methods that are subject to the boiling temperature of extraction solvents at atmospheric pressure, the microwave energy heats samples and solvents in a closed pressurized extraction vessel. As a result, the extraction of samples can be completed in minutes as opposed to hours necessary when traditional methods are used. Our laboratory has reported a series of microwave-assisted sample preparation for the analysis of major ions, organic acids, trace elements, and PAHs [13–16] in airborne particulate matter, and demonstrated their real-world applications with extensive field studies from different sources [17–19]. For total nitrogen digestion, only very few researchers have explored the use of microwave-assisted digestion in waste waters, sediments, etc. [20–25]. The quantity as well as the ratio of persulfate to sodium hydroxide used in the digestion is critically important in order to avoid the formation of chlorate (from chloride content) and high sulfate concentration (from persulfate) because of their potential interference in the IC analysis of nitrogen compounds. Furthermore, the microwave extraction can be effective even at low temperatures by using closed vessel system. To the best of our knowledge, the potential application of this sample preparation method has not been systematically evaluated for atmospheric wet and dry deposition samples yet.

In the present study, we propose a rapid microwave-assisted persulfate oxidation method followed by ion chromatographic analysis for determination of total nitrogen in wet and dry deposition samples. This study was carried out with two main objectives: (1) to optimize the oxidation reagent concentrations and the microwave operating parameters for rapid and efficient oxidation of nitrogen to nitrate and (2) to use the optimized method to measure the total nitrogen content in atmospheric wet and dry deposition samples collected in Singapore to estimate the washout ratio of nitrogen compounds including organic nitrogen. The results obtained are discussed in this paper.

2. Experimental

2.1. Reagents and standards

For preparation of reagents and standards, ultrapure water (MilliQ® Gradient A 10 System, Millipore, USA) was used. All reagents were of analytical grade. Anionic standards of chloride, nitrite, nitrate, and sulfate and that of ammonium were procured from AccuStandard, USA. Sodium hydroxide, potassium persulfate, EDTA, glycine, and urea were obtained from Merck, Germany.

SRM 1648 (Urban Particulate Matter), obtained from National Institute of Standards and Technology (NIST, Gaithersburg, MD, USA), was used for validation of the microwave-assisted extraction method. This standard consists of natural atmospheric particulate matter collected at an urban location, and is certified for its major, minor, and traces inorganic constituents.

2.1.1. Organic nitrogen standard

Nitrogen standards were prepared from ethylenediaminetetraacetic acid (ETDA), urea, and glycine by dissolving appropriate amounts in ultra pure water so as to have a stock solution of $1000 \, mg\text{-}N \, l^{-1}$. EDTA-based standard nitrogen solution was used for optimization experiments. The other two reagents were used to check the robustness of the optimized procedure.

2.2. Microwave digestion system

A closed vessel microwave digestion system (MLS-1200 mega, Milestone, Italy) was used in this study. It consists of a compact terminal touch-screen display with operator selectable 0–800 W output, temperature control up to 300 °C, five-layer PTFE coated microwave cavity, HPR/1000/10S Rotor, and 100-mL Teflon vessels (10 vessels). The Teflon vessels were cleaned with 2% hydrochloric acid and washed with deionized water at least three times before use.

2.3. Procedure for microwave oxidation

Rainwater samples (20 ml) after removal of suspended particulate matter through filtration were transferred to digestion vessels. Four millilitres of the oxidizing reagent was then added for digestion at recommended conditions in the microwave. After cooling, the digest was diluted to 10 times and filtered through 0.45 mm PTFE syringe filters and then analyzed by ion chromatography for nitrate content. The diluted digests were kept in a refrigerator at 4 °C until analysis which was carried out as soon as possible, certainly within 1 week. Optimization experiments involving oxidation reagents and microwave operating parameters were carried out using spiked standards. Pre-baked quartz filter strips (2 cm × 2 cm) were spiked with 200 µl of $1000 \, mg \, l^{-1}$ organic nitrogen standard and air-dried for 30 min. Initially, the amounts of sodium hydroxide and persulfate required for complete oxidation of organic nitrogen were determined. After fixing reagent concentrations, the microwave power and the extraction time were varied and optimized. For SRM, an accurately weighted amount (10–15 mg) of NIST SRM 1648 was transferred to the digestion vessel followed by addition of 25 ml of ultra pure water. Digestion and chemical analysis were carried out as described above.

2.4. Instrumentation

The diluted digests were analyzed for nitrate concentration by ion chromatography (IC) within a week after digestion. A compact Dionex IC system (Model ICS-2000, Dionex Corporation, USA) was used for the analysis. It consists of an eluent Generator (EG with CR-TC), isocratic pump, conductivity detector, anion self-regenerating suppressor (ASRS Ultra II-4 mm), Rheodyne six-port injection valve with 25 µl injection loop, and AS-40 auto sampler. An AS-11-HC (4 mm) analytical column in conjunction with an AG-11-HC guard column was used for nitrate determination. The peaks corresponding to different analytes in individual standards were identified according to their retention times. The whole IC operation including calibration and sample analysis was carried out using ChromeleonTM software. The ammonium ion content was also analyzed in order account for dissolved inorganic nitrogen. For this determination, the cation ion-exchange column, CS-12 (4 mm), was used with 11.0 mM H_2SO_4 as the eluent.

The choice of analytical column was important since the nitrate was to be determined in the presence of large amount of sulfate. We have employed a high capacity anionic column, AS-11-HC, for this work. The eluent strength and its flow rate were varied and optimized in order to obtain better baseline resolution. The eluent strength of 20 mM at a flow rate of 0.8 ml min^{-1} was used for

the determination of nitrate from digests. A four-point calibration (0.2, 0.5, 1.0 and 2 mg l^{-1} NO$_3^-$) in the presence of equal amounts of sulfate and chloride was performed initially. Then a second set of calibration standards was prepared containing 200 mg l^{-1} of sulfate in all standards. The slope and the regression coefficient of both calibrations were 0.1318 ($r^2 = 0.95$) and 0.1288 ($r^2 = 0.93$), respectively, indicating the nitrate determination is satisfactory even in the presence of a significantly higher amount of sulfate concentration. The repeatability and reproducibility of the IC method were assessed by injecting 0.5 mg l^{-1} nitrate standard and estimated to be 3.2% and 3.9%, respectively.

2.5. Sample collection

Wet deposition: wet deposition samples were collected for a period of 45 days at the NUS atmospheric research station using a home-made wet only sampler, based on the design proposed by Mirlean et al. [26]. Rainwater samples were transferred from the sampler to pre-cleaned HDPE bottles after the rain event and immediately filtered using 0.45 μm nylon membrane filters and refrigerated at 4 °C until analysis.
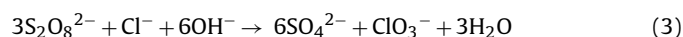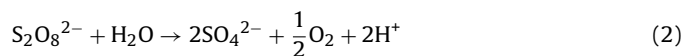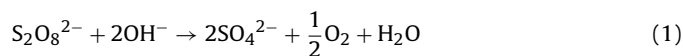
For dry deposition samples, a mini-volume air sampler was operated at 5 l min^{-1} to collect total suspended particulate matter in ambient air. Air samples were also collected at the same sampling location, but mainly during dry weather conditions. A detailed description of the dry deposition sampler can be found elsewhere [17–19]. After collection, the filters were stored in a dry box at 40% relative humidity for 1 day prior to and after sample collection to weigh the amount of particles collected. The particulate filters were stored in a refrigerator at 4 °C until extraction.

Dry and wet deposition samples were first analyzed for dissolved and water-soluble inorganic nitrogen (NO$_3^-$ and NH$_4^+$). Wet deposition samples were directly analyzed by ion-chromatography for NO$_3^-$ and NH$_4^+$ whereas dry deposition samples were analyzed after ultrasonic extraction. Half of the dry deposition sample collected onto the filter was extracted with 15 ml of DI water for 30 min in an ultrasonicator. The extract was filtered through 0.45 μm nylon membrane syringe filters and analyzed by ion-chromatography for NO$_3^-$ and NH$_4^+$. The remaining half of the filter sample was processed with 16 ml of DI water and 4 ml of persulfate oxidizing reagent following microwave digestion as described above. The digests were filtered through 0.45 μm nylon membrane syringe filters and refrigerated at 4 °C until analysis.

3. Results and discussion

3.1. Optimization of microwave-assisted persulfate oxidation

Persulfate oxidation can lead to different reactions in the presence of different ratios of sodium hydroxide as detailed below:

$$S_2O_8{}^{2-} + 2OH^- \rightarrow 2SO_4{}^{2-} + \frac{1}{2}O_2 + H_2O \tag{1}$$

$$S_2O_8{}^{2-} + H_2O \rightarrow 2SO_4{}^{2-} + \frac{1}{2}O_2 + 2H^+ \tag{2}$$

$$3S_2O_8{}^{2-} + Cl^- + 6OH^- \rightarrow 6SO_4{}^{2-} + ClO_3{}^- + 3H_2O \tag{3}$$

A high amount of chlororate can interfere with NO$_3^-$ separation in the IC analysis. Though the chloride oxidation is favored in the presence of hydroxide, Halstead et al. [27] reported that an initial ratio of perfulate to sodium hydroxide was important to control the chlorate formation rather than the absolute concentrations of either reagent. On the other hand, less amount of persulfate should be added in order to minimize the concentration
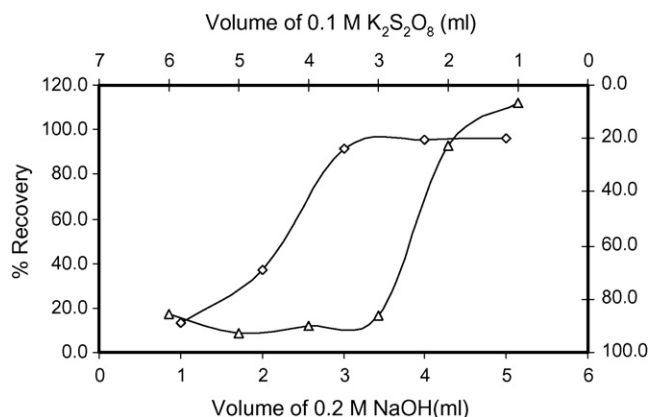

Fig. 1. Effect of oxidizing reagents (sodium hydroxide and potassium persulfate).

of the post-oxidation product, i.e. sulfate if the IC analysis of nitrogen compounds is preferred. Therefore, it was important to choose an optimum quantity of persulfate and sodium hydroxide so as to maximize nitrogen oxidation to nitrate and minimize the chlorate formation.

Pre-baked filter strips spiked with EDTA nitrogen standard were used for optimization studies. The optimum concentrations were chosen based on the recovery of nitrogen. Fig. 1 shows the effect of persulfate and sodium hydroxide concentrations on the extent of oxidation of EDTA based organic nitrogen using microwave digestion. As can be seen from this figure, even a slight increase in NaOH and K$_2$S$_2$O$_8$ favors nitrogen oxidation. Three millilitres of 0.2 M NaOH was required to complete nitrogen oxidation which remained constant above 4 ml. Hence, 3.5 ml of NaOH (0.2 M) was chosen for subsequent studies. Similarly for persulfate, 3–4 ml was the optimum quantity to be added at which a maximum oxidation took place. A chloride solution (∼40 mg/l) was also added to the pre-oxidation solution to check chlorate formation and study its influence. When more than 5 ml of persulfate solution was added, a significant reduction (20–30%) in the initial chloride concentration was observed, but there was no conversion of chloride to chlorate below 4 ml level. Therefore, it was decided to use 4.0 ml of mixed reagents containing K$_2$S$_2$O$_8$ (0.1 M) and NaOH (0.2 M). This ratio was similar to what was reported by Halstead et al. [27]. However, the concentration is half of what was used by Halstead et al. It should be noted that the ratio and the quantity of the two reagents are not critically important if the post-oxidation analysis is carried out by colorimetric technique. Maher et al. [25] reported 1:1 (K$_2$S$_2$O$_8$–NaOH) instead of 2:1 for total nitrogen and phosphorus in turbid waters.

Using an optimum quantity of oxidizing reagents, the microwave power and extraction time were then optimized. The microwave power was initially varied from 100 to 600 W with a constant extraction time of 8 min. As expected, increasing the microwave energy favored the nitrogen oxidation, and 400 W was sufficient for maximum recovery of nitrogen. The temperature of the sample mixture was around 95 °C at 400 W. This is in good agreement with the findings reported by Maher et al. [25] (95 °C; 40 min). At a fixed microwave energy of 400 W, the extraction time was then studied. It was found that 6–8 min was sufficient to achieve the maximum conversion of nitrogen compounds to nitrate. Therefore, it was decided to use a microwave energy 400 W for 7 min to complete persulfate-induced oxidation of nitrogen compounds from wet and dry deposition samples. Under the proposed experimental conditions, the extraction method is very rapid compared to previous reports [21,25], which required 30–40 min digestion time (Fig. 2).
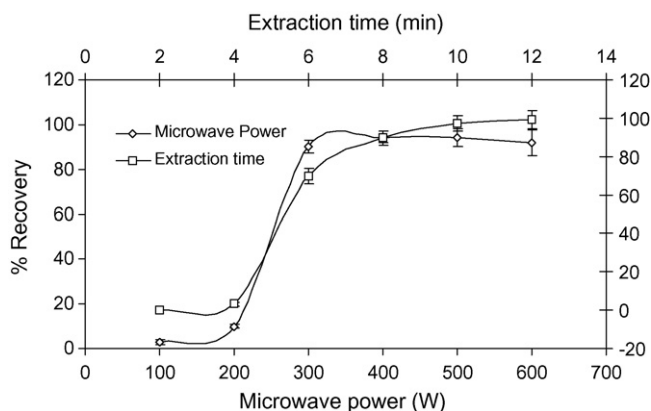
Fig. 2. Effect of microwave conditions (power and digestion time).

Table 2
Summary of nitrogen compounds concentrations in wet and dry deposition samples

	Mean ± S.D	Minimum–Maximum	LOD
Wet deposition (mg/l)[a]			
NO_3^+-N	0.54 ± 0.22	0.25–1.00	0.005
NH_4^+-N	0.39 ± 0.19	0.16–0.73	0.008
ON-N	0.10 ± 0.06	0.01–0.20	NA[b]
TN-N	1.05 ± 0.44	0.53–2.16	0.10
Dry deposition ($\mu g\,m^{-3}$)[c]			
NO_3^--N	0.65 ± 0.21	0.45–1.03	0.01
NH_4^+-N	0.73 ± 0.45	0.13–1.34	0.02
ON-N	0.60 ± 0.38	0.13–1.08	NA[b]
TN-N	1.98 ± 0.70	1.14–3.04	0.28

[a] Number of rain events = 12.
[b] ON was derived from the difference between TN and total amount of NO_3^--N and NH_4^+-N.
[c] No of samples = 7.

3.2. Validation of the proposed microwave extraction method

The optimized method was checked for its robustness by testing different forms of commonly found organic nitrogen (EDTA, urea, and glycine) in the atmosphere for a wide range of concentrations. The recovery, repeatability, and reproducibility were evaluated. The summary of those results is presented in Table 1. In all three forms of nitrogen compounds, the recoveries were better than 90% and % CV (coefficient of variance) was less than 10%, indicating the suitability of the optimized method. The method was further validated by processing NIST SRM 1648 (urban particulate matter) for its nitrogen content. Though there was no certified value available for total nitrogen, a reference value was obtained by analyzing the total nitrogen content using elemental analyzer. The total nitrogen in SRM1648 was 2.35 ± 0.16% ($n = 6$) according to the proposed digestion method which is in close agreement with the value of 2.7 ± 0.2% as obtained by CHN (elemental) analyzer. The total nitrogen content of the water-soluble extract was also determined by oxidizing water-soluble fraction of N. The nitrogen content was calculated to be 1.8% which is due to the sum of NO_3^- and NH_4^+. This result indicates that the water-soluble organic nitrogen may be negligibly small. In the case of rain water (wet precipitation), standard addition experiments were conducted with the above three forms of nitrogen (EDTA, urea, and glycine), and the recovery results were 95 ± 5% for the concentration in the range of 1–5 mg l^{-1}. In summary, it can be said that the proposed digestion method is accurate and reliable based on the validation data obtained.

3.3. Application of the proposed method

The proposed persulfate oxidation method was employed to determine total nitrogen in atmospheric dry deposition and wet deposition samples collected in Singapore. The inorganic forms of nitrogen, namely, NO_3^- and NH_4^+ were also separately determined in order to estimate the bulk organic nitrogen. The summary of the results obtained from these determinations is presented in Table 2. There were 13 rain events, accounting for 280 mm of rainfall during the study period. The concentrations of different nitrogen

compounds were in the order of $NO_3^- > NH_4^+ > ON$. The nitrate accounted for 50% of the total nitrogen while the ammonium ion accounted for 35%. There were few smoke haze episodes occurring in Singapore during the study period due to uncontrolled forest and peat fires in Indonesia. These air pollution episodes affected the local air quality in Singapore, and contributed to the increase in total nitrogen content in precipitation samples (1.5–2.2 mg l^{-1} against 0.7 mg l^{-1}). A good correlation was observed between TN and NO_3^--N ($r^2 = 0.834$) as well as with NH_4^+-N ($r^2 = 0.811$), indicating that these two nitrogen compounds were major contributors to the increase of total nitrogen. In the case of dry deposition, the concentrations of NO_3^-, NH_4^+, and ON are of the same order each contributing ~30–35% of the total nitrogen. As mentioned above, the haze episode contributed to the increase in PM (airborne particulate matter) concentration (60 $\mu g\,m^{-3}$ vs. 40 $\mu g\,m^{-3}$). Though there was an increase in total nitrogen, only ON could showed better correlation with TN ($r^2 = 0.726$). This finding suggests that uncontrolled biomass burning could be an additional source of atmospheric nitrogen compounds apart from local emissions in Singapore, which together led to their elevated concentrations since there were few smoke haze episodes reported during the study period.

The wet and dry deposition fluxes were calculated for nitrogen using the following two equations [28].

$$F_{wet} = 0.01 C_{rain} P \tag{4}$$

where F_{wet} is the wet deposition flux (kg ha^{-1} year^{-1}), C_{rain} the rainfall concentration in mg l^{-1}, P the precipitation amount in m, and 0.01 is a unit conversion factor.

$$F_{dry} = C_i V_d 315.0 \tag{5}$$

where F_{dry} is the dry deposition flux (kg ha^{-1} year^{-1}), C_i the concentration in $\mu g\,m^{-3}$, V_d the deposition velocity (m s^{-1}), used from a previous report by Poor et al. [28] and 315.0 is a unit conversion factor.

The mean flux values along with their corresponding standard deviations are shown in Fig. 3 for NO_3^-, NH_4^+, ON, and TN. As can be seen from the figure, the wet deposition flux was much higher than the dry deposition flux. The ratio was very particularly high (6–8) for NO_3^- and NH_4^+, indicating higher scavenging of inorganic nitrogen compounds by rain droplets compared to organic nitrogen. We have calculated scavenging ratios for NO_3^-, NH_4^+, and ON using the data obtained from this study. The ratios were 1104, 683, and 221 for NO_3^-, NH_4^+, and ON, respectively. Calderon et al. [29] reported that particle scavenging is responsible for most of inorganic nitrogen in rainwater and that gas scavenging of NH_3 and HNO_3 could be further considered to NO_3^- and NH_4^+ scavenging rates to explain

Table 1
Validation data on microwave-persulfate oxidation for total nitrogen

Parameters	EDTA	Glycine	Urea
Range (mg/l)	1–50	1–50	1–50
Recovery (%)	89.8	92.2	95.4
Repeatability (%) ($n = 6$)	4.7	3.8	5.0
Reproducibility (%) ($n = 3$)	6.2	6.7	5.9

Table 3
Comparison data on dry and wet deposition flux ($kg\,ha^{-1}\,year^{-1}$)

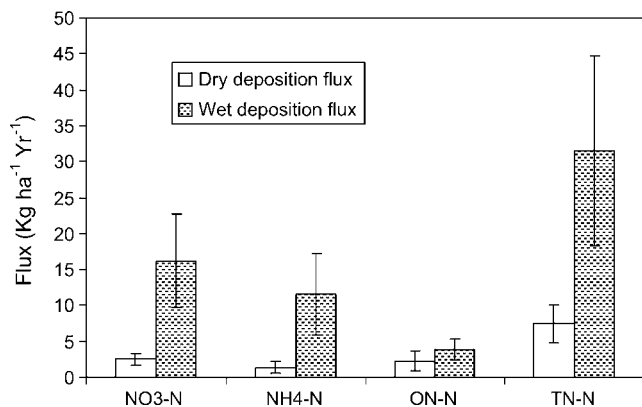| Country	Wet deposition				Dry deposition				Reference
	NO_3^-	NH_4^+	ON	TN	NO_3^-	NH_4^+	ON	TN	
Singapore	13.4	11.5	3.8	31.8	1.6	0.12	1.5	4.98	Present study
Malaysia	9.4	6.2	–	–	–	–	–	–	[30]
Hong Kong	4.0	4.5	–	–	–	–	–	–	[31]
Indonesia (Bogor)	12.7	21.3	–	–	–	–	–	–	[32]
Japan	7.0	10.0	6.5	24	0.8	12.1	4.5	18	[33]
USA	7.4	2.5	1.4	11.4	0.13	0.38	0.1	2.1	[34]

Fig. 3. Atmospheric deposition of nitrogen compounds (wet and dry).

>90% ionic concentration. Table 3 provides a comparison of wet and dry deposition of nitrogen compounds around the world. As can be seen, the deposition fluxes in terms of nitrate and ammonium, measured in Singapore are higher than those reported for Malaysia and Indonesia. This is mainly because the flux for Singapore was calculated based on 1 month data while the latter flux data were based on yearly average. Higher atmospheric concentrations of nitrate and ammonium during the study period contributed to higher flux. The mean concentration of nitrate and ammonium ion was higher than those reported from our previous study [35], which must be mainly due to contribution from biomass burning in Sumatra. The flux reported for ammonium and organic nitrogen in Japan was higher than that from our present study which indicates the agricultural activities act as a major source for these two species. However, the fluxes reported in USA and Hong Kong were found to be rather low.

Though the organic nitrogen content is relatively less compared to inorganic nitrogen, its contribution towards the nitrogen budget cannot be ignored since it adds ~15% through wet deposition and 30% through dry deposition. It is known that dissolved organic nitrogen (DON) is the most abundant organic N form and is potentially mineralized in ecosystems. Also, DON such as urea and amino acids can be directly taken up by some plants [5]. Consequently, the DON deposition rate must be one of the important factors controlling the N in ecosystems. The current deposition data obtained for Singapore resulted from 1-month sample collection. To get more insights into the atmospheric nitrogen deposition, particularly that of ON in Singapore, the collection of wet- and dry deposition samples is in progress at a network of three different sampling sites, and the data will be collected for at least 1 year. These comprehensive results will be reported elsewhere.

4. Conclusion

This report describes a simple, rapid microwave-assisted persulfate oxidation method followed by ion chromatographic determination of total nitrogen in wet deposition and dry deposition samples. These analytical data were used to estimate bulk organic nitrogen content in atmospheric samples after subtracting the total inorganic nitrogen ($NO_3^- + NH_4^+$) from the total nitrogen. The robustness and reliability of the proposed analytical method was demonstrated by thorough validation using different forms of organic nitrogen loaded in filter substrates and by using NIST SRM 1648 (urban particulate matter). The validated analytical method was employed for estimating the wet and dry deposition fluxes of nitrogen compounds in Singapore. The wet deposition flux was higher (two to five times) than the dry deposition flux. The nitrogen flux was in the order of $NO_3^- > NH_4^+ > ON$ for wet deposition samples. Our study showed that ON nitrogen contributes about 15% (wet) and 30% (dry) of the total nitrogen deposition. A few smoke haze episodes that took place in Singapore during the study period contributed to the elevated nitrogen flux. In summary, the proposed analytical method is very useful for analyzing wet and dry deposition samples collected from a network of sites for total nitrogen which is necessary for estimating bulk organic nitrogen content. The resulting database could in turn provide valuable insights into understanding the linkage between atmospheric deposition of nitrogen compounds and surface water quality degradation.

References

[1] J.N. Galloway, W.H. Schlesinger, H. Levy, A. Michaels, J.L. Schnoor, Global Biogeochem. Cycles 9 (1995) 235–252.
[2] V. Smil, Global Biogeochem. Cycles 13 (1999) 647–662.
[3] P.M. Vitousek, J.D. Aber, R.W. Howarth, G.E. Likens, P.A. Matson, D.W. Schindler, W.H. Schlesinger, D.G. Tilman, Ecol. Appl. 7 (1997) 737–750.
[4] W.A.H. Asman, M.A. Sutton, J.K. Schjorring, New Phytol. 139 (1998) 27–48.
[5] S.E. Cornella, T.D. Jickellsa, J.N. Capeb, A.P. Rowlandc, R.A. Duced, Atmos. Environ. 37 (2003) 2173–2191.
[6] R.M. Rejesus, R.H. Hornbaker, Agric. Ecosyst. Environ. 75 (1999) 41–53.
[7] J.N. Cape, A. Kirika, A.P. Rowland, D.S. Wilson, T.D. Jickells, S. Cornell, Sci. World 1 (S2) (2001) 230–237.
[8] J.C. Neff, E.A. Holland, F.J. Dentener, W.H. McDowell, K.M. Russell, Biogeochemistry 57/58 (2002) 99–136.
[9] S.P. Seitzinger, R.W. Sanders, Limnol. Oceanogr. 44 (1999) 721–730.
[10] D.A. Bronk, M.W. Lomas, P.M. Glibert, K.J. Schukert, M. Sanderson, Mar. Chem. 69 (2000) 163–178.
[11] J.G.C. Kjeldahl, Fresenius J. Anal. Chem. 22 (1883) 366–372.
[12] K.M. Russell, J.N. Galloway, S.A. Macko, J.L. Moody, J.R. Scudlark, Atmos. Environ. 32 (1998) 2453–2465.
[13] S. Karthikeyan, R. Balasubramanian, Anal. Bioanal. Chem. 381 (2005) 1604–1608.
[14] S. Karthikeyan, R. Balasubramanian, Anal. Sci. 21 (2005) 1505–1508.
[15] S. Karthikeyan, R. Balasubramanian, S.W. See, Talanta 69 (2006) 79–86.
[16] S. Karthikeyan, U.M. Joshi, R. Balasubramanian, Anal. Chim. Acta 576 (2006) 23–30.
[17] S.W. See, R. Balasubramanian, R. Elizabeth, S. Karthikeyan, D.G. Streets, Environ. Sci. Technol. 41 (2007) 3488–3494.
[18] S.W. See, S. Karthikeyan, R. Balasubramanian, J. Environ. Monit. 8 (2006) 369–376.

[19] S.W. See, Y.H. Wang, R. Balasubramanian, Environ. Res. 103 (2007) 317–324.
[20] M. Colina, P.H.E. Gardiner, J. Chromatogr. A 847 (1999) 285–290.
[21] S. Colombini, S. Polessello, S. Valsecchi, J. Chromatogr. A 822 (1998) 162–166.
[22] X.T. He, R.L. Mulvaney, W.L. Banwart, Soil Sci. Am. J. 54 (1990) 1625–1629.
[23] P.J. Johnes, A.L. Heathwaite, Water Res. 26 (1992) 1281–1287.
[24] K.V. Lo, W.T. Wong, P.H. Liao, J. Environ. Sci. Health Part A: Toxic Hazard. Subst. Environ. Eng. 40 (2005) 609–615.
[25] W. Maher, F. Krikowa, D. Wruck, H. Louie, T. Nguyen, W.Y. Huang, Anal. Chim. Acta 463 (2002) 283–293.
[26] N. Mirlean, V.E. Andrus, M.R. Casertelli, J. Environ. Monitor. 5 (2003) 591–592.
[27] J.A. Halstead, J. Edwards, R.J. Soracco, R.W. Armstrong, J. Chromatogr. A 857 (1999) 337–342.

[28] N. Poor, C. Pollman, T. Paul, M. Begum, M. Evans, S. Campbell, Water Air Soil Pollut. 170 (2006) 267–283.
[29] S.M. Calderon, N.D. Poor, S.W. Campbell, J. Air. Waste Manage. 56 (2006) 1278–1286.
[30] G.P. Ayers, L.C. Peng, R.W. Gillet, L.S. Fook, Water Air Soil Pollut. 133 (2002) 15–30.
[31] G.P. Ayers, K.K. Yeung, Atmos. Environ. 30 (1996) 1581–1587.
[32] R.W. Gillet, G.P. Ayers, P.W. Selleck, M.H.W. Tuti, H. Harjanto, Water Air Soil Pollut. 120 (2000) 205–215.
[33] Y.S. Ham, S. Tamiya, Water Air Soil Pollut. 177 (2006) 45–57.
[34] Y.Z. Luo, X.S. Yang, R.J. Carley, C. Perkins, Atmos. Environ. 36 (2002) 4517–4528.
[35] G.P. Hu, R. Balasubramanian, C.D. Wu, Chemosphere 51 (2003) 747–755.

Hybrid mesoporous materials for on-line preconcentration of Cr(VI) followed by one-step scheme for elution and colorimetric determination at ultratrace levels

Manuela L. Kim, Jorge D. Stripeikis, Mabel B. Tudino*

Laboratorio de Análisis de Trazas, Departamento de Química Inorgánica, Analítica y Química Física, INQUIMAE, Facultad de Ciencias Exactas y Naturales, Universidad de Buenos Aires, Ciudad Universitaria, 1428 Buenos Aires, Argentina

ABSTRACT

An hybrid mesoporous material synthesised in our laboratories for solid phase extraction (SPE) in flow through systems has been used for analytical purposes. The solid was obtained from mesoporous silica MCM-41 functionalized with 3-aminopropyltriethoxy silane by Sol–Gel methodology. In order to exploit the large sorption capacity of the material together with the possibility of modeling it for anions retention, a microcolumn (MC) filled with the solid was inserted in a flow system for preconcentration of Cr(VI) and its determination at ultratrace levels in natural waters. The analytical methodology involved a reverse flow injection system (rFI) holding a MC filled with the solid for the analyte extraction. Elution and colorimetric detection were carried out with 1–5 diphenylcarbazide (DPC) in sulfuric acid. DPC produced the reduction of Cr(VI) to Cr(III) together with the generation of a cationic red complex between Cr(III) and 1–5 diphenylcarbazone which was easily eluted and detected with a visible spectrophotometer. Moreover, the filling material got ready for the next sample loading remaining unspoiled for more than 300 cycles.

The effect of several variables on the analytical signal as well as the influence of cationic and anionic interferences were discussed. Particular attention was given to sulfuric acid interference since it is the required media for the complex generation.

Under optimal conditions, 99.8% of Cr(VI) recovery was obtained for a preconcentration time of 120 s (sample and DPC flow rates = 1 mL min^{-1}) and an elution volume of 250 μL. The limit of detection (3 s) was found to be 0.09 μg L^{-1} Cr(VI) with a relative standard deviation ($n = 10$, 3 μg L^{-1}) of 1.8.

Since no Cr(III) was retained by the solid material and Cr(VI) was completely adsorbed, electrothermal atomic absorption spectrometry (ET AAS) determinations of Cr(III) were also performed by simply measuring its concentration at the end of the microcolumn after Cr(VI) retention by the mesoporous solid.

Applications to the determination of Cr(VI) and Cr(III) in natural waters and the validation of the methodology were also studied.

1. Introduction

Chromium(VI) is one of the inorganic species of more ecotoxicological concern due to its already probed carcinogenic and/or mutagenic effects on living organisms [1].

Mostly, total chromium determinations are carried out by optical methods (90%), corresponding to atomic spectrometry (ET AAS, FAAS, ICP) about 65%. The rest involves fluorometry, quimiluminiscence and UV–visible spectrophotometry [2].

Flow injection analysis (FIA) is a well-established and versatile technique. This versatility allows the easy inclusion of micro-

columns (MC) filled with different solids that make the system able to the on-line isolation and preconcentration of different analytes. In this way, solid phase extraction (SPE) is a "classic" in flow systems and the pursuit of the most suitable filling materials becomes a challenge for the analyst.

During the last 10 years, the analytical applications of the hybrid mesoporous materials have been increased due to the main characteristics of these solids: large surface area, thermal and chemical resistance, high adsorption capacity, easiness of functionalization, etc. [3]. However, applications have been devoted to the isolation of metal ions in "batch" procedures since the contact time between the solution and the solid usually needs to be high [4–7]. Recent works have shown the utility of these hybrid mesoporous materials for the preconcentration of trace elements employing columns packed with small amounts of solids. However, all these studies have shown the need of multiple and time consuming steps to

* Corresponding author. Tel.: +54 1145763360; fax: +54 1145763341.
  E-mail address: tudino@qi.fcen.uba.ar (M.B. Tudino).

perform the retention, elution and detection of the analytes of interest [8,9], enabling in this way the chance for on-line operation.

In this work, we present the employment of the mesoporous silica MCM-41 functionalized with 3-aminopropyl groups (APS) for on-line analytical applications. The hybrid material employed as filling of a microcolumn held in a reverse flow injection (rFI) system, was synthesised in our laboratories by the *One Pot* procedure, employing Sol–Gel methodology.

Cr(VI) was retained on the column in anionic form and then, easily eluted as a cationic red complex with DPC in sulfuric acid. Therefore, the colorimetric reagent (CR) performs two different tasks in only one step: reduces Cr(VI) to Cr(III) allowing its rapid elution, and complexes Cr(III) developing a red color which is detected spectrophotometrically. After all, the packaging material gets ready for a new sample loading.

Optimal conditions of operation will be discussed together with the influence of cationic and anionic interferences on the analytical signal. Special attention will be given to the interference of sulfuric acid since its inclusion in CR is mandatory for the complex formation and hence, the color development.

The advantages of this methodology will be presented in terms of analytical features, including sample throughput, lifetime of the packaging material and easiness of operation. Obtained results will be fully discussed.

Taking advantage of the efficiency of the solid for the complete sorption of Cr(VI) with no interference of Cr(III), the latter was also determined by electrothermal atomic absorption spectrometry (ET AAS) by simply measuring its concentration at the end of the column and after retention of Cr(VI) onto the mesoporous solid.

Applications to the determination of Cr(VI) and Cr(III) in different kind of natural waters will be shown as well. Validation of the analytical methodology will be provided.

2. Experimental

2.1. Reagents and materials

All the reagents listed below were analytical grade. Doubly deionized water (DIW, 18 MΩ cm^{-1}) obtained from a Milli-Q water System (Millipore, Beadford, MA, USA) was used throughout the experiments.

Sodium tetraethyl-ortosilicate (TEOS) 98% (M = 208.33, d = 0.934 g mL^{-1}), cetyl-trimethylammonium bromide (CTAB) (M = 364.46) and 3-aminopropyltriethoxysilane (APTES) (M = 221.37, d = 0.942) were obtained from Sigma–Aldrich (St Louis, MO, USA).

H$_2$SO$_4$ 98% (w/w), NaOH (s), HCl 38% (w/w), H$_3$PO$_4$ 85.5% (w/w), 1–5 diphenylcarbazide (DPC), ethanol 98% (w/w) and acetone p.a. were obtained from Merck (KGaA, Darmstadt, Germany).

All standard solutions were prepared by adequate dilution of stock standard solutions of 1.000 mg L^{-1} (Merck KGaA).

All operations were performed on a laminar flow clean bench. Nalgene (Nalge, Rochester, NY, USA) laboratory ware was thoroughly cleaned with (1 + 1) nitric acid and rinsed with DIW.

Before preconcentration, Cr(VI) and Cr(III) standard solutions and water samples were kept at pH 2 by the addition of a suitable amount of HCl (c) and made up to volume with 1:4 acetone:water solution.

For preparing 100 mL of colorimetric reagent, 0.200 g de DPC were dissolved in 25 mL of acetone, and sulfuric acid was added in order to obtain a final concentration of 0.1 mol L^{-1} when made up to volume with DIW.

All solutions were sonicated during 15 min for degassing, preventing in this way the production of bubbles during the FI measurements.

2.2. Apparatus

Manifolds constructed using 0.5 mm id. PFTE tubing (Cole Parmer, Chicago, IL, USA) were assembled with zero dead volume Cheminert fittings (Valco Instruments, Houston, TX, USA). The colorimetric reagent was injected using a VICI six-port rotary valve (Valco). Standards and sample solutions were pumped using an eight channel Ismatec IPC variable speed precision peristaltic pump (Cole Parmer). Absorbance was monitored using an SPD-10AVvp UV–vis detector equipped with a 4 μL flow cell (Shimadzu, Kyoto, Japan) and interfaced to a personal computer through a data acquisition system.

FAAS determinations of total Chromium were carried out at 358.0 nm by running the standard program of the spectrometer Shimadzu AA 6800 (Shimadzu, Kyoto, Japan).

A Shimadzu 6700 Atomic Absorption Spectrometer (Kyoto, Japan) equipped with a graphite furnace accessory GFA 6000 and an autosampler ASC-6000 was used for the determination of Cr(III) after Cr(VI) retention onto the mesoporous solid. Standard pyrolitic graphite tubes (Shimadzu) were used. The standard program provided by the manufacturer was run for all the determinations. High purity argon was employed as internal gas (AGA, Argentina).

2.3. Preparation of functionalized mesoporous silica (APS)

The solid APS was prepared according to the methodology described by Fowler et al. [10]. 0.4 g of CTAB were dissolved in 5.00 g of NaOH 0.1 mol L^{-1} and 17.55 g of DIW. In a separate vessel, APTES and TEOS were mixed in different proportions giving raise to four different mixtures: 5% (m/m), 10% (m/m), 15% (m/m) and 20% (m/m) APTES/TEOS. Each mixture was treated in the same way. First, it was added to the CTAB solution slowly and under continuous agitation. Then, it was agitated during 24 h at 25 °C. The obtained solid was filtrated and washed several times with DIW and ethanol and then, it was dried in a vacuum desiccator during 10 h at 100 °C. For the surfactant extraction, the solid was refluxed with HCl 1 mol L^{-1} in ethanol at 75 °C during 24 h. Finally, it was washed again with ethanol and DIW and dried in the vacuum desiccator for 10 h at 100 °C. Amongst the four obtained solids, APS 20% (m/m) was selected for analytical purposes (see below). It was employed to fill a column constructed from an acrylic cylinder (3.0 cm long, 1.5 cm diameter) furnished with 0.25–28 female connectors. The inner part was drilled to obtain a 7.9 μL bed volume (10 mm long, 1.0 mm i.d.). The aspect ratio (length to diameter) was adjusted to keep minimal dispersion in the system together with lower resistance to the flow stream.

2.4. Analytical procedure for Cr(VI) and Cr(III) determinations

Samples and standard solutions containing Cr(VI) in HCl 0.01 mol L^{-1} were passed through the microcolumn filled with APS and pre-conditioned at pH 2 with HCl, at a volumetric flow rate of 1 mL min^{-1} during a preconcentration time (t_{pc}) of 240 s. Then, the injection valve was commutated and 250 μL (flow rate = 1 mL min^{-1}, loop length = 50 cm) of the colorimetric reagent were injected into the carrier stream. The cationic red complex formed between Cr(III) and dyphenylcarbazone [11] was released from the microcolumn and measured at 548 nm. Fig. 1 shows the FI system configuration.

Samples and standards solutions containing Cr(III) in HCl 0.01 mol L^{-1} were passed through the MC as described above. ET AAS determinations of Cr(III) were performed off-line by simply collecting the solution discarded after preconcentration and before the CR injection. A sample volume of 100 μL was directly injected in the graphite furnace and thus, Cr(III) was determined. No matrix
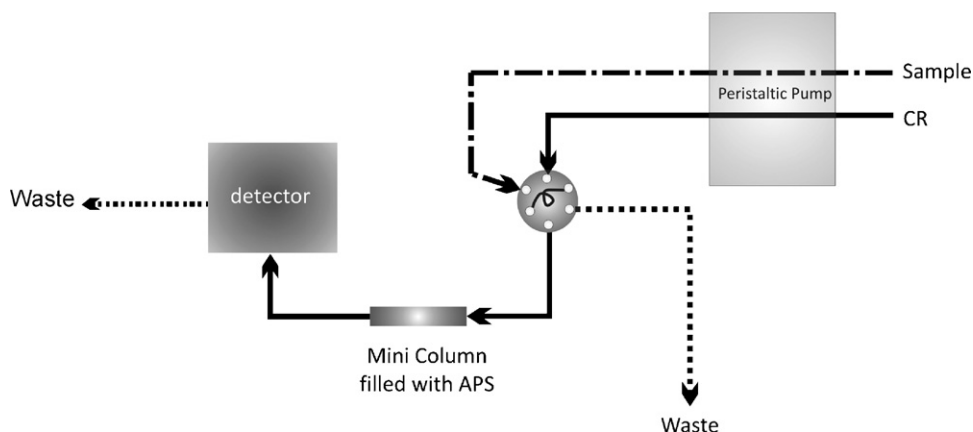
Fig. 1. rFI configuration for Cr(VI) determination. Load position: the sample preconcentrates on the column and gives background signal. Inject position: CR goes through the column and releases the analite giving a transient signal.

modifiers, either in solution or permanent were needed for complete recovery of the analyte.

3. Results and discussion

3.1. Influence of the percentage of functionalization

APTES and TEOS were employed in a 20% (m/m) proportion. Higher amounts of APTES were not assayed as the obtained solid is amorphous and looses the main features of the mesoporous one, principally the large surface area. Lower values showed lower sorption capacity for Cr(VI) at all the pH values assayed (see below). Since Cr(VI) occurs as chromate or acid chromate at low concentrations, and the capacity of sorption is established by the difference between the charge of the analyte and the surface charge of the solid, a positive surface charge improves retention. This surface charge is conditioned by the percentage of functionalization (ratio APTES/TEOS) and the pH value of the solution in contact with the solid as it will be discussed in Section 3.2.

3.2. Influence of pH on the adsorption of Cr(VI) on APS

Once the mesoporous solids with different percentages of functionalization are obtained, it is necessary to optimize its surface charge by changing the pH of the solutions in contact with them. To study the influence of pH on Cr(VI) adsorption at percentages of functionalization ranging between 5% and 20% (m/m), 5 mL of a solution containing 5 mg L^{-1} Cr(VI) at different pH values were suspended in 0.05 g of APS (the experiment was repeated for the different proportions APTES/TEOS), agitated during 24 h and centrifuged at 3000 rpm. 2 mL of the supernatant were taken and the remaining amount of Cr(VI), and thus the quantity adsorbed by the solid, was determined by FAAS. The different pH values, ranging between 0 and 9 were obtained by the addition of HCl 1 mol L^{-1} or NaOH 1 mol L^{-1}. Nitric and sulfuric acid were also tested for the acid range but the first one produces a significant drift in the baseline at the moment of the spectrophotometric determination, and the second is a serious interference for chromium sorption when goes along with chromium standards and samples. The influence of sulfuric acid (actually HSO$_4^-$ and SO$_4^{2-}$ at pH 2) will be discussed below as it is the required media for the development of the complex between Cr(III) and diphenylcarbazone.

Fig. 2 shows the influence of pH on the retention of Cr(VI) onto the microcolumn packed with APS 20% (m/m). Results found for solids containing lower proportions APTES/TEOS are not shown as poorer sorption capacities were observed at any pH. The maximum

capacity of adsorption of APS 20% is observed for pH values between 2 and 3, which is in agreement with those reported by Lam et al. [12]. At low concentrations and pH 2–3, Cr(VI) is present as HCrO$_4^-$. In this range, the surface charge of the solid should be positive as the amino groups of the filling are protonated and the net surface charge of the silica should be zero. This fact, favors the electrostatic interaction between HCrO$_4^-$ and the protonated amino groups on the surface. At higher pH values, APS develops a negative surface charge and an electrostatic repulsion between the filling and the anionic analyte is observed [13]. The sharp decrease of the adsorption capacity below pH 2 is mainly due to the conversion of HCrO$_4^-$ into its neutral form H$_2$CrO$_4$.

Even though the adsorption capacity for Cr(VI) onto APS 20% is slightly higher with HCl 0.001 mol L^{-1} (pH 3), HCl 0.01 mol L^{-1} (pH 2) was selected due to its higher buffer capacity which makes easier to keep pH constant between injections, improving reproducibility at the moment of the determination. Regarding the selectivity for Cr(VI) sorption, no significant differences were observed between both pH values. At pH 2, the adsorption capacity for Cr(VI) was 4.35 mmol g^{-1} and that for Cr(III) was 0.007 mmol g^{-1}. These values reveal that APS 20% at pH 2 is highly selective for Cr(VI) retention allowing its determination with no interference of the cationic form.

In order to match these findings with the on-line procedure, the optimum pH of sorption was also assessed by means of the FI-SPE system. These experiments were performed as described in Section 2.4 for Cr(III) determination except that Cr(VI) solutions (10 μg L^{-1}) at different pH values were preconcentrated instead. Since the capacity of sorption at low pH was extremely high, it was not easy to measure Cr(VI) in the remaining solution. However, the same values (pH 2–3) were found as optimal within the experimental error.
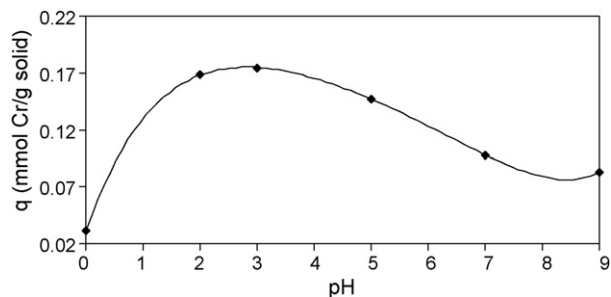

Fig. 2. Effect of pH on the retention of Cr(VI) onto APS 20%. [Cr(VI)]: 5 mg L^{-1}, 5 mL of solution in 0.05 g of APS.
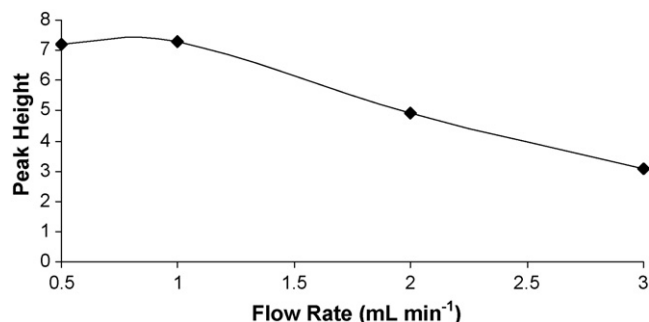
Fig. 3. Analytical signal of the Cr(III). 1.5-Diphenylcarbazone complex (at 548 nm) vs. volumetric flow rate for Chromium sorption. Flow rate: 0.5 and 3 mL min^{-1}; [Cr(VI)]: 10 μg L^{-1} in HCl 0.01 mol L^{-1} (pH 2): PCF: 16; [CR]: 0.2% (w/v) DPC in Acetone 1:4 and 0.1 mol L^{-1} H$_2$SO$_4$.

Fig. 4. Effect of the injected volume of CR on the analytical signal. [Cr(VI)] 10 μg L^{-1}; PCF: 16; flow rate of sorption/desorption: 1 mL min^{-1}; CR volume: 50–1000 μL. [CR]: 0.2% (w/v) DPC in Acetone 1:4 and 0.1 mol L^{-1} H$_2$SO$_4$.

3.3. Influence of the volumetric flow rate on the "on-line" sorption and release of Cr(VI)

The volumetric flow rate for sorption of Cr(VI) onto the filling and thus, its release by CR was varied between 0.5 and 3 mL min^{-1}. Higher values were not employed as leaks were observed as a consequence of compaction of the mesopororus solid and the development of internal pressures in the system. Lower values were not compatible with the proper operation of the peristaltic pump. Experiments were performed with a solution of 10 μg L^{-1} Cr(VI) in HCl 0.01 mol L^{-1} (pH 2) with a constant preconcentration factor (PCF) equal to 16. PCF was defined as the quotient between the volume of sample flowing through the column and the volume of CR employed to release the analyte. These volumes were fixed in 4 mL and 250 μL, respectively. Therefore, for changing the flow rate keeping constant the volume of Cr(VI) solution retained on APS, the time of contact between the analyte and the packed solid was varied between 80 and 480 s.

Fig. 3 shows the influence of the volumetric flow rate on the spectrophotometric analytical signal obtained for the complex Cr(III)/diphenylcarbazone (λ = 548 nm) after sorption of Cr(VI) onto APS and its desorption as cationic red complex.

A volumetric flow rate of 1 mL min^{-1} was chosen as the most advantageous. Lower values produce a low sample throughput. Higher values decrease the time of contact between the filling and the analyte and thus the chance for retention. Moreover, the time of contact between the filling and CR is also reduced (the pump works at the same flow rate for sortion and desorption and it is never stopped). Therefore two combined effects, efficiency of retention onto APS and efficiency of complex release, are responsible for signal decay.

All this operations were carried out in a reverse FI manifold where the sample takes the place of the carrier solution giving us the flexibility for changing the time of contact and thus, the efficiency of retention of the filling. On the other hand, CR was injected in the sample stream, obliging to the use of a fast reaction to release the analyte. These facts will be discussed below under Section 3.5 dedicated to the design of the FI system.

3.4. Influence of the injected volume of CR on the analytical signal

Fig. 4 shows the influence of the injected volume of CR on the analytical signal (peak height) of chromium. The concentration of CR was the maximum compatible with the complete dissolution of DPC in the acetone/sulfuric acid media. Lower concentrations were not employed as the volume of injection should be raised with the consequent decrease of PCF. Values ranging
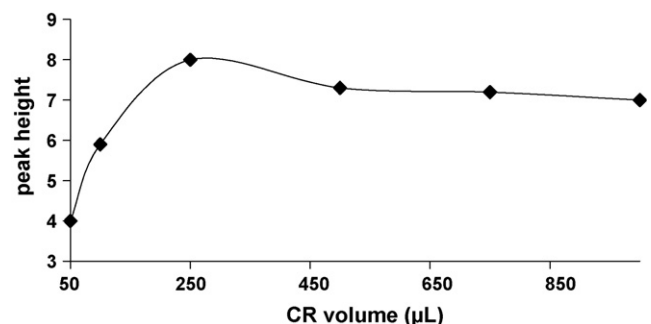
between 50 and 1000 μL were assayed, keeping the volumetric flow rate for sorption/desorption equal to 1 mL min^{-1} and t_{pc} equal to 240 s.

A value of 250 μL was found as optimal for chromium release and color development and it was employed for all the experiments throughout this work. Lower values showed a decrease in the analytical signal probably due to a lack of reagent and/or a poor interaction between Cr(VI) and CR. Higher values showed the presence of asymmetric double peaks. This fact can be ascribed to a deficiency of the analyte in the center of the sample bolus which leads to the appearance of humped peaks and thus, to a decrease of the peak height at the maximum of the transient signal.
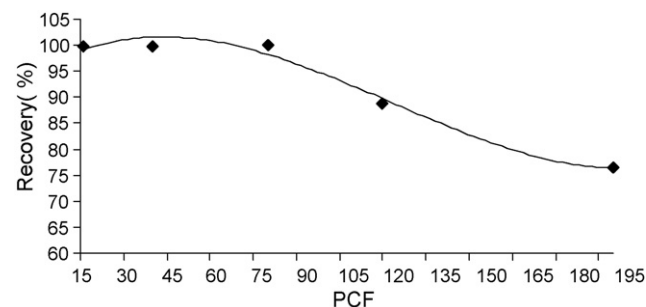
Fig. 5. Percentage of recovery of Cr(VI) for different PCF values. [Cr(VI)]:10 μg L^{-1}; PCF: 16–200; CR volume: 250 μL; [CR]: 0.2% (w/v) DPC in Acetone 1:4 and 0.1 mol L^{-1} H$_2$SO$_4$; flow rate of sorption/desorption: 1 mL min^{-1}.

Table 1a
Studies of Cr(VI) recovery with cationic and anionic interferences for 3 μg L^{-1} Cr(VI)

Interference	Concentration (μg L^{-1})	Recovery (%)[a]
Al(III)	100	97.6 $\pm$ 0.2
	250	99.3 $\pm$ 0.4
	500	97.2 $\pm$ 0.3
Cu(II)	20	98.5 $\pm$ 0.2
	200	94.7 $\pm$ 0.2
Zn(II)	100	95.3 $\pm$ 0.1
	1,000	94.0 $\pm$ 0.1
Fe(III)	100	98.7 $\pm$ 0.2
	1,000	102.0 $\pm$ 0.1
Ca(II)	50,000	77.4 $\pm$ 0.3
Mg(II)	50,000	81.3 $\pm$ 0.3
Cr(III)	100	96.7 $\pm$ 0.3

[a] Errors are expressed according to Massart et al. [17] (numbers of replicates: 3).

Table 1b
Studies of Cr(VI) recovery with anionic interferences for 3 μg L^{-1} Cr(VI)

Interference	Concentration (mol L^{-1})	Recovery (%)[a]
Sulfates	10^{-3}	86.4 ± 0.2
Phosphates	10^{-3}	99.2 ± 0.2
Chlorides	0.1	99.3 ± 0.1
Nitrates	0.1	98.5 ± 0.2

[a] Errors are expressed according to Massart et al. [17] (numbers of replicates: 3).

3.5. The design of the rFI manifold

To improve the analytical performance of the method presented in this work, it is necessary to look for the quantitative sorption of Cr(VI) on the APS filling together with its complete release in the lower volume of eluant attainable. As it was told under introduction, the time of contact analyte/mesoporous material needs to be large in order to obtain an efficient retention and thus, only "batch" procedures are reported in the literature. Therefore, "on-line" operation requires a FI manifold designed to permit rather large times for sorption of Cr(VI) even though the sample throughput is diminished. To accomplish this, we designed a reverse FI manifold where the sample flows along the carrier channel interacting for a given time with the filling. Regarding the complete release of Cr(VI), we found DPC in sulfuric acid as a very suitable eluant as it allows the reduction of Cr(VI) to Cr(III) together with the development of the colored Cr(III)-diphenylcarbazone complex in a very short time with a minimal volume of CR. So, chromium is retained in the anionic form and it is released as a cation since the filling remains protonated all along the measurement. Additionally, elution is easy as both reactions, electron transfer and complex production, are fast [14,15]. Another advantage is the lifetime of the filling material: since the redox environment is always reductor there is no place for degradation of APS and thus, more than 300 cycles are carried out with no drop of sensitivity.

As told in Section 3.4, keeping the elution volume in 250 μL and employing a solution of 10 μg L^{-1} Cr(VI), a preconcentration time of 240 s at a volumetric flow rate of 1 mL min^{-1} was found at optimum.

Fig. 5 shows the percentage of recovery of 10 μg L^{-1} Cr(VI) for different PCF values. The obtained signals were compared to those resulting from the direct colorimetric determination of solutions containing Cr(VI) concentrations equal to those expected for a 100% of recovery.

Fig. 5 shows that at PCF values around 16, a 100% recovery of Cr(VI) is found. From PFC 80 onwards an important decay is observed revealing that all the sites of sorption were already fulfilled with the analyte.

Another important issue to discuss is the interference of sulfuric acid as it is a component of CR. Luckily, a 250 μL injection volume

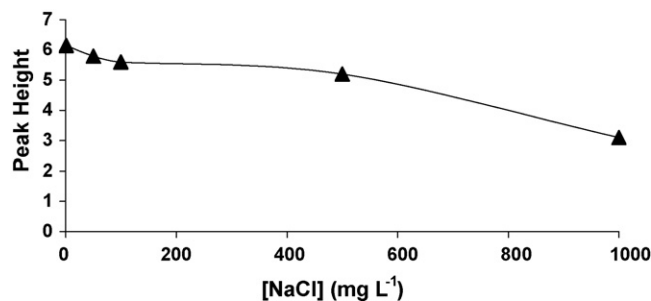**Fig. 6.** Effect of salinity on the analytical signal. [Cr(VI)]: 5 μg L^{-1}; PCF: 16; CR volume: 250 μL; [CR]: 0.2% (w/v) DPC in Acetone 1:4 and 0.1 mol L^{-1} H$_2$SO$_4$; flow rate of sorption/desorption: 1 mL min^{-1}.

passing through the column involves just 0.47 s of contact time eluant/filling (bed volume of APS equal to 7.9 μL). This time is large enough to free the analyte but short enough to impede the retention of HSO$_4^-$. In this way, there is no chance for this reagent to interfere Cr(VI) sorption during the next sample loading. So, this analytical approach reinforces the assertion of Hansen and Miró [16] regarding the possibility of executing novel procedures based on kinetic discrimination schemes by flow injection. The fortunate chances given by the rFI system presented here, meaning a large time of contact of the analyte with the filling together with short time of contact of the main interference, makes FI (or related techniques) the unique possibility for carrying out this application.

3.6. Determination of Cr(III)

Taking into account that Cr(III) occurs in higher concentrations than Cr(VI) in natural waters and that ET AAS shows more sensitivity than UV–visible spectrophotometry, it is easy to perform Cr(III) determination by ET AAS without appealing to a preconcentration process. However, it is worthy to mention that this procedure must be performed just in those cases where a 100% recovery of Cr(VI) is obtained after SPE. Otherwise, systematic positive errors should be obtained as it will be discussed below.

3.7. Study of anionic and cationic interferences on Cr(VI) sorption

A study of cationic and anionic interferences of usual occurrence in natural waters was carried out employing the analytical methodology described here (Table 1a). Al(III), Fe(III), Zn(II), Cr(III) and Cu(II) solutions of concentrations up to 10 times higher than those of river waters were assayed showing no signal decay. Ca(II) and Mg(II) showed 81.3% and 77.4% recovery, respectively, which can be attributed to the production of a non-charged complex between Cr(VI) and Ca or Mg that obliges to work with the addition

Table 2
Determination of trace levels of Cr(VI) and Cr(III) in DIW, tap, mineral osmosis and groundwaters

Sample	Cr(VI) added (μg L^{-1})	Cr(III) added (μg L^{-1})	Cr(VI) found (μg L^{-1})[a] (proposed method)	Cr(III) found (μg L^{-1})[a] (ET AAS)[b]	Total Cr (μg L^{-1})[a] (ET AAS)[b]
DIW water	0	0	0	0	0
	2	2	2.1 ± 0.1	2.1 ± 0.1	4.4 ± 0.2
Osmosis water	0	0	0.0 ± 0.1	5.8 ± 0.1	5.8 ± 0.2
	2	2	1.9 ± 0.1	7.9 ± 0.1	9.8 ± 0.2
Tap water	0	0	0.0 ± 0.1	0.8 ± 0.1	0.8 ± 0.2
	2	2	2.1 ± 0.1	3.1 ± 0.1	5.2 ± 0.2
Mineral water	0	0	0.0 ± 0.1	2.2 ± 0.1	2.2 ± 0.2
	2	2	2.0 ± 0.1	4.4 ± 0.1	6.4 ± 0.2

[a] Errors are expressed according to Massart et al. [17] (numbers of replicates: 3).
[b] Referee methodology employed for validation.

Table 3
Comparison of the analytical performance of the proposed method for Cr(IV) determination with that of SI-BI-LOV system using DPC-loaded C_{18}-PS/DVB, open tubular PTFE knotted reactors and permanent sorbet microcolumns prior to Cr(VI) determination via ET AAS

Parameter	This work	Column-in-tip-ET AAS [24]	KR PTFE-ET AAS [25]	SI-BI-LOV-ET AAS [26]
Regression equation (Cr, $\mu g\,L^{-1}$)	1.62[Cr]+0.03	0.089[Cr]+0.034	0.37[Cr]+0.034	0.27[Cr]+0.002
Correlation coefficient	0.998	0.9992	0.997	0.998
Linear range ($\mu g\,L^{-1}$)	0.09–3	0.4–8	0.01–1.25	0.12–1.5
Sample volume (mL)	4	5	2	2
Loading flow rate (mL min^{-1})	1	2	5	4.5
Limit of detection ($\mu g\,L^{-1}$, 3 s)	0.09 ($n=10$)	0.08	0.016	0.03
R.S.D.%	1.8	3.5	2.4	3.8
Enrichment factor	16.0	5.6	16.3	12.9
Sample frequency (h^{-1})	15	28	16.7	15
Lifetime	300	Not reported	Not reported	Renewable
Column dimension length (cm) × i.d.(cm)	1 × 0.1	0.5 × 0.3	125 × 0.05	0.7 × 0.16

of standards to the sample. A pre-treatment with a strong complexing agent as EDTA seems not possible due to the acid pH of the sample. Moreover, the excess of ligand, for sure in the anionic form and as sodium salt, should become in an interference even more severe than Ca and Mg themselves. This will be explained below.

Mineral acids sulfuric, nitric, hydrochloric and phosphoric were also tested (Table 1b). Nitric acid promotes a drift of the baseline at the moment of the measurement but does not produce a signal drop. HCl shows no interference up to 0.01 mol L^{-1} and it was the most suitable choice for APS conditioning. H$_2$SO$_4$ interferes for concentrations beyond 0.001 mol L^{-1}. No signal decay was noticed for H$_3$PO$_4$ (or H$_2$PO$_4^-$) up to 0.001 mol L^{-1}. We assume that there is a different accessibility to the filling pores since the size of the hydrated ion H$_2$PO$_4^-$ is larger than HSO$_4^-$ and thus, the tolerance is greater for the former.

Regarding the salinity of the samples, the effect on the analytical signal of 5 $\mu g\,L^{-1}$ Cr(VI) is shown in Fig. 6. It is observed a significant drop of sensitivity for solutions containing 1000 g L^{-1} NaCl which makes the proposed methodology unsuitable for seawater analysis. Moreover, as Cr(III) is detected at the end of the APS column, results for Cr(III) should be overestimated in those samples where the percentage of recovery of Cr(VI) falls below 100%. Conversely, Cr(VI) can be always measured with accuracy and precision by employing direct interpolation of the signal in the calibration curve (complete recovery) or the standard addition methodology.

3.8. Analytical performance and applications

The analytical performance of the system was obtained using the optimum conditions described above. Relative standard deviation (R.S.D.%) was 1.8% ($n=10$) and it was calculated through successive adsorption-elution cycles of synthetic samples of 3 $\mu g\,L^{-1}$ Cr(VI). The recovery of Chromium (PCF=16) was 99.8% and the limit of detection (LOD, calculated as three times the standard deviation of the blank signal, $n=10$) was found equal to 0.09 $\mu g\,L^{-1}$ of Cr(VI). The calibration curve was linear over the concentration range 0.09–3 $\mu g\,L^{-1}$. The sensitivity and the intercept obtained are 1.62 ± 0.02 $\mu g\,L^{-1}$ and 0.03 ± 0.5 $\mu g\,L^{-1}$, respectively (95% confidence level). The comparison of sensitivities between the proposed method and the rFI without preconcentration, showed no significant differences (95% of confidence level), which demonstrates that the efficiency of the APS microcolumn is very high.

In order to study the applicability of the proposed system, Cr(VI) was determined in several natural and spiked water samples due to the lack of water reference materials certified for Cr(VI) and Cr(III). Results are summarized in Table 2.

Cr(VI) determinations in osmosis, tap, mineral waters and groundwater samples can be performed by simple interpolation of the analytical signal in the calibration graph. By doing this, a 100% recovery of Cr(VI) was found for real samples and Cr(III) was easily

determined at the end of the MC. Standard addition methodology needs to be applied in the case the effluent water for Cr(VI) determination. Cr(III) should be overestimated in these cases and it is not a recommendable choice.

4. Conclusions

The analytical methodology described here employs for the first time an hybrid mesoporous material for the on-line retention of Cr(VI) followed by its elution as charged red complex and its simple spectrophotometric detection by means of a fast one-step procedure. It exploits the unique characteristics of FI, allowing us to employ the reproducibility of times of contact between the samples and the mesoporous filling to carry out the determination itself and to avoid serious interferences, specially that produced by sulfuric acid as part of the CR. The analytical features are improved in comparison to those already reported by several authors that employ SPE coupled to FAAS [18,19] or SPE coupled to ICP OES [20,21]. Similar results to ours were reported by other authors [22–26] who employed more sophisticated techniques for detection such as ET AAS or ICP MS (Table 3). However, it is worthy to recognize that we have limitations on seawater analysis, circumstance that is overcome by Long et al. [26]. With respect to Cr(III) determinations, they are only possible for osmosis, tap, mineral and groundwaters.

Regarding the analytical applications of hybrid mesoporous materials, they seem quite promising in conjunction with FI systems that take advantage of kinetic discrimination.

References

[1] M. Miro, J.M. Estela, V. Cerdá, Talanta 63 (2004) 201.
[2] V. Gómez, M.P. Callao, Trends Anal. Chem. 25 (10) (2006) 1006.
[3] P.K. Jal, S. Patel, B.K. Mishra, Talanta 62 (2004) 1005.
[4] H. Yoshitake, E. Koiso, H. Horie, H. Yoshimura, Micropor. Mesopor. Mater. 85 (2005) 183.
[5] D. Pérez-Quintanilla, I. del Hierro, M. Fajardo, I. Sierra, Mater. Res. Bull. 42 (2007) 1518.
[6] J. Li, X. Miao, Y. Hao, J. Zhao, X. Sun, L. Wang, J. Colloid Interface Sci. 318 (2008) 309.
[7] G. Wu, Z. Wang, J. Wang, C. He, Anal. Chim. Acta 582 (2007) 304.
[8] J. Fan, C. Wu, Y. Wei, C. Peng, P. Peng, J. Hazards Mater. 145 (2007) 323.
[9] D. Pérez-Quintanilla, A. Sánchez, I. del Hierro, M. Fajardo, I. Sierra, J. Sep. Sci. 30 (10) (2007) 1556.
[10] C.E. Fowler, S.L. Burkett, S. Mann, Chem. Commun. 18 (1997) 1769.
[11] R.T. Pflaum, L.C. Howick, J. Am. Chem. Soc. 78 (1956) 4862.
[12] K.F. Lam, K.L. Yeung, G. McKay, Micropor. Mesopor. Mater. 100 (2007) 191.
[13] M. Fritzen, A.J. Souza, T.A.G. Silva, L. Souza, R.A. Nome, H.D. Fiedler, F. Nome, J. Colloid Interface Sci. 296 (2006) 465.
[14] G.A. Crespo, F.J. Andrade, M.B. Tudino, F.A. Iñón, Anal. Chim. Acta 539 (2005) 317.

[15] F.A. Iñón, F.J. Andrade, M.B. Tudino, O.E. Troccoli, J. Flow Injection Anal. 17 (2) (2000) 174.

[16] E.H. Hansen, M. Miró, Trends Anal. Chem. 26 (1) (2007) 18.

[17] D.L. Massart, B.G.M. Vandeginste, L.M.C. Buydens, S. De Jong, P.J. Lewi, J. Verbeke, Handbook of Chemometrics and Qualimetrics (Part A and B), Elsevier Science B.V., Amsterdam, 1997.

[18] S. Pramanik, S. Dey, P. Chattopadhyay, Anal. Chim. Acta 584 (2007) 469.

[19] A.N. Anthemidis, S.J.V. Koussoroplis, Talanta 71 (2007) 1728.

[20] A.A. Menegário, P. Smichowski, G. Polla, Anal. Chim. Acta 546 (2005) 244.

[21] J. Chwastowska, W. Skwara, E. Sterlińska, L. Pszonicki, Talanta 68 (2005) 388.

[22] J. Chwastowska, W. Skwara, E. Sterlińska, L. Pszonicki, Talanta 66 (2005) 1345.

[23] B. Wen, X.Q. Shan, J. Lian, Talanta 56 (2002) 681.

[24] W. Som-Aum, S. Liawruangrath, E.H. Hansen, Anal. Chim. Acta 463 (2002) 99.

[25] M.T. Siles-Cordero, E.I. Vereda-Alonso, A. García de Torres, J.M. Cano-Pavón, J. Anal. Atom. Spectrom. 19 (2004) 398.

[26] X. Long, M. Miró, E.H. Hansen, Anal. Chem. 77 (2005) 6032.

Contents lists available at ScienceDirect

Talanta

Determination of trace cobalt(II) by adsorptive stripping voltammetry on disposable microfabricated electrochemical cells with integrated planar metal-film electrodes

Christos Kokkinos, Anastasios Economou*, Michael Koupparis

Laboratory of Analytical Chemistry, Department of Chemistry, University of Athens, 157 71 Athens, Greece

ABSTRACT

This work reports the determination of trace Co(II) by adsorptive stripping voltammetry on disposable three-electrode cells with on-chip metal-film electrodes. The heart of the sensors was a bismuth-film electrode (BiFE) with Ag and Pt planar strips serving as the reference and counter electrodes, respectively. Metals were deposited on a silicon chip by sputtering while the areas of the electrodes were patterned via a metal mask. Co(II) was determined by square wave adsorptive stripping voltammetry (SWAdSV) after complexation with dimethylglyoxime (DMG). The experimental variables (the DMG concentration, the preconcentration potential, the accumulation time and the SW parameters), as well as potential interferences, were investigated. Using the selected conditions, the 3σ limit of detection was 0.09 μg l^{-1} of Co(II) (for 90 s of preconcentration) and the relative standard deviation for Co(II) was 3.8% at the 2 μg l^{-1} level ($n = 8$). The method was applied to the determination of Co(II) in a certified river water sample. These mercury-free electrochemical devices present increased scope for field analysis and μ-TAS applications.

© 2008 Elsevier B.V. All rights reserved.

1. Introduction

Mercury electrodes, despite their advantages for electroanalysis, are associated with the use, manipulation and disposal of mercury and mercury salts. Since these compounds are toxic, they are considered unsafe and are gradually phased out of laboratories and in some cases their use is completely banned [1,2]. Over the last year, attempts have been made to replace mercury with more environmental-friendly electrode materials while retaining the advantageous analytical properties of the former. Among electrode materials proposed as alternatives to mercury, bismuth [3], and very recently antimony [4], are the most promising, their main advantage being their negligible toxicity compared to mercury. Bismuth-based electrodes, especially in the form of bismuth-film electrodes (BiFEs) – consisting of a thin bismuth film deposited on a suitable substrate – have been extensively studied and have been shown to offer comparable performance to mercury electrodes in stripping voltammetry [5–7]. There are several reports of the determination of different metals such as Pb, Cd, Tl, In, Ni, Co, Al, Cr, U, Mo, Fe, V, as well of some organics, on bismuth electrodes by anodic stripping voltammetry (ASV) and adsorptive stripping voltammetry (AdSV) [5–7].

The major difficulty associated with the use of BiFEs is the generation and maintenance of the bismuth layer that serves as the active electrode surface [5–7]. By far the most widely adopted method for fabricating a BiFE has been, and still is, electrolysis in which Bi(III) existing is solution is reduced and deposited on a conductive substrate as metallic bismuth. Yet, there are several drawbacks associated with this approach. *Ex-situ* Bi plating (preplating) requires a separate bismuth-plating step from a Bi(III) solution (which complicates the experimental procedure and extends the analysis time). *In-situ* Bi plating, which involves spiking the sample solution with Bi(III) ions, is limited to acidic or strongly alkaline media (in which Bi(III) ions are stable in solution) and is not applicable to slightly acidic, neutral or moderately alkaline media (in which Bi(III) easily hydrolyses) [4]. Also, the use of a – usually expensive – conductive support for the bismuth film is necessary. In addition, the surface of the bismuth layer is critically dependent on the chemical, physical and instrumental conditions during the deposition. Finally, as soon as the bismuth coating is damaged or inactivated, the substrate must be cleaned and the coating process repeated, resulting in a laborious and time-consuming procedure.

Recently, we proposed an alternative microfabrication method for the preparation of BiFEs, based on sputtering of a silicon substrate with bismuth [8,9]. Although thin-film sensors fabri-

---

* Corresponding author. Tel.: +30 210 7274298; fax: +30 210 7274750.
E-mail address: aeconomo@chem.uoa.gr (A. Economou).

cated by sputtering of different metals (e.g. Au, Ag and Pt) have been reported previously for electrochemical detection [10–13], Bi-sputtered electrodes have a wider scope since they can serve as substitutes of mercury electrodes. The application of this thin-film approach for the fabrication of BiFEs offers several advantages compared to electroplating. In particular, neither a Bi(III) plating solution nor a conductive substrate are required resulting in a simpler, shorter and low-cost fabrication procedure. Also, unlike their *in-situ* plated counterparts, these sputtered BiFEs are applicable to media covering a wide pH range. Besides, the fabrication technology ensures strict control and reproducibility of the surface area and morphology of the electrode. Finally, the use of standard thin-film technology offers the potential for mass-production of inexpensive and disposable devices with a variety of configurations. Although, these microfabricated BiFEs can be used as working electrodes in a conventional configuration with external counter and reference electrodes [8,9], thin-film technology can be further exploited for the fabrication of complete sensors with integrated on-chip planar electrodes. Miniaturised cells with integrated electrodes have drawn great attention since they can be easily used for on-site analysis, are low-cost and disposable and can be combined with micro-total analysis systems (μ-TAS) [14–17]. However, there is only a very limited number of applications using electrochemical cells with on-chip electrodes for stripping voltammetry and in particular utilising BiFEs as working electrodes. Recently, a plastic injection-moulded cell has been developed with integrated conductive electrodes for AdSV but the construction of theses devices is complex and *ex-situ* plating of the working electrode with Bi is required [18]. Also, a three-electrode cell fabricated by stepwise lithography has been reported featuring a sputtered Bi working electrode for ASV [19]. However, the reported limits of detection are rather high while lithography is a rather complex fabrication method exposing the thin-film electrodes to solvents with the risk of being damaged.

In this work, miniaturised cell-on-a-chip sensors featuring integrated metal-film electrodes (a Bi-film working electrode, a Ag-film reference electrode and a Pt-film counter electrode), fabricated by a non-lithographic method, were tested for the determination of Co(II) by square wave adsorptive stripping voltammetry (SWAdSV) after complexation with dimethylglyoxime (DMG) and the method developed was successfully applied to the analysis of water samples.

2. Experimental

2.1. Instrumentation

A home-made potentiostat was interfaced to a Pentium PC through a multi-function interface card (6025 E PCI, National Instruments, TX). SWASV were carried out by purpose-developed application programmes developed in LabVIEW 7.1 [20]. Experiments were carried out in a standard electrochemical cell. An atomic force microscope (AFM) (SPM SMENA, NT-MDT Co., Moscow, Russia) was used for imaging of the surface of the electrodes.

2.2. Reagents and glassware

All the chemicals were of analytical grade. Doubly distilled water was used throughout. Working metal ion solutions were prepared from 1000 mg l^{-1} atomic absorption standard solutions after appropriate dilution with water. The stock supporting electrolyte was ammonia buffer (1 mol l^{-1} in total ammonium species, pH 9.2) prepared by mixing the appropriate amounts of NH$_3$ and HCl. A 0.1 mol l^{-1} stock solution of DMG was prepared by dissolving the
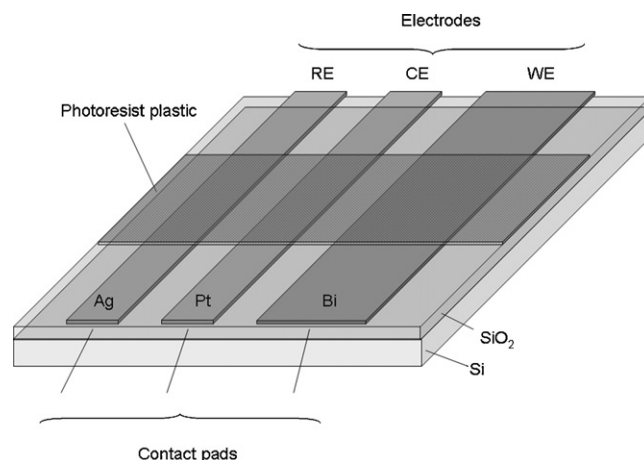

Fig. 1. Schematic diagram of the microfabricated devices.

appropriate amount of DMG in absolute ethanol. A 2 × 10^{-3} mol l^{-1} stock solution of EDTA and a 1000 mg l^{-1} stock solution of Triton X-100 (BDH, Poole, England) were prepared in water.

2.3. Fabrication of the sensors

A schematic diagram of a sensor is illustrated in Fig. 1. An aluminium plate manufactured by a thin sheet of aluminium and featuring slots for the three electrodes was used as a mask to define the area of the electrodes. Silicon wafers (3 in. in diameter, 500 μm in thickness) were covered with a layer of SiO$_2$ 1080-nm thick by means of wet thermal oxidation. The metal mask was attached firmly on the wafer and Ti was first sputtered on the silicon areas intended for the reference and counter electrodes to a thickness of 5 nm by covering the slot intended for the working electrode. This layer was found to be necessary for better adhesion of the Ag and Pt films on the wafer. Then, the three electrodes were formed by successively sputtering each metal in the order Ag (800 nm), Pt (400 nm) and Bi (400 nm) on the wafer at the respective slots by covering the other two slots with a plastic sheet. As soon as the three electrodes were formed, the sensing area of the device was isolated from the contact/grip pads using a simple photolithographic step. The final dimension of the working areas of the electrodes were: WE 4 mm × 5 mm; CE 3 mm × 5 mm; RE 3 mm × 5 mm.

Before use, the sensor was immersed into a 0.1 mol l^{-1} KCl solution and the Ag and Pt electrodes were connected to the anode and cathode, respectively, of a power supply. A current of 1 mA was applied for 10 s in order to cover the Ag reference electrode with AgCl.

2.4. Sample preparation

Five milliliter of the certified river water (TM-23.3, NWRI, Canada) was buffered to pH 9.2 using ammonia solution, the solution was transferred to a 10.0-ml volumetric flask, 1.0 ml of the 1 mol l^{-1} ammonia buffer (pH 9.2) was added and the sample was diluted to the mark with distilled water.

Five milliliter of tap-water was transferred to a 10.0-ml volumetric flask, 1.0 ml of the 1 mol l^{-1} ammonia buffer (pH 9.2) was added and the sample was diluted to the mark with distilled water.

2.5. Determination of Co(II)

The sensor was immersed into the sample solution, the sample was spiked with the required volume of the DMG solution (to give

the desired final DMG concentration) and the preconcentration was carried out at the selected preconcentration potential under stirring. After accumulation, a cathodic SW scan was applied to the working electrode to a final potential of -1.35 V while the voltammogram was recorded. After the scan, the bismuth film was cleaned of the remaining adsorbed complex by keeping the potential of the electrode at -1.35 V for 10 s. After the cleaning step, standard additions of Co(II) were made as required and the measurement procedure repeated on the same sensor.

3. Results and discussion

Macroscopic inspection of the sputtered metal films revealed a uniform shiny surface. Close examination of the fine structure was performed by inspection with AFM at different areas of the electrodes which indicated that complete coverage of the surface was achieved with no bare SiO_2 areas visible. These images also suggested that the metal layers in fact consisted of minute grains (Fig. 2). However, the Ag and Pt layers possessed smoother sur-
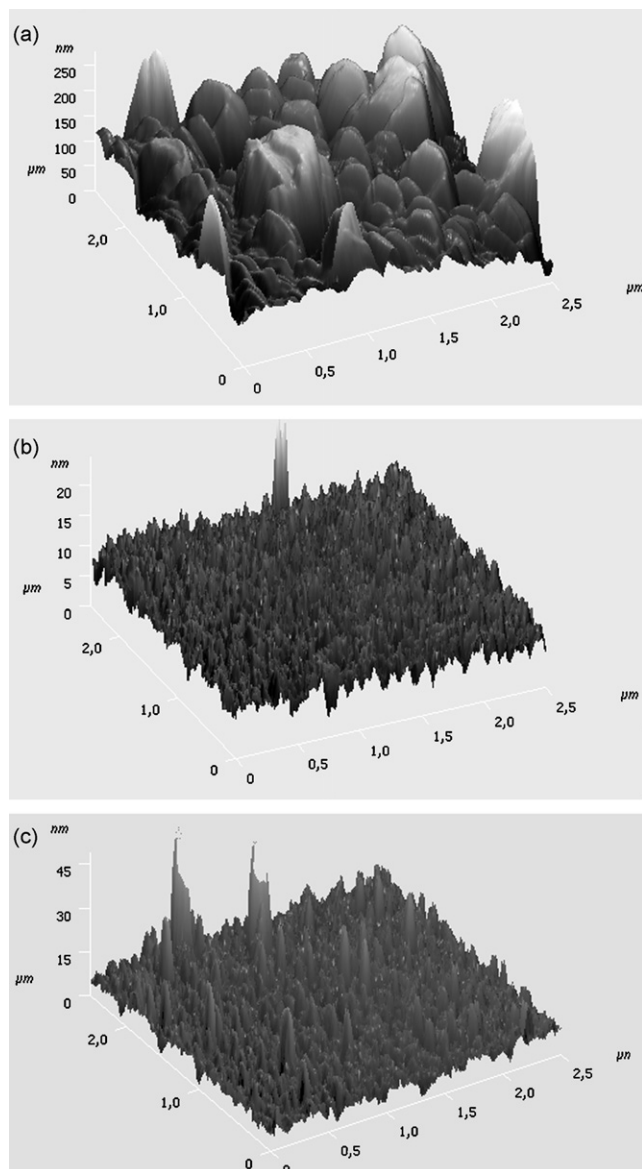
faces with smaller and more densely packed grains with average height (roughness) of a few nanometers and an average grain diameter of around 25 nm. In contrast, the bismuth layer exhibited a rougher surface with grains of columnar structure with average height (roughness) of 100 nm and an average grain diameter of 200 nm. Sputtered bismuth on different materials is known to exhibit a coarse and irregular surface [21,22]. It was assumed that the smoothness of their surface is presumably the reason why deposition of Ag and Pt required a buffer layer of Ti for good adherence onto SiO_2 (a common practice in most microfabrication applications involving those metals), otherwise the metal films would peel-off if immersed in the solution. It seems that bismuth, with its coarser surface morphology, adhered better on the SiO_2 layer and, therefore, did not require the incorporation of any buffer layer since a buffer of Ti did not offer any improvement in mechanical stability. Microscopic examination of the metal-film electrodes, an especially the Bi working electrode, after prolonged use in the ammonia buffer (pH 9.2) showed some erosion of their surface which led to inactivation of the sensors and gradual decrease in their response. Each device could be used for at least 15 preconcentration/stripping cycles in the semi-disposable mode.

A cyclic voltammogram (in the range -0.75 to -1.35 V) in a solution containing Co(II) in the presence of DMG after 30 s preconcentration on the BiFE is shown in Fig. 3. The cathodic scan revealed a peak at -1.18 V arising from the reduction of the Co(II)–DMG complex which had adsorbed on the BiFE. No peak was observed in the anodic scan suggesting that the reduction of the complex was an irreversible process which was in agreement with results obtained on electroplated BiFEs [23].

The effect of the DMG concentration on the Co peak height was investigated in the range $0.01–2.5$ mmol l^{-1} and is illustrated in Fig. 4(a). The Co peak height increased with increasing DMG concentration and essentially stabilized for DMG concentrations higher than 2 mmol l^{-1}. Therefore, a DMG concentration of 2 mmol l^{-1} was selected for subsequent experiments. A similar behavior has been documented on electroplated BiFEs [23] and MFEs [24].

The effect of the preconcentration potential on the Co peak height in a solution containing Co(II) was studied in the range -0.60 to -1.10 V and is shown in Fig. 4(b). The Co peak height increased as the deposition potential become more negative in the range -0.60 to -1.00 V. This behavior is attributed to the fact that the Co(III)–DMG complex is positively charged and has a higher adsorption affinity towards the negatively charged electrode surface [24].

Fig. 2. AFM images of: (a) the Bi working electrode; (b) the Pt counter electrode; and (c) the Ag reference electrode.
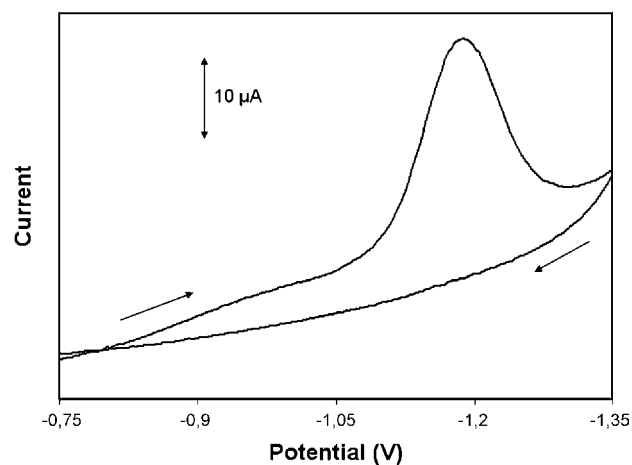

Fig. 3. A cyclic voltammogram in the potential range -0.75 to -1.35 V in a solution containing 10 μg l^{-1} of Co(II) after preconcentration for 60 s on the sputtered BiFE. DMG concentration: 2 mmol l^{-1}; deposition potential: -1.0 V; supporting electrolyte: 0.1 mol l^{-1} ammonia buffer (pH 9.2); potential scan rate: 50 mV s^{-1}.

Fig. 5. A series of SW voltammograms in a solution containing increasing Co(II) concentration in steps of $2 \mu g \, l^{-1}$ (lower trace is the blank) after preconcentration for 30 s on the sputtered BiFE (the calibration curve is shown as an inset). Other conditions as in Fig. 4.

of the adsorbed complex was approached. It is interesting to note that the equilibrium surface concentration was reached in relatively short preconcentration times (<100 s) and this was attributed to the fast adsorption of the Co(II)–DMG on the electrode surface. Indeed, it has been shown in conjunction with electroplated BiFEs that the Co(II)–DMG adsorbs preferentially on the areas of the electrode that are covered by Bi and not on the bare substrate surface [25]. The present Bi-coated electrodes, unlike electroplated BiFEs [25], are characterized by complete coverage of the electrode surface with Bi (Fig. 2(a)) and a larger surface area is therefore available for adsorption.

Next, the SW parameters of the stripping waveform (frequency, pulse height and step increment) were investigated. The effect of frequency and the scan increment was studied in the range 12.5–200 Hz and 1–16 mV, respectively, while the effect of the pulse height was examined in the range 10–80 mV. The best compromise between sensitivity, peak sharpness and background characteristics was obtained using the following conditions: SW frequency 50 Hz; SW pulse height 40 mV; SW step increment 4 mV.

Using these conditions, the linear parts of the graphs, at two deposition times of 30 and 60 s, were expressed by the equations:

30-s deposition :

$$I_{Co} \, (\mu A) = (1.02 \pm 0.03) c_{Co} \, (\mu g \, l^{-1}) + (0.65 \pm 0.27), \quad R^2 = 0.995$$

60-s deposition :

$$I_{Co} \, (\mu A) = (2.16 \pm 0.07) c_{Co} \, (\mu g \, l^{-1}) + (0.38 \pm 0.68), \quad R^2 = 0.994$$

A series of voltammograms for the concentration range $2–16 \mu g \, l^{-1}$ of Co(II) using a deposition time of 30 s is illustrated in Fig. 5. The limit of detection was calculated as $0.09 \mu g \, l^{-1}$ of Co(II) at the 3σ level (for 90 s accumulation time) and the relative standard deviation for Co(II), in terms of peak height, was 3.8% for at the $5 \mu g \, l^{-1}$ level ($n = 8$). The limit of detection were comparable with the ones obtained with electroplated BiFEs using the same complexation protocol as in the present work [23,26–28]. If lower limits of detection are desired, the microfabricated sensors could be coupled to ligands with catalytic activity that are known to provide enhancement of the Co signal [29,30].

The presence of surface-active compounds is the more serious interference in stripping analysis since such compounds can easily adsorb on the electrode and inactive its surface. Triton X-100
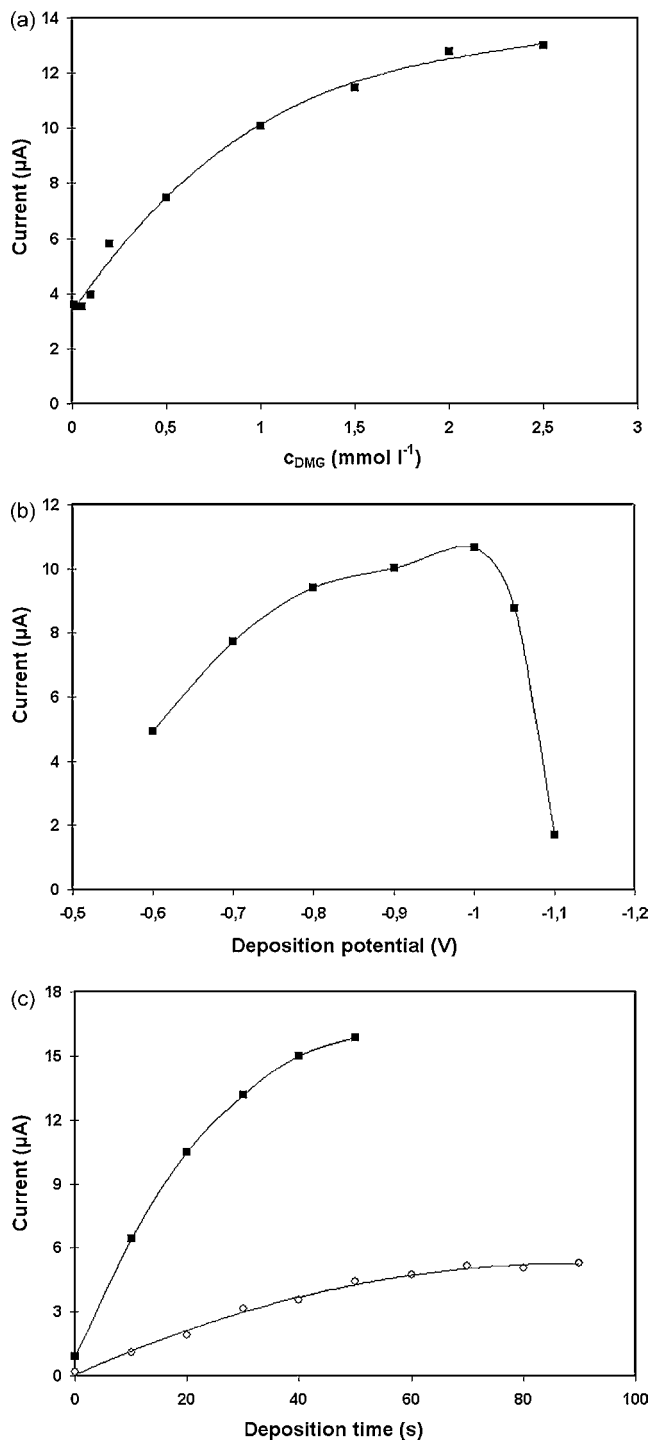

Fig. 4. Effect of: (a) the DMG concentration; (b) the preconcentration potential; and (c) the preconcentration time in a solution containing $10 \mu g \, l^{-1}$ (■) and $2.5 \mu g \, l^{-1}$ (○) of Co(II) on the Co stripping peak height after preconcentration on the sputtered BiFE. Deposition time: 30 s; SW frequency: 50 Hz; scan increment: 4 mV; pulse height: 40 mV; other conditions as in Fig. 3.

Therefore, a deposition potential of −1.00 V was selected except in cases in which Ni(II) was also present (see discussion below).

The effect of the deposition time on the Co stripping peak height in two solutions containing different Co(II) concentrations is illustrated in Fig. 4(c). The Co stripping peak height increased rectilinearly with increasing deposition time and at higher deposition times it started to level-off as the equilibrium surface concentration
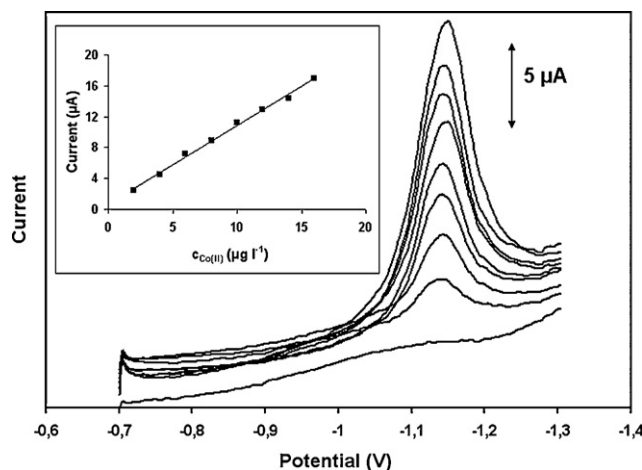
Fig. 6. The interferences by (a) Zn(II) (traces: (i) $10 \mu g l^{-1}$ Co(II); (ii) as (i) with $400 \mu g l^{-1}$ Zn(II); (iii) as (ii) with 2×10^{-3} mmol l^{-1} EDTA; (iv) as (ii) with 4×10^{-3} mmol l^{-1} EDTA); (b) Ni(II) (traces: (i) $10 \mu g l^{-1}$ Co(II) + $50 \mu g l^{-1}$ Ni(II) with deposition at -1.0 V; (ii) as (i) with deposition at -1.05 V). Other conditions as in Fig. 4.

was used to simulate the effect of typical non-ionic surfactants. It was found that the sputtered BiFE exhibited comparable sensitivity to the presence of Triton-X 100 as the electroplated BiFEs [31,32] with the Co stripping peak height being suppressed by 19, 72 and 83% in the presence of 0.1, 0.5 and 1 mg l^{-1} of Triton X-100, respectively. A number of metal ions that could potentially interfere were examined: Pb(II), Hg(II), Cu(II), Fe(II), Al(III), Cd(II), Ti(IV), Ca(II) and Mn(II) added at a 100-fold mass concentration excess over $2 \mu g l^{-1}$ Co(II) did not interfere (the criterion for interference was a $\pm 10\%$ error in the peak height of Co). Zn(II), when present at a higher than 100-fold mass concentration excess over Co(II), produced a diffusion-controlled (not adsorptive) stripping peak at -1.25 V that partially overlapped with the Co stripping peak. This interference was eliminated by the addition of EDTA that preferentially complexed Zn(II), as illustrated in Fig. 6(a). On electroplated BiFEs, Ni(II) produces a stripping peak on the anodic side of, and is well resolved from, the Co(II) peak allowing simultaneous determination of Ni(II) and Co(II) [23]. On the sputtered BiFE, Ni(II) produced a stripping peak at -1.06 V which was too close to the Co(II) peak potential to enable separation between the two peaks (Fig. 6(b)-(i)). However, it was possible to achieve selective determination of Co(II) in the presence of excess Ni(II) by judicious selection of the instrumental and chemical conditions. Indeed, it has been documented earlier,
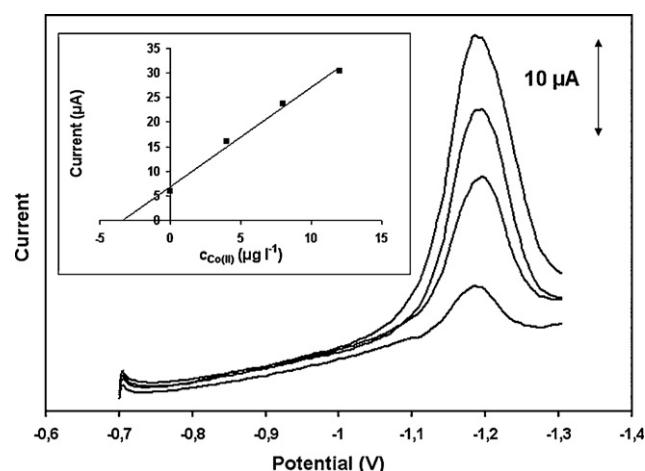

Fig. 7. SW voltammograms for the determination of Co(II) in a certified river water sample after preconcentration for 60 s on a sputtered BiFE (the standard additions plot is shown as an inset). From below: sample and three successive standard additions of $4 \mu g l^{-1}$ Co(II). Deposition at -1.05 V; other conditions as in Fig. 4.

and confirmed in the present work, that higher DMG concentrations and longer accumulation times favour the adsorption of the Co(II)–DMG complex over the Ni(II)–DMG complex on BFEs [23,33]. Also, performing the deposition at a potential more negative than -1.00 V allowed selective adsorption of the Co(II)–DMG complex and suppression of the Ni peak, as illustrated in the voltammogram of Fig. 6(b)-(ii) which was taken at an accumulation potential of -1.05 V; however, a small amount of the Ni(II)–DMG complex also adsorbed indicated by a weak Ni peak. By carrying out the deposition in the potential range -1.05 to -1.08 V, the selectivity towards Ni(II) was further increased but at the expense of sensitivity in the determination of Co(II) (since the accumulation of the Co(II)–DMG complex also decreased at more negative accumulation potentials (Fig. 4(b)). At an accumulation potential of -1.05 V, Co(II) could be determined in the presence of a 20-fold mass concentration excess of Ni(II).

The accuracy of the method was assessed by determining Co(II) in a tap-water sample and a certified river water sample. In the tap-water sample, Co(II) was under the limit of detection and the recovery was calculated by spiking the sample with $6 \mu g l^{-1}$ of Co(II) and performing the analysis by the standard addition method with a mean recovery of 108% ($n = 3$). In this case, a Zn peak also appeared that overlapped with the Co peak and this interference was eliminated by adding EDTA to a final concentration of 6×10^{-3} mmol l^{-1}, as discussed preciously. A series of voltammograms after standard additions of Co(II) in the river water sample is illustrated in Fig. 7 and the standard additions plot is shown as an inset. The Co(II) concentration determined was $7.1 \pm 0.6 \mu g l^{-1}$ ($n = 3$) compared to the reference value of $6.7 \pm 0.9 \mu g l^{-1}$.

4. Conclusions

This work reports the trace determination of Co(II) by AdSV on mercury-free and disposable microfabricated voltammetric sensors with integrated planar metal-film electrodes. The electrodes were fabricated by sputtering metals (bismuth for the working electrode, Pt for counter electrode and Ag for the reference electrode) on a silicon substrate by means of a mask. The cells were tested for the determination of trace Co(II) by SWAdSV. The relevant chemical and instrumental parameters were investigated and the devices were employed to determine Co(II) in water samples. These sensors are environmentally friendly, disposable, easy to mass produce, exhibit sensitivity comparable to mercury elec-

trodes and are ideally suited for filed measurements and μ-TAS applications.

Acknowledgements

References

[1] Swedish Chemicals Inspectorate, (KEMI) Mercury: investigation of a total ban (KEMI report No 4/04). KEMI, Stockholm, 2004, http://www.kemi.se/upload/Trycksaker/Pdf/Rapporter/Rapport4_04.pdf (accessed on May 13, 2008).
[2] European Commission, Commission proposes strategy to deal with mercury pollution including a ban on exports (Press Release IP/05/114). EC, Brussels, 2005, http://europa.eu.int/rapid/pressReleasesAction.do?reference=IP/05/114&format=HTML&aged=0&language=EN&guiLanguage=en (accessed on May 13, 2008).
[3] J. Wang, J.M. Lu, S.B. Hocevar, P.A.M. Farias, B. Ogorevc, Anal. Chem. 72 (2000) 3218.
[4] S.B. Hocevar, I. Svancara, B. Ogorevc, K. Vytras, Anal. Chem. 79 (2007) 8639.
[5] A. Economou, TrAC 24 (2005) 334.
[6] J. Wang, Electroanalysis 17 (2005) 1341.
[7] C. Kokkinos, A. Economou, Curr. Anal. Chem. 4 (2008) 183.
[8] C. Kokkinos, A. Economou, I. Raptis, C.E. Efstathiou, T. Speliotis, Electrochem. Commun. 9 (2007) 2795.
[9] C. Kokkinos, A. Economou, I. Raptis, C.E. Efstathiou, Electrochim. Acta 53 (2008) 5294.
[10] D. Xu, K. Huang, Z. Liu, Y. Liu, L. Ma, Electroanalysis 13 (2001) 882.
[11] P. Masawat, S. Liawruangrath, J.M. Slater, Sens. Actuat. B Chem. 91 (2003) 52.
[12] J. Cheng, P. Jandik, X. Liu, C. Pohl, J. Electroanal. Chem. 608 (2007) 117.
[13] J. Cheng, P. Jandik, N. Avdalovic, Anal. Chim. Acta 536 (2005) 267.
[14] Z. Zou, J. Han, A. Jang, P.L. Bishop, C.H. Ahn, Biosens. Bioelectron. 22 (2007) 1902.
[15] R.P. Baldwin, T.J. Roussel Jr., M.M. Crain, V. Bathlagunda, D.J. Jackson, J. Gullapalli, J.A. Conklin, R. Pai, J.F. Naber, K.M. Walsh, R.S. Keynton, Anal. Chem. 74 (2002) 3690.
[16] J.H. Kim, C.J. Kang, Y.S. Kim, Biosens. Bioelectron. 20 (2005) 2314.
[17] K.S. Yun, J. Gil, J. Kim, H.J. Kim, K. Kim, D. Park, M.S. Kim, H. Shin, K. Lee, J. Kwak, E. Yoon, Sens. Actuat. B Chem. 102 (2004) 27.
[18] N.G. Naseri, S.J. Baldock, A. Economou, N.J. Goddard, P.R. Fielden, Anal. Bional. Chem. 391 (2008) 1283.
[19] Z. Zou, A. Jang, E. MacKnight, P.M. Wu, J. Do, P.L. Bishop, C.H. Ahn, Sens. Actuat. B Chem. 134 (2008) 18.
[20] A. Economou, S.D. Bolis, C.E. Efstathiou, G. Volikakis, Anal. Chim. Acta 467 (2002) 179.
[21] D.H. Kim, S.H. Lee, J.K. Kim, G.H. Lee, Appl. Surf. Sci. 252 (2006) 3525.
[22] T. Yoshinoa, K. Yoshida, T. Hagihara, K. Sato, U. Morita, Y. Ishisaki, R. Fujimoto, N.Y. Yamasaki, K. Mitsuda, Nucl. Instrum. Meth. Phys. Res. A 559 (2006) 432.
[23] M. Morfobos, A. Economou, A. Voulgaropoulos, Anal. Chim. Acta 519 (2004) 57.
[24] A. Economou, P.R. Fielden, Analyst 118 (1993) 47.
[25] A. Krolicka, A. Bobrowski, Electrochem. Commun. 6 (2004) 99.
[26] E.A. Hutton, S.B. Hocevar, B. Ogorevc, M.R. Smyth, Electrochem. Commun. 5 (2003) 765.
[27] E.A. Hutton, S.B. Hocevar, B. Ogorevc, Anal. Chim. Acta 537 (2005) 285.
[28] A. Bobrowski, K. Nowak, Anal. Lett. 38 (2005) (1887).
[29] M. Korolczuk, Z.A. Moroziewicz, M. Grabarczyk, Anal. Bioanal. Chem. 382 (2005) 1678.
[30] M. Korolczuk, M. Grabarczyk, A. Moroziewicz, Electroanalysis 19 (2007) 2155.
[31] J. Wang, R.P. Deo, S. Thongngamdee, B. Ogorevc, Electroanalysis 13 (2001) 1153.
[32] G. Kefala, A. Economou, A. Voulgaropoulos, Analyst 129 (2004) 1082.
[33] C. Kokkinos, A. Economou, I. Raptis, T. Speliotis, Anal. Chim. Acta 622 (2008) 111.

A novel cobalt(II)-selective potentiometric sensor based on *p*-(4-*n*-butylphenylazo)calix[4]arene

Pankaj Kumar[b], Yoon-Bo Shim[a],*

[a] *Department of Chemistry and Center for Innovative Bio-Physio Sensor Technology, Pusan National University, Busan 609-735, South Korea*
[b] *Department of Chemistry, Hindustan College of Science and Technology, Farah, Mathura, India*

ARTICLE INFO

ABSTRACT

A new poly(vinyl chloride)-based membranes containing *p*-(4-*n*-butylphenylazo)calix[4]arene (I) as an electroactive material along with sodiumtetraphenylborate (NaTPB), and dibutyl(butyl)phosphonate in the ratio 10:100:1:200 (I:DBBP:NaTPB:PVC) (w/w) was used to fabricate a new cobalt(II)-selective sensor. It exhibited a working concentration range of 9.2×10^{-6} to 1.0×10^{-1} M, with a Nernstian slope of 29.0 ± 1.0 mV/decade of activity and the response time of 25 s. This sensor shows the detection limit of 4.0×10^{-6} M. Its potential response remains unaffected of pH in the range, 4.0–7.2, and the cell assembly can be used successfully in partially non-aqueous medium (up to 10%, v/v) without significant change in the slope of working concentration range. The sensor has a lifetime of about 3 months and exhibits excellent selectivity over a number of mono-, bi-, and tri-valent cations including alkali, alkaline earth metal, heavy and transition metal ions. It can be used as an indicator electrode for the end point determination in the potentiometric titration of cobalt ions against ethylenediaminetetraacetic acid (EDTA) as well as for the determination of cobalt ion concentration in real samples.

© 2008 Elsevier B.V. All rights reserved.

1. Introduction

Determination of cobalt assumes importance because of its widespread occurrence in sea as well as in fresh waters, earth crust, meteorites, animals, and plants. It is an essential element in animal nutrition and its total mass in an average human body is about 1.5 mg with high concentration in liver, bone and kidney. Its deficiency may cause anemia, retarded growth and loss of appetite. Cobalt ions are the component of vitamin B-12, which is required for good health [1]. On the other hand, if consumed in large doses, cobalt may be toxic and cause diarrhea, irritation of gastrointestinal tract and vomiting. Exposure to cobalt may cause lung effects, which include respiratory irritation, coughing, asthma, pulmonary edema and pneumonia [2]. The international agency for research on cancer classifies cobalt as a possible human carcinogen. A dose of 500 mg or above may be toxic and maximum tolerable limit of cobalt in diet is 10 ppm [3]. Cobalt is widely used in paint, varnish, and ink industry as a drying agent, in the preparation of pigments like cobalt blue and cobalt green, in ground coats for porcelain enamels, in lithium ion battery electrode, as catalyst in petroleum and chemical industries, in electroplating industry.

Presently, sophisticated techniques, viz., AAS, ICP, etc. are employed for the determination of trace amount of metal ions. However, these methods are disadvantageous in terms of cost and unsuitability for routine analyses of large number of samples [4–7]. Recently, ion-sensors are being used for such quantification, as these provide a convenient, fast and 'On-line' method of analysis. Some commercialized sensors for alkali and alkaline earth metals, halides, etc. are available, but more efforts are required to develop better sensors for heavy metal ions. Although a number of cobalt ion selective electrodes have been reported so far [8–13], a selective sensor for the monitoring of cobalt is still desired.

Calixarenes are fascinating objects for the study of host guest interactions with pronounced binding affinities to various metals [14]. Calixarenes have been found to bind metal ions selectively as these have electron rich interior cavities and possessing the ability to complex through dipole–dipole interactions with metal ion of compatible dimensions. These compounds also possess high lipophilicity and thermodynamic stability coupled with sufficient conformational flexibility for the rapid exchange of metal ions [15]. A large variety of cation substrates can be complexed by such macrocyclic structures due to the various available cavity sizes and this property of calixarenes has been largely exploited for the development of a number of cation selective electrodes [16–20]. The complexation ability of calixarenes largely depends upon the type of the substituents on the upper and lower rims.

Many substituted calixarenes have already been reported with the aim of modifying their binding properties with the ligands. Lower rim modifications have been explored extensively in comparison with upper rim modified calixarenes and found to have highly significant ionophoric properties for metal ions, e.g. 4-*tert*-butylcalix[4]arene tetraacetic acid tetraethyl ester, and thia-bridge modified calix[4]arene, have been used as neutral carriers to develop Na^+ and Hg^{2+} selective electrodes, respectively [21,22]. Similarly oligosiloxane-modified calix[4]arene, 5,11-dibromo-25,27-dipropozyclix[4]arene, and 5,11,17,23-tetra-*tert*-butyl-25,27-bis(hydroxy)-26-(ethoxycarbylmethoxy)-28-(diethylcarbaoyal-methoxy)calix[4]arene have been used as an ionophore to develop Na^+, Pb^{2+}, and UO_2^{2+}-selective electrodes, respectively [23–25].

In the present study, we report for the first time, a new, highly selective, and sensitive Co(II) sensor based on a synthesized ionophore, *p*-(4-*n*-butyl-phenylazo)calix[4]arene, as an excellent neutral carrier for the selective quantification of cobalt(II) ions. This calixarene derivative contains azo groups at the upper rim which can serve as the binding site for the complexation ability towards metal ions. These circularly arranged ligands, at the upper rim of the calixarene cavity, form cyclic metal ion receptors which facilitate their selective complexation with metal ions. This suitability has been further confirmed by the selective behavior of the PVC membranes based on *p*-(4-*n*-butyl-phenylazo)calix[4]arene, towards Co(II) ions. Various experimental conditions like; the composition of the membrane ingredients, suitable concentration of the internal solution of the sensor have been optimized to obtain a better working concentration range, detection limit, and other response characteristics. Also, the prepared sensor has also been used for the determination of Co(II) ion concentration in the real samples.

2. Experimental

2.1. Equipments and reagents

The potential measurements were performed with a multichannel potentiometer (Kosentech, Korea, Model AS MP8). A PerkinElmer model 3100 atomic absorption spectrophotometer (AAS) with a graphite furnace was used to determine the concentration of metal ion in the standard solutions. All the reagents used for the preparation of metal salt solutions and the membranes were of analytical reagent grade. *p*-(4-*n*-Butyl-phenylazo)calix[4]arene (I) was synthesized as described elsewhere [26], Tri-*n*-butylphosphate (TBP) and the anion excluder sodiumtetraphenylborate (NaTPB) from (BDH, England), di(butyl)butyl phosphonate (DBBP) from (Mobil, USA), 1-chloronapthalene (CN), tris(2-ethylhexyl) phosphate (TEP), dibutylphthalate (DBP), and dioctylphthalate (DOP) from (E-Merck, Germany, and high molecular weight poly(vinyl chloride) (PVC) from (Fluka, Switzerland) were used without any further treatment. Metal solutions were prepared in doubly distilled water and standardized by appropriate methods. The concentrations of the standard metal solu-
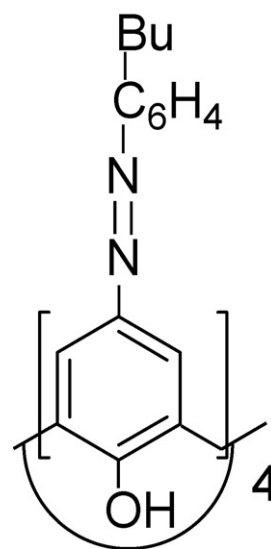
Fig. 1. Chemical structure of *p*-(4-*n*-butyl-phenylazo)calix[4]arene.

tions were confirmed by atomic absorption spectrometer also (Fig. 1).

2.2. Preparation of membranes

Varying amounts of (I), anion excluder NaTPB, plasticizers (DBBP, TEP, TBP, CN, DOP, or DBP) and PVC in different ratio were dissolved in 5 ml of tetrahydrofuran and a drop of diethyl ether. This solution was shaken slowly with a glass rod until it became homogeneous and was poured in acrylic rings resting on a smooth glass plate. The solution was allowed to evaporate at room temperature in a closed cabinet. After 24 h, the light pink-colored transparent membranes were obtained which were cut to size and glued to a hollow pyrex glass tube. A number of membranes were prepared and equilibrated in 1.0 M concentration of different metal ion solutions namely Co^{2+}, Zn^{2+}, Cu^{2+}, Hg^{2+}, Cd^{2+}, Pb^{2+}, Ag^+, Ni^{2+}, La^{3+}, Ca^{2+}, Cr^{3+}, and Mg^{2+} solutions for 2–3 days [27]. In the case of cobalt ions, conditioning was carried out in neutral environment to avoid the possible oxidation of metal ions. The ratio of membrane ingredients, time of contact and concentration of equilibrating solution were optimized so that the membrane could develop reproducible, noiseless and stable potentials. Membrane to membrane reproducibility was assured by carefully following the optimum conditions of fabrication. The composition and response characteristics of different membranes are given in Table 1.

2.3. Potential measurements

Potentials were measured by using a fixed concentration of Co^{2+} solution as the internal solution (0.1 M) and saturated calomel electrodes as reference electrodes. Potential measurements were

Table 1
Compositions and response characteristics of PVC-based membranes having *p*-(4-*n*-butyl-phenylazo)calix[4]arene as electroactive material

S. no	(I)	DOP	DBP	CN	TEP	TBP	DBBP	NaTPB	PVC	Slope (mV/decade of activity)	Response time (s)	Working concentration range (M)
1	10							1.0	200	35.0	~120	4.0×10^{-4} to 1.0×10^{-1}
2	10	150						1.0	200	31.0	90	9.5×10^{-5} to 1.0×10^{-1}
3	10		200					1.0	200	33.2	20	9.0×10^{-5} to 1.0×10^{-1}
4	10			120				1.0	200	33.6	30	7.8×10^{-5} to 1.0×10^{-1}
5	10				150			1.0	200	31.5	25	8.1×10^{-5} to 1.0×10^{-1}
6	10					200		1.0	200	31.0	30	7.0×10^{-5} to 1.0×10^{-1}
7	10						100	1.0	200	29.0	25	9.2×10^{-6} to 1.0×10^{-1}

Fig. 2. Variation of cell potential with Co^{2+} concentration for electrode nos. 1, 2, 4, and 7 (electrode nos. 3, 5, and 6 showed almost similar response to electrode no. 2).

Fig. 3. Effect of pH on cell potential; $[Co^{2+}]$ 1.0×10^{-2} M (a) and 1.0×10^{-3} M (b).

carried out at $25 \pm 0.1\,^{\circ}C$ by setting up the following cell assembly: Internal reference electrode (SCE)/internal Co^{2+} solution, 0.1 M/membrane/test solution/external reference electrode (SCE). Cobalt nitra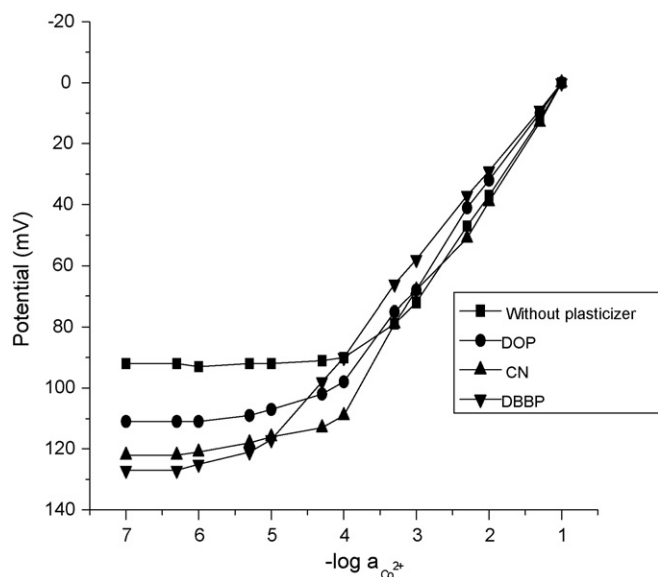te solutions were prepared with the concentration range 1.0×10^{-1} to 1.0×10^{-7} M by serial dilution of 0.1 M cobalt nitrate solution. The concentrations of the standard solutions were also confirmed by atomic absorption spectrophotometer. Each solution was stirred and potential readings were recorded when it became stable. These potential values were plotted as a logarithmic function of cobalt ion activity.

3. Results and discussion

3.1. Selection of the membrane and effect of anion excluder/plasticizers

In preliminary experiments, the ionophore was used as a neutral carrier to prepare PVC-based membranes for a variety of metal ions. Various membrane electrodes were prepared and conditioned in different metal ion solutions. The response of these electrodes was observed. The best response was recorded for Co^{2+} ions while all other ions exhibited lower emf response. This may be due to

Table 2
Effect of partially non-aqueous medium on the working of Co^{2+} ions (sensor no. 7)

% of non-aqueous content (v/v)	Slope (mV/decade of activity)	Working concentration range (M)
0	29.0	9.2×10^{-6} to 1.0×10^{-1}
Methanol		
5	28.6	9.2×10^{-6} to 1.0×10^{-1}
10	28.5	9.8×10^{-6} to 1.0×10^{-1}
15	23.8	5.5×10^{-5} to 1.0×10^{-1}
Acetone		
5	29.0	9.2×10^{-6} to 1.0×10^{-1}
10	28.6	9.7×10^{-6} to 1.0×10^{-1}
15	24.8	6.4×10^{-5} to 1.0×10^{-1}
Ethanol		
5	28.8	9.2×10^{-6} to 1.0×10^{-1}
10	28.5	9.7×10^{-6} to 1.0×10^{-1}
15	23.2	5.9×10^{-5} to 1.0×10^{-1}

the selective behavior of the ionophore against Co^{2+} in comparison to the other metal ions and the rapid exchange kinetics of the resulting ligand–metal ion complex. Therefore, this membrane was used to develop a cobalt ions selective sensor. As the properties of membranes depend on the ratio of electroactive phase and the binder material, membranes with different compositions were prepared. The primary studies showed that the membrane having the composition I:PVC (10:200) exhibits the best results. It is well known that some additives like anion excluders enhance the sensitivity and selectivity of cation selective membrane by reducing its resistance [28–30]. Also, in case of PVC-based neutral carrier membranes, plasticizers if compatible with the ionophore, can provide a smooth surface to the membrane and thus enhance the response characteristics. It can also improve the dielectric constant of the polymeric membrane and also the movement of ionophore and its metal complex [31]. Therefore, effect of the addition of anion excluder (NaTPB) and plasticizers like DBP, DOP, TEP, TBP, CN, and DBBP on the performance of the membranes was also studied.

3.2. Working concentration range and slope

The membrane containing only electroactive material in the PVC matrix exhibited a narrow working concentration range of 4.0×10^{-4}–1.0×10^{-1} M with a slope of 35.0 mV/decade of activity (Fig. 2). The characteristics of the sensor, especially response time

Table 3
The working concentration range and slope values recorded per week

No. of weeks	Working concentration range (M)	Slope (mV/decade of activity)
1	9.2×10^{-6} to 1.0×10^{-1}	29.0
2	9.2×10^{-6} to 1.0×10^{-1}	29.0
3	9.2×10^{-6} to 1.0×10^{-1}	29.0
4	9.3×10^{-6} to 1.0×10^{-1}	28.8
5	9.3×10^{-6} to 1.0×10^{-1}	28.8
6	9.5×10^{-6} to 1.0×10^{-1}	28.8
7	9.6×10^{-6} to 1.0×10^{-1}	28.8
8	9.8×10^{-6} to 1.0×10^{-1}	28.6
9	9.8×10^{-6} to 1.0×10^{-1}	28.5
10	1.0×10^{-5} to 1.0×10^{-1}	28.5
11	1.0×10^{-5} to 1.0×10^{-1}	28.4
12	1.2×10^{-5} to 1.0×10^{-1}	28.4

Table 4
Potentiometric selectivity coefficient values ($K_{Co^{2+},B}^{Pot}$) (interfering ions B), observed for fabricated Co^{2+} selective sensor, using modified fixed interference and matched potential method

Interfering ion B	Fixed interference method	Matched potential method
Li^+	1.9×10^{-2}	0.14
NH_4^+	3.0×10^{-2}	0.11
Na^+	8.1×10^{-1}	0.50
K^+	2.8×10^{-2}	0.20
Ag^+	1.1×10^{-2}	0.16
Hg^{2+}	1.0×10^{-2}	0.10
Cu^{2+}	3.6×10^{-2}	0.38
Ni^{2+}	3.7×10^{-2}	0.22
Ca^{2+}	2.3×10^{-2}	0.20
Cd^{2+}	3.4×10^{-2}	0.29
Mg^{2+}	2.2×10^{-2}	0.16
Ba^{2+}	1.4×10^{-2}	0.15
Pb^{2+}	1.7×10^{-2}	0.15
Zn^{2+}	8.8×10^{-1}	0.61
Sr^{2+}	1.6×10^{-2}	0.12
Cr^{3+}	1.1×10^{-2}	0.12
Al^{3+}	1.1×10^{-2}	0.16
Fe^{3+}	2.7×10^{-2}	0.32
Ce^{3+}	1.5×10^{-2}	0.11

Fig. 4. Variation of cell potential as a function of Co^{2+} concentration in presence of varying concentrations of Na^+ ions.

and slope were improved when the anion excluder (NaTPB) and solvent mediators (DBP, DOP, TBP, CN, TEP, and DBBP) were also added. The improvement in the working concentration range as well as the slope was almost similar for the solvent mediators DOP, DBP, TEP, and TBP (Table 1). The membrane containing DBBP as a plasticizer exhibited the best results (sensor no. 7). This sensor showed a Nernstian response (slope 29.0 ± 1.0 mV/decade of activity) and linear potential response over concentrations range of 9.2×10^{-6} to 1.0×10^{-1} M (Table 1). Repeated monitoring of potentials (20 measurements) on the same portion of sample gave a standard deviation of 0.5 mV. The standard deviation of slope was 0.7–1.0 mV which shows good reproducibility.

3.3. Effect of the concentration of internal solution

The influence of the concentration of internal solution on the potential response of the Co^{2+} ion sensor was also studied. The cobalt nitrate solution concentration was varied from 1.0×10^{-1} to 1.0×10^{-3} M and the potential values were recorded. The variation of the concentration of the internal cobalt nitrate solution does not cause any significant difference in the potential response except for an expected change in the intercept of the resulting Nernstian plots. However, a 1.0×10^{-1} M concentration of the reference solution was found quite appropriate for smooth functioning of the sensor system and it was used for all further investigations.

3.4. pH and non-aqueous effect

The pH dependence of the electrode potentials of membrane sensor no. 7 has been studied at 1.0×10^{-2} and 1.0×10^{-3} M Co^{2+} solution by varying the pH of these solutions from 1.0 to 8.0. Hexamine and nitric acid were used to adjust the pH of the solutions. The potential remained constant over the pH 4.0–7.2 (Fig. 3). Therefore,

it can be taken as the working pH range of this sensor. The sharp changes in potential below pH 4.0 may be ascribed to H^+ co-fluxing and above pH 7.2 may be due to hydrolysis of Co^{2+} ions.

The performance of the sensor no. 7 was also studied in partially non-aqueous medium by using methanol–water, acetone–water and ethanol–water mixtures (Table 2). The proposed sensor could tolerate the non-aqueous content only up to 10% (v/v). The working concentration range reduces sharply when the non-aqueous content exceeds this concentration limit though the slope remains almost unaffected for the entire concentration range.

3.5. Response time and lifetime

Response time is the average time required for the Co^{2+} ion sensor to reach a potential within ± 1 mV of the final equilibrium value after successive immersion of a series of cobalt ion solution was measured. The response time of the membranes without plasticizer was found to be about 2 min at higher concentration levels of test solution while it was observed more than 4 min at lower concentration levels, i.e. below 10^{-4} M. The addition of plasticizers improved the response time significantly. The best result was shown as 25 s by the membrane containing DBBP as a plasticizer (No. 7). The results with DBP and TEP were also found good (20 and 25 s, respectively) over the entire working concentration range. The potentials remained stable and constant for more than 3 min after which began to decrease very slowly. This sensor could be used successfully over a period of more than 3 months at a stretch without any significant change in any of the response characteristics (Table 3). After this period a drift in potentials was observed which could be corrected by re-equilibrating the membrane with 1.0 M Co^{2+} solution for 1–2 days. With this treatment the assembly could

Table 5
Data for cobalt(II) concentration determined in waste water samples by AAS and the sensor no. 7

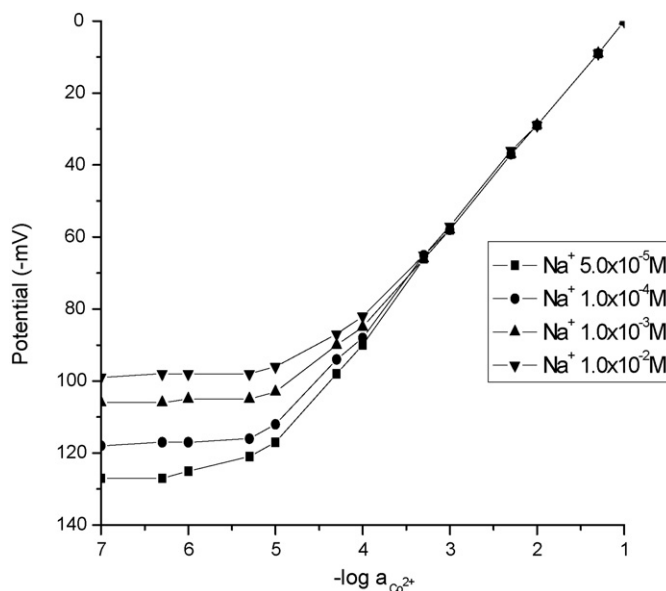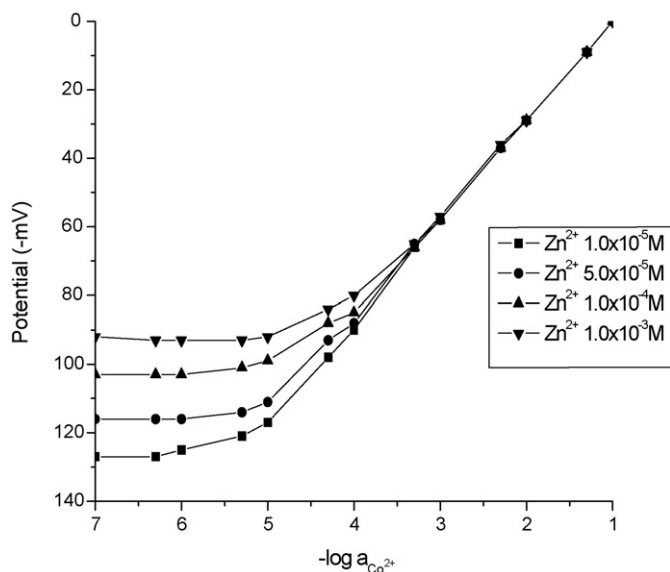| Sample no.	pH found	pH after adjustment	Co^{2+} concentration as determined by the sensor (mg/kg)	Co^{2+} concentration as determined by AAS (mg/kg)
1	5.80	5.6	43.0	41.0
2	4.90	5.4	47.0	48.0
3	5.30	5.0	47.0	48.5
4	5.20	6.1	41.0	39.5

Fig. 5. Variation of cell potential as a function of Co^{2+} concentration in presence of varying concentrations of Zn^{2+} ions.

be used over a period of about two more weeks then a fresh membrane replaced it. This is to emphasize that the sensor was placed in 0.1 M Co^{2+} solution when was not in use to avoid drying and cracking.

3.6. Potentiometric selectivity

Selectivity is measured in terms of potentiometric selectivity coefficient values ($K_{Co^{2+},B}^{Pot}$), which have been evaluated by a modified form of the fixed interference method as well as by matched potential method as suggested by the method reported earlier [32,33]. The selectivity coefficient values (Table 4) clearly indicate that the electrode is moderately selective to Co^{2+} over a number of cations. Only the presence of higher concentration of Na^+ and Zn^{2+}

Fig. 6. Titration plot of 10 ml of 1.0×10^{-4} M Co^{2+} with 1.0×10^{-3} M EDTA solution at pH 6.

are likely to cause some interference as the selectivity coefficient values are higher for these ions. Thus, to calculate the maximum tolerable concentrations of these metal ions in the estimation of Co^{2+}, some mixed run studies were carried out. Na^+ ions $\leq 5.0 \times 10^{-5}$ M do not cause any significant deviation in the original plot of pure Co^{2+} solution (Fig. 4). Thus, the electrode can tolerate Na^+ up to this concentration over the entire working concentration range. If Na^+ concentration exceeds this limit, the sensor can be used to determine Co^{2+} over a concentration range only. Fig. 4 shows that in the presence of 1.0×10^{-4}, 1.0×10^{-3}, and 1.0×10^{-2} M Na^+, the electrode assembly can be used to determine Co^{2+} in the concentration ranges 3.6×10^{-5} to 1.0×10^{-1}, 1.0×10^{-4} to 1.0×10^{-1}, and 9.2×10^{-4} to 1.0×10^{-1} M, respectively. Similarly, Zn^{2+} can be tolerated up to the concentration $\leq 1.0 \times 10^{-5}$ M over the entire working concentration range (Fig. 5). When Zn^{2+} is present at the concentration 5.0×10^{-5}, 1.0×10^{-4}, and 1.0×10^{-3} M, the sensor assembly could be used for the determination of Co^{2+} in the reduced concentration ranges 4.0×10^{-5} to 1.0×10^{-1}, 8.2×10^{-4} to 1.0×10^{-1}, and 5.5×10^{-3} to 1.0×10^{-1} M, respectively.

3.7. Analytical application

3.7.1. Wastewater analysis

The proposed sensor has been successfully used for determining cobalt ions in a real sample from a nearby electroplating industrial complex. Four samples of the electroplating waste were collected, filtered, and stored. Their pH was adjusted according to the working pH range of the sensor by using 0.1 M HNO_3 and hexamine. The data in Table 5, indicate that the amount of cobalt determined in effluent, by the proposed sensor is in close agreement with that determined by the atomic absorption spectrophotometer.

3.7.2. Potentiometric titration

The analytical applicability of the electrode was tested by using it as an indicator electrode, to determine the end point in the potentiometric titration of Co^{2+} with EDTA [34,35]. 10 ml of 1.0×10^{-4} M Co^{2+} solution was titrated against 1.0×10^{-3} M EDTA solution after adjusting the pH of the solution at 6. Hexamine and nitric acid were used to adjust the pH of the solution. The potential data were plotted against the volume of EDTA (Fig. 6). The conventional sigmoid shape plot was obtained and the sharp break point corresponds to the stoichiometry of Co(II)–EDTA complex and indicates the end point of titration.

4. Conclusion

The sensor incorporating *p*-(4-*n*-butylphenylazo)calix[4]arene as electroactive material, DBBP as plasticizer and NaTPB as anion excluder in a PVC matrix in the ratio [10:100:1:200] could be used to determine Co^{2+} in the concentration range 9.2×10^{-6} to 1.0×10^{-1} M with a detection limit of 4.0×10^{-6} M. It exhibits Nernstian behavior throughout the working concentration range. The working pH range is 4.0–7.2 and most of the metal ions do not cause any interference in the estimation of cobalt ions. The response is fast enough (25 s) and lifetime of this assembly is more than 3 months in aqueous as well as in partially non-aqueous medium. It could also be used as an indicator electrode to determine the end point in the potentiometric titration of Co^{2+} ions against EDTA solution as well as for the estimation of Co(II) ions in a real sample.
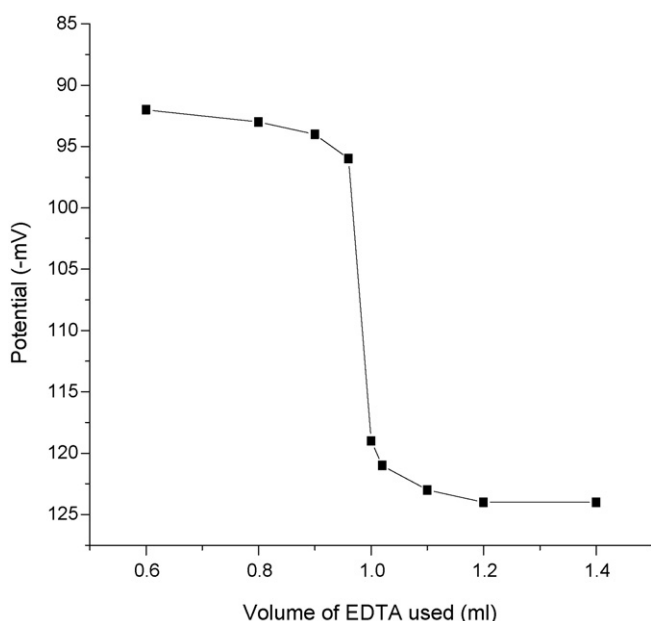
References

[1] O.R. Kirk, F.D. Othmer, Encyclopedia of Chemical Technology, 5, Wiley, 1982, p. 851.
[2] I. Pais, J.B. Jones, The Handbook of Trace Elements, St. Lucie Press, FL, 1997.
[3] S. Memon, M. Yilmaz, J. Mol. Struct. 595 (2001) 101.
[4] A. Miret, J. Ruffo, A.M. Sastre and J.L. Cortina, in: N. Piccinini, R. Delorenzo (Eds.), Chemical Industry and Environment, Politecnico di Torino, 1 (1996).
[5] R.E. Shaffer, J.O. Cross, S.L. Rose-Pehrsson, W.T. Elam, Anal. Chim. Acta 442 (2001) 295.
[6] C.M. Davidson, R.P. Thomas, S.E. McVey, R. Perala, D. Littlejohn, A.M. Ure, Anal. Chim. Acta 291 (1994) 277.
[7] M.H. Mashhadizadeh, A. Momeni, R. Razavi, Anal. Chim. Acta 462 (2002) 245.
[8] R.K. Reddy, S.J. Reddy, Int. J. Environ. Anal. Chem. 31 (1998) 283.
[9] A.K. Jain, V.K. Gupta, L.P. Singh, U. Khurana, Analyst 122 (1997) 583.
[10] H. Tsukube, Talanta 40 (1993) 1313.
[11] V.K. Gupta, A.K. Singh, S. Mahtab, B. Gupta, Anal. Chim. Acta 566 (2006) 5.
[12] A.K. Singh, S. Mahtab, P. Saxena, Sens. Actuators B 120 (2007) 455.
[13] A. Jyo, R. Minakami, Y. Kanda, H. Egawa, Sens. Actuators B 13/14 (1993) 200.
[14] C.D. Gutsche, Calixarenes, The Royal Society of Chemistry, Cambridge, 1991.
[15] N.A. Chaniotakis, A.M. Chasser, M.E. Meyerhoff, Anal. Chem. 60 (1988) 88.
[16] D. Diamond, K. Nolan, Anal. Chem. 73 (2001) (A-pages).
[17] E. Bakker, Y. Qin, Anal. Chem. 78 (2006) 3965.
[18] G.G. Talanova, N.S.A. Elkarim, V.S. Talanov, R.A. Bartsch, Anal. Chem. 71 (1999) 3106.
[19] F. Cadogan, P. Kane, M.A. Mckervey, D. Diamond, Anal. Chem. 71 (1999) 5544.
[20] M.G. Kaifer, P.A. Reddy, C.D. Gutsche, L. Echegoyen, J. Am. Chem. Soc. 119 (1997) 5222.
[21] F. Phillips, K. Kaczor, N. Gandhi, B.D. Pendley, R.K. Danish, M.R. Neuman, B. Toth, V. Horvath, E. Lindner, Talanta 74 (2007) 255.
[22] R.K. Mahajan, R. Kaur, V. Bhalla, M. Kumar, T. Hattori, S. Miyano, Sens. Actuators B 130 (2008) 290.
[23] Y. Tsujimura, M. Yokoyama, K. Kimura, Anal. Chem. 67 (1995) 2401.
[24] A.K. Jain, V.K. Gupta, L.P. Singh, J.R. Raisoni, Electrochim. Acta 51 (2006) 2547.
[25] D.M. Duncan, J.S. Cockayne, Sens. Actuators B 73 (2001) 228.
[26] H. Delligoz, N. Ercan, Tetrahedron 58 (2002) 2881.
[27] A. Craggs, G.J. Moody, J.D.R. Thomas, J. Chem. Educ. 51 (1974) 541.
[28] J.H. Kim, Y.G. Kim, K.H. Lee, S.W. Kang, K.N. Koh, Synth. Met. 117 (2001) 145.
[29] D. Ammanmm, E. Pretsch, W. Simon, E. Lindler, A. Bezegh, E. Pungor, Anal. Chim. Acta 171 (1985) 119.
[30] E. Bakker, P. Buhlmann, E. Pretsch, Chem. Rev. 97 (1997) 3083.
[31] P. Ankere, E. Wieland, D. Ammann, R.E. Dohner, R. Asper, W. Simon, Anal. Chem. 53 (1981) 1970.
[32] F.J. Sa'ezde Viteri, D. Diamond, Analyst 119 (1994) 749.
[33] V.P.Y. Gadzekpo, G.D. Christian, Anal. Chim. Acta 164 (1984) 279.
[34] M.H. Hyun, M.H. Piao, Y.J. Cho, Y.-B. Shim, Electroanalysis 16 (2004) 1785.
[35] M.A. Rahman, M.S. Won, Y.-B. Shim, Anal. Chem. 75 (2003) 1123.

Study on the phosphorescence characterizations of palmatine chloride on the solid substrate and its interaction with ctDNA

Junfen Li, Shaomin Shuang, Chuan Dong*

Center of Environmental Science and Engineering Research, Department of Chemistry, Shanxi University, Taiyuan 030006, China

ABSTRACT

The spectroscopic characterizations of solid substrate room temperature phosphorescence (SS-RTP) of palmatine (Pal) have been studied. Strong RTP signal at 615 nm can be induced on filter paper in the presence of TlAc. The interaction between calf thymus DNA (ctDNA) and Pal has been investigated at pH 6.90 using fluorescence, UV–vis, SS-RTP and cyclic voltammogram spectroscopy. Strong binding affinity of Pal with DNA is revealed from the absorption and fluorescence studies in the liquid state. With the addition of ctDNA, the fluorescence intensity of Pal is enhanced greatly and UV–vis spectra show no apparent hypochromicity and red shift, which indicates that Pal intercalates into ctDNA bases. However, this conclusion could not explain the phenomena from fluorescence polarization and denatured DNA measurements, which indicate that groove binding is at least the main binding mode. Binding constant and binding site size have been calculated to be 2.57×10^4 L/mol and 0.16 based on Scatchard plot from fluorescence titration data. Groove binding has also been supported by phosphorescence lifetime and anion quenching experiments. Above studies demonstrate that there should exist intercalative binding and groove binding in the interaction of Pal and DNA. Furthermore, cyclic voltammogram study suggests that electrostatic binding exists at the same time exactly. Taken together, the binding model obtained in this study is mixed-mode.

© 2008 Elsevier B.V. All rights reserved.

1. Introduction

The interaction of small molecules with DNA plays an important role in many biological processes [1–3]. These associative interactions can cause dramatic changes in the physiological functions of DNA, which might be responsible for the cytotoxic behavior of the small molecules. Among the biologically active molecules from natural sources, alkaloids occupy an important position because of a host of biological pharmacological properties [4–6]. Polycyclic aromatic alkaloids are potential DNA-targeting drugs [7–9]. Recently, significant attention has been focused on the cytotoxic protoberberines. Palmatine (Pal, Fig. 1) represents the most intensively studied protoberberine molecule, which possesses antitumor activity in vitro and in vivo [10–13]. Pal is found in a variety of plant tissues, such as *C. rhizome* and *P. cortex*, and is a close structural analog of berberine (Ber) bearing the same tetracyclic structure (7,8,13, 13*a*tetrahydro-9,10-dimethoxy-berberinium) but differs by the dimethoxy substituents at positions 2,3 on the benzo ring.

Pal and Ber have been known as DNA binders and bind to DNA predominantly by intercalation [9,14–17]. However, other binding modes for Ber and DNA have also been reported. For example, electrostatic force [18], minor groove orientation with preferential AT-rich sequences [19], and model of mix-mode [20] have been proposed. At the same time, binding affinities of Pal and DNA have been extensively characterized by employing several analytical techniques including absorption, fluorescence, NMR, and electrospray ionization mass spectroscopy (ESI-MS), etc., but there is still no consensus on the mode of the interaction [21–25]. Besides intercalative binding, another study has suggested groove binding rather than the former mechanism [23]. The noncovalent complexes of Ber and Pal with few oligonucleotides have been investigated by ESI-MS by Song et al. [18]. Results indicate that Pal interacts with DNA by electronic mode. In addition, model of mix-mode has been proposed in a recent report. Electric linear dichroism (ELD) spectroscopy studies on the Pal with natural DNA having heterogeneous AT and GC sequences have been interpreted by Kluza et al. [24] either by an intercalation or by an external stacking parallel to the base pairs. Pilch et al. [25] suggest a "mixed-mode" binding model rather than classic DNA intercalators, in which a portion of the molecule intercalates into the double helix, while the nonintercalated portion protrudes into the minor groove of the host duplex. A common

---

* Corresponding author. Tel.: +86 351 7018613; fax: +86 351 7018613.
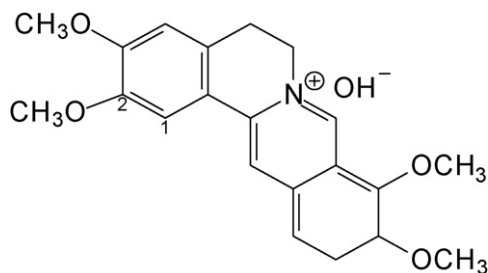 *E-mail address:* dc@sxu.edu.cn (C. Dong).

Fig. 1. The structure of palmatine.

agreement of all these studies is that drugs bind in a single type of binding site of DNA. Emerging diverse biological properties of protoberberines clearly emphasize the urgent need for understanding the molecular basis of their action more closely. So multifaceted study on the binding of the plant alkaloids with DNA is still very important.

At room temperature, only very few compounds could emit phosphorescence. Due to much longer emission wavelength and larger Stokes' shift than fluorescence, phosphorescence is possible to avoid high luminescence background in most biological and clinical samples. By employing phosphorescence probe, biological systems with weak phosphorescence or without phosphorescence could be investigated. Phosphorescence probe molecule is very sensitive to specific microenvironments. Concentration of dissolved oxygen, heavy atom and temperature could affect RTP intensity directly. Using these properties, relative information on microenvironments can be obtained by probing biological systems or biomicromolecules (interact with DNA) with phosphorescence molecules and determinating their phosphorescence properties, such as wavelength shift, emission intensity, lifetime and quantum yield.

When solid substrate room temperature phosphorescence (SS-RTP) is used, the phosphorescence of compounds will be enhanced, and the addition of a chemical oxygen scavenger is not necessary. The volume of sample applied in SS-RTP is only several microlitres, compared with the detection in aqueous solution, which is very small. Therefore, SS-RTP has been widely applied in the fields of environmental research, biochemistry, clinical chemistry and pharmaceutical analysis for its simplicity, high sensitivity and selectivity [26–29]. Although the application of RTP in the study of DNA binding can provides more useful messages and favorable evidence, very few studies have been done on solid substrate. Tong et al. [30] reported the interaction of ZnPP with ctDNA through SS-RTP and found that hydrogen bonding between the monocarboxylic acid substituent of ZnPP and the base pairs of DNA plays a crucial role in the binding. As for alkaloids, only the RTP of quinine and quinidine have been reported in liquid solutions [31]. To our knowledge, phosphorescence has not been used in the interactions of alkaloids with DNA either in aqueous or on the solid substrate. Current techniques in the literatures, including CD, NMR, and mass spectrometry, require expensive and sophisticated instruments. As for spectra methods, the above reported works only involved some absorption and fluorescence spectrometry.

In this paper, Pal was found to possess fairly strong long wavelength phosphorescence at room temperature. The SS-RTP properties of Pal and its interaction with ctDNA were investigated. To further understand the nature of the binding mode of Pal with ctDNA, UV–vis spectra, fluorescence spectra and cyclic voltammogram (CV) studies were also carried out. The binding parameters of Pal to ctDNA was quantitatively determined. Pal binds to DNA through three fixed binding modes: electrostatic interaction, binding interaction with minor groove, and intercalation between the

base pairs of DNA. As much as we know, this is the first work devoted to the spectroscopic and interaction mechanism of alkaloid with DNA by phosphorescence spectra and CV study. This study has the significance of expanding the application of SS-RTP technique in the investigation of alkaloids with DNA, and the research of binding mode would be valuable in the rational design of new and efficient DNA targeted molecules for application in chemotherapy.

2. Experimental

2.1. Regents and materials

ctDNA was purchased from Sigma Chemical Co. (USA) and used without further purification. Stock solution of ctDNA was prepared by dissolution overnight in 0.1 mol/L NaCl and was stored below 4 °C in the dark for short periods only. The concentration of ctDNA(P) was determined using $\varepsilon_{260} = 6600\,L\,mol^{-1}\,cm^{-1}$ [32]. Pal was obtained from the National Institute for the control of Pharmaceutical and Biological Products (Beijing, China). The stock solution of Pal was prepared to 1×10^{-3} mol/L and then dissolved with double distilled water and was always kept protected in the dark. Tris–HCl buffer solution was used to control the pH of the media (pH 6.90). All other reagents were analytical reagent grade and were used without further purification. Double distilled water was used throughout the experiments.

2.2. Apparatus

The fluorescence were carried out on a Cary Eclipse fluorescence spectrophotometer (Varian, USA) connected to an ultrathermostat of temperature precision ±0.1 °C with single cell peltier accessory. A standard 1 cm quartz cell was used. SS-RTP measurements were carried out on a F-4500 fluorescence spectrophotometer (HITACHI, Japan), equipped with a phosphorescence attachment and a lab-made solid sample holder for the solid substrate. A 150 W xenon arc lamp was used as the excitation light source and a piece of quartz glass (1 cm × 1 cm) covered the substrate to reduce the influence of oxygen and moisture. A drying box, equipped with a 250 W IR lamp, was used to dry the samples, and the temperature was controlled automatically (±1 °C). Filter paper purchased from Fuyang Paper Factory (Hangzhou, China) was used as solid substrate. A 5 μL microsyringe (Shanghai Medical Laser Instrument Factory, China) was used for introducing samples and salt solution. The scan speed is 240 nm/min. The absorbance monitoring was performed on a TU-1901 UV–vis spectrophotometer (Puxi Instrument Factory, Beijing, China) with 2.0 nm spectrum bandwidth and slow speed scan. The pH of solutions measurement was performed on a model pHS-29A pH-meter (2nd Analysis Instrumental Factory of Shanghai, China). Cyclic voltammetry was carried out with a computer controlled CHI 660C An electrochemistry workstation (Chenhua Instruments Co., Shanghai, China).

2.3. Procedures

2.3.1. Fluorescence or absorption titration

The effect of reaction time shows that after adding of DNA into Pal solution (7.5×10^{-6} mol/L), the maximum intensity can be observed immediately and remained constant for more than 2 h. Therefore, the fluorescence intensity was immediately measured after mixing. Spectrophotometric titrations were performed by adding aliquots of DNA to the solution of Pal at fixed concentration (1×10^{-5} mol/L) in 2 mL Tris–HCl buffer (pH 6.90). This operation ensured that the concentration of DNA increases gradually. The absorption titrations were made by addition of the ctDNA stock solution directly to the Pal solution (8.8×10^{-5} mol/L) at increasing

concentrations. The mixing was well achieved by thorough shaking and stirring for 3 min. Then the corresponding fluorescence or absorption spectra were measured.

2.3.2. Fluorescence polarization experiment

The titrations were made by addition of the ctDNA stock solution directly to a 1 cm cuvette containing 2 mL Pal solution (1.0×10^{-5} mol/L) at increasing concentrations, and the added volume of ctDNA was not more than 10 μL to avoid complications due to dilution effects. The mixture was mixed thoroughly and then equilibrated for 3 min at room temperature. The measurement of polarization follows equation in literature [26].

The fluorescence intensities were measured at the corresponding maxima of excitation (350 nm) and emission (525 nm) wavelengths. The widths of excitation and emission slits were set at 10 and 10 nm, respectively.

2.3.3. Denatured DNA study

The solutions of double-stranded DNA (ds-DNA) was converted into single-stranded DNA (ss-DNA) by incubated at 100 °C in water bath for 15 min and cooled in ice-water immediately. The process of fluorescence titration is same as Section 2.3.1.

2.3.4. SS-RTP spectra determination

The sample solutions were prepared by the addition of ctDNA stock solution directly into a 1 cm cuvette containing 2 mL Pal solution (1.0×10^{-4} mol/L) at increasing concentrations in base pairs, and the added volume of ctDNA was not more than 10 μL to avoid complication due to dilution effect within titration type experiments. The mixture was mixed thoroughly at room temperature.

The filer paper was cut into 17 mm × 14 mm strips on which a line with an interval of 4 mm was engraved with a graver at the position of the excitation light spot in order to limit the extent of sample solution. The 5 μL of 2 mol/L TlAc solution was spotted onto the surface of the filter paper strip using a 5 μL microsyringe. The paper strip was pre-dried at 95 °C for 1 min. Then 5 μL of sample solution was added at the same position and the filter paper strip was dried again for 2 min. Finally, the filter paper strip was fixed to the solid substrate holder and covered with quartz glass to avoid humidity and oxygen and transferred to the sample compartment immediately to measure the SS-RTP intensity and record the spectra. The scan speed was 240 nm min^{-1}.

2.3.5. SS-RTP lifetime experiment

Phosphorescence lifetime can be obtained from the following equation:

$$\ln I_t = \ln I_0 - t\tau \tag{1}$$

where τ is the phosphorescence lifetime; t the decay time; I_t the phosphorescence intensity at decay time t after excitation; I_0 defined as pre-exponential factor of the decay curve is the prompt transient phosphorescence intensity at zero decay time. The computer calculated the value of the lifetime automatically.

All measurements of the SS-RTP were taken at the corresponding maximum excitation (350 nm) and emission (615 nm) wavelengths and the widths of excitation and emission slits were set at 10 and 20 nm, respectively.

2.3.6. Continuous variation analysis (Job's plot)

To determine the binding stoichiometry of complexation of Pal and DNA, Job's continuation method [22] was applied. At constant temperature, the fluorescence signal of the solutions was recorded where the concentrations of DNA and Pal were varied while the sum of their concentration was kept constant at 1×10^{-4} mol/L. Difference in fluorescence intensity of Pal in the absence and presence of

Table 1
RTP intensities and signal-to-noise ratios (S/N) of Pal absorbed on several papers

Kind of filter papers	I_p[a]	S/N
Qualitative	118.2	11.36
Fast speed quantitative	135.8	12.45
Middle speed quantitative	213.7	14.68
Slow speed quantitative	258.3	16.14

[a] Net signal of RTP.

DNA at 525 nm was plotted as a function of the input mole fraction of Pal. Break point in the resulting plot corresponds to the mole fraction of Pal in the complex. The stoichiometry is obtained in terms of $[(1 - \chi_{Pal})/\chi_{Pal}]$ where χ_{Pal} denotes the mole fraction of Pal.

2.3.7. Cyclic voltammograms study

Cyclic voltammograms study was carried out in Tris–HCl buffer solution. An electrochemical cell with a conventional three electrode configuration was used for all electrochemical experiments at a scan rate of 0.1 V s^{-1}.

3. Results and discussion

3.1. Selection of SS-RTP measurement conditions

3.1.1. Selection of filter paper substrate

The interaction between the analyte molecule and the substrate plays an important role in the SS-RTP emission [26], so the first decision to be made is the choice of the type of substrate. Filter paper is widely used in SS-RTP study because of relatively low cost and wide selection [33]. The SS-RTP properties of Pal adsorbed on several types of filter papers with different spread speed were investigated. It is found that the slow speed quantitative filter paper induces the strongest SS-RTP emission intensity and lower background intensity (Table 1), which is selected as the optimum solid substrate. When different filter papers are applied there are no significant changes in the shape and position of the maximum excitation and emission spectra.

3.1.2. Selection of the external inorganic salt

The inorganic salt can enhance the SS-RTP intensity. The reason might be that the inorganic salt and the analyte molecules can occupy the interstices of the filter paper fibers, and this spatial constraint provides the rigidity required to restrict collisional quenching and radiationless deactivation of the triplet state. More than 20 inorganic salts were screened and their effects as perturber on the SS-RTP intensities of Pal adsorbed on filter paper were investigated. It is found that different inorganic salt has different enhancement effect on phosphorescence. The experiments reveal that most of acetates and nitrates have certain enhancement effect on Pal, while sulfates have slight enhancement effect, and Cl$^-$ has no obvious enhancement effect. Among all the inorganic salts investigated, TlAc could induce the strongest SS-RTP intensity (see Fig. 2) and was chosen for the further work. To obtain intense and stable SS-RTP signal, the absolute amount of inorganic salt compound should be appropriate, so the fixed volume of TlAc 5 μL and the concentration of TlAc was studied. The result shows that the TlAc concentration corresponding to the highest SS-RTP intensity of Pal is 2.0 mol/L (the figure is not shown).

3.1.3. Effect of drying conditions and stability

At room temperature, oxygen is the most persistent quencher of phosphorescence. Moisture can quench the phosphorescence severely in the presence of oxygen [34], so the drying of the sample solution is necessary before the measurement is taken. The sample
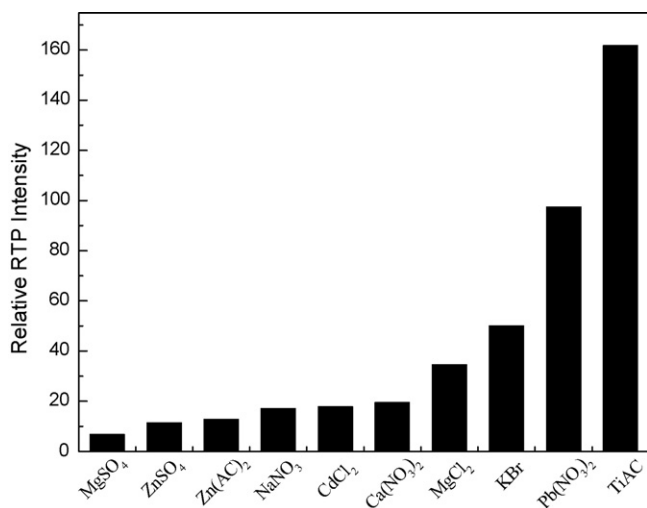
Fig. 2. Effect of the heavy atoms on SS-RTP intensity.

Fig. 3. Influence of ctDNA concentration on fluorescence spectra of Pal at pH 6.90 [Pal] = 1.00×10^{-5} mol/L, [ctDNA] $\times 10^{-5}$ mol/L (1–11) = 0, 0.97, 1.94, 3.63, 6.06, 8.48, 12.1, 14.5, 16.9, 18.4, and 19.2.

drying conditions including drying temperature and drying time were examined in detail, and following results were obtained: (1) the proper drying temperature is in the range of 90–95 °C; (2) the appropriate pre-drying time, dry the wet filter paper after spotting the inorganic salt solution before adding the sample solution, is 1 min; (3) the appropriate drying time is examined to be 2 min, at this time, the highest RTP emission was obtained.

Phosphorescence is not stable during measurement time because of many reasons. The SS-RTP stability of Pal was examined and the experiment shows that the emission intensity changes slightly within 5 min and quenches distinctly after 10 min. This stability time is long enough to meet the requirement of the determination, which needs less than 1 min.

3.1.4. Effect of pH on SS-RTP

Since quaternary ammonium cation of Pal is basic, its RTP should be sensitive to the pH of the solution. It is obvious that the pH value greatly affect the RTP emission intensity of Pal. The PS-RTP intensity of Pal increases sharply with the increase of pH (<6) of the sample solution, and reaches to the maximum in neutral solution and then decreases in basic solution. This illustrates that pH can affect the molecular configuration and the distribution of charges. Strong acid and basic medium are not fit for the compound to emit RTP. Maximum phosphorescence is observed about pH 6.5, and the RTP measurements are all performed under pH 6.90.

3.2. SS-RTP spectra of Pal alone

Under above experimental conditions, the SS-RTP spectra of Pal were measured on the solid substrate and given two emission bands. The first one at shorter wavelength of 522 nm, identical with its fluorescence spectra (525 nm), belongs to delayed fluorescence emission, and the other, peaking at about 615 nm, is phosphorescence emission. Stokes' shift of Pal reaches to 265 nm. Obviously, longer emission wavelength and larger stokes' shift are the advantages of RTP over fluorescence.

3.3. Interaction of Pal with ctDNA

3.3.1. Fluorescence titration

Like most polycyclic aromatic alkaloids, Pal exhibits a low fluorescence quantum efficiency [35] with maximum around 525 nm when excited at 350 nm in neutral pH medium. The emission peak
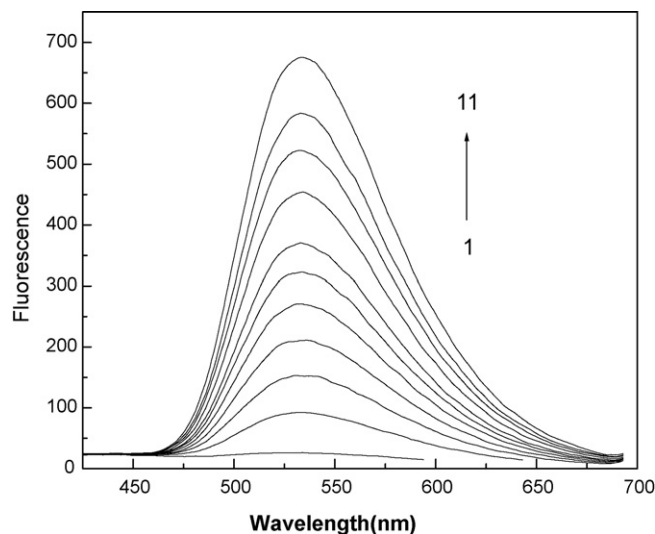
is may be assigned to a π–π^* transition and that enhances on binding with nucleic acids. The fluorescence titration spectra of Pal in various concentration of DNA were reflected in Fig. 3. It is observed that the addition of DNA leads to efficient increase in the fluorescence intensity of Pal, with almost 10 nm red shifts in excitation and 2–3 nm blue shifts in emission wavelength. This strongly indicates the interaction of Pal with DNA and makes Pal a promising fluorescent probe of DNA.

The intense fluorescence of Pal bound to DNA could be for this possible reason: The change of microenvironment does occur, and it is reflected through λ_{em} value and fluorescence intensity [36]. Pal locates in a region of much less polarity after binding, which is provided by microemulsion and with this useful microenvironment, Pal can be isolated or protected from the aqueous phase and placed in a hydropholic environment, and thus, its fluorescence intensity increases.

3.3.2. UV–vis spectra of Pal in the presence of ctDNA

Pal shows two strong and characteristic absorption bands in the visible region centered around 420 and 342 nm. Binding mode of Pal to DNA was studied by spectrophotometric titration, with a fixed concentration of Pal and increasing concentration of DNA. Binding to DNA results in significant changes in the absorption spectra of the compound. With the increasing of ctDNA concentration, the absorption spectra show hypochromicity of 8.82 and 12.24%, and red shifts of 4 and 2 nm at the two maximum bands. This indicates an effective overlap of the π electron cloud of the alkaloid with the base pairs of DNA. In addition, three well-resolved isosbestic points are observed at 350, 380, and 451 nm respectively indicating equilibrium binding [37]. The result from the absorption spectra study corroborates the intercalative binding of the Pal to the DNA bases.

3.3.3. Fluorescence polarization measurement

When small molecule chromophore intercalates into the DNA bases, its rotational motion should be restricted and the fluorescence polarization of the bound small molecule chromophore should be increased. On the other hand, if the polarization remains unchanged, the binding may belong to groove or other mode [38]. The polarized intensity parallel and vertical in the direction of the excitation were recorded and the polarization values of Pal in the
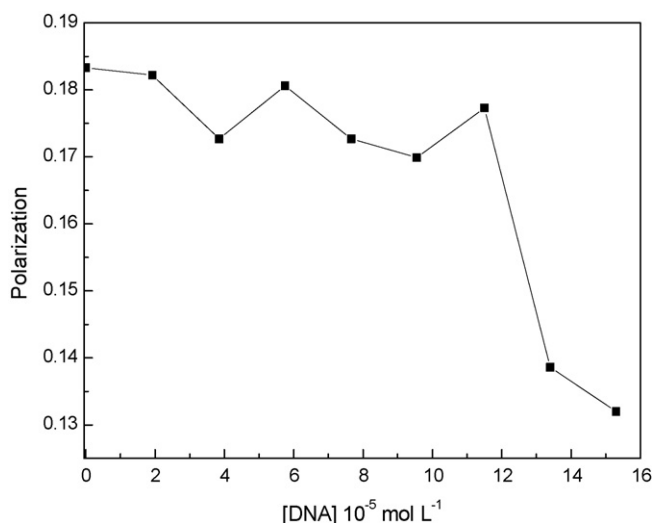
Fig. 4. Influence of ctDNA concentration on fluorescence polarization of Pal. [ctDNA] = (1) 0 mol/L, (2) 1.92×10^{-5} mol/L, (3) 3.85×10^{-5} mol/L, (4) 5.75×10^{-5} mol/L, (5) 7.66×10^{-5} mol/L, (6) 9.68×10^{-5} mol/L, (7) 1.15×10^{-4} mol/L, (8) 1.38×10^{-4} mol/L and (9) 1.54×10^{-4} mol/L.

presence of different concentration of DNA were investigated. Fig. 4 shows that the addition of increasing amounts of ctDNA does not lead to the increase of the fluorescence polarization value of Pal. That is to say, increasing the ctDNA concentration, the rotational motion of Pal is not restricted and no more fluorescence of Pal is polarized. The result above provides evidence that Pal indeed does not intercalate into the helix and ctDNA does not provide a rigid microenvironment for Pal. It illustrates groove binding interaction.

3.3.4. Fluorescence quenching study

The fluorescence quenching study was performed to determine the interaction pattern of Pal with DNA. Anionic quencher KI with increasing concentration was added into Pal or Pal–DNA solution, respectively. Stern–Volmer K_{SV} was used to evaluate the fluorescence quenching efficiency. The experiments show that the fluorescence of Pal does not affected by KI, while the magnitude of K_{SV} of the bound molecule is 61.81 L/mol, which is bigger than that of the free one. When small molecules intercalate into DNA base pairs, the base of the double helix of DNA would protect the bound molecules from the anionic quencher [39]. On the other hand, groove binding exposes the bound molecules to the solvent surrounding the helix [40], and provides much less protection for the chromophore. As a result, this phenomenon is not consistent with intercalation mode either, but consistent with groove binding.

3.3.5. Denatured DNA study

Single strand structure of DNA does not benefit for intercalation. If Pal intercalates into the helix stack, the enhancement extent of the fluorescence from Pal by ss-DNA would be noticeably smaller than that by ds-DNA. Dropping Pal with same concentrations of ss-DNA and ds-DNA, respectively, and comparing their fluorescence intensities, the result shows that both ss-DNA and ds-DNA could increase the fluorescence intensity of Pal. When the concentrations of both DNA increase from 0 to 3.2×10^{-5} mol/L, the fluorescence intensities of Pal increase to about 56 and their values are very similar. When concentrations are higher than 3.2×10^{-5} mol/L, the fluorescence intensity of Pal in ss-DNA is slightly lower than in ds-DNA. That is to say that the enhancement extent of the fluorescence of Pal by ss-DNA is not obviously smaller than that of by ds-DNA, and the binding mechanism is not supported by the intercalation mode.
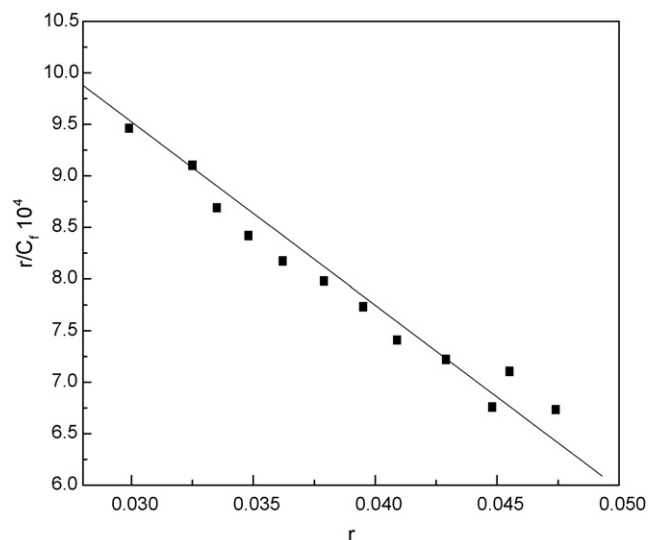
Fig. 5. Scatchard plot for pal to DNA.

3.3.6. Binding constant and stoichiometry of ctDNA and Pal

For the interaction of small molecules with macromolecules, the Scatchard plot is commonly used to characterize the binding properties in terms of the binding constant. The binding constant for DNA to Pal is estimated from the fluorescence data in the form of Scatchard plots, which were analyzed according to the formula of McGhee and Von Hippel [41]:

$$\frac{r}{C_f} = K(n - r) \tag{2}$$

Where n, apparent site size, represents the number of binding sites per nucleotide residue, r is the ratio of bound ligand to nucleotide residues at a free ligand concentration, and K is the intrinsic binding constant for the Pal binding to a site on the nucleic acid. The study yielded a K value of 2.57×10^4 L/mol, and n is 0.16 (Fig. 5). This large constant indicates that Pal has intense affinity to ctDNA base pairs. The binding affinity of 1.07×10^4 L/mol was also calculated from the data of absorption titration as reference [42]. The intrinsic binding constants obtained by the two different spectral methods were close and in the order of 10^4 L/mol, which are both similar with the result reported in the literature [43].

The binding stoichiometry of association and the possible number of binding site of Pal to DNA were determined by continuous variation analysis (Job's plots) in fluorescence (Fig. 6). The plot of difference fluorescence intensity at 525 nm for Pal versus the mole fraction of the ligand reveal a single binding mode for the binding of the alkaloid on DNA. From the inflection points at $\chi_{ligand} = 0.14$, the number of nucleotides per one ligand Pal can be estimated around 6.14 (3 base pairs). The stiochiometry of the binding is in excellent agreement with the number of occluded sites obtained from the Scatchard analysis of the fluorimetric data.

3.3.7. The possibility of Pal as SS-RTP probe for ctDNA

The reaction time for the binding of Pal and ctDNA was investigated at the ctDNA concentration two times greater than that of the Pal. The result shows that 10 min is sufficient for the interaction, so the measurements were taken after 10 min. Fig. 7 demonstrates the SS-RTP spectra of Pal in the presence of different concentration ctDNA. The SS-RTP intensities initially increase due to the ctDNA addition, and then decrease dramatically when the concentration of ctDNA increase to 9.84×10^{-5} mol/L. Upon binding to ctDNA, there is no significant change in the position of the

Fig. 6. Job's plot for pal to DNA in buffer of pH 6.90 at 25 °C.
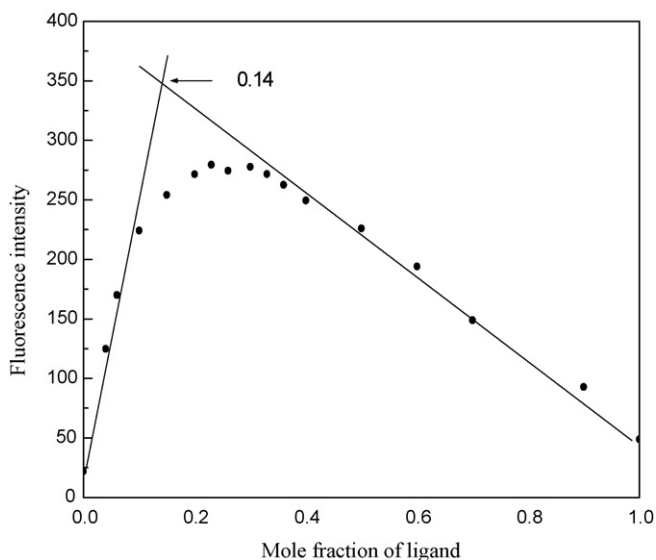

Fig. 8. Cyclic voltammograms of Pal in the absence of and in the presence of DNA; a: 1×10^{-5} mol/L Pal + 0 mol/L DNA; b: 1×10^{-5} mol/L Pal+1.97 × 10^{-5} mol/L DNA.

maximum emission spectrum of Pal. The change of phosphorescence intensity shows the possibility for Pal as phosphorescence probe of DNA. Furthermore, an alternative method to measure DNA should be founded at longer wavelength region than fluorescence. This part of work will be performed and reported elsewhere.

The observation after addition of ctDNA implies that there may exists not only one mode. It can be explained as follows. When part of Pal molecule intercalates into ctDNA bases, the highly ordered medium of ctDNA helix provides a protected microenvironment for the triplet excite state of Pal and shields the collisional quenching, so the intensity of RTP increases [44,45]. But then RTP begin to decrease and the quenching is enhanced with the increasing amount of ctDNA. So later, another part of Pal molecule may interact with DNA by groove binding, and this mode is stronger than the former. That is to say that its grooving part is affected by collision quenching and phosphorescence decrease.

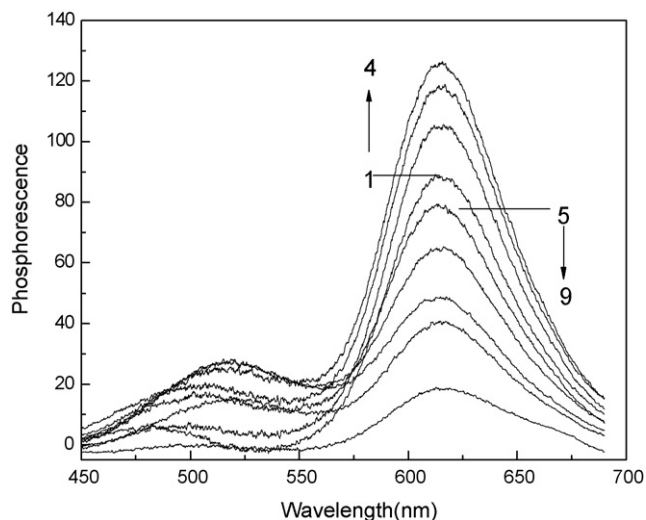Fig. 7. The phosphorescence spectra of Pal in the different concentrations of DNA. [Pal] = 6.0×10^{-5} mol/L, [ctDNA] from 1 to 9 are 0, 0.32, 0.65, 0.98, 1.31, 1.97, 2.62, 3.28 and 4.05 × 10^{-4} mol/L.

3.3.8. SS-RTP lifetime measurement

Phosphorescence lifetime is usually used to characterize the extent of immobilization and shield for phosphorescent substance. Normally, when the extent of immobilization is increased, the molecule will be difficult to be quenched. The effect of ctDNA concentration on the SS-RTP lifetime of Pal was investigated at the corresponding maximum excitation and emission wavelengths. In the absence of ctDNA, the phosphorescence lifetime of Pal is 36 ± 0.02 ms. Upon addition of ctDNA, the lifetime increases and reaches to the maximum of 39.55 ms in 1.0×10^{-5} mol/L ctDNA and then decreases slightly. This might be explained as demonstrated in Section 3.3.7 that the intercalation part of Pal into ctDNA bases leads to certain stronger rigidity and longer lifetime, while the groove binding part then makes the lifetime become shorter again, because intercalation is not the predominant binding mode.

3.3.9. SS-RTP anion quenching experiment

On the filter paper, $Fe(CN)_6^{4-}$ was chosen to quench the phosphorescence of Pal and determine the accessibility of Pal to anionic quencher in the absence and presence of ctDNA. The Stern–Volmer plots are not linear with the decreasing of phosphoresce in the presence of ctDNA, but it is obvious that the quenching extent of the bound Pal by $Fe(CN)_6^{4-}$ is not less than that of the free Pal. As the discussion in Section 3.3.4, this measurement further supports the groove binding of Pal to ctDNA.

3.3.10. Cyclic voltammogram study

Pal is a polycondensate molecule with a positive charge in C ring, it is reasonable to assume that there could be electrostatic interaction of its binding to DNA. To investigate this hypothesis, CV study was performed and showed in Fig. 8. It is obvious that the increase of DNA leads to negative shift in the potential for the two reduction peaks, and the peak electron current of the two reduction peaks decrease obviously at the same time. The formal potential E_p of Pal is −0.392 V, and shifts to −0.516 V in the presence of relatively high concentration of DNA (3.49×10^{-5} mol/L). This phenomenon supports the electrostatic binding between the positive charge on the alkaloid and the negative charge of the phosphate group on DNA helix.

3.3.11. Discussion on binding mechanism

DNA binding properties of Pal indicate that fluorescence and phosphorescence probes for DNA is available. Above characteris-

tics strongly suggest a "mix-mode" model in which a portion of the ligand molecule intercalates into the double helix, while the nonintercalated portion of the ligand molecule protrudes into the minor groove of the host duplex. In another word, part of the planar molecule binds to DNA essentially by intercalation and exert its biological activity while another part binds in the floor of minor groove through H-bonding. This conclusion is consistent with reference [25], but electrostatic binding is proposed also in this study which is expected to exist at the same time. The reason may be found in the structure of Pal molecule, which has a slightly buckled structure due to the partial saturation of the central ring like Ber [46]. Furthermore, Pal has four methoxy groups, and the steric effects of rotating C—O bonds might block the intercalation of Pal into the base stack. As a result, it may not be inserted fully like ethidium and this would probably be the reason for its observed moderate affinity and the binding is predominantly controlled by groove interactions.

4. Conclusion

Luminescence measurements in this paper attest that Pal forms stable complex with DNA, and our studies represent the first attempt to utilize SS-RTP method to study the interaction of Pal with DNA. We found that Pal can induce strong phosphorescence in longer wavelength region on filter paper substrate, which avoids the interference from the biological samples. Fluorescence polarization measurement and denatured DNA study show that Pal may interact with DNA by grooving binding, but this conclusion could not explain the result of UV–vis spectra experiment. After binding with ctDNA, the RTP intensity and lifetime determinations indicate that Pal may bind to DNA via at least some degree of intercalation besides groove binding. This result is also supported by the SS-RTP anion quenching experiment. CV study shows that electrostatic binding also exists. Taken together, we conclude that the binding model of Pal and DNA obtained in this study is mixed-mode, and groove binding is probably the predominant one. The binding properties of Pal in this paper indicate the perfect uses of fluorescence and phosphorescence DNA probes of Pal.

Acknowledgements

References

[1] H. Ihmels, K. Faulhaber, D. Vedaldi, F. Dall'Acqua, G. Viola, Photochem. Photobiol. 81 (2005) 1107.
[2] L.S. Lerman, Proc. Natl. Acad. Sci. U.S.A. 49 (1963) 94.
[3] L.H. Hurley, Nat. Rev. Cancer 2 (2002) 188.
[4] A.H. Amin, T.V. Subbaiah, K.M. Abbasi, Can. J. Microbiol. 15 (1969) 1067.
[5] W.A. Creasey, Biochem. Pharmacol. 28 (1979) 1081.
[6] T. Schmeller, B. Latz-Bruning, M. Wink, Phytochemistry 44 (1997) 257.
[7] M. Cushman, F.W. Dekow, L.B. Jacobsen, J. Med. Chem. 22 (1979) 331.
[8] M.W. Davidson, I. Lopp, S. Alexander, W.D. Wilson, Nucleic Acids Res. 1 (1977) 2697.
[9] G.S. Kumar, D. Debnath, A. Sen, M. Maiti, Biochem. Pharmacol. 46 (1993) 1665.
[10] S. Mazzini, M.C. Bellucci, Bioorg. Med. Chem. 11 (2003) 505.
[11] S. Nishida, S. Kikuichi, S. Yoshioka, M. Tsubaki, Y. Fujii, H. Matsuda, M. Kubo, K. Irimajiri, Am. J. Chin. Med. 4 (2003) 551.
[12] S. Letašiová, S. Jantová, L. Čipák, M. Múčková, Cancer Lett. 239 (2006) 254.
[13] S. Letašiová, S. Jantová, M. Miko, R. Ovadekova, M. Horvathova, J. Pharm. Pharmacol. 58 (2006) 263.
[14] H.Z. Xing, C.Q. Jiang, M.X. Guo, Spectro. Spect. Anal. 23 (2003) 755.
[15] A. Saran, S. Srivastava, E. Coutinho, M. Maiti, Indian J. Biochem. Biophys. 32 (1995) 74.
[16] D.S. Pilch, C. Yu, D. Makhey, E.J. LaVoie, A.R. Srinivasan, W.K. Olson, R.R. Sauers, K.J. Breslauer, N.E. Geacintov, L.F. Liu, Biochemistry 36 (1997) 12542.
[17] K. Bhadra, G.S. Kumar, S. Das, Md.M. Islam, M. Maiti, Bioorg. Med. Chem. 13 (2005) 4851.
[18] F.R. Song, N. Liu, C.Y. Yan, Z.Q. Liu, S.Y. Liu, Chem. J. Chin. Univ. 25 (2004) 1830.
[19] S. Mazzini, M.C. Bellucci, R. Mondelli, Bioorg. Med. Chem. 11 (2003) 514.
[20] V. Markéta, K. Vlastimil, V. Jaroslav, S. Vilím, Electrophoresis 26 (2005) 1673.
[21] T.K. Li, E. Bathory, E.J. La Voie, A.R. Srinivasan, W.K. Olson, R.R. Sauers, L.F. Liu, D.A. Pilch, Biochemistry 39 (2000) 7107.
[22] K. Bhadra, M. Maiti 1, G.S. Kumar, Biochim. Biophys. Acta 1770 (2007) 1071.
[23] W.Y. Li, H. Lu, C.X. Xu, J.B. Zhang, Z.H. Lu, Spectr. Lett. 31 (1998) 1287.
[24] J. Kluza, B. Baldeyrou, P. Colson, P. Rasoanaivo, L. Mambu, F. Frappier, C. Bailly, Eur. J. Pharm. Sci. 20 (2003) 383.
[25] D.S. Pilch, C. Yu, D. Makhey, E.J. LaVoie, A.R. Srinivasan, W.K. Olson, Biochemistry 36 (1997) 12542.
[26] W.J. Jin, H.R. Zhang, X. Yang, C.S. Liu, Appl. Spectrosc. 49 (1995) 320.
[27] J.F. Li, Y.L. Wei, X.H. Feng, C. Dong, Anal. Lett. 37 (2004) 307.
[28] J.F. Li, C. Dong, P. Yang, Anal. Lett. 32 (2002) 2319.
[29] H.Z. Xie, C. Dong, W.J. Jin, Y.S. Wei, C.S. Liu, S.S. Zhang, B.L. Zhou, Anal. Chim. Acta 319 (1996) 239.
[30] A.J. Tong, L. Liu, L.D. Li, C.W. Huie, Fresen. J. Anal. Chem. 370 (2001) 1023.
[31] X.H. Zhang, Y. Wang, W.J. Jin, Talanta 73 (2007) 938.
[32] R.F. Pasternack, E.J. Gibbs, J.J. Villagranca, Biochemisry 22 (1983) 2406.
[33] C. Dong, S.M. Shuang, K.C. Feng, C.S. Liu, Anal. Lett. 32 (1999) 9.
[34] R.T. Parker, R. Freedlander, R. Brucedunlap, Anal. Chim. Acta 119 (1980) 189.
[35] Y.L. Chung, R.D. Hong, H.W. Wu, W.H. Hung, L.J. Lai, C.M. Wang, J. Electroanal. Chem. 610 (2007) 85.
[36] J.Z. Wu, L. Wang, G. Yang, Chem. J. Chin. Univ. 17 (1996) 1010.
[37] A. Sen, M. Maiti, Biochem. Pharmacol. 48 (1994) 2097.
[38] C.V. Kumar, E.H. Asuncion, J Am. Chem. Soc. 115 (1993) 8547.
[39] H.M. Berman, P.B. Young, Annu. Rev. Biophys. Bioeng. 10 (1981) 87.
[40] E.H. Weyand, Y. Wu, S. Patel, Chem. Res. Toxicol. 4 (4) (1991) 466.
[41] J.D. McGhee, P.H. Bon Hippel, J. Mol. Biol. 86 (1974) 469.
[42] L.S. Lerman, J. Mol. Biol. 3 (1961) 18.
[43] K. Hirakawa, S. Kawanishi, T. Hirano, Chem. Res. Toxicol. 18 (2005) 1545.
[44] J.F. Li, Y.X. Wei, Y.L. Wei, C. Dong, J. Lumin. 124 (2007) 143.
[45] L.M. Guo, W.J. Dong, X.F. Tong, C. Dong, S.M. Shuang, Talanta 70 (2006) 630.
[46] L. Grycova, J. Dostal, R. Marek, Phytochemistry 68 (2007) 150.

High performance protein microarrays based on glycidyl methacrylate-modified polyethylene terephthalate plastic substrate

Yingshuai Liu, Chang Ming Li*, Weihua Hu, Zhisong Lu

School of Chemical & Biomedical Engineering, Center for Advanced Bionanosystems, Nanyang Technological University, 70 Nanyang Drive, Singapore 637457, Singapore

ARTICLE INFO

ABSTRACT

There is a great challenge to immobilize high density of probe molecules for high performance protein microarrays, and this is achieved in this work by using polyethylene terephthalate (PET) plastic substrate onto which glycidyl methacrylate (GMA) photopolymer is grafted under mild conditions to introduce high density of epoxy groups for covalent immobilization of proteins. The poly(GMA)-grafted PET (PGMA-PET) surface was characterized with atomic force microscope (AFM) and attenuated total reflectance Fourier transform infra-red (ATR-FTIR) spectroscopy. For high density of protein immobilization and good quality of microspots, experiments were conducted to optimize the printing buffer, and an optimal buffer was found out to be PBS with 10% glycerol + 0.003% triton X-100. According to the studies of loading capacity and immobilization kinetics, the optimal protein probe concentration and incubation time for the efficient immobilization are $200 \, \mu g \, mL^{-1}$ and 8 h, respectively. The performance of the PGMA-PET-based protein microarrays is evaluated with sandwich immunoassay using rat IgG and anti-rat IgG as model proteins, demonstrating a limit of detection (LOD) of $10 \, pg \, mL^{-1}$ and a dynamic range of five orders of magnitude which are better than or very comparable with the reported or commercially available immunoassays, while providing a high-throughput approach. The work renders a simple and economic method to manufacture high performance protein microarrays and is expected to have great potentials in broad applications related to clinic diagnosis, drug discovery and proteomic research.

© 2008 Elsevier B.V. All rights reserved.

1. Introduction

Bioarrays have demonstrated their increasing impact on clinic diagnostics, drug discovery, and life science research because of their advantages of high-throughput, high reliability, fast analysis and small amount of sample. With the completion of human genome project, exploration and development of various high performance protein arrays have been logically fueled up. Protein microarrays possess the ability to analyze complex biological system and have emerged for numerous important applications including screening of recombinant antibody libraries [1], monitoring of protein–protein interactions [2–4], detection of cytokines [5,6], analysis of protein expression profiling, and identification of protein structure and function [7–9].

Protein microarrays are normally fabricated by delivering various probe proteins onto different substrates such as glass [7–9], silicon [10,11] and gold [12]. Alternatively, organic polymer substrates such as polymethyl methacrylate, polycarbonate and polyurethane are also employed for DNA or protein microarrays [13–16]. Polyethylene terephthalate (PET), one of the most widely used biomaterials in tissue engineering and biomedical devices, is an inexpensive plastic material with desirable physicochemical properties. Up to date, it has not been used to fabricate protein microarrays. In this work, we use it as a potential substrate to fabricate high performance protein arrays by a surface modification.

For microarray construction, one of the most important steps is to efficiently immobilize probe proteins on a substrate. Currently, a number of strategies such as physical adsorption, specific affinity and covalent bonding are available for protein immobilization [17]. Although physical adsorption normally offers the simplest process for the immobilization, it is relatively unstable and uncontrollable. It also unfavorably damages protein activity by protein denaturation and steric hindrance [18]. Alternatively, specific affinity, such as protein A or G with Fc part of an antibody [19] and biotin–avidin/streptavidin interaction [12], are used for site-specific protein immobilization. The approach is easy to retain the native conformation and to control the orientation of immobilized protein. However, it requires conjugation of the probe protein with affinity tag and specifically modified substrate [20]. Covalent coupling provides the strongest attachment of probes onto activated

---

* Corresponding author. Tel.: +65 67904485; fax: +65 67911761.
E-mail address: ecmli@ntu.edu.sg (C.M. Li).

substrate [17]. Silanes are often used to functionalize glass slide for covalent protein immobilization [8,21,22], but its immobilization efficiency is low [23]. The steric hindrance between protein and surface from the short spacer provided by silanes also reduces the affinity of probe and the accessibility of analytes.

PET is lack of indigenous reactive functional groups. In tissue engineering and biomedical devices, it is functionalized by saponification, aminolysis and surface reduction for protein immobilization [24]. These methods cannot provide high density of functional groups [24] and require additional crosslinkers such as silanes, glutaraldehyde, aldehyde-dextran and functionalized PEG to covalently immobilize biomolecules [24–27]. Plasma postpolymerization for grafting vinyl compounds onto PET surface is explored for surface modification and biomolecules immobilization [28–32]. However, the plasma approach is slow and expensive [33].

In this work, a simple and efficient approach was investigated to functionalize PET surface by grafting glycidyl methacrylate (GMA) photopolymer for high performance protein microarrays. GMA possesses both acrylate and epoxy groups, of which the former can be employed to photopolymerize GMA in the presence of photoinitiator under UV irradiation, and the latter, can be an anchor for covalent immobilization of proteins. poly(GMA)-grafted PET (PGMA-PET) was prepared and further characterized with atomic force microscope (AFM) and attenuated total reflectance Fourier transform infra-red (ATR-FTIR) spectroscopy. The optimal printing buffer, protein immobilization kinetics and loading capacity were investigated systematically. PGMA-PET-based protein microarrays were fabricated and demonstrated by sandwich immunoassay.

2. Experiments

2.1. Materials and apparatus

1 mm thick PET sheets were purchased from goodfellow (England). Rabbit IgG, biotin-conjugated anti-rabbit IgG, Cy3-conjugated anti-goat IgG, rat IgG, anti-rat IgG, biotin-conjugated anti-rat IgG, hexamethylenediamine, glycidyl methacrylate (GMA), glycerol, triton® X-100 and 0.01 M phosphate buffered saline (PBS, pH 7.4) were received from Sigma–Aldrich. Cy3-conjugated streptavidin was obtained from GE Healthcare. Blocker™ Casein in TBS was purchased from Pierce. Deionized water was produced by a water purification system, Q-Grad® 1, Millipore Corporation.

AFM (SPM 3100, Veeco instruments Inc., USA) was used to characterize substrate surface properties. Nicolet 5700 FTIR instrument (Thermo Electron Corporation) was utilized to record the IR spectra. VersArray chip writer™ compact system (Bio-Rad, USA) was applied for microarrays fabrication. ScanArray GX Microarray Scanner (PerkinElmer, USA) was employed for imaging and quantitative analysis.

2.2. Preparation of PGMA-PET slide

The PGMA-PET slides were prepared under mild conditions by following the procedure shown in Scheme 1. For cleaning, the tailored 75 mm × 25 mm PET slides were immersed in 2-propanol for 30 min and then cleaned for 5 min in an ultrasonic water bath, followed by thoroughly rinsing with ethanol and deionized water. The precleaned PET slides were aminated with a method similar to that in the amination of polyester (polymethyl methacrylate, PMMA) [14]. In our preparation, the precleaned PET slides were incubated in 10% hexamethylenediamine for 2 h at room temperature to introduce primary amine to PET ester linkage, and then

rinsed three times with deionized water. For the conduction of photografting, GMA monomers were firstly coupled to aminated PET surface via the reaction between epoxy and amino groups to form an acrylate-activated PET surface. Specifically, aminated PET slides were soaked in 5% (v/v) GMA in 50% ethanol solution for 2 h at room temperature, and rinsed thoroughly with ethanol and dried under nitrogen flowing. The acrylate groups enable GMA photopolymer to be covalently attached onto PET surface. The acrylate-activated PET slides were immersed in GMA monomer solution (5% in 50% ethanol, v/v) containing 5 mM sodium persulfate as a photoinitiator, which was completely degassed using nitrogen flow for 30 min. Then, the mixture was exposed to UV (shuttered UV system, 400 W) for 15 min. After the polymerization, PET slides were washed with ethanol and deionized water to remove unpolymerized monomer and uncoupled oligomer or polymer.

2.3. AFM characterization

Pristine, aminated PET and PGMA-PET surfaces were characterized with AFM in a tapping mode. The scan area was 2 μm × 2 μm. All images were acquired in open air.

2.4. ATR-FTIR characterization

The IR spectra were acquired by using a Nicolet 5700 instrument equipped with an attenuated total reflection accessory. The polymerized GMA, pristine PET and PGMA-PET were placed onto the ATR crystal and pressed tightly to obtain good spectra. The examinations were performed by 32 scans with a resolution of 1 (data spacing is 0.482 cm^{-1}).

2.5. Fabrication of protein microarrays

Protein probes were prepared in printing buffer with desired concentrations and then transferred to a 384-well microtiter plate before printing. For printing buffer optimization, 0.01 M PBS containing 10% glycerol and different amount of triton X-100 range from 0.001% to 0.012% were applied as printing buffers. In other experiments, the optimal buffer was employed. For investigation of probe immobilization kinetics and loading capacity, 100 μg mL^{-1} of Cy3-conjugated anti-goat IgG and twofold diluted biotin-conjugated anti-rabbit IgG solutions from 200 μg mL^{-1} to 6.25 μg mL^{-1} were prepared. 20 μL of the protein probe solution was dispensed to each well. The contact printing process was performed by VersArray chipwriter™ (BIO RAD) with telechem printhead and stealth microspotting pins. At 60% humidity, ~0.3 nL of a sample per spot was delivered to PET surface.

Probe immobilization was carried out in a humid chamber with incubation times of 0 h, 0.25 h, 0.5 h, 1 h, 2 h, 4 h, 6 h, 8 h, 10 h and 12 h, respectively, for investigation of immobilization kinetics, and overnight for other experiments. Then, the slides were washed three times for 2 min each with PBST (0.01 M PBS with 0.05% Tween 20) to remove unbound probes. All printed array slides were immersed in Blocker™ casein in TBS solution for 1 h not only to quench the unreacted functional groups on substrate surface, but also to form a molecular layer of casein that could reduce the nonspecific binding of other proteins in subsequent steps.

2.6. Imaging and data analysis

Cy3-conjugated streptavidin, which can specifically attach to biotin-conjugated proteins through the strong affinity of biotin and streptavidin, was employed to produce fluorescent signals for detection. After applying Cy3-conjugated streptavidin, slides were thoroughly washed with PBST and deionized water three times,
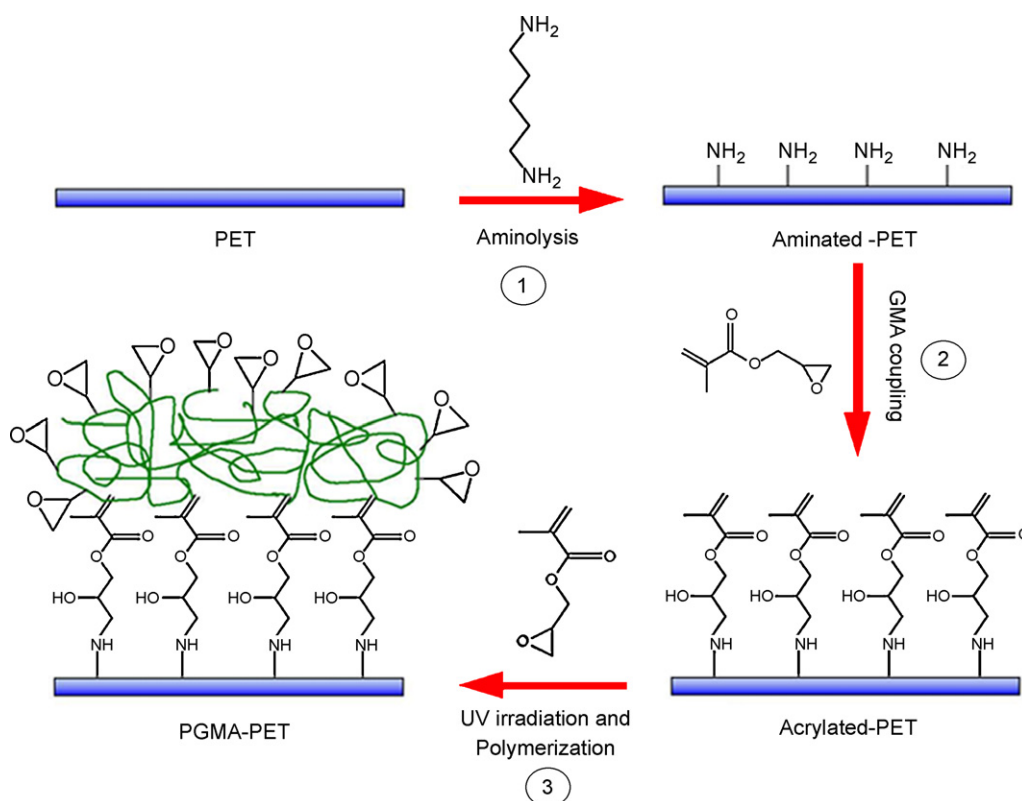
Scheme 1. Procedures for PGMA-PET slide preparation. The dimension in the scheme is not drawn to scale.

respectively. Then, the dried slides were immediately scanned with ScanArray GX Microarray Scanner. The acquired images were quantitatively analyzed with ScanArray® Express analysis software. The fluorescent intensity was local background subtracted means, which were used for downstream statistical analysis. The acquired data were inputted to Origin 7.0 for further analysis and plots.

3. Results and discussion

3.1. Topographic properties of modified PET

The topographic property of PGMA-PET surface was examined with AFM. Fig. 1 shows the images of pristine PET surface (Fig. 1A), aminated-PET surface (Fig. 1B) and PGMA-PET surface (Fig. 1C). The pristine PET exhibits a smooth and featureless surface profile (Fig. 1A), of which the root-mean-square roughness (R_q) is 0.36 ± 0.26 nm, while the morphology is much rougher with small and dense islands (Fig. 1B) after amination in hexamethylenediamine, resulting in R_q up to 2.99 ± 0.42 nm. The significant change of surface morphology should be ascribed to the attack of hexamethylenediamine during aminolysis. In comparison to pristine and aminated PET surfaces, PGMA-PET surface illustrates a drastic change (Fig. 1C), in which the islands become larger and sparser. Accordingly, the roughness rapidly increases to 17.11 ± 3.50 nm. This phenomenon clearly indicates that GMA photopolymers are successfully grafted onto PET surface via the simple and efficient strategy.

Generally, the rougher the surface is, the larger the surface area will be [10]. In order to improve protein loading capacity, one straightforward approach is to increase the surface area of the substrate by enhancing the surface roughness. From the AFM results, the roughness significantly increases from R_q 0.36 ± 0.26 nm for pristine PET to R_q 17.11 ± 3.50 nm for PGMA-PET in this work

(Fig. 1D). Therefore, the significant increase in roughness of photografted PET surface can provide larger surface areas for great improvement of protein loading capacity.

3.2. ATR-FTIR analysis

ATR-FTIR spectrophotometry was employed to characterize the presence of high density of epoxy groups on the PGMA-PET surface and to further confirm the photografting. Fig. 2 shows the IR spectra of PGMA-PET (a), pristine PET (b) and PGMA (c). Six PGMA characteristic peaks (indicated by green arrows) are observed on the spectrum of PGMA-PET as compared to that of pristine PET. Among them, two prominent absorbance peaks are located at 843 and 904 cm^{-1}, which can be assigned to epoxy group's vibration [34]. However, there is no noticeable absorbance peak at the same wavelengths for the pristine PET (b). This result verifies that high density of epoxy group survives from the successful photografting. The high density of functional groups provides high protein loading capacity, which is one of the most important factors for high performance protein microarrays. Moreover, the polymer chains as a long spacer can retain the natural conformation of immobilized probes and increase the accessibility of target molecules to the probes [35].

3.3. Optimization of printing buffer

Printing buffer can significantly affect the quality of microspots, stability of protein probes and protein loading capacity. The effect of additive triton X-100 [22,36] on microspot quality and signal intensity was investigated in this work to optimize the printing buffer for PGMA-PET-based microarrays. A series of printing buffers were prepared with 0.01 M PBS containing 10% glycerol and various concentrations of triton X-100 additive at 0.001%, 0.003%, 0.006%, 0.009% and 0.012%, respectively. Rabbit IgG as
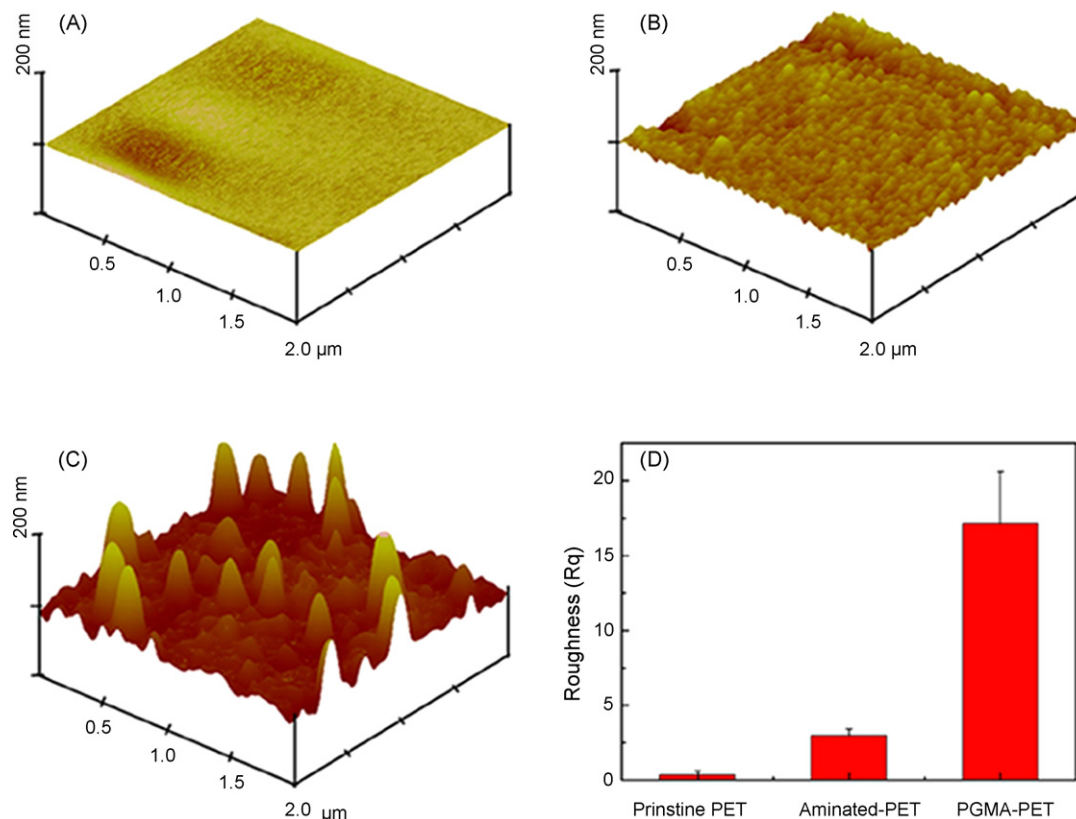
Fig. 1. AFM topographic images (2 μm × 2 μm). (A) Pristine PET surface; (B) aminated-PET surface; (C) PGMA-PET surface; (D) roughness of each surface.

probe protein dissolved in these buffers with a concentration of 100 μg mL^{-1} was spotted on PGMA-PET surface. The quality of microspots and efficiency of probe immobilization on the surface was examined using fluorescent scanner after applying of biotin-conjugated anti-rabbit IgG and Cy3-labeled streptavidin.

Fig. 3 indicates the influence of printing buffer on the quality of microarrayed spots. It is shown that a smearing profile appears when the printing buffer contains no or a low level of triton X-100 (Fig. 3I, columns A and B). The effect can be completely eliminated after using a printing buffer with higher percentage of triton X-100 (Fig. 3I, columns C–F). However, as a non-ionic detergent, excessive

triton X-100 in the buffer can damage the activity of protein and result in low immobilization efficiency since it blocks the protein immobilization on the substrate [37–39]. Fig. 3II illustrates that the signal intensity enhances first and then decreases with the increase of triton X-100. Group C (0.003% triton X-100 was applied) gives the highest fluorescent intensity (Fig. 3II). Therefore, the optimal printing buffer was determined to be PBS with 10% glycerol and 0.003% triton X-100.

3.4. Kinetics of protein immobilization on PGMA-PET surface

Study of kinetics of probe immobilization on substrate is of importance since it can quantitatively characterize the immobilization process and provide information for optimal immobilization conditions in protein microarrays fabrication. In order to determine the efficient immobilization time, protein immobilization on the PGMA-PET surface against the incubation time was investigated. The plot of fluorescence intensity versus incubation time (Fig. 4) shows that fluorescence intensity increases rapidly during the first two-hour incubation and reaches a plateau after 8 h. This result suggests the optimal incubation time for efficient protein immobilization on PGMA-PET substrate.

3.5. Protein loading capacity

The performance of protein microarrays can be greatly influenced by the amount of immobilized probes. Generally, the larger amount of probes is immobilized, the higher detection sensitivity of the microarrays is obtained. However, the amount of immobilized probe proteins does not increase linearly with its concentration in the printing buffer due to the limitation of substrates loading capacity. Since proteins (mostly antibodies or antigens) are expensive,
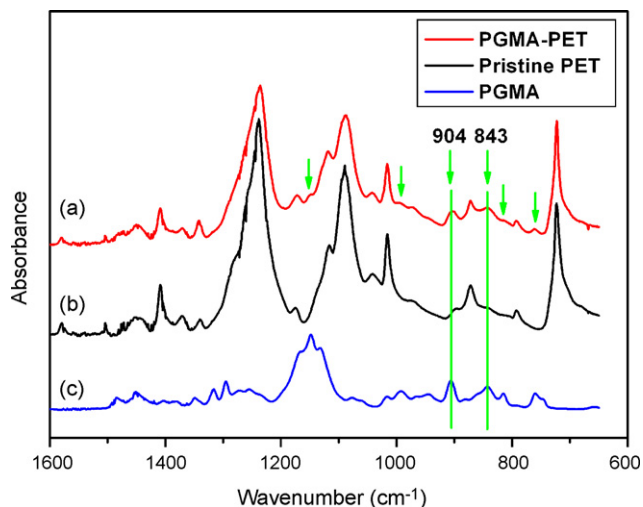
Fig. 2. ATR-FTIR spectra of PGMA-PET (a), pristine PET (b) and PGMA (c).
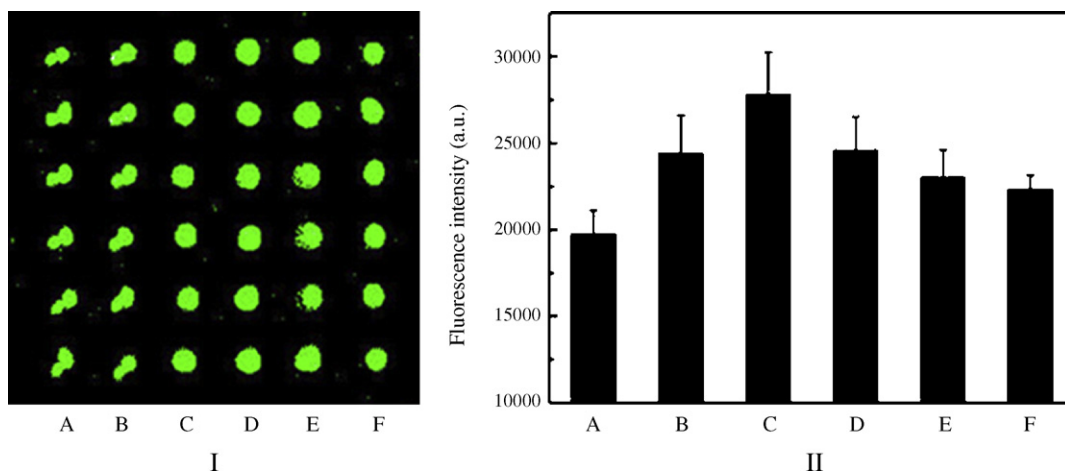
Fig. 3. Optimization of the printing buffer. Column A: 0.01 M PBS + 10% glycerol. Column B: 0.01 M PBS + 10% glycerol + 0.001% triton X-100. Column C: 0.01 M PBS + 10% glycerol + 0.003% triton X-100. Column D: 0.01 M PBS + 10% glycerol + 0.006% triton X-100. Column E: 0.01 M PBS + 10% glycerol + 0.009% triton X-100. Column F: 0.01 M PBS + 10% glycerol + 0.012% triton X-100.

the immobilization has to be efficient for both the sensitivity and economy.

In this work, the loading capacity of protein on PGMA-PET was assessed with biotin-conjugated anti-rabbit IgG as an example protein. A series of double-diluted biotinylated antibody in a range of 200–6.25 $\mu g\,mL^{-1}$ were printed on PGMA-PET surface. After post-printing incubation for overnight and blocking with Blocker^{TM} casein in TBS, Cy3-conjugated streptavidin was applied to array surface to produce fluorescence. Signal intensity as a function of printed concentrations of biotinylated anti-rabbit IgG is shown in Fig. 5. The fluorescence intensity increases rapidly with the increase of printed protein concentrations at low concentration range (below 100 $\mu g\,mL^{-1}$), and then slow increase is obtained when the concentration is higher than 100 $\mu g\,mL^{-1}$.

According to the Langmuir adsorption kinetics [40], the fraction of occupied surface anchors, θ, could be defined as

$$\theta = \frac{\Gamma_t}{\Gamma_0} \tag{1}$$

where Γ_t represents the surface concentration of immobilized proteins and Γ_0 is the maximal concentration of immobilized proteins that could be achieved on the surface (a complete coverage). Then, the surface adsorption and desorption kinetics could be described as

$$\frac{d\theta}{dt} = k_a(1-\theta)[A] - k_d\theta \tag{2}$$

where $[A]$ is the probe concentration in printing solution, k_a is the association rate constant, and k_d is the dissociation rate constant.

When the adsorption and desorption reach equilibrium, i.e. $d\theta/dt = 0$, the equilibrium surface coverage, θ_{eq}, could be given by the Langmuir adsorption isotherm

$$\theta_{eq} = \frac{K[A]}{1+K[A]}, \text{ thus}$$

$$R_{eq} = \frac{K[A]R_0}{1+K[A]} \tag{3}$$

where K is the equilibrium coefficient, defined as $K = k_a/k_d$, R_{eq} is the equilibrium fluorescence intensity in response to a certain concentration and R_0 is the fluorescence intensity for a complete coverage.

Fig. 5 also shows the fitting curve based on Eq. (3) by assuming the fluorescence intensity of complete coverage (R_0) as 45 000. The fitting result indicates that the amount of immobilized protein
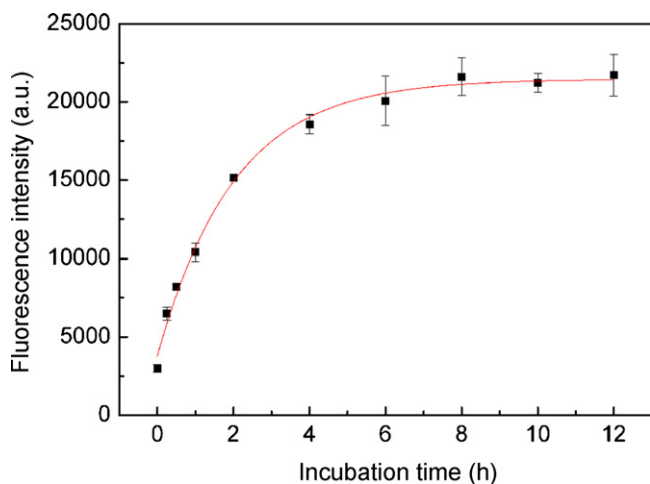
Fig. 4. Fluorescence intensity versus incubation time for immobilization of 100 $\mu g\,mL^{-1}$ Cy3-labeled anti-goat IgG on PGMA-PET surface.
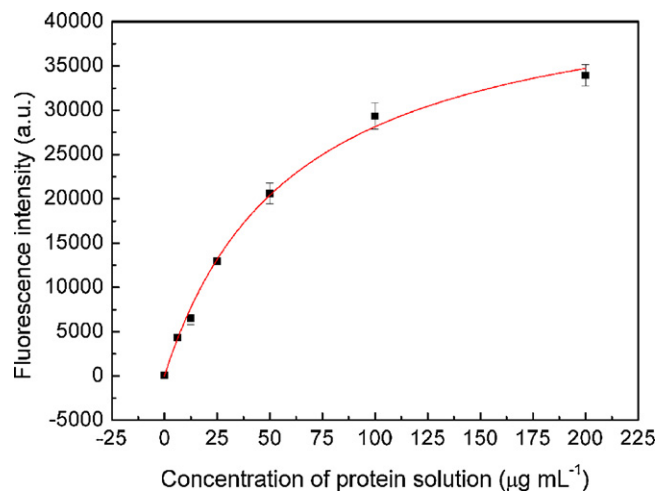
Fig. 5. Dependence of fluorescence intensity on the printed concentrations of biotinylated anti-rabbit IgG on PGMA-PET surface measured by experiments (scatter points) and the fitting curve (red line). (For interpretation of the references to color in this figure legend, the reader is referred to the web version of the article.)
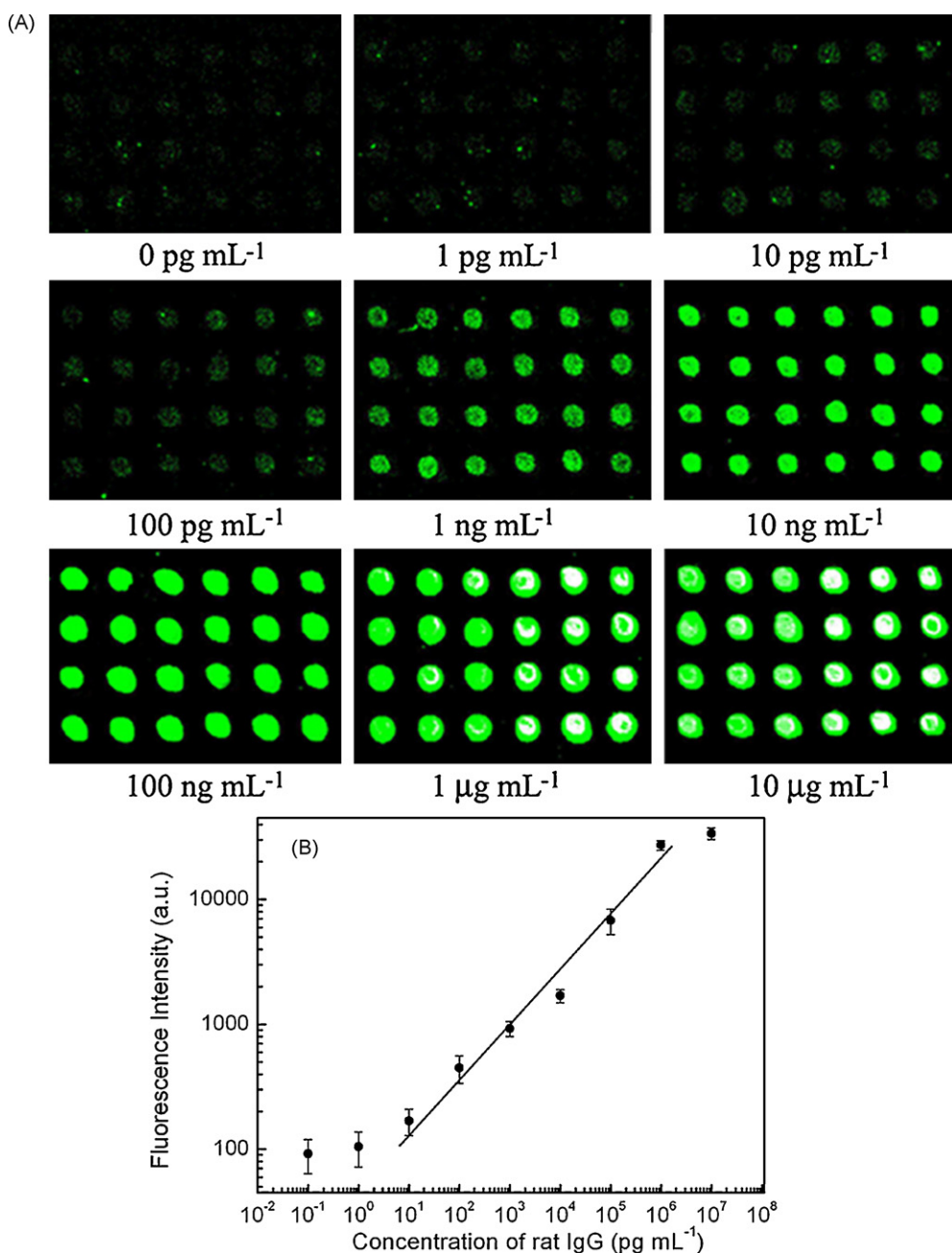
Fig. 6. Sandwich immunoassay on PGMA-PET surface. (A) Fluorescence images of antibody microarrays exposed to different concentrations of rat IgG. (B) Double logarithmic dose–response curve of rat IgG detection.

reaches ca. 76% of the maximal loading capacity of the PGMA-PET substrate when 200 μg mL^{-1} proteins are used. For both efficiency and economy considerations, the identified concentration was used in the following microarrays fabrication.

3.6. Performance of PGMA-PET-based protein microarrays

The dynamic range and limit of detection (LOD) of protein microarrays fabricated on PGMA-PET substrate was characterized by sandwich immunoassay with rat IgG and anti-rat IgG as model proteins. The antibody microarrays were produced with 200 μg mL^{-1} anti-rat IgG in the optimal printing buffer described above. Various concentrations of rat IgG from 10 μg mL^{-1} to 1 pg mL^{-1} with 10-fold dilution was used to incubate each array,

while the diluent was added to another array and regarded as a negative control. After the incubations, the biotin-conjugated anti-rat IgG and Cy3-conjugated streptavidin were subsequently applied to each array for imagining analysis as described in the experimental part.

Fig. 6A illustrates that the fluorescence intensity rises with the increase of analyte concentration. After quantitative analysis of fluorescence images in Fig. 6A, a plot of fluorescence intensity versus concentrations of the analyte, rat IgG with both logarithmic axes was obtained by using Origin 7.0. Fig. 6B shows the typical sigmoid dose–response curve for rat IgG detection. The sigmoid curve has a broad linear range from 10 pg mL^{-1} to 1 μg mL^{-1}. At the concentration above 1 μg mL^{-1}, the dose–response curve displays a plateau (Fig. 6B). It indicates that the dynamic range is from 10 pg mL^{-1} to

$1 \mu g\,mL^{-1}$. LOD (the concentration corresponding to three SDs) [20] is determined to be $10\,pg\,mL^{-1}$. The results clearly demonstrate that a broad dynamic range and excellent LOD of protein microarrays on PGMA-PET are achieved.

As for the performance of protein microarrays, the dynamic range and LOD are the most two important parameters. Currently, various strategies have been developed to improve the performance of protein microarrays. Wolter et al. prepared antibody microarrays based on poly(ethylene glycol) functionalized glass slides, then five orders dynamic range and $0.08\,ng\,mL^{-1}$ LOD were obtained [41]. Schweitzer et al. performed microarrays immunoassay based on rolling circle amplification (RCA) reporter system, and achieved a dynamic range over five logs and LOD of $1\,ng\,mL^{-1}$ IgE [42]. While Zhou et al. reported three orders dynamic range and LOD of $6\,pg\,mL^{-1}$ for protein microarrays based on 3D polyelectrolyte thin films prepared by Layer-by-Layer self-assembly [20]. Apparently, protein microarrays developed in this work show high performance in both dynamic range and LOD, which is better than or comparable with the reported works [20,41,42] and the commercialized ELISA as well [40]. The high performance of PGMA-PET-based protein microarrays could attribute to the improved surface properties, resulting in high surface area and high density of functional groups for high protein loading capacity.

4. Conclusions

In summary, a simple and efficient approach was described to introduce high density of epoxy groups to PET surface by grafting GMA photopolymer for high performance protein microarrays. The surface modification was characterized by AFM topography and IR spectroscopy. For efficient immobilization and high microspots quality, the printing buffer was optimized and determined to be PBS with 10% glycerol + 0.003% triton X-100. In addition, the optimal protein immobilization time and concentration were also examined by investigating protein immobilization kinetics and protein loading capacity. An excellent LOD of $10\,pg\,mL^{-1}$ and a wide dynamic range from $10\,pg\,mL^{-1}$ to $1\,\mu g\,mL^{-1}$ for protein microarrays is achieved, which is better than or comparable with the reported and commercialized protein microarrays. This work demonstrates that PGMA-PET substrate has great potential to be a novel polymeric platform for high performance protein microarrays through a simple and economic manufacturing process.

Acknowledgment

References

[1] R.M.T. de Wildt, C.R. Mundy, B.D. Gorick, I.M. Tomlinson, Nat. Biotechnol. 18 (2000) 989–994.
[2] A.Q. Emili, G. Cagney, Nat. Biotechnol. 18 (2000) 393–397.
[3] G. Walter, K. Bussow, D. Cahill, A. Lueking, H. Lehrach, Curr. Opin. Microbiol. 3 (2000) 298–302.
[4] H. Zhu, M. Snyder, Curr. Opin. Chem. Biol. 5 (2001) 40–45.
[5] R.P. Huang, R.C. Huang, Y. Fan, Y. Lin, Anal. Biochem. 294 (2001) 55–62.
[6] M.D. Moody, S.W. Van Arsdell, K.P. Murphy, S.F. Orencole, C. Burns, Biotechniques 31 (2001) 186-+.
[7] M.J. Dunham, P.O. Brown, B.B. Haab, Genome Biol. 2 (2001) research 0004.1–0004.13.
[8] G. MacBeath, S.L. Schreiber, Science 289 (2000) 1760–1763.
[9] H. Zhu, M. Bilgin, R. Bangham, D. Hall, A. Casamayor, P. Bertone, N. Lan, R. Jansen, S. Bidlingmaier, T. Houfek, T. Mitchell, P. Miller, R.A. Dean, M. Gerstein, M. Snyder, Science 293 (2001) 2101–2105.
[10] A.J. Nijdam, M.M.C. Cheng, D.H. Geho, R. Fedele, P. Herrmann, K. Killian, V. Espina, E.F. Petricoin, L.A. Liotta, M. Ferrari, Biomaterials 28 (2007) 550–558.
[11] A. Ressine, S. Ekstrom, G. Marko-Varga, T. Laurell, Anal. Chem. 75 (2003) 6968–6974.
[12] P. Pavlickova, N.M. Lensen, H. Paul, M. Schaeferling, C. Giammasi, M. Kruschina, W.D. Du, M. Theisen, M. Ibba, F. Ortigao, D. Kambhampati, J. Proteome Res. 1 (2002) 227–231.
[13] K. Derwinska, L.A. Gheber, C. Preininger, Anal. Chim. Acta 592 (2007) 132–138.
[14] F. Fixe, M. Dufva, P. Telleman, C.B.V. Christensen, Nucleic Acids Res. 32 (2004).
[15] F. Fixe, M. Dufva, P. Telleman, C.B.V. Christensen, Lab Chip 4 (2004) 191–195.
[16] Y.C. Li, Z. Wang, L.M.L. Ou, H.Z. Yu, Anal. Chem. 79 (2007) 426–433.
[17] I. Humphery-Smith, J.S. Albala, Protein Arrays, Biochips, and Proteomics, Marcel Dekker Inc., 2003.
[18] W. Kusnezow, J.D. Hoheisel, J. Mol. Recognit. 16 (2003) 165–176.
[19] S.Y. Seong, C.Y. Choi, Proteomics 3 (2003) 2176–2189.
[20] X.C. Zhou, J.Z. Zhou, Proteomics 6 (2006) 1415–1426.
[21] W. Kusnezow, A. Jacob, A. Walijew, F. Diehl, J.D. Hoheisel, Proteomics 3 (2003) 254–264.
[22] Y.S. Liu, C.M. Li, L. Yu, P. Chen, Front. Biosci. 12 (2007) 3768–3773.
[23] V. Afanassiev, V. Hanemann, S. Wolfl, Nucleic Acids Res. 28 (2000) e66.
[24] L.N. Bui, M. Thompson, N.B. McKeown, A.D. Romaschin, P.G. Kalman, Analyst 118 (1993) 463–474.
[25] R. Fukai, P.H.R. Dakwa, W. Chen, J. Polym. Sci. Polym. Chem. 42 (2004) 5389–5400.
[26] H. Gappa-Fahlenkamp, R.S. Lewis, Biomaterials 26 (2005) 3479–3485.
[27] S.P. Massia, J. Stark, D.S. Letbetter, Biomaterials 21 (2000) 2253–2261.
[28] I. Bisson, M. Kosinski, S. Ruault, B. Gupta, J. Hilborn, F. Wurm, P. Frey, Biomaterials 23 (2002) 3149–3158.
[29] S.H. Hyun, M.W. Kim, D.H. Oh, I.K. Kang, W.S. Kim, J. Appl. Polym. Sci. 101 (2006) 863–868.
[30] K. Sugiyama, K. Kato, M. Kido, K. Shiraishi, K. Ohga, K. Okada, O. Matsuo, Macromol. Chem. Phys. 199 (1998) 1201–1208.
[31] C. Yin, L. Ying, P.C. Zhang, R.X. Zhuo, E.T. Kang, K.W. Leong, H.Q. Mao, J. Biomed. Mater. Res. A 67A (2003) 1093–1104.
[32] L. Ying, C. Yin, R.X. Zhuo, K.W. Leong, H.Q. Mao, E.T. Kang, K.G. Neoh, Biomacromolecules 4 (2003) 157–165.
[33] J.W. Zhu, J.P. Deng, S.M. Cheng, W.T. Yang, Macromol. Chem. Phys. 207 (2006) 75–80.
[34] L. Malovic, A. Nastasovic, Z. Sandic, J. Markovic, D. Dordevic, Z. Vukovic, J. Mater. Sci. 42 (2007) 3326–3337.
[35] M. Cretich, G. Pirri, F. Damin, I. Solinas, M. Chiari, Anal. Biochem. 332 (2004) 67–74.
[36] Y. Deng, X.Y. Zhu, T. Kienlen, A. Guo, J. Am. Chem. Soc. 128 (2006) 2768–2769.
[37] K.L. Brogan, J.H. Shin, M.H. Schoenfisch, Langmuir 20 (2004) 9729–9735.
[38] J.S. Wang, J.X. Shan, Q. Xu, X. Ruan, Y.D. Gong, T.Y. Kuang, N.M. Zhao, J. Photochem. Photobiol. B 58 (2000) 136–142.
[39] S. Zampieri, A. Ghirardello, A. Doria, M. Tonello, R. Bendo, K. Rossini, P.F. Gambari, J. Immunol. Methods 239 (2000) 1–11.
[40] G.H. Yan, D. Xing, S.C. Tan, Q. Chen, J. Immunol. Methods 288 (2004) 47–54.
[41] A. Wolter, R. Niessner, M. Seidel, Anal. Chem. 79 (2007) 4529–4537.
[42] B. Schweitzer, S. Wiltshire, J. Lambert, S. O'Malley, K. Kukanskis, Z.R. Zhu, S.F. Kingsmore, P.M. Lizardi, D.C. Ward, Proc. Natl. Acad. Sci. U.S.A. 97 (2000) 10113–10119.

Magnetic solid-phase extraction based on octadecyl functionalization of monodisperse magnetic ferrite microspheres for the determination of polycyclic aromatic hydrocarbons in aqueous samples coupled with gas chromatography–mass spectrometry

Yan Liu [a,b], Haifang Li [a], Jin-Ming Lin [a,*]

[a] *The Key Laboratory of Bioorganic Phosphorus Chemistry & Chemical Biology, Department of Chemistry, Tsinghua University, Beijing 100084, China*
[b] *Beijing Center for Physical and Chemical Analysis, Beijing 100089, China*

ARTICLE INFO

ABSTRACT

Monodisperse magnetic C_{18} microspheres were prepared based on the three-step reactions of solvothermal reduction, silanization and alkylation. The microspheres are of uniform sizes in the range of 200–260 nm. The structure of synthesized magnetic C_{18} microspheres was studied by transmission electron microscopy, scanning electron microscopy, X-ray diffraction patterns, element analysis and vibrating sample magnetometry. This material has a high magnetic saturation value of 59 emu g^{-1} and is easy to manipulate under a magnet. The prepared material was used for the preconcentration of the polycyclic aromatic hydrocarbon in water. The effects of desorption solvent and the amount of adsorbent on the preconcentration were also investigated. The results showed that the developed method was beneficial for the preconcentration of PAHs of middle molecular weight.

© 2008 Elsevier B.V. All rights reserved.

1. Introduction

Polycyclic aromatic hydrocarbons (PAHs) are of concern due to their carcinogenicity and mutagenicity [1]. PAHs are a class of several hundred individual compounds defined to be composed of two or more fused aromatic rings and created when products like coal, oil, gas and garbage are burned but the burning process is not complete. EPA prior controlled 16 PAHs were in the range of 2–6 fused aromatic rings and had different physical properties (volatilization and solubility) that brought the difficulties of their simultaneous pretreatment. Simple, rapid and effective methods are the ultimate goal of developed pretreatment.

Magnetic solid-phase extraction (MSPE) is an excellent extraction method, which is a new procedure of SPE based on the use of magnetic or magnetizable adsorbents. In this procedure magnetic adsorbent is added to a solution or suspension containing the target analyte. The analyte is adsorbed onto the magnetic adsorbent and then the adsorbent with adsorbed analyte is recovered from the suspension using an appropriate magnetic separator. The analyte is consequently eluted from the recovered adsorbent

and analysed. The main advantage of using magnetic functionalized material as adsorbent makes the sample pretreatment simple [2–5]. The adsorbent need not be packed into the SPE cartridges like the traditional SPE and the phase separation could be conveniently realized by applying an external magnetic field. Some functional magnetic materials were prepared and applied to separation/preconcentration.

C_{18} materials have been widely used for the preconcentration of enviromental organic pollutants because of their favorable separation ability, excellent stability and long lifetime [6,7]. Therefore, the prepared magnetic C_{18} microspheres are expected to perform excellently in the aspects of adsorption and separation of the hydrophobic substances from water sample. Magnetic C_{18} material had been reported in the previous literatures [8,9], which had been prepared according to the direct reaction between magnetite and octadecyltrichlorosilane. The materials are not stable when they are in the preservation because the magnetite is easy to be oxidized in the air. In this work, monodisperse and homogeneous magnetic C_{18} microspheres with high magnetic saturation value were prepared based on the three-step reactions of solvothermal reduction, silanization and alkylation. Silanization produced silica as the shell of magnetite, which could not only protect the magnetite but also increase the surface area because of mesoporous coatings. Moreover, silica-coating could introduce large numbers

---

Y. Liu et al. / Talanta 77 (2009) 1037–1042

of hydroxyl group in the surface of particles and tune the magnetic properties of particles by changing its coating thickness. Mesoporous silica-magnetite materials prepared using various methods were reported [10–13]. Here, the hydrolysis of tetraethyl orthosilicate (TEOS) was chosen to produce the silica shell. Furthermore, magnetic Fe_3O_4 particle was chosen as the magnetic core due to its simple, cheap and high yield synthesis method, especially high magnetic property to satisfy the requirement of magnetic separation. To the best of our knowledge, monodisperse and homogeneous magnetic C_{18} microspheres with high magnetic saturation values are reported first. Finally, MSPE method was established and applied to the preconcentration of polycyclic aromatic hydrocarbons in water.

2. Experimental

2.1. Reagents

Reference PAHs (16 compounds, each at $2000\,\mu g\,mL^{-1}$) were obtained from Supelco (Walton-on-Thames, UK). The solution was diluted with methanol to prepare $10\,\mu g\,mL^{-1}$ stock standard solution. All solutions were stored and refrigerated at $4\,°C$. Then, the working standard solution was freshly prepared by diluting the mixed standard solution with distilled water to required concentrations. $FeCl_3\cdot6H_2O$, ethylene glycol, polyethylene glycol and NaAc were analytical reagents. Trichloro(octadecyl)silane (Aldrich), TEOS, trimethylchorosilane and triethylamine were used. Toluene and methanol were all of HPLC grade. All glasswares were cleaned thoroughly by soaking overnight in diluted HNO_3 and rinsing with ultra-pure water (Millipore, Bedford, MA, USA) and dried.

2.2. Apparatus

SEM images were obtained on an S-3000N field emission scanning electron microscope (Hitachi, Japan). TEM images were generated with an H-800 transmission electron microscopy (Hitachi, Japan). XRD analysis was carried out on a Bruker D8 advance powder X-ray diffractometer at a voltage of 40 kV and a current of 40 mA with Cu Kα radiation (λ = 1.5406 Å). Element analysis was obtained by the CE-440CHN/O/S elemental analyzer (Exeter Analytical, Inc., USA). Magnetization measurements were studied with a vibrating sample magnetometer (VSM, LakeShore7307, USA).

A Shimadzu GCMS-QP2010 (Shimadzu, Kyoto, Japan) system was equipped with a 30-m × 0.25-mm-i.d. fused-silica capillary column with a 0.1-μm Rtx-5 ms coating (5% phenyl:95% dimethylpolysioxane). The carrier gas helium was maintained at

a constant linear velocity of $37\,cm\,s^{-1}$. The injector port temperature was set to $280\,°C$ in a splitless mode with the splitter activated after 1 min. The column was held at $70\,°C$ for 1 min, increased to $180\,°C$ at the rate of $25\,°C\,min^{-1}$ for 2 min, then increased to $280\,°C$ at the rate of $15\,°C\,min^{-1}$ for 2 min, finally increased to $300\,°C$ at the rate of $10\,°C\,min^{-1}$ for 5 min. The mass spectrometer was operated in the electron impact ionization (EI) mode with an ion source temperature of $200\,°C$ and the energy of electrons was kept at 70 eV. And the interface temperature was kept at $260\,°C$.

2.3. Preparation of magnetic octadecyl modified silica gel

The process of preparation of magnetic C_{18} microspheres was illustrated in Scheme 1. Firstly, the magnetic Fe_3O_4 microspheres were synthesized by a solvothermal reduction method; secondly, the Fe_3O_4 microspheres were modified with TEOS; thirdly, C_{18} chain was bonded to the surface of silica gel modified magnetic microspheres through the Si–O–Si combination.

2.3.1. Preparation of magnetic microspheres
Magnetic microspheres were prepared by a solvothermal reduction method [14]. 1.35 g $FeCl_3\cdot6H_2O$ was dissolved in 40 mL ethylene glycol to form a clear solution, followed by the addition of 3.6 g NaAc and 1.0 g polyethylene glycol. The mixture was stirred vigorously for 30 min and then sealed in a 50 mL teflon-lined stainless-steel autoclave. The autoclave was heated and maintained at $200\,°C$ for 12 h, then was cooled to room temperature. The black Fe_3O_4 microspheres were washed several times with ethanol and dried at $60\,°C$ for 6 h in oven.

2.3.2. Preparation of magnetic silica gel
The mesoporous silica shell was formed on the surface of the Fe_3O_4 microsphere. The mesoporous silica shell was formed from sol–gel polymerization method. 30 mg of the prepared magnetite microspheres was dispersed in 80 mL ethanol by sonication for more than 30 min. 3 mL of 15 M ammonia, 5 mL of deionized water and 100 μL of TEOS were added into the microspheres solution. Finally, the mixture was placed into a $40\,°C$ water bath and vigorously stirred for 2 h.

2.3.3. Preparation of magnetic octadecyl modified silica gel
Before C_{18} functionalization, silica gel modified magnetic microspheres were dried at $100\,°C$ for 4 h under vacuum. 3 g of the dried silica modified magnetic microspheres was added to 90 mL toluene. The slurry was heated to boiling, and 10 mL of triethylamine and 1 mL of silane reagent were added in succession. The
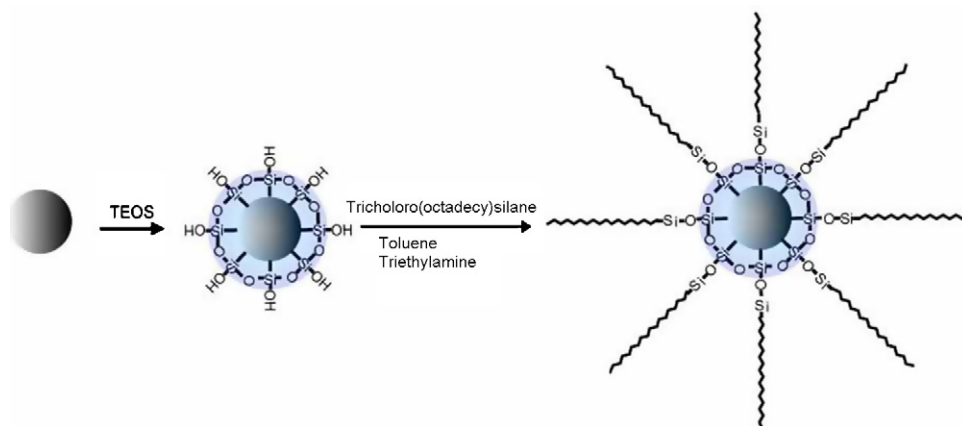
Scheme 1. Schematic synthesis of magnetic C_{18} microspheres.

mixture was then refluxed for 24 h. The magnetic C_{18} microspheres were obtained, which were washed and dried for use.

2.4. General procedure

50-mg magnetic C_{18} microspheres were put into a 40 mL beaker and firstly cleaned and activated with *n*-hexane, acetone, methanol and distilled water in sequence. Then 20 mL of 0.5 μg L^{-1} PAHs aqueous solution was added into the beaker. The mixture was sonicated at room temperature for 1 min to form a homogeneous dispersion solution. After standing for 5 min, magnetic C_{18} microspheres adsorbed PAHs were separated rapidly from the solution under a strong external magnetic field. After discarding the supernatant solution, PAHs were eluted from the magnetic C_{18} microspheres with 3× 1.5 mL of *n*-hexane. Then the solution was concentrated to 0.5 mL with a stream of nitrogen. Finally, 1.0 μL of
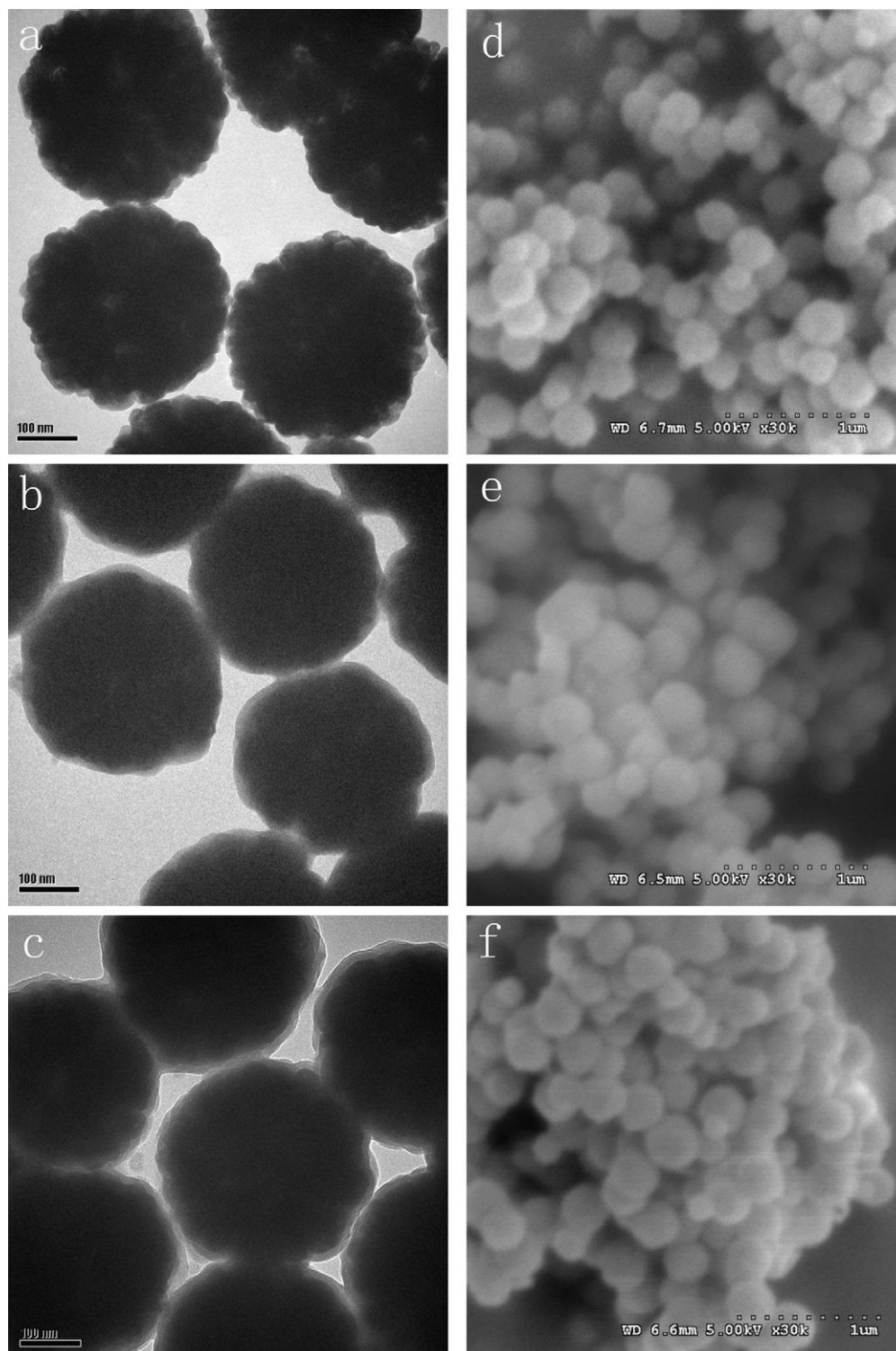
Fig. 1. TEM (a, b and c) and SEM (d, e and f) of magnetite microspheres, silica gel modified magnetic microspheres and magnetic C_{18} microspheres, respectively.
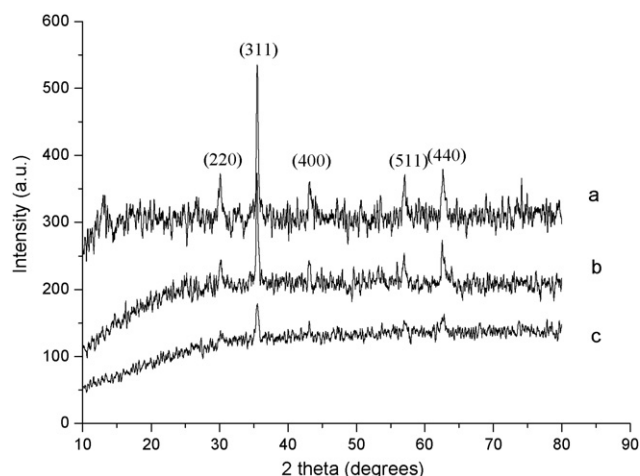
Fig. 2. XRD of (a) magnetite microspheres, (b) silica gel modified magnetic microspheres and (c) magnetic C_{18} microspheres.

Fig. 3. Room-temperature magnetization curves of (a) magnetite microspheres, (b) silica gel modified magnetic microspheres and (c) magnetic C_{18} microspheres.

the PAHs eluate was analysed by gas chromatography–mass spectrometry (GC–MS).

3. Results and discussion

3.1. Structural characterization of prepared products

The size and shape of the prepared microspheres were examined by transmission electron microscopy (TEM) and scanning electron microscopy (SEM) as shown in Fig. 1. Fig. 1a and d shows the prepared magnetite microspheres to be fairly well dispersed, having uniform sizes in the range of 200–260 nm and are spherical. The silica shell thickness was estimated about 5 nm according to Fig. 1b. The silica shell thickness could vary with the different dosage of TEOS and reaction time. But we found that 100 μL of TEOS in 80 mL ethanol was the best. If more TEOS was added, both the silica shell on the Fe_3O_4 microsphere and the pure silica particles would synchronously form, which make the prepared magnetic C_{18} microspheres impure. Fig. 1c and f shows that the prepared magnetic C_{18} microspheres are monodisperse, homogeneous and spherical.

According to the element analysis, the content of carbon of magnetite microspheres, silica gel modified magnetic microspheres and magnetic C_{18} microspheres were 1.86, 1.56 and 5.11%, respectively, which proved that C_{18} group was bonded to the surface of silica gel

modified magnetic microspheres. It was noted that since the ferrite core was very easy leaching into the reaction liquor under the low pH [15], the alkalescence of reaction solvent was necessary during the preparation of magnetic C_{18} microspheres.

In order to investigate the structure and composition of magnetite microspheres, silica gel modified magnetic microspheres and magnetic C_{18} microspheres, X-ray diffraction patterns (XRD) were employed to analyze them. As shown in Fig. 2a, the patterns of ferrite oxide were consistent with Fe_3O_4 (JCPDS 75-1609). Furthermore, the silica shell and the bonding reaction have little effect on the structure of Fe_3O_4 microspheres.

3.2. Magnetic properties of prepared products

The magnetic properties of the prepared microspheres were investigated with a vibrating sample magnetometer. As shown in Fig. 3, the magnetic saturation values are 87 emu g^{-1} for Fe_3O_4 microspheres, 59 emu g^{-1} for silica gel modified magnetic microspheres and 59 emu g^{-1} for magnetic C_{18} microspheres. When silica-coating was formed, the magnetic properties of microparticles were weaker than the original Fe_3O_4 microspheres, since the extent of dipolar coupling is related to the distance between the particles and this in turn depends on the thickness of the inert silica shell and provides hydroxyl group. The magnetic saturation values of the silica gel modified magnetic microspheres
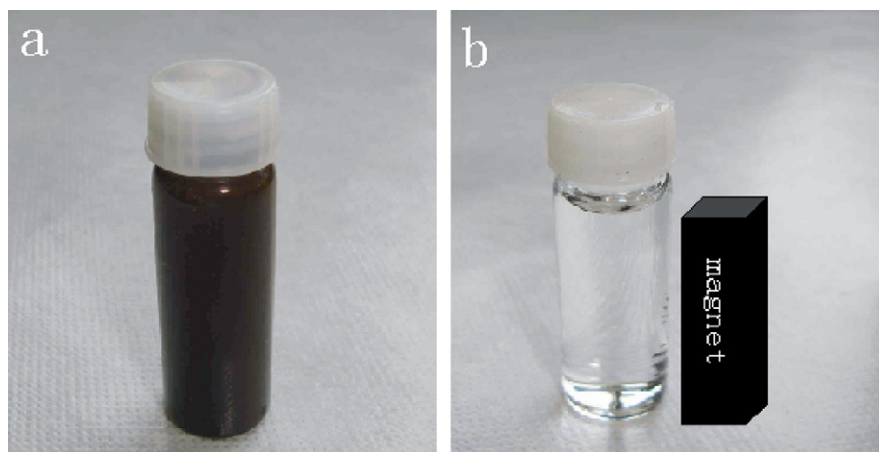
Fig. 4. The dispersion (a) and separation (b) process.
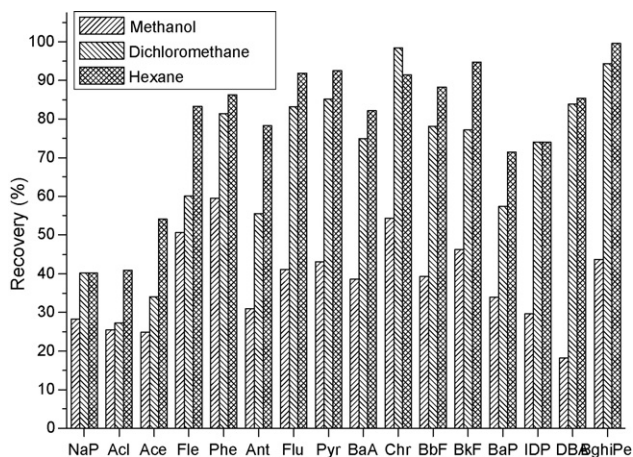
Fig. 5. The effect of desorption solvent on the extraction performance (adsorbent: 50 mg magnetic C_{18} microspheres, sample: 20 mL 0.5 μg L^{-1} spiked PAHs in aqueous sample and desorption solvent: 3× 1.5 mL).

and magnetic C_{18} microspheres are almost the same, which were strong enough to be easily separated by external magnetic field (see to Fig. 4).

3.3. Effect of desorption solvent

Three different common organic solvents (methanol, *n*-hexane, dichloromethane; 3× 1.5 mL for each solvent) were used as elution solvents to determine their impact on the recoveries and the results are shown in Fig. 5. Among the three eluents, *n*-hexane provided the best result.

3.4. Effect of the amount of adsorbent

The amount of the adsorbent was investigated so that the adsorbent not only adsorbs sufficient analysts but also remains utilized. 10, 30, 50 and 75 mg of magnetic C_{18} microspheres were discussed and the result is shown in Fig. 6. 50 mg of magnetic C_{18} microspheres could adsorb the analytes sufficiently and the recovery of most PAHs was quantitative. To the volatile PAH, there were lower recoveries in that they were high volatile and easy to loss in the process of the manipulation.
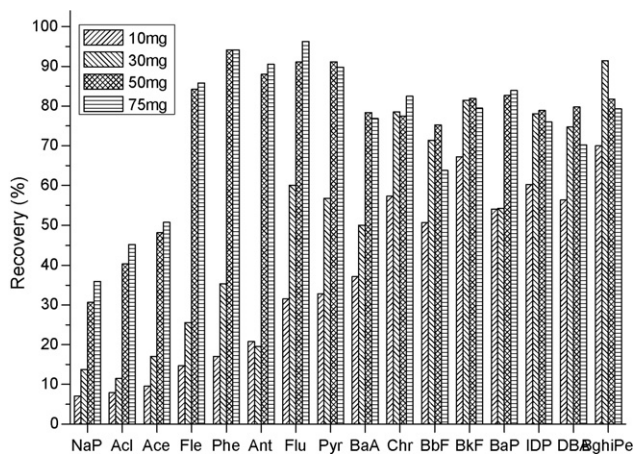
Fig. 6. The effect of the amount of adsorbent on the extraction performance (sample: 20 mL 0.5 μg L^{-1} spiked PAHs in aqueous sample, desorption solvent: 3× 1.5 mL *n*-hexane).

Table 1
Linear range, regression coefficients (R^2), limits of detection (LODs) and repeatability (R.S.D., $n = 3$) of analytical method

PAHs	Linear range (μg L^{-1})	R^2	LOD (μg L^{-1})	R.S.D. (%)
NaP	10–800	0.9984	0.8	4.1
Acl	10–800	0.9958	2.8	5.2
Ace	10–800	0.9937	4.1	5.0
Fle	10–800	0.9963	1.6	3.8
Phe	10–800	0.9985	3.4	5.2
Ant	10–800	0.9992	4.2	4.5
Flu	10–800	0.9994	3.9	4.4
Pyr	10–800	0.9992	5.1	4.0
BaA	10–800	0.9971	5.8	4.1
Chr	10–800	0.9981	4.9	5.2
BbF	10–800	0.9947	3.5	4.1
BkF	10–800	0.9989	3.6	4.6
BaP	10–800	0.9970	5.6	2.0
DBA	10–800	0.9927	36	3.5
BghiPe	10–800	0.9942	7.6	10
IDP	10–800	0.9959	7.9	7.0

3.5. Evaluation of the method performance

Linearity range, limit of detection, accuracy and repeatability of the method were investigated and the result is shown in Table 1. The linearity ranges of analytical method of 16 PAHs were in the range of 10–800 μg L^{-1}. Meanwhile, the regression coefficients (R^2) were in the range of 0.9927–0.9994. Furthermore, the limit of detections (S/N = 3) of 16 PAHs were in the range of 0.8–36 μg L^{-1} and the repeatability was calculated by the 3-time determinations of 200 μg L^{-1} standard sample. Analytical method has good repeatability.

3.6. Applications

The developed method was applied to determine 20 mL of 0.5 μg L^{-1} spiked 16 PAHs tap water sample and the chromatogram is shown in Fig. 7. The recoveries of NaP, Acl, Ace, Fle, Phe, Ant, Flu, Pyr, BaA, Chr, BbF, BkF, BaP, DBA, BghiPe and IDP were 35, 42, 50, 72, 93, 70, 90, 91, 76, 99, 74, 96, 72, 64, 70 and 85%, respectively. Relative standard deviations were less than 10% according to the 3-time determinations. From the result we can see that the recoveries of middle molecular weight PAHs were better than the low and high molecular weight PAHs, which is consistent with the previous report [16]. The possible reason is the carbon length
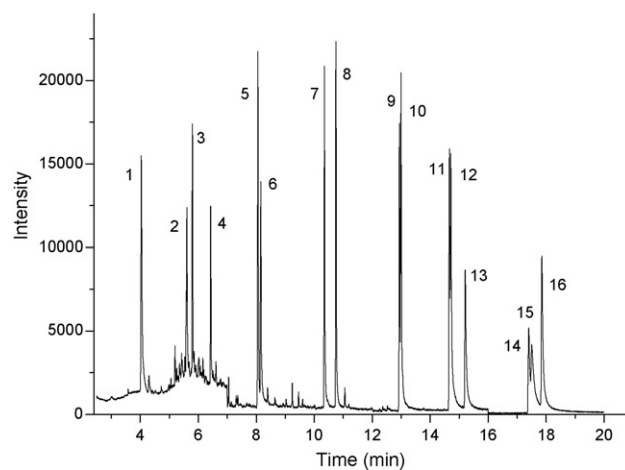
Fig. 7. Chromatogram of 16 PAHs in spiked water at a concentration of 0.5 μg L^{-1} under the optimum extraction condition. Peaks: (1) NaP; (2) Acl; (3) Ace; (4) Fle; (5) Phe; (6) Ant; (7) Flu; (8) Pyr; (9) BaA; (10) Chr; (11) BbF; (12) BkF; (13) BaP; (14) IDP; (15) DBA; (16) BghiPe.

and solubility of C_{18} adapting to the middle molecular weight PAHs retentions. Furthermore, the investigation of our group on the retention behavior of 16 PAHs on C_{30} adsorbents showed that the longer carbon chain PAHs had stronger retention ability on C_{30} than on C_{18} [17]. The study also proved that high molecular weight (5-6-ring) PAHs were retained more easily on C_{30} than on C_{18}.

4. Conclusions

Monodisperse magnetic C_{18} microspheres with a magnetic saturation value as high as $59\,emu\,g^{-1}$ were prepared successfully. A rapid, convenient and efficient pretreatment of PAHs using magnetic C_{18} microspheres as extraction materials was accomplished based on magnetic separation. Magnetic C_{18} microspheres extraction is possible to achieve automation and high-throughput with the help of a magnet. It is believed that the magnetic C_{18} microspheres have a good potential for the separation, purification and preconcentration of environmental pollutants, pesticide residues and biological molecules.

Acknowledgments

References

[1] IARC, Polynuclear aromatic compounds. Part 1, chemical, environmental and experimental data, in: IARC Monographs on the Evaluation of the Carcinogenic Risk of Chemicals to Humans, vol. 32, International Agency for Research on Cancer, Lyon, 1983, p. p. 453.
[2] M. Safarikova, I. Safarik, J. Magn. Magn. Mater. 194 (1999) 108.
[3] Y. Deng, C. Deng, D. Yang, C. Wang, S. Fu, X. Zhang, Chem. Commun. 44 (2005) 5548.
[4] J. Li, X. Zhao, Y. Shi, Y. Cai, S. Mou, G. Jiang, J. Chromatogr. A 1180 (2008) 24.
[5] X.L. Zhao, Y.L. Shi, Y.Q. Cai, S.F. Mou, Environ. Sci. Technol. 42 (2008) 1201.
[6] D.J. Anderson, Anal. Chem. 67 (1995) 475R.
[7] J.G. Dorsey, W.T. Cooper, B.A. Siles, J.P. Foley, H.G. Barth, Anal. Chem. 68 (1996) 515R.
[8] H. Katsumata, H. Asai, S. Kaneco, T. Suzuki, K. Ohta, Microchem. J. 85 (2007) 285.
[9] H.Y. Shen, Y. Zhu, X.E. Wen, Y.M. Zhuang, Anal. Bioanal. Chem. 387 (2007) 2227.
[10] H. Lu, G. Yi, S. Zhao, D. Chen, L.H. Guo, J. Cheng, J. Mater. Chem. 14 (2004) 1336.
[11] P. Wu, J. Zhu, Z. Xu, Adv. Funct. Mater. 14 (2004) 345.
[12] W. Zhao, J. Gu, L. Zhang, H. Chen, J. Shi, J. Am. Chem. Soc. 127 (2005) 8916.
[13] T. Sen, A. Sebastianelli, J. Bruce, J. Am. Chem. Soc. 128 (2006) 7130.
[14] H. Deng, X.L. Li, Q. Peng, X. Wang, J. Chen, Y. Li, Angew. Chem. Int. Ed. 44 (2005) 2782.
[15] W.J. Rieter, K.M.L. Taylor, W. Lin, J. Am. Chem. Soc. 129 (2007) 9852.
[16] F. Busetti, A. Heitz, M. Cuomo, S. Badoer, P. Traverso, J. Chromatogr. A 1102 (2006) 104.
[17] K. Li, H. Li, L. Liu, Y. Hashi, T. Maeda, J.-M. Lin, J. Chromatogr. A 1154 (2007) 74.

Clinical analysis of human urine by means of potentiometric Electronic tongue

Larisa Lvova [a,b,*], Eugenio Martinelli [c], Francesca Dini [c], Alberto Bergamini [d], Roberto Paolesse [a], Corrado Di Natale [c], Arnaldo D'Amico [c]

[a] Department of Chemical Science and Technologies, University "Tor Vergata", 00133 Rome, Italy
[b] Biological Research Institute of St. Petersburg State University, 198504 St. Petersburg, Russia
[c] Department of Electronic Engineering, University "Tor Vergata", 00133 Rome, Italy
[d] Department of Public Health and Cellular Biology, University "Tor Vergata", 00133 Rome, Italy

ARTICLE INFO

ABSTRACT

The Electronic tongue (ET) composed of different kind of potentiometric chemical sensors has been applied for the detection of urinary system dysfunctions and creatinine levels. The creatinine contents evaluated by ET were compared with those obtained by automated Jaffe's method and GC-MS, obtaining a satisfying agreement for both methods. Partial least square regression discriminate analysis (PLS-DA) and feed forward back-propagation neural network (FFBP NN) classified 51 urine specimens from healthy volunteers in four classes, according to the creatinine content, showing that both techniques can satisfactorily differentiate urines according to this parameter. The best accuracy result of 92.2% correct classification of unknown samples was achieved with FFBP NN. Moreover, the possibility of ET system to distinguish between urine samples of healthy patients, and those with malignant and non-malignant tumor diagnosis of bladder has been shown.

© 2008 Elsevier B.V. All rights reserved.

1. Introduction

Urine clinical analysis is important for human health care since it may provide parameters useful for diagnosis of some dysfunctions or pathologies. Furthermore the degree of assimilation of various remedies as far as the intake of some drugs and doping agents may be obtained by monitoring the patient urine composition [1]. Finally, the analysis of urine samples in biological monitoring is a preferred method to assess human exposures to environmental and workplace chemicals, due to a simplicity of a urine sampling and because of sufficient amounts of sample material available [2,3]. Among the different urine components, creatinine is particularly interesting, because it is the end product of muscle metabolism and it is excreted from the body by urinary system [4]. The changes in urinary creatinine amount can indicate thyroid disorders, muscle wasting diseases such as muscular dystrophy and can be widely used in a clinical analysis for the determination of the renal glomerular filtration rate as a marker of kidney dysfunction [5]. Moreover, in medical practice and particu-

larly in drug discovery and biomonitoring applications, the content of several urine components and especially of nonpersistent polluting chemicals (i.e. compounds having short biological half-lives, such as most of pesticides, metals and drugs) and drug metabolites is used to be represented in units relative to the urinary creatinine concentration, so-called creatinine-adjusted concentrations [2,6–8]. Therefore, the accurate and rapid assessment of creatinine levels in body fluids is clinically important and remains one of the most requested in clinical laboratories [9].

Since many decades, Jaffe's method is the most-used for creatinine detection among a variety of analytical methods. The method is based on the spectrophotometric detection at 500 nm (either end point or kinetic) of the orange-red colored complex formed by creatinine with picric acid under alkaline conditions [10]. Subsequently semi-automated and automated urinary creatinine detection by modified Jaffe's method were also reported [11,12]. Besides this well-established spectroscopic procedure, separation methods such as high-performance liquid chromatography (HPLS), high-performance thin-layer chromatography (HPTLC), capillary electrophoresis (CE), gas- or liquid-chromatography in combination with mass spectrometry (GC/LC-MS) have been applied recently for urinary creatinine determination [13–16]. An application of Surface Enhanced Raman Scattering Spectroscopy (SERS) on 50 nm colloidal gold particles for human urine creatinine detection

has been reported by Chiang and co-workers [17]. However, such methods often require multi-step separation and either derivation of analyte.

After pioneering works of Rechnitz and co-workers [18,19] a significant progress has been made towards developing and improving enzymatic methods for creatinine biosensing [20]. Two main enzymatic schemes are used: (a) incorporation of creatinine deiminase with following amperometric ammonia detection [21] or potentiometric monitoring of ammonium-ion [22–25] (b) application of three-enzyme system consisting of creatininase, creatinase and sarcosine oxidase with a final detection of released hydrogen peroxide [26–28]. In order to improve creatinine biosensor selectivity and stability a variety of modifications, such as the use of electron-transfer mediators [29], immobilization [30,31] or either entrapping of enzymes in polymeric films [32,33], the use of permselective membranes [34] or employing an insoluble oxidizing agent layer for removing redox-active interferences [35] have been explored. The novel approach for creatinine potentiometric sensing has been suggested by Pandey and Mishra [36]. A bi-enzymatic reactor containing creatininase and creatinase within two layers of organically modified ORMOSIL glass converts creatinine into urea and the latter is monitored by urea biosensor based on polyaniline pH electrode with immobilized urease layer. The application of In-MOS capacitors as detectors in ammonia-N-sensitive probe combined with creatinine deiminase reactor for creatinine analysis in biological fluids was reported by Winquist et al. [37]. Sant et al. reported the development of miniaturized disposable creatinine-sensitive enzymatic field effect transistor (Creatinine-EnFET) [38]. Creatinine-EnFET showed sensitivity at approximately 30 mV/pCreatinine in the 10–1000 μmol/l range. Being stored in darkness at 4 °C sensors had 1 week lifespan with decrease of sensitivity in 2 times. The same authors performed the modeling of creatinine-EnFETs in order to optimize sensors functionality in the field of hemodialysis applications [39].

However both classical spectroscopic, LGH-MS or enzymatic methods for urine components detection also if very selective, are complex, require sample pretreatment, professional operators and expensive equipment. Even if a volume of the analyzed sample is not a problem, it is often not possible to use it for other detections since these methods destruct a sample (derivatives are detected). Moreover, as mentioned above, the specific storage conditions and a short lifetime is a serious drawback of biosensors application.

An application of enzymeless chemical sensors and sensors arranged in an array may appear a possible alternative method which can be used for routine urine analysis even in a small and simply equipped laboratory. Moreover, it permits either to identify various urine samples or to detect at the same time several parameters of the same sample. An enzymeless electrochemical approach for the selective and quantitative recognition of creatinine in human urine by using a preanodized screen-printed carbon electrode (SPE) has been demonstrated by Zen and co-workers [40]. The formation of a stable carbon–carbon bond between SPE surface and active methylene group of creatinine during a preconcentration step was identified by XPS. A potentiometric solvent polymeric membrane sensor based on dibenzo-30-crown-10 ester has been described and applied for determination of serum creatinine in rats [41].

Several applications of sensor arrays for body fluids analysis have been recently reported. Thus, an integrated micro fluidic system permitting the simultaneous determination of ammonia, creatinine, and urea by use of air-gap Severunghaus-type ammonia sensors as transducers and creatinine deiminase and urease incorporated in the bottom of the flow channel have been fabricated in [42]. A family of electrochemical thick film sensors composed of screen-printed on polycarbonate plate working electrodes cov-

ered by various ion-selective PVC polymeric membranes, pO$_2$ Clark type sensor and enzymatic urea, creatinine, glucose and lactate sensors has been designed for use in biological fluids [43]. Microfluidic miniaturized system permitting a dual determination of urea and creatinine using two independent methods: electrochemical and spectrophotometric in biological fluids during hemodialysis course has been reported by Brzozka and co-workers in [44]. Bioelectronic tongue composed of enzymatically modified all-solid-state sensors together with sensors sensitive to ammonium, potassium, sodium and generic sensors to alkaline ions that allowed a simple direct determination of urea and creatinine in real urine samples without the need of eliminating the alkaline interferences has been reported in [45].

In this paper we focused on some particular applications of sensor array for analysis of human urine specimens. We have explored the possibility to classify human urine samples according to the creatinine level and detect the urinary system dysfunctions by means of the Electronic tongue (ET) composed of miniaturized metallic sensors (metal of high purity and alloys) and ion-selective electrodes with PVC solvent polymeric membranes. The urinary creatinine content evaluated by ET has been compared with the results obtained by automated Jaffe's method and GC-MS. The ability of ET to distinguish between 27 urine samples coming from healthy individuals and patients with malignant and non-malignant bladder tumor diagnosis has also been investigated, with the aim to explore the ET potentialities as a non-invasive and low cost technique for the early monitoring of urinary tumors.

2. Experimental

2.1. Reagents

Poly(vinyl chloride) (PVC) high molecular weight, bis(2-ethylhexyl) sebacate (DOS), *o*-nitrophenyl octyl ether(*o*-NPOE), tris(2-ethylhexyl)phosphate (TOP), potassium tetrakis(4-chlorophenyl)borate (KTpClPB), tetradodecyl ammonium chloride (TDACL), monensin, nonactin and thenoyltrifluoroacetone (TTA) were purchased from Fluka Chemie AG (Buchs, Switzerland). Tetrahydrofurane (THF), creatinine, billirubin, hydrocortisone, uric acid, valproic acid and urea were purchased from Sigma-Aldrich Chemie GmbH (Steinheim, Germany). 2,4-Pentanedione was from ACROS (Italy), glacial acetic acid and hexane were purchased from Carlo Erba (Italy). 2,4-Pentanedione and hexane were distilled before use. All other chemicals were of analytical grade and were used without further purification. All solutions were prepared by using distilled water.

2.2. Sensors preparation and evaluation

Electronic tongue consisted of 13 potentiometric sensors and was supplemented by pH glass electrode (AMEL, Italy). Two different types of sensors were employed: metallic electrodes and solvent polymeric PVC-based membrane electrodes. Detailed information on sensors composition is given in Table 1. Following materials were used for metallic sensors preparation: Co (99.99% pure); brass (an alloy of Cu and 20 wt.% Zn); four alloys of silver: Ag 42%–Cu 17%–Zn 16%–Cd 25%, Ag 60%–Cu 26%–Sn14%, Ag 30%–Cu 26%–Zn 32%–Sn 2%, Ag 56%–Cu 22%–Zn 17%–Sn 5% (numbers in wt.%), two component alloys Sn 40%–Pb 60% and Cu–P (copper doped with 7 wt.% of phosphorous). Metallic rods sections of 3 cm length and 3 mm in diameter were cut and embedded within Teflon tubes. Electrical copper wire connections were soldered to the parts of rods protruded from Teflon. Sensor surfaces were flat, buffed with alumina slurries, cleaned in

Table 1
Potentiometric sensors employed in Electronic tongue

N		Material of metallic electrodes
1		Ag 42%–Cu 17%–Zn 16%–Cd 25%
2		Brass: Cu–Zn 20%
3		Ag 60%–Cu 26%–Sn 14%
4		Cu–P 7%
5		Ag 30%–Cu 26%–Zn 32%–Sn 2%
6		Ag 56%–Cu 22%–Zn 17%–Sn 5%
7		Sn 40%–Pb 60%
8		Co 99.99%

N	PVC-based electrodes membrane components, wt.%		
	Plasticizer	Ionophore, wt.%	Additive, wt.%
9	o-NPOE	Monensin, 3 wt.%	TDACl, 1 wt.%
10	DEHS	Nonactin, 1 wt.%	–
11	TOP	TTA, 7 wt.%	–
12	DEHS	–	KTClPB, 5 wt.%
13	DEHS	–	TDACl, 2 wt.%

Table 2
Composition of multicomponent solutions mimicking human urine

Component	Concentration range, mol/l
Na^+	5×10^{-2}–1×10^{-1}
K^+	1×10^{-1}–1.9×10^{-1}
Phosphate$_{total}$	3.7×10^{-3}–7.3×10^{-3}
Creatinine	5×10^{-3}–2×10^{-2}
Cortisol	0–1.5×10^{-7}
pH[a]	4.6–6.8
Drugs or sickness indicators	
Valproic acid	2×10^{-8}–1.4×10^{-7}
Ethanol	2.2×10^{-3}–4.3×10^{-3}
Bilirubin	0–2×10^{-5}
Pb^{2+}	0–3×10^{-6}

[a] Adjusted by addition of HCl 37 wt.%.

2.3×10^{-5} mol/l of bilirubin. Multicomponent solutions of 36 different compositions have been used for ET training and testing. Measurements were performed three times in each of 36 solutions in a random order.

2.4. Real urine samples

Urine specimens have been collected from 64 individuals of both sexes, with the following classification: 30 healthy volunteers with unremarkable medical story, 17 patients with bladder tumor diagnosis and 17 patients under cure with urinary system dysfunctions. No dietary restriction was applied for all patients except one vegetarian female subject. Early morning collected urine samples were analyzed without any pretreatment few hours after sampling. At least two replicas were performed for each urine sample in the same day. Samples were measured in a random order. Urine samples were stored at $-20\,^\circ$C if not analyzed immediately. Between the measurements all sensors were conditioned in 0.01 mol/l KCl solution. In order to maintain a proper blank sample, the aqueous 2 wt.% urea solution has been utilized to dilute urine specimens when required.

2.5. Urine creatinine determination

2.5.1. Jaffe's spectrophotometric method

Determination of creatinine by modified Jaffe's method (rate-blanked and compensated) has been performed following a certified protocol [12]. Measurements were performed using a Hitachi 902 automated analyser (Roche, Germany), which is routinely applied for clinical biochemistry measurements. 1 ml of urine samples was diluted 20 times and measured with alkaline picrate at 505 nm.

2.5.2. GC-MS method

Since creatinine is a low volatile compound, its derivatization is required in order to facilitate the movement trough the GC column [13]. The derivatization method reported in the literature has been utilized [46]. Creatinine was converted to the ethyl ester of *N*-(4,6-dimethyl-2-pyrimidinyl)-*N*-methylglycine by reaction with 2,4-pentanedione and ethanol in the presence of acetic acid. Creatinine (6.2 mg) was dissolved in 1 ml of ethanol and 500 μl of glacial acetic acid in a glass tube. Aliquots of solution containing of 500, 800, 1000 and 1150 μg of creatinine were transferred to the reaction tubes, containing 500 μl of 2,4-pentanedione and ethanol was added to bring the total volume to 1500 μl. In the case of real urine samples 500 μl of urine were immersed in a reaction tube, containing 100 μl of glacial acetic acid and 500 μl of 2,4-pentanedione. Ethanol was added to the total mixture volume of 1500 μl. The reaction tubes were briefly shaken and placed in the

ultrasonic bath, rinsed with methanol and dried on air. In order to prevent possible contamination due to adsorption or either precipitation of poorly soluble products, the sensors working surface was mechanically cleaned with a fine emery-paper, rinsed with methyl alcohol and distilled water before each measurement.

PVC-based membrane sensors were prepared according to a common procedure. Membrane of 100 mg weight contained 1–7 wt.% of defined ionophore and varying amount of lipophilic additives distributed in PVC/plasticizer (1:2) polymeric matrix. Membrane components were dissolved in 1 ml of THF and the mixture was cast out on flat Pt electrodes (3 cm length, 3 mm in diameter) incorporated in a Teflon body (AMEL, Italy). Before membrane casting Pt electrodes were pretreated as for the other metallic sensors. THF was allowed to evaporate overnight. Freshly prepared all-solid-state sensors were soaked in 0.01 M NaCl at least for 24 h before first measurement. The potential differences between sensors in array and the Saturated Calomel reference Electrode (SCE, AMEL, Italy) have been measured using a PC equipped high-impedance 16-channel analog-to-digital converter (Smartronix, Italy) with a precision of 0.1 mV and written into PC data files. Potentiometric behavior of PVC-based membrane electrodes was examined in 0.01 M KCl background. Calibrations were performed by adjusting the calculated amounts of concentrated stock solutions varying the concentration of different ions stepwise from 10^{-5} to 10^{-1} M at every 100 s. The response of discrete metallic sensors towards aqueous solutions of several individual human urine components (urea, creatinine, valproic acid, hydrocortisone, bilirubin), in the range of their presence in urine was then examined. A content of dissociated forms of analyte in solution was calculated according to the dissociation constants K_{dis} and pH. At least two replicas with all metallic sensors were performed for every material and three individual identical sensors were evaluated at the same time, in total number of repetitions was $n = 6$.

2.3. Multicomponent solutions mimicking human urine

The measurements with ET were initially performed in mixed solutions, mimicking the composition of human urine and prepared as listed in Table 2. All solutions contained fixed amount of urea (2 wt.%), the concentration of several components (creatinine, valproic acid, ethanol, inorganic ions) was changed stepwise, while content of others varied randomly. A half of model set (18 not identical solutions) contained 1.5×10^{-7} mol/l of cortisol and

oven at 85 °C for 60–70 h. The reaction mixture was then concentrated under a stream of nitrogen at room temperature. The product was dissolved in 1 ml of hexane, transferred in silicone septum-cupped vials of 20 ml volume. These vials were heated in water bath at 50 °C for 10 min and a solid phase microextraction (SPME) of analyte from the vial headspace was performed for 20 min on carboxen-polydimethylsiloxane coated fiber (Supelco, CAR/PDMS, 75 μm coating). The sample was then injected into a chromatography column by SPME fiber stripping for 2 min at 250 °C.

A Shimadzu QP-2010 GC/MS system (Kyoto, Japan) was used. A fused-silica capillary column Equity-5 (Supelco, 30 m × 0.25 mm i.d., 0.25 μm film thickness) was used for separation. The column temperature was held at 40 °C for 5 min and then programmed to 300 °C in increments of 10 °C/min and held for 2 min. The split ratio was 3:1, helium flow rate was 3 ml/min, injection temperature and ion source temperature was 250 °C. The mass spectrometer operated at 70 eV. Under these conditions the retention time of the creatinine derivative was 20.3 min. The EI mass spectrum had most of the ion intensity concentrated at two masses: the smaller peak at m/z 223 corresponding to the molecular ions of creatinine derivative, and the base peak at m/z 150 resulting from the loss of carbethoxy group $-COOC_2H_5$.

2.6. Data analysis

Data analysis included identification, classification and quantitative validation of humane urines. Identification was performed using Principal Component Analysis (PCA) technique. Partial Least Square Discriminant Analysis (PLS DA) and Feed Forward Back Propagation Neural Network (FFBP NN) were applied for specimen classifications. The autoscaling procedure was applied to the data. When the number of measurements composing the dataset was not big enough to divide the dataset in a training and test set, a leave-one-out validation was applied. Partial Least Square regression (PLS) method was applied to train ET in multicomponent artificial solutions mimicking human urine and to correlate urinary creatinine content determined by spectroscopic Jaffe's method and GC-MS with ET response. The following commercially available software was used: Unscrambler v.9.1 (2004, CAMO PROSESS AS, Norway) and v.7.8 (CAMO AS, Norway) and Matlab v.7.0 (2005, The MathWorks, Inc., Natick, USA).

3. Results and discussion

3.1. Urines discrimination

Early morning spot urine voids of 30 healthy volunteers, 9 patients with urinary system pathologies (6 of them were then diluted in 10 and 100 times by 2 wt.% urea aqueous solution) and a blind non-urine control sample (in 3 replicates) have been measured in first experimental session. The aim was to investigate the ability of ET to differentiate various urine specimens. It has been found that ET formed of metallic electrodes 1–4, 7,8 and sensors 9, 12, 13 (see Table 1) with PVC solvent polymeric membranes based on monensine-ionophore, cation- (TpClPBK, 5 wt.%) and anion-(TDMACl, 2 wt.%) exchangers correspondingly clearly differentiates urines of healthy persons and those with urinary system dysfunctions, Fig. 1. Data were treated together with ET readings in a set of artificial solutions mimicking in some way the composition of human urine, Table 2. The purpose of this measure was to investigate the potential use of these artificial mixtures for ET training, in order to determine several individual urine components content. As can be seen from Fig. 1, the similar response of ET in real and artificial urine specimens can be noticed especially analyzing PC1-PC2 plane, while some difference in score values appears alone
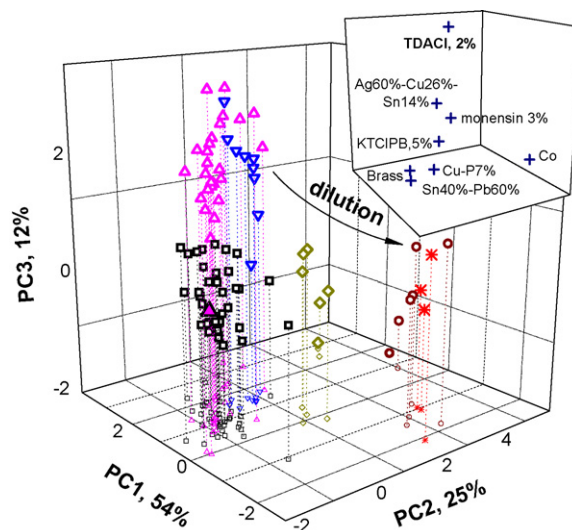
Fig. 1. A PCA score plot of urine specimens' differentiation. In the figure: (□)—artificial model solutions mimicking human urine; (△)—urine specimens of healthy volunteers, namely (▲) vegetarian person urine void; (▽)—urines of patients with urinary system pathologies; urines of sick patients diluted 10 (◇) and 100 (○) times; (✳)—blind test sample. In the insert: ET sensor loadings plot.

PC3. This difference decreases after the dilution of real urine specimens 10 and then 100 times. From the values of sensors loadings (see insert in Fig. 1), the highest loading value alone PC 3 component (and hence, the strong sensor influence on samples scores alone PC 3) can be noticed for TDMACl-based anion-exchanging solvent polymeric membrane sensor 13. This finding may indicate some misbalance in anionic composition of artificial urine samples. Nevertheless, dilute urine samples are clearly separated from both artificial calibration solutions set and non-pretreated real urines on PC1-PC2 plane, and this result support the exploitation of 36 artificial solutions set for ET training. It is interesting to note here that a urine sample provided by a person following a strict vegetarian diet
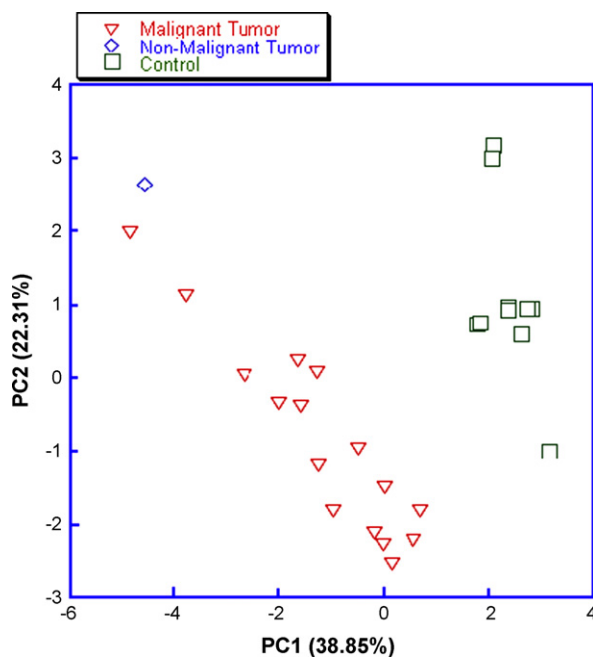
Fig. 2. ET discrimination of urine samples from patients with urinary bladder tumor and healthy patient controls.

was distinguished by ET system from other urines. Moreover, a blind sample was situated on the score plot near 100-fold diluted urine samples corresponding in this way to a very dilute or either non-urine sample (in fact, for self-control reasons, the ordinary black weak tea preparation has been analyzed in this case).

3.2. An application of Electronic tongue for monitoring of urinary system dysfunctions

The second part of the work was devoted to explore the possibility to monitor the presence of urinary system pathologies, and namely urinary bladder tumors by a non-invasive urine measurement with ET. All the sensors listed in Table 1 have been utilized for these measurements. In this experimental campaign only male subjects have been considered in order to avoid the possible influence of the patient gender on the final classification result. Twenty-seven urine specimens were collected: 16 malignant tumors, 1 non-malignant tumor, and 9 controls of healthy volunteers. No attention was paid to the age and a body mass/height index of subjects. Fig. 2 shows the scores plot of the first two principal component of the PCA model obtained with the above dataset. There is a clear separation between the tumor samples and the controls. It is also interesting to note that the urine sample coming from a patient with a non-malignant tumor is not close to the malignant tumor urines suggesting a possible deviation from the chemical composition of tumors samples. However, in order to provide more general conclusions on the last hypothesis a more deep study considering more than one subject is necessary.

3.3. Quantitative detection of urine components

An attempt to found correlations between the overall ET response and the content of several components in urine was performed employing regression method. ET (composed of all the sensors listed in Table 1 and pH glass electrode) was trained in multicomponent solutions mimicking the composition of human urine. Each of 36 solutions was repeatedly measured 4 times in a random order. All replicated measurements have been used as a training set except 4 replicated measurements of 9 randomly chosen model urine solutions which were used as a test set with unknown analyte content. PLS regression method was applied for data elaboration. In Fig. 3 the result of PLS application model

trained with 4 factors (4 PCs) is presented. The ET showed a good predictive power for total content of alkali metal ions (root mean square error of training, RMSEC, and prediction, RMSEP, values of 0.0075 and 0.0087 mol/l correspondingly; correlation coefficients for the training and validation were $R_{training} = 0.979$, $R_{val} = 0.975$, respectively), total phosphorous and chloride-anions content (RMSEC = 0.0016 mol/l, RMSEP = 0.0038 mol/l $R_{training} = 0.995$, $R_{val} = 0.993$), and creatinine content (RMSEC = 0.0018 mol/l, RMSEP = 0.0019 mol/l, $R_{training} = 0.943$, $R_{val} = 0.940$).

From the above reported results the possibility of ET to monitor the changes in urinary creatinine content seems to be the most remarkable result. Indeed, the high correlation of ET response to total content of sodium and potassium cations in artificial urine solutions could be well explained by the presence (and the highest loadings) of highly-sensitive solvent polymeric membrane sensors 9–10, 12 based on monensin (3 wt.%), and nonactine (1 wt.%) ionophors and cation-exchanger TpClPBK (5 wt.%) in the ET array. More interesting considerations can be made concerning to the detection of chloride and total phosphorous content. Solvent polymeric membrane sensor 13 based on TDMACl (2 wt.%) anion-exchanger showed the major influence on PLS regression result (with the highest loading alone PC1, 67% of total system variance), but the application of the single sensor 13 for the detection of chloride ion and especially for total ionic phosphorous content in multicomponent artificial urine solutions gave no adequate results (data not shown). The analysis of sensors loadings evaluated on PLS training step has indicated a high influence of metallic sensors 1, 3, 6 formed of high-percentage silver alloys (42, 60 and 56 wt.% of Ag correspondingly), copper containing sensors 2, 4 and metallic Co sensor 8 on the total phosphorous and chloride anions content correct determination. We explain such a phenomenon by a mixed corrosion potential aroused from the partial oxidation-reduction of the metal electrodes surface followed by a relatively fast formation of several low soluble products like AgCl, Ag_3PO_4, $Cu_3(PO_4)_2$ and $Co_3(PO_4)_2$, on the sensors surface in the presence of chloride and phosphate ions. In the literature Meruva and Meyerhoff [47] showed that the presence of phosphate ion enhances the corrosion of Co metallic potentiometric electrode, shifting the potential of Co(0) oxidation to Co(II) to more negative potentials, which results in negative shift in the mixed potential value of the system upon the addition of phosphate ions. Cobalt electrode is found to respond to all of the three forms of phosphate ions, namely, $H_2PO_4^-$, HPO_4^{2-},
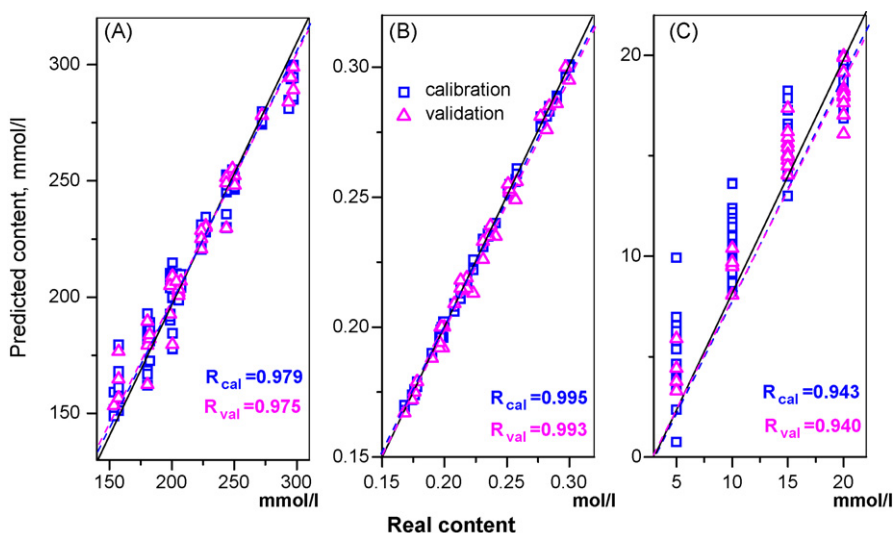

Fig. 3. The result of PLS1 prediction of (A) total alkali metal ions content, (B) inorganic anions concentration (chloride and total phosphorous), (C) creatinine content in 36 model solutions mimicking human urine composition, number of replicas $n = 4$, 9 samples have been chosen randomly and used as a test set for all 4 replicas.

and PO_4^{3-}. The similar principle may be applied for the explanation of Cu and Ag-alloy-based sensors behavior. Besides the formation of insoluble copper and silver phosphates, the Ag(0) oxidation to Ag(I) is enhanced by the chloride ion presence, AgCl precipitated of on the surface results in electrode partial transformation in chloride-sensitive pseudo-Ag/AgCl metallic electrode of second kind. The mechanical cleaning and reconditioning of electrode surface recurring after every measure ensure the sensors reproducibility.

As it was mentioned previously, the possibility of the ET system to distinguish vegetarian subject urine from urines of all the other healthy volunteers without dietary restrictions was revealed on the urine identification step. Hoogwerf et al. showed that urine creatinine values changed in conjunction with diet change [48]. Both total protein intake and red meat intake and further conversion of meat creatine to creatinine are contributing variables in urine creatinine content. This suggests why vegetarians have been shown to have lower levels of creatinine in urine [49] and permit us to suppose that the difference in urinary creatinine content influenced the vegetarian and meat-eating subjects urines differentiation, Fig. 1. This founding is in correspondence with a good PLS correlation received for evaluation of creatinine content by ET in 36 artificial solutions mimicking human urine composition, Fig. 3(B). According to a PLS result, metallic sensors 2–4 have the highest loadings alone PC1 component, explaining 79% of total variance. From the Table 1 it is possible to note that all the mentioned sensors are mixed alloys with a relatively high copper percentage (Cu content is about 90, 80 and 26 wt.% for sensors 4, 2 and 3, respectively).

We can hypothesize the particular influence of copper on metallic sensors sensitivity to creatinine. Recently Hsu et al. reported an application of disposable copper-plated screen-printed carbon electrodes (CuSPE) for the determination of urinary metabolites, creatinine in particular [50]. Detection has been performed amperometrically in pH 7.5 phosphate buffer solution (PBS) with ionic strength 0.11 mol/l at −0.05 V versus Ag/AgCl reference electrode. The mechanism of CuSPE sensitivity towards creatinine has been explained by complexation at a copper electrode in neutral medium, the same as the previously reported o-diphenol response of CuSPEs [51]. Thus, authors proposed that initially happens the partial oxidation of Cu(0) to Cu(II), then the analyte form a weak complex intermediate by chelating Cu(II) ion, followed by an electron transfer and dehydrogenation reaction with o-quinone derivative formation. A similar complexation was noticed for amino

acids at conventional copper electrodes at potential near 0 V followed by marked corrosion and dissolution of active material [52]. Since ET features the simultaneous utilization of several metallic alloy sensors with varied copper percentage, an enhanced ability to sense the change in urinary creatinine content may be achieved. It is important to note here, that by using disposable electrodes it is possible to avoid the time consuming cleaning and conditioning procedures. The work in this direction is now in process.

In order to prove the utility of ET for the determination of urinary creatinine, we performed the comparison for creatinine content obtained using ET, spectroscopic Jaffe's method and GC-MS technique. Urinary creatinine determination in 21 (11 female and 10 male) healthy subjects by Jaffe's method was performed following a certified protocol for clinical analysis laboratory. The peak area corresponding to the 223 m/z and 150 m/z molecular ions of creatinine derivative obtained from solutions with initial creatinine content 500–1150 μg (see Section 2 for details) and retained at 20.3 min were used for GC-MS calibration curve. The curve was linear in all the concentration range, and the correlation coefficient was 0.9273. Five urine specimens of 3 healthy male and 2 female subjects were analyzed (see Section 2 for details). The response of ET composed of all the 13 potentiometric sensors (Table 1) and pH electrode was then correlated with the creatinine content determined by both methods. As can be seen from Fig. 4, the result obtained from ET was in agreement with the results obtained with both techniques. The correlation coefficients for PLS regression with Jaffe's method result were $R_{training} = 0.910$ and $R_{val} = 0.857$, while for GC-MS even higher: $R_{training} = 0.972$ and $R_{val} = 0.901$, respectively. A leave-one-out validation has been performed due to a relatively small amount of analyzed samples. Nevertheless, the obtained results may indicate the high compatibility of ET with classical analytical methods and utility for fast and simple evaluation of urinary creatinine changes with sufficient precision. The ET response in individual solutions of several urine components showed no influence of urea on the urinary creatinine determination, in strict contrast of Jaffe's method, which is strongly influenced by urea. Moreover, no correlation of alkaline interferences is demanded on the contrary to the creatinine biosensors with potentiometric ammonia ion determination.

At the last stage of the work we investigated the potential exploitation of the developed procedure of urine specimen classification according to creatinine content for biomonitoring purposes. As it was already mentioned, the biological monitoring is a common
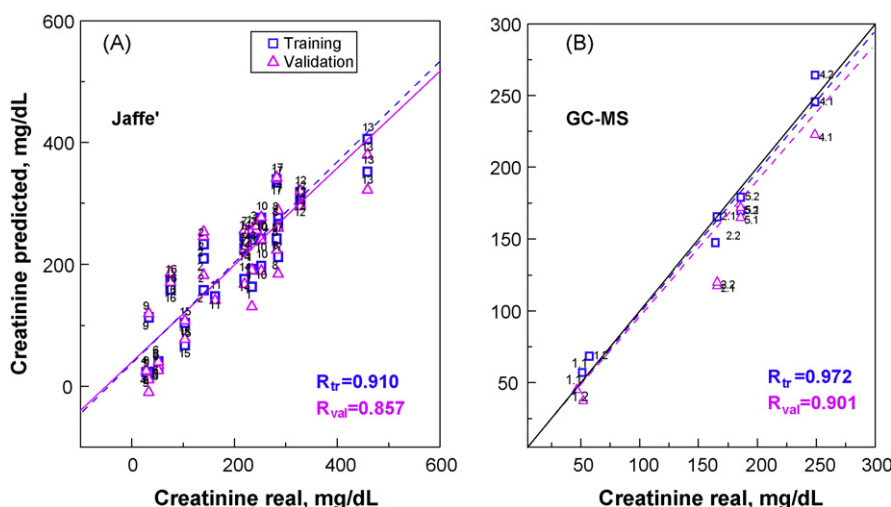
Fig. 4. The result of PLS1 prediction of creatinine content in urines of healthy volunteers by means of Electronic tongue versus creatinine concentration determined by (A) Jaffe's method, 21 urine samples (11 female and 10 male in the 25–45 years old range); (B) GC-MS in 5 urine samples (3 male and 2 female in 30–35 years old range). Number of replicas $n = 3$.
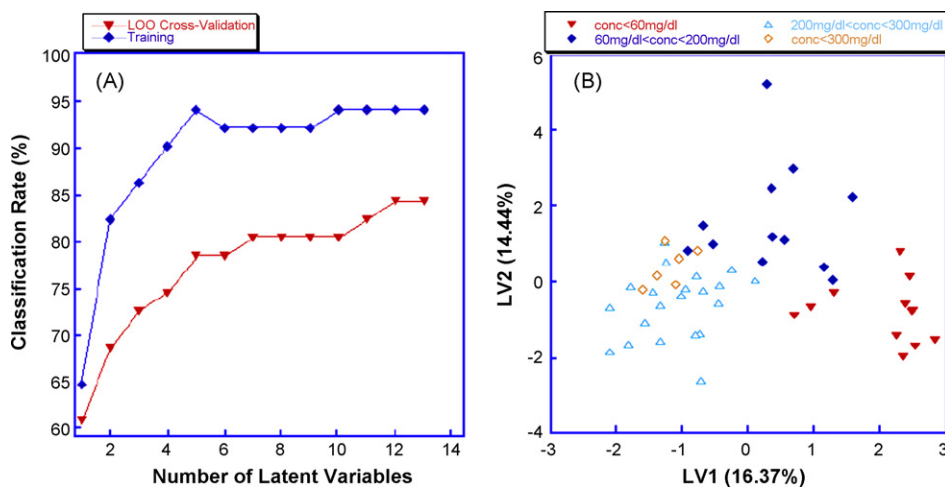
Fig. 5. PLS-DA result of ET application for urine analysis. (A) a PRESS-plot; (B) score plot of first two latent variables discrimination of 51 specimens of healthy volunteers according to the creatinine concentration.

Table 3
PLS-DA and FFBP NN classification of 51 human urine specimens according to the creatinine content

Number of correctly classified samples	PLS-DA				FFBP NN			
	Class 1	Class 2	Class 3	Class 4	Class 1	Class 2	Class 3	Class 4
Class 1[a]	11	0	1	0	11	1	0	0
Class 2[b]	1	9	2	0	0	12	0	0
Class 3[c]	0	0	20	1	1	0	20	0
Class 4[d]	0	1	2	3	0	0	2	4

[a] Class 1: creatinine content <60 mg/dL.
[b] Class 2: creatinine content in a range 60–200 mg/dL.
[c] Class 3: creatinine content in a range 200–300 mg/dL.
[d] Class 4: creatinine content >300 mg/dL.

method to assess human exposures to environmental and workplace chemicals. For biomonitoring the content of nonpersistent polluting chemicals and drug metabolites are represented in creatinine-adjusted concentrations [2]. Due to a short biologic half-life of several body pollutants (see Section 1), the spot, usually first morning urine voids, are used in biomonitoring instead of the traditional cumbersome 24 h urine collection.

Two chemometric approaches, PLS-DA and FF BPNN [53] have been applied for classification of 51 urine specimens. Considering that the normal range of human urinary creatinine is 30–300 mg/dL (although in case of disorders or pathologies the amount may exceed the upper limit), we divided the creatinine concentration in four classes according the following intervals: Class 1: less then 60 mg/dL (low content); Class 2: between 60 and 200 mg/dL (normal conditions); Class 3: between 200 and 300 mg/dL (alteration); Class 4: higher than 300 mg/dL (dangerous for health). An autoscaling procedure has been applied to the data before the utilization of the PLS-DA. In Fig. 5(A) the PRESS plot of the PLS-DA model is shown. The best result obtained with 12 latent variables was 84.31% of correct classification. The confusion matrix representing the results of correct PLS-DA classification is shown in Table 3. This result is also put in evidence in the scores plot of the first two latent variables of the PLS-DA model where the Class 4 is overlapped with the Class 2 and Class 1, Fig. 5B. The not satisfactory classification is due to a small number of samples belonging to the Class 3 respect to the other classes that produce a biasing PLS-DA model. In order to increase the system recognition performance, a FFBP NN was utilized. The network architecture has been composed by only one hidden layer of 5 neurons. The 'tansig' function has been considered as activation function for all the neurons. The classification rate in training was around 99.50% while in the validation phase

92.16%. The confusion matrix of the validation results is shown in Table 3. In this case, the recognition performance is increased for all the classes and in particular for the Class 3 there is an improvement of 16.6% respect of the PLS-DA performance (it was less than 75%). The present method can be of clinical value in preliminary diagnosis of disorders to provide a prompt and simple technique in routine analysis, due to its simplicity and reproducibility.

4. Conclusions

In the present study the application of potentiometric ET composed of miniaturized metallic sensors (metal of high purity and alloys) and ion-selective electrodes with PVC solvent polymeric membranes for clinical analysis of human urine. The ET showed a good predictive power for the total content of alkali metal ions, total phosphorous and chloride anions content and urinary creatinine. The ET response has been correlated with creatinine content determined by GC-MS and Jaffe's method and a quite good agreement have been achieved for all the techniques. The ET data analysis has shown that it is possible to predict with high accuracy (92.157%) the concentration range of the creatinine also in presence of a not well-balanced dataset. It is reasonable to suppose that in presence of a well-balanced dataset the recognition performances could further improve. Moreover, with dedicated sensors set it has been possible to divide tumors samples from the controls. Although this interesting result should be studied in deeper detail, the method could represent a first step versus a non-invasive and low cost technique for an early monitoring of urinary tumors. The good correlation with standard analytical methods, the possible modification of the sensor array composition by simple sensor extraction or replacement, long lifetime, easy maintenance and low cost of sensors

confirm usefulness of Electronic tongue for clinical applications of biological liquids.

Acknowledgement

Appendix A. Supplementary data

Supplementary data associated with this article can be found, in the online version, at doi:10.1016/j.talanta.2008.08.021.

References

[1] M. Tsivou, N. Kioukia-Fougia, E. Lyris, Y. Aggelis, A. Fragkaki, X. Kiousi, Ph. Simitsek, H. Dimopou-lou, I.-P. Leontiou, M. Stamou, M.-H. Spyridaki, C. Georgakopoulos, Anal. Chim. Acta 555 (2006) 1.
[2] D.B. Barr, L.C. Wilder, S.P. Caudill, A.J. Gonzalez, L.L. Needham, J.L. Pirkle, Environ. Health Perspect. 113 (2005) 192.
[3] C. Saieva, C. Aprea, R. Tumino, G. Masala, S. Salvini, G. Frasca, M.C. Giurdanella, I. Zanna, A. Decarli, G. Sciarra, D. Palli, Sci. Total Environ. 332 (2004) 71.
[4] M. Wyss, R. Kaddurah-Daouk, Physiol. Rev. 80 (2000) 1107.
[5] K. Spencer, Ann. Clin. Biochem. 23 (1986) 1.
[6] P. Lafolie, O. Beck, G. Blennow, L. Boreus, S. Borg, C.E. Elwin, L. Karlsson, G. Odelius, P. Hjemdahl, Clin. Chem. 37 (1991) 1927.
[7] P.J. Saudan, L. Shaw, M.A. Brown, Am. J. Hypertens. 11 (1998) 839.
[8] R. Rabinowitz, D.S. Smith, D.D. Tiemann, M.A. Hudson, J. Urol. 158 (1997) 1728.
[9] E. Bakker, D. Diamond, A. Lewenstam, E. Pretsch, Anal. Chim. Acta 393 (1999) 11.
[10] M. Jaffe, Z. Hoppe-Seyler's, Physiol. Chem. 10 (1886) 391.
[11] B.W. Steinert, J.A. Robinson, B.A. Mitchell, A.C. Diokno, Comput. Biomed. Res. 28 (1995) 211.
[12] M.L. Knapp, P. Mayne, Clin. Chim. Acta 168 (1987) 239.
[13] T. Smith-Palmer, J. Chromatogr. B 781 (2002) 93.
[14] I. Shi, Y. Ma, Y. Ma, Anal. Chim. Acta 312 (1995) 79.
[15] M. Yasuda, K. Sugahara, J. Zhang, T. Ageta, K. Nakayama, T. Shuin, H. Kodama, Anal. Biochem. 253 (1997) 231.
[16] J. Kratochvíla, B. Friedecky, M. Budina, I. Šperlingová, Accred. Qual. Assur. 12 (2007) 146.
[17] T.L. Wang, H.K. Chiang, H.H. Lu, F.Y. Peng, Opt. Quant. Electron. 37 (2005) 1415.
[18] H. Thompson, G.A. Rechnitz, Anal. Chem. 46 (1974) 246.
[19] M. Meyerhoff, G.A. Rechnitz, Anal. Chim. Acta 85 (1976) 277.
[20] A.J. Killard, M.R. Smyth, Trends Biotechnol. 18 (2000) 433.
[21] M. Trojanowicz, A. Lewenstam, T. Krawczyński Vel Krawczyk, I. Lähdesmäki, W. Szczepek, Electroanalysis 8 (1996) 233.
[22] G.G. Guilbault, P.R. Coulet, Anal. Chim. Acta 152 (1983) 223.
[23] W. Matuszewski, M. Trojanowicz, M.E. Meyerhoff, A. Moszczyńska, E. Lange-Moroz, Electroanalysis 5 (1993) 113.
[24] M. Jurkiewicz, S. Alegret, J. Almirall, M. García, E. Fabregas, Analyst 123 (1998) 1321.
[25] A. Radomska, E. Bodenszac, S. Głab, R. Koncki, Talanta 64 (2004) 603.
[26] T. Tsuchida, K. Yoda, Clin. Chem. 29 (1983) 51.
[27] H. Kinoshita, M. Torimura, K. Kano, T. Ikeda, Electroanalysis 9 (1997) 1234.
[28] E.J. Kim, T. Haruyama, Y. Yanagida, E. Kobatake, M. Aizawa, Anal. Chim. Acta 394 (1999) 225.
[29] M.A.T. Gilmartin, J.P. Hart, Analyst 120 (1995) 1029.
[30] Y.T. Shih, H.J. Huang, Anal. Chim. Acta 392 (1999) 143.
[31] V.K. Nguyen, C.M. Wolff, J.L. Seris, J.P. Schwing, Anal. Chem. 63 (1991) 611.
[32] J. Schneider, B. Grundig, R. Renneberg, K. Cammann, M.B. Madaras, R.P. Buck, K.-D. Vorlop, Anal. Chim. Acta 325 (1996) 161.
[33] T. Osaka, S. Komaba, A. Amano, Y. Fujino, H. Mori, Sens. Actuators B 65 (2000) 58.
[34] M.B. Madaras, R.P. Buck, Anal. Chem. 68 (1996) 3832.
[35] J.H. Shin, Y.S. Choi, H.J. Lee, S.H. Choi, J. Ha, I.J. Yoon, H. Nam, G.S. Cha, Anal. Chem. 73 (2001) 5965.
[36] P.C. Pandey, A.P. Mishra, Sens. Actuators B 99 (2004) 230.
[37] F. Winquist, I. Lundström, B. Danielson, Anal. Chem. 58 (1986) 145.
[38] W. Sant, M.L. Pourciel-Gouzy, J. Launay, T. Do Conto, R. Colin, A. Martinez, P. Temple-Boyer, Sens. Actuators B 103 (2004) 260.
[39] P. Temple-Boyer, J. Le Gal, M.L. Pourciel-Gouzy, W. Sant, A. Martinez, Sens. Actuators B 118 (2006) 47.
[40] J.-C. Chen, A.S. Kumar, H.-H. Chung, S.-H. Chien, M.-C. Kuo, J.-M. Zen, Sens. Actuators B 115 (2006) 473.
[41] M.A.F. Elmosallamy, Anal. Chim. Acta 564 (2006) 253.
[42] H. Suzuki, Y. Matsugi, Sens. Actuators B 98 (2004) 101.
[43] C. Ritter, H. Frebel, H. Kroneis, F.J. Krysl, S. Lang, C. Neuhold, H. Offenbacher, G. Pestitschek, B. Schaffar, M. Schinnerl, W. Schmidt, G. Steiner, Sens. Actuators B 76 (2001) 220.
[44] I. Grabowska, M. Sajnoga, M. Juchniewicz, M. Chudy, A. Dybko, Z. Brzozka, Microelectron. Eng. 84 (2007) 1741.
[45] M. Gutierrez, S. Alegret, M. del Valle, Biosens. Bioelectron. 23 (2008) 795.
[46] M.J. Welch, A. Cohen, H.S. Hertz, K.J. Ng, R. Schaffer, P. Van Der Lijn, E.V. White, Anal. Chem. 58 (1986) 1681.
[47] R.K. Meruva, M.E. Meyerhoff, Anal. Chem. 68 (1996) 2022.
[48] B.J. Hoogwerf, D.C. Lame, E. Greene, Am. J. Clin. Nutr. 43 (1986) 350.
[49] J. Delanghe, J.P. De Slypere, M. De Buyzere, J. Robbrecht, R. Wieme, A. Vermeulen, Clin. Chem. 35 (1989) 1802.
[50] C.-T. Hsu, H.-J. Lyuu, T.-H. Yang, E.D. Conte, J.-M. Zen, Sens. Actuators B 113 (2006) 22.
[51] J.M. Zen, H.H. Chung, A.S. Kumar, Anal. Chem. 74 (2002) 1202.
[52] P. Luo, F. Zhang, F.R.P. Baldwin, Anal. Chem. 63 (1991) 1702.
[53] K.H. Esbensen, Multivariate Data Analysis in Practice, fifth ed., Camo press, AS, 2004, p. 590.

Comparison of supercritical fluid and ultrasound-assisted extraction of carotenoids and chlorophyll a from *Dunaliella salina*

M.D. Macías-Sánchez [a], C. Mantell [a,*], M. Rodríguez [a], E. Martínez de la Ossa [a], L.M. Lubián [b], O. Montero [b]

[a] *Department of Chemical Engineering, Food Technology and Environmental Technologies, Science Faculty, University of Cadiz, Avda. República Saharaui s/n, 11510 Puerto Real (Cádiz), Spain*
[b] *Institute for Marine Sciences of Andalucia (CSIC), Avda. República Saharaui 2, 11510 Puerto Real (Cádiz), Spain*

ARTICLE INFO

ABSTRACT

In the work described here the extraction processes of carotenoids and chlorophylls were analysed using two extraction techniques, namely ultrasound-assisted extraction and supercritical fluid extraction, and the results are compared. The solvents used for the ultrasound-assisted extraction were *N,N'*-dimethylformamide and methanol and for the supercritical fluid extraction, carbon dioxide. The raw material studied was *Dunaliella salina*, a microalgae characterized by the high levels of carotenoids present in its cellular structure. The results indicate that the supercritical fluid extraction process is comparable to the ultrasound-assisted extraction when methanol is used as solvent. In addition, the supercritical extraction process is more selective for the recovery of carotenoids than the conventional technique since it leads to higher values for the ratio carotenoids/chlorophylls. Finally, the effects of pressure and temperature on the extraction yields of the supercritical fluid extraction process were studied.

© 2008 Elsevier B.V. All rights reserved.

1. Introduction

At present, microalgae offer great possibilities for the isolation of natural substances of significant commercial interest in industries such as pharmaceuticals, alimentary or cosmetic products. This fact makes microalgae raw materials with a great deal of added value.

Within the wide variety of microalgae types, the marine species in particular are able to produce a variety of substances with a range of properties. These include polyunsaturated fatty acids (PUFAs) [1–3] that protect from cardiovascular illnesses, carotenoids, which are precursors of vitamins and also show antioxidant activity [4,5] and prevent illnesses like cancer and cellular aging [6–8], toxins and bioactive substances with a high antitumor capacity, and micosporines that protect from UV radiation [9–11]. At present, society demands products made with additives that are natural in origin and, wherever possible, are beneficial to human health. In this sense, marine microalgae offer great possibilities as sources of these substances and have attracted close attention from the aforementioned industries due to the economic and social repercussions that the use of this type of additive has in the production of their products. Many of these products are designed for direct human consumption and the extraction technique is extremely important in terms of the appropriate technology to apply.

In this sense, the application of new techniques such as ultrasound-assisted extraction (UAE) and extraction with fluids at high pressure or under supercritical conditions (SFE) constitute extraction methods that reduce the volume of solvent and the extraction time. In addition, in the case of SFE it is possible to minimize the environmental impact of the use of volatile organic compounds (VOCs).

UAE is a good extraction method in comparison with the more traditional approaches due to its high efficiency, low energy requirements and low solvent consumption. This technique has been used systematically in the extraction of substances with low molecular weights [12] and bioactive compounds from plants [13,14]. The improvement in the extraction process on using ultrasound is related to the destruction of the cellular walls, reduction of the particle size, and enhancement of the mass-transfer through the cell wall due to the collapse of bubbles produced by cavitation [15,16].

Carotenoid extraction by SFE represents an alternative to the conventional extraction technique due to the fact that the purification stage is minimized and the extraction time is reduced [17]. The application of this technology in the recovery of pigments from marine microalgae has been widely studied in recent years. Mendes et al. analysed the supercritical extraction process on substances

---

* Corresponding author. Tel.: +34 956016458; fax: +34 956016411.
E-mail address: casimiro.mantell@uca.es (C. Mantell).

of pharmacological interest from different marine microalgae such as *Botryococcus braunii* [18], *Chlorella vulgaris* [19] and *Asthorospira (Spirulina) maxima* [20]. Careri et al. [21], Macías-Sánchez et al. [22,23], Montero et al. [24], Mendiola et al. [25], Gouveira et al. [26] and Canela et al. [27] have applied supercritical extraction to obtain carotenoids from *Spirulina platensis*, *Nannochloropsis gaditana*, *Synechococcus* sp., *Chlorella vulgaris* and *Spirulina maxima*, respectively, with satisfactory results.

Dunaliella salina is a unicellular *Chlorophyta* alga of the *Chlorophyceae* class and *Volvocales* order. The main morphological characteristic that distinguishes this alga from the rest of the *Volvocales* is the absence of a polysaccharide cell wall. For this reason, *D. salina* can be easily digested by humans and animals [28]. It is a microalgae with a high efficiency for the conversion of light energy into biomass and it is also able to accumulate high levels of β-carotene when cultivated under stress conditions [29,30].

When *D. salina* is under appropriate cultivation conditions, it can contain more than 10% of its dry weight as β-carotene (other microalgae and superior plants usually have a content of around 0.3% in β-carotene). This massive accumulation of β-carotene seems to be related to a protection mechanism to counteract the effects of solar radiation. In addition to β-carotene, this microalgae contains other pigments such as chlorophyll a and b, luteine and violaxantine. Depending on the light conditions it can also produce anteraxantine and zeaxantine [31].

There are numerous reports in the literature that describe the study of carotenoid recovery from *D. salina* using a range of extraction techniques [32]. The application of high pressure fluid extraction to this microalgae has been studied by several authors in recent years [33,34]. In relation to the use of supercritical carbon dioxide in the extraction of *D. salina*, only one study has been developed, by Mendes et al. [20], and this involved an analysis of the solubility of the *cis*- and *trans*-β-carotene isomers from this microalgae compared with the solubility of the synthetic *trans*-isomer. The results indicate that the latter compound has a lower solubility in supercritical carbon dioxide than the natural ones.

The work described here involved a comparison of the UAE process and the SFE process with carbon dioxide on carotenoids and chlorophyll. In addition, the program STATGRAPHICS plus 5.1 (1994–2001, Statistical Graphics Corp.) was used to develop empirical equations that have the capacity to predict the extraction yields in the SFE of carotenoids and chlorophyll. The same program also provides useful information concerning the influence of variables on the extraction yields of the process. In this sense, the effects of temperature and pressure in the SFE of carotenoids and chlorophyll were analysed using a multilevel factorial experimental design.

2. Experimental

2.1. Raw material

The algal matter used in this study was provided by the Microalgae Culture Collection of the Institute of Marine Sciences of Andalusia (ICMAN-CSIC, Spain). The biomass was grown in sea water enriched with f/2 medium [35], at temperature in the range 20–35 °C and with atmospheric aeration. After growth was complete, the biomass was lyophilized and stored in a refrigerator in the absence of light until the extraction process was carried out.

2.2. SFE

The experimental work was carried out in SFE equipment (micro-scale) from ISCO (Nebraska), model SFX 220. This equipment has a 0.5 mL extraction cell and the solvent is supplied by a syringe pump with a capacity of 250 mL. The flow rate was controlled manually at the exit of the installation by a thermostatic micrometric valve [22].

The experimental procedure was as follows: firstly, the extraction cartridge was loaded with approximately 0.1 g of the microalgae sample, which was homogenized in order to maintain a constant apparent density in all the experiments; the cartridge was then introduced into the extractor for 15 min to reach the operating temperature; the extractor was pressurized with the CO_2 pump; a static extraction was carried out under working conditions during 15 min; after this time, the micrometric valve was opened and kept at 60 °C. The solvent flow-rate for all experiments was 4.5 mmol/min and the extraction time was 180 min.

The extracted samples were collected in glass tubes containing methanol. After the extraction process, the solvent was removed with a flow of nitrogen at 40 °C. The extracted product was dissolved in 5 mL of methanol and was stored at 4 °C in the absence of light until the measurements were carried out. All the experiments were repeated two times.

2.3. UAE

Methanol and *N*,*N*′-dimethylformamide (DMF) were the solvents selected for the UAE of pigments from *D. salina*. A sample of 0.105 g of lyophilized microalgae was suspended in 5 mL of the solvent. The suspension was sonicated for 3 min in an ultrasound apparatus from Selecta (Spain) and stored for 24 h at 4 °C. After this time, the extract was separated from the pellet and recovered by centrifugation, immediately filtered through a 0.22 μm filter, and finally stored at 4 °C in the absence of light until analysis was carried out. The extraction process was repeated until the liquid extract did not have any coloration (approximately 6 extraction cycles for methanol and 4 extraction cycles for DMF).

2.4. Analytical methods

The total concentrations of carotenoids and chlorophyll were determined by measuring the absorbance of the samples using a U-2010 Spectrophotometer from Hitachi (Japan). The equation proposed by Wellburn [36] was used for the determination of carotenoid and chlorophyll concentrations in the samples of *D. salina*. This equation has more parameters than other equations presented in the literature and allows the determination of the chlorophyll b contained in the samples.

The concentration of total carotenoids was calculated using the following equation:

$$C_{\text{total carotenoids } (x+c)} = \frac{1000A_{470} - 1.63C_a - 104.96C_b}{221} \tag{1}$$

where A_{470} is the absorbance at 470 nm, and C_a and C_b are the concentrations of chlorophyll a and b calculated by:

$$C_a(\mu g/mL) = 16.72A_{665.2} - 9.16A_{652.4} \tag{2}$$

$$C_b(\mu g/mL) = 34.09A_{652.4} - 15.28A_{665.2} \tag{3}$$

where $A_{665.2}$ and $A_{652.4}$ are the absorbance values at 665.2 nm and 652.4 nm, respectively.

3. Experimental results

The experimental results for the extraction yields obtained in the extraction of chlorophylls and carotenoids from lyophilized *D. salina* by SFE with carbon dioxide and UAE using DMF and methanol, along with the carotenoids/chlorophylls ratios, are presented in Table 1 with the confidence limits considering a 95% of confidence

Table 1
Extraction yields of carotenoids and chlorophylls

	Pressure (bar)	Extraction yields		Ratio Car/Chlo
		μg carotenoids/mg dry microalgae	μg chlorophylls/mg dry microalgae	
Temperature (°C)				
SFE-CO₂				
40		0.207 ± 0.004	0.197 ± 0.008	1.05
50	100	0	0	–
60		0	0	–
40		6.43 ± 0.26	0.086 ± 0.003	74.78
50	200	7.03 ± 0.14	0.071 ± 0.002	99.03
60		5.75 ± 0.06	0	–
40		6.30 ± 0.50	0.033 ± 0.003	191
50	300	6.31 ± 0.31	0.184 ± 0.013	34.28
60		14.92 ± 0.89	0.268 ± 0.011	55.66
40		7.67 ± 0.69	0.061 ± 0.004	125.77
50	400	7.28 ± 0.29	0.235 ± 0.009	30.99
60		12.17 ± 0.24	0.227 ± 0.005	53.63
40		4.06 ± 0.24	0.026 ± 0.002	156.31
50	500	1.08 ± 0.03	0.161 ± 0.006	6.72
60		9.30 ± 0.37	0.376 ± 0.019	24.74
UAE-methanol		14.1 ± 1.0	2.5 ± 0.1	5.64
UAE-DMF		27.7 ± 1.4	3.1 ± 0.1	8.93

Car/Chlo: carotenoids/chlorophylls.

level. The yields are expressed in μg of pigment per mg of dry weight of microalgae.

4. Discussion of results

4.1. UAE

From the results presented in Table 1, it can be concluded that the extraction yields obtained for carotenoids and chlorophylls on using DMF as the solvent in the ultrasound-assisted extraction are higher than those obtained with methanol. These results indicate that the use of ultrasound facilitates the penetration of the DMF through the microalgae cell membrane, thus increasing the recovery of the pigments present in the raw material. This finding can be corroborated if we consider that the resulting pellet from the methanol extraction still retains coloration, which is indicative that this process is unable to extract all of the pigments present in the sample.

As far as the carotenoids/chlorophylls ratio is concerned, the extraction with DMF gives higher values than that with methanol. These results show that DMF is more selective than methanol in the recovery of carotenoids from chlorophylls. This behaviour can be attributed to the fact that chlorophyll is heterogenically bound to other compounds in the chloroplast and at least two or even three fractions of chlorophyll exist in the chloroplast. Therefore, the different polarities of methanol and DMF lead to the extraction of different types of chlorophyll and this gives rise to variations in the extraction yield of this substance [37,38].

4.2. SFE

The results of the experimental design analysis are shown in Table 2. Estimates of the effects and interactions between the range of variables under investigation are shown along with the analysis of variance of the extraction process. The sign associated with each of the effects indicates a positive or negative influence on the yield of the process. The analysis of variance with the degree of significance of each factor is represented in Table 2 by the p-value; when

a factor has a p-value below 0.05 this factor influences the process in a significant way.

The results obtained show that temperature and pressure both have a significant positive influence on the extraction process of carotenoids and chlorophylls (p value <0.05). On the other hand, the combined interaction of these two variables only has a significant positive influence on the extraction process of chlorophylls.

4.2.1. Effect of pressure

Analysis of the data presented in Table 1 shows that the maximum extraction yield of carotenoids depends on the temperature. At temperatures of 40 and 50 °C, the maximum extraction yield is achieved at 400 bar, while at 60 °C the best value it is obtained at a pressure of 300 bar. On the other hand, in the chlorophyll extraction, it can be seen that at 40 °C the values of the extraction yields are similar and significant differences are not found. At 50 °C of temperature, the highest extraction yield is obtained when the extraction is carried out at a pressure of 400 bar, while at 60 °C the highest chlorophyll yield is obtained at 500 bar.

For each temperature, an increase in the operating pressure leads to two opposing effects: an increase in the solvent power of the carbon dioxide and a decrease in its diffusivity. At relatively low temperatures (40 and 50 °C) the data obtained indicate that the dominant effect is the solvent power of the carbon dioxide until a pressure of 400 bar is reached. Above this value, this effect is unable to counteract the decrease in the solvent diffu-

Table 2
Estimated effect and analysis of variance for the supercritical extraction process for carotenoids and chlorophylls

Variable	Carotenoids		Chlorophylls	
	Effects	p-Value	Effects	p-Value
Temperature (T)	3.494	0.028	0.124	0.009
Pressure (P)	5.561	0.011	0.179	0.005
TT	5.747	0.5168	−0.047	0.517
PP	−14.742	0.3796	−0.071	0.380
TP	3.214	0.120	0.210	0.003

sivity and a decrease in the extraction yield of the process is observed.

On the other hand, at 60 °C the effect that prevails up to 300 bar in the SFE of carotenoids is the solvent power of the carbon dioxide, and above this value an increase in pressure does not compensate for the decrease in the diffusivity at 400 and 500 bar, a situation that leads to lower extraction yields. In the SFE of chlorophyll, the increase in the dissolving capacity of the solvent with pressure enables a larger amount of the solute to be recovered up to a pressure of 500 bar.

These results are consistent with those obtained in previous studies in which the microalgae *Nannochlorpsis gaditana* [22] and *Synechococcus* sp. [23] were used as raw materials, and also those obtained by Mendes et al. [20] in the extraction of carotenoids from *Clhorela vulgaris* working in the range 200–350 bar and 40–55 °C.

4.2.2. Effect of the temperature

It can be seen from Table 1 that at a pressure of 200 bar the highest extraction yields are reached when the temperature is 50 °C. This behaviour is similar to that observed in a previous study in which two different microalgae were used: *Nannochloropsis gaditana* [22] and *Synechococcus* sp. [23]. At a pressure of 200 bar, the slight increase in the extraction yield observed on increasing the temperature from 40 to 50 °C it is attributed to an increase in the vapour pressure of the solutes and the increase in the diffusivity of the carbon dioxide. On the other hand, when the temperature is increased from 50 to 60 °C, the effect that prevails is the decrease in the density of the solvent and this is not compensated by the increase in the diffusivity and the vapour pressure of the solutes to be extracted.

The best extraction yields are obtained at a temperature of 60 °C when the operation is carried out at 300, 400 and 500 bar. This behaviour is attributed to the fact that at these pressures the density of the carbon dioxide is greater and, at the same time, the increase in temperature causes increases in the solvent diffusivity and the vapour pressures of the pigments being extracted, thus favouring their dissolution and giving better extraction yields.

4.2.3. Carotenoids/chlorophylls (Car/Chlo) ratio

In order to define the best selective operating conditions for the extraction of carotenoids with respect to chlorophylls, the Car/Chlo ratios presented in Table 1 were analysed. Analysis of these data leads to two conclusions:

The first consideration is that at operating pressures of 300, 400 and 500 bar, the ratio between carotenoids and chlorophylls (Car/Chlo) shows the same variation with temperature. In other words, this ratio decreases on increasing the temperature from 40 to 50 °C, and increases to the highest values when a temperature of 60 °C is reached.

The second conclusion is that the best pressure and temperature conditions to obtain the highest ratio between carotenoids and chlorophyll are 300 bar and 40 °C. These conditions are the most appropriate to carry out the separation and purification of these two types of pigments.

4.3. Empirical correlations

The program STATGRAPHICS was used to analyse the experimental data and this enabled two empirical correlations to be obtained. These correlations are able to relate the variables that influence the SFE extraction process of carotenoids and chlorophylls with carbon dioxide.
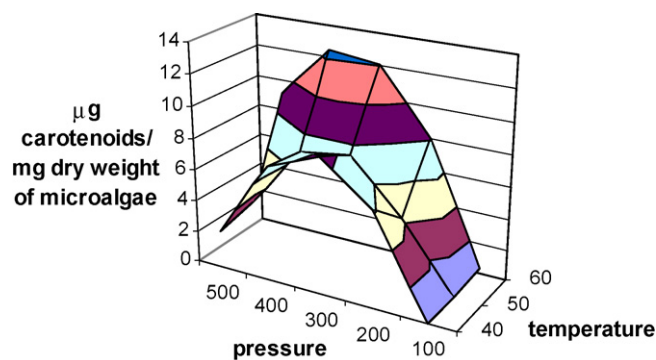
Fig. 1. Estimated values for the extraction yields of carotenoids using the empirical correlation proposed.

In the case of carotenoid extraction, the expression proposed is as follows:

$$R = 61.890 + 8.430 \times 10^{-2}P - 2.940T - 1.843 \times 10^{-4}P^2$$
$$+ 8.035 \times 10^{-4}PT + 2.873 \times 10^{-2}T^2 \qquad (4)$$

where R is the yield of the extraction of carotenoids in μg per mg of dry weight of microalgae, T the temperature [°C] and P is the pressure [bar]. The correlation coefficient obtained is 0.92.

Eq. (4) is represented in Fig. 1 for the different operating conditions. A detailed analysis of the figure indicates that the estimated values are consistent with those obtained experimentally. The highest yield is obtained between 300 and 400 bar at 60 °C.

In the case of chlorophyll extraction, the empirical correlation proposed is as follows:

$$R = -0.170 - 1.644 \times 10^{-3}P + 1.394 \times 10^{-2}T - 8.817 \times 10^{-7}P^2$$
$$+ 5.240P \times 10^{-5}T - 2.347 \times 10^{-4}T^2 \qquad (5)$$

where R is the extraction yield of chlorophylls in g per mg of dry weight of microalgae, T the temperature [°C] and P is the pressure [bar]. The correlation coefficient obtained is 0.92, which is identical to that obtained in the correlation for the carotenoids.

Eq. (5) is represented in Fig. 2 for the different operating conditions. When *D. salina* was used as the raw material it can be seen that the graph leads to a similar conclusion to that described in Section 4.2, i.e., the highest yield is obtained at a pressure of 500 bar and a temperature of 60 °C.

4.4. Comparison of SFE and UAE

A bar chart showing the comparison of the best results obtained by SFE and those obtained by UAE using methanol and DMF as sol-
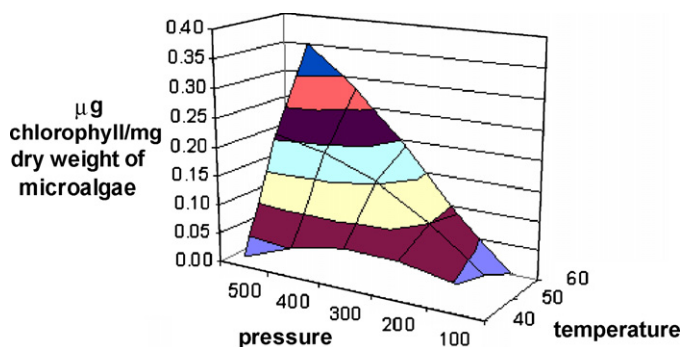

Fig. 2. Estimated values for the extraction yields of chlorophylls using the empirical correlation proposed.
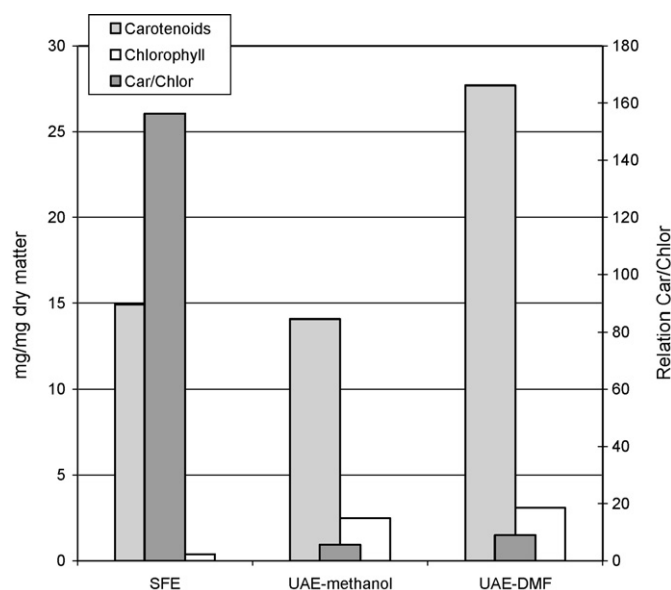
Fig. 3. Comparison of the extraction yields obtained by SFE and UAE on carotenoids and chlorophylls.

vent is shown in Fig. 3 along with the Car/Chlo ratios. Analysis of this figure shows that, for the carotenoid and chlorophyll extraction, the best extraction yields are obtained when the UAE is carried out using DMF as the solvent. On the other hand, the SFE is a more efficient method for the recovery of carotenoids than UAE using methanol as solvent. As far as the Car/Chlo ratio obtained in the SFE process using carbon dioxide is concerned, it is possible to conclude that, in all cases, this ratio is higher than that obtained in the UAE process using methanol or DMF. This suggests that the supercritical extraction process is more selective than the conventional one.

5. Conclusions

The best extraction yields of carotenoids on using *D. salina* as the raw material are obtained at the maximum operating temperature (60 °C) and at a pressure of approximately 400 bar. The best yields in the extraction of chlorophyll are achieved at 60 °C and 500 bar.

Supercritical carbon dioxide is a suitable solvent for the extraction of carotenoids due to the low polarity of these compounds. The SFE process is more selective than the UAE techniques when polar pigments, e.g. chlorophylls, are present in the raw material.

Acknowledgements

References

[1] F. García, E. Molina, M.E. Martínez, S. Sánchez, Grasas y aceites 41 (1990) 13–18.
[2] A.P. Scott, C. Middleton, Aquaculture 18 (1979) 227–240.
[3] S. Fujita, T. Watanabe, C. Kitajiwa, Aquaculture 34 (1983) 115–143.
[4] G.W. Burton, J. Nutr. 119 (1989) 109–111.
[5] P. Palozza, N.I. Krinsky, Methods Enzymol. 213 (1992) 403–420.
[6] A. Bendich, J.A. Olson, FASEB J. 3 (1989) 1927–1932.
[7] A. Bendich, in: N.I. Krinsky, M.M. Mathews-Roth, R.F. Taylor (Eds.), Carotenoids: Chemistry and Biology, Plenum Press, New York, 1990, pp. 323–335.
[8] N.I. Krinsky, Pure Appl. Chem. 66 (1994) 1003–1010.
[9] M.A. Borowitzka, L.J. Borowitzka, Microalgal Biotechnology, Cambridge University Press, Cambridge, 1988, p. 477.
[10] R.C. Cresswell, T.A.V. Rees, N. Shah, Algal and Cyanobacterial Biotechnology, Longman Scientific & Technical, 1981, p. 341.
[11] Z. Cohen, Chemicals from Microalgae, Taylor & Francis, 2002, p. 444.
[12] M. Wettasinghe, F. Shahidi, J. Agric. Food Chem. 47 (1999) 1801–1805.
[13] S. Rodrigues, G.A.S. Pinto, F.A.N. Fernandes, Ultrason. Sonochem 80 (2007) 869–872.
[14] V. Flores Péres, J. Saffi, M.I.S. Melecchi, F.C. Abad, R. Jacques, M.M. Martinez, E.C. Oliveira, E.B. Caramão, J. Chromatogr. A (2006) 115–118.
[15] L. Paniwnyk, E. Beaufoy, J.P. Lorimer, T.J. Mason, Ultrason. Sonochem. 8 (2001) 299–305.
[16] M.H. Entazani, S.H. Nazary, M.H.H. Khodaparast, Ultrason. Sonochem. 11 (2004) 379–384.
[17] L. Mathiasson, C. Turner, H. Berg, L. Dahlberg, A. Theobald, E. Anklam, R. Ginn, M. Sharman, F. Ulberth, R. Gaberning, Food Add. Cont. 19 (2002) 632–646.
[18] R.L. Mendes, H.L. Fernandes, J.P. Coelho, J.M.S. Cabral, A.M.F. Palavra, J.M. Novais, J. Appl. Phycol. 6 (3) (1994) 289–293.
[19] R.L. Mendes, H.L. Fernandes, J.P. Coelho, E.C. Reis, J.M.S. Cabral, J.M. Novais, A.F. Palavra, Food Chem. 53 (1995) 99–103.
[20] R.L. Mendes, B.P. Nobre, M.T. Cardoso, A.P. Pereira, A.F. Palavra, Inorg. Chim. Acta 356 (2003) 328–334.
[21] M. Careri, L. Furlattini, A. Mangia, M. Musci, E. Anklam, A. Theobald, J. Chromatogr. A 912 (2001) 61–71.
[22] M.D. Macías-Sánchez, C. Mantell, M. Rodríguez, E. Martínez de la Ossa, L.M. Lubián, O. Montero, J. Food Eng. 66 (2005) 245–251.
[23] M.D. Macías-Sánchez, C. Mantell, M. Rodríguez, E. Martínez de la Ossa, L.M. Lubián, O. Montero, J. Supercrit. Fluids 39 (2007) 323–329.
[24] O. Montero, M.D. Macías-Sánchez, C.M. Lama, L.M. Lubián, C. Mantell, M. Rodríguez, E. Martínez de la Ossa, J. Agric. Food Chem. 53 (2005) 9701–9707.
[25] J.A. Mendiola, L. Jaime, S. Santoyo, G. Reglero, A. Cifuentes, E. Ibañez, F.J. Señoráns, Food Chem. 102 (2007) 1357–1367.
[26] L. Gouveira, B.P. Nobre, F.M. Marcelo, S. Mrejen, M.T. Cardoso, A.F. Palabra, R.L. Mendes, Food Chem. 101 (2007) 717–723.
[27] A.P. Canela, P.T.V. Rosa, M.O.M. Marques, M.A.A. Meireles, Ind. Eng. Chem. Res. 41 (2002) 3012–3018.
[28] K.N. Chidambara Murthy, A. Vanitha, J. Rajesha, M. Mahadeva Swamy, P.R. Sowmya, G.A. Ravishankar, Life Sci. 76 (2005) 1381–1390.
[29] J. Navalho, Biotecnología de Dunaliellsa salina para produçao de betacaroteno Universidade do Algarbe. Unidade de Ciencias e Tecnología dos Recursos Acuáticos, 1997.
[30] A. Ben-Amotz, in: Z. Cohen (Ed.), Chemicals from Microalgae, Taylor & Francis Ltd., 1999.
[31] M. García-González, J. Moreno, J.C. Manzano, F.J. Florencio, M.G. Guerrero, J. Biotechnol. 115 (2005) 81–90.
[32] M.A. Hejazi, C. de Lamarliere, J.M.S. Rocha, M. Vermuë, J. Tamper, R.H. Wijffels, Biotechnol. Bioeng. 79 (1) (2002) 29–36.
[33] J.R. Denery, K. Dragull, C.S. Tang, Q.X. Li, Anal. Chim. Acta 501 (2004) 175–181.
[34] M. Herrero, L. Jaime, P.J. Martín-Álvarez, A. Cifuentes, E. Ibañez, J. Agric. Food Chem. 54 (2006) 5597–5603.
[35] R.R.L. Guillard, J.H. Ryther, J. Microb. 8 (1962) 229–239.
[36] A.R. Wellburn, J. Plant Physiol. 144 (1994) 307–313.
[37] M.E. Deroche, J.M. Briantais, Photochem. Photobiol. 19 (1974) 233–240.
[38] G. Oquist, G. Samuelsson, Physiol. Plantarum 50 (1980) 57–62.

Butene concentration prediction in ethylene/propylene/1-butene terpolymers by FT-IR spectroscopy through multivariate statistical analysis and artificial neural networks

Emilio Marengo [a,*], Valentina Longo [a], Marco Bobba [a], Elisa Robotti [a], Orfeo Zerbinati [a], Silvana Di Martino [b]

[a] Department of Environmental and Life Sciences, University of Eastern Piedmont, Via Bellini, 25/G 15100 Alessandria, Italy
[b] Polimeri Europa, Ferrara Plant, Piazzale G. Donegani, 12, 44100 Ferrara, Italy

ARTICLE INFO

ABSTRACT

This paper reports the development of calibration models for quality control in the production of ethylene/propylene/1-butene terpolymers by the use of multivariate tools and FT-IR spectroscopy.

1-Butene concentration prediction is achieved in terpolymers by coupling FT-IR spectroscopy to multivariate regression tools. A dataset of 26 terpolymers (14 coming from a constrained experimental design for mixtures, plus 12 terpolymers used for external validation) was analysed by FT-IR spectroscopy. An internal method of "Polimeri Europa" plant, based on ^{13}C NMR spectroscopy is used to determine the percentage of 1-butene in the samples. Then, different multivariate tools are used for 1-butene concentration prediction based on the FT-IR spectra recorded. Different multivariate calibration methods were explored: principal component regression (PCR), partial least squares (PLS), stepwise OLS regression (SWR) and artificial neural networks (ANNs). The model obtained by back-propagation neural networks turned out to be the best one. The performances of the BP-ANN model were further improved by variable selection procedures based on the calculation of the first derivative of the network.

The proposed approach allows the monitoring in real time of the polymer synthesis and the estimation of the characteristics of the product attainable from the concentration of 1-butene.

© 2008 Elsevier B.V. All rights reserved.

1. Introduction

Ethylene/propylene/1-butene terpolymers are synthetic rubbers or elastomeric materials able to endure high deformations under the action of relatively small efforts, and recover quickly the original shape and dimensions when the effort is removed.

An example of section of macromolecular chain of a generic ethylene–propylene–1-butene terpolymer is represented as:
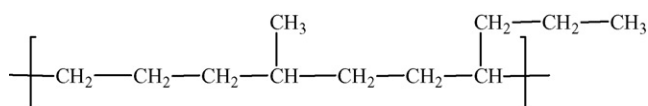
In this case, the terpolymers are statistical or random copolymers: polymer chains in which the monomeric units are randomly distributed.

The presence of 1-butene in terpolymers is studied to estimate the possible improvements of the elastomeric performances

for many different applications, regarding the automotive industry (section bars, radiating muffs, pipes, packings), the building industry (windows, electrical cables) and household appliances (packings, porthole for washing machines).

The objective of this work is to perform the fast determination of the concentration of 1-butene in ethylene/propylene/1-butene terpolymers, by the application of experimental design techniques and multivariate calibration methods. The final aim is the achievement of a reliable model to be used during the monitoring of the production process, controlling in real time the quality of the product.

The determination of ethylene and propylene in copolymers can be carried out exploiting the ratio between IR bands [1]. In the case of terpolymers the same procedure cannot be used for the determination of the % of 1-butene because of spectral superimpositions that afflict quantitative FT-IR analysis [1]. In this case, the concentration of 1-butene can be determined by ^{13}C-nuclear magnetic resonance (NMR) analysis [2], that is very precise but, in the meantime very time consuming (it supplies the result after several hours, spent for sample preparation, instrumental analysis, ^{13}C NMR spectra treatment and area integration).

This paper is mainly focused on the possibility of substituting ^{13}C NMR spectroscopy with FT-IR spectroscopy for the determination of the percentage of 1-butene in ethylene/propylene/1-butene terpolymers. A set of terpolymers coming from a constrained experimental design for mixtures is produced in the "Polimeri Europa" plant in Ferrara (Italy). The concentration of 1-butene in each final product is then determined by ^{13}C NMR spectroscopy and all products are characterised by FT-IR spectroscopy.

Finally, different calibration tools are applied to the FT-IR spectra recorded for each product obtained, to achieve a suitable regression model relating the concentration of 1-butene to the IR spectrum. The achievement of a reliable model would be of fundamental importance since the prediction of 1-butene concentration in future products could be accomplished by the use of FT-IR spectroscopy instead of NMR determinations: the great time saving could allow the monitoring of the terpolymer synthesis in real time.

Different multivariate strategies were compared here: principal component regression (PCR) [3,4], partial least squares (PLS) [3–9] and the stepwise OLS regression (SWR) [3,4]. These linear methods were compared to back-propagation artificial neural network (BP-ANN) [10–16] in order to evaluate the presence of non-linear effects.

2. Theory

2.1. Quantitative methods for monomer determination of EPDM

2.1.1. Infrared spectroscopy

IR test method ASTM D-3900 [1] covers the determination of the proportion of ethylene and propylene in copolymers and terpolymers over a range from 35% to 65% (w/w) of ethylene.

This test exploits the ratio between the absorbance of methyl groups from propylene units at 8.65 μm (1156 cm^{-1}) and the absorbance of methylene sequences from ethylene units at 13.85 μm (722 cm^{-1}). A series of known EPM polymers (whose concentration is determined through ^{13}C NMR spectroscopy) is used to build a calibration curve of $A_{8.65}/A_{13.85}$ versus % (w/w) of ethylene:

$$\text{ethylene} (\%) = a - b \ln \left(\frac{A_{8,65}}{A_{13,85}} \right) \tag{1}$$

where a and b are the regression coefficients to be calculated.

The propylene % is obtained as a complement to 100.

The ethylene % employed to build the calibration curve is obtained by the NMR spectroscopic determinations carried out on a set of samples covering the overall range of concentration.

In the case of terpolymers, the concentration of 1-butene cannot be determined through the ASTM method described because of spectral superimposition problems at about 755 cm^{-1}. So ^{13}C NMR [2] spectroscopy is normally used.

2.1.2. ^{13}C NMR spectroscopy

^{13}C NMR spectrometry is used to determine the molecular composition of a set of standard copolymers and to determine 1-butene concentration in terpolymers: the NMR method is the same used in ASTM D-3900 to determine the monomer concentration of the reference samples. The ^{13}C NMR method used to determine the 1-butene concentration is a internal procedure developed by "Polimeri Europa" company (Ferrara plant, Italy) and it is based on the linear combination of spectral peaks attributed to the presence of 1-butene.

Due to the long time of analysis, this method is not suitable for a real time monitoring of the production process of terpolymers. Therefore, calibration methods were explored to check the possibility of replacing the determination of 1-butene concentration in terpolymers by NMR spectroscopy with FT-IR spectroscopy. The use of FT-IR spectroscopy in facts would allow the monitoring of the production process in real time due to the faster instrumental procedure.

2.2. Multivariate calibration methods

2.2.1. Principal component regression (PCR) and partial least squares (PLS)

Principal component regression [3,4] is a method for relating the variations of a response (*Y*-variables) to the variation of several predictors (*X*-variables), with explanatory or predictive purposes. Principal components are first calculated from the *X*-variables matrix and then multiple linear regression is carried out on the extracted components to obtain the calibration model.

Partial least squares [3–9] models both the *X*- and *Y*-variables simultaneously, to find the latent variables (LVs) in *X* that best predict the latent variables in *Y*. These PLS-components (latent variables) are similar to principal components.

2.2.2. Stepwise ordinary least squares regression

The most exploited method for selecting a small number of variables from the original data is stepwise regression [3,4], based on two fundamental strategies: forward selection (FS) and backward elimination (BE). The FS method was used here for variable selection.

FS method starts with a model where no variables are included and gradually adds a variable at a time until a determined criterion of arrest of the procedure is satisfied.

The variable being included in the model in each step is the one providing the greatest value of an F-Fisher ratio, so that the *j*th variable is included in the model, with *p* variables already included, if:

$$F_j^+ = \max_j \left[\frac{\text{RSS}_p - \text{RSS}_{p+j}}{S_{p+j}^2} \right] > F_{\text{in}} \tag{2}$$

where: S_{p+j}^2 = variance calculated for the model with p variables plus jth variable; $\text{RSS}_p = \sum_p (y_p - \hat{y}_p)^2$ = residual sum of squares of the model with p variables; RSS_{p+j} = residual sum of squares of model with p variables plus jth variable.

The *F* value thus calculated is compared to a reference value (F_{in}) usually set at values ranging from 1 to 4: 1 corresponds to a more permissive selection, including in the final model a larger number of variables, while 4 corresponds to a more severe selection.

2.2.3. Artificial neural networks

Artificial neural networks (ANNs) [10–19] are mathematical algorithms that allow to solve complex problems by simulating the human brain functioning. In this work, the back-propagation network (Fig. 1) was applied: which is the most popular network used for calibration. It consists of:

- an input layer, where each neuron is associated to an experimental variable (in this case the wavelengths of IR spectra);
- one or more hidden layers with optimal number of neurons;
- an output layer, where each neuron is associated to a response (in this case 1-butene concentration).

The signal moves from the input layer towards the output layer (feed-forward).

In every neuron of the hidden and output layers, the signals coming from each neuron of the previous layer are accumulated by
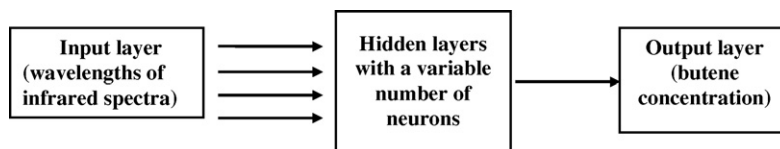
Fig. 1. Scheme of a BP-ANN.

applying a multiplying weight. The portion of signal that is transferred is regulated by a transfer function, often having a sigmoid shape.

In this process, each experiment of the training set is presented in turn to the network and the weights are corrected to decrease the error committed by the network in estimating the corresponding responses. In each cycle, constituting a learning epoch, all experiments are presented once to the network; the iterations of the learning epochs are repeated until the network produces satisfactory results.

Two parameters, called *learning rate* (set here at 0.3) and *momentum* (set here at 0.3), are used for controlling the size of weight adjustment along the descending direction and for dampening oscillations of the iterations.

The number of hidden layers and neurons in each hidden layer and the geometry of the network (i.e. the connection of the neurons of different layers) must be selected in order to achieve a satisfactory fitting ability associated, in the same time, to a satisfactory predictive ability.

The secret of building successful neural networks is to know when to stop the training phase (Fig. 2): if the net is trained for a short time it will not learn the data patterns, while if it is trained for too long, it will learn the noise and memorize the data by heart (overfitting). In order to solve the problem of overfitting the validation procedure adopted is fundamental. To this purpose, the dataset is splitted in three sets:

- *training set*, used for training the network (model building);
- *test set*, used for selecting the end of the training phase (corresponding to the minimum error committed on the test set (Fig. 2));
- *production set*, used for testing the predictive ability of the network.

A large number of variables contrast with the use of ANNs since it increases the risk of overfitting: therefore it is sometimes necessary to reduce the size of spectral datasets. In this case, this was achieved by substituting 10 subsequent wavelengths with their average absorption. This transformation reduces the number of wavelengths to 236.
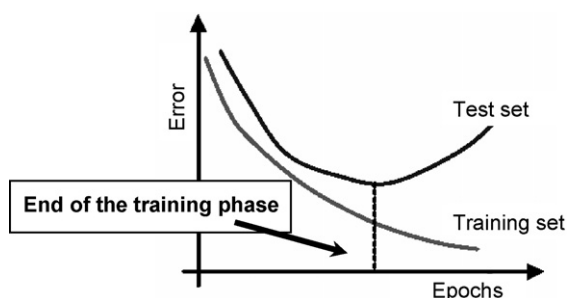
Fig. 2. Typical behaviour of the error of the training and test set during ANN training epochs.

2.2.3.1. Derivative of the network. ANNs can be considered as "black-boxes": this means that the contribution of the input variables in predicting the value of the output is difficult to disentangle within the network. Consequently, input variables are often entered into the network and an output value is generated without gaining any understanding of the inter-relationships between the variables i.e. without gaining any explanatory insight into the underlying mechanisms being modelled by the network. This disadvantage can be bypassed by the calculation of the first derivative of the network with respect to the input variables [18,19]. The first derivative allows the interpretation of the influence of each input variable on the final response; this feature can be used to perform variable selection: input variables not showing a relevant influence on the response can be eliminated allowing a more reliable predictive ability of the final model (i.e. reducing overfitting).

The value of the ANN first derivative is calculated for each input variable (variables are scaled from −1 to +1) for the samples present in the training set. Small variations are applied to one variable at a time in turn for each ith sample of the training set, keeping the original values of all the other variables. The variations applied here correspond to ±0.0001 for each jth variable:

$$x_{i,j}^+ = x_{i,j} + 0.0001 \tag{3}$$

$$x_{i,j}^- = x_{i,j} - 0.0001 \tag{4}$$

The derivative of each jth variable for each ith sample, $d_{i,j}$, is then computed as:

$$d_{i,j} = \frac{y_{i,j}^+ - y_{i,j}^-}{2 \times 0.0001} \tag{5}$$

where: $y_{i,j}^+$ = response given by the network for the ith object when a positive variation is applied to the jth variable according to Eq. (3); $y_{i,j}^-$ = response given by the network for the ith object when a negative variation is applied to the jth variable according to Eq. (4).

The values of derivative thus calculated range from −1 to +1. Values of first derivative close to the extremes (±1) correspond to variables relevant for the determination of the final response (the positive or negative sign of the value is related to variables increasing or decreasing respectively the experimental response), while values around zero correspond to non-relevant variables. The first derivative can therefore be used for variable selection: the variables not characterised by a relevant effect on the final response can be eliminated from the model in order to reduce overfitting.

2.2.4. Models evaluation

The fitting ability of artificial neural models and regression models was evaluated by the coefficient of multiple determination, R_{tr}^2, calculated as:

$$R_{tr}^2 = 1 - \frac{\sum_{i=1,n}(\hat{y}_i - y_i)^2}{\sum_{i=1,n}(y_i - \bar{y})^2} \tag{6}$$

where: n = number of samples of the training set; $\hat{y}_i$ = predicted value of the response for the ith experiment;
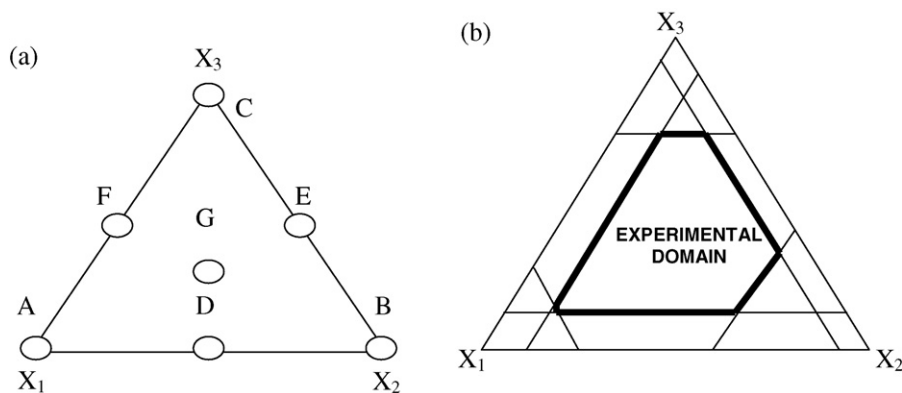
Fig. 3. Example of the distribution of experiments in simplex-centroid design (a) and example of experimental domain generated from constrained mixtures (b).

y_i = experimental value of the ith experiment; $\bar{y}$ = average response of the n experiments.

An analogous expression is used to evaluate the predictive ability of the models using the experiments of the production set: in this case the coefficient of multiple determination is indicated as R_{pro}^2. This coefficient is able to provide an estimation of the predictive ability of the network in conditions similar to the real use of the network when estimating new unknown situations, so it is a valid and efficient estimate of its genuine predictive ability.

The root mean square error (RMSE) between measured and predicted values is estimated as:

$$\text{RMSE} = \sqrt{\frac{\sum_i (\hat{y}_i - y_i)^2}{n}} \tag{7}$$

This parameter can be calculated using both the training (root mean square error of fitting, RMSEF) or the production (root mean square error of prediction, RMSEP) set of experiments, to achieve information about fitting and predicting ability respectively.

The significance of each model was calculated by ANOVA and by a F-Fisher test:

$$F_{\text{calc}} = \frac{\text{MS}_{\text{reg}}}{\text{MS}_r} = \frac{\sum_{i=1,n}(\hat{y}_i - \bar{y})^2 / 1}{\sum_{i=1,n}(y_i - \hat{y}_i)^2 / n - 2}$$

where: MS_{reg} = sum of squares due to regression divided by the corresponding degrees of freedom (1); MS_r = sum of squares due to residuals divided by the corresponding degrees of freedom $(n-2)$; n = number of samples used to build the model (training set); y_i = experimental response for the ith object of the training set; $\hat{y}_i$ = response of the ith object predicted by the model; $\bar{y}$ = average experimental response for the training set.

If it is verified the relationship:

$$F_{\text{calc}} > F_{\text{tab}(\alpha=0.05; \nu_1=1; \nu_2=n-2)}$$

the model calculated is statistically significant. The $F_{\text{tab}(\alpha=0.05; \nu_1=1; \nu_2=n-2)}$ value is tabulated for a fixed significance level (here: $\alpha = 0.05$, corresponding to a probability level of 95%) for $\nu_1 = 1$ and $\nu_2 = n - 2$, degrees of freedom. For all the models calculated, $F_{\text{tab}(\alpha=0.05; \nu_1=1; \nu_2=12)} = 4.75$.

2.3. Experimental design for mixtures

The study of mixtures [20] is of particular interest in the industrial field. The components of a mixture are not independent from each other as the sum of their concentration must be close to 100%. This means that, in the case of a three components mixture, the physical space that corresponds to all possible mixtures has the shape reported in Fig. 3(a): the physical domain is limited to the equilateral triangle, where each vertex corresponds to a pure component while points on the edges correspond to binary mixtures. Therefore, each three-component mixture can be represented by a point pertaining to this equilateral triangle, usually called *simplex*. In the case of a two-component mixture, the point correspondent to each mixture can vary on a segment, while in the case of four components the physical domain assumes the shape of a tetrahedron.

The interest is often focused on specific areas of the domain, so that it is further limited by bounds and assumes shapes like the one reported in Fig. 3. The presence of minimum and maximum bounds on a single component corresponds to cuts of the domain parallel to the faces of the simplex. In the case of ternary mixtures (Fig. 3(b)), the bounds are represented by the segments corresponding to cuts parallel to the edges of the triangle.

The experimental domain for mixtures can be sampled by several experimental design strategies: the ones more exploited are the simplex-lattice and the simplex-centroid design [20]. Here, given the presence of boundaries on the concentration of the components, the simplex was explored performing experiments on the vertices, in the centre of the edges and in the overall centre of the constrained domain.

3. Experimental

3.1. Experimental design

The problem was characterised by three factors corresponding to the three monomers used for terpolymers production, with the constraints indicated hereafter:

ethylene % (w/w) = 65–70,
propylene % (w/w) = 5–25,
butene % (w/w) = 5–25.

Because of the presence of the constraints, the experimental domain has the complex shape delimited by the nine mixtures represented in the blow-up (Fig. 4(b)). The experimental design adopted required to perform experiments in the vertices of the constrained region, in the centre of its edges and in its overall centre. Since the samples came from the production process, it was not possible to obtain mixtures perfectly coincident with those fixed by the experimental design: the mixtures used to build the calibration models were the most similar to the ideal ones (Fig. 4(c)).

Further 12 mixtures within the experimental domain were used for validating the calibration models.
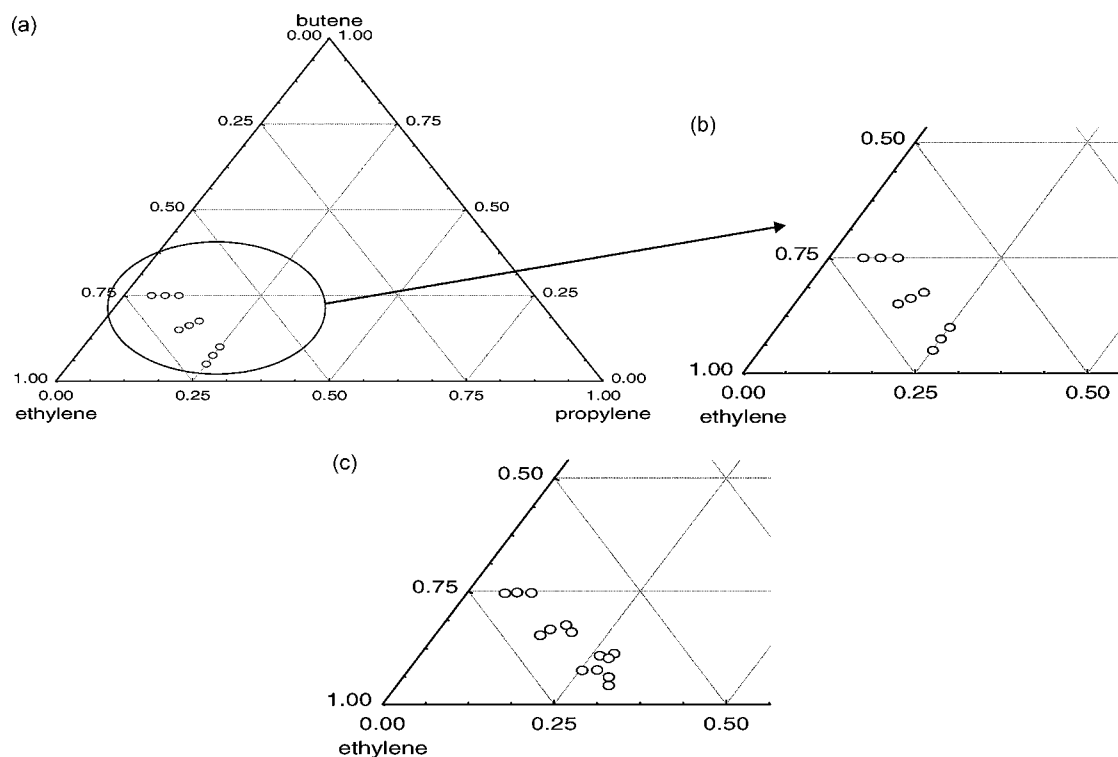
Fig. 4. Experimental domain obtained by the adopted experimental design (a and b); actual experiments performed (c).

All terpolymer samples correspond to the products obtained from the production in "Polimeri Europa" society (Ferrara plant, Italy). The dataset of terpolymers, consisting in 26 samples, was divided in three groups:

- 13 products out of the 14 defined by the experimental design in the *training set* (for the construction of the model) and the one left out in the *test set* (leave-one-out procedure): this process was iterated on all the 14 experiments on the experimental design;
- 12 products in the *production set* (to calculate the predictive ability of the model from genuine predictions).

3.2. FT-IR and NMR spectroscopy

The 26 terpolymer samples were characterised by infrared spectroscopy (range: 5000–450 cm^{-1}) and analysed through ^{13}C NMR spectroscopy to determine 1-butene concentration.

The transmittance infrared spectrum of a generic ethylene/propylene/1-butene terpolymer is shown in Fig. 5. The assignments of each band are indicated in Table 1. IR spectra were recorded on polymeric films obtained by pressing 0.2 g of sample between two aluminium sheets at 120 °C at a pressure of 10 Tons for 60 s. IR spectra were recorded by a PerkinElmer FT-Spectrum One System with
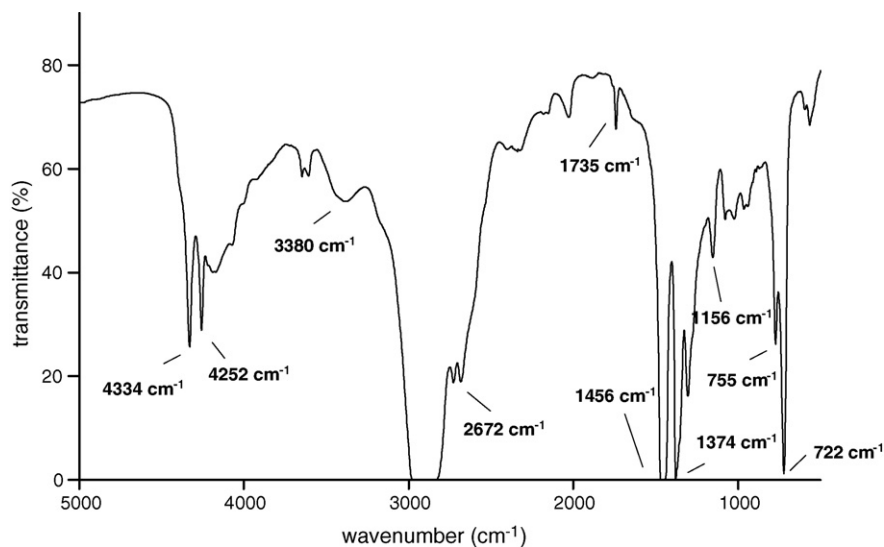
Fig. 5. Typical IR spectrum of a generic terpolymer ethylene/propylene/1-butene.

Table 1
Band assignments of the IR spectrum of Fig. 5

Band (cm^{-1})	Description
4334	Combination of vibrations of bending and stretching asymmetric of tie CH of methyls
4252	Combination of vibrations of bending and stretching asymmetric of tie CH of the methylenes
3380	Residual catalytic
2672	Armonica of the bending symmetrical of the CH$_3$
1735	Additive (anti-oxidant)
1456	Vibrations of bending of asymmetric CH$_2$ and CH$_3$
1374	Vibrations of bending of the symmetrical CH$_3$
1156	Vibration of wagging of the CH$_3$
755	Vibration of CH$_2$ of the butene
722	Vibrations of rocking of the CH$_2$

16 scans and a resolution of 2 cm^{-1}, using a deuterated triglycine sulfate (DTGS) detector.

NMR determinations were carried out by a Bruker Avance-300 spectrometer collecting 6600 scans at 120 °C with a pulse angle 90° and pulse repetition of 20 s, using tetrachloroethane-d_2 (C$_2$D$_2$Cl$_4$) as solvent. The protocol followed to calculate the 1-butene concentration in terpolymers is not reported here since it is an internal procedure of "Polimeri Europa" (Ferrara, Italy). The actual range of 1-butene concentration calculated on the 26 terpolymers by NMR spectroscopy was between 4.2% and 24.8%.

Each spectrum was described by 2358 wavenumbers; all calibration models investigated (PCR, PLS, SWR, ANN) were calculated using the first derivative of each infrared spectrum collected: this procedure was used to eliminate drift effects. For what regards PCR, PLS and SWR models, no other spectra pre-treatment was applied. For what regards instead ANNs, a smoothing procedure was applied to reduce the number of input variables at about 1/10 of the number of original variables, for calculation problems. A moving average smoothing procedure with step 10 was applied: the first derivative of 10 subsequent variables was substituted by their average, giving a total of 236 input variables.

3.3. Software

PCR and PLS models were calculated by "The Unscrambler" v. 9.5 (Camo, Norway); SWR models by Statistica v 7.1 (Statsoft, USA) and ANNs models by Neuroshell 2 (Ward Systems Group, USA). Graphical representations were built by Excel 2003 (Microsoft Corporation, USA) and Statistica.

4. Results and discussion

4.1. PCR and PLS

PCR and PLS were applied to the spectra of the 14 terpolymers of the training set. The first derivative of the wavelengths of the infrared spectra were considered as X-block variables and 1-butene concentration as the Y-variable. Data were mean centred. Table 2 reports the % of cumulative explained variance for PCR and PLS respectively.

Table 2
%Cumulative explained variance in Y of each principal component/latent variable in PCR and PLS models

Principal Components	PCR Y –%cumulative variance	Latent variables	PLS Y –%cumulative variance
PC1	28.67	LV1	81.54
PC2	93.77	LV2	96.12
PC3	98.69	LV3	99.36
PC4	99.06	LV4	99.79
PC5	99.13	LV5	99.93

The first three PCs/LVs explain 98.69% and 99.36% of the total variance of the dataset using PCR and PLS respectively, and were retained as significant. From Table 3 it can be noticed that PCR and PLS models perform satisfactorily both in fitting and prediction, even if PLS guarantees better results with respect to PCR. Both models appear statistically significant, as confirmed by the F value reported. Fig. 6 shows the predicted versus experimental values for the training (represented as asterisks) and the production sets (represented as circles) for PCR (Fig. 6(a)) and PLS models (Fig. 6(b)), respectively. It can be noticed that PLS performs better than PCR, especially in prediction: even if the coefficients of multiple determination of the training set are similar, the PLS model shows a better predictive ability ($R_{pro}^2 = 0.92$ and RMSEP = 1.83 in PCR; $R_{pro}^2 = 0.94$ and RMSEP = 1.58 in PLS).

4.2. Stepwise OLS regression

A stepwise regression was then carried out on the original variables and compared to the results obtained by PCR and PLS. The stepwise procedure was applied with forward selection. The analysis was carried out with different F_{in} values ranging from 3 to 10. Two different results were obtained depending on $F_{in} < 5$ or $F_{in} > 5$.

Table 3 shows that the best predictive ability using stepwise OLS is obtained when $F_{in} = 6$. In this case the procedure selects an optimal subset of only three original variables at 499 cm^{-1}, 750 cm^{-1} and 2447 cm^{-1}. Again, the significance of the model is confirmed by the F value. The experimental versus predicted concentrations of 1-butene for the samples of the production set for this model are shown in Fig. 6(c).

The results obtained prove that SWR, when compared to PLS, can slightly improve the predictive ability since it guarantees a lower root mean square error (RMSEP). Moreover, the SWR model provides a considerable variable reduction, confirming that the band at 750 cm^{-1} is the most related to the presence of 1-butene.

4.3. Back-propagation network

PCR, PLS and stepwise OLS assume a linear relationship between the X- and Y-variables. The presence of significant non-linear effects would lead to large prediction errors using these regression methods. Artificial neural networks can solve this problem: they have the ability to virtually approximate any function in a stable and efficient way.

Table 3
Summary of R^2, RMSE for the concentration of 1-butene and Fisher-F value for all the linear and non-linear regression procedures adopted

	R^2 (training)	R^2 (production)	RMSEF	RMSEP	$F_{calc} = MS_{reg}/MS_r$, $F_{tab(\alpha=0.05; \nu_1=1; \nu_2=12)} = 4.75$
PCR – 14 objects training set, 2358 original variables	0.98	0.92	0.78	1.83	911.41
PLS – 14 objects training set, 2358 original variables	0.99	0.94	0.54	1.58	1877.06
SWRs – F_{in} = 4 14 objects training set, 6 original variables	0.99	0.92	0.29	1.79	45881.23
SWRs – F_{in} = 6 14 objects training set, 3 original variables	0.99	0.94	0.61	1.46	3207.10
BP-ANN – 5 neurons hidden layer, 14 objects training set, 236 original variables	0.97	0.98	1.22	0.85	62.16

Fig. 6. PCR (a) and PLS results (b): predicted versus experimental concentration of 1-butene for training set (*) and for production set (○) (the regression line represents the trend of the training set); stepwise OLS results (F_{in} = 6) (c): predicted versus experimental concentration of 1-butene for production set (○) (the regression line represents the trend of the production set); best BP-ANN results without variables selection (d) and BP-ANN results with variables selection (21 input variables) (e): predicted versus experimental concentration of 1-butene for production set (○) (the regression line represents the trend of the production set).

Considering the low number of samples in the training set, the samples of the production set previously used for validating linear regression models, were used for the selection of the test set in BP-ANN. The production set of the network is constituted by the sample eliminated in turn from the test set. Therefore, at the end of the analysis, the training and the production sets of the BP-ANN are the same as for PCR, PLS and SWR.

Different architectures were investigated, changing the number of neurons in the hidden layers and number of hidden layers.

Table 4 reports the R^2 and RMSE values obtained both in fitting and in prediction for BP-ANNs with different number of neurons in the hidden layer. The best results were obtained selecting one hidden layer containing five neurons and the logistic transfer function.

The experimental versus predicted concentration of 1-butene of the production set obtained from the best network is shown in Fig. 6(d).

For what regards the R^2 values (Table 3), the BP-ANN model performs better both in fitting and prediction with respect to PCR, PLS and stepwise OLS models. The model is statistically significant but its F value is the smallest among the models considered: this is due to the fitting ability that is smaller compared to other models but that guarantees in the meantime a larger predictive ability. In general, BP-ANN succeeded in building a model that supplies the best compromise between fitting and prediction (high coefficient of multiple determination of the production set). On the other hand, it does not allow to know the most important IR bands for butene concentration prediction.

Table 4
Summary of R^2 and RMSE for the concentration of 1-butene using BP-ANNs with different number of neurons in the hidden layer

236 Neurons input layer; 1 neuron output layer; logistic transfer function	R^2 (training)	R^2 (production)	RMSEF	RMSEP
3 Neurons, 1 hidden layer	0.94	0.94	1.66	1.57
4 Neurons, 1 hidden layer	0.94	0.95	1.68	1.43
5 Neurons, 1 hidden layer	0.97	0.98	1.22	0.85
6 Neurons, 1 hidden layer	0.99	0.93	0.18	1.65
7 Neurons, 1 hidden layer	0.99	0.95	0.82	1.44
8 Neurons, 1 hidden layer	0.97	0.94	1.09	1.51
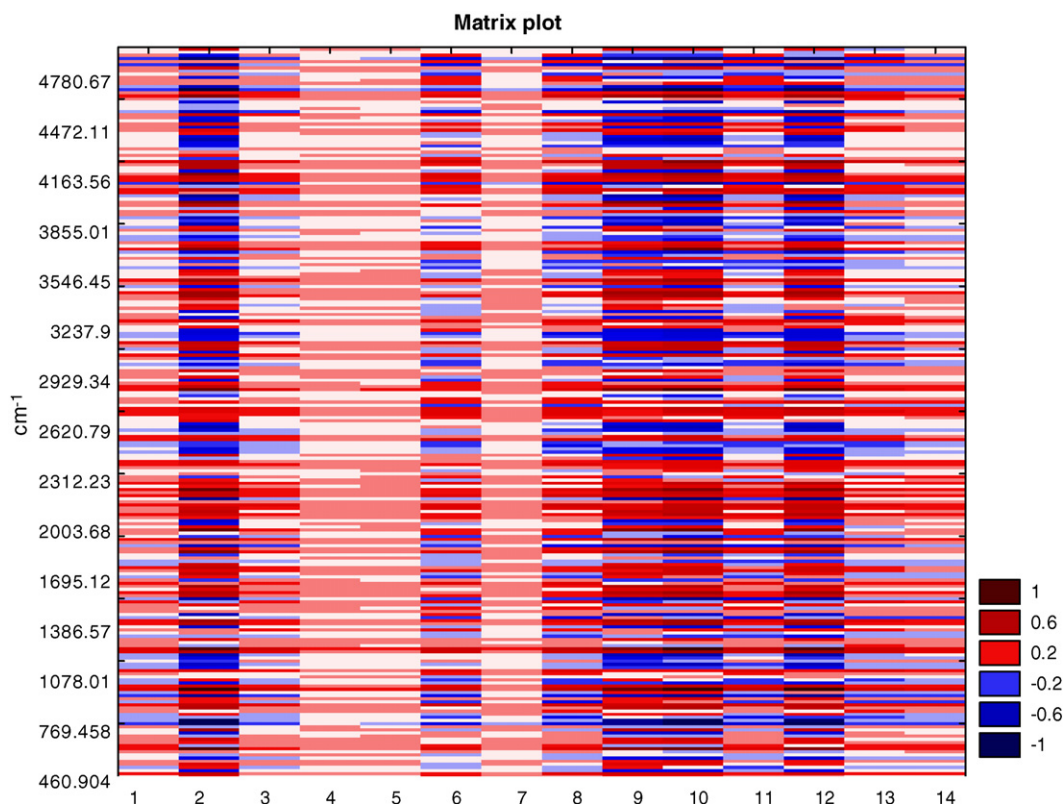
Matrix plot

Fig. 7. Matrix plot showing the first derivative of the network calculated for the samples of the training set. The 14 samples of the training set are represented on the x-axis, while the 236 wavelengths are represented on the y-axis.

The calculation of the first derivative of the best network (five neurons in the hidden layer) was performed to obtain information about the role played by the input variables in modelling 1-butene concentration.

Input variables showing a null value of the first derivative of the network do not have a high influence on the output; positive or negative values of the ANN first derivative correspond to variables with a positive or negative influence on the response.

Fig. 7 represents the first derivative of the network for the samples of the training set: the 14 samples of the training set are represented on the x-axis, while the 236 wavelengths are represented on the y-axis. The matrix plot is represented on a colour scale: red areas correspond to large positive values of the first derivative and blue areas correspond to large negative values; white areas show values around 0. From the matrix plot it is possible to point out the variables with a positive correlation with butene concentration (wavelengths represented in red) and those showing a negative correlation (wavelengths represented in blue).

The values of the first derivative of the network can be used to select a subset of significant variables in order to provide a network with a smaller number of input variables (wavelengths) and, possibly, a corresponding larger predictive ability. This variable selection procedure was repeated several times to identify the best number of input variables: a decreasing number of significant (input)

variables was selected by changing the range of derivative values considered as non-significant:

- derivatives from −0.30 to +0.30 as non-significant, producing 140 significant input variables;
- from −0.50 to +0.50: producing 59 significant input variables;
- from −0.75 to +0.75: producing 21 significant input variables;
- from −0.90 to +0.90: producing 9 significant input variables.

BP-ANN was trained again for each threshold selection value (± 0.30; ± 0.50; ± 0.75; ± 0.90) by eliminating the non-significant variables. Table 5 reports the R^2 values for training and production sets and the corresponding RMSE values. The results show that the best model corresponds to a threshold value of ± 0.75 with only 21 input variables. This model is the one that performs better both in fitting and prediction, showing the largest R^2 values (0.98 for training set; 0.99 for production set) and smallest RMSE values (RMSEF = 1.06 and RMSEP = 0.76) for training and production sets. The experimental versus predicted concentration of 1-butene of the production set obtained from this network is shown in Fig. 6(e).

The selection of the best subset of variables allowed to obtain an increase of R^2 values for training ($R^2_{without} = 0.97$ versus $R^2_{with} = 0.98$), and production sets ($R^2_{without} = 0.98$ versus $R^2_{with} = 0.99$)

Table 5
Summary of R^2 and RMSE for the concentration of 1-butene of the first derivative of the network with different range of derivative values around 0 value

Threshold selection value	R^2 (training)	R^2 (production)	RMSEF	RMSEP
±0.30 with 8 neurons in the hidden layer	0.99	0.95	0.56	1.37
±0.50 with 4 neurons in the hidden layer	0.99	0.95	0.66	1.44
±0.75 with 10 neurons in the hidden layer	0.98	0.99	1.06	0.76
±0.90 with 10 neurons in the hidden layer	0.94	0.98	1.67	0.98

while RMSE values decreased from 1.22 to 1.06 for the training set and from 0.85 to 0.76 for the production set.

The insertion of non-relevant information in the first BP-ANN model caused a loss of predictive ability due to the presence of noise in the model.

5. Conclusions

It can be asserted that it is possible to take advantage of FT-IR spectroscopy for the determination of the concentration of 1-butene in terpolymers.

PLS and stepwise regression supply, in general terms, better results with respect to PCR.

The use of the BP-ANN allowed to improve the predictive ability with respect to linear models. The fitting and predictive ability of BP-ANN was further improved by the application of a variable selection procedure based on the calculation of the first derivative of the network. In general, BP-ANN is the best method for this specific application and provides very good results in particular for what regards its predictive ability ($R^2_{pro} = 0.99$ and RMSEP = 0.76).

It can be asserted that, through the application of the BP-ANN technique to FT-IR spectroscopy, it is possible to monitor in real time the product (to predict the concentration of butene) substituting the use of ^{13}C NMR spectroscopy that is more time and money consuming.

Acknowledgment

References

[1] ASTM D 3900-95, Determination of ethylene units in EPM (ethylene–propylene copolymers) and EPDM (ethylene–propylene–diene terpolymers). American Society for testing and materials, 629.
[2] S. Di Martino, M. Kelchtermans, J. Appl. Polym. Sci. 56 (1995) 1781.
[3] H. Martens, T. Naes, Multivariate Calibration, Wiley and Sons, New York, 1989.
[4] B.G.M. Vandeginste, D.L. Massart, L.M.C. Buydens, S. De Jong, P.J. Lewi, J. Smeyers-Verbeke, Handbook of Chemometrics and Qualimetrics: Part B, Elsevier, Amsterdam, 1998.
[5] P. Bastien, V.E. Vinzi, M. Tenenhaus, Comput. Stat. Data Anal. 48 (2005) 17.
[6] H.J. Luinge, J.H. Van der Maas, T. Visser, Chemom. Intell. Lab. Syst. 28 (1995) 129.
[7] P. Geladi, B. Kowalski, Anal. Chim. Acta 185 (1986) 1.
[8] H.O.A. Wold, P.L.S. regression, in: N.L. Johnson, S. Kotz (Eds.), Encycplopaedia of the Statistical Sciences, vol. 6, Wiley, New York, 1988, p. 581.
[9] E. Marengo, R. Todeschini, Chemom. Intell. Lab. Syst. 12 (1992) 117.
[10] J. Hopfield, Neural Networks and Physical System, MIT Press, 1982.
[11] J. Zupan, J. Gasteiger, Neural Networks for Chemists: An Introduction, Weinheim, New York, 1993.
[12] K. Tanabe, T. Tamura, H. Uesaka, Appl. Spectrosc. 46 (1992) 807.
[13] J.R.M. Smits, W.J. Melssen, L.M.C. Buydens, G. Kateman, Chemom. Intell. Lab. Syst. 22 (1994) 165.
[14] G.D. Garson, AI Expert 6 (1991) 47.
[15] I. Aleksander, Introduction to Neural Computing, Thompson International Press, London, 1995.
[16] M. Smith, Neural Networks for Statistical Modeling, Van Nostrand Reinhold, New York, 1993.
[17] E. Marengo, M. Bobba, E. Robotti, M. Lenti, Anal. Chim. Acta 511 (2004) 313.
[18] E. Marengo, M. Bobba, E. Robotti, M.C. Liparota, Environ. Sci. Technol. 40 (2006) 272.
[19] E. Gabano, E. Marengo, M. Bobba, E. Robotti, C. Cassino, M. Botta, D. Osella, Coord. Chem. Rev. 250 (2006) 2158.
[20] J.A. Cornell, Experiments with Mixtures, second ed., Wiley Interscience, New York, 1990.

An optimized digestion method coupled to electrochemical sensor for the determination of Cd, Cu, Pb and Hg in fish by square wave anodic stripping voltammetry

V. Meucci [a,*], S. Laschi [b], M. Minunni [b], C. Pretti [c], L. Intorre [a], G. Soldani [a], M. Mascini [b]

[a] *Department of Veterinary Clinics, University of Pisa, viale delle Piagge 2, 56124 Pisa, Italy*
[b] *Department of Chemistry, University of Florence, via della Lastruccia 3, 50019 Sesto Fiorentino, Florence, Italy*
[c] *Department of Animal Pathology, University of Pisa, viale delle Piagge 2, 56124 Pisa, Italy*

ABSTRACT

An optimized digestion method coupled to electrochemical detection to monitor lead, copper, cadmium and mercury in fish tissues was developed. Square wave anodic stripping voltammetry (SWASV) coupled to disposable screen-printed electrodes (SPEs) was employed as fast and sensitive electroanalytical method for heavy metals detection. Different approaches in digestion protocols were assessed. The study was focused on Atlantic hake fillets because of their wide diffusion in the human nutrition. Best results were obtained by digesting fish tissue with hydrogen peroxide/hydrochloric acid mixture coupled to solid phase (SP) purification of the digested material. This combined treatment allowed quantitative extraction from fish tissue (muscle) of the target analytes, with fast execution times, high sensitivity and avoiding organic residues eventually affecting electrochemical measurements. Finally, the method has been validated with reference standard materials such as dogfish muscle (DORM-2) and mussel tissues (NIST 2977).

© 2008 Elsevier B.V. All rights reserved.

1. Introduction

The discharge of potentially toxic trace metals into the marine environment has become a global problem. Non-essential metals are held to be the most dangerous, since continuous exposure of marine organisms to their low concentrations may result in bioaccumulation, and subsequent transfer to man through the food chain. Fish represents an important source of high value proteins, vitamins, minerals and long chain polyunsaturated fatty acids (LC *n*-3 PUFAs). The intake of LC *n*-3 PUFAs, ensured through the weekly consumption of fish, is beneficial to cardiovascular health and may also benefit the fetus development [1]. The security of food from marine origin is guaranteed on one hand by the inspections carried out by the health authorities, and on the other hand, guaranteed by the regulation of the production methodologies (guidelines). The toxic risk of heavy metals in fish products has brought about a directive from the European Union 1881/2006 defining the maximum residues limits (MRL) of these contaminants in fish and molluscs.

Although the levels of heavy metals in foodstuff from fish is generally lower than the MRL and the levels of exposure in humans below the provisional tolerable weekly intake (PTWI), under certain circumstances, there is a risk that the consumption of fish and molluscs contaminated with heavy metals might bring to exposure that exceeds the PTWI [1].

Nowadays, consumers purchase fish from fish markets and supermarkets, but unfortunately no information about their contamination level is given, preventing consumers to take informed decision in buying. Thus from the point of view of inspection, the evaluation of the contamination levels of heavy metals in foodstuffs of marine origin becomes mandatory. To allow efficient control in remote places (fish markets, distribution chains, or supermarkets), simple, fast and reliable analytic protocols are the most suitable choice for heavy metals control, both in farmed and wild fish. In fact conventional approaches i.e. atomic absorption spectrometry (AAS) [2,3], inductively coupled plasma-atomic emission spectrometry (ICP-AES) [2,4] and inductively coupled plasma-mass spectrometry (ICP-MS) [2,5] are unsuitable for on-site screening since related instrumentation is not portable and requires skilled personnel and long analysis times. Electrochemical-based approaches i.e., stripping analysis using conventional electrodes [6–12] although allowing fast analysis of heavy metals, employ instrumentation still intended for laboratory use and thus unsuitable for on-site

* Corresponding author at: Section of Pharmacology & Toxicology, Department of Veterinary Clinics, University of Pisa, viale delle Piagge 2, 56124 Pisa, Italy. Tel.: +39 050 2216803; fax: +39 050 2216813.
E-mail address: vmeucci@vet.unipi.it (V. Meucci).

heavy metal analysis. More recently, stripping analysis can be performed by pocket-size portable electrochemical analyzers coupled to disposable screen-printed electrodes (SPEs), which have been largely used for many applications in sensor and biosensor technology [13,14]. This set up allows low-power, low-cost, rapid, and sensitive field analysis [15,16], as demonstrated by their use in environmental analysis for pesticide and other pollutant detection [17–24]. The coupling of disposable sensors to portable instrumentation can be also applied to control heavy metals in foodstuff extracts, allowing efficient and capillary on-site control of these analytes. Here we report the development of a simple and fast protocol for detecting heavy metals in fish, which couple a simple extraction procedure with electrochemical stripping analysis. The electrochemical technique used was square wave anodic stripping voltammetry (SWASV), and it was based on the use of portable instrumentation and disposable SPEs. The study was focused on Atlantic hake fillets. This choice is justified by the wide diffusion of this species in the human nutrition both in fresh and processed food. For this application, different digestion methods were evaluated in order to develop a simple analytical protocol suitable for on-field analysis of Pb, Cu, Cd and Hg in fish tissues, aiming also to avoid both the use of hazardous material and to minimize the waste residues. When measuring trace elements in seafood products, a prior accurate and reliable sample pre-treatment step is essential. Differently from environmental samples such as soils, sediments or plants, in fish muscle insoluble substances are not present then wet or dry decomposition treatment can be successfully applied. However, the most used decomposition treatments results too long to be compatible to fast analysis [25,26]. Most used sample pre-treatments are based on wet digestions with concentrated acids and alkaline treatments to destroy the organic matter present in the fish tissue. In this study different treatment procedures have been applied to fish samples. In particular, several methods reported by AAS or electrochemistry [4,5,9,12,27–36] for the digestion of various biological samples for the determination of Pb, Cu, Cd and Hg were studied for their suitability to digest fish samples for metal analysis by SWASV. The main drawback of using high concentrated acids consists in the presence of matrix effect in measurements. Moreover in the case of nitric acid use, the formation of toxic nitrous vapours, the presence of high blank values can occur. Furthermore perchloric acid, for its high reactivity, should be discouraged.

Most used approaches present limitations for direct application on electrochemical detection of heavy metals since the use of organic solvent in the measuring sample should be avoided. Consequently, the commonly used liquid extraction to remove the presence of the organic residues (i.e. lipids) deriving from the fat tissues cannot be applied. In order to overcome these limitations, a dedicated study was conducted to optimize the extraction step of the analytes suitable for electrochemical heavy metal detection. For these reasons different acid treatments on wet or dried fish tissue, performed at different temperatures, were evaluated and eventually coupled to liquid/liquid or solid phase (SP) treatment to remove any lipid residue. The relative recovery was evaluated by using certified reference material (CRM) and spiked fish tissue. Finally the analytical parameters (i.e. linearity, sensitivity, reproducibility and matrix effect) of the assay were evaluated.

2. Experimental

2.1. Reagents

Suprapur grade hydrochloric, nitric, perchloric acids and hydrogen peroxide were purchased from Merck (Italy). The water used for the preparation of solutions was from a Milli-Q System (Milli-

pore, Italy). High performance liquid chromatography (HPLC) grade hexane was supplied by LABSCAN (Hasselt, Belgium). Heavy metal stock solutions were prepared by diluting Pb(II), Cu(II), Cd(II) and Hg(II) standard solutions AAS grade (Fluka, Italy). Superlean ENVI-Carb columns were used for samples purification (Supelco, Italy). Certified reference material (CRM) from dogfish muscle (DORM-2) and mussel tissues (NIST 2977) were purchased from Nova Chimica (Milan, Italy).

2.2. Instrumentation and experimental conditions

Screen-printed graphite-based mercury-modified and gold-based electrodes were purchased from EcoBioServices & Researches s.r.l., Florence, Italy.

Electrodes are serigraphically screen-printed with a shape similar to that reported in [15]. They consist of a round-shaped working electrode (diameter 3 mm), of a graphite counter electrode and of a silver pseudo-reference electrode. In addition, the silver electrical contacts were covered by a graphite layer in order to prevent oxidation phenomena during storage.

Two working electrode materials were used in this work, depending on the two different measurement applications. In the case of Pb(II), Cu(II), and Cd(II) detection, graphite-based Hg-modified screen-printed electrodes were used. These are based on the use of a special coating cellulose-derivative film deposited onto the graphite working electrodes containing a Hg(II) salt, as reported in [15]; Hg(II) is reduced from the salt to the metallic form and the modified sensor can be then used for heavy metal accumulation and stripping. The use of this strategy allows to avoid the use of large amounts of Hg solutions, by keeping the high sensitivity which characterize mercury-coated electrodes.

On the contrary, gold-based screen-printed sensors were used for the detection of Hg(II). In this case, the measurement is based on the capability of Hg to form amalgam with Au [16]. The screen-printed working electrode was obtained by printing a gold-based ink, and the surface needs just a short electrochemical procedure for measurement activation.

For measurements, SPEs are the interfaced with a portable electrochemical transducer Palmsens (Palm Instrument BV, Houten, The Netherlands) for the acquisition of the analytical signal, connected to a hand-held computer iPaq (Hewlett-Packard Company, Palo Alto, CA, USA) for the elaboration of the analytical data. The applied electrochemical technique was the SWASV.

Square wave (SW) voltammetry conditions for Pb(II), Cu(II), and Cd(II) analysis were conditioning potential −0.15 V for 60 s, deposition potential −1.1 V for 120 s, equilibration time 30 s, SW amplitude (E_{amp}) 28 mV, step potential (E_{step}) 3 mV and frequency (f) 15 Hz. Each mercury-coated electrode is pre-treated, before using, by applying −1.1 V for 300 s and then SW voltammetric scans were carried out until low and stable background were obtained, as suggested in literature [15].

SW voltammetry conditions for Hg(II) analysis were conditioning potential +0.7 V for 30 s, deposition potential +0.2 V for 120 s, equilibration time (t_{eq}) 30 s, SW amplitude (E_{amp}) 28 mV, step potential (E_{step}) 3 mV and frequency (f) 15 Hz. Each sensor was pre-treated, before using for the first time, by applying five cycles of cyclic voltammetry (CV) using the following conditions: potential range 0/+0.7 V, scan rate 50 mV/s and step potential 2.44 mV. This step is necessary to obtain a stable baseline [16].

HCl 0.1 M was used as supporting electrolyte for all measurements. All measurements were performed without removing oxygen from the solution. The measurements were performed immersing the sensor in 5.0 ml of solution; stirring conditions were used during the conditioning and the accumulation steps, whereas the square wave scan was performed in quiescent solution.

2.3. Samples treatment

In this work, taking into account the above-mentioned approaches, wet acid digestion with nitric acid, nitric/perchloric acids and hydrogen peroxide/hydrochloric acid have been applied to fish muscle samples. In particular, fresh and dried muscle (hot plate or in oven) was used as starting material undergoing acid digestion. To avoid organic residues in the matrix, an additional solid phase (carb column) or liquid extraction (hexane) was performed. Samples of different commercial brands of frozen Atlantic hake (*Merluccius* spp.) fillets were purchased from local large supermarkets, although the precise hake fillets origin (Atlantic Ocean) was not specified. Several types of wet acid digestion techniques were evaluated (Methods 1–5). The digestion was always performed into a closed vessel.

- Method 1. At 5 g of wet or dried (100 °C overnight) muscle were added 5 ml of HNO_3 1N, everything was heated up at 100 °C for 4 h, the solvent was evaporated and 5 ml of HCl 0.1 M were added and refluxed until a limpid solution was formed (∼2 h).
- Method 2. The same as the previous but with HNO_3 concentrated.
- Method 3. At 5 g of wet or dried (100 °C overnight) muscle were added 10 ml of HNO_3 concentrated overnight at room temperature; then everything was heated up at 100 °C for 4 h the solvent was evaporated and 5 ml of HCl 0.1 M were added and refluxed until a limpid solution was formed (∼2 h).
- Method 4. The same as the first but with $HNO_3/HClO_4$ concentrated solution (1:1, v/v).
- Method 5. At 5 g of wet or dried (100 °C overnight) muscle were added 5 or 10 ml of H_2O_2 33%, everything was heated up at 50 °C for 2 h, cooled and 5 or 10 ml of HCl 30% were added, the sample was then heated up at 70 °C for 2 h until a limpid solution was formed. The solution was made up to 10 or 20 ml with ultra-pure water.

For all the tested methods the final sample was measured before and after extraction with hexane (5 or 10 ml) to remove lipids or elution with carbon column to remove any organic residue. The carb columns were pre-conditioned with 2 ml of methanol followed by 2 ml of ultra-pure water. These methods are summarised in Table 1.

2.4. Analytical parameters

The quantitative analysis was done by standard addition method [37–39]. To test the accuracy and the reliability of the methods described, recoveries from reference matrices of dogfish muscle, mussel tissues, and spiked hake fillets, subjected to the treatment procedure already described, were carried out. To test the stability of the digested samples, the analysis of heavy metals was performed on initially spiked hake fillets on different days (day 0: extraction day; day 1 and day 2). The measures were repeated in triplicate ($n = 3$) for each group of sample.

The linearity of the method was assessed by heavy metal standard solutions (range 1 µg/L to 1 mg/L). The limits of detection (LOD) of all the studied metals were estimated as the concentration corresponding to the three times the standard deviation of the blank divided by the slope of the calibration curve.

3. Results and discussion

3.1. Sample pre-treatment

The properties of the digests obtained with the applied treatments are summarised in Table 2. All the acid digestion protocols applied, except Methods 1 and 2, produced a clear digest. However, not all of these digests were suitable for SWASV analysis. In fact sample digested with HNO_3 (Method 3), further purified by liquid/liquid extraction in hexane, produced a large peak, not observed in reagent blanks, over the potential range using both

Table 1
Methods of digestion

	Reagents	Sample	Digestion protocol	Purification
Method 1				
A	HNO_3 1N	Wet muscle	100 °C 4 h	No
B	HNO_3 1N	Wet muscle	100 °C 4 h	Hexane
C	HNO_3 1N	Dried muscle	100 °C 4 h	No
D	HNO_3 1N	Dried muscle	100 °C 4 h	Hexane
Method 2				
A	HNO_3 conc.	Wet muscle	100 °C 4 h	No
B	HNO_3 conc.	Wet muscle	100 °C 4 h	Hexane
C	HNO_3 conc.	Dried muscle	100 °C 4 h	No
D	HNO_3 conc.	Dried muscle	100 °C 4 h	Hexane
Method 3				
A	HNO_3 conc.	Wet muscle	Overnight RT and 100 °C 4 h	No
B	HNO_3 conc.	Wet muscle	Overnight RT and 100 °C 4 h	Hexane
C	HNO_3 conc.	Dried muscle	Overnight RT and 100 °C 4 h	No
D	HNO_3 conc.	Dried muscle	Overnight RT and 100 °C 4 h	Hexane
Method 4				
A	$HNO_3/HClO_4$	Wet muscle	100 °C 4 h	No
B	$HNO_3/HClO_4$	Wet muscle	100 °C 4 h	Hexane
C	$HNO_3/HClO_4$	Dried muscle	100 °C 4 h	No
D	$HNO_3/HClO_4$	Dried muscle	100 °C 4 h	Hexane
Method 5				
A	H_2O_2/HCl	Wet muscle	H_2O_2 50 °C 2 h/HCl 70 °C 2 h	No
B	H_2O_2/HCl	Wet muscle	H_2O_2 50 °C 2 h/HCl 70 °C 2 h	Hexane
C	H_2O_2/HCl	Wet muscle	H_2O_2 50 °C 2 h/HCl 70 °C 2 h	Carb column
D	H_2O_2/HCl	Dried muscle	H_2O_2 50 °C 2 h/HCl 70 °C 2 h	No
E	H_2O_2/HCl	Dried muscle	H_2O_2 50 °C 2 h/HCl 70 °C 2 h	Hexane
F	H_2O_2/HCl	Dried muscle	H_2O_2 50 °C 2 h/HCl 70 °C 2 h	Carb column

Different letters indicate subgroup within the same acid treatment with the same acid reagent and digestion protocol.

gold- and graphite-based electrodes. This effect should be therefore attributed to incomplete destruction of organic matter or to its decomposition products. When Methods 1 and 2 were applied followed by hexan purification, no peaks were recorded, even in spiked digests. The samples obtained applying the treatment directly on fresh material, always resulted in highly impure samples, not suitable for the analysis. In fact the material obtained from visual inspection never appear colorless and/or without impurities leading to evident difficulties in metal detection. Improvement has been obtained when a further oxidizing agent has added as in Method 4 (perchloric acid) and Method 5 (hydrogen peroxide), also coupled to hexan or carb-column purification. However, this was not sufficient to obtain a clear useful analytical signal. Conversely, reproducible peaks and linear standard addition plots were observed in digested reagent blanks. This indicates a clear matrix effect due to incomplete destruction of organic matter or to its decomposition products. In the case of digestion with $HNO_3/HClO_4$ (Method 4), followed by HCl treatment (under reflux), some promising results were obtained after hexane extraction in turn of visible residues presence. However no clear peak separation was obtained in SWASV. Method 5, consisting in acid digestion in a oxidizing environment using H_2O_2/HCl performed on dried (oven 100 °C) muscle followed by elution on carb columns, was found to be the only one allowing metals' detection. Furthermore no matrix effect was observed. With this latter treatment tiny, clear, well-separated signals corresponding to the different metals (Figs. 1 and 2) were recorded by SWASV. Moreover, no metal was found to be released by the columns as checked in the digested reagents blank (data not shown). For these reasons H_2O_2/HCl digestion with carb-column purification coupled to disposable screen-printed electrode was used in further analyses.

Table 2
Properties of digests after several methods of digestion

	Clear digest produced?	Colorless digest produced?	Metals detected by SWASV?
Method 1			
A	No	No	No
B	No	No	No
C	No	No	No
D	No	No	No
Method 2			
A	No	No	No
B	No	No	No
C	No	No	No
D	No	No	No
Method 3			
A	Yes	No	No
B	Yes	No	No
C	Yes	No	No
D	Yes	No	No
Method 4			
A	Yes	No	No
B	Yes	No	Yes
C	Yes	No	No
D	Yes	No	Yes
Method 5			
A	Yes	No	No
B	Yes	No	Yes
C	Yes	Yes	Yes
D	Yes	No	No
E	Yes	No	Yes
F	Yes	Yes	Yes

Different letters indicate subgroup within the same acid treatment with the same acid reagent and digestion protocol.
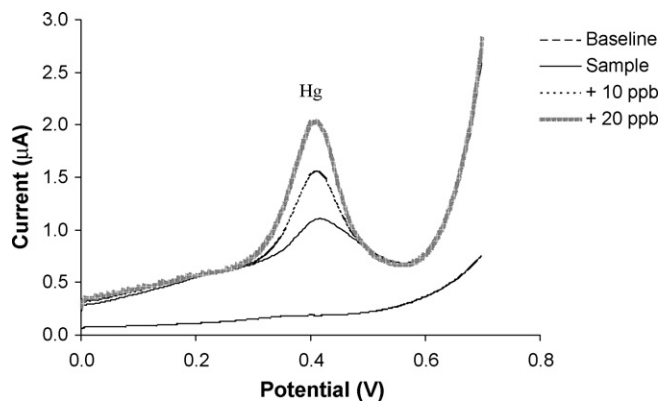
Fig. 1. SWASV scans for Hg detection in Atlantic hake sample. Gold-based screen-printed sensors were used. Applied digestion procedure: optimized H_2O_2/HCl treatment with carb-column purification. The experimental conditions were conditioning potential 0.7 V for 30 s, deposition potential 0.2 V for 120 s, equilibration time 30 s, SW amplitude 28 mV, step 3 mV and frequency 15 Hz.

3.2. Analytical parameters of the developed assay

3.2.1. Sensor calibration

Different concentrations of Pb, Cu, Cd and Hg were used to perform linear regression analysis for utilized screen-printed electrodes. The linear regression analysis, obtained by plotting the height of the peaks obtained for each concentration, gave the following equations: for Pb, $y = 0.31x$; for Cd, $y = 0.10x$; for Cu, $y = 0.25x$ and for Hg, $y = 0.04x$. In all cases, linearity ranging from 1 μg/L to 1 mg/L was obtained with a correlation ≥ 0.99 for all metals. The detection limit (DL) for each metal was estimated as the concentration corresponding to the three times the S.D. of the blank divided by the slope of the calibration curve, and are 0.3, 1, 0.5 and 0.9 μg/L for lead, cadmium, copper and mercury, respectively.

3.2.2. Application to reference material

The optimized procedure was tested on certified reference material (CRM). In Table 3 results of NIST 2977 and DORM-2 relatively for Pb, Cu, Cd and Hg are reported. Very good agreement between the certified value and the determined ones was found, indicating a recovery >91% and a relative error lower than 12%. This finding obtained with CRMs provides also a validation of the reported optimized protocol for this particular matrix.
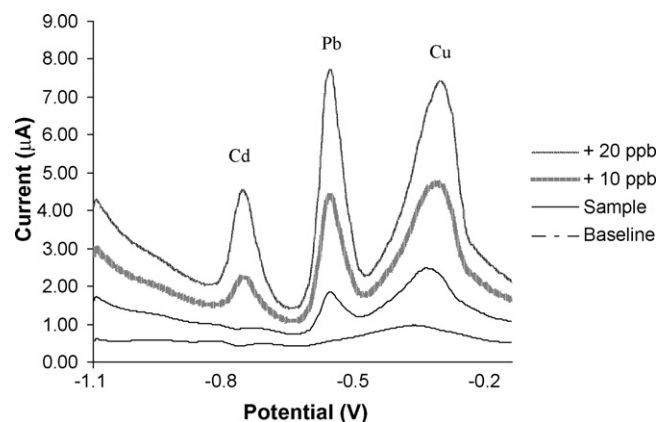
Fig. 2. SWASV scans for Pb, Cu and Cd detection in Atlantic hake sample. Graphite-based Hg-modified screen-printed electrodes were used. Applied digestion procedure: optimized H_2O_2/HCl treatment with carb-column purification. The experimental conditions were conditioning potential −0.15 V for 60 s, deposition potential −1.1 V for 120 s, equilibration time 30 s, SW amplitude 28 mV, step 3 mV and frequency 15 Hz. The electrode was conditioned before using by applying −1.1 V for 300 s.

Table 3
Comparison between certified values of certified reference material (CRM) of dogfish muscle (DORM-2) and mussel tissues (NIST 2977) and metals content found after hydrogen peroxide/hydrochloric acid digestion coupled with solid phase purification (with carb column) and SWASV analysis

Certified reference material	Element	Certified value (mg/kg)	Determined value (mg/kg), $n = 3$
Mussel tissue NIST 2977	Cd	0.18 ± 0.01	0.17 ± 0.02
	Cu	9.42 ± 0.52	9.44 ± 0.35
	Pb	2.27 ± 0.13	2.31 ± 0.20
	Hg	0.10 ± 0.01	0.10 ± 0.01
Dogfish muscle DORM-2	Cd	0.04 ± 0.01	0.05 ± 0.01
	Cu	2.34 ± 0.16	2.58 ± 0.28
	Pb	0.07 ± 0.01	0.06 ± 0.01
	Hg	4.64 ± 0.26	4.24 ± 0.35

Table 4
Metals content (±standard deviation) determined in samples of Atlantic hake fillets by SWASV analysis after sample digestion with hydrogen peroxide/hydrochloric acid treatment followed by solid phase purification with carb column

Hake fillets	Cd (mg/kg wet weight)	Cu (mg/kg wet weight)	Pb (mg/kg wet weight)	Hg (mg/kg wet weight)
1	<LOD	0.14 ± 0.05	0.08 ± 0.01	<LOD
2	0.03 ± 0.01	0.52 ± 0.06	0.18 ± 0.01	0.14 ± 0.02
3	0.04 ± 0.01	0.53 ± 0.07	0.15 ± 0.01	0.17 ± 0.02
4	0.03 ± 0.01	0.16 ± 0.03	0.14 ± 0.01	0.09 ± 0.01
5	<LOD	0.11 ± 0.02	0.09 ± 0.01	<LOD

Different numbers indicate different samples of hake fillets analysed.

Table 5
Stability of spiked Atlantic hake fillets after hydrogen peroxide/hydrochloric acid digestion coupled with solid phase purification (carb column) and SWASV analysis performed at different days (0, 1 and 2) from digestion

Metals	Metal conc. (mg/kg)	Metal added (mg/kg)	Metal expected (mg/kg)	Days	Metal found (mg/kg)
Cd	<LOD	0.20	0.20	0	0.22 ± 0.03
				1	0.18 ± 0.02
				2	0.16 ± 0.01
Pb	0.04	0.20	0.24	0	0.24 ± 0.02
				1	0.21 ± 0.04
				2	0.18 ± 0.01
Cu	0.15	0.20	0.35	0	0.34 ± 0.02
				1	0.29 ± 0.04
				2	0.18 ± 0.01
Hg	0.09	0.20	0.29	0	0.27 ± 0.02
				1	0.25 ± 0.03
				2	0.18 ± 0.03

3.2.3. Application to hake fillets samples

Then the developed analytical procedure was further applied to commercially available samples of frozen Atlantic hake (*Merluccius* spp.) fillets from different commercial brands (spiked or not). The frozen material was thawed and processed following the optimized procedure. The estimated heavy metal content is reported in Table 4.

To evaluate the stability of digested spiked samples, a different set of samples was processed with the optimized protocol; the analysis thus was performed at different days (0, 1 and 2) from digestion (Table 5). It can be seen for all the analytes comparable values were obtained at days 0 and 1. A low decrease of estimated content was observed at day 2 from the digestion, especially for Hg. Reproducibility, calculated by three determination on the same digested sample, and expressed as coefficient of variation (CV%) was found to be always <20 CV%.

4. Conclusions

Electrochemical detection, based on SWASV with disposable screen-printed electrodes, coupled to portable instrumentation has been successfully applied to heavy metal detection of fish muscle. Different approaches in digestion protocols were assessed. Among the different tested methods, best results were obtained by digesting fish tissue with hydrogen peroxide/hydrochloric acid mixture coupled with solid phase purification of the digested material. Differently from the other tested protocols, with the optimized digestion treatment no matrix effect was observed and tiny, clear, well-separated peaks corresponding to the different metals were recorded. The analytical performances of the developed protocol have been investigated. Sensitive, reproducible, fast multi-analyte detection of lead, cadmium, copper and mercury in Atlantic hake fillets by SWASV has been achieved. Validation of the method in the fish matrix was performed with CRMs (DORM-2 and NIST 2977). Extension of this fast, simple, sensitive and cheap approach for heavy metal analysis to other food tissue matrices can be foreseen. The portability of the instrumentation together with simple sample pre-treatment makes this approach particularly appealing for multi-analytes detection i.e. for inspection purposes.

References

[1] EFSA, EFSA J. 236 (2005) 1.
[2] E.P. Popek, Sampling and Analysis of Environmental Chemical Pollutants: A Complete Guide, Academic Press, San Diego, CA, USA, 2003.
[3] Ö. Dalman, A. Demirak, A. Balci, Food Chem. 95 (2006) 157.
[4] M. Türkmen, C. Ciminli, Food Chem. 103 (2007) 670.
[5] G. Falcó, J.M. Llobet, A. Bocio, J.L. Domingo, J. Agric. Food Chem. 54 (2006) 6106.
[6] T.M. Florence, Analyst 117 (1992) 551.
[7] D.F. Lambert, N.J. Turoczy, Anal. Chim. Acta 408 (2000) 97.

[8] C. Locatelli, Food Addit. Contam. 17 (2000) 769.
[9] G. Dugo, L. La Pera, A. Bruzzese, T.M. Pellicanò, V. Lo Turco, Food Control 17 (2006) 146.
[10] U. Celik, J. Oehlenschläger, Food Chem. 87 (2004) 343.
[11] U. Celik, J. Oehlenschläger, Food Control 18 (2007) 258.
[12] B.S. Sherigara, Y. Shivaraj, R.J. Mascarenhas, A.K. Satpati, Electrochim. Acta 52 (2007) 3137.
[13] N.Y. Stozhko, N.A. Malakhova, M.V. Fyodorov, K.Z. Brainina, J. Solid State Electrochem. 12 (2008) 1219.
[14] K.C. Honeychurch, J.P. Hart, Trends Anal. Chem. 22 (2003) 456.
[15] I. Palchetti, S. Laschi, M. Mascini, Anal. Chim. Acta 530 (2005) 61.
[16] S. Laschi, I. Palchetti, M. Mascini, Sens. Actuators 114 (2006) 460.
[17] I. Palchetti, M. Mascini, M. Minunni, A.R. Bilia, F.F. Vincieri, J. Pharm. Biomed. Anal. 32 (2003) 251.
[18] S. Laschi, D. Ogończyk, I. Palchetti, M. Mascini, Enzyme Microb. Technol. 40 (2007) 485.
[19] S. Centi, S. Laschi, M. Fránek, M. Mascini, Anal. Chim. Acta 538 (2005) 205.
[20] S. Centi, E. Silva, S. Laschi, I. Palchetti, M. Mascini, Anal. Chim. Acta 594 (2007) 9.
[21] S. Andreescu, J.L. Marty, Biomol. Eng. 23 (2006) 1.

[22] M. Mehrvar, M. Abdi, Anal. Sci. 20 (2004) 1113.
[23] G. Hanrahan, D.G. Patil, J. Wang, J. Environ. Monitor. 6 (2004) 657.
[24] O. Domínguez Renedo, M.A. Alonso-Lomillo, M.J. Arcos Martínez, Talanta 73 (2007) 202.
[25] M. Hoenig, Talanta 54 (2001) 1021.
[26] P. Bermejo-Barrera, A. Moreda-Piñeiro, A. Bermejo-Barrera, Talanta 57 (2002) 969.
[27] O.D. Uluozlu, M. Tuzen, D. Mendil, M. Soylak, Food Chem. 104 (2007) 835.
[28] M. Dural, M.Z. Lugal Göksu, A.A. Özak, Food Chem. 102 (2007) 415.
[29] P. Sivaperumal, T.V. Sankar, P.G. Viswanathan Nair, Food Chem. 102 (2007) 612.
[30] B. Gümgüm, E. Ünlü, Z. Tez, Z. Gülsün, Chemosphere 29 (1994) 111.
[31] G.R. Boaventura, A.C. Barbosa, G.A. East, Biol. Trace Elem. Res. 60 (1997) 153.
[32] M. Tüzen, Food Chem. 80 (2003) 119.
[33] S. Mormede, I.M. Davies, Cont. Shelf Res. 21 (2001) 899.
[34] C. Locatelli, G. Torsi, Ann. Chim. (Rome, Italy) 91 (2001) 65.
[35] C. Locatelli, G. Torsi, Environ. Monit. Assess. 75 (2002) 281.
[36] L.D. Svintsova, A.A. Kaplin, Ind. Lab. 57 (1991) 788.
[37] H. Huang, P.K. Dasgupta, Anal. Chim. Acta 380 (1999) 27.
[38] C. Locatelli, G. Torsi, J. Electroanal. Chem. 509 (2001) 80.
[39] D. Melucci, C. Locatelli, Microchem. J. 2 (2007) 321.

Evaluation of selectivity for L-glutamide-derived highly ordered assemblies in reversed-phase high-performance liquid chromatography

M. Mizanur Rahman [a,b,*], Makoto Takafuji [a], Hirotaka Ihara [a,*]

[a] *Department of Applied Chemistry and Biochemistry, Faculty of Engineering, Kumamoto University, Kumamoto 860-8555, Japan*
[b] *Department of Applied Chemistry and Chemical Technology, Faculty of Engineering and Technology, University of Dhaka, Dhaka 1000, Bangladesh*

ABSTRACT

Two dioctadecyl L-glutamic acid derivatives with amide and ester type bondings have been synthesized and immobilized from 3-aminopropyltrimethoxysilane (APS) grafted silica (Sil-APS) to be used in reversed-phase high-performance liquid chromatography (RP-HPLC). Subsequent studies showed that dioctadecyl-L-glutamide derivative (GLN) can self-assemble into highly ordered structures by forming three-dimensional fibrillar aggregates as observed in scanning and transmission electron microscopes (SEM and TEM). Variable temperature ^{1}H NMR and FT-IR spectra of organogel revealed that the special aggregation morphology shown by GLN was stabilized by inter and or intra molecular hydrogen bonding among amide moieties. However, such ordered aggregated or self-assembled structures were not observed for the dioctadecyl-L-glutamate (GLU) derivative. The stationary phases Sil-GLN and Sil-GLU were characterized by DRIFT, elemental analysis, TGA, and ^{13}C and ^{29}Si CP-MAS NMR spectroscopic measurements. The chromatographic selectivity for both stationary phases was evaluated from the retention studies of different size and shape polycyclic aromatic hydrocarbons (PAHs). The chromatographic experiment for PAHs and geometrical isomers in RP-HPLC showed that Sil-GLN demonstrated extremely enhanced selectivity than Sil-GLU. The higher selectivity attributed by Sil-GLN has been brought by multiple π–π interactions among the π-electrons of the grafted organic phase and π-electrons of the guest PAHs molecules. Thermodynamic studies for linear and nonlinear PAHs revealed that the retention behavior does not change over a temperature range from 10 to 60 °C for both stationary phases.

© 2008 Elsevier B.V. All rights reserved.

1. Introduction

The majority of separations undertaken in reversed-phase liquid chromatography (RPLC) optimize hydrophobicity as the dominant separation factor. In general, hydrophobicity is the repulsive interactions between non-polar compounds and a polar environment, such as water. Closely related compounds such as polycyclic aromatic hydrocarbons (PAHs), which contain π-electrons, can be separated via dipole-induced dipole interactions, but do not undergo electrostatic interactions (i.e., ion–dipole or dipole–dipole) because of their lack of a permanent dipole moment. Unlike hydrophobicity, electrostatic, or even hydrogen-bonding interactions, π–π interactions are subtle interactions that occur between solutes and the stationary phase, and have been found to be very important with respect to selectivity in RPLC [1]. π–π interactions occur between compounds containing π-electrons and are

significant when the stationary phase is electron-rich and the analyte is electron-poor (donor–acceptor complexes) [2], or when both have extensive π-bonding.

Alkyl amide phase shows interesting chromatographic properties [3–6], since the separation occurred due to the participation of various interaction sites, e.g., residual, unreacted silanols and unreacted amine groups as well as hydrophobic chains of the grafted molecules. In addition, the affinity of these phases to solute molecules differs significantly from observations for conventional alkyl phases. Therefore, intermolecular interactions that determine elution of solutes of different character on alkylamide phases are interesting from both practical and theoretical points of view. Self-assembling systems are very attractive, as they yield supramolecular functions beyond those of unit segment molecules in a solution state. The most successful examples can be seen in bio-organic systems, such as lipid membranes, proteins, and nucleic acids. Lipid-bilayer membrane systems, having gel (solvated crystalline state) to liquid crystalline phase transition, are attractive models for realization of self-assembled systems for separation chemistry. Furthermore, we have reported the application of comb-shaped polymer, ODA$_n$ [7] also showed phase

---
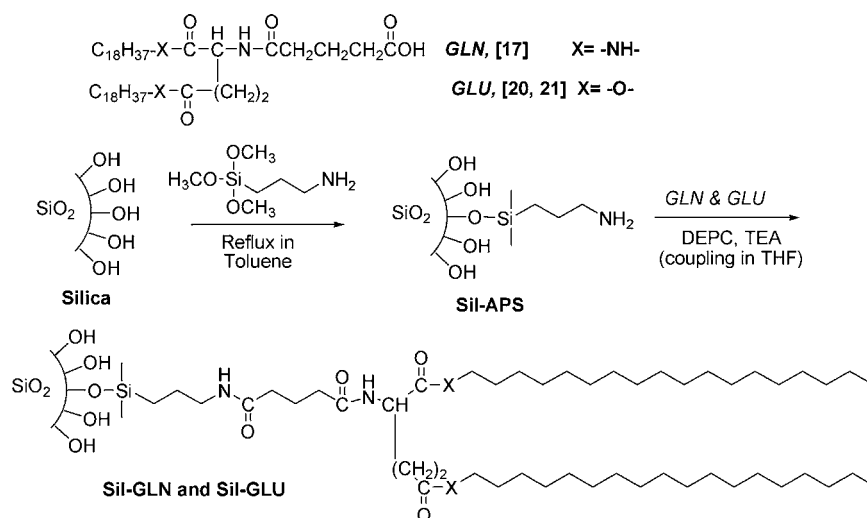
Fig. 1. Grafting process of L-glutamic acid derived stationary phases on silica.

transition and phase separation behavior and worked as a lipid membrane analogue organic phase on a silica surface. The molecular design for self-assembling compounds are based on the fact that dialkyl-L-glutamide-derived amphiphilic lipids form nano-tubes [8,9], -helices [8,9], and -fibers [10] based on bilayer structures in water and on the fact that intermolecular hydrogen bondings among the amide moieties contribute to self-assembly [11]. Similar self-organization has been realized by lipophilic derivatives of L-glutamide (didodecyl L-glutamide) even in organic solvents [12–15]. The uniqueness of these self-assemblies can be explained by ordered-to-disordered transition, phase separation behavior [16], and enhancement of chirality [13–16] and can be termed as lipid membrane analogues. These molecules have potential applications for various fields: catalysis, sensor technology, materials science and in separation science.

We have previously reported that dioctadecyl L-glutamide type lipid membrane analogue has been used as unique organic phase for HPLC that showed extremely enhanced selectivity for PAHs through multiple π–π interactions [17,18]. However, it is not established whether merely the presence of π-electrons played a key role for selectivity enhancement or the carbonyl groups in ordered assemblies was required. In this work we wish to illuminate the details of the contribution of carbonyl groups for amide bonded highly ordered assemblies in the separation behavior of PAHs and positional isomers Aiming to establish this phenomenon of π–π interactions from ordered assemblies and disordered assemblies we have introduced another L-glutamic acid derivative with dioctadecyl moieties in which the two amide linkages were replaced by ester linkages. Dioctadecyl L-glutamate with ester linkage cannot form highly ordered assemblies, however, it contains an equal number of carbonyl groups of dioctadecyl L-glutamide type. The selectivity results will be compared with two commercial monomeric and polymeric ODS (ODS-m, and ODS-p) columns and will be discussed in the following sections.

2. Experimental

2.1. Materials and methods

L-Glutamic acid (Wako, >99%), stearylamine (Wako), diethylphosphorocyanidate (DPEC) (Wako, peptide synthesis reagent) were purchased and used without further purification.

TEA (Wako, >99%) was distilled over KOH and stored under N2 atmosphere. YMC silica (YMC SIL-120-S5) having diameter 5 μm, pore size 12.0 nm, surface area 300 $m^2 g^{-1}$ (YMC-gel, Kyoto Japan) was used for grafting process. We have used two commercial ODS columns; monomeric (ODS-m) and polymeric ODS (ODS-p) for chromatographic analysis. ODS-m (Inertsil, ODS 3, column size—250 mm × 4.6 mm i.d. with particle size 5.5 μm, pore size 10 nm and surface area of silica particles are 450 $m^2 g^{-1}$ containing 13.8% C) was purchased from G. L. Science, Tokyo, Japan, and ODS-p column (Shodex, C18 P, particle size 5 μm, pore size 10 nm, surface area 300 $m^2 g^{-1}$ with end capped of the unreacted silanol group) containing 17.5% C was obtained from Shodex, Tokyo, Japan. Polyaromatic hydrocarbon (PAH) samples and six nucleosides were obtained either from Sigma or from Nacalai Tesque (Tokyo, Japan). HPLC-grade methanol was obtained from Wako (Japan). FT-IR measurements were conducted on a Jasco (Japan) FT-IR-4100 Plus instrument in KBr. For DRIFT-IR measurements, the accessory DR PRO410-M (Jasco, Japan) was used. Thermogravimetric
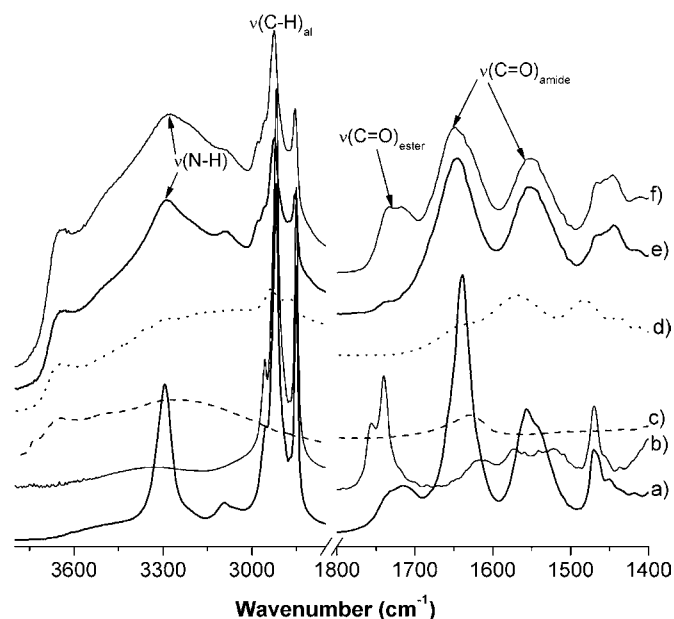
Fig. 2. DRIFT-IR spectrum; (a) GLN, (b) GLU, (c) bare silica, (d) Sil-APS, (e) Sil-GLN and (f) Sil-GLU.

(TGA) analysis was performed on a Seiko EXSTAR 6000 TG/DTA 6300 thermobalance in static air from 20 to 900 °C at a heating rate of 10 °C min^{-1}. To monitor synthesis processes, ^{1}H and ^{13}C NMR spectra used was recorded on a JEOL JNM-LA400 (Japan) instrument. Chemical shifts (δ) of ^{1}H and ^{13}C were expressed in parts per million (ppm) with use of the internal standard Me$_4$Si (δ = 0.00 ppm). Coupling constants (*J*) were reported in Hertz.

2.2. Solid-state nuclear magnetic resonance

^{13}C and ^{29}Si CP-MAS NMR spectra were carried out in a VAR-IAN UNITYINOVA AS400. For the ^{29}Si nucleus, a contact time of 5 ms and a pulse repetition time of 1.5 s were employed and for ^{13}C, the parameters used for measurement were spectral width 50,000 Hz, proton pulse width PW 90 = 11.6 µs, contact time for cross-polarization 5 ms and delay before acquisition was 2 s. High power proton de-coupling of 63 db with fine attenuation of dipole *r* = 2500 was used only during detection periods. Representative samples of 200–250 mg were spun at 4 kHz using 7 mm double bearing ZrO$_2$ rotors. Typically, 1.5 k free induction decays (FIDs) with an acquisition time of 35 ms were accumulated in 1 kilobyte (kb) data points and zero-filling to 8 kb prior to Fourier transformation. The line broadening used was 30 Hz and the spectral width for all spectra was about 25 kHz.

2.3. HPLC measurements

The chromatographic runs were performed in a system that consists of a Gulliver PU-980 intelligent HPLC pump with a Rheodyne sample injector having 20 µL loops. A Jasco multi-wave length UV detector MD 2010 plus was used. The column temperature was maintained by using a column jacket with a circulator having heating and cooling system. A personal computer connected to the detector with Jasco-Borwin (Ver.1.5) software was used for system control and data analysis. Water–1-octanol partition coefficient (log *P*) was determined by retention factor with octadecylsilylated silica, ODS (Inertsil ODS, i.d. 250 mm × 4.6 mm, GL Science): log *P* = 3.759 + 4.207 log *k* (*r* = 0.99997) [19].

2.4. Immobilization of GLN and GLU on silica surface

The synthesis and characterization of "Glutamide (GLN)" [17] and "Glutamate (GLU)" [20,21] (as shown in Fig. 1) have done according to the procedure reported elsewhere. The chemical structures in each step were identified by melting point determination, FT-IR, ^{1}H NMR, MALDI TOF-MS and elemental analysis measurements. Sil-APS was prepared by refluxing the suspension of 3-aminopropyltrimethoxysilane (APS) and silica in toluene for 24 h. ASP grafted silica was filtered and washed thoroughly with toluene, methanol and ether and dried in *vacuum*. It was characterized by DRIFT-IR, TGA and elemental analysis in order to confirm the grafting of APS on to porous silica surface. The coupling reactions between Sil-APS with GLN and GLU have carried out in a similar procedure. A typical procedure is as follows: 3 g of Sil-APS and 3 g of each compound (GLN or GLU) were suspended in 60 mL THF (anhydrous). TEA and DEPC were added into the mixture and the suspension was heated up to 55 °C for 24 h. After completion of the reaction, the mixture was filtered and washed with hot THF and CHCl$_3$, until all of the ungrafted compounds were removed and finally washed with methanol, ether and finally dried in *vacuum*. The dried materials were used as stationary phase materials Sil-GLN and Sil-GLU. The grafted particles were characterized and packed into stainless steel column for HPLC analysis.

3. Results and discussion

3.1. Synthesis and self-assembly of glutamide (GLN) and glutamate (GLU)

GLN containing three amide groups per molecule could dissolve in organic solvents at 0.5 mM in benzene, toluene and 1–3 mM concentrations in THF and chloroform upon heating to 60 °C, however, when the solution was cooled down to room temperature a distinct gelation was observed. This state is often referred as molecular gel because the gelation is brought about through the formation of three-dimensional network with self-assembled nano-fibrillar aggregates of low molecular weight compounds [22]. However, no such gelation or self-assembly was observed for GLU molecule even at concentrations as high as 50 mM. Our detailed investigation with dialkyl-L-glutamide-derived lipid, having long alkyl chain, showed that highly oriented structures with chiral arrangements below T_c can be obtained. Such molecular assembly had been brought about by complementary hydrogen bonds among the amide moieties [23,24]. SEM observation of GLN xerogel (after freeze-drying of benzene gels), as well as TEM images in benzene and in methanol, substantiated the hypothesis of the construction of three-dimensional fibrous network structures.

It is well known that hydrogen bonding is one of the driving forces for self-assembly of organogelators in organic solvents [10–16,22–24]. FT-IR of gel-state and variable temperature ^{1}H NMR spectroscopies is powerful tools to study hydrogen-bonding interactions. In general, the secondary amide groups (NH) engaged in the standard amide–amide hydrogen bonds (C=O···H–N) display stretching bands in the range 3370–3250 cm^{-1} [25]. The FT-IR spectrum of GLN in a benzene gel ([GLN] = 0.5 mM) showed d absorption bands at 3302 cm^{-1} as well as 1661 and 1634 cm^{-1}, arising from the intermolecular hydrogen-bonded amide moieties. Furthermore, variable temperature ^{1}H NMR measurements showed that as the temperature increased, the peaks for amide protons were consistently visible as representative of the associated amide function. Upon increasing the temperature, the intensity of the two bands increased and shifted up field which clearly indicated that the driving force for this aggregation was the formation of intra/intermolecular hydrogen bonding among the amide moieties similar to that reported in the literature [26].

3.2. DRIFT-IR analysis

Grafting of organic molecules on a silica surface can be monitored by DRIFT-IR measurement. Characteristic carbonyl absorption for ester bondings were clearly observed, as indicated by the intense broad peak of C=O bond stretching at 1740 cm^{-1} in spectrum (f) for Sil-GLU, however, no such absorption in this region was observed for Sil-GLN. A group of peaks at 2931 and 2859 cm^{-1}, respectively, were attributed to the C–H bond stretching of the long alkyl chain for both stationary phases in spectra (e) and (f). FT-IR and DRIFT spectra of (a) GLN, (b) GLU, (c) bare silica, (d) Sil-APS, (e) Sil-GLN, and (f) Sil-GLU are shown in Fig. 2. The spectrum (d) of Sil-GLN showed intense bands at 1634 and 1540 cm^{-1}, indicating the presence of grafted amide bonded lipids on the silica surface. Equally important is the appearance of N–H stretching (3293 cm^{-1}) in the spectrum for Sil-GLN, providing further evidence that GLN was successfully grafted on to the silica surface. However, N–H stretching at 3294 cm^{-1} and carbonyl absorption at 1635 cm^{-1} were also observed for Sil-GLU, but the intensities were lower due to the absence of amide bonding with the long alkyl moieties.
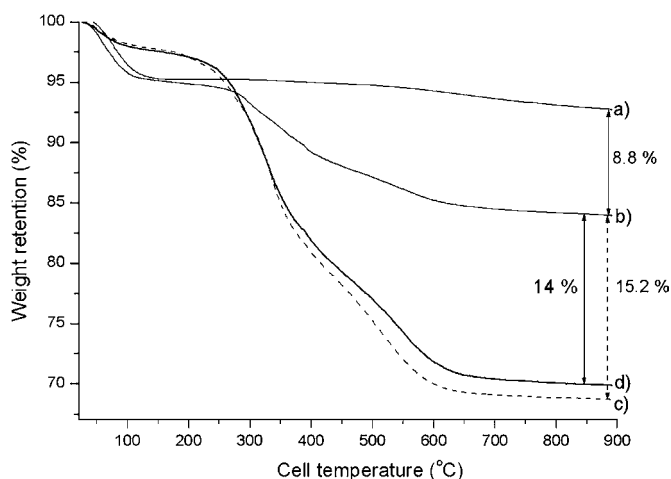
Fig. 3. TGA thermogram of the stationary phases; (a) bare silica, (b) Sil-APS, (c) Sil-GLN and (d) Sil-GLU.

3.3. Grafting density

Thermogravimetric analysis illustrates the distinct effect of silane functionality on bonded phase surface coverage to a greater extent than values from elemental analysis. The significant weight loss step from 300 to 900 °C correlates to the decomposition of the chemically bonded alkyl ligand on the silica surface. To evaluate the organic content of the APS, GLN, and GLU grafted silica, repeated TGA runs were conducted and almost identical curves were obtained. Each sample was kept under *vacuum* at 70 °C for 5 h to remove solvent traces, and then TGA measurements were run at a constant heating rate of 10 °C min^{-1} in air by using an empty Pt crucible as a reference. The heating process was continued to 900 °C, which has been demonstrated to be sufficiently high to degrade all surface bonded organosilanes [27]. Typical TGA curves for the bare silica, Sil-APS, Sil-GLN, and Sil-GLU are depicted in Fig. 3. The weight retention profile of silica and Sil-APS reached a plateau at about 110 °C (drying period), indicating the removal of surface water. After the thermal degradation of the initiator the weight of the sample was constant from 650 to 900 °C. A plateau in the weight retention curve of Sil-GLN and Sil-GLU was also observed as the temperature reached 650 °C, confirming that there is no organic content remaining on the silica at 900 °C. Using the TGA curve of silica as reference, the weight of the immobilized APS can be calculated as 8.8 wt.% of the total mass. Similarly, TGA revealed that 15.2 wt.% GLN and 14 wt.% GLU were grafted on the silica surface, using the weight retention of Sil-APS as a reference at 900 °C.

The grafted alkyl chain densities for alkyl stationary phases can also be determined from the %C obtained from elemental analysis data. The alkyl chain densities for Sil-GLN, Sil-GLU and ODS were determined according to the following modified equations, reported in our previous paper [28]. The results of elemental analysis, amount of grafting, and surface coverage are shown in Table 1. The molar amount of polymer per 1 g silica (M) can be calculated from carbon percentages of the organic phase-grafted silica particles

$$M\,(\mu\text{mol g}^{-1}) = \frac{10^6(P_\text{C}/100)}{12n} \tag{1}$$

where P_C is the percentage of carbon element according to elemental analysis and n is the number of carbon atoms present per molecule of grafted organic phase.

The weight percentage of grafted phase (P_W) can be calculated as:

$$P_\text{W} = m \times 10^{-4}M \tag{2}$$

Where m is the molecular mass of a grafted monomer unit.

In addition, surface coverage (N) can be calculated as:

$$N\,(\mu\text{mol m}^{-2}) = \frac{10^6 P_\text{C}}{12nS(100 - P_\text{W})} \tag{3}$$

Where S is surface area of bare silica (in the present case, $S = 300\,\text{m}^2\,\text{g}^{-1}$).

Alkyl chain densities (D) for double alkyl L-glutamic acid derived stationary phase can be calculated from the following equation

$$D\,(\mu\text{mol m}^{-2}) = Nf \tag{4}$$

Where the factor (f) indicate the number of alkyl chain present in the grafted molecule. For ODS, it is considered as 1, and for Sil-GLN and Sil-GLU it is 2. The grafting amount calculated from the elemental analysis data strongly corresponds to the results obtained by TGA measurements as indicated in Table 1.

3.4. Spectroscopic investigation (^{13}C and ^{29}Si CP-MAS NMR)

Solid-state ^{13}C CP-MAS NMR provides useful information of the chemical composition of modified surfaces, furthermore it reveals evidence about conformation and dynamics of immobilized alkyl groups. Fig. 4 shows ^{13}C and ^{29}Si CP MAS NMR spectrum of the Sil-GLN and Sil-GLU column materials. Looking at the spectra (a) and (b), the intense signal at 30.2 ppm representing the alkyl chains $-(CH_2)_n-$ where $n = 4$–15, was attributed to *gauche* conformation. This chemical shift arises from the average of the chemical shifts of the *trans* and *gauche* conformations of the alkyl chains [28,29], showing that the alkyl chains on the silica surface are quite mobile at room temperature. However, the intensity of the signal at 32.5 ppm due to the *trans* conformation is very low. While *trans* conformations indicate rigid, ordered chains; the *gauche* conformations characterize mobile, amorphous regions. Furthermore, it is established that the octadecyl moieties ODS-p generally exists in a highly ordered *trans*-conformational form ($\delta = 32.84$ ppm) although ODS-m this subsisted with mobile *gauche* conformational state [30,31].

^{29}Si CP-MAS NMR has the ability to ascertain the surface chemistry of silica bonded phases prepared by different bonding synthetic strategies. ^{29}Si CP-MAS NMR spectroscopy can also reveal the functionality of the silanes. The signals of trifunctional species (T^n) appear in the range of −49 to −66 ppm as shown in spectra c) and d). Obviously both phases possess high cross-linking according to the signals at −56 ppm (T^2) and at −67 ppm (T^3), while there is no signal for T^1 species visible in the spectrum. The intensity of signal at −56 ppm for T^2 is very low in both cases meaning these stationary phases contains trifunctional species with an extremely high degree of cross-linking. Since the loss of stationary phase from a chromatographic sorbent can take place due to hydrolysis of the T^1 groups binding the stationary phase to the support, the chromatographic performance in acidic and basic environments of a sorbent with large amounts of T^1 groups would be diminished. Therefore, the absence of T^1 groups on the grafted materials proves the successful grafting and furthermore implies the high stability of these phases. The species found on the silica surface are described as Q^n, where n is related to the number of Si–O–Si bonds. In ^{29}Si spectra of native bare silica, the Q^4 (tetrasiloxane), Q^3 (hydroxysiloxane), and Q^2 (dihydroxysiloxane) were detected at intense signal of −110, −101 and −92 ppm, respectively. However, in spectra of (c) and (d) dihydroxysiloxane (Q^2) or geminal silanol groups is almost undetectable indicating low degree of silanol activity for the grafted

Table 1
Comparison of physical properties of different column materials

	%C	%H	%N	C/N	Grafting (%) (elemental analysis)	Grafting (%) (TGA)	Alkyl chain density ($\mu mol\, m^{-2}$)	Dominant alkyl chain conformation	Type of carbonyl groups
Sil-APS	7.70	2.20	2.41	3.11	–	8.80	–	–	–
Sil-GLN	18.60	2.98	2.70	6.70	15.10	15.20	1.53	*gauche*	amide
Sil-GLU	17.45	2.74	2.40	7.10	13.8	14.0	1.40	*gauche*	ester
ODS-m	13.80	2.70	–	–		–	1.72	*gauche*	–
ODS-p	16.70	3.8	–	–		–	3.40	*trans*	–

materials. The reduced signal for Q^3 species in these two stationary phases as compared to native silica gave an insight about the lower amount of free OH-groups on the surface. These phases would demonstrate less silanophilic interactions in HPLC [32,33].

3.5. Retention mode and selectivity for alkylbenzenes

Conventional octadecylsilylated silica or ODS can detects the hydrophobicity of elutes; hydrophobicity is measured by the methylene activity of the elutes. It reflects the possibility of the phase to separate two molecules differing only in methylene group, e.g., amylbenzene and butylbenzene or ethylbenzene and toluene as reported by Kimata et al. [34]. The plots of log k and log P for alkylbenzenes and four linear PAHs already proved to be a good indicator for retention mode and the separation behavior of unknown stationary phases [17,22,27]. Fig. 5 represents the log k and log P plots of alkylbenzenes and PAHs for Sil-GLN, Sil-GLU and ODS-m in three different sections with similar vertical scale. The results show the retention of alkylbenzene increases with increasing methylene group activity following similar retention mode to that of conventional commercial ODS phases, i.e., hydrophobicity of elutes. Log k and log P plots of alkylbenzenes and PAHs for ODS-m are almost parallel and coincide with each other because of the fact that ODS-m only recognizes the hydrophobicity of elutes. Furthermore, there are no differences of selectivity between PAHs and alkylbenzenes with similar log P values. On the other hand, the log k versus log P plots for PAHs deviated significantly more in Sil-GLN and Sil-GLU than that of alkylbenzenes, and greater deviation was observed for the former case. For example, log P of naphthacene (5.71) is radically

lower than dodecylbenzene (8.45); however, log k value for naphthacene (0.83) is substantially higher than dodecylbenzene (0.73) on Sil-GLN column. Though log k for naphthacene (0.63) demonstrated lower value than dodecylbenzene (1.12) on Sil-GLU this still deviates from alkylbenzene with similar log P value. This extensive increase of retention for PAHs on Sil-GLN occurs due to the existence of carbonyl π and aromatic π interactions between the stationary phases and the guest molecules and thus enhanced the selectivity.

3.6. Selectivity for PAHs

Molecular shape can often provide a basis for the separation of compounds with constrained molecular structure; however, shape-selective columns are less effective for solutes with conformational freedom. Shape selectivity is exemplified by the capacity of a column to resolve isomers on the basis of molecular structure. PAH isomers typically elute in order of increasing length to breadth ratio (L/B), and nonplanar solutes elute before planar solutes with similar L/B. Contributions to shape recognition for ODS phases increases with (1) polymeric surface modification chemistry, (2) increasing bonding density, (3) increasing alkyl chain length, and (4) decreasing temperature. In general, these conditions promote increased alkyl chain order with increased *trans* conformations and reduced *gauche* defects [35]. An empirical model of solute retention for ODS, referred to as the "slot model", has been advanced to describe these differences [36]. In this model, the spaces between the alkyl chains are viewed as slots into which solute molecules penetrate. Solute shape and slot width (i.e., chain spacing) are important to this representation. Thus, planar molecules are able to fit between chains
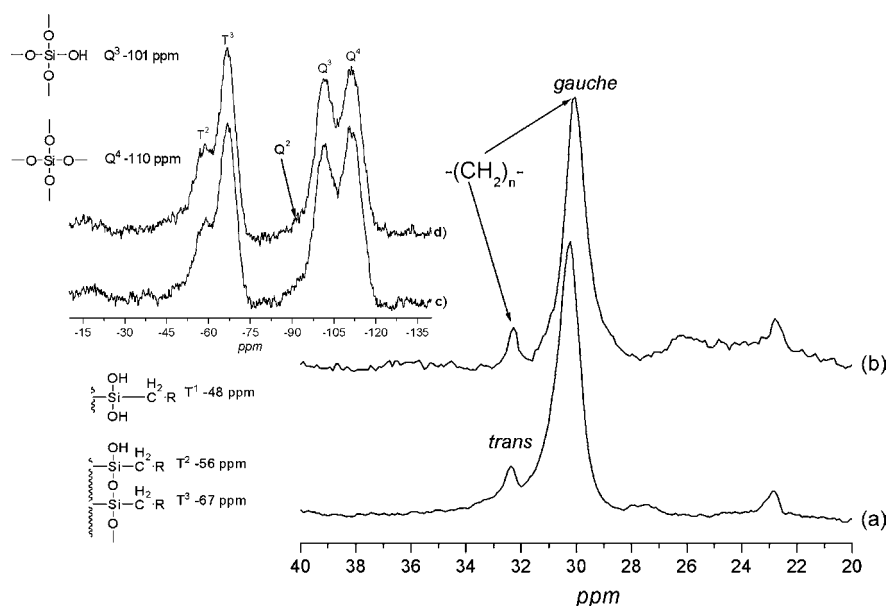
Fig. 4. ^{13}C CP-MAS NMR spectra for stationary phases (a) Sil-GLN, (b) Sil-GLU, (c) and (d) indicates ^{29}Si CP-MAS NMR for both stationary phases.
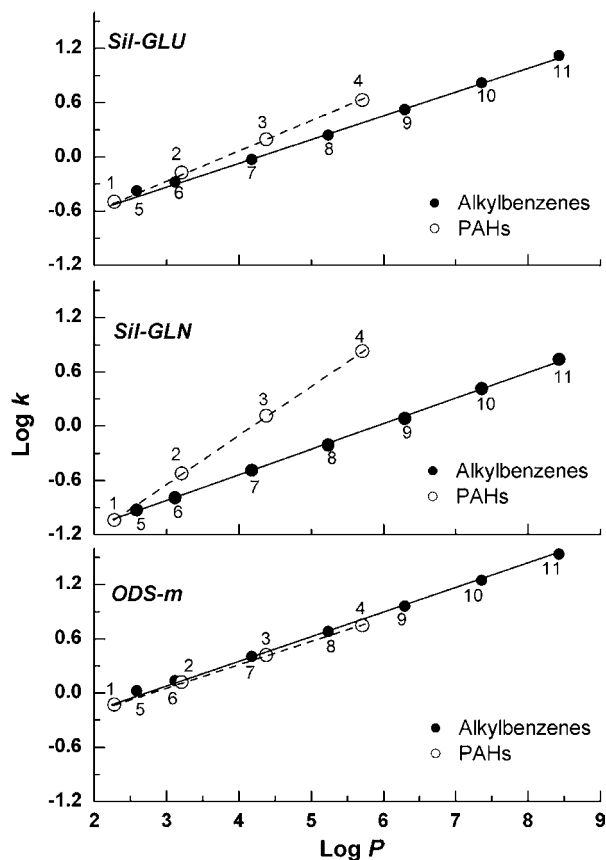
Fig. 5. Log P and log k plots for alkylbenzenes and PAHs (1—benzene, 2—naphthalene, 3—anthracene, 4—naphthacene, 5—toluene, 6—ethylbenzene, 7—butylbenzene, 8—hexylbenzene, 9—octylbenzene, 10—decylbenzene, and 11—dodecylbenzene); Chromatographic conditions; mobile phase: 90/10 for Sil-GLN and ODS-m and 80/20 for Sil-GLU, flow rate: 1.00 mL min^{-1}, column temperature: 30 °C.

more readily than nonplanar molecules, and planar molecules elute after nonplanar molecules even within isomer sets.

Molecular-planarity recognition with Sil-GLN and Sil-GLU were estimated by using triphenylene and o-terphenyl as elutes.
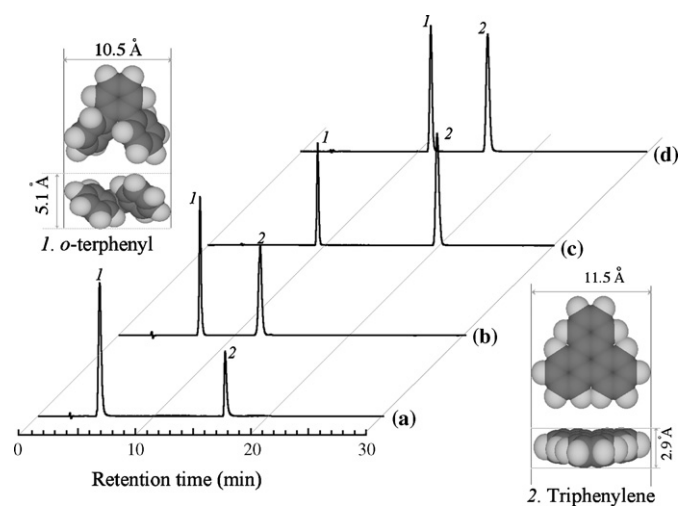
Fig. 6. Chromatogram of planarity selectivity for triphenylene and o-terpphenyl; (a) Sil-GLN, (b) Sil-GLU, (c) ODS-p and (d) ODS-m (chromatographic conditions; mobile phase: methanol/water = 90/10 for three columns, and 80/20 for Sil-GLU flow rate: 1.00 mL min^{-1}, column temperature: 30 °C).
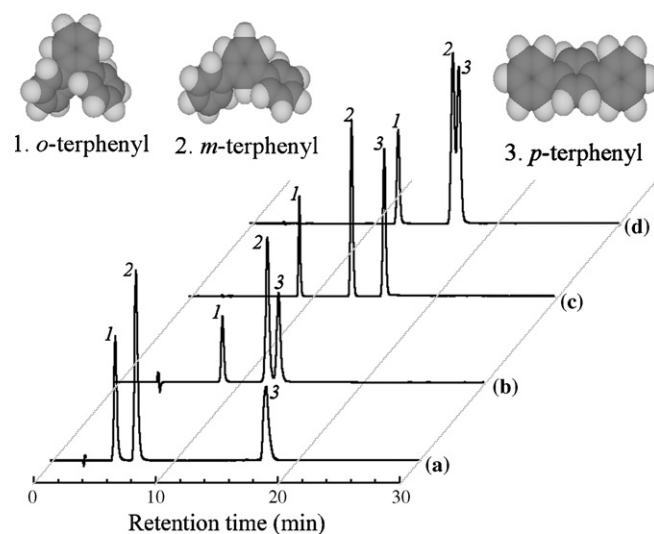
Fig. 7. Chromatogram for terphenyl isomers; (a) Sil-GLN, (b) Sil-GLU, (c) ODS-p and (d) ODS-m (chromatographic conditions same as Fig. 6).

These two compounds possess the same number of carbon atoms and π-electrons however their molecular-planarity is completely different. Therefore, the separation factor between them should be a good marker to evaluate molecular-planarity selectivity as suggested by Jinno et al. [37]. The chromatogram for triphenylene and o-terphenyl for all columns are given in Fig. 6. The results showed that Sil-GLN ($\alpha_{\text{triphenylene}/o\text{-terphenyl}} = 5.33$) demonstrated 242% higher shape selectivity than Sil-GLU ($\alpha_{\text{triphenylene}/o\text{-terphenyl}} = 2.20$). The detailed retention results for PAHs and aromatic positional isomers on different columns studied in this work are given in Table 2 along with the retention data of reference column (ODS-m and ODS-p). Further evidence of shape selectivity can also be assessed by another sample set, such as coronene/hexahelicene, trans-stilbene/cis-stilbene, etc. In every case Sil-GLN revealed enhanced selectivity. In addition, molecular length selectivity for planar PAHs on Sil-GLN and Sil-GLU can also be examined by structural isomers of four and five rings possessing same carbon numbers and π-electrons, and more importantly, all these are planar compounds. For instance, Sil-GLN gave a selectivity ($\alpha_{\text{naphthacene/triphenylene}} = 3.59$) however Sil-GLU showed ($\alpha_{\text{naphthacene/triphenylene}} = 1.30$), indicating that enriched molecular slenderness recognition can be obtained by Sil-GLN as well. Similar behavior was also noted for anthracene/phenanthrane, benz[a]pyrene/benzo[e]pyrene, dibenzo[a,h]anthracene/dinbenzo[a,c]anthracene. Furthermore, since the selectivity values are unchanged after the addition 0.01% trifluoroacetic acid to the mobile phase on both Sil-GLN and Sil-GLU the effect of unfunctionalized amine groups can be neglected.

Table 1 shows that Sil-GLN has lower surface coverage or chain density than ODS-p, hence molecular recognizibility yielded by this stationary phase (as given in Table 2) cannot explained by the common phenomena alone, as shape selectivity is high with higher bonding density and longer alkyl phase chain length [38,39]. In this connection it is noteworthy to mention that extremely enhanced molecular recognition could be achieved by self-assembled lipid membrane anlagoue grafted silica (Sil-ODA$_n$) in RP-HPLC through multiple carbonyl–π interactions. The alkyl moieties of Sil-ODA$_n$ form highly oriented structures in the crystalline state which aligned the carbonyl groups in highly ordered state thus the aligned carbonyl groups boosted molecular-shape selectivity for PAHs through multiple π–π interactions [7,40–42].

Table 2
Selectivity data of isomeric PAHs and aromatic positional isomers on different columns

PAHs	Sil-GLN		Sil-GLU		ODS-m		ODS-p	
	k	α	k	α	k	α	k	α
Linear PAHs								
Benzene	0.11		0.31		0.77		0.55	
		2.36		2.16		1.80		2.0
Naphthalene	0.26		0.67		1.39		1.10	
		3.89		2.34		2.02		2.43
Anthracene	1.01		1.56		2.81		2.67	
		9.10		2.73		2.23		3.02
Naphthacene	9.20		4.27		6.28		8.06	
Nonlinear PAHs								
Phenanthrane	0.78		1.42		2.6		2.42	
		1.92		1.68		1.57		1.70
Pyrene	1.50		2.39		4.09		4.12	
		1.70		1.36		1.22		1.28
Triphenylene	2.56		3.27		5.0		5.28	
4-Rings isomers								
Benz-*a*-anthracene	3.4		3.58		5.35		6.0	
		1.22		1.03		1.07		1.03
Chrysene	4.15		3.68		5.38		6.2	
5-Rings isomers (a)								
Benz-*e*-pyrene	1.29		5.58		0.69		1.24	
		1.26		1.01		1.04		1.24
Benz-*a*-pyrene	1.63		5.64		0.72		1.54	
		0.94		1.03		0.97		0.86
Perylene	1.54		5.8		0.70		1.32	
5-Rings isomers (b)								
Dibenz[*a,c*]anthracene	1.75		8.87		0.69		1.31	
		1.78		1.09		1.03		1.12
Dibenz[*a,h*]anthracene	3.13		9.65		0.71		1.46	
6-Rings isomers								
Hexahelicene	0.38		5.41		1.1		0.87	
		15.0		3.30		0.90		4.6
Coronene	5.7		17.83		1.0		3.97	
Positional isomers								
o-Terphenyl	0.48		1.48		2.1		2.20	
		1.77		1.72		1.12		1.68
m-Terphenyl	0.85		2.54		2.35		3.70	
		3.83		1.10		1.0		1.22
p-Terphenyl	3.26		2.80		2.35		4.51	
cis-Stilbene	2.56		1.08		2.06		1.72	
		2.51		1.35		1.08		1.27
trans-Stilbene	6.44		1.46		2.22		2.18	

Chromatographic conditions: Mobile phase, methanol/water = 90/10 and for 5 rings ethanol (100%) and methanol/water = 80/20 for Sil-GLU in all cases, column temperature = 25 °C, flow rate = 1.00 mL min^{-1}.

It is apparent that the octadecyl moieties in both Sil-GLN and Sil-GLU were of disordered, non-crystalline and mobile gauche conformational form. The unusually enhanced selectivity cannot be explained by the phenomena as mentioned in the literature for Sil-ODA$_n$. However, we can assume that the hydrogen bonding among amide moieties in Sil-GLN would play a pivotal role to orient carbonyl groups in highly oriented state suitable for interacting with π-electron containing solutes (e.g., PAHs). Although the octadecyl chains remained as disordered *gauche* conformational form, it played a significant role in the assembly of GLN promoting association in the self-assembly by van deer Walls forces. Moreover, these octadecyl moieties also produce *trans–gauche* conformation that can play significant role in self-assembling of GLN. This phenomenon was supported by studying short alkyl chain (C4-chain) with the glutamide moieties. The short chain glutamide moieties with similar molecular structure do not show self-assembly and no gelation in organic solvent was detected. This experimental observation is good evidence confirming the necessity of octade-

cyl moieties in the self-assembling process of GLN and in HPLC separation as well. As indicated inter/intra molecular hydrogen bonding stabilizes the self-assembling behavior of GLN in organic solvents. Both SEM and TEM images showed that GLN formed three-dimensional fibrous network in benzene and in methanol, but dioctadecyl-L-glutamate (GLU), in which two amide linkage were replaced by esteric linkage cannot aggregate in organic solvents and no such self-assembly was observed. Due to the absence of highly orientated microenvironment carbonyl groups of the stationary phase derived from GLU (Sil-GLU), less favored multiple carbonyls π–aromatic π interactions thus retard shape selectivity. This investigation determined that not only the presence of carbonyl groups can enhance the selectivity, but also the presence of ordered carbonyl groups is rather important in RP-HPLC separation for PAHs isomers.

A further test mixture evaluating the contributions of π–π interactions can be examined by using nitro substituted benzene sample sets. These compounds have very similar size and

Fig. 8. van't Hoff plots [ln k versus $1/T$ ($1/K$)] for linear PAHs on Sil-GLN and Sil-GLU phases.

of the partners can act as an electron-donor while the other one plays the role of an electron-acceptor.

3.7. Selectivity for positional isomers

As discussed in the previous section, *o*-terphenyl is a nonplanar polyaromatic compound that is successfully employed as an indicator for the planarity recognition test of a stationary phase with triphenylene. Due to the bulkiness of the two aryl-groups attached to the benzene ring and the rotational freedom of the attaching C–C bond, the three terphenyl-isomers differ strongly in the extent of their off-planarity. The close proximity of the two π-electron clouds of the aryl-groups in the *ortho*-position provides a strong sterical hindrance that is amplified by the repulsion of the two aromatic π-electron clouds. Therefore, the *o*-terphenyl isomer posses the highest deviation from planarity, followed by *m*-terphenyl and *p*-terphenyl [46]. The increased retentivity and selectivity for the *para/ortho* and the *para/meta* isomers resulted from Sil-GLN usage (as shown in Fig. 7). In a previous report on Sil-ODA$_n$ the authors pointed out that the selectivity for aromatic positional isomers was enhanced by the ordered carbonyl–π interactions, and this is more articulated for *trans* and *para*-isomers. The detailed investigation regarding the retention behavior of geometrical isomers showed that multiple π–π interactions for the ordered carbonyls groups of Sil-ODA$_n$ in the crystalline region was advantageous for recognition of isomers, and exhibited effectiveness for planar to planar and rigid to rigid structures [40,41]. In the present investigation the authors believes that the ordered carbonyl groups attributed by hydrogen bonded amide carbonyls groups in Sil-GLN demonstrated significantly higher carbonyl π–benzene π interactions that enhance retentivity for long, planar *p*- and *trans*-isomers more than corresponding *o*-, *m*- and *cis*-isomers.

shape but different π-electron densities. The selectivity between benzene- and nitro substituted benzene can be used as a measure of the contribution of retention from π interactions in the reversed-phase system [43]. In conventional RP-HPLC with C_8 or C_{18} stationary phases, the higher nitrated compounds are eluted first [44]. However, the elution of nitro substituted benzenes followed elution of benzenes. For instance, $\alpha_{nitrobenzene/benzene}$ = 1.16 and $\alpha_{o\text{-dinitrobenzene/benzene}}$ = 1.27 are obtained for Sil-GLN phase, on the other hand Sil-GLU yields 1.02 and 1.05. This observed behavior is an effect of specific interactions between the π-electron systems of the solutes on the one hand and the stationary phase on the other hand. The solutes are substituted with electron-drawing nitro-groups. Therefore, their aromatic ring systems possess a low π-electron density. In contrast, the ligands are substituted by weak electron-pushing carbonyl groups increasing the π-electron density in the phenyl rings. Thus, the bonded ligand can act as an electron donor, while the nitrated solutes act as electron acceptors. These functionalities result in specific π–π interactions which can lead to the formation of donor–acceptor complexes. The stability of these complexes depends on the electron density of both the solutes and the stationary phase [45]. Since the electron density of the solutes decreases with increasing numbers of nitro groups, the π–π interaction is strongest for the trinitro-substituted compounds and these solutes exhibit the longest retention times. The interaction is stronger if the π-system of one partner is electron-rich while that of the second partner is electron-poor, due to pushing or pulling groups present in the respective systems. In this case, one
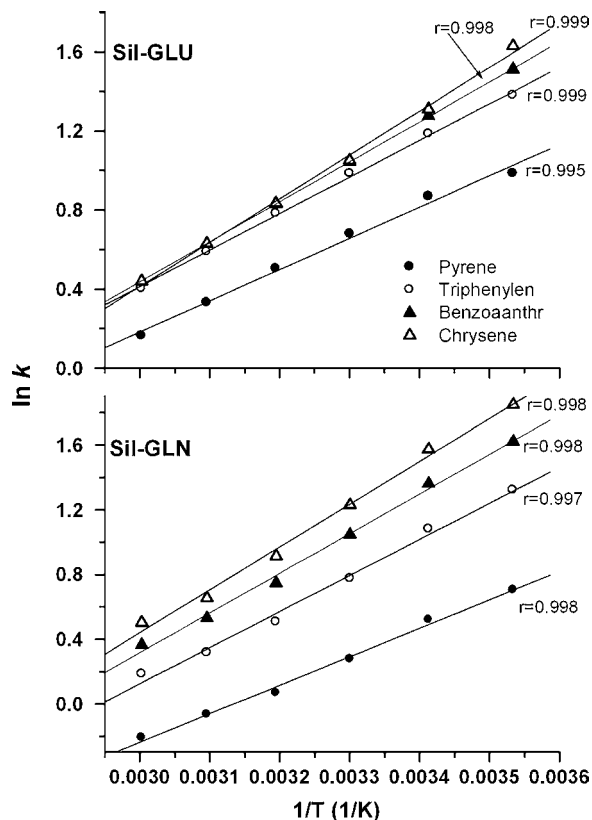

Fig. 9. van't Hoff plots [ln k versus $1/T$ ($1/K$)] for nonlinear PAHs on Sil-GLN and Sil-GLU phases.
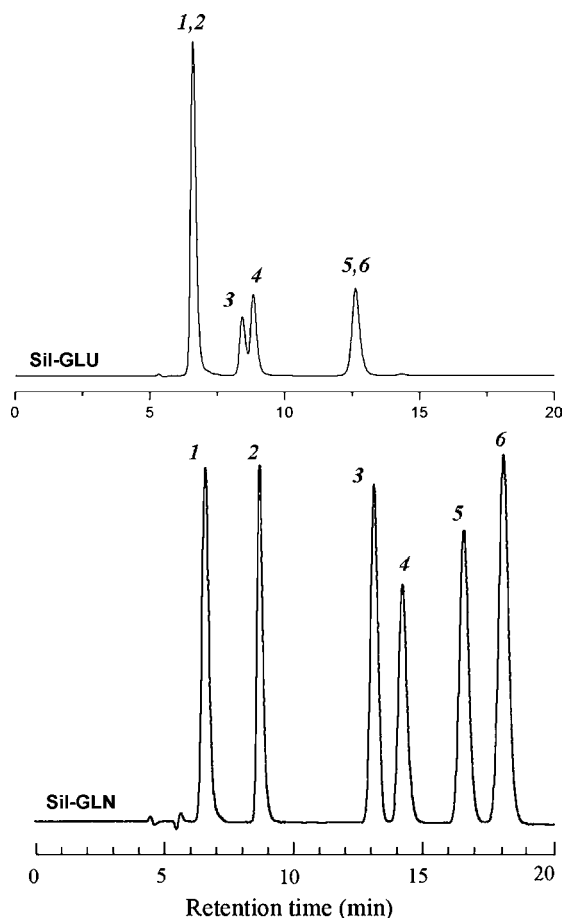
Fig. 10. Chromatogram of nucleosides (a) Sil-GLN and (b) Sil-GLU. 1—Cytidine, 2—uridine, 3—thymidine, 4—guanosine, 5—xanthosine, 6—adenosine (mobile phase: 0.2 M KH_2PO_4 buffer: methanol = 80/20, pH 4.8, flow rate: 0.5 mL min^{-1}, column temperature: 20 °C).

3.8. Thermodynamic behavior

The thermodynamic behavior of solutes can yield useful information regarding the retention behavior and retention mechanisms that take place in RP-HPLC. A basic understanding of retention behavior can be gauged by enthalpy–entropy compensation (EEC) [47,48]. In liquid chromatography, EEC relationships are used to determine the relationship between changes in the molar enthalpy and molar entropy associated with solute binding. The retention of a solute (k) is related to enthalpy and entropy changes of a system through Eq. (5).

$$\ln k = -\frac{\Delta H_x^\circ}{RT} + \frac{\Delta S_x^\circ}{RT} + \ln \phi \qquad (5)$$

Where k is the measured retention value, ΔH° the enthalpy, ΔS° the entropy, T the absolute temperature, R the gas constant and ϕ the phase ratio of the column materials. Enthalpy (ΔH°) represents the measure of energy exchange in a system and entropy (ΔS°) represents the chaos of a system. van't Hoff plots are obtained by regressing $\ln k$ versus $1/T$. Such plots are linear if ΔH° and ΔS° are independent of the temperature. The slope of the van't Hoff plot indicates the standard enthalpies of transfer. The standard entropies of transfer of the analyte from the (HPLC) experiments were performed using a mobile to the stationary phase are calculated from the intercept. Nonlinear van't Hoff plots are indicative for a change of retention mechanism: e.g., ΔH° is not constant over the whole temperature range studied [49]. van't Hoff plots

for linear and nonlinear PAHs on Sil-GLN and Sil-GLU are shown in Figs. 8 and 9. Linear van't Hoff plots for both columns results an indication that no phase transitions of the grafted organic phases occurred and the retention mechanisms of PAHs do not change over the temperature range studied.

3.9. Retention of nucleosides

It is known that any substituent on nucleosides that exists as lactam (keto) tautomeric form decreases the retention than that exists as lactim (enol) form [50]. The lactim (enol) form of nucleic acid constituents is favorable for π–π interaction with aligned carbonyl groups in Sil-GLN; thus retention is increased. It is known that nucleosides have the characteristics of typical hydrogen bonding compounds, and as a result these compounds may form a higher degree of hydrogen bonding with the stationary phase. The chromatograms for nucleosides on both phases are depicted in Fig. 10. The figure showed that using a mobile phase composition of 20% methanol with 80% KH_2PO_4 buffer at pH 4.8, complete separation of all six compounds can be possible by Sil-GLN column; however there are only four peaks were observed for Sil-GLU demonstrated its less effectiveness for analysis of nucleosides.

4. Conclusion

In this work, the role of carbonyl groups in highly ordered self-assemblies attributed by hydrogen bonded amide moieties for HPLC separation has been discussed. Significantly higher molecular recognition can be obtained by amide type stationary phase than that of ester type having an equal number of carbonyl groups. Furthermore, the chromatographic results for various size and shape PAHs demonstrated that the presence of carbonyl groups cannot enhance HPLC selectivity for PAHs; however, carbonyl groups in ordered assemblies have substantial effect that can enhance the selectivity for π-electron containing solutes (e.g., PAHs) through multiple π–π interactions.

References

[1] N. Tanaka, Y. Tokuda, K. Iwaguchi, M. Araki, J. Chromatogr. 239 (1982) 761.
[2] JL.E. Reubsaet, R. Vieskar, J. Chromatogr. A 841 (1999) 147.
[3] B. Buszewski, R.M. Gandzala-Kopciuch, M. Markuszewski, R. Kaliszan, Anal. Chem. 69 (1997) 3277.
[4] B. Buszewski, J. Schmind, K. Albert, E. Bayer, J. Chromatogr. 552 (1991) 415.
[5] B. Buszewaski, R.K. Gilpin, M. Jaroniec, J. Chromatogr. 673 (1994) 11.
[6] P. Katasuri, B. Buszewaski, M. Jaroniec, K. Gilpin, J. Chromatogr. 659 (1994) 261.
[7] T. Fukumoto, H. Ihara, S. Sakaki, H. Shosenji, C. Hirayama, J. Chromatogr. 672 (1994) 237.
[8] K. Yamada, H. Ihara, T. Ide, T. Fukumoto, C. Hirayama, Chem. Lett. (1984) 4821.
[9] H. Hachisako, H. Ihara, C. Hirayama, K. Yamada, Liq. Cryst. 13 (1993) 307.
[10] H. Ihara, M. Takafuji, C. Hirayama, D.F. O'Brien, Langmuir 8 (1992) 1548.
[11] H. Ihara, M. Takafuji, C. Hirayama, D.F. O'Brien, Langmuir 8 (1992) 1548.
[12] H. Ihara, M. Takafuji, T. Sakurai, in: H.S. Nawla (Ed.), Encyclopedia of Nanoscience and Nanotechnology, 9, American Science Publishers, USA, 2004, p. 473.
[13] H. Ihara, M. Yoshitake, M. Takafuji, T. Yamada, T. Sagawa, C. Hirayama, H. Hachisako, Liq. Cryst. 26 (1999) 1021.
[14] H. Ihara, T. Sakurai, T. Yamada, T. Hashimoto, M. Takafuji, T. Sagawa, H. Hachisako, Langmuir 18 (2002) 7120.
[15] H. Ihara, M. Takafuji, T. Sakurai, M. Katsumoto, N. Ushijima, T. Shirosaki, H. Hachisako, Org. Biomol. Chem. 1 (2003) 3004.

[16] H. Ihara, H. Hachisako, C. Hirayama, K. Yamada, J. Chem. Soc., Chem. Commun. 17 (1992) 1244.
[17] M.M. Rahman, M. Takafuji, H.R. Ansarian, H. Ihara, Anal. Chem. 77 (2005) 6671.
[18] M. Takafuji, M.M. Rahman, H.R. Ansarian, M. Derakshan, T. Sakurai, H. Ihara, J. Chromatogr. A 1074 (2005) 223.
[19] H. Ihara, T. Sagawa, Y. Goto, S. Nagaoka, Polymer 40 (1999) 2555.
[20] H. Ihara, H. Hachisako, C. Hirayama, K. Yamada, Jpn. J. Polym. Sci. Technol. 52 (1994) 606.
[21] H. Hachisako, Y. Yamazaki, H. Ihara, C. Hirayama, K. Yamada, Liq. Cryst. 15 (1993) 723.
[22] M.M. Rahman, M. Czaun, M. Takafuji, H. Ihara, Chem. Eur. J. 14 (2008) 1312.
[23] H. Ihara, K. Shudo, C. Hirayama, H. Hachisako, K. Yamada, Liq. Cryst. 20 (1996) 807.
[24] H. Hachisako, H. Ihara, T. Kamiya, C. Hirayama, K. Yamada, Chem. Commun. (1997) 19.
[25] G.P. Dado, S.H. Gelman, J. Am. Chem. Soc. 115 (1993) 4228.
[26] S. Kiyonaka, S. Shinkai, I. Hamachi, Chem. Eur. J. 9 (2003) 976.
[27] M.M. Rahman, M. Takafuji, H. Ihara, J. Chromatogr. A 1203 (2008) 59.
[28] H.R. Ansarian, M. Derakhsan, M.M. Rahman, T. Sakurai, M. Takafuji, I. Taniguchi, H. Ihara, Anal. Chim. Acta 547 (2005) 179.
[29] M. Pursch, S. Strohschein, H. Haendel, K. Albert, Anal. Chem. 68 (1996) 386.
[30] J. Clauss, K. Schmidt-Rohr, A. Adam, C. Boeffel, H. Spiess, Macromolecules 25 (1992) 5208.
[31] S. Pawsey, K. Yach, J. Halla, L. Reven, Langmuir 16 (2000) 3294.
[32] K. Albert, E. Bayer, J. Chromatogr. 544 (1991) 345.
[33] D.W. Sindorf, G.E. Maciel, J. Am. Chem. Soc. 105 (1983) 1487.
[34] K. Kimata, K. Iwaguchi, S. Onishi, K. Jinno, R. Eksteen, K. Hosoya, M. Araki, N. Tanaka, J. Chromatogr. Sci. 27 (1989) 721.
[35] L.C. Sander, M. Pursch, S.A. Wise, Anal. Chem. 71 (1999) 4821.
[36] S.A. Wise, L.C. Sander, J. High Resolut. Chromatogr. Chromatogr. Commun. 8 (1985) 248.
[37] K. Jinno, C. Okumura, M. Taniguchi, Y.L. Chen, Chromatographia 44 (1997) 613.
[38] L.C. Sander, R.M. Parris, S.A. Wise, Anal. Chem. 63 (1991) 2589.
[39] K.B. Sentell, J.G. Dorsey, Anal. Chem. 61 (1989) 930.
[40] M.A.J. Chowdhury, R.I. Boysen, H. Ihara, M.T.W. Hearn, J. Phys. Chem. B 106 (2002) 11936.
[41] Y. Goto, K. Nakashima, K. Mitsuishi, M. Takafuji, S. Sakaki, H. Ihara, Chromatographia 56 (2002) 19.
[42] H. Ihara, T. Sagawa, K. Nakashima, K. Mitsuishi, Y. Goto, M.A.J. Chowdhury, S. Sakaki, Chem. Lett. 29 (2000) 128.
[43] C.S. Sychov, M.M. Ilyin, V.A. Davankov, K.O. Sochilina, J. Chromatogr. A 1030 (2004) 17.
[44] E.S.P. Bouvier, S.A. Oehrle, LC–GC Int. 8 (1995) 338.
[45] H. Hemetsberger, in K.K. Unger (Ed.), Chromatogr. Sci., vol. 47 (Pack. Stationary Phases Chromatogr. Tech.), Marcel Dekker, New York, Basel, 1990, p. 511.
[46] J. Horak, W. Lindner, J. Chromatogr. A 1043 (2004) 177.
[47] M. Takafuji, W. Dong, Y. Goto, T. Sakurai, S. Nagaoka, H. Ihara, Polym. J. 34 (2002) 437.
[48] S. Kayillo, G.R. Dennis, R.A. Shalliker, J. Chromatogr. A 1126 (2006) 283.
[49] W. Melander, D.E. Campbell, C. Horv'ath, J. Chromatogr. 158 (1978) 215.
[50] P.R. Brown, E. Grushka, Anal. Chem. 52 (1980) 1210.

An optical redox chemical sensor for determination of iodide

Saadat Rastegarzadeh*, Nahid Pourreza, Iman Saeedi

Department of Chemistry, College of Science, Shahid Chamran University, Ahvaz, Iran

ARTICLE INFO

ABSTRACT

A novel optical sensor based on a redox reaction for the determination of iodide has been developed. The optode membrane is constructed by immobilization of methyltrioctylammonium chloride on triacetylcellulose polymer. The exchange of chloride as counter ion with iodate in the membrane changes the color to yellow, when it is placed in acidic solution of iodide. The sensor can readily be regenerated by $0.1 \, mol \, L^{-1}$ NaOH in less than 15 s. The optode has a linear range of 3.94×10^{-6} to $5.51 \times 10^{-5} \, mol \, L^{-1}$ of iodide ions with a limit of detection $7.44 \times 10^{-7} \, mol \, L^{-1}$. The relative standard deviation for eight replicate measurements of 3.94×10^{-6} and $1.57 \times 10^{-5} \, mol \, L^{-1}$ of iodide was 2.83 and 1.38%, respectively. The sensor was successfully applied to the determination of iodide in tablet, powdered milk and urine samples.

© 2008 Elsevier B.V. All rights reserved.

1. Introduction

In recent years, the optical chemical sensors (optodes or optrodes) have become a rapidly expanding area of analytical chemistry. These sensors have opened up a new perspective in the search for simple, safe, rapid and remote systems for monitoring some important substances. Recent development in this field have also been driven by such factors as the availability of low-cost, miniature optoelectronic light source and detectors, the need for multianalyte array-based sensors particularly in the area of biosensing, advances in microfluidics and imaging technology. Optical chemical sensors employ optical transduction techniques to yield analyte information. The most widely used techniques applied in optical chemical sensors are optical absorption and luminescence, but sensors based on other spectroscopies as well as on optical parameters, such as refractive index and reflectivity have also been developed [1].

In most optical sensors, a reagent is immobilized in a solid matrix usually in the form of a monolith or a thin film. The reagents immobilized into the sensor are responsible for the extraction of the analyte into the sensing material and generating an optical signal proportional to the change in the concentration of the analyte [2]. Many of the existing optodes utilize color complexion reactions between immobilized ligands and analyte [3,4].

The utilization of color redox reactions has largely been ignored despite the fact that numerous substances of analytical interest are electroactive.

Optodes for a variety of analytes such as cations, anions and gaseous species have been reported [5–8]. In comparison with cation optodes, which are predominant, anion optodes are few in number.

Iodine is an essential micronutrient in human growth and metabolism [9]. Inadequate iodine during prenatal and early development periods, can lead to several diseases, including spontaneous abortion, increased infant mortality, hypothyrodism and cretinism [10]. World Health Organization (WHO) estimates that iodine deficiency disorders are a significant public health problem in many countries. Iodine plays as important role in influencing the proper function of thyroid gland, which is an essential part of thyroid hormones triiodothyronine (T3) and thyroxin (T4). [11]. Too low or excess ingestion of iodine may lead to hypertrophy or hypothyroidism and hyperthyroidism [12]. Therefore, there has been an increase in the analytical control of iodine in food, pharmaceutical products and biological samples such as urine. Iodine contents in urine have been widely used as a marker for status assessment of iodine deficiency disorder [13].

In order to determine low concentration levels of iodine and/or iodide, many methods based on different principles have been proposed. These include gas chromatography with mass spectrometry detection [14], electrostatic ion chromatography [15], capillary electrophoresis [16], chemiluminescence [17], pulse stripping analysis [18], inductively coupled plasma-mass spectrometry [19], indirect atomic absorption spectrometry [20].

* Corresponding author. Fax: +98 611 3331042.
E-mail addresses: rastegarz@yahoo.com, rastegarz@scu.ac.ir (S. Rastegarzadeh).
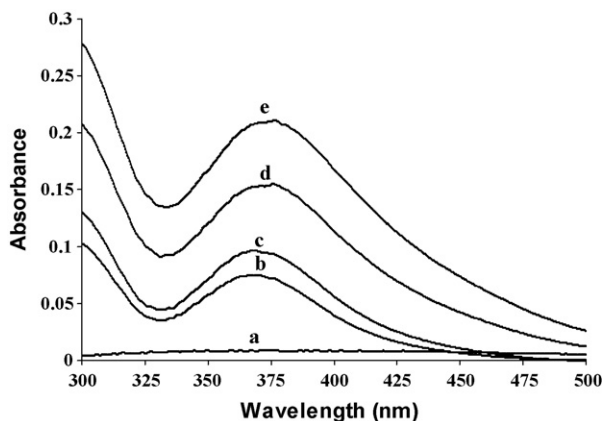
These approaches, although sensitive, suffer from the need for expensive instrumentation. Therefore the development of analytical techniques that do not need expensive or complicated equipment for the determination of iodide becomes increasingly important. As it is known the optodes have gained considerably in practical reliability, and can be considered as inexpensive alternative to certain conventional analytical methods.

Several optical sensors have been reported for determination of iodide using different reagents. Urbano et al. described optical sensor for halides and pseudohalides using acridinium quinolinium indicators, which were immobilized onto a glass surface [21]. The sensors are able to indicate the concentration of halides in solution by virtue of the decrease in fluorescence intensity due to the quenching process. Liu et al. proposed a flow-through optosensor for determination of iodide based on a chelate room-temperature phosphorescence (RTP). The sensing phase in this sensor was prepared by immobilization of chelate of aluminum with quinolin-8-ol-5-sulphonic acid on an anion exchange resin [22]. In another research, a series of thin film optical sensors based on halide-sensitive fluorophored have been developed and characterized by Geddes et al. [23]. The sensor films use rhodamine, 6-methoxyquinoline, and harman dyes which have been functionalized and bound to a hydrophilic copolymer. Geddes also presented optical thin film polymeric sensors for determination of iodide based on two acridinium fluorophores that have been synthesized and immobilized in a hydrophilic copolymer [24]. Thin films of the copolymers swell in aqueous media allowing dye fluorescence to be dynamically quenched by the diffusion of halide ions.

In this paper, we describe a novel approach to optical chemical sensing which makes use of the redox properties for determination of iodide. This optode is prepared by immobilizing methyltrioctylammonium chloride on triacetylcellulose membrane according to a simple method.

2. Experimental

2.1. Apparatus

A GBC UV–vis spectrophotometer model Cintra 101 was used for recording the spectra, and the absorbance measurements were made using a PerkinElmer UV–vis spectrophotometer model 550S. The sensing membrane was placed in a glass cell and all measurements were performed in a batch mode.

Measurement of pH was performed using a Metrohm 632 pH-meter with a combined glass electrode.

2.2. Reagents and solutions

All reagents used were of analytical grade and double distilled water was used throughout.

A 7.87×10^{-3} mol L^{-1} of iodide stock solution was prepared by dissolving 0.1307 g of potassium iodide (Merck) in water and diluting to 100 mL in a volumetric flask. Standard solutions were prepared by adequate dilution of the stock solution.

An iodate solution (0.2 mol L^{-1}) was prepared by dissolving 8.5600 g of potassium iodate (Merck) in water and diluting to 200 mL in a volumetric flask. The sulfuric acid solution 1.0 mol L^{-1} was prepared by diluting 5.44 mL of concentrated H$_2$SO$_4$ (Merck) to 100 mL in volumetric flask.

2.3. Preparation of optical sensor

The following procedure for the preparation of sensor was performed in order to immobilize methyltrioctylammonium chloride

on triacetylcellulose membrane [25]. For this purpose, the transparent triacetylcellulose membranes were produced from waste photographic films that had been previously treated with commercial sodium hypochlorite in order to remove colored gelatinous layers. The membranes were treated with a solution of 0.20 g methyltrioctylammonium chloride in 10 mL of ethylenediamine for 15 min at ambient temperature. Then, they were washed with water for removing the additional reagent. The optode membrane was stored under water when not in use.

2.4. Analytical procedure

The prepared membrane was placed in a solution of potassium iodate (0.20 mol L^{-1}) for 2 min, then it was washed and mounted into a spectrophotometer cell. A few mL of a solution containing iodide and sulfuric acid was transferred to cell, and the absorbance was measured at 370 nm after 8 min.

2.5. Preparation of powdered milk sample

14 g of milk sample was placed in a porcelain crucible, and 5 g of Na$_2$CO$_3$, 5 mL of a 6 mol L^{-1} NaOH solution and 20 mL of MeOH were added. This mixture was allowed to dry slowly in a heater at 110 °C. Then it was placed in a cold muffle furnace, the temperature of which was slowly increased to 500 °C, to prevent analyte losses. Approximately 3 h later, when incineration was complete (white ash), the crucible was cooled down in a desiccator to room temperature. Then the ash was redissolved in hot water. The dissolve residue was filtered and the appropriate amount of H$_2$SO$_4$ added, diluted to 25 mL with water and the analytical procedure was applied [20].

2.6. Preparation of tablet sample

The procedure described in Section 2.5 was performed for preparation of Levothyroxine Na tablet sample. In this procedure 2 g of Na$_2$CO$_3$, 3 mL of NaOH and 10 mL of MeOH were added to one tablet (1.8910 g).

3. Results and discussion

3.1. Principle of operation and spectral characteristics

The adsorption of methyltrioctylammonium chloride (MTA$^+$Cl$^-$) on triacetylcellulose makes the membrane to be used as an anionic exchange membrane. The preliminary experiments showed that by placing this film in iodate solution the counter ion in membrane is exchanged with iodate and it can be used as an optical redox sensor. By placing the membrane containing iodate in acidic solution of iodide, the colorless membrane changed to yellow. This color changing is due to oxidation of iodide to I$_3{}^-$ in membrane interface and then its immediate adsorption by anionic exchange phenomena, as described by following scheme:

$$MTA^+Cl^-_{(mem.)} + IO_3{}^-_{(aq.)} \rightarrow MTA^+IO_3{}^-_{(mem.)} + Cl^-_{(aq.)} \qquad (1)$$

$$\underset{(colorless)}{MTA^+IO_{3(mem.)}^-} + I^-_{(aq.)} \xrightarrow{H^+} \underset{(yellow)}{MTA^+I_{3(mem.)}^-} \qquad (2)$$

The absorption spectra of the proposed sensor in the absence and presence of iodide in different concentrations are shown in Fig. 1. As seen, upon addition of iodide the absorbance in maximum wavelength, 370 nm, increased therefore this wavelength was selected for measuring the absorbance of the optode.

Fig. 1. Absorption spectra of optode (a) in the absence and (b–e) in the presence of 3.94×10^{-6}, 7.87×10^{-6}, 1.57×10^{-5} and 2.36×10^{-5} mol L^{-1} of iodide, respectively.

3.2. The effect of variables on sensor response

The stability and sensitivity of the sensor depends significantly on the membrane composition. Therefore, the effects of solvent types, amount of methyltrioctylammonium chloride and preparation time on the response behavior were studied. The obtained results indicated that the membrane responded to iodide ions when it was prepared using ethylenediamine as solvent. The hydrolyzed cellulose film in ethylenediamine shaped the porous structure in the polymer, which minimizes barriers of mass transport between the analyte and immobilized reagent [26,27].

The amount of methyltrioctylammonium chloride had significant effect on the membrane response. At low amounts the response is low and higher values caused the membrane to be opaque. The highest response was obtained using 0.20 g of methyltrioctylammonium chloride. In another experiment, the presence time of membrane in methyltrioctylammonium chloride/ethylenediamine solution was investigated. The results indicated that the response increased with time, but over 15 min the membrane begins to dissolve and to deform. Thus, the optode was prepared by treating transparent triacetylcellulose membrane with a solution of 0.20 g methyltrioctylammonium chloride in 10 mL ethylenediamine for 15 min.

The reaction between iodate and iodide occurs when the solution is acidified with a strong acid [28]. Therefore, the influence of sulfuric acid concentration over the range of 0.02–0.10 mol L^{-1} on the response of optical sensor was studied. The results shown in Fig. 2 indicate that the sensor response increased up to 0.04 mol L^{-1} of sulfuric acid and above this value it decreased. As expected, the response increased by increasing of acid concentration, but in
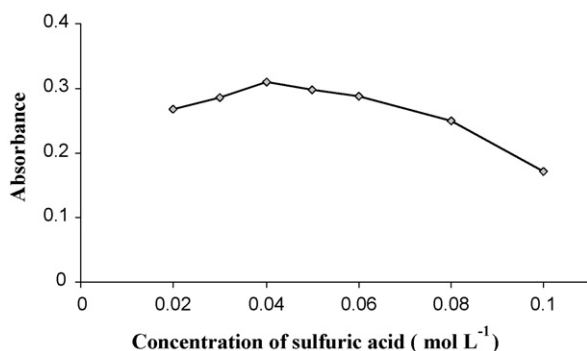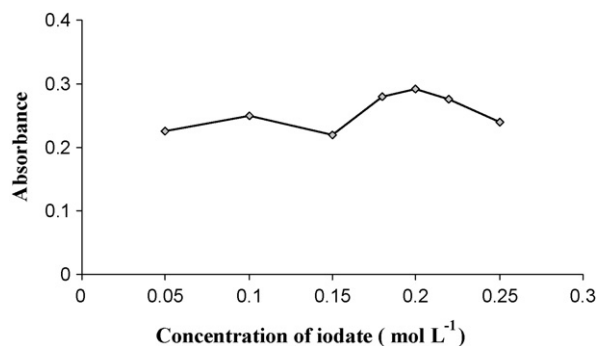

Fig. 3. Effect of iodate concentration on the optode response for the solution containing 3.94×10^{-5} mol L^{-1} of iodide and 0.04 mol L^{-1} of sulfuric acid.

higher acid concentrations the excess of iodide converted to iodine and concentration of I_3^- is decreased. Thus 0.04 mol L^{-1} of sulfuric acid was selected as optimum concentration.

The effect of potassium iodate concentration on the optode response was investigated in the range of 0.05–0.25 mol L^{-1}. Fig. 3 shows that a maximum value in the absorbance was obtained at 0.20 mol L^{-1} of potassium iodate. At concentrations higher than 0.20 mol L^{-1} of iodate the response is decreased. This is also due to conversion of excess of iodide to iodine. Therefore 0.20 mol L^{-1} was chosen for further studies.

The presence time of membrane in potassium iodate solution was also studied. The obtained results indicated that the membrane absorbance increased up to 90 s and above this value it became constant. The presence time of 120 s was selected as optimum.

The influence of electrolyte concentration on the sensor response was investigated by adding different amounts of potassium nitrate. The obtained results denoted that this parameter had no effect on the response of optical sensor up to 0.1 mol L^{-1} of potassium nitrate.

3.3. Response time and regeneration

The absorbance response of the optode versus time in selected experimental conditions for 7.87×10^{-6} and 3.94×10^{-5} mol L^{-1} of iodide was studied. Fig. 4 shows that the proposed sensor reaches the out put signal of 98% of steady-state response after 8 min. This result is the same for both concentration of iodide.

A good sensor should fully regenerate at a short time. The proposed optode was regenerated completely in 0.1 mol L^{-1} of NaOH in less than 15 s. The membrane could be regenerated about 50 times and used without any loss of sensitivity.
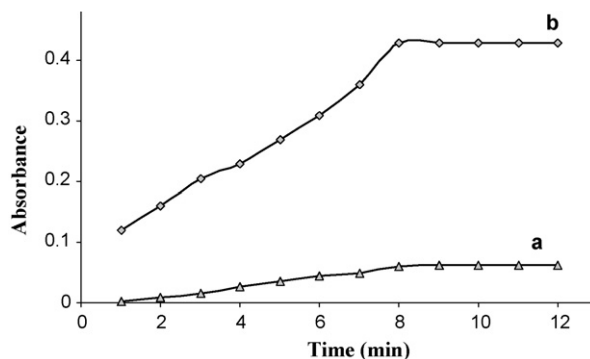

Fig. 2. Effect of sulfuric acid concentration on the optode response for solution containing 3.94×10^{-5} mol L^{-1} of iodide.

Fig. 4. Absorbance as a function of time when the concentration of iodide was (a) 7.87×10^{-6} and (b) 3.94×10^{-5} mol L^{-1}.
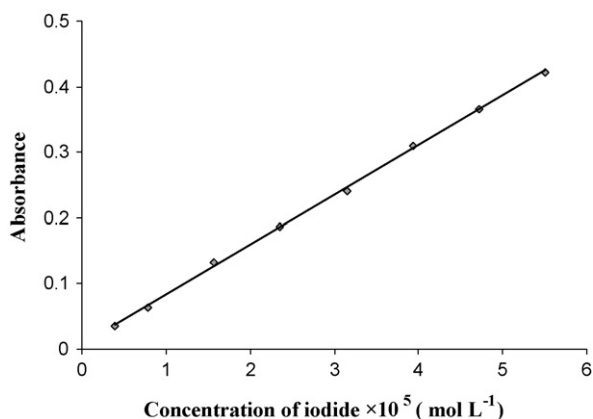
Fig. 5. Calibration curve for determination of iodide using the optode.

3.4. Analytical figure of merit

The corresponding calibration graph (Fig. 5) based on absorbance of the optode versus iodide ion concentration was linear in the range of 3.94×10^{-6} to 5.51×10^{-5} mol L^{-1} (0.5–7 μg mL^{-1}). The regression equation for the line was $A = 7.57 \times 10^3 C + 7.27 \times 10^{-3}$ with correlation coefficient (r) of 0.9995, where C is concentration of iodide in mol L^{-1} and A is absorbance of optode at 370 nm. The detection limit of the sensor based on three times the standard deviation of blank was 7.44×10^{-7} mol L^{-1}.

3.5. Reproducibility and lifetime of the optode

The reproducibility of the membrane preparation was checked for five separate membranes by measuring the absorbance under optimum conditions for 7.87×10^{-6} mol L^{-1} of iodide. The results showed that the R.S.D. for the membrane preparation was less than 3.5%.

The precision using a single membrane was tested by performing eight replicate measurements for 3.94×10^{-6} and 1.57×10^{-5} mol L^{-1} of iodide solutions. The relative standard deviation (R.S.D.) for these determinations was 2.83 and 1.38%, respectively.

In determination of the lifetime of the sensor, the change in the absorbance after keeping the membrane in water for 1 month was measured. The absorbance values of optode membrane at 370 nm only decreased about 2% over a period of 1 month. This result indicates that the optode is very stable, so it could be stored for more than 1 month without losing its characteristics.

Table 1
Effect of interfering ions on determination of 1.57×10^{-5} mol L^{-1} of iodide

Foreign ions	Tolerance ratio ([M]/[I$^-$])
CO_3^{2-}, NO_3^{-}, Cr^{3+}, Na^+	500
Ca^{2+}, Mg^{2+}	200
Co^{2+}, Mn^{2+}, Fe^{2+}, Cl^{-}[a]	100
Cu^{2+}, Cd^{2+}, Zn^{2+}	50
F^-	30
Ni^{2+}, $C_2O_4^{2-}$[b]	10
Br^-	2

[a] Masked by Cd^{2+}.
[b] Masked by Co^{2+}.

Table 2
Determination of iodide in Levothyroxine Na tablet

Sample	Iodide found[a] (mol L^{-1})	Levothyroxine Na found (mg)	Reported value (mg)
1	$1.89(\pm 0.03) \times 10^{-5}$	0.095	0.1
2	$1.87(\pm 0.03) \times 10^{-5}$	0.093	0.1

[a] Mean ± S.D. ($n = 4$).

Table 3
Determination of iodide in powdered milk and urine samples

Samples	Amount of iodide (mol L^{-1})		Recovery (%)
	Added	Found[a]	
Powdered milk	–	$8.92(\pm 0.05) \times 10^{-6}$	–
	7.87×10^{-6}	$1.69(\pm 0.05) \times 10^{-5}$	100.6
Urine	–	$1.50(\pm 0.05) \times 10^{-5}$	–
	3.94×10^{-6}	$1.89(\pm 0.03) \times 10^{-5}$	99.8
	7.87×10^{-6}	$2.31(\pm 0.04) \times 10^{-5}$	101.0

[a] Mean ± S.D. ($n = 4$).

3.6. Effect of foreign ions

In the presence of other ions, the selectivity of the optode was studied for 1.57×10^{-5} mol L^{-1} of iodide ion solution using the proposed method. The tolerance limit was defined as the maximum concentration of foreign ion causing ±5% error in the determination of iodide. The results are summarized in Table 1. As it is observed the optode is more selective to iodide than other anions under optimum conditions.

The interference of chloride and oxalate anions on the determination of iodide was eliminated using 8.9×10^{-4} mol L^{-1} of Cd(II) ion for chloride and 1.7×10^{-3} mol L^{-1} of Co(II) ion for oxalate because Cd(II) and Co(II) ions form complexes with chloride and oxalate anions, respectively.

3.7. Analytical application

3.7.1. Determination of iodide in tablet

The presented iodide optical sensor was applied to the determination of Levothyroxine Na ($C_{15}H_{10}I_4NNaO_4$) in two tablet samples (Iran Hormone). According to the obtained amount of iodide (Table 2) the average of Levothyroxine Na amount is 0.094 mg which is in good agreements with the reported values.

3.7.2. Determination of iodide in powdered milk and urine

The proposed optical sensor was also employed for the determination of iodide in powdered milk and urine samples. The possibility of applying the present optical sensor for analysis of samples was tested by determining the recovery of known amounts of iodide ion added to the samples. The given results in Table 3 show good agreement between added and detected concentration of the iodide in real samples.

4. Conclusion

This paper described a novel optical redox chemical sensor for determination of iodide. The sensing membrane was easily prepared and operated. The purposed optode can be regenerated quickly and the response of the optode is very reproducible. In comparison with other methods [21–24], the purposed sensor is more sensitive and it was prepared easily by using low-cost materials in a short time. In addition, the method is based on measuring the optode absorption by UV–vis spectrophotometry, which has the advantage of determinations by an inexpensive instrument in a rel-

atively short time. The proposed method could be widely applied to the determination of iodide in real samples with different compositions.

Acknowledgement

References

[1] C. McDonagh, C.S. Burke, B.D. MacCraith, Chem. Rev. 108 (2008) 400.
[2] Y.M. Scindia, A.K. Pandey, A.V.R. Reddy, S.B. Manohar, Anal. Chim. Acta 515 (2004) 311.
[3] S. Rastegarzadeh, V. Rezaei, Sens. Actuators B 129 (2008) 327.
[4] I.M. Steinberg, A. Lobnik, O.S. Wolfbeis, Sens. Actuators B 90 (2003) 230.
[5] N. Alizadeh, A. Moemeni, M. Shamsipur, Anal. Chim. Acta 464 (2002) 187.
[6] Z. Liu, F. Luo, T. Chen, Anal. Chim. Acta 510 (2004) 189.
[7] J.A. Ortuno, M.I. Albero, M.S. Garcia, C. Sanchez-Pedreno, M.I. Garcia, R. Exposito, Talanta 60 (2003) 563.
[8] G. Absalan, M. Soleimani, M. Asadi, M.B. Ahmadi, Anal. Sci. 20 (2004) 1433.
[9] Z. Xie, J. Zhao, Talanta 63 (2004) 339.
[10] D. Nacapricha, P. Sangkarn, C. Karuman, T. Mantim, W. Waiyawat, P. Wilairat, T. Cardwell, I.D. McKelvie, N. Ratanawimarnwong, Talanta 72 (2007) 626.
[11] K.M. Eckhoff, A. Maage, J. Food Comp. Anal. 10 (1997) 270.
[12] L. Liang, Y. Cai, S. Mou, J. Cheng, J. Chromatogr. A 1085 (2005) 37.
[13] D. Nacapricha, S. Muangkaew, N. Ratanawimarnwong, J. Shiowatana, K. Grudpan, Analyst 126 (2001) 121.
[14] Y. Bichsel, U. Von-Gunten, Anal. Chem. 77 (1999) 34.
[15] W. Hu, P.J. Yang, K. Hasebe, P.R. Haddad, K. Tanaka, J. Chromatogr. A 956 (2002) 103.
[16] K. Ito, T. Ichihara, H. Zhuo, K. Kumamoto, A.R. Timerbaev, T. Hirokawa, Anal. Chim. Acta 497 (2003) 67.
[17] T. Fujiwara, H. Mohammadzai, H. Inoue, T. Kumamaru, Analyst 125 (2000) 759.
[18] R.C. Prost, Anal. Chem. 49 (1977) 1199.
[19] L.F. Sanchez, J. Szpunar, J. Anal. Atom. Spectrom. 14 (1999) 1697.
[20] P. Bermejo-Barrera, L.M. Fernandez-Sanchez, M. Aboal-Somoza, R.M. Anllo-Sendin, A. Bermejo-Barrera, Microchem. J. 69 (2001) 205.
[21] E. Urbano, H. Offenbacher, O.S. Wolfbeis, Anal. Chem. 56 (1984) 427.
[22] Y.M. Liu, R.P. Garcia, M.E.D. Garcia, A. Sanz-Medel, Anal. Chim. Acta 255 (1991) 245.
[23] C.D. Geddes, P. Douglas, C.P. Moore, T.J. Wear, P.L. Egerton, J. Fluoresc. 9 (1999) 163.
[24] C.D. Geddes, Dyes Pigments 45 (2000) 243.
[25] A. Safavi, M. Bagheri, Sens. Actuators B 99 (2004) 608.
[26] T.P. Jones, M.D. Porter, Anal. Chem. 60 (1988) 404.
[27] Y. Kostov, S. Tzonkov, L. Yotova, M. Krysteva, Anal. Chim. Acta 280 (1993) 15.
[28] D.A. Skoog, D.M. West, F.J. Holler, Fundamentals of Analytical Chemistry, 5th ed., Saunders College Publishing, 1988, p. 343.

Microwave-assisted extraction and ultrasonic extraction to determine polycyclic aromatic hydrocarbons in needles and bark of *Pinus pinaster* Ait. and *Pinus pinea* L. by GC–MS

Nuno Ratola[a], Sílvia Lacorte[b], Damià Barceló[b], Arminda Alves[a,*]

[a] *LEPAE, Departamento de Engenharia Química, Faculdade de Engenharia da Universidade do Porto, Rua Dr. Roberto Frias, 4200-465 Porto, Portugal*
[b] *Department of Environmental Chemistry, IIQAB-CSIC, c/Jordi Girona 18-26, 08034 Barcelona, Catalonia, Spain*

ABSTRACT

Two different extraction strategies (microwave-assisted extraction (MAE) and ultrasonic extraction (USE)) were tested in the extraction of the 16 US Environmental Protection Agency (EPA) polycyclic aromatic hydrocarbons (PAHs) from pine trees. Extraction of needles and bark from two pine species common in the Iberian Peninsula (*Pinus pinaster* Ait. and *Pinus pinea* L.) was optimized using two amounts of sample (1 g and 5 g) and two PAHs spiking levels (20 ng/g and 100 ng/g). In all cases, the clean-up procedure following extraction consisted in solid-phase extraction (SPE) with alumina cartridges. Quantification was done by gas chromatography (GC) with mass spectrometry (MS), using five deuterated PAH surrogate standards as internal standards. Limits of detection were globally below 0.2 ng/g. The method was robust for the matrices studied regardless of the extraction procedures. Recovery values between 70 and 130% were reached in most cases, except for high molecular weight PAHs (indeno[1,2,3-*cd*]pyrene, dibenzo[*a,h*]anthracene and benzo[*ghi*]perylene). A field study with naturally contaminated samples from eight sites (four in Portugal and four in Catalonia, Spain) showed that needles are more suitable biomonitors for PAHs, yielding concentrations from 2 to 17 times higher than those found in bark. The levels varied according to the sampling site, with the sum of the individual PAH concentrations between 213 and 1773 ng/g (dry weight). Phenanthrene was the most abundant PAH, followed by fluoranthene, naphthalene and pyrene.

© 2008 Elsevier B.V. All rights reserved.

1. Introduction

Pine trees can be used as biomonitors to assess the occurrence of a wide range of persistent organic pollutants (POPs) in the environment, mainly through the retention properties exhibited by the waxy layer of their needles [1]. The worldwide presence of different pine species allows not only a broad estimation of the levels of several POPs such as the polycyclic aromatic hydrocarbons (PAHs) but also the collection of comparative data to establish bioaccumulation or transport patterns between different locations.

PAHs are ubiquitous priority pollutants resulting from natural (forest fires and volcanoes) and anthropogenic sources (incomplete combustion of fossil fuels and industrial processes, among others) [2,3]. Their carcinogenic and mutagenic properties [4] cause great concern, being the major routes of exposure for humans the ingestion of contaminated food and inhaled air [5].

Several studies reported the biomonitoring properties of needles from species such as *Pinus sylvestris* L. [6,7], *Pinus strobus* L. [8,9], *Pinus densiflora* Siebold & Zucc., *thumbergii* Parl., *maximartinezii* Rzed. and *taeda* L. [10,11], *Pinus nigra* Arn. [12,13], *P. pinaster* Ait. [13], *Pinus massoniana* Lamb [14] and *P. pinea* L. [15] towards PAHs. Pine bark is also known to accumulate airborne contaminants, due to its very porous and almost inert surface [16]. There is, however, less information regarding PAHs [17,18] since this particular matrix is mostly recognized for trapping metallic elements [19–22] or as a sorbent for the removal of contaminants from aqueous media [23–26].

The analysis of pine needles and bark require effective extraction and clean-up procedures to retain the target compounds and eliminate matrix interferences. Hence, several approaches are continuously being attempted in search of faster, cleaner and reliable analytical methodologies. The most frequent employ solvent extraction and gas chromatography with selective and sensitive detection, although HPLC with fluorescence detection has also been used for PAHs [7,13]. Techniques reported for the extraction of PAHs from pine needles and bark include Soxhlet [18,27], ultrasonic extraction (USE) [8,11,13,28], supercritical fluid extraction

* Corresponding author. Tel.: +351 22 5081883; fax: +351 22 5081449.
E-mail address: aalves@fe.up.pt (A. Alves).

(SFE) [9] and pressurized liquid extraction (PLE) [12,14,17,28,29]. Microwave-assisted extraction, first reported by Ganzler et al. for solid matrices [30], is also employed but to our knowledge never for PAHs in pine trees.

The main objective of the current work was to test the efficiency of microwave-assisted extraction (MAE) and ultrasound extraction followed by alumina cartridge solid-phase extraction (SPE) clean-up in the determination of the 16 EPA PAHs in pine needles and bark. *P. pinaster* Ait. and *P. pinea* L. trees were chosen once they are the two main pine species in Portugal, besides being common in the whole Mediterranean area. Two sample masses (1 g and 5 g) and two PAHs spiking levels (20 ng/g and 100 ng/g) were used for both needles and bark of each species. The two methods were compared not only in terms of validation parameters (detection limits, precision, recovery) but also through the PAHs levels detected in samples from eight field sites (four in Portugal and four in Catalonia, Spain). Comparison between such levels in needles and bark from the same tree (to our knowledge only studied for heavy metals [21]) was also possible. Analysis and quantification was performed by gas chromatography–mass spectrometry (GC–MS) in selected ion monitoring (SIM) mode, using deuterated PAHs as internal standards.

2. Experimental

2.1. Chemicals and reagents

Sixteen prioritary PAHs according to the US Environmental Protection Agency (EPA) were analysed: naphthalene, acenaphthylene, acenaphthene, fluorene, phenanthrene, anthracene, fluoranthene, pyrene, benzo[*a*]anthracene, chrysene, benzo[*b*]fluoranthene, benzo[*k*]fluoranthene, benzo[*a*]pyrene, indeno[1,2,3-*cd*]pyrene, dibenzo[*a,h*]anthracene and benzo[*ghi*]perylene. The surrogate standard was a mixture containing [2H8]naphthalene (naphthalene-d_8), [2H10]acenaphthene (acenaphthene-d_{10}), [2H10]phenanthrene (phenanthrene-d_{10}), [2H12]chrysene (chrysene-d_{12}) and [2H12]perylene (perylene-d_{12}), which were added to the samples before extraction and used as internal standards for quantification. Both standard mix solutions at 2000 μg/L in hexane were from Supelco (Bellefonte, PA, USA). Also from Supelco, [2H10]anthracene (anthracene-d_{10}) was added just before GC–MS analysis to detect possible instrumental errors. Solvents (hexane and dichloromethane SupraSolv) were from Merck (Darmstadt, Germany). International Sorbent Technology (Mid Glamorgan, UK) provided the SPE alumina cartridges (5 g, 25 mL). Nitrogen for drying (99.995% purity) was from Air Liquide (Maia, Portugal)

In order to reduce the losses of the target compounds due to adsorption upon glassware, all glass material was silanised before use by soaking it overnight in a 15% dichlorodimethylsilane solution in toluene, then rinsing with toluene and methanol and drying for 4 h at 400 °C. Dichlorodimethylsilane and toluene were provided by Aldrich (Milwaukee, WI, USA).

2.2. Pine samples

Bark and needle samples for the performance assays were collected from two trees in Porto, Portugal (one *P. pinaster* Ait. and one *P. pinea* L.) and naturally contaminated samples were collected from eight trees in the Iberian Peninsula (four in Portugal, all *P. pinaster* Ait.and four in Catalonia, Spain, all *P. pinea* L.). Porto (large urban area), Bragança (small urban area), Quintãs (rural) and Vide (mountain) were the locations chosen in Portugal and Barcelona (large urban area), Vic (small urban area), El Prat (seaside, close to the air-

port) and Montseny (mountain) in Catalonia. Needles were chosen from the bottom branches of the trees and removed in one piece while bark was collected all around the trunk from 50 to 150 cm above the soil, detaching only the most external layer.

2.3. Sample pretreatment

Whenever possible, the samples were analysed immediately after collection. If not, they were kept from light and frozen until extraction. Two sample masses (1 g and 5 g) and two spiking levels of native PAHs (20 ng/g and 100 ng/g) were used for the method performance assays. As to the naturally contaminated samples, 2 g of sample were analysed. The surrogate internal standards were added to all samples in a concentration of 50 ng/g. No further pre-treatment was needed. For both needles and bark of both pine species, two extraction methodologies were studied for the four combinations of sample amounts and PAHs spiking levels. The volume of the extracting solvent used in all assays (hexane:dichloromethane 1:1) was 90 mL. Triplicate analyses were performed for each situation, together with one method blank.

2.4. Water content of bark and needles

Water content was determined for needles and bark of both pine species based on a study of Hubert et al. [31]: three samples of 5 g each were dried at 80 °C until constant weight. *P. pinaster* Ait. needles have, on average, 59% water while bark has 11%. For *P. pinea* L. the values are very similar: 59% for needles and 13.5% for bark. These values were taken into account in order to present the results regarding PAHs contamination levels in a dry-weight basis.

2.5. Microwave-assisted extraction (MAE)

Microwave-assisted extractions were performed with a modified version of the WP700P17-3 domestic oven from Electric Co. (2,450 MHz, China), based on the work by Herbert et al. [32]. As shown in Fig. 1, the flasks were inserted in the oven and coupled to an exterior condenser connected to a 16 °C water bath, model F34 from Julabo (Seelbach, Germany). This device was used under a fume hood at all times and a microwave radiation sensor was permanently monitoring any possible leak. All glass parts (except the condenser) were previously silanised as described above.

Needles (cut into 1 cm bits) and bark (ground to <1 cm^2 bits with pestle and mortar) were inserted in 250 mL round-bottomed flasks and extraction was performed using 90 mL of hexane:dichloromethane (1:1) for 30 min at 513 W. The extract was evaporated to almost dryness (0.5 mL approximately) in a Buchi R-200 rotavapor (Flawil, Switzerland) and further purified using SPE alumina cartridges as explained in Section 2.2.3.

2.6. Ultrasonic extraction (USE)

Following almost identically the procedure adopted by Ratola et al. [15], needles (cut into 1 cm bits) and bark (ground to <1 cm^2 bits with pestle and mortar) were inserted in glass tubes with 30 mL hexane/dichloromethane (1:1) and placed for 10 min in a 720 W Selecta ultrasonic bath (J.P. Selecta, Barcelona, Spain). The procedure was repeated two more times, using fresh solvent each time. The extracts were treated as for MAE before clean-up.

2.7. Clean-up

The extracts from MAE and USE were purified following a clean-up procedure previously described by Ratola et al. [15], using SPE alumina cartridges (5 g, 25 mL). In brief, the cartridges
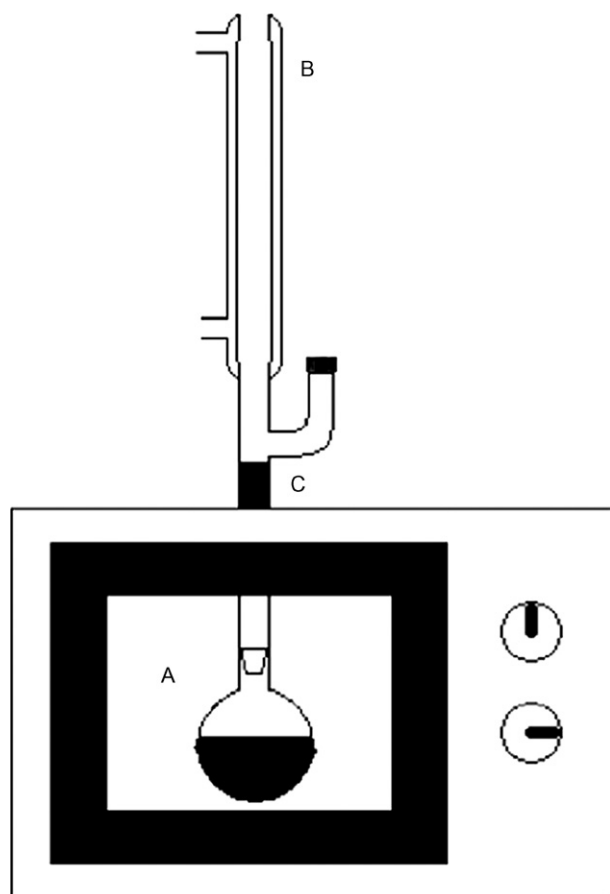
Fig. 1. Scheme of the MAE apparatus (adapted from Herbert et al. [32]). (A) 250 mL round-bottomed glass flask; (B) condenser connected to a 16 °C water bath; (C) Claisen adaptor inserted into the microwave's metallic tube attenuator, for radiation protection.

were conditioned prior to sample loading with 50 mL hexane-dichloromethane (1:1). The extract was then added to the column and eluted with 50 mL hexane-dichloromethane (1:1), followed by 50 mL dichloromethane. The two fractions were collected into the same pear-shaped flask, pre-concentrated in a rotary evaporator to 0.5 mL and transferred to 2 mL amber glass vials. Extracts were evaporated at room temperature under nitrogen and reconstituted in 1 mL of hexane. At this stage, 50 ng/mL of anthracene-d_{10} were added to account for possible instrumental errors in subsequent GC–MS analyses.

2.8. GC–MS parameters and quantification

All samples were analysed by a Trace GC 2000 Series gas chromatograph from TermoQuest (Waltham, MA, USA) coupled to a quadrupole mass spectrometer (Finnigan Trace MS 2000 Series), operating in electron impact mode (EI, 70 eV). Separation was carried out in a J&W Scientific (Folsom, CA, USA) 30 m × 0.25 mm I.D. DB-5 column coated with 5% diphenyl-polydimethylsiloxane (film thickness 0.25 μm). The oven temperature programme started at 60 °C, held for 1 min, then up to 175 °C at 6 °C/min, held for 4 min, to 235 °C at 3 °C/min and finally to 300 °C at 8 °C/min and held for 5 min. Injection (2 μL) was in splitless mode, with the split valve closed for 48 s. Carrier gas was helium (50 cm/s) and the temperatures for the injector, transfer line and ion source were 280, 250 and 200 °C, respectively. Acquisition was performed under time-scheduled selected ion monitoring using the retention time windows and ions indicated in Table 1. Total runtime was 60 min.

Table 1 presents the experimental mass conditions for the PAHs and the surrogate standards. Peak identification and integration were performed by internal standard method with the Excalibur 1.2 software from Finnigan (Waltham, MA, USA). Five surrogate PAHs (Naph-d_8, Ace-d_{10}, Phen-d_{10}, Chry-d_{12} and Pery-d_{12}, one per time window) were used for internal standard quantification mode, in order to control the extraction efficiencies (see Table 1). Anthracene-d_{10} was used to check for possible GC–MS mass variations. Retention time information and up to three ions were used to identify the base peaks.

Table 1
GC–MS retention time windows and ions monitored in the SIM mode

Time window (min)	Compound	Abbreviation	Retention time (min)	Ions (m/z)
0–16.00	Naphthalene-d_8	Naph-d_8	13.81	136, 108, 134
	Naphthalene	Naph	13.89	128, 127, 129
16.00–25.00	Acenaphthylene	Acy	19.91	152, 151, 76
	Acenaphthene-d_{10}	Ace-d_{10}	20.49	164, 162
	Acenaphtene	Ace	20.62	154, 152, 76
	Fluorene	Fluo	23.02	166, 165, 164
25.00–43.00	Phenanthrene-d_{10}	Phen-d_{10}	29.05	188, 184
	Phenanthrene	Phen	29.21	178, 89, 152
	Anthracene-d_{10}	Ant-d_{10}	29.45	188, 184
	Anthracene	Ant	29.58	178, 89, 152
	Fluoranthene	Flt	38.08	202, 200, 101
	Pyrene	Pyr	39.72	202, 200, 101
43.00–49.50	Benzo[a]anthracene	BaA	48.42	228, 226, 114
	Chrysene-d_{12}	Chry-d_{12}	48.31	240, 228
	Chrysene	Chry	48.44	228, 226, 114
49.50–60.00	Benzo[b]fluoranthene	BbF	52.71	252, 250, 126
	Benzo[k]fluoranthene	BkF	52.81	252, 126, 250
	Benzo[a]pyrene	BaP	53.82	252, 126, 250
	Perylene-d_{12}	Pery-d_{12}	54.04	264, 260
	Indeno[1,2,3-c,d]pyrene	IcdP	58.52	276, 138, 274
	Dibenzo[a,h]anthracene	DahA	58.71	278, 276, 139
	Benzo[ghi]perylene	BghiP	59.80	276, 138, 274

Underlined, the main quantifying ions. Internal standards and anthracene-d_{10} shown in italics.

Table 2

Compound	Pinus pinaster				Pinus pinea			
	Needles		Bark		Needles		Bark	
	LOD (ng/g)	Repeatability (%)	LOD (ng/g)	Repeatability (%)	LOD (ng/g)	Repeatability (%)	LOD (ng/g)	Repeatability (%)
(a) Limits of detection (LOD) and repeatability (n = 3) for MAE using spiked samples (20 ng/g, 5 g extracted)								
Naph	0.04	1.1	0.14	5.4	0.06	3.8	0.15	13.1
Acy	0.14	3.4	0.27	9.9	0.06	3.7	0.10	8.1
Ace	0.22	0.9	0.89	7.2	0.34	2.5	0.80	2.0
Fluo	0.14	3.7	0.13	6.3	0.03	5.9	0.06	11.2
Phen	0.08	11.9	0.06	3.4	0.02	0.9	0.06	7.0
Ant	0.16	3.2	0.07	1.3	0.02	2.3	0.03	4.3
Flt	0.54	8.5	0.35	4.6	0.04	4.5	0.05	6.0
Pyr	0.24	9.4	0.16	3.6	0.03	5.2	0.08	4.5
BaA	0.38	4.6	0.03	1.7	0.02	1.3	0.03	3.0
Chry	0.38	4.8	0.04	1.8	0.02	3.5	0.03	3.0
BbF	0.07	2.3	0.11	5.2	0.05	2.4	0.08	4.0
BkF	0.07	2.7	0.12	6.5	0.05	2.8	0.07	3.8
BaP	0.08	2.1	0.10	4.4	0.08	3.3	0.09	5.5
IcdP	0.10	3.0	0.08	3.5	0.05	1.6	0.11	2.9
DahA	0.24	3.1	0.14	4.0	0.07	1.7	0.19	3.1
BghiP	0.10	3.1	0.11	3.1	0.06	0.4	0.10	2.1
(b) Limits of detection (LOD) and repeatability (n = 3) for USE using spiked samples (20 ng/g, 5 g extracted)								
Naph	0.055	12.0	0.964	0.1	0.028	1.0	0.068	5.7
Acy	0.094	5.4	0.203	7.1	0.069	4.1	0.063	6.6
Ace	0.286	2.1	0.774	4.3	0.224	6.0	0.379	5.7
Fluo	0.069	3.5	0.330	11.5	0.057	11.6	0.040	5.6
Phen	0.037	12.5	0.157	1.3	0.030	6.4	0.020	3.5
Ant	0.073	3.3	0.164	1.9	0.033	4.7	0.023	4.5
Flt	0.346	2.8	0.875	12.3	0.052	0.7	0.047	5.5
Pyr	0.098	5.5	0.712	12.7	0.256	6.7	0.073	3.8
BaA	0.018	3.1	0.074	2.4	0.079	3.1	0.052	1.3
Chry	0.019	4.0	0.171	2.1	0.086	1.0	0.058	0.9
BbF	0.045	0.4	0.096	0.6	0.065	4.5	0.096	3.1
BkF	0.047	0.3	0.097	0.1	0.074	3.4	0.057	4.5
BaP	0.042	0.9	0.148	2.7	0.102	1.3	0.090	5.5
IcdP	0.067	0.4	0.061	5.4	0.108	2.6	0.093	3.4
DahA	0.094	0.3	0.136	5.8	0.226	3.8	0.172	4.1
BghiP	0.071	0.6	0.128	5.9	0.104	3.0	0.115	2.7

3. Results and discussion

3.1. Method validation

All 16 PAHs studied showed linear behaviour from 0.01 to 1 mg/L (six calibration points), with correlation coefficients varying from 0.9906 to 0.9956 and good chromatographic separation. Table 2 shows the results of the limits of detection (LODs, calculated using a signal-to-noise ratio of 3), and repeatability (average of three consecutive injections of samples spiked at 20 ng/g). LODs are shown in a dry-weight basis.

The LODs for needles ranged from 0.02 to 0.54 ng/g for MAE and from 0.02 to 0.35 for USE, but the values are generally below 0.2 ng/g for *P. pinaster* and 0.1 ng/g for *P. pinea*. These values are in line with previously released data [15,33]. The results for *pinea* needles proved to be better, with lower detection limits in most cases. Piccardo et al. [13] refer that the morphological and physiological differences between different conifer species can be a key factor when persistent organic pollutants uptake is concerned. In fact, *P. pinaster* needles proved to be a more difficult matrix to handle, showing a wider range of interfering compounds in its quantification. Maybe this can explain the differences shown particularly for Flt, Pyr, BaA and Chry in MAE and Flt in USE.

For bark samples the results are similar, with LODs ranging between 0.03 and 0.89 ng/g for MAE and from 0.02 to 0.96 ng/g for USE. However, in the latter case and for *P. pinaster* needles, the LODs were poorer for bark. Matrix differences towards the needles may explain this particular exception. Still, USE globally presented lower LODs comparing with MAE.

The overall results for repeatability are good, with most values below 10% and showing no clear differences between sample type, pine species or extraction procedure.

Carryover was checked by blank chromatographic assays. Blank samples were also performed before each set of experiments in order to subtract the contribution of the naturally present PAHs and correct the final recovery results.

3.2. Recovery assays

Two different extraction procedures were considered in this work: MAE and USE. The following sections describe the results of the recovery assays (and respective standard deviations) established to assess the performance of both methodologies applied to the quantification of PAHs in needles and bark of *P. pinaster* Ait. and *P. pinea* L. To facilitate the interpretation of the results, both species will be shown separately.

3.2.1. Extraction of Pinus pinaster Ait

Fig. 2 shows the values of the recovery assays for the needle samples (1 g and 5 g; 20 and 100 ng/g PAH spiking level).

Common trends are found in the recovery assays regardless of sample mass and spiking concentration. For both MAE and USE, the recoveries for the lower molecular weight PAHs (LMW, with 2, 3 and 4 aromatic rings) are within the 70–130% range accepted by the US Environmental Protection Agency for these types of analyses. A decrease in these values is verified for the 5- and 6-ringed PAHs (HMV), especially for IcdP, DahA and BghiP, which presented recoveries below 50% under the conditions used. This difficulty is very
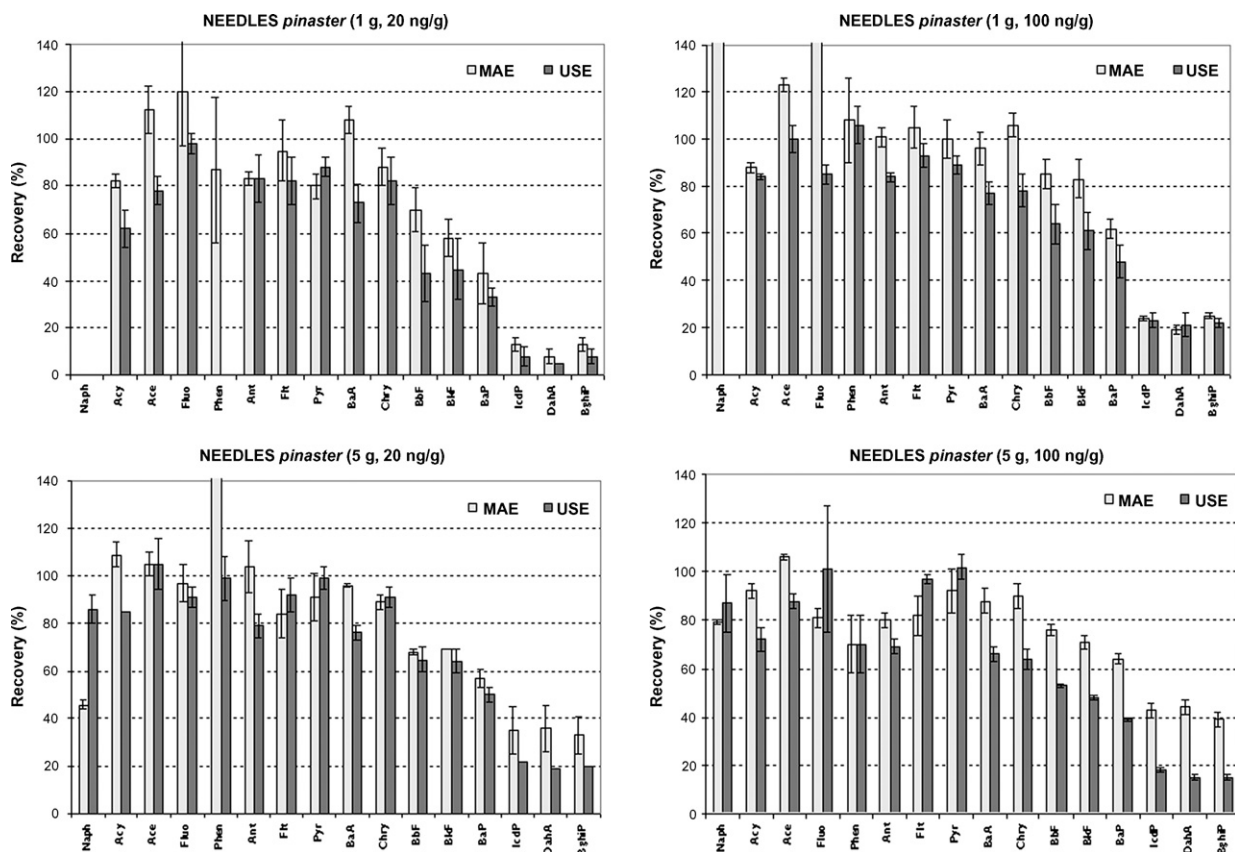
Fig. 2. Recoveries and standard deviation for MAE and USE extraction of *Pinus pinaster* Ait. needles (1 g and 5 g) spiked with 20 ng/g and 100 ng/g of each of the 16 EPA PAHs, using alumina cartridges for clean-up.

common regardless of the multi-analyte procedures, once it is not easy to quantify with the same accuracy a group of compounds with different characteristics, namely in terms of polarity and volatility. Some important parameters have to be carefully considered, such as the extracting solvent. Currently, mixtures of solvents are used in order to widen the spectrum of polarity of the extraction. Hexane:dichloromethane and hexane:acetone are very common. For MAE it is important that the solvents have a high dissipation factor in order to allow a proper excitation by the microwaves, transformed in thermal energy [34]. Acetone has such characteristic, but dichloromethane is preferable during reconcentrations due to its lower boiling point [35], thus allowing faster evaporation steps. For airborne particulate matter, Karthikeyan and Balasubramanian [36] proved the advantages of hexane:acetone (1:1), as did Yusà et al. [37] for naphthalenes in semipermeable membrane devices. For USE, Hollender et al. [38] found similar results for acetone and dichloromethane when extracting PAHs from soils and Capuano et al. [29] preferred hexane alone to extract PAHs from pine needles. Interestingly, the same authors used hexane:dichloromethane (1:1) for soils and sediments, extracted by accelerated solvent extraction (ASE). As it can be seen, there is not an "ideal" extracting solvent. Comparing several extraction procedures, Piñeiro-Iglesias et al. [39] used hexane:acetone (1:1) to extract PAHs from SRM 1650 diesel particulate matter and found similar recovery results for Soxhlet, USE and MAE. Still, they came upon the same lower recoveries for the HMW PAHs.

The clean-up is also a crucial factor, once the complexity of some matrices can lead to difficulties in the quantification. Coelutions and subsequent lack of proper selectivity are common when analyzing PAHs, since the ions formed by GC–MS in EI mode have sometimes masses comparable those of other matrix compounds (humic acids, sulphur, fats, waxes or oils) [40]. This can explain the sporadic high recoveries for some PAHs. On the other hand, inefficient ionisation can be another reason for some of the lower recoveries found. The clean-up chosen in this study is commonly used and has proven its efficiency in previous studies [15,33] but other solutions would be possible, such as additional SPE [13] or gel permeation chromatography [10], despite the risk of other types of losses. Nevertheless, and unfortunately, as stated by Jánská et al. [41] the selectivity of both "classic" and "novel" extraction procedures can be low, as in most cases increased recovery accompanies higher quantities of matrix interferences.

In terms of quantification itself, isotope-dilution is suggested for most complex matrices instead of the widespread internal standard approach [40], given the improved recoveries. The recoveries of the surrogate standards can also be an important factor, although this evaluation required the comparison the peak areas of the samples with the peak areas obtained in the calibration. This is not the procedure used for the assessment of the recovery results for the target compounds (internal standard method). However, and despite this limitation, the recoveries of the surrogate standards were calculated. Average recoveries of 89%, 99% and 97% were found for Ace-d_{10}, Phen-d_{10} and Chry-d_{12}, respectively. Naphthalene-d_8 had poorer and inconsistent values (between 7% and 102%, average 53%), which may reflect the difficulties verified in the analysis of naphthalene (only compound quantified by Naph-d_8). Regarding perylene-d_{12}, a more consistent, yet rather low recovery results were found, between 24% and 58%, with 46% average. This can also justify the lower overall recoveries obtained for the six higher molecular PAHs.

The results show other particular aspects. Recoveries are very similar when comparing MAE to USE. The only consistent differ-
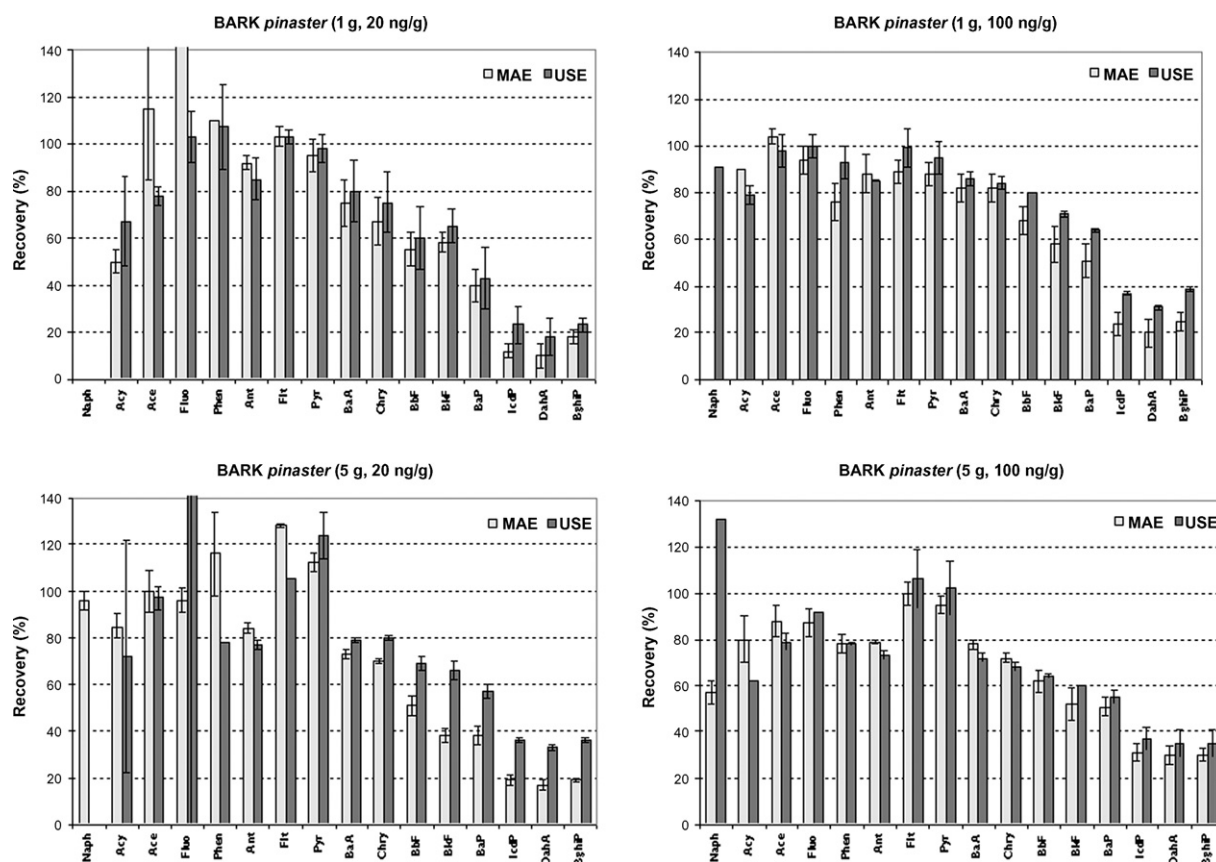
Fig. 3. Recoveries and standard deviation for MAE and USE extraction of *Pinus pinaster* Ait. bark (1 g and 5 g) spiked with 20 ng/g and 100 ng/g of each of the 16 EPA PAHs, using alumina cartridges for clean-up.

ence occurred for the HMV PAHs with 5 g and 100 ng/g, when MAE produced better results (about 20% more). However this fact can be a consequence of instrumental uncertainties rather than a specific operative reason. Furthermore, for the less sample mass and spiking concentration, the overall results were worse, probably due to the natural increase in method uncertainty when the lowest concentrations are reached. Some problems were detected in the quantification of naphthalene, which showed some inconsistency. Besides the poor recoveries for naphthalene-d_8, naphthalene is also the most volatile of all the PAHs under study and the risk of losses is amplified, especially when the methodology employs evaporation steps [39]. Cheng [42] reported recoveries of naphthalene dropping from almost 90% to less than 65% when using a rotary evaporator to reduce a volume of 300 mL–1 mL. The author suggests reducing the volume to a minimum of 3 mL, but operating factors may advise against this procedure once extra flask or vial transferences may also increase the global losses. Still, this problem occurred mostly in the 1 g experiments.

Fig. 3 shows the recoveries of PAHs in bark samples.

Given the diverse structure and composition of needles and bark, different results were expected. However, the patterns seen for needles were also found for bark. In general, there was a slight overall decrease in the recoveries for the LMW PAHs, especially when extracting 5 g of sample. Matrix effects play a crucial role in the recovery of PAHs, since a greater amount of sample yielded lower recoveries. The two extraction procedures are again reproducible, with a slight advantage for USE in this case, namely for the HMV PAHs. The problems with naphthalene were noticed again.

It is clear that in terms of validation alone, both needles and bark of *P. pinaster* Ait. are fit for PAHs level assessment, given the similarity of the methodology performances. Plus, isotope dilution

quantification allowed the correction of some inconsistencies in the recovery results for naphthalene and the low recoveries found for high molecular PAHs.

3.2.2. Extraction of Pinus pinea L.

The same experiments (1 g and 5 g; 20 and 100 ng/g PAH spiking level) were performed with samples of *P. pinea* L. The results of the recovery assays are not displayed since they were similar to *P. pinaster*, showing the same merits and problems.

However, for the needle samples a clear difference was now noticed between the assays with 1 g and 5 g, in favour of the latter. Up to a point where matrix interferences are very influential, having more initial sample usually produces better identification and quantification results. In a previous work with samples of this species [15] good results were found for USE with up to 10 g of sample. On the other hand, attempts with the same amount of *P. pinaster* needles proved unfruitful due to the amount of matrix interferences which made compound identification virtually impossible under the specified operative conditions. As mentioned before, the morphological and physiological differences between different conifer species can account for the difference between the two species. In *pinaster*, matrix interferences are stronger and fewer amounts of needle samples are necessary.

Taking the 5 g assays, the results are good and the decrease for the HMVs is clearly noticed only for IcdP, DahA and BghiP, with fewer than 40% recovery for either extraction method. In fact, the similarity between MAE and USE is even stronger in this case. Naphthalene only presented problems in the 1 g, 20 ng/g assays.

The trends for bark samples are also in agreement with the ones presented for *P. pinaster*. Good recoveries except for the HMV PAHs, problems in the quantification of naphthalene (in this case only

Table 3
Concentration of the 16 EPA PAHs in naturally contaminated pine needle (need) and bark samples collected from four different locations (extracted by MAE)

Compound	Porto		Bragança		Quintãs		Vide		Barcelona		Vic		El Prat		Montseny	
	Need	Bark	Need	Bark	Need	Bark	Need	Bark	Need	Bark	Need	Bark	Need	Bark	Need	Bark
Naph	19	7	29	25	23	69	n.a.	n.a.	70	7	37	10	29	9	n.a.	8
Acy	7	1	38	1	57	1	4	1	20	1	6	3	6	1	4	3
Ace	9	8	19	5	37	9	35	6	41	6	16	7	26	5	23	5
Fluo	38	7	126	2	161	6	20	3	57	5	19	50	32	4	24	17
Phen	273	41	648	20	799	24	84	7	171	16	64	42	181	7	54	17
Ant	13	2	47	1	29	1	7	1	9	1	5	2	4	1	2	1
Flt	104	23	253	11	268	24	21	4	49	10	30	20	56	10	14	8
Pyr	89	13	49	9	119	12	21	3	140	12	51	32	49	8	58	9
BaA	5	2	12	2	9	2	99	1	10	2	10	3	10	1	4	1
Chry	18	4	43	4	37	5	9	1	24	2	19	10	29	3	4	3
BbF	7	3	5	2	5	3	4	1	14	7	6	2	10	3	5	2
BkF	2	1	2	1	2	1	1	1	5	2	2	2	4	1	2	1
BaP	1	1	2	1	1	1	1	1	2	3	4	2	2	1	4	2
IcdP	1	1	1	1	1	1	1	1	2	2	2	2	2	1	7	3
DahA	n.d.	n.d.	1	1	1	n.d.	1	1	1	n.d.	3	2	2	1	10	4
BghiP	2	1	1	1	1	1	1	1	4	4	2	2	2	1	7	3
Σ PAH	590	116	1276	85	1552	159	310	31	619	81	277	189	446	58	221	85

n.a. – not available; n.d. – not detected. All values in ng/g (dry weight).

for MAE samples) and similarity of responses for MAE and USE, although it is perceptible that for the 5 g, 20 ng/g assay the latter presents better results for the HMV PAHs.

These sets of results show the overall suitability and versatility of two different extraction methods to quantify PAHs from pine trees and of two pine species to act as biomonitors for the aforementioned pollutants. Recovery of PAHs is possible at low and high concentrations, with relatively small sample amounts. The next step would be to validate such findings for field samples.

3.3. Field study

In order to assess the application of MAE and USE to the detection of PAHs in naturally contaminated samples and to compare both pine species and, especially, the differences between needles and bark in the same tree, eight sampling sites from different socio-environmental locations were chosen: four in Portugal (all *P. pinaster* Ait. trees) and four in Catalonia, Spain (all *P. pinea* L. trees). All target PAHs were identified (except for naphthalene in two occasions) and the individual and total concentrations (dry weight) are presented in Tables 3 and 4, for MAE and USE, respectively.

One fundamental aspect stands out from the analysis of the results on both tables: the total concentration of PAHs is clearly higher in needles than in bark, considering the same tree and the sum of all 16 PAHs. Furthermore, the most volatile PAHs were more frequently detected and at higher concentrations, thus indicating atmospheric deposition as their major source. In the field, the differences in structure between needles and bark seem to play an important role. To our knowledge, there is no evidence of comparative studies between the ability of needles and bark for the accumulation of PAHs. Such data was only reported for heavy metal contamination by Sameka-Cymerman et al. [21]. However, their study shows that in some cases, different heavy metals have different affinities towards needles and bark. In the case of PAHs and other airborne organic pollutants, pine needles have been recognized as good biomonitors by several studies reported in literature. For bark, this is not the case, and studies mainly focus on heavy metal accumulation. The surface of bark is very porous and almost inert in the presence of organic and organic substances [17] and the accumulation of contaminants is mainly by deposition from the atmosphere onto the outer layer [16], which also occurs for needles. However, being inert, bark does not have the same means of "entrapment" for organic pollutants. Although some materials of the bark, namely suberin, favour the partitioning of organochlorine pollutants [43], the waxy surface of the needles composed mainly of fatty acids (methyl esters), polyesters, paraffins [44] and sec-

Table 4
Concentration of the 16 EPA PAHs in naturally contaminated pine needle (need) and bark samples collected from four different locations (extracted by USE)

Compound	Porto		Bragança		Quintãs		Vide		Barcelona		Vic		El Prat		Montseny	
	Need	Bark	Need	Bark	Need	Bark	Need	Bark	Need	Bark	Need	Bark	Need	Bark	Need	Bark
Naph	66	27	22	21	27	12	34	n.a.	135	10	50	10	58	8	n.a.	7
Acy	7	1	35	1	65	1	4	1	24	1	7	1	12	1	3	2
Ace	7	6	17	4	27	4	10	4	47	3	17	4	59	3	13	3
Fluo	45	15	149	4	210	4	18	2	73	2	37	14	70	1	23	8
Phen	276	72	854	26	955	31	80	4	189	14	71	18	181	7	30	15
Ant	16	2	65	1	35	1	4	n.d.	9	1	4	1	6	1	1	1
Flt	138	38	289	13	271	25	23	4	64	8	32	12	87	8	9	5
Pyr	54	20	48	10	124	12	20	2	174	9	70	14	95	7	24	5
BaA	5	2	14	2	9	2	4	1	11	2	10	2	8	1	7	1
Chry	17	5	34	3	39	5	9	1	32	2	21	2	28	3	7	1
BbF	6	3	5	2	4	3	2	1	16	6	7	3	7	3	13	3
BkF	4	1	1	1	1	1	1	1	5	2	4	1	2	1	15	2
BaP	4	1	2	1	1	1	1	n.d.	4	2	4	2	2	1	15	3
IcdP	3	1	1	1	1	1	1	n.d.	3	1	4	1	2	1	4	1
DahA	2	1	1	1	1	1	1	1	n.d.	1	4	1	2	1	35	6
BghiP	4	2	1	1	1	1	1	1	5	4	4	1	2	1	35	7
Σ PAH	655	196	1537	90	1773	103	213	22	790	66	347	90	620	48	235	70

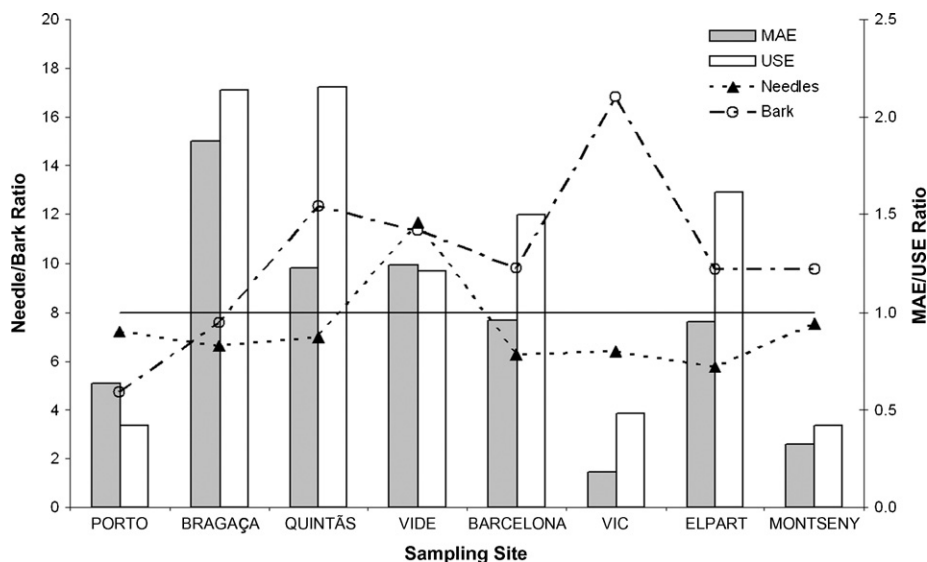n.a. – not available; n.d. – not detected. All values in ng/g (dry weight).

Fig. 4. Needle/bark Σ PAHs ratio (left side axis) for MAE (grey bars) and USE (white bars) and MAE/USE Σ PAHs ratio (right side axis) for needles (black triangle line) and bark (white circle line).

ondary alcohols [45] is probably more effective in trapping such contaminants. The different behaviour between needles and bark is elucidated in Fig. 4. Referring to the left hand side axis, it can be seen that the ratio needles/bark is always above 2 for both MAE and USE (except in Vide with MAE) and easily reaches values of 10 or higher. These evidences favour needles over bark as biomonitors of PAHs.

Still, further elements can be analyzed. Also noticeable is the similarity between the results of the two extraction strategies, especially for needles. In fact, ranking the sampling sites from the most to the least contaminated, we have, for MAE: Quintãs > Bragança > Barcelona > Porto > El Prat > Vide > Vic > Montseny. For USE the sequence is almost the same, only with Vide in the last position. In terms of absolute values the differences are negligible, as can be seen on the right hand side axis in Fig. 4. Taking the ratio 1 as reference, corresponding to the same value for both extraction procedures, USE is slightly favoured in terms of total PAHs concentration, but with a ratio very close to 1. The exception is Vide, where MAE obtained a higher value, but since this is one of the least contaminated sites, the uncertainty of the analytical methodologies can account for such minor deviations to the general rule. Interestingly, the values for bark are also not so different when comparing MAE and USE, but the PAHs contamination ranking is somewhat different from the one seen for needles: Vic > Quintãs > Porto > Bragança > Montseny > Barcelona > El Prat > Vide for MAE and USE almost the same, with Quintãs preceding Porto and Vic instead. Again the structural differences of the two materials can explain the diverse behaviour, although for bark the levels of PAHs found are so much lower that the method uncertainty is probably the key factor. Still, seemingly low concentrations for bark are also reported by other authors. Schulz et al. [17] found values for BaP of 9.14 ± 1.08 ng/g on *P. sylvestris* L. in a heavily polluted area and Di Lella et al. [18] in a study performed in Kabul could only identify four of the 16 EPA PAHs (Phe, Ant, Flt and Pyr), with total concentrations between 59.4 and 161.2 ng/g. Fig. 4 also demonstrates that for bark MAE extracted higher concentrations than USE, except for Porto and Bragança. It is clear that needles should be considered more reliable as biomonitors for PAHs and that both MAE (with an adapted domestic microwave oven) and USE are equally fit to perform the extraction step successfully.

Taking a closer look into the degree of contamination of each site (needles only) for USE (since it presents the highest concentrations of total PAHs), the ranking follows the expectations considering that urban sites should be more polluted than rural or mountain sites. The exceptions are two flagrant cases: Quintãs (a rural site) and Bragança (a small interior city), which presented by far the heaviest contaminations. A good explanation could be that in the first case, heavy road construction had been occurring for some time and that the tree in the second case is placed right next to a very busy gas station. The other results seem to follow the socio-environmental trends. Porto and Barcelona, two mass urban sites have very similar results with slightly higher concentrations for the bigger city, but closely followed by El Prat. Although being a seaside location, it is surrounded by the Barcelona airport, which can enhance the levels of contamination. The small interior city of Vic follows the trend and the two more remote mountain sites (Montseny and Vide) are the least contaminated. Phenanthrene was the most abundant PAH in all needle samples except Montseny and also in the majority of the bark samples. Such evidence is widely confirmed in literature and is probably due to its stability in pine needles [10,11].

The values or ranges of contamination by PAHs reported in literature for pine needles are similar to the levels presented in this study. A previous work by the same authors with *P. pinea* L. needles revealed the same trends of contamination, although with slightly lower levels [15]. For *P. pinaster* Ait. Piccardo et al. [13] reported values between 21.88 ng/g in a remote site and 817.41 ng/g near a heavy traffic road (dry weight) and also that values for *Pinus nigra* Arn. in rural areas seem to be, on average, 2.3 times higher than for *P. pinaster* Ait. Regarding other pine species, Tremolada et al. [7] found a range of 19–3091 ng/g and an average of 323 ng/g (dry weight) in UK rural sites, whereas Migaszewski et al. [46] obtained values between 78 and 216 ng/g for the 16 EPA PAHs plus perylene in forest sites, both for *P. sylvestris* L. For the same PAHs, Hwang et al. [10] found values of 62 and 166 ng/g for two rural sites, 204, 243 and 384 ng/g in semi-urban and urban sites and 1126 ng/g in an industrial site (all dry weight and for *Pinus densiflora* Siebold & Zucc., *maximartinezii* Rzed. and *taeda* L.). Finally, Liu et al. [14] reported a range between 280 and 3000 ng/g (dry weight) of the 16 EPA PAHs minus naphthalene in *Pinus massoniana* Lamb from heavily populated regions of China.

4. Conclusions

Two different extraction strategies (MAE and USE) were tested in the extraction of the 16 EPA PAHs from pine trees of two different species (*P. pinaster* Ait. and *P. pinea* L.) and obtained very similar recovery results for both needles and bark. Values between 70 and 130% were reached in the majority of the cases. However, for indeno[1,2,3-*cd*]pyrene, dibenzo[*a,h*]anthracene and benzo[*ghi*]perylene recoveries were all below 50% but these low results were compensated using isotope dilution quantification. Limits of detection were globally below 0.2 ng/g. Both methods were considered reliable to perform the extraction under the given experimental conditions.

The field study with samples from eight natural sites revealed levels of contamination within the ranges previously reported in literature. Furthermore, it showed that needles are more suitable biomonitors for PAHs than bark, reaching concentrations from 2 to 17 times higher. Both MAE and USE displayed similar results for both matrices separately.

References

[1] S. Simonich, R. Hites, Environ. Sci. Technol. 29 (1995) 2905.
[2] L.H. Lim, R.M. Harrison, S. Harrad, Environ. Sci. Technol. 33 (1999) 3538.
[3] A.M. Mastral, M.S. Callén, Environ. Sci. Technol. 34 (2000) 3051.
[4] R. Fuoco, S. Giannarelli, M. Onor, A. Ceccarini, V. Carli, Microchem. J. 79 (2005) 69.
[5] T. Pena, L. Pensado, C. Casais, C. Mejuto, R. Phan-Tan-Luu, R. Cela, J. Chromatogr. A 1121 (2006) 163.
[6] I. Holoubek, P. Korínek, Z. Seda, E. Schneiderová, I. Holoubková, A. Pacl, J. Tríska, P. Cudlín, J. Cáslavský, Environ. Pollut. 109 (2000) 283.
[7] P. Tremolada, V. Burnett, D. Calamari, K.C. Jones, Environ. Sci. Technol. 30 (1996) 3570.
[8] D.M. Wagrowski, R.A. Hites, Environ. Sci. Technol. 31 (1997) 279.
[9] Q. Lang, F. Hunt, C.H. Wai, J. Environ. Monit. 2 (2000) 639.
[10] H.-M. Hwang, T.L. Wade, J.L. Sericano, Atmos. Environ. 37 (2003) 2259.
[11] X.-P. Wang, T.-D. Yao, Z.-Y. Cong, X.-L. Yan, S.-C. Kang, Y. Zhang, Sci. Total Environ. 372 (2006) 193.
[12] E. Lehndorff, L. Schwark, Atmos. Environ. 38 (2004) 3793.
[13] M.T. Piccardo, M. Pala, B. Bonaccurso, A. Stella, A. Redaelli, G. Paola, F. Valério, Environ. Pollut. 133 (2005) 293.
[14] G. Liu, G. Zhang, J. Li, X. Li, X. Peng, S. Qi, Atmos. Environ. 40 (2006) 3134.
[15] N. Ratola, S. Lacorte, A. Alves, D. Barceló, J. Chromatogr. A 1114 (2006) 198.
[16] L. Harju, K.-E. Saarela, J. Rajander, J.-O. Lill, A. Lindroos, S.-J. Heselius, Nucl. Instr. Methods B 189 (2002) 163.
[17] H. Schulz, P. Popp, G. Huhn, H.-J. Stärk, G. Schüürmann, Sci. Total Environ. 232 (1999) 49.
[18] L.A. Di Lella, S. Loppi, G. Protano, F. Riccobono, Atmos Environ. 40 (2006) 225.
[19] G. Huhn, G. Schulz, H.-J. Stärk, R. Tölle, G. Schüürmann, Water Air Soil Pollut. 84 (1995) 367.
[20] I. Türkan, E. Henden, Ü. Çelik, S. Kivilcim, Sci. Total Environ. 166 (1995) 61.
[21] A. Sameka-Cymerman, G. Koisor, A.J. Kempers, Ecotoxicol. Environ. Saf. 65 (2006) 108.
[22] S.R. Oliva, M.D. Mingorance, Chemosphere 65 (2006) 177.
[23] S. Al-Asheh, Z. Duvnjak, J. Hazard. Mater. 56 (1997) 35.
[24] I.P. Brás, L. Santos, A. Alves, Env. Sci. Technol. 33 (1999) 631.
[25] N. Ratola, C. Botelho, A. Alves, J. Chem. Technol. Biotechnol. 78 (2003) 347.
[26] B. Acemioğlu, Bioresour. Technol. 93 (2004) 99.
[27] M. Barriada-Pereira, E. Graña, E. Fernández, J. Chromatogr. A 1008 (2003) 115.
[28] K.-D. Wenzel, A. Hubert, M. Manz, L. Weissflog, G. Werner Engewald, Schüürmann, Anal. Chem. 70 (1998) 4827.
[29] F. Capuano, B. Cavalchi, G. Martinelli, G. Pecchini, E. Renna, I. Scaroni, M. Bertacchi, G. Bigliardi, Chemosphere 58 (2005) 1563.
[30] K. Ganzler, A. Salgo, K. Valkó, J Chromatogr. A 371 (1986) 299.
[31] A. Hubert, P. Popp, K.-D. Wenzel, W. Engewald, G. Schüürmann, Anal. Bioanal. Chem. 376 (2003) 53.
[32] P. Herbert, A.L. Silva, M.J. João, L. Santos, A. Alves, Anal. Bioanal. Chem. 386 (2006) 324.
[33] E. Martinez, M. Gros, S. Lacorte, D. Barceló, J. Chromatogr. A 1047 (2004) 181.
[34] M. Tomaninová, J. Hajšlová, J. Pavelka Jr., V. Kocourek, K. Holadová, I. Klímová, J. Chromatogr. A 827 (1998) 21.
[35] M. Letellier, H. Budzinski, Analusis 27 (1999) 259.
[36] S. Karthikeyan, R. Balasubramanian, S.W. See, Talanta 69 (2006) 79.
[37] V. Yusà, A. Pastor, M. de la Guardia, Anal. Chim., Acta 565 (2006) 103.
[38] J. Hollender, B. Koch, C. Lutermann, W. Dott, Intern. J. Environ. Anal. Chem. 83 (2003) 21.
[39] M. Piñeiro-Iglesias, P. Lopez-Mahia, E. Vazquez-Blanco, S. Muniategui-Lorenzo, D. Prada-Rodriguez, Polycyclic Aromat. Compd. 22 (2002) 129.
[40] A.R. Boden, E.J. Reiner, Polycyclic Aromat. Compd. 24 (2004) 309.
[41] M. Jánská, M. Tomaninová, J. Hajšlová, V. Kocourek, Anal. Chim. Acta 520 (2004) 93.
[42] C.C. Cheng, Polycyclic Aromat. Compd. 32 (2003) 315.
[43] M.L. Meredith, R.A. Hites, Environ. Sci. Technol. 21 (1987) 709.
[44] H. Kylin, E. Grimvall, C. Oestman, Environ. Sci. Technol. 28 (1994) 320.
[45] E. Stabentheiner, H.W. Pfeifhofer, J. Peters, M.S. Jiménez, D. Morales, D. Grill, Flora 199 (2004) 90.
[46] Z.M. Migaszewski, A. Gałuszka, P. Pasławski, Environ. Int. 28 (2002) 303.

A microband lactate biosensor fabricated using a water-based screen-printed carbon ink

F.J. Rawson [a], W.M. Purcell [b], J. Xu [c], R.M. Pemberton [a], P.R. Fielden [d], N. Biddle [e], J.P. Hart [a],*

[a] Centre for Research in Analytical, Materials and Sensors Science, Faculty of Health and Life Sciences, University of the West of England, Bristol, UK
[b] University of Plymouth, Drake Circus, Plymouth, UK
[c] Centre for Research in Biomedicine, Faculty of Health and Life Sciences, University of the West of England, Bristol, UK
[d] School of Chemical Engineering and Analytical Science, Faculty of Engineering and Physical Sciences, The University of Manchester, Manchester, UK
[e] Gwent Electronic Materials Ltd., Monmouth House, Mamhilad Park, Pontypool, UK

ARTICLE INFO

ABSTRACT

The present study demonstrated for the first time that screen-printed carbon microband electrodes fabricated from water-based ink can readily detect H_2O_2 and that the same ink, with the addition of lactate oxidase, can be used to construct microband biosensors to measure lactate. These microband devices were fabricated by a simple cutting procedure using conventional sized screen-printed carbon electrodes (SPCEs) containing the electrocatalyst cobalt phthalocyanine (CoPC). These devices were characterised with H_2O_2 using several electrochemical techniques. Cyclic voltammograms were found to be sigmoidal; a current density value of $4.2\,mA\,cm^{-2}$ was obtained. A scan rate study revealed that the mass transport mechanism was a mixture of radial and planar diffusion. However, a further amperometric study under quiescent and hydrodynamic conditions indicated that radial diffusion predominated. A chronoamperometric study indicated that steady-state currents were obtained with these devices for a variety of H_2O_2 concentrations and that the currents were proportional to the analyte concentration. Lactate microband biosensors were then fabricated by incorporating lactate oxidase into the water-based formulation prior to printing and then cutting as described. Voltammograms demonstrated that lactate oxidase did not compromise the integrity of the electrode for H_2O_2 detection. A potential of +400 mV was selected for a calibration study, which showed that lactate could be measured over a dynamic range of 1–10 mM which was linear up to 6 mM; a calculated lower limit of detection of 289 μM was ascertained. This study provides a platform for monitoring cell metabolism in-vitro by measuring lactate electrochemically via a microband biosensor.

© 2008 Elsevier B.V. All rights reserved.

1. Introduction

Screen-printing technology has been used extensively to develop biosensors for important biomedical markers [1]. Lactate is an important marker in cell metabolism and the purpose of the current study was to develop an electrochemical biosensor to monitor this metabolite. In order to monitor cell metabolism for a 24 h period it is necessary to produce microband biosensors to avoid any significant perturbation of the system and avoid any adverse effects on the cells. Microelectrodes can be formed by a variety of methods including laser micromachining [2], sonoelectrochemistry [3,4] and photolithography techniques [5]; and by direct cutting as shown by Chang and Zen [6] and Authier et al. [7]. The method of Authier et al. and one previously reported by our group [8] are considered to be the simplest to use and a similar method was used in the present study to produce microband electrodes. Microband electrodes have several advantages over conventional sized electrodes (mm^2) including low ohmic drop, steady-state currents, independence of signal on stir rate and increased signal-to-noise ratios, leading to lower detection limits [9,10].

In this investigation, microband biosensors were fabricated using screen-printed carbon electrodes (SPCEs) produced from a water-based carbon ink. This ink has key advantages over an organic-based ink, as it is less toxic, and does not denature enzymes; this allows for a one-step printing process which greatly reduces the cost of production. This approach has been used successfully to produce glucose biosensors in which glucose oxidase was incorporated into a water-based ink and printed in a one-step print process [11,12]. In the present study, the enzyme lactate oxidase was incorporated directly into the water-based ink, together with the electrocatalyst cobalt phthalocyanine (CoPC).

* Corresponding author. Tel.: +44 1173282469.
  E-mail address: john.hart@uwe.ac.uk (J.P. Hart).

Lactate oxidase catalyses the oxidation of lactate to pyruvate with the production of hydrogen peroxide (H_2O_2). This H_2O_2 can then be followed electrochemically via its electrocatalytic oxidation by CoPC; the reaction scheme can be seen in Eqs. (1) and (2). The reaction mechanism for this process has been previously reported by our group [13,14].

$$2Co^{2+}PC + H_2O_2 \rightarrow 2Co^+PC + 2H^+ + O_2 \qquad (1)$$

$$2Co^+PC \rightarrow 2Co^{2+}PC + 2e^- \qquad (2)$$
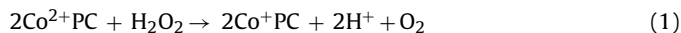
This study demonstrates for the first time that screen-printed carbon microband electrodes, fabricated from water-based ink can readily detect H_2O_2 and that the same ink, with the addition of lactate oxidase, can be used to construct biosensors for lactate measurements. To our knowledge, this is the first report of a microband biosensor for lactate measurements using such an approach.

2. Experimental

2.1. Chemicals and reagents

All chemicals were purchased from Sigma–Aldrich. A 0.5 M sodium lactate stock solution in 0.25 M phosphate buffer pH 7.3 was made up fresh on each experimental day. The supporting electrolyte was phosphate buffer prepared at 0.25 M by combining appropriate amounts of di-sodium hydrogen orthophosphate and sodium di-hydrogen orthophosphate. A stock solution of 0.5 M H_2O_2 solution was made up fresh in 0.25 M phosphate buffer pH 7.3 and any further concentrations of H_2O_2 were prepared via dilution of the stock with phosphate buffer. The lactate oxidase was from *Aerococcus viridans* obtained from Genzyme UK (code 1381).

2.2. Apparatus

All electrochemical measurements were carried out using a dual screen-printed electrode design. A CoPC-SPCE based on an ink code C207070501R2 containing no lactate oxidase and ink code C20727D3 which incorporated the enzyme lactate oxidase (microband lactate biosensors) was used to screen-print electrodes (Gwent Electronic Materials Ltd. (GEM)). These inks were screen-printed on one side of the 0.5 mm thick PVC substrate and a defined area of 9 mm^2 was created using dielectric tape; an Ag/AgCl reference electrode was printed around the working electrode (conventional sized Fig. 1A). Microbands were formed by cutting through the working electrode and insulator layer using scissors, thus exposing the edge of the electrodes (Fig. 1B). The geometrical area of the edge was calculated to be 5.28×10^{-4} cm^2 by multiplying the length (*l*) by the width (*w*). The value of *w* (17.6 μm) was measured using a TESA digital micrometer obtained from Radio Spares, Switzerland. The SPCEs were connected to the potentiostat by two gold clips attached to the ends of two electrical leads. All electrochemical measurements were made with an Autolab Pstat10 potentiostat (Windsor Scientific, Slough) and accompanying software. The electrochemical cell was a Metrohm tapered-wall glass cell with water jacket. The temperature was fixed at 25 °C by means of a circulating water bath (HAAKE D3).

2.3. Cyclic voltammetric measurements of hydrogen peroxide at microband SPCEs

Cyclic voltammograms were obtained by scanning from 0 to +1 V at a scan rate of 20 mV s^{-1} using a 10 ml aliquot of 5 mM H_2O_2. This was done using both plain microband SPCEs which did not contain the electrocatalyst CoPC and microband SPCEs that contained the electrocatalyst (CoPC-SPCEs). This was performed to show that
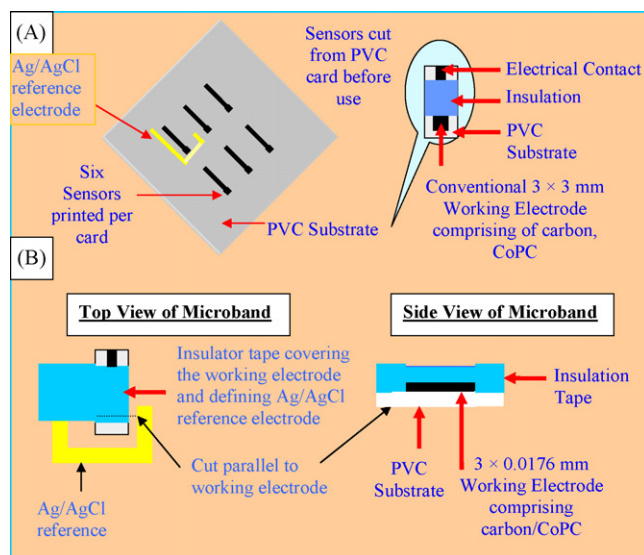

Fig. 1. Schemic diagram of SPCEs used and method to produce (A) conventional and (B) microband electrodes.

the signal generated occurred via the electrocatalytic oxidation of H_2O_2. A scan rate study using 1, 10, 20 and 50 mV s^{-1} for H_2O_2 was carried out to establish whether microelectrode behaviour occurred as indicated by the appearance of steady-state currents [9].

2.4. Cyclic voltammetric measurements of lactate using microband CoPC-SPCEs and microband biosensors

Cyclic voltammograms were obtained by scanning from 0 to +1 V at a scan rate of 20 mV s^{-1} using a 10 ml aliquot of 5 mM lactate solution. These voltammograms were generated at, microband CoPC-SPCEs without lactate oxidase, and microband biosensors containing both CoPC and lactate oxidase (microband biosensors).

2.5. Effect of stirring on the amperometric response for H_2O_2 using microband CoPC-SPCEs

Amperometry was used to obtain current versus potential plots in quiescent and stirred solution containing 5 mM H_2O_2 and blank 0.25 M pH 7.3 phosphate buffer solutions. This was done by transferring a 10 ml aliquot of H_2O_2 solution or blank solution to the cell, stepping the potential from open circuit to 0 V, then stepping from 0 to +0.1 V and continuing in this way to a final potential of +1 V. The voltammograms constructed using the mean value from triplicate measurements were used to ascertain the effect of stirring on the response and also, to deduce the potential to be used in later amperometric studies.

2.6. Calibration study on H_2O_2 using chronoamperometry with microband CoPC-SPCEs

Standard solutions containing 0.07, 0.21, 0.7, 2.1 and 7 mM H_2O_2 were prepared in 0.25 M pH 7.3 phosphate buffer. Chronoamperograms were then recorded using a fresh microband CoPC-SPCE and 10 ml aliquots of each H_2O_2 solution. Each solution was examined by inserting the electrode and leaving at open circuit for 5 s before applying a potential of +400 mV for a period of 100 s. One electrode was used for all solutions examined, and this procedure repeated using a further four electrodes to give a total of five replicate measurements at each concentration.

2.7. Optimisation of the potential for amperometric measurements of lactate using microband biosensors

In order to deduce the optimum applied potential for calibration studies, amperometric measurements were made at various potentials in lactate and blank buffer solutions. The microband biosensors were placed in 5 mM lactate solution for 500 s for the first two potential steps then 2000 s for the succeeding application of each potential step up to +1 V. The resulting data was used to plot a voltammogram from which the potential to be used in amperometric studies was deduced. It should be added that the time taken to reach a steady current is considerably less at the lower potentials, i.e. below +200 mV; consequently shorter analysis times are required for the current data sets in this region.

2.8. The effect of pH on the response generated at microband biosensors for lactate determination

The effect of pH was investigated over the pH range 6–8 at a constant phosphate buffer strength of 0.25 M with microband biosensors. A calibration study was performed by adding 40 μl aliquots of a 0.25 M solution of lactate to a 10 ml solution of 0.25 M phosphate buffer giving 1 mM additions of lactate. A fixed potential of +400 mV versus a Ag/AgCl reference electrode was used throughout the study under quiescent conditions.

2.9. The Effect of buffer strength on the response generated at microband biosensors for lactate determination

The effect of buffer strength over the range 0.1, 0.25, and 0.5 M pH 7.3 phosphate buffer was investigated with microband biosensors. Cyclic voltammograms were obtained by scanning from 0 to +1 V at a scan rate of 20 mV s^{-1}, using a 10 ml aliquot of 5 mM lactate in the different buffer; blank buffers without the lactate present were also examined under the same conditions. This was done in triplicate using a fresh electrode for each voltammogram.

2.10. Calibration study using amperometry with microband biosensors for lactate detection

Calibration studies were carried out with microband biosensors by making 40 μl additions of a 0.25 M solution of lactate to a 10 ml solution of 0.25 M pH 7.3 phosphate buffer containing 0.1 M NaCl equating to 1 mM additions of lactate. Amperograms were recorded using a fresh microband biosensor for each calibration curve. After switching to +400 mV for a period 1000 s, to ensure that a steady-state was reached, lactate additions were made every 300 s up to a 10 mM lactate concentration.

3. Results and discussion

3.1. Cyclic voltammetric measurements of hydrogen peroxide at microband CoPC-SPCEs and plain microband SPCEs

An initial cyclic voltammetric study was performed to establish whether H_2O_2 could be measured using the new microband CoPC-SPCEs. The voltammogram is shown in Fig. 2IA for H_2O_2 at this electrode and clearly exhibits an electrocatalytic oxidation signal at approximately +0.5 V (Fig. 2I(A); the lack of a peak on the voltammogram obtained in the plain buffer solution (Fig. 2I(B)) demonstrates that H_2O_2 is responsible for the response [8]. We also carried out the equivalent experiment but with microband SPCEs that contained no electrocatalyst; clearly no signal for H_2O_2 was observed (Fig. 2I(C)). From these results it can be deduced
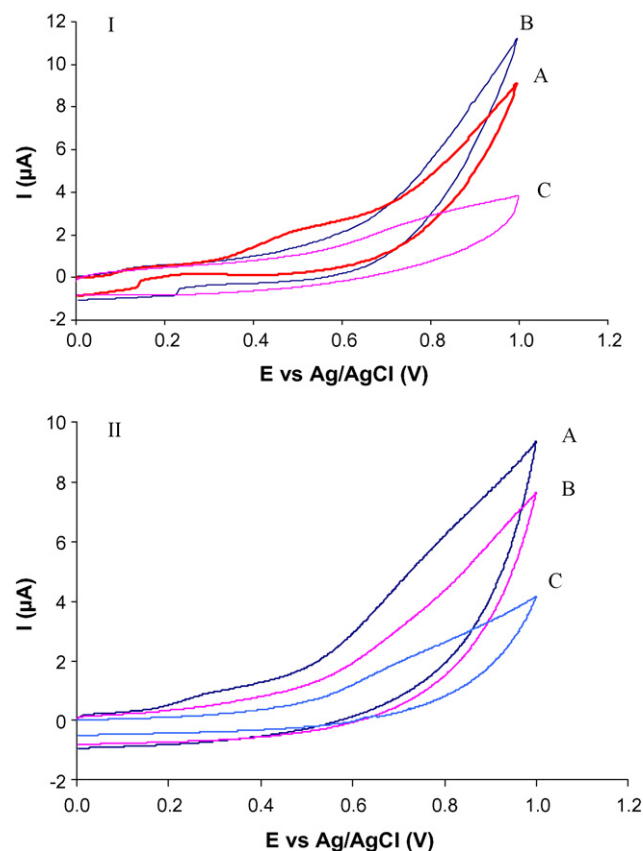

Fig. 2. (I) Typical cyclic voltammogram obtained using a microband CoPC-SPCE (A and B): for 5 mM H_2O_2 (A) and plain 0.25 M phosphate buffer pH 7.3 (B). A typical voltammogram obtained using microband SPCEs (no electrocatalyst) for 5 mM H_2O_2 (C). (II) Typical cyclic voltammograms obtained for 5 mM lactate using microband biosensors (A and B): for 5 mM lactate (A) and plain 0.25 M phosphate buffer pH 7.3 (B). Typical voltammograms are also shown obtained using microband CoPC-SPCEs (C) that contained no enzyme obtained for 5 mM lactate.

that H_2O_2 is catalytically oxidised through Co^{2+}/Co^+ redox couple [8,14]. It is also interesting to note that the new design microband CoPC-SPCEs gave a current density value calculated from Fig. 2I(A) of 4.2 mA cm^{-2} compared to 290 μA cm^{-2} for conventional sized CoPC-SPCEs; this is due to the more efficient mass transport at the microband electrode surface, where radial diffusion is occurring, compared to the planar diffusion which is seen at the conventional sized electrode surface. Such high current density values have been seen previously for screen-printed tubular microband electrodes [8].

A scan rate study was performed with the new microband electrodes and the resulting voltammograms and steady-state currents are plotted in Fig. 3. Voltammograms in Fig. 3A show steady-state currents are obtained for the electrocatalytic oxidation of hydrogen peroxide at a CoPC-SPCE microband electrode over the range 1–50 mV s^{-1}. This behaviour is indicative of mass transport by radial diffusion. This supports our earlier conclusion regarding the mechanism of diffusion control, where current density of 4.2 mA cm^{-2} was calculated compared to 290 μA cm^{-2} seen for a conventional sized electrode. The plot of mean steady-state currents (Fig. 3B) suggests that mass transport does not occur by planar diffusion as currents would be expected to increase with the square root of scan rate. However, the signals do not appear to be completely independent of scan rate, which may indicate a mixed mechanism of mass transport involving both radial and planar diffusion.
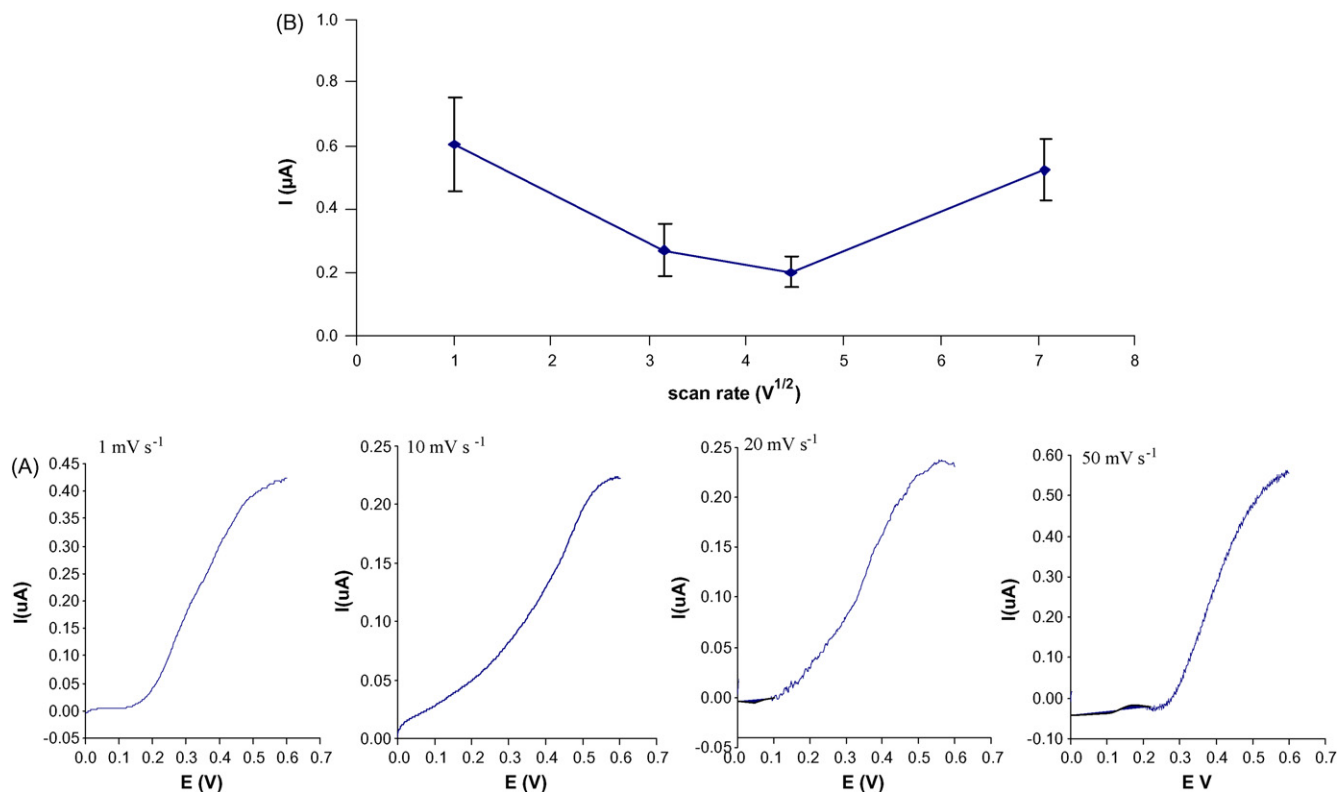
Fig. 3. Typical voltammograms (A) and mean steady-state currents (B) obtained at various scan rates: 1, 10, 20 and 50 mV s^{-1} for 5 mM $H_2O_2 \pm 1$ S.D. ($n = 3$).

3.2. Effects of stirring on the amperometric response for H_2O_2

In order to further examine the mass transport behaviour of H_2O_2 at a microband CoPC-SPCE, amperometric studies were performed under quiescent and hydrodynamic conditions over the potential range +0.1 to +1 V. The resulting voltammograms are shown in Fig. 4. It can be seen that there is no significant difference in the maximum currents observed at around +0.5 V. This confirms that radial diffusion is the predominant mechanism of H_2O_2 transport to the electrode.

3.3. Calibration study on H_2O_2 using chronoamperometry with microband CoPC-SPCEs

The next stage of the investigation was to establish whether these microband electrodes could form the basis for the proposed

lactate biosensors and an applied potential of +0.4 V was used in this study. It should be mentioned that this potential was selected for calibration rather than the potential where current is at a maximum for two reasons: first, less interference will occur at the lower potentials; second, we wish to avoid the possibility of the irreversible reaction which is known to occur with this electrocatalyst at potentials around +0.5 to +0.6 V. This reaction results in a loss of sensitivity over time and has been reported previously [8,14]. Fig. 5 shows the chronoamperograms obtained for several different concentrations of H_2O_2 and it is apparent that steady-state currents were obtained with these devices, as is expected when radial diffusion predominates. The magnitude of the signals was shown to be directly proportional to the concentration of H_2O_2 over the range
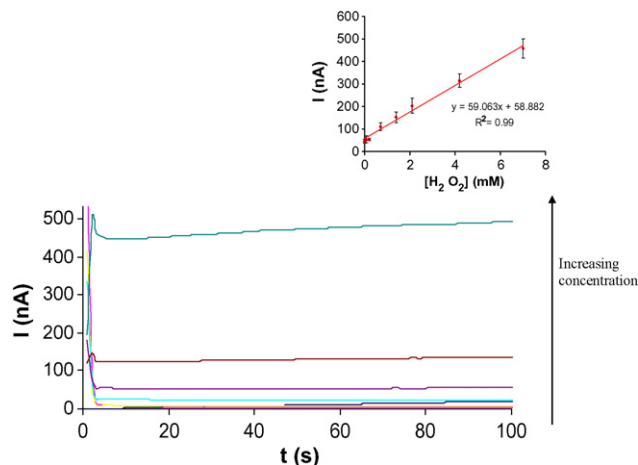

Fig. 4. Voltammograms for 5 mM H_2O_2 obtained by stepping the potential from open circuit voltage in +100 mV steps in stirred (♦) and quiescent (▲) solution using microband CoPC-SPCE electrodes. The supporting electrolyte was 0.25 M phosphate buffer at pH 7.3 and blank voltammograms have been subtracted in each case.

Fig. 5. Typical chronoamperograms obtained for various H_2O_2 concentrations and calibration graph (inset) obtained using an applied potential of +400 mV error bars ± 1 S.D. ($n = 5$).
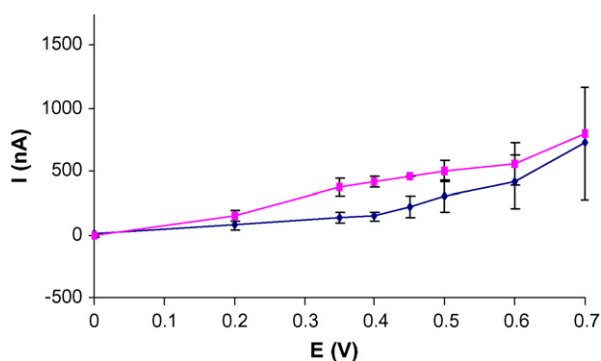
Fig. 6. Voltammograms obtained by stepping the potential from open circuit voltage in +100 mV steps in 5 mM lactate (■) or buffer solution (▲) using microband lactate biosensors.

studied as seen in the inset in Fig. 5. From this plot the linear range was deduced to be 0.07–7 mM H_2O_2, with a sensitivity value of 59 nA mM^{-1} and the theoretical limit of detection calculated via twice the standard deviation of the noise (0.44 nA) divided by the sensitivity gave a lower limit of 15 μM. Typical coefficients of variation were obtained in the range 9–18.5%. These results indicated that the devices could readily form the basis of a lactate microband biosensor.

3.4. Cyclic voltammetric measurements of lactate at microband CoPC-SPCEs and microband biosensors

Cyclic voltammograms were obtained with a 5 mM lactate solution and blank pH 7.3 0.25 M phosphate buffer using microband lactate biosensors fabricated from WB-CoPC-SPCEs. An oxidation signal for lactate was seen at +300 mV (Fig. 2II(A)) that is not apparent in the blank buffer solution (Fig. 2II(B)). Cyclic voltammograms were also obtained for lactate with microband CoPC-SPCEs without enzyme; the resulting voltammogram did not show a peak at +300 mV (Fig. 2II(C)). These results demonstrate that it is not possible to detect lactate by direct oxidation at the CoPC-SPCE but that it is readily measured with a microband lactate biosensor; the latter operates by the detection of H_2O_2 produced by lactate oxidase.

3.5. Optimisation of applied potential for the lactate microband biosensor

Fig. 6 shows the voltammograms obtained with the microband biosensor using a 5 mM lactate solution at pH 7.3 or plain buffer solutions. As mentioned earlier, the lactate response results from the electrocatalytic oxidation of H_2O_2 which is enzymatically produced during the enzymatic oxidation of lactate to pyruvate by the lactate oxidase. The voltammetric profile is similar to that obtained for H_2O_2 with plain microband CoPC-SPCEs (Fig. 4). This indicates that there is no significant effect on the response when the enzyme is incorporated into the ink. For analytical purposes a potential of +400 mV was selected for calibration studies.

3.6. The effect of pH and buffer strength on the current response generated at microband biosensors for lactate determination

The effect of pH on biosensor performance can be seen in Fig. 7; clearly maximum sensitivity was obtained at pH 8 but the largest linear range was obtained at pH 6. pH 7 offered intermediate linear range and sensitivity. This is perhaps expected, as the optimum has been reported to be pH 6.4 [15]. Although this behaviour is interesting, our proposed application for microband biosensors is to monitor cell metabolism in culture medium of pH 7.3. Conse-
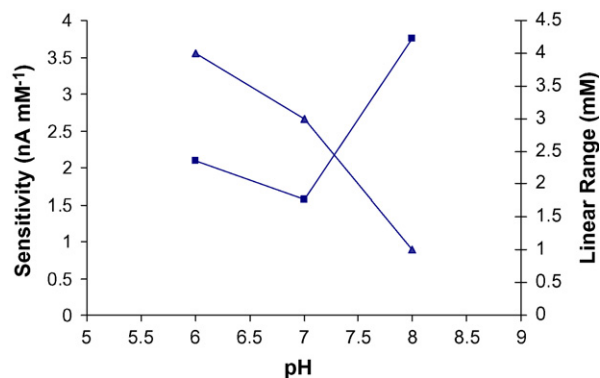

Fig. 7. The effect of pH on microband biosensor performance, showing both lactate sensitivity (squares) and linear range (triangles). Data obtained from amperograms obtained from fixed potential current curves obtained using standard additions of 1 mM lactate.

Table 1
Table of steady-state currents obtained for cyclic voltammograms recorded in 5 mM lactate solutions at different ionic strengths

	Ionic strength of phosphate buffer (M)		
	0.125	0.25	0.5
Ip (μA)	0.248	1.518	0.12
	0.322	1.289	0.13
	0.348	1.287	0.1
Mean	0.31	1.36	0.12
Standard deviation	0.05	0.13	0.02
Coefficients of variation (%)	16.9	9.7	13.1

quently, we have selected pH 7.3 for further studies. However, for some applications which do not involve live cells such as milk analysis, a biosensor operating at a pH of 6 may be of benefit. The effect of buffer strength on the steady-state current generated for cyclic voltammograms obtained with 5 mM lactate solution can be seen in Table 1. The buffer strength that yielded the highest steady-state currents was 0.25 M phosphate buffer; this concentration was used in further studies.

3.7. Calibration studies for lactate at microband screen-printed biosensors

Fig. 8 shows a typical amperometric response for lactate additions to a microband biosensor immersed in 0.25 M pH 7.3 phosphate buffer solution. The additions correspond to added con-
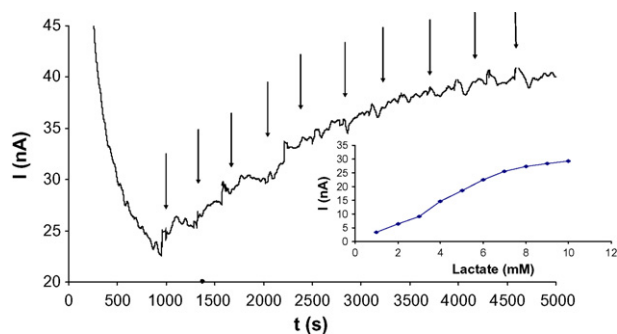

Fig. 8. Typical amperometric responses obtained for standard lactate additions using an applied potential of +400 mV with microband lactate biosensors and the resulting calibration graph (each data point is the mean of current value obtained at five calibration studies).

centrations of 1 mM. It is evident that, even though solutions were not stirred, the responses to lactate were reasonably rapid and steady-state currents were obtained; lactate could be measured over the range 1–10 mM. A linear range was obtained up to 6 mM lactate ($y = 3.6258x$) giving a R^2 value of 0.98 and an intra-electrode coefficient of variation over this range of 9% ($n = 6$). A sensitivity value over this range of 3.63 nA mM^{-1} was obtained with a theoretical lower detection limit of 289 μM based on three times the mean noise. The sensors were stable for up to two weeks. These results compare relatively well to other published data on macrosized biosensors incorporating lactate oxidase to detect lactate with values recorded recently in the literature of 4.4 μM [16], 10 μM [17], and 300 μM [18].

4. Conclusions

It has been shown that microband SPCEs fabricated using a water-based screen-printing ink incorporating CoPC gave a well-defined electrocatalytic response for H$_2$O$_2$. The resulting voltammogram was similar to that previously described for a tubular microband electrode, fabricated using an organic-based carbon ink [8]. Evidence that our electrodes behave as microband devices may be deduced by the higher current density compared to conventional planar screen-printed electrodes. This behaviour suggests that a significant proportion of the current is generated by radial diffusion. Further evidence to support this diffusion behaviour was demonstrated by the observation that the voltammetric response did not increase proportionally with the square root of scan rate. The microband CoPC-SPCEs could be used to detect H$_2$O$_2$ over a wide concentration range from 70 to 7000 μM and significantly, steady-state currents were obtained by chronoamperometry.

It was demonstrated that our microband lactate biosensor could readily measure the analyte over a linear range 1–6 mM (Fig. 8). This study represents the first report on the manufacture and use of microband biosensors based on screen-printing technology for lactate determination. These lactate microband biosensors will form the platform for future work in measuring cell metabolism, via the release of lactate, in quiescent solutions over extended incubation times.

References

[1] J.P. Hart, A. Crew, E. Crouch, K.C. Honeychurch, R.M. Pemberton, in: S. Alegret, A. Merkoci (Eds.), Comprehensive Analytical Chemistry, vol. 49, 2007, p. 497 (Chapter 23).
[2] C. Ball, D.L. Scott, J.K. Lump, S. Daunert, J. Wang, L.G. Bachas, Anal. Chem. 72 (2000) 497.
[3] K.A. Law, S.P.J. Higson, Biosens. Bioelectron. 20 (2005) 1914.
[4] J. Pritchard, K. Law, A. Vakurvov, P. Millner, S.P.J. Higson, Biosens. Bioelectron. 20 (2004) 765.
[5] J. Burmeister, M. Palmer, G.A. Gerhardt, Biosens. Bioelectron. 20 (2005) 1772.
[6] J.-L. Chang, J.-M. Zen, Electrochem. Commun. 8 (2006) 571.
[7] L. Authier, C. Groissiord, P. Brossier, Anal. Chem. 73 (2001) 4450.
[8] F.J. Rawson, W.M. Purcell, J. Xu, D.C. Cowell, P.R. Fielden, N. Biddle, J.P. Hart, Electrochim. Acta 52 (2007) 7248.
[9] X. Xie, D. Stueben, Z. Berner, Anal. Lett. 38 (2005) 2281.
[10] A.M. Bond, Analyst 119 (1994) R1.
[11] E. Crouch, D.C. Cowell, S. Hoskins, R.W. Pittson, J.P. Hart, Anal. Biochem. 347 (2005) 17.
[12] E. Crouch, D.C. Cowell, S. Hoskins, R.W. Pittson, J.P. Hart, Biosens. Bioelectron. 21 (2005) 712.
[13] J.P. Hart, A. Crew, E. Crouch, K.C. Honeychruch, R.M. Pemberton, Anal. Lett. 37 (2004) 789.
[14] M.A.T. Gilmartin, R.J. Ewen, J.P. Hart, C.L. Honeybourne, Electroanalysis 7 (1995) 547.
[15] J. Huang, J. Li, Y. Yang, X. Wang, B. Wu, J. Anzai, T. Osa, Q. Chen, Mater. Sci. Eng. 28 (2007) 1071.
[16] D. Lowinsohn, M. Bertotti, Anal. Biochem. 365 (2007) 260.
[17] F. Ghamouss, S. Ledru, N. Ruille, F. lantier, M. Boujtita, Anal. Chim. Acta 570 (2006) 158.
[18] N. Sato, H. Okuma, Anal. Chim. Acta 565 (2006) 250.

Fluorescence quantification of tetracycline in the presence of quenching matrix effect by means of a four-way model

N. Rodríguez [a], M.C. Ortiz [a,*], L.A. Sarabia [b]

[a] *Department of Chemistry, Faculty of Science, University of Burgos, Plza. Misael Bañuelos s/n, 09001 Burgos, Spain*
[b] *Department of Mathematics and Computation, Faculty of Science, University of Burgos, Plza. Misael Bañuelos s/n, 09001 Burgos, Spain*

ABSTRACT

In this work, a four-way tensor is used to model the quenching effect in fluorescent measurements. By means of the analysis of excitation–emission matrices obtained in the determination of tetracycline in tea, which acts as quencher, it is shown as the impossibility to use a calibration, or an addition standard based on a three-way model. It is analysed the quencher multiplicative effect made on the tetracycline signal by means of an ANOVA. However, by arranging the experimental data in a four-way tensor, it is viable to perform a calibration based on the parallel factor analysis, PARAFAC, decomposition and a four-way partial least squares, 4-PLS, regression to quantify the tetracycline in the presence of the matrix quencher effect. 4-PLS calibration provides better results. In the range from 40 to 220 μg L^{-1} gives an average of relative errors in absolute value equal to 8.02% in prediction (3.40% in calibration). The repeatability as standard deviation in this range is 5.08 μg L^{-1} and the method is accurate, slope and intercept being statistically equal to 1 and 0, respectively when a regression calculated *versus* true concentration is performed. Moreover, it has a decision limit (CCα) of 13.87 μg L^{-1} for a probability of false positive, α, equal to 0.05 and a capability of detection (CCβ) of 26.63 μg L^{-1} (for probabilities of false positive, α, false negative, β, equals to 0.05).

© 2008 Elsevier B.V. All rights reserved.

1. Introduction

One of the main disadvantages of fluorescence as an analytical tool is its dependence on environmental factors, such as temperature, pH or ionic strength [1]. Among many other facts, it can mention the photochemical decomposition of the fluorescent compound or the viscosity of the medium, but it is the presence of the phenomenon called quenching which frequently causes a great number of problems when an analyte calibration must be carried out. It is known as quenching the decrease in intensity of fluorescence produced by a wide variety of processes. This phenomenon does not imply any modification in the shape of the analytes spectra, but only in their magnitude. This fact takes importance when comparing with other problems usually present in fluorescence spectroscopy such as the inner filter effects.

The inner filter effects appear when a component (either fluorescent or not) absorbs the energy of excitation or the emission corresponding to another sample component (or both), leading to different emission and excitation profiles for the affected analytes from sample to sample, not only in intensity but also in shape [2]. As an example, the determination of chrysene under a strong inner filter effect produced by benzopyrene is analysed in [3] showing how the unfolded-partial least squares/residual bilinearization modelling, (among many other approaches, such as parallel factor analysis or multivariate curve resolution-alternating least squares) is the most appropriate algorithm in this case.

The presence of several fluorophores in the matrix makes difficult the use of fluorescence with quantitative purposes. Multivariate curve resolution in combination with addition standard method is the strategy employed in [4] to avoid the matrix effect in the quantification of triphenyltin in sea-water. Standard addition is also the chosen method, but now combined with the use of PARAFAC modelling in the determination of salicylic acid in plasma [5]. Here, the necessity to employ this methodology and the application of second order advantage are justified by the presence of a strong matrix effect caused by the quenching of the proteins present in the plasma. Otherwise, quenching is caused in [6] by the addition of nitromethane in the analysis of mixtures of polycyclic aromatic hydrocarbons (PAHs). In this case, qualitative information about the composition of those real mixtures was provided by means of trilinear decomposition.

Four-way PARAFAC has also been applied in the quantification of catecholamines [7], pesticides [8], polycyclic aromatic hydrocarbons [9], or folic acid and methotrexate [10] by means of a kinetic excitation–emission fluorescence study. This means that four-way data are induced by including the time as an additional dimension

* Corresponding author.
  E-mail address: mcortiz@ubu.es (M.C. Ortiz).

in the analysis. Kinetic measurements are also the ones used in [11] to constitute four-way data in the determination of two anticancer drugs. In this case, trilinear least squares and unfolded-PLS coupled to residual trilinearization are the chemometric tools employed.

A wide range of algorithms has been created in the approach of second- and third-order multivariate calibration. Escandar et al. in [12] made a recent review of applications with this kind of data obtained through excitation–emission fluorescence spectroscopy and other techniques.

In the present study, quenching effect is not provoked by the addition of any other molecule, it is the own matrix which causes that effect. Thus, a four-way data array was used with the aim of quantifying the analyte in study concentration under the strong quenching effect made by tea. The appropriateness of the four-way data array is based on the alteration of the fluorescence quantum yield by changing the quantity of quencher, which produces the decrease in the fluorescence intensity [13]. Therefore, a four-way PARAFAC decomposition provides successful results in contrast with the impossibility to use a three-way PARAFAC decomposition. Results obtained when calibrating the same four-way tensor by means of PLS are also studied in a comparative way.

2. Theory

2.1. PARAFAC

There are several ways of introducing the PARAFAC model for the analysis of fluorescent data. For example, PARAFAC can be considered a generalization to N-way arrays of principal components analysis (PCA), a well-established method in analytical chemistry. This section focuses on how PARAFAC corresponds to a physical model of fluorescent data, including quenching effect, under some common assumptions.

Although quenching can also occur by a variety of trivial, i.e., non-molecular mechanisms, such as attenuation of the incident light by the fluorophore itself or other absorbing species, it can be divided into two categories: static and dynamic. Static quenching refers to the process which occurs in the ground state and does not rely on diffusion or molecular collisions; in this case fluorophores can form non fluorescent complexes with other molecules in solution, which are called quenchers. Dynamic or collisional quenching occurs when the excited-state flourophore is deactivated on contact with quenchers. The fluorophore is returned to the ground state during a diffusive encounter with the quencher. The molecules are not chemically altered in the process.

In Leurgans and Ross [13] it is shown as the multi-way approach to describe the fluorescence spectroscopy, including the quencher effect, the inner effect and time resolved spectroscopy. Afterwards, only models employed in this work will be described to fix the notation, other details should be consulted in Leurgans and Ross paper.

In fluorescence spectroscopy, the amount of light emission measured is separately linear in the number of photons absorbed and in the fraction of photons absorbed that lead to emission at a specific wavelength. Therefore, when sample i-th, $i = 1, \ldots, I$, containing F fluorophores is illuminated with light of wavelength λ_j^{ex}, $j = 1, \ldots, J$, and the consequent emission of light is measured at wavelength λ_k^{em}, $k = 1, \ldots, K$ then, in theory, we have the trilinear equation for the fluorescence intensity

$$x(i, j, k) = \sum_{f=1}^{F} a_{if} b_{jf} c_{kf}, \quad i = 1, ..., I, \ j = 1, ..., J, \ k = 1, ..., K \tag{1}$$

where a_{if} is the concentration of fluorophore f in the sample i-th, b_{jf} is the relative absorption (extinction coefficient) of fluorophore

f at wavelength λ_j^{ex} and c_{kf} is the relative emission at wavelength λ_k^{em}.

The application of three-way model, Eq. (1), requires that sample absorbance be small and that excitation not to be transferred between chromophores (inner effect), however nonlinearity due to inner effect can be corrected and energy transfer can be treated with a T2 multilinear model which incorporates the correlation between two factors in the two spectral modes [13] or by means of unfolded-partial least squares/residual bilinearization modelling [3].

In presence of a fluorescence quencher we have an additional independent variable by treating the sample in some manner that differentially affects the total amount of light emission from different fluorophores. Of all excitations, only some fraction leads to light emission, this fraction, d_{fl}, is the fluorescence quantum yield and by changing their quantities ($l = 1, \ldots, L$) we then have the quadrilinear model

$$x(i, j, k, l) = \sum_{f=1}^{F} a_{if} b_{jf} c_{kf} d_{lf}, \quad i = 1, ..., I, \ j = 1, ..., J,$$
$$k = 1, ..., K, \ l = 1, ..., L \tag{2}$$

where a_{if}, b_{jf} and c_{kf} are as defined previously.

If relative concentration of each analyte, a_{if}, is fixed, the model in Eq. (2) is reduced to a trilinear model with profiles: excitation, emission and quencher. This model is useful in the structural analysis of biological molecules, such as proteins, where the relative concentration of different fluorophores is fixed because they are all part of the same large molecule. But depending on the fluorophore position, in the surface or in the center of the molecule, this can be reached or not by the quencher, and as a consequence, changing the quencher quantity the fitting of experimental data to trilinear model (excitation, emission and quencher) allows getting information about the intact molecule (by example a protein), which is not possible to study in other way because the chemical separation of the fluorophores would have destroyed the system being studied.

Applications of this procedure, always from a qualitative point of view, are in reference [13] with simulated data, in [14] to describe the underlying structure of fluorescence spectra obtained from pigment complexes in pea thylakoids and in [15] to analyse the properties of hydrogen-bonded tyrosine.

When quencher effect is not taken into account, fluorescent intensities form a three-way tensor $\underline{\mathbf{X}}$ with dimensions ($I \times J \times K$) whose element, $x(i, j, k)$, is the fluorescence of sample i-th at excitation wavelength λ_j^{ex} and emission wavelength λ_k^{em}. For this tensor a trilinear model of rank F can be expressed as:

$$x(i, j, k) = \sum_{f=1}^{F} a_{if} b_{jf} c_{kf} + \varepsilon_{ijk},$$
$$i = 1, ..., I, j = 1, ..., J, k = 1, ..., K \tag{3}$$

where ε_{ijk} is the residual not explained by the trilineal model.

On the contrary, if quencher effect is taken into account, the experimental intensities form the four-way tensor $\underline{\mathbf{X}}$ with dimensions ($I \times J \times K \times L$) whose general term, $x(i, j, k, l)$, is the fluorescence of sample i-th at excitation wavelength λ_j^{ex}, emission wavelength λ_k^{em} and l-th level of quencher. The quadrilinear model of rank F for this tensor is:

$$x(i, j, k, l) = \sum_{f=1}^{F} a_{if} b_{jf} c_{kf} d_{lf} + \varepsilon_{ijkl},$$
$$i = 1, ..., I, j = 1, ..., J, k = 1, ..., K, l = 1, ..., L \tag{4}$$

It can be observed that the model of Eq. (3) and that of Eq. (4) correspond to the physical model in Eqs. (1) and (2), respectively.

Therefore if the experimental data are trilinear, Eq. (3) or quadrilinear, Eq. (4) and there are F fluorescent components in the samples, the model of F components can be used to estimate: (i) the extinction coefficients for each analyte f at all wavelengths, i.e., their excitation profile $\boldsymbol{b}_f = (b_{1f}, b_{2f}, ..., b_{Jf})$ or excitation spectrum. (ii) the relative emission at all wavelengths, i.e., their emission profile $\boldsymbol{c}_f = (c_{1f}, c_{2f}, ..., c_{Kf})$ or emission spectrum of each analyte and (iii) the relative concentration of every analyte in all samples, i.e., sample profile $\boldsymbol{a}_f = (a_{1f}, a_{2f}, ..., a_{If})$. If the quenching effect is considered, Eqs (2) and (4), also the fluorescence quantum yield, i.e., the quencher profile $\boldsymbol{d}_f = (d_{1f}, d_{2f}, ..., d_{Lf})$ can be estimated for each analyte f in all samples.

When experimental data correspond to models (3) and (4), that is the data are trilinear (or quadrilinear), the PARAFAC decomposition method [16,17] provides unique profiles estimations [18]. This means that, provided the rank of the PARAFAC model corresponds to the number of fluorescent compounds, each PARAFAC component, f, can be assigned to a compound and the loadings (a_{fi}, b_{fj}, c_{fk} and d_{fl}) can be interpreted as an estimation of the relative concentrations of the analytes, excitation spectra, emission spectra and quantum yield for this compound, respectively.

Andersen and Bro present a dedicated investigation and practical description of how to apply PARAFAC modelling to fluorescence excitation–emission measurements [19] and a review of recent chemical applications of PARAFAC can be seen in ref. [20].

2.2. PARAFAC based calibration

A calibration of fluorescence N-way data, based in a PARAFAC decomposition consists basically of the following steps:

(i) Record the EEM matrix of dimension $J \times K$ for each sample, where J is the number of excitation wavelengths and K that of emission. Using these data, if a trilinear model as that of Eq. (3) is used, build the three-way array, $\underline{\mathbf{X}}$, formed by the calibration samples at I levels of analyte and at L levels of quencher. In this case the tensor $\underline{\mathbf{X}}$ has dimension $(I \times L) \times J \times K$ because there are $(I \times L)$ different samples. Alternatively, if a quadrilinear model, Eq. (4), is fitted, the four-way tensor, $\underline{\mathbf{X}}$, has dimension $I \times J \times K \times L$. That is, for each sample with level i ($i = 1, 2, ..., I$) of analyte concentration we had a cube of data (with dimension $J \times K \times L$) formed by the EEM matrices recorded at the L levels of quencher.

(ii) Perform the PARAFAC decomposition. This gives the spectral and the sample profiles of the analytes; also the quencher profile is provided if a quadrilinear model is fitted. The internal validation of the decomposition is done using the indices T^2 and Q such that the absence of anomalies in the spectral, sample or quencher profile is guaranteed.

(iii) Identify the factor, f_0, which corresponds to the analyte of interest.

(iv) Once the factor associated with the analyte has been identified, one has the loadings (coordinates) of the sample profile, $\boldsymbol{a}_{f_0} = (a_{1f_0}, a_{2f_0}, ..., a_{If_0})$. The calibration curve is build by means of regression loading *versus* spiked concentration.

(v) Using the concentration values calculated by the calibrations in step (iv) the decision limit (CCα) and the capability of detection (CCβ) will be estimated.

(vi) With the same procedure, regression of the concentration obtained with the PARAFAC decomposition *versus* true concentration, the trueness, intermediate precision and linear range are established.

(vii) Determination of the concentration of a problem sample. Once the matrix of data, EEM$_p$, has been recorded for this sample, it will be added to the array $\underline{\mathbf{X}}$ and the joint decomposition

will be carried out. Q and T^2 values of the problem sample in the three ways must be below the threshold values established with the calibration samples, in order to guarantee that the problem sample is similar to the calibration ones. There is another approach for apply PARAFAC decomposition to a problem sample: project the EEM$_p$ matrix on the factors obtained previously, but in practice better results are obtained with the former option [21]. Step (iii) allow one to unequivocally identify the analyte and the linked sample loading allows one to determine the concentration by means of the calibration curve in step (iv) even in the presence of non-modelled interferents in the calibration step [19,22], this property is known as the second order advantage and is related to the uniqueness of the PARAFAC decomposition.

In the univariate regression used in steps (iv) and (v) one must detect the outliers, for example, by means of a least median squares regression, LMS. Once the outliers has been eliminated a least squares regression is performed. Furthermore, one must verify the hypotheses underlying a least squares regression [23] (normality, independence of residues, homocedasticity and lack of fit).

The PARAFAC based calibration can be used with experimental data provided by other analytical techniques, a recent review in the case of chromatographic ones can be seen in ref. [24].

2.3. N-way partial least squares, N-PLS

A calibration of N-way data based on a decomposition PARAFAC has two steps: the decomposition PARAFAC, step (ii) in Section 2.2, and the regression univariate sample loadings linked to analyte *versus* true concentration, step (iv) in Section 2.2. But the PARAFAC profiles have been obtained without considering the true analyte concentration. It is a situation similar to the regression on principal components for two-way data. By contrast, the two-way PLS search latent variables that explain the variability in the space signals, as principal components, but at the same time the most correlated with the analyte concentration.

To generalize the PLS approach to multi-way data, a general multilinear PLS (N-PLS) regression model has been developed [25,26]. In the N-way version of PLS, the N-way tensor $\underline{\mathbf{X}}$ is decomposed into a N-linear model similar to the PARAFAC model; however, for N-PLS, the model is not fitted in a least squares sense but seeks, in accordance with the philosophy of PLS, to describe the covariance of the response and the predictor variables. This is achieved by simultaneously fitting a linear model of the response variable, a $(N-1)$-linear model of the predictor variables, and a regression model relating the two decomposition models.

Unlike to the most common two-way PLS, N-PLS models do not have orthogonal scores. The computational procedure is more complicated than two-way PLS because after the scores, weights and regression coefficients are all determined a Tucker3-like core is introduced to provide appropriate $\underline{\mathbf{X}}$-residuals for outlier detection and other purposes. Thus, the interpretation of the N-PLS model of $\underline{\mathbf{X}}$ is usually performed as for a PARAFAC model.

In general a N-PLS calibration model has not the second order property, so it is not assuring the spectral identification of the analyte. The step (v) and (vi) of procedure described in Section 2.2 are applicable also to the N-PLS calibration model.

With the same four-way data tensors (sample $\times$ excitation $\times$ emission $\times$ quencher), an analyte concentration can be calibrated by means of 4-PLS method [17] which sometimes lead to better analytical quality calibrations [27] than the calibration based on a PARAFAC decomposition previously described in Section 2.2.

3. Experimental

3.1. Chemicals and reagents

Analytical-reagent grades were used without further purification. Tetracycline standards were obtained from Sigma (Steinheim, Germany) and stored below 0 °C away from light. Stock solutions (1 g L^{-1}) were prepared in methanol HPLC grade and kept at 4 °C in brown glass vials for a maximum period of a month. A dilute standard solution (1250 mg L^{-1} tetracycline) was also arranged in methanol.

Buffer solution was prepared from 2 M NH$_4$Cl (Panreac, Barcelona, Spain) and 2 M NH$_3$ (Merck, Darmstadt, Germany) solutions and a basic pH higher than 9 was fitted.

To obtain the quencher solution, tea leaves contained in a commercial tea-bag were added to 150 ml of hot water and stirred for 1 min. The solution obtained was filtered in order to remove tea particles that produce scattering of the incident excitation light. The filtrate was collected and stored in a glass flask to allow the brew to cool to room temperature before being used in the preparation of working solutions.

3.2. Experimental procedure

Two procedures were applied. Procedure A: a set of nine standards solutions five times performed, was prepared by dilution of the standard tetracycline solution to appropriate concentrations (0–160 µg L^{-1}) with 1 ml of both, NH$_3$/NH$_4$Cl buffer and quencher solution (tea). Procedure B: seven levels of tetracycline concentration (40–220 µg L^{-1}) were studied at four different volumes of quencher solution (1.0, 1.5, 2.0 and 2.5 ml) by preparing a set of 28 standard solutions that was performed in duplicate. All solutions in both procedures were diluted with deionised water until 10 ml. Deionised water was obtained from a Milli-Q water purification system (Millipore). Samples were measured immediately after being prepared.

3.3. Instrumentation and software

Measurements were performed at room temperature on a PerkinElmer LS50B Luminescence Spectrometer equipped with a xenon discharge lamp and a gated photomultiplier. Excitation and emission slits were both set to 10 nm and the scan speed was 1500 nm min^{-1}. The emission spectra were recorded between 440 and 560 nm (intervals of 1 nm) at excitation wavelengths between 320 and 400 nm (regular steps of 10 nm). The size of the data tensors is described in the corresponding section.

The FL WinLab software (PerkinElmer) was used for measurements, the data were imported to Matlab using the INCA software [28] which avoids the non-trilinear parts of the spectrum by setting them to missing values. The PLS Toolbox for Matlab [29] was employed for PARAFAC and PLS calculations. Data were analysed using STATGRAPHICS [30] for building and validating regressions, PROGRESS [31] for detecting outliers that is very useful in the linear calibration step [32] and a home-made program NWAYDET (available from the authors on request) was used to obtain the capability of detection as is described in ref. [21].

4. Results and discussion

4.1. Analysis of fluorescent signals

Five independent calibration sets (1, 2, 3, 4 and 5) were measured with a fixed quantity of 1 ml of tea solution. Each calibration set has nine samples with tetracycline concentrations between 0
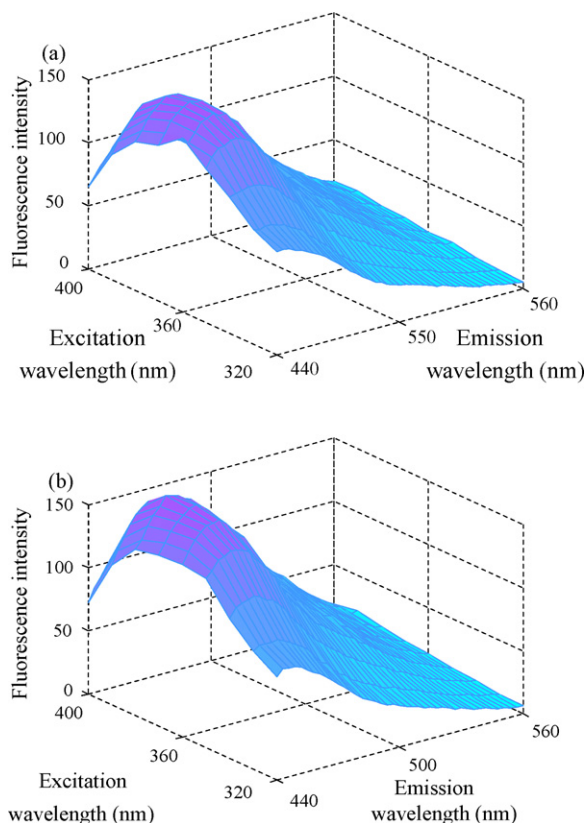

Fig. 1. EEM (landscape) of two samples corresponding to calibration set 1 with 1 ml of tea solution. (a) Spiked with 20 µg L^{-1} of tetracycline. (b) Spiked with 160 µg L^{-1} of tetracycline.

and 160 µg L^{-1}. Fig. 1 shows the excitation–emission landscapes of two tea samples spiked with 20 and 160 µg L^{-1} of tetracycline corresponding to calibration set 1.

On the other hand, when tetracycline was determined at different levels of tea, four independent sets of seven samples with tetracycline concentrations between 40 and 220 µg L^{-1} were measured. They are calibration sets 6, 7, 8 and 9. Another similar group of seven samples (for each level of tea) will be used as problem samples. Fig. 2 shows the excitation–emission matrices of four samples spiked with the same quantity of tetracycline (100 µg L^{-1}) and four levels of tea volume: 1.0, 1.5, 2.0 and 2.5 ml.

Comparing Figs. 1 and 2, it can be seen that the presence of tea, both in fixed quantities (Procedure A) or at different levels of concentration (Procedure B), modifies the magnitude of tetracycline signal. Fluorescence intensity increases when tetracycline concentration rises at fixed quantities of tea solution, as it is shown in Fig. 1; whereas fluorescence intensity decreases at a fixed tetracycline concentration and increasing quantities of tea solution, Fig. 2. This quenching effect is due to the matrix (tea) not to the addition of any other substance.

4.2. Three-way decomposition

If the matrix has fluorophores which act as quenchers, as it happens with tea in our case, a calibration function for the analyte, tetracycline, cannot be obtained, because its effect over the signal is multiplicative, as it is checked when comparing Eqs. (1) and (2). In order to show it, a three-way PARAFAC decomposition by means of Eq. (3) will be fitted in this first analysis with the experimental data. The tensor **X** (73 × 121 × 9) containing the whole excitation–emission matrices of Procedure A and Procedure B, was
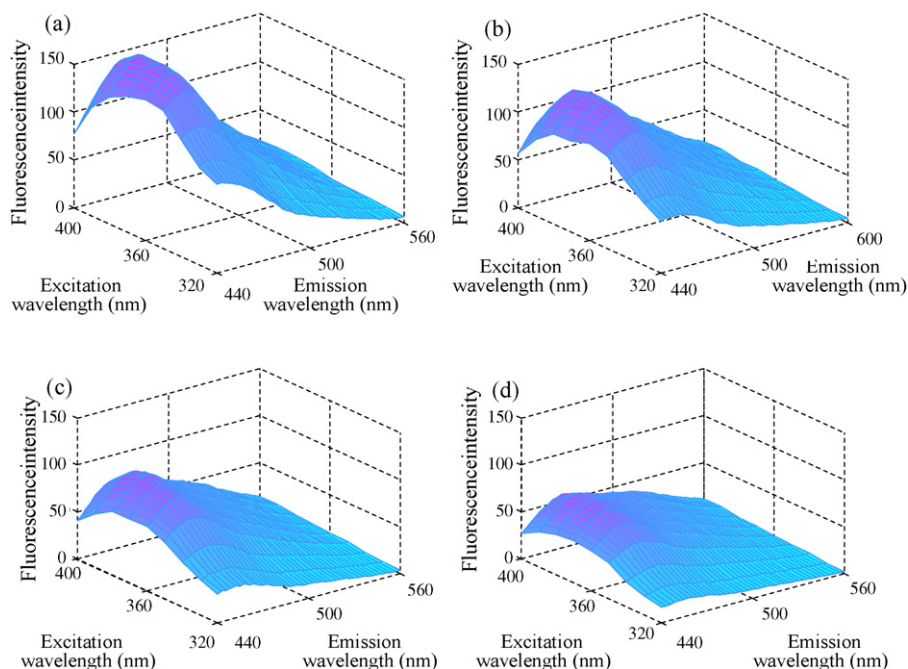
Fig. 2. EEM (landscape) of four samples spiked with 100 µg L^{-1} of tetracycline and different quantities of tea solution: (a) 1 mL; (b) 1.5 mL; (c) 2 mL; (d) 2.5 mL.

used. The first mode corresponds to the number of samples, (the first 45 samples are those from Procedure A, and the rest 28 correspond to the first replicate of Procedure B), whereas 121 and 9 are the number of emission and excitation wavelengths, respectively, where fluorescence intensity has been recorded. No pre-processing step has been performed over the experimental tensor **X**, but non-negativity restrictions in the two spectral modes were applied.

The number of components is determined through the global consistency index, CORCONDIA [33], which is of 99.99% when two components are chosen. The outlier data diagnostic is performed through the sum of squared residuals (Q index) and Hotelling's T^2 to detect samples or spectral intensities that do not correspond to the expected one (step (ii) in Section 2.2). At the significance level of 99%, there is not any outlier data. Loadings obtained for the two components PARAFAC model are shown in Fig. 3.

However, although the three-way PARAFAC decomposition properly fits the experimental data, the loadings from sample mode show a behaviour that do not correspond to the variation of the tetracycline concentration, as it can be seen in Fig. 3a. Loadings from the first 45 samples with 1 ml of tea (Procedure A) have been separated from the next 28 with increasing tea concentrations (Procedure B) with a vertical line. These samples (Procedure B) with the same tetracycline concentration have different loading, in factor related to the Tetracycline, depending on the level of quencher. This decrease in the tetracycline loadings in the first way of PARAFAC decomposition points out the existence of an interaction between the two factors in study (tetracycline concentration and level of quencher solution) which is not observed in the loadings from samples with tea quantity fixed (Procedure A) in the same Fig. 3a.

In order to show the multiplicative effect of the quencher over the loadings and therefore, the necessity for its modelling by means of Eq. (4), a two-way ANOVA was employed. Loadings from the related to tetracycline PARAFAC factor in samples from Procedure B are the data in this ANOVA. The factors, which must be obviously significant, are the tetracycline concentration at seven fixed levels and quencher volume at four fixed levels. To evaluate the signification of the interaction between both factors, the ANOVA sum of squares, which is not explained by the factors, has to be

distributed in the due to the interaction part and the residual one. As there is only an observation per cell it is not possible to evaluate the pure error and the technique given by Tukey [34] has been applied. Computational details can be also consulted in page 45 and next from Anderson and McLean [35] book. With this approach, the mean square estimated for the interaction with one degree of freedom is 8947.92. Table 1 shows the analysis of variance with interaction. Once the residual mean square is calculated, the corresponding hypothesis tests are carried out. As it can be clearly seen, again in Table 1, calculated *F* statistics are in all cases much higher than the theoretical ones, having to reject the null hypothesis (H$_0$: there is no effect) at a significance level of 0.05. Therefore, it is statistically proved the influence of both factors in study just as their interaction.

4.3. Standard addition method

As a consequence of results showed in previous Section 4.2, a calibration with loadings obtained with samples from Procedure A cannot be used for samples in Procedure B because a tetracycline concentration less than the true one will be provided. If data are trilinear, the PARAFAC decomposition accomplishes the second order property and the corresponding to the analyte loading is estimated in a unique way. That is why, to solve the strong matrix effect caused by the quenching effect, the standard addition method has been proposed by other authors [5]. The idea to couple a trilinear decomposition with the standard addition method has been employed with other analytical techniques, for example with spectroelectrochemical data in [36]. However, the use of this method requires that the loadings related with the analyte calibrated be under two constraints: (a) it must depend linearly on the increase of the analyte concentration, (b) it must be zero when the analyte concentration is zero. This second condition is not fulfilled in our case.

To corroborate the impossibility to apply the standard addition method, this is applied to multivariate data through a plot of the related to tetracycline loadings from three-way PARAFAC decomposition as a function of the amount of analyte added with the
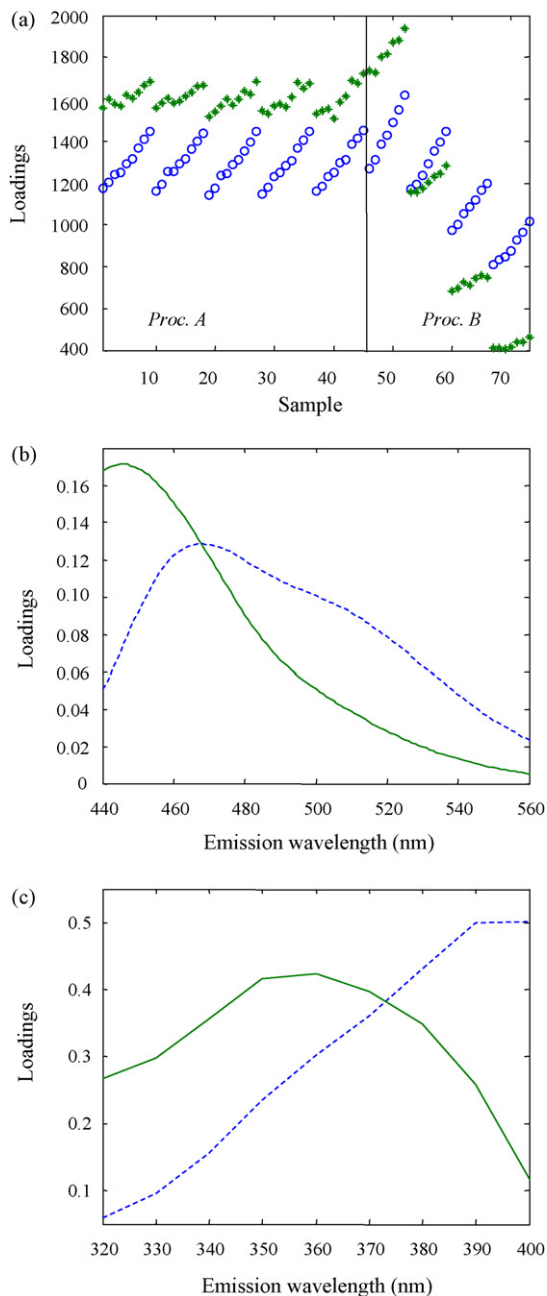
Fig. 3. Two factors loadings obtained in the PARAFAC decomposition fitted with three-way tensor $\underline{\mathbf{X}}$ (73 × 121 × 9): (a) sample mode; (b) emission mode; (c) excitation mode. The related to tetracycline factor is shown with circles (○) and a dashed line (- - -). Experimental Procedures A and B are explained in Section 3.2.

Table 2
Regression lines fitted from plotting related to tetracycline loadings from three-way PARAFAC decomposition (y) *versus* the amount of analyte added in the different levels of quencher solution (x)

Level of quencher solution (mL)	Regression line	R^{2*}	$[tc]_{calculated}^{\dagger}$ ($\mu g\,L^{-1}$)
1.0	$y = 1.949x + 1375.8$	0.991	705.9
1.5	$y = 1.738x + 1239.6$	0.997	713.2
2.0	$y = 1.255x + 1048.4$	0.998	835.4
2.5	$y = 1.389x + 842.68$	0.993	606.7

* R^2 is the coefficient of determination.

† $[tc]_{calculated}$ is the tetracycline concentration obtained by standard addition method for samples spiked with $100\,\mu g\,L^{-1}$.

purpose of predicting samples spiked with $100\,\mu g\,L^{-1}$ of tetracycline. Table 2 shows the corresponding regression lines fitted for each level of quencher, the coefficient of determination is in all cases higher than 0.99, that is regressions explain more than 99% of the loadings variability, they are very significant and do not have outlier data. However, the tetracycline concentrations obtained in each case are wrong as can be seen in Table 2. It is important to stand out the different values of slope obtained for the different levels of quencher solution which shows up once again, the multiplicative effect that the two factors (tetracycline concentration and volume of quencher solution) make on the loadings.

4.4. Four-way PARAFAC decomposition

According to model in Eq. (2), now the dimension of the four-way tensor is $14 \times 121 \times 9 \times 4$, where 14 corresponds to the sample mode, 121 to the emission mode, 9 to the excitation mode and 4 to the quencher mode. A PARAFAC model is built for both replicates in Procedure B in order to achieve the quantitative analyte determination in the presence of quenching effect. The first seven samples will be used as a calibration set, whereas the next seven will be used as a test set. The model fitted with two factors, has a CORCONDIA equal to 75.16% and no outlier data were found, once Q and T^2 Hotelling indices diagnostic was applied. The representation of their loadings in the four modes is shown in Fig. 4. The correlation between the spectra estimated for the two factors in the four-way (Fig. 4b and c) and the three-way (Fig. 3b and c) PARAFAC decompositions are 0.99 in the two cases. Therefore, both decompositions obtain the same two factors, but sample mode and quencher mode were estimated jointly in the three-way PARAFAC decomposition.

4.5. Performance criteria from calibration with four-way tensor

In order to carry out tetracycline calibration with data from the four-way tensor, the two different calibration procedures described in Section 2 will be used. The number of latent variables in the 4-PLS regression is determined by cross-validation with leave one out procedure, reaching the RMSCV minimum with four latent variables. This model explains 99.17% of the predictor variables variance and 99.91% of the response variance. None of the calibration samples have significant values of Q and T^2. This means that none

Table 1
Two-way analysis of variance for sample loadings, related to tetracycline, from the three-way PARAFAC decomposition

Source	Sum of squares	Degrees of freedom	Mean square	F (statistic) calculated	F^*
Tetracycline	2.24×10^5	6	37276.20	389.95	2.70
Volume of tea	1.18×10^6	3	393063.00	4111.83	3.20
Interaction	8.95×10^3	1	8947.92	93.60	4.45
Residual	1.63×10^3	17	95.59		
Total	1.41×10^6	27	52348.89		

* Critical value of an F distribution at a significance level of 0.05.
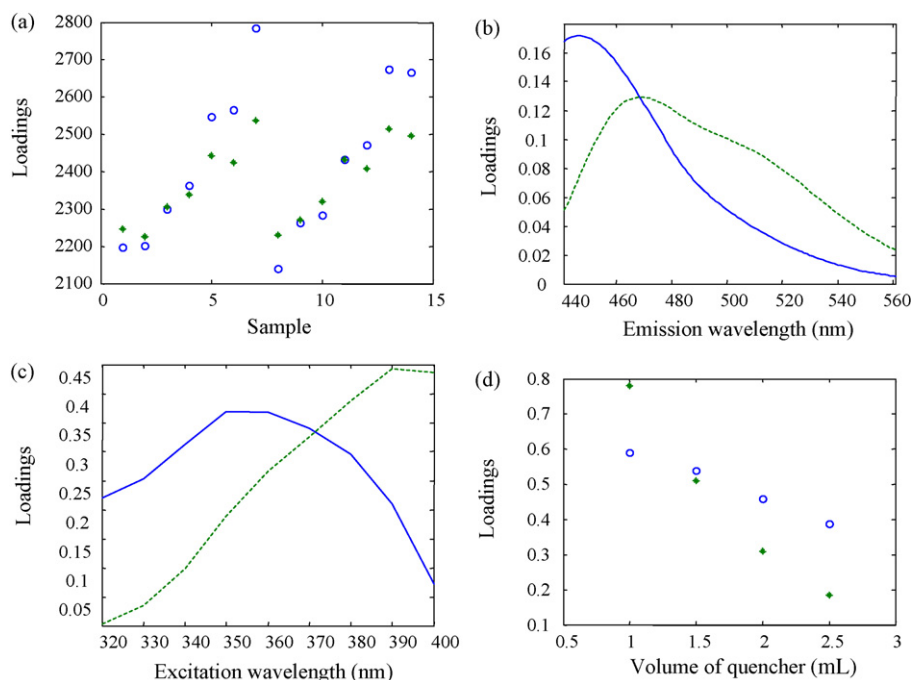
Fig. 4. Loadings from the PARAFAC decomposition with four-way tensor $\underline{\mathbf{X}}$ ($14 \times 121 \times 9 \times 4$): (a) sample mode; (b) emission mode; (c) excitation mode; (d) quencher mode. The related to tetracycline factor is showed with circles (○) and a dashed line (- - -).

of them can be considered as outlier. With regard to calibration samples, the average of relative errors (in absolute value), ARE, is 3.40%.

Table 3 shows the comparison between both calibration procedures. In both cases intercept and slope are significantly equal to 0 and 1, respectively at a significant level of 5%, because the *p*-values are always greater than 0.05, therefore both calibration methods accomplish the property of trueness, so much in calibrated like in prediction. 4-PLS calibration is obviously more precise than the one based on PARAFAC because the residual standard deviation is almost three times lower for the calibration samples, which means a higher correlation coefficient and a better ARE in calibration. These advantages are kept also for the samples of prediction.

Another figures of merit such as CCα and CCβ have been evaluated according to Commission Decision [37], ISO [38] and IUPAC [39] recommendations. The decision limit (CCα) means the limit at and above which it can be concluded with an error probability

of α that a sample has analyte. The capability of detection (CCβ) of a method is the smallest content of the substance that may be detected, identified and/or quantified in a sample with a false negative probability equal to β and a false positive probability equal to α. The multivariate multi-way version of CCα and CCβ can be consulted in ref. [21,40]. Regarding these definitions, the capability of detection and the decision limit depend on the regression slope and on its standard deviation, and also on desired values of both probabilities of false positive (α) and false negative (β). In our case, values of decision limit for $\alpha = 0.05$ and values of capability of detection for $\alpha = \beta = 0.05$ have been calculated for one future determination in the sample problem and they are shown in Table 3. As a consequence of the lower residual standard deviation, CCα and CCβ values are slightly the half with the 4-PLS calibration than with the one based on PARAFAC. Finally, the ARE in prediction is 8.02% for 4-PLS and of 15.64% for the calibration based on PARAFAC which falls to 10.75% when the relative error (44.95%) corresponding to

Table 3
Figures of merit so much in calibrated like in prediction obtained by means of the regression between the tetracycline concentration found *versus* true tetracycline concentration for both *N*-way based procedures

	Calibration (training set, *N* = 7)		Prediction (test set, *N* = 7)	
	Based on PARAFAC	4-PLS	Based on PARAFAC	4-PLS
Slope (*p*-value[a])	1.0001 (0.999)	0.9944	1.0575 (0.654)	1.1069 (0.312)
Intercept (*p*-value[b])	0.0084 (0.999)	0.7405	−6.2540 (0.732)	−15.6724 (0.302)
Correlation coefficient	0.979	0.997	0.9689	0.9821
Residual standard deviation	14.51	5.08	19.18	15.09
ARE[c]	8.09	3.40	15.64 (10.75)[d]	8.02
CCα[e] (μg L^{-1})	28.53	13.87	–	–
CCβ[f] (μg L^{-1})	54.80	26.63	–	–

[a] Hypothesis test for slope equal to one.
[b] Hypothesis test for null intercept.
[c] ARE means for average of relative errors in absolute value.
[d] In brackets the ARE value without the sample of 40 μg L^{-1} (less than CCβ).
[e] Probability of false positive α equal to 0.05.
[f] Both probabilities of false positive and false negative equal to 0.05.

sample with $40\,\mu g\,L^{-1}$. This sample should be eliminated because it is under the $CC\beta$.

5. Conclusions

This work opens a new approach to quantification in presence of a strong quenching effect caused by the matrix. The fluorescence spectrophotometry determination of tetracycline in a tea solution is used to show the ineffectiveness of a three-way PARAFAC decomposition and the standard addition method in these conditions in spite of the trilinear model fitted with the experimental tensor. A procedure based in an ANOVA is proposed to verify the multiplicative effect of quencher over the loadings.

Therefore, it is the alteration of the fluorescence quantum yield by changing the levels of quencher quantity providing a four-way tensor which let us the determination of tetracycline concentration. A 4-PLS regression and other one based on PARAFAC as calibration models are tested with suitable results, which are better for 4-PLS.

Acknowledgments

References

[1] G.G. Guilbault, Practical Fluorescence, Marcel Dekker, Inc., New York, 1990.
[2] J.R. Lakowicz, Principles of Fluorescence Spectroscopy, Springer, New York, 2006.
[3] D. Bohoyo, A. Muñoz de la Peña, J.A. Arancibia, G.M. Escandar, A.C. Olivieri, Anal. Chem. 78 (2006) 8051–8058.
[4] J. Saurina, R. Tauler, Analyst 125 (2000) 2038–2043.
[5] M.M. Sena, M.G. Trevisan, R.J. Poppi, Talanta 68 (2006) 1707–1712.
[6] P.D. Wentzell, S.S. Nair, R.D. Guy, Anal. Chem. 73 (2001) 1408–1415.
[7] R.P.H. Nikolajsen, K.S. Booksh, A.M. Hansen, R. Bro, Anal. Chim. Acta 475 (2003) 137–150.
[8] M.L. Nahorniak, G.A. Cooper, Y. Kim, K.S. Booksh, Analyst 130 (2005) 85–93.
[9] Y. Kim, J.A. Jordan, M.L. Nahorniak, K.S. Booksh, Anal. Chem. 77 (2005) 7679–7686.
[10] A. Muñoz de la Peña, I. Durán, A. Jiménez, Anal. Bioanal. Chem. 385 (2006) 1289–1297.
[11] J.A. Arancibia, A.C. Olivieri, D. Bohoyo, A. Espinosa, I. Durán-Merás, A. Muñoz de la Peña, Chemom. Intell. Lab. Syst. 80 (2006) 77–86.
[12] G.M. Escandar, N.M. Faber, H.C. Goicoechea, A. Muñoz de la Peña, A.C. Olivieri, R.J. Poppi, Trends Anal. Chem. 26 (2007) 752–765.
[13] S. Leurgans, R.T. Ross, Stat Sci. 7 (1992) 289–319.
[14] R.T. Ross, C.H. Lee, C.M. Davis, B.M. Ezzedune, E.A. Fallad, S.E. Leurgans, Biochim. Biophys. Acta 1056 (1991) 317–320.
[15] J.K. Lee, R.T. Ross, S. Thampi, S. Leurgans, J. Phys. Chem. 96 (1992) 9158–9162.
[16] R.A. Harshman, UCLA Working Pap. Phonetics 16 (1970) 1–84.
[17] R. Bro, Ph.D. Thesis, University of Amsterdam, Amsterdam. http://www.mli.kvl.dk/staff/foodtech/brothesis.pdf, 1998 (last access: April 2008).
[18] R.B. Cattell, Psychometrika 9 (1944) 267–283.
[19] C.M. Andersen, R. Bro, J. Chemom. 17 (2003) 200–215.
[20] R. Bro, Crit. Rev. Anal. Chem. 36 (2006) 279–293.
[21] M.C. Ortiz, L.A. Sarabia, I. García, D. Giménez, E. Meléndez, Anal. Chim. Acta 559 (2006) 124–136.
[22] D. Giménez, L.A. Sarabia, M.C. Ortiz, Analyst 130 (2005) 1639–1647.
[23] D.L. Massart, B.G.M. Vandeginste, L.M.C. Buydens, S. De Jong, P.J. Lewi, J. Smeyers-Verbeke, Handbook of Chemometrics and Qualimetrics: Parts A and B, Elsevier, Amsterdam, 1997.
[24] M.C. Ortiz, L. Sarabia, J. Chromatogr. A 1158 (2007) 94–110.
[25] R. Bro, J. Chemom. 10 (1996) 47–61.
[26] A. Smilde, R. Bro, P. Geladi, Multi-way Analysis. Applications in the Chemical Sciences, John Wiley and Sons Inc., Chichester, 2004.
[27] I. García, L. Sarabia, M.C. Ortiz, J.M. Aldama, Anal. Chim. Acta 515 (2004) 55–63.
[28] C.A. Andersson, INCA 1.41, Department of Dairy and Food Science, Frederiksberg, Denmark. Freely available at http://www.models.kvl.dk/source/inca/, 2002.
[29] M. Wise, N.B. Gallagher, R. Bro, J.M. Shaver, PLS Toolbox 3. 02, Eigenvector Research Inc., Manson, WA, 2003.
[30] STATGRAPHICS plus for Windows, Ver. 4.0. Statistical Graphics Corp. Rockville, 1998.
[31] P.J. Rousseeuw, A.M. Leroy, Robust Regression and Outlier Detections, John Wiley and Sons Inc., Hoboken, NJ, 2001.
[32] M.C. Ortiz, L. Sarabia, A. Herrero, Talanta 70 (2006) 499–512.
[33] R. Bro, H.A.L. Kiers, J. Chemom. 17 (2003) 274–286.
[34] J.W. Tukey, Biometrics 5 (1949) 99–114.
[35] V.L. Anderson, R.A. MacLean, Design of Experiments. A Realistic Approach, Marcel Dekker, New York, 1974.
[36] A. Herrero, S. Zamponi, R. Marassi, P. Conti, M.C. Ortiz, L.A. Sarabia, Chemom. Intell. Lab. Syst. 61 (2002) 63–74.
[37] European Decision (EC) No. 2002/657/EC of 12 August 2002 implementing Council Directive 96/23/EC concerning the performance of analytical methods and the interpretation of results, Off. J. L 221, 17/8/2002, pp. 8–36.
[38] International Standard ISO 11843-1, Capability of detection. Terms and definitions, International Standard ISO 11843-2, Capability of detection. Methodology in the linear calibration case, International Organization for Standardization, Genève, 1997.
[39] J. Inczédy, T. Lengyel, A.M. Ure, A. Gelencsér, A. Hulanicki, IUPAC, Compendium of Analytical Nomenclature, Blackwell, Oxford, 1998.
[40] M.C. Ortiz, L.A. Sarabia, A. Herrero, M.S. Sánchez, M.B. Sanz, M.E. Rueda, D. Giménez, M.E. Meléndez, Chemom. Intell. Lab. Syst. 69 (2003) 21–33.

Determination of chemical composition of siderite in concretions by wavelength-dispersive X-ray spectrometry following selective dissolution

Rafał Sitko [a,*], Beata Zawisza [a], Tomasz Krzykawski [b], Ewa Malicka [a]

[a] Institute of Chemistry, Silesian University, Szkolna 9, 40-006 Katowice, Poland
[b] Department of Earth Sciences, Silesian University, 41-200 Sosnowiec, Poland

A B S T R A C T

Determination of chemical composition of siderite $(Fe, Me)CO_3$ (where Me = Mg, Ca, Mn) present in siderite concretion is developed. An accurate and precise determination of Mg, Ca, Mn and Fe in siderite required complete separation of this mineral from other materials, e.g. calcite, quartz. For this purpose, selective dissolution in acetic acid (HAc) was applied. HAc concentration from 0.1 to 1 mol L^{-1} and extraction time from 0.5 to 8 h were investigated. In each step of investigation of selective dissolution, the X-ray diffraction measurements (XRD) of the residues was performed and also calcium (complexometric titration) and iron (XRF) in solution were determined. HAc of concentration 0.25 mol L^{-1} and extraction time of 2 h was adopted for siderite separation because in these conditions the siderite was not dissolved and, simultaneously, calcite was completely dissolved. In the next step, the nondissolved sample was digested in hydrochloric acid. The solution of the separated siderite was pipetted onto membrane filter and Mg, Ca, Mn and Fe were determined by wavelength-dispersive X-ray fluorescence (WDXRF) spectrometry. The calibration was performed using 11 certified reference materials of iron ores. Matrix effects were corrected using empirical coefficient model for intermediate-thickness samples.

© 2008 Elsevier B.V. All rights reserved.

1. Introduction

Heavy metals are present in geological materials in various phases: silicates, carbonates, hydroxides, oxides, phosphate, adsorbed ions, etc. Element speciation in these materials is usually performed by using sequential extraction (selective dissolution), e.g. three-step BCR procedure based on Tessier scheme [1]. The BCR can be successfully applied to a variety of matrices, including sludges [2,3], soils [4,5], sediments [6,7] and fly ash samples [8]. Advances and difficulties of sequential selective extraction techniques used to fractionate the solid-phase forms of metals are discussed in a review paper [9]. Analytical procedures of sequential extraction differ from each other in many steps, including sample preparation, time of extraction, type and concentration of leachates, etc. The sequential extraction procedure can be modified for particular chemical composition of analyzed material, e.g. for soils with high carbonate content [10] or for analysis of selected analyte, e.g. the iron speciation in soils and sediments [11,12]. Poulton and Canfield developed procedure of sequential extraction for iron in sediments [13]. The procedure allows identifying the follow-ing phases: carbonate associated Fe (siderite and ankerite), easily reducible oxides (ferrihydrite and lepidocrocite), reducible oxides (goethite, hematite and akaganeite), magnetite, poorly reactive sheet silicate Fe, pyrite Fe and unreactive silicate Fe.

The selective dissolution can be applied not only for element speciation but also for separation of selected mineral from the others. Then separated mineral can be accurately analyzed by, e.g. X-ray fluorescence spectrometry (XRF). The aim of this study was to work out the analytical procedure for the determination of chemical composition of siderite $(Fe^{2+}, Me^{2+})CO_3$ (where $Me^{2+} = Mg^{2+}$, Ca^{2+}, Mn^{2+}) which is present in siderite concretions together with other minerals, e.g. calcite, quartz. Knowledge of chemical composition of these interesting geological materials allows for petrological studies on these minerals origin [14].

The micro-characterization of siderite concretions can be successfully performed using electron-probe microanalysis (EPMA) [15]. Nevertheless, this technique, suitable for microanalysis, should be carefully applied for determination of bulk composition, even if many micro-areas are analyzed. An accurate and precise determination of Mg, Ca, Mn and Fe in siderite requires complete separation of this mineral from other minerals, e.g. calcite, quartz.

For this purpose, selective dissolution in acetic acid (HAc) was applied. After dissolution, the liquid samples were pipetted onto membrane filters and measured by wavelength-dispersive

---

Fig. 1. The siderite concretion collected in Gnaszyn (Częstochowa, Poland).

X-ray spectrometry (WDXRF) [16]. Applying this method of sample preparation allows obtaining satisfactory detection limits for Mg, Ca and Mn which substitute Fe in siderite. The analyzed siderite concretions were collected in Gnaszyn (Czestochowa, Poland). The size of concretions ranged from a few centimeters to a few dozen centimeters in diameter. An exemplary siderite concretion from Gnaszyn is presented in Fig. 1. Early diagenetic concretions appearing within the Czestochowa Ore Bearing Clay Formation are cemented of rhombohedra siderite crystals and vary in grain size from 5 to 20 μm.

2. Experimental

2.1. Equipment

A wavelength-dispersive X-ray spectrometer with the side-window silver target X-ray tube was used for the measurements. The incidence and take-off angles were 60° and 40°, respectively. The X-ray tube was operated at 50 kV and 40 mA for determination of Mn, Ca, Fe and at 40 kV and 60 mA for determination of Mg. The measurements were performed in a vacuum with rotation of the sample. K lines were used for the determination of all elements. For detection, a flow-proportional counter (counter gas 90% Ar + 10% CH_4) was used. LiF (2 0 0) analyzing crystal was used for determination of Ca, Mn, Fe, whereas ADP was used for Mg. The counting times were 100, 40, 40 and 10 s for Mg, Ca, Mn and Fe determination, respectively. The net intensities were determined for each sample by the measurement of the fluorescent radiation of the analyte element (peak) and the measurement of the continuum close to the peak.

X-ray diffraction (XRD) analysis was performed on Philips PW 3710 using graphite monochromatized Co Kα radiation. The X-ray tube was operated at 45 kV and 30 mA. Counting times were 2, 3 or 8 s. Scans were conducted in the range from 3° to 75° with a step size of 0.01° or 0.02°.

Microanalysis was performed with EDS analyzer (EDAX, Sapphire) associated to scanning electron microscope (Philips XL 30 ESEM); accelerating voltage was 15 kV; takeoff angle 35°; 10 mm^2 area Si(Li) detector with super-ultra-thin window and 140 eV energy resolution.

2.2. Reagents

All chemicals used were of p.a. grade, obtained from POCh (Gliwice, Poland). The membrane filters were from Millipore (1.2 μm pore size, White RAWP, 25 mm diameter). The 11 certified reference materials of iron ores were used for calibration: 2-61/2, 2-62/2, 2-63/2, 2-64/2, 2-65/2, 2-66/2, 2-67/2 Iron ores (Institute of Ferrous Metals, Gliwice, Poland); 676-1 Iron Ore Sinter (Bureau of Analyzed Samples Limited, Newham Hall, Middlesbrough, England); JK 30 Iron ore (Granges Gruvor, Strassa, Sweden); Siderite GBW 07222 (Iron and Steel Research Institute, Wuhan Iron and Steel Corporation, Wuhan, China); ECRM 627-2 (Federal Institute for Materials Research and Testing (BAM), Berlin, Germany).

2.3. Influence of time extraction and concentration of acetic acid on the separation of calcite from siderite

The siderite concretion was crushed and pulverized in agate ball mill. 1 g of the sample was shaken in 150 mL of HAc of concentration 0.10, 0.25, 0.50, 0.75 and 1 mol L^{-1}. For each HAc concentration, the extraction was performed during the times of 0.5, 1, 2, 4, 5, 6 and 8 h.

After extraction, the sample was rinsed with water and dried. Then XRD measurements were performed for each sample. The calcium and iron were determined in each solutions obtained after extraction. Calcium was determined by complexometric titration in 5 mL of the solution obtained after extraction. Iron was determined by WDXRF. For this purpose, 1 mL of the solution obtained after extraction was pipetted onto Millipore filter and dried.

2.4. Reference sample preparation

Each certified reference material was additionally pulverized in an agate mortar and weighed in an amount of 100 mg. Then, the material was digested in platinum crucible in 3 mL of concentrated hydrofluoric acid. Digestion was carried out to achieve complete evaporation. The digestion in hydrofluoric acid was repeated three times to complete the evaporation of silica. Then, the residue was digested in 5 mL of concentrated hydrochloric acid. The solution was transferred into a 50-mL volumetric flask and filled up to the mark with water. Each solution of certified reference material was pipetted onto Millipore membrane filter in the amounts of 1.0, 1.5 and 2.0 mL. Finally, the 33 reference samples were obtained. Masses per unit area of the analytes were in the ranges: 0.2–10 μg cm^{-2} Mg, 0.3–56 μg cm^{-2} Ca, 0.1–3.7 μg cm^{-2} Mn, 43–298 μg cm^{-2} Fe. The membrane filters were mounted onto a plastic rings by means of a two-sided adhesive tape. The sample was dried under an IR heater at 50 °C.

2.5. Sample preparation

The sample was prepared in the following stages: the siderite concretion was crushed and pulverized in agate ball mill. Then, the analyzed material was weighed in an amount of 1 g and shaken
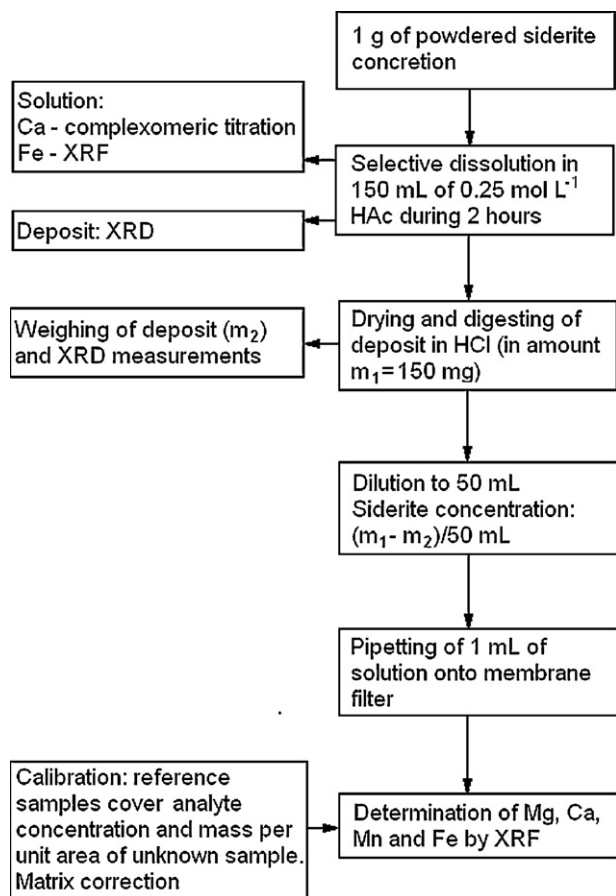
Fig. 2. Analytical procedure for determination of chemical composition of siderite present in concretion.

Fig. 3. Back-scattered electron (BSE) image of quartz crystal surrounded by siderite in selected area of concretion. (a) and (b) are micro-areas analyzed by EPMA.

formed using electron-probe microanalysis (EPMA). Nevertheless, results obtained by this technique can be loaded with an inadmissible error resulting from material inhomogeneity, geometric effects, etc. Fig. 3 presents back-scattered electron (BSE) image of quartz crystal surrounded by siderite in selected area of concretion. EPMA was performed for two micro-areas marked in Fig. 3 as points (a) and (b). The following results were obtained for these points 52.9% FeO, 4.7% CaO, 3.1% MgO and 48.2% FeO, 9.5% CaO, 2.5% MgO, respectively. Such high differences between these places can result from inhomogeneous distribution of Mg and Ca cations (Mn was not detected) in siderite. Moreover, the micro-areas of siderite in concretion are selected for EPMA measurements on the basis of BSE image. Fig. 4 presents two situations possible in EPMA. In the first one, only the elements in siderite are excited by electrons. In

in 150 mL of 0.25 mol L^{-1} HAc during the time of 2 h. The suspension was filtered and the deposit was rinsed with water and dried. Next, the deposit (siderite and mainly quartz) was weighed in an amount $m_1 = 150$ mg and digested in 10 mL of hydrochloric acid (1:1). After digestion, the solution was filtered, the deposit (mainly quartz) on the filter was rinsed with water and the filtrate was transferred into a 50-mL volumetric flask and filled up to the mark with water. Then, 1 mL of the obtained solution was pipetted onto Millipore membrane filter. The sample was dried under an IR heater at 50 °C. Because each concretion contained various quantities of the siderite, the deposit (remaining after digestion in hydrochloric acid) was dried and weighed (m_2) for calculation of the concentration of siderite solution: $(m_1 - m_2)/50$ mL. The complete analytical procedure for determination of chemical composition of siderite is presented in Fig. 2.

3. Results and discussion

The aim of this study was to work out a procedure for XRF analysis of siderite (Fe^{2+}, Me^{2+})CO$_3$ (where Me^{2+} = Mg^{2+}, Ca^{2+}, Mn^{2+}) that was present in siderite concretion together with other minerals like calcite and quartz and also with minor minerals: kaolinite, sphalerite and pyrite, etc. XRD analysis indicated that the mineralogical composition of investigated concretions varied within the limits: 64–93% siderite, 6–30% calcite, 0.3–17% quartz.

In the siderite, the Fe^{2+} cation can be substituted with other cations like Mg^{2+}, Ca^{2+} and Mn^{2+}. Therefore, these elements were determined together with iron. The analysis of siderite which is presented in concretion together with other minerals can be per-
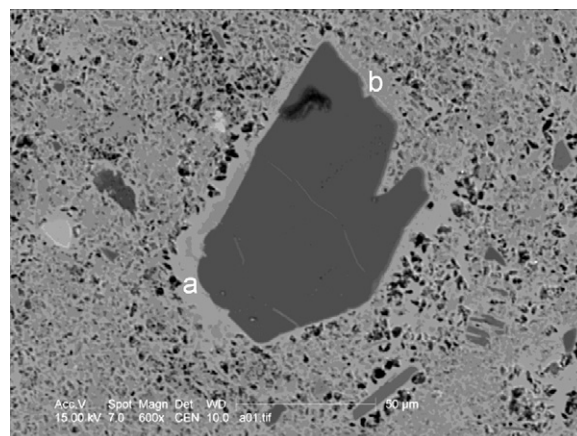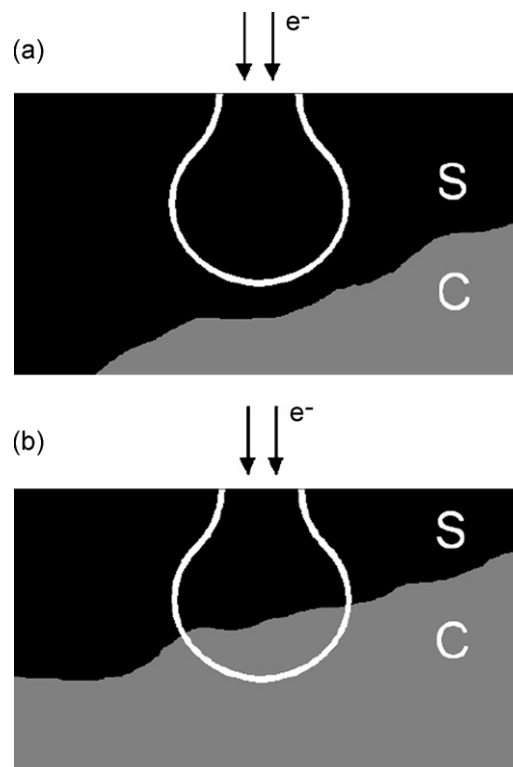

Fig. 4. The possible situations in EPMA: (a) siderite analysis; (b) analysis of siderite and calcite; S—siderite; C—calcite.

No. of analyzed micro-area	MgO, % (m/m)	CaO, % (m/m)	FeO, % (m/m)
1	3.1	4.7	52.9
2	2.5	9.5	48.2
3	2.8	7.1	50.6
4	2.1	8.6	49.7
5	2.8	6.3	51.5
6	2.3	5.6	52.8
7	1.7	11.6	46.9
8	2.8	7.8	49.7
9	3.6	4.1	52.7
10	3.2	3.3	54.2
11	2.8	7.9	49.6
Mean ± S.D.	2.7 ± 0.5	7 ± 2	51 ± 2
CV%	19	29	4

S.D.—standard deviation and CV—coefficient of variation.

the second one, elements in both siderite and calcite are excited and detected, which is not observed in the BSE image. In this case, concentration of Ca can be significantly overestimated. Thus, the EPMA results should be carefully interpreted in the analysis of siderite, when other minerals are also presented. Moreover, EPMA cannot be recommended for determination of bulk chemical composition of the whole siderite in concretion or selected areas, even if the analysis is performed in many places and then the average result is calculated. For instance, Table 1 presents EPMA data obtained for 11 analyzed micro-areas of siderite in concretion. The analyte concentrations vary within the ranges: 1.7–3.6%, 3.3–11.6% and 46.9–54.2% for MgO, CaO, FeO, respectively. The very high dispersion of results for calcium can be explained by inhomogeneous distribution of Ca cations in siderite or by a situation presented in Fig. 4.

This study focuses on determining of the bulk chemical composition of siderite in concretions. The selective dissolution was used for separation of siderite from other minerals present in concretion. The acetic acid, ammonium acetate and sodium acetate solutions were used for selective dissolution of calcite. Nevertheless, satisfactory results were obtained only for HAc solution. The selective extraction was performed using HAc of concentration from 0.1 to 1 mol L^{-1} during the times from 0.5 to 8 h (for each concentration). The following measurements were performed for each solution after extraction and for each residue:

- calcium and iron were determined in the solution after extraction. The calcium concentration indicates the degree of dissolution of calcite. The quantity of iron indicates whether the siderite is dissolved.
- XRD measurement of residue was performed to confirm the complete dissolution of calcite.

The calcium determined in solutions after extraction (one selected concretion) performed during the time above 1 h (expressed as concentration of calcite in concretion) vary within the range from 29.4 to 30.9% (m/m) CaCO$_3$ (the mean value 30.3 ± 0.4% (m/m)). These results indicate complete dissolution of calcite in these cases. The dispersion of the results can be explained by certain inhomogeneity of the material and an uncertainty of the complexometric titration method. The X-ray diffraction measurements of residue confirm complete dissolution of calcite as well.

Fig. 5 presents influence of HAc concentration and extraction time on iron concentration in the solution after extraction. The influence of time extraction from 0.5 to 8 h for HAc of concentrations of 0.1 and 0.25 mol L^{-1} on iron concentration was rather insignificant. The mean iron concentration equaled 0.67 ± 0.03% (m/m) for these extraction conditions. This quantity of iron resulted
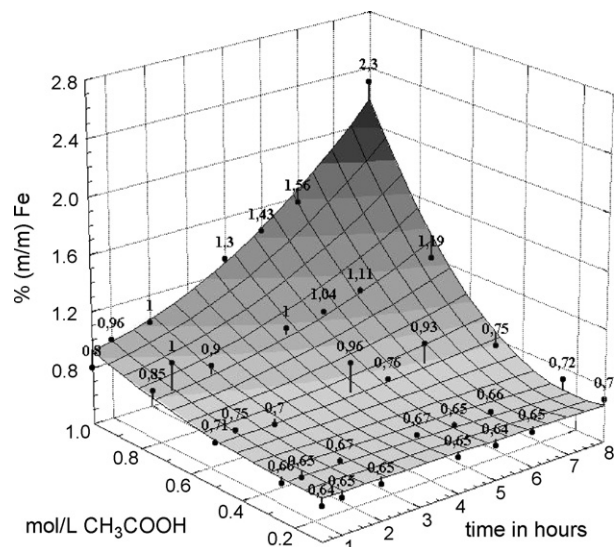
Fig. 5. Influence of HAc concentration and extraction time on the iron concentration in the solution after extraction.

from the presence of this element in dissolved calcite. The partial dissolution of the siderite was observed when HAc of concentration higher than 0.25 mol L^{-1} was applied, especially if extraction was performed for longer than 4 h. HAc of concentration 0.25 mol L^{-1} and extraction time of 2 h was adopted for the following experiments because in these conditions the siderite was not dissolved and, simultaneously, we were certain that calcite is dissolved completely.

Fig. 6a and b present diffraction patterns obtained for concretion before and after dissolution in 0.25 mol L^{-1} HAc performed during 2 h. In diffraction pattern obtained for concretion after dissolution, the calcite phase was not observed. After dissolution in 0.25 mol L^{-1} HAc, the deposit was dissolved in hydrochloric acid. Fig. 6c presents diffraction pattern for residue after digestion in hydrochloric acid. Besides quartz, the kaolinite, pyrite and sphalerite phases were also detected because these minerals were enriched as a result of digestion of calcite and siderite.

After selective dissolution in HAc, the sample was dried and weighed. Then, the sample was digested in hydrochloric acid and undissolved residue (mainly quartz) was separated by filtration.
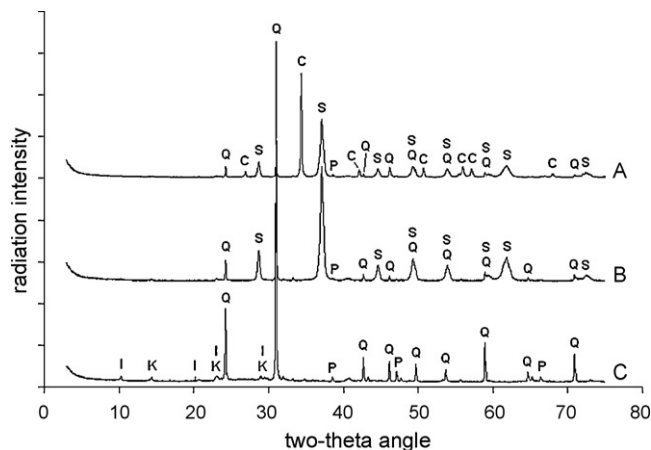

Fig. 6. Diffraction patterns obtained for concretion before extraction (A), after extraction in 0.25 mol/L HAc performed during 2 h (B) and after digestion in hydrochloric acid (C); Q—quartz, C—calcite, S—siderite, I—illite, K—kaolinite, P—pyrite and sphalerite.

Table 2
Residual errors RMS before and after matrix correction

Analyte	Mass range (μg cm^{-2})	RMS	
		Before matrix correction	After matrix correction
Mg	0.2–10	0.41	0.24
Ca	0.3–56	1.4	0.53
Mn	0.1–3.7	0.068	0.039
Fe	43–298	4.2	3.6

Because each sample of siderite concretion contained various content of quartz, various concentrations of siderite solutions were obtained. Thus, the samples of various mass per unit areas were obtained if solutions of analyzed siderites were pipetted onto filter in the same volume, i.e. 1 mL. In this case, the increasing absorption effects with regard to the mass per unit area of the sample should be expected. Therefore, in these samples, the radiation intensity of an analyte depended on matrix composition and sample mass per unit area. This problem can be simply solved using appropriate matrix correction method. In the previous papers, the empirical and theoretical coefficient models deduced from the Sherman equation were proposed for the correction of matrix effects in intermediate-thickness samples [17,18]. In the analysis of samples pipetted onto filters, the empirical coefficient model is more appropriate than the theoretical algorithm, especially if a suitable number of reference samples is available. The following equation was applied for matrix correction:

$$m_i = K_i I_i \left(1 + a_i m + \sum_{j=1}^{n} m_j \alpha_{ij} \right) + B_i$$

$$m = m_i + \sum_{j=1}^{n} m_j \qquad W_i = (m_i/m)$$

(1)

where m_i and m_j are masses per unit area of the analyte i and matrix element j, respectively; m is mass per unit area of the sample, K_i and B_i are slope and intercept, respectively; a_i is the coefficient that is constant for given range of the masses per unit area of the samples; α_{ij} is the influence coefficient of matrix element j on analyte element i; W_i is the weight fraction of analyte.

The values of the coefficients K_i, a_i, α_{ij} and B_i in Eq. (1) were determined by the leastsquares fit on the basis of solutions of the reference materials pipetted onto the membrane filter. Table 2 presents the residual errors RMS (root of the mean square of the sum of the differences between the measured value and the calculated values) before and after matrix correction using Eq. (1). Residual errors RMS were calculated according to the following formula:

$$\text{RMS} = \sqrt{\frac{\sum_k (m_{\text{chem},k} - m_{\text{calc},k})^2}{p - q}}$$

(2)

where $m_{\text{calc},k}$ is calculated mass per unit area of analyte in standard k; $m_{\text{chem},k}$ is mass per unit area of analyte in standard k; p is the number of standards; q is the number of coefficients in Eq. (1).

The values of RMS indicated an improvement of the results after matrix correction. This improvement resulted not only from the matrix effects in the samples of the same thickness (mass per unit area) but also from the increase of self-absorption effects together with sample thickness. Table 3 presents WDXRF analysis of certified reference material of siderite GBW 07222. The standard deviations were calculated for three samples and three measurements were carried out for each of them. The differences between certified val-

Table 3
WDXRF analysis of certified reference material of siderite GBW 07222 (three samples and three measurements for each analyte)

Analyte	Certified values, % (m/m)	WDXRF, %(m/m)
MgO	4.20	4.3 ± 0.2
CaO	5.20	5.3 ± 0.1
MnO	0.25	0.23 ± 0.01
FeO	50.8	50.4 ± 0.2

Table 4
Precision of WDXRF analysis (three measurements for each analyte)

Sample no.	MgO, % (m/m)	CaO, % (m/m)	MnO, % (m/m)	FeO, % (m/m)
1	2.1	6.1	0.15	52.4
2	2.4	6.1	0.15	51.9
3	2.4	6.2	0.15	51.9
4	2.3	6.2	0.16	52.0
5	2.2	6.3	0.16	52.0
6	2.4	6.5	0.17	51.6
Mean ± S.D.	2.3 ± 0.1	6.2 ± 0.2	0.16 ± 0.01	52.0 ± 0.3
CV%	4.3	3.2	6.3	0.6

S.D.—standard deviation and CV—coefficient of variation.

ues and WDXRF analysis could be explained by sample preparation (e.g. inhomogeneity of masses per unit area), counting statistics as well as some errors of empirical matrix correction. Nevertheless, the agreement between certified values and WDXRF analysis is satisfactory and indicates the usefulness of the sample preparation for siderite analysis. Precision of XRF analysis including sample inhomogeneity, selective dissolution, sample preparation and counting statistics was also investigated. Six samples of selected powdered siderite concretion were selectively dissolved in HAc, the residues were digested in hydrochloric acid and pipetted onto membrane filters and WDXRF measurements were carried out for each of them. The results included in Table 4 can be regarded as satisfactory and useful to geological studies. Results of exemplary analysis of siderites after separation from other minerals present in concretions are included in Table 5. The concentrations of all determined elements were above obtained detection limits (DL) which are presented in Table 6 (DL $= (3/k)(R/t)^{1/2}$, where k is the sensitivity in counts cm^2 s^{-1} μg^{-1}, R is background count rate in counts s^{-1} and t is counting time). The chemical composition of siderite (Table 5) is useful for inferring the palaeoenvironments (pore water chemistry

Table 5
WDXRF analysis of exemplary siderites (three samples and three measurements for each analyte)

Concretion no.	MgO, % (m/m)	CaO, % (m/m)	MnO, % (m/m)	FeO, % (m/m)
1	2.6	3.6	0.21	54.4
2	2.5	4.3	0.17	53.9
3	2.6	4.0	0.19	54.0
4	2.1	6.1	0.15	52.4
5	2.5	5.3	0.17	52.7
6	2.1	5.4	0.14	53.1
7	1.9	8.0	0.13	50.6
8	2.0	3.6	0.17	55.2
9	0.8	23.3	0.11	35.1
10	1.4	11.9	0.12	46.9

Table 6
Detection limits

Analyte	μg cm^{-2}	% (m/m)
Mg	0.21	0.04
Ca	0.013	0.003
Mn	0.036	0.007
Fe	0.087	0.02

and microbial influence). Precipitation of siderite from pore water with different Mg:Ca ratio (3:1, as in seawater, 1:1 as in brackish water and 1:3 as in freshwater) should reflect this ratio in the chemical composition. The precipitation of the concretionary siderite from Gnaszyn was probably a microbially moderated process. Mortimer et al. [19] suggest that microbially precipitated concretions do not simply retain the chemistry of the water from which they precipitate. The trace metal composition also reflects the community structure, activity and nutritional status of the incipient microorganisms. The proposed method of separation can be successfully applied if apatite is not present in concretions. Otherwise, Ca concentration determined in siderite can be overestimated because of incomplete dissolution of apatite in HAc. Thus, apatite concentration has to be controlled by XRD measurement of residue after extraction. However, in the investigated siderite concretions collected in Gnaszyn, the apatite was not detected by XRD.

4. Conclusions

Accurate determination of chemical composition of siderite present in concretion requires a complete separation of this mineral from other minerals. The precise separation of siderite from calcite is especially important for accurate determination of calcium. Otherwise, calcium concentration can be significantly overestimated if separation is incomplete. Selective dissolution in HAc of concentration $0.25 \, mol \, L^{-1}$ during 2 h allows to separate siderite completely from calcite, which was confirmed by XRD measurements of the residue and determination of Ca and Fe in the solution.

The worked out analytical procedure was successfully applied for the analysis of siderite in concretions whose mineralogical composition varied within the limits: 64–93% siderite, 6–30% calcite, 0.3–17% quartz. After the digestion of the residue, the solution was pipetted onto membrane filters. This method of sample preparation, suitable for liquid samples, allows to obtain satisfactory sensitivity and detection limits.

References

[1] A. Tessier, P.G.C. Campbell, M. Bisson, Anal. Chem. 51 (1979) 844.
[2] E.D. van Hullebusch, S. Utomo, M.H. Zandvoort, P.N.L. Lens, Talanta 65 (2005) 549.
[3] R. Zufiaurre, A. Olivar, P. Chamorro, C. Nerin, A. Callizo, Analyst 123 (1998) 255.
[4] M. Žemberyová, J. Barteková, I. Hagarová, Talanta 70 (2006) 973.
[5] M. Žemberyová, R. Jankovič, I. Hagarová, H.-M. Kuss, Spectrochim. Acta B 62 (2007) 509.
[6] P. Pazos-Capeáns, M.C. Barciela-Alonso, A. Bermejo-Barrera, P. Bermejo-Barrera, Talanta 65 (2005) 678.
[7] C.M. Davidson, R.P. Thomas, S.E. McVey, R. Perala, D. Littlejohn, A.M. Ure, Anal. Chim. Acta 291 (1994) 277.
[8] C. Brunori, Z. Mester, C. Cremisini, P. Fodor, R. Morabito, Ann. Chim. 89 (1999) 891.
[9] C. Gleyzes, S. Tellier, M. Astruc, TrAC-Trend. Anal. Chem. 21 (2002) 451.
[10] M. Sulkowski, A.V. Hirner, Appl. Geochem. 21 (2006) 16.
[11] T.T. Chao, L. Zhou, J. Soil Sci. Soc. Am. Proc. 47 (1983) 225.
[12] G.E.M. Hall, J.E. Vaive, R. Beer, M. Hoashi, J. Geochem. Explor. 56 (1996) 59.
[13] S.W. Poulton, D.E. Canfield, Chem. Geol. 214 (2005) 209.
[14] H.A. Middleton, C.S. Nelson, Sediment. Geol. 103 (1996) 93.
[15] K.S. Choi, B.K. Khim, K.S. Woo, Mar. Geol. 202 (2003) 17.
[16] R. Sitko, B. Zawisza, M. Czaja, J. Anal. At. Spectrom. 20 (2005) 741.
[17] R. Sitko, X-ray Spectrom. 34 (2005) 11.
[18] R. Sitko, X-ray Spectrom. 35 (2006) 93.
[19] R.J.G. Mortimer, M.L. Coleman, J.E. Rae, Sedimentology 44 (1997) 759.

Review

A review of analytical techniques for determination of oxicams, nimesulide and nabumetone

Małgorzata Starek*, Jan Krzek

Jagiellonian University, Collegium Medicum, Department of Inorganic and Analytical Chemistry, 9 Medyczna Str., 30-688 Cracow, Poland

ARTICLE INFO

ABSTRACT

Non-steroidal anti-inflammatory drugs (NSAIDs) are the group most often used in human health care, since they are available without prescription for treatment of fever and minor pain. The present review submitted the use of various analytical techniques for the determination of oxicams, nimesulide and nabumetone. This review covers the time period from 1990 to 2008 during which over 200 analytical methods including all types of chromatographic, spectrophotometric and voltammetric techniques were reported. Presented application concerns analysis of chosen NSAIDs from pharmaceutical formulations and biological samples.

© 2008 Elsevier B.V. All rights reserved.

Contents

1. Introduction

Non-steroidal anti-inflammatory drugs (NSAIDs) are a group of drugs of diverse chemical composition and different therapeutic potentials having a minimum of three common features: identical basic pharmacological properties, similar basic mechanism of action as well as similar adverse effects. Moreover, all drugs in this group exhibit acidic character. pK_a values are in the range of 3–5 (acids of medium strength).

NSAID molecules contain hydrophilic groups (carboxylic or enolic group) and lipophilic ones (aromatic ring, halogen atoms). In accordance with their acidic character, NSAIDs occur in the gastric juice in the protonated (lipophilic) form. Also in the small intestine, there are conditions favourable for absorption of weak acids. NSAID exist in highly ionized forms in plasma. Low values defining NSAIDs distribution volume (from 0.1 to 1) in tissues may be a proof of poor distribution of these drugs in extravascular systems. A very high degree of binding with plasma proteins (>97%) is the result of favourable amiliphilic properties and accounts for the fact of displacing other drugs from protein binding of NSAIDs [1,2].

NSAIDs are classified according to their chemical structure into the following groups: salicylic acid derivatives (i.e. acetylsalicylic acid, salicylamid, sodium salicylate); aniline and p-aminophenol derivatives (i.e. paracetamol, phenacetyne); pyrazolone derivatives (i.e. phenylbutazone, propyphenazone); indoleacetic acid derivatives (i.e. indomethacin, sulindac); phenylacetic acid derivatives (i.e. diclofenac); propionate acid derivatives (i.e. ibuprofen, naproxen, ketoprofen, tiaprofenic acid); enolic acid derivatives (i.e. piroxicam, meloxicam, tenoxicam); antranil acid derivatives (i.e. mefenamic acid, flufenamic acid); nicotinic acid derivatives (i.e. niflumic acid); pyranocarboxylic acid derivatives (etodolac); pyrrolepyrroles (ketorolac); coxibes (i.e. celecoxib, etoricoxib); naphtylbutanone derivatives (nabumetone); sulphonamides (nimesulide); benzoxazocine derivatives (nefopam) [3,4].

NSAIDs are easily available and effective and thus are extensively used by patients. The growing demand for these agents stimulate a search for new even more effective drugs, but also calls for higher level of quality control of these therapeutic substances and preparations, so that they are in the highest possible degree free from any impurities that may come from the production process, as well as from decomposition products of active or auxiliary substances. Therefore, it seems appropriate to develop new analytical methods regarding their qualitative and quantitative analysis [5–7].

The progress of analytical chemistry in the scope of instrumentalisation of the methods of chemical analysis is reflected in the use thereof in pharmacopeia monographs as well as in the standards adopted by manufacturers. A constant place is occupied by chromatographic methods (high-performance liquid chromatography (HPLC), thin layer chromatography (TLC), and gas chromatography (GC)). Unification of the equipment used necessitates preparation of a very accurate and detailed description of conditions for carrying out the analysis. Other meaningful methods having a big meaning are also ultraviolet-visible (UV–vis) and infrared (IR) spectrophotometry, atomic absorptive spectrometry (AAS), nuclear magnetic resonance (NMR), mass spectrometry (MS) or spectrofluorimetry. Among the analytical methods used for determining NSAIDs are also electromigrational (capillary electrophoresis (CE), capillary zone electrophoresis (CZE), and micellar electrokinetic capillary chromatography (MEKC)) and voltamperometric methods. One that has been gaining more and more applications is the flow injection analysis (FIA), whose main advantage is the full automation of the analysis, considerably minimises the effects of side reactions and thus increases the sensitivity and selectivity of this method.

Introduction of new methods, enabling carrying out determinations with maximum accuracy, contributes to increased interest in analytical methods as such. They should enable to simultaneously determine the individual components in multi-component preparations and in biological material. Range of guidelines, standardising requirements concerning the quality of drugs, have been issued. Fulfilment confirms them the appropriate quality of the product and of the analytical method used. These are numerical parameters that validate reliability of the results and enable comparing efficiency of the methods used. The process that is used to determine the above parameters is the so-called method validation [8].

Oxicams are a group of NSAIDs derived from the benzene(thieno)thiazine heterocyclic system, where the group of N-heterocyclic carboxamide include the triazine sulphur, and in position 4 there is an enolic group. Condensation of benzene ring or thiophene with the heterocyclic system as well as substitution of the amide group in position 3 imparts acidic properties to the enolic group. This is a group of drugs of diverse chemical composition whose common feature is high affinity for both cyclooxygenase (COX) isomers, with some predominance to inhibit COX-2 activity [3,4]. The structures of the investigated drugs are illustrated in Fig. 1.

Oxicams, nimesulide and nabumetone are the recent development of NSAIDs and there is a great need to review the analytical work reported so far in the literature. Our objective was to compile the published analytical methods dealing with formulated, unformulated drugs, biological samples including metabolites and degradation studies. Efforts have been made to collect the literature from 1990 up to the present and the analytical procedures have been tabulated in the proceeding sections. Techniques like spectrophotometric, fluorimetric, chromatographic (HPLC, TLC, and GC), capillary electrophoresis (CE, CZE, and MEKC), voltammetric and others have been used for analysis. The percentage of their utility is shown in Fig. 2, from which it can be seen that HPLC and spectrophotometric methods have been used most extensively.

2. Analytical methods for drug determination

2.1. Piroxicam

Piroxicam (4-hydroxy-2-methyl-N-(pyridine-2-yl)-2H-1,2-benzothiazine-3-carboxamide-1,2-dioxide) is a well-known non-steroidal anti-inflammatory and analgesic drug, indicated for acute or long-term treatment of inflammation associated with musculoskeletal and joint disorders, such as osteoarthritis, rheumatoid arthritis and ankylosing spondylitis. Piroxicam acts as an anti-inflammatory agent mainly by prostaglandin synthesis inhibition, as well as by leucocytes migration and phagocyte activity inhibition. The chemoprevention effect of piroxicam is attributed to its property of reducing levels of prostaglandins which are associated with carcinogenesis in the colon. However, the inhibitory effect of piroxicam in prostaglandin E_2 (PGE_2) synthesis is responsible for the ulcerogenic action of piroxicam on the gastrointestinal tract. Piroxicam strongly inhibits COX-2 activity as well as migration of neutrocytes to inflammatory foci in the presence of prostaglandins. It is fully biotransformed in the liver by hydroxylation of the pyridol ring of the side chain and by coupling with gluconic acid, to inactive metabolites excreted with urine and faeces [1–4].

Potentiometric titration in anhydrous acetic acid with 0.1 M perchloric acid as titrant is recommended by pharmacopoeal monographies for the determination of piroxicam [9,10]. However, USP 24 LC method on L1 (3.9 mm × 30 mm) column with

buffer mixture: aqueous solutions of anhydrous acid and dibasic sodium phosphate + methanol (55 + 45, v/v) as a mobile phase is recommended. Solutions ought to be prepared in 0.01 M methanolic hydrochloric acid and the detection wavelength should be at $\lambda = 254$ nm. However, for substance identification infrared absorption spectrophotometry [9,11], colorimetry (reaction with sodium hydrogen carbonate, potassium hexacyanoferrate(III) and mercury; reddish color product) [10] and thin-layer chromatography (stationary phase: silica gel; mobile phase: toluene + glacial acetic acid (95 + 5, v/v); solutions in mixture: chloroform:methanol (1:1, v/v), detection under short-wavelength ultraviolet light) are recommended [11].

Techniques as chromatography (about 40%), spectrophotometry (about 30%), also electrophoresis (about 7%), voltammetric (about 10%) and FIA (about 10%) have been used most often for determination of piroxicam. Among chromatographic methods HPLC is the most popular technique [12–14]. It has been used with spectrophotometric [15–34], fluorimetric [35], amperometric [36,37],

mass spectrometry [29,38–41] or NMR [25] detection. The LC-chromatographic conditions are presented in Table 1. The majority of studies concern determination of piroxicam content in pharmaceutical preparations or biological material, in various conditions of chromatographic separation or different processes of a sample preparation. Yritia et al. proposed two solid-phase extraction (SPE) methods. Off-line extraction consists of activating SPE cartridges (Bond-Elut C_8 100 me) with methanol and conditioning with water and phosphate buffer (0.15 mM) at pH 3.5. Thereafter, the sample (blank, plasma) with internal standard (I.S.) was transferred to the cartridges. The cartridges were washed with buffer and eluted with mobile phase, and injected into HPLC system. In the on-line extraction process, SPE cartridges were activated with methanol and water. The vials containing sample with I.S. were placed in the autosampler and programmed to apply sample to every cartridge. Then, the cartridge was rinsed with phosphate buffer (0.15 M, pH 3.5) and solutions were eluted with mobile phase [26]. Gaudiano et al. developed a method for determination of
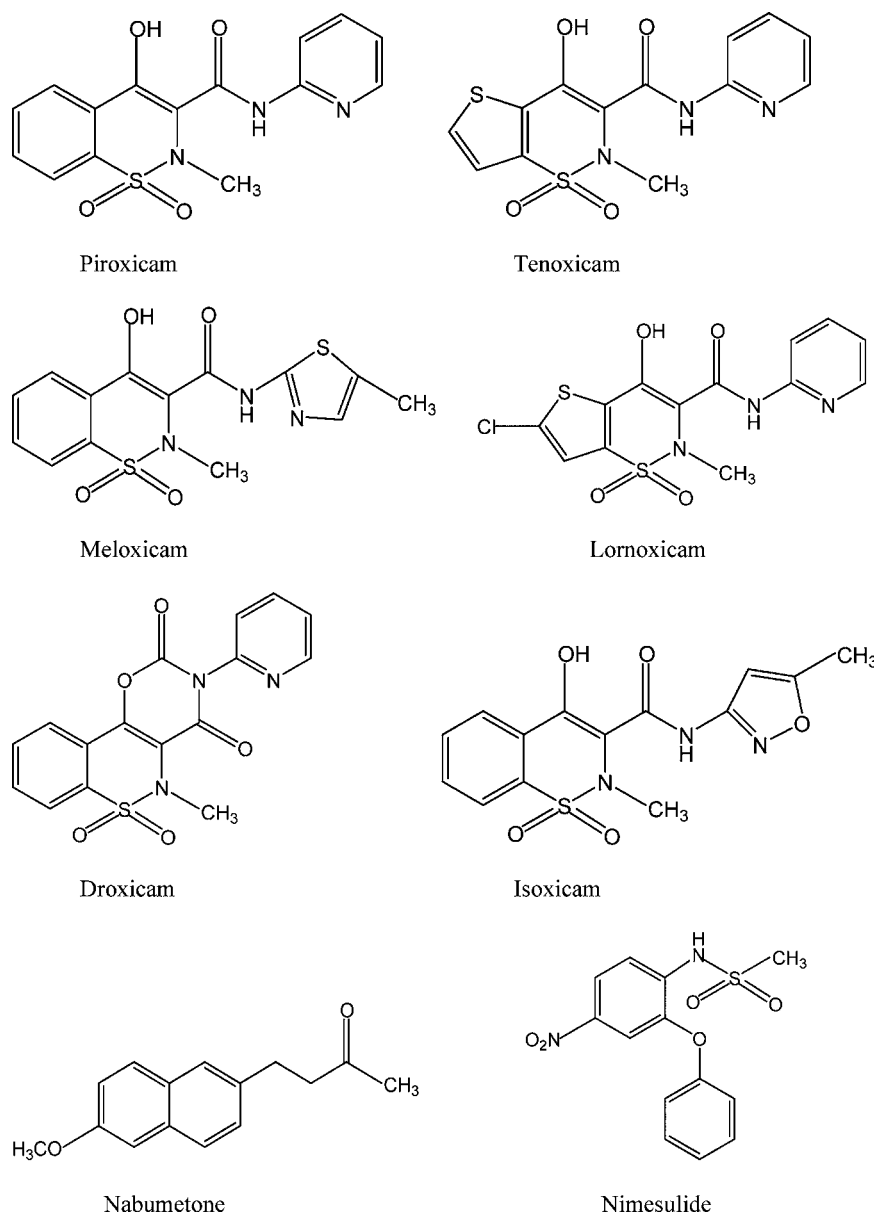

Fig. 1. Chemical structures of analyzed substances.

diclofenac and piroxicam by RP-HPLC after reaction with OH• free radicals to detect newly formed oxidation and degradation products. OH• free radicals were obtained by means of ferrous sulphate and ʟ-ascorbic acid mixtures. During the reaction the mixtures were exposed to irradiation by a tungsten lamp to obtain an increased and more reproducible formation of hydroxyl radicals [27]. After addition of I.S. and protein precipitation using acetonitrile, human serum samples were transferred with mobile phase (gradient system: 30% $CH_3CN + n$-propanol (954 + 45) solvent and 70% dilute NaOH) to autosampler vials for direct analysis. Autosampler was connected directly to the MS–MS with approximately 0.5 m (poly 1,4-phenylene ether ketone) tubing. Injection of an air bubble with the sample and a multiple reaction monitoring method using argon collision-induced dissociation of analyte $[M-H]^-$ ions permitted integration of the product ion peak areas to produce reproducible quantitative data over the range of concentrations expected in serum [41].

Apart from HPLC, HPTLC method was used for the determination of piroxicam using silica gel aluminium plate 60 F_{254} as stationary phase and mixture: toluene + acetic acid (8 + 2, v/v) as mobile phase, with densitometric detection at $\lambda = 360$ nm [42]. Bartsch et al. exposed the samples to radiation in the Suntest in three concentration ranges, and then they performed determination of the solutions obtained on HPTLC silica gel 60 F_{254} plates, rinsing them before use with a mixture of methanol and dichloromethane (1:1, v/v), and using chloroform + 96% acetic acid (9 + 1, v/v) as the mobile phase. Densitometric detection was carried out at $\lambda = 280$ nm, and peaks were obtained for piroxicam of retention distance value of 27 mm [23]. TLC matrix-assisted laser desorption/ionization (MALTI) TOF MS was used for preparing the matrix on the plate in order to minimise interference. The piroxicam determination studies were carried out with four methods, and the best results were obtained by pre-development of the TLC plates in mobile phase (chloroform + methanol (9 + 1, v/v)) to which the I.S. (tenoxicam) was added. Thereafter, analyte solutions (in dichloromethane) were applied onto plates and the plates were developed again in the same mobile phase, obtaining peaks of $R_f \approx 0.63$ (piroxicam) and 0.37 (tenoxicam). MS analysis was executed directly from TLC strip with a modified linear Laser TOF 1500 mass spectrometer, equipped with a nitrogen laser ($\lambda = 337$ nm). The TLC strip were scanned over a distance of 50 or 55 mm and mass spectra were recorded every 0.5 mm [43]. Other separation methods used in studies of piroxicam are electrophoretic methods, i.e. CE [23,44], CZE [45,46] or MEKC [45,47].

Also spectrophotometric methods were frequently used wherein detection was carried out within the UV [47,48] or VIS range [49–54]. For the determination of piroxicam UV difference spectrophotometry [31], first-derivative spectrophotometry [19,55,56] and spectrofluorimetry [57–64] were used too. Nepote et al. described conventional spectrophotometry combined with partial-least squared (PLS-1ver.) multivariate calibration in spectral range of 351–380 nm. Multivariate calibration methods such as PLS involve a calibration step in which the relation between spectra and substance concentration is estimated from a set of reference samples and a prediction step in which the results of the calibration are used to estimate the substance concentration in an unknown sample spectrum. The PLS-1ver. is optimized for the determination of a single analyte [47]. The spectrophotometric conditions for determination of piroxicam are presented in Table 2.

Piroxicam content was determined by adsorptive stripping voltammetric techniques, using conventional and chemically modified carbon paste electrodes in micellar media [65–67]. The methods based on the oxidation behaviors of piroxicam at the carbon paste electrode (CPE) are presented [68–70]. Square wave and
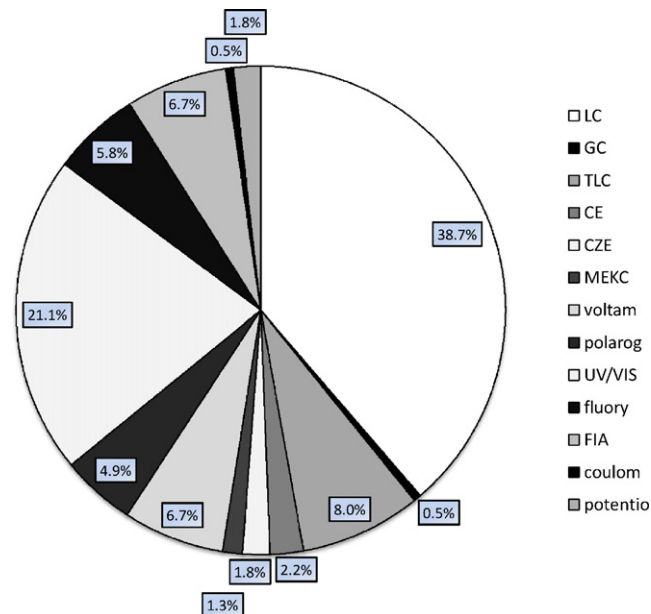

Fig. 2. Different techniques employed for determination of oxicams, nimesulide and nabumetone during 1990–2008.

square-wave adsorptive stripping voltammetric measurements were used by El-Maali et al. The potentials are referred to the Ag/AgCl/KCl(s) reference electrode and a platinum wire was used as a counter electrode with initial potential -0.6 V [71]. The electrochemical behavior of piroxicam was determined by classical and differential pulse mode adsorptive cathodic stripping voltammetry (AdCSV) in methanol with water (20:80, v/v) and acetonitrile with water (20:80, v/v) [72]. Norouzi et al. used fast Fourier transform continuous cyclic voltammetry (FFTCV) at a gold microelectrode for determining piroxicam in pharmaceutical formulations. The best effect was obtained at pH 2, scan rate value of 40 V/s, accumulation potential of 400 mV and time of 0.4 s [73]. Nikolic et al. reported a method for determination of piroxicam by coulometrically titrating with electrogenerated chloride in the presence of methyl orange as indicator [74]. Potentiometry with ion-selective membrane electrode in range of pH 4.0–7.5 [75] and potentiometric titration with 2×10^{-3} M N-bromosuccinimide solution in acid medium [51] were described. Among analytical methods for determination of piroxicam FIA with detection in the UV range [76], at $\lambda = 520$ nm after reaction with Fe(III) in methanol [77] and at $\lambda = 425$ nm after post-chemiluminescence reaction with N-bromosuccinimide and luminal [78] were reported. FIA methods are based on the luminescence sensitization of europium(III) (EuCl$_3$) by complexation with piroxicam ($\lambda_{ex} = 358$ nm and $\lambda_{em} = 615$ nm) [79] and by formation of complex with piroxicam in the presence of trioctylphosphine oxide and Tween-80 as surfactant ($\lambda_{ex} = 359$ nm and $\lambda_{em} = 615$ nm) [80]. Al-Momani developed a method based on the oxidation of piroxicam by N-bromosuccinimide in an acidic medium with chloranilic acid, to bleach purple color ($\lambda = 530$ nm) [81].

2.2. Tenoxicam

Tenoxicam (4-hydroxy-2-methyl-N-(pyridine-2-yl)-2H-thieno [2,3-e]-1,2-thiazine-3-carboxamide-1,1-dioxide) inhibits COX which catalyses the formation of cyclic endoperoxides. It is a derivative of oxicam with a thiophene ring replacing the benzene ring in piroxicam. Due to its accentuated hydrophilic character against other oxicam, tenoxicam is characterized by lower penetration into tissues, what explains reduced incidence of adverse

Table 1
LC methods used for the analysis of oxicams, nimesulide and nabumetone.

Compound	Sample matrix	I.S.	Chromatographic conditions				Ref.
			Column	Mobile phase (v/v)	Flow rate (mL min^{-1})	Detection	
Piroxicam	Human plasma, urine, bile	–	RP-C 10CN	ACN + water + dihydrogen phosphate solution	–	–	[14]
	Human plasma, urine	Naproxen	C$_{18}$ Spherisorb	ACN + 0.1 M sodium acetate (33 + 67) (pH 3.3)	–	330 nm	[15]
	Human plasma	Isoxicam	CN Spherisorb (5 μm)	ACN + water (6 + 94) containing 10 mM Na$_2$HPO$_4$, adjusted to pH 2	–	363 nm	[16]
	Tablets	–	HPODShypersil RP C$_{18}$ (100 mm × 3.9 mm; 5 μm)	Phosphate buffer (pH 7.8; 0.05 M) + methanol (6 + 4)	1.0	254 nm	[19]
	Hairless rat skin	Tenoxicam	Scharlau C$_{18}$ (12 cm × 0.46 cm; 5 μm)	ACN + acetate acid 4% (pH 2.8) (45 + 55)	1.0	354 nm	[20]
	Rat plasma	Tenoxicam	μBondapak ODS C$_{18}$ (300 mm × 3.9 mm; 10 μm)	Methanol + 10 mM phosphate buffer pH 2 (45 + 55)	1.5	361 nm	[21]
	Human plasma	–	NovaPak C$_{18}$ (25 cm × 4.6 mm; 4 μm) with C$_{18}$ precolumn (20 mm × 3.9 mm; 10 μm)	0.1 M sodium acetate + ACN + TEA (61 + 39 + 0.05) adjusted to pH 4 with glacial acetic acid	1.5	330 nm	[22]
	Substance	–	LiChrospher 100 RP18 (119 mm × 3 mm; 5 μm)	Isocratic elution: methanol + acetate buffer (pH 4.3; 0.4 M) (45 + 55)	–	254 nm; 280 nm	[23]
	Substance	–	Phenomenex Luna C$_{18}$ (150 mm × 4.6 mm; 5 μm)	ACN + water + acetic acid (45 + 47 + 8)	1.5	254 nm	[24]
	Substance	–	Spherisorb NH$_2$ (250 mm × 4.6 mm; 5 μm)	Phosphate buffer (50 mM NaH$_2$PO$_4$; pH 3.4, 5.5, 6.7, 8.0) + methanol (40 + 60)	1.0	247 nm ^{1}H NMR	[25]
	Substance	Tenoxicam	Kromasil C$_{18}$ (150 mm × 4 mm; 5 μm)	ACN + phosphate buffer (20 mM, pH 3.1) (50 + 50)	1.0	486 nm; 484 nm	[26]
	Substance	–	Hypersil BDS C$_{18}$ (250 mm × 4.6 mm; 5 μm)	ACN + KH$_2$PO$_4$ solution (6.81 g L^{-1}; pH 3) (28 + 72)	1.0	230 nm	[27]
	Human urine	–	RP Inertsil ODS-2 (150 mm × 4.6 mm; 5 μm)	50 mM phosphate buffer + ACN (58 + 42) at pH 5	0.9	230 nm	[28]
	Homeopathic preparations	Benzoic acid	Agilent Zorbax Eclipse XDB C-18 (150 mm × 4.6 mm; 5 μm)	ACN + water with acetic acid 0.1%, pH 3.18; isocratic elution (A:B) 3 min → (15 + 85), 7 min → (30 + 70), 20 min → (90 + 10)	1.0	245 nm; ESI-MS m/z 330	[29]
	Pharmaceutical preparations	Isoxicam	LiChrospher RP18	Tris acetic acid buffer + TBA reagent + tetrahydrofuran + ACN	–	360 nm	[30]
	Capsules, tablets	–	LiChrospher 100 RP-18 (5 μm); LiChrocart 125-4	Buffer solution: citric acid + Na(OH)$_2$PO$_4$ (pH 3) (55 + 45)	–	254 nm	[31]
	Blood, plasma, solutions	–	Nucleosil C$_{18}$	ACN + distilled water + acetic acid (58 + 38 + 4)	1.0	365 nm	[32]
	Human blood	Isoxicam	Devolsil ODS-5 (250 mm × 1.5 mm; 5 μm)	ACN + 0.1 M acetate buffer (pH 5) + methanol	0.1	365 nm	[34]
	Human serum, capsules	Naproxen	ACE C-18 with trimethylsilane (150 mm × 4.6 mm; 5 μm)	ACN + 0.1% aqueous H$_3$PO$_4$, using "dual-mode" gradient	–	λ_{ex} = 90 nm; λ_{em} = 45 nm	[35]
	Human plasma	–	RP-C$_{18}$	Methanol + water + phosphate buffer	–	Amperometric V = +0.9 V	[36]
	Human plasma, tissue	–	Higgins Haisil 120 BD C$_{18}$ (120 mm × 3 mm; 5 μm)	30 mM H$_3$PO$_4$ + methanol + tetrahydrofuran (600 + 320 + 80) containing 150 mg L^{-1} KCl, adjusted to pH 2.7 with 4 M NaOH	–	Amperometric V = +0.65 V	[37]
	Urine	–	Phenomenex Synergi Hydro-RP (1 mm × 150 mm) + Opti-Guard C$_{18}$ (1 mm × 15 mm)	100% formic acid 25 mM + ACN; gradient elution: 1–9 min to final proportion of 80%	0.075	MS/MS; m/z 332; 330	[38]
	Tablets, capsules	–	Shim-Pack	ACN + 1% acetic acid solution (4 + 1)	–	MS; m/z 332	[39]
	Human plasma	Isoxicam	Sunfire (2.1 nm × 100 nm; 5 μm)	Methanol + ammonium formate (15 mM, pH 3) (60 + 40)	0.2	MS/MS; m/z 332 → 95	[40]
Tenoxicam	Pharmaceutical preparations	Isoxicam	LiChrospher RP18	Tris acetic buffer + TBA + tetrahydrofuran + ACN	–	360 nm	[30]

Table 1 (*Continued*)

Compound	Sample matrix	I.S.	Chromatographic conditions				Ref.
			Column	Mobile phase (v/v)	Flow rate (mL min^{-1})	Detection	
	Plasma, blood, solutions	–	Nucleosil C_{18}	ACN + distilled water + acidic acid (58 + 38 + 4)	1.0	365 nm	[32]
	Human blood	Isoxicam	Devolsil ODS-5 (250 mm × 1.5 mm; 5 μm)	ACN + 0.1 M acetate buffer (pH 5) + methanol	0.1	365 nm	[34]
	Urine	–	Phenomenex Synergi Hydro-RP (1 mm × 150 mm) + Opti-Guard C_{18} (1 mm × 15 mm)	100% formic acid 25 mM + ACN; gradient elution: 1–9 min to final proportion of 80%	0.075	MS/MS; *m/z* 338; 336	[38]
	Tablets, capsules	–	Shim-Pack	ACN + 1% acetic acid solution (4 + 1)	–	MS; *m/z* 338.4	[39]
	Human plasma	Isoxicam	Sunfire (2.1 mm × 100 mm; 5 μm)	Methanol + formate ammonium (15 mM, pH 3) (60 + 40)	0.2	MS/MS; *m/z* 332 → 95	[40]
	Human plasma	Ketorolac	Nucleosil C_{18}	ACN + water + phosphate buffer (pH 2.8) (35 + 65)	–	355 nm	[84]
	Human plasma	Piroxicam	Zorbax 5B C_{18} (50 mm × 4.6 mm; 1.8 μm) + Phenomenex C_{18} (2 mm × 4.6 mm; 1.8 μm)	0.1% H_3PO_4 aqueous solution + ACN (65 + 35)	2.0	368 nm	[87]
	Tablets	2,4-Dinitrochlorobenzene	RP-C_8 Lichrosorb (250 mm × 4.6 mm; 10 μm)	0.02 M sodium acetate + methanol + ACN (11 + 8 + 1) with 0.005 M heptane sulphonic acid sodium salt (pH 3.5)	1.5	300 nm; 375 nm	[88]
	Tablets, ampoules, capsules	–	NovaPak C_{18} (150 mm × 3.9 mm; 4 μm)	Methanol + ACN + acetate buffer, pH 4.6 (1.9 + 0.1 + 3.0)	0.8	280 nm	[89]
Meloxicam	Pharmaceutical preparations	Isoxicam	LiChrospher RP18	Tris acetic acid + TBA + tetrahydrofuran + ACN		360 nm	[30]
	Human plasma	Isoxicam	Sunfire (2.1 mm × 100 mm; 5 μm)	Methanol + ammonium formate (15 mM, pH 3) (60 + 40)	0.2	MS/MS; *m/z* 352 → 115	[40]
	Tablets, ampoules, capsules	–	Nova-Pak C_{18} (150 mm × 3.9 mm; 4 μm)	Methanol + ACN + acetate buffer pH 4.6 (4.5 + 0.5 + 5)	0.8	280 nm	[89]
	Human plasma	–	RP-C 18	Methanol + phosphate buffer (pH 3.2) (60 + 40)	–	346 nm	[99]
	Tablets	Piroxicam	μBondapak 125 AC 18 (10 μm)	Methanol + water (70 + 30)	2.0	230 nm	[100]
	Tablets	Isoxicam	RP C_{18}	0.05 M tris acetic acid buffer + TBA + ACN	–	360 nm	[101]
	Human plasma	Tenoxicam	Prevail C_8 (150 mm × 4.6 mm; 5 μm)	ACN + water + 10 mM acetic acid (20 + 80)	–	MS/MS	[112]
	Plasma	Piroxicam	LiChrocart RP-18 (125 mm × 4 mm; 5 μm) + LiChrocart RP-18 (4 mm × 4 mm; 5 μm)	$(NH_4)_2HPO_4$ aqueous solution + methanol + ACN (5 + 4 + 1)	1.0	364 nm	[103]
	Human plasma	Piroxicam	Sunfire C_{18} (150 mm × 4.6 mm; 5 μm)	20 mM KH_2PO_4 + ACN (60 + 40) adjusted to pH 3.5 with H_3PO_4	1.2	355 nm	[104]
	Rat plasma		Gemini C_{18} (150 mm × 4.6 mm; 5 μm)	I: 50 mM phosphate buffer (pH 3.2) + ACN (40 + 60); II: 50 mM phosphate buffer (pH 3.2) + methanol (65 + 35)	1.0	I: 360 nm; II: 320 nm	[105]
	Human plasma	Piroxicam	LiChrospher C_{18} (125 mm × 4 mm; 5 μm)	Acetate buffer (pH 3.3, 170 mM) + ACN (62 + 38)	1.0	355 nm	[106]
	Horse plasma	–	LiChrocart 25-4 + LiChrospher RP-8 ADS	0.05 M phosphate buffer + ACN (70 + 30) and 25 mM t-butylamine at pH 7	0.8	364 nm	[107]
	Tablets	–	Phenomenex Luna C_{18} (250 mm × 4.6 mm; 5 μm)	Methanol + isopropanol + 50 mM phosphate buffer (pH 5.9) (51 + 9 + 40)	1.0	225 nm	[108]
	Tablets, suppository	–	Spherisorb ODS (250 mm × 4.6 mm; 5 μm)	Acetate buffer pH 4.3 + methanol (55 + 45)	–	UV	[109]
	Human plasma	Piroxicam	Phenomenex Luna C_{18} (150 mm × 2 mm; 5 μm)	ACN + 0.2% aqueous formic acid (65 + 35), pH 3.1	0.3	MS/MS; *m/z* 352 → 115	[113]

Table 1 (*Continued*)

Compound	Sample matrix	I.S.	Chromatographic conditions				Ref.
			Column	Mobile phase (v/v)	Flow rate (mL min^{-1})	Detection	
	Human plasma	Piroxicam	Zorbax SB C$_{18}$ (150 mm × 4.6 mm; 5 μm) + Security Guard C$_{18}$ (4 mm × 3 mm)	ACN + water + formic acid (80 + 20 + 0.2)	0.5	MS/MS; m/z 352 → 115	[114]
	Animal tissue	Flunixin-D3	Xterra (150 mm × 2.1 mm; 5 μm)	Formic acid 10 mM + methanol (A:B); gradient program: 0.1–1 min → 70% B, 10–13 min → 90% B, 13–23 min → 70% B	0.25	MS; m/z 352 → 115, 141, 184	[115]
Lornoxicam	Pharmaceutical preparations	Isoxicam	LiChrospher RP 18	Tris acetic acid buffer + TBA + tetrahydrofuran + ACN	–	360 nm	[30]
	Human blood	Isoxicam	Devolsil ODS-5 (250 mm × 1.5 mm; 5 μm)	ACN + 0.1 M acetate buffer (pH 5) + methanol	0.1	365 nm	[34]
	Tablets, ampoules, capsules	–	Nova-Pak C$_{18}$ (150 mm × 3.9 mm; 4 μm)	Methanol + ACN + acetate buffer (pH 4.6) (4.5 + 0.5 + 5)	0.8	280 nm	[89]
	Plasma	Tenoxicam	Hypersil C$_{18}$ (250 mm × 4.6 mm; 5 μm)	0.1 M NaH$_2$PO$_4$ buffer (pH 6) + methanol (50 + 50)	1.5	372 nm	[129]
	Human plasma	Isoxicam	Sunfire C$_{18}$	Methanol + ammonium formate (10 mM, pH 3) (70 + 30)	–	MS/MS	[132]
Isoxicam	Substance	–	LiChrospher 100 RP18 (150 × 3.9 mm; 4 μm)	Methanol + acetate buffer (pH 4.6; 0.4 M) (40 + 60)	0.8	254 nm; 280 nm	[127]
Nabumetone	Pharmaceutical preparations	–	Kromasil C$_{18}$	0.06 M cetyltrimethylammonium bromide (pH 7) with 10% 1-butanol	1.0	–	[136]
	Tablets, plasma	4-Methoxyacetophenone	Supercosil LC-8 (150 mm × 4.6 mm; 5 μm)	ACN + TEA + glacial acetic acid (500 + 1.5 + 8) diluted to 1000 ml with distilled deionized water	–	270 nm	[137]
	Pharmaceutical preparations	Methyl p-toluate	Wakosil 5C$_{18}$ (150 mm × 4.6 mm; 5 μm)	0.5 g 1-heptanesulphonic acid sodium salt diluted in ACN + water + TEA (500 + 500 + 1) adjusted to pH 3 by H$_3$PO$_4$	1.0	270 nm	[138]
	Human urine	Methyl p-toluate	Wakosil 5C$_{18}$ (150 mm × 4.6 mm; 5 μm)	0.5 g 1-heptanesulphonic acid sodium salt diluted in: ACN + water + TEA (500 + 500 + 1) adjusted H$_3$PO$_4$ to pH 3	1.0	λ$_{ex}$ = 80 nm; λ$_{em}$ = 50 nm	[138]
	Substance	4-Chloro-2-nitroaniline	RP Inertsil C$_{18}$ ODS (250 mm × 4.6 mm; 5 μm)	Methanol + 0.05% aqueous solution of glacial acetic acid (68 + 32)	1.0	230 nm	[139]
	Serum	–	Pinkerton ISRP (GFF-S5-80; 150 mm × 4.6 mm)	ACN + phosphate buffer (0.1 M, pH 7) (10 + 90)	–	254 nm	[140]
	Human plasma	Cisapride	Nova-Pak C$_{18}$ (150 mm × 3.9 mm; 5 μm) preceded by 4 mm × 3 mm C$_{18}$ guard column	ACN + 0.02% TEA adjusted to pH 7 by 85% H$_3$PO$_4$ (50 + 50)	1.4	λ$_{ex}$ = 30 nm; λ$_{em}$ = 56 nm	[141]
Nimesulide	Homeopathic preparations	Benzoic acid	Agilent Zorbax Eclipse XDB C-18 (150 mm × 4.6 mm; 5 μm)	ACN + water with 0.1% acetic acid (pH 3.16) (A + B); elution (15 + 85) for 3 min, then (30 + 70) in 7 min and finally to (90 + 10) in 20 min	1.0	245 nm; ESI-MS; m/z 307 → 170	[29]
	Substance	4-Chloro-2-nitroaniline	RP Inertsil C$_{18}$ ODS (250 mm × 4.6 mm; 5 μm)	Methanol + 0.05% aqueous solution of acetic acid (68 + 32)	1.0	230 nm	[139]
	Human plasma	Phenacetin	RP Supercosil LC-18 (150 mm × 4.6 mm; 5 μm)	Methanol + phosphate buffer (pH 3.5, 0.01 M) (55 + 45)	–	258 nm	[148]
	Rabbit aq. Humor	–	Ultracarb ODS(30) C$_{18}$ (150 mm × 4.6 mm; 5 μm)	60% methanol + 40% water, with 1% TEA, adjusted to pH 3.2 by 85% H$_3$PO$_4$	1.0	300 nm	[149]
	Urine	–	Supercosil LC-18 DB (250 mm × 4.6 mm; 5 μm) + Supelgard LC-18 (150 mm × 4.6 mm; 5 μm)	Sodium phosphate buffer (50 mM) adjusted to pH 3 with 85% H$_3$PO$_4$ (3.5 mM) (A) + ACN (B); gradient elution: start 22% B, increasing linearly to 30% B (18 min) and to 50% B over 50 min	1.0	230 nm	[150]

Table 1 (*Continued*)

Compound	Sample matrix	I.S.	Chromatographic conditions		Flow rate (mL min^{-1})	Detection	Ref.
			Column	Mobile phase (v/v)			
	Human plasma	DRF-4367	Kromasil KR 100-5C$_{18}$ (250 mm × 4.6 mm; 5 μm)	Gradient elution: 0.05 M formic acid (pH 3) + ACN + methanol + water	1.0	235 nm	[151]
	Drugs	–	Shimpac C$_{18}$ (150 mm × 4.6 mm; 5 μm)	Methanol + water + acetic acid (67 + 32 + 1)	1.0	230 nm	[152]
	Substance	Propylparaben	Separon SGXC$_{18}$ (250 mm × 4.6 mm; 7 μm)	ACN + (NH$_4$)$_3$PO$_4$ solution (pH 7.9, 0.02 M) (35 + 65)	0.6	245 nm	[153]
	Rat plasma	NS 398	Waters Symmetry C$_{18}$ (150 mm × 4.6 mm; 3.5 μm) with Waters Sentry Symmetry C$_{18}$ guard column	ACN + 50 mM sodium citrate buffer, pH 3 (53 + 47)	1.1	240 nm	[154]
	Human plasma	–	Nucleosil 120-5 C$_{18}$ (50 mm × 4 mm)	ACN + methanol + 15 mM KH$_2$PO$_4$ buffer, pH 7.3, adjusted with KOH (30 + 5 + 65)	1.0	404 nm	[155]
	Human plasma	–	RP ODS Zorbax (250 mm × 4.6 mm; 5 μm) with guard column ODS Zorbax (100 mm × 4.6 mm; 5 μm)	Phosphate buffer (pH 5.5) + methanol + ACN (50 + 20 + 30)	1.4	230 nm	[156]
	Human plasma	Tolbutamide	Supercosil LC-18 DB (33 mm × 4.6 mm; 3 μm) with LiChrocart 25-4 manufix containing a LiChrospher 100 RP-18 (5 μm) guard column	Gradient elution: 0.05 M phosphate buffer (pH 5.5) + methanol (80 + 20) was changed to (20 + 80) within 16 min; after next 4 min brought again to (80 + 20)	0.4	230 nm	[157]
	Human plasma	Tolbutamide	LiChrospher 100 RP-18 (250 mm × 4 mm; 5 μm) with LiChrospher 25-4 manufix containing a LiChrospher 100 RP-18 (5 μm) guard column	Gradient elution: 0.05 M phosphate buffer (pH 5) + methanol (55 + 45) after 3 min changed to (40 + 60) within 15 min; kept 8 min and brought again to (55 + 45)	1.0	230 nm	[157]
	Rat plasma	–	Shandon Hypersil BDS C$_{18}$ (250 mm × 4.6 mm; 5 μm) with BDS C$_{18}$ guard column	Methanol + citrate phosphate buffer (pH 3) (68 + 32)	1.0	240 nm	[158]
	Pharmaceutical preparations	Ibuprofen	CLC C$_{18}$ (250 mm × 4.6 mm; 5 μm)	ACN + 0.05 M KH$_2$PO$_4$ buffer (pH 7) (55 + 45)	–	230 nm	[159]
	Pharmaceutical preparations	Piroxicam	Inertsil (250 mm × 4.6 mm; 5 μm)	Water + ACN (2 + 3) adjusted to pH 3.5 with H$_3$PO$_4$	1.0	240 nm	[160]
	Tablets	–	Chromosorb RP 18	0.1 M ammonium acetate + methanol + ACN (3 + 5 + 2) at pH 6	–	210 nm	[161]
	Pharmaceutical preparations	–	Agilent Zorbax Extend C$_{18}$ (150 mm × 4.6 mm; 5 μm)	ACN + TEA + water (45 + 0.5 + 54.5) adjusted to pH 5.2 with formic acid	1.0	230 nm	[162]
	Tablets	–	ODS C$_{18}$	Methanol + water (65 + 35) adjusted to pH 4.15 with H$_3$PO$_4$	1.4	307 nm	[163]
	Human plasma	Celecoxib	X-Terra TM-MS C$_{18}$ (150 mm × 4.6 mm; 3.5 μm)	ACN + water (80 + 20) with 5 mM ammonia solution	0.5	MS/MS; m/z 307 → 229	[164]
	Tablets	–	μBondapak/μPorasil C-18 (150 mm × 3.9 mm)	pH 3 phosphate buffer + methanol (40 + 60)	1.0	Electrochem. 1200 mV	[165]

reactions due to this drug. Tenoxicam also shows analgesic and antipyretic properties. It is strongly bound to plasma proteins (99%) and is characterized by extended plasma half-life, usually 72 ± 28 h. The main therapeutic indications are: rheumatoid arthritis, osteoarthritis, enkylosing spondylitis, extraarticular inflammation and acute gout. The side effect profile of tenoxicam appended similar to that seen with other non-steroidal anti-inflammatory drugs. The most common side effects are gastrointestinal (e.g. epigastric pain, nausea, dyspepsia, indigestion). Tenoxicam should not be used in patients with known salicylate or NSAID-induced asthma, rhinitis or urticaria, or a history of severe

gastrointestinal disease. It should not be administered before an aesthesia or surgery in elderly, or in patients with an increased risk of renal failure or bleeding [1–4].

Pharmacopoeias suggest that tenoxicam content should be determined with the potentiometric titration method with 0.1 M perchloric acid in anhydrous acetic acid. For confirmation of substance identity the IR spectrophotometry is recommended [9,10]. Among methods for the determination of tenoxicam in pharmaceutical preparations and in biological material, the most commonly used are LC and TLC chromatography (about 38%), spectrophotometric methods (about 26%) and voltamperometric

Table 2
Spectrophotometric and spectrofluorimetric methods for analysis of oxicams, nimesulide and nabumetone.

Compound	Sample matrix	Reagent used	Detection, λ (nm)	Linearity range	Ref.
Piroxicam	Tablets	UV	261.4	2.4–20 µg mL^{-1}	[19]
	Pharmaceutical preparations	UV	333	3–8.5 µg mL^{-1}	[31]
	Pharmaceutical preparations	UV	327	5–15 µg mL^{-1}	[31]
	Pharmaceutical preparations	Fe(III) + o-phenanthroline in acetate buffer (pH 4.8)	510	2–26 µg mL^{-1}	[50]
	Tablets, capsules	Potassium iodate in 30% sulphuric acid + cyclohexane	522	0.05–1.1 mg mL^{-1}	[51]
	Tablets, capsules, suppositories	I: alizarin; II: alizarin red S; III: alizarin yellow G; IV: qualizarin	I: 538; II: 529; III: 355; IV: 579	0.05–2.4 µg mL^{-1}	[52]
	Tablets	2,2′-Bipyridyl + ferric ammonium sulphate dodecahydrate + 1 M HCl	522	0.05–6.5 µg mL^{-1}	[53]
	Tablets	1,10-Phenanthroline + ferric ammonium sulphate dodecahydrate + 1 M HCl	510	0.2–6.5 µg mL^{-1}	[53]
	Tablets, capsules	Ceric ammonium sulphate in acidic medium + promethazine hydrochloride	515	0.4–7.5 µg mL^{-1}	[54]
	Tablets, capsules	Ceric ammonium sulphate in acidic medium + methdilazine hydrochloride	513	0.2–10 µg mL^{-1}	[54]
	Human plasma	Hydrochloric and trichloroacetic acid	337	8–10 mg L^{-1}	[55]
	Human plasma	UV	343.5	0.5–12 µg mL^{-1}	[56]
	Pharmaceutical preparations, human serum	0.05 M sodium dodecyl sulphate surfactant (pH 1.5–2; nitric acid)	λ$_{ex}$/λ$_{em}$	0.05–1.5 µg mL^{-1}; 0.2–10 µg mL^{-1}	[58]
	Pharmaceutical preparations	2.77×10^{-4} M aqueous N-bromosuccinimide + 1.68×10^{-5} M aqueous methdilazine hydrochloride	λ$_{ex}$ = 343; λ$_{em}$ = 377	0.2–8 µg mL^{-1}	[59]
	Capsules	–	λ$_{ex}$ = 330; λ$_{em}$ = 440	0.01–1.25 µg mL^{-1}	[60]
	Pharmaceutical preparations	Dimethylformamide + dioxane	λ$_{ex}$ = 340; λ$_{em}$ = 470	0.2–1.2 µg mL^{-1}	[61]
	Pharmaceutical preparations	0.1 M sulphuric acid	λ$_{ex}$ = 345; λ$_{em}$ = 470	0.2–2 µg mL^{-1}	[61]
	Pharmaceutical preparations	–	λ$_{ex}$ = 320; λ$_{em}$ = 440	0.03–0.2 µg mL^{-1}	[62]
	Serum	–	λ$_{ex}$ = 320; λ$_{em}$ = 440	0.02–0.22 µg mL^{-1}	[63]
	Gel	–	λ$_{ex}$ = 320; λ$_{em}$ = 465	0.3–4 µg mL^{-1}	[64]
Tenoxicam	Tablets, capsules	Potassium iodate + 30% sulphuric acid	522	0.05–0.6 mg mL^{-1}	[51]
	Tablets, capsules, suppositories	I: alizarin; II: alizarin red S; III: alizarin yellow G; IV: qualizarin	I: 546; II: 531; III: 370; IV: 579	0.05–2.4 µg mL^{-1}	[52]
	Pharmaceutical preparations	Dimethylformamide + dioxane	λ$_{ex}$ = 360; λ$_{em}$ = 480	0.3–2.4 µg mL^{-1}	[61]
	Tablets	–	368	2–10 µg mL^{-1}	[88]
	Laboratory mixtures	3-Methylbenzothiazolinone hydrazone hydrochloride + ceric ammonium sulphate in acid medium	λ$_{ex}$ = 300; λ$_{em}$ = 360	1–10 µg mL^{-1}	[90]
	Laboratory mixtures	3-Methylbenzothiazolinone hydrazone hydrochloride + ceric ammonium sulphate in acid medium	465	2–20 µg mL^{-1}	[90]
	Tablets, vials, ampules, capsules	0.4% 7-chloro-4-nitrobenz-2-oxa-1,3-diazol (NBD-Cl) + acetone	535	1–10 µg mL^{-1}	[91]
	Tablets, vials, ampules, capsules	0.4% 7-chloro-4-nitrobenz-2-oxa-1,3-diazol (NBD-Cl) + methanol	λ$_{ex}$ = 450; λ$_{em}$ = 535	50–1000 ng mL^{-1}	[91]
	Tablets, vials, suppositories	Al(III) ions	λ$_{ex}$ = 350; λ$_{em}$ = 450	16–200 ng mL^{-1}; 40–200 ng mL^{-1}	[92]
Meloxicam	Laboratory mixtures	3-Methylbenzothiazoline hydrazone hydrochloride + ceric ammonium sulphate in acid medium	λ$_{ex}$ = 300; λ$_{em}$ = 360	1–10 µg mL^{-1}	[90]
	Laboratory mixtures	3-Methylbenzothiazoline hydrazone hydrochloride + ceric ammonium sulphate in acid medium	450	2–20 µg mL^{-1}	[90]
	Tablets, vials, ampoules, capsules	0.4% 7-chloro-4-nitrobenz-2-oxa-1,3-diazol (NBD-Cl) + acetone	535	0.5–4.0 µg mL^{-1}	[91]
	Tablets, ampoules, capsules	0.4% 7-chloro-4-nitrobenz-2-oxa-1,3-diazol (NBD-Cl) + methanol	λ$_{ex}$ = 450; λ$_{em}$ = 535	25–400 ng mL^{-1}	[91]
	Tablets	0.1% basic methylene blue in phosphate buffer (pH 8)	653.5	1–5 µg mL^{-1}	[109]
	Tablets	0.1 M NaOH	362	0.5–20 mg L^{-1}	[121]
	Tablets	0.01 M FeCl$_3$ × 6H$_2$O in methanol	570	5–250 mg L^{-1}	[121]

Table 2 (*Continued*)

Compound	Sample matrix	Reagent used	Detection, λ (nm)	Linearity range	Ref.
	Tablets, suppositories	0.1% safranin T	$\lambda_{ex}=520$; $\lambda_{em}=582$	0.4–1.2 µg mL^{-1}	[122]
	Tablets, suppositories	0.1 M ethanolic HCl and NaOH	333.9–384.7	2–10 µg mL^{-1}	[122]
Lornoxicam	Tablets, vials, ampoules, capsules	0.4% 7-chloro-4-nitrobenz-2-oxa-1,3-diazol (NBD-Cl) + acetone	535	1–10 µg mL^{-1}	[91]
	Tablets, vials, ampoules, capsules	0.4% 7-chloro-4-nitrobenz-2-oxa-1,3-diazol (NBD-Cl) + methanol	$\lambda_{ex}=450$; $\lambda_{em}=535$	5–1000 µg mL^{-1}	[91]
Nabumetone	Tablets	4-Carboxyl-2,6-dinitrobenzene diazonium	470	1–6 µg mL^{-1}	[143]
	Tablets	0.2 M sodium dodecyl sulphate + 0.25 M thallium(I) nitrate + sodium sulphite	$\lambda_{ex}=271$; $\lambda_{em}=520$	25–1000 ng mL^{-1}	[145]
Nimesulide	–	Thymol 5-methyl-2-(1-methylethyl)phenol in ammonium medium	476	5–40 µg per sample	[175]
	Bulk, dosage form	Nitrous acid + phloroglucinol	400	4–20 meug mL^{-1}	[176]
	Bulk, dosage form	p-Dimethylaminobenzaldehyde	415	4–24 meug mL^{-1}	[176]
	Tablets	Alcoholic iminodibenzyl in acid medium	600	0.1–7.5 µg mL^{-1}	[178]
	Tablets	3-Aminophenol in acid medium	470	0.4–12 µg mL^{-1}	[178]
	Pure, dosage forms	–	300	10–50 µg mL^{-1}	[180]
	Tablets, sachets	I. ethanol; II. chloroform	$200 \rightarrow 500$ ($\Delta\lambda=21$)	I: 2–90 µg mL^{-1}; II: 2–50 µg mL^{-1}	[181]

(about 27%). Among separation techniques HPLC [82,83] with UV-spectrophotometric [30,32,33,84–89] or MS detection [33,38–40,86] is frequently used. The chromatographic parameters are presented in Table 1. Taha et al. applied TLC-densitometry for the determination of tenoxicam in pharmaceutical preparations using TLC silica gel F$_{254}$ plates as stationary phase and ethyl acetate + methanol + 25% ammonia (17 + 3 + 0.35, v/v/v) as mobile phase. Chromatograms undergo densitometric detection at λ = 370 nm [89]. HPTLC-densitometry was used for the photostability test of tenoxicam. The stability indicating capability of the respective assays is proven with sample solutions irradiation from a xenon source. Bartsch et al. reported quantification of tenoxicam using capillary electrophoresis [83].

For the determination of tenoxicam, UV–vis spectrophotometric methods [49,51,52,88,90,91] as well as spectrofluorimetric methods [61,90–92] are also used. Taha et al. described determination of meloxicam and tenoxicam in the presence of their degradation products using spectrophotometric and spectrofluorimetric methods [90]. Quantitative determination by infrared spectrophotometry was reported, using KBr technique and dehydrochloric acid as I.S. The analysis was run in the range of 0.15–0.35% (w/w) in KBr. The absorption band at 1420 cm^{-1} was chosen [93]. The spectrophotometric methods for determination of tenoxicam are presented in Table 2. Voltammetric methods using CPE [68], square wave and square-wave adsorptive stripping voltammetric [71], direct current (DC), differential pulse (DPP), superimposed constant amplitude pulse (SCAP) and superimposed increasing amplitude pulse (SIAP) polarographic techniques were reported [66,94–96]. Potentiometric titration of drug with tenoxicam in reaction with N-bromosuccinimide in sulphuric acid [51] and using ion-selective membrane electrodes were described [75]. Mohamed et al. described the ionization constant and stability constants of the complexes formed with metal ions. The stability constants of complexes formed with tenoxicam decrease in the order Fe(III) > Bi(III) > Al(III) > Cr(III) > Cd(II) > Sb(III), which is in agreement with the decrease in the ionic potential of metal ions [92]. Nikolic et al. presented coulometric titration of tenoxicam with electrogenerated chloride in the presence of methyl orange [74]. Two FIA methods for determination of tenoxicam in methanol

using Fe(III) and 2 M HCl to produce an orange-brown compound and with spectrophotometric detection (540 and 355 nm) were reported [97]. Al-Tamrah described FIA method based on the reaction of tenoxicam with Fe(NO$_3$)$_3$ × 9H$_2$O. The produced ion Fe(II) reacts with 0.1 M K$_3$Fe(CN)$_6$ forming Prussian blue measureable at 724 nm [98]. FIA system with spectrophotometric detection at λ = 530 nm was used for the analysis of complex drugs containing tenoxicam. The method is based on the oxidation of a drug by a known excess of N-bromosuccinimide in 1 M HCl, followed by a reaction of excess oxidant with chloranilic acid to bleach its purple color [81].

2.3. Meloxicam

Meloxicam (4-hydroxy-2-methyl-N-(5-methyl-1,3-thiazol-2-yl)-2H-1,2-benzothiazine-3-carboxamide-1,1-dioxide) is a piroxicam analogue, in which the pyridyl group in the amidic part of the molecule was substituted with the 5-methylthiazole system. It exerts anti-inflammatory effect by inhibiting more strongly the enzymatic activity of COX-2 than of COX-1. This preferential operation causes, that meloxicam inhibits synthesis of prostaglandins in the inflammatory places, but within the alimentary tract and kidneys considerably weakly. Clinical studies demonstrated a lower rate of adverse symptoms than while using other NSAIDs. In the body, the drug is subjected to intensive metabolic changes (oxidation) and less than 5% of the daily dose is excreted in unchanged form with faeces, while only trace amounts of the drug are excreted in unchanged form in urine. Meloxicam is indicated for the treatment of rheumatoid arthritis, osteoarthritis and other joint diseases. Its therapeutic benefits combined with a good gastrointestinal tolerability make it a valuable therapeutic agent. However, meloxicam should not be used in patients sensitive to sulphonamides (it has a sulphamide group built in the ring), with bronchial asthma, angioneurotic oedema and urticaria, developed as a consequence of using other NSAIDs [1–4].

Pharmacopoeia recommends potentiometric titration with 0.1 M perchloric acid as a titrant in anhydrous acetic acid for the determination of meloxicam content. For identification of meloxicam, IR and UV (λ = 354 nm) spectrophotometry are used [10].

Table 3
Validation data for analyzed drugs.

Compound	Method	Linear range	LOD	LOQ	Precision (R.S.D. %)		Recovery (%) (R.S.D. %)	Ref.
					Intra-day	Inter-day		
Piroxicam	LC	0.05–10 µg mL^{-1}	0.05 µg mL^{-1}	–	<8%		–	[16]
		5–20 µg mL^{-1}	–	–	0.94–1.47	0.94–1.04	–	[19]
		0.05–10 µg mL^{-1}	0.025 µg mL^{-1}	0.05 µg mL^{-1}	2.4–9.8		–	[20]
		0.2–20 µg mL^{-1}	0.02 µg mL^{-1}	–	2.2–2.3	4.6–7.9	82.0 (6.0)	[21]
		0.1–6 µg mL^{-1}	0.02 µg mL^{-1}	0.06 µg mL^{-1}	3.17–5.21	3.23–5.37	100.09 (6.52)	[22]
		8.8–44 µg mL^{-1}; 60–300 µg mL^{-1}; 0.44–2.2 µg mL^{-1}	–	–	0.86–1.35	2.22–2.83	–	[23]
		0.2–0.5 µg mL^{-1}	–	–	0.4	0.2–0.4	99.1–100.5	[24]
		0.144 × 10^{-3} to 7.24 × 10^{-3} M; 0.129 × 10^{-3} to 6.49 × 10^{-3} M	1 × 10^{-7} M	3 × 10^{-7} M	–		(0.06–0.63)	[25]
		0.05–2.5 µg mL^{-1}	–	0.05 µg mL^{-1}	2.48–9.05	3.31–9.01	91.64–101.54	[26]
		0.1–10 µg mL^{-1}	–	–	1.3–8.8		73.1–80.0	[28]
		0.1–25 µg mL^{-1}	0.16 ng	–	1.0–7.0		87.0–95.0	[29]
		50–400 µg mL^{-1}	1.15 ng	–	1.35–1.48		87.0–95.0	[29]
		10–100 µg mL^{-1}	–	–	0.45	0.90	97.13	[31]
		10–1000 ng mL^{-1}	4.2 ng mL^{-1}	–	0.7–6.2	0.5–8.4	96.6–99.7	[34]
		0.15–106 µM	0.075 µM	0.15 µM	–		93.3–99.8	[35]
		0.72–600 ng mL^{-1}	–	0.72 ng mL^{-1}	3.8–10.7	7.7–13.5	–	[37]
		10–160 ng mL^{-1}	<10 ng mL^{-1}	–	–		85.0	[38]
		0.5–200 ng mL^{-1}	–	0.5 ng mL^{-1}	2.3–4.7	3.5–5.0	78.3–85.6	[40]
		0.2–100 µg mL^{-1}	0.2 µg mL^{-1}	1.0 µg mL^{-1}	6.9	7.8	≥45% at the LOD	[41]
	TLC	8.8–44 µg mL^{-1}; 60–300 µg mL^{-1}; 0.44–2.2 µg mL^{-1}	–	–	1.5–3.32	2.38–3.5	–	[23]
		400–800 ng mL^{-1}	40 ng mL^{-1}	150 ng mL^{-1}	1.32	1.08	(1.58–1.68)	[42]
		400–800 ng mL^{-1}	39 ng mL^{-1}	131 ng mL^{-1}	1.3–8.9	3.2–6.4	(0.7–2.9)	[43]
	CE	8.8–44 µg mL^{-1}; 60–300 µg mL^{-1}; 0.44–2.2 µg mL^{-1}	–	–	1.74–3.61	3.74–4.35	–	[23]
	CZE	40–500 µM	10 µM	–	<5		> 95	[46]
	MEKC	0–100 mg L^{-1}	–	–	–		99.0–103.0	[47]
	Spectrophotometry	2.4–20 µg mL^{-1}	–	–	0.94–1.47	0.94–1.04	99.7	[19]
		3–8.5 µg mL^{-1}	–	–	0.02	0.33	100.22	[31]
		5–15 µg mL^{-1}	–	–	0.05	0.47	99.02	[31]
		3–7 mg L^{-1}	0.33 mg L^{-1}	–	–		99–101	[47]
		0.05–1.1 mg mL^{-1}	–	–	–		99.7–100.0 (0.62–2.6)	[51]
		0.05–2.4 µg mL^{-1}	12 µg mL^{-1}	40 µg mL^{-1}	0.49–1.6		Close to 100% (0.8–1.2)	[52]
		0.05–6.5 µg mL^{-1}	–	–	–		98.95–99.54	[53]
		0.2–6.5 µg mL^{-1}	–	–	–		98.88–99.64	[53]
		0.4–7.5 µg mL^{-1}; 0.2–10 µg mL^{-1}	–	–	–		98.74–99.68 (<1.1)	[54]
		8–10 mg L^{-1}	–	0.27 mg L^{-1}	–		–	[55]
		0.5–12 µg mL^{-1}	–	0.29 µg mL^{-1}	0.12–2.0		89.4	[56]
	Spectrofluorimetry	0.05–1.5 µg mL^{-1}	0.015 µg mL^{-1}	–	–		–	[58]
		0.2–10 µg mL^{-1}	0.1 µg mL^{-1}	–	–		–	[58]
		0.2–8 µg mL^{-1}	–	–	0.56–0.67		99.77–101.1 (<1.1)	[59]
		0.01–1.25 µg mL^{-1}	0.012 µg mL^{-1}	–	–		89.0–99.6 (1.0–8.0)	[60]
		0.2–2 µg mL^{-1}	0.034 µg mL^{-1}	0.113 µg mL^{-1}	1.12–1.2		100.33 (1.21)	[61]
		0.2–1.2 µg mL^{-1}	0.045 µg mL^{-1}	0.15 µg mL^{-1}	0.91–1.06		100.47 (0.91)	[61]
		0.03–0.2 µg mL^{-1}	0.01 µg mL^{-1}	0.032 µg mL^{-1}	–		100.3 (2.9)	[62]
		0.02–0.22 µg mL^{-1}	0.03 µg mL^{-1}	0.09 µg mL^{-1}	–		81.0–112.0	[63]
		0.3–4 µg mL^{-1}	0.22 µg mL^{-1}	–	–		104.0	[64]
	Voltammetry	0.15–5 µg mL^{-1}	0.1 µg mL^{-1}	–	0.73		96.0–104.18 (0.98–3.0)	[70]
		2 × 10^{-9} to 2 × 10^{-7} M; 2 × 10^{-9} to 6 × 10^{-8} M	5 × 10^{-8} M	–	3.2		–	[71]
	Potentiometry	1 × 10^{-2} to 5.2 × 10^{-5} M	2.4 × 10^{-6} M	–	<2.0		98.8–102.1	[75]
	FIA	1.5–364,000 pg mL^{-1}	0.33 pg mL^{-1}	1.5 pg mL^{-1}	–		–	[73]
		0.5–10 µg mL^{-1}	0.1 µg mL^{-1}	0.33 µg mL^{-1}	<5%		95.7–104.5	[76]
		0.1–1.0 ppm	23 ppm	–	–		98.8–101.2 (1.5–3.8)	[79]
		200–1000 ppb	29 ppb	–	3.8		97.5–102.0 (0.5–3.9)	[80]
		10–160 mg mL^{-1}	6 mg L^{-1}	20 mg L^{-1}	<5.0		98.0–101.0 (1.0–2.0)	[81]
Tenoxicam	LC	10–1000 ng mL^{-1}	2.3 ng mL^{-1}	–	1.7–9.4	0.7–12.7	97.0–100.6	[34]
		10–160 ng mL^{-1}	<10 ng mL^{-1}	–	–		75.0	[38]
		0.5–200 ng mL^{-1}	–	0.5 ng mL^{-1}	1.7–5.4	2.9–3.4	80.0–87.1	[40]
		0.1–10 µg mL^{-1}	0.5 µg mL^{-1}	–	–		–	[82]
		10–40 ng mL^{-1}	40 ng mL^{-1}	–	3.9–7.7		87.0–102.0	[84]
		5–2000 ng mL^{-1}	5 ng mL^{-1}	–	–		98.99 (4.3)	[85]
		25–5500 ng mL^{-1}	–	48.3 ng mL^{-1}	0.74–2.47	1.17–6.76	91.2–96.3 (1.7–2.3)	[87]

Table 3 (*Continued*)

Compound	Method	Linear range	LOD	LOQ	Precision (R.S.D. %) Intra-day	Inter-day	Recovery (%) (R.S.D. %)	Ref.
		$2–10\,\mu g\,mL^{-1}$	–	–	–		99.5–100.2	[88]
		$0.5–20\,\mu g\,mL^{-1}$	$0.045\,\mu g\,mL^{-1}$	$0.15\,\mu g\,mL^{-1}$	0.9–1.58	0.1–0.68	98.9 (1.61)	[89]
	TLC	$0.25–6.0\,\mu g$ per spot	$0.4\,\mu g$ per spot	$1.36\,\mu g$ per spot	–		100.57 (1.34)	[89]
	Spectrophotometry	$0.05–0.6\,mg\,mL^{-1}$	–	–	–		100.0–102.0 (0.6–3.4)	[51]
		$0.05–2.4\,\mu g\,mL^{-1}$	12–16 ng mL^{-1}	40–50 ng mL^{-1}	0.76–1.45		Close to 100% (1.0–1.2)	[52]
		$2–10\,\mu g\,mL^{-1}$	–	–	–		99.6–100.7	[88]
		$1–10\,\mu g\,mL^{-1}$	–	–	0.8	1.0	99.7–101.5 (0.5–0.6)	[91]
	Spectrofluorimetry	$0.3–2.4\,\mu g\,mL^{-1}$	$0.041\,\mu g\,mL^{-1}$	$0.137\,\mu g\,mL^{-1}$	0.67–0.88		100.37–100.45	[61]
		50–1000 ng mL^{-1}	–	–	1.1	1.2	98.7–101.3 (0.6–0.9)	[91]
		40–200 ng mL^{-1}; 16–100 ng mL^{-1}	10.8 ng mL^{-1}; 4.68 ng mL^{-1}	–	–		98.58–102.22	[92]
	Voltammetry	1×10^{-8} to 8×10^{-10} M	1×10^{-10} M	–	3.6		–	[71]
	Polarography	$0.025–20\,\mu g\,mL^{-1}$	–	–	–		99.1–99.6	[95]
		1×10^{-5} to 1×10^{-7} M	3×10^{-8} M	1×10^{-7} M	–		–	[96]
	Potentiometry	$0.05–0.6\,mg\,mL^{-1}$	–	–	–		100.0–102.0 (0.6–3.4)	[51]
		1×10^{-2} to 1×10^{-5} M	6×10^{-6} M	–	<2.0		97.3–102.1	[75]
	FIA	$0.5–8.5\,mg\,L^{-1}$	$0.08\,mg\,L^{-1}$	–	1.05–1.4	4.2	99.3–101.0	[97]
		$7–320\,mg\,L^{-1}$	$1.1\,mg\,L^{-1}$	–	0.58–0.6	3.9	99.4–100.7	[97]
		$0.5–100\,\mu g\,mL^{-1}$	$0.4\,\mu g\,mL^{-1}$	–	–		100.5–100.6	[98]
		$20–200\,mg\,L^{-1}$	$10\,mg\,L^{-1}$	$32\,mg\,L^{-1}$	<5.0		97.0–103.0 (1.0–4.0)	[81]
Meloxicam	LC	0.5–200 ng mL^{-1}	–	0.5 ng mL^{-1}	1.0–2.1	1.5–4.1	81.8–85.5	[40]
		$1.25–50\,\mu g\,mL^{-1}$	$0.03\,\mu g\,mL^{-1}$	$0.09\,\mu g\,mL^{-1}$	0.47–0.76	0.3–1.12	100.86 (1.55)	[89]
		$0.52–52\,\mu g\,mL^{-1}$	$0.029\,\mu g\,mL^{-1}$	$0.1\,\mu g\,mL^{-1}$	<2.0		92.7	[103]
		10–2400 ng mL^{-1}	–	10 ng mL^{-1}	1.6–4.3	2.4–7.3	98.3–114.0	[104]
		50–1500 ng mL^{-1}	10 ng mL^{-1}	50 ng mL^{-1}	6.41–7.23		>85.0	[106]
		5–25 ng mL^{-1}; 25–140 ng mL^{-1}; 50–3500 ng mL^{-1}; 140–700 ng mL^{-1}; 700–3500 ng mL^{-1}	3 ng mL^{-1}	20 ng mL^{-1}	0.46–3.02	1.42–8.29	97.9–101.8 (0.37–1.72)	[107]
		$100–500\,\mu g\,mL^{-1}$	$3.65\,\mu g\,mL^{-1}$	$12.16\,\mu g\,mL^{-1}$	0.36		98.05–99.83 (0.2–0.91)	[109]
		8.96–2059 ng mL^{-1}	–	8.96 ng mL^{-1}	1.3–3.8	3.3–8.9	103.6–113.0	[113]
		0.1–50 ng mL^{-1}	–	0.1 ng mL^{-1}	3.0–7.0	2.7–5.7	92.8–97.2	[114]
		$33.7–61.8\,mg\,L^{-1}$	$0.22\,mg\,L^{-1}$	$1.7\,mg\,L^{-1}$	0.4	0.7	99.37–100.69	[115]
		$10–500\,\mu g\,ng^{-1}$ of muscle; $65–1000\,\mu g\,kg^{-1}$ of liver	–	–	<15.0		91.0–110.0	[115]
	TLC	$0.5–10\,\mu g$ per spot	$0.14\,\mu g$ per spot	$1.4\,\mu g$ per spot	–		100.71 (1.57)	[89]
	CE	$5–100\,\mu g\,mL^{-1}$	$1\,\mu g\,mL^{-1}$	$3\,\mu g\,mL^{-1}$	0.34–0.99	0.26–0.84	>95.0	[119]
	CZE	$0.55–150\,\mu g\,mL^{-1}$	$0.3\,\mu g\,mL^{-1}$	$0.5\,\mu g\,mL^{-1}$	0.31–1.41	1.25–1.86	99.67–99.72 (0.12–0.29)	[120]
	Spectrophotometry	$0.5–4\,\mu g\,mL^{-1}$	–	–	1.1	1.3	98.8–101.8 (0.3–1.7)	[91]
		$40–160\,\mu g\,mL^{-1}$	$3.38\,\mu g\,mL^{-1}$	$11.28\,\mu g\,mL^{-1}$	0.95	0.81	96.57–98.91 (0.3–0.86)	[109]
		$1–5\,\mu g\,mL^{-1}$	2.7 ng mL^{-1}	9.09 ng mL^{-1}	0.99	0.45	97.14–99.54 (0.42–0.81)	[109]
		$0.5–20\,mg\,L^{-1}$	$0.04\,mg\,L^{-1}$	–	0.36		99.2–101.9	[121]
		$5–250\,mg\,L^{-1}$	$0.72\,mg\,L^{-1}$	–	0.47		98.3–102.3	[121]
		$1–10\,\mu g\,mL^{-1}$	$0.07\,\mu g\,mL^{-1}$	–	0.37–1.316		99.03–99.53	[122]
		$4–12\,\mu g\,mL^{-1}$	$0.33\,\mu g\,mL^{-1}$	–	0.24–0.454		99.14–99.53	[122]
	Spectrofluorimetry	25–400 ng mL^{-1}	–	–	1.2	1.6	99.3–99.7 (0.6–1.7)	[91]
		$0.4–1.2\,\mu g\,mL^{-1}$	$8.7 \times 10^{-3}\,\mu g\,mL^{-1}$	–	0.5–1.09		99.24–99.76	[122]
	Voltammetry	5×10^{-5} to 5×10^{-7} M	1.6×10^{-7} M	–	2.2		–	[127]
		5×10^{-6} to 1×10^{-8} M	2.9×10^{-9} M	–	4.2		–	[128]
		50–250 ng mL^{-1}	0.14 ng mL^{-1}	–	–		99.4 (0.3)	[129]
	Polarography	$0.38–15\,\mu g\,mL^{-1}$	$0.02\,\mu g\,mL^{-1}$	$0.38\,\mu g\,mL^{-1}$	0.67–1.65	0.12–2.11	98.88–98.9 (0.08–0.27)	[125]
	FIA	$10–160\,mg\,L^{-1}$	$6\,mg\,L^{-1}$	$20\,mg\,L^{-1}$	<5.0		100.0–104.0 (1.0–4.0)	[81]
Lornoxicam	LC	25–1000 ng mL^{-1}	6.4 ng mL^{-1}	–	0.5–3.4	0.5–7.4	98.2–99.8	[34]
		$0.5–20\,\mu g\,mL^{-1}$	$0.01\,\mu g\,mL^{-1}$	$0.04\,\mu g\,mL^{-1}$	0.18–1.76	0.54–0.97	99.81 (1.01)	[89]
		$0.927c–0.0021 = P$	10 ng mL^{-1}	–	0.6–4.5	3.2–3.5	93.0–101.0	[129]
		$1.159c–0.0034 = P$	40 ng mL^{-1}	–	2.2–4.0	3.8–5.5	93.0–101.0	[129]
		0.5–500 ng mL^{-1}	–	0.5 ng mL^{-1}	0.7–4.2	4.5–5.0	87.8	[132]
	TLC	$0.25–6\,\mu g$ per spot	$0.08\,\mu g$ per spot	$0.26\,\mu g$ per spot	–		99.8 (1.32)	[89]
	Spectrophotometry	$1–10\,\mu g\,mL^{-1}$	–	–	0.7	1.1	99.0–101.3 (0.8–1.5)	[91]
		$0.5–35\,\mu g\,mL^{-1}$	$0.13\,\mu g\,mL^{-1}$	$0.5\,\mu g\,mL^{-1}$	1.27–2.13	0.78–2.12	100.6–100.95 (0.53–0.67)	[133]
		$0.2–75\,\mu g\,mL^{-1}$	$0.06\,\mu g\,mL^{-1}$	$0.2\,\mu g\,mL^{-1}$	0.63–2.01	0.78–2.12	100.04–100.07 (0.49–0.58)	[133]
	Spectrofluorimetry	5–1000 ng mL^{-1}	–	–	1.3	1.6	100.3–100.5 (0.8–2.0)	[91]
	Voltammetry	25–1025 ng mL^{-1}	5.4 ng mL^{-1}	–	2.7		>95.0 (<3.0)	[134]
Isoxicam	LC	$8.8–44\,\mu g\,mL^{-1}$; $60–300\,\mu g\,mL^{-1}$; $0.44–2.2\,\mu g\,mL^{-1}$	$0.32\,\mu g\,mL^{-1}$	$1.25\,\mu g\,mL^{-1}$	1.5–2.57	2.48–2.78	–	[135]

Table 3 (*Continued*)

Compound	Method	Linear range	LOD	LOQ	Precision (R.S.D. %)		Recovery (%) (R.S.D. %)	Ref.
					Intra-day	Inter-day		
	TLC	8.8–$44\,\mu g\,mL^{-1}$; 60–$300\,\mu g\,mL^{-1}$; 0.44–$2.2\,\mu g\,mL^{-1}$	$5\,\mu g\,mL^{-1}$	$10\,\mu g\,mL^{-1}$	1.98–3.3	2.14–2.94	–	[135]
	CE	8.8–$44\,\mu g\,mL^{-1}$; 60–$300\,\mu g\,mL^{-1}$; 0.44–$2.2\,\mu g\,mL^{-1}$	$1\,\mu g\,mL^{-1}$	$5\,\mu g\,mL^{-1}$	1.42–3.47	2.54–3.6	–	[135]
Nabumetone	LC	32–$16\,\mu g\,mL^{-1}$	$1.5\,\mu g\,mL^{-1}$	$120\,\mu g\,mL^{-1}$	–		–	[138]
		24–$288\,ng\,mL^{-1}$	$1.5\,ng\,mL^{-1}$	$120\,ng\,mL^{-1}$	–		–	[138]
		1–$20\,\mu g\,mL^{-1}$	$0.127\,\mu g\,mL^{-1}$	$0.385\,\mu g\,mL^{-1}$	0.23–1.72		97.291–99.62 (0.02–1.71)	[139]
		1.5–$40\,ng\,mL^{-1}$	$700\,ng\,mL^{-1}$	$1500\,ng\,mL^{-1}$	1.06–2.71	1.88–9.73	90.0–98.0	[140]
		0.313–$20\,ng\,mL^{-1}$	$0.05\,ng\,mL^{-1}$	$0.313\,ng\,mL^{-1}$	2.59–6.25	2.45–7.81	81.26–83.78	[141]
	Voltammetry	1×10^{-6} to $8 \times 10^{-5}\,M$	$2.31 \times 10^{-7}\,M$	$7.69 \times 10^{-7}\,M$	0.33–0.72	0.53–0.87	100.04 (0.09–0.31)	[146]
	FIA	2.8×10^{-5} to $1.4 \times 10^{-6}\,M$	$4.4 \times 10^{-7}\,M$	$1.3 \times 10^{-6}\,M$	<2.6%		99.0	[144]
		25–$1000\,ng\,mL^{-1}$	$18.2\,ng\,mL^{-1}$	–	1.8		99.5–103.0	[145]
Nimesulide	LC	50–$400\,\mu g\,mL^{-1}$	$1\,ng\,mL^{-1}$	–	1.41–1.54		85.0–101.0	[29]
		0.1–$25\,\mu g\,mL^{-1}$	$0.035\,ng\,mL^{-1}$	–	2.0–4.0		77.0–136.0	[29]
		1–$20\,\mu g\,mL^{-1}$	$0.71\,\mu g\,mL^{-1}$	$2.155\,\mu g\,mL^{-1}$	0.23–1.72		98.36–100.46 (0.21–2.31)	[139]
		0.2–$5\,\mu g\,mL^{-1}$	$40\,ng\,mL^{-1}$	–	–		–	[147]
		0.05–$2.5\,\mu g\,mL^{-1}$	–	$50\,ng\,mL^{-1}$	1.26–9.6	1.0–13.3	99.0–105.0	[149]
		25–$5000\,ng\,mL^{-1}$	$10\,ng\,mL^{-1}$	$15\,ng\,mL^{-1}$	2.21–5.21	1.8–6.73	96.22–96.45	[150]
		0.5–$50\,\mu g\,mL^{-1}$	–	$0.5\,\mu g\,mL^{-1}$	0.97–7.06	3.21–7.37	90.0–116.0	[151]
		100–$1000\,\mu g\,mL^{-1}$	4 ppm	–	–		99.1–100.1	[152]
		150–$500\,\mu g\,mL^{-1}$	$0.12\,\mu g\,mL^{-1}$	–	0.22–0.43		99.35–99.7	[153]
		Plasma: 25–$10,000\,ng\,mL^{-1}$; brain: 20–$5000\,ng\,g^{-1}$; CSF: 20–$5000\,ng\,mL^{-1}$	–	$25\,ng\,mL^{-1}$; $25\,ng\,g^{-1}$; $20\,ng\,mL^{-1}$	1.7–10.7	2.3–10.8	97.5–98.3; 91.3–94.5	[154]
		80–$10,000\,ng\,mL^{-1}$	0.2 ng	$79.55\,ng\,mL^{-1}$	1.7–4.5	2.5–3.5	–	[155]
		0.05–$5\,\mu g\,mL^{-1}$	$30\,ng\,mL^{-1}$	–	0.43–1.02	0.3–0.7	98.8–101.4	[156]
		250–$5000\,ng\,mL^{-1}$	–	$25\,ng\,mL^{-1}$	4.2–7.8	2.4–7.1	79.6–92.8	[157]
		50–$5000\,ng\,mL^{-1}$	–	$50\,ng\,mL^{-1}$	4.4–19.2	3.6–7.9	97.9–101.1	[157]
		0.5–$10\,\mu g\,mL^{-1}$	–	–	2.6–7.2	3.6–6.6	91.5–96.2	[158]
		0.5–$100\,\mu g\,mL^{-1}$	–	–	–		99.23–100.13 (<0.97)	[159]
		50–$150\,\mu g\,L^{-1}$	$0.3\,\mu g\,L^{-1}$	–	–		100.12–100.77	[160]
		10–$100\,\mu g\,mL^{-1}$	0.09 ppm	–	–		101.38 (0.775)	[161]
		0.016–$0.165\,mg\,mL^{-1}$	–	$5.8\,\mu g\,mL^{-1}$	0.05–0.20		97.98–102.14	[162]
		10–$50\,\mu g\,mL^{-1}$	–	–	0.0047		100.67	[163]
		10–$2000\,ng\,mL^{-1}$	–	$10\,ng\,mL^{-1}$	2.1–6.3	2.0–9.2	97.8	[164]
	TLC	100–$900\,ng$	60 ng	100 ng	–		100.11–102.89	[166]
		0.0607–$0.1822\,mg\,mL^{-1}$	–	–	–		98.0–102.0	[167]
		20–$200\,ng\,\mu L^{-1}$	$0.26\,ng\,\mu L^{-1}$	–	–		99.76–100.27 (0.4–1.36)	[168]
		1–$2.8\,\mu g\,mL^{-1}$	–	–	–		99.92–100.31 (0.568–1.111)	[169]
		–	$0.1\,mg\,L^{-1}$	–	2.8–4.5	4.8–8.5	99.0 (8.0)	[170]
	GC	–	4 ppm	–	–		99.21–100.2	[152]
	CZE	40–$500\,\mu M$	$20\,\mu M$	–	<5.0%		> 95.0	[46]
		1.1×10^{-4} to $2.2 \times 10^{-5}\,M$	$2.21 \times 10^{-6}\,M$	$6.69 \times 10^{-6}\,M$	1.98–2.29	2.05–2.86	99.6 (1.59)	[174]
	Spectrophotometry	5–$40\,\mu g$ per sample	$0.99\,\mu g$ per sample	$3.32\,\mu g$ per sample	1.7	<2.2	97.66–102.69	[175]
		0.1–$7.5\,\mu g\,mL^{-1}$	$0.075\,\mu g\,mL^{-1}$	$0.251\,\mu g\,mL^{-1}$	–		99.6–100.3 (0.25–0.3)	[178]
		0.4–$12\,\mu g\,mL^{-1}$	$0.214\,\mu g\,mL^{-1}$	$0.714\,\mu g\,mL^{-1}$	–		99.6–100.2 (0.18–0.25)	[178]
		10–$50\,\mu g\,mL^{-1}$	$0.46\,\mu g\,mL^{-1}$	$1.04\,\mu g\,mL^{-1}$	–		–	[180]
		2–$90\,\mu g\,mL^{-1}$	$0.5\,\mu g\,mL^{-1}$	$2\,\mu g\,mL^{-1}$	–		99.89 (2.04)	[181]
		2–$50\,\mu g\,mL^{-1}$	$1\,\mu g\,mL^{-1}$	$2\,\mu g\,mL^{-1}$	–		99.96 (2.97)	[181]
	Voltammetry	3.85×10^{-7} to $3.32 \times 10^{-9}\,M$	$1.33 \times 10^{-9}\,M$	$4.43 \times 10^{-9}\,M$	0.3–0.6		98.6–105.0	[182]
		1×10^{-5} to $1 \times 10^{-7}\,M$	$5 \times 10^{-8}\,M$	–	–		96.4–105.0	[183]
	Potentiometry	1×10^{-2} to $1 \times 10^{-6}\,M$	$3.2 \times 10^{-7}\,M$	–	–		98.64–98.71	[186]
	FIA	3×10^{-4} to $5 \times 10^{-5}\,M$	$3.1 \times 10^{-6}\,M$	–	–		99.1–102.8 (0.4–1.1)	[187]

Determination of meloxicam by separation methods was carried out using in the first place HPLC with UV [30,89,99–110] or MS detection [40,111–116]. The LC-chromatographic conditions for determination of meloxicam are presented in Table 1. Meloxicam was determined in the presence of its alkaline degradation products on TLC silica gel F$_{254}$ plates using: chloroform + *n*-hexane + 96% acetic acid (18 + 1 + 1, v/v/v) as a mobile phase. Densitometric detec-tion was performed at λ = 364 nm [89]. TLC densitometric method at 365 nm was described for the determination of meloxicam and tetracaine hydrochloride in the presence of their degradation prod-ucts [117]. Oxicams have been separated by videodensitometric TLC on silica and silanized gels with toluene + acetic acid + methanol (11 + 1 + 0.5, v/v/v) as mobile phase. The compounds were iden-tified by UV at λ = 254 nm [118]. A CE using 20% acetonitrile as

anionic surfactant with UV detection at $\lambda = 200$ nm was described. These separations were performed in an uncoated fused-silica capillary (40.2 cm × 50 µm) at 25 °C in Tris-buffer (10 mM, pH 11) with sodium octanesulphonate (60 mM) [119]. Nemutlu and Kir used CZE for the determination of meloxicam in tablets after extraction to methanol with diode array detection (DAD) at 205 nm [120].

Meloxicam was determined using UV-VIS spectrophotometric [90,91,101,109,117,121,122] and spectrofluorimetric methods [90,91,122]. The spectrophotometric methods are presented in Table 2. Hassan reported two methods: first based on the formation of an ion-association complex between the drug and 0.1% safranin T in Kolthoff's borax–phosphate buffer solution (pH 8) and absorption measurement at 518 nm; the second, based on the ^{1}D-values at 322–368 nm and ^{2}D-values at 343.2–385.6 nm [122]. Spectrophotometry methods based on a specific reaction between meloxicam and 0.01% 2,3-dichloro-5,6-dicyano-p-benzoquinone resulting in the formation of an orange red product ($\lambda = 455$ nm) and between 0.1% basic methylene blue in phosphate buffer (pH 8) were described [109].

Flow-injection procedures with UV-detection were used [81,121,123,124]. FIA based on the formation of a green complex between meloxicam and Fe(III) (2:1) in methanol with UV–vis detection (362 and 570 nm) are reported [121]. Liu et al. developed the flow-injection chemiluminescence method based on the reaction with N-bromosuccinimide in alkaline medium [124]. Voltammetric behavior of meloxicam was studied using direct current differential pulse voltammetry, cyclic voltammetry and square-wave cathodic adsorptive stripping voltammetry [125–129].

2.4. Lornoxicam

Lornoxicam (chlorotenoxicam; 6-chloro-4-hydroxy-2-methyl-N-2-pyridyl-5H-thieno-[2,3-e]-1,2-thiazine-2-carboxamide-1,1-dioxide) is a new non-steroidal drug of the oxicam class with analgesic, anti-inflammatory and antipyretic properties. It is distinguished from established oxicams by a relatively short elimination half-life, which may be advantageous from a tolerability standpoint. Lornoxicam and its metabolites strongly bind to plasma albumin.

Pharmacopoeias do not provide any monograph for lornoxicam. Bibliography data indicate that the liquid chromatography method with UV [30,34,89,130], coulometric [131] or MS detection [132] have been used for the determination of lornoxicam. The LC-chromatographic parameters are presented in Table 1. Radhofer-Welte and Dittrich made research in plasma of human and laboratory animals. After addition of I.S., samples are acidified and extracted with dichloromethane via Extrelut-1 columns or by solid-phase extraction using C_{18} SPE columns [130]. TLC-densitometry method was used to determine lornoxicam in the presence of its alkaline degradation products on TLC F_{254} plates with ethyl acetate + methanol + 25% ammonia (17 + 3 + 0.35, v/v/v) as mobile phase and detection at $\lambda = 380$ nm [89]. Spectrophotometric methods in VIS [91] and zero- and first-order derivative in UV [133] were reported. The spectrophotometric conditions for the determination of lornoxicam are presented in Table 2. Ghoneim et al. described square-wave adsorptive stripping voltammetry using static mercury drop electrode (drop area: 0.017 cm^2) with an Ag/AgCl/KCl as reference electrode and a platinum wire as a counter electrode. Cathodic peak, corresponding to the reduction of the adsorbed drug was observed at −1.028 V [134].

2.5. Droxicam

Droxicam (5-methyl-3-(2-pyridyl)-2H,5H-oxazino(5,6-c)-1,2-benzothiazine-4,4(3H)-dione-6,6-dioxide) is a new anti-inflammatory compound from the oxicam group, of remarkable gastrointestinal tolerance and potency.

Pharmacopoeias do not provide any monograph for droxicam. There is only one analytical method available for this drug in the literature. Acuña et al. used TP and DPP with Ag/AgCl/KCl as reference electrode, a platinum wire as counter and a Metrohm 6.1230.010 capillary as working electrode. Determination was made in: methanol + Britton-Robinson aqueous buffer (0.1 M) (4 + 96, v/v) at pH 4–5 (linearity from 1×10^{-5} to 1×10^{-7} M; LOD = 2.8×10^{-8} M; LOQ = 9.3×10^{-8} M) [96].

2.6. Isoxicam

Isoxicam (4-hydroxy-2-methyl-N-5-methyl-3-isoxolyl-2H-1,2-benzothiazine-3-carboxamide-1,1-dioxide) is a potent long acting anti-inflammatory agent from the oxicam group, highly effective in relieving the symptoms of rheumatoid arthritis and degenerative joint disease.

Pharmacopoeias do not provide any monograph for isoxicam. In literature HPLC with UV-detection and capillary electrophoresis with diode array detection at 214, 254 and 280 nm were reported [135]. Bartsch et al. made analysis on HPTLC silica gel 60 F_{254} plates. Plates are prewashed before use with methanol + dichloromethane (1:1, v/v). Chloroform + 1-propanol + 96% acetic acid (9 + 0.5 + 0.5, v/v/v) was used as mobile phase. Densitometric detection at $\lambda = 280$ nm was made [135]. Isoxicam is a substance frequently used as I.S. in LC methods [16,30,34,40,101,132]. The LC-chromatographic conditions are presented in Table 1.

2.7. Nabumetone

Nabumetone (4-(6-methoxynaphthalen-2-yl)-butan-2-one) is a non-steroidal anti-inflammatory drug from a class of 2,6-disubstitued naphthyl-alkanones and is almost devoid of activity itself; the real action is exerted by its active metabolite 6-methoxy-2-naphthylacetic acid (6-MNA), which more strongly inhibits the action of COX-2 than that of COX-1. Being a pro-drug, and devoid of the carboxylic group, nabumetone is not subject to the "ion trap" within the stomach and duodenum, and 6-MNA does not enter the enterohepatic circulation. This metabolite is almost entirely conjugated and only ≤1% of the active form is excreted with urine. This causes that not only the alimentary tract but also kidneys are relatively seldom damaged by nabumetone. By reason of such operation, at first it exhibits anti-inflammatory action, only later analgesic one. The drug has proved to be effective in the treatment of rheumatoidal arthritis, osteoarthritis and acute soft tissue injuries. Nabumetone to a small extent affects platelet aggregation; it can, however, induce chromosome aberration in lymphocytes [1–4].

The pharmacopoeal method for the determination of nabumetone content is LC. The analytical procedure is as follows: acetonitrile solutions are subjected to analysis on a column with base-deactivated octadecylsilyl silica gel (0.15 m × 4.6 mm, 4 µm) as the stationary phase. Gradient elution is carried out using a mixture of tetrahydrofuran + acetonitrile + 0.1% aqueous solution of acetic acid in different proportions; the retention time of nabumetone is about 11 min. As detector, a spectrophotometer at $\lambda = 254$ nm was used [9,10]. For the determination of nabumetone LC [136] with UV [137–140] or fluorimetric detection [138,141] was used. The LC-chromatographic conditions for the determination of nabumetone are presented in Table 1. Reddy et al. used two spectrophotometric methods for the determination of nabumetone in pharmaceutical preparations and biological samples. The first was based on the reaction with 3-methyl-2-benzothiazoline hydrazone in the presence of ceric ammonium sulphate to form a pink complex

(λ = 520 nm). The second method was based on the reaction with ferric chloride in the presence of potassium ferricyanide to form a green complex (λ = 760 nm) [142]. The parameters of spectrophotometric methods are presented in Table 2. FIA for the determination of nabumetone were also used. Can et al. used solvent system of ethanol + water (30 + 70, v/v) and UV-detection at 228.8 nm [144]. Pulgarin et al. developed a method based on obtaining a phosphorescence signal using 0.2 M sodium dodecyl sulphate as micellar agent, 0.25 M thallium(I) nitrate (TlNO$_3$) as heavy atom and 0.25 M sodium sulphite (Na$_2$SO$_3$) as deoxygenator agent. This technique (MS-RTP; micelle-stabilized room temperature phosphorescence) has been used in combination with the stopped-flow mixing technique [145]. Altun et al. described voltammetric techniques (CV, DPP, and OSW) in pH 3.7 acetate buffer [146].

2.8. Nimesulide

Nimesulide (N-(4-nitro-2-phenoxyphenyl)-methane-sulphonamide) is a relatively new non-steroidal anti-inflammatory drug with analgesic and antipyretic properties, that does not induce gastrointestinal ulceration. Nimesulide is a methanesulphonic acid anilide derivative. In the aromatic ring, phenoxylic group (aromatic ether) and nitric group are substituted. Its analgesic and anti-inflammatory action does not fully depend on cyclooxygenase inhibition. Nimesulide is a strong inhibitor of metalloproteases, enzymes that along with free radicals account for matrix decomposition of the articular molecule in the degenerative process. It also exerts indirect inhibiting effect on A$_2$ phospholipase. Showing a good tolerability with a lower incidence of gastrointestinal problems nimesulide is currently administered in the treatment of several different pathologies. Its application is found in the treatment of chronic rheumatoid arthritis or osteoarthritis, inflammation of genitourinary system, otorhinolaryngological diseases, odontostomatological practice and in postoperative pain. Nimesulide is almost completely transformed to 4-hydroxynimesulide in both free and conjugated forms and this metabolite appears to contribute to the anti-inflammatory activity of the compound [1–4].

For the determination of nimesulide content, pharmacopoeia recommends potentiometric titration in water–acetone (30:20, v/v) using 0.1 M sodium hydroxide as a titrate [9]. For the determination of nimesulide in drugs and biological samples separation (about 65%), spectrophotometric (about 26%) and electroanalytical (about 9%) methods are used. Most of all the applications, HPLC with spectrophotometry [110,139,147–163], MS [29,164] and electrochemical detection [165] was described. The LC-chromatographic analytical parameters are presented in Table 1. Carini et al. detected nimesulide and metabolites in human urine by HPLC and TLC–MS. TLC analysis was performed on Kieselgel GF 254 nm plates using two mobile phases: toluene + ethylformate + formic acid (50 + 40 + 10, v/v/v) (first run) and toluene + ethylacetate + isopropanol + 25% ammonium hydroxide (30 + 30 + 30 + 10, v/v/v/v) (second run). Plates were visualized under UV light (254 nm) and after spraying with the mixtures: 2% FeCl$_3$ in 2 M HCl and 1% aqueous potassium ferricyanide, or 1% sodium nitrite in 1 M HCl followed by 0.2% β-naphtol in 1 M NaOH. The metabolites were extracted from silica gel plates with methanol and the extract subjected to EI MS. Electron impact (EI) mass spectra of nimesulide shows a [M]$^+$ at *m/z* 308 [150]. TLC was used in analysis of drugs containing nimesulide [152,153,166–169]. TLC-densitometry (at λ = 310 nm) was applied in pharmacokinetic studies, to analyse nimesulide ($R_f \approx 0.5025$) on silica gel 60 F$_{254}$ plates with toluene + acetone (100 + 10, v/v) as mobile phase [170] and also for its determination in human plasma with a single-stage extraction procedure without the use of an I.S. [171]. Nimesulide and its metabolites were detected in a blood and urine samples

by TLC. They were identified as resulting from the reduction of the nitro group on nimesulide to an amino group [172]. Syed et al. used GC on stainless steel OV-17 on 125–150 mesh Chromosorb (3 m × 2 mm) column (19,536 theoretical plates/m) [152]. A MEKC for the analysis of nimesulide in electrolyte composed of 35 mM borate buffer and 35 mM of anionic detergent SDS (pH 9.75) + acetonitrile (95 + 5, v/v) was reported. Detection at 234 nm using a DAD was made [173]. A CZE was also reported. The separation was run using borate buffer (60 mM L^{-1}, pH 8.5) containing 13% of methanol (v/v), at 20 kV and detection at 200 nm [46]. Dogrukol-Ak et al. presented separation using electrolyte of 10 mM borate buffer containing 10% ethanol (v/v) (pH 8.1) and detection at 200 nm [174].

For the analysis of nimesulide spectrophotometric methods were also frequently used following derivatisation to a colored chromogen [175–179] or in UV [180] and using second order derivative UV spectrophotometry [181]. The spectrophotometric methods for determination of nimesulide are presented in Table 2. Nimesulide content was determined by AdCSV with hanging drop working electrode, an Ag/AgCl as the reference and a platinum wire as auxiliary electrodes at −0.33 V [182]. For determination of nimesulide in human serum Wang et al. used CNTs (carbon nanotubes) with cysteic acid and electrochemical oxidation of L-cysteine to form a novel composite thin film material at a glassy carbon electrode (GCE) for differential pulse voltammetry [183]. Polarographic methods have been developed for the analysis of drugs containing nimesulide [184,185]. Kumar et al. described potentiometric method in the pH range of 5–8. The electrochemical cell: saturated calomel electrode/internal filling solution (1 × 10^{-1} M NaCl solution + 1 × 10^{-3} M drug solution in methanol)/PVC membrane test solution/KCl salt bridge//saturated calomel electrode was used [186]. Catarino et al. developed a new flow-injection system. The injector–commutator besides functioning as an injector device for the sample plugs, allowed the movement of the tubular voltammetric detector between the two flow channels of the manifold. Analytical signal was obtained in potential 1.2 V in the case of nimesulide [187].

3. Simultaneous determination of analyzed drugs

Besides the analytical methods for single components, some of the simultaneous determinations are also included in this review. Oxicams, nabumetone and nimesulide were simultaneously determined by LC–UV [29,30,32–34,89,110,139,160,161,163], LC–MS [29,38–40], TLC-densitometry [89,167], CZE [46], spectrophotometry UV–vis [49,51,52,90,91], spectrofluorimetry [61,90,91], FIA [81] and electrochemical methods [51,66,68,71,74,75,96].

LC with UV and fluorimetry detection was used for determination of 12 non-steroidal drugs (naproxen, indomethacin, sulindac, piroxicam, loxoprofen, ketoprofen, felbinac, fenbufen, flurbiprofen, diclofenac, ibuprofen and mefenamic acid) in human urine [28]; naproxen, ketoprofen, ibuprofen, diclofenac, piroxicam, nimesulide and paracetamol in homeopathic preparations [29]; piroxicam, mefenamic acid, salicylic acid and acetylsalicylic acid in human serum [35]; meloxicam and pyridinol mesylate [108]; clobutinol hydrochloride together with diclofenac, meloxicam and nimesulide in urine [110]; naproxen, nabumetone and its major metabolite in human urine [138]; ketoprofen, fenbufen, sulindac, probenecid, nabumetone and indomethacin [140]; etoricoxib, salicylic acid, valdecoxib, ketoprofen, nimesulide and celecoxib in human plasma [151]; nimesulide and chlorzaxazone in pharmaceuticals [160] and tizanide and nimesulide in tablets [161,163]. By LC–MS–MS, acetylsalicylic acid, flunixin, phenylbutazone, tolfenamic acid, meloxicam and ketoprofen [111] and meloxicam, flunixin meglumine, carprofen and tolfenamic acid [115] have been analyzed. Micellar liquid

chromatography was used to determine acemethacin, diclofenac, indomethacin, ketoprofen, nabumetone, naproxen, piketoprofen and tolmentin in pharmaceutical preparations [136]. Meloxicam and tetracaine hydrochloride [117] and paracetamol, chlorzaxazone and nimesulide [167] were determined by TLC-densitometry. Capillary electrophoresis was reported for the determination of sulindac, ketoprofen, indomethacin, piroxicam, nimesulide, ibuprofen, naproxen [46]; meloxicam, rofecoxib and celecoxib [119]; nimesulide and valdecoxib [173] and for simultaneous analysis of 13 NSAIDs at 36 °C (niflumic acid, flufenamic acid, piroxicam, alclofenac, tiaprofenic acid, flurbiprofen, suprofen, ketoprofen, naproxen, indomethacin, carprofen, indoprofen and sulindac) and 11 NSAIDs at 25 °C in nonaqueous electrolyte made of 50 mM ammonium acetate + 13.75 mM ammonia in methanol [44].

Spectrophotometry (conventional and derivative mode) was applied for the analysis of piroxicam in the presence of vitamin B6, B2 and dexamethasone sodium phosphate [47]; promethazine, chlorhexidine, benzydamine, ketoprofen, ibuprofen, fentiazac, piroxicam, fluorouracil, crotamiton and hydrocortisone acetate in cream components [48]; amoxicillin, ciprofloxacin and piroxicam after oxidation by Fe(III) present in 1,10-phenanthroline or 2,2′-bipyridyl [53]; propranolol hydrochloride and piroxicam with ceric ammonium sulphate in acidic medium [54]; meloxicam, tetracaine hydrochloride and their degradation products [117]. Simultaneous determination of piroxicam and pyridoxine (vitamin B6) by spectrofluorimetry was reported [64].

Voltammetric determination of indomethacin, acemethacin, piroxicam and tenoxicam was reported [66]. Catarino et al. used FIA with amperometric detection for the determination of nimesulide and diltiazem [187].

4. Validation of the methods

Validation of a method is the planned and documented procedure to establish its performance characteristics. Typical parameters that characterize each analytical method include selectivity, specificity, range, linearity, accuracy (recovery), detection limit (LOD), quantitation limit (LOQ), precision (repeatability and reproducibility), robustness and ruggedness [8]. They define what the method can do under optimized conditions of matrix solution, analyte isolation, instrumental settings and other experimental features.

The analytical procedures presented in this review have been validated in terms of basic parameters, i.e. linearity, LOD, LOQ, precision and recovery. Validation parameters of the methods used for the determination of oxicams, nimesulide and nabumetone are presented in Table 3. The data obtained makes it possible to choose the proper analytical procedure, adopted to the kind of sample (pharmaceutical preparations, biological matrices), method of the determination or detection. Comparing validation parameters of already researched methods, it can be concluded which one of them is more sensitive (low LOD and LOQ values), accurate (precision and recovery) and allows markings in a broad linearity scope.

5. Conclusions

This review presents analytical methods applied for the determination of oxicams as well as nimesulide and nabumetone between 1990 and 2008. A great number of studies on piroxicam, tenoxicam, meloxicam or nimesulide can be noted, whereas for droxicam, isoxicam or nabumetone there are only a few. Among all of the published methods, liquid chromatography with UV–vis or MS–MS detection is the most popular technique which is used both for the analysis of pharmaceutical preparations and biological material. It is applied not only for the determination of active

components, purity and stability studies, but also for pharmacokinetic analysis. Other chromatographic methods, i.e. TLC, GC, are not so popular. Another technique used for mixture components separation is electrophoresis, in which after separation, the individual components can be analysed in the buffer solution using a spectrophotometric or electrochemical detector. Modifications in the design of capillaries or the buffers used, combined with modern detection techniques allow for further development of these techniques and more and more widespread use thereof in the analysis. Spectrophotometric methods in UV–vis (classical and for consecutive derivatives) as well as fluorimetric are also quite common, being most frequently used for quantification or confirmation of substance identity. Despite wide availability of the equipment, their use is however still limited, especially with a complicated matrix. Various voltamperometric techniques are becoming more and more popular especially because they allow obtaining correct results with great accuracy and sensitivity. The stage of preliminary concentration enables determination within the concentration range of 10^{-5} to 10^{-8} M. A permanent place in the analysis is occupied by classical methods, i.e. potentiometry and coulometry, with the use of different modified indicator electrodes, although they are used very rarely. Automation of some stages in the analytical procedure as well as combining many methods increase the potential of analysis and detection of components and lead to the development of new methods, e.g. flow-injection analysis, and modification of those already used. The ultimate goal is to obtain results with more and more precision and accuracy and at increasingly lower concentration levels of the substances being determined. This also facilitates the course of analysis by reducing the impact of the matrix, without prior labour-consuming preparation of the samples (especially the biological ones).

References

[1] W. Janiec, Kompendium farmakologii, PZWL, Warszawa, 2005.
[2] A. Danysz, Z. Kleinrok, Podstawy farmakologii, Volumed, Wrocław, 1996.
[3] A. Zejc, M. Gorczyca, Chemia leków, PZWL, Warszawa, 2002.
[4] M. Zając, E. Pawełczyk, Chemia leków, AM, Poznań, 2000.
[5] J. Sherma, Anal. Chem. 72 (2000) 9R.
[6] R.N. Rao, S. Meena, A.R. Rao, J. Pharm. Biomed. Anal. 39 (2005) 349.
[7] K. Ferenczi-Fodor, Z. Végh, A. Nagy-Turák, B. Renger, M. Zeller, J. AOAC Int. 84 (2001) 1265.
[8] ICH Harmonised Tripartite Guideline, ICH Steering Committee, Nov 1996, inc. Nov 2005.
[9] European Pharmacopoeia, 6th edn. (Suppl. 6.2), Council of Europe, Strasbourg, France, 2007.
[10] British Pharmacopoeia, 3rd edn., The Stationery Office, London, 2000.
[11] United States Pharmacopoeia USP24, 12601 Twinbrook Parkway, Rockville, MD 20852, 1999.
[12] M.T. Maya, J.P. Pais, J.A. Morais, J. Pharm. Biomed. Anal. 13 (1995) 319.
[13] L. Edno, F. Bressolle, B. Combe, M. Galtier, J. Pharm. Biomed. Anal. 13 (1995) 785.
[14] P.A. Milligan, J. Chromatogr. 576 (1992) 121.
[15] A. Avgerinos, S. Axarlis, J. Dragatsis, Th. Kardas, S. Malamataris, J. Chromatogr. B: Biomed. Sci. Appl. 673 (1995) 142.
[16] S. Wanwimolruk, S.Z. Wanwimolruk, A.R. Zoest, J. Liq. Chromatogr. Rel. Technol. 14 (1991) 2373.
[17] D. Cerretani, L. Micheli, A.I. Fiaschi, G. Giorgi, J. Chromatogr.: Biomed. Sci. Appl. 614 (1993) 103.
[18] K. Saeed, M. Becher, J. Chromatogr.: Biomed. Sci. Appl. 567 (1991) 185.
[19] H. Basan, N.G. Göğer, N. Ertaş, M.T. Orbey, J. Pharm. Biomed. Anal. 26 (2001) 171.
[20] A. Doliwa, S. Santoyo, M.A. Campanero, P. Ygartua, J. Pharm. Biomed. Anal. 26 (2001) 531.
[21] M. Amanlou, A.R. Dehpour, J. Chromatogr. B 696 (1997) 317.
[22] S. Dadashzadeh, A.M. Vali, N. Rezagholi, J. Pharm. Biomed. Anal. 28 (2002) 1201.
[23] H. Bartsch, A. Eiper, H. Kopelent-Frank, J. Pharm. Biomed. Anal. 20 (1999) 531 (21 (2005) 1275 (erratum)).
[24] B. Boneschans, A. Wessels, J. Van Staden, M. Zovko, B. Zorc, J. Bergh, Drug Dev. Ind. Pharm. 29 (2003) 155.
[25] S. Rozou, A. Voulgari, E. Antoniadou-Vyza, Eur. J. Pharm. Sci. 21 (2004) 661.
[26] N. Yritia, P. Parra, J.M. Fernández, J.M. Barbanoj, J. Chromatogr. A 846 (1999) 199.

[27] M.C. Gaudiano, L. Valvo, P. Bertocchi, L. Manna, J. Pharm. Biomed. Anal. 32 (2003) 151.
[28] T. Hirai, S. Matsumoto, I. Kishi, J. Chromatogr. B 692 (1997) 375.
[29] A. Panusa, G. Multari, G. Incarnato, L. Gagliardi, J. Pharm. Biomed. Anal. 43 (2007) 1221.
[30] J. Joseph-Charles, M. Bertucat, J. Liq. Chromatogr. Rel. Technol. 22 (1999) 2009.
[31] E.R.M. Hackmann, E.A. Dos Santos Gianotto, M.I.R.M. Santoro, Anal. Lett. 26 (1993) 259.
[32] J.I. Troconiz, L.G. Lopez-Bustamante, D. Fos, Arzneimittelforschung 43 (1993) 679.
[33] M. Sultan, G. Stecher, W.M. Stöggl, R. Bakry, P. Zaborski, C.W. Huck, N.M. El Kousy, G.K. Bonn, Curr. Med. Chem. 12 (2005) 573.
[34] A. Nakamura, M.N. Nakashima, M. Wada, K. Nakashima, Bunseki Kagaku 54 (2005) 755.
[35] H. Ibrahim, A. Boyer, J. Bouajila, F. Couderc, F. Nepveu, J. Chromatogr. B 857 (2007) 59.
[36] A.G. Kazemifard, D.E. Moore, J. Chromatogr.: Biomed. Sci. Appl. 533 (1990) 125.
[37] A.D. De Jager, H. Ellis, H.K.L. Hundt, K.J. Swart, A.F. Hundt, J. Chromatogr. B 729 (1999) 183.
[38] A.R. McKinney, C.J. Suann, A.M. Stenhouse, Rapid Commun. Mass Spectrom. 18 (2004) 2338.
[39] M.E. Abdel-Hamid, J. Liq. Chromatogr. Rel. Technol. 23 (2000) 3095.
[40] H.Y. Ji, H.W. Lee, Y.H. Kim, D.W. Jeong, H.S. Lee, J. Chromatogr. B 826 (2005) 214.
[41] J. De Kanel, W.E. Vickery, X. Diamond, J. Am. Soc. Mass Spectrom. 9 (1998) 255.
[42] S.P. Puthli, P.R. Vavia, J. Pharm. Biomed. Anal. 22 (2000) 673.
[43] A. Crecelius, M.R. Clench, D.S. Richards, V. Parr, J. Pharm. Biomed. Anal. 35 (2004) 31.
[44] M. Fillet, I. Bechet, V. Piette, J. Crommen, Electrophoresis 20 (1999) 1907.
[45] M.G. Donato, W. Baeyens, W. Van Den Bossche, P. Sandra, J. Pharm. Biomed. Anal. 12 (1994) 21.
[46] Y.L. Chen, S.M. Wu, Anal. Bioanal. Chem. 381 (2005) 907.
[47] A.J. Nepote, L. Vera-Candiotti, M.R. Williner, P.C. Damiani, A.C. Olivieri, Anal. Chim. Acta 489 (2003) 77.
[48] D. Bonazzi, V. Andrisano, R. Gatti, V. Cavrini, J. Pharm. Biomed. Anal. 13 (1995) 1321.
[49] M.A. El Ries, Anal. Lett. 31 (1998) 793.
[50] A.M. El-Didamony, A.S. Amin, Anal. Lett. 37 (2004) 1151.
[51] M.A. El-Ries, G. Mohamed, S. Khalil, M. El-Shall, Chem. Pharm. Bull. 51 (2003) 6.
[52] A.S. Amin, J. Pharm. Biomed. Anal. 29 (2002) 729.
[53] B.S. Nagaralli, J. Seetharamappa, M.B. Melwanki, J. Pharm. Biomed. Anal. 29 (2002) 859.
[54] B.G. Gowda, J. Seetharamappa, M.B. Melwanki, Anal. Sci. 18 (2002) 671.
[55] V. Ródenas, M.S. García, C. Sánchez-Pedreño, M.I. Albero, Analyst 123 (1998) 1749.
[56] A. Klopas, I. Panderi, M. Parissi-Poulou, J. Pharm. Biomed. Anal. 17 (1998) 515.
[57] G.M. Escandar, Analyst 124 (1999) 587.
[58] J.L. Manzoori, M. Amjadi, Microchim. Acta 143 (2003) 39.
[59] K.C. Ramesh, B.G. Gowda, J. Seetharamappa, J. Keshavayya, J. Anal. Chem. 58 (2003) 933.
[60] P.C. Damiani, M. Bearzotti, M. Cabezón, A.C. Olivieri, J. Pharm. Biomed. Anal. 17 (1998) 233.
[61] M.H. Barary, M.H. Abdel-Hay, S.M. Sabry, T.S. Belal, J. Pharm. Biomed. Anal. 34 (2004) 221.
[62] G.M. Escandar, A.J. Bystol, A.D. Campiglia, Anal. Chim. Acta 466 (2002) 275.
[63] J.A. Arancibia, G.M. Escandar, Talanta 60 (2003) 1113.
[64] H. Abdollahi, M.H. Sororaddin, A. Naseri, Anal. Sci. 22 (2006) 263.
[65] J.A. Acuña, C. de la Fluente, M.D. Vãzquez, M.L. Tascón, P. Sánchez-Batanero, Talanta 40 (1993) 1637.
[66] C. Reguera, M.C. Ortiz, M.J. Arcos, Electroanalysis 14 (2002) 1699.
[67] A.M. Beltagi, O.M. Abdallah, M.M. Ghoneim, Chem. Anal. 52 (2007) 387.
[68] N.A. El-Maali, R.M. Hassan, Bioelectrochem. Bioenerg. 24 (1990) 155.
[69] A.R. Paniagua, M.D. Vázquez, M.L. Tascón, P. Sánchez-Batanero, Electroanalysis 6 (1994) 265.
[70] A. Abbaspour, R. Mirzajani, J. Pharm. Biomed. Anal. 44 (2007) 41.
[71] N.A. El-Maali, J.-C. Vire, G.J. Patriarche, M.A. Ghandour, G.D. Christian, Anal. Sci. 6 (1990) 245.
[72] A. González, M.D. Vázquez, M.L. Tascón, P. Sánchez-Batanero, Electroanalysis 6 (1994) 497.
[73] P. Norouzi, M.R. Ganjali, S. Labbafi, A. Mohammadi, Anal. Lett. 40 (2007) 747.
[74] K. Nikolic, M. Bogavac, L. Arsenijevic, Farmaco 48 (1993) 1131.
[75] S. Khalil, N. Borham, M.A. El-Ries, Anal. Chim. Acta 414 (2000) 215.
[76] C. Sánchez-Pedreño, M.S. Garcia, M.I. Albero, J. Rodriguez, J. Pharm. Biomed. Anal. 11 (1993) 933.
[77] M.I. Pascual-Reguera, M.J. Ayora-Cañada, M.S.C. Ruiz, Eur. J. Pharm. Sci. 15 (2002) 179.
[78] H. Bai, F. Nie, J. Lu, Anal. Sci. 23 (2007) 1301.
[79] S.M.Z. Al-Kindy, A. Al-Wishahi, F.E.O. Suliman, Talanta 64 (2004) 1343.
[80] S.M.Z. Al-Kindy, F.E.O. Suliman, A.A. Al-Wishahi, H.A.J. Al-Lawati, M. Aoudia, J. Lumin. 127 (2007) 291.
[81] J.F. Al-Momani, Anal. Sci. 22 (2006) 1611.
[82] G. Carlucci, P. Mazzeo, G. Palumbo, J. Liq. Chromatogr. Rel. Technol. 15 (1992) 683.
[83] H. Bartsch, A. Eiper, H. Kopelent-Frank, E. Sakka, J. Liq. Chromatogr. Rel. Technol. 25 (2002) 2821.
[84] J.L. Mason, G.J. Hobbs, J. Chromatogr. B: Biomed. Sci. Appl. 665 (1995) 410.
[85] M.I. Múnera-Jaramillo, S. Botero-Garcés, J. Chromatogr.: Biomed. Sci. Appl. 616 (1993) 349.
[86] A. Marland, P. Sarkar, R. Leavitt, J. Anal. Toxicol. 23 (1999) 237.
[87] I. Sora, T. Galaon, S. Udrescu, J. Negru, V. David, A. Medvedovici, J. Pharm. Biomed. Anal. 43 (2007) 1437.
[88] A.F.M. El Walily, S.M. Blaih, M.H. Barary, M.A. El Sayed, H.H. Abdine, A.M. El Kersh, J. Pharm. Biomed. Anal. 15 (1997) 1923.
[89] E.A. Taha, N.N. Salama, L.El-S.A. Fattah, J. AOAC Int. 87 (2004) 366.
[90] E.A. Taha, N.N. Salama, L.El-S.A. Fattah, Spectrosc. Lett. 35 (2002) 501.
[91] E.A. Taha, N.N. Salama, L.El-S.A. Fattah, Chem. Pharm. Bull. 54 (2006) 653.
[92] H.A. Mohamed, H.M.A. Wadood, O.A. Farghaly, J. Pharm. Biomed. Anal. 28 (2002) 819.
[93] O. Atay, F. Dinçol, Anal. Lett. 30 (1997) 1675.
[94] Z. Atkopar, M. Tunçel, Anal. Lett. 29 (1996) 2383.
[95] N. Özaltin, Anal. Chim. Acta 406 (2000) 183.
[96] J.A. Acuña, M.D. Vázquez, M.L. Tascón, P. Sánchez-Batanero, J. Pharm. Biomed. Anal. 36 (2004) 157.
[97] M.S. Garcia, C. Sánchez-Pedreño, M.I. Albero, M.J. Gimenez, J. Pharm. Biomed. Anal. 21 (1999) 731.
[98] S.A. Al-Tamrah, Anal. Chim. Acta 375 (1998) 277.
[99] A. Abd Elbary, N. Foda, M. Elkhateeb, Anal. Lett. 34 (2001) 1175.
[100] M.S. Arayne, N. Sultana, F.A. Siddiqui, Pak. J. Pharm. Sci. 18 (2005) 58.
[101] J. Joseph-Charles, M. Bertucat, Anal. Lett. 32 (1999) 2051.
[102] G. Marcelin-Jiménez, J.A. Hernández, A.P. Ángeles, L. Contreras, A. Garcia, M. Hinojosa, M. Morales, L. Rivera, L. Martinez-Rossier, A. Fernández, Biopharm. Drug Dispos. 26 (2005) 167.
[103] T. Velpandian, J. Jaiswal, R.K. Bhardwaj, S.K. Gupta, J. Chromatogr. B 738 (2000) 431.
[104] J.-W. Bae, M.-J. Kim, Ch.-G. Jang, S.-Y. Lee, J. Chromatogr. B 859 (2007) 69.
[105] H.-K. Han, H.-K. Choi, Eur. J. Pharm. Biopharm. 65 (2007) 99.
[106] B. Dasandi, Shivaprakash, H. Saroj, K.M. Bhat, J. Pharm. Biomed. Anal. 28 (2002) 999.
[107] W.R.G. Baeyens, G. Van der Weken, E. D'haeninck, A.M. García-Campaña, T. Vankeirsblick, A. Vercauteren, P. Deprez, J. Pharm. Biomed. Anal. 32 (2003) 839.
[108] S.E. Vignaduzzo, P.M. Castellano, T.S. Kaufaman, J. Pharm. Biomed. Anal. 46 (2008) 219.
[109] N.H. Zawilla, M. Abdul-Azim Mohammad, N.M. El Kousy, S.M. El-Moghazy Aly, J. Pharm. Biomed. Anal. 32 (2003) 1135.
[110] E.T. Malliou, C.K. Markopoulou, J.E. Koundourellis, J. Liq. Chromatogr. Rel. Technol. 27 (2005) 1565.
[111] N. Van Hoof, K. De Wasch, S. Poelmans, N. Noppe, H. De Brabander, Rapid Commun. Mass Spectrom. 18 (2004) 2823.
[112] H.M. Rigato, G.D. Mendes, N.C. do Carmo Borges, R.A. Moreno, Int. J. Clin. Pharmacol. Ther. 44 (2006) 189.
[113] J.J. Wiesner, A.D. De Jager, F.C.W. Sutherland, H.K.L. Hundt, K.J. Swart, A.F. Hundt, J. Els, J. Chromatogr. B 785 (2003) 115.
[114] Y. Yuan, X. Chen, D. Zhong, J. Chromatogr. B 852 (2007) 650.
[115] C. Igualada, F. Moragues, J. Pitarch, Anal. Chim. Acta 586 (2007) 432.
[116] V. Hormazabal, T. Fosse, B. Ranheim, J. Liq. Chromatogr. Rel. Technol. 29 (2006) 1291.
[117] L.I. Bebawy, Spectrosc. Lett. 31 (1998) 797.
[118] H. Hopkała, A. Pomykalski, J. Planar Chromatogr.-Modern TLC 16 (2003) 107.
[119] Y.-H. Hsieh, S.-J. Lin, S.-H. Chen, J. Sep. Sci. 29 (2006) 1009.
[120] E. Nemutlu, S. Kir, J. Pharm. Biomed. Anal. 31 (2003) 393.
[121] M.S. Garcia, C. Sánchez-Pedreño, M.I. Albero, J. Martí, Eur. J. Pharm. Sci. 9 (2000) 311.
[122] E.M. Hassan, J. Pharm. Biomed. Anal. 27 (2002) 771.
[123] E. Sener, G. Altiokka, Z. Atkosar, M. Tuncel, Pharmazie 56 (2001) 186.
[124] H.Y. Liu, L. Zhang, Y.H. Hao, Q.J. Wang, P.G. He, Y.Z. Fang, Anal. Chim. Acta 541 (2005) 187.
[125] S. Altinöz, E. Nemutlu, S. Kir, Il Farmaco 57 (2002) 463.
[126] G. Altiokka, Z. Atkosar, M. Tuncel, Pharmazie 56 (2001) 184.
[127] A. Radi, M.A. El Ries, F. El-Anwar, Z. El-Sherif, Anal. Lett. 34 (2001) 739.
[128] A.M. Beltagi, M.M. Ghoneim, A. Radi, J. Pharm. Biomed. Anal. 27 (2002) 795.
[129] A.-E. Radi, M. Ghoneim, A. Beltagi, Chem. Pharm. Bull. 49 (2001) 1257.
[130] S. Radhofer-Welte, P. Dittrich, J. Chromatogr. B 707 (1998) 151.
[131] T. Suwa, H. Urano, Y. Shinohara, J. Kokatsu, J. Chromatogr.: Biomed. Sci. Appl. 617 (1993) 105.
[132] Y.H. Kim, H.Y. Ji, E.S. Park, S.W. Chae, H.S. Lee, Arch. Pharm. Res. 30 (2007) 905.
[133] E. Nemutlu, Ş. Demircan, S. Kir, Pharmazie 60 (2005) 421.
[134] M.M. Ghoneim, A.M. Beltagi, A. Radi, Anal. Sci. 18 (2002) 183.
[135] H. Bartsch, A. Eiper, K. Habiger, H. Kopelent-Frank, J. Chromatogr. A 846 (1999) 207.
[136] L.E. Gilabert, Y.M. Biosca, S. Sagrado, R.M.V. Camanas, M.J.M. Hernandez, Chromatographia 55 (2002) 283.
[137] I.F. Al-Momani, Anal. Lett. 30 (1997) 2485.
[138] E. Mikami, T. Goto, T. Ohno, H. Matsumoto, M. Nishida, J. Pharm. Biomed. Anal. 23 (2000) 917.
[139] R.N. Rao, S. Meena, D. Nagaraju, A.R.R. Rao, Biomed. Chromatogr. 19 (2005) 362.

[140] A. Haque, J.T. Stewart, Biomed. Chromatogr. 13 (1999) 51.
[141] K. Kobylińska, M. Barlińska, M. Kobylińska, J. Pharm. Biomed. Anal. 32 (2003) 323.
[142] G.K. Reddy, J.V.L.N.S. Rao, R.L.B. Varma, D.G. Sankar, Indian Drugs 38 (2001) 336.
[143] A.O. Adegoke, S.O. Idowu, A.A. Olaniyi, Afr. J. Med. Med. Sci. 36 (2007) 249.
[144] N.O. Can, M. Tuncel, H.Y. Aboul-Enein, Pharmazie 58 (2003) 22.
[145] J.A.M. Pulgarin, A.A. Molina, M.T.A. Pardo, Anal. Chim. Acta 528 (2005) 77.
[146] Y. Altun, B. Dogan, S.A. Ozkan, B. Uslu, Acta Chim. Slov. 54 (2007) 287.
[147] M.C. Carrasco-Portugal, V. Granados-Soto, G.A. Camacho-Vieyra, J. Pérez-Urizar, F.J. Flores-Murrieta, J. Liq. Chromatogr. Rel. Technol. 23 (2000) 2237.
[148] C.M. Rolim, V. Porta, S. Storpirtis, Arzneimittelforschung 57 (2007) 537.
[149] A. Maltese, F. Maugeri, C. Bucolo, J. Chromatogr. B 804 (2004) 441.
[150] M. Carini, G. Alolini, R. Stefani, C. Marinello, R.M. Facino, J. Pharm. Biomed. Anal. 18 (1998) 201.
[151] V.V.P. Kumar, M.C.A. Vinu, A.V. Ramani, R. Mullangi, N.R. Srinivas, Biomed. Chromatogr. 20 (2006) 125.
[152] A.A. Syed, M.K. Amshumali, N. Devan, Acta Chromatogr. 12 (2002) 95.
[153] P. Kovařiková, M. Mokrý, J. Klimeš, J. Pharm. Biomed. Anal. 31 (2003) 827.
[154] P. Ferrario, M. Bianchi, J. Chromatogr. B 785 (2003) 227.
[155] P. Ptáček, J. Macek, J. Klima, J. Chromatogr. B 758 (2001) 183.
[156] G. Kraksa, N. Udupa, J. Chromatogr. B 727 (1999) 241.
[157] C. Giachetti, A. Tenconi, Biomed. Chromatogr. 12 (1998) 50.
[158] D.J. Jaworowicz Jr., M.T. Filipowski, K.M.K. Boje, J. Chromatogr. B 723 (1999) 293.
[159] B.S. Nagaralli, J. Seetharamappa, B.G. Gowda, M.B. Melwanki, J. Anal. Chem. 58 (2003) 778.
[160] S.S. Zarapkar, N.P. Bhandari, U.P. Halkar, Indian Drugs 37 (2000) 469.
[161] B. Raman, D. Patil, Indian Drugs 39 (2002) 392.
[162] B. Tubić, B. Ivković, M. Zečević, S. Vladimirov, Acta Chim. Slov. 54 (2007) 583.
[163] H. Nimje, S.P. Wate, D.P. Dharkar, R. Razdan, Indian J. Pharm. Sci. 69 (2007) 281.
[164] R.E. Barrientos-Astigarraga, Y.B. Vannuchi, M. Sucupira, R.A. Moreno, M.N. Muscará, G. De Nucci, J. Mass Spectrom. 36 (2001) 1281.
[165] A. Álvarez-Lueje, P. Vásquez, L.J. Núñez-Vergara, J.A. Squella, Anal. Lett. 31 (1998) 1173.
[166] V.B. Patravale, S. D'Souza, Y. Narkar, J. Pharm. Biomed. Anal. 25 (2001) 685.
[167] R.T. Sane, M. Gadgil, J. Planar Chromatogr.-Modern TLC 15 (2002) 76.
[168] A.P. Argekar, J.G. Sawant, J. Planar Chromatogr.-Modern TLC 12 (1999) 152.
[169] S.G. Navalgund, P.S. Sahasrabudhe, D.H. Kanolkar, P.S. Prabhu, R.T. Sane, Indian Drugs 35 (1998) 757.
[170] B. Miljković, B. Brzaković, I. Kovacević, D. Agbaba, M. Pokrajac, J. Planar Chromatogr.-Modern TLC 16 (2003) 211.
[171] K.K. Pandya, M.C. Satia, I.A. Modi, R.I. Modi, B.K. Chakravarthy, T.P. Gandhi, J. Pharm. Pharmacol. 49 (1997) 773.
[172] P. Sarkar, J.M. McIntosh, R. Leavitt, H. Gouthro, J. Anal. Toxicol. 21 (1997) 197.
[173] S.L. Dalmora, M. Fronza, D.R. Nogueira, R.B. Souto, R.M. Bernardi, J. Liq. Chromatogr. Rel. Technol. 30 (2007) 2863.
[174] D. Dogrukol-Ak, M. Tuncel, H.Y. Aboul-Enein, J. Sep. Sci. 24 (2001) 743.
[175] A.C. Perju, M. Mândrescu, A.F. Spac, V. Dorneanu, Rev. Med. Chir. Soc. Med. Nat. Iasi. 111 (2007) 535.
[176] K.P.R. Chowdary, K.G. Kumar, G.D. Rao, Indian J. Pharm. Sci. 61 (1999) 86.
[177] Ch.S.R. Lakshimi, M.N. Reddy, Microchim. Acta 132 (1999) 1.
[178] P. Nagaraja, H.S. Yathirajan, H.R. Arunkumar, R.A. Vasantha, J. Pharm. Biomed. Anal. 29 (2002) 277.
[179] S.G. Navalgund, P.S. Prabhu, P.S. Sahasrabudhe, H.K. Deepa, R.T. Sane, Indian Drugs 37 (2000) 209.
[180] S. Chandran, S. Saggar, K.P. Priya, R.N. Saha, Drug Dev. Ind. Pharm. 26 (2000) 229.
[181] S. Altinöz, Ö.Ö. Dursun, J. Pharm. Biomed. Anal. 22 (2000) 175.
[182] S. Furlanetto, S. Orlandini, G. Aldini, R. Gotti, E. Dreassi, S. Pinzauti, Anal. Chim. Acta 413 (2000) 229.
[183] Ch. Wang, X. Shao, Q. Liu, Q. Qu, G. Yang, X. Hu, J. Pharm. Biomed. Anal. 42 (2006) 237.
[184] A. Álvarez-Lueje, P. Vásquez, L.J. Núñez-Vergara, J.A. Squella, Electroanalysis 9 (1997) 1209.
[185] Y.V.R. Reddy, P.R.K. Reddy, C.S. Reddy, S.J. Reddy, Y.V.R. Reddy, P.R. Kumar, C.S. Reddy, S.J. Reddy, Indian J. Pharm. Sci. 58 (1996) 96.
[186] K.G. Kumar, P. Augustine, S. John, Portug. Electrochem. Acta 25 (2007) 375.
[187] R.I.L. Catarino, C.L. Conceição, M.B.Q. Garcia, M.L.S. Gonçalves, J.L.F.C. Lima, M.M.C. Dos Santos, J. Pharm. Biomed. Anal. 33 (2003) 571.

Electrochemical detection of a breast cancer susceptible gene using cDNA immobilized chitosan-*co*-polyaniline electrode

Ashutosh Tiwari [a,*], Shaoqin Gong [a,b,**]

[a] *Department of Mechanical Engineering, University of Wisconsin-Milwaukee, 3200 North Cramer Street, Milwaukee, WI 532011, USA*
[b] *Department of Materials, University of Wisconsin-Milwaukee, 3200 North Cramer Street, Milwaukee, WI 532011, USA*

ABSTRACT

An electrochemical breast cancer biosensor based on a chitosan-*co*-polyaniline (CHIT-*co*-PANI) copolymer coated onto indium–tin-oxide (ITO) was fabricated by immobilizing the complementary DNA (cDNA) probe (42 bases long) associated with the breast cancer susceptible gene BRCA1. Both the CHIT-*co*-PANI/ITO and the cDNA/CHIT-*co*-PANI/ITO electrodes were characterized with Fourier transform infrared (FTIR) spectroscopy, atomic force microscopy (AFM), cyclic voltammetry (CV) and electrochemical impedance spectroscopy (EIS). For the cDNA/CHIT-*co*-PANI/ITO electrode, the amperometric current decreased linearly with an increasing logarithm of molar concentration of the single-stranded target DNA (ssDNA) within the range of 0.05–25 fmol. The bioelectrode exhibited a sensitivity of 2.104 μA/fmol with a response time of 16 s. The cDNA/CHIT-*co*-PANI/ITO electrode had a shelf life of about six months, even when stored at room temperature.

© 2008 Elsevier B.V. All rights reserved.

1. Introduction

Breast cancer starts in the breast cells of men and women. Worldwide, breast cancer is the second most common type of cancer and the second-leading cause of cancer death in women. Although considerable advancements have been made in detection and treatment in recent years, the majority of breast cancers are still detected in their last stage of advancement [1,2].

The advent of gene technology provides the hope of discovering novel biological sensors for early breast cancer detection, disease diagnosis, prognostication, and predicting responses to therapy. Abnormalities in the expression of specific genes have been linked to a huge and increasing number of diseases, including cancers. Specific genetic mutations occur in the cancerous breast cells that acquire mutations in the oncogenes and tumor suppressor genes [3].

Most breast cancers have gene mutations; thus, gene expression sensing is a promising technique for early detection. However, the existing nucleic acid detection techniques, including Northern blotting [4], ribonuclease protection assays [5], and reverse transcription-polymerase chain reaction (RT-PCR) [6,7] have limitations, including low sensitivity, poor selectivity and nonlinearity to the target strength [8]. These limitations affect the precision and quality of the biosensor and often provide distorted information on the gene expression for the breast carcinoma.

In order to rapidly detect primary-stage breast carcinoma, there is a significant need for low-cost, sensitive, and selective biosensors. In recent years, electrochemical nucleic acid biosensors have received much attention due to their rapid response, high sensitivity, and inherent selectivity [9–11]. The electrochemical detection technique provides a simple, accurate, and inexpensive platform for molecular detection. This approach is promising for the early detection of breast carcinoma using a breast cancer susceptible gene-1 (BRCA1; 5592 bp) specific cDNA probe (synthesized from mRNA of the cancerous breast tissue using RT-PCR) [12].

The performance of electrochemical biosensors generally depends on the physico-chemical properties of the electrode materials, as well as the sensing element immobilized over the electrode surface [13]. Most of the reported electrochemical biosensors must apply a high positive charge potential on the working electrode, which minimizes the interference effects from the reducing species [14].

Chitosan (CHIT) is a moderately inexpensive and stable electroactive material that allows for mass-production of biosensors. It is one of the most widely used biopolymers for sensor applications due to its nontoxic nature, excellent film forming ability, good mechanical strength, high permeability, and cost-effectiveness [15]. CHIT is a non-conducting biomaterial; however, it has an excellent biocompatible property that favors the immobilization of biomolecules over its surface [16]. The surface immobilization and protection of the biosensing element, i.e., the ssDNA or cDNA probe,

---

* Corresponding author.
** Co-corresponding author. Tel.: +1 414 229 5946; fax: +1 414 229 6958.
E-mail addresses: tiwari@uwm.edu (A. Tiwari), sgong@uwm.edu (S. Gong).

is one of the key challenges for fabricating a highly sensitive DNA biosensor [17–20]. It was also reported that modifying CHIT with conducting polymers such as polyaniline (PANI) improves its redox properties that influence the electron-transfer kinetics during the course of electrochemical detection [21,22].

PANI is a unique polymer whose variable conductivity can be controlled by the protonation of the imine sites on the main polymer chain [23]. Although pure PANI is not compatible for the genetical specimens, its composites usually provide a sustainable matrix for the biological molecules [24]. It was reported that the sensitivity and selectivity of PANI to genetical substances such as DNA, mRNA, and nucleic acids can be improved through copolymerization with polymers that have a variety of functional groups such as –OH, –NH$_2$, –COOH, and acetyl [25–28]. Thus, CHIT-*co*-PANI has been investigated as a promising sensing electrode for the early detection of breast carcinoma.

During this study, cDNA probe sequences associated with the breast cancer gene BRCA1 was immobilized onto the surface of a CHIT-*co*-PANI/ITO electrode. Using this electrode, the ssDNA was electrochemically detected by a change in current due to DNA hybridization. The advantageous features of this biosensor include a low price, ease of preparation, high sensitivity, and good selectivity.

2. Experimental

Aniline (Aldrich, 99.5%) and CHIT (Aldrich, >85% deacetylated) were used without further purification. All solutions were prepared with 18.2 MΩ deionized water. Indium–tin-oxide (ITO) coated glass (Balzers) sheets with a resistance of 15 Ω/cm were used as substrates for the deposition of CHIT-*co*-PANI copolymer electrodes.

The breast cancer specimens were obtained from a woman undergoing surgery for primary breast cancer. The breast tumor tissues were stored in liquid nitrogen immediately after surgical resection, transported to the laboratory, and then stored at −70 °C until mRNA extractions were performed.

2.1. Preparation of CHIT solution

To prepare the CHIT solution, 1.0 g of CHIT flakes was dissolved into 100 mL of 1.0% acetic acid. The resulting mixture was stirred for 3 h at room temperature until the CHIT flakes were completely dissolved. The CHIT solution was stored in a refrigerator at 4 °C.

2.2. Fabrication of CHIT-co-PANI/ITO electrode

Aniline (150 μL) and 1.0% CHIT solution (85 μL) were mixed with 10 mL of 0.5 M HCl in an electrochemical cell and the mixture was ultrasonically agitated for about 4 h. The CHIT-*co*-PANI was chronoamperometrically synthesized onto an ITO coated glass surface using a three-electrode assembly with the ITO glass as working, platinum as counter, and Ag/AgCl as reference electrodes at a potential of 0.9 V and a duration of 240 s.

2.3. mRNA isolation and cDNA preparation

The mRNA of the breast tumor tissues was extracted by homogenization in Trizol reagent (Invitrogen), and cDNA was prepared using oligo(dT) primer (Boehringer Mannheim) with Superscript^{TM} II reverse transcriptase (Invitrogen) for 50 min at 42 °C [29].

The following sequences of the primers were designed by PCR using SuperScript^{TM} II: target DNA: 5′ AGCTCGCT-GAGACTTCCTGGATCC CCCACAGCCGACTACTGA 3′; probe cDNA: 5′ TCGAGCGACTCTGAAGGACCTAGG GGGTGTCGGCTGATGACT 3′; mismatch DNA: 5′ AGCACGCTGAGACTTGCTGGA TCCCCCTCAGCC-GACTACAGA 3′.

2.4. Immobilization of cDNA probe onto CHIT-co-PANI/ITO electrode

The CHIT-*co*-PANI/ITO electrode was upturned and 15 μL of cDNA probe (350 nmol) was pipetted over the electrode surface and kept at room temperature for 5 h. The resulting cDNA probed CHIT-*co*-PANI/ITO bioelectrode was thoroughly washed with water and rinsed with a phosphate buffer solution (PBS) of pH 7.0 to rinse off any loosely bound cDNA from the electrode (Fig. 1).

2.5. Hybridization of cDNA onto CHIT-co-PANI/ITO electrode

The hybridization reaction was carried out by pipetting 15 μL of buffer containing 10 mM Tris–HCl, 1.0 mM EDTA, and 0.10 M NaCl on the surface of the electrode hold with a different molar concentration of the ssDNA. The resulting electrode was kept at 42 °C for 50 min, and then washed with PBS of pH 7.0 to remove the unhybridized ssDNA over the CHIT-*co*-PANI/ITO electrode. A similar procedure was adopted for the mismatched ssDNA (Fig. 1).
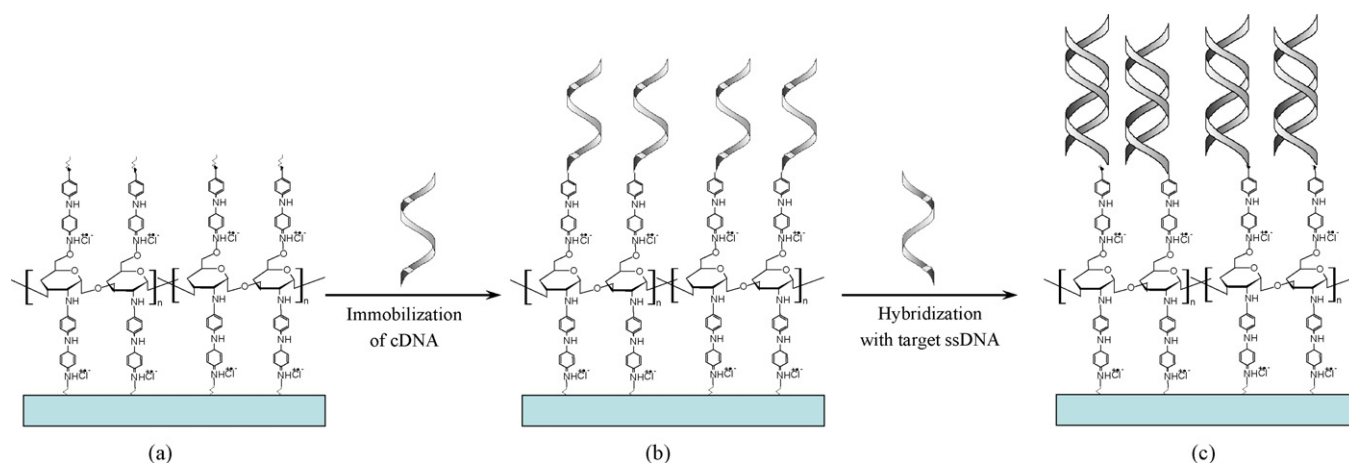
Fig. 1. Schematic presentation of the (a) fabrication of CHIT-*co*-PANI/ITO electrode; (b) immobilization of cDNA (BRCA1) over CHIT-*co*-PANI/ITO electrode; and (c) hybridization of the ssDNA onto cDNA/CHIT-*co*-PANI/ITO electrode.

2.6. Electrochemical detection

The electrochemical detection was performed by cyclic voltammetry (CV) with a three-electrode cell configuration comprising Ag/AgCl as a reference electrode, platinum foil as a counter electrode, and cDNA/CHIT-*co*-PANI/ITO as a working electrode in PBS of pH 7.0 containing 5 mM $Fe(CN)_6^{3-/4-}$ at 30 mV s^{-1} scan rate.

2.7. Characterization

Electrochemical measurements of the electrodes were carried out on a potentiostat/glavanostat (Princeton Applied Research, 273 A) unit with three electrodes in PBS of pH 7.0. The working electrode was one of the following three electrodes fabricated: CHIT-*co*-PANI/ITO; cDNA/CHIT-*co*-PANI/ITO; and target DNA hybridized CHIT-*co*-PANI/ITO. Platinum foil and Ag/AgCl were used as the counter and reference electrodes, respectively. Fourier transform infrared (FTIR) spectra were recorded on a PerkinElmer, Spectrum BX II spectrophotometer. The surface topology of the electrodes was studied using atomic force microscopy (AFM) (Veeco DICP2) under the tapping mode. All measurements were carried out at 25 °C.
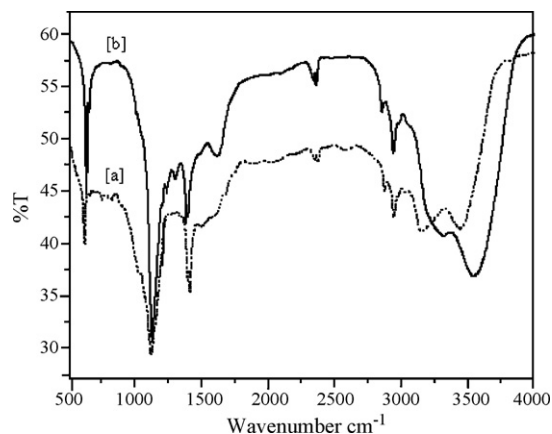
Fig. 2. FTIR spectra of the (a) CHIT-*co*-PANI/ITO and (b) cDNA/CHIT-*co*-PANI/ITO electrodes.

3. Results and discussion

During the electrochemical copolymerization, the aniline monomer initially became protonate with HCl and propagated to form an intermediate called PANI radical cation [30].

Aniline.HCl　　　　　**PANI radical cation [a]**
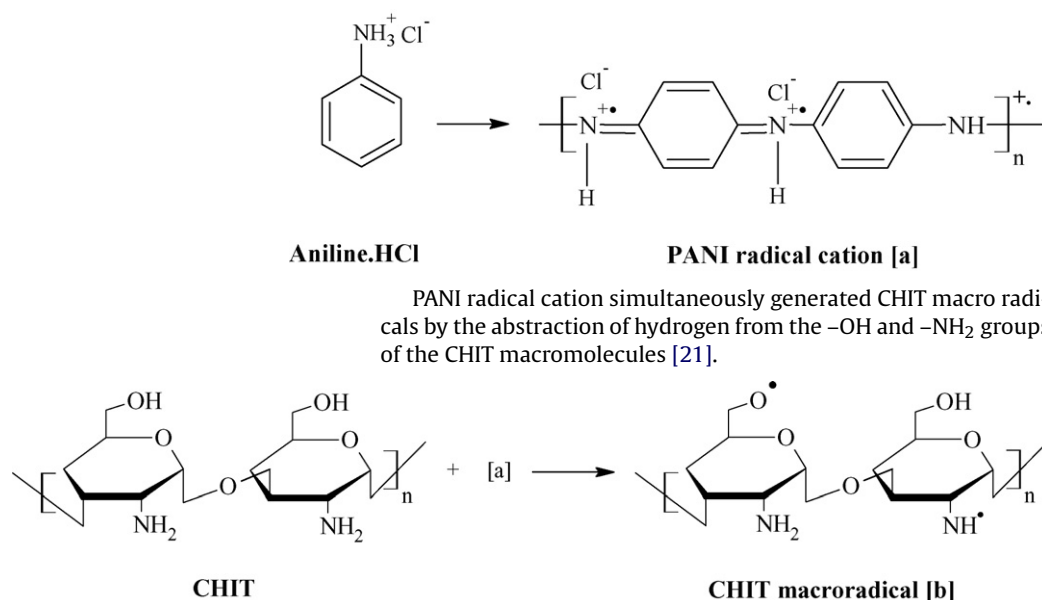
PANI radical cation simultaneously generated CHIT macro radicals by the abstraction of hydrogen from the –OH and –NH$_2$ groups of the CHIT macromolecules [21].

CHIT　　　　　**CHIT macroradical [b]**
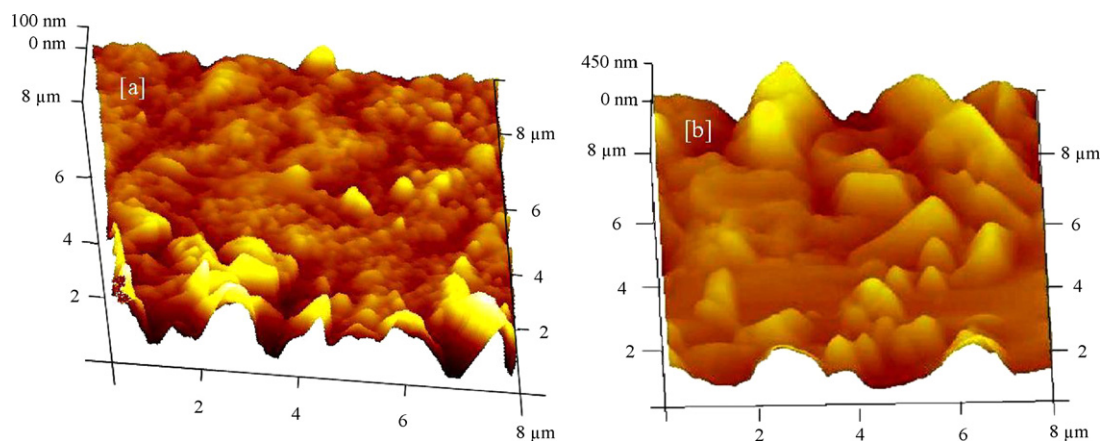
Fig. 3. AFM micrographs of the (a) CHIT-*co*-PANI/ITO and (b) cDNA/CHIT-*co*-PANI/ITO electrodes.

The PANI cation radicals and CHIT macro radicals then copolymerized and yielded CHIT-*co*-PANI.

hybridization of the target ssDNA in the case of cDNA/CHIT-*co*-PANI/ITO electrode.
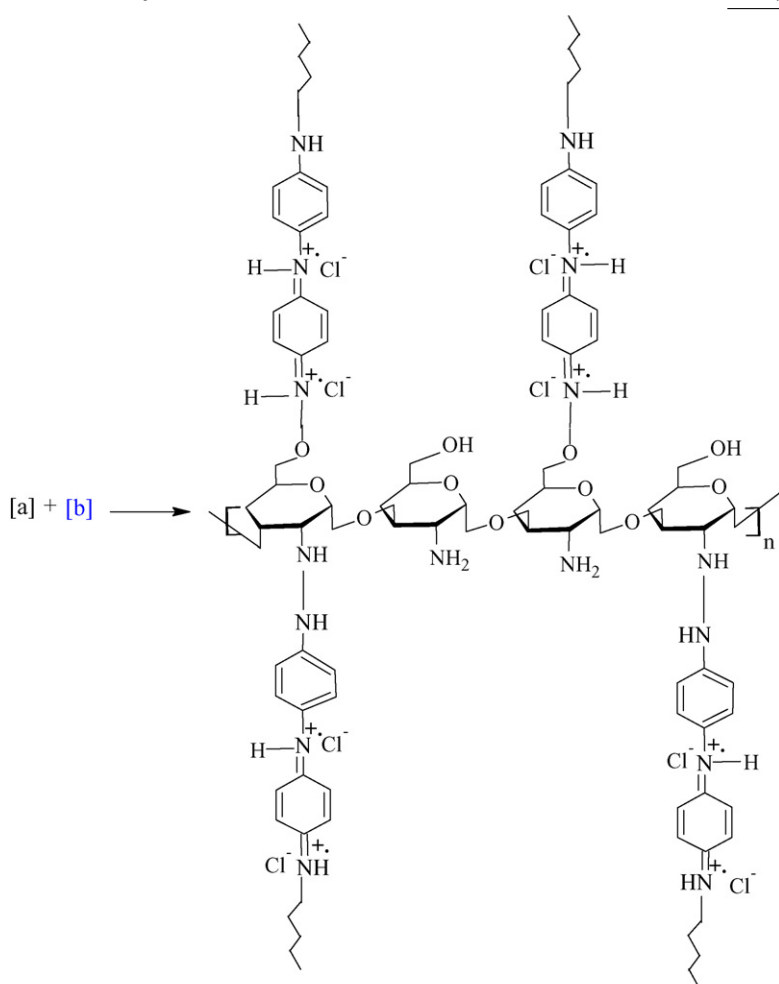
CHIT-co-PANI

The FTIR spectrum of the CHIT-*co*-PANI/ITO electrode (Fig. 2a) illustrated the characteristic peaks of PANI, as well as CHIT [21]. The following key characteristic bands were observed: (1) 3110–3532 cm^{-1} (free O—H stretching and N—H stretching with hydrogen bonded secondary amino groups); (2) 3023 cm^{-1} (aromatic C—H stretching); 2926 and 2865 cm^{-1} (aliphatic C—H stretching); (3) 1636 cm^{-1} (C=O stretching of carbonyl group, typical saccharide absorption); (4) 1588 cm^{-1} (C=C stretching of quinoid rings); (5) 1489 cm^{-1} (C=C stretching vibration of benzenoid rings); and (6) 1248 cm^{-1} (C—N stretching).

The absorption band of the N=Q=N bending vibration of protonated pure PANI was observed at 1238 cm^{-1}, but shifted to 1121 cm^{-1} in the CHIT-*co*-PANI copolymer due to the steric effect of CHIT [21]. The FTIR spectrum of the cDNA/CHIT-*co*-PANI/ITO electrode (Fig. 2b) showed phosphate vibration at 1226 cm^{-1} (accredited from phosphate backbone of immobilized cDNA) with the peaks broadening at (1) 3105–3364 cm^{-1} (addition of N—H stretching vibration); (2) 2922–2863 cm^{-1}; and (3) 1632–1668 cm^{-1} due to the attachment of cDNA with the CHIT-*co*-PANI matrix. Hence, FTIR spectra confirmed the immobilization of cDNA onto the CHIT-*co*-PANI/ITO electrode.

The surface morphology of the electrodes was observed with AFM and is shown in Fig. 3. Both electrodes exhibited a relatively rough surface topology, which may facilitate the immobilization of cDNA in the case of the CHIT-*co*-PANI/ITO electrode and the

Fig. 4 shows the electrochemical characteristics of bare, cDNA immobilized, and DNA hybridized CHIT-*co*-PANI/ITO electrodes. The CHIT-*co*-PANI/ITO electrodes illustrated admirable electrochemical performance. It was observed that the CHIT-*co*-
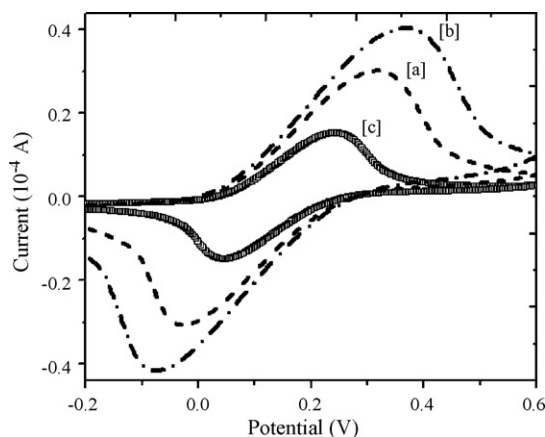
Fig. 4. Cyclic voltammograms of the (a) CHIT-*co*-PANI/ITO; (b); cDNA/CHIT-*co*-PANI/ITO and (c) DNA hybridized CHIT-*co*-PANI/ITO electrodes in PBS (50 mM, pH 7.0, and 5 mM Fe(CN)$_6^{3-/4-}$) at 30 mV s^{-1} scan rate.
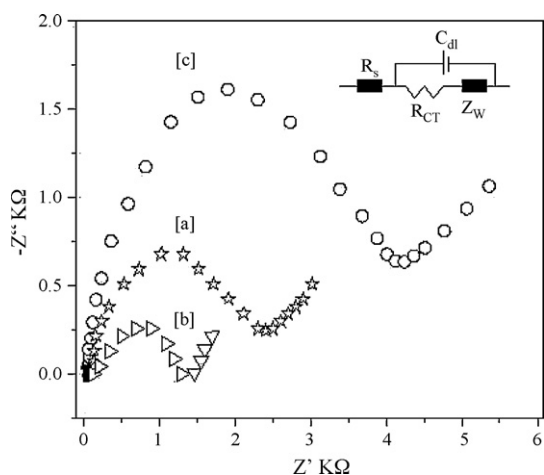
Fig. 5. EIS of the (a) CHIT-*co*-PANI/ITO; (b) cDNA/CHIT-*co*-PANI/ITO; and (c) DNA hybridized CHIT-*co*-PANI/ITO electrodes in PBS (50 mM, pH 7.0, and 5 mM $Fe(CN)_6^{3-/4-}$).

Fig. 6. Steady-state current dependence calibration curve of the biosensor (cDNA/CHIT-*co*-PANI/ITO) to logarithm of molar concentration of the single-stranded target DNA. Working conditions: supporting electrolyte: PBS 50 mM, pH 7.0, and 5 mM $Fe(CN)_6^{3-/4-}$ at potential 0.32 V vs. Ag/AgCl.

PANI/ITO electrodes could enhance the electrochemical response of $Fe(CN)_6^{3-/4-}$, which could be attributed to PANI's excellent electronic conductivity and CHIT's strong ability to interact with the negatively charged $Fe(CN)_6^{3-/4-}$ ions (due to the presence of –NH_2 groups in CHIT) [31]. Among the three types of electrodes investigated, the peak current of the cDNA/CHIT-*co*-PANI/ITO electrode was the highest while that of the DNA hybridized CHIT-*co*-PANI/ITO electrode was the lowest. The increase in the peak current observed with the cDNA/CHIT-*co*-PANI/ITO electrode was attributed to the prompt redox behavior of cDNA [32]. The decrease in the peak current measured with the DNA hybridized CHIT-*co*-PANI/ITO electrode may be related to the electrostatic repulsion between the polyanionic hybridized DNA on the CHIT-*co*-PANI/ITO electrode and the anionic redox couple ions [33].

Electrochemical impedance spectroscopy (EIS) is an excellent technique to study the interfacial properties of surface modified electrodes [34,35]. In EIS, the total impedance is measured by various parameters, including solution resistance (R_s), double layer capacitance (C_{dl}), charge transfer resistance (R_{CT}) and Warburg coefficient (Z_w). The R_s and Z_w are usually not affected by the biochemical reactions that occur at the electrode interface; however, both C_{dl} and R_{CT} vary with the interfacial electron-transfer resistances at the electrode–solution interfaces [36]. Fig. 5 shows EIS as Nyquist plot ($-Z'$ vs. Z') of the CHIT-*co*-PANI, cDNA/CHIT-*co*-PANI, and ssDNA hybridized CHIT-*co*-PANI electrodes using 5 mM $[Fe(CN)_6]^{4-/3-}$ as marker ions at EIS frequency from 0.1 Hz to 10 kHz. The Nyquist plot consisted of two steps: first a semicircle and then a straight line. The semicircle diameter of the EIS spectra provides the R_{CT} value that reveals the electron-transfer kinetics of the redox probe at the electrode interface, while the straight line is a typical characteristic of a diffusion limit step. The R_{CT} values for the CHIT-*co*-PANI, cDNA/CHIT-*co*-PANI, and ssDNA hybridized cDNA/CHIT-*co*-PANI electrodes were 2.41 kΩ (curve a), 1.37 kΩ (curve b), and 4.16 kΩ (curve c), respectively. The relatively low R_{CT} value observed with the CHIT-*co*-PANI electrode indicates that the CHIT-*co*-PANI copolymer matrix could have an excellent ability to carry the charge over the electrode surface. In addition, the lower R_{CT} value observed with the cDNA/CHIT-*co*-PANI electrode indicates that immobilizing cDNA on the CHIT-*co*-PANI electrode enhanced the electron transfer between the electrode and solution.

Fig. 6 shows the calibration curve of the peak current measured with CV using the cDNA/CHIT-*co*-PANI/ITO electrode at varying molar concentrations of the ssDNA ranging from 0.05 to 25 fmol.
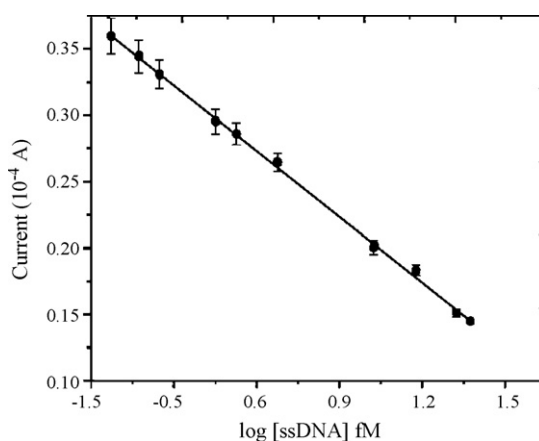
It was found that the peak oxidation current observed at about 0.32 V decreased with an increasing concentration of the target ssDNA until 25 fmol, beyond which the peak oxidation current remained as a constant. In fact, as shown in Fig. 6, the peak oxidation current decreased linearly with an increasing logarithm of ssDNA molar concentration within the range of 0.05–25 fmol. This result indicates that binding of cDNA with the ssDNA at the cDNA/CHIT-*co*-PANI/ITO electrode surface had occurred. Moreover, it shows that 25 fmol of ssDNA is sufficient to saturate the cDNA immobilized CHIT-*co*-PANI/ITO electrode surface, and 0.05 fmol was detection limit of the biosensor. The sensitivity of the cDNA/CHIT-*co*-PANI/ITO bioelectrode measured was 2.104 μA/fmol and it responded in 16 s. In addition, the surface concentration of the ionic species on the cDNA/CHIT-*co*-PANI/ITO was 6.072 mmol/cm^2, calculated by measuring the oxidation current of CV at different scan rates.

The selectivity of the biosensor was investigated by the hybridization of the cDNA immobilized CHIT-*co*-PANI/ITO bioelectrode with one-base-mismatch ssDNA sequences. After incubation with the mismatched ssDNA sequence, the bioelectrode showed a negligible decrease in the peak oxidation current at 0.32 V, indicating that the biosensor had good selectivity only for the ssDNA.

The reproducibility of the biosensor was measured with a 15 fmol ssDNA sequence. The response currents with seven cDNA/CHIT-*co*-PANI/ITO electrodes fabricated under similar conditions were 2.78, 2.80, 2.78, 2.76, 2.80, 2.81 and 2.78 ($\times 10^{-4}$ A). The seven cDNA/CHIT-*co*-PANI/ITO electrodes had an average current response of 2.79×10^{-4} A with a standard deviation of ±0.02. Thus, the biosensor showed excellent reproducibility.

The shelf life of the cDNA/CHIT-*co*-PANI/ITO bioelectrode was determined by measuring the current at an interval of seven days for up to six months. The amperometric current decreased slowly with an increase in time. The decrease in current measured about 5% after the cDNA/CHIT-*co*-PANI/ITO electrode was stored at room temperature for six months.

4. Conclusions

The cDNA of the breast cancer susceptible gene (BRCA1) was immobilized onto the CHIT-*co*-PANI/ITO electrode. The cDNA/CHIT-*co*-PANI/ITO bioelectrode was employed for the hybridization of the ssDNA, which had a detection limit of 0.05 fmol and showed an excellent sensitivity and reproducibility. The voltammetric sensitivity of the biosensor was 2.104 μA/fmol. In the presence of one-base-mismatched DNA, the amperometric response of the

cDNA/CHIT-*co*-PANI/ITO bioelectrode for the ssDNA was barely affected. Current efforts aim to exploit the cDNA/CHIT-*co*-PANI/ITO electrode for the efficient and precise detection of breast carcinoma at its early stage.

References

[1] C. Bouchardy, G. Fioretta, H.M. Verkooijen, G. Vlastos, P. Schaefer, J.F. Delaloye, I.N. Caspar, S.B. Majno, Y. Wespi, M. Forni, P. Chappuis, A.P. Sappino, E. Rapiti, Br. J. Cancer 96 (2007) 1743.
[2] A.H. Sims, A. Howell, S.J. Howell, R.B. Clarke, Nat. Clin. Pract. Oncol. 4 (2007) 516.
[3] J.D. Fackenthal, O.I. Olopade, Nat. Rev. Cancer 7 (2007) 937.
[4] J. Watson, M. Gilman, J. Witkowski, M. Zoller, Recombinant DNA, vol. 2, W.H. Freeman & Co., New York, 1992, pp. 127–30.
[5] S.D.H. Chan, K. Dill, J. Blomdahl, H.G. Wada, Anal. Biochem. 242 (1996) 214.
[6] F. Cottrez, C. Auriault, A. Capron, H. Groux, Nucleic Acids Res. 22 (1994) 2712.
[7] G. Totze, A. Sachinidis, H. Vettre, Y. Ko, Mol. Cell Probes 10 (1996) 427.
[8] R. Baugh, A.A. Hill, E.L. Brown, C.P. Brown, Nucleic Acids Res. 29 (2001) E29.
[9] J.C. Liao, M. Mastali, Y. Li, V. Gau, M.A. Suchard, J. Babbitt, J. Gornbein, E.M. Landaw, E.R.B. McCabe, B.M. Churchill, D.A. Haake, J. Mol. Diagn. 9 (2007) 158.
[10] J.C. Liao, M. Mastali, V. Gau, M.A. Suchard, A.K. Møller, D.A. Bruckner, J.T. Babbitt, Y. Li, J. Gornbein, E.M. Landaw, E.R.B. McCabe, B.M. Churchill, D.A. Haake, J. Clin. Microbiol. 44 (2006) 561.
[11] A.M. Tencaliec, S. Laschi, V. Magearu, M. Mascini, Talanta 69 (2006) 365.
[12] W.D. Tilley, M. Marcelli, J.D. Wilson, M.J. McPhaul, Proc. Natl. Acad. Sci. 86 (1989) 327.
[13] M. Yang, Y. Yang, H. Yang, G. Shen, R. Yu, Biomaterials 27 (2006) 246.
[14] S.J. Updike, G.P. Hicks, Nature 214 (1967) 986.
[15] X.L. Luo, J.J. Xu, J.L. Wang, H.Y. Chen, Chem. Commun. (2005) 2169.
[16] M. Zhang, X.H. Li, Y.D. Gong, N.M. Zhao, X.F. Zhang, Biomaterials 23 (2002) 2641.
[17] K.J. Feng, Y.H. Yang, Z.J. Wang, J.H. Jiang, G.L. Shen, R.Q. Yu, Talanta 70 (2006) 561.
[18] A. Abbaspour, M.A. Mehrgardi, Anal. Chem. 76 (2004) 5690.
[19] M.H. Tonya, M.J. Tarlov, J. Am. Chem. Soc. 119 (1997) 8916.
[20] C. Tlili, H. Korri-Youssoufi, L. Ponsonnet, C. Martelet, N.J. Jaffrezic-Renault, Talanta 68 (2005) 131.
[21] A. Tiwari, V. Singh, Express Polym. Lett. 1 (2007) 308.
[22] X. Xin, R. Guang, C. Juan, L. Qiang, L. Dong, C. Qiang, J. Mat. Sci. 41 (2006) 3147.
[23] S.V. Kuzmin, P. Sáha, N.T. Sudar, V.A. Zakrevskii, I. Sapurina, S. Solosin, M. Trchova, J. Stejskal, Thin Solid Films 516 (2008) 2181.
[24] H. Tai, Y. Jiang, G. Xie, J. Yu, X. Chen, Z. Ying, Sens. Actuators B: Chem. 129 (2008) 319.
[25] A. Tiwari, V. Sen, S.R. Dhakate, A.P. Mishra, V. Singh, Polym. Adv. Technol. 19 (2008) 909.
[26] A. Tiwari, S.P. Singh, J. Appl. Polym. Sci. 108 (2008) 1169.
[27] A. Tiwari, J. Polym. Res. 15 (2008) 337.
[28] A. Tiwari, J. Mcromol. Sci. A 44 (2007) 735.
[29] B.K. Zehentner, D.C. Dillon, Y. Jiang, J. Xu, A. Bennington, D.A. Molesh, X.Q. Zhang, S.G. Reed, D.H. Persing, R.L. Houghton, Clin. Chem. 48 (2002) 1225.
[30] A. Tiwari, V. Singh, Carbohydrate Polymers 74 (2008) 427.
[31] C. Xu, H. Cai, Q. Xu, P.G. Gang, Y.Z. Fang, Fresenius J. Anal. Chem. 369 (2001) 428.
[32] C.M.H. Yaua, H.L. Chana, S.F. Suib, M. Yang, Thin Solid Films 413 (2002) 218.
[33] I.O.K. Owino, O.A. Sadik, Electroanalysis 17 (2005) 2101.
[34] X. Chen, Y. Wang, J. Zhou, W. Yan, X. Li, J.J. Hu, Anal. Chem. 80 (2008) 2133.
[35] Y.M. Yan, R.T. Vered, O. Yehezkeli, Z. Cheglakov, I. Willner, Adv. Mater. 20 (2008) 2365.
[36] E. Katz, I. Willner, Electroanalysis 15 (2003) 913.

Method development for the determination of teicoplanin in patient serum by solid phase extraction and micellar electrokinetic chromatography

I.-Lin Tsai [a], Fe-Lin Lin Wu [a,b,c], Churn-Shiouh Gau [a], Ching-Hua Kuo [a,c,*]

[a] *School of Pharmacy, College of Medicine, National Taiwan University, Taiwan*
[b] *Graduate Institute of Clinical Pharmacy, College of Medicine, National Taiwan University, Taiwan*
[c] *Department of Pharmacy, National Taiwan University Hospital, Taiwan*

ARTICLE INFO

ABSTRACT

In-hospital deaths caused by the infection of methicillin-resistant *Staphylococcus aureus* (MRSA) are on the increase worldwide. Teicoplanin is a potent glycopeptide antibiotic against MRSA. A rapid and cost-saving micellar electrokinetic chromatography (MEKC) method combined with solid phase extraction (SPE) was developed and then validated to quantify teicoplanin in patient serum in this work. The method includes the following steps: (1) pretreatment of the serum samples with 10 M urea to denature proteins, (2) application of SPE by using an OASIS HLB cartridge to clean up and concentrate the serum samples, and (3) use of MEKC for sample analysis. Under the optimized conditions, the SPE recovery of teicoplanin is higher than 90%. The six major components of teicoplanin could be baseline-separated from one another and endogenous materials in 12 min with a background electrolyte composed of 20 mM sodium tetraborate buffer pH 8.8, 40 mM sodium dodecyl sulfate, and 11% (v/v) ACN. The relative standard deviation (R.S.D.) of the peak area ratios for method repeatability ($n=6$) and intermediate precision (inter-day, $n=3$) were found to be lower than 4.18% and 5.30%, respectively. The calibration curves were linear between the chromatographic response and total teicoplanin concentration over the range of 5 μg/mL to 55 μg/mL. Limit of detection (LOD) for each of the six components was found to be lower than 0.06 μg/mL. Pearson's correlation revealed that a good correlation ($r=0.98$) was obtained between the SPE–MEKC method and the fluorescence polarization immunoassay (FPIA) method. The developed method can be used to quantitatively determine serum teicoplanin concentration in patients for dose monitoring and clinical research.

© 2008 Elsevier B.V. All rights reserved.

1. Introduction

Staphylococcus aureus is a major cause of serious hospital- and community-acquired infections. Compared to patients infected with methicillin-susceptible *S. aureus* (MSSA), those infected with methicillin-resistant *S. aureus* (MRSA) tend to have higher mortality rate, longer hospital stays, and higher hospital charges [1]. A recent research in the *JAMA* (Journal of the American Medical Association) showed that, in 2005, an estimate of 18,650 in-hospital deaths were due to invasive MRSA infections in the United States [2]. The emergence of MRSA is one of the most important aspects of nosocomial infections in the last two decades worldwide. Teicoplanin is a glycopeptide antibiotic having good activity against MRSA [3]. Based on the data sheet of the ABPI (Association of the British

Pharmaceutical Industry), it is recommended that the steady-state trough concentrations of teicoplanin should be kept above 10 mg/L in serious infections [4]. In addition, for optimal monotherapy of *S. aureus*-incited endocarditis, the maintaining of a minimal trough concentration of teicoplanin above 20 mg/L has also been suggested. When patients are undergoing treatment with teicoplanin, it is important to monitor their blood teicoplanin concentrations to ensure that safe and adequate therapeutic level be attained [4].

Teicoplanin has six major components: A3-1, A2-1, A2-2, A2-3, A2-4, and A2-5. These components are closely related but their antimicrobial activities against microbial species are different [5]. The chemical structures of the six major components are shown in Fig. 1. Determination of teicoplanin in biological matrix has been performed by microbiological assay, high performance liquid chromatography (HPLC) [6–12], and fluorescence polarization immunoassay (FPIA) methods [13–15]. The FPIA method is the analytical method most commonly used to determine teicoplanin in serum samples. However, this method is costly and unable to determine the level of individual teicoplanin components. Bourget et al.

* Corresponding author at: School of Pharmacy, College of Medicine, National Taiwan University, No. 1, Section 1, Jen-Ai Road, Taipei 100, Taiwan.
Tel.: +886 2 23123456; fax: +886 2 23919098.
E-mail address: kuoch@ntu.edu.tw (C.-H. Kuo).

(1) A 3-1   **R=H**

GROUP A2   **R=**

(2) A 2-1	**R'=**	-(CH$_2$)$_2$-CH=CH-C$_5$H$_{11}$
(3) A 2-2	**R'=**	-(CH$_2$)$_6$-CH(CH$_3$)$_2$
(4) A 2-3	**R'=**	-C$_9$H$_{19}$
(5) A 2-4	**R'=**	-(CH$_2$)$_6$-CH(CH$_3$)(C$_2$H$_5$)
(6) A 2-5	**R'=**	-(CH$_2$)$_7$-CH(CH$_3$)$_2$

Teicoplanin
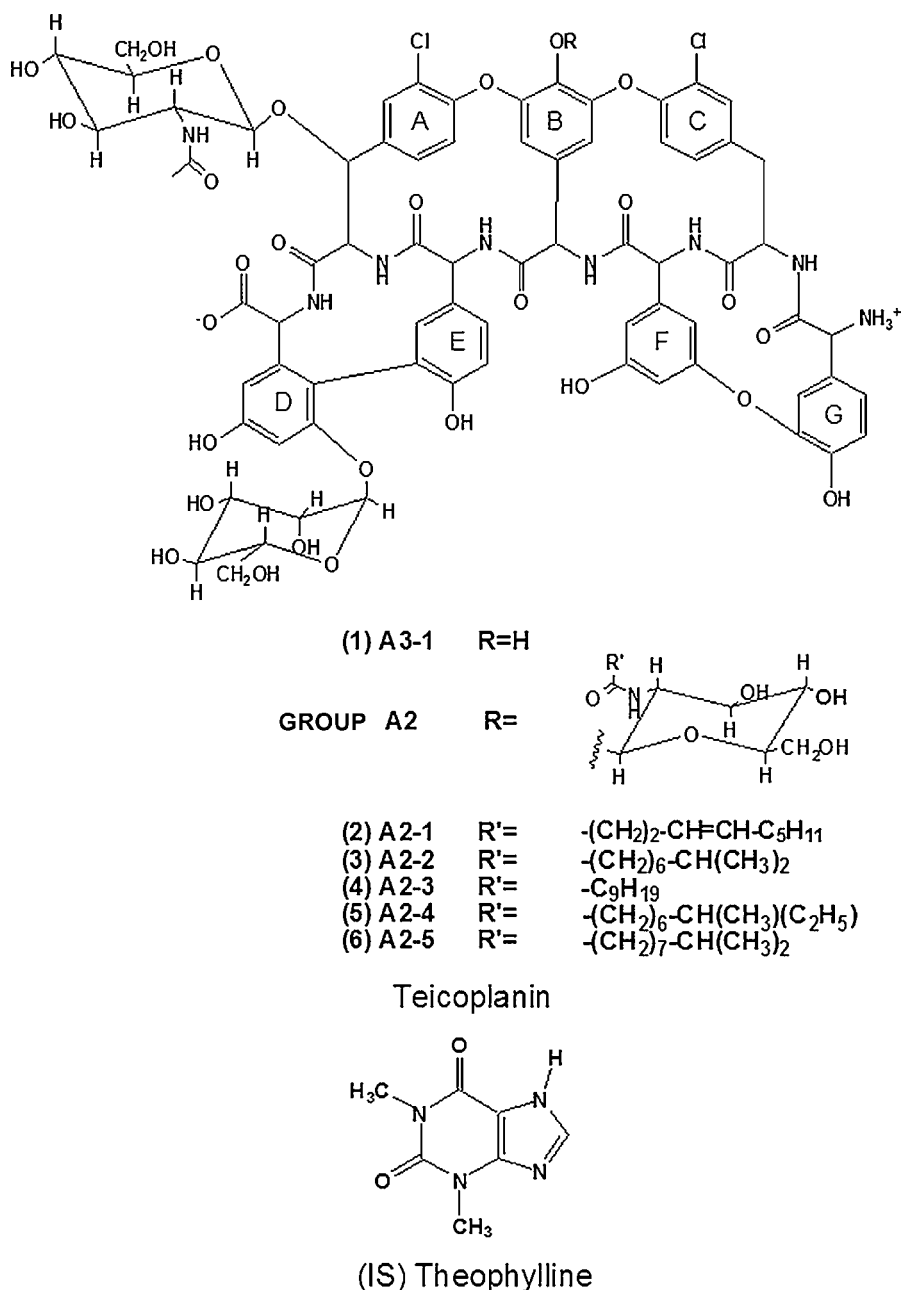
(IS) Theophylline

Fig. 1. Chemical Structures of the six major components of teicoplanin and the internal standard, theophylline.

compared the teicoplanin quantitation results obtained from FPIA and HPLC analysis and found that the FPIA method was not accurate for the analysis of teicoplanin concentrations lower than 12 μg/mL [17]. They concluded that the HPLC method should be preferable than FPIA in the assay of teicoplanin in pharmacokinetic studies and pharmacological research. Although more accurate, the HPLC method is more time-consuming. It requires about an hour to complete a single analysis. Mochizuki et al. recently developed an HPLC method with electrochemical detection to analyze teicoplanin in cerebrospinal fluid. The method has great sensitivity, but the analytical time is still long (>60 min) [11].

Due to its high resolution, short analysis time and low reagent and sample consumption, the capillary electrophoresis (CE) method has become a powerful tool in pharmaceutical analysis. One study which used the CE method to analyze teicoplanin was reported [16]. However, the selectivity of the method to patient serum components was not demonstrated and the applicability to clinical analysis was unknown.

The high salt and protein concentrations in serum often result in band broadening and poor repeatability in CE analyses. Co-extractive cleanup of serum sample has been developed to eliminate potential interfering substances in teicoplanin analysis [7]. However, there are disadvantages of the method such as that emulsion may form during extraction and it is difficult to carry out the procedure in batches. Several studies using solid phase extraction (SPE) method to remove endogenous components in serum were reported. However, the recovery rate was either unsatisfactory [6] or not studied [17].

The primary goal of our research was to develop a sensitive and efficient electrophoretic method to facilitate clinical research works

of teicoplanin. To achieve this goal, a SPE method was developed for sample concentration and MEKC conditions were optimized for fast separation. The developed SPE–MEKC method was validated and then applied to the analysis of serum teicoplanin in patients who received teicoplanin treatment. The results are compared to those obtained using the FPIA method. To the best of our knowledge, this is the first time that a SPE–MEKC method was developed to quantitatively determine the six teicoplanin components in patient serum.

2. Experimental

2.1. Chemicals

Teicoplanin standard was purchased from Dongkook Pharm. (Seoul, Korea). The teicoplanin components were identified according to HPLC/MS/MS method reported by Ackermann and Brian [18]. Sodium dodecyl sulfate (SDS) was purchased from Sigma–Aldrich (St. Louis, MO, USA). Hydrochloric acid, sodium hydroxide, and sodium tetraborate were purchased from Merck (Darmstadt, Germany). Cetyltrimethylammonium bromide (CTAB) was purchased from Acros (Geel, Belgium). Acetonitrile (ACN) and Methanol (MeOH) were purchased from Mallinckrodt (Paris, KY, USA). All reagents and solvents used were of analytical or chromatographic grade. Serum samples obtained from patients on teicoplanin treatment (200–400 mg/day) were provided by National Taiwan University Hospital. The study was approved by the ethical committee. The signed inform consents were received for all patients participated in the study. The serum samples were stored and frozen at −80 °C before use. Fluorescence polarization immunoassay kit was purchased from Seradyn Inc. (Indianapolis, IN, USA). Oasis HLB SPE cartridges were purchased from Waters (Milford, MA, USA). The SPE procedure was performed on a Waters extraction manifold system.

2.2. Instrumentation

The MEKC experiments with UV detection were carried out in a system consisting of a Prince programmable injector (Lauer Labs, Emmen, The Netherlands) and a 30 kV high-voltage supply connected to a UV absorbance detector (Dynamax, Rainin, Emeryville, CA, USA). A fused-silica capillary (Polymicro Technologies, Phoenix, AZ, USA) was used for the separation. The electropherograms were recorded using an EZChrom (Scientific Software, San Ramon, CA, USA) chromatographic data system.

2.3. Separation conditions

MEKC separations were performed on a 75 cm (60 cm effective length) × 50 μm I.D. fused-silica capillary. The background electrolyte solution was prepared by adding 40 mM SDS to a 20 mM sodium tetraborate buffer solution. The pH of the buffer solution was adjusted to 8.8 with 1.0 M HCl. ACN was then added to make up the electrophoresis running solution (containing 11% v/v of ACN). The applied voltage was 30 kV. Sample solutions were injected into the capillary with hydrodynamic mode of 50 mbar for 9 s. Detection wavelength was 240 nm and capillaries were thermostatted at 25 °C with air controlling system. New fused-silica capillaries were conditioned by flushing, in sequence, with 1.0 M NaOH for 10 min, 0.2 M NaOH for 10 min, water for 10 min and running solution for 10 min. At the beginning of each experiment, the capillary was washed with 0.2 M NaOH for 3 min, followed by water for 2 min and then running solution for 5 min.

All solutions were filtered through a 0.45 μm filter (Millipore, Bedford, MA, USA) before use.

2.4. Preparation of standard solution

Teicoplanin stock solution with concentration of 1 mg/mL was prepared in water. Blood samples were collected from healthy volunteers and were centrifuged at 3000 rcf for 15 min to obtain blank serum samples. Teicoplanin stock solution was spiked into the blank serum to obtain 25 μg/mL teicoplanin. Theophylline, at concentration of 100 μg/mL in the standard solution, was used as an internal standard.

2.5. Sample preparation

Oasis HLB cartridges (1 mL; 30 mg) were used for sample extractions. Cartridges were conditioned with 1 mL MeOH and 1 mL water prior to use. Six-tenth milliliter (0.6 mL) of 10 M urea was added to 0.6 mL serum sample and vortex-mixed. One milliliter (1 mL) of the resulting solution was transferred to the pre-conditioned SPE cartridge. The cartridge was then washed with 1 mL of water and 15% MeOH. Teicoplanin was then eluted with 2 mL of 53% MeOH. The extraction cartridge was placed on the vacuum manifold and the vacuum pressure was adjusted to 3 mm Hg to control the flow rate during the loading and eluting steps. The vacuum pressure was kept at 10 mmHg in conditioning and washing steps.

The eluent was collected, evaporated to dryness in a rotary evaporator, and then reconstituted in 50 μL of water containing 100 μg/mL theophylline. The reconstituted solution was subjected to MECK for analysis.

2.6. Preparation of calibration curves

Aliquots of the teicoplanin stock solution were added to blank human serum to obtain 5, 15, 25, 35, 45 and 55 μg/mL teicoplanin spiked solutions. The spiked serum samples were subjected to sample preparation procedures as described in Section 2.5. Linear regression lines were obtained by plotting peak area ratios against teicoplanin concentrations.

3. Results and discussion

3.1. Sample preparation method development

Teicoplanin is 90% bound to protein in serum. In our study, the protein denaturation step was performed to increase the recovery rate of teicoplanin. To achieve a higher recovery rate, we evaluated several protein denaturation methods. Typical additives to denature serum protein are acetonitrile, methanol, perchloric acid, sodium hydroxide, zinc sulfate and urea. Since teicoplanin is unstable in extreme pH conditions and it is insoluble in dilute mineral acids, only acetonitrile, methanol and urea were used to evaluate their efficiency in protein denaturation. Hanada et al. studied protein denaturation using acetonitrile. In their study, the plasma samples were diluted with water before adding acetonitrile [9]. The recovery of teicoplanin was improved for more than 20% with the serum dilution step. The Hanada procedure was evaluated in our study. Unfortunately, the serum dilution step was found to be insignificant in improving teicoplanin recovery rate. Therefore, direct addition of acetonitrile to serum samples was applied to evaluate the efficacy for acetonitrile denaturation. The recovery of teicoplanin obtained by acetonitrile, methanol and, urea denaturation methods were $90.92 \pm 1.44\%$, $23.61 \pm 0.64\%$, and $90.93 \pm 0.24\%$, respectively. The recovery studies were tested at total teicoplanin concentration of 25 μg/mL. The values of recovery were calculated by comparing the relative peak area of teicoplanin components in the protein denaturation sample to that of sample without protein denaturation treatment. The results demonstrate that similar

recoveries were obtained from the acetonitrile and urea denaturation methods. Urea treated samples showed the lowest elution strength, and could be directly loaded into SPE cartridge without any dilution steps. It was therefore chosen as the protein denaturant agent in this study.

The SPE extraction method was applied to concentrate teicoplanin components and to eliminate endogenous materials in serum. It was found that increasing the washing solvent strength to greater than 15% methanol resulted in reduction of the recovery of A3-1. Fifteen percent (15%) methanol was therefore used as the washing solution. When 100% methanol was used as the elution solvent, capillary electrophoretic separation of teicoplanin components A2-2–A2-5 were significantly interfered by endogenous substances. To overcome the interference problem, solvent strength of the eluent was adjusted to improve the selectivity between teicoplanin components and endogenous substances. It was found that decreasing the solvent strength of the eluent could reduce the interference significantly. Fifty-three percent (53%) methanol was then selected as the optimum elution solution. It was also found that further decreasing in the elution strength reduced the recovery of teicoplanin. This was due to teicoplanin components A2-4 and A2-5 which were not eluted with low elution strength. As a result of the above findings, the optimum extraction procedure for spiked human serum samples using Oasis HLB as extraction cartridges was set up as firstly by using methanol and deionized water as conditioning solvent, followed by using water and 15% methanol for washing, and finally by using 53% methanol as the elution solvent. The recovery of teicoplanin from the spiked sample was higher than 90% with the optimum extraction conditions.

Taylor and Reid used C_8 cartridges [6] and Bourget et al. used C_{18} cartridges [17] to extract teicoplanin from patient serum. Their extraction procedures were evaluated in this study. It was found that our sample pre-treatment procedures provided higher extraction yield and less interference. The structure of teicoplanin contains both hydrophilic and lipophilic moieties (Fig. 1). The higher extraction yield could be attributed to the hydrophilic–lipophilic balance property of Oasis HLB extraction cartridges.

3.2. Analytical method development

Teicoplanin-spiked serum samples were used as standard solutions in the optimization of the electrophoretic separation method. Teicoplanin consists of six major components, each being represented as A3-1 and A2-1–A2-5. A3-1 is the hydrolyzed product with higher polarity. Components A2-1–A2-5 are similar in their polarity as they only differ in acyl chain of *N*-acylglucosamine which is attached to B-4 phenol. As depicted in Fig. 1, A2-2 and A2-3 have the same molecular weight, so do as A2-4 and A2-5. Due to the high similarity of mass to charge ratio of the individual teicoplanin components, capillary zone electrophoresis of teicoplanin always led to co-migration of these analytes. The MEKC mode which could separate molecules according to their lipophilicities was therefore used to resolve the co-migration issue. MEKC conditions developed by Taylor et al. was tested first [16]. The running buffer was composed of tris–HCl buffer at pH 7.2, 100 mM SDS, and 40% ACN. Under such conditions, poor peak shapes accompanied with disturbed baselines were observed. Besides, the peaks of teicoplanin components were seriously overlapped with endogenous matters in serum, which hampered these conditions to be directly used in clinical analysis. A new analytical conditions had to be sought to meet clinical requirement. Three micellar systems including, sodium dodecyl sulfate, sodium cholate and cetyltrimethylammonium bromide were tested in this study. It was found that the resolution of teicoplanin components was poor when using sodium

cholate and CTAB as adding surfactant. The investigated concentration range was 10–50 mM for sodium cholate and 5–30 mM for CTAB. The literature survey revealed that, the HPLC methods using octadecylsilane (C_{18}) as stationary phase showed good selectivity for teicoplanin components in their analysis (although these HPLC methods were time consuming) [6–11]. SDS micellar systems are reported to be similar to the C_{18} phase in HPLC for separations of moderately water-soluble compounds [19]. As manifested by later experiments, SDS micellar systems provided the best resolving power for teicoplanin components in this study. Various parameters, including ACN%, buffer pH, buffer concentration and SDS concentration were subsequently investigated for optimization in terms of selectivity, speed, and peak efficiency.

3.2.1. ACN%

Organic modifier alters the retention mechanism by changing the polarity of the aqueous phase and shifting the partition coefficient of the analytes. This leads to the change of separation selectivities. Teicoplanin components A2-1–A2-3 were significantly overlapping with the endogenous materials when acetonitrile was not added to the background electrolyte (Fig. 2A). Although the migration time of teicoplanin components increased due to the change of zeta potential of the capillary wall, adding 10% of ACN dramatically improved the peak shapes and separation result (Fig. 2B). Further increase the concentration of acetonitrile from 10% to 13% (Fig. 2B–E) decrease the migration time of A2-1–A2-5. This was due to the addition of acetonitrile which reduced the affinity of these components to SDS. The migration time of endogenous substances and A3-1 remained unchanged with the addition of acetonitrile. The different effects of acetonitrile on the migration time led to a better separation of teicoplanin from endogenous substances. As a result by taking peak shape, selectivities and analytical time into consideration, the best separation result was obtained when 11% ACN was added to the background electrolyte (Fig. 2C).

3.2.2. Effect of pH

Teicoplanin molecules carry several ionizable functional groups. The pKa value for the carboxyl group is 5.0; that for the amino group is 7.1, and those for the phenolic groups are between 9 and 12.5 [5]. Experiments showed that the selectivity of separation was significantly affected by the change of buffer pH value at a range of 8.4–9.2. This could be due to the dissociation of phenolic groups and to a minor extent to the amino groups. As shown in Fig. 3, the peaks of A2-2 and A2-3 were overlapped at pH 8.4. At a higher pH, the phenolic groups of these components started to ionize and this incurred the changes of their lipophilicities. The resolution between A2-2 and A2-3 was greatly improved at pH 8.6. In addition, owing to the electrorepulsion effect, the retention of teicoplanin A2-1–A2-5 in SDS micelles was reduced by the ionization of the phenolic groups and this resulted in total shorter analysis time. As depicted in Fig. 3, the decrease in migration time was larger for teicoplanin components than that for endogenous materials. In contrast with teicoplanin A2-1–A2-5, the migration time of A3-1 was increased with increasing of pH. This could be attributed to the lowest affinity of the component A3-1 to SDS micelles. Because of the interaction between the components and SDS micelles, the electrorepulsion was rendered greater by increasing ionization of the components, and the migration time became shorter. Increasing ionization could also increase the mobility of A3-1 to the opposite direction, which led to the increase of migration time. Since component A3-1 has low affinity to SDS, the influence of ionization on decreasing of migration time was the least. The influence of ionization on mobility became dominant and this resulted in the increase of migration time. When pH was higher than 9.0, A2-1 was
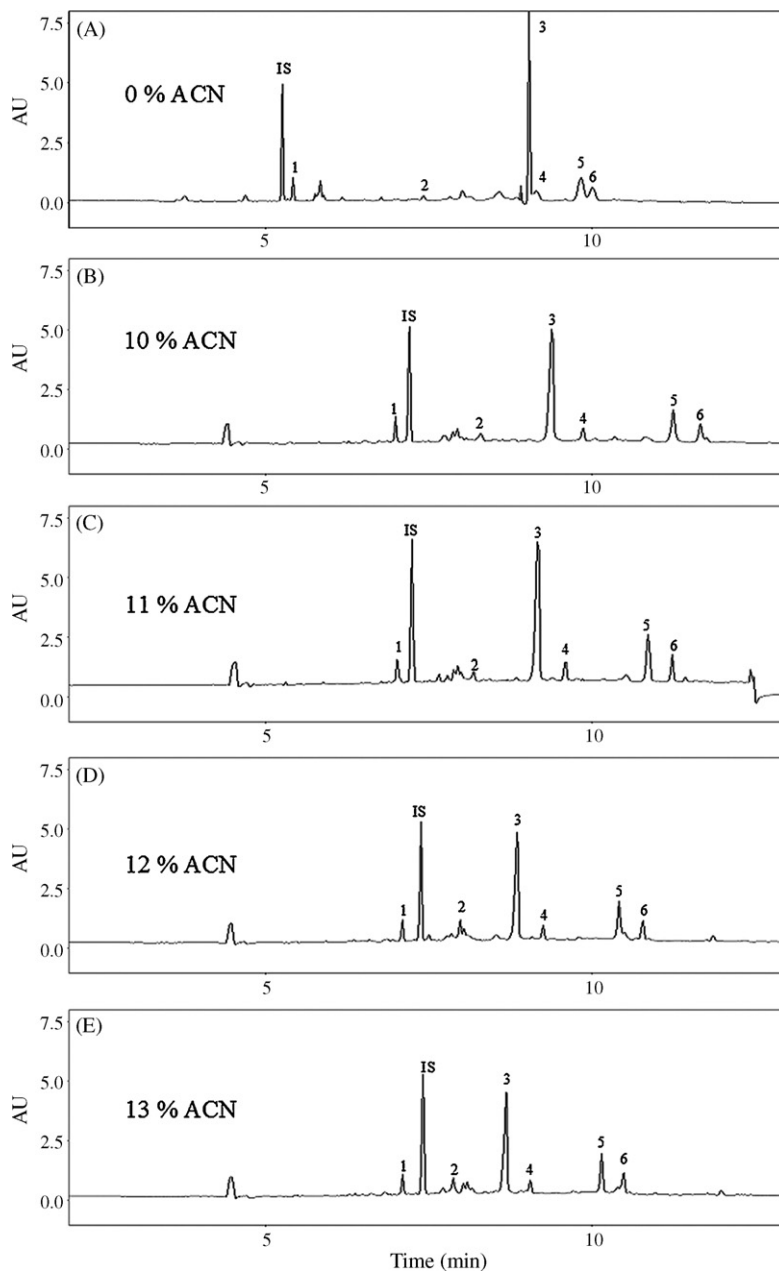
Fig. 2. Influence of ACN on separation of teicoplanin components. Separation conditions: fused-silica capillary: 75 cm × 50 μm I.D., 60 cm effective length; background electrolyte: 20 mM sodium tetraborate, pH 8.8, 40 mM SDS; applied voltage: 30 kV; temperature: 25 °C; injection: 50 mbar for 9 s. The ACN percentages are as indicated in the figure. The numbering of peaks corresponds to those in Fig. 1. Teicoplanin concentration was 25 μg/mL.

found to be significantly overlapped with the endogenous materials. At pH 8.8, teicoplanin components were well separated from endogenous materials. Because of the shorter analysis time and better selectivity, pH 8.8 was selected as the optimum separation pH value.

3.2.3. Effect of buffer concentration

Teicoplanin components are hydrophobic compounds and they tend to be adsorbed onto the capillary, especially in solutions at low pH and low ionic strength. To minimize Joule heats generated and analyte adsorption, sodium tetraborate of concentrations between 15 mM and 35 mM at pH 8.8 were tested to investigate the effect of buffer concentration on peak efficiencies. Poor peak shapes occurred at the buffer concentration higher than 30 mM, and it was

proposed to be caused by Joule heating. When buffer concentration was at 25 mM, A2-1 co-migrated with endogenous materials. Therefore, 20 mM sodium tetraborate was chosen in terms of best peak efficiencies and shortest analytical time.

3.2.4. Effect of SDS concentration

Teicoplanin components A2-1–A2-5 have long aliphatic chains (C9 and C10) (Fig. 1). They showed higher affinity to SDS micelles than component A3-1. The partition coefficients (micelles/water) of them increased with the increased concentration of SDS. These increases in partition coefficient gave longer retention time. In contrast to teicoplanin components, retention times of endogenous materials in serum changed only slightly with the increase of SDS concentration as indicated in Fig. 4. Component A2-1
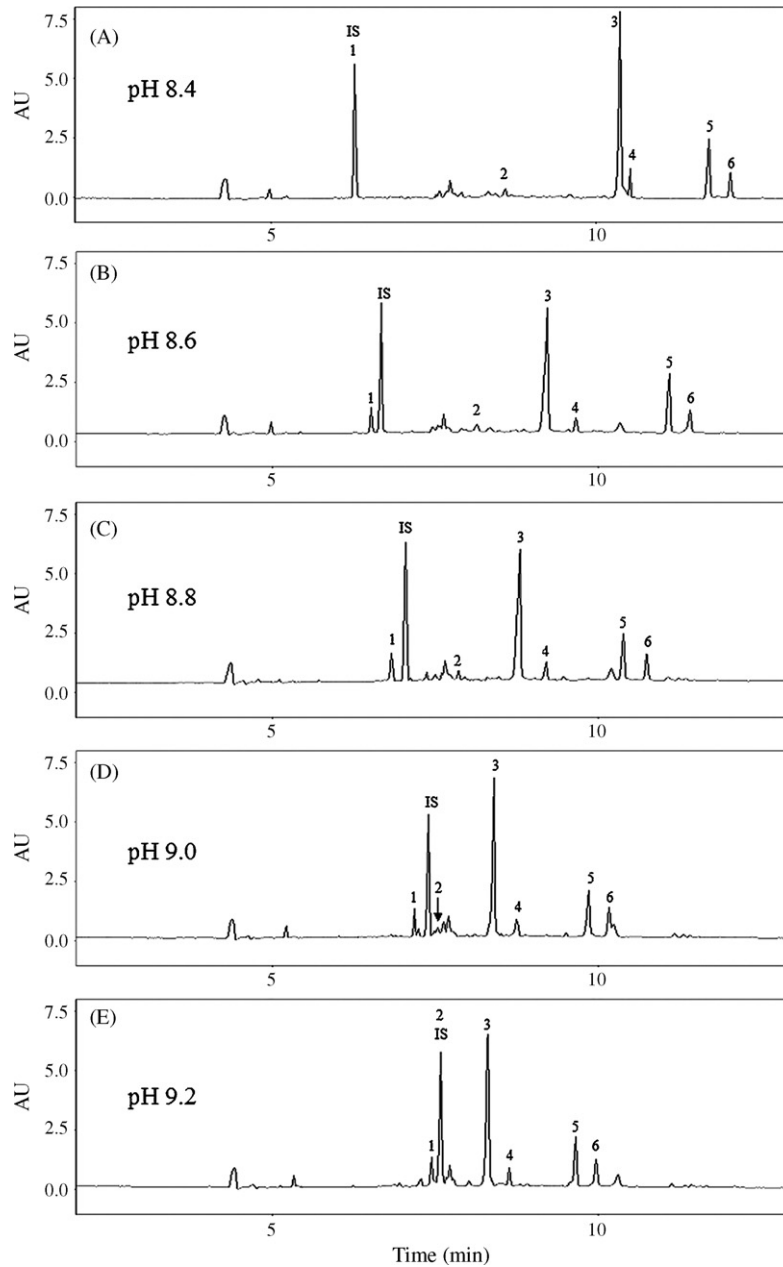
Fig. 3. Influence of pH on separation of teicoplanin components. Separation conditions: 20 mM sodium tetraborate, 40 mM SDS, 11% v/v ACN. The pH values are as indicated in the figure. Other conditions are the same as those described in Fig. 2. The numbering of peaks corresponds to those in Fig. 1. Teicoplanin concentration was 25 μg/mL.

significantly overlapped with endogenous materials at SDS concentrations lower than 35 mM. At 40 mM SDS, each of the teicoplanin components was completely separated from the endogenous materials. Further increase in SDS concentration resulted in longer analytical time without selectivity improvement. 40 mM SDS was found to give best selectivity within the shortest time and therefore was chosen as optimum concentration.

The highest applicable voltage (30 kV) of the CE apparatus was used to reduce the analysis time, and the injection time was selected to give the best sensitivity without peak broadening. The optimum background electrolyte was composed of 20 mM pH 8.8 sodium tetraborate buffer, 40 mM SDS, and 11% ACN. The applied voltage was set at 30 kV and the injection was 50 mbar for 9 s. The electropherogram obtained under the optimum separation conditions is shown in Fig. 4C. Six teicoplanin components were well separated from the endogenous materials within 12 min.

3.3. Analytical method validation

Clinically, the total serum teicoplanin concentration is in the range of 5–55 μg/mL [6]. The quality of the developed SPE–MEKC method was therefore investigated within this range. All validation studies were preformed by spiking suitable amount of teicoplanin in the blank serum. To ensure high precision of the developed method, internal standard was added to the standard solution. Vancomycin was first investigated because of its structure similarity to teicoplanin. However, the peak shape and migration time of vancomycin were unsatisfactory. Further investigation was conducted from which theophylline was selected as the internal standard due to its favorable migration time and peak shape. Relative standard deviation (R.S.D.) of the repeatability ($n = 6$) and intermediate precision (inter-day, $n = 3$) of the retention times of six teicoplanin components were found to be lower than of 0.79% and 1.13%,
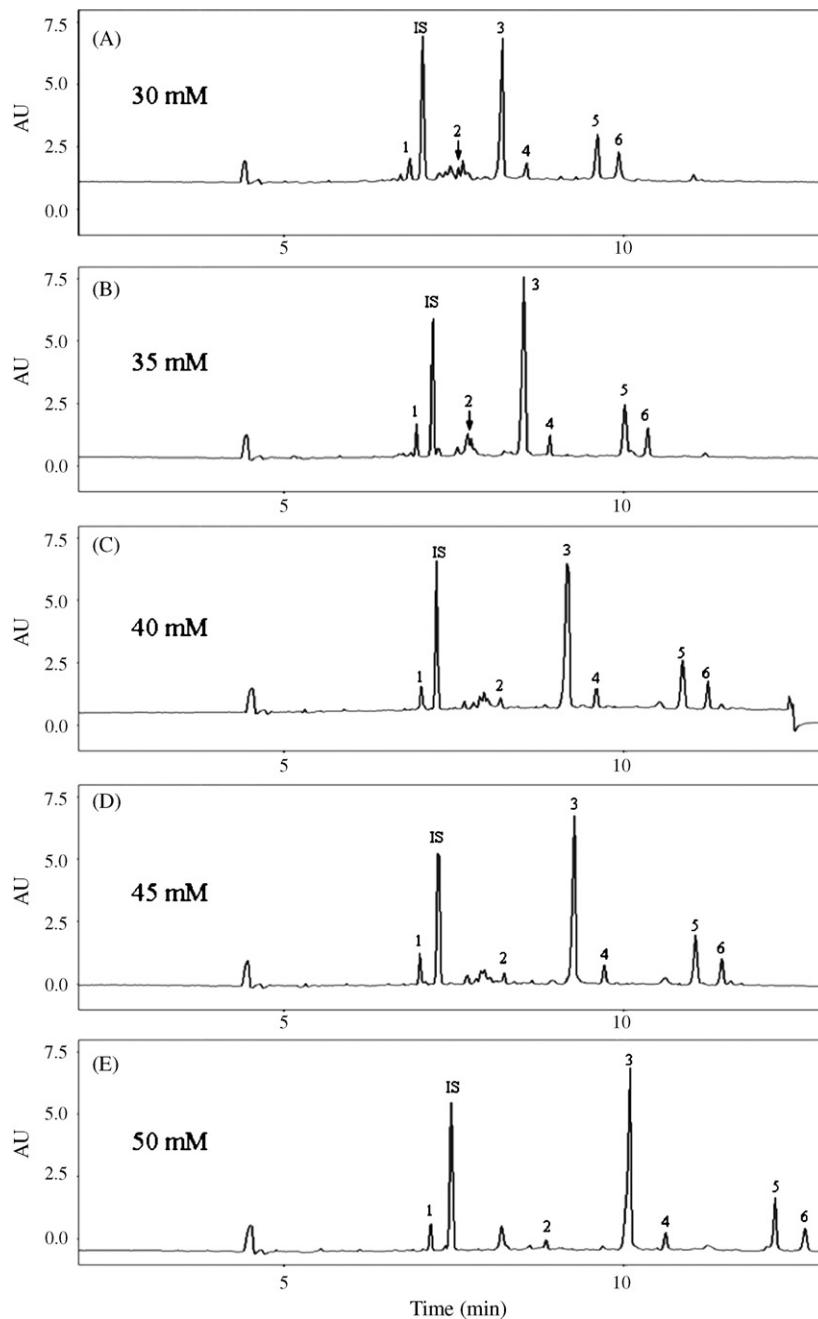
Fig. 4. Influence of SDS concentration on separation of teicoplanin components. Separation conditions: 20 mM sodium tetraborate, pH 8.8, 11% v/v ACN. The SDS concentrations are as indicated in the figure. Other conditions are the same as those described in Fig. 2. The numbering of peaks corresponds to those in Fig. 1. Teicoplanin concentration was 25 µg/mL.

Table 1
Linear relationships between peak area ratios (y) and concentrations (µg/mL) (x), LODs and LOQs for the teicoplanin components

Teicoplanin components	Linear range (µg/mL)	Intercept	Slope	R^a	LOQ (µg/mL)	LOD (µg/mL)
A3-1	0.27–2.96	0.0056	0.1109	0.999	0.15	0.05
A2-1	0.14–1.54	−0.0019	0.1348	0.999	0.14	0.06
A2-2	2.92–32.12	0.0111	0.1106	0.998	0.18	0.06
A2-3	0.27–2.98	0.0113	0.1195	0.998	0.17	0.06
A2-4	0.91–10.02	−0.0062	0.1082	0.999	0.17	0.06
A2-5	0.49–5.38	0.0014	0.1120	0.998	0.13	0.05

[a] R: correlation coefficient.
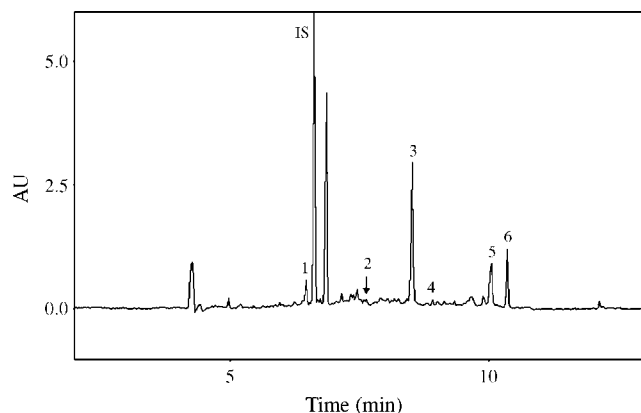
Fig. 5. Electropherogram of serum sample for a patient undergoing teicoplanin treatment. Separation conditions are the same as those described in Fig. 2. (11% ACN). The numbering of peaks corresponds to those in Fig. 1.

respectively. The precision of the peak area ratios of A3-1 and A2-1–A2-5 to the internal standard, was tested at total teicoplanin concentration of 5 μg/mL. Relative standard deviation of the repeatability ($n = 6$) and intermediate precision (inter-day, $n = 3$) were found to be lower than 4.18% and 5.30%, respectively. Due to the lack of pure standard materials of the individual components, the peak area normalization method was used to calculate the concentration of individual components with the assumption that the UV absorption coefficients of these components are identical. Linearity of the method was tested with the total teicoplanin concentration in the range of 5–55 μg/mL. The regression equations of A3-1–A2-5 are shown in Table 1. The linear range was presented for the concentration of each teicoplanin component. The correlation coefficients were found to be higher than 0.998. Accuracy of the method was determined at the lowest, intermediate and highest concentration levels of the linearity range. The recoveries were within 95.86% and 114.08% for six components at three concentration levels. The limit of detection (LOD) was determined as the concentration at which the signal-to-noise ratio (S/N) equaled to 3. Limit of quantitation (LOQ) was determined as the concentration at which the signal-to-noise ratio (S/N) equaled to 10. The LODs and LOQs of the individual teicoplanin components are shown in Table 1.

3.4. Determination of teicoplanin in patient serum

A total of 36 serum samples were collected from patients receiving the teicoplanin treatment. The concentration of each teicoplanin component was calculated from six calibration curves shown in Table 1. Fig. 5 shows the representative electropherogram of the patient serum analysis. Comparing to the data presented in Fig. 4C, the relative signal intensity of A2-4 and A2-5 are obviously higher in patient serum due to their higher lipophilicity and tendency to accumulate in human body [20]. The concentration of teicoplanin in patient serum was tested by both SPE–MEKC and FPIA methods. Because FPIA method can only give total concentration, the concentrations of six teicoplanin components obtained from SPE–MEKC method were added up and the sum was compared with the concentration obtained from FPIA method. The data obtained from both methods are provided in Fig. 6. Pearson's correlation analysis was applied to data obtained from the two methods and it revealed a good correlation between the SPE–MEKC and FPIA method ($r = 0.98$).

When patients are treated with teicoplanin, it is important to monitor their blood teicoplanin concentrations to ensure that safe and adequate therapeutic level is achieved. The maintaining of a
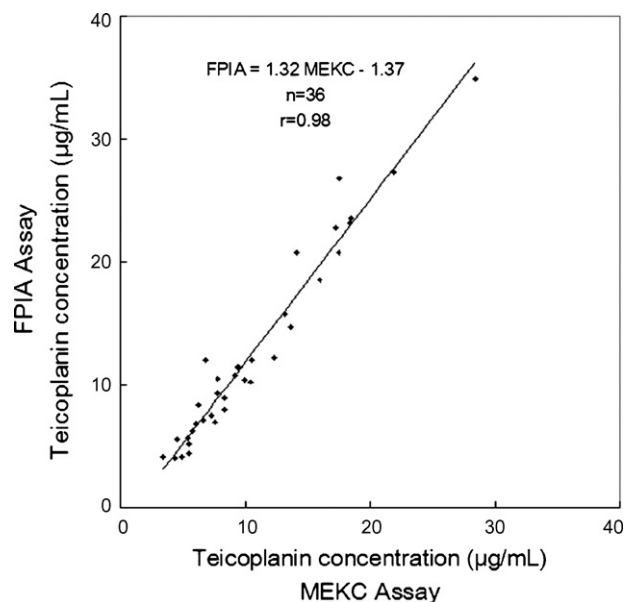
Fig. 6. Correlation of teicoplanin concentration measured by MEKC and FPIA.

minimal trough concentration of teicoplanin above 20 mg/L has been suggested. Our test results demonstrate that the developed method could be used for therapeutic drug monitoring.

4. Conclusion

In this study, a simple, efficient, and cost-saving SPE–MEKC method for the assay of teicoplanin in patient serum is developed for the first time. The method is capable of separating components with similar structures within 12 min, attaining a fourfold time's saving when compared with the previous HPLC analysis [9,11]. The sample preparation procedure was simplified by using urea as the protein denaturation reagent. When coupling with SPE extraction, interference caused by endogenous materials was greatly reduced. Moreover, the developed SPE method was able to concentrate serum teicoplanin level for more than 10-fold such that the developed method can be used for clinical analysis. Hanada et al. used co-extractive method for serum sample pre-treatment with recovery rate between 72% and 93%. Compared with their method, our SPE procedures provide more consistent recovery with recovery rate being at 90.93 ± 0.24% and besides, they could be run in batch. With regard to the sample SPE procedures developed by Taylor and Reid [6] and Bourget et al. [17], the recovery of the present study was higher for more than 10%.

Currently, FPIA is the analytical method most widely used to determine the concentration of teicoplanin in patient serum [13–15]. Although efficient, the FPIA method used the reagent which cost far more (65 USD per specimen) than the SPE–MEKC method. In addition, with the high selectivity of the SPE–MEKC method, the potential cross-reactivity that might be encountered on using the FPIA method could be minimized. The SPE–MEKC method is able to separate the individual teicoplanin components, this making it available for the pharmacokinetic characterization of each single component of teicoplanin in serum samples [20].

In conclusion, this present study demonstrates that the SPE–MEKC method is more efficient than the HPLC procedures and, on the other hand, more selective and cost-effective than the FPIA procedure for the analysis of teicoplanin in patient serum. The developed SPE–MEKC method can be applied to therapeutic drug monitoring and clinical research.

Acknowledgements

References

[1] S.E. Cosgrove, Y. Qi, K.S. Kaye, S. Harbarth, A.W. Karchmer, Y. Carmeli, Infect. Control Hosp. Epidemiol. 26 (2005) 166.
[2] R.M. Klevens, M.A. Morrison, J. Nadle, S. Petit, K. Gershman, S. Ray, L.H. Harrison, R. Lynfield, G. Dumyati, J.M. Townes, A.S. Craig, E.R. Zell, G.E. Fosheim, L.K. McDougal, R.B. Carey, S.K. Fridkin, JAMA 298 (2007) 1763.
[3] J.C.J. Barna, D.H. Williams, D.J.M. Stone, T.-W.C. Leung, D.M. Doddrell, J. Am. Chem. Soc. 106 (1984) 4895.
[4] A.H. Williams, R.N. Grüneberg, J. Antimicrob. Chemother. 14 (1984) 441.
[5] A. Borghi, C. Coronelli, L. Faniuolo, G. Allievi, R. Pallanza, G.G. Gallo, J. Antibiot. 32 (1984) 615.
[6] R.B. Taylor, R.G. Reid, J. Chromatogr. 563 (1991) 451.
[7] M. Cociglio, H. Peyrière, D. Hillaire-Buys, R. Alric, J. Chromatogr. B 705 (1998) 79.
[8] S.J. McCann, L.O. White, B. Keevil, J. Antimicrob. Chemother. 50 (2002) 107.
[9] K. Hanada, A. Kobayashi, Y. Okamori, T. Kimura, H. Ogata, Biol. Pharm. Bull. 28 (2005) 2023.
[10] B. Joos, R. Lűthy, Antimicrob. Agents Chemother. 31 (1987) 1222.
[11] N. Mochizuki, K. Ohno, T. Shimamura, H. Furukawa, S. Todo, S. Kishino, J. Chromatogr. B 847 (2007) 78.
[12] J. Shen, Z. Jiao, Y. Zhou, H. Zhu, Z. Song, Chromatographia 65 (2007) 9.
[13] L.O. White, C. McMullin, A.J. Davis, A.P. MacGowan, I. Harding, D.S. Reeves, J. Antimicrob. Chemother. 38 (1996) 701.
[14] S.H. Mastin, R.L. Buck, P.A. Mueggler, Diagn. Microbiol. Infect. Dis. 16 (1993) 17.
[15] H. Cox, M. Whitby, G. Nimmo, G. Williams, Antimicrob. Agents Chemother. 37 (1993) 1924.
[16] R.B. Taylor, S. Vorarat, R.G. Reid, S.P. Boyle, R.R. Moody, J. Capill. Electrophor. Microchip Technol. 6 (1999) 131.
[17] P. Bourget, A. Lesne-Hulin, A. Sertin, A. Maillot, M. Alaya, C. Martin, Int. J. Pharm. 146 (1997) 167.
[18] B.L. Ackermann, T.R. Brian, J. Am. Soc. Mass Spectrom. 7 (1996) 1227.
[19] R. Kuhn, S. Hoffstetter-Kuhn, Capillary Electrophoresis: Principles and Practice, Springer-Verlag Berlin Heidelberg, 1993, p.198.
[20] A. Bernareggi, A. Danese, A. Cometti, G. Buniva, M. Rowland, J. Pharmacokinet. Biopharm. 18 (1990) 525.

A portable, inexpensive and microcontrolled spectrophotometer based on white LED as light source and CD media as diffraction grid

Germano Veras [a,b], Edvan Cirino Silva [a,*], Wellington Silva Lyra [a], Sófacles Figueredo Carreiro Soares [a], Thiago Brito Guerreiro [a], Sérgio Ricardo Bezerra Santos [c]

[a] *Universidade Federal da Paraíba, Departamento de Química, 58.051-970, João Pessoa, PB, Brazil*
[b] *Universidade Estadual da Paraíba, Departamento de Química, 58.109-753, Campina Grande, PB, Brazil*
[c] *Centro Federal de Educação Tecnológica da Paraíba, 58.015-430, João Pessoa, PB, Brazil*

ARTICLE INFO

ABSTRACT

A portable, microcontrolled and low-cost spectrophotometer (MLCS) is proposed. The instrument combines the use of a compact disc (CD) media as diffraction grid and white light-emitting diode (LED) as radiation source. Moreover, it employs a phototransistor with spectral sensitivity in visible region as phototransductor, as well as a programmable interrupt controller (PIC) microcontroller as control unit. The proposed instrument was successfully applied to determination of food colorants (tartrazine, sunset yellow, brilliant blue and allura red) in five synthetics samples and Fe^{2+} in six samples of restorative oral solutions. For comparison purpose, two commercial spectrophotometers (HP and Micronal) were employed. The application of the t-paired test at the 95% confidence level revealed that there are not significant differences between the concentration values estimated by the three instruments. Furthermore, a good precision in the analyte concentrations was obtained by using MLCS. The overall relative standard deviation (R.S.D.) of each analyte was smaller than 1.0%. Therefore, the proposed instrument offers an economically viable alternative for spectrophotometric chemical analysis in small routine, research and/or teaching laboratories, because its components are inexpensive and of easy acquisition.

Published by Elsevier B.V.

1. Introduction

Since the seventies of the last century, when researchers as Flaschka et al. [1] developed photometers based on light-emitting diode (LED), LEDs have been applied on spectrophotometric instrumentation as radiation sources having relatively small effective bandwidth [2,3]. However, the increasing demand for chemical analyses makes necessary to develop LED-based instruments to work in a wide range of wavelengths what requires multiple radiation sources. The approach increases cost and complexity of the optical and electronic system. For example, optical fibers are usually employed to direct the radiation towards the detector and a more elaborated hardware is necessary to control the LED drift.

Nowadays, it is easy to acquire white LEDs that substitutes the complex optical system obtained when monochromatic LEDs are used as sources of several wavelengths in the visible region.

Therefore, it is possible to develop simple spectrophotometers using a single white LED with an adequate disperser of the white light. For this purpose, the literature reports two works only that employ white LED as radiation source [4,5]. Shimazaki et al. [4] were pioneers in the development of a white LED-based spectrophotometer which was used in determination of Fe^{2+} in river water by the *o*-phenantroline method. Li et al. [5] described a portable multi-function instrument using different spectrophotometric techniques. As application, the spectrophotometric determination of Cr^{6+} and Al^{3+} was carried out using diphenylcarbazide and pyrocatechol violet as chelant and chromogenic reagents, respectively.

Commercial spectrophotometric instrumentation commonly employs absorption or interference optical filters, prisms or diffraction grids as radiation dispersers. In most of these instruments, the dispersive device is a diffraction grid, an optical component containing series of grooves traced on a glass plate or polished metal. In this context, a compact disc (CD) media could be used as diffraction grid due to its grooves. Despite the use of CD media as radiation disperser [6], no application in spectrophotometric instrumentation has been found.

---

* Corresponding author.
E-mail address: edvan@quimica.ufpb.br (E.C. Silva).

In the present work, a portable, microcontrolled and low-cost spectrophotometer (MLCS) having a white LED as radiation source and a CD media as diffraction grid for measurements using the visible region was developed. In order to increase the signal-to-noise ratio in the spectrophotometric measurements, a phototransistor with maximum spectral sensitivity in the visible region was used. In the MLCS, pulsed radiation from the white LED is dispersed by the CD media generating monochromatic radiation that is focalized in the phototransistor by a stepper motor. The control of the proposed instrument, the acquisition and treatment of data are accomplished by an electronic circuit based on a programmable interrupt controller (PIC) microcontroller. Two analytical applications were elected to illustrate the performance of the MLCS. The first is represented by individual determinations of four food colorants (tartrazine, brilliant blue, allura red and sunset yellow). The second concerns to the determination of Fe^{2+} in restoratives by using the 1,10-phenantroline method.

2. Experimental

2.1. Reagents, solutions and samples

Food colorants tartrazine (E-102), sunset yellow (E-110), allura red (E-129), and brilliant blue (E-133) were purchased from Sigma–Aldrich. Stock solutions of $1000\,mg\,L^{-1}$ of each colorant were prepared dissolving its necessary amount in phosphate buffer
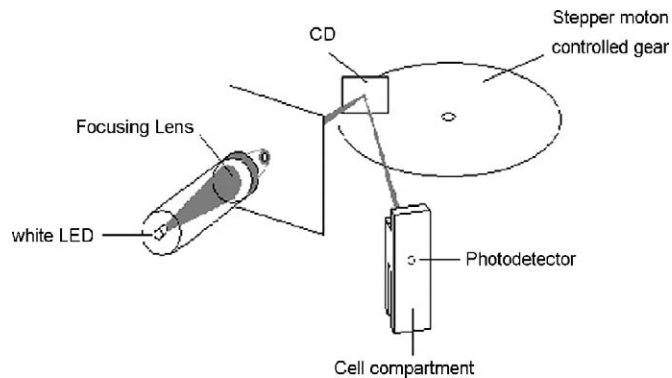
Fig. 1. Schematic diagram illustrating the optical system of the MLCS.

solution at pH 7.00. Standard solutions of synthetic samples of each colorant were prepared by the appropriated dilution of the respective stock solution. The standard solutions were prepared in authentic triplicates at the concentrations 2.0, 4.0, 6.0, 8.0, 10.0, 12.0, 14.0, 16.0, 18.0, 22.0, and $26.0\,mg\,L^{-1}$.

$FeCl_3 \cdot 6H_2O$ was used to prepare stock solutions of Fe^{3+} $1000\,mg\,L^{-1}$. Working solutions (Fe^{2+} 2.0–$10.0\,mg\,L^{-1}$) were prepared from the stock solution after reduction of the Fe^{3+} using ascorbic acid 1.0% (w/v). Six samples of restorative oral solutions (containing Fe^{2+}) from different marks were acquired in drugstores at João Pessoa city, Brazil. These pharmaceutical for-
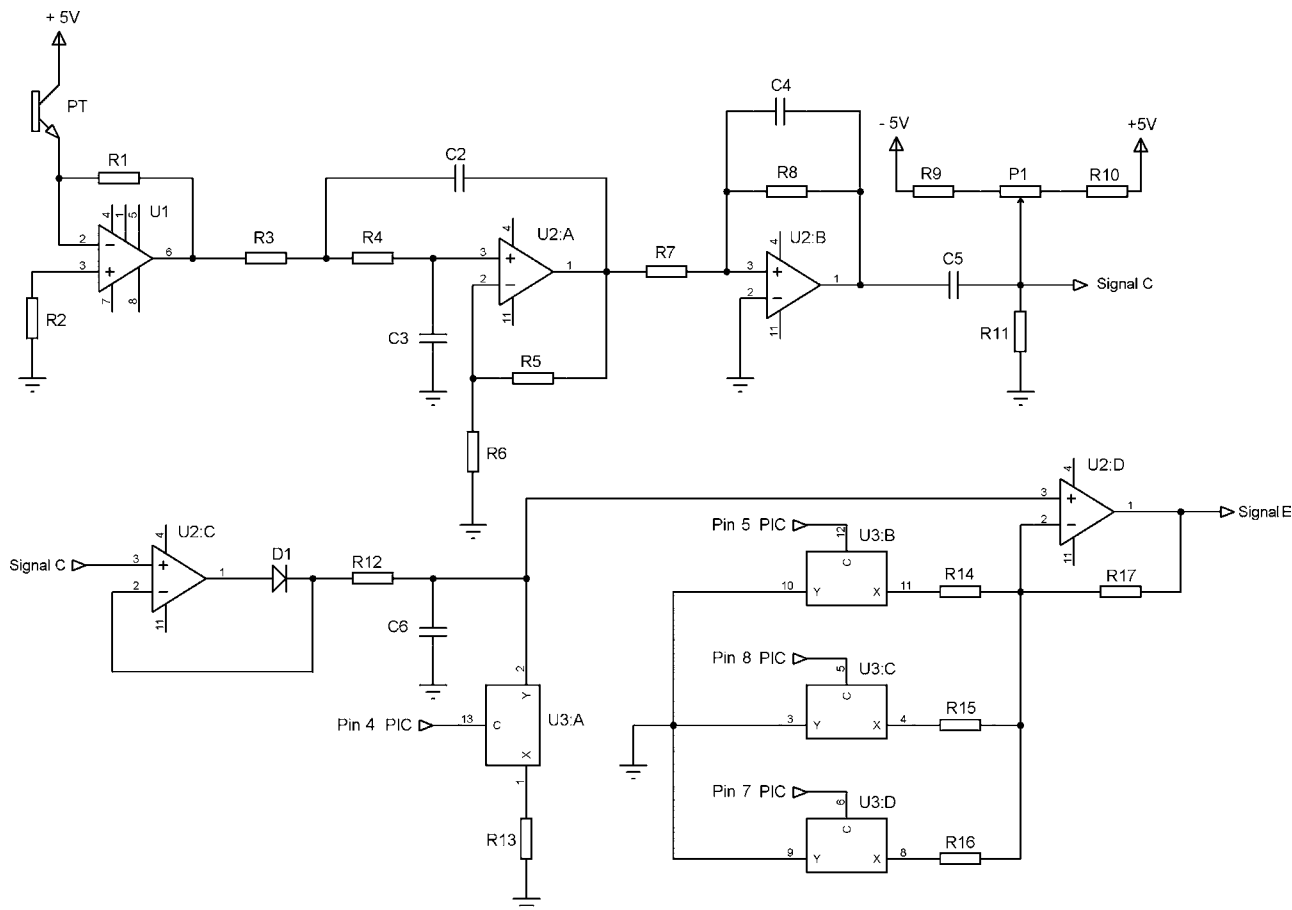
Fig. 2. Electronic layout of the MCLS detector. Legend: PT = phototransistor; C = polyethylene capacitors; R = resistors; U1 = operational amplifier; U2 = quadruple operational amplifier; U3 = quadruple switches. Details in text.

mulations were diluted to fit in the linear range of the analytical curve.

Recently distilled water was used to prepare all solutions.

2.2. Description of the proposed instrument

Fig. 1 illustrates the optical components employed in the MLCS and Fig. 2, the electronic layout of the detection unit. This instrument was assembled into a box with 30 cm front, 20 cm height and 30 cm length. The optical–mechanical system is composed by white LED, focus lens to create a small light image (2 mm diameter) on the diffraction grid (CD) and stepper motor with gear to move the diffraction grid and to promote the scan of the spectral region of interest. To increase the spectral resolution, the position of the stepper motor was adjusted so that the phototransistor can detect the radiation from the second overtone.

The instrument uses a PIC 16F877 programmable microcontroller as control unit driven by a stabilized power supply. The control software was elaborated with C language. The microcontroller presents a 10-bit multi-channel analog to digital converter (A/D), $8k \times 14$ words of flash program memory, 256×8 bytes of EEPROM data memory, 368×8 bytes of RAM, three timers and three ports with eight channels (multiplexed pins) each, for general purpose, that can be configured for data acquisition. The microcontroller allows drastic reduction of the number of electronic components in the spectrophotometer and makes possible to introduce or alter functionalities in the instrument without any hardware modification.

The white LED Control Module pulses the white LED radiation at 7 Hz. The module turns the white LED on for readings of the analytical signals and off for determination of instrumental noise. The signals are detected, filtered and amplified in the Detection Module of the MLCS, showed in Fig. 2. In the layout, five operational amplifiers are used for different purposes: to convert the photocurrent into voltage (U1), to filter the high frequency noise (U2:A) as a high-pass Butterworth filter; to amplify the analytical signal (U2:B), to detect the peak signal as a sample-hold unit (U2:C) and to fit the analytical signal (U2:D) in the A/D scale (5 V) using CMOS switches (U3:B–D) to change the gain depending on the value of the input signal. C5 and R11 are used as low-pass filter and P1 is used for off-set. CMOS switch U3:A is used to discharge the capacitor of the sample-hold circuit. The switches are controlled by the PIC. The processed signal E is sent to the A/D converter of the PIC to be converted into absorbance values. To calculate the absorbance values, the logarithm function used the measurement of blank (water) as reference. Both blank and sample measurements were registered turning the LED on to consider maximum light power and off in order to consider the dark signal. After digitalization, the absorbance values are sent by the microcontroller to the liquid crystal display (LCD) module, a TECH2004D-FL-GBS-S character type LCD with two buses: eight bits for data and three bits for control. In this work, the communication between microcontroller and LCD was always carried out with six bits, four being used for data transmission and two for data control. The Stepper Motor Control Module controls the angular displacement of the CD media.

A clock elaborated with a 4-MHz piezoelectric crystal is used for synchronization of the microcontroller internal functions.

3. Results and discussion

3.1. Calibration of the MLCS optical–mechanical system

An ocean optics spectrometer, model USB450, which substituted the phototransistor as detector, was used to calibrate the MLCS optical–mechanical system. Since the slit for the light entrance on the probe and the sensitive area of the phototransistor have the same dimensions (ca. 0.3 mm), the spectra registered by the ocean optics spectrometer represent the profile of the radiation that reaches the phototransistor. In this process, the spectrometer registers the reflected spectrum resulting from the radiation diffracted on the CD media. It was carried out five scans to obtain an average spectrum for each step of the stepper motor. Average spectra were used to build a calibration curve between the number of steps and the wavelength of maximum emission of the spectrum. In this case, an equation was estimated by using the linear least-squares and the result is presented below.

$$Step = wavelength \times 0.50246 - 214.7837$$

The number of steps and peak wavelengths are linearly correlated in the spectral range 440–640 nm with a correlation coefficient of 0.99968. Therefore, practically the entire visible spectral region can be exploited for spectrophotometric measurements by the MLCS. The overall standard deviation at the peak wavelengths was 0.30 nm, indicating a good repeatability associated to the wavelengths obtained starting from the number of steps.

The collected data were also employed to establish the effective bandwidths at maximum wavelength for each step and the value 13 nm was estimated in the range 440–640 nm.

The dispersion of the maximum signals measured for each step was also assessed and the overall relative standard deviation (R.S.D.) was estimated as 2.6%. This result indicates a good repeatability of the signals associated to the radiant power of the white LED.

3.2. Determination of food colorants in synthetic samples

The performance of the MLCS was initially evaluated by analyzing food colorants in the synthetic samples. The absorbance measurements were accomplished at the wavelengths of its maximum absorption: 486 nm (sunset yellow), 500 nm (allura red) and 582 nm (brilliant blue). However, in the case of tartrazine solutions, the measurements were performed at 440 nm due to the low sensibility of the MLCS in the wavelength of maximum absorption of this colorant (426 nm). For reference measurements, the food colorants were also analyzed by an HP diode-array, model 8453, and a Micronal spectrophotometer, model B34211.

In order to investigate the maximum concentration for linear response (the limit of linearity—LOL), ANOVA (analysis of variance) and F-test for lack of fit were applied to the models elaborated with the concentration range 2.0–26.0 mg L^{-1}, for each colorant. The results showed no lack of fit up to the LOL as presented in Table 1. An F-test for the regression significance revealed that the performed linear regressions are highly significant up to the LOL values.

The values of limits of detection (LOD) and limits of quantification (LOQ), which were estimated according to IUPAC recommendations [7], are also shown in Table 1. It is worth noting that LOL, LOD and LOQ present similar values for the three instruments and for the four food colorants.

After the study above, the analytical curves were constructed employing the following concentration ranges: 2.0–12.0 mg L^{-1} for allura red and 3.0–18.0 mg L^{-1} for the other colorants. In Table 2 are presented the results for the colorants determinations in synthetic samples.

As can be seen, there is a good agreement between the results of concentration determined by the proposed instrument and those

Table 1
Values of LOD, LOQ and LOL obtained for the four colorants

Colorant	Instrument	LOD (10^{-2} mg L^{-1})	LOQ (10^{-2} mg L^{-1})	LOL (mg L^{-1})
Allura red	Micronal	3.1	9.4	14.0
	HP	0.7	2.2	14.0
	MLCS	0.1	0.2	12.0
Sunset yellow	Micronal	3.2	9.7	18.0
	HP	0.7	2.1	18.0
	MLCS	13.0	39.4	18.0
Tartrazine	Micronal	2.6	7.8	18.0
	HP	0.8	3.6	18.0
	MLCS	8.1	24.7	18.0
Brilliant blue	Micronal	5.5	16.6	18.0
	HP	7.8	23.8	18.0
	MLCS	3.1	9.3	18.0

Table 2
The average concentration values of food colorants and confidence intervals obtained in the analyses of synthetic samples

Colorant	Sample	Expected value (mg L^{-1})	Estimated value (mg L^{-1})		
			Micronal	HP	MLCS
Allura Red	01	3.0	2.9 ± 0.1	2.9 ± 0.2	2.9 ± 0.1
	02	5.0	4.7 ± 0.0	4.8 ± 0.1	4.7 ± 0.2
	03	7.0	6.9 ± 0.1	7.0 ± 0.2	7.0 ± 0.3
	04	9.0	8.9 ± 0.0	8.7 ± 0.1	8.9 ± 0.1
	05	11.0	11.0 ± 0.1	11.0 ± 0.2	11.0 ± 0.4
Sunset Yellow	01	4.0	4.0 ± 0.0	4.1 ± 0.1	4.1 ± 0.2
	02	8.0	7.8 ± 0.1	7.8 ± 0.1	7.9 ± 0.2
	03	10.0	10.1 ± 0.1	10.0 ± 0.1	10.0 ± 0.3
	04	14.0	13.9 ± 0.1	13.9 ± 0.1	13.8 ± 0.5
	05	16.0	15.9 ± 0.1	15.8 ± 0.1	15.6 ± 0.2
Tartrazine	01	4.0	4.0 ± 0.1	3.9 ± 0.1	4.1 ± 0.1
	02	8.0	8.0 ± 0.1	7.9 ± 0.1	7.7 ± 0.1
	03	10.0	10.2 ± 0.5	10.2 ± 0.1	10.2 ± 0.2
	04	14.0	13.9 ± 0.5	13.9 ± 0.1	14.0 ± 0.6
	05	16.0	15.7 ± 0.0	15.8 ± 0.0	15.8 ± 0.1
Brilliant Blue	01	4.0	4.1 ± 0.1	4.3 ± 0.1	4.2 ± 0.0
	02	8.0	8.0 ± 0.0	7.8 ± 0.1	8.0 ± 0.0
	03	10.0	9.9 ± 0.0	9.9 ± 0.1	10.1 ± 0.1
	04	14.0	13.9 ± 0.1	13.7 ± 0.1	13.8 ± 0.1
	05	16.0	15.9 ± 0.1	15.8 ± 0.1	15.9 ± 0.1

obtained by using the commercial spectrophotometers. In fact, the application of the *t*-paired test at the 95% confidence level revealed that there are not significant differences between the concentrations estimated by the three instruments.

Concerning to the precision of results, in Table 2 is shown that the confidence intervals are narrow and similar for the concentration values obtained by the three instruments. Moreover, the overall R.S.Ds. associated to the results from the three instruments

Tabela 3
Average values of Fe^{2+} concentration and confidence intervals obtained in the analyses of samples of restorative oral solutions

Sample	Estimated values (mg L^{-1})		
	Micronal	HP	MLCS
01	4.9 ± 0.1	4.9 ± 0.0	4.9 ± 0.1
02	5.8 ± 0.1	5.7 ± 0.0	5.8 ± 0.1
03	4.2 ± 0.1	4.1 ± 0.1	4.3 ± 0.1
04	6.3 ± 0.1	6.3 ± 0.1	6.2 ± 0.1
05	4.5 ± 0.0	4.4 ± 0.0	4.5 ± 0.0
06	9.0 ± 0.1	8.9 ± 0.1	8.9 ± 0.0
R.S.D.	0.8%	0.5%	0.7%

Tabela 4
Recovery percentage obtained for Fe^{2+} in six samples of restorative oral solutions

Sample	Added Fe^{2+} (mg L^{-1})	Recovery (%)		
		Micronal	HP	MLCS
01	3.0	99.31	100.34	97.18
	5.0	98.86	100.19	100.56
	7.0	98.98	97.99	96.41
02	3.0	99.65	100.00	97.18
	5.0	98.67	99.24	98.05
	7.0	96.81	97.27	97.25
03	3.0	96.19	94.56	93.85
	5.0	96.01	98.48	99.86
	7.0	98.55	99.28	99.05
04	3.0	101.39	98.30	98.72
	5.0	99.62	100.19	105.29
	7.0	99.27	98.28	98.10
05	3.0	104.51	103.74	97.69
	5.0	97.91	99.05	97.50
	7.0	99.42	101.72	100.84
06	3.0	104.51	95.58	103.85
	5.0	97.91	97.92	94.16
	7.0	99.42	99.43	97.68

were smaller than 1.0%. Such finding indicates a good precision in the estimative of the colorants concentrations by using the three instruments.

3.3. Determination of Fe^{2+} in restoratives oral solutions

In these analyses, the measurements of absorbance were carried out at 515 nm in the three instruments. Restorative oral samples of six different manufacturers were analyzed by using analytical curves built in the concentration ranges 2.0–10.0 mg L^{-1}, which were validated by using ANOVA and *F*-test for lack of fit and for regression significance at the 95% confidence level.

Table 3 presents the results in terms of average values of Fe^{2+} concentration and the confidence intervals estimated at 95% level. The results show that good agreements of the results were obtained employing the three instruments and it is corroborated by the application of the *t*-paired test at the 95% confidence.

Table 3 also presents the values of overall R.S.Ds., which indicate a good precision in the estimation of the Fe^{2+} concentrations by the three instruments.

In spite of the *t*-test to reveal absence of systematic error (bias) it does not guarantee its actual absence in the results. In order to check the eventual presence of bias, a recovery test was carried out according to the procedure described elsewhere [8]. For this purpose, known quantities of the analyte were added into the restorative samples and the measured recovery taxes are presented in Table 4. As can be seen, satisfactory recovery taxes were obtained for all fortified samples. Therefore, this result evidences the absence of bias associated to the estimated values of Fe^{2+} concentration employing the three instruments.

4. Conclusions

A portable, inexpensive and microcontrolled spectrophotometer was developed in this work. Such advantageous characteristics were achieved due to the incorporation of a CD media as diffraction grid and a white LED as radiation source. Other relevant characteristic of the proposed instrument concerns to the use of a phototransistor with spectral sensitivity in the visible region as phototransductor.

The MLCS was successfully applied to the determination of food colorants (sunset yellow, tartrazine, allura red and brilliant blue) in synthetic samples and Fe^{2+} in restorative oral solutions. In all applications, the proposed instrument lead to results similar to the obtained by the commercial instruments employed for comparison. Therefore, the proposed instrument offers an economically viable alternative for spectrophotometric chemical analysis in small routine, research and/or teaching laboratories.

Acknowledgement

References

[1] H. Flaschka, C. Mckeithan, R. Barnes, Anal. Lett. 6 (1973) 585.
[2] P.K. Dasgupta, I.Y. Eom, K.J. Morris, J. Li, Anal. Chim. Acta 500 (2003) 337.
[3] E.N. Gaião, E.P. Medeiros, W.S. Lyra, P.N.T. Moreira, P.C. Vasconcelos, E.C. Silva, M.C.U. Araújo, Quim. Nova 28 (2005) 1102.
[4] Y. Shimazaki, S. Watanabe, M. Takahashi, M. Iwatsuki, Anal. Sci. 16 (2000) 1091.
[5] Q. Li, K.J. Morris, P.K. Dasgupta, I.M. Raimundo Jr., H. Temkin, Anal. Chim. Acta 479 (2003) 151.
[6] M.A. Cavalcante, A. Benedetto, Rev. Bras. Ensino Física 21 (1999) 437.
[7] IUPAC—Nomenclature, symbols, units and their usage in spectrochemical analysis. II. Data interpretation. Pure Appl. Chem. 45 (1976) 99.
[8] P. Bruce, P. Minkkinen, M.-L. Riekkola, Microchip. Acta 128 (1998) 93.

CdTe nanocrystals sensitized chemiluminescence and the analytical application

Zhouping Wang[a,b], Jun Li[a], Bin Liu[a], Jinghong Li[a,*]

[a] *Department of Chemistry, MOE Key Laboratory of Bioorganic Phosphorus Chemistry & Chemical Biology, Tsinghua University, Beijing 100084, China*
[b] *State Key Laboratory of Food Science and Technology, School of Food Science and Technology, Jiangnan University, Wuxi 214122, China*

ARTICLE INFO

ABSTRACT

It was found that the mixing of CdTe semiconductor nanocrystals (NCs) with luminol in the presence of $KMnO_4$ can induce a great sensitized effect on chemiluminescence (CL) emission. When the concentration of luminol, $KMnO_4$ and NaOH were fixed at 1 μM, 1 μM and 0.05 M, respectively, the most excellent performance can be obtained for the CdTe NCs sensitized CL. By means of CL and photoluminescence spectra, we suppose the enhanced CL signals resulted from the accelerated luminol CL induced by the oxidized species of CdTe NCs. Based on the finding, using thioglycolic acid-capped CdTe NCs as label and immunoglobulin G (IgG) as a model analyte, a CL immunoassay protocol for IgG content detection was developed. The strong inhibition effect of phenol compounds on luminol–$KMnO_4$–CdTe NCs CL system was also observed. All these findings demonstrated the possibility of semiconductor nanocrystals induced chemiluminescence to be utilized for more practical applications.

© 2008 Elsevier B.V. All rights reserved.

1. Introduction

Semiconductor nanocrystals, also referred to as quantum dots, with the superior emitting properties, attracted the growing attention to applications of these materials in LED and display devices [1,2], as well as in biological luminescent labels [3]. In general, luminescent semiconductor nanocrystals (NCs) is concerned with the potential to overcome problems encountered by their organic fluorophore counterparts. It has been utilized for fluorescent tagging applications with the advantages of high photobleaching threshold, good chemical stability, and readily tunable spectral properties [3–8].

Luminescent properties of colloidal semiconductor nanocrystals, including photoluminescence (PL) produced with photoexcitation [9,10], electrochemiluminescence (ECL) generated by electron injection [11–13], and cathodoluminescence given from electron impact [14], have been extensively investigated and applied in many areas of fundamental and technical importance [15,16]. Recently, Talapin et al. described the CL property of CdSe/CdS core/shell nanostructure dealing with the emitting state related to the quantum-confined orbitals [17]. Li et al. [18] and Wang et al. [19] then reported the CL of CdTe NCs and CdS NCs directly oxidized by some oxidants, such as H_2O_2 and $KMnO_4$, and its size-dependent and surfactant-sensitized effects. However, it is still quite lack for the information involving in chemiluminescence (CL) of semiconductor nanocrystals.

In recent years, CL and related analytical techniques with the advantages of high sensitivity, wide linear rage and no interference from background scattering light have intrigued people extensive interest and have been developed to be an important and powerful tool in various fields [20–27]. The investigation on the CL of semiconductor nanocrystals would therefore be promising for broadening the applications of luminescent semiconductor nanocrystals.

Herein, upon previous work [18], we introduced CdTe NCs into the classic luminol CL system. It was found the mixing of CdTe NCs with luminol in the presence of $KMnO_4$ could induce a great of enhancement on CL radiation. Possible sensitized CL mechanism was further investigated by means of CL and PL spectra. Based on it, using TGA capped CdTe NCs as label, a CL immunoassay procedure for IgG content detection was further developed. Moreover, it was found that some phenols compounds acutely inhibit the CL intensity of luminol–$KMnO_4$–CdTe NCs system. All the results proved that semiconductor nanocrystals-induced chemiluminescence can be successfully applied for many practical purposes, such as bioassay and trace detection of analyte.

2. Experimental

2.1. Chemicals and materials

Analytical reagent-grade chemicals and ultra-purification water prepared with a Milli-Q system were used throughout. Luminol

* Corresponding author. Tel.: +86 10 62795290; fax: +86 10 62795290.
E-mail address: jhli@mail.tsinghua.edu.cn (J. Li).

was obtained from Merck (Germany). Te powder, CdCl$_2$, NaHB$_4$, thioglycolic acid (TGA), 1-ethyl-3-(3-dimethylaminopropyl) carbodiimide hydrochloride (EDC), N-hydroxysuccinimide (NHS), and 1,9-nonanedithiol were purchased from Acros Organics (Geel, Belgium). H$_2$O$_2$, KMnO$_4$, ascorbic acid, catechol, resorcin, hydroquinone and NaOH were obtained from Beijing Chemical Reagent Plant (Beijing, China). Dopamine hydrochloride, adrenaline hydrochloride, noradrenaline bitartrate, and isoprenaline hydrochloride were gotten from Drug and Biological Products Examination Bureau of China, Beijing. Adrenaline hydrochloride and isoprenaline hydrochloride injections are the products of Shanghai Harvest Pharmaceutical Co., Ltd. and Sanjing pharmaceutical Co., Ltd. of Harbin Pharmaceutical Group. Highly pure gold plate was gotten from Shanghai Chenhua Instrument Co., China. All other chemicals were of the best grade available and used as received. The possibly minimum number of dilution steps was used to prepare more diluted solutions.

Bovine serum albumin (BSA), human immunoglobulin G (IgG) and sheep anti-human immunoglobulin G (anti-IgG) obtained from Dingguo Biological Technology Co. (Beijing, China) were used for the CL immunoassay. IgG and anti-IgG solution were prepared in phosphate buffer solution (PBS) and stored in a refrigerator (4 °C).

2.2. Preparation of CdTe NCs

TGA-capped CdTe NCs were synthesized as the procedure described in Ref. [28,29] with little modification. Briefly, N$_2$-saturated cadmium chloride solution was added to NaHTe solution which was prepared by the reaction between NaHB$_4$ and tellurium powder in the presence of thioglycolic acid (TGA). The concentration of Cd^{2+} was 2 mM, and the molar ratio of Cd^{2+}:Te^{2-}:TGA was fixed at 1:0.5:2.5. After mixed, the solution was heated with microwave for 1 h.

CdTe NCs samples used in the present work were purified by selective precipitation with isopropanol and re-dispersed in ultra-purification water. The free CdCl$_2$ and TGA were further removed via dialysis for 2 days in 0.01 M NaOH solution. Dialysis membrane with molecular weight of cutoff 7000 was used for the purification of CdTe NCs. The concentration of CdTe NCs was defined by the number of cadmium atoms contained in the sample.

2.3. Preparation of (anti-IgG)–CdTe NCs conjugates

According to the literatures with little modification [3,30], anti-IgG labeled with TGA-capped CdTe NCs was prepared as following: 500 μL containing 1 mM CdTe NCs, 10 mg/mL NHS, and 20 mg/mL EDC was added to 1 mg/mL anti-IgG solution and mixed for 1 h at room temperature. The resulting solution contained stable (anti-IgG)-CdTe NCs conjugation without obvious aggregates then was treated by repeated centrifugation to remove the excess proteins, CdTe NCs, free EDC and NHS. The purified conjugates were stored in PBS solution at room temperature.

2.4. Procedure for CdTe NCs sensitized CL

A flow-injection CL system was employed for performing the CdTe NCs sensitized CL. A peristaltic pump was used to deliver flow streams in this system. PTFE tubing (0.8 mm i.d.) was used as the connection material in the flow system. In order to obtain good mechanical and thermal stability, the instruments were run for 10 min before the first measurement. Flow lines were inserted into luminol, KMnO$_4$, water carrier and CdTe NCs sample solution, respectively. The flow rate was fed at 2.0 mL/min for all lines. The pumps were started to wash the whole system until a stable baseline was recorded. Sample solution (50 μL) was injected into the carrier stream (water) using an six way injection valve equipped with a 50-μL sample loop, merged with the mixture of luminol (in 0.05 M NaOH) and KMnO$_4$ and then reached the flow cell, producing CL emission. The flow cell was made by coiling 30 cm of colorless glass tube (1 mm i.d. and 2 mm o.d.) into a spiral disk shape with a diameter of 2 cm and was located directly facing the window of the CR-105 photomultiplier tube (PMT) (Hammamatsu, Tokyo, Japan). The CL signal produced in the flow cell was detected and recorded with the computerized MPI-B ultra-weak luminescence analyzer. Data acquisition and treatment were performed with MPI-B software running under Windows XP.

The kinetics characteristics of the CL reactions was recorded with a static system consisted of a colorless glass beaker (10 mL) and the MPI-B ultra-weak luminescence analyzer. The glass beaker was located directly on the window of the CR-105 photomultiplier tube of the luminescence analyzer. Luminol solution, CdTe NCs sample
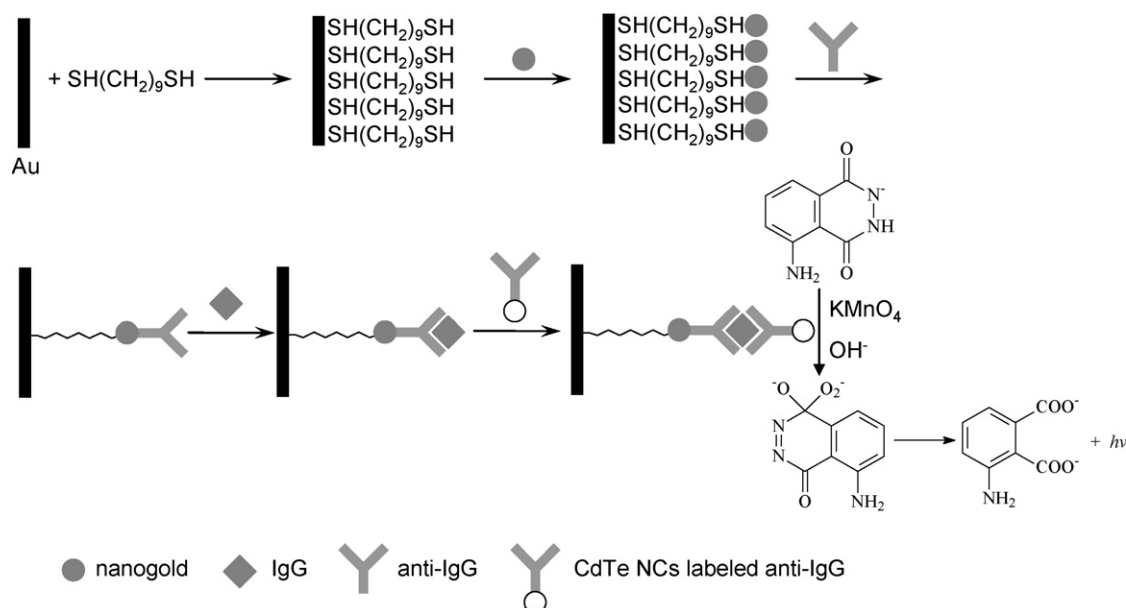
Scheme 1. CL immunoassay of IgG using CdTe NCs as label.

solution, and NaOH solution were placed into the glass beaker, respectively. $KMnO_4$ solution was injected into the beaker using a 200-μL injector through the rubber plug in the lid of detector of the luminescence analyzer. Data acquisition and treatment were still performed with MPI-B software running under Windows XP.

2.5. Procedure for IgG immunoassay

Similar to literature method, we prepared anti-human IgG–CdTe NCs conjugate [30]. Sandwich-type conjugate of (anti-human IgG)/IgG/(anti-human IgG–CdTe NCs) was assembled on a gold substrate as follows: we firstly pretreated the gold substrates with "piranha" solution (98% H_2SO_4:H_2O_2, 7:3, v/v) prior to use and rinsed with ultra-purified water. The pretreated gold substrate was firstly immersed in 1,9-nonanedithiol ethanol solution to form the self-assembly monolayer of 1,9-nonanedithiol. Then, the thiol functionalized gold substrates were dipped into the spherical gold colloid solution in darkness, which was synthesized as a well-known method [31]. The spherical nanogold-modified gold substrates were further immersed in 0.5 mL PBS at pH 7.4 with 0.1 mg/mL of the anti-human IgG and incubated overnight at 4 °C in order to immobilize more anti-human IgG stably on the substrate (or anti-IgG/spherical nanogold/SH(CH$_2$)$_9$SH/gold substrate). Then thoroughly rinsing the gold substrates with 0.02 M PBS (pH 7.4) to remove the weakly absorbed anti-IgG. Bovine serum albumin (BSA) in 0.02 M PBS (pH 7.4) then was introduced to saturate the possible bare spherical nanogold for 30 min and rinsed with 0.02 mol/L PBS (pH 7.4). Next the substrates were dipped into a pH 7.4 PBS containing various concentrations of IgG at 37 °C for 30 min, then rinsed by 0.02 M PBS (pH 7.4) solution to remove unbound IgG [26]. Finally it was immersed in anti-IgG–CdTe NCs conjugate solution at 37 °C for 30 min, and then rinsed by 0.02 M PBS (pH 7.4) to remove unbound (anti-IgG)–CdTe NCs conjugate. The processes of the immobilization of antibody onto the gold substrate and the formation of sandwich-type (anti-IgG)/IgG/(anti-IgG-CdTe NCs) are shown in Scheme 1. Ten same gold substrates were used for the immobilization, assembly, and consequent measurements.

After the formation of the sandwich-type complexes of (anti-IgG)/IgG/(anti-IgG–CdTe NCs), the assembled gold substrates were located in a colorless glass tube directly facing to the window of PMT of CL detector, and connecting into the flow lines of the flow-injection CL setup (Fig. 1). 1×10^{-6} M luminol and 1×10^{-6} M $KMnO_4$ were injected into the system, which were sensitized by probe CdTe NCs to produce enhanced CL in alkaline medium. The concentrations of IgG are quantified via the relative CL intensity.

2.6. Procedure for inhibited CL detection of phenols compounds

The schematic diagram of the flow system employed for inhibited chemiluminescent determination of phenols compounds is shown in Fig. 2. In order to obtain good mechanical and thermal
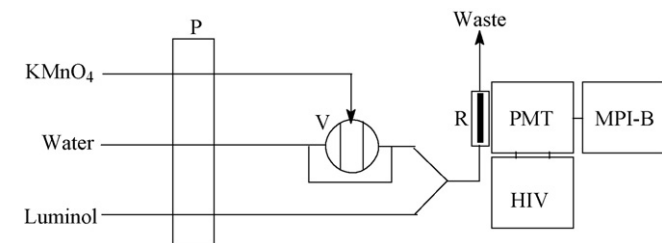
Fig. 1. Schematic diagram of lab-built flow-injection chemiluminescence immunoassay system. P, peristaltic pump; V, injection valve; C, flow cell; R, CL immunoassay reactor; PMT, photomultiplier tube; HIV, negative high voltage; MPI-B, luminescence analyzer controlled by personal computer.
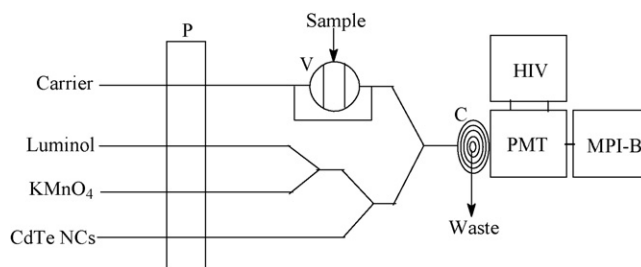
Fig. 2. Schematic diagram of lab-built flow-injection inhibited chemiluminescence detection system for phenols compounds and ascorbic acid. P, peristaltic pump; V, injection valve; C, flow cell; PMT, photomultiplier tube; HIV, negative high-voltage supply; MPI-B, luminescence analyzer controlled by personal computer.

stability, the instruments were run for 10 min before the first measurement. Flow lines were inserted into luminol solution, $KMnO_4$ solution, CdTe NCs solution, water carrier and sample solution, respectively. The flow rate was fed at 2.0 ml/min for all lines. The pumps were started to wash the whole system until a stable baseline was recorded. The 50 μl of sample solution was injected into the carrier stream. This stream was merged with the mixture of $KMnO_4$, luminol and CdTe NCs solution and then reached the flow cell, accompanying a decreased CL signal. The concentration of samples was quantified by the relative decreased CL intensity.

2.7. Apparatus

The CL measurements were performed with an ultra-weak luminescence analyzer (type MPI-B, manufactured at Remax Analytical Instrument Co. Ltd., Xi'an, China). PL spectra of CdTe NCs were examined by LS-55 luminescence spectrophotometer (PE Elmer, U.K.). CL spectra of the proposed systems were obtained with a modified Model RF-5301 Spectrofluorometer (Shimadzu, Japan). UV–vis absorption spectra were achieved with a Model UV-2100s Spectrophotometer (Shimadzu, Japan). The size of the as-prepared CdTe NCs was calculated according to Peng's method [32].

3. Results and discussions

As described in Section 2, we synthesized TGA-capped CdTe NCs. The TEM image of the as-prepared TGA-capped CdTe NCs was referred in our previous work [28]. Fig. 3 shows the PL and absorption spectra of the as-prepared CdTe NCs with a maximum PL emission ~565 nm and a peak absorption at ~536 nm. According to Peng's method [32], the size of the as-prepared CdTe NCs is ~3.05 nm, which was calculated according to the following equation:

$$D = (9.8127 \times 10^{-7})\lambda^3 - (1.7147 \times 10^{-3})\lambda^2 + (1.0064)\lambda - (194.84)$$

where D (nm) is the size of CdTe NCs, and λ (nm) is the wavelength of the absorption peak of CdTe NCs.

3.1. Sensitized effect of CdTe NCs on luminol–KMnO$_4$ CL

In previous experiments, it was found that CdTe NCs could be directly oxidized by $KMnO_4$ or H_2O_2 to generate relative strong CL radiation. Aiming to further enhance the CdTe NCs induced CL intensity and exploit the applied potential of CdTe NCs induced CL, we introduced luminol into CdTe NCs induced CL system. In the presence of oxidant, such as $KMnO_4$, H_2O_2, $K_3Fe(CN)_6$, and N-succinimide, the CL response of luminol–CdTe NCs system was investigated firstly. The results show when $KMnO_4$ was used as oxidant the mixing of CdTe NCs and luminol could result in the strongest CL light radiation.
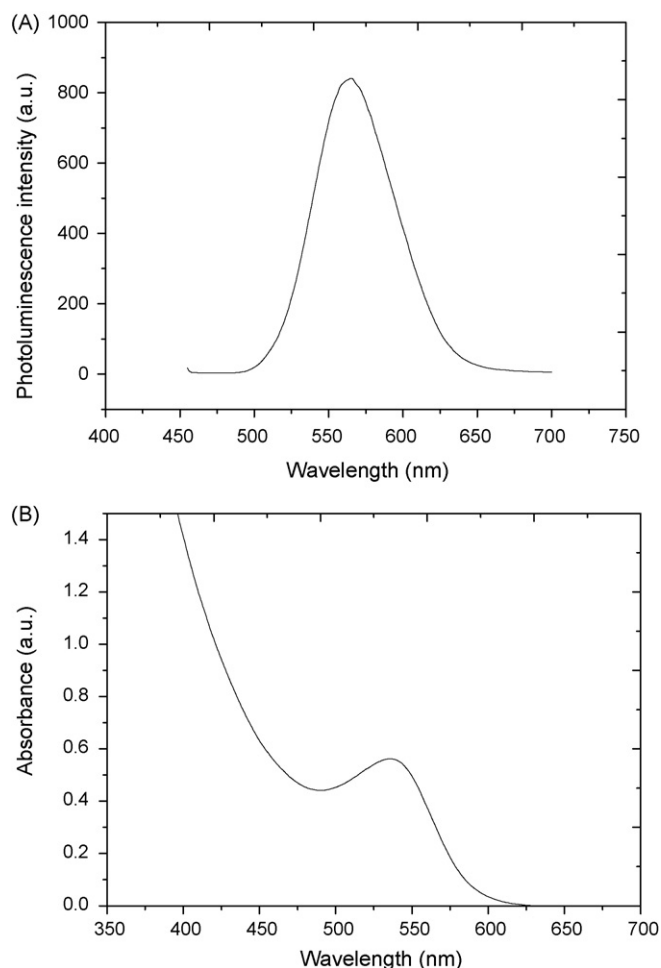
Fig. 3. Photoluminescence (A) and absorption (B) spectra of as-prepared CdTe NCs colloid solution.

Consequently, the dynamic CL intensity-time profiles of the luminol and luminol–CdTe NCs in the presence of KMnO$_4$ were acquired in static-injection mode. It indicated (Fig. 4) that the CL reactions were very quick and the CL intensity reached a maximum
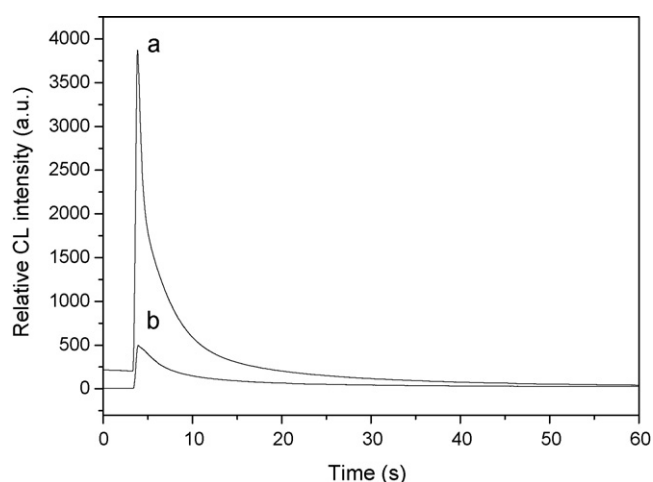
after ~0.55 s for luminol system and ~0.5 s for luminol–CdTe NCs system after initiating the reactions with KMnO$_4$. And the CL intensity of luminol–KMnO$_4$–CdTe NCs system is far stronger than that of luminol–KMnO$_4$ system, indicating the great sensitized effect of CdTe NCs on luminol–KMnO$_4$ CL reaction.

Parameters influencing the CL signals of luminol–KMnO$_4$–CdTe NCs system were then investigated systematically to establish the optimal conditions for the CL reaction. The results show when luminol and KMnO$_4$ were all fed at 1×10^{-6} M and NaOH at 0.05 M the most excellent performance can be obtained for the luminol–KMnO$_4$–CdTe NCs CL reaction.

The sensitized effects of CdTe NCs with different size (3.05, 3.33, 3.50, 3.73 nm), which was prepared by microwave heating with different time, on luminol–KMnO$_4$ CL reaction were also examined. The results revealed that the CL intensity increased with the increment of the size of CdTe NCs.

3.2. Possible CL reaction mechanisms

In general, the ascertainment of the final CL luminophor is the key to clarify the CL reaction mechanisms. In previous work, we have demonstrated that the CL spectra of CdTe NCs directly oxidized by oxidant are identical with the PL spectra of CdTe NCs, namely, the emitter is the excited state of CdTe NCs. For the present CdTe NCs enhanced luminol–KMnO$_4$ CL system, we suppose there possibly exist two luminescent approaches. Firstly, the luminophor is the excited state of 3-aminophthalate molecule, luminophor of luminol CL system, and there have no energy transfer from excited state of 3-aminophthalate to CdTe NCs during the CL reaction. In this case CdTe NCs participated in the enhanced CL reaction only as a sensitizer. The second one possibly involves in the energy-transfer from excited state of 3-aminophthalate to CdTe NCs and the final emitter is the excited state of CdTe NCs. It is well known the maximum light emission of luminol CL is around 425 nm. At the same time, CdTe NCs possesses broad excite band, it is possible for it to accept the energy released from excited state of 3-aminophthalate and to be excited to its excited state.

We examined the CL spectra of luminol–CdTe NCs system in the presence of KMnO$_4$. A modified Model RF-5301 spectrofluorometer was employed for the acquirement of the CL spectra (turn off the excitation light source). The results displayed (Fig. 5) that there is only one peak emission around 425 nm for luminol–CdTe

Fig. 4. Kinetic curves for the luminol–KMnO$_4$–CdTe NCs (a) and luminol–KMnO$_4$ (b) CL systems. (a) 100 μL 2.5 μM KMnO$_4$ solution was injected into a mixture of 1 mL 1 μM luminol (in 0.01 M NaOH) and 1 mL 1 μM CdTe NCs sample solution; (b) 100 μL 2.5 μM KMnO$_4$ solution was injected into a mixture of 1 mL 1 μM luminol (in 0.01 M NaOH) and 1 mL water; High voltage, −400 V.
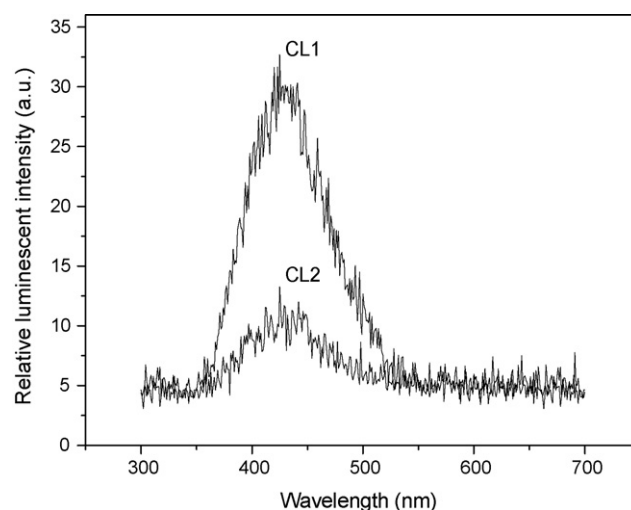
Fig. 5. CL spectra of luminol–KMnO$_4$ in the presence of CdTe NCs (CL1) and luminol–KMnO$_4$ in the absence of CdTe NCs (CL2). Conditions: luminol, 1×10^{-5} M (in 0.01 M NaOH); KMnO$_4$, 1×10^{-5} M; CdTe NCs, 1×10^{-3} M.
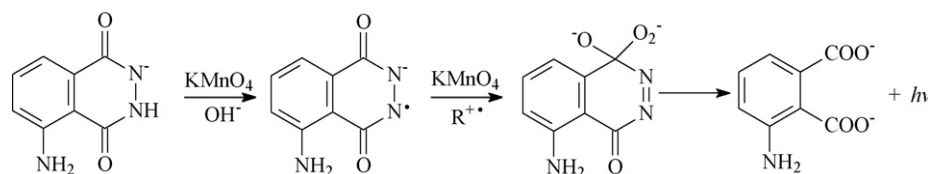
Scheme 2. Possible luminol CL mechanism in the presence of CdTe NCs and KMnO$_4$.

NCs–KMnO$_4$ system when scanned from 300 to 700 nm, which is in agreement with that of luminol–KMnO$_4$ system. Moreover, the CL intensity of luminol–KMnO$_4$–CdTe NCs system (CL1) is obviously stronger than that of luminol–KMnO$_4$ system (CL2), indicating the sensitized effect of CdTe NCs on luminol–KMnO$_4$ CL reaction. Fig. 3 gives the PL spectrum of CdTe NCs with a maximum emission around 565 nm. Based on these facts, we propose the main emitter of luminol–CdTe NCs–KMnO$_4$ CL system is closely related to the excited state of 3-aminophthalate molecule with a characteristic maximum emission of around 425 nm. The supposed energy-transfer process does not occur during the CL reaction, or the light radiation from energy-transfer process is very weak and cannot be observed by the testing instruments used for CL spectra.

In general, the CL reaction mechanism of luminol oxidized by oxidant has been specified in many literatures [33,34].

In meanwhile, many literatures involving in the electrogenerated chemiluminescence of semiconductor nanocrystals have indicated that electron-transfer annihilation of electrogenerated anion and cation radicals results in the production of excited states [35–37].

$$R^{-\bullet} + R^{+\bullet} \rightarrow R* + R \tag{1}$$

$$R* \rightarrow R + h\nu \tag{2}$$

In the present system, we suppose that the oxidant KMnO$_4$ can also oxidize CdTe NCs to produce the cation radicals R$^{+\bullet}$, or oxidized species (CdTe NCs)$^{+\bullet}$, which served as the sensitizer or co-oxidant of luminol–KMnO$_4$ CL reaction to accelerate the enhanced CL radiation. Possibly due to the differences of the oxidation ability or energy-matching degree, for the proposed CdTe NCs induced enhancement CL reaction, the stronger enhancement signals were recorded in the presence of KMnO$_4$ instead of other studied oxidants. Meanwhile, the use of KMnO$_4$ as oxidant is probably in favor of performing the luminescent approach of luminol rather than that of CdTe NCs exciton luminescence.

Therefore, the possible mechanism of the enhanced CL reaction induced by CdTe NCs can be concluded in a simple form as showing Scheme 2. (R$^{+\bullet}$ refers to cation radicals (CdTe NCs)$^{+\bullet}$).

At the same time, we found that Cd^{2+} can sensitize the CL of luminol–KMnO$_4$ system in a small magnitude. If the nanostructure of CdTe NCs was demolished to form Cd^{2+} by the oxidation of KMnO$_4$, it would contribute to the CL of luminol–CdTe NCs–KMnO$_4$ with a few degrees. We also examined the response of capping reagent, TGA, to the CL of luminol in the presence of KMnO$_4$, and compared with that of purified CdTe NCs. The results showed that the increased CL intensity induced by TGA is far small than that of purified CdTe NCs at the same concentration. Therefore, it suggested that the main factor enhancing the CL emission of luminol in the presence of KMnO$_4$ is CdTe NCs instead of TGA.

3.3. Immunoassay of IgG

Based on the sensitized effect of CdTe NCs on luminol–KMnO$_4$ CL, as an application of CdTe NCs, we proposed using CdTe NCs as label and IgG as model analyte for CL immunoassay. As described in Section 2, CdTe NCs conjugated with anti-human IgG

Table 1
Precision and accuracy for the recovery of spiked IgG in diluted human plasma samples

Background content (10^{-6} M)	Added concentration (10^{-6} M)	Detected concentration (mean ± S.D.) ($n = 5$) (10^{-6} M)	Recovery ratio (%)[b]
0.82[a]	0.8	1.63 ± 0.11	101.25
	1	1.79 ± 0.17	97.00
	3	3.89 ± 0.23	102.33
	5	5.81 ± 0.21	99.80
	7	7.86 ± 0.35	100.57

[a] The plasma sample was diluted 100 folds step by step.

[b] Recovery(%) = (Detected concentration − Background content)/Added concentration × 100%. Conditions: luminol, 1×10^{-6} M (in 0.05 M NaOH); KMnO$_4$, 1×10^{-6} M; flow rate, 2.0 mL/min; high voltage, −400 V.

and a sandwich-type immunoassay procedure was developed for human IgG immunoassay. The principle of the noncompetitive CL immunoassay with CdTe NCs label is depicted in Scheme 1. Primary antibodies-specific anti-human IgG was immobilized on the surface of gold substrates via nanogold and 1,9-nonanedithiol. The human IgG analyte was first captured by the primary antibody and then sandwiched by secondary antibody labeled with CdTe NCs. Next, the unbound CdTe NCs-labeled antibody was discarded, and the remained labeled CdTe NCs were quantitatively determined by the proposed CdTe NCs sensitized luminol–KMnO$_4$ CL reaction. The CL signals were directly proportional to the amount of target analyte (human IgG) in the standard or samples.

Under the used conditions, calibration curves for the IgG ($\Delta I = 19.13 + 5.70$ [IgG]·10^7 (M), $R^2 = 0.9913$) show good correlation, demonstrating the linear response over the concentrations tested (0.05–5 μM for IgG). The limit of detection, calculated based on 50 μL of a solution of calibrators, was 17 nM for IgG, with a signal-to-noise ratio of 3. The relative standard deviation (R.S.D.) for 5 parallel determinations of 0.5 μM IgG on five gold substrates with same size and thickness was 5.1%.

Recovery experiments of standard human IgG from spiked human plasma samples listed in Table 1 also indicated the excellent accuracy and precision of the proposed CdTe NCs labeled CL immunoassay method. Compared with some published IgG immunoassay methods, the proposed CdTe NCs method can be completed in about 1.5 h and the detection limit is enough for real IgG samples detection.

Table 2
Analytical performance of the proposed inhibition CL system for the determination of adrenaline, isoprenaline and ascorbic acid

Compound	Linear range[a]	Calibration curve	Correlation coefficient
Adrenaline	1×10^{-8} to 1×10^{-6} M	$\Delta I = 86.783C + 1796.5$	$R^2 = 0.9833$
Isoprenaline	2×10^{-10} to 2×10^{-8} M	$\Delta I = 9.0841C + 888.89$	$R^2 = 0.986$
Ascorbic acid	1×10^{-7} to 1×10^{-5} M	$\Delta I = 19.895C + 1027.8$	$R^2 = 0.9989$

[a] Conditions: luminol, 1×10^{-5} M; KMnO$_4$, 1×10^{-5} M; CdTe NCs, 5×10^{-5} M; NaOH, 0.1 M; flow rate, 2 mL/min; high voltage, −500 V.

Table 3
Results for the determination of adrenaline and isoprenaline in commercial formulations

Sample	Label (mg/ml)	Found (mg/ml)[a]	Proposed method	Official method [29]
Adrenaline hydrochloride	Injection 1	1	0.97 (±2.7%)	0.95 (±2.5%)
	Injection 2	1	0.98 (±3.1%)	0.96 (±2.2%)
Isoprenaline hydrochloride	Injection 1	0.5	0.48 (±1.5%)	0.47 (±2.3%)
	Injection 2	0.5	0.47 (±1.3%)	0.47 (±1.7%)

[a] Values are mean of three replicates (±R.S.D.).

3.4. Inhibited CL determination of phenols compounds

Inhibited CL system was often developed for sensitive trace analysis in various applications. In the present work, we investigated the response of catecholamines and other phenols compounds as well as ascorbic acid to luminol–$KMnO_4$–CdTe NCs CL reaction.

As described in Section 2, a flow-injection CL set-up (Fig. 2) was employed to get the response signals of these compounds on luminol–$KMnO_4$–CdTe NCs CL emission. The results revealed that the studied compounds, including dopamine, adrenaline, noradrenaline, isoprenaline, catechol, resorcin, and hydroquinone, as well as ascorbic acid could sharply inhibit the CL of luminol–$KMnO_4$–CdTe NCs system. We optimized the conditions for the inhibited CL, and found that the optimal parameters for the flow-injection inhibited CL system as follows: luminol, 1×10^{-5} M; $KMnO_4$, 1×10^{-5} M; CdTe NCs, 5×10^{-5} M; NaOH, 0.1 M; flow rate, 2 mL/min; high voltage, −500 V. And the inhibited CL intensity is linear with the concentration of some studied compounds in certain range, listed in Table 2. Due to the reductive properties of the studied compounds, the inhibited CL mostly results from the consumption of the oxidant $KMnO_4$ in luminol–$KMnO_4$–CdTe NCs system by the studied compounds. Fig. 6 displayed a typical recording output for the measurement of isoprenaline with different concentrations. Moreover, just owing to all these studied compounds can sensitively respond to the proposed CL system, the strong luminol–$KMnO_4$–CdTe NCs CL system therefore offers the potential of being used as the post-column detector system for the simultaneous determination of these compounds after HPLC or capillary electrophoresis separation.

The proposed inhibited CL system was then preliminarily applied to the analysis of adrenaline and isoprenaline in their injec-

tion formulations. The results obtained by the proposed method are shown in Table 3. They are in excellent agreement with the labeled values and compare well with the values obtained by the official method [38].

4. Conclusions

In summary, we observed the drastically sensitized effect of CdTe NCs on luminol CL in the presence of $KMnO_4$. This provides us with a sensitive CL strategy to utilize CdTe NCs for more practical applications. According to PL and CL spectra, the sensitized CL was suggested to be the accelerated luminol CL induced by the oxidative species of CdTe NCs. As an application of the CdTe NCs sensitized CL, we successfully developed a sandwich-type CL immunoassay of human IgG using CdTe NCs as label. Although the analytical performance, especially the sensitivity, of the immunoassay can not be compared with the more sensitive protocols recently developed for IgG immunoassay, but the sensitivity of the CdTe NCs presented CL can be further improved by modifying the reaction condition, increasing the reaction substrate area or optimizing the nanostructures of CdTe NCs. We also observed the inhibited effect of phenols compounds and ascorbic acid on luminol–$KMnO_4$–CdTe NCs CL radiation. All the finding would be promising to broaden the applications of CdTe NCs sensitized CL into many cases, such as clinical immunoassay and DNA hybridization analysis, or as end-column CL detection system of HPLC and capillary electrophoresis.
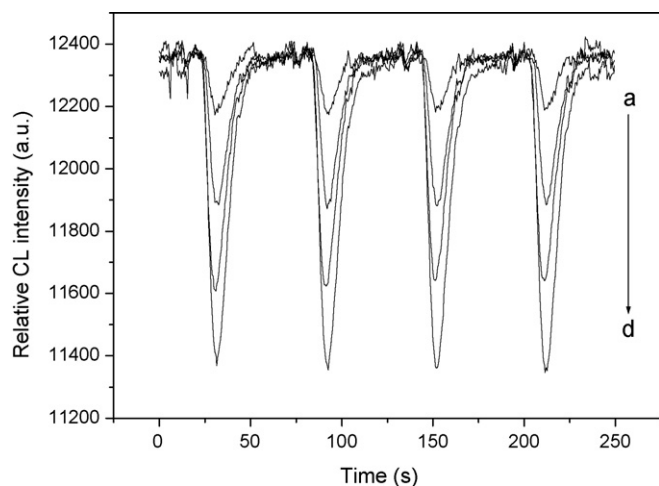
Acknowledgment

Fig. 6. A typical recording output of the proposed inhibited CL system for the measurements of different concentrations of isoprenaline hydrochloride. a, b, c, and d correspond to 2, 4, 6, and 8 nM, respectively. Conditions: $KMnO_4$, 1×10^{-5} M; luminol, 1×10^{-5} M (NaOH, 0.1 M); CdTe NCs, 5×10^{-5} M; flow rate, 2.0 mL/min; high voltage, −500 V.

References

[1] S. Coe, W.-K. Woo, M. Bawendi, V. Bulovic, Nature 420 (2002) 800.
[2] N. Tessler, V. Medvedev, M. Kazes, S.-H. Kan, U. Banin, Science 295 (2002) 1506.
[3] W.C.W. Chan, S.M. Nie, Science 281 (1998) 2016.
[4] M.P. Bruchez, M. Moronne, P. Gin, S. Weiss, A.P. Alivisatos, Science 281 (1998) 2013.
[5] H. Weller, Adv. Mater. 5 (1993) 8.
[6] A.P. Alivisatos, Science 277 (1996) 933.
[7] D.Y. Wang, A.L. Rogach, F. Caruso, Nano Lett. 2 (2002) 857.
[8] H. Mattoussi, J.M. Mauro, E.R. Goldman, G.P. Anderson, V.C. Sundar, F.V. Mikulec, M.G. Bawendi, J. Am. Chem. Soc. 122 (2000) 12142.
[9] L.H. Qu, X.G. Peng, J. Am. Chem. Soc. 124 (2002) 2049.
[10] W. Chen, J.Z. Zhang, A.G. Joly, J. Nanosci. Nanotechnol. 4 (2004) 919.
[11] Y. Bae, N. Myung, A.J. Bard, Nano Lett. 4 (2004) 1153.
[12] G.Z. Zou, H.X. Ju, Anal. Chem. 76 (2004) 6871.
[13] J.J. Miao, T. Ren, L. Dong, J.J. Zhu, H.Y. Chen, Small 1 (2005) 802.
[14] J. Rodriguez-Viejo, K.F. Jensen, H. Mattoussi, J. Michel, B.O. Dabbousi, M.G. Bawendi, Appl. Phys. Lett. 70 (1997) 2132.
[15] M. Han, X. Gao, J.Z. Su, S. Nie, Nat. Biotechnol. 19 (2001) 631.
[16] S.W. Chen, L.A. Truax, J.M. Sommers, Chem. Mater. 12 (2000) 3864.
[17] S.K. Poznyak, D.V. Talapin, E.V. Shevchenko, H. Weller, Nano Lett. 4 (2004) 693.
[18] Z.P. Wang, J. Li, B. Liu, J.Q. Hu, X. Yao, J.H. Li, J. Phys. Chem. B 109 (2005) 23304.
[19] Y. Li, P. Yang, P. Wang, X. Huang, L. Wang, Nanotechnology 18 (2007) 225602.
[20] A.M. Garc-Campa, W.R.G. Baeyens, Chemiluminescence in Analytical Chemistry, Marcel Dekker, New York, 2001.
[21] A.M. Powe, K.A. Fletcher, N.N. St. Luce, M. Lowry, S. Neal, M.E. McCarroll, P.B. Oldham, L.B. McGown, I.M. Warner, Anal. Chem. 76 (2004) 4614.

[22] J. Yakovleva, R. Davidsson, A. Lobanova, M. Bengtsson, S. Eremin, T. Laurell, J. Emneus, Anal. Chem. 74 (2002) 2994.
[23] F.M. Li, C.H. Zhang, X.J. Guo, W.Y. Feng, Biomed. Chromatogr. 17 (2003) 96.
[24] J.G. Lv, Z.J. Zhang, J.D. Li, L.R. Luo, Forensic Sci. Int. 148 (2005) 15.
[25] C. Dodeigne, L. Thunus, R. Lejeune, Talanta 51 (2000) 415.
[26] J.H. Lin, H.X. Ju, Biosens. Bioelectron. 20 (2005) 1461.
[27] C. Chen, F.K. Liu, X.P. Qi, J.S. Li, World J. Gastroenterol. 9 (2003) 242.
[28] J. Li, X. Hong, Y. Liu, D. Li, Y.W. Wang, J.H. Li, Y.B. Bai, T.J. Li, Adv. Mater. 17 (2005) 163.
[29] J. Li, X. Hong, D. Li, K. Zhao, L. Wang, H.Z. Wang, Z.L. Du, J.H. Li, Y.B. Bai, T.J. Li, Chem. Comm. (2004) 1740.
[30] G.T. Hermanson, Bioconjugate Techniques, Academic Press, New York, 1996.
[31] G. Frens, Nat. Phys. Sci. 241 (1973) 20.
[32] W.W. Yu, L. Qu, W. Guo, X. Peng, Chem. Mater. 15 (2003) 2854.
[33] G. Merényi, J. Lind, T.E. Eriksen, J. Biolumin. Chemilumin. 5 (1990) 53.
[34] T.G. Burdo, W.R. Seitz, Anal. Chem. 47 (1975) 1639.
[35] Z.F. Ding, B.M. Quinn, S.K. Haram, L.E. Pell, B.A. Korgel, A.J. Bard, Science 296 (2002) 1293.
[36] N. Myung, Z.F. Ding, A.J. Bard, Nano Lett. 2 (2002) 1315.
[37] T. Ren, J.Z. Xu, Y.F. Tu, S. Xu, J. Zhu, J. Electrochem. Commun. 7 (2005) 5.
[38] Society of Pharmacopoeia of Hygiene Department, The Pharmacopoeia of P.R. China, Part 2, China Chemical Industry Press, Beijing, 2000, p. 110, 601.

Derivatized silver nanoparticles as sensor for ultra-trace nitrate determination based on light scattering phenomenon

Chien C. Wang [c], Marta O. Luconi [a], Adriana N. Masi [b,c], Liliana P. Fernández [a,c,*]

[a] Área de Química Analítica, Facultad de Química, Bioquímica y Farmacia, Universidad Nacional de San Luis, San Luis, Argentina
[b] Área de Bromatología- Ensayo y Valoración de Medicamentos, Facultad de Química, Bioquímica y Farmacia, Universidad Nacional de San Luis, San Luis, Argentina
[c] Instituto de Química de San Luis (INQUISAL-CONICET), Chacabuco y Pedernera, 5700 San Luis, Argentina

ARTICLE INFO

ABSTRACT

New silver nanoparticles coated with EDTA (EDTA-AgNPs) have been synthesized by citrate reduction method and characterized by UV–vis spectroscopy, molecular fluorescence and scanning electron microscopy (SEM). The derivatized nanoparticles show fluorescent emission and second order scattering (SOS) signals which in presence of nitrate are both attenuated. The SOS decreasing is greater than its fluorescent quenching; considering this fact, a new ultra sensitive methodology using the derivatized silver nanoparticles as sensor for nitrate determination has been developed. Under optimal established conditions, a linear response has been obtained within the range of 6.4×10^{-4} to $3.0\,\mu g\,mL^{-1}$ nitrate concentrations, with a detection limit of $1.8 \times 10^{-4}\,\mu g\,mL^{-1}$. This novel technique provides a sensitive and selective methodology for nitrate determination and has been satisfactorily applied to its quantification in parenteral solutions.

© 2008 Elsevier B.V. All rights reserved.

1. Introduction

Nitrate is an important anion in environmental and biological analysis [1]. Because it has direct impact on health after chemical transformations, excessive amount of the nitrate anion in water supplies typically indicates pollution from sewage on agricultural effluents. The over exposure of infants to nitrates can lead to methemoglobinemia, commonly known as blue baby syndrome [2].

Nitrate analysis is commonly based on indirect determination after reduction from nitrate to nitrite, either by reducing metals such as zinc [3] or by enzymatic reaction of nitrate reductase [4,5]. Several instrumental techniques for its determination include chromatography [6,7], potentiometry [8], polarography [9], Raman spectroscopy [10], spectrophotometry [11], chemiluminescence [12,13] and spectrofluorimetry [14,15]. From these previously mentioned methods, spectrofluorimetry is the most sensitive for trace analysis, which is based on the diazotation reactions of nitrite with different reagents [16–19]. However, it has disadvantages such as the toxicity of used reagents, time-consuming extraction processes and the presence of serious interferences [20].

Since in parenteral solutions the bioavailability of pharmaceuticals is greatest, their contents have rapid and direct influence on health. The development of sensitive methods for nitrate determination in liquid pharmaceutical formulations acquires main importance and constitutes a challenge for actual researcher.

Nanoparticles in liquid phase have long fascinated scientists because of their novel chemical and physical properties [21–26]. Particularly, silver nanoparticles have attracted the attention for their unique optical properties; particles size may influence all physical properties of such nanoparticles. One of the simplest syntheses consists is the chemical hot reduction of silver salt by the action of sodium citrate. Experimental conditions as reagent concentrations, time and temperature of heating, cleanliness of glassware must be carefully controlled to achieve stable and reproducible colloids. The obtained products tend to form agglomerates and/or change the size or shape during the storage. As silver nanoparticles are fairly unstable in solution [27], the derivatization step is necessary to obtain monodispersed nanoparticles.

For analytical chemistry, any signal, if its intensities have simple functional relationship with analyte concentration, can be applied with analytical purposes. The light scattering signals and fluorescence signals are twins in fluorospectroscopy and the light scattering signals are frequently sources of interferences in spectrofluorimetry [28]. In recent years, the light scattering technique has been increasingly applied to analytical chemistry; the most

---

* Corresponding author at: Área de Química Analítica, Facultad de Química, Bioquímica y Farmacia, Universidad Nacional de San Luis, Chacabuco y Pedernera, 5700 San Luis, Argentina. Fax: +54 2652 430224.
E-mail address: lfernand@unsl.edu.ar (L.P. Fernández).

common method used is resonance light scattering. The strong scattering of light at double incident wavelength ($\lambda_{em} = 2\lambda_{ex}$) is named as second order scattering (SOS) [29]. In fluorimetric analytical methodology, scattering signals can appear as potential spectral interference and the instrumental conditions are selected to minimize this harmful phenomenon [30].

Since Liu et al. first studied SOS as an analytical technique and applied in the determination of metal ions in 1995 [31,32], it has been used as a new analytical technique with application prospects to ultra-trace determinations [33–36].

Till date no research has been reported on the quenching effect of nitrate on fluorescence signal of silver nanoparticles or SOS decrease phenomenon. Based on this approach, a novel methodology for nitrate ultra-traces determination employing Ag-EDTA NPs as luminescent sensor is presented. The novel nanomaterial has been characterized by UV–vis spectroscopy, molecular fluorescence and SEM images.

2. Experimental

2.1. Apparatus

The SOS spectra and fluorescent intensities were measured on a RF-5301PC spectrofluorimeter (Shimadzu Corporation, Analytical Instrument Division, Kyoto Japan) equipped with a Xenon discharge lamp and 1 cm × 1 cm quartz cell.

A pHmeter (Orion Expandable Ion Analyzer, Orion Research, Cambridge, MA, USA) Model EA 940 with combined glass electrode was used for monitoring pH adjustment.

A Hewlett-Packard spectrophotometer with 10 mm optical path cells was used to record UV–vis absorption spectra.

The microphotographies were taken from a screening electron microscopy model LEO 450 VP (Carl Zeiss).

2.2. Reagents

All reagents and solvents were of analytical grade (Each origin is specified in the text); ultra-pure water was provided from MiliQ system.

2.3. Synthesis and derivatization of silver nanoparticles

Silver nanoparticles were prepared by citrate reduction of silver nitrate as described in literature [37]. 17.0 mg of AgNO$_3$ (Sigma–Aldrich) was dissolved in 100 mL ultra pure water in a 250 mL tri-neck flask. The solution was heated to boiling with a hemisphere heating mantle under vigorous magnetic stirring. After boiling for 2 min, a 10 mL aqueous solution of sodium citrate (3×10^{-3} mol L^{-1}, Sigma–Aldrich) was rapidly added to the flask. The solution gradually turned yellow within a few minutes, indicating the formation of Ag nanoparticles. The solution was kept boiling for an additional 6 min. After cooled, the solution containing the silver nanoparticles was transferred to a 250 mL flask. 1.0 mL of EDTA (0.10 mol L^{-1}, Merck) and 0.5 ml of NaOH (3.0 mol L^{-1}) were added and the vigorous magnetic stirring was maintained for 30 min till complete reaction.

Immediately after adding the derivatizing reagent, the color of reaction system turned to violet and after few minutes the homogeneous colloidal solution suffered a flocculation process forming flaks which were separated from the aqueous medium by centrifugation to remove the excess of reagents. The derivatized nanoparticles deposited on the bottom of centrifugal tube were removed with chloroform and collected in flask crystallizers. 100 mL of ultra pure water were added to each system. The

magnetic stirring at 333 K was applied to contribute with the complete removal of chloroform, obtaining a transparent solution of derivatized nanoparticles.

2.4. General procedure

0.50 mL Ag-EDTA NPs, 1.0 mL buffer Tris (0.10 mol L^{-1}) and nitrate standard solution or 1.0 mL of sample solution were added to graduated volumetric flasks and then diluted to 10 mL with ultra pure water.

The synthesized Ag-EDTA NPs presented an excitation and emission maximum at 225 and 295 nm, respectively.

In order to choose the optimal SOS peak, different exciting wavelengths, from 220 to 350 nm, were used; the SOS signals were recorded from 440 to 700 nm ($\lambda_{sos} = 2\lambda_{ex}$). 225 nm was chosen as excitation wavelength and 450 nm as measurement wavelength, both with slit width of 5 nm. All SOS intensities were measured against the blank which was prepared in the same way.

2.5. Pharmaceutical samples

The samples A and B were NaCl physiological solution (NaCl 0.90 mol L^{-1}) and dextrose isotonic solution (glucose 5%) respectively for intravenous use, both purchased from Lab. Roux-Ocefa (Buenos Aires, Argentina).

3. Results and discussion

3.1. Formation of nanosized Ag particles

The use of EDTA allowed the stability of these nanoparticles to be monodispersed in aqueous medium.

During the silver nanoparticles synthesis by conventional heating it was observed that after citrate was added, the color of reaction solution changed from colorless to yellow, making evident the formation of colloidal silver. SEM images (Fig. 1A) show that in this instance the particles which were nearly spherical were not well separated and stuck together to form many small groups. This typical behavior has been reported by other researchers [38,39]. The introduction of derivatization step resulted necessary to stabilize the silver nanoparticles as monodispersed material in aqueous medium.

The chelating reagent EDTA has been used as derivatizing agent for obtaining stable nanoparticles [40]. This coater suffers a chemisorption process onto the surface of AgNP through carboxylate groups. The two oxygen atoms of the carboxylate groups are coordinated symmetrically to the Ag atoms. The surface of AgNP remains negatively charged and, in presence of counter ions, acquires an electrostatic double layer. This double layer provides a repulsive force enabling to silver colloid to be stable in aqueous solution [41–43].

Attending that the possibility of using EDTA-AgNPs with analytical purposes depends on obtaining nanomaterial of high pure grade, it was necessary to add a purification step to eliminate all excess of reactant. With this aim, concentrated NaOH aqueous solution was added to EDTA-AgNPs solution and, after 15 min of reacting time, the flocculation process took place [38]. It was observed that the solution color changed immediately from yellow to violet. The dramatical diminution of their Z potential led to form the big flaks of nanoparticles, which facilitated the phases separation by flocculation. This phenomenon was reversible once removing the hydroxide by subsequently washing steps, obtaining a transparent solution of monodispersed nanoparticles with average size of 40 nm (Fig. 1B).
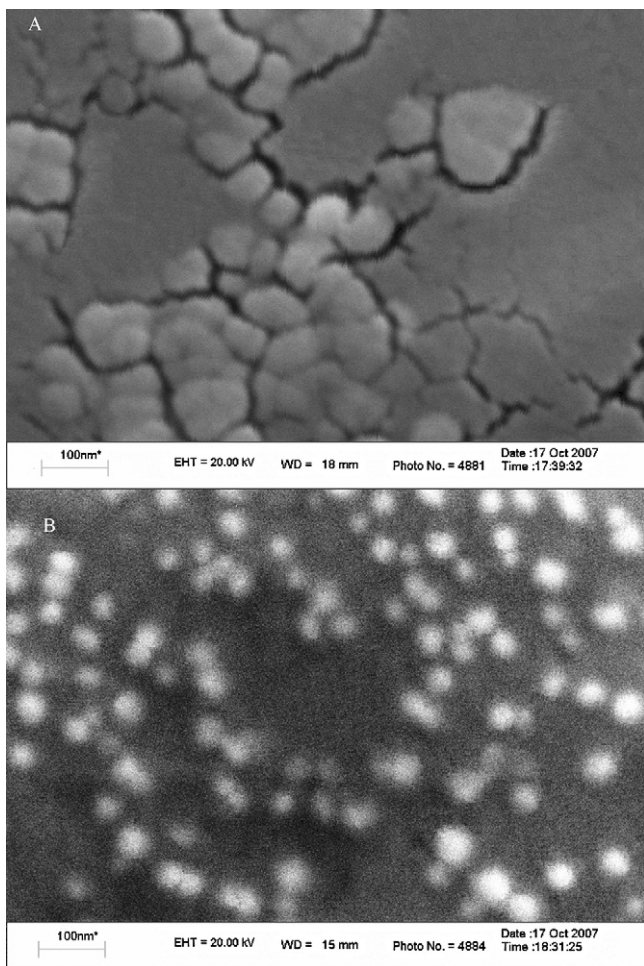
Fig. 1. SEM micrographics of synthesized AgNPs before and after of EDTA derivatization. (A) AgNPs and (B) AgNPs-EDTA.

3.2. Spectral characteristics of EDTA-AgNPs

UV–vis absorption spectra have proved to be quite sensitive to the presence of silver colloids because these nanoparticles exhibit an intense absorption peak due to the surface plasmon excitation [44]. The absorption band in visible light region (350–550 nm) is
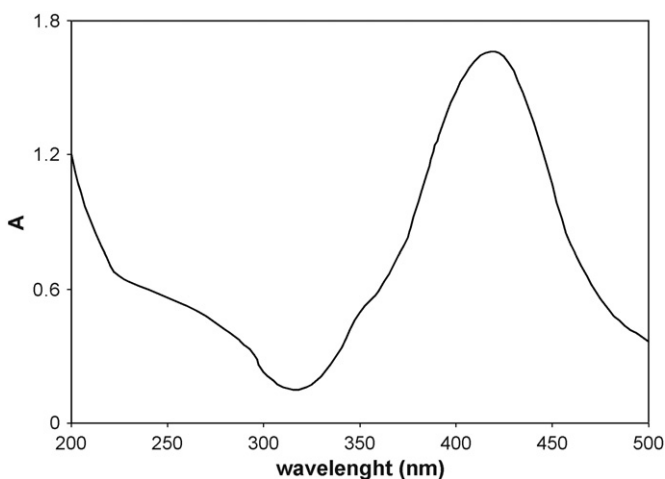

Fig. 2. Absorption spectrum of synthesized AgNPs-EDTA (λ_{max} = 415 nm).
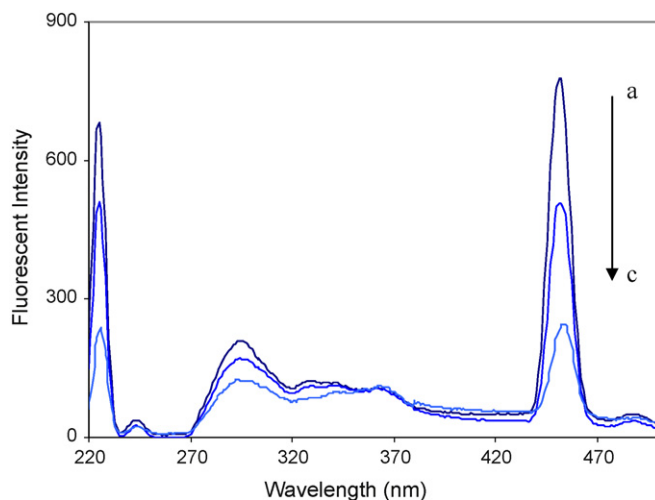
Fig. 3. Fluorescence spectra and SOS spectra of AgNPs-EDTA in absence and presence of NO_3^-. (a) Blank of the AgNPs-EDTA system (prepared as described in general procedure); (b) 1.25 μg mL^{-1} of NO_3^-; (c) 2.5 μg mL^{-1} of NO_3^-. Instrument conditions: λ_{ex} = 225 nm; slits of excitation and emission, both 5 nm.

typical for silver nanoparticles. With increasing particles size, the plasmon absorption shifts toward red.

The EDTA-AgNPs obtained showed an UV–vis absorption spectrum with a maximum at 415 nm [27,35,45] (Fig. 2). Proceeding with the spectral studies the synthesized nanomaterial was explored by fluorescent spectroscopy. These nanosized colloids presented an excitation and emission maximum at 225 and 295 nm, respectively (Fig. 3).

In presence of nitrate, the fluorescent emission decreased significantly; simultaneously to the fluorescence quenching, the SOS peak also decreased but in a more pronounced way (see Section 4.3). This observation led to the development of an ultra sensitive methodology using the derivatized silver nanoparticles as luminescent sensor for nitrate determination. Fig. 4 shows the SOS spectra beginning at excitation wavelength of 220 nm in step of 5 nm, in presence and absence of nitrates; the maximum ΔI is located at 225/450 nm for $\lambda_{ex}/\lambda_{em}$, respectively.

3.3. Quenching proposed mechanism

There exist a wide variety of substances which act as quenchers of fluorescence as well as different types of quenching process. Nitrate is considered an electron scavenger. This kind of quencher probably involves donation of electrons from the surface of nanoparticles to the quencher, deactivating the excitate state
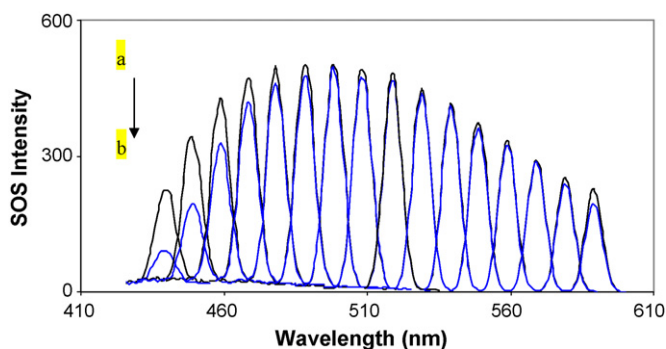
Fig. 4. SOS spectra of AgNPs-EDTA in presence and absence of NO_3^-. (a) AgNPs-EDTA system (prepared as described in general procedure); (b) system "a" with [NO_3^-]: 1.75 μg mL^{-1}. Instrumental condition: slit of excitation, 3 nm; slit of emission, 5 nm.

Table 1
K_{sv} values[a] for different experimental temperatures

Temperature (K)	K_{sv} value ($\mu g\,mL^{-1}$)
293	0.736
303	0.991
313	1.213
323	1.456

[a] EDTA-AgNPs systems prepared and measured as described in general procedure; [NO_3^-]: 0.00, 0.30, 0.60, 0.90, 1.20 $\mu g\,mL^{-1}$.

responsible of fluorescence [46]. It is well known that fluorescent emission and SOS are associated phenomena; consequently the fluorescence quenching of EDTA-AgNPs by nitrates affects directly to its SOS signals.

In order to determine the quenching type, a study of the K_{sv} (Stern–Volmer constant) from the modified Stern–Volmer equation (Eqs. (1) and (2)) was carried out at different experimental temperature conditions submerging the systems in thermostatic bath.

$$\frac{F_o}{F} = 1 + K_{sv}C_q \qquad (1)$$

Stern–Volmer equation for fluorescent quenching, where F_o and F are fluorescent emissions of the fluorofore in absence and presence of the quencher respectively; K_{sv} is the Stern–Volmer constant; and C_q is the concentration of the quencher.

Replace the term F_o/F by I_o/I:

$$\frac{I_o}{I} = 1 + K_{sv}C_q \qquad (2)$$

modified Stern–Volmer equation for SOS decrease; where I_o and I are SOS intensities of EDTA-AgNPs in absence and presence of nitrates, respectively.

The obtained K_{sv} values for each studied temperature are listed in Table 1. The linearity of the Stern–Volmer plot, as the value of K_{sv} which enhanced with increasing temperature (Fig. 5), indicated that the quenching mechanism of Ag-EDTA NPs by presence of nitrate is a single dynamic quenching [46].

The experimental results of decreasing SOS signals by nitrates showed a good fit to Stern–Volmer plots, giving linear relationship with quencher concentration. Additionally, the SOS signals present better sensitivity than the fluorescent emission; thus, the SOS signals were chosen for nitrate determination.
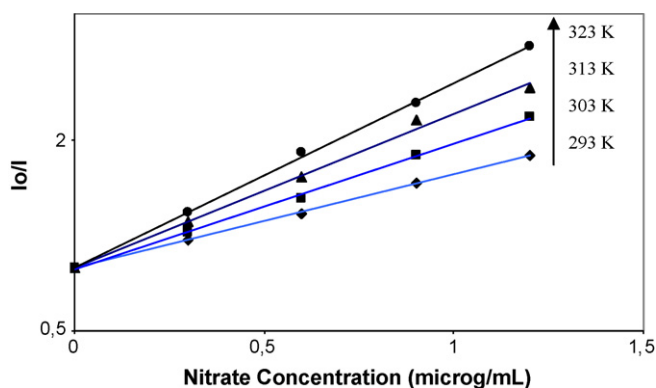
Fig. 5. Influence of temperature on AgNPs-EDTA SOS signals in presence of nitrate. [NO_3^-]: 0.00; 0.30; 0.60; 0.90; 1.20 $\mu g\,mL^{-1}$. Instrument conditions: $\lambda_{ex} = 225$ nm; $\lambda_{em} = 450$.
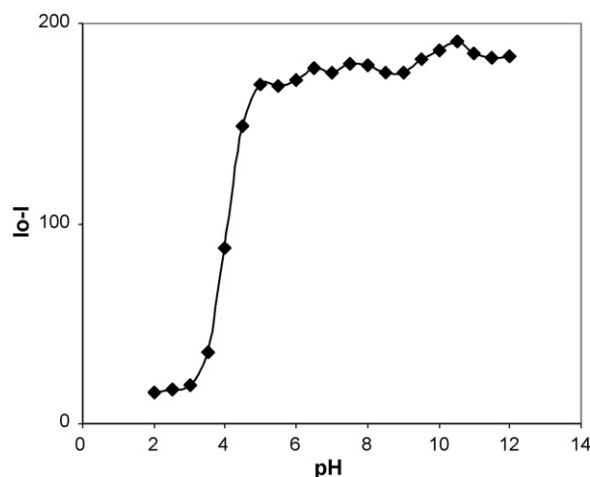
Fig. 6. Influence of pH on ΔI_{sos} of AgNPs-EDTA in presence of 1.25 $\mu g\,mL^{-1}$ NO_3^-; buffer: Tris (1×10^{-2} mol L^{-1}) adjusted with NaOH (d) or HCl (d).

4. Optimization of analytical parameters

4.1. Influence of pH

In order to study the influence of pH on the SOS signal, different buffers (TRIS, borax, phosphoric acid/phosphate, and acetic acid/acetate) were tested over pH range of 2.0–12.0 (Fig. 6). The SOS decrease value (ΔI_{SOS}) enhanced with increasing pH. At pH 10.5, ΔI_{SOS} reached a maximum value. Below pH 5.0, the ΔI_{SOS} decreased greatly and the EDTA-AgNPs solution color turn to red, regardless the assayed buffer nature. This change in color accompanied with bathochromic shift of plasmon absorbance, indicated the growth on the particles size [47]. The results showed that TRIS buffer provokes the most intensive luminescence and consequently, the best ΔI_{SOS}. Additionally, in this experimental condition, the stability of the system was optimal. Thus, 0.10 mol L^{-1} TRIS buffer was used for further experiments.

4.2. Effects of size and concentration of EDTA-AgNPs

When the time of AgNPs synthesis process is extended, a larger size of nanoparticles is obtained and in the fluorescence spectrum, the huge dispersion of the light produces an increase of the noise. After derivatization, the noise of fluorescent spectrum was

Table 2
Tolerance of potentially interfering substances[a]

Foreign substance	Tolerance ($\mu g/mL$)	Relative error (%)
Na^+	4600	−1.5
K^+	310	−2.2
Ca^{2+}	100	+2.1
Cu^{2+}	3.10	−3.7
Cd^{2+}	5.60	+2.3
Mg^{2+}	30	+1.2
Zn^{2+}	0.91	+4.5
Al^{3+}	16	+1.5
Fe^{3+}	6.70	−1.2
Pb^{2+}	0.20	+3.6
CH_3COO^-	630	−2.3
SO_4^{2-}	1900	+1.6
ClO_4^-	1000	−2.6
PO_4^{3-}	550	+3.1
Br^-	650	−4.5
Glucose	9000	+3.6

[a] Conditions: EDTA-AgNPs systems prepared and measured as described in general procedure, with coexisting concentration of NO_3^- of 0.1 $\mu g\,mL^{-1}$.

Table 3
Nitrate determination in parenteral solutions (recovery of the method[a])

Samples	Base value	Added ($\mu g\,mL^{-1}$)	Found ($\mu g\,mL^{-1}$)	Recovery[b] $\pm$ R.S.D.[c] (%)
A	–	0.000	0.006	–
	0.006	0.250	0.252	98.43 $\pm$ 1.89
	0.006	0.500	0.503	99.40 $\pm$ 1.77
	0.006	0.750	0.768	101.50 $\pm$ 2.21
B	–	0.000	0.009	–
	0.009	0.250	0.263	101.54 $\pm$ 1.45
	0.009	0.500	0.507	99.60 $\pm$ 2.10
	0.009	0.750	0.749	98.68 $\pm$ 1.87

[a] AgNPs-EDTA systems prepared and measured as described in general procedure.

[b] Recovery = $100 \times [(found-base)/added)]$.

[c] $n = 6$.

minimized; nevertheless, the decreasing of SOS and fluorescence quenching for these nanoparticles in presence of nitrate was not efficient. This phenomenon maybe due to the superficial activities diminution produced by the increase of the particles size and simultaneously, the reduced capability of nitrate to produce the deactivation process of the excited state.

The effect of EDTA-AgNPs concentration was studied for $1.25\,\mu g\,mL^{-1}$ of nitrate varying the volume of EDTA-AgNPs within the range of 0.25–3.0 mL. The SOS signals in absence and presence of nitrates (I_o and I) were both enhanced with the increase of EDTA-AgNPs concentration, remaining ΔI practically constant. Therefore, the concentration of EDTA-AgNPs chosen is given by the maximal intrinsic intensity obtained (blank signal) with constant excitation and emission slit widths. A volume of 1 mL EDTA-AgNPs was chosen as optimal.

4.3. Interference of foreign ions

The effects of the coexisting ions were tested according to the standard procedure and the results are listed in Table 2. The ions were considered no interference if the variation of the intensity was $< \pm 5\%$. The results indicated that the most of assayed ions could coexist at high concentration with nitrite, and for substances present in tested real samples like NaCl and glucose, the developed methodology could tolerate higher level of concentration than labeled values.

4.4. Analytical performance

Under the optimal experimental conditions, calibration curves for the determination of nitrate by SOS and fluorescence were obtained. By SOS decrease, the results showed a good linear relationship over the range 6.4×10^{-4} to $3.0\,\mu g\,mL^{-1}$. The linear regression equation was $\Delta I_{sos} = 228.50\,C\,(\mu g\,mL^{-1}) + 0.84$ with regression coefficient $r = 0.997$. The limit of detection (LOD) and quantification (LOQ) were calculated in accordance to the official compendia methods by $k(Sb)/m$, where $k = 3$ for LOD and $k = 10$ for LOQ, Sb is the standard deviation from 10 replicate blank measurements (Sb = 0.0146) and m is the slope of the calibration curve. The LOD estimated was $1.8 \times 10^{-4}\,\mu g\,mL^{-1}$; while for quenching of fluorescence emission the equation of calibration curve was $\Delta F = 34.40\,C\,(\mu g\,mL^{-1}) + 1$, value means lost of sensitivity compared with SOS technique.

4.5. Nitrate determination in parenteral solutions

The proposed method was applied to nitrate present in 1.0 mL commercial parenteral samples solutions giving values of 6 ppb of nitrate in sample A and 9 ppb in sample B. In order to validate the developed methodology, a recovery test was carried out

giving satisfactory results and presented in Table 3. Compared to other methodologies for nitrate determination [8,48,49] the present work has lower detection limit with the additional advantage of direct analysis of sample without pretreatment.

5. Conclusions

In this paper, a new modified silver nanoparticles (EDTA-AgNPs) have been synthesized and characterized (SEM, UV–vis and fluorescence spectroscopy). Through SEM images we could confirm that these EDTA-AgNPs were monodispersed in aqueous medium in contrast to before be derivatized. The fluorescent quenching and SOS decrease of these nanoparticles by presence of nitrate was studied. Quenching mechanism was proposed for SOS phenomenon. An innovative methodology was developed for ultra-trace nitrates quantification and successfully applied for its determination in commercial parenteral solutions. The main advantage of the proposed method is the possibility of direct nitrates determination with very good accuracy, sensitivity and tolerance, without the need of previous reduction to nitrite, neither any previous treatment for samples used. The obtained results showed that the EDTA-AgNPs can be applied as sensor for nitrate determination in real pharmaceutical samples.

References

[1] W. Lijinsky, Chemistry and Biology of N-Nitroso Compounds, Cambridge Monographs on Cancer Research, Cambridge University Press, Cambridge, 1992.
[2] S.W. Boese, V.S. Archer, J.W. O'Laughlin, Anal. Chem. 49 (1977) 479.
[3] K. Matsunaga, M. Nishimura, Anal. Chim. Acta 45 (1969) 350.
[4] F. Egami, S. Taniguchi, H.U. Berdmeyer (Eds.), Method of Enzymatic Analysis, Academic Press, New York, 1974, p. 2260.
[5] G. Wu, J.T. Brosnan, Biochem. J. 281 (1992) 45.
[6] S.B. Butt, M.Z. Iqbal, Talanta 55 (2001) 789.
[7] D. Connolly, B. Paull, Anal. Chim. Acta 441 (2001) 53.
[8] R.K. Mahajan, R. Kaur, H. Miyake, H. Tsukube, Anal. Chim. Acta 584 (2007) 89.
[9] N.V. Bondareva, L.P. Sadimenka, A.A. Kozhin, Zh. Anal. Khim. 51 (1996) 602.
[10] E. Wada, A. Hattori, Anal. Chim. Acta 56 (1971) 233.
[11] M.N. Abbas, G.A. Mostafa, Anal. Chim. Acta 410 (2000) 185.
[12] B. Paolo, A. Tiziana, B. Fugenio, Life Sci. 68 (2001) 2789.
[13] T. Aoki, S. Fukuda, Y. Hosoi, H. Mukai, Anal. Chim. Acta 349 (1997) 11.
[14] H. Wang, W. Yang, S.C. Liang, H.S. Zhang, Anal. Chim. Acta 419 (2000) 169.
[15] X. Zhang, H. Wang, S.C. Liang, H.S. Zhang, Talanta 56 (2002) 499.
[16] L.J. Dombrowski, E.J. Pratt, Anal. Chem. 44 (1972) 2268.
[17] G. Oshima, K. Nagasawa, Chem. Pharm. Bull. 20 (1972) 1492.
[18] E.D. Coppola, A.F. Wickroski, J.G. Hanna, J. Assoc. Off. Anal. Chem. 59 (1976) 783.
[19] H.D. Axelrod, N.A. Engel, Anal. Chem. 47 (1975) 922.

[20] J.S. Li, H. Wang, X. Zhang, H.S. Zhang, Talanta 61 (2003) 797.
[21] J.A. Creighton, D.G. Eadon, J. Chem. Soc. Faraday Trans. 87 (1991) 3881.
[22] Z.L. Jiang, F. Li, T.S. Li, H. Liang, Chem. J. Chin. Univ. 21 (2000) 1488.
[23] A.M. Qin, Z.L. Jiang, T.S. Li, L. Liao, Chin. J. Appl. Chem. 20 (2002) 1150.
[24] R.F. Pasternack, P.J. Collings, Science 269 (1995) 935.
[25] S.P. Liu, X.L. Hu, H.Q. Luo, Sci. China Ser. B 32 (2002) 18.
[26] O.P. Siwach, P. Sen, Spectrochim. Acta Part A 69 (2007) 659.
[27] Y. Luo, X. Sun, Mater. Lett. 61 (2007) 1622.
[28] S.F. Chen, Y.F. Li, C.Z. Huang, Talanta 70 (2006) 52.
[29] X.F. Long, H. Zhang, S.P. Bi, Spectrochim. Acta Part A 60 (2004) 1631.
[30] G.Z. Chen, X.Z. Huang, Z.Z. Zheng, J.G. Xu, Z.B. Wang, Fluorescence Analysis Method, Science Press, Beijing, 1990, p. 102.
[31] S.P. Liu, Z.F. Liu, M. Li, Acta Chim. Sinica 53 (1995) 1178.
[32] S.P. Liu, Z.F. Liu, M. Li, Acta Chim. Sinica. 53 (1995) 1185.
[33] N.B. Li, S.P. Liu, H.Q. Luo, Anal. Chim. Acta 472 (2002) 89.
[34] F. Ding, H.C. Zhao, S.L. Chen, J. Ouyang, L.P. Jin, Anal. Chim. Acta 536 (2005) 171.
[35] F. Ding, H. Zhao, L. Jin, D. Zheng, Anal. Chim. Acta 566 (2006) 136.

[36] X. Wang, B. Shen, H. Zhao, L. Jin, Anal. Sci. 23 (2007) 1373.
[37] http://Schererlab.uchicago.edu/pubs/100_Jin_JACS127_2005_suppl.pdf.
[38] B. He, J.J. Tan, K.Y. Liew, H. Liu, J. Mol. Catal. A Chem. 221 (2004) 121.
[39] Z. Jiang, W. Yuan, H. Pan, Spectrochim. Acta Part A 61 (2005) 2488.
[40] H. Pan, X. Tao, C. Mao, J.J. Zhu, F. Liang, Talanta 71 (2007) 276.
[41] J.A. Creighton, C.G. Blatchford, M.G. Albrecht, J. Chem. Soc. Faraday Trans. II 75 (1979) 790.
[42] S.M. Heard, F. Grieser, C.G. Barraclough, J. Colloid Interface Sci. 93 (1983) 545.
[43] B. Vickova, D. Tsai, X. Gu, M. Moskovits, J. Phys. Chem. 100 (1996) 3169.
[44] X. Gao, G. Gu, Z. Hu, Y. Guo, X. Fu, J. Song, Colloid Surface A 254 (2005) 57.
[45] P.C. Lee, D. Meisel, J. Phys. Chem. 86 (1982) 3391.
[46] J.R. Lakowicz, Principles of Fluorescence Spectroscopy, 2nd ed., Plenum Press, New York, 1999, pp. 239–240.
[47] Y. Xia, N.J. Halas, MRS Bull. 30 (2005) 338.
[48] J. Davis, M.J. Mooreroft, S.J. Wilkins, R.G. Compton, M.F. Cardosi, Analyst 125 (2000) 737.
[49] E. Ballesteros, A. Rios, M. Valcarcel, Analyst 122 (1997) 309.

On-line coupling of sequential injection lab-on-valve to differential pulse anodic stripping voltammetry for determination of Pb in water samples

Yang Wang, Zaiqing Liu, Xiaoya Hu*, Jinglian Cao, Fei Wang, Qin Xu, Chun Yang

College of Chemistry and Chemical Engineering, Yangzhou University, Yangzhou 225002, China

ABSTRACT

Sequential injection lab-on-valve (LOV) was first proposed for analyzing ultra-trace amounts of Pb using differential pulse anodic stripping voltammetry (DPASV) with a miniaturized electrochemical flow cell fabricated in the LOV unit. Deposition and stripping processes took place between the renewable mercury film carbon paste electrode and sample solution, the peak current was employed as the basis of quantification. The mercury film displayed a long-term stability and reproducibility for at least 50 cycles before next renewal, the properties of integrated miniature LOV unit not only enhanced the automation of the analysis procedure but also declined sample/reagent consumption. Potential factors that affect the present procedure were investigated in detail, i.e., deposition potential, deposition time, electrode renewable procedure and the volume of sample solution. The practical applicability of the present procedure was demonstrated by determination of Pb in environmental water samples.

© 2008 Published by Elsevier B.V.

1. Introduction

Differential pulse anodic stripping voltammetry (DPASV) has proved a powerful method for the characterization and quantitative detection of trace metals, analyte preconcentration onto a working electrode surface and metal deposition/stripping detection steps were involved during one electroanalytical circulation. Compared with many other analytical techniques, this procedure was recognized as the sensitive technique by features such as simplicity of use, great sensitivity and low cost of instrument [1,2]. However, routine DPASV procedure was laborious and large sample/reagent consumption when using batch mode operations, from this respect, which was not suitable for expensive samples analysis.

Sequential injection lab-on-valve (SI-LOV) introduced by Ruzicka provided an excellent alternative for sample pretreatment [3–8], which integrated all necessary laboratory facilities for a variety of sample manipulation operations, precise liquid manipulation, microliter levels sample and reagent consumption. So far, the sequential injection LOV system has exhibited many practical applications as the sample pretreatment front end [9–14]. In valve renewable beads were utilized as adsorption materials to separate and preconcentrate trace analytes coupled to electrother-

mal atomic absorption spectrometry (ETAAS) [15–18], inductively coupled plasma mass spectrometry (ICPMS) [19], atomic fluorescence spectrometry (AFS) [20] and liquid chromatography (LC) [21], these schemes eliminated the disadvantages of the conventional solid-phase extraction approaches. The lab-on-valve has also proved to be a new platform for miniaturization of instrumentation, a miniature atomic fluorescence spectrometric in the lab-on-valve system was designed for mercury and arsenic analysis, respectively [22–24]. In addition, by inserting optical fiber into the channels of multi-purpose flow cell in the lab-on-valve, fluorescence detection mode can be obtained and the applications of the above-mentioned procedure were demonstrated by DNA detection and purification [25,26].

The purpose of this study is to develop a simple, low sample/reagent consumption and automatic on-line anodic stripping voltammetry detection procedure coupled with SI-LOV system. The electrochemical flow cell (EFC) was designed as a part of the LOV unit, three electrodes were fabricated into the channels of LOV EFC, by on-line plating mercury solution onto the surface of carbon paste working electrode, a rapid separation/enrichment and determination procedure can be achieved when the sample solution passing through the EFC, the produced current during the stripping step can be associated with the amount of the analyte in the solution.

The feasibility of the established system was demonstrated by lead detection in environmental water samples. It has been widely recognized that exposure to the excessive lead can result in high

---

* Corresponding author. Tel.: +86 514 87975587; fax: +86 514 87975587.
E-mail address: xyhu@yzu.edu.cn (X. Hu).

blood pressure and hypertension, damage to the brain and nervous system with high levels of lead accumulation in their bodies [27,28]. In this respect, particular attention should be paid to screen the concentration of lead in the environmental samples because of their irreversible deleterious effects on the natural environment and the health of human [29,30]. Thus, lead was chosen as a model analysis material. Compared with batch mode operations, not only sample and reagent consumption were reduced, but also sampling frequency was enhanced, this characteristic is especially beneficial for minimizing electrochemical sample/reagent consumption and automatic analysis.

2. Experimental

2.1. Instrument

The sequential injection lab-on-valve system used in the present work consists of three independent components, as described in Fig. 1. A FIAlab-3000 sequential injection system (FIAlab Instruments, Bellevue, WA, USA) equipped with a 2.5 mL syringe pump (Cavro, Sunnyvale, CA, USA) was employed for sample and reagent delivery. The central part of the system, i.e., a homemade LOV unit, which was made of transparent plexiglass, incorporated an electrochemical flow cell with a volume of *ca*, 200 μL. The sampling port was set to port #3 while the waste was destined for port #8, the central channel was connected to a holding coil and other remaining ports were individually communicated with the central channel for fluidic arranged. The electrochemical signals measurements were performed with CHI660A electrochemical workstation (Chenhua Instrument, Shanghai, China).

A detailed electrochemical flow cell configuration is illustrated in Fig. 1, a three-electrode system consists of a 3 mm i.d. homemade carbon paste working electrode (CPE), a Ag/AgCl (3 mol L^{-1} KCl) reference electrode (RE) and a platinum wire auxiliary electrode. These electrodes were encapsulated into the LOV unit in line and the CPE was placed in the middle of the flow cell. In addition, the air bubbles in the solutions may adsorb on the electrode surface, which could cause negative effect in the deposition/stripping procedure. To minimize such effect, the port #7 of flow cell was designed to connect port #6 in the valve via a connecting tube, thus, the air bubbles adsorption could effectively minimize through this interface design.

All externally used tubes were made of 0.8 mm i.d. PTFE tubing (Upchurch Scientific, Oak Harbor, WA, USA) and the capacity of holding coil was 2.5 mL. The operations of the sequential injection lab-on-valve and date acquisition systems were synchronously controlled by FIAlab software and CHI660A Electrochemical Workstation for Windows, respectively.

2.2. Chemicals

All reagents used were at least of analytical reagent grade, and de-ionized water (18 MΩ cm^{-1}) was used throughout.

A 1000 mg L^{-1} Pb stock solution were prepared by dissolving 0.1598 g Pb(NO$_3$)$_2$ (Jinshan Chemicals, Shanghai, China) in 100 mL 1% (v/v) nitric acid. A 500 mg L^{-1} Hg (II) stock solution were prepared by dissolving 0.06778 g HgCl$_2$ (Tongyin Chemicals, Guizhou, China) in 100 mL 1% (v/v) hydrochloric acid. Working standard solutions were obtained by step-wise dilution. 0.1 mol L^{-1} acetate buffer (pH 4.6) was prepared by mixing the appropriate amounts of sodium acetate (Shanghai Chemicals Co., Shanghai, China) and glacial acetic acid (99.5%, Shanghai Chemicals Co., Shanghai, China). De-ionized water was employed as carrier stream and nitrogen gas (99.999%) was used for purging oxygen in a solution to provide an inert atmosphere inside the flow cell.

2.3. Preparation and activation of the carbon paste electrode

The working electrode was pretreated as follows: 0.5 g spectroscopic grade carbon powder and 0.3 g silicone oil were blended in an agate mortar and homogenized by a pestle, then the mixture were firmly packed into a 3 mm i.d. PTFE tube, into which a copper wire was plugged to establish electrical contact with the exterior equipment. Prior to measurement, the electrode surface was polished manually to obtain a fresh surface, then, the CPE was immersed in the 0.5 mol L^{-1} H$_2$SO$_4$ supporting electrolyte and cycled from −1.0 to 1.0 V at the scan rate of 100 mV s^{-1} until the reproducible background was obtained.
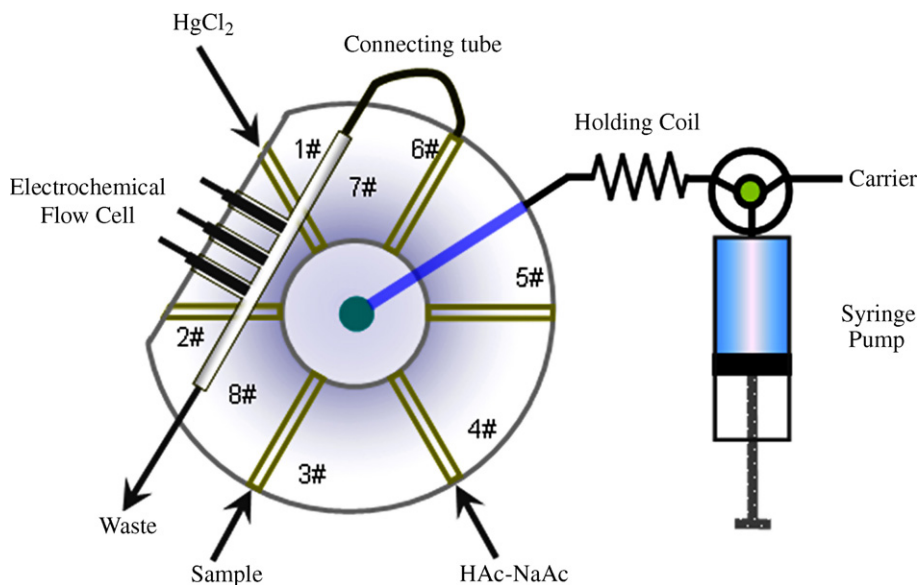
Fig. 1. Flow manifold of the sequential injection lab-on-valve (LOV) system with an integrated electrochemical flow cell for Pb determination with differential pulse anodic stripping voltammetry.

2.4. The operating procedure

The flow manifold used for the determination of Pb was illustrated in Fig. 1, a total operating cycle runs through the following steps:

2.4.1. Mercury film preparation

600 µL HgCl$_2$ solution from port #1 and 500 µL carrier solution from reservoir were sequential aspirated by syringe pump and stored in the holding coil, then the solutions were afterward dispensed through port #6 and transferred into the electrochemical flow cell at a flow rate of 5 µL s^{-1}, a potential of −1.0 V was subsequently applied to the CPE for 3 min and a thin layer of mercury film (MF) was plated onto the working electrode surface.

2.4.2. Deposition/stripping

400 µL sample and 500 µL buffer solutions were sequential aspirated into holding coil at a flow rate of 20 µL s^{-1} via ports #3 and #4. Afterwards, the mixed solutions were immediately dispensed through the electrochemical flow cell via port #6 at a flow rate of 17 µL s^{-1}, the analyte were deposited onto the MF electrode surface which was held at a −0.9 V to form alloys, afterwards, the Pb deposits were stripped from the electrode by scanning the potential from −0.9 to 0 V after a rest period of 10 s.

2.4.3. Renewal of MF electrode

The main disadvantage of MF electrode is its surface structural changes caused by amalgam formation in conventional DPASV analysis, which directly deteriorated its analytical performance. Moreover, the time-consuming cleaning treatments procedure did not beneficial to rapid and automatic analysis. The construction of renewal MF electrode in the LOV unit offered itself a suitable candidate for solving the aforementioned aspects, that is, the electrode surface was renewed to obtain the same electrochemical surface before each measurement or the electrode performance became deteriorated. In the present work, after *ca*, 50 deposition and stripping operation cycles, the MF was afterward directed to be electrochemically cleaned at a potential of 0.3 V for 20 s and another mercury (II) solutions would be aspirated to form a new MF for the ensuing processes.

3. Results and discussion

3.1. The optimization of the electrochemical parameters

In this assay, deposition time was tested for MF preparation, by fixing the concentration of mercury (II) at 500 mg L^{-1} and deposition potential at −1.0 V. The result indicated that only some areas of the CPE were coated with a deposition time of 1 min. With increasing deposition time up to 3 min, a thin layer of MF was full plated onto the CPE surface and high current intensity was obtained with good peak shape. Exceeding this deposition time, e.g., 5 min, the stripping shape, analytical precision became poor and the detection frequency was also reduced. After a compromise made by considering the analysis time and the current intensity, a deposition time of 3 min was employed for the MF preparation.

The supporting electrolytes were crucial to the performance of stripping procedure and different kinds of solutions were tested, including hydrochloric acid, sulfuric acid, nitric acid, acetate buffer and phosphate buffer. In the present assay, acetate buffer was found to give stable and sufficient signal from sample solutions, which was used for subsequent experiments. The pH of buffer was an important parameter for the stripping procedure, the effect of
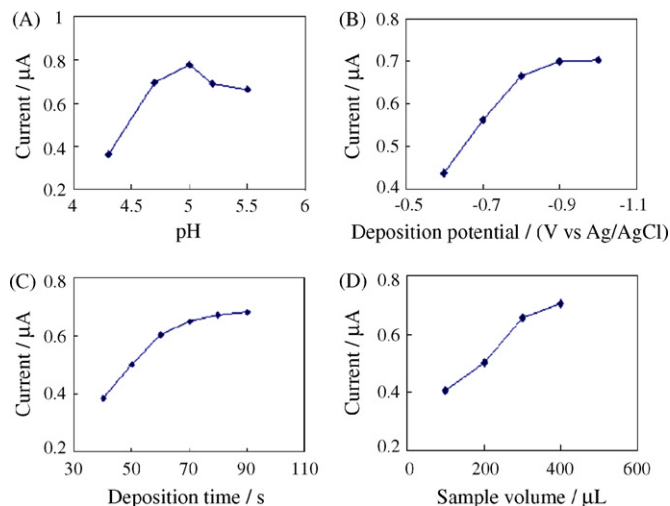
Fig. 2. The effects of chemical variables on the current intensity, the concentration and flow rate of the solution: 20 µg L^{-1} and 17 µL s^{-1}. (A) Deposition potential, −0.9 V; deposition time, 70 s; sample volume, 400 µL; (B) pH, 5.0; deposition time, 70 s; sample volume, 400 µL; (C) pH, 5.0; deposition potential, −0.9 V; sample volume, 400 µL; (D) pH, 5.0; deposition potential, −0.9 V; deposition time, 70 s.

acetate buffer pH on the stripping peak current was evaluated from 3.5 to 5.5. Fig. 2A demonstrated the relationship between the peak signal and the pH of acetate buffer, the signal intensity of the analyte increased with the pH from 3.5 to 5.0, thereafter, a decline of signal intensity was observed by further increasing the pH up to 5.5. This phenomenon indicated that the ionic strength of the supporting electrolyte had a large effect on the metal accumulation procedure. An appropriate pH value could enhance the stripping current intensity. However, the metals would like to form deposition compounds at a higher pH solution, resulting in the decline of the signal intensity, similar results have been also reported [31,32]. For further experiments a pH of 5.0 was used.

The effect of the deposition potential on the peak current was tested at a fixed Pb concentration of 20 µg L^{-1} and the results were shown in Fig. 2B. It was obvious that the peak current intensity was systematically improved with the increasing of deposition potential with a range from −0.6 to −0.8 V, which afterwards remained constant with further increase of deposition potential until −1.0 V. However, when more negative deposition potential was employed, the stability of peak current was deteriorated. This phenomenon could be explained by the reduced procedures of some other chemicals in the solution. Especially, the hydrogen evolution from the electrolyte solutions at such negative potential might destroy the metal alloys deposited process and produced negative effect on the subsequent signal determination [33]. Therefore the deposition potential of −0.9 V was selected as the best condition. The effect of deposition time was also studied and the obtained results were illustrated in Fig. 2C, an increase of analyte peak current was achieved with a deposition time from 40 to 90 s. When deposition time exceeds 70 s, the peak current changed slowly and the background current increased quickly. This can be attributed to the signal intensity would be limit to the defined volume and concentration of sample solution injected into the flow cell, which would resulted in the current signal obtained a maximal value in such system. At the same time, the ratio of signal to noise became poor with the deposition time prolonged, thus, a deposition time of 70 s was employed for the ensuing experiments in this assay, as a compromise of analysis frequency and signal intensity.
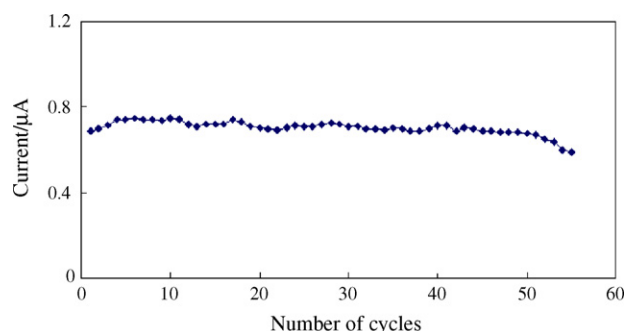
Fig. 3. The stability of the MF obtained within 55 cycles in the sequential injection lab-on-valve system. Pb concentration: $20 \, \mu g \, L^{-1}$; R.S.D.: 4.53% ($n = 55$).

3.2. The optimization of the SI-LOV parameters

The influence of sample flow rate on the electrochemical preconcentration process was researched. It was found that the current intensity increased linearly up to a sample flow rate of $17 \, \mu L \, s^{-1}$, this phenomenon could be explained that less dispersion was observed at higher flow rate, though the sample solution remains inside the flow cell for a long time at slower flow rate [34]. While afterwards a worsen peak signal was encountered with further increase in flow rate, probably due to the deterioration of MF on the electrode surface, which would directly lead the system performance, e.g., repeatability and precision became unacceptable. Accordingly, a sample flow rate of $17 \, \mu L \, s^{-1}$ was employed for further work.

The effect of sample volume ranged from 100 to $400 \, \mu L$ was investigated. As illustrated in Fig. 2D, the current intensity increased almost linearly up to $400 \, \mu L$. However, if a too large sample volume was employed, a longer sample loading and preconcentration time should be demanded. With consideration to the signal intensity as well as the sample analysis frequency, a sample volume of $400 \, \mu L$ was employed throughout.

3.3. The renewal of the MF electrode

The experiments indicated that the MF electrode surface was quite stable for dealing with the deposition and stripping procedure even after 50 successive scans with only $600 \, \mu L$ mercury (II) consumption. From this aspect, it is rational to employ MF electrode as a semipermanent component of the system and it is renewed only when peak current has been dropped during the stripping step or the analytical performance of the system has deteriorated. As illustrated in Fig. 3, after approximate 50 cycles, a rapidly declined peak current was observed, after which an electrochemical rinsing and a electrode surface renewable procedures were carried out as described in the previous operating procedure, where a fresh MF was deposited and made ready for the next circulation.

3.4. Effect of foreign species

To demonstrate the selectivity of the present developed procedure, the potential interferences in environmental samples were

Table 1
Comparison of the linear range and detection limit of a few published methods for determination Pb.

Electrode modifier	Linear range ($\mu g \, L^{-1}$)	Detection limit ($\mu g \, L^{-1}$)	Reference
Poly(3,4-ethylenedioxythiophene)	5–300	0.5	[35]
A Nafion-coated bismuth film	4–36	0.17	[36]
Bismuth film	5–45	0.5	[37]
Bismuth nano-powder	3–300	0.07	[38]
Bismuth/poly(p-aminobenzene sulfonic acid) film	1–130	0.8	[39]
Graphite-Epoxy	100–500	10	[40]
Mercury film	10–100	2.0	[41]
Mercury film	1–100	0.43	This work

tested by adding various concomitant substances into a standard solution containing $20 \, \mu g \, L^{-1}$ Pb. The tolerance level was defined, as the relative error produced by concomitant species not exceeded ±5%. The concentrations of alkali and alkaline earth metals in water samples have no evident influences during the deposition and stripping procedure. The common examined ions, e.g., $5.0 \times 10^{-3} \, g \, L^{-1}$ of Co^{2+}, Al^{3+}, Cr^{3+}, Mn^{2+}, Ni^{2+}, Zn^{2+}, Cl^-, Br^-, I^-, NO_3^-, CO_3^{2-}, $1.0 \times 10^{-3} \, g \, L^{-1}$ of Cd^{2+} and Cu^{2+} did not interfere (no tests for higher concentration levels). In addition, the present results indicated the coexisting organic ligands came from water samples also have no evident disturb in the determination of Pb stripping signal because of their low concentration in water samples. From the estimation results we can see the established system can be used to analysis practical samples without any masking reagent or dilution.

3.5. Performance of the procedure

All the experimental parameters in the present protocol were optimized using a univariate approach by fixed sample/reagent flow rate and concentration. The response was linear in the concentration range from 1.0 to $100.0 \, \mu g \, L^{-1}$ ($R^2 = 0.9989$) for Pb determination. With sample consumption of $400 \, \mu L$, a detection limit of $0.43 \, \mu g \, L^{-1}$ (3σ) was obtained with a precision of 3.14% R.S.D. at the level of $20 \, \mu g \, L^{-1}$, Regression equation of the calibration curves was $i_p = 0.0353 C_{Pb} + 0.0219$ (i_p: 10^{-6} A, C: $\mu g \, L^{-1}$) along with a sampling frequency of $45 \, h^{-1}$. Furthermore, the mercury film on the electrode can be used at least 50 times before next renewal.

It is obvious that the linear range and detection limit of the present protocol are superior to or at least at the same level as those of the published procedures using other electrode modifier with detection by DPASV, which are summarized in Table 1. It is also worth mentioning that the mercury (II) consumption of this assay is considerably decreased, moreover, the sample economy is evidently enhanced in comparison with the conventional electrochemical analytical system.

The developed procedure was validated by the analysis of two practical environmental samples: slim west lake water and tap water, which were filtrated through a $0.45 \, \mu m$ filter before immediately analyzed after collection. The analytical results were given in Table 2 and the spiked concentrations were obtained with good recoveries.

Table 2
Determination of trace levels of Pb in environmental waters by on-line hyphenation of SI-LOV with DPASV[a].

Samples	Determined by present method ($\mu g \, L^{-1}$)	Spiked ($\mu g \, L^{-1}$)	Found ($\mu g \, L^{-1}$)	Recovery (%)	R.S.D. (%)
Tap water ($n = 3$)	1.09 ± 0.32	0.50	1.58 ± 0.08	98.0	2.0
		1.00	2.12 ± 0.13	103.0	2.4
Slim west lake water ($n = 3$)	3.68 ± 0.62	3.00	6.75 ± 0.49	102.3	2.9
		8.00	11.99 ± 0.63	103.9	2.1

[a] The results were obtained at 95% confidence level.

4. Conclusions

This paper has described a novel SI-LOV-DPASV approach, the design of the integrated electrochemical flow cell in the LOV unit with renewable electrode surface manipulation made it as a promising electrochemical detection platform. The total processing was carried out in a closed channel system, which enhanced the repeatability of analysis procedure and minimized sample/reagent consumption. The feasibility of the present study was demonstrated by Pb determination in practical samples and the recoveries for the spiked water samples were satisfactory. Nevertheless, taking into consideration the pollution of mercury solution, the limited mercury solution consumption made it alternative electrode material in the field of electrochemical analysis.

Acknowledgements

References

[1] J.F. Van Staden, M.C. Matoetoe, Anal. Chim. Acta 411 (2000) 201–207.
[2] E.P. Achterberg, C. Braungradt, Anal. Chim. Acta 400 (1999) 381–397.
[3] J. Ruzicka, Analyst 125 (2000) 1053–1060.
[4] Y. Wang, J.H. Wang, Z.L. Fang, Anal. Chem. 77 (2005) 5396–5401.
[5] J.H. Wang, E.H. Hansen, Trends Anal. Chem. 24 (2005) 1–8.
[6] J.H. Wang, Anal. Bioanal. Chem. 381 (2005) 809–811.
[7] X.W. Chen, J.H. Wang, Anal. Chim. Acta 602 (2007) 173–180.
[8] H. Erxleben, J. Ruzicka, Analyst 130 (2005) 469–471.
[9] E.H. Hansen, M. Miró, Trends Anal. Chem. 26 (2007) 18–26.
[10] X.B. Long, M. Miró, R. Jensen, E.H. Hansen, Anal. Bioanal. Chem. 386 (2006) 739–748.
[11] X.B. Long, M. Miró, E.H. Hansen, J. Anal. Atom. Spectrom. 20 (2005) 1203–1211.
[12] M. Yang, Y. Xu, J.H. Wang, Anal. Chem. 78 (2006) 5900–5905.
[13] M. Yang, Y. Xu, J.H. Wang, Talanta 72 (2007) 1710–1716.
[14] J. Jakmunee, L. Pathimapornlert, S.K. Hartwell, K. Grudpan, Analyst 130 (2005) 299–303.
[15] J.H. Wang, E.H. Hansen, Anal. Chim. Acta 424 (2000) 223–232.
[16] J.H. Wang, E.H. Hansen, Anal. Chim. Acta 435 (2001) 331–342.
[17] M. Miró, S. Jończyk, J.H. Wang, E.H. Hansen, J. Anal. Atom. Spectrom. 18 (2003) 89–98.
[18] X.B. Long, M. Miró, E.H. Hansen, Anal. Chem. 77 (2005) 6032–6040.
[19] J.L. Burguera, M. Burguera, Spectrochim. Acta Part B 56 (2001) 1801–1829.
[20] Y. Wang, M.L. Chen, J.H. Wang, J. Anal. Atom. Spectrom. 21 (2006) 535–538.
[21] J.B. Quintana, M. Miró, J.M. Estela, V. Cerda, Anal. Chem. 78 (2006) 2832–2840.
[22] Y.L. Yu, Z. Du, J.H. Wang, J. Anal. Atom. Spectrom. 22 (2007) 650–656.
[23] H. Erxleben, J. Ruzicka, Anal. Chem. 77 (2005) 5124–5128.
[24] Y.L. Yu, Z. Du, M.L. Chen, J.H. Wang, J. Anal. Atom. Spectrom. 23 (2008) 493–499.
[25] X.W. Chen, W.X. Wang, J.H. Wang, Analyst 130 (2005) 1240–1244.
[26] X.W. Chen, Z.R. Xu, B.Y. Qu, Y.F. Wu, J. Zhou, H.D. Zhang, J. Fang, J.H. Wang, Anal. Bioanal. Chem. 388 (2007) 157–163.
[27] P.C. Kao, I. Schloegel, R. Cyr, Y.S. Leung, K. Dees, Clin. Chem. 43 (1997) 1251–1257.
[28] H.T. Delves, Analyst 95 (1970) 431–438.
[29] M. Tuzen, E. Melek, M. Soylak, J. Hazard. Mater. 136 (2006) 597–603.
[30] M. Yaman, Y. Dilgin, S. Gucer, Anal. Chim. Acta 410 (2000) 119–125.
[31] S.B. Hocevar, B. Ogorevc, J. Wang, B. Pihlar, Electroanalysis 14 (2002) 1707–1712.
[32] W.W. Zhu, N.B. Li, H.Q. Luo, Talanta 72 (2007) 1733–1737.
[33] R. Pauliukaite, C.M.A. Brett, Electroanalysis 17 (2005) 1354–1359.
[34] K.Y. Chumbimuni-Torres, P. Calvo-Marzal, J. Wang, E. Bakker, Anal. Chem. 80 (2008) 6114–6118.
[35] P. Manisankar, C. Vedhi, G. Selvanathan, P. Arumugam, Microchim. Acta 163 (2008) 289–295.
[36] H. Xu, L.P. Zeng, D.K. Huang, Y.Z. Xian, L.T. Jin, Food Chem. 109 (2008) 834–839.
[37] C. Kokkinos, A. Economou, I. Raptis, C.E. Efstathiou, Microchim. Acta 53 (2008) 5294–5299.
[38] G.J. Lee, H.M. Lee, C.K. Rhee, Electrochem. Commun. 9 (2007) 2514–2518.
[39] Y. Wu, N.B. Li, H.Q. Luo, Sens. Actuator B 133 (2008) 677–681.
[40] S. Carregalo, A. Merkoc, S. Alegret, Microchim. Acta 147 (2004) 245–251.
[41] S. Suteerapataranon, J. Jakmunee, Y. Vaneesorn, Talanta 58 (2002) 1235–1242.

Determination of nicardipine and amlodipine in human plasma using on-line solid-phase extraction with a monolithic weak cation-exchange column

Xiaoyi Wei [a,b], Gengliang Yang [a,*], Li Qi [a], Yi Chen [a]

[a] Beijing National Laboratory for Molecular Sciences, Laboratory of Analytical Chemistry for Life Science, Institute of Chemistry, Chinese Academy of Sciences, Beijing 100190, China
[b] Graduate School, Chinese Academy of Sciences, Beijing 100049, China

A B S T R A C T

An on-line solid-phase extraction (SPE)-HPLC method was developed for simultaneous screening of nicardipine and amlodipine in human plasma. A short monolithic poly(glycidyl methacrylate-co-ethylene glycol dimethacrylate) [p(GMA-EDMA)]-based weak cation-exchange (WCX) column was prepared and employed as the selective extraction sorbent, which exhibited good permeability and biocompatibility. During the on-line SPE protocol, high-abundance proteins (human serum albumin, immunoglobulin G, immunoglobulin A and transferrin) and most matrixes in plasma were fast removed while nicardipine and amlodipine were effectively trapped on this monolithic column. Furthermore, the monolithic WCX sorbent could be continuously reused more than 300 times without obvious changes in analytes extraction and proteins cleanup. The proposed method was linear over a range of 0.5–50.0 ng mL^{-1} for both analytes with a linear regression coefficient greater than 0.998, and the limit of detection (LOD) for each analyte was 0.2 ng mL^{-1}. Validation assays also demonstrated acceptable precision and adequate recovery for simultaneous quantitative screening of nicardipine and amlodipine in human plasma. Real plasma samples from hypertensive patients receiving a dosing of 5 mg antagonists were examined by using the proposed method. Results indicated that the on-line SPE-HPLC method could be applied for simultaneously monitoring of nicardipine and amlodipine in clinical plasma samples.

© 2008 Elsevier B.V. All rights reserved.

1. Introduction

Nicardipine and amlodipine (Fig. 1) are calcium antagonists with highly potent vasodilating activity and have been widely used for the treatment of hypertension, angina pectoris and cerebrovascular disease [1,2]. Because of their rapid absorption and extensive biotransformation in the liver [3,4], dihydropyridine (DHP) drugs including nicardipine and amlodipine often display relatively low concentrations (typically at a level of nanogram per milliliter) in human plasma after chronic oral administration. Therefore, sensitive and specific methods are essential for monitoring of DHP drugs in clinical samples. Various approaches have been reported for the quantitative analysis of nicardipine and amlodipine in plasma or serum [5–10]. Nevertheless, most approaches involve laborious and tedious extraction procedures prior to HPLC detection, which highly limits their applications in handling of a large number of samples from clinical researches. Fast and high-throughput sample pretreat-ment protocols are highly required. For this purpose, on-line SPE methods are proposed to enhance the analysis throughput and accuracy in virtue of their advantages of being less labor intensive and having better sensitivity [11,12].

Recently, a new type of SPE sorbents, monolithic material, has attracted considerable attention in sample pretreatments due to its superior porosity, good permeability and simple prepara-tion [11]. Our previous studies [13–15] showed the preparation of monolithic polymer columns and their versatile applications in selective extractions of β-lactam antibiotics and α$_1$-adrenergic receptor antagonists in human plasma and urine. We found that such biocompatible polymeric monoliths could greatly reduce the undesirable interactions between the stationary phase and the matrixes (typically human serum albumin) in biological fluids, thus allowing a great level of re-use, which was superior to the conven-tional SPE sorbents such as ODS C18 and silica particles.

In this study, a poly(glycidyl methacrylate-co-ethylene gly-col dimethacrylate) [poly (GMA-EDMA)]-based monolithic weak cation-exchange (WCX) column was prepared and subjected to an on-line SPE for sample cleanup and analytes trapping. High-abundance proteins in human plasma, including human serum albumin (HSA), immunoglobulin G (IgG), immunoglobulin A (IgA), and transferrin, were effectively eliminated whereas nicardipine

* Corresponding author at: Institute of Chemistry, Chinese Academy of Sciences, Zhongguancun North First Street 2, Beijing 100190, PR China. Tel.: +86 10 82627290; fax: +86 10 62559373.
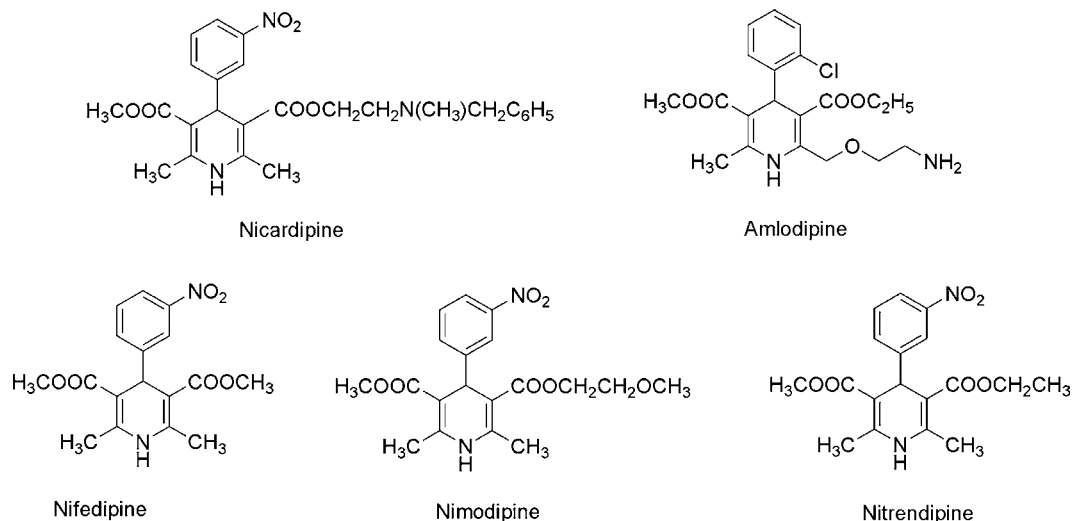 E-mail address: glyang@iccas.ac.cn (G. Yang).

Fig. 1. Chemical structures of the dihydropypidines.

and amlodipine were strongly retained, therefore the detection sensitivity and accuracy were correspondingly improved. Coupled with the HPLC system, the proposed method was successfully applied to simultaneously screen nicardipine and amlodipine in human plasma.

2. Experimental

2.1. Chemicals and materials

Glycidyl methacrylate (GMA) and ethylene glycol dimethacrylate (EDMA) were purchased from Acros (NJ, USA). 2,2′-Azobisisobutyronitrile (AIBN) was produced by Shanghai Chemical Plant (Shanghai, China) and refined before use. 1-Dodecanol and cyclohexanol were from Fuchen Chemical Plant (Tianjin, China). Ethylenediamine and chloroacetic acid were obtained from Xingjin Chemical Plant (Beijing, China). Nicardipine, amlodipine, nitrendipine, nifedipine and nimodipine were kindly provided by North China Pharmaceutical Co. (Shijiazhuang, China). Human serum albumin (HSA), human immunoglobulin G (IgG), human immunoglobulin A (IgA) and transferrin were all purchased from Xinjingke Biotechnology Co. Ltd. (Beijing, China). Other reagents were all of analytical reagent grade. Water was prepared from a triple distilled water system and solutions were filtered through a 0.45 μm membrane before use.

2.2. Preparation of the weak cation-exchange monolithic column

The monolithic WCX column was prepared as described elsewhere [15]. Briefly, a polymerization mixture of 0.5 mL GMA, 0.5 mL EDMA, 0.25 mL dodecanol, 1.75 mL cyclohexanol and 30.0 mg AIBN was prepared and homogenized in an ultrasonic bath for 10.0 min, and then purged with nitrogen for 5.0 min before being drawn by the stainless-steel tube (50.0 mm × 4.6 mm i.d.). The tube was then sealed at both ends and allowed to proceed at a 60 °C water bath for 24.0 h. After the polymerization, the column was flushed with methanol to remove the porogen and other soluble compounds present in the polymer rod. Then a mixture of ethylenediamine with tetrahydrofuran (1:1, v/v) solutions and a solution of 14.0% chloroacetic acid (pH 12.0) adjusted by sodium hydroxide were pumped through the column (at 0.05 mL min^{-1}) in steps at 80 °C for 24.0 h. Finally, the column was washed with 0.05 mol L^{-1} acetate buffer followed by deionized water until the eluent was neutral.

2.3. On-line SPE-HPLC procedure

The monolithic WCX rod was cut into 10.0-mm long pieces, and one of them was then fixed into a guard column (10.0 mm × 4.6 mm i.d.). Such column was used as an on-line SPE sorbent, which was placed in the sample-loop position of the injection valve. Firstly, when the six-port injector valve was on its "load" position, 50 μL of spiked plasma standards was directly injected into the column, and then 300 μL of 20 mM NaH$_2$PO$_4$ buffer (pH 7.2) was employed for selected washing at a flow rate of 0.2 mL min^{-1} (Fig. 2a). The direc-
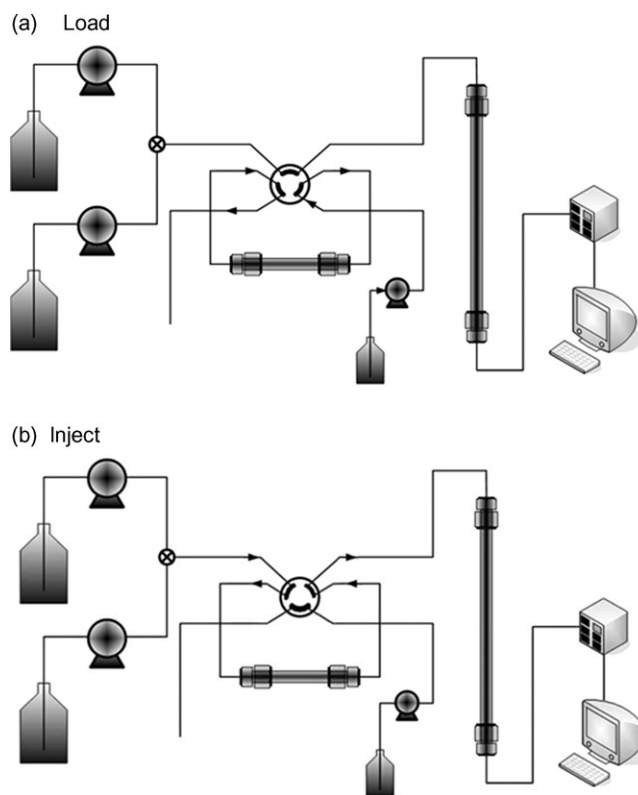
Fig. 2. Schematic diagrams of the proposed on-line SPE-HPLC method for the determination of analytes process. (a) "Load" position of six-port injector valve. (b) "Inject" position of six-port injector valve.

tion of the mobile phase flow during this step was indicated by arrows in the schematic. Most matrix materials (high-abundance proteins) were removed from the column to waste, while the analytes were focused and retained on the SPE monolith. After 1.5 min of washing, the six-port valve switched to "inject" position so that the pre-column and the analytical support were coupled online, as shown in Fig. 2b. The target analytes could be eluted in the back-flush mode by the mobile phase at an optimized flow rate of 1.0 mL min^{-1}, and then separated on the analytical column (Chromolith Performance RP-18e). Thus, a complete cycle of the on-line SPE pre-concentration and HPLC separation of the analytes was accomplished.

2.4. HPLC analysis

Chromatographic investigations were carried out with a Shimadzu LC-20A HPLC system (Shimadzu, Japan) consisting of a LC-20AT HPLC pump and a SPD-20A UV–Vis detector. Data processing was performed with a HW-2000 chromatography workstation (Nanjing Qianpu Software, China). Chromatographic separations were carried out on a Chromolith Performance RP-18e column (100 mm × 4.6 mm i.d. Merck Co.). The optimized mobile phase was 20 mM NaH$_2$PO$_4$ buffer at pH 3.0 and methanol, 40:60 (v/v). The flow rate was 1.0 mL min^{-1}, and the detection wavelength was 254 nm.

2.5. Preparation of plasma samples

A standard stock solution (100 μg mL^{-1}) of nicardipine and amlodipine samples was prepared in methanol, and then diluted in order to obtain six working solutions from 10.0 to 1000.0 ng mL^{-1}. Aliquots of 1.0 mL of blank human plasma were spiked with 50 μL each of working solutions to yield the plasma standards corresponding to 0.5, 1.0, 2.0, 5.0, 10.0, 50.0 ng mL^{-1}. These calibration standard solutions were vortex-mixed for 2.0 min and allowed to equilibrate at room temperature for 15.0 min.

Clinical plasma samples were obtained from anonymous hypertensive patients receiving an oral administration of 5.0 mg of nicardipine or amlodipine, respectively. Then the plasma standards and the clinical samples were stored at −20 °C prior to be applied on the on-line SPE-HPLC protocol.

3. Results and discussion

3.1. Online protein removal

Our previous study [15] showed that pH of the mobile phase might influence the surface electrical property of HSA, thereby affecting the retention of the protein on the WCX monolithic column. In the case of the human serum, albumin constitutes an overwhelming content of the total protein. Even following albumin
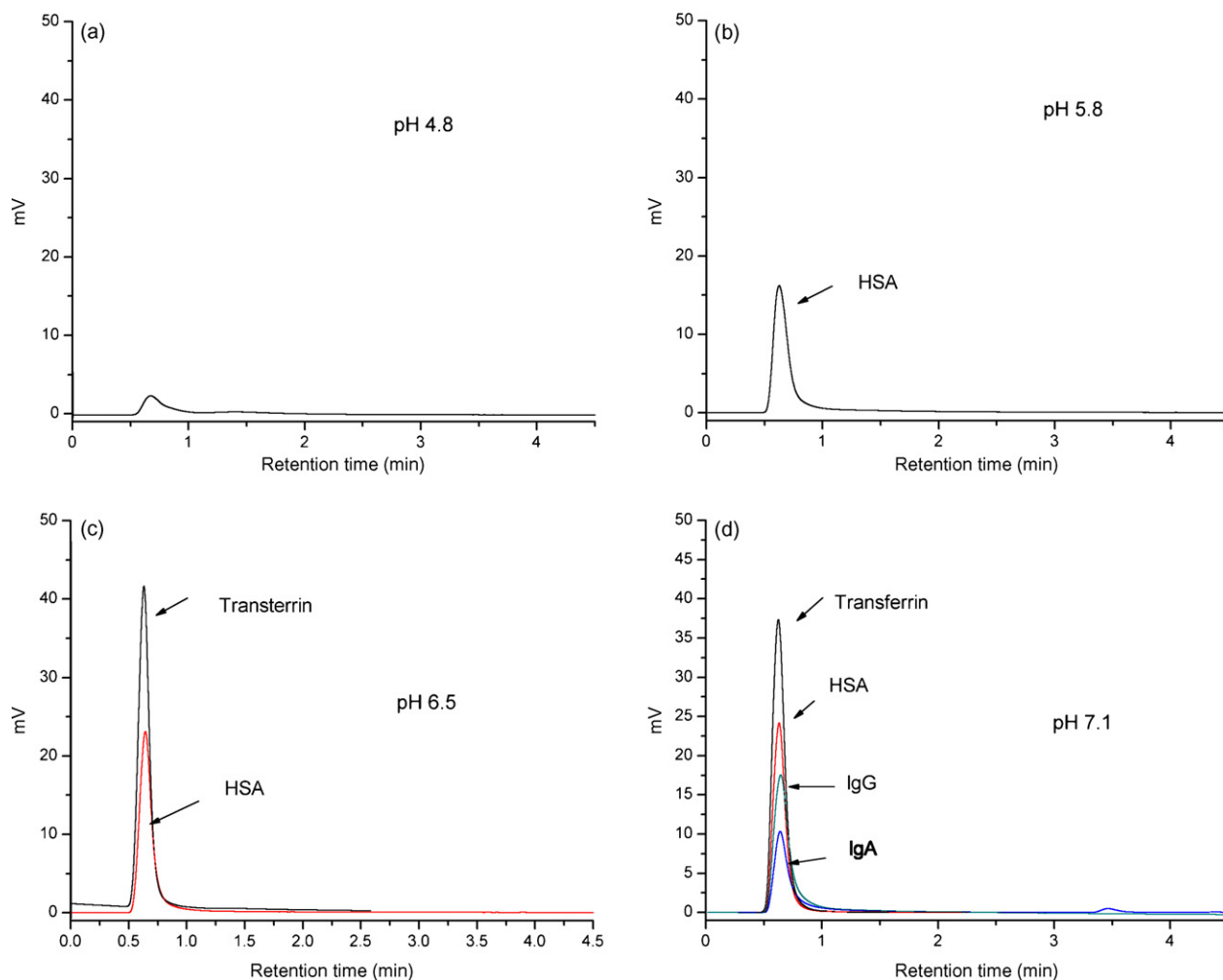
Fig. 3. Chromatograms for each protein at different pH. Experimental conditions: column, monolithic WCX column (50 mm × 4.6 mm i.d.); mobile phase, 20 mM phosphate buffer with different pH; detection wavelength, 280 nm.

removal, serum still remains a complex protein mixture with the inclusion of other high-abundance proteins (such as IgG, IgA, transferrin, haptoglobin, and antitrypsin) [16–18]. Collectively, these four-highest abundance proteins (HSA, IgG, IgA, and transferrin) constitute over 85.0% of the human serum proteome [19]. Therefore, removal of these proteins represents a fundamental improvement toward sample pretreatment of the biological fluids.

In this experiment, the effects of pH (phosphate buffer in the mobile phase) on the removal of the high-abundance proteins in human plasma were investigated, and the representative eluting chromatograms were shown in Fig. 3. As seen in Fig. 3a, four proteins were all retained on the column, and no peak was found when the pH of the phosphate buffer in the mobile phase was 4.8. As pH of the buffer increased to 5.8, only HSA (pI 4.9) was rapidly eluted while others were still retained. Subsequently, transferrin tended to be unretained when the value of pH was 6.5 over its pI 5.7 and eluted together with HSA (Fig. 3c). IgG and IgA, whose pI are near 7.0, were not eluted until pH of the mobile phase was above 7.1, where the four proteins were all eluted at pH higher than their isoelectric point (Fig. 3d). The results had been explained previously either that retention was dominated by the interactions between the negatively charged groups of the stationary phase and localized positively charged residues on the protein surface or that Donnan potential effects determined the protein partitioning into the stationary phase [20]. In this study, a higher pH elution was needed for removal of all four proteins at pH 7.2, with a high protein recovery of over 90.0%. It should be considered that besides these four high-abundance proteins, theoretically, other acidic proteins found in whole plasma [21], might also be eluted if the pH of the mobile phase was above their pI. Thus it would be speculated that most acidic matrixes were unretained and eluted rapidly at pH 7.2, the same as the four high-abundance proteins. Due to the removal of proteins in human plasma, there was less interference with the analytes, therefore "cleaner" chromatograms and higher detection sensitivity were obtained. In addition, due to the rapid removal of the proteins from the biocompatible monolith, it suggested that there was less undesirable irreversible adsorption between the matrixes in biological fluids and the column. As a result, this kind of SPE sorbents could be used more than 300 times while the permeability and the chemical property of the monolith were still suitable for sample pretreatment.

3.2. Characteristics of the monolithic WCX column

Due to the carboxyl groups at the surface of a hydrophobic skeleton, the prepared monolithic column can provide selectivity for alkali compounds mainly through ion-exchange and hydrophobic interactions. A total ion-exchange capacity of the column was calculated to be 1.6 mM g^{-1} according to the method described by Wei et al. [22]. To demonstrate the special selectivity of the monolith, five dihydropyridines (DHPs), including nicardipine, amlodipine, nitrendipine, nimodipine and nifedipine were used for further evaluation by varying the pH or ionic strength of the mobile phase.

The effects of pH on the retention of five analytes were investigated in Fig. 4. As can be seen, the analytes could be divided into two categories based on their chromatographic behaviors. Both nicardipine and amlodipine had a distinct change in the retention time within the pH range 2.0–7.0. However, the retention time of the other three analytes (nitrendipine, nimodipine, and nifedipine) kept almost constant during the experiments. This could be attributed directly to the changes in ionization of the carboxylate group on the polymeric monolithic stationary phase and the analytes. Considering the acid–base equilibrium of the analytes and the surface groups on the monolithic WCX column, nicardipine and amlodipine were dissociated due to their high pK_a (8.6, 9.0, respec-
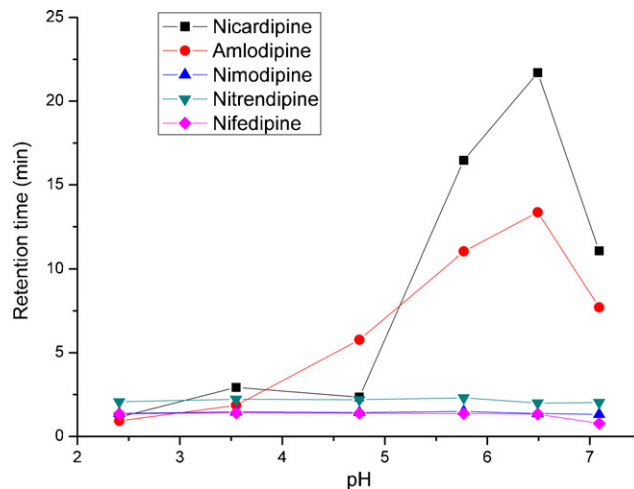

Fig. 4. Effects of pH in the mobile phase on the retention times of the DHPs. Experimental conditions: column, monolithic WCX column (50 mm × 4.6 mm i.d.); mobile phase, 20 mM phosphate buffer with different pH; detection wavelength, 254 nm.

tively) at low pH, thus a strong interaction between the negatively charged carboxylate functionality of the monolithic WCX column and the positively charged amine groups on the basic analytes took place. When the pH continued to increase to 7.0 near their pK_a, they tended to be in neutral forms, and the ion-exchange interaction was reduced. However, the hydrophobic interaction between the analytes and the polymer main chains was intensified and compensated for the reduction, leading to a slight decrease in the retention time [23]. On the other hand, nifedipine and the other two analytes were always in a state of deionization because of their low pK_a (especially the pK_a of nifedipine was below 1) during the whole pH range of the experiment. As a consequence, it was anticipated that the ion-exchange interaction was so weak that they had a constant and short retention time on the monolithic stationary phase. This result can probably be attributed to a number of interactions (mainly ion-exchange and hydrophobic interaction competition) between analytes and the stationary phase.

Further investigations were carried out into the effects of the different phosphate buffer concentrations in the mobile phase on the retention times of the five analytes at pH 7.2, and the data were shown in Fig. 5. It could be seen that the retention time of nicardipine and amlodipine decreased as the ionic strength of eluent increased, which is a typical behavior for separation of analytes in ion-exchange chromatography [24]. However, the retention times of the other three analytes had no obvious relation to the ionic strength of the eluent, which was also attributed to their weak ion-exchange interaction.

3.3. On-line SPE-HPLC protocol

As described above, HSA, IgG, IgA, transferrin and other matrixes in human plasma were rapidly removed when pH of the phosphate buffer in mobile phase was 7.2, where only nicardipine and amlodipine could be strongly retained on the WCX monolith. Therefore, nicardipine and amlodipine had been chosen for the next on line SPE-HPLC protocol. In the on-line SPE steps, the selective washing procedure was performed with 300 μL 20 mM NaH$_2$PO$_4$ buffer (pH 7.2). The protein matrixes in human plasma were removed from the column, whereas the two target analytes were focused and retained. If a higher pH value (>8) or larger amounts (>400 μL) of the buffer were used for washing, lower recoveries of the analytes were found. When sample pretreatment was carried out by means of this on-line SPE procedure, two target analytes were back
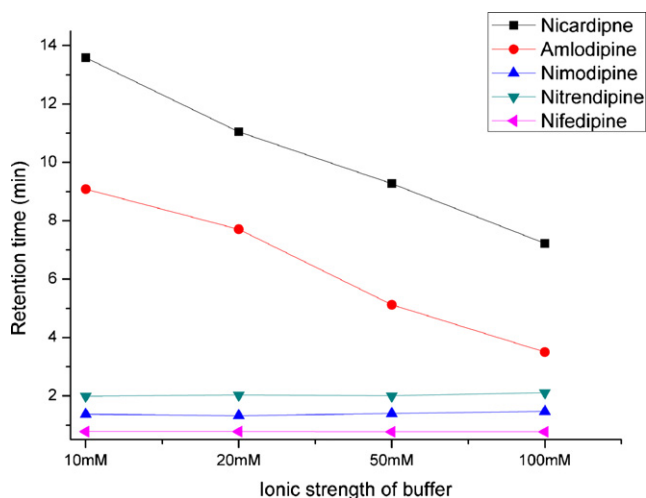
Fig. 5. Influences of phosphate buffer concentration on the retention times of the DHPs. Experimental conditions were similar with Fig. 4, except the mobile phase with various concentrations of phosphate buffer at pH 7.2.
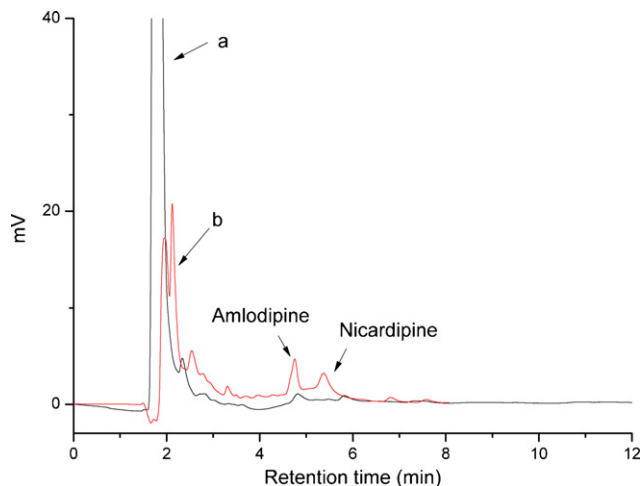

Fig. 6. Chromatograms for the determination of 50 μL nicardipine and amlodipine plasma samples at the concentration of 5.0 ng mL^{-1} with buffer (b) and 50 μL blank plasma without buffer (a). Mobile phase: 20 mM phosphate buffer at pH 3.0 and methanol, 40:60 (v/v); flow rate: 1.0 mL min^{-1}; column: 100 mm × 4.6 mm i.d.; UV detection at 254 nm.

eluted off the monolithic column to the analytical column for chromatographic separation. The sample elution solvent employed was 20 mM NaH$_2$PO$_4$ buffer (pH 3.0)/methanol (40:60, v/v), in order that the target analytes could be rapidly eluted, and the band broadening effect reduced before they entered the analytical column.

Under the optimized conditions, the on-line SPE-HPLC method was applied for determination of nicardipine and amlodipine in human plasma samples, and the chromatograms are shown in Fig. 6. From Fig. 6b, most proteins in human plasma were cleaned up dur-

Table 2
Concentrations of the target analytes in the clinical plasma samples

Sample	Analytes	Dosage (mg)	Sampling time (h)	Concentration (ng mL^{-1})
Sample 1	Nicardipine	5.0	2.0	0.87
Sample 2	Amlodipine	5.0	6.0	1.45
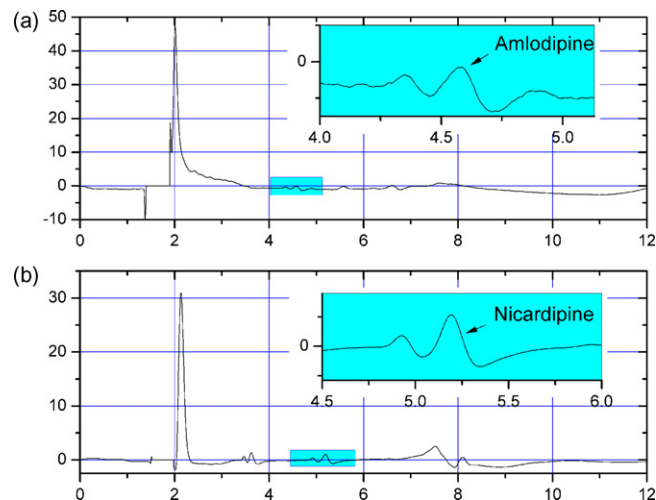
Fig. 7. Chromatograms of amlodipine (a) and nicardipine (b) in clinical plasma samples. Mobile phase: 20 mM phosphate buffer at pH 3.0 and methanol, 40:60 (v/v); flow rate: 1.0 mL min^{-1}; column: 100 mm × 4.6 mm i.d.; UV detection at 254 nm. "Retention time (min)" was used as abscissa, while "mV" was as ordinate.

ing the online SPE step, while nicardipine and amlodipine were well separated from interfering matrix components within 6 min. A control experiment (blank plasma) was investigated using similar conditions but without buffer eluting in the SPE procedure (Fig. 6a). Results showed that this on-line SPE technique was a highly selective and efficient samples preparation method for proteins removal.

3.4. Method validation

Quantitative analysis of nicardipine and amlodipine spiked in human plasma samples over the range of 0.5–50.0 ng mL^{-1} was accomplished using the on-line SPE-HPLC protocol.

Standard calibration curves were generated by spiking the standard solutions at six different concentrations of the two analytes in plasma. The correlation coefficient for each regression equation was better than 0.998 (Table 1). The limits of detection (LOD) and quantitation (LOQ) calculated at a signal-to-noise ratio of 3 and 10 were determined as 0.2 and 0.5 ng mL^{-1}, respectively. The intra-day precision was determined from the analysis on five independent quality control (QC) samples at three different concentrations (0.5, 5.0 and 50.0 ng mL^{-1}), while the inter-day precision was calculated by testing the same QC samples over three consecutive days. The recovery assays of the target analytes were assessed at 5.0 ng mL^{-1} by adding six replicates of the analyte standards to the blank

Table 1
Calibration curves, precision and recovery of analytes

Analytes	Range (ng mL^{-1})	Correlation coefficient	Intra-day precision[a]			Inter-day precision[a]			Recovery (%)
			0.5[b]	5.0[b]	50.0[b]	0.5[b]	5.0[b]	50.0[b]	
Amlodipine	0.5–50.0	0.9995	14.5	12.5	2.9	20.5	13.7	5.2	83.0
Nicardipine	0.5–50.0	0.9987	14.6	8.8	4.6	14.9	10.7	8.9	75.5

[a] Expressed as % relative standard deviation (R.S.D.).

[b] Concentration of the samples (ng mL^{-1}).

plasma. The results were shown in Table 1. The recoveries of two analytes were low, probably due to the serious adsorption between analytes and the glassware [25], however, the proposed method showed acceptable results for quantitative assay.

3.5. Clinical application

The proposed method was subsequently employed to analyze real clinical plasma samples. Samples were obtained from anonymous hypertensive patients who had taken orally 5.0 mg doses of nicardipine or amlodipine tablets, respectively. By interpolating the peak area on the calibration curve, the contents of each analyte in clinical plasma samples were obtained as listed in Table 2, and the chromatograms were shown in Fig. 7.

4. Conclusion

In this study, a poly(GMA-EDMA)-based monolithic weak cation-exchange column was successfully introduced into an on-line SPE-HPLC protocol for removing high-abundance proteins (HSA, IgG, IgA, and transferrin) and simultaneous screening nicardipine and amlodipine in human plasma. The developed method was also validated with linearity, inter- and intra-precision, recovery and applied for real clinical plasma samples.

The proposed method could reduce sample preparation steps and enable effective pre-concentration and cleanup of biological fluids. Besides, due to the good permeability and biocompatibility of the monolithic column, this SPE sorbent could avoid the undesirable interactions between the matrixes and the stationary phase, and be reused more times. Although the assay of recovery was not satisfactory this on-line SPE-HPLC method was still effective to remove most proteins in human plasma and appropriate for routine therapeutic analytes monitoring in plasma samples.

References

[1] E. Sorkin, S. Clissold, Drugs 33 (1987) 296.
[2] M. Haria, A.J. Wagstaff, Drugs 50 (1995) 560.
[3] S. Higuchi, Y. Shrobara, Xenobiotica 10 (1980) 447.
[4] D.A. Stopher, A.P. Beresford, P.V. Macrae, M.J. Humphrey, J. Cardiovasc. Pharmacol. 12 (1988) 55.
[5] K. Li, X. Zhang, Y. Yuan, F. Zhao, Biomed. Chromatogr. 12 (1998) 326.
[6] C.M. Fernandes, F.J.B. Veig, Biomed. Chromatogr. 17 (2003) 33.
[7] M. Qi, P. Wang, X. Jin, J. Chromatogr. B 830 (2006) 81.
[8] Y. Ma, F. Qin, X. Sun, X. Lu, F. Li, J. Pharm. Biomed. Anal. 43 (2007) 1540.
[9] A. Mohammadia, N. Rezanour, M.A. Dogaheh, F.G. Bidkorbeh, M. Hashem, R.B. Walker, J. Chromatogr. B 846 (2007) 215.
[10] K.R. Naidu, U.N. Kale, M.S. Shingare, J. Pharm. Biomed. Anal. 39 (2005) 147.
[11] J. Bones, K. Thomasb, P.N. Nesterenko, B. Paull, Talanta 70 (2006) 1117.
[12] J. Li, L. Chen, X. Wang, H. Jin, L. Ding, K. Zhang, H. Zhang, Talanta 75 (2008) 1245.
[13] G. Yang, H. Liu, Y. Zhang, S. Wang, J. Yin, B. Yin, Y. Chen, J. Chromatogr. A 1129 (2006) 231.
[14] G. Yang, S. Feng, H. Liu, J. Yin, L. Zhang, L. Cai, J. Chromatogr. B 854 (2007) 85.
[15] X. Wei, J. Yin, G. Yang, C. He, Y. Chen, J. Sep. Sci. 30 (2007) 2851.
[16] B.A. Chromy, A.D. Gonzales, J. Perkins, M.W. Choi, M.H. Corzett, B.C. Chang, C.H. Corzett, S.L. McCutchen-Maloney, J. Proteome Res. 3 (2004) 1120.
[17] Y. Tanaka, H. Akiyama, T. Kuroda, G. Jung, K. Tanahashi, H. Sugaya, J. Utsumi, H. Kawasaki, H. Hirano, Proteomics 6 (2006) 4845.
[18] D. Sitnikov, D. Chan, E. Thibaudeau, M. Pinard, J.M. Hunter, J. Chromatogr. B 832 (2006) 41.
[19] M.D. Seferovic, V. Krughkov, D. Pinto, V.K.M. Han, M.B. Gupta, J. Chromatogr. B 865 (2008) 147.
[20] T.M. Pabst, D. Antos, G. Carta, N. Ramasubramanyan, A.K. Hunter, J. Chromatogr. A 1181 (2008) 83.
[21] B. Herbert, P.G. Righetti, Electrophoresis 21 (2000) 3639.
[22] Y. Wei, X. Huang, R. Liu, Y. Shen, X. Geng, J. Sep. Sci. 29 (2006) 5.
[23] Y. Fan, Y. Feng, J. Zhang, S. Da, M. Zhang, J. Chromatogr. A 1074 (2005) 9.
[24] J. Dong, J. Ou, X. Dong, R. Wu, M. Ye, H. Zou, J. Sep. Sci. 30 (2007) 2986.
[25] P.Y. Cheah, K.H. Yuen, M.L. Liong, J. Chromatogr. B 745 (2000) 439.

Optical fiber evanescent wave absorption spectrometry of nanocrystalline tin oxide thin films for selective hydrogen sensing in high temperature gas samples

Qiangu Yan[a,*], Shiquan Tao[a,b,*], Hossein Toghiani[a]

[a] Dave C. Swalm School of Chemical Engineering, Box 9595, Mississippi State University, MS 39762, United States
[b] Department of Mathematics, Chemistry and Physics, WTAMU, Box 60787, West Texas A&M University, Canyon, TX 79016, United States

ABSTRACT

SnO_2 nanocrystalline material was prepared with a sol–gel process and thin films of the nanocrystalline SnO_2 were coated on the surface of bent optical fiber cores for gas sensing. The UV/vis absorption spectrometry of the porous SnO_2 coating on the surface of the bent optical fiber core exposed to reducing gases was investigated with a fiber optical spectrometric method. The SnO_2 film causes optical absorption signal in UV region with peak absorption wavelength at around 320 nm when contacting H_2–N_2 samples at high temperatures. This SnO_2 thin film does not respond to other reducing gases, such as CO, CH_4 and other hydrocarbons, at high temperatures within the tested temperature range from 300 °C to 800 °C. The response of the sensing probe is fast (within seconds). Replenishing of the oxygen in tin oxide was demonstrated by switching the gas flow from H_2–N_2 mixture to pure nitrogen and compressed air. It takes about 20 min for the absorption signal to decrease to the baseline after the gas sample was switched to pure nitrogen, while the absorption signal decreased quickly (in 5 min) to the baseline after switching to compressed air. The adhesion of tin oxide thin films is found to be improved by pre-coating a thin layer of silica gel on the optical fiber. Adhesion increases due to increase interaction of optical fiber surface and the coated silica gel and tin oxide film. Optical absorption spectra of SnO_2 coating doped with 5 wt% MoO_3 were observed to change and red-shifted from 320 nm to 600 nm. SnO_2 thin film promoted with 1 wt% Pt was found to be sensitive to CH_4 containing gas.

© 2008 Elsevier B.V. All rights reserved.

1. Introduction

Metal oxide gas sensors are the most commercialized type of gas sensors. Semiconductor metal oxides, such as tin oxide, zinc oxide, titanium oxide, zirconium oxide, indium oxide, etc. have long been investigated as sensing materials for sensing reducing gas, such as H_2, CO, CH_4 and other hydrocarbons, NH_3, H_2S [1–7]. These materials are usually made in the form of film, which is coated on a substrate, such as a silicon wafer or a glass. Traditionally, the films are insensitive to reducing gas at room temperature. However, if heated to a temperature above 200 °C, the resistance of such a film changes when exposed to a reducing gas component [8]. The working temperature range for this type of sensor are usually from 200 °C to 700 °C [9]. Tin oxide based semiconductor sensors have been reported for sensing reducing gas for a long time, and commercial products are available [10]. Titania (TiO_2) based semiconductor sensors have been used for sensing NO_2, NO and CO [11,12] and silicon carbide film for sensing hydrocarbons [13]. These sensors can

be operated at temperatures from 300 °C to 700 °C or even higher, and can detect gas components down to ppm levels [14]. One of the most important factors limiting the application of this class of sensors is that the sensors' lack of selectivity. SnO_2 film sensors can detect hydrocarbons, CO, NO and H_2 without distinguishing them. A TiO_2 semiconductor sensor responds similarly to NO, CO and NO_2. Although efforts have been made to improve the selectivity of these sensors, the results are not satisfactory [15,16].

Recently, optical fiber gas sensors for high temperature gas sensing have been attracting attention owing to several advantages over conventional electricity-based gas sensors. An optical fiber chemical sensor (OFCS) senses the existence and/or measures the concentration of a compound through detecting the interaction of the compound with light guided inside an optical fiber. These interactions include the absorption of light by the target compound, the excitation of the compound by light guided inside an optical fiber, and scattering of light guided inside an optical fiber caused by the compound. Therefore, almost all the traditional analytical spectroscopic techniques, such as ultra violet/visible (UV/vis) absorption spectrometry, infrared (IR) absorption spectrometry, Raman scattering spectrometry, and fluorescence (FL) spectrometry, can be used in

* Corresponding author. Tel.: +1 662 325 2480.
E-mail addresses: qy8@ra.msstate.edu (Q. Yan), stao@wtamu.edu (S. Tao).

OFCS development [17]. In addition, evanescent wave interaction based fiber optical spectrometric techniques are well suited for observing surface phenomenon because penetration depth of the evanescent wave is comparable to the wavelength (from several hundred nanometers to several microns) of light guided inside an optical fiber. Recent developments in surface plasma spectrometry and surface enhanced Raman spectrometry with fiber optical techniques are examples of surface phenomenon observation [18,19]. The advantages of fiber optical sensor techniques over conventional electric sensors for high temperature gas sensing include immunity to electromagnetic noise, less danger of fire ignition, capability of remote sensing, compatibility with optical fiber techniques to form sensor network, capability of selective sensing with spectroscopic recognition, and multi-component sensing [20–22].

The optical absorbance changes of nanomaterials have been reported in gas atmospheres [23]. Yasumoto et al. [24,25] found that some gas-sensing semiconductors, which were synthesized by sol–gel and sputtering methods, could change their optical transmittance by exposure to nitrogen monoxide. For example, CoO/SiO_2 nanocomposite films were deposited on a quartz-glass substrate with pulsed laser deposition in Ar without heating of the substrate. The optical transmittance changes caused by trace CO in dry air were measured in the wavelength of 625 nm at 350 °C using a spectrophotometer with a special quartz cell. The reversible transmittance change by 200 ppm as well as the sensing mechanisms was studied [26]. Guo and Tao synthesized silver and palladium nanoparticles with reversed micelle techniques and immobilized the metal particles in porous silica with sol–gel processes [27,28]. The obtained nanocomposite materials have been coated on the surface of optical fibers for designing fiber optical sensors for gas sensing at ambient temperature. A Pd/SiO_2 nanocomposite coating has been used for selectively sensing hydrogen and an Ag/SiO_2 nanocomposite coating has been used for selectively sensing ammonia [28]. Sensitivity and selectivity of metal oxide gas sensors can be modified by doping a small amount of second or third components [29–32]. Usually the doping method is based on the selection of the most effective catalyst that modifies some specific chemical reaction on the surface of the solid state gas sensor.

In this paper, we report the optical spectrometric response of a nanocrystalline SnO_2 material coated on the surface of an optical fiber core to reducing gases at high temperatures. The nanocrystalline SnO_2 material was coated on the surface of a bent optical fiber probe with a sol–gel process. A fiber optical evanescent wave absorption spectrometric method was used to observe the response of the nanocrystalline SnO_2 coating to gas samples containing reducing gas components at high temperatures. It was found that the SnO_2 coating absorbs UV light with peak absorption wavelength at around 320 nm when exposed to hydrogen containing nitrogen $(H_2–N_2)$ gas samples. However, this SnO_2 coating does not respond to other reducing gases, such as CO, CH_4 and other hydrocarbon gases, in the tested temperature range from 300 °C to 800 °C. To the best knowledge of the authors, no reports are available on the optical properties of a semiconductor metal oxide film. Pre-coating the optical fiber with a layer of silica gel was used to improve the mechanical strength of the tin oxide thin film. The influences of additional metal oxide MoO_3, and Pt metal on the optical spectrometric response of the SnO_2 film to hydrogen and methane gases were also investigated.

2. Experimental

2.1. Materials

Tin(IV)-isopropoxide $(Sn[OC_3H_7]_4)$ (10%, w/v) in isopropanol (72 vol%) and toluene (18 vol%), corresponding to the concentration of 0.23 M of tin-isopropoxide, was purchased from Alfa Aesar (USA) and used as received. A gold-jacketed optical fiber was received from Fiberguide Industries, Inc. (AFS300/330G, Stirling, NJ). This optical fiber has silica as a fiber core, porous silica as a cladding and a thin layer of gold on the top of the cladding as a jacket for mechanical protection. This fiber can work at temperature up to 800 °C. Gas samples (10 vol% $H_2–N_2$, 5 vol% $CH_4–N_2$, 10 vol% $CO–N_2$) were obtained from AirGas Inc. (Marietta, GA).

2.2. Instruments

An optical fiber compatible UV/vis spectrometer (Model SD-2000, Ocean Opticals Inc., Dunedin, FL) was used for recording evanescent wave absorption spectrum of specially prepared optical fiber probes. An optical fiber compatible deuterium/tungsten combo light source (Model DT-100 CE, Analytical Instrument System Inc., Flemington, NJ) was used to provide light in the wavelength region from 200 nm to 850 nm for the UV/vis spectrometric investigation. A split tube furnace (Model HST12/–/300/301, Carbolite Inc., Watertown, WI) with a programmable controller (Model HST 12/300, Carbolite Inc.) was used to control gas sample temperature. A specially designed quartz tube flow cell (30 mm inner diameter, 800 mm length) was used with this tube furnace. A dynamic gas calibrator (Model 146, Thermo Environmental Instruments Inc., Franklin, MA) was used to dilute a gas sample of high analyte concentration with nitrogen gas for making testing gas samples of lower analyte concentrations.

2.3. Preparing a bent optical fiber probe using a gold jacketed optical fiber

A bent optical fiber probe was prepared with a previously reported procedure [33,34]. In order to make a bent optical fiber probe, two ends of a gold-jacketed optical fiber were polished. A small part in the middle of the end-prepared optical fiber was inserted into a flame to melt the golden jacket. The resulting optical fiber core portion of the optical fiber was then further bent into a "U" shape while in the flame. After the optical fiber was cooled to room temperature, the bent fiber core part was soaked in a solution of $K_2Cr_2O_7/H_2SO_4$ for 30 min to wash off any organic materials possibly sticking on the surface of the bent part. The bent fiber core was then taken out from the solution and rinsed with deionized (DI) water. The bent part of the fiber was further soaked in a 2 M NaOH solution for at least 24 h to activate its surface hydroxyl groups.

2.4. Coating nanocrystalline SnO_2 material on the bent optical fiber core by sol–gel technique

Two coating methods were used for the tin oxide coating on optical fiber, in situ dip coating and ex situ sol–gel dip coating. These two coating methods were compared. Tin oxide coated on the optical fiber surface can be processed via in situ sol–gel dip-coating technique. For synthesizing pure SnO_2 thin films, a pre-cleaned bent optical fiber probe was dipped in the solution of tin-isopropoxide in isopropanol and toluene. After the dip-coating process, the probe was exposed to air for several hours. During this process, tin-isopropoxide on the surface of the bent optical fiber core was hydrolyzed and a tin oxide gel was formed on the surface of the fiber. The gel-coated fiber probe was then inserted into the split tube furnace and dried at 150 °C for 1 h while air was flowed through the tube flow cell. The substrates were dip-coated again using the respective solutions under similar conditions and then dried again at 150 °C for 1 h in air. Finally, the coated probe was calcined at 600 °C in air for 1 h, and then cooled to room tempera-

ture inside the furnace. Only thin film coating was obtained by this technique, the thickness of the film is under sub-micron level.

In order to obtain thick film coating, an ex situ sol–gel dip-coating method was used. Tin oxide gel was first prepared via sol–gel process: take 1 g of DI water in a bottle. Slowly add 1 g of the solution of tin-isopropoxide in isopropanol and toluene into the bottle, and then add 1 drop of 1 M HNO_3 into the solution while stirring for 1 h. Tin oxide gel was formed and ready for coating. Thick film coating can be obtained by dip coating tin oxide gel.

2.5. Improve adhesion of the optical fiber to the tin oxide thin film by pre-coating with a layer of silica gel film

Sol–gel technique has proved to improve the mechanical quality of thin film deposited on the optical fiber surface. The pre-treated optical fiber was first coated with a layer of silica gel thin film. The silica sol solution used in this work was made by hydrolyzing TMOS with trace hydrochloric acid as a catalyst. To prepare the sol solution: 2 ml of TMOS was mixed with 1 ml water (30 μl of 0.1 M HCl solution was added) for ∼5 min. A clear solution was obtained after hydrolysis. This solution was used to coat the bent part of the optical fiber. The silica gel coated optical fiber was dried at room temperature in the air overnight, and then the SnO_2 thin film was coated following the procedure described in Section 2.3.

2.6. Doping MoO_3 and platinum on tin oxide thin films

Thin films of MoO_3 and platinum-doped tin oxide were also prepared by the sol–gel dip-coating experimental setup. 5 wt% MoO_3 and 1 wt% Pt were doped in the tin oxide thin film, respectively. The coated probe was calcined at 600 °C in air for 1 h, and then cooled to room temperature inside the furnace.

2.7. Optical fiber evanescent wave absorption spectrometry (OF-EWAS)

The OF-EWAS is different from traditional optical absorption spectrometry. When light travels through a fiber, total internal reflection produces an "evanescent wave" on the interface between the fiber core and the sol–gel coating. The evanescent wave is a kind of wave tending to vanish along the direction perpendicular to the interface of the two media. In this method, a conventional optical fiber, which has a coating on the surface of the optical fiber core, is used. The optical fiber core is used for sensing light from a light source to a sample, which is the cladding coated on the surface of the fiber core. This specially coated fiber is connected with a light source and an optical fiber compatible optical spectrometer. The optical absorption signal of OF-EWAS can be described by using the Lambert–Beer law described by the following equation [35,36]:

$$A_{EW} = \log\left(\frac{1}{T}\right) = \gamma\varepsilon CL = \gamma\varepsilon C\left(\frac{d_p}{n_2 \sin\theta / a(n_1^2 - n_2^2 \sin^2\theta)^{1/2}}\right)$$

In this equation, A_{EW} is the absorbance; T is the transmittance; γ is the ratio of optical power flowing in the cladding over total light power guided through the optical fiber; ε is the absorption coefficient of the analyte in the coating, C is the concentration of the analyte; L is the length of the interaction, which equals the penetration depth (d_p) times the number of total internal reflections; the number of total internal reflections is calculated as $(1/n_2 \sin\theta)/a(n_1 - n_2^2 \sin^2\theta)^{1/2}$, as light travels a length of inside the optical fiber; the penetration depth depends on the wavelength of the incident light (λ), the refractive indices of the fiber core

(n_1) and the sol–gel coating (n_2), and the angle of incidence (θ) according to the relationship:

$$d_p = \frac{\lambda}{2\pi\sqrt{n_1^2 \sin^2\theta - n_2^2}}$$

In an optical fiber the evanescent wave propagates in the sol–gel tin oxide coating parallel to the interface of the fiber core and the sol–gel coating. The amplitude of its electric field decays exponentially along the direction perpendicular to the incident plane. The evanescent wave penetrates a certain distance into the sol–gel coating. The penetration depth describes the distance from the interface to where the intensity of the evanescent field has decreased to 1/e of the initial intensity. Hence the higher the penetration depth, the higher is the sensing signal. The sensitivity of the fiber optical evanescent field absorption sensor based on a U-shaped probe increases with the decrease in the bending radius of the probe [37]. The increment occurs up to a certain value of the bending radius which depends on the fiber numerical aperture and core diameter. Therefore a U-shape bent probe was used in the current experiments.

2.8. Investigating the optical spectrometric properties of the tin oxide thin film with an OF-EWAS

The optical properties of the SnO_2 thin film were investigated with an OF-EWAS method. The optical absorption signal of the tin oxide coated on the surface of the optical fiber core is observed. The instrument set-up for this investigation is shown in Fig. 1. Light from the deuterium/tungsten combo light source was connected to one end of the coated bent optical fiber probe. The second end of the bent optical fiber probe was connected to the optical fiber compatible UV/vis spectrometer. The coated bent optical fiber probe was deployed inside the quartz gas flow cell which is inserted into the split tube furnace. During the test, the tube furnace was heated to certain temperature and kept at the temperature. A gas sample was flowed through the quartz flow cell and the optical absorption spectrum of the coated optical fiber probe was recorded with the optical fiber compatible spectrometer.

2.9. Characterization of the tin oxide thin films

Temperature-programmed reaction (TPR) of tin oxide was performed by means of an automated catalyst characterization system AutoChem II 2910, which incorporates a thermal conductivity detector (TCD). However, all the processes were monitored and measured by an on-line Quadrupole MS. Before starting TPR runs, the sample, 0.02 g, was activated under flowing air at 600 °C for 60 min. TPR experiments were carried out at a heating rate of 10 °C/min. The reactive gas compositions were H_2 (10.2 vol%)/Ar for
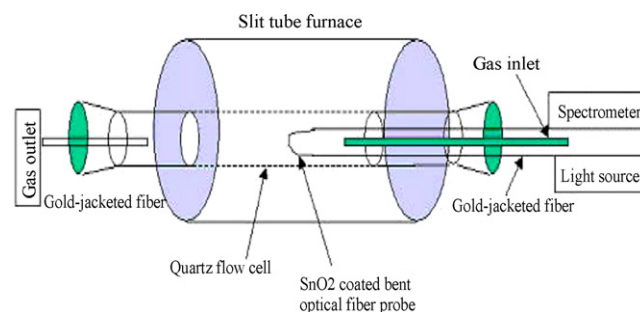

Fig. 1. A diagram of the testing system for investigating the optical properties of sol–gel derived silica optical fibers.

TPR. The TPR experiments were performed up to a temperature of 900 °C.

The physical properties (BET area, etc.) of tin oxide samples have been determined by N_2 adsorption–desorption (Quantachrome, Autosorb-1). Prior to measurements, the samples were degassed at 300 °C overnight.

The morphology of the tin oxide samples was investigated with a scanning electron microscopy (SEM) equipped with an energy-diffusive X-ray spectroscopy (EDX) attachment (JEOL JSM-6500F), which could simultaneously provide the surface elemental composition information. Tin oxide coated optical fiber samples were pre-coated with gold before introduced into the vacuum chamber. Adhesion was measured by direct pull-off (DPO) method [38].

3. Results and discussion

3.1. SnO₂ thin film structure, morphology and properties

The surface morphology of the SnO_2 coating on the bent optical fiber probe and the thickness of the coating were analyzed with SEM. Fig. 2a shows a SEM image of the SnO_2 thin film coated on an optical fiber surface by in situ sol–gel coating. Detailed SEM analysis was conducted for the SnO_2 film (Fig. 2b) to determine the nature of the crystalline aggregates that were observed. The particle diameter evaluated from Fig. 2b was found to be 10–20 nm. The SnO_2 thin film in Fig. 2b is homogeneously dispersed and porous network version over the optical fiber surface. It can be seen clearly that the crystalline SnO_2 crystal clusters in the SEM image. The thickness of the coating is below 1 μm (Fig. 2c). Thick film coating can be obtained by ex situ sol–gel coating with alumina sol–gel. The coating thickness can be between 1 μm and 5 μm. The BET surface area of the tin oxide sample was 129.75 m²/g.

The reducibility of the fresh tin oxide was examined by temperature programmed reduction. Prior to temperature programmed reduction experiments, the tin oxide sample was activated under flowing O_2 (10 vol%; balance He) at 600 °C for 90 min. TPR experiments were carried with a heating rate of 10 °C/min. The reactive gas compositions were H_2 (10.2 vol%/balance Ar). Fig. 3 shows TPR profiles of the fresh tin oxide prepared by sol–gel method. At least three hydrogen consumption regions are observed in the tin oxide profile. The first region is from 120 °C with peak centered at around 270 °C and could be attributed to the reduction of chemisorbed oxygen or surface hydroxyl on the tin oxide surface. The second region of hydrogen consumption is observed at 400 °C, this peak can correspond to surface O^{2-} species in tin oxide. Bulk SnO_2 shows a broad reduction band with one peak at ∼850 °C.

3.2. OF-EWAS of SnO₂ coating exposed to reducing gas at 600 °C

The optical absorption spectrum of the SnO_2 coating on the surface of a bent optical fiber probe exposed to a 1 vol% H_2–N_2 gas sample was investigated by using optical fiber evanescent wave absorption spectrometry. In this experiment, the temperature of the furnace was kept at 600 °C. Pure N_2 gas was first flowed through the quartz flow cell and light intensity guided through the SnO_2 coated bent optical fiber probe was recorded as reference intensity. A 1 vol% H_2–N_2 gas sample was then flowed through the quartz flow cell and the absorption spectrum of the coated optical fiber was recorded. Fig. 4 shows the recorded evanescent wave absorption spectrum in UV/vis region. In the UV/vis region, an absorption spectrum with peak absorption wavelength at around 320 nm was recorded when a 1 vol% H_2–N_2 gas sample was flowed through the quartz flow cell, while there is no absorption peak was found when the tin oxide thin film coated optical fiber was exposed to either
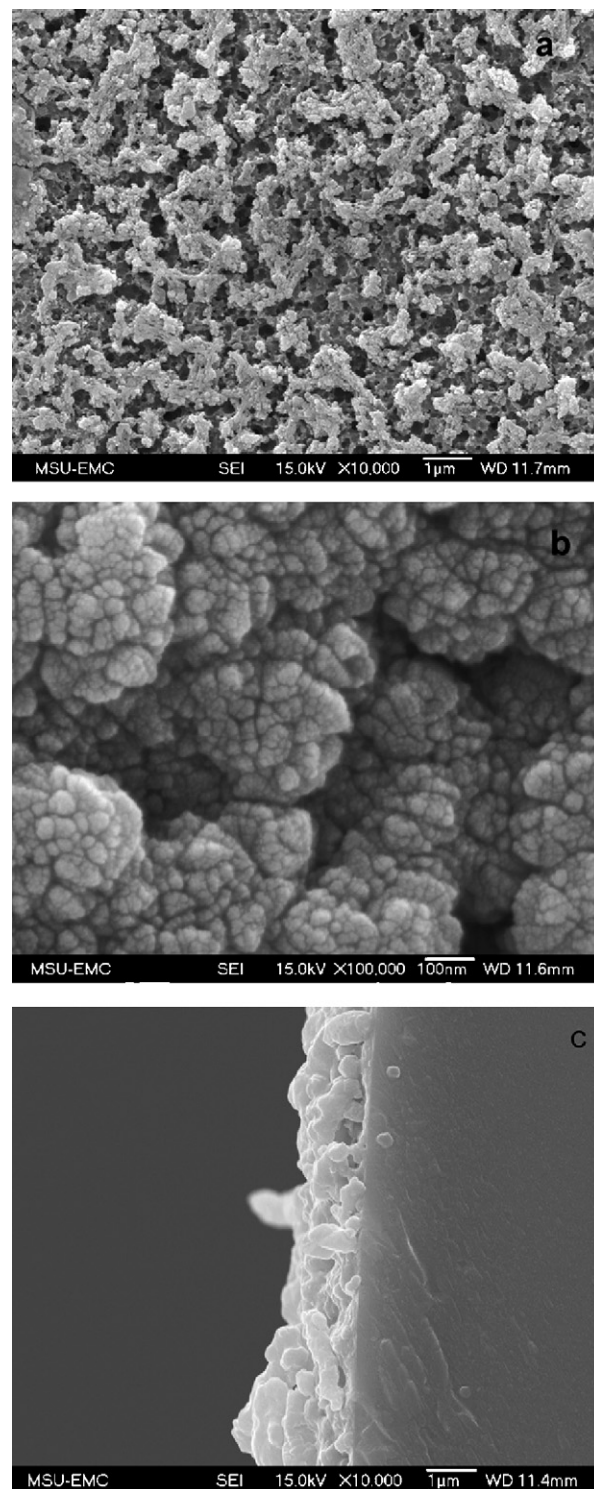

Fig. 2. SEM image of the coated SnO_2 thin film over an optical fiber.

of CH_4–N_2 or CO–N_2 gas samples. When the SnO_2 coating on the optical fiber probe was exposed to nitrogen gas samples containing 5% CH_4, there was no optical absorption signal observed in the UV/vis region. When the SnO_2 coating on the optical fiber probe was exposed to nitrogen gas samples containing 5% CO, optical absorption signal in the UV/vis region was not observed even when the temperature of the gas sample was increased up to 800 °C. In traditional semiconductor metal oxide membrane sensors, almost all
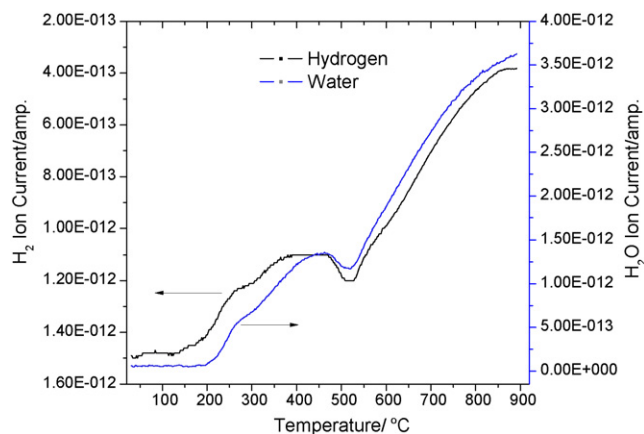
Fig. 3. TPR spectra of tin oxide prepared by sol–gel technique.

the reducing gases cause the change of resistance of the film. These sensors can only detect the existence of reducing gases, but cannot discriminate between the gases, and therefore, the sensors lack of selectivity for sensing individual reducing gases. From the recorded evanescent wave absorption spectra in this work, it is clear that the optical absorption spectrum can be used as a finger-print to discriminate between H_2, CH_4 and CO, and selective sensing of these gases can be achieved.

3.3. OF-EWAS of SnO_2 coating exposed to reducing gas at different temperatures

The optical properties of the SnO_2 coating on the optical fiber probe exposed to reducing gas at different temperatures were investigated following the method described above. When a 1 vol% H_2–N_2 mixture was used as a sample gas, the SnO_2 coating starts to show absorption signal from ca. 300 °C. The intensity of the absorption signal increased with the increase of temperature in the tested range up to 800 °C (Fig. 5). It is expected that with the increase of temperature more hydrogen molecules diffused into the pores of the SnO_2 coating, will be decomposed and more nascent hydrogen atoms are available to react with surface absorbed oxygen ions. Thus, with the increase of temperature, the absorption signal increased. It was also observed that with the increase of temperature, the peak absorption wavelength of the absorption spectrum
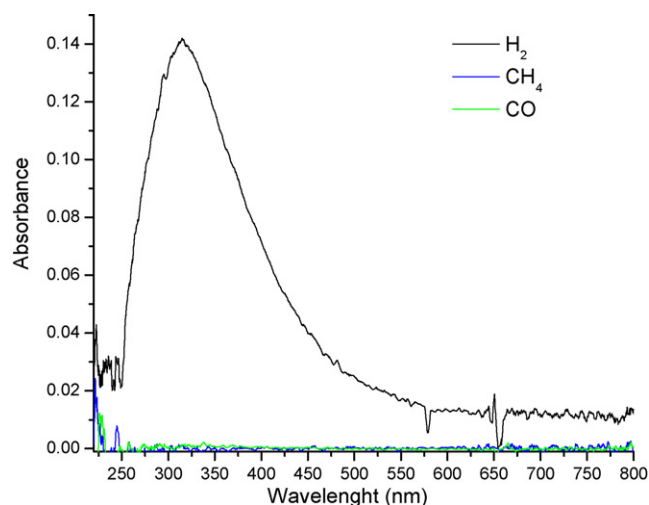
Fig. 4. UV–vis absorption spectra of a SnO_2 thin film optical fiber sensor response to 1 vol% H_2, 5 vol% CH_4 and 5 vol% CO in N_2 flows at 600 °C, respectively.
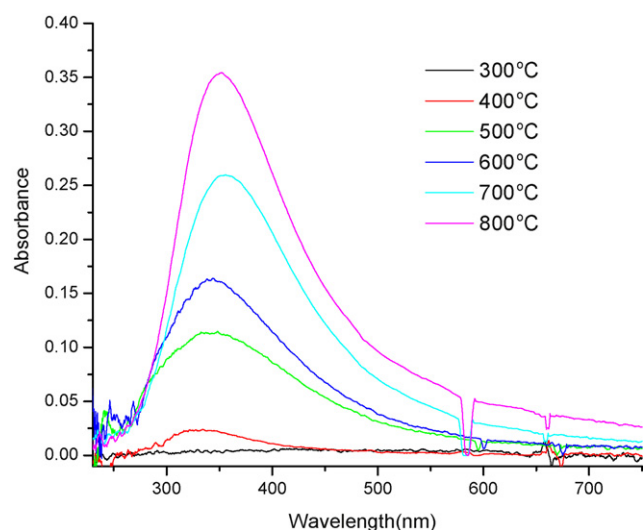
Fig. 5. UV–vis absorption spectra of a SnO_2 thin film optical fiber sensor response to a 1 vol% H_2–N_2 flow under different temperatures.

was a little red-shifted. The peak wavelength shift was considered to be the result of energy level shifting accompanying the increase of temperature.

3.4. Calibration of the SnO_2 coating on the optical fiber probe for quantitatively sensing H_2 in an inert gas sample

The evanescent wave absorption signal of the SnO_2 coating on the surface of the optical fiber probe in UV/vis region has been evaluated for quantitatively sensing hydrogen concentration in a nitrogen gas sample. In this test, the 10 vol% hydrogen containing nitrogen gas sample was diluted with pure nitrogen by using the dynamic calibrator and the obtained gas samples were flowed through the quartz cell inside the split tube furnace. The temperature of the furnace was kept at 600 °C. The obtained absorption spectra of the probe exposed to nitrogen gas samples containing hydrogen of different concentrations are shown in Fig. 6a. With the increase of hydrogen concentration in the gas sample, the absorption signal increased. The relationship of the absorbance (Abs.) with the concentration of hydrogen (C_{H_2}) in the nitrogen sample is shown in Fig. 6b; these data were calibrated; the calibration curve can be described by follow equation:

$$Abs. = 0.082 \ln(C_{H_2}) + 0.145.$$

3.5. OF-EWAS and response times of thick and thin SnO_2 coating films exposed to reducing gas

Fig. 7a shows the dependence of sensitivity to 1 vol% H_2 in N_2 under 600 °C operating temperature for the thick coated and thin films spin-coated tin oxide and sintered at 600 °C. The maximum absorbance of tin oxide film in H_2 flow increased with increasing the thickness of the film.

The time response of the SnO_2 coating on the bent optical fiber probes for sensing H_2 in a nitrogen gas sample was tested. In this test, the source gas sample was switched from pure N_2 to 1 vol% H_2–N_2 mixture and the evanescent wave optical absorption signal of the SnO_2 coated bent optical fiber probe deployed inside the quartz gas flow cell was continuously monitored. The recorded result is presented in Fig. 7b. As shown in Fig. 7b, under the experimental conditions in this study, the absorption signal
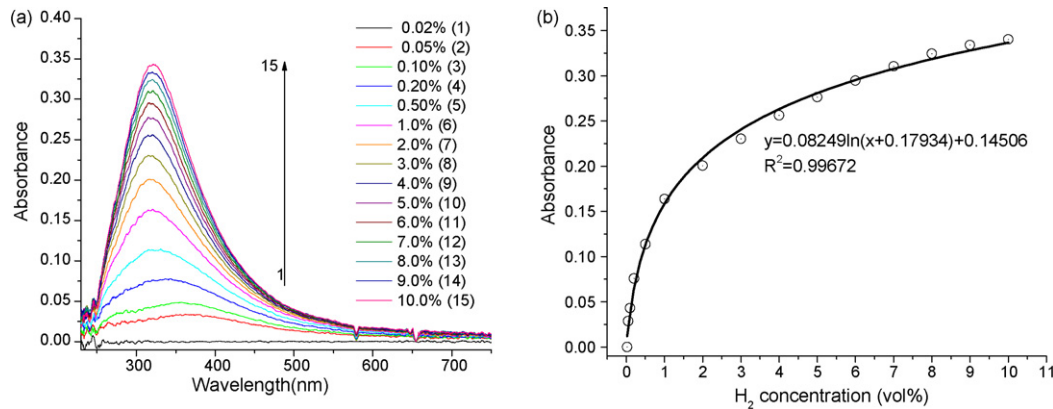
Fig. 6. UV–vis absorption spectra of a SnO_2 thin film optical fiber sensor response to H_2–N_2 flows with different H_2 concentrations at 600 °C (a) and correlation between the gas-sensitive absorbance of the thin film optical fiber sensor and the concentration of H_2 at a wavelength of 320 nm (b).

of the thin film reaches the steady-state signal intensity within 10 s, while it takes the thick film more than 10 min to achieve steady absorbance. The volume of the quartz flow cell used in this work is 0.24 L. The flow rate of the gas sample is 1 L/min. The change of hydrogen concentration in the flow cell from zero (pure nitrogen) to 1% needs approximately 1 min under the experimental conditions used in this work. Therefore, the response time of the SnO_2 coating for gas sensing should be within seconds.

The response time of this SnO_2 coating for sensing H_2 is faster compared with the response time of some reported semiconductor metal oxide membrane based sensors [16,26]. It was believed that the capability of using a very thin SnO_2 coating in this work is responsible of this fast response of this sensing technique. In optical fiber evanescent wave absorption spectrometry, the penetrate depth of evanescent wave is comparable to the wavelength of the light guided through the fiber. Therefore, it is possible to using a coating with thickness in the sub-micron range as a sensing film.

3.6. Replenishing of oxygen in tin oxide thin films

The restoring of oxygen in the tin oxide thin films was investigated in this study. When the sample gas was switched from 1 vol% H_2–N_2 to nitrogen, the optical absorption signal decreased with time. Fig. 8 shows the recorded changes of the absorbance signal. It takes about 20 min for the absorption signal to reach the baseline after the gas sample was switched to nitrogen since

there is trace of oxygen/moisture in nitrogen gas (Fig. 8a). If the gas sample was switched to compressed air, the absorption signal decreased quickly (in 5 min) to the baseline (Fig. 8b). These results also suggest that the change of surface-adsorbed oxygen-ion concentration is responsible for the probe's ability to sense H_2 gas.

3.7. Improvement in the mechanical properties of tin oxide thin films with SiO_2 modification

Numerous researchers have reported the electrical and optical properties of tin oxide but very few on the mechanical properties. Adhesion is one of the important properties, which provides the information about the interaction between the film–substrate interfaces. The adhesion of the tin oxide thin film to the surface of the optical fiber was investigated. The adhesion was measured by direct pull off method [38]. The adhesion of tin oxide thin films to the optical fiber is around 3.8×10^5 N/m^2, while the adhesion of the thin films to the optical fiber pre-deposited with a layer of silica gel is above 5×10^5 N/m^2. So, a SiO_2 thin layer can improve the adhesion of the contacts to the SnO_2 film, adhesion increases may due to increased interaction of optical fiber surface and the coated silica gel and tin oxide film. Fig. 9 presents the UV–vis absorption spectra of a SnO_2 thin film optical fiber sensor pre-coated with a layer of silica gel response to H_2–N_2 flows at 600 °C, it is found that pre-coated a layer of silica gel does not change the UV–vis absorption spectra of the tin oxide thin film.

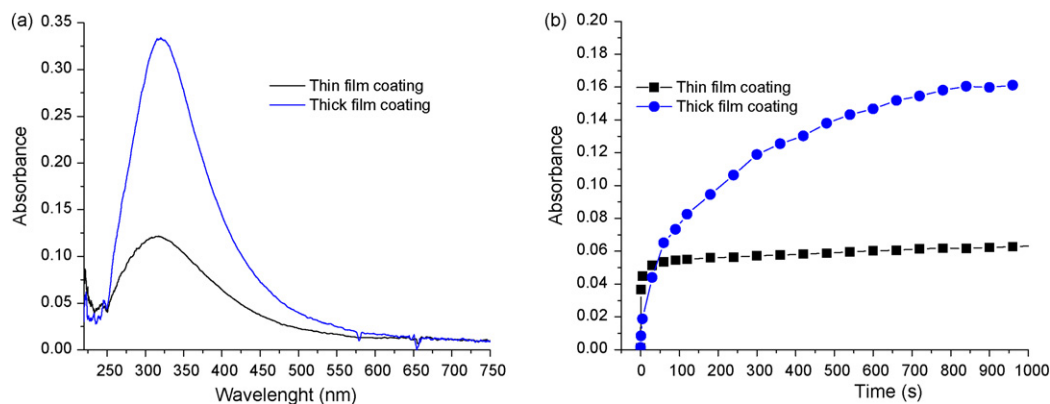**Fig. 7.** Typical UV–vis absorption spectra of SnO_2 thin film and thick film coated optical fiber sensor response to a H_2–N_2 flow at 600 °C (a) and time response of the absorbance of SnO_2 thin film and thick film coated optical fiber sensors to a 1 vol% H_2–N_2 flow at a wavelength of 320 nm under 600 °C (b).
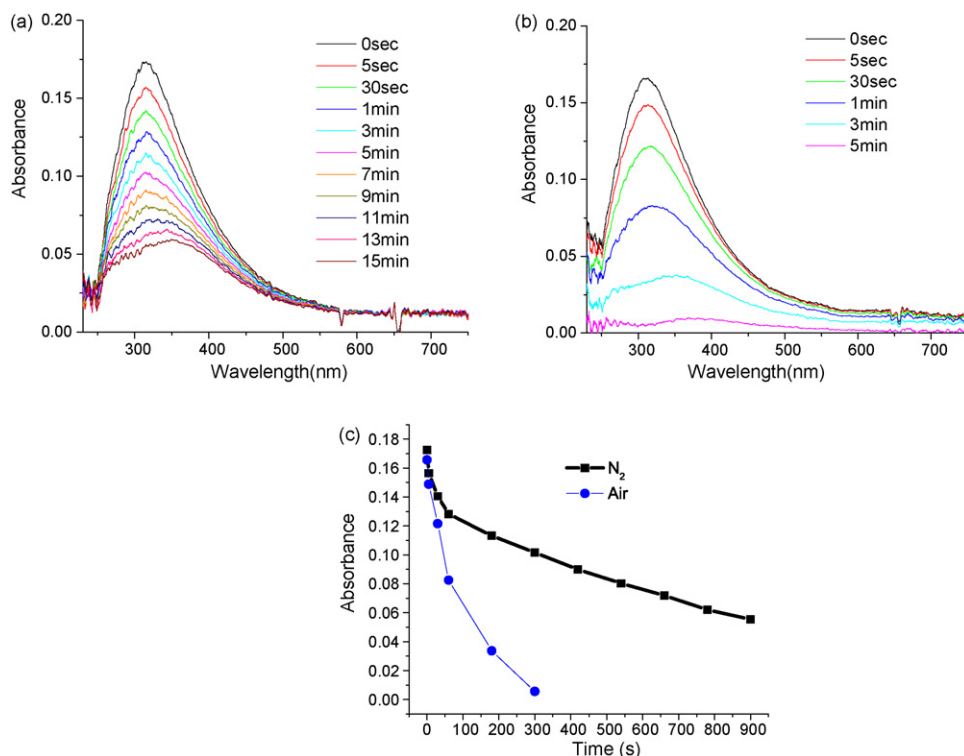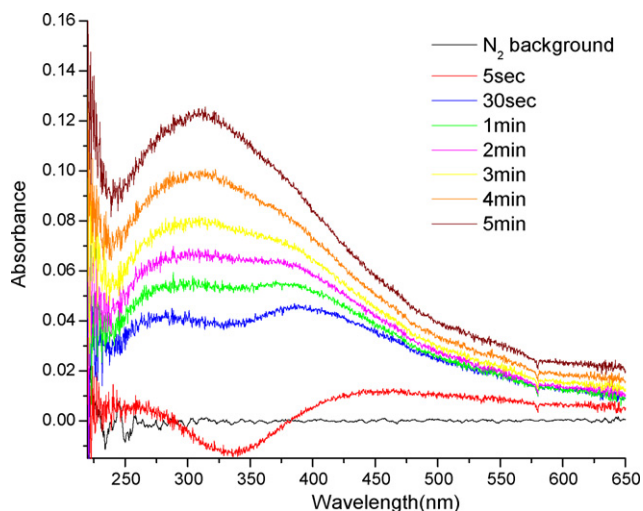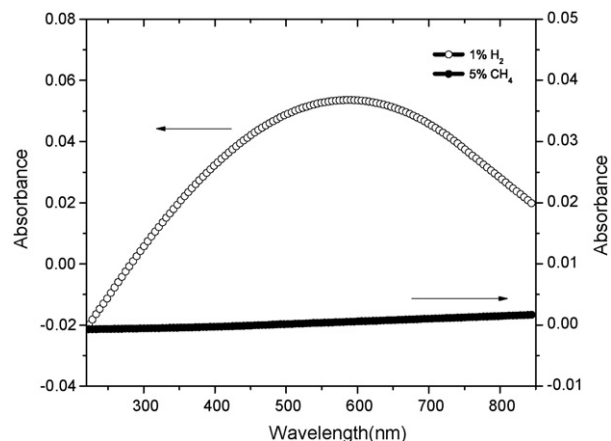
Fig. 8. UV–vis absorption spectra of a SnO_2 thin film optical fiber sensor recovery response from 1 vol% H_2–N_2 flow to a (a) N_2 flow, (b) air flow at 600 °C and (c) time response of the absorbance of SnO_2 thin film coated optical fiber sensors from 1 vol% H_2–N_2 flow at a wavelength of 320 nm under 600 °C.

3.8. Effects of 5 wt% MoO_3 doping on the optical absorption spectra of the SnO_2 thin film exposed to reducing gas

Doping is one of the strategies to tune the sensitivity and selectivity of SnO_2-based gas sensors. The dopant used was 5% by weight of MoO_3 in this study. The influence of MoO_3 is illustrated in Fig. 10 by the UV–vis absorption spectra of a SnO_2 thin film optical fiber sensor doped with 5 wt% of MoO_3 response to 1 vol% H_2–N_2 and 5 vol% CH_4–N_2 flows at 600 °C. It was observed that with doping 5 wt% MoO_3, the peak absorption wavelength of the absorption spectrum to hydrogen has been widened from 230 nm to 850 nm, and peak red-shifted to 600 nm. The peak wavelength shift was considered to be the result of energy level shifting accompanying the dopants. There is no absorbance for the MoO_3 modified tin oxide film to CH_4 in UV–vis range under operation conditions.

3.9. Effects of Pt doping on the optical absorption spectra of the SnO_2 thin film exposed to reducing gas

The influence of 1 wt% Pt is illustrated by the UV–vis absorption spectra of a SnO_2 thin film optical fiber sensor doped with 1 wt% of Pt response to 1 vol% H_2–N_2 and 5 vol% CH_4–N_2 flows at 600 °C in Fig. 11. It was observed that with doping 1 wt% Pt, the peak absorption wavelength of the absorption spectrum to hydrogen has been red-shifted to 625 nm. The peak wavelength shift was considered to be the result of energy level shifting accompanying the dopants.

Fig. 9. UV–vis absorption spectra of a SnO_2 thin film optical fiber sensor pre-coated with a layer of silica gel response to H_2–N_2 flows at 600 °C.

Fig. 10. UV–vis absorption spectra of a SnO_2 thin film optical fiber sensor doped with 5 wt% of MoO_3 response to H_2–N_2 and N_2–CH_4 flows at 600 °C.
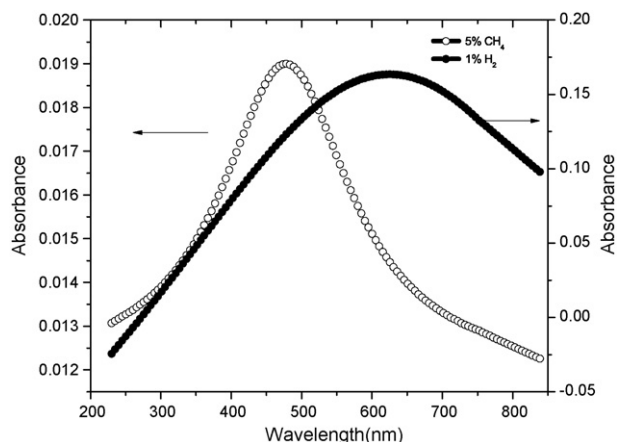
Fig. 11. UV–vis absorption spectra of a SnO_2 thin film optical fiber sensor doped with 1 wt% of Pt response to H_2–N_2 and N_2–CH_4 flows at 600 °C.

There is an absorption peak centered at 400 nm for the Pt doped tin oxide film to CH_4 in UV–vis range under operation conditions.

4. Discussion

Tin oxide is one of the transparent conductive oxides. The oxide films are stable, strongly adherent to the substrate, mechanically hard and resistant to moisture and acids [39,40]. SnO_2 is also an unusual material that is both electrically conductive and visually transparent [41,42]. Tin oxide films have large transmittance in the visible region of the electromagnetic spectrum as a consequence of the large band gap. Owing to its outstanding electrical, optical and electrochemical properties, SnO_2 is extensively used in many applications such as catalytic support materials, transparent electrodes for flat panel displays and solar cells and gas sensors. In particular, SnO_2 thin films have drawn much interest because of their potential application in microsensor devices [43]. Optical and structural properties of tin oxide films has been reported [44]. In the UV/vis region, an absorption spectrum with peak absorption wavelength at around 320 nm was recorded when a 1 vol% H_2–N_2 gas sample was flowed through the quartz flow cell.

The most possible cause of the change of band gap could be related only with oxygen species in the tin oxide thin film. We cannot identify which one of the two species $O_2{}^-$ or O^- are the most essential for an increase of the optical absorption. The observed optical absorbance signal may be associated with a decrease in the surface-adsorbed oxygen-ion concentration on the tin oxide surface while some oxygen vacancies are generated in the tin oxide during its interaction with H_2. The optical absorbance peak decreased to baseline as the recovery of the oxygen in tin oxide thin films indicates that the change of oxygen species concentration is responsible for the probe's ability to sense H_2 gas.

It is well-known that oxygen-ions exist on the surface of semiconductor metal oxide particles [45,46]. The propensities to reduce the oxygen species present on the tin oxide were investigated by TPR. The reduction of tin oxide by H_2 takes place between 30 °C and 900 °C as is shown in Fig. 3. Three distinct hydrogen uptake peaks occurred at T_{max} = 270 °C, 400 °C and 850 °C, respectively. The presence of three reduction peaks may indicate the presence of three different oxygen species on tin oxide. The peak centered at around 270 °C could be attributed to the reduction of chemisorbed oxygen or surface hydroxyl on the tin oxide surface. The hydrogen consumption peak observed at 400 °C can correspond to surface O^{2-} species in tin oxide. Bulk SnO_2 shows a broad reduction band with one peak at ∼850 °C.

Tin dioxide is generally used in gas sensing applications due to its environment dependent surface chemistry. The oxygen chemistry at the grain surfaces of the porous SnO_2 materials is strongly dependent on the surrounding gas atmosphere and the process variables, and it is reflected in the easily measurable electric conductance, and in the optical absorption in this study.

The porous surface of the SnO_2 thin film has a high surface area of 129.75 m^2/g. It has strong tendency to react with H_2 molecules from the gas phase. Hydrogen with the smallest molecular size can easily pass through the surface dense layer, is activated on the surface of tin oxide and reacts very quickly with surface adsorbed oxygen species with negative charges, resulting in water and free electrons. When hydrogen gas diffused into the porous SnO_2 coating, hydrogen molecules were decomposed on the tin oxide surface to hydrogen atoms, which lose electrons to the conduction band of semiconductor oxide. The generated protons get associated with the surface-adsorbed oxygen ions and hop from one oxygen ion to another. Two adjacent OH groups condense and eliminate H_2O. In the process, net one electron is injected into the conduction band of SnO_2 film, reduces the film's resistance and changes the energy band gap of the tin oxide, therefore, there comes an absorption spectrum for tin oxide film when it contacts with hydrogen. At higher temperature, tin oxide is subjected to severe reduction even at a low hydrogen gas concentration (∼100 ppm) because hydrogen is more effectively diffused and interaction with oxygen in tin oxide. As a result, tin oxide is exposed in a vigorous reduction atmosphere, with hydrogen at a high temperature; lattice oxygen ions (O^{2-}), as well as surface adsorbed oxygen species with negative charges, contribute to the oxidation of hydrogen, resulting in a significant change in surface stoichiometry with formation of divalent tin (O^-). The intensity of the SnO_2 thin film optical absorbance increased with the increase of temperature in the tested range up to 800 °C. It is expected that with the increase of temperature more surface absorbed oxygen ions reacting with hydrogen molecules diffused into the pores of the SnO_2 coating. Thus, with the increase of temperature, the absorption signal increased. It was also observed that with the increase of temperature, the peak absorption wavelength of the absorption spectrum has been red-shifted. The peak wavelength shift was considered to be the result of energy level shifting accompanying the increase of temperature.

Doping is the most popular method for the improvement of sensitivity and selectivity of SnO_2-based gas sensors [47–52]. Various metallic dopants have been tested for this purpose. The doping method is usually based on the selection of an appropriate metal, which is the most effective catalyst for the modification of certain chemical reaction on the surface of a solid-state gas sensor. The effect of Pt doping on the methane gas sensitivity can be interpreted in the terms of the surface catalytic activity contributing to the chemical reactions on the surface of solid-state sensors [46–52]. Tin thin film shows chemical sensitization to methane after it was doped with 1 wt% platinum. Methane molecular is catalytic dissociated to carbon species and atomic hydrogen over surface Pt clusters and hydrogen species subsequently spill-over from the Pt clusters onto the tin oxide surface [53]. These hydrogen products then cause the gas sensing response. Hydrogen reduces the oxide support and consumes chemisorbed oxygen species at the SnO_2 surface.

5. Conclusions

Optical fiber probes for sensing hydrogen in a H_2–N_2 flow were developed. The characteristics of the probes for sensing hydrogen in hydrogen–nitrogen flow were studied with fiber optical UV–vis absorption spectrometry. The tin oxide sol–gel coating has porous structure with thickness and pore size in the nanometer range. This

SnO$_2$-based fiber optical sensor is used for detecting H$_2$, CO, CH$_4$ and other combustible gases. A SnO$_2$ sensor is found to cause a strong UV absorption signal with peak absorption wavelength at around 320 nm when the sensor is exposure to a hydrogen sample flow (H$_2$ concentration varies from 0.1% to 10%). Moreover, this optical fiber sensor shows high selectivity, and it does not respond to other reducing gas, such as CH$_4$ and CO. This is a significant progress when compared with traditional semiconductor SnO$_2$ sensor, which detects the electrical property of a SnO$_2$ film. The sensor is tested under the temperature from 300 °C to 800 °C and the sensor is found to selective sensing to H$_2$ under this wide temperature range. The response time of this sensor is within seconds. Replenishing of the oxygen in tin oxide was demonstrated by switching the gas flow from H$_2$–N$_2$ mixture to pure nitrogen and compressed air. The absorption signal decreased quickly (in 5 min) to the baseline when the gas sample was switched to compressed air. These results also suggest that the change of surface-adsorbed oxygen-ion concentration is responsible for the probe to sense H$_2$ gas. Surface silica gel modification technique is successfully used to improve the mechanical properties of tin oxide thin films. The adhesion of tin oxide thin films to the optical fiber is around 3.8×10^5 N/m^2, while the adhesion of the thin films to the optical fiber pre-deposited with a layer of silica gel is above 5×10^5 N/m^2. So, a SiO$_2$ thin layer can improve the adhesion of the contacts to the SnO$_2$ film, adhesion increases may due to increase interaction of optical fiber surface and the coated silica gel and tin oxide film. The influence of MoO$_3$ on the UV–vis absorption spectra of a SnO$_2$ thin film optical fiber sensor doped with 5 wt% of MoO$_3$ response to 1 vol% H$_2$–N$_2$ and 5 vol% CH$_4$–N$_2$ flows at 600 °C was examined. It was observed that with doping 5 wt% MoO$_3$, the peak absorption wavelength of the absorption spectrum to hydrogen has been widen from 230 nm to 850 nm, and peak red-shifted to 600 nm. The SnO$_2$ thin film optical fiber sensor doped with 1 wt% of Pt response to 1 vol% H$_2$–N$_2$ and 5 vol% CH$_4$–N$_2$ flows at 600 °C was also investigated, and it was observed that with doping 1 wt% Pt, the peak absorption wavelength of the absorption spectrum to hydrogen has been red-shifted to 625 nm. The peak wavelength shift was considered to be the result of energy level shifting accompanying the dopants. There is an absorption peak centered at 400 nm for the Pt doped tin oxide film to CH$_4$ in UV–vis range under operation conditions. Based on these research results, a fiber optical sensor for selectively monitoring hydrogen in high temperature gas samples can be developed in further work.

Acknowledgements

References

[1] G. Korotcenkov, I. Boris, V. Brinzari, Yu. Lychkovsky, G. Karkotsky, V. Golovanov, A. Cornet, E. Rossinyol, J. Rodriguez, A. Cirera, Sensors and Actuators B 103 (2004) 13–22.
[2] N. Barsan, U. Weimar, Journal of Physics: Condensed Matter 15 (2003) R1–R27.
[3] N. Yamazoe, Sensors and Actuators B 5 (1991) 7–19.
[4] U. Kirner, K.D. Schierbaum, W. Göpel, B. Leibold, N. Nicoloso, W. Weppner, D. Fischer, W.F. Chu, Sensors and Actuators B 1 (1990) 103–107.
[5] G.N. Advani, L. Nanis, Sensors and Actuators 2 (1981/1982) 201.
[6] T.W. Capehart, S.C. Chang, The Journal of Vacuum Science and Technology 18 (1981) 393–397.
[7] Y. Liu, E. Koep, M. Liu, Chemical Material 17 (15) (2005) 3997–4000.
[8] M. Fleischer, H. Meixner, Sensors and Actuators B 4 (1991) 437–441.
[9] W. Göpel, in: G. Sberveglieri (Ed.), Gas Sensors, Kluwer, Dordrecht, 1992, pp. 365–410 (Chapter 11).
[10] G. Sberveglieri, Sensors and Actuators B: Chemical 6 (1992) 239–247.
[11] V. Guidi, M. Carotta, M. Ferroni, G. Martinelli, L. Paglialonga, P. Nelli, G. Sberveglieri, Sensors and Actuators B 5 (1999) 197–200.
[12] H. Kokusen, S. Matsuhara, Nishino, Y.S. Hasegawa, K. Kubono, Catalysis Today 28 (1996) 191.
[13] H. Wingbrant, H. Svenningstorp, P. Salomonsson, D. Kubinski, J.H. Visser, M. Löfdahl, A. Lloyd Spetz, IEEE Sensors Journal 5 (2005) 1099.
[14] K. Zakrzewska, Thin Solid Films 391 (2001) 229–238.
[15] A. Fort, S. Rocchi, M.B. Serrano-Santos, R. Spinicci, N. Ulivieri, V. Vignoli, IMTC 2004—Instrumentation and Measurement, 2004, p. 599.
[16] D.P. Mann, T. Paraskeva, K.F.E.I. Pratt, P. Parkin, D.E. Williams, Measurement Science and Technology 16 (2005) 1193.
[17] S. Tao, in: C.A. Grimes, E.C. Dickey, M.V. Pishko (Eds.), Encyclopedia of Sensor, vol. 3, American Scientific Publishers, Stevenson Ranch, CA, 2006, p. 467.
[18] Y.C. Kim, S. Banerji, J.F. Masson, W. Peng, K.S. Booksh, Analyst 130 (2005) 838–843.
[19] K.I. Mullen, D. Wang, L.G. Grane, K.T. Karron, Analytical Chemistry 64 (1992) 930–936.
[20] G. Ghiotti, A. Chiorino, F. Boccuzzi, Sensors and Actuators 19 (1989) 151–157.
[21] F.J. Xu, W.H. Weng, D.Y. Lin, Journal of Transduction Technology 4 (1995) 16–18.
[22] W.R. Seitz, Analytical Chemistry 56 (1984) 16A.
[23] K. Eguchi, in: G. Sberveglieri (Ed.), Gas Sensors, Kluwer, Dordrecht, 1992, p. 307.
[24] A. Yanase, H. Komiyama, Surface Science 264 (1992) 147.
[25] K. Yasumoto, N. Koshizaki, K. Suga, in: J.D. Mackenzie (Ed.), Proceedings of SPIE: International Society of Optical Engineering, Bellingham, WA, USA, 1992, pp. 604–611.
[26] H.-J. Nam, T. Sasaki, N. Koshizaki, J. Phys. Chem. B. 110 (2006) 23081.
[27] H. Guo, S. Tao, IEEE Sensors Journal 7 (2007) 323–328.
[28] H. Guo, S. Tao, Sensors and Actuators B: Chemical 123 (2007) 578–582.
[29] N. Butta, M. Meli, S. Pizzini, Sensors and Actuators B 2 (1990) 151–161.
[30] K.D. Schierbaum, J. Geiger, U. Weimar, W. Göpel, Sensors and Actuators B 13–14 (1993) 145–147.
[31] J. Mizsei, Sensors and Actuators B 15–16 (1993) 328–333.
[32] J. Tamaki, T. Maekawa, N. Miura, N. Yamazoe, Sensors and Actuators B 9 (1992) 197–203.
[33] L. Xu, J.C.K. Fanguy, K. Soni, S. Tao, Optical Letters 29 (2004) 1191.
[34] S. Tao, L. Xu, J.C. Fanguy, Sensors and Actuators B: Chemical B115 (2006) 158.
[35] S. Tao, S.-F. Gong, L. Xu, J.C. Fanguy, Analyst 129 (342) (2004).
[36] S. Tao, in: C.A. Grimes, E.C. Dickey, M.V. Pishko (Eds.), Encyclopedia of Sensors, vol. 3, American Scientific Publishers, Stevenson Ranch, CA, 2006, p. 467.
[37] S.K. Khijwania, B.D. Gupta, Optics Communications 175 (2000) 135–137.
[38] P.V. Patil, R.K. Puri, V. Puri, Materials Chemistry and Physics 49 (1997) 156.
[39] V. Matsui, Y. Yamamoto, S. Takeda, Material Research Symposium Proceedings 621 (2000) Q4.9.1–Q4.9.6.
[40] K.L. Chopra, S.R. Das, Thin Film Solar cells, Plenum Press, New York, 1983, pp. 321–327.
[41] S.H. Jeong, S.B. Lee, J.H. Boo, Current Applied Physics 4 (2004) 655–658.
[42] B. Thangaraju, P. Kaliannan, Journal of Physics D: Applied Physics 33 (2000) 1054–1059.
[43] J.E. Dominguez, L. FU, X.Q. Pan, Applied Physics Letters 79 (5) (2001) 614–616.
[44] M.N. Islam, C.A. Hogarth, Journal of Material Science 8 (1989) 989.
[45] P.T. Moseley, B.C. Tofield (Eds.), Solid State Gas Sensors, Adam Hinger, Bristol, 1987.
[46] G. Sberveglieri, Sensors and Actuators B: Chemical 23 (2–3) (1995) 103–109.
[47] K.D. Schierbaum, J. Geiger, U. Weimar, W. Göpel, Sensors and Actuators B 13–14 (1993) 145.
[48] J. Mizsei, Sensors and Actuators B 15–16 (1993) 328.
[49] G.S.V. Coles, S.E. Bond, G. Williams, Sensors and Actuators B 4 (1991) 485.
[50] S.J. Gentry, T.A. Jones, Sensors and Actuators 10 (1986) 141.
[51] D. Kohl, Sensors and Actuators 18 (1989) 71.
[52] N. Butta, M. Meli, S. Pizzini, Sensors and Actuators B 2 (1990) 151.
[53] P. Dutronc, C. Lucat, F. Menil, M. Loesch, M.C. Horrillo, I. Sayago, J. Gutierrez, J.A. de Agapito, Sensors and Actuators B: Chemical 16 (1993) 384–389.

Nucleic acids detection using cationic fluorescent polymer based on one-dimensional microfluidic beads array

Xiaohai Yang, Xiang Zhao, Xinbing Zuo, Kemin Wang*, Jianhui Wen, He Zhang

State Key Laboratory of Chemo/Biosensing and Chemometrics, College of Chemistry and Chemical Engineering, Engineering Center for Biomedicine, Institute of life science and Biotechnology, Key Laboratory for Bio-Nanotechnology and Molecular Engineering of Hunan Province, Changsha 410082, PR China

ABSTRACT

An assay for rapid and direct detection of DNA/mRNA using cationic fluorescent polymer based on one-dimensional microfluidic beads array (1-D chip) has been developed. The cationic water-soluble polythiophene derivatives can easily transduce hybridization events into measurable optical signal due to the conformational changes of the conjugated backbone, when mixed with single-stranded or double-stranded oligonucleotides. In this paper, the polymer was introduced into 1-D chip for fluorescence detection of nucleic acids, and demonstrated its capability on rapid detection of p53 complementary DNA (cDNA) with different concentration. Using this system, we have evaluated the mRNA expression changes of three tumor-associated genes (p53, c-myc and cyclin-d1) in human nasopharyngeal carcinoma CNE2 cell lines before and after 5-flouorouracil (5-FU) stimuli. These results were validated by the conventional reverse transcriptase-PCR. The most important advantage of this assay is not needed target or report labeling prior to hybridization, which makes the experiment process easy to handle and low-cost for multi-target measurement.

© 2008 Elsevier B.V. All rights reserved.

1. Introduction

Nucleic acids analysis plays a key role in life science research and clinical diagnosis of inherited diseases and particular cancers [1,2]. The growing number of nucleic acid-based tests has stimulated a demand for automated, miniaturized and inexpensive testing platforms that also afford rapid, sensitive and multianalyte assays. Biochip, as one of the promising tools for the nucleic acids detection, was widely used in gene expression studies, disease diagnosis and drug discovery for its characteristics of micromation, efficiency and high-throughput [3–5]. Generally, biochips are fabricated from glass, silicon, or plastic substrates on which several chains of single-stranded DNA probe have been immobilized. Target molecules that hybridize with specific probes are usually detected through optical or electrical means. However, the conventional strategies for on-chip nucleic acids detection require labeling each report probe or target with fluorophores or other indicators, which make the assay time-consuming, laborious and high-cost [6,7]. For this reason, several unlabeled methods have been developed and

have attracted increasing attentions. Surface plasmon resonance (SPR) [8,9], atomic force microscopy (AFM) nanoshaving approach [10], and mass based methods such as quartz crystal microbalance [11,12], have been suggested and developed. Although they are label-free, most of these methods involve relatively specific instruments and complex operation steps.

Recently, many studies have been focused on the chemical and biological sensors based on fluorescent conjugated polymers because they provide a new mode to obtain simple, reversible and high sensitive systems [13–20]. Some of fluorescent conjugated polymers were utilized as hybridization transducers in view of their unique transduction mechanism. Leclerc's groups have developed a water-soluble cationic polythiophene derivatives, which can undergo conformational changes upon complexes with single- or double-stranded oligonucleotides [17]. Rapid, direct and specific detection of nucleic acids at the zeptomole level can be achieved using such fluorescent polymeric transducer in homogeneous media [18]. Furthermore, biochips using water-soluble cationic polymers have also been reported, and they can transduce hybridization events into an optical signal without any labeling of the probe or analyte [19,20].

In this paper, we introduce the cationic water-soluble polythiophene derivatives into one-dimensional microfluidic beads array (1-D chip) [21–24] for fluorescence detection of nucleic acids. As a demonstration, the oligonucleotides synthesized according to

* Corresponding author at: State Key Laboratory of Chemo/Biosensing and Chemometrics, Hunan University, Changsha 410082, PR China.
Tel.: +86 731 8821566; fax: +86 731 8821566.
E-mail address: kmwang@hnu.cn (K. Wang).

a special fraction of human gene p53 were detected on the chip. The achieved detection limit is ~50 pM. Furthermore, we have examined simultaneously the transcripts expression changes of p53, c-myc and cyclin-d1 in CNE2 before and after anti-tumor drug treatment. This design integrates the advantages of both 1-D chip and the fluorescent polymeric transducer. A more desirable feature is that it offers a label-free, low-cost and sensitive approach for multiple targets detection. This methodology extends upon our prior efforts of the 1-D chip, and represents important step to make this system serve as a universal, inexpensive and multianalyte detection platform.

2. Experimental

2.1. Reagents

Cationic water-soluble poly [3-(3′-N,N,N-triethylamino-1′-propyloxy)-4-methyl-2, 5-thiophene hydrochloride] was prepared according to the literature [17,25]. All chemicals for synthesis were purchased form J&K Chemical Ltd. (Beijing, China). Distilled water was used.

Poly(dimethylsiloxane) (PDMS) prepolymer and curing agent were obtained from Dow Corning Corporation (Midland, MI, U.S.A.); avidin–agarose beads (Ø = 50 μm), polybrene (PB) were purchased from Sigma (St. Louis, MO, U.S.A.); Dextran sulphate (DS) was purchased from H&Y Bio. Co. Ltd. (Tianjin, China).

RNase inhibitor, AMV reverse transcriptase, DNA Taq polymerase and dNTPs mixtures were obtained from Takara Corporation (Dalian, China). The biotinylated capture probes, target sequence, primers for reverse transcriptase-PCR (RT-PCR), and other oligonucleotides used in this study were also synthesized and purified by Takara Corporation (summarized in Tables 1 and 2). Trizol reagent kit was provided by Invitrogen Corporation (Carlsbad, U.S.A.).

2.2. Fabrication of chip and modification of microbeads

The 1-D chip was fabricated according to the previous methods reported by our group [21]. Briefly, a PDMS replica was molded on

Table 1
Names and sequences (5–3 orientation) of three capture probes and targets used in the experiments

Name	Sequence
p53 capture probe	5′-CCTCTGTGCGCCGGTCTCTCCCAGGACAGGAAA-biotin-3′
c-myc capture probe	5′-GGAGGGAGGCGCTGCGTAGTTGTGCTGATGAAA-biotin-3′
cyclin-d1 capture probe	5′-AGGAAGCGTGTGAGGCGGTAGTAGGACAGGAAA-biotin-3′
p53 target	5′-CCTGTCCTGGGAGAGACCGGCGCACAGAGG-3′
c-myc target	5′-CATCAGCACAACTACGCAGCGCCTCCCTCC-3′
cyclin-d1 target	5′-CCTGTCCTACTACCGCCTCACACGCTTCCT-3′

Table 2
Primer sequences for PCR

Gene	Primer sequence for PCR
p53	Forward primer: 5′-GGCCCATCCTCACCATCAT-3′ Reverse primer: 5′-AGTTCCAAGGCCTCATTCAGC-3′
c-myc	Forward primer: 5′-AGCCCACTGGTCCTCAAGA-3′ Reverse primer: 5′-GTTCGCCTCTTGACATTCTCC-3′
cyclin-d1	Forward primer: 5′-GACCTTCGTTGCCCTCTGTGC-3′ Reverse primer: 5′-GTCCACCTCCTCCTCCTCCTCTTC-3′
β-actin	Forward primer: 5′-TCCTGGAGAAGAGCTACTA-3′ Reverse primer: 5′-GTACTTGCGCTCAGGAGGAG-3′

the silica stencil-plate, which was fabricated by Research Institute of Micro/Nano Science and Technology (Shanghai, China). To reduce the none-specific absorption of regents or samples, the inner walls of the channel were treated by dynamic coating with 5% PB and 3% DS [26].

To functionalize the microbeads, avidin–agarose beads were incubated with 2 μM biotinylated capture probes for 1 h. The probes can be easily immobilized on the bead surface by the biotin–avidin linkage. After washing three times with water, the microbeads modified with capture probes were transferred into the micro-chambers using a vacuum tweezer (Nikon Narishige, model: NT88NEN, Nikon Corp, Japan) under the microscope. After manipulation, PDMS replica was sealed with a cleaned quartz glass slide.

2.3. Optical measurements in homogeneous solution

For optical measurements, the cationic water-soluble polymer was firstly diluted to 2 μM (on a monomeric unit basis) with the 10 mM Tris–HCl (pH 7.8) containing 0.1 M NaCl and 0.3 mM Triton X-100. This mixture was heated to 50 °C, followed by the addition of 5 μl of 5 nM p53 capture probes, and the resulting solution was kept at 50 °C for 5 min. The 1.0 equivalent of the p53 complementary DNA (cDNA) was then added to the solution, and the optical signals were measured for a period of approximately 50 min allowed for hybridization and stabilization. All UV–vis absorption spectra were obtained by a DU800 spectrophotometer (Beckman Coulter). All fluorescence spectra were recorded by fluorescence spectrophotometer (F-2500, Hitachi). Excitation was set at 400 nm and scanning of the emission from 450 to 700 nm.

2.4. Total RNA extraction and RT-PCR

Two bottles of human nasopharyngeal carcinoma CNE2 cell lines were grown in RPMI-1640 medium supplemented with 10% fetal bovine serum (FBS) under 5% CO_2 at 37 °C. One of them was treated with 10 μg/ml 5-flouorouracil (5-FU) for 18 h. Total RNA was isolated from CNE2 cell lines and 5FU-CNE2 cell lines by using Trizol kit according to the standard manufacturer's instructions, and then quantified by a DU800 Spectrophotometer.

Total RNA samples were firstly purified with RNase-free DNase I and RNase inhibitor to remove DNA contaminant. Same amount RNA of CNE2 and 5FU-CNE2 was used for reverse transcription in 20 μl volumes with 4 μl 5 × reverse transcriptase buffer, 1 μg RNA template, 1 mM each nucleotide mixture, 30 U RNase inhibitor, 5 U AMV RTase, 50 pM oligo(dT)$_{18}$ primer at 42 °C for 1 h, followed by inactivation of RTase at 94 °C for 2 min. PCR was performed in 50 μl volumes containing reaction mixture of 5 μl 10 × PCR buffer, 200 μM each nucleotide, 0.4 μM each primer, 2.5 U of Taq DNA Polymerase and 0.5 μl of sample per reaction. Amplification reactions were carried out in a thermocycler (GeneAmp, PCR system 2700, Applied Biosystems) with preliminary denaturation for 5 min at 94 °C, followed by 30 cycles at 94 °C for 50 s, 55 °C for 50 s, 72 °C for 60 s, and a final extension at 72 °C for 10 min. 5 μl of each PCR product was electrophoresed on 2% agarose gels, stained with ethidium bromide, and visualized by UV transillumination.

2.5. Detection of cDNA and mRNA samples on 1-D chip

After assembly of the linear microbeads array, 100 nM fluorescent polymers (on a monomeric unit basis) were introduced into microchannel via gravity-driven flow by chip slope of 15°. The complex was formed between the polymer and capture probes, followed by elution with water for 5 min to wash off the superabundance polymers. Then 2 μl of p53 cDNA with different concentrations were added and hybridized for 50 min at 50 °C. For
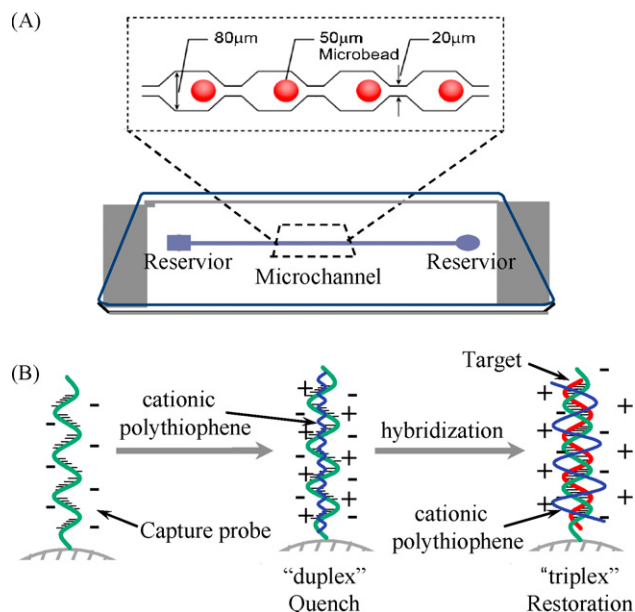
Fig. 1. (A) Schematic of the 1-D Chip. (B) Sketch of the interaction between cationic polymer and nucleic acids. The capture probes were modified on the surface of the microbeads through a biotin–avidin linkage and the polymer bind the capture probes via electrostatic interactions.

Fig. 2. (A) The UV-visible absorption spectra for p53 cDNA detection. (B) Fluorescence spectra with excitation at 400 nm. (a) polymer; (b) polymer/probe duplex; (c) polymer/probe/target triplex. Spectra were recorded in 10 mM Tris–HCl (pH 7.8) containing 0.1 M NaCl and 0.3 mM Triton X-10, at 50 °C.

the mRNA detection, the samples were firstly denatured at 90 °C for 10 min and all samples had the same RNA concentration of 40 μg/100 μl. The RNA hybridization with capture probes under the same conditions for the purified DNA samples. Fluorescence images of the beads were captured using an inversed fluorescence microscope (Nikon TE2000, Exciter: 387(11) nm; Emitter: 520(35) nm; Dichroic: 495 nm) equipped with a cooled charge coupled device (CCD) camera (Leica DC 300F) and the data were analyzed using Image J analysis software. A nucleic acid sample could be detected in about one hour.

3. Results and discussion

3.1. Design of the 1-D chip and principle of the assay

The scheme of the 1-D chip is shown in Fig. 1A. A PDMS replica with many periodic chambers (80 μm wide × 60 μm deep) along a linear microfluidic flow channel (20 μm wide × 60 μm deep) is the central component of this chip. Each of the microfabricated chambers holds a single microbead modified with DNA probes, with interconnecting channels for liquid flow. When samples flowing through the microchannel, targets can be recognized and captured by the corresponding bio-functional microbeads. 1-D chip integrates the technique of both beads array and microfluidic system, which can offer advantages of little sample consumption, low potential of contaminations, easy operation, cost favorable and reusage. Moreover, such a design makes it convenient to pursue multianalyte detections in a single channel.

As shown in Fig. 1B, interpolyelectrolyte complex (duplex) was firstly prepared through electrostatic interactions by mixing the cationic polymer and the capture probes, in which the polymer take a highly conjugated and planar conformation. The intrinsic fluorescence of the polymer is quenched due to close proximity and stiffening of the polythiophene chains [17]. When the target nucleic acids flowing through and hybridizing with the duplexes to form triplex, the polymeric transducer exhibits great fluorescence enhancement and the conformation turns into less conjugated,
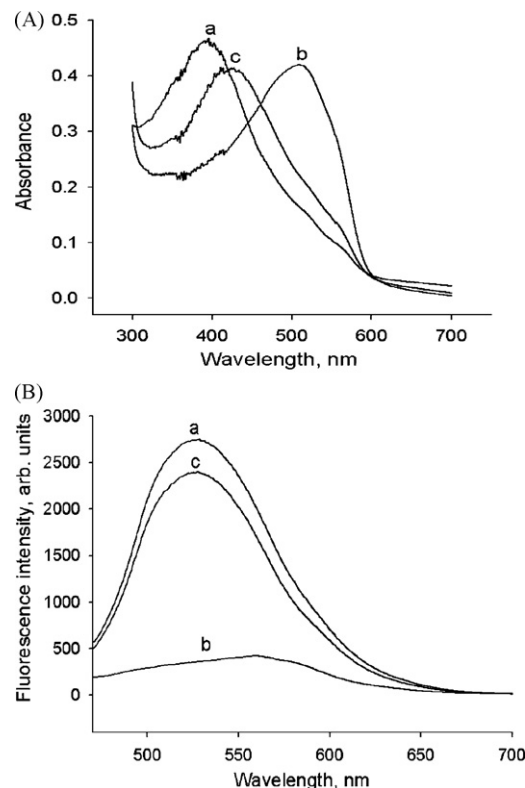
nonplanar. With the use of 1-D chip, this scheme allows simultaneous multiple nucleic acids detection.

3.2. The performance of the polymer in homogeneous solution

The p53 cDNA detection was carried out based on different electrostatic interactions and conformational structures between the cationic polymer and single-stranded or hybridized double-stranded oligonucleotide. As shown in Fig. 2A, the aqueous solution of the cationic polymer was yellow with a maximum absorption wavelength at 399 nm, corresponding to a random-coil conformation. When given capture probes were added, the mixture became red ($\lambda_{max} = 527$ nm) because of the formation of so-called duplex. In addition, precipitation occurred after several hours presumably owing to the aggregation of the duplex mixture. After 50 min of mixing with one equivalent of complementary oligonucleotides at 50 °C, the solution became yellow ($\lambda_{max} = 425$ nm) again due to the formation of more steady triplex. The solubility of the mixture increased and precipitation was not observed even after several days.

A fluorometric detection of nucleic acids hybridization is also possible based on the difference in the fluorescence quantum yield of the positively charged polymer in the random coil or in the aggregated state. As illustrated in Fig. 2B, when excited at 400 nm, the polymer emitted intense fluorescence at 525 nm. But upon addition of negatively charged capture probes, the fluorescence intensity of the polymer decreases strongly (quenched). In the case of hybridization with target sequences, the polymer of triplex complex gave obviously fluorescence restoration.
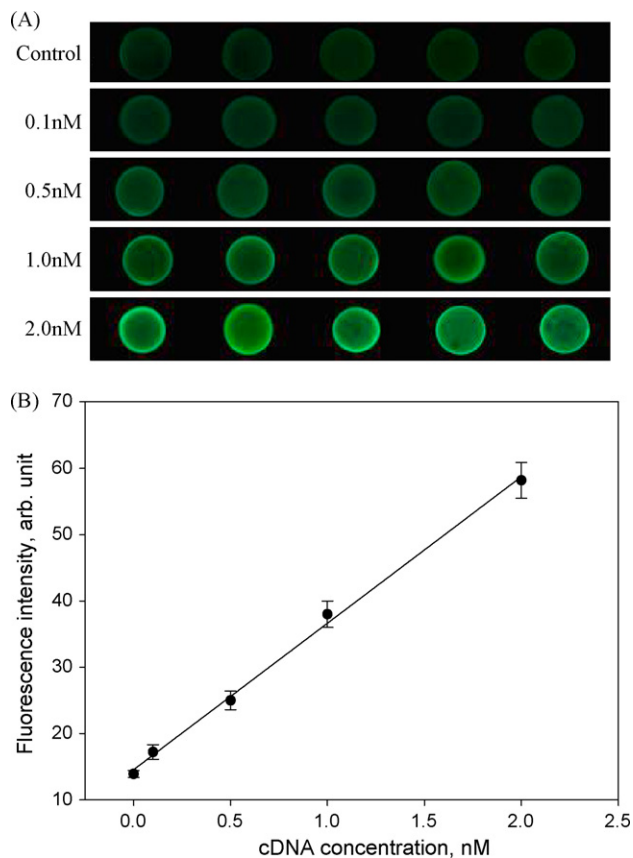
(A)

(B)

Fig. 3. Detection of p53 target cDNA using 1-D chip. (A) The fluorescence images of five-fold redundant beads. (B) Calibration curve of fluorescence intensity versus p53 cDNA concentration, showing a linear relationship between 0.05 and 2 nm target.

3.3. The cDNA target detection on chip

In this section, avidin-labeled agarose microbeads were selected to prevent non-specific adsorption of polymer. The avidin presented positive charge in the given buffer (pH 7.8), which effectively avoids unwanted electrostatic interactions with the cationic polymer on the surface of beads. Fig. 3A describes the fluorescence images of the five-fold redundant beads array of hybridization with various concentration of p53 target cDNA, and the fluorescence intensities on the beads respond to different concentrations of cDNA proportionally. The blank of the beads and beads with capture DNA were both measured by some ways, and the fluorescences were fainter than the control in Fig. 3A. The limit of detection (LOD), defined as the minimum concentration corresponding to a signal above three times of standard deviations, is found to be ~0.05 nM, and a linear response was observed with target concentrations ranging from 0.05 to 2 nM, Linear regression equation is $F = 22.1C + 14.5$ with a correlation coefficient of 0.9976, as shown in Fig. 3B. Comparing with similar method in ref [23], the detection limits are of the same order of magnitude.

3.4. Multiple transcripts expression analysis on chip and validation by RT-PCR

Based on the results obtained from the purified samples, the 1-D chip has further been applied to multiple transcripts expression detection in various cells extracts. Cyclin-d1, p53 and c-myc are three tumor-associated genes and their expression products play key roles in regulation of cell cycle, proliferation and malignant transformation. We selected CNE2 nasopharyngeal carcinoma cell
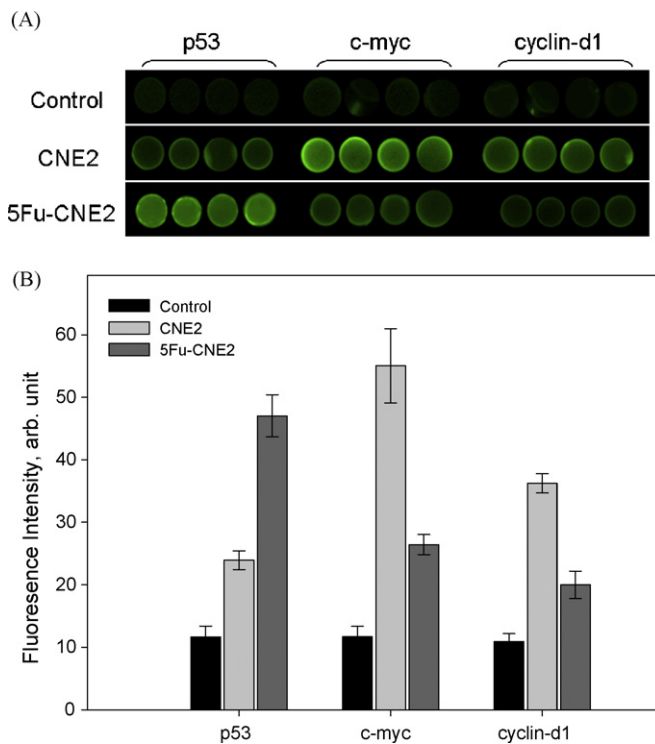
(A)

(B)

Fig. 4. Detection of mRNA samples using 1-D chip. (A) Fluorescence images of beads detecting three intracellular transcripts. Control beads images were obtained using the same experimental conditions without adding RNA samples. (B) A fluorescence intensity quantification quantitative result of the beads images.

lines as a model for the transcripts expression analysis of these genes. The responses of these three genes expression in CNE2 cells to anticancer drug 5-Fu stimuli were also assessed. Each mRNA samples was introduced into the sample reservoir respectively for on-chip hybridization. Meanwhile, blank sample was used for the control experiment. Fig. 4A shows the fluorescence images of the beads array for three cellular RNA samples in CNE2 and 5-FU mediated CNE2. Fig. 4B is the corresponding fluorescence intensity profiles for the beads array. According to the result, c-myc and cyclin-d1 have relative high expression to p53 in CNE2. After 5-FU inducement to the CNE2 cells, p53 expression shows obvious upregulation, while expressions of c-myc and cyclin-d1 decrease obviously.
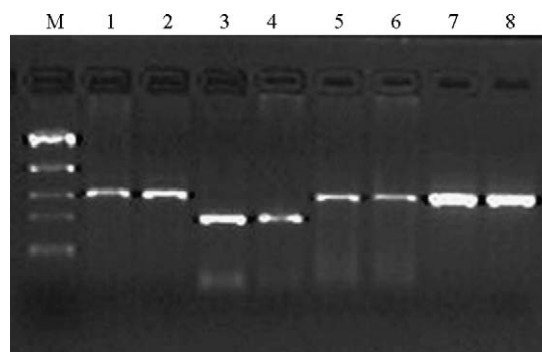

Fig. 5. The electrophoretic result of RT-PCR. Lane M is DNA maker. Lane 1, 3, 5 are the CNE2 cell PCR products of gene p53, c-myc and cyclin-d1, respectively. Lanes 2, 4, 6 are the 5FU-CNE2 cell PCR product of gene p53, c-myc and cyclin-d1, respectively. And lanes 7, 8 are the β-actin RT-PCR products of CNE2 and 5-FU treated CNE2, respectively as invariant expression reference.

To validate the data obtained by the 1-D chip, RT-PCR was performed on the same RNA samples. β-actin has invariant intracellular expression and was used as an internal control for the expression analysis of p53, c-myc and cyclin-d1. As shown in Fig. 5, the results reveal that CNE2 carcinoma cells have higher c-myc and cyclin-d1 expression. After drug treatment, p53 in CNE2 cells is significantly upregulated, while c-myc and cyclin-d1 show an opposite trend. The RT-PCR results are consistent with results obtained by linear microfluidic beads array.

4. Conclusion

In this paper, a simple, rapid and label-free nucleic acid detection method was developed to extend the application of 1-D chip. With the use of fluorescent polymeric transducer, the cDNA samples with different concentration were detected, transcriptional expression of three tumor-associated genes extracted from cells and expression changes of these genes in CNE2 after drug stimuli were also assessed. This method combines the various advantages of microfluidic beads array and fluorescent conjugated polymer, such as little sample consumption, easy operation, and no need of nucleic acids labeling prior to hybridization or any chemical reaction of the probes.

Acknowledgements

References

[1] F.S. Collins, E.D. Green, A.E. Guttmacher, M.S. Guyer, Nature 422 (2003) 835.
[2] A.P. Dale, E.K. Ian, N. Selim, S. Dennis, M.K. Carolyn, R.M. Jeffrey, R. Gregory, P. Kornelia, Cancer Res. 61 (2001) 5697.
[3] J.R. Epstein, I. Biran, D.R. Walt, Anal. Chim. Acta 469 (2002) 3.
[4] A.M. Talaat, P. Hunter, S.A. Johnston, Nat. Biotechnol. 18 (2000) 679.
[5] T.C. Mockler, J.R. Ecker, Genomics 85 (2005) 1.
[6] X.J. Zhao, R. Tapec-Dytioco, W.H. Tan, J. Am. Chem. Soc. 125 (2003) 11474.
[7] R.I. Stears, T. Martinsky, M. Schena, Nat. Med. 9 (2003) 140.
[8] A.W. Peterson, R.J. Heaton, R.M. Georgiadis, Nucleic Acids Res. 29 (2001) 5163.
[9] A.W. Peterson, L.K. Wolf, R.M. Georgiadis, J. Am. Chem. Soc. 124 (2002) 14601.
[10] D. Zhou, K. Sinniah, C. Abell, T. Rayment, Angew. Chem. Int. Ed. 42 (2003) 4934.
[11] X.C. Zhou, L.Q. Huang, S.F.Y. Li, Biosens. Bioelectron. 16 (2001) 85.
[12] M. Passamano, M. Pighini, Sensors Actuators B 118 (2006) 177.
[13] B.S. Gaylord, A.J. Heeger, G.C. Bazan, Proc. Nat. Acad. Sci. 99 (2002) 10954.
[14] B. Liu, G.C. Bazan, Chem. Mater. 16 (2004) 4467.
[15] C.H. Xue, S.P. Jog, P. Murthy, H.Y. Liu, Biomacromolecules 7 (2006) 2470.
[16] H.M. Huang, K.M. Wang, W.H. Tan, D.L. An, X.H. Yang, S.S. Huang, Q.G. Zhai, L.J. Zhou, Y. Jin, Angew. Chem. Int. Ed. 43 (2004) 5635.
[17] H.A. Ho, M. Boissinot, M.G. Bergeron, G. Corbeil, K. Dore, D. Boudreau, M. Leclerc, Angew. Chem. 41 (2002) 1548.
[18] K. Doré, S. Dubus, H.A. Ho, I. Lévesque, M. Brunette, G. Corbeil, M. Boissinot, G. Boivin, M.G. Bergeron, D. Boudreau, M. Leclerc, J. Am. Chem. Soc. 126 (2004) 4240.
[19] F.R. Raymond, H.A. Ho, R. Peytavi, L. Bissonnette, M. Boissinot, F.J. Picard, M. Leclerc, M.G. Bergeron, BioMed. Central Biotechnol. 5 (2005) 10.
[20] K.P.R. Nilsson, O. Inganäs, Nat. Mater. 2 (2003) 419.
[21] L.J. Zhou, K.M. Wang, W.H. Tan, Y.Q. Chen, X.B. Zuo, J.H. Wen, B. Liu, H.X. Tang, L.F. He, X.H. Yang, Anal. Chem. 78 (2006) 6246.
[22] X.B. Zuo, X.H. Yang, K.M. Wang, W.H. Tan, J.H. Wen, Anal. Chim. Acta 587 (2007) 9.
[23] J.H. Wen, X.H. Yang, K.M. Wang, W.H. Tan, L.J. Zhou, X.B. Zuo, H. Zhang, Biosens. Bioelectron. 22 (2759) (2007).
[24] H. Zhang, X.H. Yang, K.M. Wang, W.H. Tan, L.J. Zhou, X.B. Zuo, J.H. Wen, Y.Q. Chen, Electrophoresis 28 (2007) 4668.
[25] J. Lukkari, A.S. Viinikanoja, A.T. Aäritalo, J. Paukkunen, N. Kocharova, J. Kankare, J. Am. Chem. Soc. 123 (2001) 6083.
[26] Y. Liu, J.C. Fanguy, J.M. Bledsoe, C.S. Henry, Anal. Chem. 72 (2000) 5939.

Synthesis, characterization and analytical application of a new inorganic cation exchanger—Titanium(IV) molybdophosphate

R. Yavari [a,*], S.J. Ahmadi [a], Y.D. Huang [b], A.R. Khanchi [a], G. Bagheri [a], J.M. He [b]

[a] Nuclear Science and Technology Research Institute, P.O. Box 11365/8486, Tehran, Iran
[b] Polymer Materials and Engineering Division, Department of Applied Chemistry, Faculty of Science,
Harbin Institute of Technology, Harbin 150001, People's Republic of China

ARTICLE INFO

ABSTRACT

A novel polyoxometalate-cation exchanger, titanium(IV) molybdophosphate (TMP) has been synthesized under varying conditions. The material was characterized by X-ray diffraction, infrared spectroscopy, inductively coupled plasma and thermogravimetry techniques. Its stability was investigated in water, dilute acids, alkaline solutions, and high temperature up to 750 °C. Ion-exchange capacity and distribution coefficients (K_d) for twenty-nine radionuclides and metal ions have been determined. It was found that the TMP has high affinity for Cs^+, Sr^{2+}, UO_2^{2+}, Ba^{2+}, Pb^{2+}, Tl^+, Zn^{2+}, Rb^{2+} and Zr^{4+} ions. The results of binary separation of metal ions showed that TMP can be potentially useful for analytical applications.

© 2008 Elsevier B.V. All rights reserved.

1. Introduction

In recent years, synthetic inorganic ion exchangers have gained much attention owing to their high selectivity for certain elements, good kinetics of sorption, good selectivity and specially their greater stability to heat, ionizing radiation doses and acidic to moderately alkaline medium. Most investigations have been concerned with the use of these materials in the separation and removal of heavy toxic metal ions which are generated as untreated or partially treated by products of various industries into public wastewater and safe storage of hazardous radioactive elements from nuclear waste solutions [1–6]. The radionuclides and toxic metal ions when present in water are injurious to the health. Hence, it is very important to treat such water to remove these hazardous ions before it is supplied for any useful purpose [7]. Thus, by synthesizing new inorganic ion exchanger, having affinity and selectivity for a particular metal ion, one can separate the undesired metal from effluents.

Amongst these synthesized crystalline or amorphous materials, three component inorganic ion exchangers (polyoxometalates) were found to show relatively increased ion-exchange capacity and selectivity in comparison to others. Various types of these useful compounds have been synthesized until now [8,9]. These materials are usually acid salts of multivalent metals. When these compounds are immersed in the aqueous solution they provide exchangeable hydrogen ions, thus exhibiting cation-exchange properties. They may be tetravalent metals such as Sn, Ce, Ti, and Zr in combination with either two anions, e.g. W, P, Mo, Si, As, V, and I. Within the ever-growing field of polyoxometalates, the molybdophosphate system occupies a special place as being one of the most extensively studied and quite well understood systems [10]. However, no work has yet been reported on the preparation and analytical applications of titanium molybdophosphate (TMP).

Titanium(IV) based ion exchangers have been known to be chemically and thermally stable in a comparative study under identical conditions of synthesis [11], so the synthesis of a new inorganic ion exchanger based on titanium is worthwhile. Molybdosilicate, tungstoarsenate, tungstosilicate, tungstophosphate, phosphosilicate, vanadophosphate, arsenosilicate and arsenomolybdate are three component salts of Ti(IV) element that have been synthesized and reported in the literature [12–19].

In continuation to our work on synthesis of new inorganic ion exchangers and their use in the separation of radionuclides and toxic ions [20–23], we present in this paper the synthesis, characterization, ion-exchange behavior and analytical applications of TMP.

* Corresponding author. Mobile: +98 9124572037; fax: +98 2188008933.
E-mail address: yavariramin@yahoo.com (R. Yavari).

Table 1
Synthesis and properties of titanium(IV) molybdophosphate

No.	Sample code	Conditions of synthesis		Properties		
		Concentration(mol L^{-1}) of reagents TiCl$_4$, MPA[a]	Mixing volume ratio, Ti:MPA	Final pH	Composition molar ratio Ti:Mo:P	Cation-exchange capacity (meq g^{-1})
1	TMP-11	0.1, 0.05	1:1	0.8	30.5, 31.2, 1.5	0.82
2	TMP -21	0.1, 0.05	2:1	1.0	28.6, 31.4, 1.1	1.3
3	TMP -31	0.1, 0.05	3:1	1.3	29.3, 31.4, 1.0	0.72

pH = pH of the reaction mixture, meq g^{-1} = ion-exchange capacity as milliequivalent per gram of the ion exchanger.

[a] Solution of titanium(IV) chloride and molybdophosphoric acid (MPA).

2. Experimental

2.1. Chemical and reagents

All the chemicals and reagents used were of Analytical Grade obtained from E. Merck or Fluka. The radioactive tracers used in ion-exchange experiments (^{51}Cr, ^{64}Cu, ^{85}Sr, ^{95}Zr, ^{131}Ba, ^{134}Cs, ^{140}La, ^{141}Ce, ^{147}Nd, ^{60}Co, ^{99}Mo, ^{187}W, ^{115}Cd, ^{86}Rb, and ^{153}Sm) were prepared by the neutron irradiation of natural radioisotopes of elements and were supplied by the Nuclear Science Research School at NSTRI, AEOI, Tehran, Iran.

2.2. Apparatus

Bruker Spectrometer (Vector 22) was used for IR studies. pH measurements were made with a Schott CG841 pH-meter (Germany). Thermogravimetric analysis was performed on a thermobalance (PL-STA 1500, PL Thermal Science). The quantitative determinations of inorganic ions were carried out using an inductively coupled plasma ((ICP) Varian Turbo Model 150-Axial Liberty), atomic absorption spectrometer (AAS Model, Spectra AA-220 Varian), a Gamma Spectrometer (Ortec EG&G, HPGe) comprising a high-resolution coaxial GMX detector with 4096 channels and an Alpha-Counter (Model LB-770). X-ray diffraction studies were made with a Philips diffractometer (model PW 1130/90) and a Waterbath shaker (model CH-4311, Infors AG) was used throughout the work.

2.3. Synthesis of titanium(IV) molybdophosphate

Three samples of TMP were synthesized by adding gradually aqueous solution of molybdophosphoric acid (MPA) to titanium(IV) chloride solutions (dissolved in ethanol) under varying conditions given in Table 1. While the reaction mixture was thoroughly stirred with a magnetic stirrer at room temperature (25 °C), the pH of the system was increased slowly by adding NaOH for completion of the precipitation formation. Then the solution containing precipitate was stirred for 1 h and was refluxed at 75–80 °C for 24 h. The resulting precipitate was decanted and washed five times with demineralized water (DMW), filtered by suction and dried at 50 ± 2 °C for 24 h. It was further treated with excess of 0.1 mol L^{-1} nitric acid solutions for complete replacement of counter ions by H$^+$ ions. The excess of acid was removed by repeated washing with DMW. Finally the material was dried in an oven at 50 ± 2 °C.

2.4. Ion-exchange capacity (IEC)

The column method was used for the determination of the ion-exchange capacity of each sample (which generally taken as a measure of the hydrogen ion liberation by neutral salt). For this purpose, one gram of dry ion exchanger samples (in H$^+$ form) was loaded into a column (i.d.: 1 cm, length: 40 cm) with a glass wool

supported at the bottom. 100 mL of 1 mol L^{-1} KCl solution was used to elute the H$^+$ ions with flow rate of 0.2 mL min^{-1}. The released H$^+$ ions were determined titrimetrically using a standard 0.01 mol L^{-1} sodium hydroxide solution. Table 1 shows the ion-exchange capacity values of the samples.

2.5. Chemical composition

The composition of each sample was determined by dissolving 250 mg of samples in 20 mL hot concentrated hydrochloric acid. The solution was cooled and diluted to 250 mL by DMW and the elements were determined by ICP.

2.6. Chemical stability

The chemical stability of the samples was assessed in some minerals and organic solvents: HCl, HNO$_3$, H$_2$SO$_4$, NaOH, ethanol, methanol, acetone and ether. 20 mL from each solvent was poured on a 50 mg of TMP in the 50 mL beaker and kept for 24 h with continuous shaking at room temperature. When heated in conc. HCl or aqua regia or 2 mol L^{-1} NaOH solution for more than 20 min, they dissolved. The released metal ions from TMP were analyzed with ICP. Detailed quantitative studies on the stability of the exchangers were made in different solutions as reported earlier [24]. The results are given in Table 2.

2.7. Distribution coefficients

The distribution coefficients (K_d) for different metal ions were determined by batch method. 200 mg of each TMP in H$^+$ form was kept in 20 mL of 1.2×10^{-4} mol L^{-1} metal ion solutions at 25 °C ± 1 °C for 5 h, with intermittent shaking to reach equilibrium. The solution was then filtered and metal ions were determined using ICP, AAS or Gamma spectrometer techniques [25]. Blank solutions were prepared without ion exchanger, having the same concentration of metal ions. This solution was treated in the same way as above. The K_d values were calculated by the following equation;

$$K_d = \left[\frac{(I - F)}{F} \right] \frac{V}{W} \, (\text{mL g}^{-1})$$

where I and F are the initial and final activity (cps^{-1}) or concentration (mg L^{-1}) of metal ions in the solution phase, V is volume of initial solution in mL, and W is the dry mass of the ion exchanger in g. Standard deviation for K_d values were checked by two determinations and were less than 10%. The results are given in Table 3.

2.8. Infrared absorption spectra

Infrared spectra of samples were measured by the standard KBr disk method. The spectrum of TMP-2 in H$^+$ form is shown in Fig. 1.

Table 2
stability of titanium molybdophosphate in different solutions (weight dissolved (mg) from 50 mg)

No	Solvent (mol L^{-1})		TMP-11			TMP-21			TMP-31		
			Mo (mg)	P (mg)	Ti (mg)	Mo (mg)	P (mg)	Ti (mg)	Mo (mg)	P (mg)	Ti (mg)
1		0.1	0.00	0.00	0.00	0.00	0.00	0.00	0.00	0.00	0.00
2	HCl	0.5	1.25	0.02	0.74	0.36	0.00	0.23	0.13	0.00	0.08
3		1	2.44	0.08	1.66	0.83	0.02	0.70	0.23	0.00	0.24
4		4	11.03	0.652	13.00	5.05	0.21	5.56	1.86	0.05	2.05
5		0.1	0.00	0.00	0.00	0.00	0.00	0.00	0.00	0.00	0.00
6	HNO$_3$	0.5	0.20	0.04	0.16	0.27	0.00	0.21	0.10	0.00	0.08
7		1	2.47	0.08	1.49	0.67	0.01	0.5	0.23	0.00	0.19
8		4	7.79	0.42	7.5	3.05	0.12	2.98	0.95	0.00	0.89
9		0.1	0.00	0.00	0.00	0.00	0.00	0.00	0.00	0.00	0.00
10	H$_2$SO$_4$	0.5	4.83	0.272	4.08	0.27	0.00	0.21	0.59	0.02	0.62
11		1	8.54	0.49	8.91	0.67	0.01	0.5	1.02	0.03	1.11
12		4	11.4	0.72	13.17	3.05	0.12	2.98	1.66	0.05	1.84
13		0.1	0.00	0.00	0.00	0.00	0.00	0.00	0.00	0.00	0.00
14	NaOH	0.5	10.98	0.81	0.00	11.92	0.68	0.01	11.79	0.55	0.00
15		1	11.45	0.82	0.00	12.2	0.68	0.01	12.79	0.57	0.00
16		4	11.98	0.82	0.05	12.2	0.68	0.08	12.99	0.61	0.03
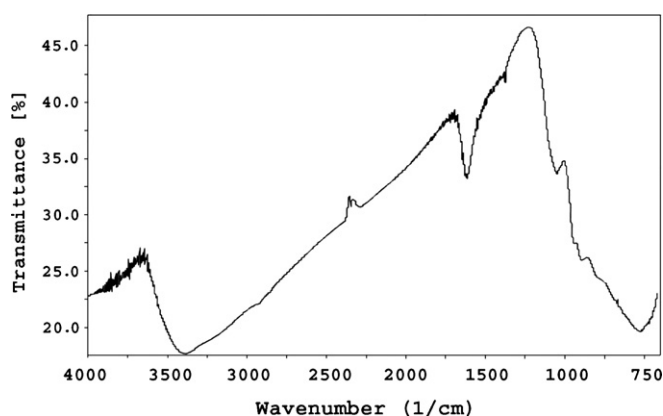
Fig. 1. Infrared spectrum of titanium(IV) molybdophosphate (TMP-21).

Fig. 3. XRD spectrum of titanium(IV) molybdophosphate (TMP-21).

2.9. Thermogravimetric studies

The thermal analysis of all samples was performed in H$^+$ form. A 20 mg from each sample was analyzed by TGA with sample holder made up of Al$_2$O$_3$ in nitrogen atmosphere at flow rate of 50 mL min^{-1} with heating rate of at 10 °C min^{-1} up to 1000 °C. The thermogram for TMP-2 in H$^+$ form is given in Fig. 2.
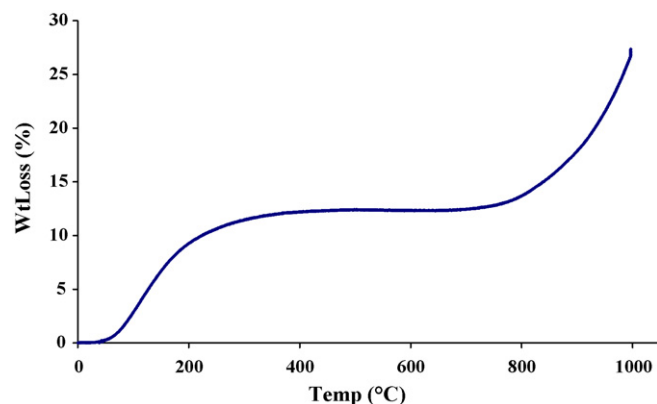

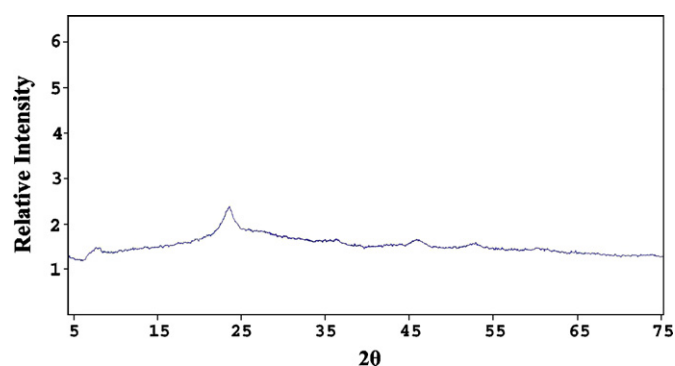Fig. 2. Thermogram of titanium(IV) molybdophosphate (TMP-21).

2.10. X-ray analysis

X-ray powder diffraction method using nickel-filtered Cu Kα radiation at 298 K was used for X-ray studies of samples in H$^+$ form. The study was done between 4° and 75° 2θ values with step size of 0.05. XRD spectrum of TMP-2 is given in Fig. 3.

2.11. Binary separation of metal ions

Important quantitative separations of metal ions were performed on columns containing TMP. One gram of TMP in H$^+$ form (mesh size 50–100 mm) was placed in glass column with inner diameter of 0.8 cm. The column was washed thoroughly with DMW. Then the mixture of the two metal ions (Table 4) to be separated was loaded by passing the mixture through the column at slow flow-rate (0.2 mL min^{-1}). The column was washed with DMW so that the metal ions (which were not exchanged) could be removed. The metal ions adsorbed on the exchanger were then eluted with different concentrations of HNO$_3$ (0.1, 0.2 and 0.5 mol L^{-1}). The mobile phase flow-rate was maintained at 0.2 mL min^{-1} until the metal ions were completely eluted from the column. The effluents were collected in 2 mL fractions and determined by Gamma Spectrometer or ICP. The metal ions solutions were either concentrated or diluted as required so as to ensure detection.

Table 3
Distribution coefficients of elements on titanium(IV) molybdophosphate: K_d value (mL g^{-1}) for different samples

Sample									
Species	TMP-11			TMP-21			TMP-31		
	DMW	0.001 mol L^{-1} HNO$_3$	0.1 mol L^{-1} HNO$_3$	DMW	0.001 mol L^{-1} HNO$_3$	0.1 mol L^{-1} HNO$_3$	DMW	0.001 mol L^{-1} HNO$_3$	0.1 mol L^{-1} HNO$_3$
Ba(NO$_3$)$_2$	>10^4	504	27	7565	491	19	831	125	11
Sr(NO$_3$)$_2$	6300	759	7	2500	121	5	161	91	2
Co(NO$_3$)$_2$	1918	821	11	112	39	1	24	6	N.A.
Cu(NO$_3$)$_2$	>10^4	3231	162	4869	2178	19	1954	761	27
Pb(NO$_3$)$_2$	>10^4	7560	23	>10^4	>10^4	34	2365	1172	42
BiONO$_3$	416	225	4	1641	780	28	174	144	11
TlNO$_3$	>10^4	7888	219	>10^4	9331	121	6374	3879	74
In(NO$_3$)$_3$	>10^4	6860	184	145	43	5	77	36	2
Cr(NO$_3$)$_3$	589	320	18	99	60	1	26	12	N.A.
Na$_2$CrO$_4$	25	20	11	4	N.A.	N.A.	59	12	N.A.
(NH$_4$)$_6$Mo$_7$O$_{24}$	N.A.	N.A.	N.A.	N.A.	N.A.	N.A.	N.A.	N.A.	N.A.
Na$_2$WO$_4$	14	15	10	36	8	N.A.	43	N.A.	N.A.
Th(NO$_3$)$_4$	412	195	3	745	302	12	398	154	6
UO$_2$(NO$_3$)$_2$	7900	933	14	257	88	4	199	65	2
Zn(NO$_3$)$_2$	>10^4	8657	498	1658	851	24	598	244	19
Cd(NO$_3$)$_2$	>10^4	7845	298	2865	1540	39	857	387	21
ZrOCl$_2$	7590	4172	91	>10^4	>10^4	174	6992	1458	48
HfOCl$_2$	4990	2564	29	>10^4	>10^4	299	>10^4	5229	167
LiNO$_3$	N.A.	N.A.	N.A.	4	N.A.	N.A.	5	N.A.	N.A.
NaNO$_3$	50	4	N.A.	150	15	N.A.	99	8	N.A.
KNO$_3$	1108	362	38	>10^4	2135	25	935	287	7
RbCl	1955	499	77	>10^4	1672	67	4110	526	41
CsNO$_3$	3323	871	101	>10^4	2841	88	4651	745	47
YCl$_3$	5505	704	13	21	12	4	24	6	N.A.
La(NO$_3$)$_3$	1542	756	120	19	N.A.	N.A.	54	N.A.	N.A.
Ce(NO$_3$)$_3$	1097	446	78	687	432	15	267	145	6
Nd(NO$_3$)$_3$	1255	970	93	121	43	3	15	3	N.A.
Sm(NO$_3$)$_3$	3610	2630	12	99	36	2	75	31	3
Dy(NO$_3$)$_3$	1293	957	64	25	17	N.A.	23	9	N.A.

N.A. = negligible adsorption.

Table 4
Separation of metal ions on titanium(IV) molybdophosphate at room temperature

No.	Metal ions separated	Amount loaded (μg)	Amount found (μg)	Total elution volume (mL)	Eluent used	The type of ion exchanger
1	La	350	350	35	H_2O	TMP-21
	Ce	450	410	40	$0.2\,mol\,L^{-1}\,HNO_3$	
2	Mo	720	720	35	H_2O	TMP-21
	Zr	240	240	30	$0.5\,mol\,L^{-1}\,HNO_3$	
3	Nd	1080	1050	45	H_2O	TMP-31
	Ce	400	390	35	$0.1\,mol\,L^{-1}\,HNO_3$	
4	Bi	1568	1490	50	$0.1\,mol\,L^{-1}\,HNO_3$	TMP-11
	Zn	200	190	40	$0.5\,mol\,L^{-1}\,HNO_3$	
5	Mo	960	960	50	H_2O	TMP-21
	Pb	522	505	25	$0.5\,mol\,L^{-1}\,HNO_3$	
6	Li	105	105	20	H_2O	TMP-21
	K	98	90	25	$0.2\,mol\,L^{-1}\,HNO_3$	
7	Dy	1625	1550	45	H_2O	TMP-21
	Ce	400	380	30	$0.2\,mol\,L^{-1}\,HNO_3$	
8	Y	1000	950	60	H_2O	TMP-21
	Tl	510	500	45	$0.5\,mol\,L^{-1}\,HNO_3$	
9	Li	140	140	20	H_2O	TMP-21
	Rb	440	440	30	$0.2\,mol\,L^{-1}\,HNO_3$	
10	Mo	1000	990	55	H_2O	TMP-21
	Cs	660	660	25	$0.2\,mol\,L^{-1}\,HNO_3$	
11	Mo	1000	990	20	H_2O	TMP-21
	Sr	440	430	20	$0.1\,mol\,L^{-1}\,HNO_3$	

3. Results and discussion

Various samples of TMP were synthesized under different conditions (see Table 1). The conditions used for the preparation of inorganic ion exchanger have considerable effect on the degree of hydration and the composition of the exchanger. These two factors are responsible for the shape and size of cavities inside the ion exchanger and for other properties of the exchanger (resulting in unusual ion-exchange behaviors) [4,5,26]. All TMP samples were as hard green granules and suitable for use in the column operation. The ion-exchange capacity of these materials shows that TMP has a higher ion-exchange capacity than titanium tungstophosphate and smaller than titanium tungstosilicate [14]. This is probably due to the strong affinity for the hydrogen ions in the following sequence.

Silicate > Molybdate > Phosphate

The chemical stability studies (Table 2) show that TMP samples are highly stable in water and dilute mineral acids and bases as well as in ethanol, methanol, acetone and ether. However, in basic and acidic media with the concentration higher than 0.1 and $0.4\,mol\,L^{-1}$, respectively, these materials should not be used because they gradually decompose. This is due to the hydrolysis of these materials at the higher pH values.

The X-ray diffraction pattern (Fig. 3) shows weak intensities, thereby suggesting that the various forms of TMPs are amorphous in nature.

The infrared spectrum of TMP in H^+ form is shown in Fig. 1. The asymmetric absorption broad and strong band between 3000 and $3500\,cm^{-1}$ is attributed to interstitial water molecules and hydroxyl groups while a sharper peak in the region of 1500–$1700\,cm^{-1}$ with the maximum at $1600\,cm^{-1}$ is a characterization for the deformation vibration of free water molecules. A broad peak in the region around $734\,cm^{-1}$ is due to metal–oxygen bond [27]. The bands at 1200 and $1000\,cm^{-1}$ may be assigned to symmetric and antisymmetric stretching of

the P–O bond in PO_3 groups in the IR spectra of TMP samples [28].

According to the thermogram of TMP recorded in Fig. 2, there is no loss in weight up to $50\,°C$. From 50 to $350\,°C$, the continuous loss in weight (about 13%) is recorded which is due to the removal of free external water molecules and condensation of hydroxyl groups [29] and that is usual in synthetic of inorganic ion exchangers. The curve pattern shows that the ion exchanger is stable up to $750\,°C$.

The ion-exchange properties of the product materials were studied by measuring the distribution coefficients (K_d) of 29 elements using batch experiments in DMW and nitric acid media. In addition to the nature of the ion exchanger, various factors such as swelling, formation of complexes, nature of the chemical bond and solvent distribution may be responsible for the wide variation in the distribution coefficient values [11]. The obtained values for K_d (given in Table 3.) show that TMP is a useful ion exchanger. According to this table the affinity sequences for alkali metal ions were $Cs^+ > Rb^+ > K^+ > Na^+ > Li^+$. That may be due to the size of the hydrated radii of the exchanging ions [30,31]. Ions with the smaller radii easily enter the pores of the exchanger, resulting in greater adsorption [32]. It was also observed that for most of the metal ions, K_d values decreased with the increase in concentration of nitric acid. Low K_d values of the metal ions in high concentration of nitric acid are due to slower replacement of the metal ions in acidic media and competition of H_3O^+ ions with metal ions as expected. The results of experiments on TMP show that Cs^+, Sr^{2+}, UO_2^{2+}, Ba^{2+}, Pb^{2+}, Tl^+, Zn^{2+}, Rb^{2+} and Zr^{4+} are more strongly adsorbed than other metal ions and therefore TMP can be used for selective removal of these ions from complex systems. Based on the K_d values for above-mentioned elements in aqueous and nitric acid medium on TMP, eleven binary metal separations have been performed (Table 4). Some of these separations may be actually used for practical samples of nuclear waste, alloys, minerals and heavy metals/trace metals. TMP is also more effective in the separating special radioactive ions in micro level quantitative analysis.

4. Conclusion

Amorphous ion exchanger, TMP was found to have good ion-exchange capacity, high chemical and thermal stabilities and was suitable for column separation. In addition the different behaviors of the exchanger towards some heavy metal and radiotoxic ions showed that it could be used for separation possibilities of toxic metal ions and radionuclides from each other. For example, Sr^{2+} and Cs^+ can be removed quantitatively from the nuclear wastes by TMP-11 and TMP-21, respectively.

Acknowledgements

References

[1] C.B. Amphelt, Inorganic Ion Exchangers, Elsevier, Amsterdam, 1964.
[2] A. Clearfield, Inorganic Ion Exchange Materials, CRC Press, New York, 1982.
[3] M. Abe, T. Kataoka, T. Suzuki, New Developments in Ion Exchange, Elsevier, Kodansha, Tokyo, 1991.
[4] B.P. Nikolskii, P.G. Ramoankov, Ion Exchange in Chemical Technology, Khimia, Moscow, 1980.
[5] M. Qureshi, K.G. Varshney, Inorganic Ion Exchange in Chemical Analysis, C.R.C. Press, Boca Raton, FL, 1991.
[6] G. Alberti, Acc. Chem. Res. 11 (1978) 168.
[7] V.K. Gupta, P. Singh, N. Rahman, J. Colloid Interface Sci. 275 (2004) 398.
[8] A.P. Gupta, G.L. Verma, S. Ikram, React. Funct. Polym. 43 (2000) 33.
[9] V.K. Gupta, P. Singh, N. Rahman, Anal. Bioanal. Chem. 381 (2005) 471.
[10] E. Dumas, S.C. Sevov, Inorg. Chem. 41 (2002) 144.
[11] M. Qureshi, N. Zehra, S.A. Nabi, V. Kumar, Talanta 20 (1973) 609.
[12] S.A. Nabi, A.H. Shalla, A.M. Khan, S.A. Ganie, Colloids Surf. A 302 (2007) 241.
[13] S.K. Srivastava, Satish Kumar, C.K. Jain, Surender Kumar, J. Radioanal. Nucl. Chem. 90 (1985) 255.
[14] Z.M. Siddiqi, D. Pathania, J. Chromatogr. A 987 (2003) 147.
[15] S.J. Naqvi, D. Huys, L.H. Baetsle, J. Inorg. Nucl. Chem. 33 (1971) 4317.
[16] J.P. Rawat, R.A. Khan, Ind. J. Chem. Sect. A 19 (1980) 925.
[17] N.J. Singh, S.N. Tandon, Ind. J. Chem. Sect. A 19 (1980) 502.
[18] K.G. Varshney, K. Agarwal, S. Agarwal, W. Saxena, R.A. Khan, Colloids Surf. A 29 (1988) 175.
[19] A.P. Gupta, J. Indian Chem. Soc. 61 (1984) 265.
[20] R. Yavari, A.R. Khanchi, M.G. Maragheh, S. Waqif-Husain, J. Radioanal. Nucl. Chem. 297 (2006) 685.
[21] R. Yavari, S.J. Ahmadi, Y.D. Huang, G. Bagheri, Sep. Sci. Technol., in press.
[22] M.G. Maragheh, S. Waqif-Husain, A.R. Khanchi, J. Appl. Radiat. Isot. 50 (1998) 459.
[23] M.G. Maragheh, S. Waqif-Husain, A.R. Khanchi, S.J. Ahmady, Sep. Sci. Technol. 34 (1999) 219.
[24] M. Qureshi, S. Waqif-Husain, J. Chem. Soc. (A) (1970) 1204.
[25] R.K. Winge, V.A. Fassel, V.J. Peterson, M.A. Floyed, Inductively Coupled Plasma Atomic Emission Spectoscopy, Elsevier Science, Amsterdam, 1985.
[26] A. Dyer, M.J. Hudson, P.A. Williams, Ion Exchange Processes: Advances and Applications, Royal Society of Chemistry, London, 1993.
[27] G. Socrates, Infrared Characteristic Group Frequencies, John Wiley & Sons, Ltd., New York, 1980.
[28] V.V. Pechkovaskii, R.Y. Melnikova, E.D. Dzyuba, Atlas of Infrared Spectra of Phosphates, Orthophosphate, Nauka, Moscow, 1985.
[29] S. Waqif Husain, M. Ghannadi-Maragheh, S. Rasheedzad, J. Radioanal. Nucl. Chem. 84 (1984) 239.
[30] A.A. Khan, M. Inamuddin, A. Mezbaul, React. Funct. Polym. 63 (2005) 119.
[31] S.A. Nabi, A.M. Khan, React. Funct. Polym. 66 (2006) 495.
[32] S.A. Nabi, S. Usmani, N. Rahman, Ann. Chim. Sci. Mater. 21 (1996) 521.

A new mixed micellar electrokinetic chromatography method for analysis of natural and synthetic anabolic steroids

Lan Zhang [a,b], Jinfeng Chen [a,c], Yu He [a], Yuwu Chi [a], Guonan Chen [a,*]

[a] *Ministry of Education Key Laboratory of Analysis and Detection for Food Safety (Fuzhou University), Fuzhou, Fujian, 350002, China*
[b] *The Sport Science Research Center, Fuzhou University, Fuzhou, Fujian, 350002, China*
[c] *Longyan Entry-Exit Inspection and Quarantine Bureau, Longyan, Fujian, 364000, China*

ARTICLE INFO

ABSTRACT

A simple, rapid and low-costing new mixed surfactant MEKC method has been developed for the analysis of five neutral anabolic steroids in this paper. It was found that the bile salt coupling with Triton X-100 was a suitable bi-micellar surfactant for the separation of these anabolic steroids with similar structure. The separation conditions were optimized in detail. The five natural and synthetic anabolic steroids, such as androstenedione (AD), 19-norandrostenedione (NAD), 1,4-androstadiene-3,17-dione (ADD), methandrostenolone (MA) and methyltestosterone (MT) were separated and detected in an alkaline buffer system (pH 9.0) containing 15 mM Britton-Robinson (BR) buffer, 50 mM sodium cholate (SC) and 0.1% (v/v) Triton X-100 with detection wavelength at 241 nm and 18 kV of separation voltage. Under the optimal conditions, five coexistence neutral steroids were completely separated within 12 min with the detection limits ranged from 0.20 to 0.51 µg/mL. This method was successfully used for detection and confirmation of the anabolic steroid methandrostenolone in methandrostenolone tablets and in the real human urine, GC–MS method was applied to confirm the free methandrostenolone existence in the urine sample in order to validate the reliability of MEKC method.

© 2008 Elsevier B.V. All rights reserved.

1. Introduction

Anabolic steroids, including natural and synthetic anabolic steroids, have a hydrophobic tetracyclic perhydro-1,2-cyclopentanophenanthrene ring in their molecular structures. Most synthetic anabolic steroids are derived from testosterone, which is natural anabolic steroid [1]. Thus, they have very similar molecular structures. Natural anabolic steroid plays a very important role on male animals [2,3]. In order to improve the anabolic activity and effect for therapeutic disease, a series of synthetic anabolic steroids called anabolic androgenic steroids (AAS) have been developed. When AAS were abused in the sports, excess hormone would seriously injure athletes' physical and mental health. Hence, anabolic steroids have been included in the International Olympic Committee doping list due to their illegal use in some sports [4].

GC–MS has been used as an official method to detect the illegal anabolic steroids using in sport [5–7]. However, GC–MS methods always require tedious sample preparation and complex chemical derivation procedures [8,9]. And other analytical technologies, such as LC–MS and LC–MS–MS have been applied for determination of the anabolic steroids [10,11]. However, all above mentioned equipments are expensive.
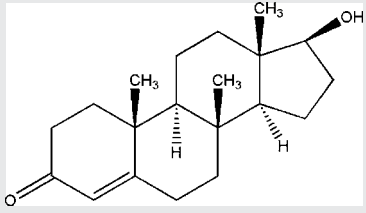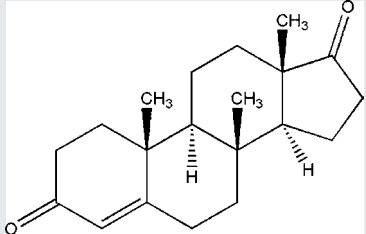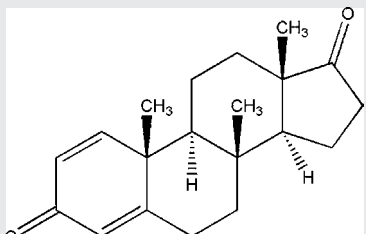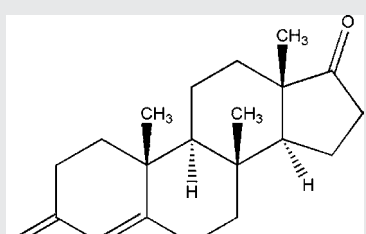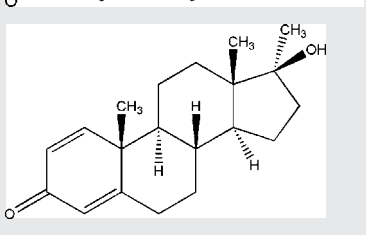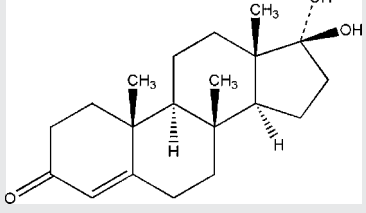
CE has many advantages, such as high resolution, minimal sample volume, short analytical time and high separation efficiency [12]. It has been proved to be a powerful tool for drug quality control in recent years [13–23]. The high efficiency and the possibility for separating both neutral and ionized solutes in the same system are the two most attractive advantages of MEKC. Compared with the official GC–MS method, MEKC method has some evident superiority including simple preparation, time saving and low cost. Thus, introducing MEKC method into the analysis of anabolic steroids may be an alternative direction.

Abubaker et al. has separated the six steroids by hydrophobic MEKC [24]. SDS mixed micellar system was reported to separate steroids by Valbuena et al., Lin et al. and Fernandez et al. [25–27]. Recently, for the purpose of coupling with ESI-MS, partial filling MEKC method has also been introduced by Amundsen et al. to separate endogenous steroid hormones and synthetic anabolic steroids, compared with normal MEKC the separation efficiency was relatively lower due to an additional band broadening mechanism in PF-MEKC [28,29].

* Corresponding author at: Department of Chemistry, Fuzhou University, Fuzhou, Fujian, 350002, China. Tel.: +86 591 87893315; fax: +86 591 83713866.
  E-mail address: gnchen@fzu.edu.cn (G. Chen).

Table 1
Molecular structures of the typical anabolic steroids

Abbreviation	Compound	Synonyms	Chemical structure	MW
T	Testosterone	17-Hydroxy-(17-beta)-androst-4-en-3-one		288
NAD	19-Norandrostenedione	Estr-4-ene-3,17-dione		272
ADD	1,4-Androstadiene-3,17-dione	Androsta-1,4-diene-3,17-dione		284
AD	Androstenedione	Androst-4-ene-3,17-dione		286
MA	Methandrostenolone	Androsta-1,4-dien-3-one,17-beta-hydroxy-17-alpha-methyl-		300
MT	Methyltestosterone	Androst-4-en-3-one, 17-beta-hydroxy-17-methyl		302

In this paper, a mixture of anionic surfactant sodium cholate (SC) (50 mM) and Triton X-100 (0.1% (v/v)) was chosen as the micellar system, and the typical five anabolic steroids, such as androstenedione (AD), 19-norandrostenedione (NAD), 1,4-androstadiene-3,17-dione (ADD), methandrostenolone (MA) and methyltestosterone (MT) were selected as the targets for elevation of this mixed micellar system. These anabolic steroids, expect AD was a natural anabolic steroid, the other four were synthetic steroids, their molecular structures were very similar, and were all neutral compounds (see Table 1). Our experimental results demonstrated that the mixed micellar system has much better resolution than the single micellar system, and five analytes was basic separated in 12 min. Compared with the previous anabolic steroids detecting method, the established MEKC method was simpler, quicker, what is more important, it was more economical.

2. Experimental

2.1. Apparatus

All experiments were carried out using a CAPEL 105 Capillary Electrophoresis System (Lumex, Russia) with UV detector. Electrophoresis was performed in a 62 cm (54 cm effective length)×50 μm i.d. bare fused-silica capillary (Yongnian Optical Fiber Factory, Yongnian, Heibei Province, China). The water used was purified by Milli-Q water purification system (Millipore, Bedford, MA, USA). PHS-3c pH meter (Leizi Instrumentation Factory, Shanghai, China) was used for pH measurement.

2.2. Reagents

AD, NAD and MA were purchased from Sigma (St. Louis, MO, USA). ADD was obtained from TCI (Tokyo Kasei Kogyo Co., Japan). MT was purchased from National Institute for the Control of Pharmaceuticals and Biological Products (Beijing, China). SC was obtained from Acros Organics (Phillipsburg, New Jersey, USA). SDS was purchased from Sigma, and Triton X-100 was got from Sinopharm Chemical reagent Co. Ltd. (Shanghai, China). β-Glucuronates was purchased from Sigma (Sigma–Aldrich, USA). Ethanol was HPLC grade, and the other chemicals used were all analytical grade.

2.3. Preparation of running buffer and standard solution

Preparation of Britton-Robinson (BR, pH 9.0) buffer solution: 4.9464 g boric acid was accurately weighted into a beaker, and 4.6 mL of glacial acetic acid, 5.33 mL of strong phosphoric acid were added sequentially. Then diluting the mixed solution to 1000 mL with water. Thus, 0.040 M three-acid mixed liquor was obtained. Subsequently, 0.20 M NaOH solution was prepared by dissolving 8.0 g NaOH with water, then also exactly diluting to 1000 mL. NaOH solution was then added in drops to that three-acid mixed liquor to obtain BR buffers with different acidity. And the pH value was adjusted and marked with precise acidity instrument.

The running buffer was composed of 15 mM of Britton-Robinson (pH 9.0), 50 mM of SC and 0.1% (v/v) of Triton X-100. All buffers were freshly prepared everyday. Stock solutions (1.00 mg/mL) containing all analytical target compounds were prepared using ethanol. The five standard solutions could be stable within 2 months when stored in dark at 4 °C. The working solutions were prepared by diluting the stock solutions using a mixture of ethanol–buffer solution (pH 9.0 and 50:50, v/v).

2.4. Sample preparation

2.4.1. For CE method

Urine samples were collected from healthy volunteers (men) at the age of 23 in large containers without any preservative. Each candidate took three pills (30 mg) of MA tablets orally and then collected their total amounts of urine within 12 h, respectively. Blank urine samples were collected before taking the MA tablets.

Urine sample was extracted simply by liquid–liquid extraction: 5 mL N-hexane were added into the urine sample (5 mL), and the mixture was shaken for about 5 min and centrifuged for 10 min at 4000 rpm. The organic layer was separated and dried under N_2 stream at temperature of 40 °C. The dry residue was redissolved in 200 μL of ethanol solution (1:10, v/v) before analysis. The whole pre-treatment could be completed within 30 min.

Moreover, all the sample solutions, standard solutions and running buffers should be filtered through an injection cellulose acetate filter (0.22 μm) and ultrasonically degassed prior to use.

2.4.2. For GC–MS method

Since steroids are non-volatile and non-polar compounds, it is inevitable to do the derivatization before GC–MS detection. The steroid sample preparation for GC–MS determination could be summarized as the following three steps.

(1) Preconcentration and purification: The methyltestosterone (50 μL, 50 ng/μL) which acted as ISTD was added to 5 mL real urine samples. After urine sample was centrifuged for 10 min at 4000 rpm, the solution was forced to pass through a C18 SPE cartridge and then washed by 3 mL H_2O and eluted by 5 mL MeOH. The resulting solution was dried under N_2 stream at the temperature of 60 °C.

(2) Enzyme hydrolyzation: It was reported that before excretion in urine the steroid was strongly metabolized in human body. 6β-Hydroxylation is the major metabolic pathway, so the metabolites are both free and conjugated forms which mainly exist as steroid glucuronates [30,31]. Thus, before GC–MS analysis, derivatization enzyme hydrolyzation should be conducted to transfer the conjugated steroids into free steroids completely. Then the urine sample, which only contained free steroid was treated by 1.0 mL, 0.1 mol/L phosphate buffer (pH 7.0) and 5000 U β-glucuronates and incubated for 3 h at the temperature of 55 °C.

(3) Derivatization reaction: After cooling, 100 mg Na_2CO_3:$NaHCO_3$ (1/8, w/w) was added to retain alkalinity. Steroid fraction was extracted with 5 mL tert-butylmethylether and centrifuged for 10 min at 4000 rpm, and then the organic layer was separated and dried by N_2 stream at the temperature of 60 °C. Finally, the derivatization reaction was carried out for 30 min at 70 °C by methyl-trimethyl-silyl-trifluoroacetamide, trimethylsilyl imidazole and dithio-erythritol, whose functions were silylating reagent, catalytic agent and antioxidant, respectively.

2.5. Procedure for separation

New capillary was washed successively with 0.5 mM of hydrochloric acid for 30 min, deionized water for 10 min and 0.5 mM of sodium hydroxide for 30 min. After that the capillary was washed by deionized water for 10 min again. All the washing procedures were helpful to restore the proper condition of the internal surface. Before the Capillary Electrophoresis System was used everyday, the capillary should be flushed sequentially with deionized water for 5 min, 0.1 M NaOH for 10 min and deionized water for 5 min and finally equilibrated with running buffer for 10 min.

The sample was introduced by 30 mbars pressure for 10 s. The analysis was carried out in the above-mentioned buffer system under 18 kV running voltage. 241 nm was used as the detection wavelength. All experiments were performed at 25 °C. After each running, the capillary was flushed with running buffer for 3 min.

2.6. GC–MS detection

The Agilent 6890N gas chromatography-Agilent 5973i mass detector system was used in the study. Chromatographic separation was performed with an Agilent Capillary Column (HP-1MS, 30 m length × 0.25 mm i.d. × 0.1 μm film thickness) with the following instrumental conditions: Ultra-pure helium flow: 0.9 mL/min; injector temperature 280 °C; transfer line temperature 290 °C; energy of electron 70 eV; the oven temperature was set at 180 °C, increased to 220 °C at 3.3 °C/min, then increased to 310 °C at
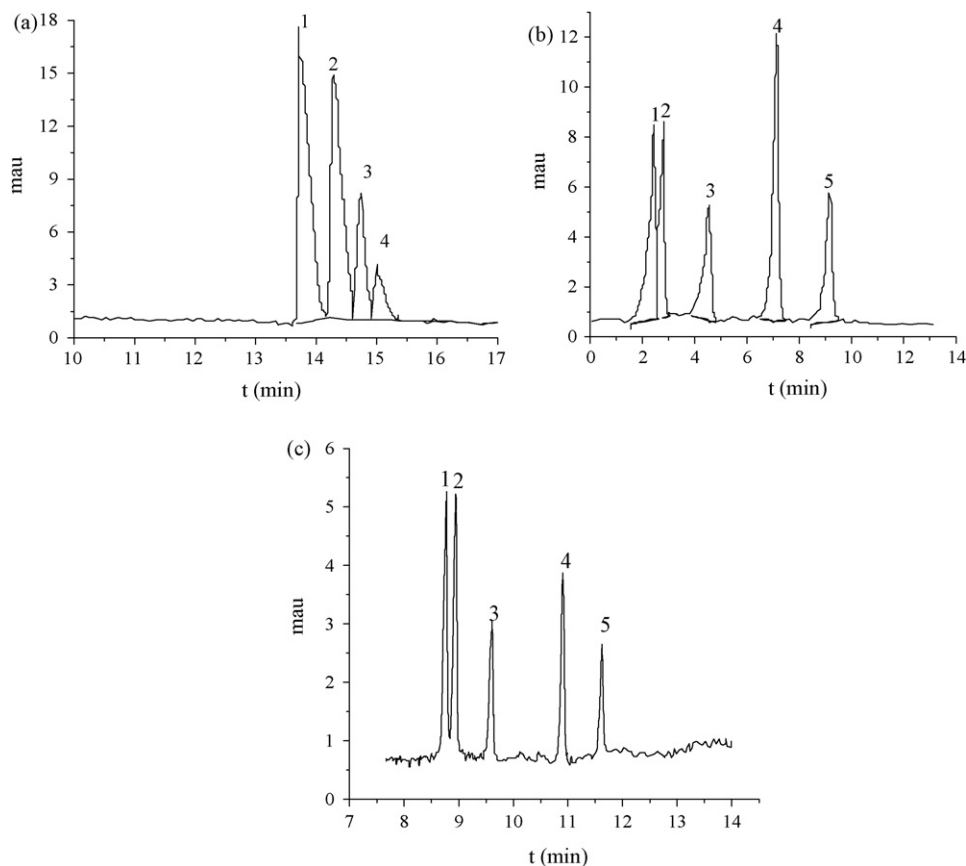
Fig. 1. Comparison of the effect on the separation by use of different surfactants. Analytical conditions: buffer solution: pH 9.0 BR (15 mM); applied voltage: 18 kV; detection UV: 241 nm; injection conditions: 30 mbar × 10 s. (a) SDS 20 mM, 1. NAD and ADD; 2. AD; 3. MA; 4. MT. (b) SC 50 mM, 1. NAD; 2. ADD; 3. AD; 4. MA; 5. MT. (c) SC 50 mM-0.1% (v/v) Triton X-100, 1. NAD; 2. ADD; 3. AD; 4. MA; 5. MT.

30 °C/min, and held for 3 min. The parameters of HP 5973i mass detector were: ion mass/charge ratio, 50–550 m/z; scan mode.

3. Results and discussion

Due to the similar structures and neutral character, it was difficult to separate the five steroids in a normal running buffer solution when CZE was employed. Therefore, MEKC was considered in the study for its superior separation efficiency to the neutral compounds [30,32].

3.1. Effects of electrolyte pH value and concentration

It was reported that the pH value of buffer solution was the most important parameter affecting the separation efficiency of CZE mode. However, in this MEKC mode, when bi-micellar surfactant containing 50 mM SC and 0.1% (v/v) Triton X-100 were used, the change of pH value from 5.0 to 10.0 did not affect the resolution. In order to get a short analytical time, pH 9.0 was employed in this study.

Increasing the concentration of buffer solution would influence the viscosity coefficient of the running solution, which would lead to decreasing the eletroosmotic flow (EOF). When the buffer concentration increased from 10 to 30 mM, the migration time was prolonged and meanwhile the current intensity turned to be higher and more instable. In order to save analytical time and get the good separation, BGE containing 15 mM BR was chosen as the optimal concentration.

3.2. Selection of the surfactants

As a kind of surfactant widely used in MEKC, SDS was firstly examined in our work. The effect of SDS on separation efficiency was firstly studied on our five targets substances by adding certain amount of SDS into the BR solution in the presence of 0.1% (v/v) Triton X-100. The concentration of SDS varied in the range of 10–40 mM. It was found that when the concentration of SDS increased, AD, MA and MT could be separated gradually, but the other two steroids (NAD and ADD) could not be separated any more (peaks were overlapped completely) (see Fig. 1a). In the meantime the migration time was prolonged obviously and the widths of the corresponding peaks were enlarged greatly.

Since the five steroids could not be separated completely by SDS, another surfactant SC was tried in this study. SC is a kind of bile salts, which have a large, rigid and planar hydrophobic structure in their steroid nucleus with two or three hydroxyl groups. Due to the special molecular structures of bile salts, they belong to a special group of biosurfactants and have different properties compared with other surfactants. Some reports have indicated that bile salts provided better selectivity and greater micelle polarity compared with SDS [33]. Our experiment confirmed this viewpoint. The SC in the running buffer had a significant effect on the separation of AAS. When the concentration of SC was higher than its CMC (14 mM), the neutral steroids interacted with SC micelles and caused different migration behavior of the various anabolic steroids. The effects of SC on the migration behavior of the target analytes were examined under the concentration of 15, 25, 35, 45, 50, 55 and 60 mM, respectively. When the concentration of SC was higher than 50 mM,

Table 2
Results of regression analysis on calibration curves and the detection limits[a]

Analyte	Regression equation ($y = ax + b$)	Correlation coefficient (R^2)	Linear range (µg/mL)	Detection limits (µg/mL)
NAD	$y = 1.9276x + 3.9512$	0.9987	0.7–100.0	0.31
ADD	$y = 1.6366x + 1.3995$	0.9986	0.6–50.0	0.22
AD	$y = 1.5387x + 2.3995$	0.9987	1.0–60.0	0.43
MA	$y = 1.1879x + 1.6227$	0.9984	0.6–70.0	0.20
MT	$y = 3.4643x + 6.2123$	0.9991	1.2–80.0	0.51

y: peak area (mAU × s); x: amount concentration (µg/mL).

[a] Other conditions are the same as in Fig. 1(c).

not only AD, MA and MT separated well, but also NAD and ADD (peak 1 and peak 2 in Fig. 1b) had a trend to be separated. Another profit was that the separation time would greatly shorten when SC was adopted as the surfactant instead of SDS. As a compromise, the 50 mM SC was selected as the optimal concentration.

In order to further improve the separation of NAD and ADD, the mixed surfactants were taken into consideration for adjusting the resolution or peak distribution in MEKC [34,35]. So in this experiment, methanol, carbamide and Triton X-100 were tested as the additives of BR buffer and SC surfactant. Only when Triton X-100 was used as additives, NAD and ADD could be separated completely. The reason might be that Triton X-100 was a kind of nonionic surfactant, when it was applied in CE, it could be used as a false static phase inside the capillary to control the EOF at the same time [36]. The effect of Triton X-100 concentration on the separation of NAD and ADD was investigated carefully in the range of 0–0.25%. The result showed that the satisfied resolution ($R_s = 1.63$) for the two analytes could be obtained when the concentration of Triton X-100 was 0.1% (v/v). Fig. 1c shows the good separation when Triton X-100 was used as additive in the SC surfactants. At last, bi-micellar surfactant containing 50 mM SC and 0.1% (v/v) Triton X-100 were utilized in this study.

3.3. Optimization of instrument parameters

The parameters of the instrument, such as separation voltage, injection time and detection wavelength were also optimized to get the best separation and detection of these five analytes.

The effect of separation voltage on the migration time of the analytes had been investigated. The results showed that the migration time was decreased with the increasing voltage for all five compounds. However, when the separation voltage was higher than 18 kV, the separation efficiency was not good. Thus, 18 kV was chosen as the optimal working voltage. Injection time is another important factor influencing the analytical sensitivity and selec-

tivity. Injection time experiment gave the result that peak area would be increased with the injection time increasing from 6 to 14 s at the intervals of 2 s under the injection pressure of 30 mbar. However, peak broadening appeared obviously when injection time was longer than 10 s. Therefore, 10 s was selected as the optimal injection time.

UV spectrometer was used to look for the maximum wavelength of the five steroids. The experimental result showed that the maximum wavelength was always in the range of 238–244 nm. As a compromise of the sensitivities of five analytes, 241 nm was selected as the most suitable wavelength for this method.

To sum up, the optimum conditions for separation and detection could be described as follows. The BGE containing the mixture surfactants of 50 mM SC and 0.1% (v/v) Triton X-100 in a 15 mM BR (pH 9.0) buffer were used as running solution. In addition, 18 kV was applied for CE separation. The injection condition was 30 mbar × 10 s and the detection wavelength was 241 nm. Under these conditions, a typical separation electropherogram of a standard mixture solution is illustrated in Fig. 1(c). The chromatogram showed these five similar neutral compounds could be completely separated in a short time (12 min).

3.4. Linear range, detection limit and repeatability

A series of the standard mixture solution of NAD, ADD, AD, MA and MT were determined and then quantitative result of this method is given in Table 2. The linear relation was based on the concentration of the compound and the corresponding peak area. The regression equations, linear ranges, correlation coefficients and detection limits are shown in Table 2. The linear ranges (with correlation coefficients $R^2 > 0.9984$) were 0.7–100.0, 0.6–50.0, 1.0–60.0, 0.6–70.0 and 1.2–80.0 µg/mL for NAD, ADD, AD, MA and MT, respectively. The detection limits of the five analytes were in the range of 0.20–0.51 µg/mL (signal to noisy, S/N = 3).

Table 3
Recovery of the spiked urine sample[a]

Analyte	Added (µg/mL)	Found (µg/mL)	Recovery (%)	R.S.D. (%) ($n = 3$)
NAD	10.0	8.15	81.5	3.9
	5.00	4.39	87.8	4.8
	15.0	15.2	101	1.9
ADD	11.0	10.6	96.6	2.1
	5.50	5.09	92.5	5.7
	16.5	18.7	113	2.6
AD	9.00	7.43	82.6	1.6
	4.50	4.59	102	2.6
	13.5	12.0	88.9	3.1
MA	12.0	10.2	85.0	4.5
	6.00	5.42	90.4	3.7
	18.0	18.9	105	3.3
MT	10.5	9.79	93.2	2.7
	5.20	4.51	86.7	2.9
	15.7	13.7	87.3	3.7

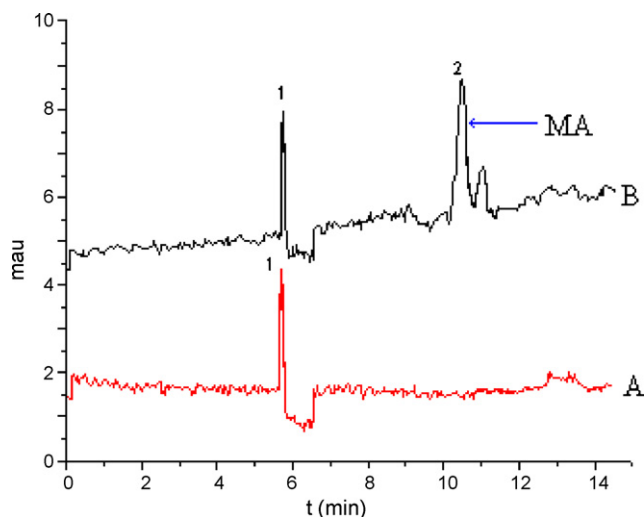[a] Other conditions are the same as in Fig. 1(c).

Fig. 2. The electropherograms of the blank urine sample (A) and urine sample after volunteer's oral administration of methandrostenolone tablets (B). The conditions were the same as in Fig. 1(c), 1. ethanol; 2. MA.
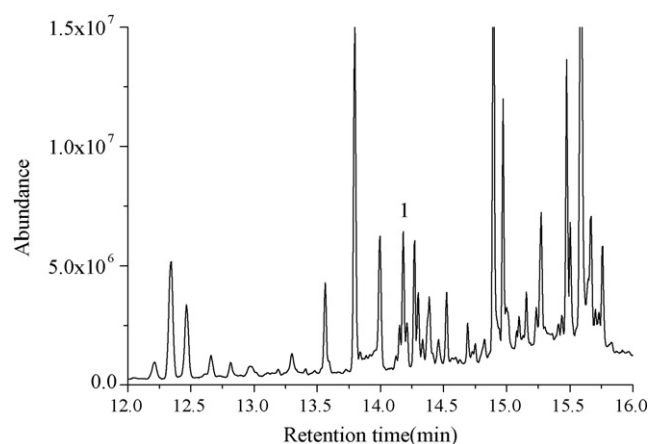

Fig. 3. GC–MS total ion chromatogram of scan analysis of urine sample 1. methandrostenolone-2TMS. GC–MS conditions are as shown in Section 2.6.

A standard mixture solution of five analytes was analyzed to evaluate the repeatability of the peak area and migration time under the optimum conditions. The results showed that the R.S.D. ($n = 7$) of the migration times and the peak areas were less than 0.7%, and 2.7%, respectively.

3.5. Applications to the real urine sample

3.5.1. Spiked urine sample

The content of MA in MA tablet was determined firstly, the detected content was 88.2 mg/g compared with the marked content in the brand (92.5 mg/g), and the accuracy was 95.4% (R.S.D. = 2.5%, $n = 5$). Then mixed solutions of five standard analytes were added into the blank urine following the simple sample pre-treatment (see Section 2.4.1). The result showed that no interference was observed when the endogenous matter and the target compounds were coexisted in urine samples. In order to verify the reliability of the method, the recoveries of these compounds in the urine samples were also investigated, and the repeatability was determined by repeated injection of solution ($n = 3$). The method recoveries of the five analytes ranged from 81.5 to 113% with the R.S.D. <5.7% (see Table 3).

3.5.2. Real urine sample

AAS have been widely used to improve athletic performance because of their myotrophic action. Hence, the determination of the anabolic steroids in urine is one of the essential parts of doping control.

In order to validate the feasibility of this method, MA, the main component of methandrostenolone tablets, was measured in the real urine sample after volunteer's oral administration. The real urine samples were simply prepared according to the procedure described in Section 2.4.1. As illustrated in Fig. 2, the free MA component was successfully detected, and target peak was traced by adding standard MA solution. This result demonstrated that no significant endogenous matter was interfered with the targeted MA.

Moreover, GC–MS method had been used to make the further confirmation whether the MA remained in the real urine sample. The sample preparation for GC–MS detection was according to Section 2.4.2. The GC–MS method validated the existence of the MA in urine, Fig. 3 refers to the total ion chromatogram of derivatization product ion. The conditions of GC–MS are described in detail in Section 2.5. Fig. 4 shows the mass spectra of MA-2TMS (derivatization product) obtained by GC–MS. As shown in Fig. 4, it points out that the ion ($m/z = 444$) is the characteristic ion fraction of MA-2TMS, and confirmation ions 206 and 143 are assigned to the fragmentation of rings B and D, respectively (molecular mass of -OTMS is 88).

The result of GC–MS analysis confirmed that the MEKC method established in this paper could be successfully applied to the determination of the anabolic steroids in the real urine samples.
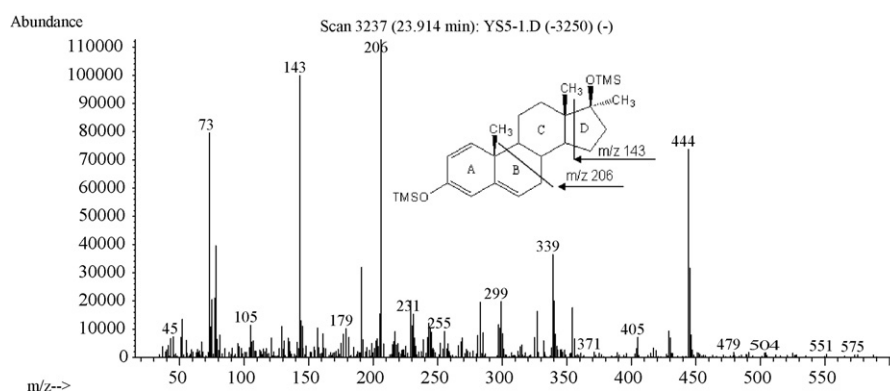

Fig. 4. The mass spectrum of methandrostenolone-2TMS. A, B, C and D represent ring A, ring B, ring C and ring D, respectively. GC–MS conditions are as shown in Section 2.6.

4. Conclusion

A MEKC method has been developed for the determination of five anabolic steroids including natural and synthetic ones. A new mixed micelle solution consisting of SC and Triton-100 was originally studied to solve the hard separation problem of these neutral steroids with the similar structures. Under the optimum conditions, baseline separation of the five analytes was achieved within 12 min. The free MA in the candidate's urine who orally took methandrostenolone tablets was detected, and GC–MS method confirmed this conclusion.

This method compared with the conventional GC–MS method had some evident advantages: (1) rapid analysis, only 12 min was consumed while at least 30 min for GC–MS; (2) simple sample preparation. For GC–MS tedious sample precondition especially derivatization reaction was usually requested. The total time for sample preparation should be more than 2 days. However, without derivatization the simple sample preparation for MEKC was only within 30 min; (3) low analytical expense. One sample would need at least 10–20 dollar for GC–MS determination, but only 2 dollar was sufficient for MEKC. To sum up, the MEKC established in this paper was promised to be a simple, rapid and low-cost method for the determination of the anabolic steroids in human urine. Future work will be focused on developing the undersized and mobile equipment for the field doping determination.

Acknowledgements

References

[1] Z.Y. Yang, M.Y. Qu, C.L. Yu, Sports Medicine, Peking University Medical Press, Beijing, 2003, p. 315.
[2] Z. Xu, Q.D. You, Pharmaceutical Chemistry, Chemical Industry Press, Beijing, 2004, p. 548.
[3] S. Wang, W.B. Chang, Univ. Chem. 18 (2003) 35.
[4] S.B. Karch, Drug Abuse Handbook, CRC Press, Boca Raton, Boston, London, 1998, p. 653.
[5] W. Schänzer, M. Donike, Anal. Chim. Acta. 275 (1993) 23.
[6] C. Ayotte, D. Goudreault, A. Charlebois, J. Chromatogr. B 687 (1996) 3.
[7] A. Huenerbein, M.A.S. Marques, A.S. Pereira, et al., J. Chromatogr. A. 985 (2003) 375.
[8] K. Van Uytfanghe, D. Stöckl, J.M. Kaufman, et al., Clin. Chem. 50 (2004) 2101.
[9] B.K. Yap, R. Kazlauskas, K. Elghazi, et al., J. Chromatogr. B 687 (1996) 117.
[10] F. Guan, C.E. Uboh, L.R. Soma, et al., J. Chromatogr. B. 829 (2005) 56.
[11] R. Gonzalo-Lumbreras, R. Izquierdo-Hornillos, J. Chromatogr. B 742 (2000) 47.
[12] M.L. Marina, M. Torre, Talanta 41 (1994) 1411.
[13] L. Zhang, G.N. Chen, Q. Hu, et al., Anal. Chim. Acta 431 (2001) 287.
[14] L. Zhang, P. Tong, G.N. Chen, J. Chromatogr. A 1098 (2005) 194.
[15] N. Anastos, N.W. Barnett, S.W. Lewis, Talanta 67 (2005) 269.
[16] L. Zhang, Q. Hu, G.N. Chen, et al., Anal. Chim. Acta. 424 (2000) 257.
[17] L. Zhang, Y.H. Liu, G.N. Chen, J. Chromatogr. A 1043 (2004) 317.
[18] K. Altria, A. Marsh, C. Sänger-van de Griend, Electrophoresis 27 (2006) 2263.
[19] R. Jabeen, D. Payne, J. Wiktorowicz, et al., Electrophoresis 27 (2006) 2413.
[20] X.Y. Zheng, M.H. Lu, L. Zhang, et al., Talanta 76 (2008) 15–20.
[21] Q. Zhang, Y.F. Li, C.Z. Huang, Talanta 76 (2008) 44–48.
[22] R. Injac, N. Kocevar, S. Kreft, Anal. Chim. Acta. 594 (2007) 119.
[23] N. Helali, N.T. Tran, L. Monser, et al., Talanta 74 (2008) 694.
[24] M.A. Abubaker, J.R. Petersen, M.G. Bissell, J. Chromatogr. B 674 (1995) 31.
[25] G.A. Valbuena, L.V. Rao, J.R. Petersen, et al., J. Chromatogr. A 781 (1997) 467.
[26] W.C. Lin, C.C. Sue, C.H. Kuei, Chromatographia 49 (1999) 454.
[27] C. Fernandez, G. Egginger, I.W. Wainer, et al., J. Chromatogr. B 677 (1996) 363.
[28] L.K. Amundsen, J.T. Kokkonen, S. Rovio, et al., J. Chromatogr. A 1040 (2004) 123.
[29] L.K. Amundsen, H. Sirén, J. Chromatogr. A 1131 (2006) 267.
[30] B.G. Wolthersa, G.P.B. Kraan, J. Chromatogr. A 843 (1999) 247.
[31] W. Schänzer, S. Horning, M. Donike, Steroids 60 (1995) 353.
[32] J.G. Bumgarner, M.G. Khaledi, Electrophoresis 15 (1994) 1260.
[33] H. Nishi, T. Fukuyama, M. Matsuo, et al., J. Chromatogr. A 498 (1990) 313.
[34] C.E. Lin, M.J. Chen, H.C. Huang, et al., J. Chromatogr. A 924 (2001) 83.
[35] Y. Esaka, M. Kobayashi, T. Ikeda, et al., J. Chromatogr. A 736 (1996) 273.
[36] Y.M. Li, A. Van Schepdael, E. Roets, et al., J. Pharm. Biomed. Anal. 15 (1997) 1063.

Kinetic study of uranium speciation in model solutions and in natural waters using Competitive Ligand Exchange Method

Jiujiang Zhao, Ismail I. Fasfous[1], John D. Murimboh[2], Tahir Yapici[3], Parthasarathi Chakraborty[4], Sheren Boca, Chuni L. Chakrabarti[*]

Department of Chemistry, Carleton University, 1125 Colonel By Drive, Ottawa, Ontario, K1S 5B6, Canada

ARTICLE INFO

ABSTRACT

Kinetic speciation of uranium in model solutions containing uranium and humic acid (HA) and in natural waters has been investigated by Competitive Ligand Exchange Method (CLEM). In alkaline freshwaters, most of uranium species were uranium–carbonate species, which were labile in the CLEM experiment. The uranium speciation of every sample was characterized either as "labile" or "non-labile" uranium complexes depending on the dissociation rate coefficients of the complexes. The results showed that as the U(VI)/HA ratio was decreased, the dissociation rate coefficients decreased and the labile fraction decreased as well. When the U(VI)/HA ratio was 0.1, the labile fraction of the U(VI)-HA increased with increasing pH; however, there was no pH effect on the dissociation of U(VI)-HA complexes at lower U(VI)/HA ratios. Chelex-100 had some limitations in its use for the study of dissociation of U(VI)-HA complex at very low U(VI)/HA ratios. By developing an analytical method and procedure for quantitative determination of kinetic parameters for the dissociation of uranium-HA complexes in model solutions and natural waters, this work has made a substantial contribution to analytical chemistry.

© 2008 Elsevier B.V. All rights reserved.

1. Introduction

Uranium is one of the heaviest naturally occurring elements on Earth. It has 16 known isotopes, all of which are radioactive. In nature, U consists of a mixture of three isotopes, ^{238}U (99.276%), ^{235}U (0.718%), and ^{234}U (0.0056%) [1]. The chemical toxicity of uranium in natural water systems depends not only on the total uranium concentration, but also on the chemical speciation of uranium [2]. Uranium exists as various chemical species in natural waters, including the free metal ions (UO_2^{2+}), and complexes with inorganic and organic ligands (both anion and cation) [3]. Humic substances (fulvic acid, humic acid, and humin), which represent typically 40–99% of dissolved organic carbon (DOC) [4], are important complexing agents for uranium in natural waters at neutral or low pH. Fulvic acid (FA) apparently reduces the bioavailability of U with increasing pH, by reducing the activity of UO_2^{2+} [5]. The binding of U(VI) by humic acid (HA) is stronger than that by fulvic acid and exhibits a larger pH-dependence [6]. Several kinetic studies of other metals complexation with humic substances have been done using Competitive Ligand Exchange Method (CLEM) [7–10]. However, published literature on the kinetics of uranium binding to the humic substances is relatively scarce. This work presents the results of our investigation of kinetics of uranium binding to humic acid, studied using CLEM combined with inductively coupled plasma mass spectrometry (ICP-MS).

2. Competitive Ligand Exchange Method

The kinetic model proposed by Olson and Shuman [11] was adapted to the study of speciation of uranium(VI) complexes as described below.

Consider a metal complex, ML_i, undergoes a first-order or pseudo-first-order dissociation, as follows:

$$ML_i \underset{k_{f,i}}{\overset{k_{d,i}}{\rightleftharpoons}} M + L_i \quad \text{(slow)} \tag{1}$$

* Corresponding author. Tel.: +1 613 5202600; fax: +1 613 5203749.
E-mail address: chuni_chakrabarti@carleton.ca (C.L. Chakrabarti).
[1] Current address: Department of Chemsitry, The Hashemite University, P.O. Box 150459, Zarqa 13115, Jordan.
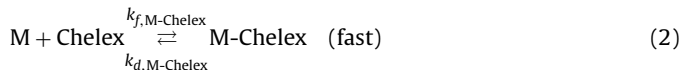[2] Current address: Department of Chemistry, Acadia University, University Avenue Wolfville, NS B4P 2R6, Canada.
[3] Current address: Health Canada, Environmental Health Centre, room B16, 50 Colombine Driveway, Tunney's Pasture, 0800B3, Ottawa (Ont.), Canada, K1A 0K9.
[4] Current address: Laboratory of Physical Chemistry and Colloid Science Wageningen University, Chemistry building (building number 316), Dreijenplein 6, 6703 HB Wageningen, The Netherlands.

where M is a metal ion and L_i is a complexant such as $CO_3{}^{2-}$ or humic acid, $k_{d,i}$ and $k_{f,i}$ are the rate coefficients of dissociation and formation of ML_i, respectively. The charges have been omitted for simplicity.

Assuming that the metal reacts with a large excess of a competing ligand, Chelex-100 chelating resin, resulting in the formation of a strong M–Chelex complex:

$$M + Chelex \underset{k_{d,\text{M-Chelex}}}{\overset{k_{f,\text{M-Chelex}}}{\rightleftarrows}} M\text{-Chelex} \quad (\text{fast}) \qquad (2)$$

where $k_{f,\text{M-Chelex}}$ and $k_{d,\text{M-Chelex}}$ are the rate coefficients of formation and dissociation of M–Chelex, respectively. Since the competing ligand has been added in large excess, the net reaction, Eq. (3), lies far to the right, and is considered as pseudo-first-order and irreversible

$$ML_i + Chelex \rightarrow M\text{-Chelex} + L_i \qquad (3)$$
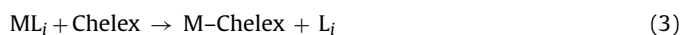
The concentration of ML_i can be described by a pseudo-first-order rate law.

$$-\frac{dc_{ML_i}}{dt} = k_{d,i} c_{ML_i} \qquad (4)$$

Integrating Eq. (4) and get Eq. (5):

$$c_{ML_i}(t) = c_{ML_i}^0 exp(-k_{d,i}t) \qquad (5)$$

where $c_{ML_i}^0$ is the initial concentration of the ML_i complex and $cML_i(t)$ is the concentration of the ML_i complex at any time, t, $k_{d,i}$ is dissociation rate coefficient of ML_i.

Since it has been assumed that the ML_i complexes dissociate simultaneously and independently, the total concentration of metal c_M remaining in the solution, at any time, t, is shown by Eq. (6)

$$c_M(t) = \sum_{i=1}^{n} c_{ML_i}^0 exp(-k_{d,i}t) \qquad (6)$$

In M-HA system, Eq. (6) can be simplified as consisting of two components: fast (labile) and slow (non-labile) component, and re-written as Eq. (7)

$$c_M k(t) = c_1 exp(-k_{d1}t) + c_2 exp(-k_{d2}t) \qquad (7)$$

where c_1 and c_2 are the initial concentrations of the fast and the slow component and k_{d1} and k_{d2} are the dissociation coefficients of these components, respectively. The percentage of the total metal remaining in the solution, $C_M(t) = c_M(t)/c_M(0) \times 100\%$, at any time t, was used in this work to avoid the bias error. Eq. (7) can be re-written as:

$$C_M(t) = C_1 exp(-k_{d1}t) + C_2 exp(-k_{d2}t) \qquad (8)$$

where C_1 and C_2 are the percentage of the fast and the slow component, respectively, in the initial solution; $C_1 = c_1/c_M(0) \times 100\%$ and $C_2 = c_2/c_M(0) \times 100\%$.

3. Experimental

3.1. Reagents

Chelex-100 chelating resin (Bio-Rad 100–200 mesh) was conditioned for the work by soaking Chelex-100 resin sequentially in methanol, 1 mol/L HCl, 3 mol/L NH_4OH and 0.1 mol/L HCl [12]. The ICP-MS/AES uranium standard solution (SCP SCIENCE, 1000 mg/L) was used to prepare uranium model solutions in ultra pure water of resistivity of 18.2 MΩ cm, obtained direct from a Milli-Q Academic (Millipore, USA) ultrapure water system. Nitric acid (Optima, Fisher Scientific) and sodium hydroxide (Caledon Laboratories Ltd.) were

used to adjust the pH. Ammonium acetate (BDH Inc.) was used to prepare 0.01 mol/L ammonium acetate solutions.

Humic acid was supplied by Dr. Les Evans (University of Guelph, Guelph, Ontario), who characterized and purified the HA according to the procedure recommended by the International Humic Substances Society. The bidentate complexing capacity of HA was calculated to be 4.88 mmol/g [13]. A stock solution of 1.0 g/L HA was prepared by dissolving approximately 1.0 g HA in sodium hydroxide, and the solution was made up to 1 L of ultrapure water. The solution was stored in the dark at 4 °C.

3.2. Model solutions, the synthetic lake water sample, and the natural water sample

A series of model solution was prepared by spiking known amounts of uranium standard solution into the HA solutions to make the concentration ratio of U(VI)/HA 0.1, 0.01 and 0.001. The total uranium concentration in these solutions was fixed at 20 µg/L (8.4×10^{-8} mol/L), whereas the HA concentration was varied: 0.2, 2.0 and 20 mg/L. The above concentration range corresponded to the range found in natural waters. Ammonium acetate was added to those model solutions as pH buffer (final concentration 0.01 mol/L). The mole/mass ratio of U(VI)/HA in the above three solutions was 0.42, 0.042 and 0.0042 mmol/g. The pH of these model solutions was adjusted to 6.0, 7.0 or 8.0, using aqueous solutions of NaOH and HNO_3. The model solutions were then equilibrated for 48 h in the dark at room temperature.

Samples of natural waters (surface waters) were collected from St. Lawrence River at Morrisburg (Ontario, Canada), using 2.2 L Teflon bottles. Major cations and anions were quantitatively determined by using atomic emission spectrometry (AES) and ion-exchange chromatography (IEC), respectively. Total dissolved organic carbon and inorganic carbon were determined using TOC Analyzer (Shimadzu TOV-V$_{CPH}$). The synthetic lake water sample simulating the natural lake water was prepared in our laboratory by adding inorganic chemicals and humic acid to ultrapure water of resistivity 18 MΩ cm.

300 mL of the test sample of above solutions was stirred with a Teflon-coated magnetic stirring bar in a Teflon reactor. About 3 g Chelex 100 resin (1 g/100 mL), which had been soaked in 0.01 mol/L ammonium acetate buffer at the same pH as that of the test sample solution, was added to the test sample. The test sample was filtered with a 8 µm polycarbonate membrane filter (Whatman), which was placed at the end of the reactor tube to filter out the Chelex 100 resin before introducing the filtrate into Elan 6100 DRC ICP-MS (PerkinElmer SCIEX). The total experimental time was 1–2 h.

4. Results and discussion

The U(VI)-HA systems were very complex, even in a simple model solution. The complexation kinetics of U(VI)-HA could be influenced by many factors, such as the deprotonation of HA at different pH, the hydrolysis of uranyl ion and the formation of uranyl complexes. The experimental data were analyzed using Marquardt–Levenberg algorithm, an advanced non-linear regression algorithm. All the data were fitted using one, two or three distinct components to find the best-fitting curve, using SigmaPlot 10 computer program (Systat Software Inc.).

The kinetic curves and kinetically distinguishable components are presented in Figs. 1–3 and Tables 1–3. The error bars in the figures represent standard deviation of the average of three measurements. In the kinetic curves, the initial steep part represents the fast component, which is the labile fraction (C_1), whereas the plateau part is the slow component or non-labile fraction
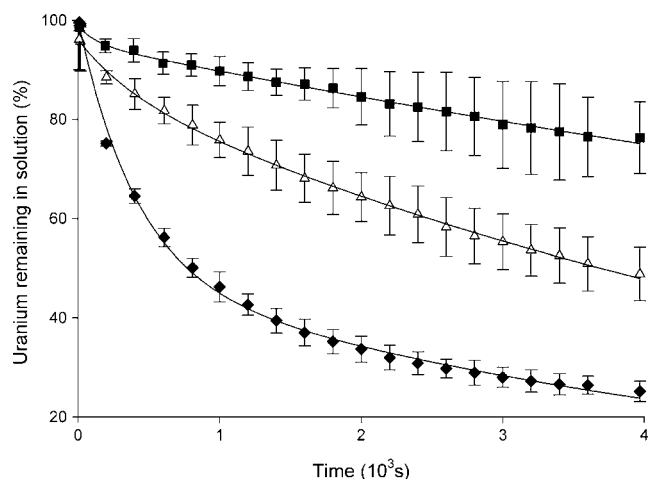
Fig. 1. Ligand exchange kinetics for three U(VI)/HA ratios in model solutions at pH 6.0. Uranium concentration was 20 μg/L (8.4×10^{-8} mol/L) and ammonium acetate concentration was 0.01 mol/L, whereas humic acid concentration was varied. (♦) U/HA ratio 0.1 and HA 0.2 mg/L, (△) U/HA ratio 0.01 and HA 2.0 mg/L and (■) U/HA ratio 0.001 and HA 20.0 mg/L. Error bars represent standard deviations for the average of three measurements.
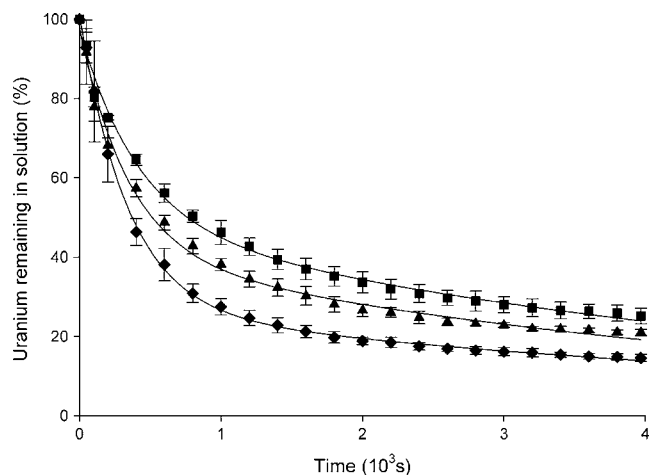

Fig. 2. Ligand exchange kinetics for U(VI)/HA in model solutions with U(VI)/HA ratio 0.1 at different pH values. Uranium concentration was 20 μg/L (8.4×10^{-8} mol/L), HA concentration is 0.2 mg/L, ammonium acetate 0.01 mol/L. (■) pH 6.0, (▲) pH 7.0, (♦) pH 8.0. Error bars represent standard deviations for the average of three measurements.

(C_2). As reported by Sekaly et al. [14,15], the binding sites of humic substances can be differentiated into recognizable groups, approximated by a small collection of rate coefficients. The binding sites of heterogeneous, natural organic complexants, such as

Table 1

Kinetically distinguishable components in U(VI)-HA model solutions, ammonium acetate concentration 0.01 mol/L, uranium concentration 20 μg/L

U/HA ratio	pH	C_1 (%)	k_{d1} (10^{-3} s^{-1})	C_2 (%)	k_{d2} (10^{-5} s^{-1})
0.1	6	50.2 ± 5.6	2.0 ± 0.1	44.6 ± 2.7	15.3 ± 0.5
	7	58.1 ± 5.4	2.3 ± 1.0	34.6 ± 12.4	12.7 ± 11.5
	8	78.5 ± 6.7	2.5 ± 0.4	20.9 ± 0.9	7.4 ± 1.4
0.01	6	31.2 ± 1.6	0.6 ± 0.04	62.6 ± 0.7	9.4 ± 0.6
	7	24.0 ± 2.7	0.6 ± 0.1	66.7 ± 3.0	9.9 ± 0.5
	8	26.2 ± 4.7	0.4 ± 0.1	71.6 ± 5.7	6.6 ± 1.0
0.001	6			94.0 ± 3.4	4.3 ± 0.8
	7			82.3 ± 3.1	3.3 ± 0.5
	8			83.1 ± 5.1	2.8 ± 0.5

Table 2

Kinetically distinguishable components in U(VI)-HA model solutions without the ammonium acetate buffer, pH 7.0, uranium in 0.01 mol/L ammonium acetate buffer, pH 7.0, and uranium in 0.004 mol/L sodium bicarbonate, pH 10

U/HA ratio	C_1 (%)	k_{d1} (10^{-3} s^{-1})	C_2 (%)	k_{d2} (10^{-5} s^{-1})
0.1	46.3 ± 3.1	1.1 ± 0.2	51.3 ± 1.6	11.9 ± 1.9
0.01	16.6 ± 2.3	2.4 ± 2.2	77.1 ± 6.3	10.3 ± 2.6
0.001	3.2 ± 1.3	1.8 ± 0.8	95.4 ± 2.1	4.9 ± 0.5
U, buffer only	73.1 ± 10.6	10.5 ± 3.7	25.3 ± 10.8	46.3 ± 3.5
U, NaHCO$_3$	90.8 ± 10.5	19.9 ± 4.7	20.4 ± 4.9	20.6 ± 6.5

Uranium concentration 20 μg/L.

humic substances, have continuous distributions and it is therefore impossible to define the individual binding sites. Two kinetically distinguishable components (fast and slow) were found to be the best fitting for the data.

4.1. Effect of the U(VI)/HA ratio on kinetic parameters

Fig. 1 presents the ligand exchange kinetics for the three U(VI)/HA ratios in model solutions at pH 6.0. The data for the other pH values are not shown. Table 1 shows the kinetic parameters obtained by fitting the data for all the pH values to the Kinetic Model. The concentration of uranium bound to strong binding sites of humic acid (slow or non-labile component) increased with decreasing U(VI)/HA ratio at all pH values, whereas the concentration of uranium bound to weak binding sites (fast or labile component) decreased. The dissociation rate coefficients of U(VI) bound to humic acids decreased with decreasing U(VI)/HA ratios, probably because uranium was bound to stronger binding sites at lower U(VI)/HA ratios. Saito et al. [16] reported two apparent complex formation constants for uranium–humic acid complex, indicating two different types of binding sites for uranium in humic acid. However, the rate coefficients (k_{d1} and k_{d2}) do not correspond to two precisely defined binding sites or complexes because there is a large number of binding sites in humic acid and the physical and chemical nature of the sites vary widely. Hence, the rate coefficients probably represent the average dissociation coefficient of similar binding sites.

The first-order dissociation rate coefficient of the fast kinetically distinguishable component (k_{d1}) is around 10^{-3} s^{-1}, whereas that of the slow component (k_{d2}) is about 10^{-5} s^{-1}. Compared to the previous studies on nickel-HA model solutions [7], the first-order
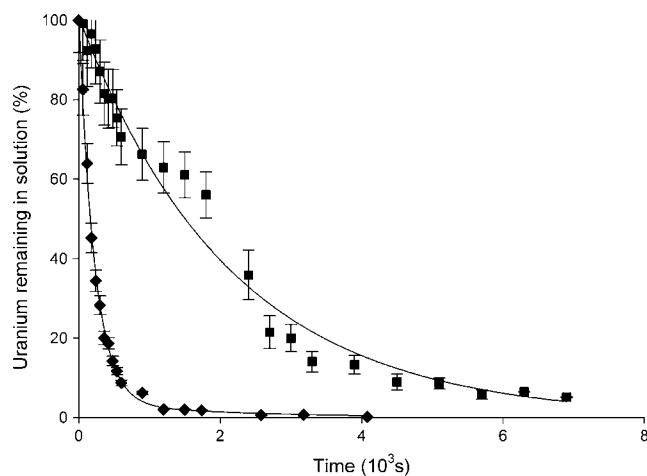

Fig. 3. Ligand exchange kinetics of uranium species in St. Laurence River and synthetic lake water sample. Uranium concentration was 10 μg/L. (■:) Synthetic lake water and (♦) St. Laurence River water sample. Error bars represent standard deviations for the average of three measurements.

dissociation rate coefficients of uranium are higher than that of nickel, which are about $10^{-4}\,\text{s}^{-1}$ (fast), and $10^{-6}\,\text{s}^{-1}$ (slow), suggesting that the UO_2^{2+} binds less strongly than Ni^{2+} to humic acid.

To study the effect of pH buffer on the kinetics parameters of U-HA complexes, U(VI) model solutions with the ammonium acetate buffer and without the buffer were investigated using CLEM. Table 2 presents the kinetic parameters for uranium in 0.01 mol/L ammonium acetate buffer and U(VI)-HA model solution without pH buffer, at pH 7.0. In the U-ammonium acetate system (pH 7), the major uranium species are $UO_2(OH)_2$ (aq.) (38%) and UO_2OH^+ (33%), calculated by Visual MINTEQ program, whereas U-acetate species is about 12%. The "labile" and the "non-labile" fraction can be obtained from the data fitting, which may, however, interfere with the determination of speciation parameters of U-HA. The "labile fraction" of uranium in the ammonium acetate buffer is much greater than that in the U(VI)-HA model solution without the buffer. The rate coefficients for both fast and slow components in the ammonium acetate buffer are about 10 times higher than those in the U(VI)-HA model solution without the buffer, which indicates that the uranium species in ammonium acetate buffer is more labile than that in U-HA model solution. The ammonium acetate buffer can affect the results of the uranium kinetic speciation. Compared with the data of U(VI)-HA model solution with the buffer at pH 7.0 in Table 1, the labile component in the U(VI)-HA model solution with the buffer is greater than that without the buffer, probably because of the formation of uranium–acetate complex in the U(VI)-HA model solution with the buffer. The uranium bound to weak binding sites of humic acid and uranium–acetate complex are not distinguishable in CLEM, probably because the dissociation rate coefficients of the two uranium complexes are very close. Table 2 also shows the kinetic parameters for uranium in 0.004 mol/L sodium bicarbonate. Uranium-carbonate species predominate in the presence of bicarbonate and carbonate, and in CLEM experiment these species are identified as labile species.

4.2. Effect of pH on kinetic parameters

There is no significant pH effect on the kinetic parameters in the model solutions having the U (VI)/HA ratio 0.01 and 0.001. However, at the U (VI)/HA ratio 0.1, as pH values increases from 6.0 to 8.0, the labile component increases with a corresponding decrease in the non-labile component. Fig. 2 presents the ligand exchange kinetics for U(VI)/HA in model solutions having the U(VI)/HA ratio 0.1 at different pH values. In freshwater systems, free uranyl ion (UO_2^{2+}) is the predominant species only at low pH. With increasing pH, the proportions of hydrolysis products of U(VI), such as UO_2OH^+, $UO_2(OH)_3^-$ and $(UO_2)_2(OH)_2^{2+}$, increase. In the kinetic study, formation of uranium-hydroxide decreases the percentage of non-labile component and increases the percentage of labile component. At the U(VI)/HA ratio 0.1, this effect could be more significant than at lower U(VI)/HA ratios because an increase in the HA concentration suppresses the hydrolysis of U(VI) and promotes the formation of U(VI)-HA complex [17]. Furthermore, at the lower U(VI)/HA ratios, a greater proportion of uranium binds to the strong binding sites, resulting in an increase in the non-labile fraction.

4.3. Kinetic parameters in the natural waters and the synthetic lake water sample

The total uranium concentration in the St. Lawrence River water (Ontario, Canada) sample was $0.35 \pm 0.01\,\mu\text{g/L}$ (determined by ICP-MS), which was not able to give a signal strong enough to do the computer program fitting. Therefore, the natural water sample and synthetic lake water sample were spiked with uranium standard solution so as to produce the final concentration of $10\,\mu\text{g/L}$. Fig. 3

Table 3
Major inorganic ions, total organic and inorganic carbons in St. Lawrence River and in synthetic lake water samples

	St. Lawrence River sample (mg/L)	Synthetic lake water sample (mg/L)
Ca^{2+}	41.9 ± 0.3	35.2
Mg^{2+}	8.8 ± 0.8	8.9
Na^+	20.2 ± 0.3	19
K^+	2.5 ± 0.2	1.7
SO_4^{2-}	26.6 ± 0.2	35.5
NO_3^{2-}	0.55 ± 0.03	2.8
Cl^-	33.7 ± 0.4	62
TOC	2.8 ± 0.5	–
TIC	19.9 ± 0.4	–
HCO_3^-	–	50
Humic acid	–	1

presents ligand exchange kinetics of uranium species in the St. Lawrence River water sample and the synthetic lake water sample. The percentage of uranium remaining in both the St. Lawrence River water sample and the synthetic lake water sample decreased very fast to about 5% and 20%, respectively, in the first 2000 s of the experiment. At the end of experiment, the uranium remaining in the St. Lawrence River water sample was almost 1%, whereas the uranium remaining in synthetic lake water sample was about 5%.

The major inorganic cations and anions of these two samples are presented in Table 3 as well as total organic carbon (TOC) and total inorganic carbon (TIC). The kinetically distinguishable components of uranium species in the two samples are presented in Table 4. The labile components in the two samples were greater than 90% of all uranium species, and only the tightly bound uranium remained after 4000 s, indicating that the dissociation rate coefficient of slow components were very small (less than $10^{-6}\,\text{s}^{-1}$); these components were considered as inert. There are many factors that can affect the binding capacity and affinity of the heterogeneous complexants such as HA for metal binding, such as the number and type of ligands, the position of the binding sites in the structure of the complexants, the metal-to-binding site ratio, and the pH [18]. The pH value of St. Lawrence River water sample was 8.3, whereas that of synthetic lake water sample was 7.8. In pH range of 6 to 8, $UO_2(OH)$-HA(I) complex is dominant in the absence of CO_2, as reported by Sachs using laser-induced fluorescence spectroscopy, where HA(I) means that one proton exchanging functional groups of HA takes part in the reaction [17]. However, under usual environmental conditions, at high pH, hardness and alkalinity, the uranium–carbonate and uranium-hydroxide–carbonate becomes more dominant species than uranium–humic substances complexes [2].

Fig. 4 presents the predicted distribution of uranium species as a function of pH (2–12) in synthetic lake water sample, calculated using Visual MINTEQ program. At pH 7.8, about 92% uranium species is $Ca_2UO_2(CO_3)_3$ (aq.), whereas U-HA species is about 3%. Therefore, the U/HA ratio of U-HA species in the synthetic lake sample is about 0.0003. The non-labile uranium species is probably the uranium bound to the strong binding sites of humic acid. For the St. Lawrence River water sample, the pH and the concentration of CO_3^{2-} are higher than that of the synthetic lake water sample, and

Table 4
Kinetically distinguishable components of uranium species in St. Lawrence River water and in synthetic lake water samples

	C_1 (%)	k_{d1} ($10^{-3}\,\text{s}^{-1}$)	C_2 (%)	k_{d2} ($10^{-5}\,\text{s}^{-1}$)
St. Lawrence River	94.3 ± 1.8	2.7 ± 2.8	5.1 ± 3.0	$<10^{-6}$ (Inert)
Synthetic lake water	91.0 ± 12.8	0.6 ± 0.1	11.8 ± 9.8	$<10^{-6}$ (Inert)

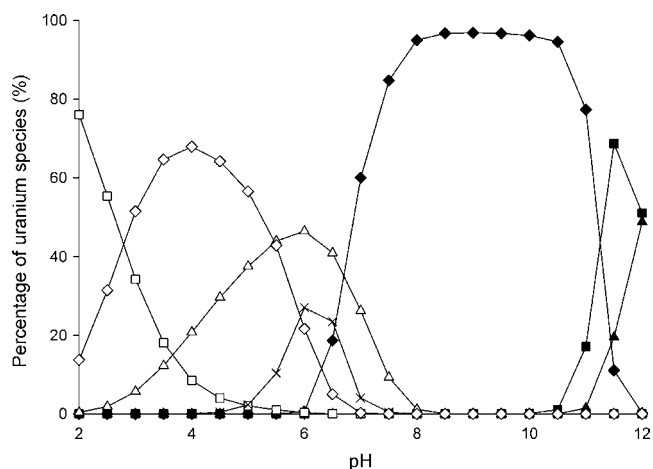Uranium concentration was $10\,\mu\text{g/L}$.

Fig. 4. Predicted uranium speciation (% total uranium) in synthetic lake water as function of pH (2–12), calculated using Visual MINTEQ version 2.51. Total uranium concentration 10 μg/L, major cation and anion concentrations are shown in Table 4. (□) UO_2^{2+}, (◇) $HA-UO_2^+$, (△) $HA-UO_2$, (×) UO_2CO_3 (aq.), (◆) $Ca_2UO_2(CO_3)_3$ (aq.), (■) $UO_2(OH)_3^-$ and (▲) $UO_2(OH)_4^{2-}$.

about 97% of total uranium is U-carbonate species in spite of the fact that it has a higher DOC concentration (2.8 mg/L).

Li et al. [19] studied the uranium speciation in St. Lawrence River using diffusive gradients in thin films (DGT) technique and reported that the DGT labile fraction was about 73% for the DE81 anion-exchange filter and 60% for the Chelex DGT cation-exchange resin. In their study, the major uranium species was $UO_2(CO_3)_2^{2-}$ (72.88%) and $UO_2(CO_3)_3^{4-}$ (26.70%) in the calculated uranium speciation distribution at pH 8.2; therefore, the DGT labile species for DE 81 was most likely $UO_2(CO_3)_2^{2-}$. In our work, the CLEM/ICP-MS results show trends similar to those of the above DGT study. The labile component in our study was most probably uranium–carbonate species, whereas the non-labile component was the uranium bound to the strong binding sites of DOC.

4.4. Adjunctive and Disjunctive Pathways

Two reaction pathways for the overall ligand-exchange reactions may be considered:

(i) Slow dissociation of ML to give M and L, followed by a fast reaction with the competitive ligand, Chelex 100, which is known as the Disjunctive Pathway, shown in Eqs. (1) and (2).
(ii) Direct attack by the competitive ligand followed by loss of the original ligand, L, which is known as the Adjunctive Pathway, shown in Eqs. (9) and (10).

$$ML_i + Chelex \rightarrow M-Chelex - L_i \tag{9}$$

$$M-Chelex - L_i \rightarrow M-Chelex + L_i \tag{10}$$
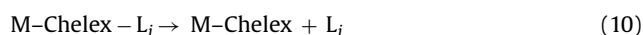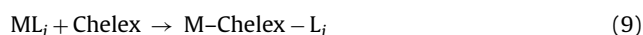
Both the Disjunctive and Adjunctive Pathway may contribute to the observed overall rate coefficient.

The metal binding to Chelex-100 resin is a surface reaction. If the reaction is simplified as unimolecuar adsorption reaction, it can be treated in terms of the Langmuir isotherm as follows [20].

$$M + S \underset{k_{-a}}{\overset{k_a}{\rightleftharpoons}} M-S \tag{11}$$
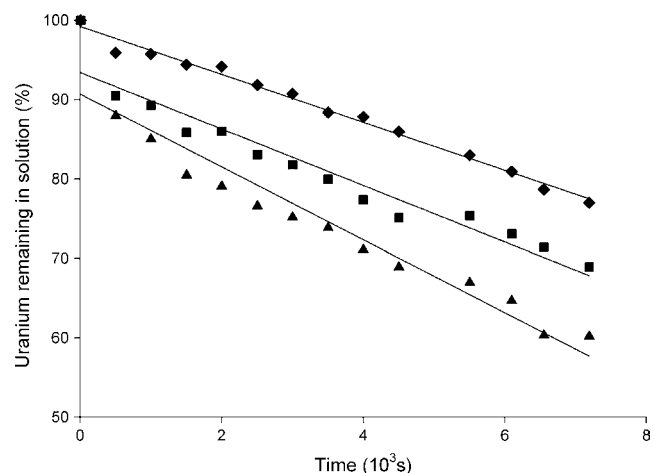
$$K = \frac{k_a}{k_{-a}} \tag{12}$$

Fig. 5. Ligand exchange kinetics for U(VI)/HA in model solutions with U(VI)/HA ratio 0.001 at pH 7. Chelex was added in various amounts, as shown below. Uranium concentration was 20 μg/L (8.4×10^{-8} mol/L), HA concentration is 20 mg/L, ammonium acetate concentration is 0.01 mol/L. (◆) Chelex 1 g/100 mL, (■) chelex 2 g/100 mL and (▲) chelex 3 g/100 mL.

$$\theta = \frac{K[M]}{1 + K[M]} \tag{13}$$

$$v = k\theta = \frac{kK[M]}{1 + K[M]} \tag{14}$$

where M is metal ions, S is the binding sites, k_a is the rate coefficient for the forward reaction, k_{-a} is rate coefficient for the reverse reaction, and K is equilibrium constant for the adsorption process. The rate v is proportional to θ, which is the fraction of the surface that is covered. If the concentration of M is high, the surface is well covered, $\theta \approx 1$, $v = k$, and the kinetics is zeroth order. If the concentration of M is low, $K[M] \approx 0$, the surface is sparsely covered, $v = k\theta = kK[M]$ and the kinetics is first-order.

The pore size of Chelex-100 resin, which is about 1.5 nm [21], is smaller than the size of humic acid, whose hydrodynamic radii range from 2 to 7 nm [22]. In CLEM experiments, free metal ions can bind with both the internal binding sites and surface binding sites of Chelex-100 resin, whereas the larger metal-humic acid complexes can only react with the surface binding sites of the Chelex-100 resin. The binding of free metal ions on surface binding sites of Chelex-100 can be ignored because the surface binding sites contribute little to the total adsorptive capacity of the resin [23]. Since the internal binding sites in Chelex-100 resin are in excess of the free metal ions, the binding of free metal ions follows the first-order kinetics. However, the surface binding sites of Chelex-100 resin are limited to metal humic substances complexes, so the reaction of U-HA complex with Chelex-100, which can only occur on the surface, follows zeroth order kinetics.

To validate the above hypothesis, different concentrations of Chelex-100 resin (1, 2 and 3 g/100 mL) were tested in model solutions having U(VI)/HA ratio 0.001. As shown in Fig. 5, as more Chelex-100 was added to the model solution, the dissociation rate coefficient increased, indicating that the rate coefficient was dependent on the concentration of Chelex-100. Therefore, as the U/HA ratio is very small, the Adjunctive Pathway is predominant. Since the surface of Chelex-100 resin is limited and is fully covered by U-HA complexes, the kinetics is zeroth order.

The rate coefficient of zeroth order kinetics (Adjunctive Pathway), is represented by Eq. (15) and Eq. (16)

$$-\frac{dC_{ML}}{dt} = k \tag{15}$$

$$C_{ML}(t) = C_{ML}^0 - kt \tag{16}$$

where $C_{ML}(t)$ is the percentage of uranium remaining in solution, at any time t, C_{ML}^0 is the initial C_{ML} at time 0, which is expected to be 100%, and k is the rate coefficient.

The data of ligand exchange kinetics for U–HA in model solutions having the U(VI)/HA ratio 0.001 at three pH values are fitted to Eq. (16). The rate coefficients for pH 6, 7 and 8 are $4.1 \times 10^{-3}\%\,s^{-1}$, $3.5 \times 10^{-3}\%\,s^{-1}$ and $3.3 \times 10^{-3}\%\,s^{-1}$, whereas the initial percentage of U–HA complexes for the three pHs are 94.8%, 90.7% and 92.6%, respectively, indicating there is probably only one component (non-labile) in U–HA complexes at the U/HA ratio 0.001. In the case of zeroth order kinetics, the CLEM with Chelex-100 as the competitive ligand is not able to determine the dissociation rate coefficient of complexes of metal-humic substance.

Acknowledgements

References

[1] E.H.P. Cordfunke, The Chemistry of Uranium, Elsevier Pub. Co., Amsterdam, New York, 1970, p. 21.
[2] S.J. Markich, Sci.World J. 2 (2002) 707–729.
[3] R.J. Silva, H. Nitsche, Radiochim. Acta 70/71 (1995) 377–396.
[4] F. Morel, Principles of Aquatic Chemistry, J. Wiley, New York, 1983, pp. 266–267.
[5] S.D. Ebbs, D.J. Brady, L.V. Kochian, J. Exp. Bot. 49 (1998) 1183–1190.
[6] J.J. Lenhart, S.E. Cabaniss, P. MacCarthy, B.D. Honeyman, Radiochim. Acta 88 (2000) 345–353.
[7] J.W. Guthrie, R. Mandal, M.S.A. Salam, N.M. Hassan, J. Murimboh, C.L. Chakrabarti, M.H. Back, D.C. Gregoire, Anal. Chim. Acta 480 (2003) 157–169.
[8] A.L.R. Sekaly, J. Murimboh, N.M. Hassan, R. Mandal, M.E. Ben Younes, C.L. Chakrabarti, M.H. Back, D.C. Gregoire, Environ. Sci. Technol. 37 (2003) 68–74.
[9] A.L.R. Sekaly, R. Mandal, N.M. Hassan, J. Murimboh, C.L. Chakrabarti, M.H. Back, D.C. Gregoire, W.H. Schroeder, Analytica Chimica Acta 402 (1999) 211–221.
[10] C.H. Langford, D.W. Gutzman, Anal. Chim. Acta 256 (1992) 183–201.
[11] D.L. Olson, M.S. Shuman, Geochim. Cosmochim. Acta 49 (1985) 1371–1375.
[12] N.M. Price, G.I. Harrison, J.G. Hering, R.J. Hudson, P.M.V. Nirel, F.M.M. Morel, Biol. Oceanogr. 6 (1989) 443–461.
[13] K.A. Bolton, S. Sjoeberg, L.J. Evans, Soil Sci. Soc. Am. J. 60 (1996) 1064–1072.
[14] A.L.R. Sekaly, M.H. Back, C.L. Chakrabarti, D.C. Gregoire, J.Y. Lu, W.H. Schroeder, Spectrochim. Acta, Part B 53B (1998) 847–858.
[15] A.L.R. Sekaly, M.H. Back, C.L. Chakrabarti, D.C. Gregoire, J.Y. Lu, W.H. Schroeder, Spectrochim. Acta, Part B 53B (1998) 837–846.
[16] T. Saito, S. Nagasaki, S. Tanaka, Radiochim. Acta 90 (2002) 27–33.
[17] S. Sachs, V. Brendler, G. Geipel, Radiochim. Acta 95 (2007) 103–110.
[18] P. Chakraborty, Y. Gopalapillai, J. Murimboh, I.I. Fasfous, C.L. Chakrabarti, Anal. Bioanal. Chem. 386 (2006) 1803–1813.
[19] W. Li, J. Zhao, C. Li, S. Kiser, R.J. Cornett, Anal. Chim. Acta 575 (2006) 274–280.
[20] K.J. Laidler, Chemical kinetics, 3rd ed., Harper & Row, New York, 1987, pp. 229–245.
[21] T.M. Florence, Water Res. 11 (1977) 681–687.
[22] M. Kawahigashi, H. Sumida, K. Yamamoto, J. Colloid Interface Sci. 284 (2005) 463–469.
[23] A. Tessier, D.R. Turner, Metal speciation and bioavailability in aquatic systems, John Wiley, New York, 1995, pp. 262–263.

Highly sensitive electrochemical impedance spectroscopic detection of DNA hybridization based on Au$_{nano}$–CNT/PAN$_{nano}$ films

Na Zhou, Tao Yang, Chen Jiang, Meng Du, Kui Jiao[*]

*Key Laboratory of Eco-chemical Engineering (Ministry of Education), College of Chemistry and Molecular Engineering,
Qingdao University of Science and Technology, Qingdao 266042, China*

ARTICLE INFO

ABSTRACT

A polyaniline nanofibers (PAN$_{nano}$)/carbon paste electrode (CPE) was prepared via dopping PAN$_{nano}$ in the carbon paste. The nanogold (Au$_{nano}$) and carbon nanotubes (CNT) composite nanoparticles were bound on the surface of the PAN$_{nano}$/CPE. The immobilization and hybridization of the DNA probe on the Au$_{nano}$–CNT/PAN$_{nano}$ films were investigated with differential pulse voltammetry (DPV) and cyclic voltammetry (CV) using methylene blue (MB) as indicator, and electrochemical impedance spectroscopy (EIS) using [Fe(CN)$_6$]$^{3-/4-}$ as redox probe. The voltammetric peak currents of MB increased dramatically owing to the immobilization of the probe DNA on the Au$_{nano}$–CNT/PAN$_{nano}$ films, and then decreased obviously owing to the hybridization of the DNA probe with the complementary single-stranded DNA (cDNA). The electron transfer resistance (R_{et}) of the electrode surface increased after the immobilization of the probe DNA on the Au$_{nano}$–CNT/PAN$_{nano}$ films and rose further after the hybridization of the probe DNA. The remarkable difference between the R_{et} value at the DNA-immobilized electrode and that at the hybridized electrode could be used for the label-free EIS detection of the target DNA. The loading of the DNA probe on Au$_{nano}$–CNT/PAN$_{nano}$ films was greatly enhanced and the sensitivity for the target DNA detection was markedly improved. The sequence-specific DNA of phosphinothricin acetyltransferase (PAT) gene and the polymerase chain reaction (PCR) amplification of nopaline synthase (NOS) gene from transgenically modified beans were determined with this label-free EIS DNA detection method. The dynamic range for detecting the PAT gene sequence was from 1.0×10^{-12} mol/L to 1.0×10^{-6} mol/L with a detection limit of 5.6×10^{-13} mol/L.

© 2008 Elsevier B.V. All rights reserved.

1. Introduction

Last decades, astonishing achievements in the cultivation of the transgenic plants have been obtained all over the world [1,2]. However, their security has been brought into focus. The accurate, sensitive, and rapid detection of the transgenic plant products is of significance for understanding the security of the transgenic plants. Phosphinothricin acetyltransferase (PAT) gene and nopaline synthase (NOS) gene are two important screening detection transgenes of the transgenic plants. Detection of these two transgenes can be utilized to identify the transgenic plants.

DNA electrochemical biosensors have been successfully applied for the transgene detection of the transgenic plants [3–5]. In order to improve the sensitivity, selectivity, and stability of the biosensor, various kinds of nanomaterial have been prepared and utilized recently for the biosensor fabrication [6–12]. One of these nano-

materials is polyaniline nanomaterial (PAN$_{nano}$). PAN$_{nano}$ has the properties of mechanical flexibilities, high surface area, chemical specificities, tunable conductivities and easy processing [13–16], which make this conducting polymer as a kind of the promising sensing material for ultrasensitive, trace-level biological and electrochemical nanosensors [17,18]. At present, combination of carbon paste with polyaniline is under intense investigation in order to get fast, sensitive and selective biosensors in different fields [19–21]. Ambrosi et al. [22] fabricated an ascorbic acid sensor via the drop-casting of dodecylbenzene sulphonic acid (DBSA)-doped polyaniline nanoparticles onto a screen-printed carbon paste electrode (CPE). The sensor was compared to a range of other conducting polymer-based ascorbate sensors and found to be comparable or superior in terms of analytical performance. More recently, hybrid nanomaterials, such as hybrid of gold nanoparticles and carbon nanotubes (CNTs), have also been applied for the construction of DNA biosensors [23]. The components of the hybrid have obvious synergistic effect on the performance of the sensor, such as high catalytic activity, enhanced conductivity, strengthened biosensing ability, improved sensitivity and selectivity.
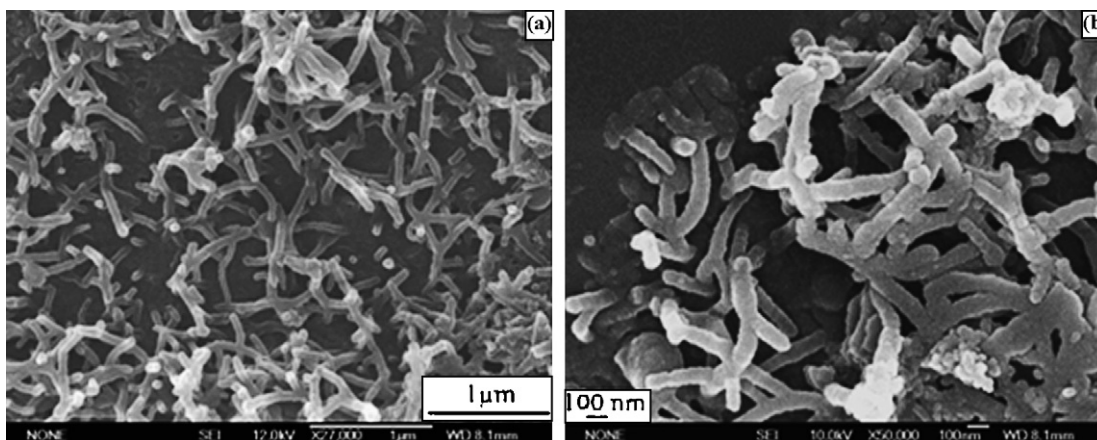
Fig. 1. SEM images of dendritic polyaniline nanofibers at different magnification.

In this paper, polyaniline nanofibers (PAN_{nano}) were used as a kind of dopping material to prepare a modified carbon paste electrode, denoted as PAN_{nano}/CPE, which showed a good electric conductivity and served as an excellent affinity interface for the subsequent immobilization of the hybrid of carbon nanotubes and gold nanoparticles (Au_{nano}–CNT). The Au_{nano}–CNT/PAN_{nano} nanocomposite films could greatly enhance the loading of the DNA probe and hence markedly improved the sensitivity for the target DNA detection. The sequence-specific DNA of the PAT gene and the polymerase chain reaction (PCR) amplification of the NOS gene from a transgenic-modified bean sample were satisfactorily detected with the label-free electrochemical impedance spectroscopic (EIS) method.

2. Materials and methods

2.1. Apparatus and reagents

A CHI 660C electrochemical analyzer (Shanghai CH Instrument Company, China), which was in connection with a home-made carbon paste-modified working electrode ($\Phi = 4$ mm), a Ag/AgCl reference electrode and a platinum wire auxiliary electrode, was used for the electrochemical measurement. The pH values of all solutions were measured by a model pHS-25 digital acidometer (Shanghai Leici Factory, China). Scanning electron microscopy (SEM) was carried out using a JSM-5900 machine (JEOL, Japan). The PCR amplification was performed by an Eppendorf Mastercycler Gradient PCR system (Germany). Aquapro ultrapure water system (Chongqing Yihe Company, China).

Graphite powder and paraffine were purchased from Shanghai Colloid Laboratory and Shanghai Hua Ling Healing Appliance Factory, respectively. Polyaniline nanofibers were provided by College of Material Science and Engineering, Qingdao University of Science and Technology, and used without further purification [24]. The SEM image was shown as Fig. 1. $HAuCl_4 \cdot 4H_2O$ (Sigma, St. Louis, MO, USA). Multi-wall carbon nanotubes (Shenzhen nanotech. Port Co., Ltd., China). $K_3[Fe(CN)_6]$ and $K_4[Fe(CN)_6]$ (Shanghai No. 1 Reagent Factory and Shanghai Heng Da Chemical Co. Ltd., respectively, China). Methylene blue (MB) (Shanghai Reagent Company, China). All the chemicals were of analytical grade and solutions were prepared with ultrapure water.

The 20-base oligonucleotides probe (probe DNA), its complementary sequence DNA (cDNA, target DNA, namely a 20-base fragment of PAT gene sequence), single-base mismatched DNA, double-base mismatched DNA and noncomplementary sequence DNA (ncDNA) were synthetized by Beijing SBS Gene Technology Limited Company. The base sequences of above DNAs and the preparation of their stock solutions (1.0 μmol/L), and materials for the PCR amplification of NOS gene sample and the amplification procedure were as described in Ref. [9].

The DNA sample for PCR amplification was extracted from one kind of transgenic soybean according to the method of plant DNA mini prep kit (Shanghai Academy of Agricultural Sciences).

All oligonucleotides stock solutions of 20-base oligomers (1.0 μmol/L) were prepared using Tris–HCl solution (5.0 mmol/L Tris–HCl, 50.0 mmol/L NaCl, pH 7.0), and stored at 4 °C. More diluted solutions were obtained via diluting aliquot of the stock solution with ultrapure water prior to use.

The hybridization solution was diluted with $2 \times SSC$ (pH 7.0), which was consisted of 0.30 mol/L NaCl and 0.030 mol/L sodium citrate tribasic dihydrate ($C_6H_5Na_3O_7 \cdot 2H_2O$).

2.2. Procedure

2.2.1. Synthesis of Au_{nano}–CNT hybrid

The Au_{nano}–CNT hybrid was synthesized according to the literature [25]. Briefly, CNT was ultrasonically dispersed in citric acid aqueous solution. Then 50 mL of 4 g/L $HAuCl_4$ solution was added dropwise to the as-prepared CNT suspension at 70 °C under vigorous stirring, and kept for stirring for another 1 h. After that, the temperature of the hybrid suspension was controlled at 80 °C for 8 h.

2.2.2. Preparation of polyaniline nanofibers-modified carbon paste electrode and Au_{nano}–CNT hybrid films

3.0 g graphite powder, 1.0 g solid paraffin and 1.0 g polyaniline nanofibers were heated at 80 °C for 2 h and mixed by hand to produce a homogenous carbon paste. It was tightly packed into a glass tube from one end by using a stainless steel rod and a copper wire was introduced into the other end for electrical contact. A fresh electrode surface was generated rapidly by extruding a small plug of the paste with the stainless steel rod and a smooth surface was obtained by smoothing the surface on a white paper. The prepared electrode was rinsed with absolute ethanol and ultrapure water for 5 min, respectively.

20 μL of 1 mg/mL Au_{nano}–CNT gelatin solution was dripped onto the fresh surface of the polyaniline nanofibers-modified carbon paste electrode and naturally dried in the air to form Au_{nano}–CNT/PAN_{nano}/CPE.

2.2.3. Immobilization and hybridization of DNA

The immobilization of the DNA probe on the electrode surface was carried out with following procedure: the

Au$_{nano}$–CNT/PAN$_{nano}$/CPE was immersed in 2.0 mL Tris–HCl buffer solution (pH 7.0) containing 1.0 μmol/L probe DNA at +0.6 V for 500 s, followed by washing the electrode with 0.2% SDS solution for removing the unimmobilized ssDNA and then rinsing it with ultrapure water. The ssDNA/Au$_{nano}$–CNT/PAN$_{nano}$/CPE electrode was immersed into hybridization solution of 1.0 μmol/L target DNA with the working potential at +0.4 V for 600 s to complete the DNA hybridization. The electrode was washed with 0.2% SDS to remove the unhybridized DNA and this hybridization-modified electrode was denoted as dsDNA/Au$_{nano}$–CNT/PAN$_{nano}$/CPE. The hybridization reaction of the probe DNA with the single-base mismatched DNA, double-base mismatched DNA and noncomplementary DNA was respectively conducted with the same procedure.

2.2.4. Electrochemical measurements

Cyclic voltammetry (CV) and differential pulse voltammetry (DPV) were used in this study. The following parameters were employed for CV and DPV, respectively—CV: scan rate 100 mV/s; DPV: pulse amplitude 50 mV, pulse width 60 ms, pulse period 0.2 s. The test solution was 1.5×10^{-5} mol/L MB in the B–R buffer solution of pH 6.0 including 25.0 mmol/L NaCl or the 1.0 mmol/L K$_3$[Fe(CN)$_6$]/K$_4$[Fe(CN)$_6$] (1:1) solution containing 0.1 mol/L KCl. In order to obtain reliable response of MB at the working electrode, the background value was recorded after the working electrode was immersed into the B–R supporting electrolyte solution for 5 min to ensure equilibration. The electrode was then transferred into the MB solution and the signal was recorded after accumulation for 5 min. The response of MB was obtained by subtracting the background value from above recorded signal.

The EIS measurement was also carried out with the CHI 660C electrochemical analyzer. Supporting electrolyte solution was 1.0 mmol/L K$_3$[Fe(CN)$_6$]/K$_4$[Fe(CN)$_6$] (1:1) solution containing 0.1 mol/L KCl. The AC voltage amplitude was 5 mV and the voltage frequencies ranged from 10 kHz to 0.1 Hz. The applied potential was 172 mV.

The reported result for every electrode in this paper was the mean value of three parallel measurements.

3. Results and discussion

3.1. Morphology of polyaniline nanofibers

The morphologies of polyaniline nanofibers were characterized by SEM. Typical SEM images of dendritic polyaniline nanofibers were shown in Fig. 1. It was clear that these polyaniline nanofibers were interconnected to form dendritic or network structures, rather than isolated nanofibers or bundles. The diameters of the polyaniline branches ranged from 60 nm to 90 nm, and the lengths were several hundred nanometers. These polyaniline nanofibers took on exoteric porotic structure in evidence, which were propitious to enhance the sensitivity of chemical sensor.

3.2. Cyclic voltammetry of MB at Au$_{nano}$–CNT/PAN$_{nano}$/CPE

Fig. 2 showed the cyclic voltammogram of 1.0 mol/L HCl solution at PAN$_{nano}$/CPE. The typical redox peaks of polyaniline in the acidic environment indicated that the PAN$_{nano}$ doped in the CPE retained its good electroactivity, which was consistent with the previous report [26].

MB is a well-known hybridization indicator of DNA [27–29]. Fig. 3 showed the cyclic voltammograms of 1.5×10^{-5} mol/L MB at different kinds of modified electrodes. The curve 'a' at the bare CPE had a couple of small redox peaks in the potential range of 0.1 V to −0.7 V. The curve 'b' at the PAN$_{nano}$/CPE had a couple of well-defined redox peaks, the current peaks of which were much larger
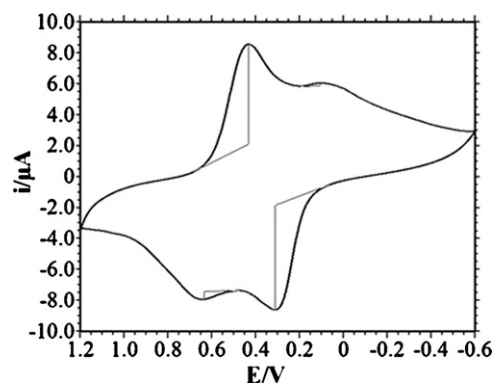

Fig. 2. Cyclic voltammogram of 1.0 mol/L HCl at PAN$_{nano}$/CPE, scan rate: 10 mV/s.

than those of the curve 'a', indicating that the properties of the modified electrode had been significantly changed. After PAN$_{nano}$ was doped in the bare CPE, PAN$_{nano}$ had a strong electrocatalytic activity toward the redox of MB.

The curve 'c' at the Au$_{nano}$–CNT/PAN$_{nano}$/CPE had a couple of obviously enhanced redox peaks as compared with the curve 'b', which meant that Au$_{nano}$–CNT film has been coated onto the PAN$_{nano}$/CPE successfully, and the Au$_{nano}$–CNT/PAN$_{nano}$/CPE had a much larger electroactive surface.

3.3. Electrochemical characterization of DNA immobilization and hybridization at Au$_{nano}$–CNT/PAN$_{nano}$/CPE

3.3.1. Differential pulse voltammetry

Fig. 4 showed the hybridization detection of DNA by using DPV method. The curve 'a' was the DPV curve of MB at the bare CPE electrode. As can be seen, the electrode modified by PAN$_{nano}$ could enhance MB signal (curve b). The DPV signal of MB at the Au$_{nano}$–CNT/PAN$_{nano}$/CPE (curve c) was significantly enhanced as compared with that at the PAN$_{nano}$/CPE. Immobilization of the ssDNA on the Au$_{nano}$–CNT/PAN$_{nano}$/CPE resulted in a further increase of the DPV signal of MB (curve d), which was attributed to the affinity of MB to the exposed guanine bases of ssDNA molecule [27,28]. After hybridization of the probe ssDNA with the target DNA, the DPV signal of MB decreased markedly (curve e) as expected. The reason was that the guanine bases were embedded in the double helix configuration after hybridization, which prevented MB from accessing the electrode [29]. These phenomena indicated that the Au$_{nano}$–CNT/PAN$_{nano}$/CPE could be a fine platform for the immobilization and hybridization of DNA.
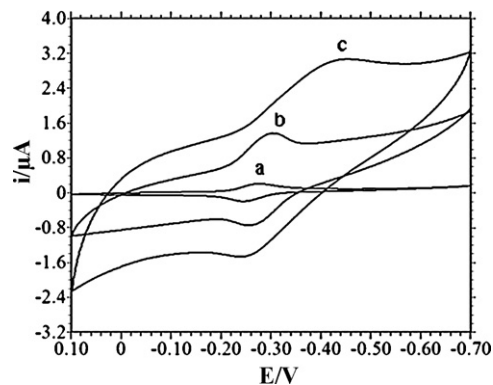

Fig. 3. Cyclic voltammograms of 1.5×10^{-5} mol/L MB in B–R buffer solution (pH 6.0) at (a) CPE; (b) PAN$_{nano}$/CPE; (c) Au$_{nano}$–CNT/PAN$_{nano}$/CPE, scan rate: 100 mV/s.
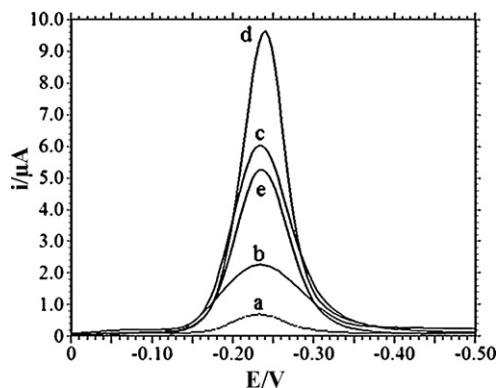
Fig. 4. Differential pulse voltammograms of 1.5×10^{-5} mol/L MB in B–R buffer solution at (a) CPE; (b) PAN_{nano}/CPE; (c) Au_{nano}–CNT/PAN_{nano}/CPE; (d) ssDNA/Au_{nano}–CNT/PAN_{nano}/CPE and (e) dsDNA/Au_{nano}–CNT/PAN_{nano}/CPE. DPV parameters—amplitude: 50 mV, pulse period: 0.2 s, pulse width: 60 ms.

3.3.2. Electrochemical impedance spectroscopy

Label-free electrochemical DNA biosensor may be characterized by the electrochemical impedance spectroscopic method [30–33]. In order to obtain more information from EIS results, the working electrode was modeled using a modified Randles equivalent circuit (inset of Fig. 5). Where, R_s is the electrolyte solution resistance, R_{et} the surface electron transfer resistance, Z_w the Warburg impedance resulting from the diffusion of ions, and C_{dl} the double layer capacitance. In EIS, the semicircle diameter of the Nyquist diagram equals to the surface electron transfer resistance (R_{et}) of the electrode. The immobilization and hybridization of DNA on the electrode surface can change the R_{et} value. Therefore, the properties of DNA immobilization and hybridization may be known by the EIS measurement.

Nyquist diagrams of $[Fe(CN)_6]^{3-/4-}$ at different modified electrodes were illustrated in Fig. 5. The curves a, b, c and d were the Nyquist diagrams of $[Fe(CN)_6]^{3-/4-}$ at the PAN_{nano}/CPE, Au_{nano}–CNT/PAN_{nano}/CPE, ssDNA/Au_{nano}–CNT/PAN_{nano}/CPE and dsDNA/Au_{nano}–CNT/PAN_{nano}/CPE, respectively. Compared with the PAN_{nano}/CPE, the Au_{nano}–CNT/PAN_{nano}/CPE had a much larger electroactive surface and higher conductivity because of the Au_{nano}–CNT film.

After the probe DNA was immobilized at the Au_{nano}–CNT/PAN_{nano}/CPE, the negatively charged phosphate
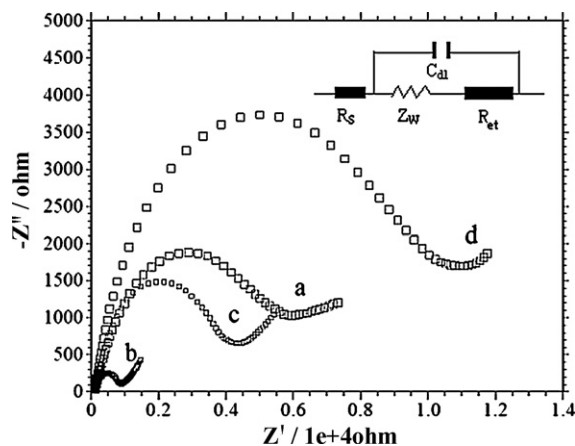

Fig. 5. Nyquist diagrams recorded at (a) PAN_{nano}/CPE, (b) Au_{nano}–CNT/PAN_{nano}/CPE, (c) ssDNA/Au_{nano}–CNT/PAN_{nano}/CPE and (d) dsDNA/Au_{nano}–CNT/PAN_{nano}/CPE. Supporting electrolyte solution is 1.0 mmol/L $K_3[Fe(CN)_6]$ and 1.0 mmol/L $K_4[Fe(CN)_6]$ containing 0.1 mol/L KCl. Inset: equivalent circuit used to model impedance data in the presence of redox couples.

backbone of the probe DNA prevented $[Fe(CN)_6]^{3-/4-}$ from reaching the electrode surface, and led to a larger R_{et} value (curve c) than that at the Au_{nano}–CNT/PAN_{nano}/CPE (curve b). When the probe DNA was hybridized with its complementary target DNA (cDNA) in solution, the R_{et} was further enhanced to a much larger value (curve d). After hybridization, the negative charges on the electrode surface increased remarkably and the surface membranes become thicker, which might raise the R_{et} value. Therefore, from the change of the R_{et} value, the immobilization and hybridization of DNA on this Au_{nano}–CNT/PAN_{nano}/CPE platform could be understood clearly.

3.3.3. Optimization of conditions for DNA immobilization and hybridization

3.3.3.1. The selection of potential for immobilization of the probe DNA.
The Nyquist diagram at the Au_{nano}–CNT/PAN_{nano}/CPE in the $[Fe(CN)_6]^{3-/4-}$ solution was recorded. Then, after the probe DNA was immobilized at the electrode at 0.4 V, the Nyquist diagram at the probe DNA-immobilized electrode was again recorded. The difference (ΔR_{et}) of the impedance values between before and after immobilization of the probe DNA was calculated. We performed the similar experiments as above except at 0.5 V, 0.6 V, 0.7 V and 0.8 V, respectively. The results indicated that ΔR_{et} value increased with the positive shift of the potential from 0.4 V to 0.6 V. With further positive shift of the immobilization potential, the ΔR_{et} did not increase anymore. An immobilization potential of 0.6 V was generally used in our experiments.

3.3.3.2. The selection of the immobilization time of the probe DNA.
The probe DNA was immobilized at 0.6 V for from 100 s to 800 s, and the Nyquist diagrams at the electrode before and after every immobilization of the probe DNA were respectively recorded. The results showed that the ΔR_{et} value rose with the increase of the immobilization time from 100 s to 500 s and reached a constant level beyond 500 s. 500 s was selected for the immobilization of the probe DNA.

3.3.3.3. The selection of potential for DNA hybridization.
The probe DNA was hybridized with cDNA at different constant potentials from 0.2 V to 0.6 V, and the Nyquist diagrams at the electrode before and after hybridization of the probe DNA were respectively recorded. The ΔR_{et} value calculated from the hybridization of the probe DNA indicated that the response of hybridization rose gradually with the positive shift of the hybridization potential from 0.2 V to 0.4 V and reached a constant level beyond 0.4 V. A hybridization potential of 0.4 V was generally used in our experiments.

3.3.3.4. The selection of the hybridization time of DNA.
The probe DNA was hybridized with cDNA at 0.4 V for from 100 s to 800 s. The results showed that the ΔR_{et} value rose with the increase of the hybridization time from 100 s to 600 s and reached a constant level beyond 600 s. 600 s was optimal for the hybridization.

3.4. Detection of sequence-specific DNA of PAT gene

The selectivity of DNA hybridization could be judged by the hybridization of the probe DNA with different DNA sequences. As shown in Fig. 6A, the curve 'a' was the Nyquist diagram of $[Fe(CN)_6]^{3-/4-}$ at the probe DNA-modified electrode, which was the same as curve 'c' in Fig. 5. After hybridization of the probe DNA with the complementary DNA under the optimal experimental conditions, the Nyquist diagram of $[Fe(CN)_6]^{3-/4-}$ was shown as the curve 'b'. The R_{et} value rose obviously. When the noncomplementary sequence was used for the hybridization, the R_{et} value (curve c)
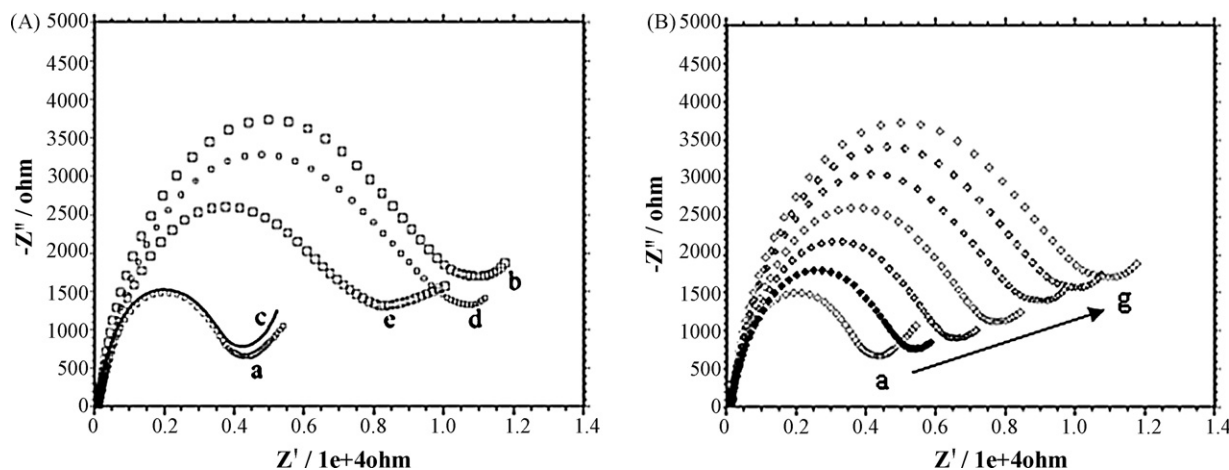
Fig. 6. (A) Nyquist diagrams recorded at (a) ssDNA/Au$_{nano}$−CNT/PAN$_{nano}$/CPE, (b) dsDNA/Au$_{nano}$−CNT/PAN$_{nano}$/CPE (hybridized with cDNA), (c) the electrode hybridized with ncDNA, (d) the electrode hybridized with single-base mismatched DNA, (e) the electrode hybridized with double-base mismatched DNA. (B) Nyquist diagrams recorded at ssDNA/Au$_{nano}$−CNT/PAN$_{nano}$/CPE (a) and after hybridization reaction with its complementary PAT gene sequence of different concentrations: (b) 1.0×10^{-12} mol/L, (c) 1.0×10^{-11} mol/L, (d) 1.0×10^{-10} mol/L, (e) 1.0×10^{-9} mol/L, (f) 1.0×10^{-8} mol/L and (g) 1.0×10^{-7} mol/L. Supporting electrolyte solution is 1.0 mmol/L K$_3$[Fe(CN)$_6$] and 1.0 mmol/L K$_4$[Fe(CN)$_6$] containing 0.1 mol/L KCl.

varied little as compared with the probe DNA-modified electrode. The single-base mismatched sequence (curve d) and the double-base mismatched sequence (curve e) could also be recognized via comparing the change of the DNA R_{et} value of [Fe(CN)$_6$]$^{3-/4-}$. The results demonstrated that this DNA biosensor displayed a high selectivity for the hybridization detection.

The difference between the R_{et} value (namely ΔR_{et}) of 1.0 mmol/L [Fe(CN)$_6$]$^{3-/4-}$ solution containing 0.1 mol/L KCl at the probe DNA/Au$_{nano}$−CNT/PAN$_{nano}$/CPE and that at the hybridization-modified electrode (dsDNA/Au$_{nano}$−CNT/PAN$_{nano}$/CPE) was used to be the measurement signal to determine the sequence-specific related to the PAT gene fragment. The concentration of the PAT gene fragment in the hybridization solution was changed from 1.0×10^{-7} mol/L to 1.0×10^{-12} mol/L, and the Nyquist diagrams of the above [Fe(CN)$_6$]$^{3-/4-}$ solution at the DNA-modified electrode before and after hybridization were respectively recorded. The results were shown as in Fig. 6B. The ΔR_{et} value versus the logarithm of the PAT gene fragment concentration presented a good linear correlation. The dynamic determination range for the PAT gene fragment was from 1.0×10^{-12} mol/L to 1.0×10^{-6} mol/L with the regression equation: ΔR_{et} (Ω) = −961.5 lgC + 17064 and the correlation coefficient: $\gamma = 0.9950$. The detection limit was

5.6×10^{-13} mol/L using 3σ, where σ was the standard deviation of the blank solution with 11 parallel measurements.

3.5. Reproducibility and regeneration of DNA sensor

The reproducibility of any biosensor is extremely important to practical applications. In our test, the probe DNA was hybridized with 1.0 μmol/L complementary DNA for seven parallel measurements and relative standard deviation (R.S.D.) of 3.6% was estimated, showing the high reproducibility of the DNA electrochemical biosensor.

The regeneration ability as for this impedance-based DNA hybridization sensor was also evaluated. The dsDNA on the hybridized electrode was hot denatured by immersing the electrode into boiling water for 8 min and then cooling it with the ice salt bath. The Nyquist diagrams of 1.0 mmol/L [Fe(CN)$_6$]$^{3-/4-}$ solution at the regenerated probe DNA/Au$_{nano}$−CNT/PAN$_{nano}$/CPE was recorded. The results indicated that the R_{et} values were almost the same values as that obtained in the first experiment. Successive experiments showed that the DNA biosensor could be reproduced for six times without losing its sensitivity, indicating the fine regeneration ability of the DNA electrochemical biosensor.

3.6. Detection of the PCR amplification of NOS gene sample

This label-free DNA electrochemical biosensor has been combined with the PCR technology for the detection of the NOS transgene in a kind of real transgenic soybean. The NOS gene template was extracted from this soybean sample with the DNA Mini preparation kit, which was purchased from Shanghai Academy of Agricultural Sciences. Then the template was amplified according to the PCR procedure.

The purification of the PCR amplification was carried out as follows: added 5 μL of agarose gel loading dye and loaded the above PCR reaction solution into a well of 1.0% low melting temperature agarose gel. Electrophosresed it for 30–60 min at 100–200 mA, and then excised the desired band visualized under UV light with a clean razor blade. Followed by purifying the DNA in a gel using the purification kit (TIANgel Maxi purification kit DP 210-02, Beijing, China). After the purification, the weight product of single molecule was obtained, and the A_{260}/A_{280} value of the PCR amplification sample was 1.82, indicating that it was pure enough.
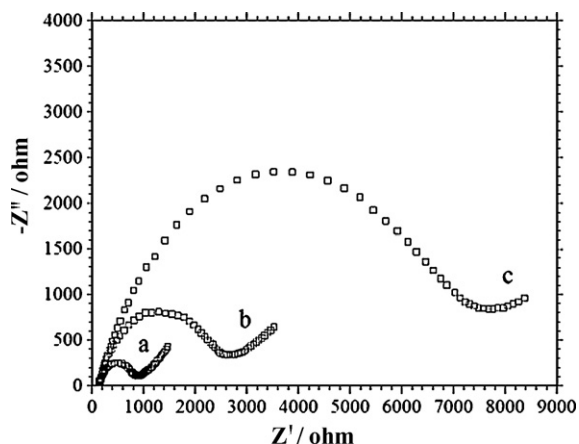

Fig. 7. Nyquist diagrams in 1.0 mmol/L K$_3$[Fe(CN)$_6$] and 1.0 mmol/L K$_4$[Fe(CN)$_6$] recorded at (a) Au$_{nano}$−CNT/PAN$_{nano}$/CPE, (b) the NOS gene probe-modified electrode and (c) the electrode hybridized with the PCR amplified real NOS sample.

The purified PCR amplification of NOS gene sample was diluted with 5.0 mmol/L Tris–HCl buffer, and denatured by heating it in boiling water for 5 min and then cooled in an ice bath. After the immobilization of the NOS gene probe on the Au_{nano}–CNT/PAN_{nano}/CPE, the electrode was immersed in 2 mL denatured PCR amplification for hybridization under the optimal conditions. The detection result was shown in Fig. 7. The curves a, b and c were the Nyquist diagrams of 1.0 mmol/L $[Fe(CN)_6]^{3-/4-}$, respectively, at the Au_{nano}–CNT/PAN_{nano}/CPE, the NOS probe DNA/Au_{nano}–CNT/PAN_{nano}/CPE and the hybridized electrode of the NOS probe with the PCR amplification of the NOS gene sample. Obviously, the R_{et} value of the curve 'c' was markedly larger than that of the curve 'b', whereas the latter was distinctly larger than that of the curve 'a'. The impedance measurements confirmed that the ssDNA/Au_{nano}–CNT/PAN_{nano}/CPE could successfully recognize and detect the PCR amplification of the NOS transgene in the real transgenic soybean sample.

4. Conclusion

Nanogold (Au_{nano}) and CNT hybrid was coated on the PAN_{nano}–modified CPE surface to form a Au_{nano}–CNT/PAN_{nano}/CPE electrode. The Au_{nano}–CNT and PAN_{nano} composite film is a very good platform for the immobilization and hybridization of DNA. The nanomaterials Au_{nano}, CNT and PAN_{nano} in the composite film had remarkable synergistic effect on the recognition of DNA hybridization. The immobilization and hybridization of the probe DNA were characterized by DPV and EIS. The sequence-specific DNA of the PAT gene and polymerase chain reaction (PCR) amplification of the NOS gene from transgenically modified beans were detected by this electrochemical DNA biosensor with label-free EIS method.

References

[1] C. James, Global status of commercialized biotech/GM crops: 2007, International Service for the Acquisition of Agri-biotech Applications brief 37-2007 http://www.isaaa.org/resources/publications/briefs/37/executivesummary/default.html.
[2] Y. Takahashi, T. Tojo, S. Nagahora, K. Yamazaki, J. Agric. Food Chem. 55 (2007) 2923.
[3] J. Yang, T. Yang, Y.Y. Feng, K. Jiao, Anal. Biochem. 365 (2007) 24.
[4] J. Yang, K. Jiao, T. Yang, Anal. Bioanal. Chem. 389 (2007) 913.
[5] K. Jiao, T. Yang, J. Yang, Y.Y. Feng, Sci. China Ser. B 50 (2007) 538.
[6] C. Staii, D.W. Wood, G. Scoles, J. Am. Chem. Soc. 130 (2008) 640.
[7] Y. Li, H.L. Qi, F. Fang, C.X. Zhang, Talanta 72 (2007) 1704.
[8] C. Jiang, T. Yang, K. Jiao, H.W. Gao, Electrochim. Acta 53 (2008) 2917.
[9] T. Yang, W. Zhang, M. Du, K. Jiao, Talanta 75 (2008) 987.
[10] S. Wu, H.X. Ju, Y. Liu, Adv. Funct. Mater. 17 (2007) 585.
[11] N. Li, R. Yuan, Y.Q. Chai, S.H. Chen, H.Z. An, W.J. Li, J. Phys. Chem. C 111 (2007) 8443.
[12] H.L. Qi, X.X. Li, P. Chen, C.X. Zhang, Talanta 72 (2007) 1030.
[13] N.N. Zhu, Z. Chang, P.G. He, Y.Z. Fang, Electrochim. Acta 51 (2006) 3758.
[14] A. Morrin, F. Wilbeer, O. Ngamna, S.E. Moulton, A.J. Killard, G.G. Wallace, M.R. Smyth, Electrochem. Commun. 7 (2005) 317.
[15] H.X. Chang, Y. Yuan, N.L. Shi, Y.F. Guan, Anal. Chem. 79 (2007) 5111.
[16] X. Luo, G.D. Vidal, A.J. Killard, A. Morrin, M.R. Smyth, Electroanalysis 19 (2007) 876.
[17] A. Morrin, O. Ngamna, A.J. Killard, S.E. Moulton, M.R. Smyth, G.G. Wallace, Electroanalysis 17 (2005) 423.
[18] H.H. Zhou, H. Chen, S.L. Luo, J.H. Chen, W.Z. Wei, Y.F. Kuang, Biosens. Bioelectron. 20 (2005) 130.
[19] R.S. Fábio, H.C.M. Luiz, M.P.V. Carlos, Sensor Lett. 2 (2004) 221.
[20] A. Morrin, O. Ngamna, E. O'Malley, N. Kent, S.E. Moulton, G.G. Wallace, M.R. Smyth, A.J. Killard, Electrochim. Acta 53 (2008) 5092.
[21] A.M. Rojas, Y.O. Maldonado, L.M.T. Rodríguez, J. Membr. Sci. 300 (2007) 2.
[22] A. Ambrosi, A. Morrin, M.R. Smyth, A.J. Killard, Anal. Chim. Acta 609 (2008) 37.
[23] S.H. Lim, J. Wei, J. Lin, Chem. Phys. Lett. 400 (2004) 578.
[24] G.C. Li, Z.K. Zhang, Macromolecules 37 (2004) 2683.
[25] L.Q. Jiang, L. Gao, Carbon 41 (2003) 2923.
[26] G.C. Li, S.P. Pang, J.H. Liu, Z.B. Wang, Z.K. Zhang, J. Nanopart. Res. 8 (2006) 1039.
[27] M.T. Carter, R. Marisol, A.J. Bard, J. Am. Chem. Soc. 111 (1989) 8901.
[28] A.A. Gorodetsky, J.K. Barton, Langmuir 22 (2006) 7917.
[29] O. Panke, A. Kirbs, F. Lisdat, Biosens. Bioelectron. 22 (2007) 2656.
[30] B. Piro, J. Haccoun, M.C. Pham, J. Electroanal. Chem. 577 (2005) 155.
[31] C. Gautier, C. Cougnon, J. Pilard, J. Electroanal. Chem. 587 (2006) 276.
[32] C. Tlili, H.K. Youssoufi, L. Ponsonnet, C. Martelet, N.J. Renault, Talanta 68 (2005) 131.
[33] D.L. Li, X.Q. Zou, Q. Shen, S.J. Dong, Electrochem. Commun. 9 (2007) 191.